# Comptes Rendus de l'Académie des sciences

1778-7025 (electronic)


# Géoscience
## Sciences de la Planète

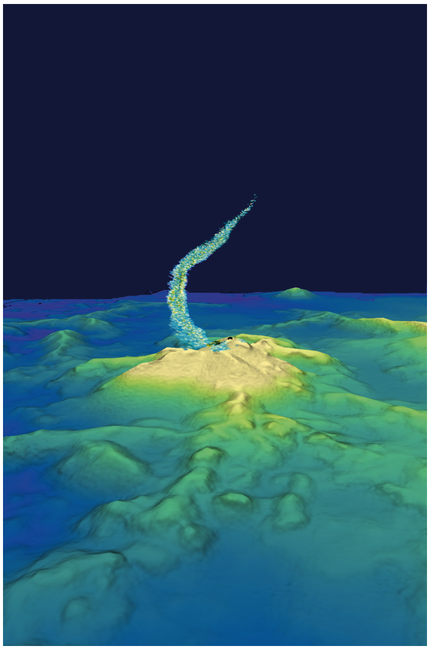


Volume 354, Special Issue S2, 2022


**Special issue / *Numéro thématique***

The Mayotte seismo-volcanic crisis of 2018-2021 in the Comoros archipelago (Mozambique channel) / *La crise sismo-volcanique de 2018-2021 de Mayotte dans l'archipel des Comores (Canal du Mozambique)*

**Guest editors / *Rédacteurs en chef invités***

Jérôme Van der Woerd, Vincent Famin, Eric Humler


**Académie des sciences — Paris**

INSTITUT DE FRANCE
Académie des sciences

CENTRE MERSENNE

# *Comptes Rendus*

# *Géoscience*

**Objective of the journal**

*Comptes Rendus Géoscience* is an internationally peer-reviewed electronic journal covering the full range of earth sciences and sustainable development. It publishes original research articles, review articles, historical perspectives, pedagogical texts, and conference proceedings of unlimited length, in English or French. *Comptes Rendus Géoscience* is published according to a virtuous policy of diamond open access, free of charge for authors (no publication fees) as well as for readers (immediate and permanent open access).



**About the journal**

All journal's information, including the text of published articles, which is fully open access, is available from the journal website at https://comptes-rendus.academie-sciences.fr/geoscience/.

**Author enquiries**

For enquiries relating to the submission of articles, please visit this journal's homepage at https://comptes-rendus.academie-sciences.fr/geoscience/.

**Contact**

Académie des sciences
23, quai de Conti, 75006 Paris, France
Tel: (+33) (0)1 44 41 43 72
CR-Geoscience@academie-sciences.fr

*Comptes Rendus*
*Géoscience — Sciences de la Planète*
**2022**, 354, nº S2

# Contents / *Sommaire*

*Comptes Rendus*
*Géoscience — Sciences de la Planète*
**2022**, Vol. 354, Special Issue S2, p. 1-6
https://doi.org/10.5802/crgeos.196

The Mayotte seismo-volcanic crisis of 2018-2021 in the Comoros archipelago (Mozambique channel) / *La crise sismo-volcanique de 2018-2021 de Mayotte dans l'archipel des Comores (Canal du Mozambique)*

# Special issue *Comptes-Rendus Geoscience*: The Mayotte seismo-volcanic crisis of 2018–2021 in the eastern Comoros archipelago (Mozambique channel)

**Jérôme van der Woerd** [*, a], **Vincent Famin** [b, c] **and Eric Humler** [d]

[a] Institut Terre et Environnement de Strasbourg, CNRS UMR 7063, Université de Strasbourg, 67000 Strasbourg, France

[b] Université de Paris, Institut de physique du globe de Paris, CNRS, UMR 7154, F-75005 Paris, France

[c] Université de La Réunion, Laboratoire GéoSciences Réunion, F-97744 Saint-Denis, France

[d] Laboratoire de Planétologie et Géodynamique, CNRS UMR 6112, Université de Nantes, 44322 Nantes, France

*E-mails:* jerome.vanderwoerd@unistra.fr (J. van der Woerd), vincent.famin@univ-reunion.fr (V. Famin), eric.humler@cnrs-dir.fr (E. Humler)

*Published online: 17 January 2023, Issue date: 17 January 2023*

The challenges posed by unexpected and poorly known natural hazard are manifold: scientific, technical and societal. Until 2018, Mayotte was classified as a zone of moderate seismicity and low probability of volcanism among French territories. The onset of the seismic crisis offshore Mayotte in May 2018, which appeared to be volcanic in the course of its discovery, has triggered an unprecedented mobilization of the French scientific, administrative and political communities (Figure 1). Understanding the event, building a message, communicating to the population: all had to be constructed and invented, with the additional difficulty that nothing was visible given that the eruption happened offshore on the several kilometers deep oceanic floor.

Even though it is not possible to cite all the actions of the French scientific and institutional communities in response to the seismo-volcanic crisis of Mayotte, some milestones appear in the chronology of crisis management. After the first earthquake swarms of 10 May 2018, the local bureau of the BRGM in Mayotte in charge of seismic risk was mobilized and issued an alert. The large chock of magnitude Mw5.9 occurred on 15 May 2018, 5 days after continuous

* Corresponding author.

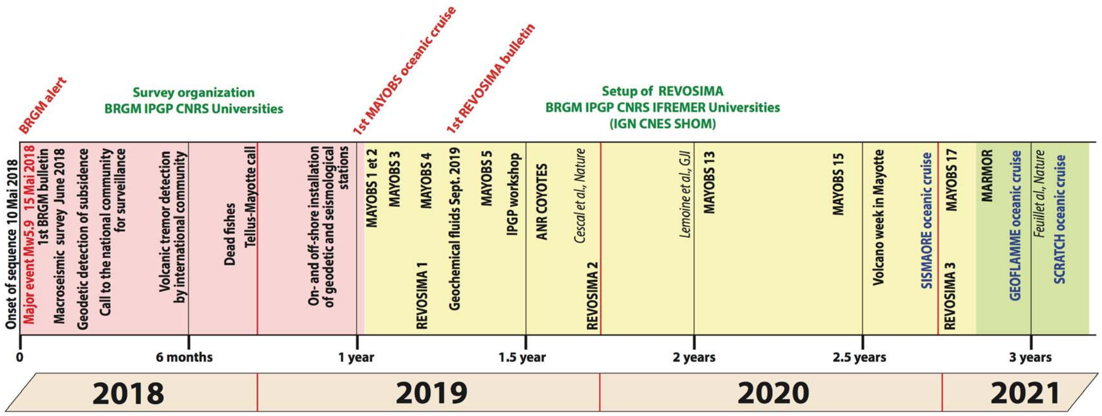


**Figure 1.** Summary of major events, decisions and actions triggered by the seismo-volcanic events starting 10 May 2018 in Mayotte.

and increasing seismicity that worried the population in a time of social unrest and tension, with the difficulty for the authorities to transmit an audible message on an unexpected and worrisome event. A macroseismic survey was launched in June 2018. As the seismicity remained important, the seismological community outlined projects for on- and off-shore deployment of seismic stations based on preliminary locations with an inadequate network. In July 2018, the French geodetic survey (IGN) noticed an unexplained change in ground motions recorded by the GNSS stations. The scientific community interpreted these ground motion changes as due to the deflation of magmatic chamber in the crust or in the mantle, with or without seafloor eruption [Lemoine et al., 2020]. Later in November 2018, a strong and long single-frequency, very low frequency seismic signal is observed several thousand kilometers from Mayotte on global seismic networks. Such a "tremor" is usually associated with magmatic circulation or reservoir draining [Cesca et al., 2020].

Governmental and scientific institutions convened and organized their effort towards understanding the seismo-volcanic event in November 2018, leading to the creation of the "Réseau de surveillance Volcanique et Sismologique de Mayotte"—REVOSIMA (Volcanic and Seismological Monitoring Network of Mayotte), with the requirement to develop scientific knowledge, identify and transmit alerts, disseminate regular information. CNRS-INSU opened a call for survey projects at the beginning of 2019. This rapidly mobilized funding allowed the deployment of ocean bottom seismometers, and the first MAYOBS-1 cruise that led to the discovery of a new submarine volcano [Feuillet, 2019, Feuillet et al., 2021], later called "Fani Maoré". Since then, recurrent campaigns have been organized to monitor the evolution of the Fani Maoré volcano (up to MAYOBS-27 at the time of writing). In addition, three oceanographic cruises have been conducted to better understand the geologic and geodynamic setting of this volcanic eruption in 2021 (Figure 2), "SISMAORE" and "GEOFLAMME" with the R/V Pourquoi Pas?, and "SCRATCH" using the R/V Marion Dufresnes II. These surveys deployed a huge panel of marine geophysical techniques and resulted in the collection of 16 sediment cores and 18 dredges over the northern Mozambique channel, which will give work to scientists for several decades.

To sustain this unprecedented scientific effort, the French National Research Agency (Agence Nationale de la Recherche—ANR) granted pluri-annual funding to three ambitious projects involving international and multidisciplinary scientific teams: "COYOTES" aiming at understanding the geodynamics of the northern Mozambique channel, "SUBSILAKE" with the objective of monitoring geochemical changes in a crater lake of Mayotte in response to the submarine eruption, and "MARMOR" aiming at building a multi-technique geophysical network of submarine eruption monitoring in the area. The newly discovered geo-hazard in the northern Mozambique channel also motivated the Comorian and French authorities to reinforce their international collabora-

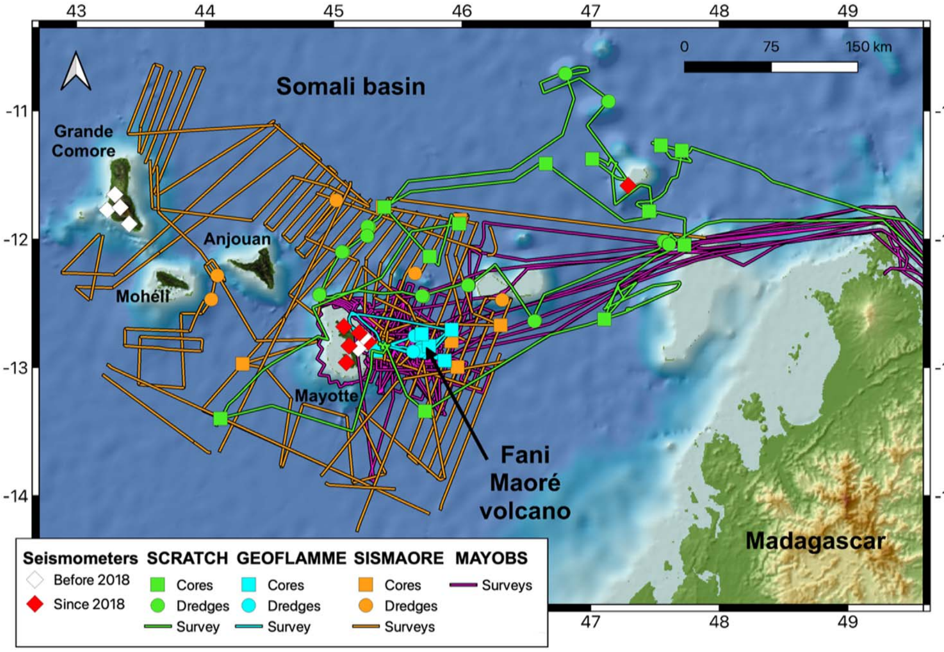


**Figure 2.** Summary of research efforts since the 2018 Mayotte seismic and volcanic crisis. Elements shown include seismic/GNSS stations installed in the Comoros archipelago, the number of which has doubled since 2018. Also shown are the oceanographic cruises and their main operations (geophysical surveys, sediment coring and or seafloor dredging): SISMAORE (December 2020–February 2021), GEOFLAMME (April–May 2021), SCRATCH (July 2021), and MAYOBS-1 to -23 (March 2019–July 2022).

tion through the "HATARI" Interreg project funded by the European Union and coordinated by the Réunion Regional Council.

Four years after the onset of the crisis, while it is apparently coming to a rest, efforts to understand what is happening and to put in place an efficient monitoring network are still ongoing, at the national and international level. For the French community, scientific and risk managers, the implementation of an underwater volcano monitoring network is not only a challenge but may set an example (Marmor project https://www.marmor-project.org/). The recent Mayotte seismo-volcanic crisis has triggered already a large set of scientific studies as can be seen from the many scientific articles and communications over the last 4 years. In this special issue, our aim is to gather a wide spectrum of scientific works around the event, without being exhaustive, in order to give an overall understanding of the crisis. It is composed of 19 articles, including details of the seismic and volcanic sequence, the various risks associated to its occurrence, its societal impact, but also first local and regional understanding of the geological, volcanic and geodynamic context of Mayotte and the Comoros archipelago.

The first part of this thematic issue is a compilation of the latest advances about the geological and geodynamic context of the Mozambique channel. Most of these advances are direct outcomes from the ANR COYOTES project (https://anr.fr/Projet-ANR-19-CE31-0018), from oceanic cruises such as SISMAORE (doi:10.17600/18001331), and from the now regular MAYOBS surveys (doi:10.18142/291). In Thinon et al. [2022] for instance, extension of the submarine volcanism in the northern Mozambique channel is evidenced, and the regional geodynamics is investigated by means of marine geophysics. This first part also questions the nature of the lithosphere beneath the Comoros archipelago, by probing its thermal state from literature and newly published heat flow measurements [Rolandone et al., 2022] and its structure from teleseismic receiver functions [Dofal et al., 2022]. Seismic reflection across the new volcano East of Mayotte provides unprecedented insights about the chronology and architecture of volcanic seamount construction in this zone [Masquelet et al., 2022]. Ocean bottom volcanic geomorphology is also investigated from high-resolution bathymetry and towed camera on the eastern submarine slope of Mayotte [Puzenat et al., 2022].

In a second part of the thematic issue, a set of studies on seismicity, geodesy, petrology, and gas emissions focuses on the development of the Mayotte seismo-volcanic sequence and its evolution. Despite an inadequate network before 2019, the first year of seismicity of the Mayotte sequence has been carefully analyzed and is now presented in a new catalogue of seismicity [Mercury et al., 2022]. A teleseismic source study of the largest events at the onset of the sequence reveals their link to magmatic fracturing and transport [Morales-Yáñez et al., 2022]. With the seafloor and onland seismic monitoring in place since 2019, the large amount of data is investigated using automatic detection techniques [Retailleau et al., 2022]. Although disseminated on few oceanic islands, large ground deformations (20–25 cm) are monitored via geodesy, which are explained by magma transfer at depth in the volcanic edifice [Peltier et al., 2022]. Eruptive material collected on the seafloor thanks to oceanographic campaigns helps constraining eruptive scenarios [Berthod et al., 2022]. The conditions required for the genesis and eruption of phonolitic lavas such as those found in this new volcano are explored [Andújar et al., 2022]. Monitoring lavas flows with an hydroacoustic network seems a promising development for the study of the eruptive sequence [Bazin et al., 2022]. Onland gases emissions on Petite Terre offer a window on magmatic processes occurring at depth during volcanic unrest [Liuzzo et al., 2022]. The co-eruptive evolution of these emissions also impacts the water chemistry of maars as shown by geochemical monitoring and modeling of the Dziani Dzaha Lake on Petite Terre in Mayotte [Cadeau et al., 2022].

In a third part, the possible consequences and impacts of the eruption and its possible evolution are explored in term of hazard and risk assessment. Knowledge of the geological nature of the surface rocks and deposits constrain possible site effects during seismic shaking [Roullé et al., 2022]. Being prepared and preventing damages in case of seismic shaking can be explored for crisis management [Taillefer et al., 2022]. The unstable submarine slopes of Mayotte could be prone to landslides themselves triggering tsunamis [Poulain et al., 2022].

The last part addresses how one communicates in the midst of a crisis with so many unknowns. A study based on news accounts reveals the various facets of the narrative from the various communities involved [Devès et al., 2022]. Another study explores the perception of the crisis and how it is revealed in the languages [Mori, 2022].

This issue is a step toward the better understanding of the multiple sides of a volcanic eruption. It gathers together a wide spectrum of scientific approaches and studies, which testify of the strong involvement of the scientific community for assessing natural hazard and risk to the populations. In addition, the organization of an operational multipartner monitoring system in emergency and in a little known geological area may serve as a model for other regions subject to equivalent hazards and risks.

## Conflicts of interest

Authors have no conflict of interest to declare.

## Acknowledgements

The authors are grateful towards François Chabaux for his suggestion to publish a special issue on the Mayotte seismo-volcanic crisis and for his constant support during the preparation of the issue. They also thank Adenise Lopes and the Comptes Rendus Geoscience team for their help in the editorial processing.

## References

Andújar, J., Scaillet, B., Moreira, M., Di Carlo, I., Le Friant, A., Bickert, M., Paquet, F., Jorry, S. J., and Feuillet, N. (2022). Experimental evidence for the shallow production of phonolitic compositions at Mayotte. *C. R. Géosci.*, 354(S2), 225–256.

Bazin, S., Royer, J.-Y., Dubost, F., Paquet, F., Loubrieu, B., Lavayssière, A., Deplus, C., Feuillet, N., Jacques, É., Rinnert, E., Thinon, I., Lebas, É., Pierre, D., Retailleau, L., Saurel, J.-M., Sukhovich, A., and Bonnet, R. (2022). Initial results from a hydroacoustic network to monitor submarine lava flows near Mayotte Island. *C. R. Géosci.*, 354(S2), 257–273.

Berthod, C., Komorowski, J.-C., Gurioli, L., Médard, E., Bachèlery, P., Besson, P., Verdurme, P., Chevrel, O., Di Muro, A., Peltier, A., Devidal, J.-L., Nowak, S., Thinon, I., Burckel, P., Hidalgo, S., Deplus, C., Loubrieu, B., Pierre, D., Bermell, S., Pitel-Roudaut, M., Réaud, Y., Fouchard, S., Bickert, M., Le Friant, A., Paquet, F., Feuillet, N., Jorry, S. L., Fouquet, Y., Rinnert, E., Cathalot, C., and Lebas, E. (2022). Temporal magmatic evolution of the Fani Maoré submarine eruption 50 km east of Mayotte revealed by in situ sampling and petrological monitoring. *C. R. Géosci.*, 354(S2), 195–223.

Cadeau, P., Jézéquel, D., Groleau, A., Di Muro, A., and Ader, M. (2022). Impact of the seismo-volcanic crisis offshore Mayotte on the Dziani Dzaha Lake. *C. R. Géosci.*, 354(S2), 299–316.

Cesca, S., Letort, J., Razafindrakoto, H. N. T., Heimann, S., Rivalta, E., Isken, M. P., Nikkhoo, M., Passarelli, L., Petersen, G. M., Cotton, F., and Dahm, T. (2020). Drainage of a deep magma reservoir near Mayotte inferred from seismicity and deformation. *Nat. Geosci.*, 13, 87–93.

Devès, M. H., Moirand, S., Le Vagueresse, L., and Robert, G. (2022). Mayotte's seismo-volcanic "crisis" in news accounts (2018–2021). *C. R. Géosci.*, 354(S2), 391–415.

Dofal, A., Michon, L., Fontaine, F. R., Rindraharisaona, E., Barruol, G., and Tkalčić, H. (2022). Imaging the lithospheric structure and plumbing system below the Mayotte volcanic zone. *C. R. Géosci.*, 354(S2), 47–64.

Feuillet, N. (2019). MAYOBS1 cruise. (RV Marion Dufresne), https://doi.org/10.17600/18001217.

Feuillet, N., Jorry, S., Crawford, W. C., Deplus, C., Thinon, I., Jacques, E., Saurel, J. M., Lemoine, A., Paquet, F., Satriano, C., Aiken, C., Foix, O., Kowalski, P., Laurent, A., Rinnert, E., Cathalot, C., Donval, J.-P., Guyader, V., Gaillot, A., Scalabrin, C., Moreira, M., Peltier, A., Beauducel, F., Grandin, R., Ballu, V., Daniel, R., Pelleau, P., Gomez, J., Besançon, S., Geli, L., Bernard, P., Bachelery, P., Fouquet, Y., Bertil, D., Lemarchand, A., and Van der Woerd, J. (2021). Birth of a large volcanic edifice offshore Mayotte via lithosphere-scale dyke intrusion. *Nat. Geosci.*, 14, 787–795.

Lemoine, A., Briole, P., Bertil, D., Roullé, A., Foumelis, M., Thinon, I., Raucoules, D., de Michele, M., Valty, P., and Hoste Colomer, R. (2020). The 2018–2019 seismo-volcanic crisis east of Mayotte, Comoros islands: seismicity and ground deformation markers of an exceptional submarine eruption. *Geophys. J. Int.*, 223, 22–44.

Liuzzo, M., Di Muro, A., Luca Rizzo, A., Grassa, F., Coltorti, M., and Ader, M. (2022). The composition of gas emissions at Petite Terre (Mayotte, Comoros): inference on magmatic fingerprints. *C. R. Géosci.*, 354(S2), 275–316.

Masquelet, C., Leroy, S., Delescluse, M., Chamot-Rooke, N., Thinon, I., Lemoine, A., Franke, D., Watremez, L., Werner, P., Paquet, F., Berthod, C., Cabiativa Pico, V., and Sauter, D. (2022). The East-Mayotte new volcano in the Comoros Archipelago: structure and timing of magmatic phases inferred from seismic reflection data. *C. R. Géosci.*, 354(S2), 65–79.

Mercury, N., Lemoine, A., Doubre, C., Bertil, D., Van Der Woerd, J., Hoste-Colomer, R., and Battaglia, J. (2022). Onset of a submarine eruption east of Mayotte, Comoros archipelago: the first ten months seismicity of the seismo-volcanic sequence (2018–2019). *C. R. Géosci.*, 354(S2), 105–136.

Morales-Yáñez, C., Duputel, Z., and Rivera, L. (2022). Exploring the link between large earthquakes and magma transport at the onset of the Mayotte volcano-seismic crisis. *C. R. Géosci.*, 354(S2), 137–152.

Mori, M. (2022). Storytelling, language, and the earthquake swarm of May 2018: insights into Shimaore and Kibushi from narrative analysis. *C. R. Géosci.*, 354(S2), 417–437.

Peltier, A., Saur, S., Ballu, V., Beauducel, F., Briole, P., Chanard, K., Dausse, D., De Chabalier, J.-B., Grandin, R., Rouffiac, P., Tranchant, Y.-T., Bès de Berc, M., Besançon, S., Boissier, P., Broucke, C., Brunet, C., Canjamalé, K., Carme, E., Catherine, P., Colombain, A., Crawford, W., Daniel, R., Dectot, G., Desfete, N., Doubre, C., Dumouch, T., Griot, C., Grunberg, M., Jund, H., Kowalski, P., Lauret, F., Lebreton, J., Pesqueira, F., Tronel, F., Valty, P., and van der Woerd, J. (2022). Ground deformation monitoring of the eruption offshore Mayotte. *C. R. Géosci.*, 354(S2), 171–193.

Poulain, P., Le Friant, A., Pedreros, R., Mangeney, A., Filippini, A. G., Grandjean, G., Lemoine, A., Fernández-Nieto, E. D., Castro Díaz, M. J., and Peruzzetto, M. (2022). Numerical simulation of submarine landslides and generated tsunamis: application to the on-going Mayotte seismo-volcanic crisis. *C. R. Géosci.*, 354(S2), 361–390.

Puzenat, V., Feuillet, N., Komorowski, J.-C., Escartín, J., Deplus, C., Bachèlery, P., Berthod, C., Gurioli, L., Scalabrin, C., Cathalot, C., Rinnert, E., Loubrieu, B., Pierre, D., Pitel-Roudaut, M., Tanguy, N., Fouquet, Y., Jorry, S. J., Lebas, E., Paquet, F., and Thinon, I. (2022). Volcano-tectonic structures of Mayotte's upper submarine slope: insights from high-resolution bathymetry and in-situ imagery from a deep-towed camera. *C. R. Géosci.*, 354(S2), 81–104.

Retailleau, L., Saurel, J.-M., Laporte, M., Lavayssière, A., Ferrazzini, V., Zhu, W., Beroza, G. C., Satriano, C., and Komorowski, J.-C. (2022). Automatic detection for a comprehensive view of Mayotte seismicity. *C. R. Géosci.*, 354(S2), 153–170.

Rolandone, F., Poort, J., Masquelet, C., Leroy, S., Thinon, I., Lemoine, A., and Paquet, F. (2022). Heat flow measurements in the Northern Mozambique Channel. *C. R. Géosci.*, 354(S2), 35–46.

Roullé, A., Baillet, M., Bertil, D., and Cornou, C. (2022). Site effects observations and mapping on the weathered volcanic formations of Mayotte Island. *C. R. Géosci.*, 354(S2), 317–341.

Taillefer, N., Bertil, D., Negulescu, C., Roullé, A., Iasio, C., Auclair, S., and Quique, R. (2022). Seismic damage scenarios for Mayotte: a tool for disaster management. *C. R. Géosci.*, 354(S2), 343–359.

Thinon, I., Lemoine, A., Leroy, S., Paquet, F., Berthod, C., Zaragosi, S., Famin, V., Feuillet, N., Boymond, P., Masquelet, C., Mercury, N., Rusquet, A., Scalabrin, C., Van der Woerd, J., Bernard, J., Bignon, J., Clouard, V., Doubre, C., Jacques, E., Jorry, S. J., Rolandone, F., Chamot-Rooke, N., Delescluse, M., Franke, D., Watremez, L., Bachèlery, P., Michon, L., Sauter, D., Bujan, S., Canva, A., Dassie, E., Roche, V., Ali, S., Hamid Sitti Allaouia, A., Deplus, C., Rad, S., and Sadeski, L. (2022). Volcanism and tectonics unveiled in the Comoros Archipelago between Africa and Madagascar. *C. R. Géosci.*, 354(S2), 7–34.

*Comptes Rendus*
*Géoscience — Sciences de la Planète*
**2022**, Vol. 354, Special Issue S2, p. 7-34
https://doi.org/10.5802/crgeos.159

The Mayotte seismo-volcanic crisis of 2018-2021 in the Comoros archipelago (Mozambique channel) / *La crise sismo-volcanique de 2018-2021 de Mayotte dans l'archipel des Comores (Canal du Mozambique)*

# Volcanism and tectonics unveiled in the Comoros Archipelago between Africa and Madagascar

## *Volcanisme et tectonique découverts le long de l'archipel des Comores entre l'Afrique et Madagascar*

**Isabelle Thinon**[*, a], **Anne Lemoine**[a], **Sylvie Leroy**[b], **Fabien Paquet**[a], **Carole Berthod**[c, d], **Sébastien Zaragosi**[e], **Vincent Famin**[f, d], **Nathalie Feuillet**[d], **Pierre Boymond**[d], **Charles Masquelet**[b], **Nicolas Mercury**[a, g], **Anaïs Rusquet**[f, d], **Carla Scalabrin**[h], **Jérôme Van der Woerd**[g], **Julien Bernard**[a], **Julie Bignon**[e], **Valérie Clouard**[i], **Cécile Doubre**[g], **Eric Jacques**[d], **Stephan J. Jorry**[h], **Frédérique Rolandone**[b], **Nicolas Chamot-Rooke**[j], **Matthias Delescluse**[j], **Dieter Franke**[k], **Louise Watremez**[l], **Patrick Bachèlery**[f], **Laurent Michon**[f, d], **Daniel Sauter**[g], **Stéphane Bujan**[e], **Albane Canva**[m], **Emilie Dassie**[e], **Vincent Roche**[b], **Said Ali**[n], **Abdoul Hamid Sitti Allaouia**[o], **Christine Deplus**[d], **Setareh Rad**[a] and **Ludivine Sadeski**[a]

[a] French Geological Survey (BRGM), France

[b] Sorbonne Université, CNRS-INSU, Institut des Sciences de la Terre de Paris, ISTeP, Paris, France

[c] Université Clermont Auvergne, CNRS, IRD, OPGC, Laboratoire Magmas et Volcans, 6 avenue Blaise Pascal, 63178 Aubière, France

[d] Université de Paris, Institut de physique du globe de Paris, CNRS, UMR 7154; F-75005 Paris, France

[e] Université de Bordeaux, CNRS, EPOC, EPHE, UMR 5805; F-33600 Pessac, France

[f] Université de La Réunion, Laboratoire GéoSciences Réunion, F-97744 Saint-Denis, France

[g] Institut Terre et Environnement de Strasbourg (ITES), Université de Strasbourg CNRS UMR 7063; 5 rue Descartes, FR-67084 Strasbourg, France

[h] Ifremer, Univ Brest, CNRS, Ifremer, Geo-Ocean, F-29280 Plouzané, France

[i] GET, UMR 5563; Observatoire Midi Pyrénées, Université Paul Sabatier, CNRS, IRD, Toulouse, France

* Corresponding author.

[j] Laboratoire de Géologie, Ecole Normale Supérieure (ENS), PSL Univ., CNRS UMR 8538; Laboratoire de Géologie, France

[k] BGR Bundesanstalt für Geowissenschaften und Rohstoffe, Germany

[l] Université de Lille, CNRS, IRD, Université Littoral Côte d'Opale, UMR 8187 – LOG – Laboratoire d'Océanologie et de Géosciences, Lille, France

[m] Université Côte d'Azur, CNRS, Observatoire de la Côte d'Azur, IRD, Géoazur, 250 rue Albert Einstein, Sophia Antipolis 06560 Valbonne, France

[n] Faculté des Sciences et Techniques - Université des Comores, Union des Comores, Comoros

[o] CNDRS (centre national de documentation et des recherches scientifiques) Union des Comores, Comoros

*Current address:* BRGM - DGR/GBS, 3 avenue Claude Guillemin, BP 36009, 45060 Orléans Cedex 2, France (I. Thinon)

*E-mails:* i.thinon@brgm.fr (I. Thinon), a.lemoine@brgm.fr (A. Lemoine), sylvie.leroy@sorbonne-universite.fr (S. Leroy), f.paquet@brgm.fr (F. Paquet), carole.berthod@uca.fr (C. Berthod), sebastien.zaragosi@u-bordeaux.fr (S. Zaragosi), vincent.famin@univ-reunion.fr (V. Famin), feuillet@ipgp.fr (N. Feuillet), boymond@ipgp.fr (P. Boymond), charles.masquelet@sorbonne-universite.fr (C. Masquelet), n.mercury@brgm.fr (N. Mercury), rusquet@ipgp.fr (A. Rusquet), Carla.Scalabrin@ifremer.fr (C. Scalabrin), jerome.vanderwoerd@unistra.fr (J. Van der Woerd), j.bernard@brgm.fr (J. Bernard), julie.julie-bignon@etu.u-bordeaux.fr (J. Bignon), valerie.clouard@get.omp.eu (V. Clouard), Cecile.Doubre@unistra.fr (C. Doubre), jacques@ipgp.fr (E. Jacques), stephan.jorry@ifremer.fr (S. J. Jorry), frederique.rolandone@upmc.fr (F. Rolandone), rooke@geologie.ens.fr (N. Chamot-Rooke), delescluse@geologie.ens.fr (M. Delescluse), Dieter.Franke@bgr.de (D. Franke), louise.watremez@univ-lille.fr (L. Watremez), p.bachelery@opgc.fr (P. Bachèlery), laurent.michon@univ-reunion.fr (L. Michon), Daniel.Sauter@unistra.fr (D. Sauter), stephane.bujan@u-bordeaux.fr (S. Bujan), Albane.CANVA@geoazur.unice.fr (A. Canva), emilie.dassie@u-bordeaux.fr (E. Dassie), vincent.roche@sorbonne-universite.fr (V. Roche), nasaidali@gmail.com (S. Ali), alawia.abdoulhamid@gmail.com (A. H. Sitti Allaouia), deplus@ipgp.fr (C. Deplus), s.rad@brgm.fr (S. Rad), l.sadeski@brgm.fr (L. Sadeski)

**Abstract.** Geophysical and geological data from the North Mozambique Channel acquired during the 2020–2021 SISMAORE oceanographic cruise reveal a corridor of recent volcanic and tectonic features 200 km wide and 600 km long within and north of Comoros Archipelago. Here we identify and describe two major submarine tectono-volcanic fields: the N'Droundé province oriented N160°E north of Grande-Comore Island, and the Mwezi province oriented N130°E north of Anjouan and Mayotte Islands. The presence of popping basaltic rocks sampled in the Mwezi province suggests post-Pleistocene volcanic activity. The geometry and distribution of recent structures observed on the seafloor are consistent with a current regional dextral transtensional context. Their orientations change progressively from west to east (~N160°E, ~N130°E, ~EW). The volcanism in the western part appears to be influenced by the pre-existing structural fabric of the Mesozoic crust. The 200 km-wide and 600 km-long tectono-volcanic corridor underlines the incipient Somalia–Lwandle dextral lithospheric plate boundary between the East-African Rift System and Madagascar.

**Résumé.** Des données géophysiques et géologiques ont été acquises lors de la campagne océanographique SISMAORE (2020–2021). Deux grands champs tectono-volcaniques sous-marins ont été découverts tout le long et principalement au nord de l'archipel des Comores : la province N'Droundé orientée N160°E au nord de Grande-Comore, et la province Mwezi orientée N130°E au nord d'Anjouan-Mayotte où des roches basaltiques de type popping-rocks suggèrent une activité volcanique possiblement actuelle à pléistocène. La géométrie et la distribution des structures récentes sont cohérentes avec un contexte régional actuel transtensif dextre. Leurs orientations évoluent d'Ouest en Est (~N160°E, ~N130°E, ~EW), suggérant pour la partie occidentale, une mise en place du volcanisme influencée par la structuration crustale préexistante. Le corridor tectono-volcanique de

200 km de large et de 600 km de long dessine une limite de plaque lithosphérique Somalie-Lwandle immature en décrochante dextre entre le système du rift est-africain et Madagascar.

**Keywords.** Volcanic province, Active tectonics, Incipient plate boundary, Bathymetry, Backscatter, Northern Mozambique Channel, Comoros Archipelago.

**Mots-clés.** Province volcanique, Tectonique active, Frontière de plaque naissante, Bathymétrie, Rétrodiffusion, Canal du Mozambique Nord, Archipel des Comores.

*Published online: 19 December 2022, Issue date: 17 January 2023*

## 1. Introduction

The Comoros Archipelago, in the Mozambique Channel between east Africa and northern Madagascar (Figure 1), is located along the poorly constrained plate boundary between the Lwandle and Somalia lithospheric plates [Famin et al., 2020, Kusky et al., 2010, Stamps et al., 2018, 2021]. This boundary has probably evolved jointly with the southward propagation of the East African Rift System (EARS) [e.g., Franke et al., 2015, Mougenot et al., 1986].

Seismicity in the Mozambique Channel is of moderate intensity and is concentrated along two large-scale structures: Davie Ridge and the Comoros Archipelago [Bertil and Regnoult, 1998, Bertil et al., 2021, Lemoine et al., 2020; Figure 1]. Focal mechanisms mainly indicate regional E–W extension along Davie Ridge, considered to be a N–S trending offshore arm of the EARS [Courgeon et al., 2018, Déprez et al., 2013, Deville et al., 2018]. West of the Comoros Archipelago, sparse focal mechanisms along approximately N–S trending normal faults are also compatible with E–W extension and may be related to the EARS [e.g., Klimke and Franke, 2016]. In contrast, seismicity in the Comoros Archipelago indicates ESE–WNW distribution west of Mayotte and ENE–WSW distribution east of Mayotte [Bertil et al., 2021]. Elsewhere in the Archipelago, sparse focal mechanisms suggest mainly strike-slip faulting with a normal component, including the seismo-volcanic sequence associated with the 2018–2021 East Mayotte eruption [Cesca et al., 2020, Feuillet et al., 2021, Lemoine et al., 2020, Lavayssière et al., 2022, Mercury et al., 2022]. Holocene tectonic and volcanic activity is also evident on the islands of Anjouan and Mayotte [Famin et al., 2020, Quidelleur et al., 2022] and in the abyssal plain north of the Archipelago [Tzevahirtzian et al., 2021]. Recent studies [e.g., Bertil et al., 2021, Famin et al., 2020, Feuillet et al., 2021, Kusky et al., 2010, Lemoine et al., 2020, Michon et al., 2016, Stamps et al., 2018, 2021] have suggested that the Comoros Archipelago is located along a diffuse or incipient plate boundary between the Lwandle and Somalia plates, although the sense of displacement is poorly constrained, being consistent with transtension, pure strike-slip, or transpression.

Early work has focused on the Comoro Islands, and few papers have treated the offshore parts of the Archipelago (Figure 2). Using bathymetric data, Audru et al. [2006] and Tzevahirtzian et al. [2021] provide overviews of the volcanic structures and slope instabilities on the flanks of the islands. Since 2019, Mayotte Volcanological And Seismological Monitoring Network [REVOSIMA (Mayotte Volcanological And Seismological Monitoring Network), 2022] has closely monitored the ongoing seismo-volcanic events and reported detailed information, such as seafloor morphology and seismic and volcanic activity on the eastern slope of Mayotte, where ~6.55 km$^3$ of magma erupted in January 2021), as well as the lithology of volcanic structures [e.g., Berthod et al., 2021a,b, Deplus et al., 2019, Feuillet et al., 2021, Foix et al., 2021, Jacques et al., 2019, Lavayssière et al., 2022, REVOSIMA newsletter, 2021, Saurel et al., 2022]. Yet, the age and nature of the volcanic Comoros Archipelago and surrounding areas are constrained only by analysis of onshore samples [Class et al., 2005, Michon et al., 2016, Pelleter et al., 2014, Quidelleur et al., 2022] and rare marine rock samples, mostly from east of Mayotte [Berthod et al., 2021a,b, Feuillet et al., 2021].

To fill this data gap, the geophysical and geological SISMAORE oceanographic cruise, linked to the COYOTES project (COmoros & maYotte: vOlcanism, TEctonics and Seismicity), took place off the Comoros Archipelago from December 2020 to February 2021 [Thinon et al., 2020b]. This cruise acquired high-resolution multibeam bathymetry and backscatter data, shallow and deep seismic reflection profiles and refraction data, heat flow, magnetic and gravity data, and rock and sediment samples. In this paper, we focus on the main characteristics of the recent volcanic and tectonic structures at a regional scale, to bet-

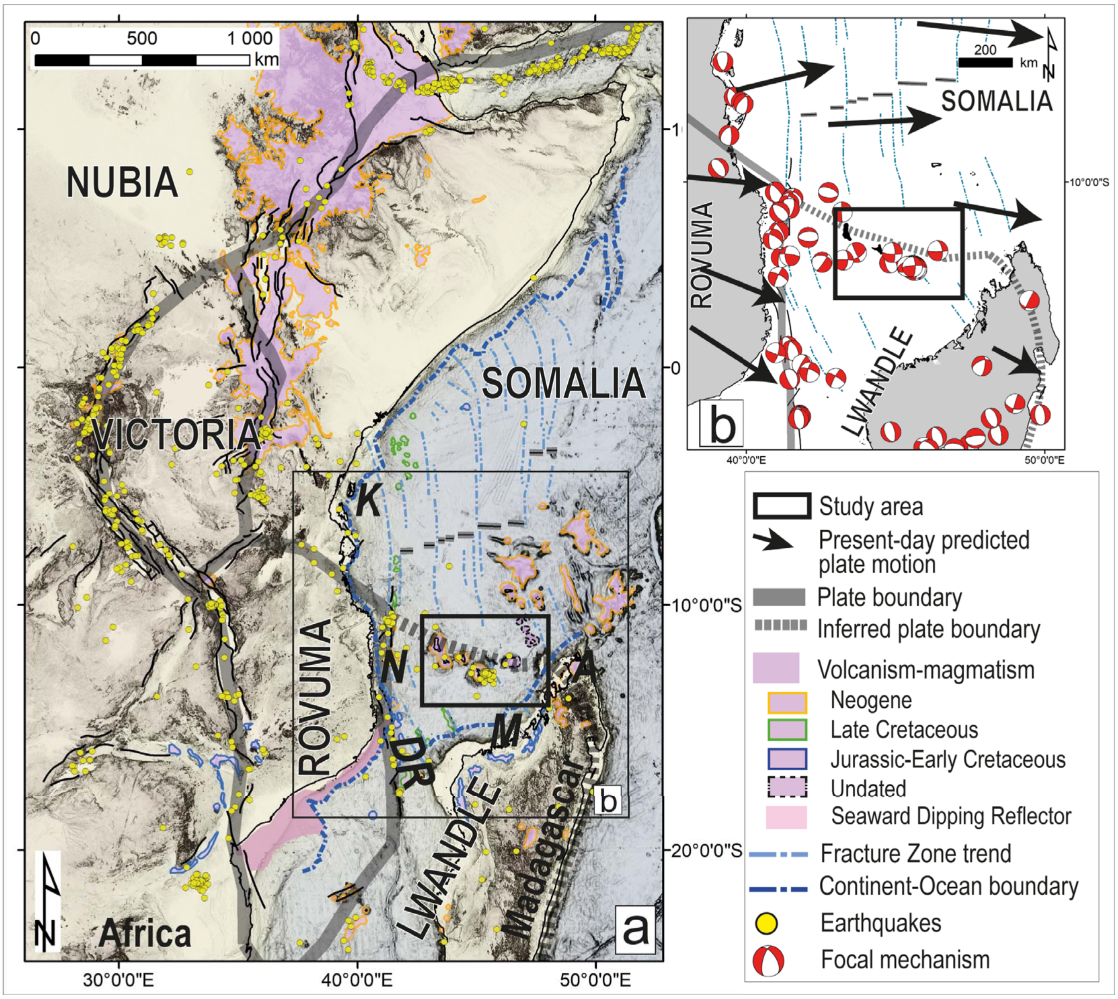


**Figure 1.** (a) Regional geological context of the study area. Volcanism in the northern Mozambique Channel from Michon et al. [2022] and Roche and Ringenbach [2022]. Earthquake locations from the database of the International Seismological Centre [2021]; plate boundaries from Michon et al. [2022]; fracture zones from Davis et al. [2016]; boundary of oceanic crust and exhumed mantle (COB) from Roche and Ringenbach [2022]; major faults of the East African Rift System (heavy black lines) from Michon et al. [2022]; bathymetry from GEBCO, 2014 [Weatherall et al., 2015]. A, Ambilobe basin; DR, Davie Ridge; K, Kerimbas basin; M, Majumba basin; N, Nacada basin. (b) Focal mechanisms compilation [Bertil et al., 2021, and references therein] and present-day relative plate motions with respect to Nubia plate [Stamps et al., 2021].

ter map the distribution of deformation around the Archipelago. Better knowledge of active structures and their regional geodynamic context will improve the identification and assessment of regional volcanic, seismic, tsunamigenic, and landslide hazards.

In this paper, we propose a geodynamic configuration that takes into account the pre-volcanism history of the northern Mozambique Channel and current regional kinematics.

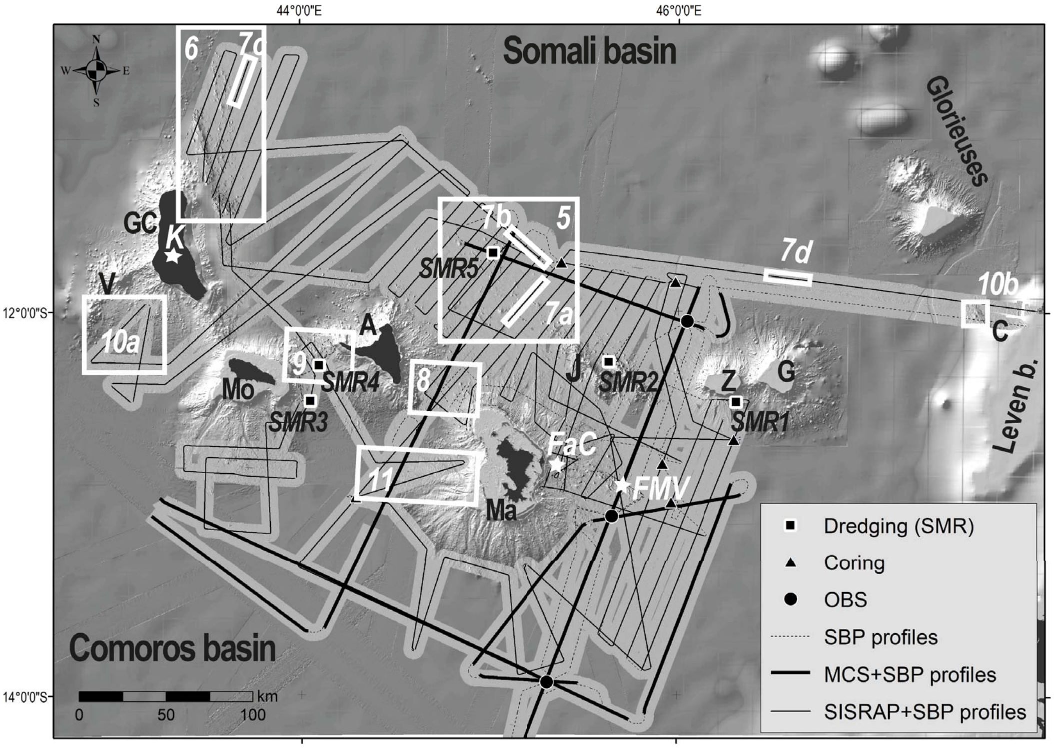


**Figure 2.** Map of major geographic features of the study area and data acquired during the 2020–2021 SISMAORE cruise. SBP, sub-bottom profiler lines; thin lines, SISRAP, 48-channel seismic reflection; Multichannel seismic (MCS) data, 960-channel seismic reflection Masquelet et al. [2022]; OBS, ocean bottom seismometer. Multibeam echosounder system (MBES) and water column acoustic data were obtained along all black lines Thinon et al. [2020b]. Volcanic islands: GC, Grande-Comore; Mo, Mohéli; A, Anjouan; Ma, Mayotte. Major seamounts and chains: V, Vailheu; J, Jumelles; Z, Zélée Bank; G, Geyser Bank; L, Leven Bank; C, Cordelière Bank. White stars: K, Karthala volcano; FMV, Fani Maore volcano; FaC, Fer à Cheval volcanic complex [Feuillet et al., 2021]. Detailed bathymetry from the compilation of Tzevahirtzian et al. [2021] (surveys listed in references and in Counts et al. [2018]) superimposed on GEBCO regional low-resolution bathymetry [Weatherall et al., 2015]. White outlines correspond to other figures in this paper.

## 2. Regional settings

### 2.1. *Volcanism of the Comoros Archipelago*

The Comoros Archipelago includes the four main islands, Grande-Comore, Mohéli, Anjouan and Mayotte, as well as submerged features including the Jumelles seamounts, Vailheu seamount and the Zélée–Geyser banks [e.g., Tzevahirtzian et al., 2021; Figure 2]. Seismic stratigraphy [Leroux et al., 2020] indicates that the main volcanic phase of Mayotte (late Paleogene to Neogene) is much younger than Zélée–Geyser banks (Cretaceous-Paleogene transition), which in turn are younger than the Glorieuses seamounts (Late Cretaceous). Mayotte, oldest of the four main islands, has a low elevation and a well-developed insular shelf, as does Mohéli [Tzevahirtzian et al., 2021]. The onset of Mayotte's volcanism was estimated at about 20 Ma by Michon et al. [2016] and between 26 and 27 Ma by Masquelet et al. [2022]. For Anjouan and Grande-Comore, high-elevation volcanic islands with young relief, volcanism could have started at 7 to 10 Ma [Michon et al., 2016].

Subaerial Mayotte is made up of three morphologically and structurally distinct units corresponding to three eruptive phases, which date from 10.6 to 1.5 Ma in the south part, from 7.1 to 1.0 Ma in the northwest part and from 2.4 Ma to 0.15 Ma in the northeast part and the nearby islet Petite-Terre [Debeuf, 2004, Nehlig et al., 2013]. Volcanic ash layers in dated lagoon sediments suggest that the most recent volcanic and explosive activity on land is younger than 7 ka [Zinke et al., 2003, 2005, and references therein]. On the northern slope off Mayotte, several small volcanic edifices are part of a longer line of volcanoes trending N140°E from Anjouan to Petite-Terre [Audru et al., 2006]. On the seafloor east of Mayotte, the MAYOBS monitoring cruises [Rinnert et al., 2019, REVOSIMA newsletter, 2021] during the 2018–2021 Mayotte seismo-volcanic crisis have documented the N110°E trending Eastern Volcanic Chain of Mayotte (EVCM; Figure 2), a line of numerous volcanic structures with a new active volcanic edifice 800 m high and 5 km in diameter at its tip [Berthod et al., 2021a,b, Cesca et al., 2020, Feuillet et al., 2021, Lemoine et al., 2020]. This active submarine volcano is called Fani Maor'e volcano (name submitted to the UNESCO's International Marine Chart Commission, Figure 2).

Before the 2018–2021 Mayotte eruption, the only volcano with known historic activity (since the early 18th century) is Karthala volcano on Grande-Comore [Bachèlery et al., 1995, 2016b]. Late Holocene activity (from $^{14}$C ages of 1300 ± 65 yr BP and 740 ± 130 yr BP) is known for La Grille volcano on Grande-Comore [Bachèlery and Coudray, 1993, Bachèlery et al., 2016b], and early Holocene activity is known for Anjouan [$^{14}$C ages of 8335 ± 50 yr BP; e.g., Quidelleur et al., 2022].

The origin of the volcanism of the Comoros Archipelago is debated [Michon et al., 2016]. A mantle plume model, proposed mainly based on large-scale geomorphological arguments and scant early K–Ar dates, is inconsistent with the inferred dextral transtension between the Somalia and Lwandle plates [Calais et al., 2006, Stamps et al., 2018] and by geochronological data showing no clear age progression through the islands [Debeuf, 2004, Quidelleur et al., 2022, Tzevahirtzian et al., 2021]. One alternative explanation is that the volcanism represents an offshore extension of the EARS to the east of Davie Ridge, possibly along a diffuse or incipient Somalia–Lwandle plate boundary [e.g., Deville et al., 2018 and references therein; Famin et al., 2020, Feuillet et al., 2021, Lemoine et al., 2020, Michon et al., 2022, Stamps et al., 2018].

## 2.2. *Distribution of recent and old deformation*

Deformation onshore on Mayotte took place predominantly on thrust and strike-slip faults consistent with the N135°E trend in earthquake focal mechanisms [Famin et al., 2020]. Offshore structures trending N130°E include the Jumelles volcanic chain and some alignments of volcanic cones, mounds and faults [e.g., Tzevahirtzian et al., 2021]. Moreover, Lemoine et al. [2020] and Feuillet et al. [2021] have suggested that the deep dyke feeding the current Mayotte eruption is oriented NW–SE, consistent with the context of transtension.

Toward Davie Ridge on the west side of Mozambique Channel, Neogene strike-slip and normal faults imply a transtensional component associated with volcanism [Franke et al., 2015, Roche and Ringenbach, 2022]. Other than there and in associated basins such as the Kerimbas and Nacala basins [Courgeon et al., 2018, Mahanjane, 2014, Mougenot et al., 1986, Roche and Ringenbach, 2022, Vormann and Jokat, 2021], no Quaternary deformation has been described in the Comoros basin or in the Majunga basin in the NW Madagascar margin (Figure 1).

## 2.3. *Regional geological history—inheritance*

Recent studies suggest that rifting of Gondwana began in late early to early Middle Jurassic time, ~170 Ma to ~185 Ma [Davis et al., 2016, Eagles and König, 2008, Gaina et al., 2015, Leinweber and Jokat, 2012, Mueller and Jokat, 2019, Senkans et al., 2019]. However, precise dating is difficult given the poorly developed seafloor spreading anomalies from this time. North of the Comoros Archipelago, kinematic reconstructions [e.g., Davis et al., 2016] and limited gravity and magnetic data suggest that the Somali basin consists of oceanic crust with an extinct EW trending oceanic spreading axis and transform faults trending N–S to NW–SE [see Figures 4 and 8 in Davis et al., 2016 and Figures 5 and 9 in Phethean et al., 2016] (Figure 1). Seafloor spreading is thought to have begun during the Jurassic Magnetic Quiet Zone (~166 Ma) and ceased at ~120 Ma [Davis et al., 2016, Segoufin and Patriat, 1980]. In

Mozambique and Tanzania to the west, the breakup unconformity is of early Middle Jurassic (Aalenian) age [Fossum et al., 2021, Roche et al., 2021, Senkans et al., 2019]. The age and the nature of the crust beneath the Comoro Islands and the Comoros Basin are still debated. On the one hand, an oceanic crust is supported by isostatic data, magnetic and gravity anomalies, P-wave velocities, and seismic reflection data [Coffin and Rabinowitz, 1987, Coffin et al., 1986, Klimke et al., 2016, Phethean et al., 2016, Roche and Ringenbach, 2022, Talwani, 1962, Vormann and Jokat, 2021, Vormann et al., 2020]. On the other hand, the presence of quartzite inclusions in volcanic rocks and a massif of quartzite on Anjouan [Flower, 1972, Flower and Strong, 1969, Montaggioni and Nougier, 1981, Quidelleur et al., 2022, Wright and McCurry, 1970] and low $V_p/V_s$ ratios [Dofal et al., 2021] suggest that the Archipelago is built on continental crust or at least upon a succession of continental sediments [Dofal et al., 2021, Roach et al., 2017]. In Figure 1, we choose to represent the crust as oceanic [Roche and Ringenbach, 2022].

Whatever the nature of the crust, gravity data appear to indicate some relict structural segmentation of both continental and oceanic domains beneath the Comoros Archipelago. Both transforms and fracture zones [Davis et al., 2016, Phethean et al., 2016] could be pre-existing structures in the Comoros and Somali Basins (Figure 1) that have influenced later structures.

## 3. Dataset from SISMAORE cruise and methods

The SISMAORE cruise (December 2020 to February 2021) of R/V (Research Vessel) *Pourquoi Pas?* collected 80,000 km$^2$ of multibeam bathymetry and backscatter data around the Comoros Archipelago with the vessel-mounted MultiBeam Echosounder System (MBES RESON 7150 at 12 or 24 kHz) that complemented previous surveys around Mayotte [Figure 2; Thinon et al., 2020b; for details, see Supplementary Information]. In addition, the ship acquired 10,000 km of sub-bottom profiler (SBP) data and 6730 km of 48-channel seismic reflection profiles (for details, see Supplementary Information), imaging the subsurface down to 0.1 s two-way travel time (TWT) with very high resolution and down to ~3 s TWT below the seafloor, respectively. Five dredging operations (Figures 2 and 3) collected mainly volcanic rocks on the flanks of Zélée Bank (sample set SMR1), the Jumelles volcanic chain (SMR2), Mohéli (SMR3), the Chistwani volcanic chain (SMR4) and a seamount in the abyssal plain north of Mayotte (SMR5) [Thinon et al., 2020b]. These rocks are macroscopically similar to those described on land in the Comoro Islands [Bachèlery and Hémond, 2016, Debeuf, 2004, Pelleter et al., 2014, and references therein] and offshore of Mayotte [Berthod et al., 2021a,b]. The rocks in the SMR5 dredge samples are $CO_2$-rich fresh basaltic rocks called popping rocks (Supplementary Figure S1) that contain arkose and quartzite xenoliths, occasionally with melted shapes, and rare olivine xenocrysts [Thinon et al., 2020b].

## 4. Observations and interpretation

On the basis of the new regional MBES bathymetric and backscatter reflectivity data (Figure 3), we prepared a new regional geomorphological map around the Comoros Archipelago (Figure 4). In addition to the islands and seamounts previously mentioned, it portrays two newly mapped large volcanic fields with tectonic structures (the N'Droundé and Mwezi provinces, and the Domoni, Chistwani and Safari submarine volcanic chains that extend between the islands [first described by Tzevahirtzian et al., 2021].

The depth of the abyssal plain ranges between 3000 m and 3800 m (Figure 3a). North of the Comoros Archipelago, the smooth abyssal plain of the Somali basin is interrupted by two large fields of heterogeneous bathymetric features (Figure 3a) and strong reflectivity contrasts (Figure 3b). The first of these, north of Anjouan and Mayotte, is here named the Mwezi Province ("Moon" in Comorian; Figures 4 and 5), and the second, north of Grande-Comore, is here named the N'Droundé Province (from the town of N'Droundé on Grande-Comore; Figures 4 and 6). In the eastern part of the Somali basin are two major valleys trending N–S to NNE–SSW, one on the seabed between the Glorieuses Islands and Leven Bank at 3800 m water depth and one north of Jumelles Seamount and Zélée–Geyser banks at 3600 m (Figures 3a and 4).

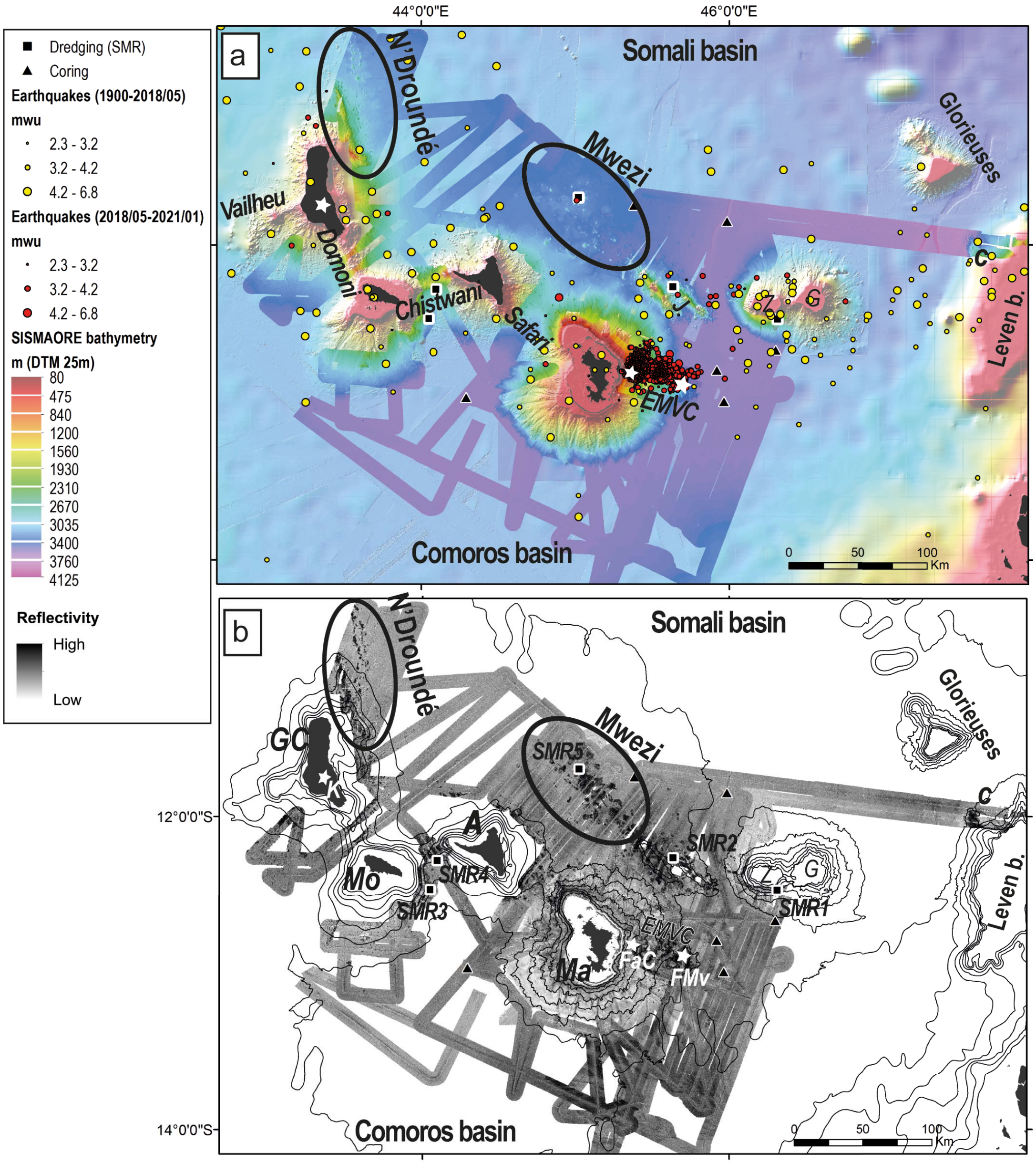


**Figure 3.** Maps showing (a) bathymetry and (b) acoustic backscatter imagery from the SISMAORE cruise combined with previous bathymetric data. Also shown are locations of newly described features: Vailheu, Domoni, Chistwani and Safari volcanic chains and N'Droundé and Mwezi provinces. Yellow and red circles represent earthquakes from Bertil et al. [2021]. All other symbols as in Figure 2.

The abyssal plain south of the Archipelago, in the Comoros Basin, has a homogeneous and flat morphology at 3500 m depth (Figure 3a) without strong reflectivity contrasts (Figure 3b). Small reflectivity variations of the flat seabed southeast of Mayotte (Figures 3b and 4) appear to be associated with the distribution of surficial sediment.

East of Mayotte, the EVCM (Figures 3 and 4) comprises elongated ridges, several volcanic cones up to 500–900 m high including the submarine volcano

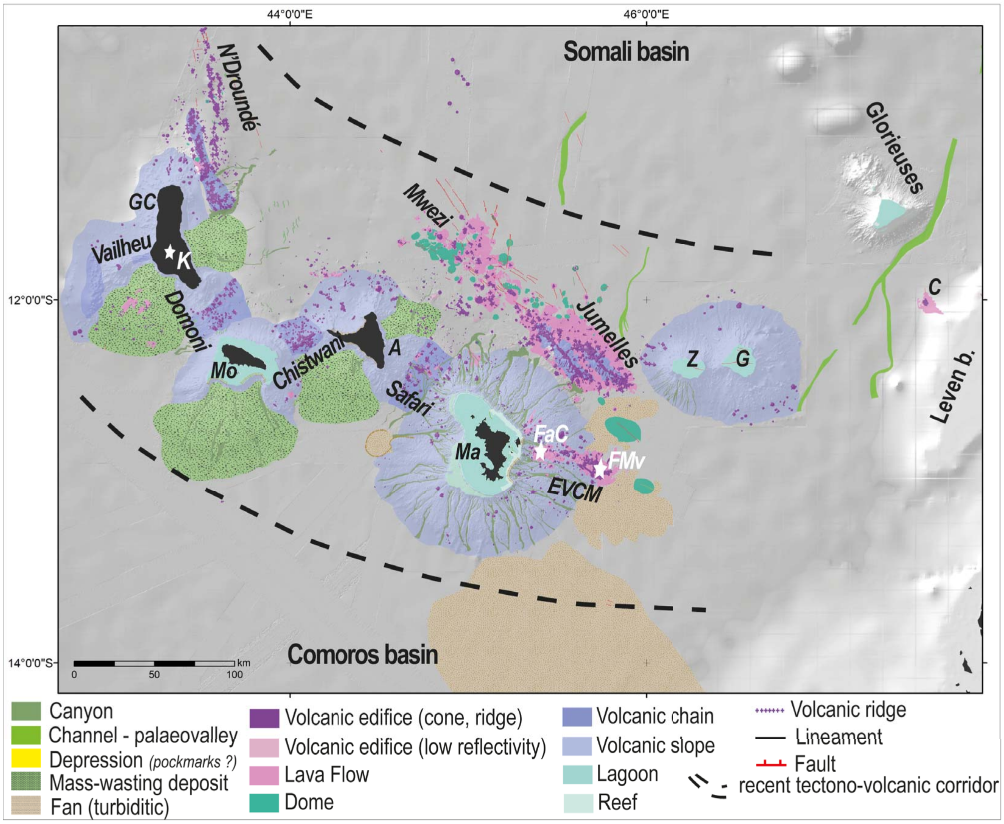


**Figure 4.** Geomorphological map of the study area showing major structural, volcanic and sedimentary features identified on the SISMAORE bathymetry and backscatter maps (Figure 3) plus features on the insular slopes from earlier work [Feuillet et al., 2021, Paquet et al., 2019, Tzevahirtzian et al., 2021]. The two grey dashed lines mark the boundaries of the Comoros tectono-volcanic corridor described in this paper.

formed during the 2018–2021 eruption, lava flows, and a horseshoe-shaped volcanic complex with current activity [MAYOBS cruises, REVOSIMA newsletter, 2021, Feuillet et al., 2021, Rinnert et al., 2019]. Two great dome-shaped forced folds, faults, and possible submarine mass transport deposits described by Paquet et al. [2019] are also imaged (Figure 4).

On the insular slopes, the map depicts the major mass-wasting deposits identified by Tzevahirtzian et al. [2021] and Audru et al. [2006] in new detail. On the abyssal plain, seismic profiles (Figure 7) show that the thickness of the entire sedimentary cover can exceed 2.5 s TWT, or ~3.1 km based on an average 2500 $m \cdot s^{-1}$ velocity in the sediments [Masquelet et al., 2022].

## 4.1. *North of the Comoros Archipelago*

### 4.1.1. *The Mwezi tectono-volcanic province*

The Mwezi Province covers an area 100 by 60 km (~6000 $km^2$) in the flat abyssal plain of the Somali basin (~3400 m depth) and represents a westward extension of the N130°E trending Jumelles volcanic chain (Figure 5). It contains abundant bathymetric features (Figures 5a and d) corresponding to patches with moderate to strong reflectivity (Figures 5b and e). These relief structures include a large number of elongated and steep-sided ridges and conical features (Figure 5d). The ridges are typically 1–4 km in length and reach heights of several hundred metres above the surrounding seafloor. The highest seamount in this area (C1 on Figures 5d

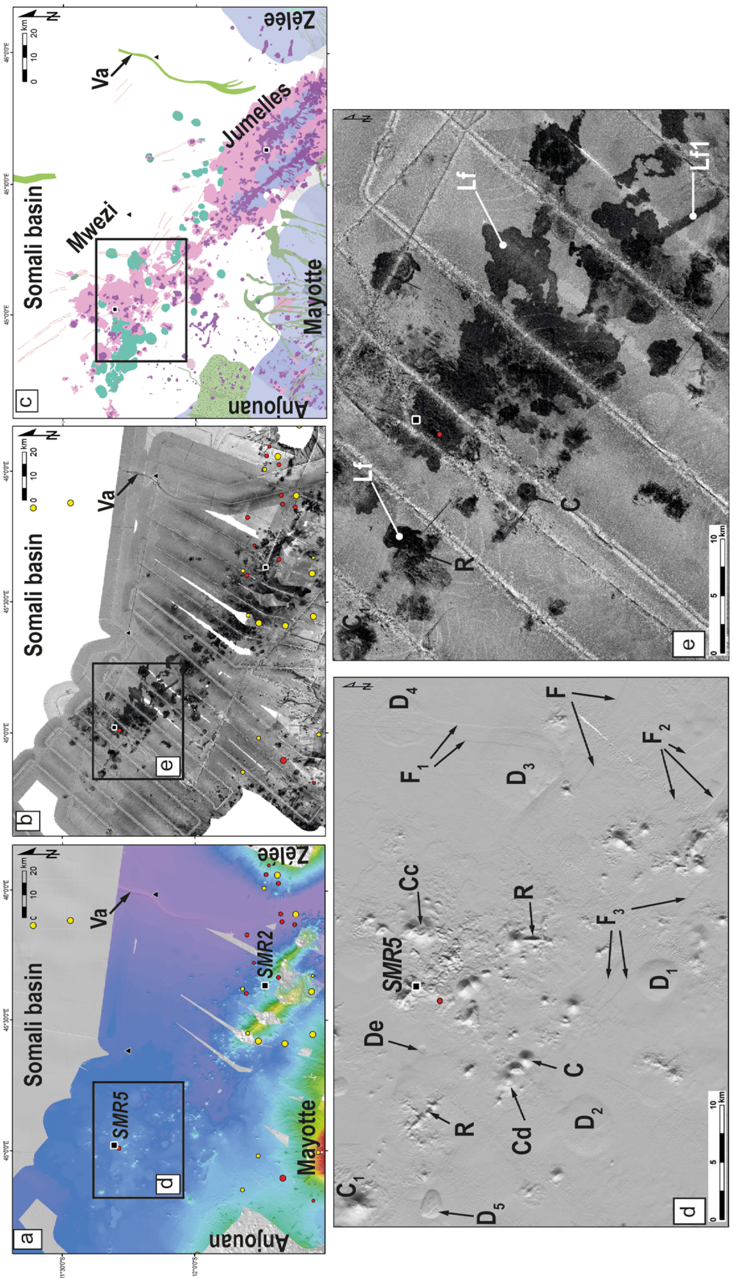


**Figure 5.** (a) Bathymetric map and (b) backscatter map of the Somali basin north of Anjouan and Mayotte, showing seismicity and an incised valley (Va). Outlined regions are shown in (d) and (e), respectively. (c) Interpretive map showing the Mwezi province, Jumelles volcanic chain, Zélée–Geyser Bank and other structural, volcanic, and sedimentary features (for legend see Figure 4). (d) Detail map of seafloor morphology and (e) reflectivity in the central Mwezi Province. Red circle indicates the 24 July 2018 earthquake [3.62 mwu, 15 km depth; Bertil et al., 2021]. C, conical feature; Cc, seamount with summit crater; Cd, seamount with summit dome; D, dome-shaped forced fold; De, depression; F, fault; Lf, lava flow; R, ridge. Supplementary Figure S2 presents oblique views of this area.

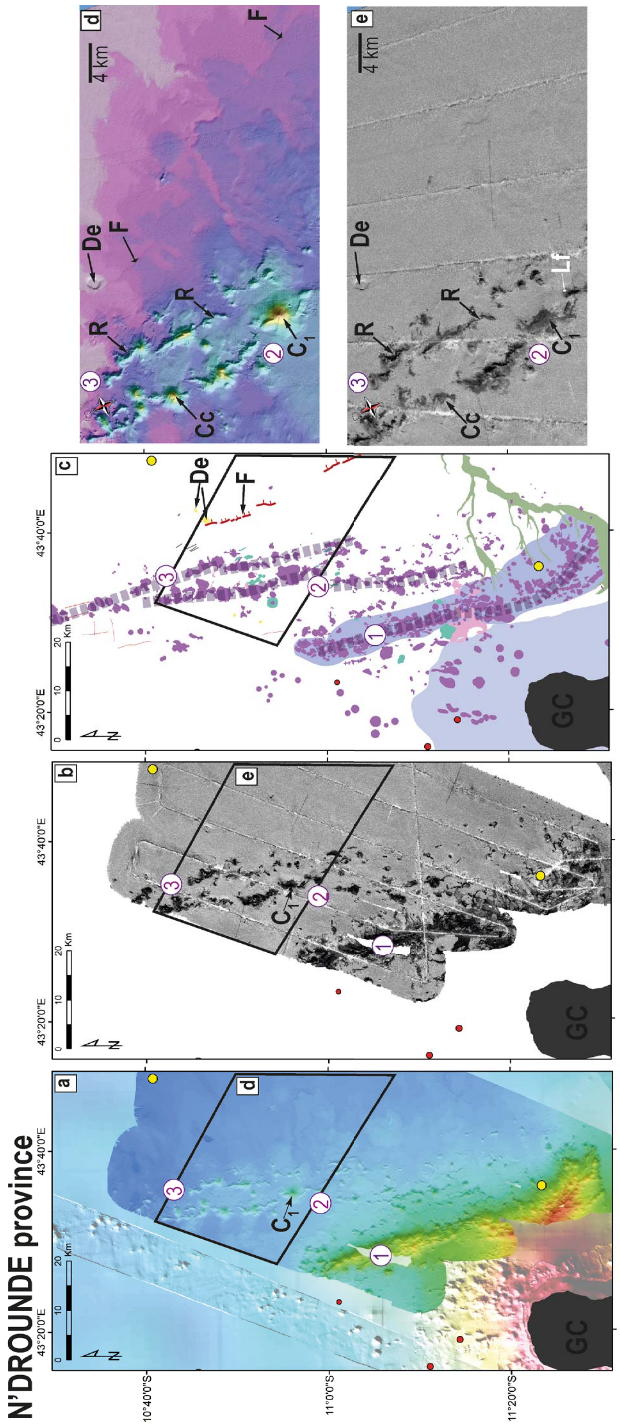


**Figure 6.** (a) Bathymetric, (b) backscatter and (c) interpretive maps of the N'Droundé Province. Three sub-parallel volcanic chains (numbered circles) are marked with thick dashed lines in (c). Note that volcanic chain 1 changes orientation from NNW–SSE to NW–SE as it approaches Grande-Comore (GC), unlike chains 2 and 3. (d) Details of bathymetry and (e) backscatter maps. See Figure 5 for explanation of symbols.

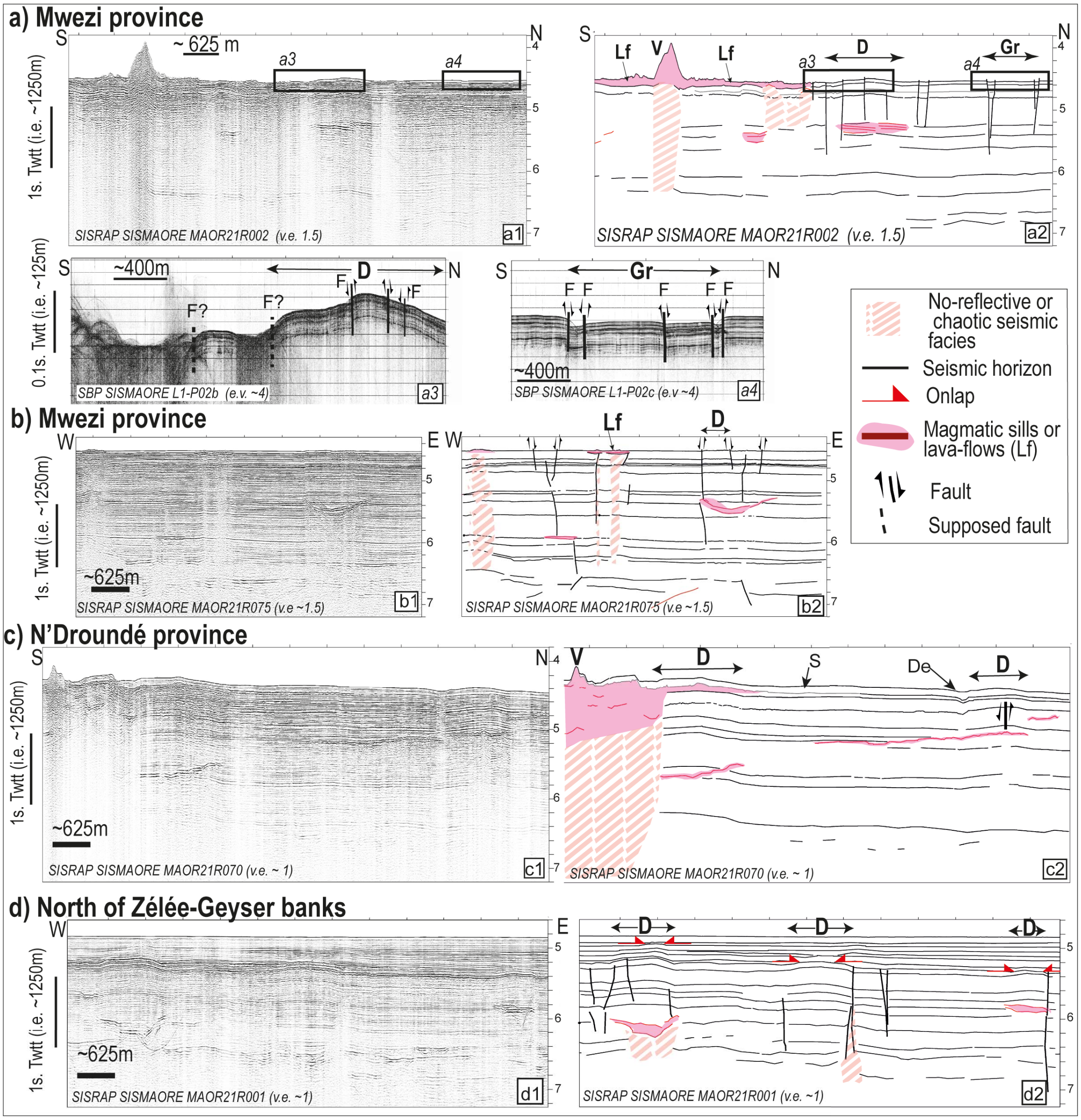


**Figure 7.** Selected 48-channel seismic reflection and SBP profiles and their interpretations, showing the subsurface architecture of different volcanic structures visible on the seafloor. Locations shown in Figure 2. (a, b) Orthogonal profiles in the Mwezi Province (MAOR21R002 and MAOR21R075, respectively), (c) NNE–SSW profile in the N'Droundé Province (MAOR21R070) and (d) WNW–ESE profile in the Somali basin north of Zélée–Geyser Bank (MAOR21R001). Gr, graben; V, volcanic edifice; v.e., vertical exaggeration; other abbreviations as in Figure 5.

and e) stands ~600 m above a basal depth of 3355 m. The conical features may contain craters (Cc) or domes (Cd) at their summits, and they typically reach diameters of a few kilometres (up to 4 km) and heights up to 600 m. The reflectivity of these features suggests a hard seabed consisting of rocky outcrops or bedrock lightly covered with sediment [Le Gonidec et al., 2003]. Dredge sample SMR5 from one of these seamounts contained popping rocks (Supplementary Figure S1). We interpreted these features as volcanic edifices [Wessel et al., 2010]. They have the same morphology and geophysical characteristics of volcanic edifices to the EMVC, where popping rocks have been sampled from the summit area and fresh lava flows of Fani Maor'e volcano [Berthod et al., 2021a,b, Feuillet et al., 2021], and features of similar bathymetry and reflectivity on the slopes of the Comoro Islands [Audru et al., 2006, Feuillet et al., 2021, Tzevahirtzian et al., 2021].

The backscatter map contains patches of strong reflectivity, some reaching more than 15 km in extent (Lf on Figure 5e), that have little bathymetric relief (Figure 5d). Generally associated with complex roughness and various shapes (commonly lobes), only one patch has a linear shape (Lf1 on Figure 5e, oriented N160°E). We interpret these patches as lava flows, cropping out on the seafloor or lightly covered by very fine sediment. The shapes and sizes of these lava flows suggest low-viscosity lavas like those observed and sampled during the 2018 eruption east of Mayotte [Berthod et al., 2021a,b, Feuillet et al., 2021].

The bathymetric map displays many large and flat circular domes with smooth seabed that reach elevations of 100 m and diameters of several kilometres (D on Figure 5d). They have no reflectivity signature (Figure 5e). Seismic profiles across these domes show an uplifted and faulted sedimentary cover overlying an abrupt, high-amplitude terminating reflector, often displaying a saucer-shaped profile (Figure 7a,b). These deep reflectors are consistent with shallow magmatic intrusions (sills or laccoliths), which would induce domal uplift and faulting of the overlying sedimentary cover [Kumar et al., 2022, Medialdea et al., 2017, Montanari et al., 2017, Omosanya et al., 2017, and references therein]. We interpret these domes as forced folds by analogy to the description of Paquet et al. [2019] and other sources [Montanari et al., 2017, and references therein]. The analogue modelling of Montanari et al. [2017] shows that the growth of dome-shaped forced folds produces tensional and compressional deformation (normal and reverse faults) in the sedimentary cover. Some of the dome-shaped forced folds in the Mwezi province are accompanied by faults with sub-vertical offsets reaching 10 m (Figure 7a2–a4, b). The disruption of seismic signals under and over the sills may result from the presence of overlying lava flows (acoustic masking) or fluid migration pathways (chimneys) [Masquelet et al., 2022, and references therein].

Most of the volcanic structures, ridges and seamounts are distributed along ~N130°E trend (Figure 5c). In addition, steep escarpments identified on the seafloor are mainly oriented ~N130°E in the centre of the Mwezi province and mainly oriented ~N–S on the northern edge. They are as long as 10 km and have vertical offsets of up to 10 m (see $F_1$, $F_2$, $F_3$ on Figures 5d and 7a3). Some of these escarpments consist of discontinuous, slightly shifted segments (Supplementary Figure S2). Some connect seamounts or domes, and some cut across domes producing vertical offsets of 10–20 m (see $F_1$ cutting domes $D_3$ and $D_4$ on Figure 5d; Supplementary Figure S2). We interpret these escarpments as faults with sub-vertical components.

#### 4.1.2. *The N'Droundé tectono-volcanic province*

The N'Droundé Province covers an area 40 by 100 km (~4000 km$^2$) at the western end of the Comoros Archipelago, north of Grande-Comore, and consists of three subparallel NNW–SSE striking submarine topographic features (Figure 6). The southernmost of these is 60 km long and ~15 km wide, with a summit reaching a depth of 1230 m above a base at 3000 m (feature 1 in Figure 6). Near its southeastern tip, its orientation changes smoothly from N160°E to N130°E. The other two are parallel lines of relief features, oriented N160°E, about 130 km long and averaging 5 km in width at 3100 to 3400 m depth (features 2 and 3 in Figure 6). They have a wide variety of shapes, including narrow ridges and conical edifices some of which have craters or breached craters at their summits (Figure 6d). These are between 1 and 5 km in diameter and a few kilometres long and reach heights of several hundred metres above the surrounding seafloor. The highest seamount rises 735 m to a depth of 2472 m (C1 on Figure 6a). We interpret these seamounts as volcanic edifices. Some dome-shaped forced folds appear in seismic profiles in the N'Droundé Province (D on Figure 7c), but few affect the seafloor and have elevations less than 100 m. Most of them are covered by a thin layer of a chaotic or non-reflective unit (max. 0.1 s TWT; V and S on Figure 7c). Significant deposition of sediments from the Grande-Comore may result in a smoother bathymetry here than in the sediment-starved Mwezi

Province. Alternatively, the N'Droundé seamounts are older than those in the Mwezi Province and have a thicker sedimentary cover. Along with the seamounts are N160°E-trending sub-vertical escarpments a few metres high, forming relays that cut the seafloor (F on Figure 6d).

### 4.2. *Other evidence of recent volcanism in the Comoros Archipelago*

#### 4.2.1. *Submarine volcanic chains*

The Safari volcanic chain between the islands of Anjouan and Mayotte has several volcanic edifices consisting of conical seamounts, ridges, eruptive fissures and lava flows (Figures 3, 4 and 8). The conical seamounts are aligned in a 130°E trend and reach heights of up to 400 m and diameters of 1 to 1.5 km (Figure 8, Supplementary Figure S3). Large high-reflectivity patches near them are interpreted as lava flows, and low-reflectivity patches are interpreted as lava flows covered by a thin layer of sediment (Figure 8b,e). The ridges, which trend NW–SE, are up to several kilometres long, hundreds of metres wide, and 200 m high (R on Figure 8d) and may contain depressions on their summits as deep as about 20 m (Ef1 on Figure 8d–f). One of these ridges transitions into a crack 2 km long with walls up to 20 m high and a high-reflectivity signature (Ef2 on Figure 8e,f). Similar features on Axial Seamount (Juan de Fuca Ridge) have been interpreted as eruptive fissures [Chadwick Jr et al., 2019, Clague et al., 2011].

Other major submarine volcanic chains, such as the Domoni and Chistwani chains (Figures 4 and 9, Supplementary Figure S4) contain volcanic edifices including conical seamounts, ridges and lava flows. The dredged rocks from the SE flank of the Chistwani chain (SMR4) are basaltic [Thinon et al., 2020a]. This widespread array of volcanic structures is evidence of several phases of volcanism that have formed submarine volcanic chains throughout the Comoros Archipelago, both between the islands (Domoni, Chistwani, and Safari chains) and beyond them (Vailheu chain and the EMVC).

#### 4.2.2. *Other volcanic evidence*

Grande-Comore, Mohéli, and Anjouan have rugged insular slopes covered with mass-wasting deposits (detrital cones) and outcropping blocks [Tzevahirtzian et al., 2021; Figure 4]. In the volcanoclastic deposits on the south slope of Grande-Comore, some small conical edifices and various patches with high reflectivity have been identified (Figure 10a).

Unlike the other Comoro Islands, the slopes of Mayotte (except the eastern slope) have a relatively smooth bathymetry and a mottled appearance [Audru et al., 2006, Tzevahirtzian et al., 2021; Figures 4 and 11a]. Major mass-wasting deposits are absent, and only a superficial submarine landslide deposit no higher than 20 m is apparent at the foot of the western flank (Figure 11a,b). In this area, the strongest reflectivity features mainly correspond to canyons and a few small isolated seamounts not covered by sediments (Figure 11c,d). Seismic profiles indicate that the smooth and mottled-bathymetry features correspond to sediment deposits (Figure 11e,f). The sedimentary unit covering the acoustic basement off Mayotte can reach thicknesses of ~0.5 s TWT (roughly 500 m in using 2000 $m \cdot s^{-1}$ velocity) and often covers volcanic edifices. On the western slope of Mayotte, three nearly conical seamounts exhibit a N160°E alignment (Figure 11a,c,d). By creating a barrier for sediment transport on the western slope, these seamounts potentially control the shape of a submarine canyon. A larger number of conical seamounts on the northern slope of Mayotte lie in a N130°E trending corridor between the Safari volcanic chain and Fani Maor'e volcano, in agreement with previous observations [Audru et al., 2006, Famin et al., 2020, Tzevahirtzian et al., 2021].

On the flanks of Zélée Bank, dredging sample SMR1 consists of volcanic rocks [Figure 3; Thinon et al., 2020a]. In the abyssal plain north of Zélée–Geyser banks, 0.2 s TWT high dome-shaped forced folds are observed in the seismic profiles (i.e. ~200 m with 2000 $m \cdot s^{-1}$ velocity; Figure 7d). However, they have no surface expression owing to the thick sediment cover (0.15 to 0.4 s TWT), which is thicker than the cover on the dome-shaped forced folds in the Mwezi (quasi-nonexistent) and N'Droundé Provinces (max. 0.1 s TWT). Dome-shaped forced folds and sills exist also east of Mayotte near Fani Maor'e volcano [Figure 4; Masquelet et al., 2022, Paquet et al., 2019, Rolandone et al., 2022].

To the east of the Comoros Archipelago, we identified evidence of volcanism near the Madagascar margin. A small conical seamount and an 85 $km^2$ high-reflectivity patch with lobe-shaped and roughened facies were identified at the foot of the western slope

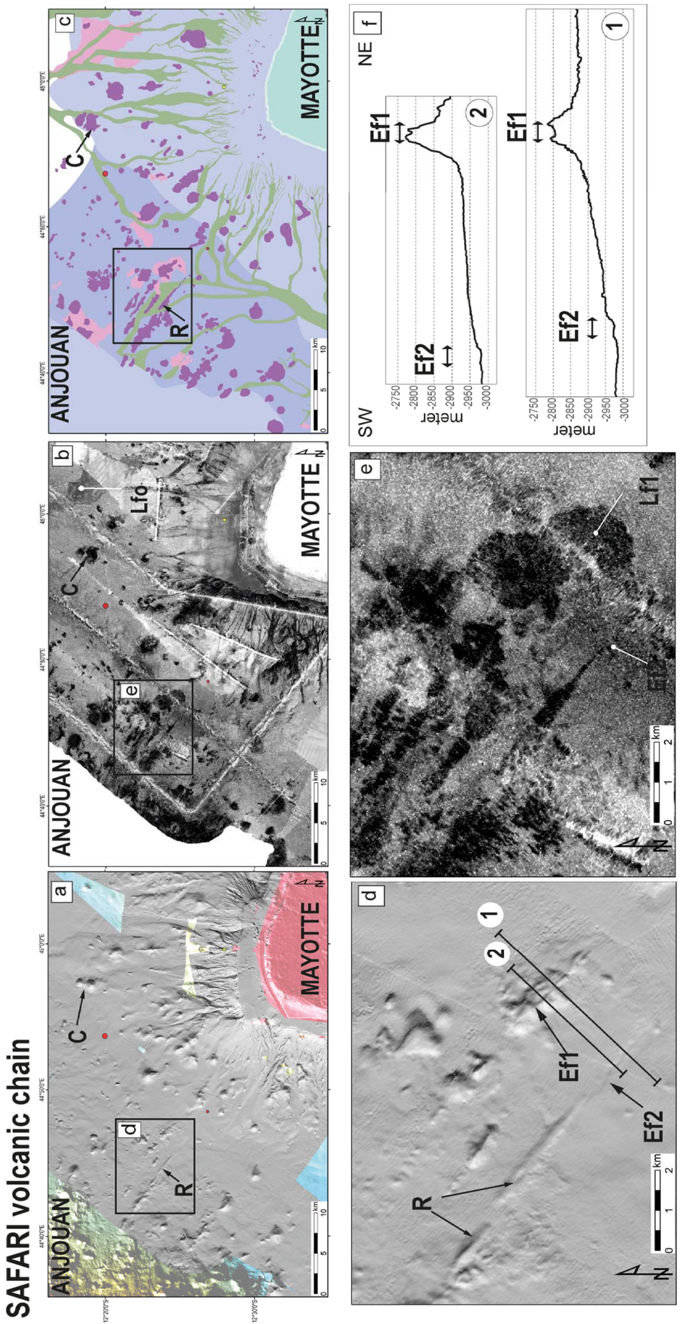


**Figure 8.** (a) Morphology of the Safari volcanic chain between Anjouan and Mayotte islands from SISMAORE MBES bathymetry data (greyscale) and previous surveys (colour, from Tzevahirtzian et al., 2021). (b) Backscatter map. (c) Interpretive map showing conical volcanic edifices (C), ridges (R), lava flows (Lf) and eruptive fissures (Ef). (d) Detail of (a) and (e) detail of (b). (f) Cross-sections across the ridges (R) and crack fissures (Ef2) observed on the seafloor. Supplementary Figure S3 presents oblique views of this area.

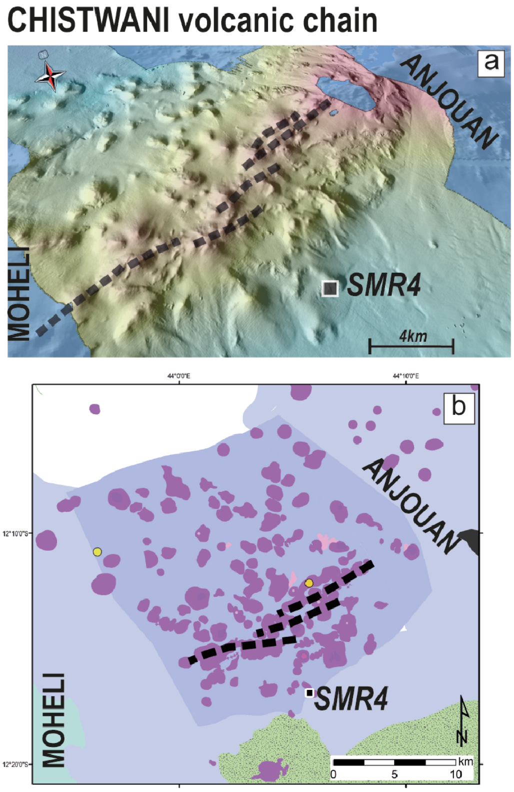


**Figure 9.** (a) Oblique view showing the morphology of the Chistwani volcanic chain between Mohéli and Anjouan. Oriented N 55°E, the chain is narrow (~20 km wide), asymmetric (steeper SE flank), and rises ~500 m (up to 2830 m depth) above the surrounding abyssal plain (3400 m depth). (b) Interpretive map showing volcanic edifices (purple) and lava flows (pink) at the top of the volcanic chain. Black dashed lines indicate en echelon lineaments that may represent a dextral motion.

of Cordelière Bank (Figure 10b). Their morphology and reflectivity suggest that they are recent volcanic structures, in agreement with the evidence of volcanism suggested by dredge sampling in this area [Daniel et al., 1972].

### 4.3. *Distribution of volcanic and tectonic structures in the Archipelago*

The great N'Droundé and Mwezi volcanic provinces in the Somali abyssal plain, together with the four Comoro Islands and the major seafloor volcanic chains around them, constitute a volcanic corridor 600 km long and 200 km wide (Figure 4). Mapping based on the SISMAORE cruise data shows on the seafloor the presence of up to 2200 recent volcanic edifices and lava flows, covering an area of ~5300 km$^2$ (~2500 km$^2$ of cones and ridges and ~2800 km$^2$ of lava flows), plus dome-shaped forced folds on the seafloor with an area larger than 972 km$^2$ throughout the Comoros Archipelago.

At the western end of the Comoros Archipelago, volcanic features are distributed mainly along a N160°E direction (N'Droundé, Grande-Comore, Domoni). To the east of Mohéli and Anjouan, the volcanism is distributed mainly along a N130°E direction (Mwezi, Jumelles, Safari, EMVC). The topography of the Mwezi Province and the two northernmost volcanic chains in the N'Droundé Province is less significant than that of the highest volcanic chains (Jumelles, Domoni, Chistwani, EMVC). The Mwezi and N'Droundé volcanic fields thus may be nascent volcanic chains, younger than the major and polyphase chains elsewhere in the corridor.

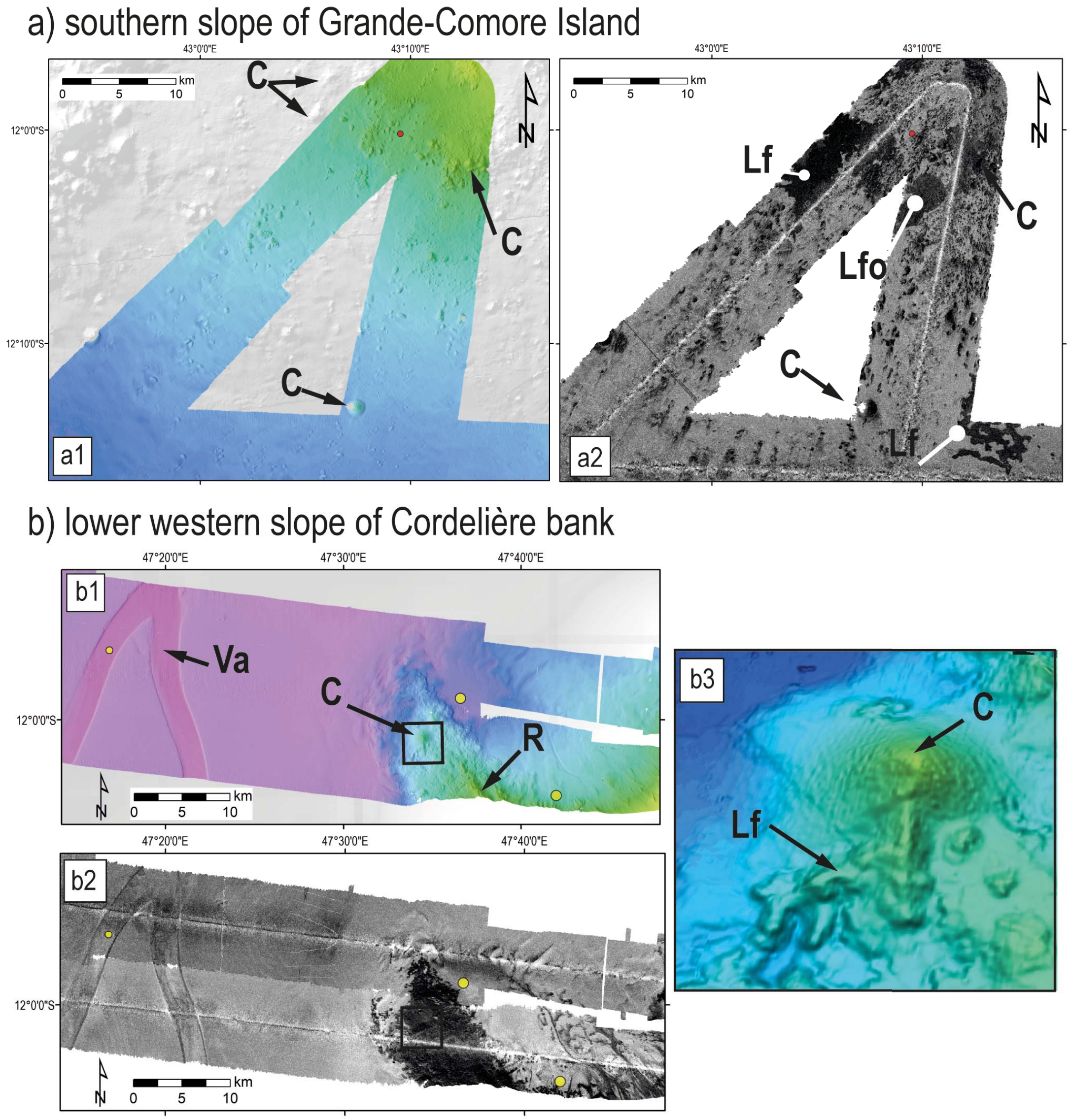


**Figure 10.** Bathymetric (left) and backscatter (right) maps of (a) the southern slope of Grande-Comore Island and (b) the lower western slope of Cordelière Bank. Also shown in (b) is detailed bathymetry of a conical volcanic edifice (C) with a potential lava flow (Lf). Lf0, lava flow with relatively low reflectivity due to sediment cover; other symbols as in Figure 5.

The faults identified in the abyssal plain of the Somali basin and east of Mayotte display two main orientations. Faults trending N130°E are mainly in the Mwezi province, east of Mayotte, and in the Safari volcanic chain, and faults trending N160°E are mainly in the N'Droundé province, in the Domoni volcanic chain and on the western upper slope of Mayotte (Figure 4). North–south to NNE–SSW trending faults exist in the northern part of the Mwezi Province. These sets of faults and volcanic structures, both too recent to be covered by sediments, appear to be coeval as they crosscut each other in many cases. Some of the faults cut the surface of the dome-shaped forced folds or connect two major structures (e.g., fault Lf1 in Figure 5e, Supplementary Figure S2). They can form graben systems (e.g., Figures 5d, 7a2

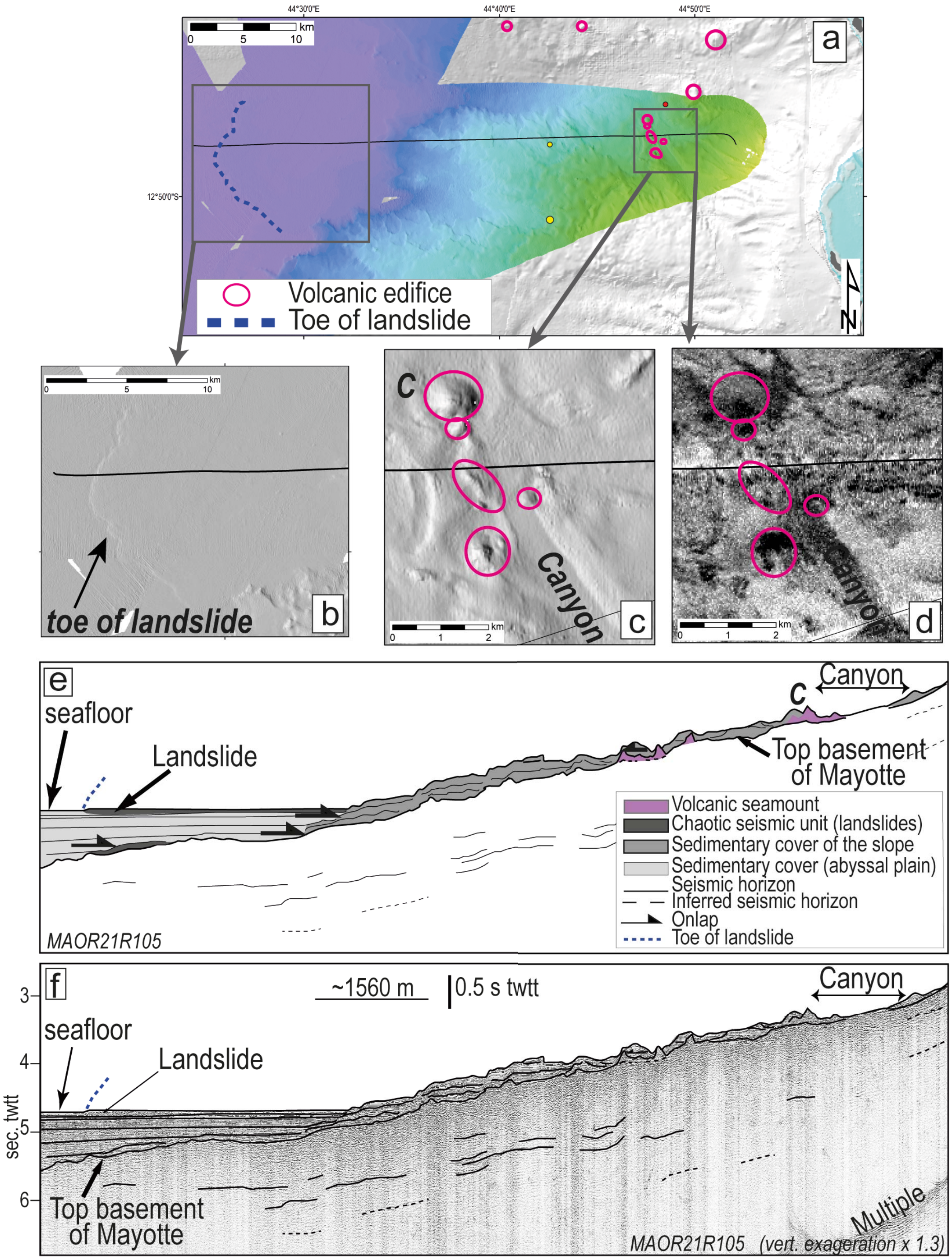


**Figure 11.** (a) Shaded bathymetric map of the western slope of Mayotte with location of MARO21R105 seismic line (black line). Small cluster of volcanic edifices (C) forms a NW–SE trend and outlines the western rim of a major canyon. (b) Detail of (a) showing the mass-wasting deposit—at the foot of the slope (3544–3521 m depth). (c) Detail of (a) showing the N160°E alignment of volcanic cluster. (d) Reflectivity map of the area in (c). (e) Interpreted and (f) migrated 48-channel seismic profile MARO21R105, oriented EW (location in (a)).

and 7a4) or lines of offset segments (e.g., Figure 6c,d). Most of the faults show sub-vertical offsets reaching 20 m, often with a normal component (Figure 7, Supplementary Figure S2). Strike-slip motion could exist, but is not easy to identify in the seismic profiles.

The eastern flank of the Chistwani volcanic chain contains three lines of volcanic edifices and ridges with ENE–WSW (N60°E to N90°E) orientations (Figure 9). Some east-facing scarps are present. These lineaments are arranged en echelon, as if they reflected the influence of a dextral motion.

## 5. Discussion

Our interpretations of bathymetry and backscatter maps and seismic profiles revealed a widespread regional distribution of recent volcanic and tectonic deformation that allows us to propose a geodynamic context for the Comoros Archipelago and address questions about the role of the structural inheritance (Figure 12).

### 5.1. *Tectono-volcanism events in the Comoros Archipelago*

The volcanic and tectonic structures in the abyssal plain rest on a sedimentary sequence ~3 km thick (Figures 7 and 11), in agreement with previous authors [Coffin et al., 1986, Leroux et al., 2020, Masquelet et al., 2022].

In the sediment-starved Mwezi Province (Figures 4 and 5), the near-absence of sediments on lava flows, volcanic edifices, forced folds, and faults suggests that volcano-tectonic activity, though undated, is very recent. The high-reflectivity of these seafloor features is similar to that of the lava flows from the 2018–2021 Fani Maor'e volcano eruption [Deplus et al., 2019, Feuillet et al., 2021]. Moreover, the presence of popping rocks in dredge sample SMR5, in the Mwezi province (Supplementary Figure S1), implies that the residence time of these seafloor basalts has been too short to permit complete degassing. The evidence is consistent with very young volcanic activity in the Mwezi Province. We propose that fresh outcrops and seafloor features represent similarly recent volcanic and tectonic activity throughout the Comoros Archipelago, including in the N'Droundé Province, on the slope of Grand-Comore, in the Safari volcanic chain, at the foot of the Jumelles volcanic chain and on the Cordelière Bank (as shown in purple in Figures 4 and 12). However, no current volcanic eruptions or fluid activity were apparent in the water column acoustic data from the SISMAORE cruise except east of Mayotte [REVOSIMA newsletter, 2021, Thinon et al., 2020b].

There are more lava flows and dome-shaped forced folds visible on the seafloor in the Mwezi Province than in the N'Droundé Province. This difference could be due to magmatic events of differing intensities or ages; however, in the N'Droundé Province, many dome-shaped forced folds and lava flows are covered by as much as 100 m (0.1 s TWT in using 2000 $m \cdot s^{-1}$ velocity) of sedimentary deposits or other volcanic products (Figure 7c). This province receives an abundant sediment supply from wave erosion and coastal hydrodynamic processes at Grande-Comore, whereas the Mwezi Province is more distant from sediment sources.

North of the Zélée–Geyser banks, a significant sedimentary cover onlaps the dome-shaped forced folds (0.15–0.4 s TWT or 100–400 m in using 2000 $m \cdot s^{-1}$ velocity, Figure 7d), hides the surface deformation induced by magmatic intrusions. Even if sedimentation rates differ between the two areas, these forced folds appear to be older than those in the Mwezi province, which disrupt the seafloor. This difference is consistent with the long-term magmatic history of the north Mozambique Channel [Michon et al., 2016], and with the emplacement of the Zélée–Geyser banks, which are older than the Comoro Islands to the west [Leroux et al., 2020]. We suggest that the Mwezi and N'Droundé provinces consist mainly of monogenetic volcanic cones and lava flows whereas submarine volcanic chains (Jumelles, Chistwani and Domoni) and Zelée–Geyser banks are products of a complex evolution and are akin to multiphase constructional structures such as the EVCM [Feuillet et al., 2021, Masquelet et al., 2022] or islands such as Mayotte [e.g., Nehlig et al., 2013]. Based on our comparisons of topographic features and backscatter signatures, we propose that most of the volcanic and tectonic structures in the Mwezi and N'Droundé provinces are younger than those of volcanic chains and Zelée–Geyser banks.

The evidence of widespread recent volcanic activity on submarine volcanic chains and islands (purple shades on Figure 4) suggests the occurrence of

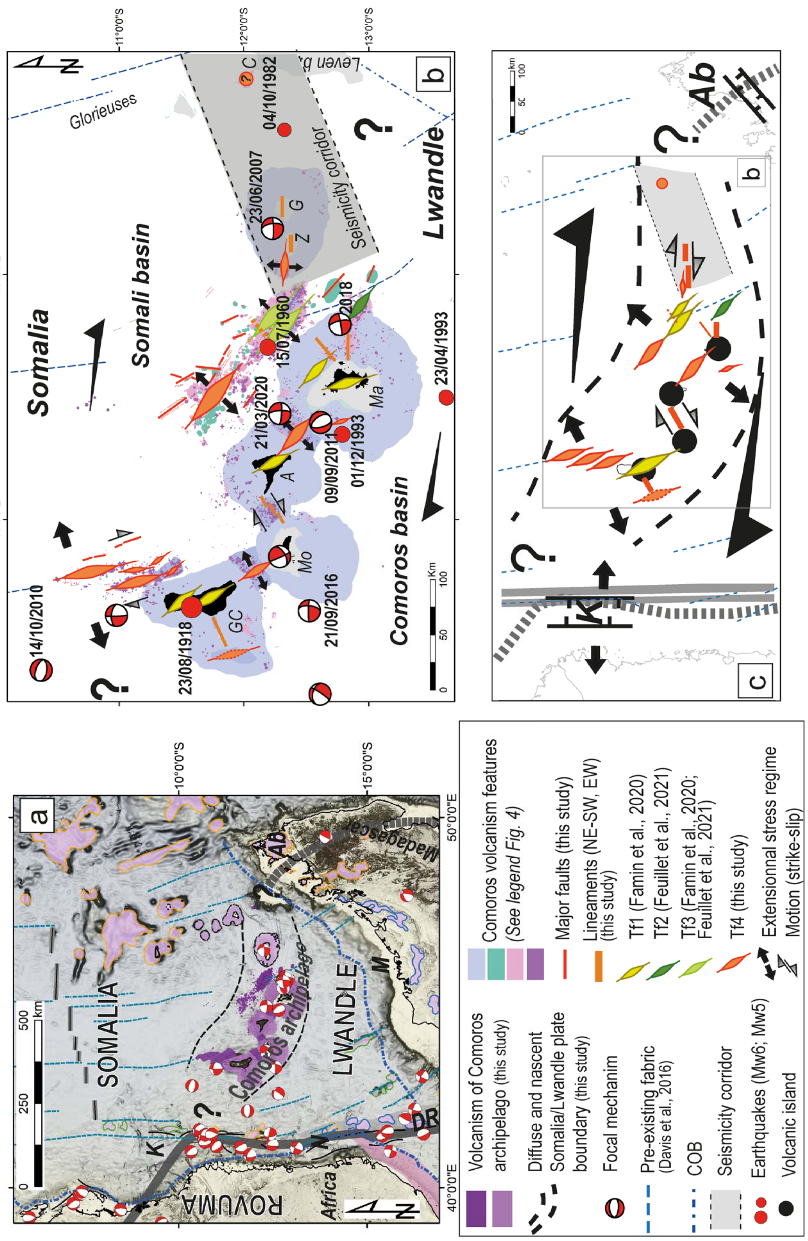


**Figure 12.** (a) Regional geological context of the Comoros Archipelago, including the distribution of recent volcanism and tectonics identified from this study and the proposed diffuse and nascent Somalia–Lwandle plate boundary. See Figure 1 for legend. (b) Geodynamic interpretation of recent tectonic and volcanic structures and the fossil Mesozoic crustal fabric of the study area. Shown are major faults and lineaments from this study as well as tensile fractures from this study (Tf4) and from Famin et al. [2020] and Feuillet et al. [2021] (Tf1, Tf2, Tf3). Locations, focal mechanisms and dates of earthquakes (up to Mw 5) are from Bertil et al. [2021] and references therein and pre-existing crustal fabric, derived from magnetic data, is from Davis et al. [2016]. (c) Regional tectonic setting between the EARS and Madagascar. K, Kerimbas basin; A, Ambilobe basin. Grey dashed lines mark the diffuse, immature Somalia–Lwandle plate boundary.

multiple volcanic events throughout the Comoros Archipelago. The volcanic structures identified on Cordelière Bank (conical edifices and lava flows; Figure 10b) appear to be the products of recent eruptive events from their morphology and strong reflectivity, more recent than those of the Glorieuses Islands [Late Cretaceous according to Leroux et al., 2020]. A pattern of multiple phases separated by periods of quiescence would be similar to that of Mayotte, where volcanic activity occurred between 10.6 and 1.9 Ma and then resumed during the Pleistocene [Bachèlery et al., 2016a, Michon et al., 2016, Pelleter et al., 2014].

These faults and volcanic structures appear to be coeval as they crosscut each other in many instances yet are both too recent to be covered by sediments. Some of the faults form and grow in response to local stress fields caused by magmatic intrusions and eruptions [see Sections 4.1 and 4.2; Figure 7; Montanari et al., 2017]. However, the major fault trends (N130°E and N160°E to N–S) and the alignment of seamounts in the Mwezi and the N'Droundé provinces are consistent with the regional stress field. During the ongoing eruption off Mayotte, magma appears to ascend through NW–SE trending lithospheric structure, consistent with the regional stress field [Berthod et al., 2021b, Feuillet et al., 2021, Lemoine et al., 2020].

### 5.2. *Spatial distribution of deformation and current kinematic context*

From the distribution of recent volcanic and tectonic structures, we identified geologically recent diking events throughout the Comoros Archipelago (Figure 12a), including the Mwezi Province (N130°E), N'Droundé Province (N160°E), Safari volcanic chain (N130°E) and Domoni volcanic chain (N160°E). Figure 12a shows groups of tensile fractures (Tf1–Tf4) corresponding to the main tectono-volcanic provinces and volcanic chains that were identified from the SISMAORE data and previous studies [Famin et al., 2020, Feuillet et al., 2021], as well as major faults and lineaments. These observations suggest the presence of major en echelon tensile fractures and secondary Riedel shears (Figure 12) in the Comoro Islands, Jumelles volcanic chain, Zélée–Geyser banks, and north of Anjouan. Feuillet et al. [2021] also interpreted the EVCM as a tensile fracture. Features with roughly orthogonal (ENE–WSW) azimuths in the Comoros Archipelago, such as those in the Chistwani volcanic chain (Figure 9), may have originated in diking events with right-lateral strike-slip motions.

The shift in the orientation of principal tensile fractures from N160°E in the west to N130°E to E–W in the east suggests a segmentation of the Archipelago (Figure 12). At the western end, the azimuths of the major volcanic structures tend to be parallel to the offshore branches of the EARS, such as the N–S trending Kerimbas graben along the Tanzanian/Mozambican coast [Franke et al., 2015, McGregor, 2015, Mougenot et al., 1986; Figures 1 and 12]. Taken as a whole, seismicity in the Comoros Archipelago outlines a rather narrow deformation zone that changes direction around Mayotte (Figure 12b). On the east, recent seismicity is distributed within an ENE–WSW (N80°E) corridor from west of Jumelles to Madagascar [especially from 2018; Bertil et al., 2021], and on the west it is concentrated in an NW–SE direction to the west of Mayotte. The N80°E trend of the eastern segment is parallel to the ENE–WSW Ambilobe sedimentary basin of northern Madagascar, of Cenozoic age [Piqué et al., 1999, Roig et al., 2012]. The observed tectono-volcanic structures on Zélée–Geyser banks are oriented roughly E–W. The same change in the orientation of tectono-volcanic structures corresponds to a change in the pattern of earthquakes, which are relatively diffuse to the west, where the structures trend from NNW–SSE to NW–SE, and less diffuse to the east, where they form a corridor trending N80°E and the tectono-volcanic structures trend approximately E–W. The few available focal mechanisms support a transtensional stress regime (Figure 12b). The current stress regime is consistent with a NE–SW direction of least stress ($\sigma 3$) and a NW–SE direction of greatest stress ($\sigma 1$), which implies an overall right-lateral deformation pattern that produces en echelon tensile fractures parallel to $\sigma 1$ and perpendicular to $\sigma 3$ in alignment with the principal volcanic chains. The transtensional stress field promotes dikes, as attested by the recent Mayotte eruptions.

The new data presented in this paper show that the recent volcanic and tectonic structures on the seafloor form a corridor some 200 km wide and 600 km long that includes the southern abyssal plain of the Somali Basin and the Comoro Islands from west of Grande-Comore to Madagascar (Figures 4 and 12). Volcanism and faulting are absent on the seafloor in the Comoros basin south of the Comoro Islands. Note that this tectono-volcanic corridor does not closely match the "broad zone of deformation" proposed by Stamps et al. [2021] from GNSS modelling, which extends 1000 km from the Comoros Archipelago, including the northern half of the Lwandle plate, and the Comoros basin. Indeed, the regional GNSS network is not optimally configured [Bousquet et al., 2020] to clearly constrain the regional kinematics. The tectono-volcanic corridor shown in Figure 12 more closely corresponds to the Somalia–Lwandle plate boundary previously proposed by previous studies [e.g., Calais et al., 2006, Famin et al., 2020, Stamps et al., 2021].

In this tectono-volcanic corridor, no major fault systems affect the seafloor like those observed, for example, along the NE–SW Atlantic plate boundary in the Azores region [Sanchez et al., 2019]. The faults in the corridor are small (less than 10 km long with apparent vertical throws no greater than 20 m) and discontinuous (Figures 4 and 12). The absence of large (M6+) earthquakes and the fact that the largest reported events are associated with volcanic events, such as the 1918 eruptions of Karthala in Grande-Comore [Bachèlery et al., 1995, 2016b] and the 2018–2021 offshore Mayotte eruption, are further evidence of the lack of major faults in the Comoros Archipelago. If a dextral transform boundary between the Somalia and Lwandle plates is present in the Comoros Archipelago, the low intensity of deformations suggests that it is very immature or incipient.

### 5.3. *Relationships between plate boundary forces, the role of inheritance and magmatism*

The study area is the locus of interactions between deformation at plate boundaries and intense magmatism.

We propose that the young tectonic and volcanic structures identified in this study mark the location of a diffuse, immature Somalia–Lwandle plate boundary between the EARS and Madagascar (dashed lines in Figures 4 and 12). A recent to current regional regime of dextral transtension explains well the location and orientation of volcanic and tectonic structures like the Mwezi province and the part of the EMVC associated with the active Fani Maor'e volcano. Particularly to the west of Mayotte, these features are well aligned with the pre-existing crustal fabric of the Somalia basin, interpreted from magnetic and gravity data as Mesozoic transform fault zones by Davis et al. [2016] and Phethean et al. [2016] (Figure 12a). We propose that these pre-existing oceanic fracture zones play a role in the distribution of the N–S to N160°E younger seafloor features by acting as weak zones, prone to reactivation in the current regional stress field (dextral shear with NE–SW tension axis or transtension), as Sauter et al. [2018] have established in the northwestern Somali basin. The volcanic complexes of the Comoro Islands appear to be located at intersections between tensile fractures guided by pre-existing fracture zones and NE–SW trending volcanic chains lying nearly parallel to the lithospheric fabric evident from magnetic anomalies in the southern Somali basin. These observations are consistent with a reactivated fossil fabric that guides magma ascent and controls the sites of volcanism on the seafloor.

However, the relationship between young seafloor features and earlier tectonic fabric is less clear east of longitude 44.5°E, from Anjouan to Madagascar. The N160°E trend of free-air gravity anomalies is subdued in this region, and the N130°E and E–W orientations of tectono-volcanic features in the Mwezi Province, the Jumelles and Safari volcanic chains, the EVCM, and the Zélée–Geyser banks are clearly oblique to the N–S to N160°E orientation of the fossil fabric. It may be that the N130°E trending structures have formed in response to the current geodynamic context of an immature plate boundary, independent of the inherited lithospheric structure. However, studies of other regions with heterogeneous lithosphere and active regional and local geodynamic contexts, especially in the Wharton basin in the Indian Ocean [Delescluse and Chamot-Rooke, 2007, Deplus et al., 1998, Hananto et al., 2018, Stevens et al., 2020, and references therein] have reported that the orientations of new and reactivated faults, and of deep and surface structures, may be different. They also suggest that shallow deformations can be influenced by both pre-existing structures and local or regional stress fields. A strong influence of a mantle melting anomaly or mantle convection cannot be excluded [Tsekhmistrenko et al., 2021]. Thus, clarifying the relationship between recent seafloor deformations, fossil fabrics of the oceanic crust, and the presence or absence of oceanic crust under the Comoros Archipelago, requires further work that is being conducted in the framework of the ANR COYOTES project [e.g., Boymond et al., 2022, Masquelet et al., 2022, Rolandone et al., 2022, Thinon et al., 2020a].

## 6. Conclusions

Our SISMAORE cruise has shed light on a hitherto poorly known area around the volcanic Comoros Archipelago. Bathymetric and backscatter data, seismic profiles and dredge samples have revealed up to 2200 volcanic edifices and lava flows on the seafloor of the Comoros Archipelago, in the abyssal plain, on the submarine volcanic chains and on the slopes of the Comoro Islands. Other newly identified features include dome-shaped forced folds linked to sill intrusions in the thick sedimentary cover of the abyssal plain. The majority of these structures are located two great volcanic and tectonic fields in the abyssal plain: the N'Droundé Province, north of Grande-Comore and the Mwezi Province, north of Anjouan and Mayotte. Dredge samples of fresh rich-gas basaltic rocks in the Mwezi Province suggest that volcanic activity, although still undated, is very recent. The Comoro Islands, the major submarine volcanic chains and the N'Droundé and Mwezi provinces are interpreted as tensile fractures associated with diking events, consistent with the current regional tectonic setting of right-lateral transtension. Although the distribution of present-day to Pleistocene tectonic and volcanic structures in the western part of the Comoros Archipelago appears fairly congruent with the pre-existing crustal fabric, in the eastern part the role of inheritance is less clear. The distribution of recent deformation appears mainly compatible with the current kinematic context, with possible influence from the pre-existing crustal fabric and heterogeneities in the lithosphere. A strong influence of a mantle melting anomaly or mantle convection cannot be excluded.

The recent volcanic and tectonic structures, as well as the regional seismicity, are distributed within a corridor at least 200 km wide, including the Comoro Islands and the abyssal plain to their north, that extends 600 km between the EARS and Madagascar. The distribution of volcanic and tectonic structures, and by inference the orientation of major tensile fractures, shifts in segments from a roughly N–S orientation in the west, to N160°E, to N130°E to E–W in the east. The Comoro Islands tend to lie at the junctions between tensile fractures (N160°E and N130°E) and ENE–WSW lineaments. This regional distribution of the recent structures is consistent with seismicity patterns in the Comoros Archipelago.

We interpret the Comoros tectono-volcanic corridor as a marker of the Somalia–Lwandle plate boundary. Although the corridor is prone to episodes of intense volcanism, the low intensity and style of deformation tends to confirm the very immature state of this dextral strike-slip plate boundary.

## Conflicts of interest

Authors have no conflict of interest to declare.

## Acknowledgments

The SISMAORE cruise was mainly funded by the Flotte Océanographique Française and the French geological survey (BRGM). We thank Captains P. Moimeaux and G. Ferrand of R/V *Pourquoi Pas?* and its crews and technicians especially and GENAVIR team for the bathymetry processing and the seismic deployment. Thanks to the BRGM regional department of Mayotte, Ifremer, REVOSIMA and the Délégation interministérielle aux risques majeurs Outremer for their assistance during the COVID health crisis. We also thank the Rectorate of Mayotte and two of its teachers (J. Jacquot, P. Deparis) for their participation, the Mission Sismaoré blog (https://sismaore.ac-mayotte.fr/) and the primary and high school students for the richness of exchanges. Thanks to the laboratory of BRGM for gas analysis and to D. Bertil for discussions on regional seismicity.

This paper is a contribution of the COYOTES (COmores & maYotte: vOlcanisme, TEctonique et Sismicité) and SISMAORE teams. This paper benefited from the previous works of the REVOSIMA community. The reviewers are greatly acknowledged for their comments and recommendations, which helped us to significantly improve an early draft of the manuscript. We also thank M. A. Alden for language editing. The processing and the detailed analysis of these geophysical and geological data are carried out mainly in the framework of the COYOTES project (ANR-19-CE31-0018; https://anr.fr/Projet-ANR-19-CE31-0018) funded by the French Agence Nationale de Recherche and the BRGM.

## Supplementary data

Supporting information for this article is available on the journal's website under https://doi.org/10.5802/crgeos.159 or from the author.

## References

Audru, J.-C., Guennoc, P., Thinon, I., and Abellard, O. (2006). Bathymay : La structure sous-marine de Mayotte révélée par l'imagerie multifaisceaux. *C. R. Géosci.*, 338, 1240–1249.

Bachèlery, P., Ali, D. B., Desgrolard, F., Toutain, J. P., and Coudray, J. (1995). L'éruption phréatique du Karthala (Grande-Comore) en Juillet 1991. *C. R. Acad. Sci. Sér. 2. Sciences de la terre et des planètes*, 320(8), 691–698.

Bachèlery, P. and Coudray, J. (1993). *Carte volcano-tectonique (1/50000e) de la Grande-Comore et notice explicative*. The French Embassy in Moroni, Comores, and The University of La Réunion, St. Denis de La Réunion.

Bachèlery, P. and Hémond, C. (2016). Geochemical and petrological aspects of Karthala volcano. In *Active Volcanoes of the Southwest Indian Ocean*, pages 367–384. Springer, Berlin, Heidelberg.

Bachèlery, P., Lenat, J. F., Di Muro, A., and Michon, L. (2016a). *Active Volcanoes of the Southwest Indian Ocean: Piton de la Fournaise and Karthala*. Springer, Berlin.

Bachèlery, P., Morin, J., Villeneuve, N., Soulé, H., Nassor, H., and Ali, A. R. (2016b). Structure and eruptive history of Karthala volcano. In *Active Volcanoes of the Southwest Indian Ocean*, pages 345–366. Springer, Berlin, Heidelberg.

Berthod, C., Médard, E., Bachèlery, P., Gurioli, L., Di Muro, A., Peltier, A., et al. (2021a). The 2018-ongoing Mayotte submarine eruption: Magma migration imaged by petrological monitoring. *Earth Planet. Sci. Lett.*, 571, article no. 117085.

Berthod, C., Médard, E., Di Muro, A., Hassen Ali, T., Gurioli, L., Chauvel, C., Komorowski, J.-C., et al. (2021b). Mantle xenolith-bearing phonolites and basanites feed the active volcanic ridge of Mayotte (Comoros archipelago, SW Indian Ocean). *Contrib. Mineral. Petrol.*, 176(10), 1–24.

Bertil, D., Mercury, N., Doubre, C., Lemoine, A., and Van der Woerd, J. (2021). The unexpected Mayotte, 2018–2020 seismic sequence: a reappraisal of the regional seismicity of the Comoros. *C. R. Géosci.*, 353(S1), 211–235.

Bertil, D. and Regnoult, J. M. (1998). Seismotectonics of Madagascar. *Tectonophysics*, 294, 57–74.

Bousquet, O., Lees, E., Durand, J., Peltier, A., Duret, A., Mekies, D., et al. (2020). Densification of the Ground-Based GNSS Observation Network in the Southwest Indian Ocean: Current Status, Perspectives, and Examples of Applications in Meteorology and Geodesy. *Front. Earth Sci.*, 8, article no. 566105.

Boymond, P., Feuillet, N., Thinon, I., Scholtès, L., Leroy, S., Rusquet, A., Masquelet, C., and Jacques, E. (2022). Volcano-tectonic interactions within two recently discovered submarine volcanic fields: implication for geodynamics in the Comoros. In *EGU General Assembly 2022, Vienne, Talk*.

Calais, E., Ebinger, C., Hartnady, C., and Nocquet, J. M. (2006). Kinematics of the east African rift from GPS and earthquake slip vector data. *Geol. Soc., Lond. Spec. Publ.*, 259(1), 9–22.

Cesca, S., Letort, J., Razafindrakoto, H. N., Heimann, S., Rivalta, E., Isken, M. P., et al. (2020). Drainage of a deep magma reservoir near Mayotte inferred from seismicity and deformation. *Nat. Geosci.*, 13(1), 87–93.

Chadwick Jr, W. W., Rubin, K. H., Merle, S. G., Bobbitt, A. M., Kwasnitschka, T., and Embley, R. W. (2019). Recent eruptions between, 2012 and, 2018 discovered at west mata submarine volcano (NE Lau Basin, SW Pacific) and characterised by new ship, AUV, and ROV data. *Front. Mar. Sci.*, 6, article no. 495.

Clague, D. A., Paduan, J. B., Caress, D. W., Thomas, H., Chadwick Jr, W. W., and Merle, S. G. (2011). Volcanic morphology of west mata volcano, NE Lau Basin, based on high-resolution bathymetry and depth changes. *Geochem. Geophys. Geosystems*, 12(11), 1–21.

Class, C., Goldstein, S. L., Stute, M., Kurz, M. D., and Schlosser, P. (2005). Grand Comore Island: a well-constrained "low 3He/4He" mantle plume. *Earth Planet. Sci. Lett.*, 233(3–4), 391–409.

Coffin, M. F. and Rabinowitz, P. D. (1987). Reconstruction of Madagascar and Africa: evidence from the Davie Fracture Zone and Western Somali Basin. *J. Geophys. Res.*, 92(B9), 9385–9406.

Coffin, M. F., Rabinowitz, P. D., and Houtz, R. E. (1986). Crustal structure in the western Somali Basin. *Geophys. J. Int.*, 86(2), 331–369.

Counts, J. W., Jorry, S. J., Leroux, E., Miramontes, E., and Jouet, G. (2018). Sedimentation adjacent to atolls and volcano-cored carbonate platforms in the Mozambique Channel (SW Indian Ocean). *Mar. Geol.*, 404, 41–59.

Courgeon, S., Bachélery, P., Jouet, G., Jorry, S. J., Bou, E., Boudagher-Fadel, M. K., Révillon, S., Camoin, G., and Poli, E. (2018). The offshore east African rift system: neo insights from the Sakalaves seamounts (Davie Ridge, SW Indian Ocean). *Terra Nova*, 30(5), 380–388.

Daniel, J., Dupont, J., and Jouannic, C. (1972). Relations Madagascar-Archipel Des Comores (Nord-Est Du Canal De Mozambique): Sur La Nature Volcanique Du Banc Du Leven. *C. R. Acad. Sci. Ser. D: Sci. Naturelles*, 274(12), 1784–1787.

Davis, J. K., Lawver, L. A., Norton, I. O., and Gahagan, L. M. (2016). Neo Somalie basin magnetic anomalies and a plate model for the early Indian Ocean. *Gondwana Res.*, 34, 16–28.

Debeuf, D. (2004). *Etude de l'évolution volcano-structurale et magmatique de Mayotte (Archipel des Comores, Océan Indien): approches structurale, petrographique, geochimique et geochronologique*. PhD thesis, Université De La Réunion. Unpublished.

Delescluse, M. and Chamot-Rooke, N. (2007). Instantaneous deformation and kinematics of the India–Australia Plate. *Geophys. J. Int.*, 168(2), 818–842.

Deplus, C., Diament, M., Hébert, H., Bertrand, G., Dominguez, S., Dubois, J., et al. (1998). Direct evidence of active deformation in the eastern Indian oceanic plate. *Geology*, 26(2), 131–134.

Deplus, C., Feuillet, N., Bachelery, P., Fouquet, Y., Jorry, S., et al. (2019). Early development and growth of a deep seafloor volcano: preliminary results from the MAYOBS Cruises. In *AGU Fall Meeting Abstracts*, volume 2019, pages V43I–0227.

Déprez, A., Doubre, C., Masson, F., and Ulrich, P. (2013). Seismic and aseismic deformation along the East African Rift System from a reanalysis of the GPS velocity field of Africa. *Geophys. J. Int.*, 193(3), 1353–1369.

Deville, E., Marsset, T., Courgeon, S., Jatiault, R., Ponte, J. P., Thereau, E., Jouet, G., Jorry, S. J., and Droz, L. (2018). Active fault system across the oceanic lithosphere of the Mozambique channel: implications for the Nubia–Somalia southern plate boundary. *Earth Planet. Sci. Lett.*, 502, 210–220.

Dofal, A., Fontaine, F. R., Michon, L., Barruol, G., and Tkalčić, H. (2021). Nature of the crust beneath the islands of the Mozambique channel: constraints from receiver functions. *J. African Earth Sci.*, 184, article no. 104379.

Eagles, G. and König, M. (2008). A model of plate kinematics in Gondwana breakup. *Geophys. J. Int.*, 173(2), 703–717.

Famin, V., Michon, L., and Bourhane, A. (2020). The Comoros archipelago: a right lateral transform boundary between the Somalia and Lwandle plates. *Tectonophysics*, 789, article no. 228539.

Feuillet, N., Jorry, S., Crawford, W., Deplus, C., Thinon, I., Jacques, E., Saurel, J.-M., et al. (2021). Birth of a large volcano offshore Mayotte through lithosphere-scale rifting. *Nat. Geosci.*, 14(10), 787–795.

Flower, M. F. J. (1972). Petrology of volcanic rocks from Anjouan, Comores Archipelago. *Bull. Volcanol.*, 36(1), 238–250.

Flower, M. F. J. and Strong, D. F. (1969). The significance of sandstone inclusions in lavas of the Comores Archipelago. *Earth Planet. Sci. Lett.*, 7(1), 47–50.

Foix, O., Aiken, C., Saurel, J. M., Feuillet, N., Jorry, S. J., Rinnert, E., and Thinon, I. (2021). Offshore Mayotte volcanic plumbing revealed by local passive tomography. *J. Volcanol. Geotherm. Res.*, 420, article no. 107395.

Fossum, K., Dypvik, H., Haid, M. H., Hudson, W. E., and van den Brink, M. (2021). Late Jurassic and early Cretaceous sedimentation in the Mandawa Basin, coastal Tanzania. *J. African Earth Sci.*, 174, article no. 104013.

Franke, D., Jokat, W., Ladage, S., Stollhofen, H., Klimke, J., Lutz, R., and Schreckenberger, B. (2015). The offshore east African rift system: structural framework at the toe of a juvenile rift. *Tectonics*, 34(10), 2086–2104.

Gaina, C., Van Hinsbergen, D. J. J., and Spakman, W. (2015). Tectonic interactions between India and Arabia since the Jurassic reconstructed from marine geophysics, ophiolite geology, and seismic tomography. *Tectonics*, 34, 875–906.

Hananto, N., Boudarine, A., Carton, H., Singh, S. C., Avianto, P., Dyment, J., et al. (2018). Evidence of pervasive trans-tensional deformation in the northwestern Wharton Basin in the 2012 earthquakes rupture area. *Earth Planet. Sci. Lett.*, 502, 174–186.

International Seismological Centre (2021). International Seismograph Station Registry (IR). https://doi.org/10.31905/EL3FQQ40.

Jacques, E., Feuillet, N., Aiken, C., Lemoine, A., Crawford, W. C., Deplus, C., et al. (2019). The 2018–2019 Mayotte seismic crisis: evidence of an upper Mantle rifting event? In *AGU Fall Meeting Abstracts*, volume 2019, pages V43I–0221.

Klimke, J. and Franke, D. (2016). Gondwana breakup: no evidence for a Davie fracture zone offshore northern Mozambique, Tanzania and Kenya. *Terra Nova*, 28(4), 233–244.

Klimke, J., Franke, D., Gaedicke, C., Schreckenberger, B., Schnabel, M., Stollhofen, H., and Chaheire, M. (2016). How to identify oceanic crust-evidence for a complex break-up in the Mozambique channel, off east Africa. *Tectonophysics*, 693, 436–452.

Kumar, P. C., Niyazi, Y., Eruteya, O. E., Moscariello, A., Warne, M., Ierodiaconou, D., and Sain, K. (2022). Anatomy of intrusion related forced fold in the offshore Otway Basin, SE Australia. *Mar. Pet. Geol.*, 141, article no. 105719.

Kusky, T., Toraman, E., Raharimahefa, T., and Rasoazanamparany, C. (2010). Active tectonics of the Alaotra–Ankay Graben system, Madagascar: possible extension of Somalian–African diffusive plate boundary? *Gondwana Res.*, 18, 274–294.

Lavayssière, A., Crawford, W. C., Saurel, J. M., Satriano, C., Feuillet, N., Jacques, E., and Komorowski, J. C. (2022). A new 1D-velocity model and absolute locations image the Mayotte seismo-volcanic region. *J. Volcanol. Geotherm. Res.*, 421, article no. 107440.

Le Gonidec, Y., Lamarche, G., and Wright, I. C. (2003). Inhomogeneous substrate analysis using EM300 backscatter imagery. *Mar. Geophys. Res.*, 24(3–4), 311–327.

Leinweber, V. T. and Jokat, W. (2012). The Jurassic history of the Africa–Antarctica corridor—new constraints from magnetic data on the conjugate continental margins. *Tectonophysics*, 530, 87–101.

Lemoine, A., Briole, P., Bertil, D., Roullé, A., Foumelis, M., Thinon, I., et al. (2020). The 2018–2019 seismo-volcanic crisis east of Mayotte, Comoros islands: seismicity and ground deformation markers of an exceptional submarine eruption. *Geophys. J. Int.*, 223(1), 22–44.

Leroux, E., Counts, J. W., Jorry, S. J., Jouet, G., Révillon, S., et al. (2020). Evolution of the Glorieuses seamount in the SW Indian Ocean and surrounding deep Somali Basin since the Cretaceous. *Mar. Geol.*, 427, article no. 106202.

Mahanjane, E. S. (2014). The Davie fracture zone and adjacent basins in the offshore Mozambique margin—a neo insight for the hydrocarbon potential. *Mar. Pet. Geol.*, 57, 561–571.

Masquelet, C., Leroy, S., Delescluse, M., Chamot-Rooke, N., Thinon, I., Lemoine, A., Franke, D., Watremez, L., Werner, P., and Sauter, D. (2022). The east-Mayotte new volcano in the Comoros archipelago: structure and timing of magmatic phases inferred from seismic reflection data. *C. R. Géosci.*, 354(S2), 65–79.

McGregor, D. (2015). History of the development of the east African rift system: a series of interpreted maps through time. *J. African Earth Sci.*, 101, 232–252.

Medialdea, T., Somoza, L., González, F. J., Vázquez, J. T., de Ignacio, C., Sumino, H., et al. (2017). Evidence of a modern deep-water magmatic hydrothermal system in the Canary Basin (eastern central Atlantic Ocean). *Geochem. Geophys. Geosystems*, 18(8), 3138–3164.

Mercury, N., Doubre, C., Lemoine, A., Van Der Woerd, J., Bertil, D., Hoste-Colomer, R., and Battaglia, J. (2022). Onset of a submarine eruption east of Mayotte, Comoros archipelago: the first ten months seismicity of the seismo-volcanic sequence (2018–2019). *C. R. Géosci.*, 354(S2), 105–136.

Michon, L. et al. (2016). The volcanism of the Comoros archipelago integrated at a regional scale. In Bachèlery, P. et al., editors, *Active Volcanoes of the Southwest Indian Ocean*, pages 333–344. Springer, Berlin, Heidelberg.

Michon, L., Famin, V., and Quidelleur, X. (2022). Evolution of the east African rift system from trap-scale to plate-scale rifting. *Earth-Sci. Rev.*, 231, article no. 104089.

Montaggioni, L. F. and Nougier, J. (1981). Les enclaves de roches détritiques dans les Volcans d'Anjouan

(Archipel des Comores), Origine et interprétation dans le cadre de l'évolution du Canal de Mozambique. *Bull. Soc. Géol. Fr.*, 7(6), 595–601.

Montanari, D., Bonini, M., Corti, G., Agostini, A., and Del Ventisette, C. (2017). Forced folding above shallow magma intrusions: insights on supercritical fluid flow from analogue modelling. *J. Volcanol. Geotherm. Res.*, 345, 67–80.

Mougenot, D., Recq, M., Virlogeux, P., and Lepvrier, C. (1986). Seaward extension of the east African rift. *Nature*, 321(6070), 599–603.

Mueller, C. O. and Jokat, W. (2019). The initial Gondwana break-up: a synthesis based on new potential field data of the Africa–Antarctica corridor. *Tectonophysics*, 750, 301–328.

Nehlig, P., Lacquement, F., Bernard, J., Audru, J.-C., Caroff, M., et al. (2013). *Notice Explicative, Carte Géologique France (1/30 000), Feuille Mayotte (1179).* BRGM, Orléans. Carte géologique par Lacquement F., Nehlig P., Bernard J., 2013.

Omosanya, K., Johansen, S., Eruteya, O. E., and Waldmann, N. (2017). Forced folding and complex overburden deformation associated with magmatic intrusion in the Vøring Basin, offshore Norway. *Tectonophysics*, 706–707, 14–34. ISSN 0040-1951.

Paquet, F., Jorry, S., Deplus, C., Le Friant, A., Bernard, J., et al. (2019). The Mayotte seismo-volcanic crisis: characterising a reactivated volcanic ridge from the upper slope to the abyssal plain using multibeam bathymetry and backscatter data. In *AGU Fall Meeting Abstracts*, volume 2019, pages V43I–0219.

Pelleter, A. A., Caroff, M., Cordier, C., Bachèlery, P., Nehlig, P., Debeuf, D., and Arnaud, N. (2014). Melilite-bearing lavas in Mayotte (France): an insight into the mantle source below the Comores. *Lithos*, 208, 281–297.

Phethean, J. J., Kalnins, L. M., van Hunen, J., Biffi, P. G., Davies, R. J., and McCaffrey, K. J. (2016). Madagascar's escape from Africa: a high-resolution plate reconstruction for the western Somali Basin and implications for supercontinent dispersal. *Geochem. Geophys. Geosystems*, 17(12), 5036–5055.

Piqué, A., Laville, E., Chotin, P., Chorowicz, J., Rakotondraompiana, S., and Thouin, C. (1999). L'extension à Madagascar du Néogène à l'Actuel: arguments structuraux et géophysiques. *J. African Earth Sci.*, 28(4), 975–983.

Quidelleur, X., Michon, L., Famin, V., Geffray, M. C., Danišík, M., Gardiner, N., Rusquet, A., and Zakaria, M. G. (2022). Holocene volcanic activity in Anjouan Island (Comoros archipelago) revealed by new Cassignol-Gillot groundmass K–Ar and $^{14}C$ ages. *Quart. Geochronol.*, 67, article no. 101236.

REVOSIMA (Mayotte Volcanological And Seismological Monitoring Network) (2019–2022). Institut de Physique du Globe de Paris (IPGP), Bureau de Recherches Géologiques et Minières (BRGM), Institut Français de Recherche pour l'Exploitation de la MER (IFREMER), Centre National de la Recherche Scientifique (CNRS). Data collection of the Mayotte volcanological and seismological monitoring network (V.1.0). Institut de Physique du Globe de Paris (IPGP).

REVOSIMA newsletter (2021). Bulletin REVOSIMA n°25 (janvier 2021) de l'activité sismo-volcanique à Mayotte. IPGP, Université de Paris, OVPF, BRGM, Ifremer, CNRS, January, 6th, 2021. http://www.ipgp.fr/sites/default/files/ipgp_1er_bulletin_info_sismo_volcanique_mayotte-cor.pdf.

Rinnert, E., Feuillet, N., Fouquet, Y., Jorry, S. J., Thinon, I., and Lebas, E. (2019). MD228/MAYOBS.

Roach, P., Milsom, J., Toland, C., Matchette-Downes, C., Budden, C., Riaroh, D., and Houmadi, N. (2017). Neo evidence supports presence of continental crust beneath the Comoros. In *Pesgb/Hgs Africa Conference, August, 2017*.

Roche, V., Leroy, S., Guillocheau, F., Revillon, S., Ruffet, G., Watremez, L., et al. (2021). The Limpopo Magma-rich transform margin, south Mozambique—2: implications for the Gondwana breakup. *Tectonics*, 40(12), article no. e2021TC006914.

Roche, V. and Ringenbach, J.-C. (2022). The Davie fracture zone: a recorder of continents drifts and kinematic changes. *Tectonophysics*, 823, article no. 229188.

Roig, J.-Y., Tucker, R. D., Peters, S. G., Delor, C., and Théveniaut, H. (2012). Carte géologique de la république de Madagascar à 1 / 1 000 000. Ministère des Mines, PGRM, Antananarivo, République de Madagascar, 1 color sheet.

Rolandone, F., Poort, J., Masquelet, C., Leroy, S., Thinon, I., Lemoine, A., and Paquet, F. (2022). Heat flow measurements in the northern Mozambique channel. *C. R. Géosci.*, 354(S2), 35–46.

Sanchez, G., Merle, R., Hinschberger, F., Thinon, I., and Girardeau, J. (2019). Post-spreading deformation and associated magmatism along the Iberia–Morocco Atlantic margins: insight from submarine volcanoes of the Tore-Madeira Rise. *Mar. Geol.*, 407, 76–93.

Saurel, J. M., Jacques, E., Aiken, C., Lemoine, A., Retailleau, L., Lavayssière, A., et al. (2022). Mayotte seismic crisis: building knowledge in near real-time by combining land and ocean-bottom seismometers, first results. *Geophys. J. Int.*, 228(2), 1281–1293.

Sauter, D., Ringenbach, J. C., Cannat, M., Maurin, T., Manatschal, G., and Mcdermott, K. G. (2018). Intraplate deformation of oceanic crust in the west Somali basin: insights from long-offset reflection seismic data. *Tectonics*, 37, 588–603.

Segoufin, J. and Patriat, P. (1980). Existence d'anomalies Mésozoïques dans le Bassin de Somalie. Implications Pour Les Relations Afrique–Antarctique–Madagascar. *C. R. Acad. Sci. Sér. IIa: Sciences De La Terre Et Des Planètes*, 291b, 85–88.

Senkans, A., Leroy, S., d'Acremont, E., Castilla, R., and Despinois, F. (2019). Polyphase rifting and break-up of the central Mozambique margin. *Mar. Pet. Geol.*, 100, 412–433.

Stamps, D. S., Kreemer, C., Fernandes, R., Rajaonarison, T. A., and Rambolamanana, G. (2021). Redefining east African rift system kinematics. *Geology*, 49(2), 150–155.

Stamps, D. S., Saria, E., and Kreemer, C. (2018). Geodetic strain rate model for the east African rift system. *Sci. Rep.*, 8(1), article no. 732.

Stevens, D. E., McNeill, L. C., Henstock, T. J., Delescluse, M., Chamot-Rooke, N., and Bull, J. M. (2020). A complete structural model and kinematic history for distributed deformation in the Wharton basin. *Earth Planet. Sci. Lett.*, 538, article no. 116218.

Talwani, M. (1962). Gravity measurements on HMS Acheron in south Atlantic and Indian Oceans. *Geol. Soc. Am. Bull.*, 73(9), 1171–1182.

Thinon, I., Lemoine, A., Feuillet, N., Michon, L., Leroy, S., et al. (2020a). ANR COYOTES project (Comoros, maYotte: vOlcanism, TEctonics and Seismicity). In *AGU Fall Meeting Abstracts 2020-Online*, volume 2020, pages V040–0003.

Thinon, I., Leroy, S., and Lemoine, A. (2020b). SISMAORE cruise, RV Pourquoi Pas?

Tsekhmistrenko, M., Sigloch, K., Hosseini, K., and Barruol, G. (2021). A tree of Indo–African mantle plumes imaged by seismic tomography. *Nat. Geosci.*, 14(8), 612–619.

Tzevahirtzian, A., Zaragosi, S., Bachèlery, P., Biscara, L., and Marchès, E. (2021). Submarine morphology of the Comoros volcanic archipelago. *Mar. Geol.*, 432, article no. 106383.

Vormann, M., Franke, D., and Jokat, W. (2020). The crustal structure of the southern Davie Ridge offshore northern Mozambique—a wide-angle seismic and potential field study. *Tectonophysics*, 778, article no. 228370.

Vormann, M. and Jokat, W. (2021). The crustal structure of the Kerimbas basin across the offshore branch of the east African Rift System. *Geophys. J. Int.*, 226(3), 2073–2102.

Weatherall, P., Marks, K. M., Jakobsson, M., Schmitt, T., Tani, S., et al. (2015). A new digital bathymetric model of the world's oceans. *Earth Space Sci.*, 2(8), 331–345.

Wessel, P., Sandwell, D. T., and Kim, S. S. (2010). The global seamount census. *Oceanography*, 23(1), 24–33.

Wright, J. B. and McCurry, P. (1970). The significance of sandstone inclusions in lavas of the Comores Archipalago, M.F.J. Flower and D.F. Strong: (Earth Planet. Sci. Lett. 7 (1969) 47–50). *Earth Planet. Sci. Lett.*, 8, 267–268.

Zinke, J., Reijmer, J. J., Taviani, M., Dullo, W. C., and Thomassin, B. (2005). Facies and faunal assemblage changes in response to the Holocene transgression in the Lagoon of Mayotte (Comoro Archipelago, SW Indian Ocean). *Facies*, 50(3–4), 391–408.

Zinke, J., Reijmer, J. J. G., Thomassin, B. A., Dullo, W. C., Grootes, P. M., and Erlenkeuser, H. (2003). Postglacial flooding history of Mayotte lagoon (Comoro archipelago, southwest Indian Ocean). *Mar. Geol.*, 194(3–4), 181–196.

*Comptes Rendus*
*Géoscience — Sciences de la Planète*
**2022**, Vol. 354, Special Issue S2, p. 35-46
https://doi.org/10.5802/crgeos.130

The Mayotte seismo-volcanic crisis of 2018-2021 in the Comoros archipelago (Mozambique channel) / *La crise sismo-volcanique de 2018-2021 de Mayotte dans l'archipel des Comores (Canal du Mozambique)*

# Heat flow measurements in the Northern Mozambique Channel

## *Mesures de flux de chaleur dans le nord du canal du Mozambique*

**Frédérique Rolandone** [*, a], **Jeffrey Poort** [a], **Charles Masquelet** [a], **Sylvie Leroy** [a], **Isabelle Thinon** [b], **Anne Lemoine** [b] **and Fabien Paquet** [b]

[a] Sorbonne Université, CNRS, Institut des Sciences de la Terre de Paris (ISTeP), Paris, France

[b] Bureau de Recherches Géologiques et Minières (BRGM), Orléans, France

*E-mails:* frederique.rolandone@sorbonne-universite.fr (F. Rolandone), jeffrey.poort@sorbonne-universite.fr (J. Poort), charles.masquelet@sorbonne-universite.fr (C. Masquelet), sylvie.leroy@sorbonne-universite.fr (S. Leroy), i.thinon@brgm.fr (I. Thinon), A.Lemoine@brgm.fr (A. Lemoine), f.paquet@brgm.fr (F. Paquet)

**Abstract.** Heat flow in the Northern Mozambique Channel is poorly constrained, with only a few old measurements indicating relatively low values of 55–62 $mW/m^2$. During the SISMAORE cruise to the Northern Mozambique Channel, we obtained new heat flow measurements at four sites, using sediment corers equipped with thermal probes. Three of the sites yield values of 42–47 $mW/m^2$, confirming low regional heat flow in this area. Our values are consistent with a Jurassic oceanic lithosphere around Mayotte, although the presence of very thin continental crust or continental fragments could also explain the observed heat flow. Our values do not support a regional thermal anomaly and so do not favor a hotspot model for Mayotte. However, at a fourth site located 30 km east of the submarine volcano that appeared in 2018 east of Mayotte, we measured a very high heat flow value of 235 $mW/m^2$, which we relate to the circulation of hot fluids linked to recent magmatic activity.

**Résumé.** Le flux de chaleur dans le nord du canal du Mozambique, basé sur des mesures anciennes et peu nombreuses, est faible (55–62 $mW/m^2$). Durant la campagne à la mer SISMAORE, nous avons obtenu quatre nouvelles mesures de flux de chaleur. Nos mesures donnent des valeurs de 47, 45 et 42 $mW/m^2$ qui confirment un flux de chaleur régional faible. Ces valeurs sont cohérentes avec une lithosphère océanique d'âge Jurassique autour de Mayotte, mais elles peuvent aussi être expliquées par une croûte continentale amincie, ou des enclaves de croûte continentale dans une croûte océanique. Nos faibles valeurs de flux ne sont pas en faveur d'une anomalie thermique régionale ni du modèle point chaud pour expliquer le volcanisme de Mayotte. Cependant, nous avons une mesure de flux,

* Corresponding author.

pour un site à 30 km du volcan sous-marin actif à l'est de Mayotte, qui donne une valeur très élevée de 235 mW/m$^2$, pouvant être reliée à la circulation de fluides chauds.

**Keywords.** Heat flow, Oceanic lithosphere, Volcanism, Northern Mozambique Channel, Comoros archipelago, 2018–2021 Mayotte eruption.

**Mots-clés.** Flux de chaleur, Lithosphère océanique, Volcanisme, Canal du Mozambique, Archipel des Comores, 2018–2021 crise volcanique de Mayotte.

*Published online: 19 December 2022, Issue date: 17 January 2023*

## 1. Introduction

The Northern Mozambique Channel lies between the east coast of Africa and the northern tip of Madagascar, where the Comoros Islands form an archipelago of four volcanic edifices (Figure 1). The volcanic islands are located between the Comoros Basin to the south and the Somali Basin to the north (Figure 1) and their activity started during the Miocene after the Mesozoic opening of the Mozambique Channel. The Somali Basin is considered to be underlain by oceanic crust, based on sonobuoy experiments and reflection seismic data [Coffin et al., 1986, Sauter et al., 2018]. An oceanic nature is also known from magnetic anomalies trending WSW–ENE, which indicate the oldest oceanic crust to be of Jurassic age, about 150 Ma [Rabinowitz et al., 1983, Davis et al., 2016, Phethean et al., 2016]. The age and nature of the crust beneath the Comoros Basin and the archipelago is a matter of ongoing debate. The area has been proposed to contain an abnormal oceanic crust [Talwani, 1962], a thinned continental crust [Roach et al., 2017], or a normal oceanic crust [Klimke et al., 2016]. Based on one receiver function computation, it has been proposed that the Comoros Archipelago may be built on an isolated block of continental crust [Dofal et al., 2021]. The origin of volcanism within the Comoros Archipelago is also the subject of debate, with proposals linking the islands to a mantle plume [the "hotspot" model, e.g., Class et al., 1998], or to a diffuse or incipient tectonic plate boundary [Michon, 2016, Famin et al., 2020, Feuillet et al., 2021].

The remarkable reports of submarine volcanic activity since May 2018 east of Mayotte, at the eastern end of the Comoros Archipelago [Figure 1, Lemoine et al., 2020, Feuillet et al., 2021, Cesca et al., 2020], have stimulated a number of sea and land surveys of the area [e.g., Rinnert et al., 2019, REVOSIMA, 2021]. To better understand the geodynamics of the Northern Mozambique Channel, geophysical and geological data were acquired during the 2020–2021 SISMAORE cruise [Thinon et al., 2020, 2022]. In this article, we focus on heat flow measurements acquired during the SISMAORE cruise at four stations (Figure 1), using a sediment corer equipped with autonomous thermal sensors. We present these measurements and then compare them with the few existing measurements of surface heat flow in the Northern Mozambique Channel [von Herzen and Langseth, 1965], in order to assess models for the nature of the crust and the origin of volcanic activity in this area.

## 2. Heat flow measurements

### 2.1. *Methods*

Heat flow density represents the Earth's heat loss per surface unit and can be obtained from the Fourier law as the product of the vertical temperature gradient and the thermal conductivity of rocks where the gradient is measured. We estimate heat flow using autonomous thermal probes attached to sediment corers with lengths of either 23 m or 12 m. We use four high-precision probes (THP from NKE®) that measure temperature with a precision of 0.005 °C. The four probes are placed along the lower 12 m or 6 m of the 23 m or 12 m core barrels, respectively. The probes measure the water temperature up to the seafloor and then the equilibrium temperature of the sediments after penetration. Because penetration of the probes in the sediment is associated with frictional heating, the temperature is recorded continuously for about ten minutes, which in general is not enough to reach equilibrium but allows its extrapolation. A separate device (S2IP from NKE®) provides pressure and tilt values. Unlike conventional heat flow instruments, thermal conductivity was not measured *in situ*, but aboard the ship on recovered sediment cores using a needle probe instrument (Hukseflux TPSYS02). The measurement method is based on the transient line source method: from the response to a heating step the thermal conductivity

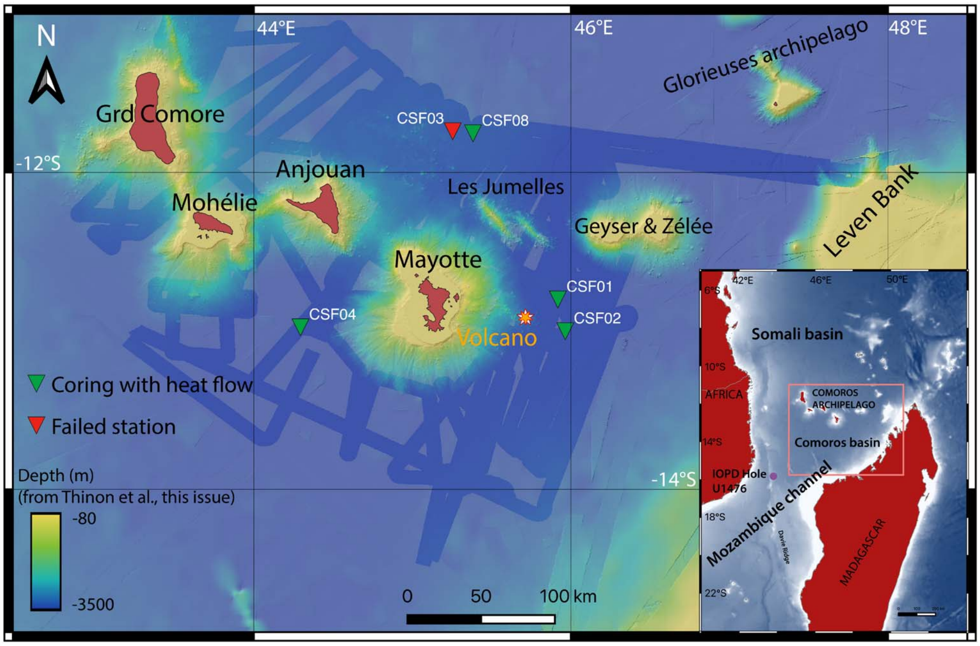


**Figure 1.** Location of heat flow measurements (green triangles) acquired during SISMAORE relative to bathymetric data compilation [Thinon et al., 2022]. A submarine volcano formed during the 2018–2021 eruption (called New Volcano Edifice) is shown with an orange star [Feuillet et al., 2021]. The inset shows the Somali and Comoros basins as well as the location of IODP site U1476.

**Table 1.** Heat flow measurements obtained during the SISMAORE cruise

| Site name | Latitude | Longitude | Water depth (m) | Sediment core length (m) | $n$T | Thermal gradient (mK/m) | $n\lambda$ | Thermal conductivity (W/m/K) | Heat flow (mW/m$^2$) |
|---|---|---|---|---|---|---|---|---|---|
| CSF01 | −12.7958 | 45.9173 | 3540 | 18.2 | 4 | 46.6 | 35 | 1.01 | 47 |
| CSF02 | −12.9965 | 45.9638 | 3525 | 4.0 | 2 | 240.0 | 12 | 0.98 | 235 |
| CSF04 | −12.9708 | 44.2927 | 3546 | 2.6 | 4 | 50.9 | 9 | 0.89 | 45 |
| CSF08 | −11.7472 | 45.3819 | 3417 | 11.0 | 4 | 49.3 | 34 | 0.85 | 42 |

$n$T, number of temperature determinations; $n\lambda$, number of thermal conductivity determinations.

of sediments can be calculated [Von Herzen and Maxwell, 1959, Blum, 1997]. We measured the conductivity at intervals of about 30 cm all along the sediment cores (Table 1).

Analysis of the cores shows that recent sediments include siliciclastic, volcanoclastic, and carbonate components. Sedimentation may affect heat flow by decreasing the temperature gradient as a function of the sedimentation rate [e.g., Manga et al., 2012]. Sedimentation rates are estimated at low values of 2–4 cm/1000 yr (Zaragosi, personal communication), comparable to values of 3 cm/1000 yr at IODP site U1476 [see inset Figure 1; Hall et al., 2017] and of 2–5 cm/1000 yr based on the thickness and estimated ages of sediment layers observed on seismic profiles from SISMAORE cruise [Thinon et al., 2022, Masquelet et al., 2022]. Such low rates of sedimentation imply a negligible heat flow correction [Von Herzen and Uyeda, 1963, Manga et al., 2012].

### 2.2. *Results at four sites*

We measured temperature and thermal conductivity at four sites, using a 23 m corer at sites CSF01 and CSF02 and a 12 m corer at sites CSF04 and CSF08

(Figures 1 and 2, Table 1). The thermal gradient is defined by three or four temperatures at all sites except CSF02, where only two temperatures were measured. We determined the thermal gradient value from a linear regression of the *in-situ* sediment temperature data. Thermal gradients are in the range of 46–51 mK/m, while mean thermal conductivity is in the range 0.85–1.01 W/m/K.

The first two measurements were performed using a 23 m long corer.

CSF01 is located east of Mayotte Island, in the abyssal plain. Good penetration resulted in a sediment core 18.2 m long. A linear thermal gradient is defined by three temperatures, whereas a fourth, higher value at a depth of 16.9 m lies above the linear trend (Figure 2). This value occurs too deep below seafloor to invoke the effect of bottom water temperature variations on sediment equilibrium temperatures [Davis et al., 2003]. We note a change in thermal conductivity at this depth, with values higher than 1.8 W/m/K (Figure 2). The high conductivity values could be related to siliciclastic sediments prone to fluid circulation and potential temperature perturbations [Vasseur et al., 1993, Poort and Polyansky, 2002]. We exclude the high temperature value at 16.9 m to calculate a linear thermal gradient of 46.6 mK/m. Thermal conductivity within the core varies from 0.71 to 1.89 W/m/K, which is high but cannot account for the thermal non-linearity observed at 16.9 m (Figure 2, Table 1). The mean thermal conductivity is 1.01 W/m/K, higher than in the other cores, which is probably related to the low porosity of the sediments. The core contains a record of hemipelagic sedimentation with turbidites. The estimated heat flow for CSF01 is 47 mW/m$^2$.

CSF02 is also located east of Mayotte, on the border of a topographic dome 10 km in diameter and 30 m in height (Figure 3). In volcanic areas, such morphology corresponds to a forced fold, often related to the intrusion of a saucer-shaped sill at depth and described in various geological contexts [Jackson et al., 2013, Medialdea et al., 2017, Magee et al., 2017], as well as experimentally reproduced [Galland, 2012]. On a seismic profile across the site, we observe that doming affects the underlying sedimentary succession (0.5 s twtt) down to an older volcanic layer that affects the seismic image and precludes sill localization (Figure 3). The morphological expression at the seabed suggests that the sill intrusion occurred in recent geological time, though it is not possible to be precise before the validation of a proper local age model. The forced fold lies at the eastern end of a WNW-ESE active volcanic ridge, the Eastern Volcanic Chain of Mayotte, 30 km east of the new Volcano Edifice [orange star in Figure 1; Paquet et al., 2019, Thinon et al., 2022, Deplus et al., 2019, Feuillet et al., 2021]. The penetration of the corer at site CSF02 was low as it stopped on a sandy quartzitic layer (6 m for a 23 m barrel). Due to this low penetration, temperatures were measured at only two sensors. The thermal gradient is therefore poorly constrained, but is very high at 240 mK/m. The mean thermal conductivity is 0.98 W/m/K, yielding a high heat flow of 235 mW/m$^2$ (Figure 2, Table 1), maybe linked to the presence of the underwater volcano (Figure 1) but a new measurement is needed to confirm this hypothesis.

Following loss of the 23 m corer and temperature probes at the site CSF03 (Figure 1), the following heat flow measurements were obtaining using a 12 m corer. CSF04 is located west of Mayotte in the Comoros Basin. Complete penetration of the corer resulted in temperature measurements in all four sensors. Nonetheless, due to technical problems, the sediment core recovered was very short (2.6 m). The thermal gradient is 50.9 mK/m, and the mean thermal conductivity of the shallow sediments is 0.89 W/m/K. Despite the fact that we only determined the conductivity in the upper part of the core, this value falls in the range of the mean conductivities measured at the other sites (Figure 2, Table 1). The heat flow estimate for CSF04 is 45 mW/m$^2$.

CSF08 is located North of Mayotte in the Somali Basin. Good penetration resulted in a core length of 11 m. The sediment core contains a record of hemipelagic sedimentation with turbidites. The thermal gradient is 49.3 mK/m and the mean thermal conductivity is 0.85 W/m/K (Figure 2, Table 1). The heat flow for CSF08 is estimated to be 42 mW/m$^2$.

## 3. Discussion

The heat flow measurements from the SISMAORE cruise add to the regional understanding of the Northern Mozambique Channel, where only six measurements have previously been acquired (Figure 4). Five of these heat flow values come from the NGHF database [Lucazeau, 2019] and date from the

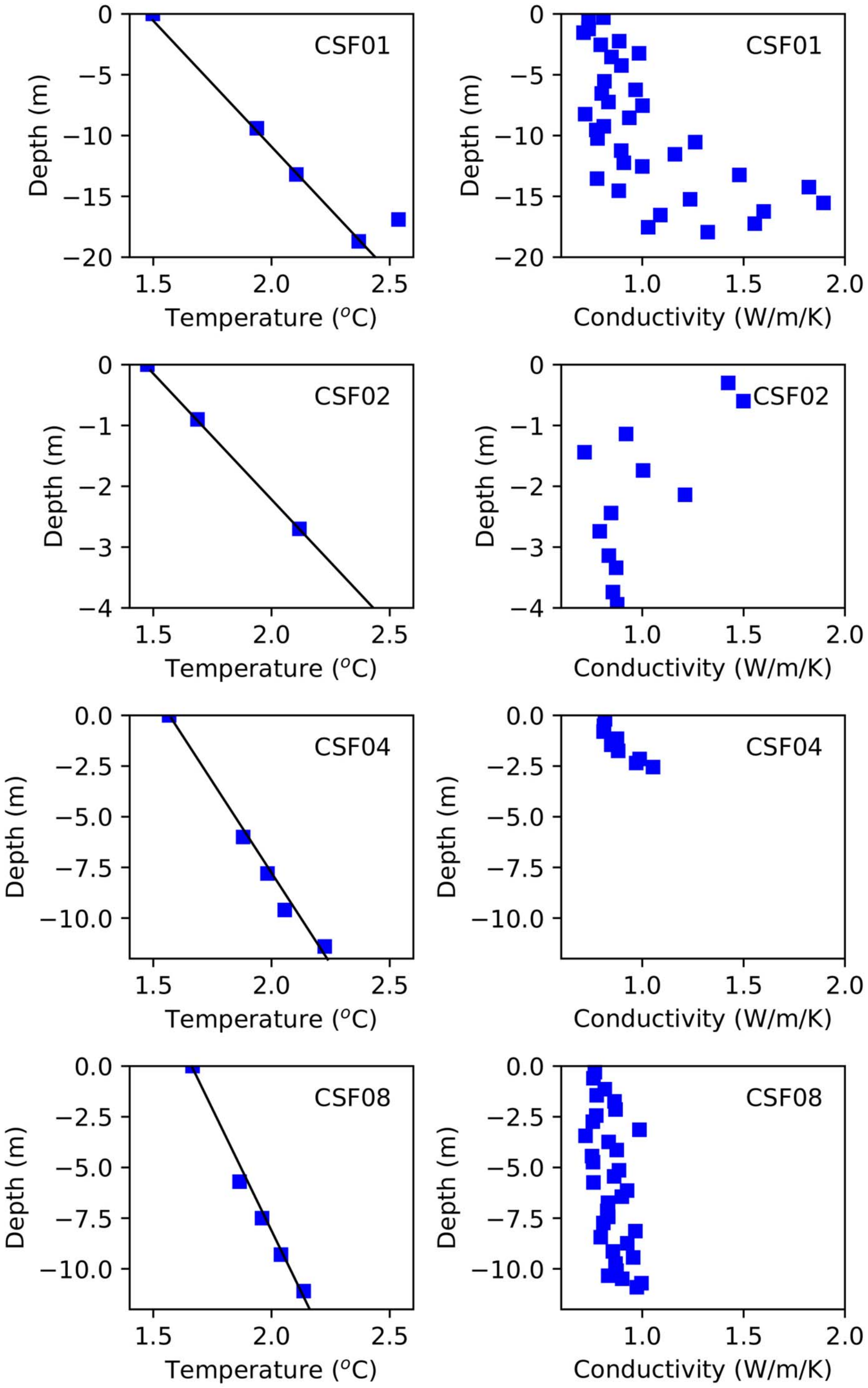


**Figure 2.** Temperature–depth and thermal conductivity–depth profiles obtained at each of the four core locations. The black lines indicate the mean thermal gradient derived from a linear regression of all or selected temperature data and extrapolated to the surface. The bottom water temperature measured before the penetration is also shown.

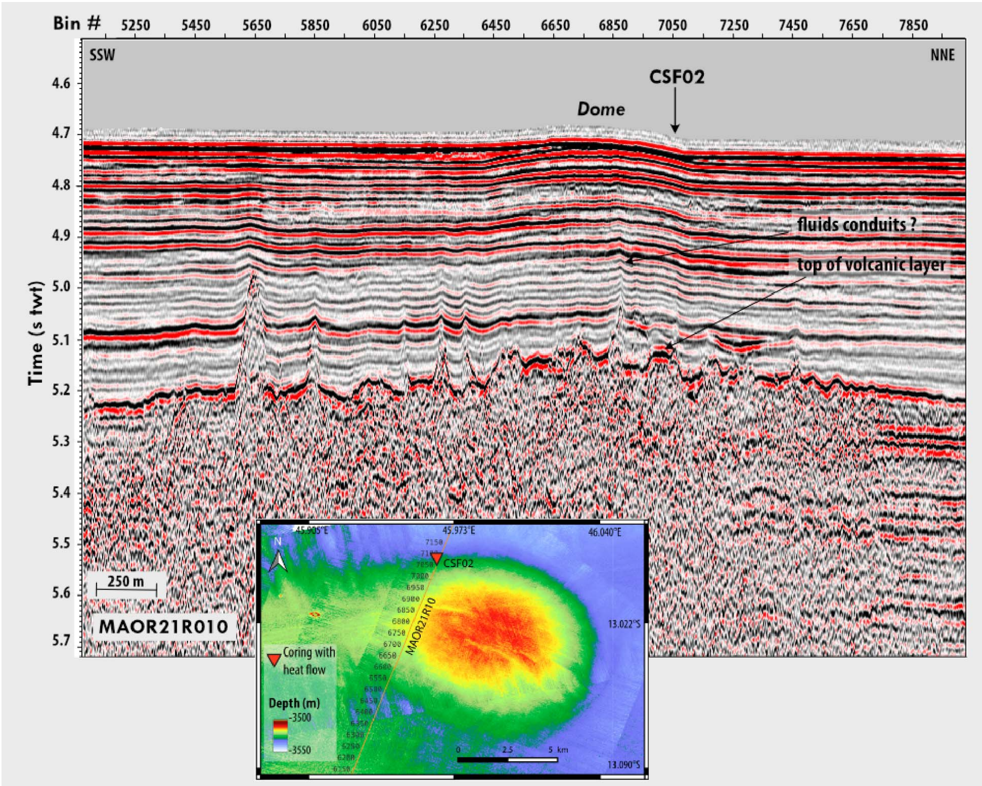


**Figure 3.** Seismic reflection profile crossing the location of core CSF02, at the edge of a topographic dome (location shown on inset bathymetric map). The dome is underlain at depth by a basaltic layer and possible fluid conduits are imaged in the overlying sediment succession that may record the vertical migration of fluids.

1960–70s (Table 2). One is a value of 29 mW/m$^2$ obtained in the Davie Ridge during DSDP leg 25 [Marshall and Erickson, 1974]. Two measurements in the Somali Basin provide heat flow values of 61 and 62 mW/m$^2$ [von Herzen and Langseth, 1965], while two measurements in the Comoros Basin have values of 57 and 55 mW/m$^2$ [von Herzen and Langseth, 1965]. In addition, during the recent PAMELA-MOZ1 cruise [Olu, 2014, Jorry et al., 2020], a heat flow measurement of 37 mW/m$^2$ was obtained close to the Glorieuses Islands (Table 2, Figure 4). Our new measurements include heat flow values of 47, 45 and 42 mW/m$^2$ for sites CSF01, CSF04 et CSF08 (Table 1, Figure 4). Taken together, available data from the Northern Mozambique Channel concur that regional heat flow is low.

It is of interest to compare our heat flow value of 45 mW/m$^2$ at site CSF04 in the Comoros Basin with a nearby older measurement at site V19-100 (Figure 4), which yielded a heat flow of 57 mW/m$^2$ [von Herzen and Langseth, 1965]. Thermal conductivity values at the two sites are similar (0.88 W/m/K versus 0.89 W/m/K, Tables 1 and 2), whereas the thermal gradient is higher for the older measurement (65.2 mK/m versus 50.9 mK/m, Tables 1 and 2). All the older measurements (Figure 4, sites V19 in Table 2) were acquired using a shorter (2 m) corer and only two thermal probes, whereas we used four probes at depths below seafloor greater than 6 m (Figure 2). Therefore, the older gradient measurements have much higher uncertainties because of possible perturbations by deep-ocean temperature variations [Davis et al., 2003] and because of technical bias before 1990 [Lucazeau, 2019]. The higher heat flow at the older sites is much less reliable than the values obtained with more recent and longer instruments.

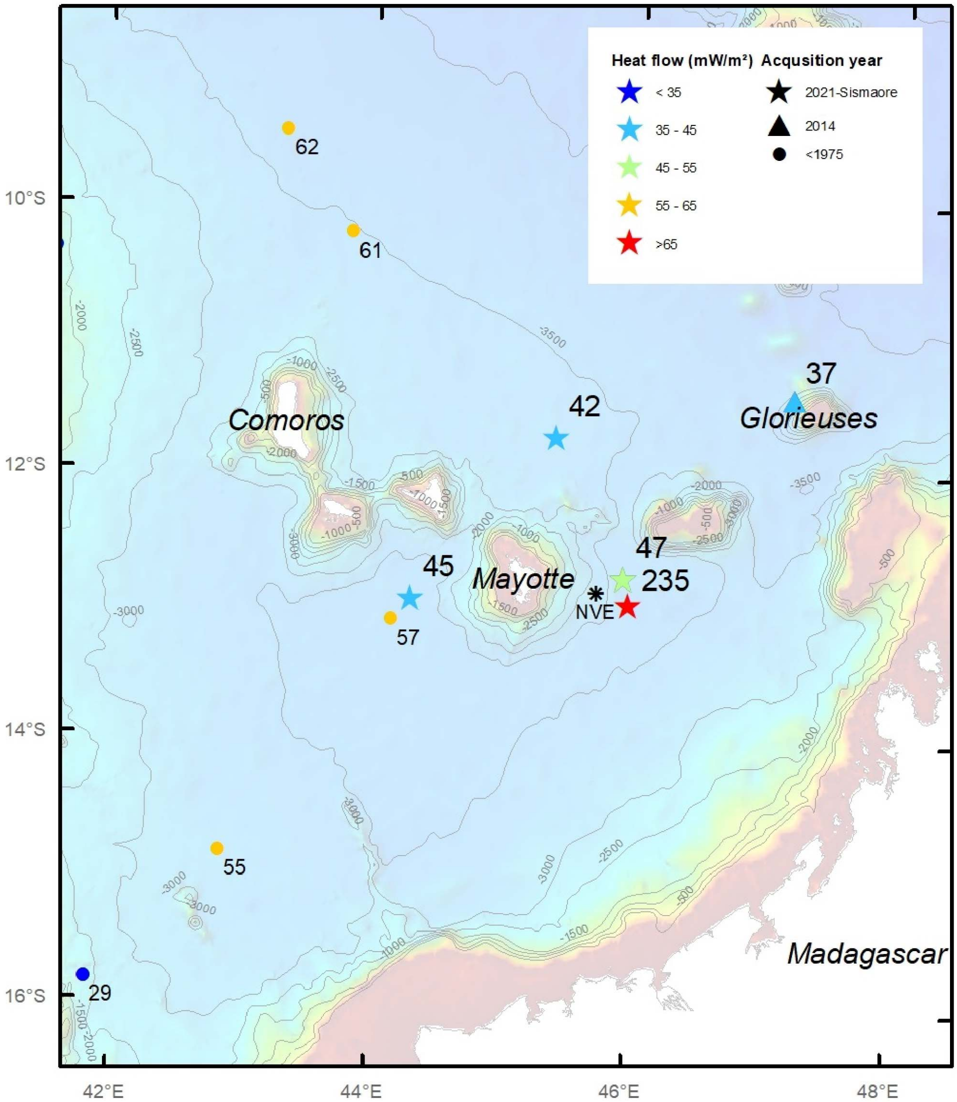


**Figure 4.** Bathymetric map of the Northern Mozambique Channel with previous heat flow measurements (colored dots) from the NGHF database [Lucazeau, 2019] and from the PAMELA-MOZ1 survey (colored triangle) [Olu, 2014], along with our new measurements (colored stars) from SISMAORE. The submarine volcano NVE (New Volcano Edifice) formed during the 2018–2021 eruption is shown with a black star.

**Table 2.** Heat flow measurements from previous cruises

| Site name | Latitude | Longitude | Thermal gradient (mK/m) | Thermal conductivity (W/m/K) | Heat flow (mW/m$^2$) | References |
|---|---|---|---|---|---|---|
| V19-98 | −9.4666 | 43.3167 | 68.8 | 0.90 | 62 | Herzen and Langseth [1965] |
| V19-99 | −10.2317 | 43.8166 | 67.0 | 0.91 | 61 | Herzen and Langseth [1965] |
| V19-100 | −13.1333 | 44.1499 | 65.2 | 0.88 | 57 | Herzen and Langseth [1965] |
| V19-101 | −14.8833 | 42.8500 | 57.8 | 0.96 | 55 | Herzen and Langseth [1965] |
| KSF06 | −11.4400 | 47.1850 | 38.8 | 0.96 | 37 | Olu [2014] |

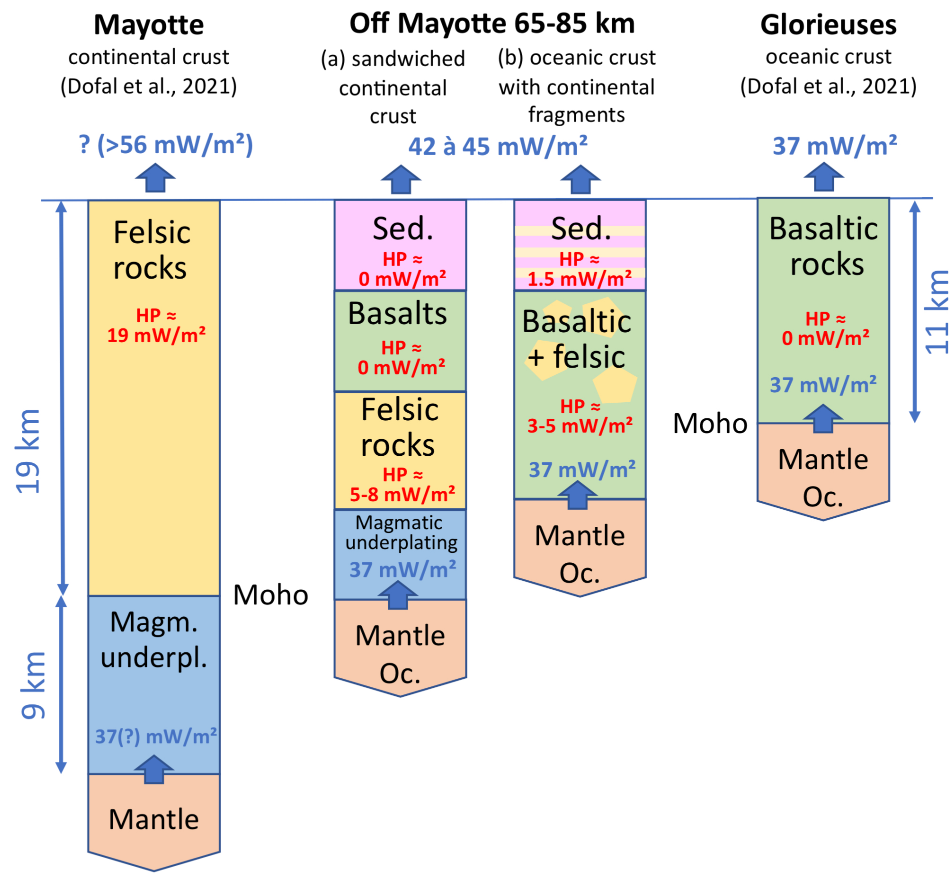


**Figure 5.** Conceptual sketch showing two hypotheses (two central columns) for the structure of the crust off Mayotte, both consistent with heat flow data, compared to heat flow measured or expected for Mayotte and Glorieuses Islands and based on information on crustal structure from Dofal et al. [2021]. See text for discussion.

We obtained heat flow values of 42 mW/m$^2$ in the Somali Basin, of 45 mW/m$^2$ in the Comoros Basin, and of 47 mW/m$^2$ east of Mayotte within the Cormoros archipelago. Our values are consistent with an oceanic lithosphere of Jurassic age, for which the mean global heat flow is $51 \pm 11$ mW/m$^2$ [Lucazeau, 2019]. The value of 37 mW/m$^2$ measured recently near the Glorieuses Islands, where receiver functions indicate an oceanic crust with a shallow Moho at 11 km depth [Dofal et al., 2021], is lower than this global mean, while our new value of 42 mW/m$^2$ in the Somali basin is at the lower end of the global mean. In the Comoros Basin, a comparable value of 45 mW/m$^2$ could also point to an oceanic crust of Jurassic age in this area. However, from a thermal point of view, it is difficult to differentiate old oceanic crust from thinned continental crust for which heat production contribution is weak [e.g., Louden et al., 1997].

From a receiver function study [Dofal et al., 2021], it was proposed that the crust under Mayotte is of continental nature, with a thickness of 19 km, and is underlain by magmatic underplating, with a 27-km deep Moho. This implies a surface heat flow of not less than 56 mW/m$^2$ if we apply a mean value of crustal heat production of 1 μW/m$^3$ [Hasterok and Webb, 2017]: 19 mW/m$^2$ due to radiogenic heat production in the crust and 37 mW/m$^2$ from mantle input as observed at the Glorieuses Islands (Figure 5). Our data indicate lower heat flow values of 42–47 mW/m$^2$ at a 65–85 km distance of Mayotte, implying that the proposed continental block under

Mayotte Island is of limited lateral extent. New investigations by Dofal et al. [2022] do not provide conclusive data on the nature of the crust, that could be either an abnormally thick oceanic crust or a thinned continental crust abandoned during the southern drift of Madagascar.

We propose two hypotheses for the crust off Mayotte that are in agreement with the heat flow observations (Figure 5): (a) a very thin continental crust of felsic material overlain by effusive basalts, and perhaps underplated by basalts as for Mayotte, or (b) a basaltic oceanic crust, with additional heat production from incrusted continental fragments and/or from quartz-rich sediment eroded from the nearby island [Flower and Strong, 1969]. Heat flow data alone cannot discriminate between these models, and the nature of the crust off Mayotte needs to be further defined by seismic methods.

At a regional scale, the low heat flow does not represent a thermal signature that can be readily associated with a mantle plume. A "hotspot" model has been proposed for the Comoros Archipelago [e.g., Class et al., 1998], but has been questioned by several authors [see discussions in Michon, 2016, Thinon et al., 2022]. On the one hand, heat flow anomalies on hot spot swells are small and sometimes difficult to constrain [Bonneville et al., 1997]. On the other hand, our measured heat flow lie in the lower range of those for Jurassic oceanic lithosphere [Hasterok, 2013, Lucazeau, 2019], and thus do not support a regional thermal anomaly.

Since May 2018, submarine volcanic activity has been taking place 50 km east of Mayotte, with evidence of a large eruption [Lemoine et al., 2020, Cesca et al., 2020, Feuillet et al., 2021, Berthod et al., 2021a,b, Deplus et al., 2019]. These studies all indicate a deep reservoir of magma (>55 km depth), which is migrating to the surface through dykes that intrude the lithosphere. Due to slow thermal diffusivity, such a deep reservoir has no present-day thermal signature at the Earth's surface. As exemplified in the Gulf of Aden, to produce a high heat flow at the surface the emplacement of the heat source must be both shallow and recent [Lucazeau et al., 2009]. As presented above, we have one very high heat flow measurement of 235 mW/m$^2$, at site CSF02, 30 km east of the active volcano (NVE, Figure 4). This value is not representative of regional heat flow but is clearly the result of a local process. Several factors suggest that it can be linked with the circulation of hot fluids. The measurement is aligned with the eastern Volcanic Chain of Mayotte and located at the border of a recent forced fold, 10 km wide and 30 m high, underlain by a magmatic sill (Figure 3). Seismic reflection data from SISMAORE cruise show conduit-like features or chimneys within the sedimentary succession that may record the vertical migration of fluids towards the surface in the area [Masquelet et al., 2022]. Upward migration of hot fluids could be triggered by the renewed activity at the east Volcanic Chain of Mayotte, or by the recent sill intrusion that formed the forced fold.

## 4. Conclusions

Heat flow measurements acquired in the Northern Mozambique Channel during the SISMAORE cruise are low, with values in the range of 42–47 mW/m$^2$. Together with other recent data in the area, these values are among the lowest heat flow reported for oceanic lithosphere of Jurassic age. Regarding the nature of the crust, two hypotheses are proposed that fit with the new heat flow data. The first is that off Mayotte the crust is mainly oceanic, with some heat production from felsic continental fragments in the crust or in sedimentary deposits. The second is that the crust is composed of a thin continental layer overlain by effusive basalts and possibly underplated as proposed for Mayotte. The low regional heat flow observed in the Northern Mozambique Channel appears inconsistent with a mantle plume. One very high heat flow value of 235 mW/m$^2$ at a site 30 km east of the active volcano is believed to be related to the circulation of hot fluids induced by the recent magmatic activity, maybe by the latest pulse that started in 2018 east of Mayotte.

## Conflicts of interest

Authors have no conflicts of interest to declare.

## Acknowledgments

We thank Captain P. Moimeaux, the crew and technicians from R/V Pourquoi Pas ? (FOF by Ifremer/GENAVIR), and the scientific COYOTES and SISMAORE teams. The SISMAORE cruise (https://doi.org/10.17600/18001331) is mainly funded by the FOF (Flotte Océanographique Française), the French Geological Survey (BRGM) and the COYOTES project (Agence Nationale de Recherche; ANR-19-CE31-0018). The Pamela-MOZ1 heat-flow measurement comes from the PAMELA project (PAssive Margin Exploration Laboratories) which is a scientific project led by Ifremer and TotalEnergies in collaboration with Université de Bretagne Occidentale, Université Rennes, Sorbonne Université, CNRS and IFPEN. Finally, we thank the two reviewers, Alain Bonneville and Daniel Praeg, for their valuable comments and suggestions.

## References

Berthod, C., Médard, E., Bachèlery, P., Gurioli, L., Di Muro, A., Peltier, A., Komorowski, J.-C., Benbakkar, M., Devidal, J.-L., Langlade, J., Besson, P., Boudon, G., Rose-Koga, E., Deplus, C., Le Friant, A., Bickert, M., Nowak, S., Thinon, I., Burckel, P., Hidalgo, S., Kaliwoda, M., Jorry, S., Fouquet, Y., and Feuillet, N. (2021a). The 2018-ongoing Mayotte submarine eruption: Magma migration imaged by petrological monitoring. *Earth Planet. Sci. Lett.*, 571, article no. 117085.

Berthod, C., Médard, E., Di Muro, A., Hassen Ali, T., Gurioli, L., Chauvel, C., Komorowski, J.-C., Benbakkar, M., Devidal, J.-L., Besson, P., Le Friant, A., Deplus, C., Nowak, S., Thinon, I., Burckel, P., Hidalgo, S., Feuillet, N., Jorry, S., and Fouquet, Y. (2021b). Mantle xenolith-bearing phonolites and basanites feed the active volcanic ridge of Mayotte (Comoros archipelago, SW Indian Ocean). *Contrib. Mineral. Petrol.*, 176(10), 1–24.

Blum, P. (1997). Physical properties handbook: a guide to the shipboard measurement of physical properties of deep-sea cores. Technical Report 26, Ocean Drilling Project. http://www-odp.tamu.edu/publications/tnotes.

Bonneville, A., Von Herzen, R. P., and Lucazeau, F. (1997). Heat flow over Reunion hot spot track: Additional evidence for thermal rejuvenation of oceanic lithosphere. *J. Geophys. Res. Solid Earth*, 102(B10), 22731–22747.

Cesca, S., Letort, J., Razafindrakoto, H. N., Heimann, S., Rivalta, E., Isken, M. P., and Dahm, T. (2020). Drainage of a deep magma reservoir near Mayotte inferred from seismicity and deformation. *Nat. Geosci.*, 13(1), 87–93.

Class, C., Goldstein, S. L., Altherr, R., and Bachèlery, P. (1998). The process of plume–lithosphere interactions in the ocean basins—the case of Grande Comore. *J. Petrol.*, 39(5), 881–903.

Coffin, M. F., Rabinowitz, P. D., and Houtz, R. E. (1986). Crustal structure in the western Somali Basin. *Geophys. J. Int.*, 86(2), 331–369.

Davis, E. E., Wang, K., Becker, K., Thomson, R. E., and Yashayaev, I. (2003). Deep-ocean temperature variations and implications for errors in seafloor heat flow determinations. *J. Geophys. Res.*, 108(B1), article no. 2034.

Davis, J. K., Lawver, L. A., Norton, I. O., and Gahagan, L. M. (2016). Neo Somalie Basin magnetic anomalies and a plate model for the early Indian Ocean. *Gondwana Res.*, 34, 16–28.

Deplus, C., Feuillet, N., Bachelery, P., Fouquet, Y., Jorry, S., Thinon, I., et al. (2019). Early development and growth of a deep seafloor volcano: Preliminary results from the MAYOBS Cruises. In *AGU Fall Meeting Abstracts*, volume 2019. AGU, Washington, D.C. V43I-0227.

Dofal, A., Fontaine, F. R., Michon, L., Barruol, G., and Tkalčić, H. (2021). Nature of the crust beneath the islands of the Mozambique Channel: Constraints from receiver functions. *J. African Earth Sci.*, 184, article no. 104379.

Dofal, A., Michon, L., Fontaine, F. R., Rindraharisaona, E., Barruol, G., and Tkalčić, H. (2022). Imaging the lithospheric structure and plumbing system below the Mayotte volcanic zone. *C. R. Géosci.*, 354(S2), 47–64.

Famin, V., Michon, L., and Bourhane, A. (2020). The Comoros archipelago: a right-lateral transform boundary between the Somalia and Lwandle plates. *Tectonophysics*, 789, article no. 228539.

Feuillet, N., Jorry, S., Crawford, W., Deplus, C., Thinon, I., Jacques, E., Saurel, J.-M., Lemoine, A., Paquet, F., Daniel, R., Gaillot, A., Satriano, C., Peltier, A., Aiken, C., Foix, O., Kowalski, P., Laurent, A., Beauducel, F., Grandin, R., Ballu, V., Bernard, P., Donval, J. P., Géli, L., Gomez, J., Guyader, V., Pelleau, P., Rinnert, E., Besançon, S., Bertil, D., Lemarchand, A., and Van Der Woerd, J. (2021). Birth of a large volcanic edifice offshore Mayotte via lithosphere-scale dyke intrusion. *Nat. Geosci.*, 14(10), 787–795.

Flower, M. F. J. and Strong, D. F. (1969). The significance of sandstone inclusions in lavas of the Comores archipelago. *Earth Planet. Sci. Lett.*, 7(1), 47–50.

Galland, O. (2012). Experimental modelling of ground deformation associated with shallow magma intrusions. *Earth Planet. Sci. Lett.*, 317–318, 145–156.

Hall, I. R., Hemming, S. R., and LeVay, L. J. (2017). South African climates (Aguhlas LGM Density profile). In *Proceedings of the International Ocean Discovery Program*, volume 361.

Hasterok, D. (2013). A heat flow based cooling model for tectonic plates. *Earth Planet. Sci. Lett.*, 361, 34–43.

Hasterok, D. and Webb, J. (2017). On the radiogenic heat production of igneous rocks. *Geosci. Front.*, 8(5), 919–940.

Jackson, C. A.-L., Schofield, N., and Glenkov, B. (2013). Geometry and controls on the development of igneous sill-related forced folds: A 2-D seismic reflection case study from offshore southern Australia. *GSA Bull.*, 125, 1874–1890.

Jorry, S. J., Jouet, G., Edinger, E. N., Toucanne, S., Counts, J. W., Miramontes, E., Courgeon, S., Vázquez Riveiros, N., Le Roy, P., and Camoin, G. F. (2020). From platform top to adjacent deep sea: New source-to-sink insights into carbonate sediment production and transfer in the SW Indian Ocean (Glorieuses archipelago). *Mar. Geol.*, 423, article no. 106144.

Klimke, J., Franke, D., Gaedicke, C., Schreckenberger, B., Schnabel, M., Stollhofen, H., et al. (2016). How to identify oceanic crust—evidence for a complex break-up in the Mozambique Channel, Off East Africa. *Tectonophysics*, 693, 436–452.

Lemoine, A., Briole, P., Bertil, D., Roullé, A., Foumelis, M., Thinon, I., Raucoules, D., de Michele, M., Valty, P., and Hoste Colomer, R. (2020). The 2018–2019 seismo-volcanic crisis east of Mayotte, Comoros islands: seismicity and ground deformation markers of an exceptional submarine eruption. *Geophys. J. Int.*, 223(1), 22–44.

Louden, K. E., Sibuet, J. C., and Harmegnies, F. (1997). Variations in heat flow across the ocean—continent transition in the Iberia abyssal plain. *Earth Planet. Sci. Lett.*, 151(3–4), 233–254.

Lucazeau, F. (2019). Analysis and mapping of an updated terrestrial heat flow data set. *Geochem. Geophys. Geosyst.*, 20, 4001–4024.

Lucazeau, F., Leroy, S., Autin, J., Bonneville, A., Goutorbe, B., Watremez, L., d'Acremont, E., Düsünur, D., Rolandone, F., Huchon, P., Bellahsen, N., and Tuchais, P. (2009). Post-rift volcanism and high heat-flow at the ocean–continent transition of the eastern Gulf of Aden. *Terra Nova*, 21(4), 285–292.

Magee, C., Bastow, I. D., van Wyk de Vries, B., Jackson, C. A.-L., Hetherington, R., Hagos, M., and Hoggett, M. (2017). Structure and dynamics of surface uplift induced by incremental sill emplacement. *Geology*, 45(5), 431–434.

Manga, M., Hornbach, M. J., Le Friant, A., Ishizuka, O., Stroncik, N., Adachi, T., et al. (2012). Heat flow in the Lesser Antilles island arc and adjacent back arc Grenada basin. *Geochem. Geophys. Geosyst.*, 13(8), article no. Q08007.

Marshall, B. V. and Erickson, A. J. (1974). Heat flow and thermal conductivity measurements, Leg 25, Deep Sea Drilling Project. In *Initial Reports of the Deep Sea Drilling Project Covering Leg 25 of the Cruises of the Drilling Vessel Glomar Challenger, Port Louis, Mauritius to Durban, South Africa*, volume 25, pages 349–355.

Masquelet, C., Leroy, S., Delescluse, M., Chamot-Rooke, N., Thinon, I., Lemoine, A., Franke, D., Watremez, L., and Werner, P., Sauter and SISMAORE team. (2022). The East-Mayotte new volcano in the Comoros archipelago: structure and timing of magmatic phases inferred from seismic reflection data. *C. R. Géosci.*, 354(S2), 65–79.

Medialdea, T., Somoza, L., Gonzalez, F. J., Vazquez, J. T., de Ignacio, C., Sumino, H., Sanchez-Guillamon, O., Orihashi, Y., Leon, R., and Palomino, D. (2017). Evidence of a modern deep water magmatic hydrothermal system in the Canary Basin (eastern central Atlantic Ocean). *Geochem. Geophys. Geosyst.*, 18, 3138–3164.

Michon, L. (2016). The volcanism of the Comoros archipelago integrated at a regional scale. In Bachelery, P. et al., editors, *Active Volcanoes of the Southwest Indian Ocean*, pages 333–344. Springer, Berlin, Heidelberg.

Olu, K. (2014). PAMELA-MOZ01 cruise, L'Atalante R/V.

Paquet, F., Jorry, S., Deplus, C., Le Friant, A., Bernard, J., Bermell-Fleury, S., Feuillet, N., Gaillot, A., Guérin, C., and Thinon, I. (2019). The Mayotte seismo-volcanic crisis: characterizing a reactivated volcanic ridge from the upper slope to the abyssal plain using multibeam batymetry and backscatter data. In *AGU Fall Meeting Abstracts*. AGU, Washington, D.C.

Phethean, J. J., Kalnins, L. M., van Hunen, J., Biffi, P. G., Davies, R. J., and McCaffrey, K. J. (2016). Madagascar's escape from Africa: A high-resolution plate reconstruction for the Western Somali Basin and implications for supercontinent dispersal. *Geochem. Geophys. Geosyst.*, 17(12), 5036–5055.

Poort, J. and Polyansky, O. (2002). Heat transport by groundwater flow during the Baikal rift evolution. *Tectonophysics*, 351(1–2), 75–89.

Rabinowitz, P. D., Coffin, M. F., and Falvey, D. (1983). The separation of Madagascar and Africa. *Science*, 220(4592), 67–69.

REVOSIMA (Mayotte Volcanological And Seismological Monitoring Network) (2021). Institut de Physique du Globe de Paris (IPGP), Bureau de Recherches Géologiques et Minières (BRGM), Institut Français de Recherche pour l'Exploitation de la MER (IFREMER), Centre National de la Recherche Scientifique (CNRS). Data collection of the Mayotte volcanological and seismological monitoring network (V.1.0). Institut de Physique du Globe de Paris (IPGP).

Rinnert, E., Feuillet, N., Fouquet, Y., Jorry, S., Thinon, I., and Lebas, E. (2019). MD 228/MAYOBS.

Roach, P., Milsom, J., Toland, C., Matchette-Downes, C., Budden, C., Riaroh, D., and Houmadi, N. (2017). New evidence supports presence of continental crust beneath the Comoros: Pesgb. In *Hgs Africa Conference*.

Sauter, D., Ringenbach, J. C., Cannat, M., Maurin, T., Manatschal, G., and Mcdermott, K. G. (2018). Intraplate deformation of oceanic crust in the west Somalie Basin: Insights from long-offset reflection seismic data. *Tectonics*, 37, 588–603.

Talwani, M. (1962). Gravity measurements on HMS Acheron in south Atlantic and Indian Oceans. *Geol. Soc. Am. Bull.*, 73(9), 1171–1182.

Thinon, I. et al. (2022). Volcanism and tectonics unveiled between the EARS and Madagascar: toward a better understanding of the geodynamics of the Comoros archipelago. *C. R. Géosci.*, 354(S2), 7–34.

Thinon, I., Leroy, S., and Lemoine, A. (2020). SISMAORE cruise, RV Pourquoi Pas?

Vasseur, G., Demongodin, L., and Bonneville, A. (1993). Thermal modelling of fluid flow effects in thin-dipping aquifers. *Geophys. J. Int.*, 112(2), 276–289.

Von Herzen, R. and Maxwell, A. E. (1959). The measurement of thermal conductivity of deep-sea sediments by a needle-probe method. *J. Geophys. Res.*, 64(10), 1557–1563.

von Herzen, R. P. and Langseth, M. G. (1965). Present status of oceanic heat flow measurements. *Phys. Chem. Earth*, 6, 385–407.

Von Herzen, R. P. and Uyeda, S. (1963). Heat flow through the eastern Pacific Ocean floor. *J. Geophys. Res.*, 68(14), 4219–4250.

*Comptes Rendus*
*Géoscience — Sciences de la Planète*
**2022**, Vol. 354, Special Issue S2, p. 47-64
https://doi.org/10.5802/crgeos.190

The Mayotte seismo-volcanic crisis of 2018-2021 in the Comoros archipelago (Mozambique channel) / *La crise sismo-volcanique de 2018-2021 de Mayotte dans l'archipel des Comores (Canal du Mozambique)*

# Imaging the lithospheric structure and plumbing system below the Mayotte volcanic zone

**Anthony Dofal** [*, a, b], **Laurent Michon** [a, b], **Fabrice R. Fontaine** [b, c], **Elisa Rindraharisaona** [a, b], **Guilhem Barruol** [d] and **Hrvoje Tkalčić** [e]

[a] Université de La Réunion, Laboratoire Géosciences Réunion, F-97744 Saint Denis, France

[b] Université Paris Cité, Institut de physique du globe de Paris, CNRS, F-75005 Paris, France

[c] Observatoire Volcanologique et Sismologique de la Martinique, Institut de physique du globe de Paris, F-97250 Fonds Saint Denis, France

[d] Université Grenoble Alpes, CNRS, IRD, Grenoble INP, IGE, 38000 Grenoble, France

[e] Research School of Earth Sciences, The Australian National University, Canberra, ACT 2601, Australia

*Current address:* Parc National de La Réunion, PNRun, F-97431 La Plaine Des Palmistes, France (A. Dofal)

*E-mails:* anthony.dofal@univ-lille.fr, anthony.dofal@reunion-parcnational.fr (A. Dofal), laurent.michon@univ-reunion.fr (L. Michon), frfont@ipgp.fr (F. R. Fontaine), elisa.rindraharisaona@univ-reunion.fr (E. Rindraharisaona), Guilhem.Barruol@univ-grenoble-alpes.fr (G. Barruol), hrvoje.tkalcic@anu.edu.au (H. Tkalčić)

**Abstract.** Teleseismic receiver-functions and Rayleigh-wave dispersion curves are jointly inverted for quantifying $S$-wave velocity profiles beneath the active volcanic zone off Mayotte. We show that the lithosphere in the east-northeast quadrant is composed of four main layers, interpreted as the volcanic edifice, the crust with underplating, the lithospheric mantle, and the asthenosphere, the latter two presenting a main low-velocity zone. The depths of the *old* (10–11 km) and *new Moho* (28–31 km) coincide with the two magma reservoirs evidenced by recent seismological and petrological methods. We propose that the main magma reservoir composed of mush with an increasing amount of liquid extends down to 54 km depth. This magma storage develops from a rheological contrast between the ductile lower and brittle upper lithospheric mantle and accounts for most of the volcanic eruption-related seismicity. Finally, the abnormally small thickness of the lithospheric mantle (33 km) is likely a result of a thermal thinning since the onset of Cenozoic magmatism.

**Keywords.** Mayotte, Comoros archipelago, Magmatic plumbing system, Lithosphere, Receiver function, Joint inversion, Rheological controls.

*Published online: 19 December 2022, Issue date: 17 January 2023*

* Corresponding author.

## 1. Introduction

The Comoros archipelago is composed of four volcanic islands displaying contrasted morphologies from west to east, with the high-standing, uneroded relief of Grande Comore and the presently active Karthala volcano to the west, to the low-lying island of Mayotte surrounded by a vast lagoon to the east (Figure 1A). This morphology, typical of the evolution of volcanoes along a hot-spot track [Darwin, 1842, Peterson and Moore, 1987], combined with the increase of the estimated age of volcanism from west to east [Emerick and Duncan, 1982] and the isotopic signature of the lavas emitted at Karthala [Class et al., 1998, 2005], have been the main arguments for proposing that the volcanism of the Comoros archipelago could result from a fixed mantle plume [Emerick and Duncan, 1982] rising beneath a moving tectonic plate, as initially proposed by Morgan [1971]. However, the trend of the volcanic track is not aligned with the recent plate motion vector [Müller et al., 1993, Morgan and Morgan, 2007]. In addition, the recent growth of a submarine volcano east of Mayotte since July 2018 [Cesca et al., 2020, Lemoine et al., 2020, Feuillet et al., 2021], at the opposite end of the present-day active Karthala volcano, can hardly be explained with a simple model of punctual and vertically rising mantle plume piercing a moving lithosphere. It has also been recently shown that abundant Holocene eruptions occurred in Anjouan Island, 130 km east of the putative hotspot expression [Quidelleur et al., 2022]. Altogether, these elements bring credit to tectonic interpretations which propose that the whole archipelago either results from the reactivation of lithospheric transform zones [Nougier et al., 1986], or grew at the right-lateral transform boundary between the Somali and Lwandle plates [Famin et al., 2020, Michon et al., 2022].

The seismo-volcanic crisis east of Mayotte initiated in May 2018, preceded the onset of the island eastward subsidence and was associated with a complex seismicity [Cesca et al., 2020, Lemoine et al., 2020, Feuillet et al., 2021]. The dominant strike-slip earthquake focal mechanisms of the largest events agree well with a control of the maximum NW–SE oriented horizontal stress in the magma intrusion process [Famin et al., 2020, Lemoine et al., 2020]. Furthermore, the large number of seismic events located 5 to 40 km east of the island at a depth of 20 to 45 km below sea level (REVOSIMA report; 2021), concentrated in three independent clusters, has been recently interpreted as evidencing a poly-stage magma ascent through successive lithospheric magma reservoirs [Berthod et al., 2021a] and a diking episode before the eruption [Cesca et al., 2020, Lemoine et al., 2020, Feuillet et al., 2021]. Petrological and geochemical analyses of erupted lavas indicate that the magmas of Mayotte would be fed by mantle partial melting in the spinel/garnet to garnet lherzolitic sources [Pelleter et al., 2014, Berthod et al., 2021a].

Seismological and petrological studies allowed to greatly improve our knowledge of the magmatic plumbing system above 50 km depth [Cesca et al., 2020, Lemoine et al., 2020, Saurel et al., 2021, 2022, Berthod et al., 2021a,b, Lavayssière et al., 2022]. Moreover, SKS splitting revealed that this plumbing system is developed in a strongly anisotropic lithosphere [Scholz et al., 2018]. Yet, the geometry of the plumbing system below 50 km, the role of the lithospheric interfaces in the location of the magma reservoirs, and the potential impact of the E–W lithospheric anisotropy in the magma migration are still poorly constrained. In this study, we analyze teleseismic receiver functions (RFs) and invert them jointly with the Rayleigh wave dispersion data. This allows us to provide new constraints on the lithospheric and asthenospheric structures down to 100 km and on crustal and mantle shear wave velocities beneath the eruptive zone. The rationale behind such a joint inversion of these two independent geophysical datasets is that they help together constraining both the interfaces' depths and absolute velocities. Armed with both types of data, we probe the structure of the lithosphere beneath Mayotte and show the occurrence of low-velocity zones (LVZ) that may correspond to magma ponding zones. We also provide a new absolute velocity model that may significantly improve the localization of seismic events related to the seismo-volcanic crisis.

## 2. Receiver functions and surface wave dispersion data

For more than 40 years, teleseismic $P$-coda RFs have become a major tool for exploring the internal structure of the Earth beneath seismic stations in various environments [e.g., Langston, 1977, Ammon, 1991, Zhu and Kanamori, 2000, Vergne et al., 2002, Zheng

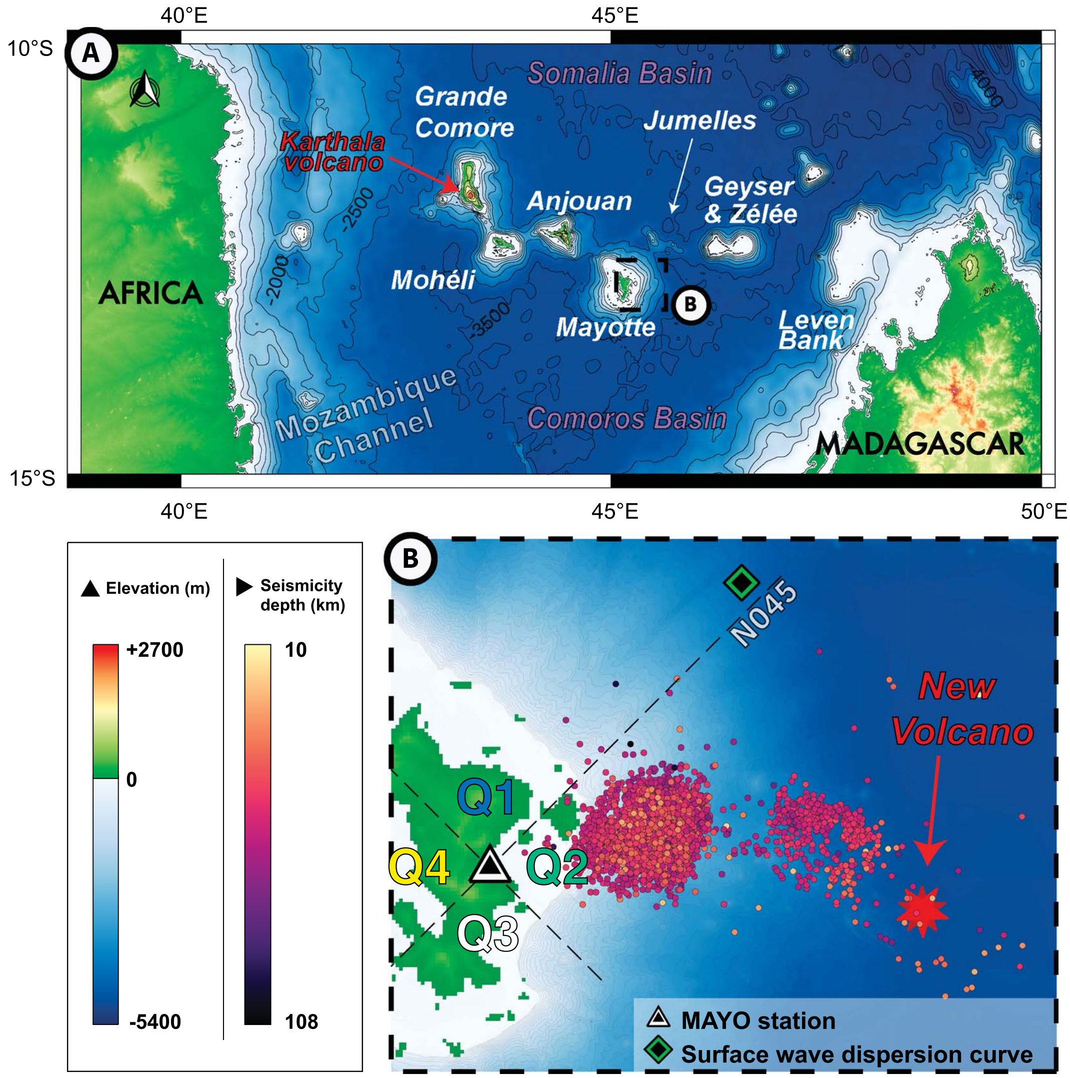


**Figure 1.** (A) The Comoros archipelago located north of the Mozambique channel between Africa and Madagascar. (B) Location of the MAYO seismic station in Mayotte, the sampling point of the Rayleigh wave dispersion data, the seismicity catalogue from 2019-02-25 to 2020-05-10 available for the Mayotte seismo-volcanic crisis [from Saurel et al., 2022] and the new submarine volcano forming the Mayotte volcanic zone [Feuillet et al., 2021]. Bathymetric data from SHOM (2016) around Mayotte and GMRT elsewhere [GMRT version 3.9; Ryan et al., 2009]. Elevation data from the ASTER Global Digital Elevation Model (GDEM, 2019).

et al., 2005, Leahy et al., 2010, Schlaphorst et al., 2018]. This method seeks to enhance *Ps* conversions and reverberations associated with crustal and mantle structures beneath the receiver by removing sensor-related, source-related, and mantle-path effects.

In this study, we computed RFs at the MAYO temporary broad-band station deployed on Mayotte Island (https://doi.org/10.15778/RESIF.YV2011, network code: YV, Lat: 12.8456° S; Long: 45.1868° E) during the RHUM-RUM experiment [Barruol and Sigloch, 2013]. This station has recorded 2 years and

10 months of seismic data (2011-04 to 2014-01). The MAYO station Probabilistic Power Spectral Densities (PPSDs) showing the frequency of occurrence of different noise level is available online (https://seismology.resif.fr/networks/#/YV__2011/MAYO/).
To calculate RFs, we selected seismic waveforms of events occurring at epicentral distance from the station between 25° and 90°, with a magnitude greater than 5.5 and a signal-to-noise ratio greater than 2. These selection criteria are considered as standards [e.g., Fontaine et al., 2015, Lamarque et al., 2015]. The $P$-arrivals were manually picked on waveforms, and the seismic signals were cut 5 s before and 30 s after the $P$-wave arrival time. A low-pass filter of ~1.2 Hz was applied to reduce the contributions of ambient noise and crustal heterogeneities to the signal recording. The iterative time-domain deconvolution method of Ligorría and Ammon [1999] was used to calculate the radial RFs (RRFs; Figure 2). The RRFs were grouped into 90° back-azimuth quadrants (Q1 to Q4) centered on the E–W and N–S axes [e.g., Tkalčić et al., 2011] to evaluate the azimuthal variations in the lithospheric properties (Figure 2).

The RFs were inverted using the Neighborhood Algorithm (NA) inversion method [Sambridge, 1999] to compute an ensemble of solutions of $S$-wave velocities profiles for different ray parameters ($p$) within the range of $\pm 0.006$ s·km$^{-1}$ of the median ray parameter [Figure 3; see selection and stacking procedure in Fontaine et al., 2013a, Dofal et al., 2021]. Note that this method gives convergent results with reflection [Fontaine et al., 2013b] and refraction profiles or transdimensional hierarchical Bayesian approach [Fontaine et al., 2015]. We used data from the different quadrants for the stacking procedure in order to image the potential presence of lithospheric anisotropies or dipping interfaces [e.g., Savage, 1998]. During the RFs inversion procedure, synthetics RFs were generated for 45,200 models using the Thomson–Haskell matrix method [Thomson, 1950, Haskell, 1990]. A calculation of the $\chi^2$ misfit function was applied to verify the coherency of the synthetics with the data. This misfit function, a L2-norm, is defined as the sum of the squares of the difference between the observed amplitude of the radial RF and the amplitude of the synthetic radial RF from a 6-layer model. Fontaine et al. [2013b] showed an example of the misfit function obtained using the NA (see their Figure 3A). An *a priori* parametrization was used to generate the $S$-wave velocity structure. It corresponds to a 6 layers model, each characterized by 4 parameters: $V_P/V_S$ ratio, thickness of the layer, $S$-wave velocities at the top and at the base of the layer. Full details of the *a priori* parameter space bounds can be found in Supplementary Material A. The velocity interfaces were determined from the $S$-wave velocities profiles, considering the 1000 best-fitting models (black curve in Figure 3).

We also extracted the Rayleigh wave dispersion curve from the regional (1° × 1° grid) group velocity model of Mazzullo et al. [2017] at the closest point to the station (12.5° S; 45.5° E). In the tomography model, the lithosphere is densely sampled with 170 seismic rays at the point where the dispersion data were extracted. This dispersion curve has periods ranging from 16 s to 100 s, allowing to constrain the lithospheric structures. The joint inversion enables us to take advantage of the constraints provided by two different datasets on complementary parameters. On the one hand, the receiver function inversion allows constraining the $S$-wave velocity contrasts at the sampled interfaces by a set of ascending seismic rays. It gives relative velocities with depth. On the other hand, surface waves provide absolute velocity information as a function of depth without being sensitive to interfaces [e.g., Özalaybey et al., 1997, Julià et al., 2000, Tkalčić et al., 2006]. Recent developments in inversion methods include the influence of noise in the inversion by treating it as a free parameter, such as the initial number of layers [e.g., Bodin et al., 2012 for the transdimensional hierarchical Bayesian inversion method; TB]. Therefore, TB method allows greater resolution of the velocity variation because models with a larger number of layers are recovered from the inversion. However, at the time of the study, the main objective is to determine the most significant lithospheric structures in this region where this information is not yet available. Therefore, we used the linear joint inversion method of Herrmann and Ammon [2002] and applied it to the RRFs and a Rayleigh wave dispersion curve. The information carried by each dataset is equally used during the inversion.

The stability of our inversion results was tested by performing inversions with several initial models. The used models are derived from PREM [Dziewoński and Anderson, 1981], ak135 [Kennett et al., 1995], HSak135 (halfspace starting model), and

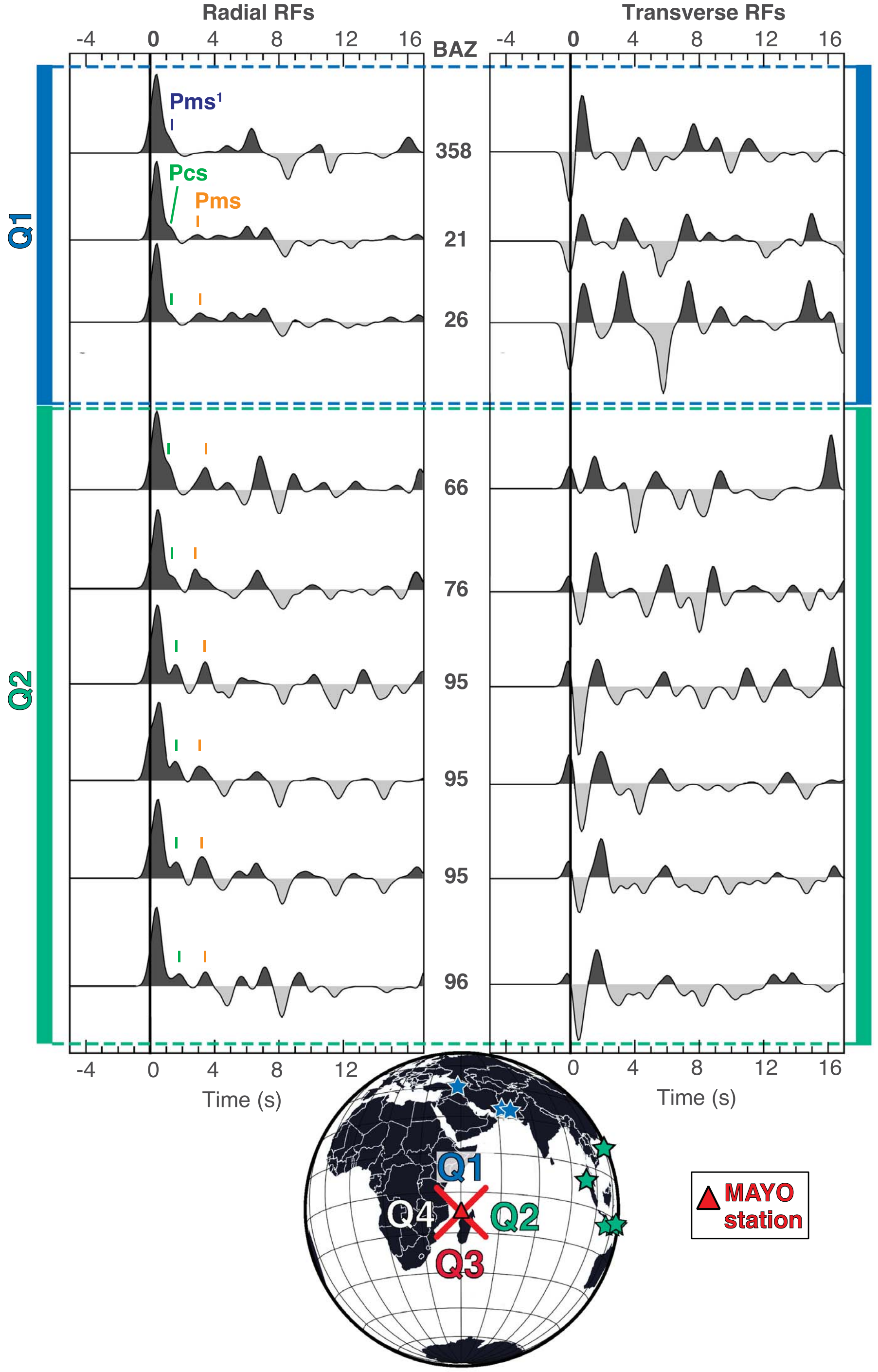


**Figure 2.** Radial (left) and transverse (right) receiver functions (RFs) grouped from their back-azimuths at the same scale. The teleseismic events used to perform RFs are indicated by stars with the same color scale as back-azimuthal Q1 and Q2 quadrants. Quadrants correspond to 90° sectors bounded by NW–SE and SW-NE axes. Q1 and Q2 correspond to the north and east sectors respectively. The *P*-wave direct arrival time is picked at the origin time. Positive and negative phases are shown in dark and light grey, respectively. Blue, green and orange ticks indicate arrival times of $Pms^1$, *Pcs* and *Pms* phases (see text for details).

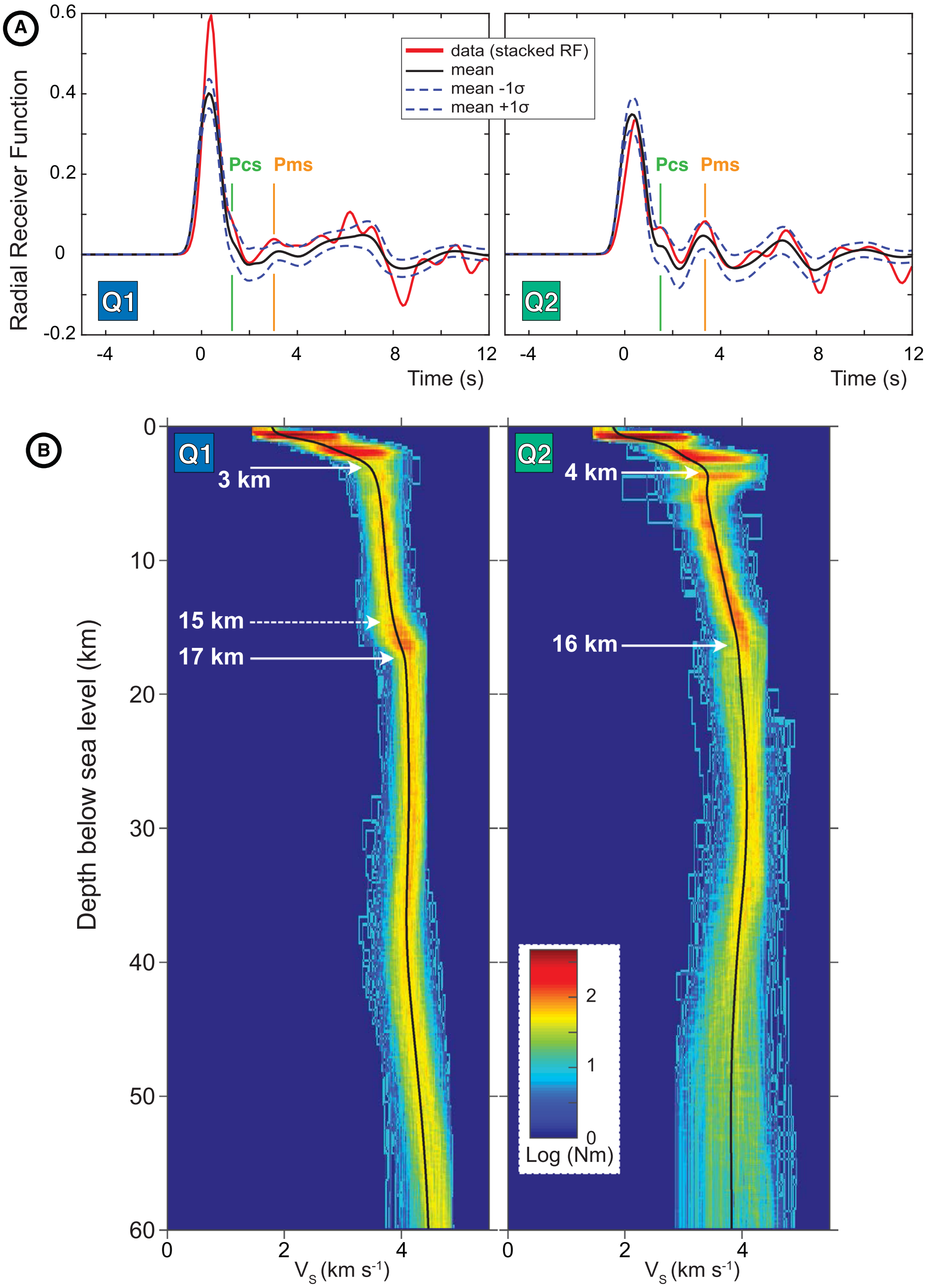


**Figure 3.** Results of the NA inversion of the RF in the two quadrants (Q1 and Q2) of the MAYO seismic station. (A) Comparison between the stacked measured radial RFs and the mean RF determined from the best 1000 models resulting from the inversion with the ±1 standard deviation limits around the average. Orange and green vertical lines account for the *Pms* and *Pcs* phases. (B) Density plot of the best 1000 velocity-depth models over the 45,200 models calculated for each quadrant. The color scale is logarithmically proportional to the number of models (Nm). The black line shows the average of the 1000 best models. White plain and dotted arrows indicate clear and gentle variations of velocity gradients in the *S*-wave velocity ($V_s$) profiles, respectively.

SURF (surface wave inversion based on halfspace starting model) and adapted in depth to the previous velocity model obtained by Dofal et al. [2021]. The uppermost mantle velocity of ak135 (i.e., $V_S$ of 4.48 km·s$^{-1}$) was fixed for the halfspace-starting model. The thickness of the two uppermost layers of the initial models was fixed at 1 and 2 km, respectively, while the thicknesses of the following layers were 2.5 km down to a depth of 100 km. We also tested the stability of the inversions by varying the layer thickness of the initial models (Supplementary Material B). During the inversion, a smoothing parameter was defined in order to prevent important velocity contrasts for two consecutive layers. This parameter was set at 0.8 for the first 30 km [i.e., in the crust and magmatic underplating; Dofal et al., 2021]. The influence of the smoothing parameter is limited as presented in Supplementary Material C.

In the NA RF inversions, we cut the traces 12 s after the direct *P* wave arrival time, whereas the signal was cut after 17 s for the joint inversions. For both inversions, the RF started at −5 s.

As for any geophysical inversion, the method used has its own limitations, in particular related to the noise not accounted for in the inversion and assumed to be zero, so the complexity of the final model is not driven by the data only but is also influenced by the subjective choice of the parameterization. Another limitation is induced by the small number of events, the poor back-azimuthal coverage and the possible influence of anisotropies or tilted reflectors, known as theory errors. Indeed, we were able to use only a limited number of RFs used in our study due to a thorough selection that increases the robustness of our inversions. Yet, the consistency of the RFs in each quadrant suggests a relative structure homogeneity in these back-azimuthal zones. Overall, if first order information may provide well-constrained results, these limitations imply that our second order interpretations should be taken as hypothetical and should be confirmed by further investigations.

## 3. Results

From the 447 events satisfying the selected criteria exposed before (epicentral distance, magnitude), we retain only 9 of them to calculate 9 individual RFs (data with a signal-to-noise ratio ≥2). The location of Mayotte relative to the global seismogenic zones strongly limits the number of teleseismic events in the usable epicentral distance (list of selected events available in Supplementary Material D). Most of them occur within the northern and eastern sectors only (3 and 6 RFs in Q1 and Q2, respectively; Figure 2).

Most of the RRFs (8 out of 9) show two positive amplitude peaks at about 1 and 3 s, labeled *Pcs* and *Pms* (Figure 2). The *Pcs* phase denotes the phase generated at the crust-to-magmatic underplating boundary [Leahy et al., 2010]. The *Pms* phase results from the conversion at the *crust-to-mantle boundary* and here it is at the *magmatic underplating-to-lithosphere mantle interface* [e.g., Leahy et al., 2010, Dofal et al., 2021]. On the 358° back-azimuth RF, the first phase following the *P*-direct cannot be the *Pcs* phase that corresponds to the crust-to-magmatic underplating interface because no clear phase appears at 3 s (the phase corresponding to the bottom of magmatic underplating). Therefore, the 1 s phase called *Pms*[1] on the 358° RF could not be generated at the same geological structure that generated the 1 s phase (*Pcs*) on eight other RFs (Figure 2). Other explanations include dipping interfaces or anisotropy. Nevertheless, with only one RF, it is not reliable to look at the velocity structure at this back-azimuth. Another difference between RFs from both quadrants is that RRFs from Q2 show a negative phase that do not appear on RRFs of Q1 and could be related to an anisotropic structure within the lithosphere. Finally, we notice that the main difference between the RFs recorded in the two quadrants stands in the polarity of the first peak of the Transverse RFs (TRFs), which is negative and positive in Q1 and Q2, respectively. The origin of this polarity inversion will be discussed in the next section.

Two of the six RFs falling in Q2 do not match the ray parameter criteria (RFs characterized by 76 and 96° of back-azimuth) and are not considered for computing the stacked RF of Q2 for the inversion with the neighborhood algorithm (NA). The ensemble of RFs (i.e., 3 and 4 RFs for Q1 and Q2, respectively) and the stacked RFs obtained for the NA shows a slight shift of the *P*-direct phase from the 0 time. This may be related to an important velocity contrast between the first two layers [e.g., Zelt and Ellis, 1999]. This observation is confirmed by the ensemble of best data-fitting *S*-wave velocity profiles that shows a sharp velocity hinge at 3 and 4 km beneath the station for Q1 and Q2, respectively (Figure 3B). RFs also reveal two positive peaks that follow the main *P* phase arrival (Figure 3A). The first peak arrives at around 1.5 s while the second one is recorded at 3–3.5 s. The former is interpreted as the *Pcs* phase, and the latter may correspond to the *Pms* phase. The modeled RFs describing the average of the 1000 best velocity models for Q1 and Q2 reproduce well the first 7 s after the *P*-direct phase but fail at fitting the high negative peak at ~8 s (Figure 3A). Beneath the 3–4 km depth boundary, the *S*-wave velocity profiles present either a constant, low gradient down to 15 km depth in Q1 or a slight velocity decrease until 6 km depth followed by a constant, low gradient down to 16 km depth in Q2. Below these depths (16–17 km), the *S*-wave velocity slightly increases at a constant rate in both quadrants until 30–35 km depth, where a weakly pronounced LVZ seems to be initiated (Figure 3B). The geometry of this LVZ is poorly constrained in Q2, as demonstrated by the larger scattering of the velocity-depth models than in Q1. To deal with this limitation, we take advantage of the sensitivity of surface wave dispersion data to investigate the geometry of the lithosphere down to 100 km depth and to better determine the evolution of the *S*-wave velocity with depth (Figure 4).

We therefore perform a joint inversion of RFs and surface wave dispersion data in both quadrants. To perform the joint inversion of RFs and surface wave dispersion data, we use the four initial models described in Section 2 as input (Figure 4). This inversion strategy is applied to the sets of RFs recorded for each quadrant (3 and 6 RFs for Q1 and Q2, respectively). The full set of models generated for these inversions is available in Supplementary Material E. The resulting velocity profiles for each quadrant and for the four selected models are presented in Figure 4. It shows first a general consistency between the profiles computed with the different models as they all present a similar overall evolution of the *S*-wave velocity with depth. The slight differences between the computed profiles for each quadrant stand in the occurrence of discrete steps related to velocity changes in the ak135 and PREM models and in higher and lower velocity values in the profile with ak135 model than with the others. Therefore, we consider an average of the four profiles to minimize the effect of each individual *a priori* model and to describe the structure of the lithosphere in quadrants Q1 and Q2 (Figure 4).

The average velocity models for both quadrants show, at first glance, a similar overall evolution characterized by (1) *S*-velocities of 1.6 and 1.9 $km\cdot s^{-1}$ near the surface increasing rapidly to 3.5 $km\cdot s^{-1}$ at around 4–6 km depth, (2) a change in velocity gradient with a slow velocity increase followed by a rapid one until around 4.5 $km\cdot s^{-1}$ at 28–30 km depth, (3) a decrease of the velocity to minimum values reached at 49 and 54 km depth in Q1 and Q2, respectively, and (4) a second LVZ with slower velocities than in the shallow one from 62–64 to 92–93 km depth (Figure 4).

The shallowest layer L1, 4, and 6 km in thickness in Q1 and Q2, respectively, is characterized by the highest velocity gradient (0.25–0.4 $km\cdot s^{-1}\cdot km^{-1}$; Table 1). In both Q1 and Q2, the velocity continues to increase in the layer L2 down to its base at 29–31 km depth (Figure 4). Below L2, the velocity decreases, forming a LVZ visible in both sectors that we define as L3 (Figure 4). This low-velocity layer is marked by a continuous (in Q2) and discontinuous (in Q1) velocity decrease down to 54 and 49 km, respectively. The velocity drop in this LVZ is larger in Q2 than in Q1 (−11.6 and −6.3% of the velocity measured at its top; Table 1). The base of L3 lies at 62–64 km depth (Figure 4; Table 1). Below the L3 layer, we define L4, which is mainly made by a second large LVZ visible on the velocity profiles. The velocity drops of around 12.5% at 75 km depth. The base of this LVZ is around 92 km depth in both quadrants.

Thus, the joint inversion of receiver functions and Rayleigh wave dispersion data suggests a similar first-order structure of the lithosphere in Q1 and Q2. L1 and L2 are characterized by positive gradients, whereas L3 and L4 represent two successive LVZ (Figure 4). Interestingly, the main difference between Q1 and Q2 is the amplitude and the size of the LVZ in L3, which is broader and slower in the quadrant sampling the eastern sector (Q2) than in the northern one (Q1).

## 4. Discussion

### 4.1. *Lithospheric anisotropy/dipping interface*

At first glance, the lithosphere sampled by rays arriving from the northern and eastern azimuths presents a similar overall geometry. Despite a sparse

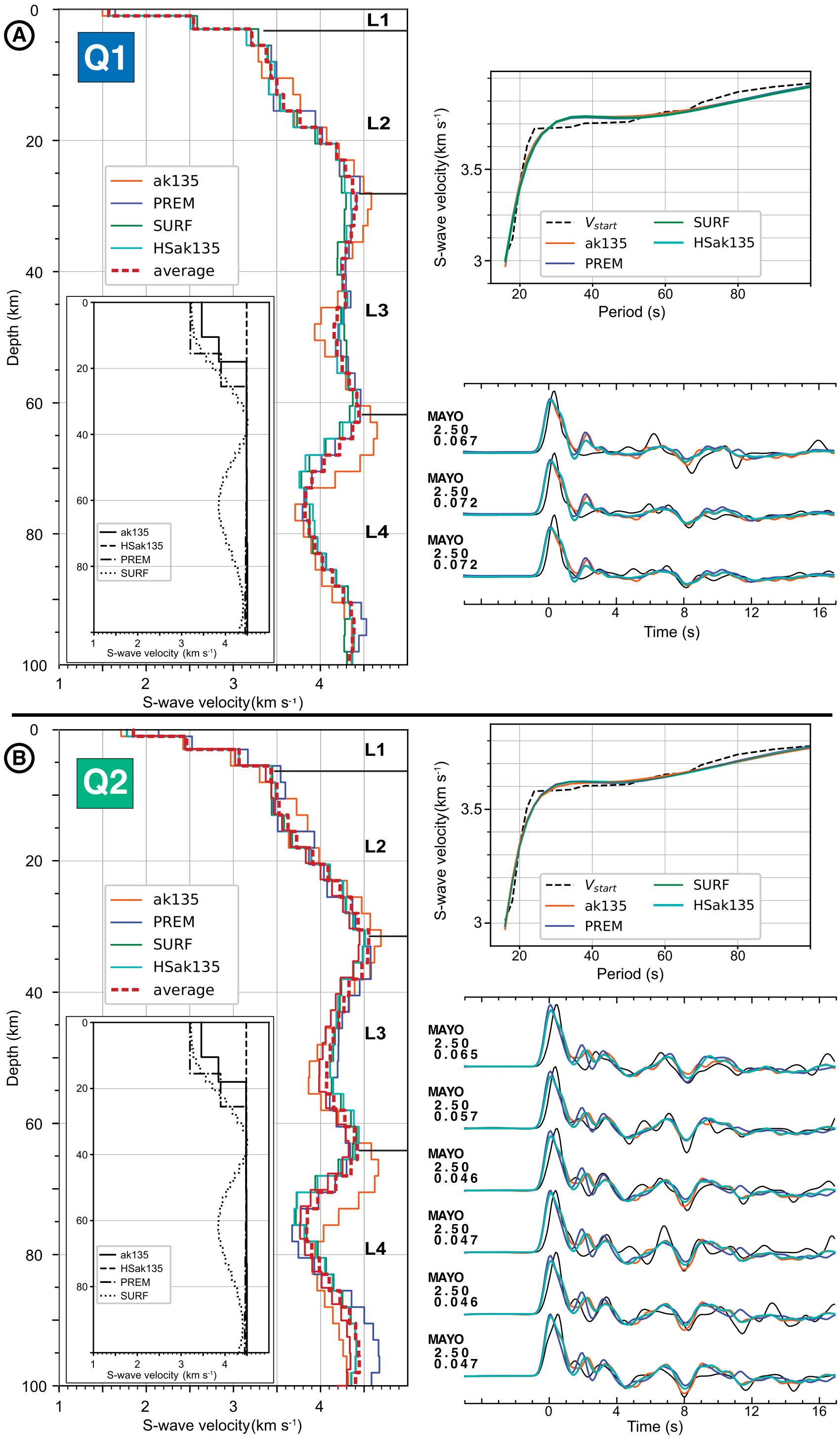


**Figure 4.** Joint RF and Rayleigh dispersion curves inversion results for Q1 and Q2 quadrants (A and B). Left, individual absolute *S*-wave velocity profiles obtained for four starting models (detailed in the legend) and the corresponding mean model, in red. Upper right panels, plot of modeled dispersion curves, and the data. Bottom right panels, plots of modeled and observed RFs. Colors correspond to the starting models used to obtain modeled RFs and dispersion curves. L1, L2, L3 and L4 refers to geological layers that are discussed in the text.

**Table 1.** Summary of the lithospheric structure in Q1 and Q2 determined from the joint inversion of receiver functions and Rayleigh wave dispersion data

| | Layers | Layer basal depth | Layer thickness | Velocity ($km \cdot s^{-1}$) at the base of the layer | Average velocity gradient ($km \cdot s^{-1} \cdot km^{-1}$) | Minimum velocity value (If LVZ) | LVZ velocity decrease (%) |
|---|---|---|---|---|---|---|---|
| Q1 | L1 | 4 | 4 | 3.2 | 0.40 | | |
| | L2 | 29 | 25 | 4.4 | 0.05 | | |
| | L3 | 62 | 33 | 4.45 | LVZ | 4.17 | −6.3 |
| | L4 | | | 4.3 | LVZ | 3.8 | −11.6 |
| Q2 | L1 | 6 | 6 | 3.4 | 0.25 | | |
| | L2 | 31 | 25 | 4.55 | 0.05 | | |
| | L3 | 64 | 33 | 4.4 | LVZ | 4.05 | |
| | L4 | 93 | 19 | 4.4 | LVZ | 3.8 | −13.6 |

back-azimuthal coverage (e.g., no RFs in Q3 and Q4) impeding unambiguous interpretation [e.g., Owens and Crosson, 1988, Cassidy, 1992], several lines of evidence indicate the occurrence of heterogeneities and anisotropic structures within the lithosphere beneath Mayotte. The first evidence is the non-zero TRFs [e.g., Cassidy, 1992, Bertrand and Deschamps, 2000] showing clear peaks of opposite polarities in Q1 and Q2 (Figure 2). Such a pattern may indicate the presence of anisotropic structures within a multi-layered lithosphere [e.g., Nagaya et al., 2008, Bar et al., 2019]. Although the anisotropy cannot be precisely characterized from RFs due to the little number of observations, the azimuthal seismic anisotropy obtained at MAYO station from surface and body waves suggests a complex anisotropy down to 100–150 km depth with two fast directions trending E–W and NE–SW [Mazzullo et al., 2017, Scholz et al., 2018]. The E–W trend was proposed to be caused by ridge-parallel mantle flow inherited from the N–S opening of the Somali basin, while the NE–SW one still remains enigmatic [Scholz et al., 2018]. The occurrence of dipping interfaces may also contribute to the inversion of peak polarity on the TRFs between Q1 and Q2, and to the occurrence of high amplitude TRFs [e.g., Savage, 1998]. As for the anisotropy, due to the sparsity of data, the dips of the interfaces cannot be well constrained and are considered by simplicity as horizontal. Note that the uncertainty on the Moho depth increases with the increase of dip angle. Synthetic analysis shows that a dip angle >4° introduces an error on the depth estimation of the interface >2 km [Zhang et al., 2009].

Finally, all RRFs but one show two peaks arriving at around 1.5 s and 3–3.5 s (Figure 2). Only the 358° back-azimuth RF has a single positive phase after the *P*-direct phase at almost 1 s, suggesting a distinct structure. This feature, together with the arrival times of the direct *P* phase on the set of RRFs could originate from multi-scale heterogeneities within the lithosphere.

### 4.2. *Structure of the lithosphere*

Our combined analysis of receiver functions and the joint inversion of receiver function and Rayleigh wave dispersion data allows us to characterize the lithospheric structure and to further constrain the geometry proposed from receiver functions and $H$-$\kappa$ staking [Dofal et al., 2021]. In a previous analysis, we imaged three interfaces (at 4, 17 and 26–27 km depth), which we interpreted as the base of the Mayotte volcanic edifice, the interface (called "*old Moho*") between a thinned continental crust and an underlying magma underplating, and the base of the magmatic underplating (called "*new Moho*"), respectively [Dofal et al., 2021]. Our new approach brings additional constraints to this geometry and allows us to discuss possible differences in the lithospheric structure between the northern and eastern quadrants, as supported by variations on radial RFs (Figure 2; see Section 3). Both velocity profiles computed from the NA and the joint inversion identify a shallow interface around 4 km depth (NA inversion: 3 and 4 km depth and joint inversion: 4 and 6 km depth for Q1 and Q2, respectively). Note that the slight differences in depth are in the range of the uncertainty, which is commonly assumed to be around 2 km for the Moho depth [e.g., Fontaine et al., 2015]. Another explanation could be the occurrence of a dipping interface toward Q2, which may explain part of the high energy on the transverse component. Nevertheless, this interface is interpreted as the base of the volcanic edifice of Mayotte Island that is lying 3.5 km below sea level [Audru et al., 2006]. The base of L2, lying at 29–31 km depth, is close to the interface evidenced at 26–27 km depth [Dofal et al., 2021]. Given the range of uncertainty, it is likely that our joint inversion imaged the same interface as the one identified by these authors. Meanwhile, our approach brings more detailed information on the structures located between 4 km and around 29 km depth. Indeed, the *S*-wave velocity profiles of Figure 4 both show a ramp-like increase with a sub-layer with a moderate velocity gradient between two sub-layers with smaller velocity gradients. The depth of the base of the first sublayer in Q1 and Q2 is located at 14 and 17 km, respectively, and coincides with that of the *old Moho* proposed in Dofal et al. [2021]. Note that the *S*-wave velocities determined for the base of this layer (3.5–3.7 $km \cdot s^{-1}$) in Q2 are compatible with the ones proposed for the oceanic crust [3.4–3.6 $km \cdot s^{-1}$; Christensen, 1996, Leahy et al., 2010], but also for a bulk continental crust [3.65 $km \cdot s^{-1}$; Christensen, 1996]. Thus, our velocity data do not allow to discriminate the oceanic or continental nature of this sub-layer. Its thickness (10–11 km) suggests however, that this unit either corresponds to an abnormally thick oceanic crust, which is regionally 6–7 km thick [Vormann et al., 2020, Dofal et al., 2021], or to a thinned continental crust abandoned during the southern drift of Madagascar [Dofal et al., 2021].

Below the *old Moho*, velocity gradients are constant until *S*-wave velocities reach 4.2 to 4.55 $km \cdot s^{-1}$ at the base of L2. Such a velocity range is comparable to that of magmatic underplating [around 4.2 $km \cdot s^{-1}$; Watts et al., 1985, Caress et al., 1995, Leahy et al., 2010], suggesting an endogenous crustal thickening of 14–15 km due to magma crystallization.

Below the *new Moho*, the L3 layer interpreted as the lithospheric mantle presents a ~20-km-thick LVZ characterized by minimum *S*-wave velocities at 49–54 km depth (Table 1; Figure 4). The origin of this LVZ is discussed in the next section. Finally, our data suggest a LAB at 62–64 km depth and a well-expressed LVZ in the upper part of the asthenosphere, with an average drop of 12.5% in shear wave velocities (Table 1). The LAB depth determined in the present paper agrees with the range of depths (50–90 km) proposed by Barruol et al. [2019] for the Comoros archipelago and indicates that the lithosphere is abnormally thin (64 km instead of around 110 km) for a lithosphere dated at around 140 Ma [Coffin and Rabinowitz, 1987]. Nonetheless, this value is similar to the lithospheric thickness of Madagascar [60 km; Rakotondraompiana et al., 1999], where the thinning of the lithospheric mantle is thought to result from the emplacement of an asthenospheric thermal anomaly in the Cenozoic [Stephenson et al., 2021].

## 5. Lithospheric-scale magma transfer

The renewal of volcanic activity east of Mayotte that started in spring 2018 was associated with a major seismic crisis, the events of which allowed to characterize the magma transfer in the upper lithosphere from a first magma reservoir located at 25–35 km depth by Cesca et al. [2020] and at $28 \pm 3$ km by Lemoine et al. [2020]. The seismicity is concentrated into two deep clusters located east of Mayotte at 20–50 km and 25–50 km depth [Lemoine et al., 2020, Bertil et al., 2021, Saurel et al., 2021]. The analysis of the submarine lavas emitted by the new volcano suggests two additional reservoirs located at $17 \pm 6$ km and between 37–48 km depth [Berthod et al., 2021a]. Finally, tomographic models computed from both terrestrial and ocean bottom seismometers recently imaged several low *S*-wave velocity zones interpreted as magma reservoirs located at about 10, 28, and 44 km depth, the deepest one being the largest in size [Foix et al., 2021].

The locations of the seismic clusters, of the magma reservoirs, and of the structures of the lithosphere that we determine from the present RF analysis strongly suggest that magma reservoirs are located at 17 km and 28 km, i.e., at the rheological interfaces between the crust and the underplating (the *old Moho)*, and between the underplating and the lithospheric mantle, respectively (the *new Moho*, Figure 5). Interestingly, magnetotelluric soundings

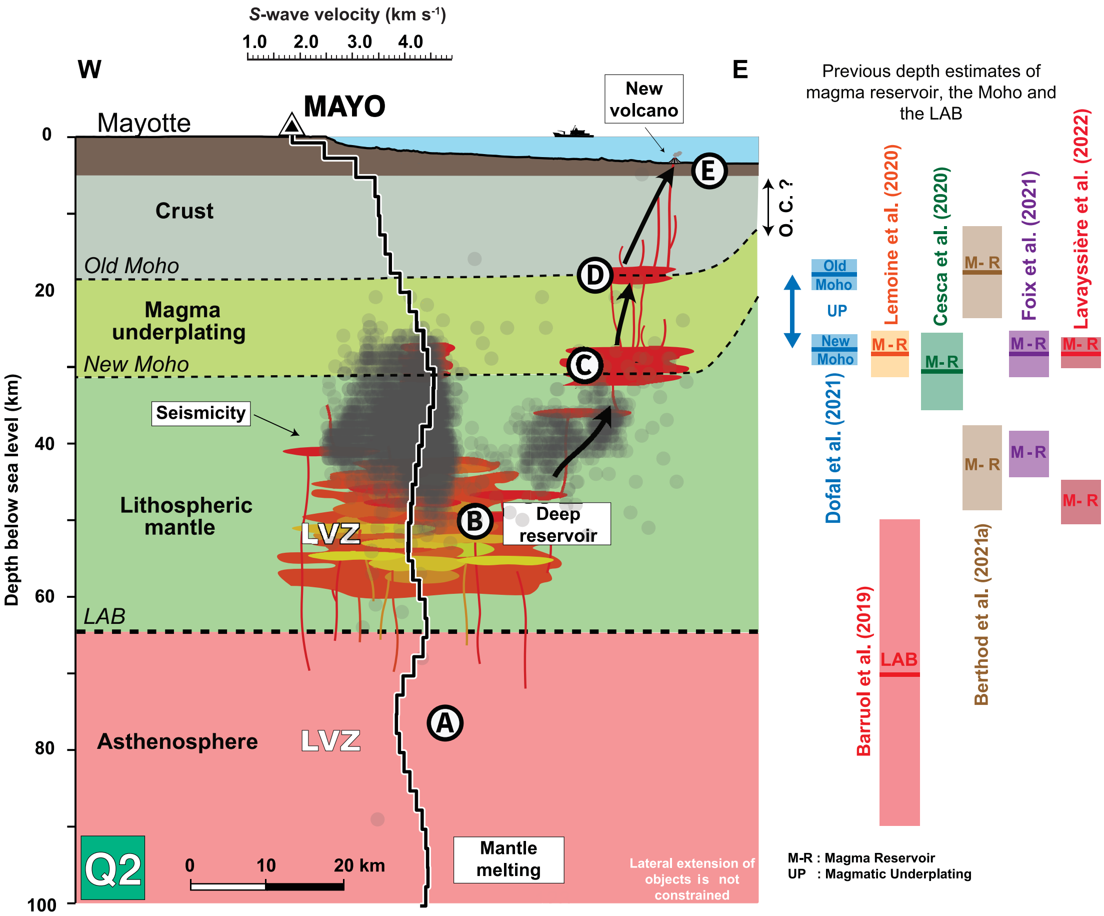


**Figure 5.** Conceptual model of the magmatic plumbing system below the currently active eruptive zone of Mayotte (quadrant Q2). In black, the *S*-wave velocity profile of the Q2 quadrant obtained at the MAYO station (this study). Grey dots indicate the hypocenters of the seismicity recorded during the Mayotte seismo-volcanic crisis from 2019-02-25 to 2020-05-10 [Saurel et al., 2022]. The red symbols represent areas of potential magma accumulation. Black arrows indicate possible magma migration paths from 80 km depth to the surface. On the right, the depth location of some interfaces provided by the literature. The lateral extent of objects is not constrained.

show the occurrence of two orders of magnitude of resistivity drop at 15 km depth interpreted as the presence of partial melt [Darnet et al., 2020]. The rheological effect of successive lithological layers is known to control the progressive growth of magma reservoirs by incremental sill injections [Kavanagh et al., 2006, Menand, 2011, and references therein]. We, therefore, propose that the *old Moho* acted as a ponding zone since the initiation of the Cenozoic volcanism [e.g., Michon, 2016], allowing the progressive development of a thick magma underplating that subsequently cooled and became part of the crust. The upper and lower interfaces of the newly formed underplating have likely played a role of mechanical heterogeneities that favored horizontal magma accumulation and the formation of independent magma reservoirs.

Both petrological and seismological data indicate a major magma reservoir located within the lithospheric mantle at a depth range of 37–52 km below sea level [Berthod et al., 2021a,b, Foix et al., 2021], which corresponds to the upper part of the LVZ that we obtain via the *S*-wave velocity profile determined for Q2 (i.e., from rays sampling the eastern quadrant where the current seismicity and volcanic activity occur). It is worth noting that the seismic data used by Foix et al. [2021] for their passive tomography does not allow to investigate mantle structures at depths greater than about 45 km and consequently, cannot image a downward continuity of the magma reservoir. Furthermore, the petrological pressure constraints were calculated from clinopyroxene crystals [Berthod et al., 2021a,b] that may have not sampled the entire storage zone. We, therefore, interpret the LVZ imaged with our joint inversion approach as a large magma storage zone between 38 and 58 km depth (Figure 5).

Our data cannot access the detailed structure and the heterogeneities within this large-scale molten body. It is therefore unlikely that this entire volume corresponds to a huge magma chamber filled by a sole magmatic phase. Instead, the *S*-wave velocity profile of Q2 reveals a progressive velocity decrease down to 54 km depth, which could sign the presence of partial melt and of a mush with an increasing amount of liquid phase from 38 to 54 km. Interestingly, the characteristics of the LVZ in Q1 (a discontinuous velocity decrease and higher *S*-wave velocities) suggest that a smaller amount of magma is stored in the lithospheric mantle in the northern quadrant beneath Mayotte than in the eastern one below the submarine volcanic ridge along which the new volcano formed [Feuillet et al., 2021]. The development of deep magma storage within the lithospheric mantle where no obvious interface exists raises the question of its controls. Analog experiments have suggested that the rigidity contrast between a stiff upper layer and a lower, less rigid unit prevents a vertical magma ascent and magma stalling in horizontal magma intrusions [Kavanagh et al., 2006]. Such a process can explain the development of sill injections right below the Conrad discontinuity, in the uppermost part of the viscous lower crust [Sparks et al., 2019]. A similar strength profile does exist in the lithospheric mantle where the lower part is viscous while the upper one remains brittle [Ranalli and Murphy, 1987, Buck, 1991]. Thus, we propose that the magma ascending from the asthenosphere stalls in the viscous lower lithospheric mantle, underneath a more rigid upper layer. The pressure decrease related to the magma emission along the submarine ridge may explain the intense seismicity that developed in the upper rigid layer, between 20–25 km and 50 km depth [Cesca et al., 2020, Lemoine et al., 2020, Feuillet et al., 2021, Saurel et al., 2021].

Although our approach does not allow to determine the precise location of the magmatic structures in the eastern quadrant (Q2), it provides results that remarkably agree with the suspected location of magma reservoirs [Lemoine et al., 2020, Cesca et al., 2020, Foix et al., 2021, Berthod et al., 2021a,b]. Our results provide insights and independent constraints into the deep plumbing system, i.e., from the surface down to the asthenosphere, revealing the existence of a substantial magma-rich zone within the lithospheric mantle. Finally, our results suggest that magma stalling beneath Mayotte is primarily controlled by brittle/ductile rheological contrasts in both the lithospheric mantle and the crust.

## 6. Conclusion

Despite a limited dataset due to the short duration of deployment of the MAYO seismic station, we are able to bring new elements to constrain the structure of the lithosphere beneath Mayotte and its northern and eastern submarine flanks. We identify deep magma storage within the lithospheric mantle (between 38 and 54 km depth) whose dynamics yields seismicity since 2018 in the brittle part of the lithospheric mantle. We propose that a shallow magma reservoir lies at the interface between the lithospheric mantle and the overlying crust, favoring the formation of thick magma underplating, and that two other magma reservoirs occur at ∼17 km and 28 km at the upper and lower boundaries of this underplating. Finally, our results suggest that the development of the plumbing system is controlled by the rheological contrasts existing within the lithosphere, contrasts that act as mechanical boundaries in which magma stalls and may progressively contribute to the formation of a thick magma underplating in areas of long-lasting activity. To better constrain the lateral and depth extents of the lithospheric structures and of the magma plumbing system at a more regional scale, future work should combine data recorded (1) by permanent onshore broadband stations, (2) by ocean bottom seismometers deployed at large scale around Mayotte and at smaller scale around the eruptive site [cf. REVOSIMA, 2020, Saurel et al., 2021], and (3) by long term and multiparameter offshore geophysical observatory, as proposed by the future French MARMOR initiative.

## Conflicts of interest

Authors have no conflict of interest to declare.

## Acknowledgments

AD's research was supported by a PhD grant from the University of La Réunion. Station MAYO installation was supported by the Programme Iles Eparses funded by the CNRS-INSU (Institut National des Sciences de l'Univers), CNRS-INEE (Institut National Ecologie et Environnement), TAAF (Terres Australes et Antarctiques Françaises). MAYO portable seismometer was provided by the Alfred Wegener Institute (AWI) in Bremerhaven. The RHUM-RUM data (http://dx.doi.org/10.15778/RESIF.YV2011) are hosted and served by the French RESIF data center (http://seismology.resif.fr). We thank C. Berthod for discussions on the magmatic plumbing system. We also thank A. Mazzullo for providing Rayleigh wave dispersion curve data and E. Stutzmann for discussions on the dispersion curve data. Finally, we would like to express our deepest thanks to the two anonymous reviewers who helped to improve the quality of the paper.

## Supplementary data

Supporting information for this article is available on the journal's website under https://doi.org/10.5802/crgeos.190 or from the author.

## References

Ammon, C. J. (1991). The isolation of receiver effects from teleseismic P waveforms. *Bull. Seismol. Soc. Am.*, 81(6), 2504–2510.

Audru, J.-C., Guennoc, P., Thinon, I., and Abellard, O. (2006). Bathymay : la structure sous-marine de Mayotte révélée par l'imagerie multifaisceaux. *C. R. Géosci.*, 338(16), 1240–1249.

Bar, N., Long, M. D., Wagner, L. S., Beck, S. L., Zandt, G., and Tavera, H. (2019). Receiver function analysis reveals layered anisotropy in the crust and upper mantle beneath southern Peru and northern Bolivia. *Tectonophysics*, 753, 93–110.

Barruol, G. and Sigloch, K. (2013). Investigating La Réunion hot spot from crust to core. *Eos Trans. Am. Geophys. Union*, 94(23), 205–207.

Barruol, G., Sigloch, K., Scholz, J.-R., Mazzullo, A., Stutzmann, E., Montagner, J.-P., Kiselev, S., Fontaine, F. R., Michon, L., Deplus, C., and Dyment, J. (2019). Large-scale flow of Indian Ocean asthenosphere driven by Réunion plume. *Nat. Geosci.*, 12(12), 1043–1049.

Berthod, C., Médard, E., Bachèlery, P., Gurioli, L., Di Muro, A., Peltier, A., Komorovski., J.-C., Benbakkar, M., Devidal, J.-L., Langlade, J., Besson, P., Boudon, G., Rose-Koga, E., Deplus, C., Le Friant, A., Bickert, M., Nowak, S., Thinon, I., Burckel, P., Hidalgo., S., Kaliwoda, M., Jorry, S. J., Fouquet, Y., and Feuillet, N. (2021a). The 2018-ongoing Mayotte submarine eruption: magma migration imaged by petrological monitoring. *Earth Planet. Sci. Lett.*, 571, article no. 117085.

Berthod, C., Médard, E., Di Muro, A., Hassen Ali, T., Gurioli, L., Chauvel, C., Komorowski, J.-C., Bachèlery, P., Peltier, A., Benbakkar, M., Devidal, J.-L., Besson, P., Le Friant, A., Deplus, C., Nowak, S., Thinon, I., Burckel, P., Hidalgo, S., Feuillet, N., Jorry, S., and Fouquet, Y. (2021b). Mantle xenolith-bearing phonolites and basanites feed the active volcanic ridge of Mayotte (Comoros archipelago, SW Indian Ocean). *Contrib. Mineral. Petrol.*, 176, article no. 75.

Bertil, D., Mercury, N., Doubre, C., Lemoine, A., and Van der Woerd, J. (2021). The unexpected Mayotte 2018–2020 seismic sequence: a reappraisal of the regional seismicity of the Comoros. *C. R. Géosci.*, 353(S1), 211–235.

Bertrand, E. and Deschamps, A. (2000). Lithospheric structure of the southern French Alps inferred from broadband analysis. *Phys. Earth Planet. Inter.*, 122(1–2), 79–102.

Bodin, T., Sambridge, M., Tkalčić, H., Arroucau, P., Gallagher, K., and Rawlinson, N. (2012). Transdimensional inversion of receiver functions and surface wave dispersion. *J. Geophys. Res.*, 117, article no. B02301.

Buck, W. R. (1991). Modes of continental lithospheric extension. *J. Geophys. Res. Solid Earth*, 96(B12), 20161–20178.

Caress, D. W., McNutt, M. K., Detrick, R. S., and Mutter, J. C. (1995). Seismic imaging of hotspot-related crustal underplating beneath the Marquesas Islands. *Nature*, 373(6515), 600–603.

Cassidy, J. F. (1992). Numerical experiments in broadband receiver function analysis. *Bull. Seismol. Soc. Am.*, 82(3), 1453–1474.

Cesca, S., Letort, J., Razafindrakoto, H. N. T., Heimann, S., Rivalta, E., Isken, M. P., Nikkhoo, M., Passarelli, L., Petersen, G. M., Cotton, F., and Dahm, T. (2020). Drainage of a deep magma reservoir near Mayotte inferred from seismicity and deformation. *Nat. Geosci.*, 13(1), 87–93.

Christensen, N. I. (1996). Poisson's ratio and crustal seismology. *J. Geophys. Res. Solid Earth*, 101(B2), 3139–3156.

Class, C., Goldstein, S. L., Altherr, R., and Lery, P. B. (1998). The process of plume–lithosphere interactions in the ocean basins—the case of Grande Comore. *J. Petrol.*, 39(5), 881–903.

Class, C., Goldstein, S. L., Stute, M., Kurz, M. D., and Schlosser, P. (2005). Grand Comore Island: A well-constrained "low 3He/4He" mantle plume. *Earth Planet. Sci. Lett.*, 233, 391–409.

Coffin, M. F. and Rabinowitz, P. D. (1987). Reconstruction of Madagascar and Africa: evidence from the Davie fracture zone and western Somali basin. *J. Geophys. Res. Solid Earth*, 92, 9385–9406.

Darnet, M., Wawrzyniak, P., Tarits, P., Hautot, S., and D'Eu, J. F. (2020). Mapping the geometry of volcanic systems with magnetotelluric soundings: Results from a land and marine magnetotelluric survey performed during the 2018–2019 Mayotte seismovolcanic crisis. *J. Volcanol. Geotherm. Res.*, 406, article no. 107046.

Darwin, C. (1842). *The Structure and Distribution of Coral Reefs*. Smith Elder and Co, London, 2nd edition.

Dofal, A., Fontaine, F. R., Michon, L., Barruol, G., and Tkalčić, H. (2021). Nature of the crust beneath the islands of the Mozambique Channel: constrains from receiver functions. *J. African Earth Sci.*, 184, article no. 104379.

Dziewoński, A. M. and Anderson, D. L. (1981). Preliminary reference Earth model. *Phys. Earth Planet. Inter.*, 25(4), 297–356.

Emerick, C. M. and Duncan, R. A. (1982). Age progressive volcanism in the Comores Archipelago, western Indian Ocean and implications for Somali plate tectonics. *Earth Planet. Sci. Lett.*, 60(3), 415–428.

Famin, V., Michon, L., and Bourhane, A. (2020). The Comoros archipelago: a right-lateral transform boundary between the Somalia and Lwandle plates. *Tectonophysics*, 789, article no. 228539.

Feuillet, N., Jorry, S. J., Crawford, W. C., Deplus, C., Thinon, I., Jacques, E., Saurel, J.-M., Lemoine, A., Paquet, F., Satriano, C., Aiken, C., Foix., O., Kowalski, P., Laurent, A., Rinnert, E., Cathalot, C., Donval, J.-P., Guyader, V., Gaillot, A., Scalabrin, C., Moreira, M., Peltier, A., Beauducel, F., Grandin, R., Ballu, V., Daniel., R., Pelleau, P., Gomez, J., Besançon, S., Géli, L., Bernard, P., Bachèlery, P., Fouquet, Y., Bertil, D., Lemarchand, A., and Van der Woerd, J. (2021). Birth of a large volcanic edifice offshore Mayotte via lithosphere-scale dyke intrusion. *Nat. Geosci.*, 14(10), 787–795.

Foix, O., Aiken, C., Saurel, J.-M., Feuillet, N., Jorry, S. J., Rinnert, E., and Thinon, I. (2021). Offshore Mayotte volcanic plumbing revealed by local passive tomography. *J. Volcanol. Geotherm. Res.*, 420, article no. 107395.

Fontaine, F. R., Barruol, G., Tkalčić, H., Wölbern, I., Rümpker, G., Bodin, T., and Haugmard, M. (2015). Crustal and uppermost mantle structure variation beneath La Réunion hotspot track. *Geophys. J. Int.*, 203(1), 107–126.

Fontaine, F. R., Tkalčić, H., and Kennett, B. L. N. (2013a). Crustal complexity in the Lachlan Orogen revealed from teleseismic receiver functions. *Aust. J. Earth Sci.*, 60(3), 413–430.

Fontaine, F. R., Tkalčic, H., and Kennett, B. L. N. (2013b). Imaging crustal structure variation across southeastern Australia. *Tectonophysics*, 582, 112–125.

Haskell, N. A. (1990). The dispersion of surface waves on multilayered media. In Ben-Menahem, A., editor, *Vincit Veritas: A Portrait of the Life and Work of Norman Abraham Haskell, 1905–1970*, pages 86–103. American Geophysical Union, Washington, DC.

Herrmann, R. B. and Ammon, C. J. (2002). *Computer Programs in Seismology: Surface Waves, Receiver Functions and Crustal Structure*. St. Louis University, St. Louis, MO.

Julià, J., Ammon, C. J., Herrmann, R. B., and Correig, A. M. (2000). Joint inversion of receiver function and surface wave dispersion observations. *Geophys. J. Int.*, 143(1), 99–112.

Kavanagh, J. L., Menand, T., and Sparks, R. S. J. (2006). An experimental investigation of sill formation and propagation in layered elastic media. *Earth Planet.*

*Sci. Lett.*, 245(3–4), 799–813.

Kennett, B. L., Engdahl, E. R., and Buland, R. (1995). Constraints on seismic velocities in the Earth from traveltimes. *Geophys. J. Int.*, 122(1), 108–124.

Lamarque, G., Barruol, G., Fontaine, F. R., Bascou, J., and Menot, R.-P. (2015). Crustal and mantle structure beneath the Terre Adelie Craton, East Antarctica: insights from receiver function and seismic anisotropy measurements. *Geophys. J. Int.*, 200(2), 807–821.

Langston, C. A. (1977). Corvallis, Oregon, Crustal and upper mantle receiver structure from teleseismic P and S Waves. *Bull. Seismol. Soc. Am.*, 67(3), 713–724.

Lavayssière, A., Crawford, W. C., Saurel, J.-M., Satriano, C., Feuillet, N., Jacques, E., and Komorowski, J.-C. (2022). A new 1D velocity model and absolute locations image the Mayotte seismo-volcanic region. *J. Volcanol. Geotherm. Res.*, 421, article no. 107440.

Leahy, G. M., Collins, J. A., Wolfe, C. J., Laske, G., and Solomon, S. C. (2010). Underplating of the Hawaiian Swell: evidence from teleseismic receiver functions. *Geophys. J. Int.*, 183(1), 313–329.

Lemoine, A., Briole, P., Bertil, D., Roullé, A., Foumelis, M., Thinon, I., Raucoules, D., de Michele, M., Valty, P., and Hoste Colomer, R. (2020). The 2018–2019 seismo-volcanic crisis east of Mayotte, Comoros islands: seismicity and ground deformation markers of an exceptional submarine eruption. *Geophys. J. Int.*, 223(1), 22–44.

Ligorría, J. P. and Ammon, C. J. (1999). Iterative deconvolution and receiver-function estimation. *Bull. Seismol. Soc. Am.*, 89(5), 1395–1400.

Mazzullo, A., Stutzmann, E., Montagner, J.-P., Kiselev, S., Maurya, S., Barruol, G., and Sigloch, K. (2017). Anisotropic tomography around la ayleig island from ayleigh waves: tomography of the western Indian Ocean. *J. Geophys. Res. Solid Earth*, 122(11), 9132–9148.

Menand, T. (2011). Physical controls and depth of emplacement of igneous bodies: a review. *Tectonophysics*, 500(1–4), 11–19.

Michon, L. (2016). The volcanism of the Comoros archipelago integrated at a regional scale. In Bachèlery, P., Lenat, J.-F., Di Muro, A., and Michon, L., editors, *Active Volcanoes of the Southwest Indian Ocean*, pages 333–344. Springer, Berlin, Heidelberg.

Michon, L., Famin, V., and Quidelleur, X. (2022). Evolution of the East African Rift System from trap-scale to plate-scale rifting. *Earth-Sci. Rev.*, 231, article no. 104089.

Morgan, W. J. (1971). Convection plumes in the lower mantle. *Nature*, 230, 42–43.

Morgan, W. J. and Morgan, J. P. (2007). Plate velocities in the hotspot reference frame. In Foulger, G. R. and Jurdy, D. M., editors, *Plates, Plumes, and Planetary Processes*, Geological Society of America Special Paper, 430, pages 65–78. Geological Society of America.

Müller, R. D., Royer, J. Y., and Lawyer, L. A. (1993). Revised plate motions relatives to the hotspots from combined Atlantic and Indian hotspot tracks. *Geology*, 21, 275–278.

Nagaya, M., Oda, H., Akazawa, H., and Ishise, M. (2008). Receiver functions of seismic waves in layered anisotropic media: application to the estimate of seismic anisotropy. *Bull. Seismol. Soc. Am.*, 98, 2990–3006.

Nougier, J., Cantagrel, J.-M., and Karche, J. P. (1986). The Comores archipelago in the western Indian Ocean: volcanology, geochronology and geodynamic setting. *J. African Earth Sci.*, 5, 135–144.

Owens, T. J. and Crosson, R. S. (1988). Shallow structure effects on broadband teleseismic P waveforms. *Bull. Seismol. Soc. Am.*, 78(1), 96–108.

Özalaybey, S., Savage, M. K., Sheehan, A. F., Louie, J. N., and Brune, J. N. (1997). Shear-wave velocity structure in the northern Basin and Range province from the combined analysis of receiver functions and surface waves. *Bull. Seismol. Soc. Am.*, 87(1), 183–199.

Pelleter, A.-A., Caroff, M., Cordier, C., Bachèlery, P., Nehlig, P., Debeuf, D., and Arnaud, N. (2014). Melilite-bearing lavas in Mayotte (France): An insight into the mantle source below the Comores. *Lithos*, 208–209, 281–297.

Peterson, D. W. and Moore, J. G. (1987). Geologic history and evolution of geologic concepts, Island of Hawaii. In Decker, R. W., Wright, T. L., and Stauffer, P. H., editors, *Volcanism in Hawaii*, volume 1 of *United States Geological Survey Professional Paper, 1350*, pages 149–189. Chapter 7.

Quidelleur, X., Michon, L., Famin, V., Geffray, M. C., Danišík, M., Gardiner, N., Rusquet, A., and Zakaria, M. G. (2022). Holocene volcanic activity in Anjouan Island (Comoros archipelago) revealed by new

Cassignol-Gillot groundmass K–Ar and 14C ages. *Quat. Geochronol.*, 67, article no. 101236.

Rakotondraompiana, S. A., Albouy, Y., and Piqué, A. (1999). Lithospheric model of the Madagascar island [western Indian Ocean]: a new interpretation of the gravity data. *J. African Earth Sci.*, 28(4), 961–973.

Ranalli, G. and Murphy, D. C. (1987). Rheological stratification of the lithosphere. *Tectonophysics*, 132(4), 281–295.

REVOSIMA (2020). Bulletin n° 25 de l'Activité Sismo-Volcanique à Mayotte. IPGP/BRGM. Sismer. Retrieved from https://campagnes.flotteoceanographique.fr/campagnes/18001729/.

Ryan, W. B. F., Carbotte, S. M., Coplan, J. O., O'Hara, S., Melkonian, A., Arko, R., Weissel, R. A., Ferrini, V., Goodwillie, A., Nitsche, F., Bonczkowski, J., and Zemsky, R. (2009). Global multi-resolution topography synthesis. *Geochem. Geophys. Geosyst.*, 10, article no. Q03014.

Sambridge, M. (1999). Geophysical inversion with a neighbourhood algorithm-I. Searching a parameter space. *Geophys. J. Int.*, 138(2), 479–494.

Saurel, J.-M., Jacques, E., Aiken, C., Lemoine, A., Retailleau, L., Lavayssière, A., Foix, O., Dofal, A., Laurent, A., Mercury, N., Crawford, W., Lemarchand, A., Daniel, R., Pelleau, P., Bès de Berc, M., Dectot, G., Bertil, D., Roullé, A., Broucke, C., Coombain, A., Jund, H., Besançon, S., Guyavarch, P., Kowaski, P., Roudaut, M., Aprioual, R., Battaglia, J., Bodihar, S., Boissier, P., Bouin, M.-P., Brunet, C., Canjamale, K., Catherine, P., Desfete, N., Doubre, C., Dretzen, R., Dumouche, T., Fernagu, P., Ferrazzini, V., Fontaine, F., Gaillot, A., Géli, L., Griot, C., Grunberg, M., Can Guzel, E., Hoste-Colomer, R., Lambotte, S., Lauret, F., Léger, F., Maros, E., Peltier, A., Vergne, J., Satriano, C., Tronel, F., Van der Woerd, J., Fouquet, Y., Jorry, S., Rinnert, E., Thinon, I., and Feuillet, N. (2022). 2019-02-25 to 2020-05-10 Mayotte eruption earthquake catalog relocated with OBS. https://doi.org/10.18715/IPGP.2021.kq136bzh. IPGP Research Collection, V1.

Saurel, J.-M., Jacques, E., Aiken, C., Lemoine, A., Retailleau, L., Lavayssière, A., Foix, O., Dofal, A., Laurent, A., Mercury, N., Crawford, W., Lemarchand, A., Daniel, R., Pelleau, P., Bès de Berc, M., Dectot, G., Bertil, D., Roullé, A., Broucke, C., Coombain, A., Jund, H., Besançon, S., Guyavarch, P., Kowaski, P., Roudaut, M., Aprioual, R., Battaglia, J., Bodihar, S., Boissier, P., Bouin, M.-P., Brunet, C., Canjamale, K., Catherine, P., Desfete, N., Doubre, C., Dretzen, R., Dumouche, T., Fernagu, P., Ferrazzini, V., Fontaine, F., Gaillot, A., Géli, L., Griot, C., Grunberg, M., Can Guzel, E., Hoste-Colomer, R., Lambotte, S., Lauret, F., Léger, F., Maros, E., Peltier, A., Vergne, J., Satriano, C., Tronel, F., Van der Woerd, J., Fouquet, Y., Jorry, S., Rinnert, E., Thinon, I., and Feuillet, N. (2021). Mayotte seismic crisis: building knowledge in near real-time by combining land and ocean-bottom seismometers, first results. *Geophys. J. Int.*, 228(2), 1281–1293.

Savage, M. K. (1998). Lower crustal anisotropy or dipping boundaries? Effects on receiver functions and a case study in New Zealand. *J. Geophys. Res. Solid Earth*, 103, 15069–15087.

Schlaphorst, D., Melekhova, E., Kendall, J.-M., Blundy, J., and Latchman, J. L. (2018). Probing layered arc crust in the Lesser Antilles using receiver functions. *R. Soc. Open Sci.*, 5(11), article no. 180764.

Scholz, J.-R., Barruol, G., Fontaine, F. R., Mazzullo, A., Montagner, J.-P., Stutzmann, E., Michon, L., and Sigloch, K. (2018). SKS splitting in the Western Indian Ocean from land and seafloor seismometers: Plume, plate and ridge signatures. *Earth Planet. Sci. Lett.*, 498, 169–184.

Sparks, R. S. J., Annen, C., Blundy, J. D., Cashman, K. V., Rust, A. C., and Jackson, M. D. (2019). Formation and dynamics of magma reservoirs. *Philos. Trans. R. Soc. A*, 377, article no. 20180019.

Stephenson, S. N., White, N. J., Carter, A., Seward, D., Ball, P. W., and Klöcking, M. (2021). Cenozoic dynamic topography of Madagascar. *Geochem. Geophys. Geosyst.*, 22, article no. e2020GC009624.

Thomson, W. T. (1950). Transmission of elastic waves through a stratified solid medium. *J. Appl. Phys.*, 21(2), 89–93.

Tkalčić, H., Chen, Y., Liu, R., Zhibin, H., Sun, L., and Chan, W. (2011). Multistep modelling of teleseismic receiver functions combined with constraints from seismic tomography: Crustal structure beneath southeast China. *Geophys. J. Int.*, 187(1), 303–326.

Tkalčić, H., Pasyanos, M. E., Rodgers, A. J., Gök, R., Walter, W. R., and Al-Amri, A. (2006). A multistep approach for joint modeling of surface wave dispersion and teleseismic receiver functions: Implications for lithospheric structure of the Arabian

Peninsula. *J. Geophys. Res. Solid Earth*, 111, article no. B11311.

Vergne, J., Wittlinger, G., Hui, Q., Tapponnier, P., Poupinet, G., Mei, J., Herquel, G., and Paul, A. (2002). Seismic evidence for stepwise thickening of the crust across the NE Tibetan plateau. *Earth Planet. Sci. Lett.*, 203(1), 25–33.

Vormann, M., Franke, D., and Jokat, W. (2020). The crustal structure of the southern Davie Ridge offshore northern Mozambique—A wide-angle seismic and potential field study. *Tectonophysics*, 778, article no. 228370.

Watts, A. B., ten Brink, U. S., Buhl, P., and Brocher, T. M. (1985). A multichannel seismic study of lithospheric flexure across the Hawaiian–Emperor seamount chain. *Nature*, 315(6015), 105–111.

Zelt, B. C. and Ellis, R. M. (1999). Receiver-function studies in the Trans-Hudson Orogen, Saskatchewan. *Can. J. Earth Sci.*, 36(4), 585–603.

Zhang, H. S., Tian, X. B., and Teng, J. W. (2009). Estimation of crustal Vp/Vs ratio with dipping Moho from receiver functions. *Chin. J. Geophys.*, 52(5), 1243–1252.

Zheng, T., Zhao, L., and Chen, L. (2005). A detailed receiver function image of the sedimentary structure in the Bohai Bay Basin. *Phys. Earth Planet. Inter.*, 152(3), 129–143.

Zhu, L. and Kanamori, H. (2000). Moho depth variation in southern California from teleseismic receiver functions. *J. Geophys. Res. Solid Earth*, 105(B2), 2969–2980.

*Comptes Rendus*
*Géoscience — Sciences de la Planète*
**2022**, Vol. 354, Special Issue S2, p. 65-79
https://doi.org/10.5802/crgeos.154

The Mayotte seismo-volcanic crisis of 2018-2021 in the Comoros archipelago (Mozambique channel) / *La crise sismo-volcanique de 2018-2021 de Mayotte dans l'archipel des Comores (Canal du Mozambique)*

# The East-Mayotte new volcano in the Comoros Archipelago: structure and timing of magmatic phases inferred from seismic reflection data

# *Le nouveau volcan de l'Est-Mayotte dans l'archipel des Comores : structure et chronologie des phases magmatiques déduites des données d'imagerie sismique*

**Charles Masquelet**[*, a], **Sylvie Leroy**[a], **Matthias Delescluse**[b], **Nicolas Chamot-Rooke**[b], **Isabelle Thinon**[c], **Anne Lemoine**[c], **Dieter Franke**[d], **Louise Watremez**[e], **Philippe Werner**[f], **Fabien Paquet**[c], **Carole Berthod**[g], **Victor Cabiativa Pico**[a] **and Daniel Sauter**[f]

[a] Sorbonne Université, CNRS, Institut des Sciences de la Terre de Paris (ISTeP), Paris, France

[b] Laboratoire de Géologie de l'École Normale Supérieure (ENS), CNRS UMR 8538, PSL University, Paris, France

[c] Bureau de Recherches Géologiques et Minières (BRGM), Orléans, France

[d] Bundesanstalt für Geowissenschaften und Rohstoffe (BGR), Hannover, Deutschland

[e] Université de Lille, CNRS, Université Littoral Côte d'Opale, IRD, UMR 8187 – LOG – Laboratoire d'Océanologie et de Géosciences, Lille, France

[f] Institut Terre et Environnement de Strasbourg (ITES), CNRS Université de Strasbourg, Strasbourg, France

[g] Laboratoire Magma et Volcans, Aubière, France

*E-mails:* charles.masquelet@sorbonne-universite.fr (C. Masquelet), sylvie.leroy@sorbonne-universite.fr (S. Leroy), delescluse@geologie.ens.fr (M. Delescluse), rooke@geologie.ens.fr (N. Chamot-Rooke), I.thinon@brgm.fr (I. Thinon), A.lemoine@brgm.fr (A. Lemoine), Dieter.Franke@bgr.de (D. Franke), louise.watremez@univ-lille.fr (L. Watremez), ph.werner@orange.fr (P. Werner), F.Paquet@brgm.fr (F. Paquet), carole.berthod@uca.fr (C. Berthod), victor.cabiativa_pico@sorbonne-universite.fr (V. Cabiativa Pico), Daniel.Sauter@unistra.fr (D. Sauter)

[*] Corresponding author.

**Abstract.** A multichannel seismic reflection profile acquired during the SISMAORE cruise (2021) provides the first in-depth image of the submarine volcanic edifice, named Fani Maore, that formed 50 km east of Mayotte Island (Comoros Archipelago) in 2018–2019. This new edifice sits on a ~140 m thick sedimentary layer, which is above a major, volcanic layer up to ~1 km thick and extends over 120 km along the profile. This volcanic unit is made of several distinct seismic facies that indicate successive volcanic phases. We interpret this volcanic layer as witnessing the main phase of construction of the Mayotte Island volcanic edifice. A ~2.2–2.5 km thick sedimentary unit is present between this volcanic layer and the top of the crust. A complex magmatic feeder system is observed within this unit, composed of saucer-shape sills and seal bypass systems. The deepest tip of this volcanic layer lies below the top-Oligocene seismic horizon, indicating that the volcanism of Mayotte Island likely began around 26.5 Ma, earlier than previously assumed.

**Résumé.** Un profil de sismique réflexion multitrace acquis lors de la campagne océanographique SISMAORE (2021) apporte la première image en profondeur du volcan sous-marin Fani Maore, qui s'est formé à 50 km à l'est de l'île de Mayotte (archipel des Comores) en 2018–2019. Ce nouvel édifice repose sur une première couche sédimentaire d'environ 140 m d'épaisseur au-dessus d'une couche volcanique majeure épaisse de 1 km et qui s'étend sur 120 km le long du profil. Cette dernière unité volcanique est constituée de plusieurs faciès sismiques distincts qui indiquent des phases volcaniques successives. Nous interprétons cette couche volcanique comme le témoin de la phase principale de construction de l'édifice volcanique de l'île de Mayotte. Une couverture sédimentaire de ~2.2–2.5 km d'épaisseur est présente entre cette couche volcanique et le toit de la croûte. On y observe de nombreux sills en forme de soucoupe ainsi que des zones à faciès de remontées de fluides, dessinant un système d'alimentation magmatique complexe sous la principale couche volcanique. L'extrémité la plus profonde de cette couche volcanique se place en dessous de l'horizon sismique de l'Oligocène supérieur et indique que le volcanisme de l'île de Mayotte a probablement commencé vers 26.5 Ma, plus tôt que ce qui était supposé auparavant.

**Keywords.** Comoros Archipelago, Mayotte, Fani Maore volcano, Volcanism, Seismic reflection.

**Mots-clés.** Archipel des Comores, Mayotte, Volcan Fani Maoré, Volcanisme, Sismique réflexion.

*Published online: 9 December 2022, Issue date: 17 January 2023*

## 1. Introduction

The East-Mayotte seismo-volcanic crisis that started in May 2018 [Cesca et al., 2020, Lemoine et al., 2020] and gave birth to a large—820 m high and 5 km in diameter—submarine volcanic edifice sitting at approximately 3500 m water depth [Feuillet et al., 2021]. Following an application submitted to the UNESCO's International Marine Chart Commission, the new volcano was named Fani Maore. The new volcano grew in the abyssal plain of the North Mozambique Channel, some 50 km east of Mayotte Island (Comoros Archipelago), at the end of a NW–SE trending volcanic ridge (Figure 1). Before May 2018, no recent eruption or notable seismic activity was reported around Mayotte [Lemoine et al., 2020]. Moreover, no recent volcanic edifice was mapped during successive bathymetric surveys in 2014 and 2016 at the position of the Fani Maore volcano [Feuillet et al., 2021]. Since May 2019, multiple scientific cruises collected geophysical and geochemical data to document this active submarine eruption, which is one of the largest ever witnessed [MAYOBS cruises; Rinnert et al., 2019]. The petrological signatures of dredged lavas integrated with geophysical data show that this large effusive eruption is fed by a deep (≥37 km) and large (≥10 km$^3$) pre-existing mantle reservoir and that the eruption was tectonically triggered [Berthod et al., 2021a, Lavayssière et al., 2021]. The magma transfer from mantle depth up to the seafloor is syn-eruptive [Berthod et al., 2021a]. Yet, direct information at the crustal scale is missing and both the structure and the nature of the basement below the Fani Maore volcano are unknown.

In February 2021, the SISMAORE cruise aboard R/V (Research Vessel) "Pourquoi Pas?" collected deep seismic reflection data along several profiles within the abyssal plains surrounding the volcanic islands of the Comoros Archipelago (Figure 1). This article presents an interpretation of a multichannel seismic profile (MAOR21D01) acquired across the new submarine East-Mayotte volcano. This profile reveals the submarine structure of the Fani Maore volcano as well as widespread magmatic features around, sills in particular, imaged within the ~3 km thick sedimentary cover from the seafloor down to the top of the

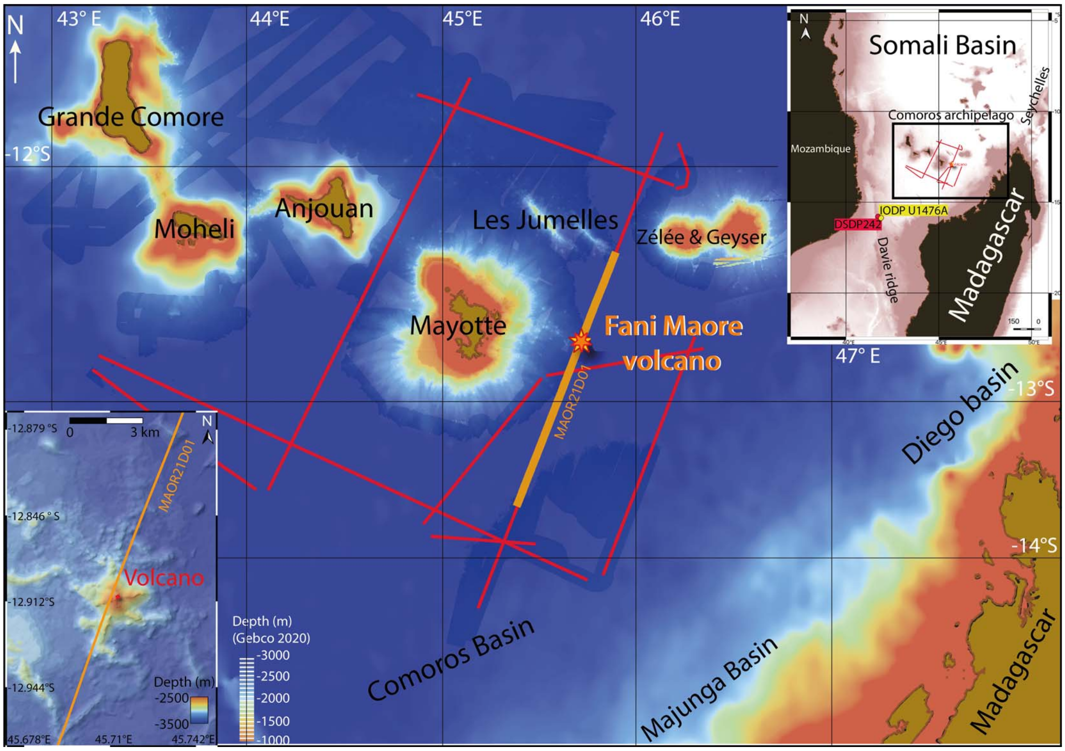


**Figure 1.** Location of the multichannel seismic profile MAOR21D01 (orange line) from SISMAORE MCS dataset (red lines) in the south of the Somali basin offshore the Comoros Archipelago, in the western Indian Ocean [see top-right inset; bathymetric data from Compilation Group GEBCO Grid, 2020]. Lower-left inset: bathymetric map of the Fani Maore volcano to the east of Mayotte [Thinon et al., 2020].

crust. We constrain the age of the onset of volcanic activity in the survey area by identifying a basaltic layer at depth that we relate to the early construction of Mayotte Island and correlating seismic horizons above and below, using known seismic stratigraphy.

## 2. Geological background

Volcanism in the northern Mozambique Channel is widespread since the Early Cretaceous [Sauter et al., 2018]. It initiated soon after the onset of seafloor spreading between Madagascar and Africa and continued as several phases until the present-day. In the West Somali Basin and the Mozambique Channel, the oldest regional magmatic phase occurred in Late Cretaceous times in relation to the breakup of Madagascar and Greater India [Torsvik et al., 2000]. Widespread flood basalts erupted between 92–83 Ma both onshore and offshore Madagascar [Leroux et al., 2020, Storey et al., 1995]. Renewed volcanic activity around the Mozambique Channel appeared to have started during Late Oligocene [Michon, 2016]. Based on geochronological data, the oldest volcanic activity recorded in the Comoros Archipelago has been dated around 11 Ma ago [Pelleter et al., 2014], but the timing of onset and main growth phase of the Archipelago remains poorly constrained [Michon, 2016]. Assuming an average long-term magma production rate for the Comoros Archipelago of 0.05 $m^3/s$, Michon [2016] suggested that volcanic activity initiated earlier in Mayotte, at about 20 Ma ago. The nature of the crust beneath the volcanic edifices remains a major open question. Both oceanic and extended continental crust have been proposed [Famin et al., 2020]. Using one receiver function, Dofal et al. [2021] recently proposed that the volcanic edifice of Mayotte Island was emplaced on top of an isolated continental block, abandoned during the Gondwana break-up and thickened afterward by magmatic underplating. However, these data were compatible with both continental and oceanic crust, and the continental block model mainly relies on the presence of a quartzite massif, on Anjouan Island, which is west (i.e., oceanward) of Mayotte [Roach et al., 2017]. Thus, the nature of the crust under Mayotte is still subject to debate.

## 3. Data acquisition and processing

Multichannel seismic (MCS) data were recorded with a 6000 m long streamer with 960 channels spaced every 6.25 m and towed at 10 m depth. The streamer position was computed using a tail buoy GPS and compasses. The seismic reflection source was composed of 16 airguns in two clusters, with a total volume of ~82 L (4990 cu. in.), also towed at 10 m depth. The airgun array was triggered every 40 s, i.e., every 100 m with a mean vessel speed of 4.8 knots. The record length was 20 s with a sampling rate of 2 ms. The distance between each common depth point (CDP) is 3.25 m. During processing, supergather CDPs were built by merging 4 CDPs in a bin of 12.5 m, allowing for a fold of 60.

Processing followed a fairly typical workflow using Geovation® software (developed by CGG) in pre-stack time for almost all steps: trace editing, amplitude correction, normal move-out correction, FK-filtering, multiple attenuation and predictive deconvolution. Post-stack time migration was performed using velocity analysis. Velocities were manually picked every 200 CDP to update the velocity model (Figure 2 and Supplementary Figure 1). The first picking round resulted in a significant signal loss below ~5.25 s TWT (two-way travel time) after stacking (example around CDP 8001, Figure 2Aa, Ab and Ac, assuming a linear velocity increase with depth shown as red line in B). We iteratively improved the stack by increasing the RMS (root mean square) velocity at that depth (resulting interval velocities shown as black line in Figure 2B, improved stack in Ca, Supplementary Figure 1). The clearest reflectivity in the entire sedimentary column was obtained with a strong increase of the interval velocity followed by a velocity inversion defining a 4000 m/s layer between 5.25 s and 5.55 s TWT (at CDP 8001) (Supplementary Figure 2). Seismic reflectors beneath (Figure 2Ca, Cb and Cc) gain more coherency when the velocity inversion is included. Although we may sometimes miss the exact location of the velocity inversion due to the low resolution of velocity picking, a weak reflector marking the base of the layer can be followed consistently along most of the profile (Figure 3B, Ca, Cb). Below this layer, velocities must be back to levels expected for typical sedimentary layers (2000–3000 m/s; Figure 2A).

## 4. Description of the multichannel seismic reflection profile

The most striking shallow feature of the seismic reflection profile is the recent Fani Maore volcano, centered at CDP 12800 (distance ~99 km) (Figure 3A, B). The volcanic edifice is ~1 s TWT high and 10 km wide at its base. An important observation is that it sits on a series of subparallel reflectors, corresponding to a 0.12 s TWT thick sedimentary unit (quoted $\alpha$ in Figure 3B). Two smaller edifices, ~0.3 s TWT high and 1.3–1.8 km wide, are located on each side of the new volcano (centered at CDP 12400 and 13400). A strong reflector located below the volcanic edifices can be traced at ~4.75 s TWT all the way to the southern and northern ends of the profile, within the sedimentary unit (Figure 3A, B, C). This reflector corresponds to a strong velocity gradient at the top of the 4000 m/s interval velocity layer (see Section 3, Figure 2 and Supplementary Figure 2). Considering that this interval velocity is representative of typical basaltic rocks [Telford et al., 1990] and that the strong reflector at the top of the layer is below the volcanic edifices, we are confident that this reflector corresponds to the top of a basaltic unit. Sub-parallel reflectors, corresponding to sedimentary layers, are observed both above and below this volcanic layer (Figure 3). The entire sedimentary cover is thinner in the northernmost part of the profile (~2.5 s TWT thick converting to ~3.1 km using an average 2500 m/s velocity in the sediments) than at the southern end of the profile (3 s TWT, ~3.8 km) (Figure 3). The top basement is defined by a strong reflector at 7–8 s TWT below which continuous and fine layering is no longer observed, replaced by a series of discontinuous very low frequency phases.

### 4.1. *Seismic stratigraphy*

Calibration of MCS data in previous works [Franke et al., 2015, Klimke et al., 2016] is based on the stratig-

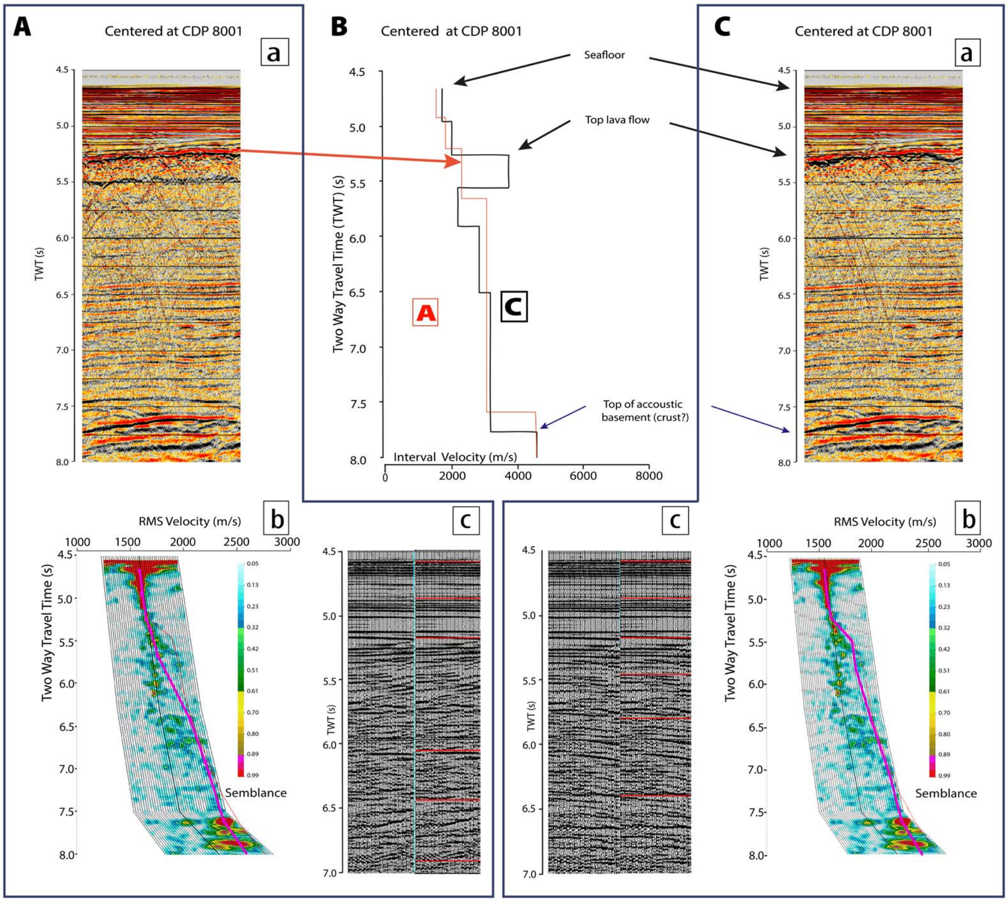


**Figure 2.** (A) Seismic processing using the velocity picking in red line (B) (a) Seismic image centered at CDP 8001 with the velocity model presented in (B) (red line); (b) RMS velocities (purple lines) as a function of TWT (s), shown on the semblance. These RMS velocities profiles have been applied to the stacked profile shown in (Aa); (c) Supergather 8001 after Normal Move Out correction (NMO) (red lines) corresponding to the stacked section (Aa). (B) Example of interval velocity of the supergather CDP 8001 as a function of the two-way travel time for two different velocity pickings (the red line corresponds to the RMS velocity picking shown in (Ab); the black line corresponds to the RMS velocity picking shown in (Cb)) (C) Seismic processing using the velocity picking in black line (B) (a) Seismic image centered around CDP 8001 after application of the full processing workflow with velocity inversion (B: black line), (b) RMS velocities (purple lines) as a function of TWT (s), shown on the semblance. These RMS velocities profiles have been applied to the stacked profile shown in Ca. (c) Stack section centered around CDP 8001 after NMO velocity picking, based on the first determination of velocities presented in Cb and B black line.

raphy obtained at DSDP (Deep Sea Drilling Project) hole 242 and IODP (Integrated Ocean Drilling Program) hole 1476, both located ~500 km west of Mayotte (inset in Figure 1), as well as ties with seismic lines of offshore Madagascar [Leroux et al., 2020]. Our revised seismic stratigraphy builds on these studies and the identification of four remarkable seismic markers in the sedimentary cover: top Miocene, top Oligocene, Cretaceous-Paleogene unconformity (K/Pg), and the Turonian volcanism event (Figures 3 and 4). Since they bracket the basaltic layer, they put strong constraints on the timing of Mayotte volcan-

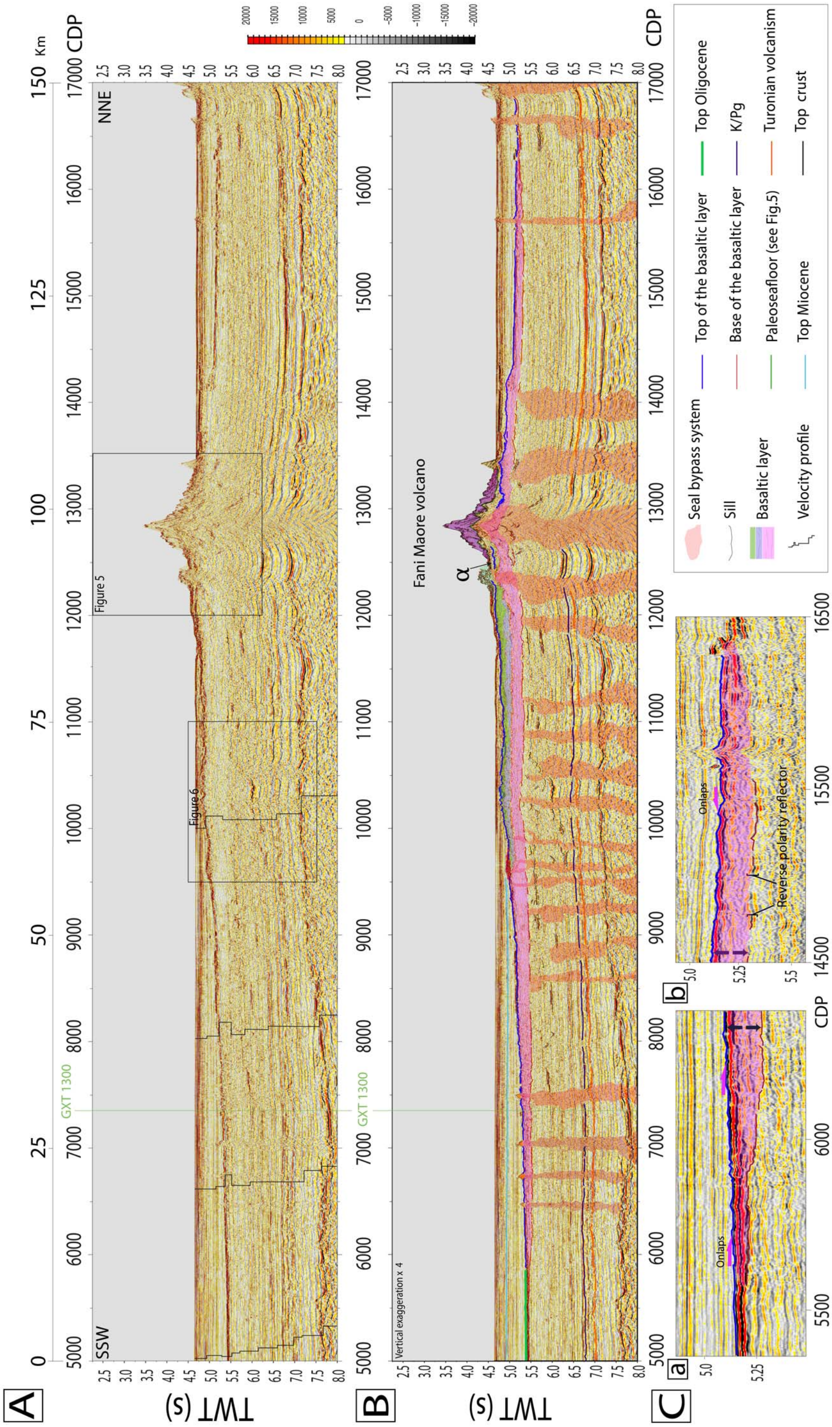


**Figure 3.** (A) Migrated profile MAOR21D01 with (B) interpretation from CDP 5000 to CDP 17000 (150 km, see Figure 1 for the location of the profile. The Fani Maore volcano is located at CDP 12900. (C) Termination of the basaltic layer on the southern (a) (vertical exaggeration ×4) and in the northern (b) (vertical exaggeration ×8) part of the line. Sediments are onlapping on its top.

ism. These markers are distinctively followed in the southern part of the profile but are more difficult to identify to the north of the new volcano.

The K/Pg unconformity is a distinct event recognized in the seismic profiles throughout the West Somali basin [Franke et al., 2015, Mahanjane, 2014]. Offshore northern Madagascar, this unconformity is well marked in the lines crossing the offshore Majunga Basin [Leroux et al., 2020]. One of these lines (ION GXT 1300) crosses our MAOR21D01 profile at CDP 7400 (Figure 3A, B, green vertical line) allowing us to correlate the medium amplitude reflector, more clearly visible at 6.75 s TWT at CDP 6000 (Figure 4), to the K/Pg unconformity (K/Pg blue line in Figures). A series of reflectors is onlapping the K/Pg unconformity at the southern end of the profile. Below the K/Pg reflector, we interpret a package of high amplitude and low-frequency discontinuous reflectors (TV in Figures 3 and 4, orange line) as corresponding to the Turonian volcanism that has been evidenced in the Diego and Majunga basins offshore Madagascar [Coffin and Rabinowitz, 1987, Leroux et al., 2020].

We identify a strong reflector as the top Oligocene horizon, based on the seismic stratigraphy used in Franke et al. [2015, TO in Figures 3 and 4] and the DSDP hole 242. This Oligocene horizon is well defined in the Rovuma basin [Mougenot et al., 1986] and can be followed from there up to the eastern flank of the Davie Ridge [Franke et al., 2015] and toward the Comoros Archipelago. Finally, we identify a top Miocene horizon (TM in Figures 3 and 4) at the same depth than the top-Miocene unit found in the IODP hole 1476 [235 m below sea floor, location in Figure 1; Hall et al., 2017].

### 4.2. *Description of the basaltic layer*

The top of the basaltic layer is a clear, strong reflector all along the MCS line (Figures 3A, B, and 4). To the south of the new volcano, this reflector gently dips ~1° southward, in continuity with the slope of the Mayotte edifice, measured from the bathymetric data in a sediment-free area. From the seismic image, it is clear that the sedimentary layers on top of the basaltic layer are progressively onlapping the top reflector on both sides of the Fani Maore volcano (Figure 3Ca). The top of the basaltic layer is highly reflective and smooth except where conic-shaped edifices are locally observed. Small conic-shaped edifices, ~500 m wide and ~200 m high, are most clearly imaged around CDP 7000 in the distal part of the volcanic layer (Figure 3). Another volcano around 4 km large and 150 m tall is observed at CDP 9600. To the north of this edifice, the top basaltic basement becomes rougher and irregular for ~20 km, before stepping upward and reaching the recent volcano area. A medium amplitude discontinuous flat reflector at ~5.7 s TWT is identified as the base of the basaltic layer. This reflector is characterized by his reverse polarity, more clearly visible on the northern part of the profile (see the red line in Figures 3Cb, 4, 5 and 6). This layer thins southward and ends as a single reflector at ~5.7 s TWT depth at the southernmost end of the MCS line (Figure 3).

In the southern part of the MCS line, three seismic facies are identified within the basaltic layer (pink, blue and green units to the south of the Fani Maore volcano in Figures 3–5). To the north, the facies of the basaltic layer appears more or less uniform (cyan layer to the north of the new volcano in Figures 3B and 5c). We interpret the deepest seismically transparent layer with a mean thickness of ~0.5 s TWT (~1000 m) as representing the main volcanic flow unit (see the pink layer in Figures 3B and 4c). It extends from CDP 5590 to CDP 12800 along ~91 km. Closer to the submarine volcano, a second basaltic unit overlays the bottom one, but still below the seismically distinct top reflection of the flow unit (blue layer in Figures 3B and 5c). This layer has a smaller extent (~33 km) and thickness (~0.25 s TWT, i.e., ~500 m on average) when compared to the main volcanic unit. The thickness of the upper part of the basaltic layer is highly variable and reaches 0.4 s TWT (800 m) close to the new volcanic edifice (see the green layer in Figures 3 and 5). To the north of the Fani Maore volcano, the basaltic layer extends from CDP 13500 to CDP 16500 (~35 km) and is made of a flat-lying unit (cyan layer in Figures 3B and 5c). A distinct step in the top reflector of this layer at CDP 14200 might represent a lava front. Close to the new volcano, the volcanic unit is ~0.3 s TWT thick (~700 m) while it thins to ~0.2 s TWT (~400 m) to the north of the step.

### 4.3. *The seal bypass systems*

Below the volcanic layer, numerous seal bypass systems [as defined by Cartwright et al., 2007] are ob-

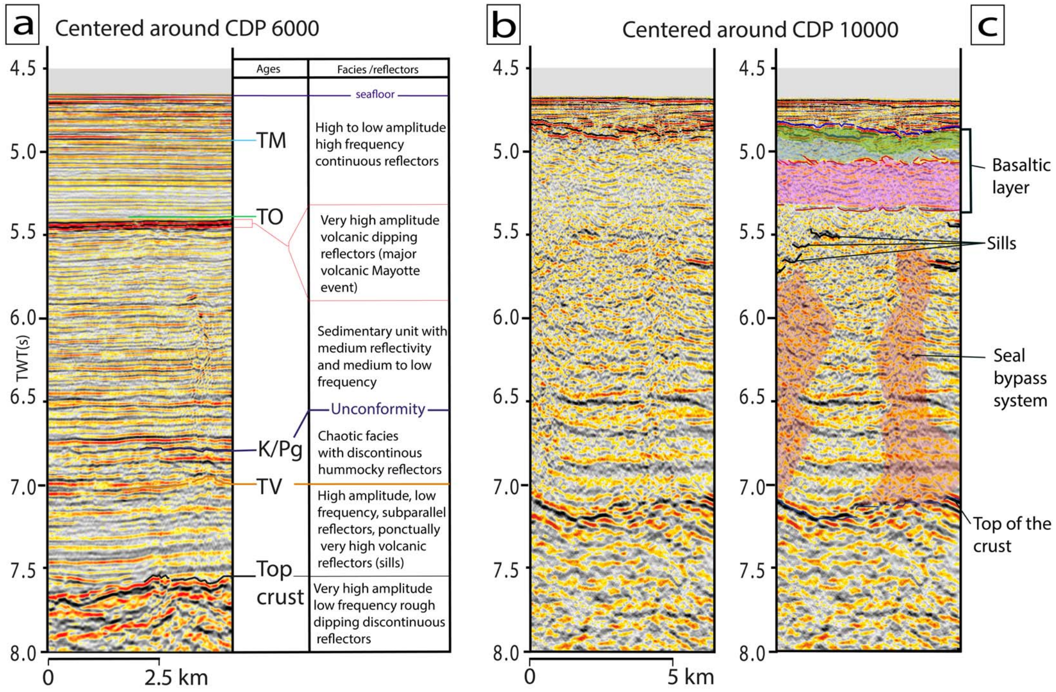


**Figure 4.** (a) Seismic stratigraphic horizons and associated facies identified at CDP 6000 (line MAOR21D01) TM: Top Miocene, TO: Top Oligocene, K/Pg: Cretaceous/Paleogene unconformity, TV: Turonian volcanism; (b, c) same profile at CDP 10000 and identification of seismic facies: basalt layer, sills, seal bypass system, and the top of the acoustic basement.

served (reddish domains in Figures 3–5). These seal bypass systems are recognized as chaotic chimney-like seismic facies running vertically through the sedimentary units. There, the typical continuous reflection pattern of the sedimentary units is replaced by scattered and strongly attenuated reflections. Locally, pull-up effects, due to vertical variations in velocity resulting from the occurrence of high-velocity magmatic material, disturb the geometry of the sedimentary units (as observed in TWT). Because there is often a progressive change of the seismic facies toward the centers of the seal bypass systems, defining precisely the edges of this seismic facies is difficult. The high-velocity basaltic layer above also acts as a screen filter and masks the imaging of the lower parts. Therefore, we only show the largest and best-defined seal bypass systems in Figures 3, 5 and 6. Such seal bypass systems are more numerous to the south of the new volcano while the chaotic seismic facies is more pervasive at a small scale in the northernmost part of the profile. There, beside smaller systems, we observe two seal bypass systems that cuts through the volcanic layer and the recent sedimentary layer rising up to the seafloor (Figure 3A, B; CDP 15700 and CDP 16600). At the end of the profile (CDP 17000) we observe some seal bypass system corresponding to the volcanic activity of the Jumelles ridges (Figure 1). All other seal bypass systems (without counting the seal bypass system present under the Fani Maore volcano) are sealed by the main volcanic layer. Seal bypass systems are narrow below small volcanic edifices and wider below the larger edifices, the largest one being observed beneath the new East-Mayotte volcano (Figure 5b, c). Numerous saucer-shaped bright reflectors, often organized step-wise, are observed both inside and at the border of the seal bypass systems. Although their shape might result from pull-up effects or migration artifacts (CDP 12700; at 5.0 s TWT), we interpret most of these bright amplitude reflectors as sills (Fig-

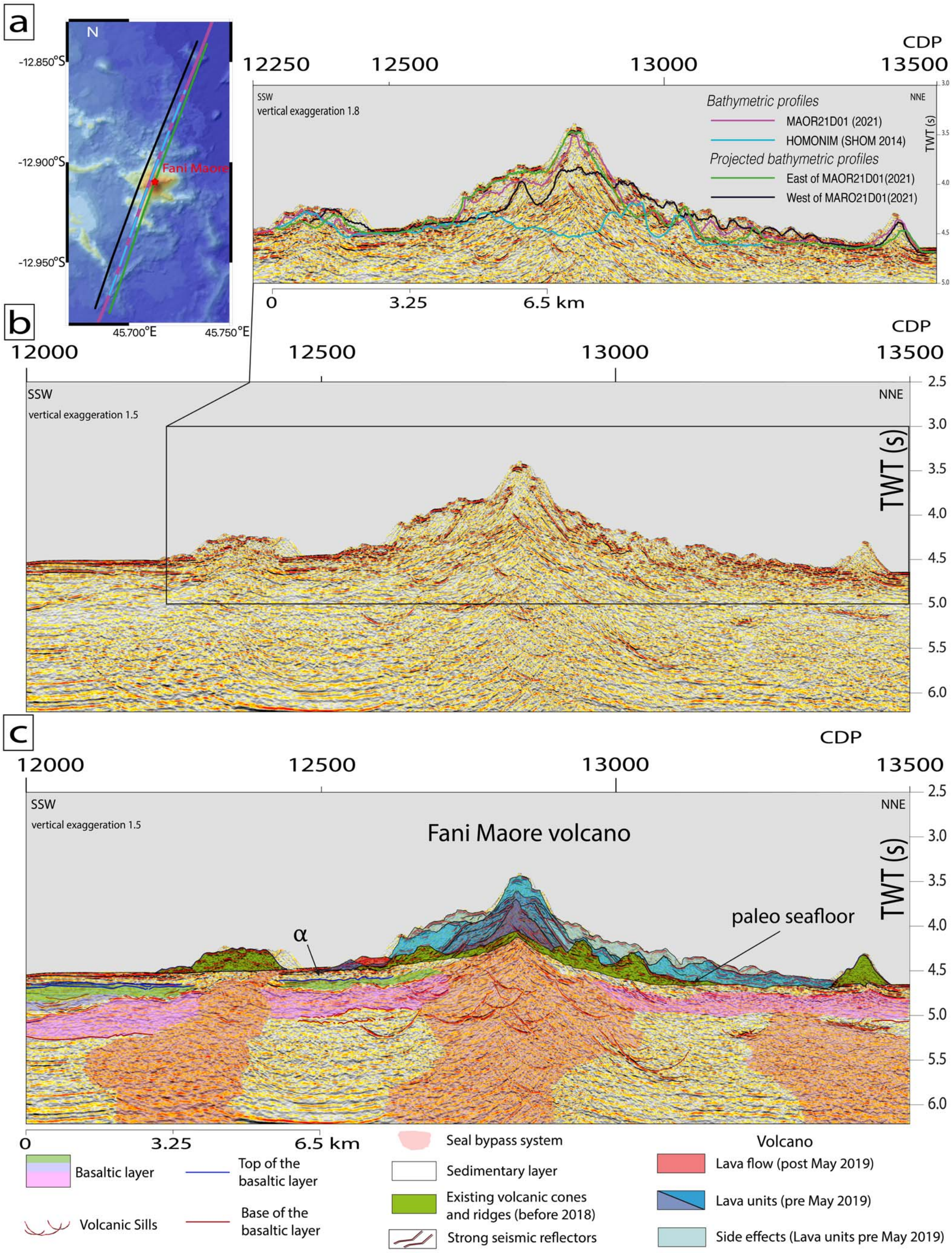


**Figure 5.** (a) Bathymetric profiles converted in s TWT plotted on the seismic profile MAOR21D01. Purple is from SISMAORE cruise [Thinon et al., 2020, 2022] dark blue from the HOMONIM project [SHOM, 2016a]. Parallel bathymetric profiles from SISMAORE cruise on either side of the seismic profile are projected onto the seismic profile. Seismic reflections above the purple line in the northern and southern parts of the volcano could be seismic side echoes from late flows on its flanks. (b, c) Close up view of the Fani Maore volcano from CDP 12000 to 13500 (18.75 km length, see Figure 3 for the location) and its interpretation. We identify the latest lava flows building the volcano since 2018 (in blue, purple and orange) and the paleo-seafloor (top of green surface); we define distinct facies into the basaltic layer (see Figure 6 for explanations).

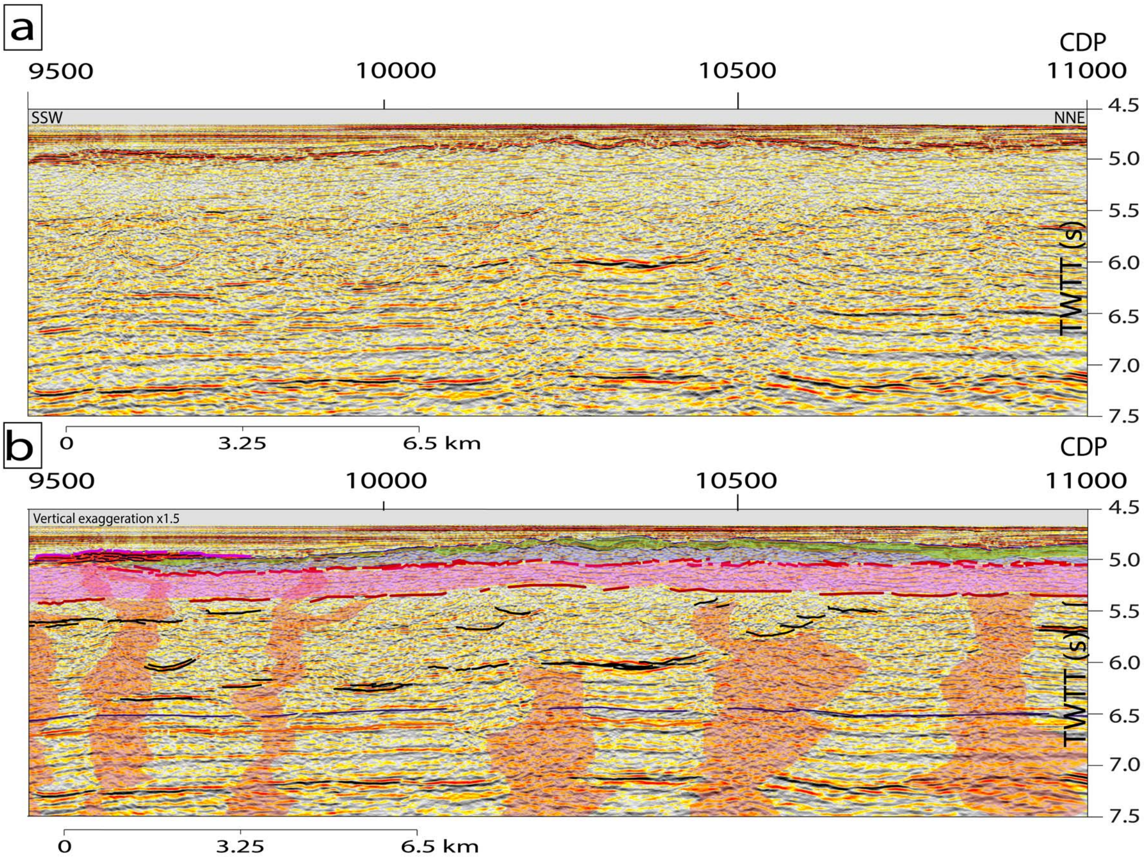


**Figure 6.** (a, b) Close-up view of the southern part of the MAOR21D01 profile from CDP 9500 to 11000 showing the seismic facies within the basaltic layer and below it within the seal bypass systems (see Figure 3 for the location).

ures 3A, B, 4, 6, and 7) [Medialdea et al., 2017]. We thus interpret the disturbed seismic facies in the seal bypass systems as the result of a network of almost vertical dykes or fractures, not imaged in seismic reflection, in which fluids and/or melt are rising from crustal or sub-crustal levels, up to the submarine volcanic edifices.

### 4.4. *The new volcanic edifice*

We use the bathymetric grid collected by the SHOM (Service hydrographique et océanographique de la marine) in 2014 [SHOM, 2016b, 2014] to obtain a time converted profile of the paleo-seafloor, using water interval velocity (the pull-up is not corrected). We superimpose this paleo-seafloor on the MCS profile (see the blue line in Figure 5a). This paleo-seafloor is not flat but shows some conic-shaped edifices that can be correlated with a strong undulating reflector in the MCS profile (see the green layer in Figures 3b and 5c). This reflector joins the seafloor at CDP 12500 to the south and CDP 13300 to the north defining the 10 km wide base of the new volcano (Figure 5b, c). To the north, the recent volcanic material abuts the adjacent smaller and older edifice (green in Figures 5, 7). To the south, the seafloor at the foot of the new volcano is flat if corrected for the pull-up effect from high-velocity material and at the same depth as the small older volcanic edifice to the south (CDP 12500 Figures 3, 5 and 7). This strongly argues for the presence of sediments at the seafloor there, rather than a magmatic flow unit. Indeed, between

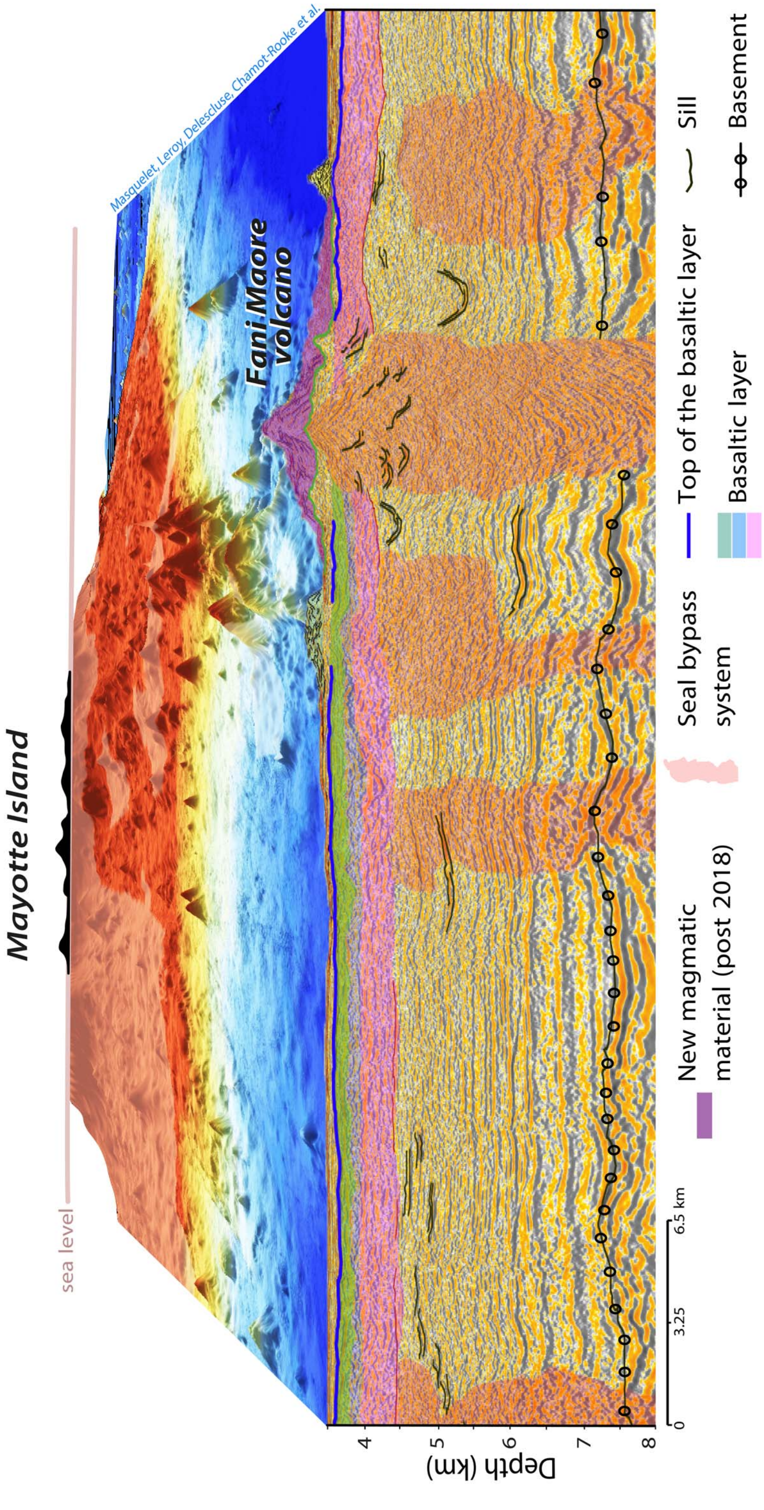


**Figure 7.** 3D close-up view of the Fani Maore volcano area with the interpreted seismic line MAOR21D01, converted in depth using our stack velocity model (see Supplementary material 1).

this paleo-seafloor and the main volcanic layers at depth (pink and cyan layers in Figures 3 and 5) we identify a ~0.11 s TWT (~140 m) thick unit which contains locally some fine reflectors that we propose to correspond to sedimentary layers. A few bright reflectors are also observed within this unit that could correspond to volcanic flows ($\alpha$ in Figures 3B and 5). Finally, under the Fani Maore volcano and below the basaltic layer, a series of subparallel reflectors corresponding to a sedimentary unit 1.75–2 s TWT thick (~2.2–2.5 km) is identified lying on the top of the acoustic basement (Figures 5 and 7). Numerous bright saucer-shaped reflectors (i.e., sills) are imaged both within and outside the large seal bypass system delineated below the new volcano.

Above the paleo-seafloor, i.e., within the Fani Maore volcano, we attempt to identify different seismic units based on their more or less transparent facies and specific geometries of reflectors (Figure 5c). Superimposing time corrected bathymetric profiles from either side of the seismic profile onto the seismic image (Figure 5a, black and green lines) shows that the southern and northern upper parts of the new volcanic edifice may correspond to seismic side echoes generated by late lava flows on the flanks (light blue areas in Figure 5c). The strongest reflectors, which are almost parallel to each other and are dipping away from the central and shallowest part of the volcano, are marking changes of seismic facies. Therefore, we interpret them as corresponding to the main lava flows at the end or start of the volcanic events building the successive volcanic cones (Figure 5c in purple and blue). Smaller and weaker reflectors within some of these seismic facies look similar to those found in lava deltas (see within the blue domain in darkest blue Figure 5c) indicating lateral progradation of the edifice flanks during the volcanic events. Thanks to a previous bathymetric survey in May 2019 [Feuillet et al., 2021] we could identify a single small post May 2019 lava flow in our profile (in orange in Figure 5).

## 5. Evolution of the volcanism

Parallel lava flows dipping away from the volcano's shallowest part indicate that they were likely fed by a single magma conduit. We propose that the new volcano was formed through successive eruptive events building stacked cones and associated flows. These lava flows covered the pre-existing conic-shaped edifices of the paleo seafloor. Following the results from Berthod et al. [2021b] and Berthod et al. [2022], the single small post May 2019 lava flow (in red in Figure 5) shows that most of Fani Maore edifice imaged by our seismic reflection profile was built between May 2018 and May 2019, correlated to the beginning of the seismic crisis. This lava flow and the underlying one appear to cover an about 140 m-thick sedimentary unit with minor volcanic additions in it (see $\alpha$ in Figure 5). Assuming a 3 cm/ky sedimentation rate, measured at IODP well 1476 [Hall et al., 2017], a ~4.6 Ma long period of tectonic quiescence with little volcanism, if any, is roughly estimated at this location.

The main magmatic phase that resulted in the formation of the deep basaltic units is obviously older. The distinct seismic facies of this main basaltic layer together with the numerous seal bypass systems feeding several volcanic edifices on top of it reveal a complex volcanic evolution around Mayotte Island with at least three volcanic phases. The thickest, deepest, and thus oldest, basaltic layer with its flat base parallel to the underlying sedimentary units, has the widest extent. Considering the location of the seismic line on the flank of Mayotte Island and the gentle slope of the basaltic layer inline with the one of the Mayotte edifice, it is likely that this volcanic layer corresponds to the submarine portion of the Mayotte Island volcanic edifice (Figures 3A, B, 6a, b, and 7). Following Leroux et al. [2020], we attribute this volcanic episode to the very early formation of Mayotte Island. The southern end of this volcanic layer lies below the inferred top-Oligocene seismic horizon (~23 Ma, Figures 3 and 4). Volcanism at Mayotte Island may thus have begun significantly earlier than previously thought [20 Ma, Michon, 2016]. We estimate the onset of this volcanism between 26 and 27 Ma ago by taking the 0.13 s TWT difference between the top-Oligocene horizon and the most distal part of the main volcanic layer (130 m at 2 km/s) and assuming a 30–35 m/Ma constant sedimentation rate during the Oligocene. We will reassess this age of the onset of volcanism at Mayotte and the nearby Comoros islands using the other MCS lines from the SISMAORE cruise in a forthcoming paper. We note that this age coincides with the beginning of the rift-related volcanism in the southern East African Rift System [26–25 Ma in the Rukwa Basin; Roberts et al., 2012], as well as in Central Madagascar [28 Ma in the Ankaratra province, Bardintzeff et al., 2010]. Following Michon [2016] and Michon et al. [2022], this contemporary onset of volcanism suggests a genetic link at a regional scale.

## 6. Conclusions

The interpretation of a newly acquired multichannel seismic reflection profile across the new volcano in the east of Mayotte reveals that several distinct magmatic phases affected the area. The most recent phase resulted in the formation of the Fani Maore volcano through eruptive events building successive cones with associated flows since May 2018. The geometry of the lava flows around the submarine volcano suggests a melt supply through a single magma conduit. The new volcano sits on a ~140 m thick sedimentary layer, as inferred from the seismic reflection pattern, suggesting a period of volcanic quiescence. Beneath this sedimentary layer exists a major, volcanic layer up to ~1 km thick and extends as far as ~91 km to the south and ~33 km to the north of the recently formed submarine volcano. This unit is made up of several different seismic facies that may indicate successive volcanic phases. We interpret this major volcanic layer as being part of the early construction of the Mayotte volcanic edifice, with the presence of a complex magmatic feeder system below, being composed of many saucer-shaped sills and seal bypass systems. A ~2.2–2.5 km thick sedimentary unit is found between the main volcanic layer, below the new volcano, and the top of the crust. The identification of the top-Oligocene seismic horizon above the deepest tip of the main volcanic layer indicates that the onset of the volcanism at Mayotte Island may be older than previously thought.

## Conflicts of interest

Authors have no conflict of interest to declare.

## Acknowledgments

This paper is a contribution of COYOTES and SISMAORE teams (http://www.geocean.net/coyotes/doku.php?id=start). It benefited from the previous works of the REVOSIMA community. The processing and the detailed analysis of these geophysical and geological data are carried out mainly in the framework of the ANR COYOTES (ANR-19-CE31-0018, https://anr.fr/Projet-ANR-19-CE31-0018) project funded by the French ANR (Agence Nationale de Recherche) and the BRGM. The SISMAORE cruise was mainly funded by the Flotte Océanographique Française (FOF) and by the BRGM. We thank CGG for allowing us to use the CGG Geovation software in CNRS labs. We thank Captains P. Moimeaux and G. Ferrand, the crews and technicians from the R/V Pourquoi Pas? (FOF by IFREMER/GENAVIR). Thanks to the BRGM regional department of Mayotte. Thanks to REVOSIMA and DIRMOM for their assistance with the cruise during the COVID sanitary crisis. Masquelet's Ph.D. is funded by Sorbonne Université, via the ANR COYOTES.

## Supplementary data

Supporting information for this article is available on the journal's website under https://doi.org/10.5802/crgeos.154 or from the author.

## References

Bardintzeff, J.-M., Liégeois, J.-P., Bonin, B., Bellon, H., and Rasamimanana, G. (2010). Madagascar volcanic provinces linked to the Gondwana break-up: geochemical and isotopic evidences for contrasting mantle sources. *Gondwana Res.*, 18, 295–314.

Berthod, C., Komorowski, J.-C., Gurioli, L., Médard, E., Besson, P., Bachèlery, P., Verdurme, P., Chevrel, O., Di Muro, A., Devidal, J.-L., Nowak, S., Thinon, I., Burckel, P., Hidalgo, S., Deplus, C., Bermell, S., Réaud, Y., Fouchard, S., Bickert, M., Le Friant, A., Feuillet, N., Jorry, S., Fouquet, Y., Rinnert, E., Cathalot, C., and Lebas, E. (2022). Temporal evolution of the Mayotte eruption revealed by in situ submarine sampling and petrological monitoring. *C. R. Géosci.*, 354(S2), 195–223.

Berthod, C., Médard, E., Bachèlery, P., Gurioli, L., Di Muro, A., Peltier, A., Komorowski, J.-C., Benbakkar, M., Devidal, J.-L., Langlade, J., Besson, P., Boudon, G., Rose-Koga, E., Deplus, C., Le Friant, A., Bickert, M., Nowak, S., Thinon, I., Burckel, P., Hidalgo, S., Kaliwoda, M., Jorry, S. J., Fouquet, Y., and Feuillet, N. (2021a). The 2018-ongoing Mayotte submarine eruption: magma migration imaged by petrological monitoring. *Earth Planet. Sci. Lett.*, 571, article no. 117085.

Berthod, C., Médard, E., Di Muro, A., Hassen Ali, T., Gurioli, L., Chauvel, C., Komorowski, J.-C., Bachèlery, P., Peltier, A., Benbakkar, M., Devidal, J.-L., Besson, P., Le Friant, A., Deplus, C., Nowak, S., Thinon, I., Burckel, P., Hidalgo, S., Feuillet, N., Jorry, S., and Fouquet, Y. (2021b). Mantle xenolith-bearing phonolites and basanites feed the active volcanic ridge of Mayotte (Comoros archipelago, SW Indian Ocean). *Contrib. Mineral. Petrol.*, 176, article no. 75.

Cartwright, J., Huuse, M., and Aplin, A. (2007). Seal bypass systems. *Bulletin*, 91, 1141–1166.

Cesca, S., Letort, J., Razafindrakoto, H. N. T., Heimann, S., Rivalta, E., Isken, M. P., Nikkhoo, M., Passarelli, L., Petersen, G. M., Cotton, F., and Dahm, T. (2020). Drainage of a deep magma reservoir near Mayotte inferred from seismicity and deformation. *Nat. Geosci.*, 13, 87–93.

Coffin, M. F. and Rabinowitz, P. D. (1987). Reconstruction of Madagascar and Africa: evidence from the Davie Fracture Zone and western Somali Basin. *J. Geophys. Res.*, 92, article no. 9385.

Compilation Group GEBCO Grid (2020). Gridded Bathymetry Data.

Dofal, A., Fontaine, F. R., Michon, L., Barruol, G., and Tkalčić, H. (2021). Nature of the crust beneath the islands of the Mozambique Channel: constraints from receiver functions. *J. Afr. Earth Sci.*, 184, article no. 104379.

Famin, V., Michon, L., and Bourhane, A. (2020). The Comoros archipelago: a right-lateral transform boundary between the Somalia and Lwandle plates. *Tectonophysics*, 789, article no. 228539.

Feuillet, N., Jorry, S., Crawford, W. C., Deplus, C., Thinon, I., Jacques, E., Saurel, J. M., Lemoine, A., Paquet, F., Satriano, C., Aiken, C., Foix, O., Kowalski, P., Laurent, A., Rinnert, E., Cathalot, C., Donval, J.-P., Guyader, V., Gaillot, A., Scalabrin, C., Moreira, M., Peltier, A., Beauducel, F., Grandin, R., Ballu, V., Daniel, R., Pelleau, P., Gomez, J., Besançon, S., Geli, L., Bernard, P., Bachelery, P., Fouquet, Y., Bertil, D., Lemarchand, A., and Van der Woerd, J. (2021). Birth of a large volcanic edifice offshore Mayotte via lithosphere-scale dyke intrusion. *Nat. Geosci.*, 14, 787–795.

Franke, D., Jokat, W., Ladage, S., Stollhofen, H., Klimke, J., Lutz, R., Mahanjane, E. S., Ehrhardt, A., and Schreckenberger, B. (2015). The offshore East African Rift System: structural framework at the toe of a juvenile rift: THE OFFSHORE EAST AFRICAN RIFT. *Tectonics*, 34, 2086–2104.

Hall, I. R., Hemming, S. R., LeVay, L. J., and Scientists, E. (2017). South African climates (Agulhas LGM Density Profile). In *Proceedings of the International Ocean Discovery Program*, volume 361. International Ocean Discovery Program, College Station, TX.

Klimke, J., Franke, D., Gaedicke, C., Schreckenberger, B., Schnabel, M., Stollhofen, H., Rose, J., and Chaheire, M. (2016). How to identify oceanic crust—evidence for a complex break-up in the Mozambique Channel, off East Africa. *Tectonophysics*, 693, 436–452.

Lavayssière, A., Crawford, W. C., Saurel, J.-M., Satriano, C., Feuillet, N., Jacques, E., and Komorowski, J.-C. (2021). A new 1D velocity model and absolute locations image the Mayotte seismo-volcanic region. *J. Volcanol. Geotherm. Res.*, 421, article no. 107440.

Lemoine, A., Briole, P., Bertil, D., Roullé, A., Foumelis, M., Thinon, I., Raucoules, D., de Michele, M., Valty, P., and Hoste Colomer, R. (2020). The 2018–2019 seismo-volcanic crisis east of Mayotte, Comoros islands: seismicity and ground deformation markers of an exceptional submarine eruption. *Geophys. J. Int.*, 223, 22–44.

Leroux, E., Counts, J. W., Jorry, S. J., Jouet, G., Révillon, S., BouDagher-Fadel, M. K., Courgeon, S., Berthod, C., Ruffet, G., Bachèlery, P., and Grenard-Grand, E. (2020). Evolution of the Glorieuses seamount in the SW Indian Ocean and surrounding deep Somali Basin since the Cretaceous. *Mar. Geol.*, 427, article no. 106202.

Mahanjane, E. S. (2014). The Davie Fracture Zone and adjacent basins in the offshore Mozambique Margin—a new insights for the hydrocarbon potential. *Mar. Pet. Geol.*, 57, 561–571.

Medialdea, T., Somoza, L., González, F. J., Vázquez, J. T., de Ignacio, C., Sumino, H., Sánchez-Guillamón, O., Orihashi, Y., León, R., and Palomino, D. (2017). Evidence of a modern deep water magmatic hydrothermal system in the Canary Basin (eastern central Atlantic Ocean). *Geochem. Geophys. Geosyst.*, 18, 3138–3164.

Michon, L. (2016). The volcanism of the Comoros Archipelago integrated at a regional scale. In

Bachelery, P., Lenat, J.-F., Di Muro, A., and Michon, L., editors, *Active Volcanoes of the Southwest Indian Ocean, Active Volcanoes of the World*, pages 333–344. Springer, Berlin, Heidelberg.

Michon, L., Famin, V., and Quidelleur, X. (2022). Evolution of the East African Rift System from trap-scale to plate-scale rifting. *Earth-Sci. Rev.*, 231, article no. 104089.

Mougenot, D., Recq, M., Virlogeux, P., and Lepvrier, C. (1986). Seaward extension of the East African Rift. *Nature*, 321, 599–603.

Pelleter, A.-A., Caroff, M., Cordier, C., Bachelery, P., Nehlig, P., Debeuf, D., and Arnaud, N. (2014). Melilite-bearing lavas in Mayotte (France): an insight into the mantle source below the Comores. *Lithos*, 208–209, 281–297.

Rinnert, E., Feuillet, N., Fouquet, Y., Jorry, S., Thinon, I., and Lebas, E. (2019). MAYOBS Cruises.

Roach, P., Milsom, J., Toland, C., Matchette-Downes, C., Budden, C., and Riaroh, D. (2017). New evidence supports presence of continental crust beneath the Comoros. In *Proceedings of the PESGB/HGS Africa Conference*, volume 18.

Roberts, E. M., Stevens, N. J., O'Connor, P. M., Dirks, P. H. G. M., Gottfried, M. D., Clyde, W. C., Armstrong, R. A., Kemp, A. I. S., and Hemming, S. (2012). Initiation of the western branch of the East African Rift coeval with the eastern branch. *Nat. Geosci.*, 5, 289–294.

Sauter, D., Ringenbach, J. C., Cannat, M., Maurin, T., Manatschal, G., and McDermott, K. G. (2018). Intraplate deformation of oceanic crust in the West Somali Basin: insights from long-offset reflection seismic data. *Tectonics*, 37, 588–603.

SHOM (2014). Transit valorisé de Mayotte à Brest.

SHOM (2016a). Homonin Project.

SHOM (2016b). MNT Bathymétrique de la Façade de Mayotte.

Storey, M., Mahoney, J. J., Saunders, A. D., Duncan, R. A., Kelley, S. P., and Coffin, M. F. (1995). Timing of hot spot—related volcanism and the breakup of Madagascar and India. *Science*, 267, 852–855.

Telford, W. M., Geldart, L. P., and Shériff, R. E. (1990). *Applied Geophysics*. Cambridge University Press, New York.

Thinon, I., Lemoine, A., Leroy, S., Paquet, F., Berthod, C., Zaragosi, S., Famin, V., Feuillet, N., Boymond, P., Masquelet, C., Mercury, N., Rusquet, A., Scalabrin, C., Van der Woerd, J., Bernard, J., Bignon, J., Clouard, V., Doubre, C., Jacques, E., Jorry, S., Rolandone, F., Chamot-Rooke, N., Delescluse, M., Franke, D., Watremez, L., Bachèlery, P., Michon, L., Sauter, D., Bujan, S., Canva, A., Dassie, E., Roche, V., Ali, S., Sitti Allaouia, A. H., Deplus, C., Rad, S., and Sadeski, L. (2022). Volcanism and tectonics unveiled in the Comoros archipelago between Africa and Madagascar. *C. R. Géosci.*, 354(S2), 7–34.

Thinon, I., Leroy, S., and Lemoine, A. (2020). SISMAORE cruise, RV Pourquoi pas ?

Torsvik, T. H., Tucker, R. D., Ashwal, L. D., Carter, L. M., Jamtveit, B., Vidyadharan, K. T., and Venkataramana, P. (2000). Late Cretaceous India-Madagascar fit and timing of break-up related magmatism. *Terra Nova*, 12, 220–224.

*Comptes Rendus*
*Géoscience — Sciences de la Planète*
**2022**, Vol. 354, Special Issue S2, p. 81-104
https://doi.org/10.5802/crgeos.175

The Mayotte seismo-volcanic crisis of 2018-2021 in the Comoros archipelago (Mozambique channel) / *La crise sismo-volcanique de 2018-2021 de Mayotte dans l'archipel des Comores (Canal du Mozambique)*

# Volcano-tectonic structures of Mayotte's upper submarine slope: insights from high-resolution bathymetry and in-situ imagery from a deep-towed camera

**Valentine Puzenat [*, a], Nathalie Feuillet [a], Jean-Christophe Komorowski [a], Javier Escartín [b], Christine Deplus [a], Patrick Bachèlery [c], Carole Berthod [c], Lucia Gurioli [c], Carla Scalabrin [d], Cécile Cathalot [d], Emmanuel Rinnert [d], Benoît Loubrieu [d], Delphine Pierre [d], Mathilde Pitel-Roudaut [d], Nina Tanguy [d], Yves Fouquet [d], Stephan J. Jorry [d], Elodie Lebas [a], Fabien Paquet [e] and Isabelle Thinon [e]**

[a] Université Paris Cité, Institut de Physique du Globe de Paris, CNRS, F-75005 Paris, France

[b] Laboratoire de Géologie – CNRS, UMR 8538, École Normale Supérieure, PSL University, Paris, France

[c] Université Clermont-Auvergne, CNRS, IRD, OPGC, Laboratoire Magmas et Volcans, 6 avenue Blaise Pascal, 63178 Aubière, France

[d] Geo-Ocean, Univ Brest, CNRS, Ifremer, UMR6538, F-29280 Plouzane, France

[e] French Geological survey—BRGM, DGR/GBS, Orléans, France

*Current address:* Institut de Physique du Globe de Paris – 1 rue Jussieu – 75238 Paris cedex 05, France (V. Puzenat)

*E-mails:* puzenat@ipgp.fr (V. Puzenat), feuillet@ipgp.fr (N. Feuillet), komorow@ipgp.fr (J.-C. Komorowski), escartin@geologie.ens.fr (J. Escartín), deplus@ipgp.fr (C. Deplus), p.bachelery@opgc.fr (P. Bachèlery), carole.berthod@uca.fr (C. Berthod), lucia.gurioli@uca.fr (L. Gurioli), carla.scalabrin@ifremer.fr (C. Scalabrin), cecile.cathalot@ifremer.fr (C. Cathalot), emmanuel.rinnert@ifremer.fr (E. Rinnert), Benoit.Loubrieu@ifremer.fr (B. Loubrieu), Delphine.Pierre@ifremer.fr (D. Pierre), Mathilde.Pitel@ifremer.fr (M. Pitel-Roudaut), Nina.Tanguy@ifremer.fr (N. Tanguy), Yves.Fouquet@ifremer.fr (Y. Fouquet), Stephan.Jorry@ifremer.fr (S. J. Jorry), elebas@ipgp.fr (E. Lebas), F.Paquet@brgm.fr (F. Paquet), i.thinon@brgm.fr (I. Thinon)

* Corresponding author.

**Abstract.** Unlike subaerial volcanic activity, deep submarine eruptions are difficult to detect, observe and monitor. The objective of this paper is to describe a large and complex volcanic region, named the Horseshoe area, recently discovered at ~1500 m below sea level on the eastern upper submarine slope of Mayotte Island. The area is crucial because, since 2018, it has experienced an exceptionally deep seismic activity associated with the ongoing submarine eruption that formed a new volcanic edifice, Fani Maoré, about 40 km to the east. We present the results of a multiscale study, based on high-resolution bathymetry and in-situ seafloor observations carried out with autonomous underwater vehicles (AUVs) and deep-towed camera systems. In-situ imagery provides ground-truth for the geological interpretation of seafloor textures mapped with the bathymetry. The combination of both datasets allows us to discuss the nature of the volcanic structures and to propose a relative chronology of previous eruptive events in the Horseshoe area. Based on our analyses, we propose the following chronology: (a) the emplacement of a large explosive volcanic cone, the Horseshoe edifice, (b) the later collapse of this edifice that resulted in the formation of an elongated, 2 km wide horseshoe-shaped depression, crosscutting older hummocky lava flows, (c) the development of an E–W eruptive fissure associated with numerous explosive craters, east of the Horseshoe edifice, and (d) late volcanism emanating from the rim of the horseshoe-shaped depression that fed elongated thin lava flows both towards and away from the depression. While all volcanic features mapped at the Horseshoe area were emplaced prior to the 2018 eruption, our study shows that this region has still been volcanically active in the recent past. Our results thus document a complex geological history at small spatial scales involved in the construction of major submarine edifices, and that are controlled by volcano-tectonic processes at larger scales.

**Keywords.** Mayotte, Submarine volcanism, Geological mapping, High-resolution bathymetry, In-situ imagery.

*Published online: 19 December 2022, Issue date: 17 January 2023*

## 1. Introduction

Most of the Earth's volcanic activity occurs underwater, particularly along mid-ocean ridges, building the oceanic crust [Crisp, 1984]. To constrain the setting and overall structure of submarine volcanic systems, detailed bathymetric and optical surveys of the seafloor are needed for comprehensive geological mapping. These combined data are crucial to better understand the distribution, geometry and nature of volcanic products, and to extrapolate local seafloor observations to more general submarine volcanic processes. Systematic seafloor mapping also provides a baseline for temporal studies, while providing a context for in-situ measurements. Such comprehensive studies [e.g., Dziak et al., 2001, Embley et al., 2010, Wessel et al., 2010, Nomikou et al., 2013, Anderson et al., 2017] can constrain the history and time evolution of submarine volcanism, document the processes leading to the formation of the present-day seafloor volcanic morphologies and in some cases, allow us to envision potential scenarios of future volcanic activity. To date, only a few active submarine volcanoes have been monitored, either along the axis of mid-ocean ridges [e.g., Axial Seamount, Clague et al., 2017, Chadwick Jr. et al., 2022], or at seamounts away from mid-ocean ridges [e.g., West Mata, Chadwick Jr. et al., 2019, Lōʻihi, Clague et al., 2019; Havre, Carey et al., 2018, Ikegami et al., 2018; NW Rota-1, Embley et al., 2006, Chadwick Jr. et al., 2008, Schnur et al., 2017].

Since May 2018, Mayotte Island (Comoros archipelago) has been undergoing a major seismo-volcanic crisis [Cesca et al., 2020, Lemoine et al., 2020] that has led to the formation of a major new deep sea (~2500 m) volcanic edifice, Fani Maoré, about 50 km east of the island [Deplus et al., 2019, Berthod et al., 2021a, Feuillet et al., 2021, Masquelet et al., 2022]. This eruption is the largest submarine event ever documented. While earlier studies have focused on the understanding of the geodynamic setting of the Comoros archipelago [Nougier et al., 1986, Famin et al., 2020, Bertil et al., 2021, Tzevahirtzian et al., 2021, Thinon et al., 2022], the source of volcanic activity in the area is still poorly understood [Bachèlery et al., 2016, Famin et al., 2020, Quidelleur et al., 2022]. The present seismo-volcanic crisis thus provides a unique opportunity to better understand the interactions between different processes on the submarine flanks of Mayotte (e.g., volcanism, tectonic activity, deep seismic activity, hydrothermal activity), and to improve our knowledge of deep submarine volcanism in general. All these phenomena impact the local ecosystems, while representing a potential risk for the human population on the island. As a result, the Mayotte Volcanological and Seismological Monitoring Network [REVOSIMA, 2022] consortium was created and a series of oceanographic cruises have been carried out since 2019, to both monitor and study the area, providing a wide range of datasets (e.g., bathymetry, imagery, petrology, seismicity, geochemistry, biology, etc.), and involving numerous multidisciplinary research groups.

Here we do not focus on the new post-2018 Fani Maoré volcanic edifice, but we present a multi-spatial-scale geomorphological study of the Horseshoe area, located 10 km east of Mayotte Island, on its eastern upper submarine slope. This area shows complex and diverse volcanic morphologies, active fluid outflow, and lies directly above the main cluster of seismicity, which is located at a depth of more than 30 km [Lavayssière et al., 2022, Saurel et al., 2022].

Specifically, we analyze very high-resolution bathymetry, acquired with Autonomous Underwater Vehicles (AUVs named Idef$^{X}$ and Aster$^{X}$), to document the different volcanic features and morphologies in this complex Horseshoe area. The analysis of in-situ seafloor imagery from a deep-towed camera system (Scampi) coupled to that of the AUV bathymetry provides ground-truth for geological interpretations. Hence, using a multiscale approach from regional maps down to outcrop-scale visual observations we interpret (a) the morphological nature and architecture of volcanic structures, (b) the eruptive modes at several spatial and temporal scales and their links to other processes, and (c) possible links between the present-day morphologies observed in the area and the recent Fani Maoré eruption and associated phenomena.

## 2. Geological setting

The Comoros archipelago is located north of the Mozambique Channel (Indian Ocean), between the Mozambique and Madagascar (Figure 1a). The archipelago is composed of four volcanic islands (Grande Comore, Mohéli, Anjouan and Mayotte) aligned in an overall east–west (E–W) trend: [Daniel et al., 1972, Tzevahirtzian et al., 2021]. Grande Comore is the most frequently active volcanic island with the Karthala volcano [Bachèlery et al., 2016]. This region was affected by an episode of NW–SE rifting through the Permo-Triassic which was associated with the fragmentation of Gondwana [~170–185 Ma, Eagles and König, 2008, Gaina et al., 2015, Leinweber and Jokat, 2012, Mueller and Jokat, 2019, Senkans et al., 2019], opening the Mozambique, Comores and Somali basins, during which Madagascar drifted southward [Mahanjane, 2012, Davis et al., 2016]. The nature of the lithosphere (continental vs. oceanic) underlying the Comoros archipelago continues to be debated and has been diversely interpreted over the years [Nougier et al., 1986, Michon, 2016, Masquelet et al., 2022, Rolandone et al., 2022]. The origin of volcanism in the area is also poorly understood, and proposed hypotheses include: (a) hot spot activity [Emerick and Duncan, 1982], (b) lithospheric fracture zones facilitating melt transport [Nougier et al., 1986], or (c) coupling of both processes, with the interaction of extensional tectonics and deeper astenospheric processes [e.g., Courgeon et al., 2018, Deville et al., 2018, Famin et al., 2020, Franke et al., 2015, Kusky et al., 2010, Michon, 2016, O'Connor et al., 2019, Wiles et al., 2020]. Several authors [e.g. Kusky et al., 2010, Stamps et al., 2018, Famin et al., 2020, Lemoine et al., 2020, Thinon et al., 2022] suggest the presence of a diffuse and immature Lwandle-Somalia plate boundary along the Comoros archipelago. Feuillet et al. [2021], based on data recently acquired offshore Mayotte, propose that the present-day morphology of the archipelago results from an E–W transtensional boundary that transfers the strain between the offshore branches of the East-African rift and the grabens of Madagascar.

Mayotte, the oldest and easternmost cluster of volcanic edifices in the Comoros archipelago, is composed of two main volcanic islands: Grande-Terre and Petite-Terre (Figure 1). The onset of main magmatic activity in Mayotte has been estimated between 15–30 Ma [Emerick and Duncan, 1982, Nougier et al., 1986, Debeuf, 2004, Pelleter et al., 2014, Michon, 2016], and in more recent studies between 26–27 Ma [Masquelet et al., 2022]. Mayotte is now made of three morphologically and structurally distinct units corresponding to three distinct eruptive phases [Debeuf, 2004, Nehlig et al., 2013]. Volcanic activity continued in the Late Quaternary (≤12 ka), and volcanic ash layers occurring just above coral from lagoon sediments dated at 7305 ± 65 years cal BP [Zinke et al., 2003, 2005] suggest that the last volcanic and explosive activity on land occurred less than 7 ka ago and perhaps as recently as between

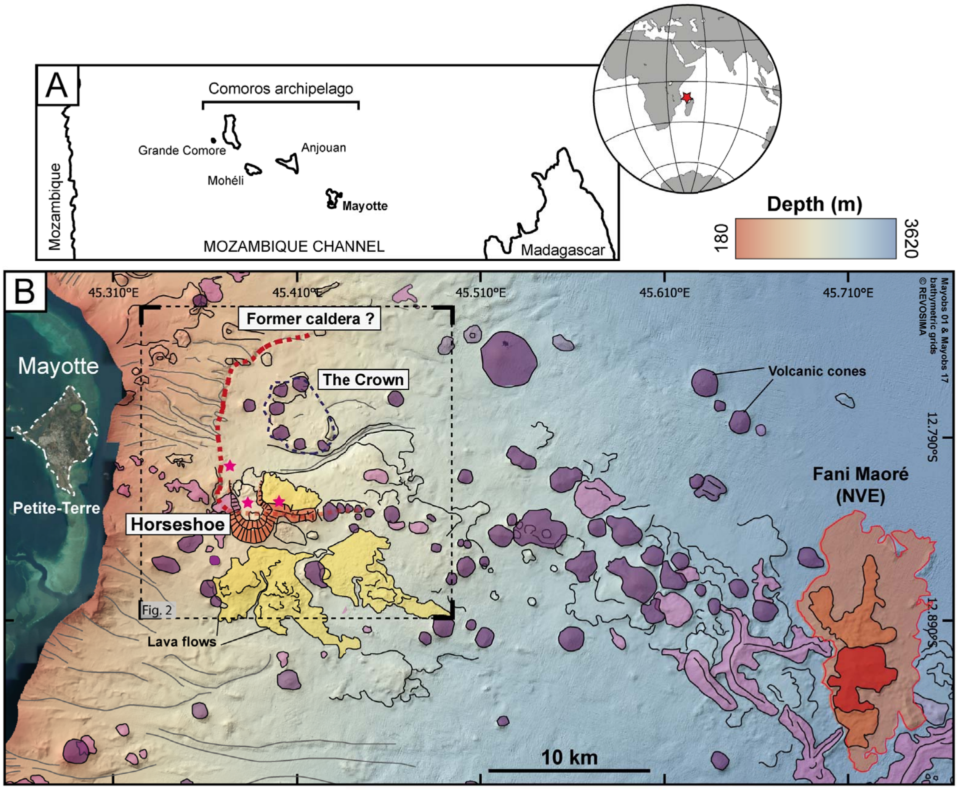


**Figure 1.** (A) Simplified map of the Comoros archipelago showing the location of Mayotte Island. (B) Map of the East-Mayotte Volcanic Chain (EMVC) modified from Feuillet et al. [2021] showing the Horseshoe, the Crown—a structure likely associated with a former caldera collapse (red dashed line), and the New post-2018 Volcanic Edifice (Fani Maoré). The central part of Fani Maoré is in red and the radial ridges and associated lava flows are in orange (outlines were defined by Feuillet et al. [2021] based on depth changes between 2014 and 2019). Purple patches represent pre-2018 volcanic features (mainly cones). Pink patches represent pre-2018 lava flows and elongated features. Yellow patches represent the upper submarine slope's highly reflective pre-2018 lava flows (see Figure 2).

6–4 ka BP as reported by Zinke et al. [2000]. Markers of this subaerial volcanic activity include cones, tuff rings, tuff cones and maar craters, that are well preserved [Nehlig et al., 2013, Pelleter et al., 2014]. The volcanic activity also extends offshore, east of Petite-Terre, where numerous submarine basanitic and phonolitic volcanic cones and lava fields are aligned along a 50 km long, WNW–ESE trending volcanic chain [Figure 1b; Audru et al., 2006, Berthod et al., 2021a,b, Feuillet et al., 2021, Tzevahirtzian et al., 2021], called the East-Mayotte Volcanic Chain (EMVC).

A major seismic crisis began in Mayotte on May 10th 2018, in a previously seismically quiet area [Audru et al., 2010, Lemoine et al., 2020]. Since the beginning of the crisis, thousands of exceptionally deep (25–50 km) earthquakes have been recorded offshore Mayotte, with a major swarm detected ~10 km east of Petite-Terre [Cesca et al., 2020, Lemoine et al., 2020, Feuillet et al., 2021, Lavayssière et al., 2022, Saurel et al., 2022]. The strongest earthquake ($M_w$ = 5.9) was felt on May 15th 2018, and is the strongest seismic event ever reported in the Comoros archipelago. Very-long-period seismic signals were also detected [Cesca et al., 2020, Lemoine et al., 2020, Feuillet et al., 2021, Lavayssière et al., 2022, Saurel et al., 2022], and could be generated by the resonance of a fluid-filled cavity [Feuillet et al., 2021, Laurent et al., 2021]. At the same time, GNSS stations recorded significant ground deformation of the island, with ~20 cm of subsidence, and a horizontal displacement of ~15 cm eastward [Lemoine et al., 2020, REVOSIMA, 2022, Peltier et al., 2022]. It was later proposed that the intense seismicity and significant surface deformation were linked to the drainage of a deep magma reservoir through dykes, leading to a deep submarine eruption [Cesca et al., 2020, Lemoine et al., 2020, Feuillet et al., 2021]. Recent geophysical and petrological studies have suggested the presence of a main magma reservoir at mantle depths (>30 km) 5–10 km east of Petite-Terre (below the Horseshoe area), together with reservoirs at shallower depths that may be present further east along the volcanic chain [Darnet et al., 2020, Berthod et al., 2021a,b, Foix et al., 2021, Lavayssière et al., 2022].

This major seismo-volcanic crisis led to the discovery of a new active volcanic edifice (NVE, recently named Fani Maoré) in 2019, at the eastern tip of the EMVC, at a 3500 m water depth [Feuillet et al., 2021]. To date, this new volcano is 820 m tall, has a base diameter of ~5 km and has produced more than 6.5 $km^3$ of lavas [REVOSIMA, 2022] with various morphologies, making it the largest effusive eruption since Iceland's Laki eruption in 1783 [>10 $km^3$, Thordarson and Self, 1993]. The main edifice is also associated with extensive lava flows (Figure 1).

No recent (post-2018) eruption sites have been detected on Mayotte's eastern submarine slope. However, the upper slope, east of Petite-Terre, is still underlain by significant deep seismic activity [25–50 km deep, Lavayssière et al., 2022, Saurel et al., 2022] and very active, with evolving fluid emissions [REVOSIMA, 2022]. This region is the focus of our study (Figure 2), and is characterized by numerous young volcanic cones, highly acoustically reflective lava flows that are widespread, and other features linked to mass-wasting processes subsequent to volcanic activity. North of the Horseshoe area, Feuillet et al. [2021] describe a large 10 km-wide depression that is bounded to the west by cross-cutting submarine faults and canyons (red dashed outline on Figures 1 and 2). They propose that this depression could be the vestige of a former caldera. A circular, 4 km-wide structure, hereafter called the Crown, was found inside the depression, composed of seven 1 km-wide, 100–150 m-high volcanic cones that have been interpreted by Feuillet et al. [2021] as post-caldera domes [Cole et al., 2005]. In this region, Feuillet et al. [2021] also described the so-called "Horseshoe area", including a 3.5 km-wide horseshoe-shaped volcanic edifice, located on the southern edge of the proposed caldera and whose peculiar morphology, likely to have resulted from complex collapse processes. This study is an in-depth investigation of the Horseshoe area, through the analysis of high-resolution bathymetry and in-situ imagery.

## 3. Data and methods

### 3.1. *Seafloor textures derived from ship-based and near-bottom high-resolution bathymetry*

This study combines two different bathymetry datasets: ship-based bathymetry, gridded with different cell sizes that vary from ~10 to 20 m per pixel (Figure 3a), and near-bottom bathymetry acquired during AUV dives, at a spatial resolution of ~1 m (Figure 3b).

Ship-based bathymetry and seafloor backscatter data were acquired during three oceanographic cruises (MAYOBS cruises, https://doi.org/10.18142/291). The MAYOBS 1 and MAYOBS 4 data (Table 1) were acquired using a 1° × 1° beam width Kongsberg EM122 multibeam echosounder. In the study area (water depths of 1000–1500 m), the data were gridded with a 20-m cell size. In January 2021, another survey was carried out during the MAYOBS17 cruise (Table 1) using a 0.5° × 0.5° beam width multibeam echosounder (Reson Seabat 7150 at 24 kHz), which resulted in a bathymetry grid with a cell size of 10 m over the same area.

Near-bottom, high-resolution multibeam bathymetry data were obtained during two cruises: the MAYOBS 4 and MAYOBS 15 cruises (Table 1), with IFREMER's AUVs Aster$^X$ and Idef$^X$ respectively, both equipped with a Kongsberg EM2040 multibeam echosounder. The near-bottom surveys were run at an altitude of ~70 m, yielding bathymetry with 1-m spatial resolution.

In this study, we use bathymetry data processed using the GLOBE software (doi: 10.17882/70460) to conduct a geomorphological analysis of volcanic and tectonic features, and those linked to later mass-wasting processes. We analyze the fine scale seafloor morphologies provided by near-bottom

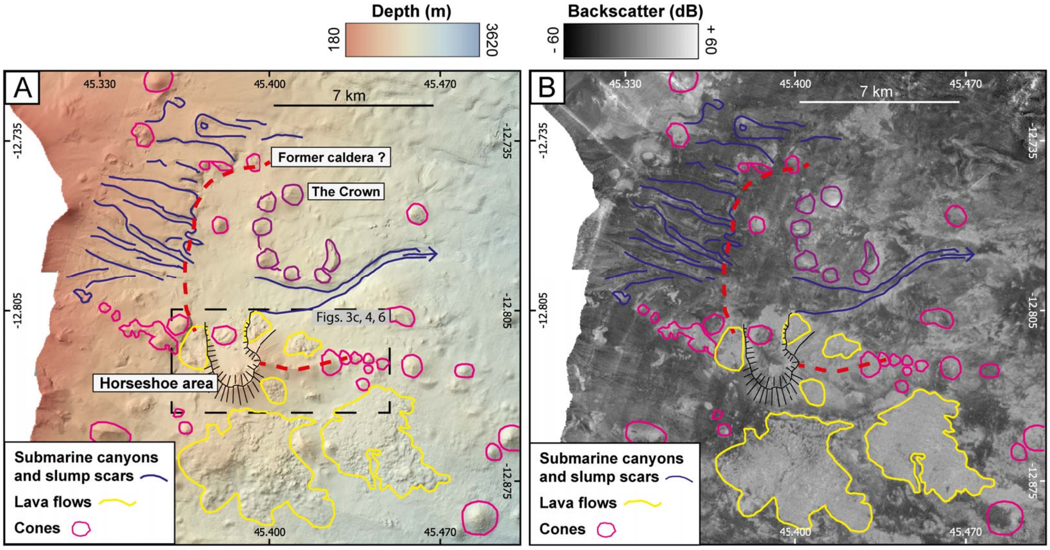


**Figure 2.** (A) General shaded bathymetric map focusing on Mayotte's eastern upper submarine slope showing the Horseshoe edifice, the Crown, deep submarine canyons, lava flows and volcanic cones. All interpreted features are pre-2018 and have been defined in Feuillet et al. [2021]. Bathymetry data used for this map were acquired during the MAYOBS 1 and MAYOBS 17 cruises (Table 1). (B) General backscatter map that corresponds to the extent of Figure 2a, only using reflectivity data from the MAYOBS 01 cruise. Relative scale is from −60 dB (black, low reflectivity) to +60 dB (white, high reflectivity).

**Table 1.** Monitoring oceanographic cruises conducted along the East-Mayotte Volcanic Chain (EMVC) by the REVOSIMA consortium used in this study

| Cruise | Date | P.I. | R/V | DOI |
|---|---|---|---|---|
| MAYOBS 1 | May 2019 | Feuillet, N. | Marion Dufresne | https://doi.org/10.17600/18001217 |
| MAYOBS 4 | July 2019 | Feuillet, N. and Fouquet, Y. | Marion Dufresne | https://doi.org/10.17600/18001238 |
| MAYOBS 15 | October 2020 | Feuillet, N., Rinnert, E. and Thinon, I. | Marion Dufresne | https://doi.org/10.17600/18001745 |
| MAYOBS 17 | January 2021 | Thinon, I., Rinnert, E. and Feuillet, N. | Pourquoi Pas? | https://doi.org/10.17600/18001983 |

high-resolution data through a combination of shaded digital terrain models (Figure 4a), slope maps (Figure 4b), and topographic profiles (Figure 5). The seafloor textures and features identified are then digitized at a scale of 1:10,000–1:20,000, depending on the resolution of the underlying bathymetric grid, and georeferenced (Figure 6) using the QGIS software (https://www.qgis.org/). For our interpretations we solely use geomorphological criteria, without considering other data such as rock composition or geochemistry, as these data are currently being processed and will be integrated in a later study. Other seafloor features are clearly visible in the study area on the ship-based data, although they were not surveyed during AUV dives. We map these features separately (grey dashed outlines on Figure 6) for indicative purposes but do not include them in our interpretations as they were not identified with the same resolution and hence reliability as the rest of the morphologies identified in AUV near-bottom data (Figure 6).

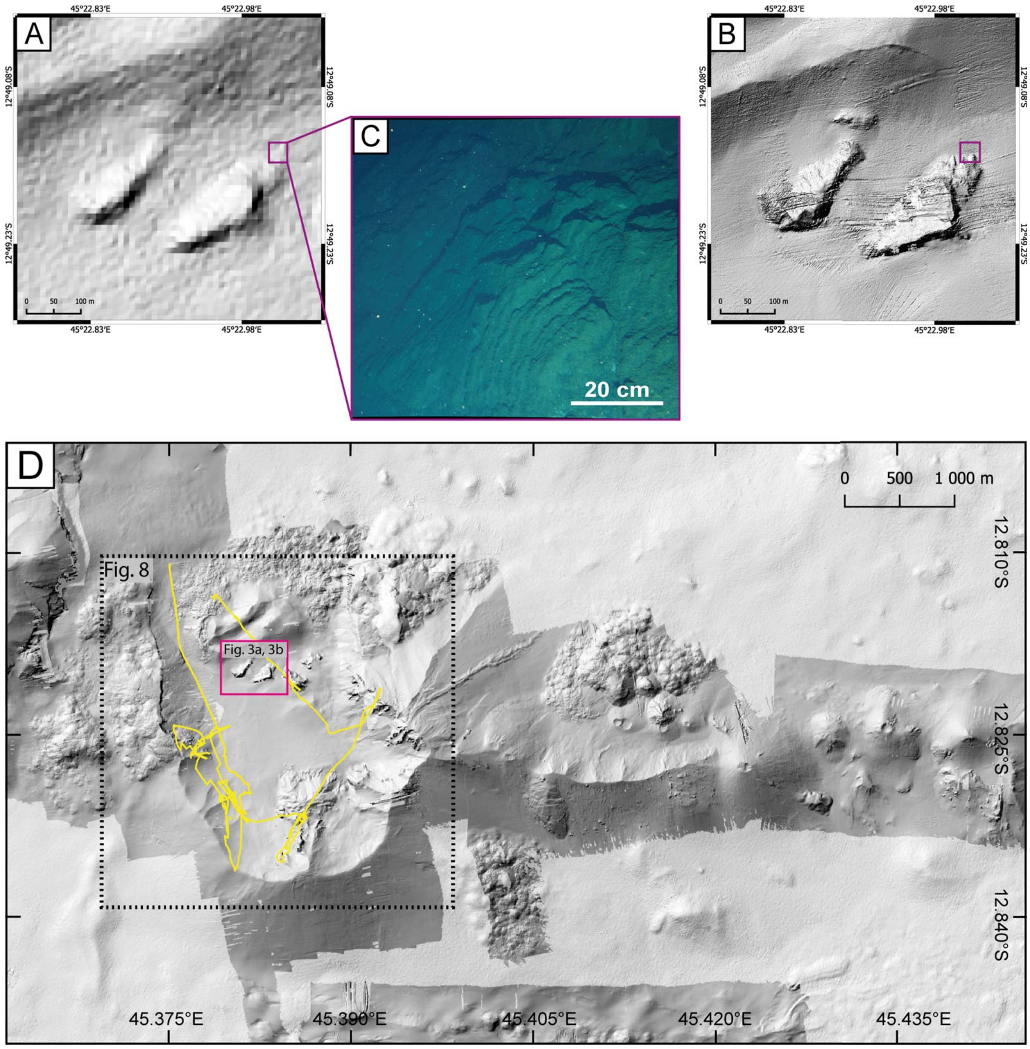


**Figure 3.** Multi-scale approach, from regional mapping to high-resolution mapping, and to visual ground truthing of seafloor outcrops. Example of an area mapped with (A) ship-based multibeam echosounder system (MBES) bathymetry, (B) AUV near-seafloor multibeam bathymetry, (C) Scampi image relocated on the shipboard bathymetric grid (purple square), and (D) General bathymetric map of the study region: the Horseshoe area. Darker shaded bathymetry grids correspond to AUV grids coverage (cell size ~1 m), that is superimposed on ship-based bathymetry (cell size ~10 m). The continuous yellow lines locate Scampi dives from the MAYOBS 4 and MAYOBS 15 cruises (Table 1). Location of this figure is indicated in Figure 2.

### 3.2. *Ground truthing with in-situ observations*

Seafloor images were obtained from a deep-towed camera system named Scampi, a submarine seafloor imaging system from IFREMER that is towed behind the ship along predefined tracks. The Scampi is flown a few meters above the seafloor to acquire images and video with a vertically mounted camera and light sources (Figure 3c). It was deployed during the MAYOBS 4 and MAYOBS 15 cruises (Table 1). Seven camera tows were made along the volcanic chain, and four specifically targeted the Horseshoe area, providing ~21 h of video imagery (Figure 3d).

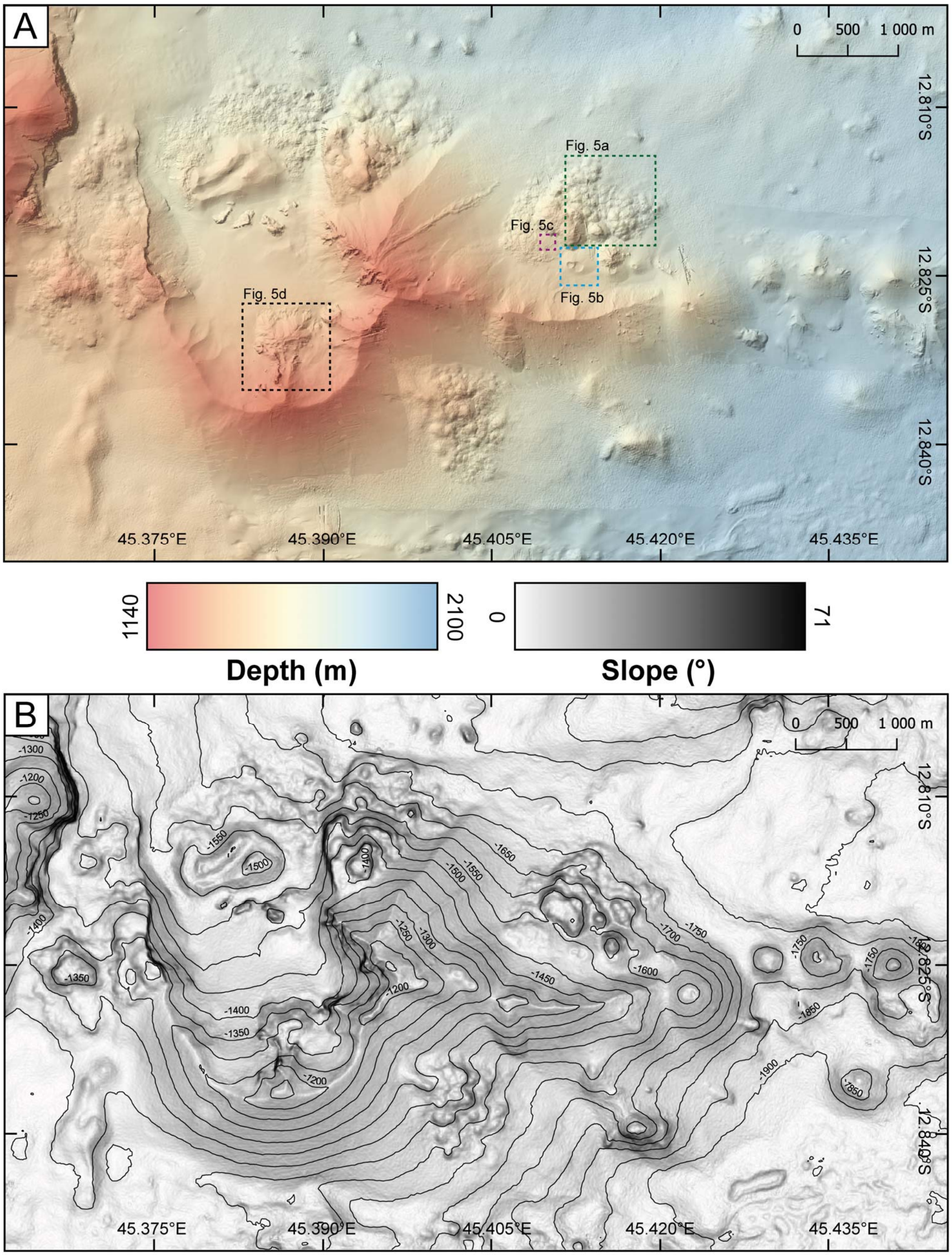


**Figure 4.** (A) General shaded bathymetric map of the Horseshoe area (compilation AUV+MBES). The different squares indicate details of the AUV derived bathymetric maps from Figure 5. (B) General slope map of the Horseshoe area, with 50 m spaced bathymetric contours.

Visual seafloor observations provide ground-truth of the geomorphological seafloor textures mapped on the bathymetry, and are required to better understand their geometry, nature, and distribution. These visual data are used to define several facies that provide clues regarding their origin (e.g., volcanic deposits, mass wasting, etc.). Qualitative comparison and spatial correlation of the

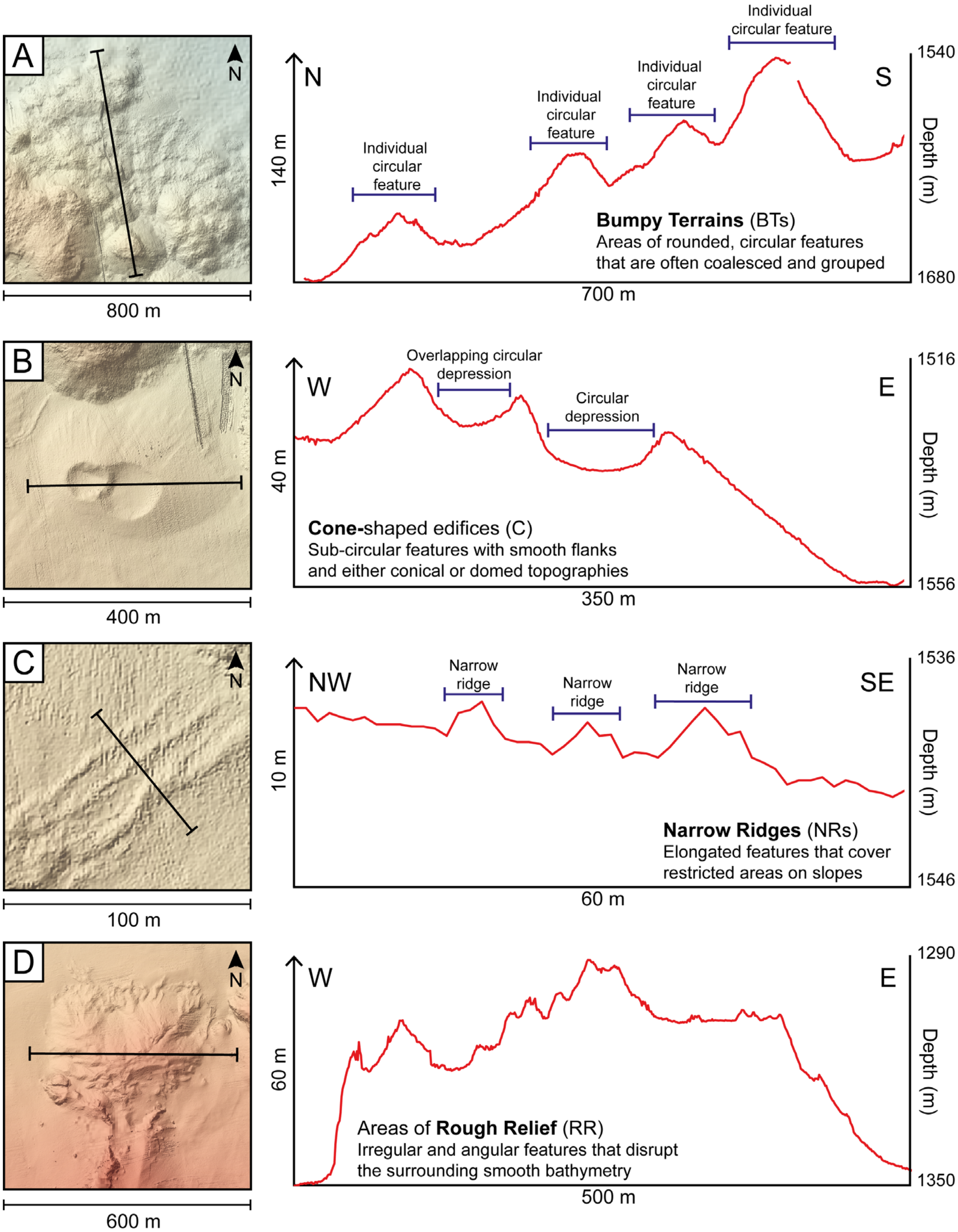


**Figure 5.** (A–D) Details of seafloor textures identified on AUV bathymetry maps at the Horseshoe area. Location of these details are indicated in Figure 4. Associated cross-sections are extracted from bathymetry grids. Location of these cross-sections are indicated on the corresponding shaded bathymetry map.

distribution of the geomorphological seafloor textures and visual facies mapped with high-resolution bathymetry and in-situ imagery allows us to determine whether local in-situ observations can be extrapolated to broader areas using the high-resolution bathymetry, or if more systematic and

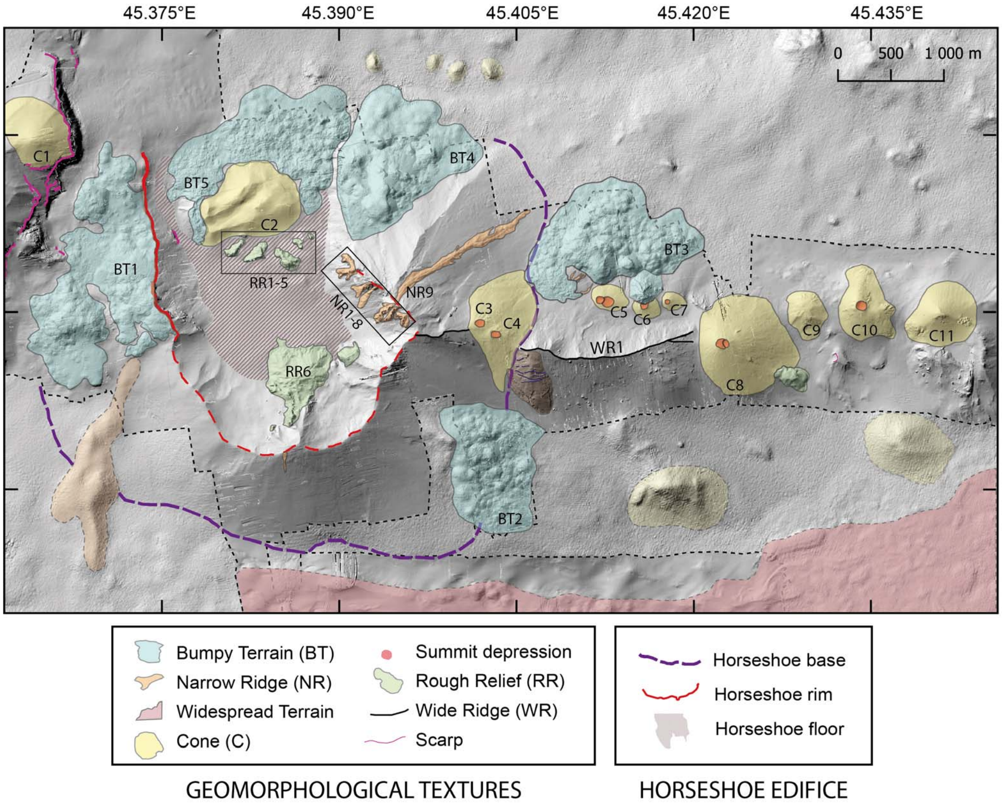


**Figure 6.** Geomorphological features of the Horseshoe area from seafloor textures and features mapped on the shaded bathymetry map, combining high-resolution AUV data (limited by black dashed lines) and ship-based data. Dashed outlined features are mapped for indicative purposes but are not used for the discussion as they are located outside the AUV surveyed area (black dashed outline; see Figure 3d).

in-situ observations are needed to ground-truth the bathymetry data.

All the images and videos from the Scampi tows conducted within the Horseshoe area were inspected visually, and from this systematic review we are able to distinguish various visual facies based on textures (e.g., size of blocks, surface texture; Figure 7). This visual interpretation was conducted independently from the geomorphological interpretation described above for objectivity and to avoid biases. We systematically classified each image according to the different visual facies along the Scampi tracks, thus providing a precise along-track map of the distribution of the different facies (Figure 8). The superposition of visual facies along the Scampi tracks over the seafloor textures mapped on the bathymetry then allows us to discuss the results presented in the following section.

## 4. Results

### 4.1. *Geomorphological characteristics and distribution of seafloor textures in the Horseshoe area*

Near-seafloor, high-resolution AUV bathymetry data (~1 m) acquired along Mayotte's upper eastern submarine slope document variations in seafloor morphology (Figures 4, 5). Figure 5 presents the main geomorphological seafloor textures that we observe in the Horseshoe area between water depths of 1100–1500 m.

The Horseshoe edifice was first described in Feuillet et al. [2021] as a large cone with smooth slopes and a large irregular U-shaped scar, based on ship-based bathymetry data. With the new high-resolution AUV bathymetry, we can now describe this structure in

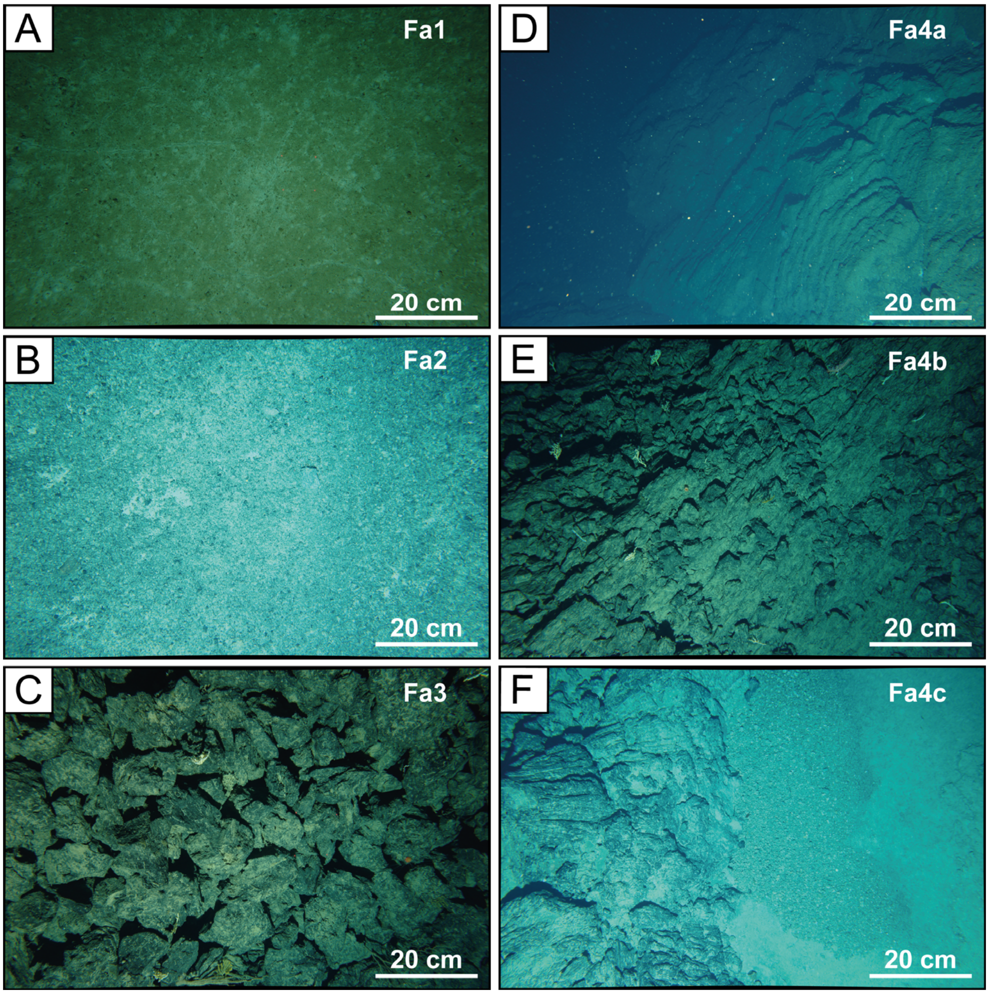


**Figure 7.** (A–F) In-situ image examples of the different seafloor facies encountered in Scampi imagery and reported on Figure 8. Fa1: fine clastic material with little to no blocks. Fa2: angular blocks a few cm to a few 10 s of cm across with very little matrix. Fa3: clusters of angular blocks up to a meter across with no matrix. Fa4a–Fa4c: stratified, consolidated, to massive in-situ outcrops.

finer detail. The base of the edifice (purple dashes on Figure 6) is ~4 km wide, as inferred from the break in slope, from 15° to 25° on the cone compared to the flat surrounding seafloor (Figure 4b). The center of the edifice shows a 2 km-wide depression that is open to the north. Its crest is marked by a sharp and well-defined U-shaped limit: the Horseshoe's rim (red dashes on Figure 6). To the west, the depression is bounded by a ~N–S striking, steep (~60°) 60 m-high, eastward facing cliff (solid red line on Figure 6). To the south, the depression is bounded by slopes that are both smoother and more gently dipping. To the east, the Horseshoe's rim is kinked in a NW–SE direction.

#### 4.1.1. *Bumpy terrains*

First, we identify bumpy terrains (BTs) characterized by rounded, circular features that are often coalesced and grouped (Figure 5a). Individual circular features have typical diameters of a few tens to up to ~200 m, heights of 10–100 m and display either rough or smooth textures in the high-resolution

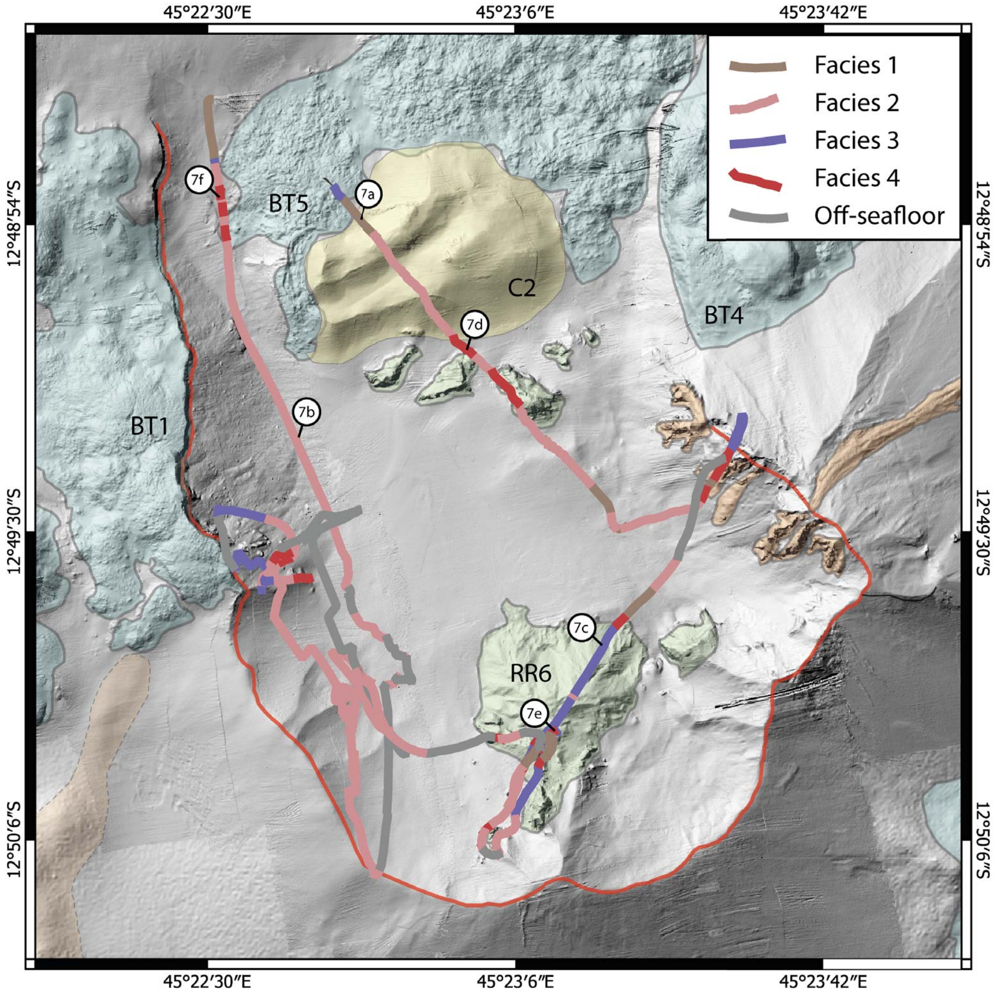


**Figure 8.** Seafloor textures throughout the Horseshoe's depression from the AUV high-resolution bathymetry and Scampi imagery. The colors along the navigation track of the scampi diving (Dives 01 and 02 of MAYOBS 4 (Table 1) and Dives 02 and 03 of MAYOBS 15 (Table 1; see location on Figure 3d)) correspond to the different seafloor types indicated in the text and are underlain by the seafloor textures mapped on the bathymetry (Figure 6). The small white circles locate the images from Figure 7. Owing to navigation and flight conditions of the Scampi, the vehicle was off-bottom during part of the transects and no images could be acquired. In addition to the visual facies described above, we also report these track sections as off-seafloor with no visual ground-truth.

bathymetry. We map five areas of bumpy terrains (BT1–BT5) on the western and eastern outer flanks of the Horseshoe edifice as well as in the center of its depression (Figure 6). These zones cover surfaces of ~1–2 km$^2$. The westernmost terrain BT1 is clearly truncated on its eastern edge by the sharp scarp bounding the Horseshoe's depression.

#### 4.1.2. *Cone-shaped edifices*

We identify well-preserved cone-shaped edifices (C1–C11 on Figure 6) that all display a sub-circular plan-view base with either conical or domed topographies (Figure 5b). Their flanks are smooth in the high-resolution bathymetry with gentle slopes ranging from 10° to 25° (Figure 4b). These structures show basal diameters of a few hundreds of meters to ~1 km and heights of up to ~200 m relative to the adjacent seafloor. West of the Horseshoe edifice, we map a large cone (C1; 500 m in diameter at the base, 140 m-high). North of the Horseshoe's depression and surrounded by BT5, we map a smooth 100 m-high edifice (C2) with gentle slopes and having a conical shape elongated in a WSW–ENE direction. A 20 m-deep, 180 m-wide depression elongated in the same direction is visible at its center. East of the Horseshoe edifice, we identify three distinct sets of cones (Figure 6). C3 and C4 (SC 1) are irregular cones, overlap each other and present well-defined small circular depressions (up to 100 m in diameter) at their summits. C5–C7 (SC 2) are much smaller (diameter up to 350 m), have clear circular bases and also show summit depressions. Lastly, C8–C11 (SC 3) are larger (diameter up to 950 m), more irregularly shaped and do not systematically show summit depressions. The three sets of cones are aligned in an overall E–W direction.

#### 4.1.3. *Wide ridges*

The three sets of cones (SC 1–SC 3) are aligned with a sharp E–W to N 70° E striking Wide Ridge (WR1 on Figure 6). The northern and southern slopes of this 1.2 km long ridge gently dip northwards by 25° and southwards by 20° and show a very smooth texture in the bathymetry (Figure 4b). This ridge appears to extend from the kinked eastern part of the Horseshoe's rim and shows a sharp crest at its summit. South of WR1 and just east of the base of the Horseshoe, we identify an ellipsoidal feature with a smooth surface that is disrupted by northward dipping scarps (brown patch on Figure 6).

#### 4.1.4. *Narrow ridges*

We also identify narrow ridges (NRs) that cover more restricted areas on slopes (Figure 5c). In particular, originating from the kinked, eastern part of the Horseshoe's rim we map eight narrow ridges (NR 1–8, Figure 6) that are 120–250 m long, 30–60 m wide and that are directed towards the center of the depression. Originating from the eastern part of the Horseshoe's rim, we map a longer narrow ridge (NR 9; ~1500 m) that goes away from the Horseshoe's depression, on its outer flank. We observe a depression in the center of NR 9. Shorter NRs also originate from BT3 and from the southern part of the Horseshoe's rim, displaying widths of ~30 m and lengths of 100–200 m.

#### 4.1.5. *Areas of rough relief*

Within the Horseshoe's depression and along WR1 we map irregularly shaped features that distinctly disrupt the surrounding smooth bathymetry (Figure 5d). In particular, we identify five ~70 m–~280 m long and up to 40 m high areas of rough relief (RR1–RR5 on Figure 6). Another angular and irregular relief with a similar rough morphology is located further south at the foot of the southern part of the Horseshoe's rim (RR6). This RR6 relief is higher (up to 100 m-high) and larger (0.3 km$^2$) than those identified further north and appears to be a "spur" originating from the Horseshoe's rim. Two other outcrops of smaller size are also visible east and west of the "spur" structure, and other angular features can be identified throughout the study area, but we have chosen to only digitize the most prominent structures.

#### 4.1.6. *Other features*

Northwest of the Horseshoe edifice we note a set of steep N–S striking scarps arranged in an en-echelon trend with the steep cliff bounding the northwest edge of the Horseshoe's depression (pink lines on Figure 6). Lastly, south of the study area, we identify a widespread terrain (WT) that has smoother surfaces than those observed with the BTs.

### 4.2. *Visual seafloor facies from in-situ imagery*

In-situ imagery of the seafloor documents the outcrop textures and detailed seafloor morphology at smaller scales (~ a few m or less; Figure 7). In this section we describe the different seafloor textures observed at the Horseshoe area based solely on visual criteria, for objectivity. The interpretation of these facies and their comparison to those observed elsewhere is detailed in Section 5.1. The distribution of these visual seafloor facies is shown in Figure 8 along the Scampi tracks that go over the different geomorphological seafloor textures we described.

We identify four different visual facies (Fa1 to 4). The first facies (Fa1; Figure 7a; Table 2) is characterized by fine (<1 cm), clastic, matrix rich material with few or no blocks and a muddy aspect. In some areas the material seems consolidated, forming crusts that are often cracked. This Fa1 facies is encountered in three distinct areas: (a) north of the Horseshoe's depression, (b) in the eastern region of the Horseshoe's floor, where it alternates with coarser deposits and (c) along the southern inner flank of the Horseshoe edifice (Figure 8), especially within the "spur" region (RR6), where it covers some areas with more abrupt topography and higher relief.

The most frequently encountered facies (Fa2; Figure 7b; Table 2) is characterized by small angular blocks that are a few centimeters across, do not appear to be consolidated, and with very little clastic matrix. There is a significant variability in the visual distribution and size of clasts, with some areas displaying larger blocks that are placed over units with smaller sized clasts. The density of larger blocks shows lateral (along-track) variations and qualitatively we observe that their abundance increases upslope, or close to steep scarps. This Fa2 facies is found in the Horseshoe's central depression and on its southwestern inner flank, The Horseshoe's floor is thus mainly composed of this facies, at least along the tracks imaged by the Scampi (Figure 8).

The third facies (Fa3; Figure 7c; Table 2) is characterized by clusters of larger angular blocks that are tens of cm to one meter in diameter with no clastic matrix. This facies is found throughout the area, at the base of cliffs, along sloping areas, or within areas of rough relief. In particular, we observe this facies on the top of the large area of rough relief (RR6) at the foot of the southern part of the Horseshoe's rim, west of BT1, as well as along its kink-shaped northeastern rim. This facies is also found locally on the top surface of BT5, just north of the smooth relief (C2, Figure 8) that it surrounds.

The last facies (Fa4) features in-situ, consolidated, stratified or massive structures. We identify three sub-facies within Fa4, based on the apparent alteration and stratification of outcrops (Fa4a–Fa4c). Some structures are made up of brecciated, stratified material (Fa4a, Figure 7d; Table 2). Fa4b consists of clear angular, massive blocks 10 s of m across (Figure 7e; Table 2) while the last sub-facies (Fa4c) shows overall flat morphologies with clear striations, resembling subaerial ropy lava surfaces (Figure 7f; Table 2). The areas mapped north of the Horseshoe's depression, west of the "spur" (RR6) and originating from the eastern kink-shaped part of the Horseshoe's rim all display brecciated, stratified outcrops often showing fractures and thus correspond to the sub-facies Fa4a. Facies observed around the spur region are less fractured, often marking clear breaks in the topography, as is the case east of BT1, below the western part of the rim and are thus interpreted as the subfacies Fa4b. Lastly, north of the Horseshoe's depression, west of BT5, we identify a massive area with an overall flat morphology that we characterize as part of the Fa4c sub-facies.

### 4.3. *Comparisons and correlations between high-resolution bathymetry and in-situ imagery*

Qualitative comparisons of the seafloor geomorphological textures mapped on the bathymetry and of the visual facies identified on the in-situ imagery allows us to determine if local, outcrop-scale data can be extrapolated to broader areas. Visual seafloor facies Fa1 and Fa2 both are composed of relatively fine (>10 cm) clastic material that corresponds to smooth seafloor texture on the high-resolution bathymetry, with no significant relief or changes in topography. Both visual facies are composed of material that is too fine to be associated to a specific sub-texture (i.e. Fa1 or Fa2) in the smooth bathymetry areas. Hence, all visual facies composed of elements with scales lower than the resolution of the bathymetry and lacking distinctive topographic features cannot be regionally extrapolated using only local in-situ observations. We thus restrict our interpretations to the Scampi tracks for these facies.

The visual facies Fa3 cannot be directly correlated with any of the seafloor textures and features identified in the bathymetry for the same reasons (the material is coarser but still too fine to be identified in bathymetry). However, we do observe that this facies tends to be found over features that show small-scale roughness (at scales of a few m), especially along slopes associated with scarps, ridges, or clear topographic markers.

In the Horseshoe area, the visual facies Fa4 identified on the Scampi imagery can be directly associated to the areas of rough relief mapped on the bathymetry (e.g., RR1–5). The sharp edges visible on both the imagery and bathymetry provide general ground-truth of these features, but systematic in-situ observations are necessary to characterize the finer

**Table 2.** Characteristics and location of high-resolution visual seafloor facies identified solely on deep-towed camera images and videos

| Facies | | Description | Location |
|---|---|---|---|
| Fa1 | | • Fine (<1 cm) clasts<br>• Few to no blocks<br>• Matrix rich | • North of the Horseshoe's depression<br>• Eastern region of the depression<br>• Within RR6 region |
| Fa2 | | • Small angular blocks (>1 cm, <10 cm)<br>• Not consolidated<br>• Very little matrix | • Most of the Horseshoe's floor (most frequently encountered facies) |
| Fa3 | | • Large angular blocks (>10 cm, <1 m)<br>• Not consolidated<br>• No matrix | • Within RR6 region<br>• Eastern part of the Horseshoe's rim<br>• West of BT1<br>• On top of BT5 |
| Fa4 | Fa4a | Stratified/brecciated in-situ structures | • North of the Horseshoe's depression<br>• West of RR6 region<br>• Eastern part of the Horseshoe's rim |
| | Fa4b | Massive angular in-situ blocks (>10 m) | • Around RR6 region<br>• East of BT1 |
| | Fa4c | Flat, striated in-situ surfaces | • West of BT5 |

scale morphologies, and to detect the presence of lineations, fissures or breccia within the outcrops.

## 5. Discussion

### 5.1. *Interpretation of seafloor textures and facies*

To date, only a few seamounts have been studied systematically over a wide range of scales [e.g., Axial Seamount, Chadwick Jr. et al., 2013, Clague et al., 2017, West Mata, Chadwick Jr. et al., 2018; Havre, Carey et al., 2018; NW Rota-1, Embley et al., 2006]. The geodynamic context offshore Mayotte is complex and different from those regions, and the volcanic features and morphologies that we identify along Mayotte's eastern upper submarine slope cannot be directly compared. However, we propose here an interpretation of the seafloor features of our study area, based on preexisting subaerial and submarine geomorphological studies.

Bumpy terrains, widespread terrains and narrow ridges likely correspond to different types of lava flows that were emplaced through different processes. While we do not yet have clear ground-truth for the bumpy terrains identified from the high-resolution bathymetry, we propose that BTs 1–5 are similar to hummocky lava flows that are made of pillow lava [Smith and Cann, 1990, Clague et al., 2017]. The latter are commonly observed at slow-spreading mid-ocean ridges [Smith et al., 1995, Yeo et al., 2012, Yeo and Searle, 2013], or at other submarine volcanic settings [e.g., Mariana back-arc spreading center, Chadwick Jr. et al., 2018; West Mata seamount, Chadwick Jr. et al., 2019; Lō'ihi seamount, Clague et al., 2019]. However, individual hummocks observed at BTs 1–5 show a texture that visually appears rougher than that described previously, and similar to what has been observed by Embley and Rubin [2018] in the Lau Basin, or by Portner et al. [2021] on the Alarcon Rise segment of the East Pacific Rise. We propose that the eruption processes might be similar, but the fine-scale rougher morphology of hummocks observed at the Horseshoe area may be due to lavas that are more evolved, and therefore more viscous [Berthod et al., 2021b], than those usually erupted along mid-ocean ridges. We suggest that the narrow ridges that we map at the Horseshoe area correspond to narrow lava flows that originate from restricted and focused vent areas. Lastly, the widespread terrain that we identify corresponds to the highly reflective lava flows visible on both shipboard bathymetry and backscatter data (Figure 2). They have a finer, smoother and more homogeneous aspect than that of the hummocky lava flows and are thus possibly associated with lavas that are erupted at a higher effusion rate and possibly a slightly lower viscosity [Gregg and Fink, 1995, White et al., 2015a].

The cone-shaped edifices mapped throughout the Horseshoe area show smooth and regular slopes in the high-resolution bathymetry and circular bases. Some cones display sharp, circular summit depressions which can be interpreted as summit craters resulting from (a) an explosive volcanic activity or (b) minor collapse (e.g., pit craters). In subaerial volcanic settings, summit craters are usually associated with explosive volcanic activity that results in the formation of monogenetic volcanic edifices [e.g., cinder cones, spatter cones, tuff rings, tuff cones; Acocella, 2021]. High-resolution geomorphological studies on deep submarine volcanic cones have also highlighted the presence of summit craters [e.g., Davis and Clague, 2006, Chadwick Jr. et al., 2008, Minami and Ohara, 2018, Nomikou et al., 2012, Cronin et al., 2017, Iezzi et al., 2020]. In submarine volcanic settings, the interactions of magma with seawater and the effects of pressure and temperature mean that explosive eruptions are less common, but not impossible [Head III and Wilson, 2003, White et al., 2015b].

We were able to correlate some of the geomorphological features mapped on the bathymetry with the in-situ visual facies. That is the case for the areas of Rough Relief, which appear to match the visual facies Fa4. Yet, the morphologies we observe in these areas are complex and likely result from different processes. They are thus difficult to interpret confidently based solely on images and videos from a subvertical 2D camera. Nevertheless, we propose that these features are also the result of different volcanic processes, some of which could be of effusive origin.

Features at scales below the resolution of the AUV bathymetry (~1 m) cannot be regionally extrapolated using only local in-situ observations. That is the case for Fa3 regions, that we interpret as "talus", as observed at other submarine areas [e.g. West Mata, Chadwick Jr. et al., 2019]. Here we make no distinction as to their origin (e.g. lava dome talus, rock-fall talus, lava flow levee rubble) as they are found at the base of cliffs, along sloping areas, or within chaotic volcanic outcrops.

That is also the case for visual facies Fa1 and Fa2, that are both composed of deposits that are too fine to be associated to a specific sub-texture, and hence all correspond to a smooth texture on the bathymetry. At the Horseshoe area, visual facies Fa1 and Fa2 correspond to fine and coarse clastic deposits that can be interpreted as pyroclastic deposits (Berthod, Gurioli, Komorowski, MAYOBS 15 cruise unpublished report, https://doi.org/10.18142/291). Such volcanic facies have already been observed at other submarine settings [e.g. West Mata, Chadwick Jr. et al., 2019; North Arch volcanic field, Davis and Clague, 2006; Gakkel Ridge, Sohn et al., 2008].

Hence, based on visual observations, preliminary dredge results and on the morphological comparison of the volcanic cones mapped at the Horseshoe area combined with those observed at submarine volcanoes elsewhere, we infer that some of the volcanic cones that we observe are likely to result from explosive activity. We also propose that the wide ridge WR1 might be the result of the combination of explosive and effusive volcanic processes, as suggested by the elevated morphology of the cones, the presence of summit craters and the presence of several coalesced cones. We thus interpret this ridge as the cumulative result of the activity along an eruptive fissure.

The focus of our study, and the most striking feature that we observe in the area is the Horseshoe edifice itself. We infer that this structure may have been emplaced during a large explosive eruption, based on its overall sub-circular shape at its base (~4 km in diameter), with smooth and regular slopes (Figures 4, 6), similar to that of the other volcanic cones mapped in the area. It is also consistent with the presence of fine and coarse likely pyroclastic deposits which are visible throughout the study area, suggesting its formation as a large tuff cone. The Horseshoe's summit is now marked by a clear U-shaped rim that shows strong variations at very small scales. The western part of the rim is characterized by a steep scarp clearly disrupting BT1 and indicating a collapse stage postdating the emplacement of this BT1 unit. The morphology of the southern part of the rim is different: the associated slopes are much smoother and more gently dipping than to the west of the rim. The kinked, eastern part of the Horseshoe's rim shows steeper slopes but is covered with narrow lava flows (NR 1–9). While this part of the rim is also reminiscent of some type of collapse processes, our interpretation is blinded by new volcanic features that emplaced over the original rim. We propose that the overall morphology of the Horseshoe edifice could be the result of complex vertical and/or lateral collapse processes, followed by new constructional volcanism.

### 5.2. *Relative chronology and geological history of the Horseshoe area*

Our multiscale study also provides preliminary constraints on the chronological evolution of the seafloor morphologies and the interactions and timing of the different volcano-tectonic processes identified. We propose a simplified relative chronology of eruptive events, based solely on geomorphological cross-cutting relationships (Figure 9). Other relevant multidisciplinary data (e.g., petrology, geochemistry, textural analysis of dredge samples) are currently the scope of other projects and will be published in the future. Here we discuss some of the main processes that have recurrently shaped the formation and evolution of the Horseshoe area within the East-Mayotte Volcanic Chain (EMVC).

The first event we identify is the emplacement of the Horseshoe edifice, one of the most prominent geomorphological structures in the area on which other features have subsequently developed (Figure 9a). The geometry of the Horseshoe's collapse scar and the distribution of hummocky lava flows (bumpy terrains), provide temporal constraints on their emplacement. The westernmost hummocky lava flow (BT1) is clearly cross-cut by the rim of the Horseshoe edifice (Figure 9b). This indicates that this lava flow postdates the formation of the Horseshoe edifice, emplaced on its flanks, but predates the Horseshoe's collapse stage (Figure 9c). The northernmost hummocky lava flow (BT5) was emplaced within the Horseshoe's depression, thus clearly postdating the collapse stage (Figure 9d).

Subsequent volcanic features do not display clear cross-cutting relationships and hence their subsequent relative history is not as well defined. In particular, it is not possible to clearly determine if the Horseshoe edifice and all other seafloor features are coeval or their emplacement postdated the formation of the Horseshoe edifice. Hence, these are grouped as part of a "recent eruptive zone" resulting from a recent eruptive fissure (WR1) that likely emplaced over older seafloor (Figure 9e). The volcanic cones with morphological features that lack evidence of erosion were emplaced on top or on a subparallel alignment to this recent eruptive fissure (SC 1–SC 3). The close association of these features suggests that volcanic activity at local scales may be controlled by larger scale pre-existing structures (e.g., faults, ring faults of a possible older postulated caldera). The other two volcanic cones (C1–C2) that are emplaced west and within the Horseshoe edifice are aligned with the recent eruptive fissure and imply a structural control of the subseafloor pre-existing structures on the emplacement of new volcanic material. Another recent volcanic event is associated with the emplacement of narrow lava flows mapped on the eastern rim of the Horseshoe along the eruptive fissure (NR 1–9). These features formed both within the Horseshoe's depression and on the outside along its eastern outer flank. These lava flows are thus likely emplaced after the collapse stage, as they appear to flow over mass-wasted deposits.

Lastly, the massive volcanic outcrops mapped as RR1–RR5 north of the Horseshoe's floor have peculiar morphologies and lack clear cross-cutting relationships to provide clues regarding their timing. Given the complex and chaotic structure of these outcrops, it is possible that they formed at the time of the Horseshoe collapse stage and might correspond to outcrops of partially buried volcanic features. The spur region (RR6), south of the Horseshoe could either be: (a) a young lava dome that formed directly after the collapse stage; (b) a lava dome or lava flow emplaced later, after the collapse stage due to resumption of eruptive activity within the depression; or (c) pre-collapse older host-rock uplifted by magma movement at shallow depth [Fouquet et al., 2018].

### 5.3. *Implications for the recent seismo-volcanic crisis*

The regional morphology of the eastern upper submarine slope of Mayotte Island suggests that caldera collapses may have occurred in the past in the Horseshoe area. The area is located on the southern boundary of what is believed to be the remnant of former large caldera structure (~10 km wide)

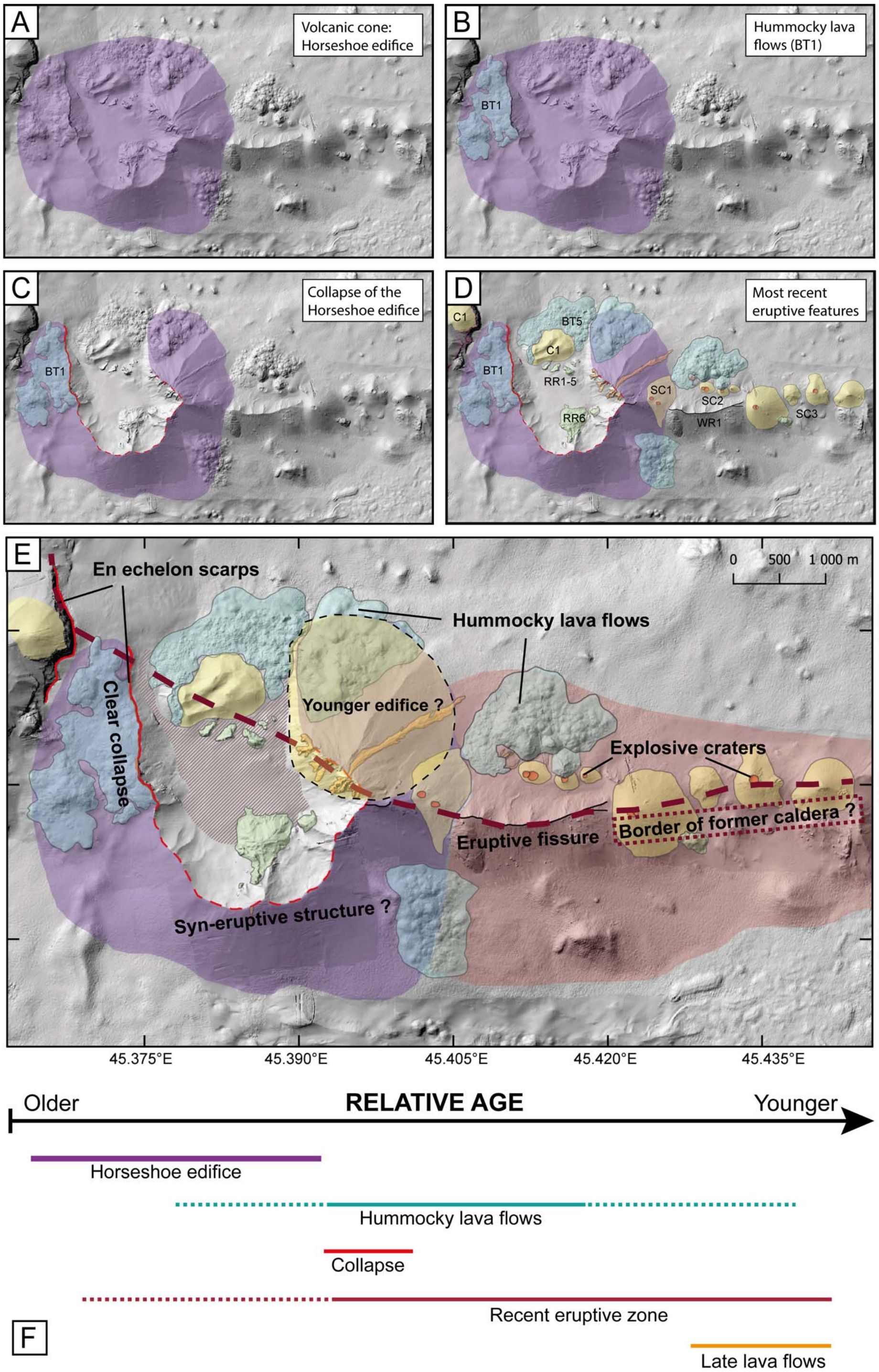


**Figure 9.** (A–D) Interpreted simplified relative chronology of the eruptive events that occurred within the Horseshoe area, based solely on crosscutting geomorphological relationships. (E) Geomorphological map with seafloor features interpreted as in Section 5.1 (Cones in yellow, hummocky lava flows in blue, and areas of rough relief in green). We identify two main units: the Horseshoe edifice (purple) and a recent eruptive zone associated with scattered volcanic activity and explosive processes. (F) Summary of relative chronological time chart.

[Figures 1b and 2; Feuillet et al., 2021]. It also lies directly above a major seismic swarm that was recorded during the seismo-volcanic crisis and that was likely associated with the drainage of a deep magma reservoir that fed the recent Mayotte eruption ~40 km to the east [Cesca et al., 2020, Lemoine et al., 2020, Berthod et al., 2021a, Feuillet et al., 2021, Jacques et al., 2021, Mercury et al., 2022].

While no sign of eruptive activity was detected on the upper submarine slope since the submarine eruption began in 2018, this study clearly shows that the Horseshoe area has been volcanically active in the recent past. Moreover, the multibeam echosounder surveys have documented active fluid emission sites throughout the area [Scalabrin et al. in preparation; REVOSIMA, 2022]. These fluid emission sites are located within and north of the Horseshoe's depression with an apparent progression of new emission sites northwards, southwards and away from the Horseshoe edifice itself [*Bulletin 45 du 1 au 31 Août 2022*, REVOSIMA, 2022]. This supports the idea that the Horseshoe area might be one volcanic field on the boundary of a larger scale volcano-tectonic structure, reusing previous subvertical zones of weakness as pathways for new volcanic and hydrothermal emissions.

While Mayotte's eastern upper submarine slope has not experienced any volcanic activity since 2018, this area is important for understanding and forecasting the potential long-term evolution and consequences of the current eruption. For example, a potential future scenario could include a new caldera collapse due to the drainage of the deep magma reservoir beneath this area. Given the uncertainties, the impacts of such a scenario are currently difficult to quantify and are the subject of ongoing geological scenarios elaboration and numerical modelling. Alternative scenarios could involve renewed explosive or effusive eruptive activity in the Horseshoe area or even the reactivation of the magmatic plumbing system that was responsible for Holocene explosive subaerial volcanic activity on Petite-Terre and on the north side of Grande-Terre on Mayotte.

## 6. Conclusions

This study of Mayotte's eastern submarine slope aims to characterize the types and chronology of previous volcanic activity, the interactions between tectonic and volcanic activity in the area, and the relation to deep seismicity beneath it. This paper focuses on the Horseshoe area, a submarine volcanic field located ~10 km east of Mayotte Island.

Using a multiscale high-resolution mapping approach, we discuss the nature of the observed volcanic features and propose a relative chronology of eruptive events in the area. We identify different volcanic textures including volcanic cones, hummocky terrains and lava flows. The observed morphologies likely result from both effusive and explosive volcanic processes. The Horseshoe edifice is a 4 km wide volcanic cone that underwent a major collapse, resulting in the formation of a 2 km wide depression opened to the north. Its collapse scar clearly cross-cuts hummocky lava flows and shows the emplacement of younger lava flows emanating from the rim. The Horseshoe edifice likely predates the emplacement of a prominent E–W trending volcanic fissure zone, that is associated with a series of volcanic cones that are also aligned E–W. The formation of this diverse set of volcanic features in the Horseshoe area may be related to their location on the southern rim of a proposed caldera structure. We plan on improving our understanding of the nature of the Horseshoe area through analyses of additional imagery and through the correlation of this study with on-going petrological and geochemical studies. A fuller understanding of the volcanic hazards that this area poses will have to await until then, but for now, this study has documented that the Horseshoe area has been volcanically active in the recent past and has experienced both effusive and explosive eruptive activity. Its location above the deep seismicity observed since 2018 suggests that the features that we have mapped may be earlier deposits from the same deep magmatic system that fed the 2018 eruption at Mayotte.

## Conflicts of interest

Authors have no conflict of interest to declare.

## Acknowledgements

MAYOBS 1 cruise was funded by the CNRS-INSU TELLUS MAYOTTE program (SISMAYOTTE project). MAYOBS 1, 4, 15, 17 cruises were conducted by several French research institutions and laboratories (IPGP/CNRS/BRGM/IFREMER/IPGS). All marine operations are performed as part of the MAYOBS set of cruises (https://doi.org/10.18142/291) and we thank the captains and crews of the R/V Marion Dufresne (TAAF/IFREMER/LDA), R/V Pourquoi Pas? (GENAVIR/IFREMER, SHOM), Beautemps-Beaupré (SHOM), Gauss (FUGRO), and the scientific parties of the different cruises. We thank the mission chiefs of the MAYOBS cruises (E. Rinnert, N. Feuillet, Y. Fouquet, S. Jorry, I. Thinon, E. Lebas, F. Paquet) for conducting marine operations that benefited this study. Analyses were funded by the Service National d'Observation en Volcanologie (SNOV, INSU) and the Réseau de Surveillance Volcanologique et Sismologique de Mayotte (REVOSIMA), a partnership between the Institut de Physique du Globe de Paris (IPGP), the Institut Français de Recherche pour l'Exploitation de la Mer (IFREMER), the Bureau de Recherches Géologiques et Minières (BRGM), the Centre National de la Recherche Scientifique (CNRS) and the REVOSIMA consortium. The REVOSIMA's operational daily monitoring is under the responsability of the Piton de la Fournaise volcanological observatory (OVPF-IPGP). We thank A. Peltier (OVPF-IPGP) and C. Mucig (BRGM Mayotte) respectively the Operational Leader and Co-leader of the REVOSIMA. Since June 2019, all activities on Mayotte are funded by le ministère de l'Enseignement Supérieur, de la Recherche et de l'Innovation (MESRI), le Ministère de la Transition Ecologique (MTE), le Ministère des Outremers (MOM), with the support of the Ministère de l'Intérieur (MI), the Ministère des Armées, the DIRMOM (Direction Interministérielle aux Risques Majeurs en Outremer) and the MAPPPROM (Mission d'appui aux politiques publiques pour la prévention des risques majeurs en Outremer). We thank the IPGP for general funding to the Observatoires Volcanologiques et Sismologiques (OVS). The data contributes to the Service National d'Observation en Volcanologie (SNOV). The authors would like to thank E. Humler for his support and national funding coordination (CNRS, REVOSIMA). Lastly, we also thank the editors and the two reviewers for their comments that helped us clarify and improve this manuscript.

## References

Acocella, V. (2021). Volcano flank instability and collapse. In *Volcano-Tectonic Processes*, pages 205–244. Springer, Cham.

Anderson, M. O., Chadwick Jr., W. W., Hannington, M. D., Merle, S. G., Resing, J. A., Baker, E. T., Butterfield, D. A., Walker, S. L., and Augustin, N. (2017). Geological interpretation of volcanism and segmentation of the Mariana back-arc spreading center between 12.7° N and 18.3° N. *Geochem. Geophys. Geosyst.*, 18, 2240–2274.

Audru, J. C., Bitri, A., Desprats, J. F., Dominique, P., Eucher, G., Hachim, S., Jossot, O., Mathon, C., Nédellec, J.-L., Sabourault, P., Sedan, O., Stollsteiner, P., and Terrier-Sedan, M. (2010). Major natural hazards in a tropical volcanic island: a review for Mayotte Island, Comoros archipelago, Indian Ocean. *Eng. Geol.*, 114(3–4), 364–381.

Audru, J. C., Guennoc, P., Thinon, I., and Abellard, O. (2006). BATHYMAY: underwater structure of Mayotte Island revealed by multibeam bathymetry. *C. R. Géosci.*, 338(16), 1240–1249.

Bachèlery, P., Lénat, J. F., Di Muro, A., and Michon, L. (2016). *Active Volcanoes of the Southwest Indian Ocean.* Springer, Cham.

Berthod, C., Médard, E., Bachèlery, P., Gurioli, L., Di Muro, A., Peltier, A., Komorowski, J.-C., Benbakkar, M., Devidal, J., Langlade, J., Besson, P., Boudon, G., Rose-Koga, E., Deplus, C., Le Friant, A., Bickert, M., Nowak, S., Thinon, I., Burckel, P., Hidalgo, S., Jorry, S., Fouquet, Y., and Feuillet, N. (2021a). The 2018-ongoing Mayotte submarine eruption: magma migration imaged by petrological monitoring. *Earth Planet. Sci. Lett.*, 571, article no. 117085.

Berthod, C., Médard, E., Di Muro, A., Hassen Ali, T., Gurioli, L., Chauvel, C., Komorowski, J.-C., Bachèlery, P., Peltier, A., Benbakkar, M., Devidal, J.-L., Besson, P., Le Friant, A., Deplus, C., Nowak, S., Thinon, I., Burckel, P., Hidalgo, S., Feuillet, N., Jorry, S., and Feuillet, N. (2021b). Mantle xenolith-bearing phonolites and basanites feed the active volcanic ridge of Mayotte (Comoros archipelago, SW Indian Ocean). *Contrib. Mineral. Petrol.*, 176, article no. 75.

Bertil, D., Mercury, N., Doubre, C., Lemoine, A., and Van der Woerd, J. (2021). The unexpected Mayotte 2018–2020 seismic sequence: a reappraisal of the regional seismicity of the Comoros. *C. R. Géosci.*, 353(S1), 211–235.

Carey, R., Soule, S. A., Manga, M., White, J. D., McPhie, J., Wysoczanski, R., Jutzeler, M., Tani, K., Yoerger, D., Fornari, D., Caratori-Tontini, F., Houghton, B., Mitchell, S., Ikegami, F., Conway, C., Murch, A., Fauria, K., Jones, M., Cahalan, R., and McKenzie, W. (2018). The largest deep-ocean silicic volcanic eruption of the past century. *Sci. Adv.*, 4(1), article no. e1701121.

Cesca, S., Letort, J., Razafindrakoto, H. N. T., Heimann, S., Rivalta, E., Isken, M. P., Nikkhoo, M., Passarelli, L., Petersen, G. M., Cotton, F., and Dahm, T. (2020). Drainage of a deep magma reservoir near Mayotte inferred from seismicity and deformation. *Nat. Geosci.*, 13, 87–93.

Chadwick Jr., W. W., Cashman, K. V., Embley, R. W., Matsumoto, H., Dziak, R. P., de Ronde, C. E. J., Lau, T.-K., Deardorff, N., and Merle, S. G. (2008). Direct video and hydrophone observations of submarine explosive eruptions at NW Rota-1 Volcano, Mariana Arc. *J. Geophys. Res.: Solid Earth*, 113, article no. B08S10.

Chadwick Jr., W. W., Clague, D. A., Embley, R. W., Perfit, M. R., Butterfield, D. A., Caress, D. W., Paduan, J. B., Martin, J. F., Sasnett, P., Merle, S. G., and Bobbitt, A. M. (2013). The 1998 eruption of Axial Seamount: new insights on submarine lava flow emplacement from high-resolution mapping. *Geochem. Geophys. Geosyst.*, 14, 3939–3968.

Chadwick Jr., W. W., Merle, S. G., Baker, E. T., Walker, S. L., Resing, J. A., Butterfield, D. A., Anderson, M. O., Baumberger, T., and Bobbitt, A. M. (2018). A recent volcanic eruption discovered on the central Mariana back-arc spreading center. *Front. Earth Sci.*, 6, article no. 172.

Chadwick Jr., W. W., Rubin, K. H., Merle, S. G., Bobbitt, A. M., Kwasnitschka, T., and Embley, R. W. (2019). Recent eruptions between 2012 and 2018 discovered at West Mata Submarine Volcano (NE Lau Basin, SW Pacific) and characterized by New Ship, AUV, and ROV Data. *Front. Mar. Sci.*, 6, article no. 495.

Chadwick Jr., W. W., Wilcock, W. S. D., Nooner, S. L., Beeson, J. W., Sawyer, A. M., and Lau, T.-K. (2022). Geodetic monitoring at Axial Seamount since its 2015 eruption reveals a Waning magma supply and tightly linked rates of deformation and seismicity. *Geochem. Geophys. Geosyst.*, 22, article no. e2021GC010153.

Clague, D. A., Paduan, J. B., Caress, D. W., Chadwick Jr., W. W., Saout, M. L., Dreyer, B., and Portner, R. A. (2017). High-resolution AUV mapping and targeted ROV observations of three historical lava flows at Axial Seamount. *Oceanography*, 30, 82–99.

Clague, D. A., Paduan, J. B., Caress, D. W., Moyer, C. L., Glazer, B. T., and Yoerger, D. R. (2019). Structure of Lō‘ihi Seamount, Hawai'i and lava flow morphology from high-resolution mapping. *Front. Earth Sci.*, 7, article no. 58.

Cole, J. W., Milner, D. M., and Spinks, K. D. (2005). Calderas and caldera structures: a review. *Earth-Sci. Rev.*, 69(1–2), 1–26.

Courgeon, S., Bachèlery, P., Jouet, G., Jorry, S. J., Bou, E., BouDagher-Fadel, M. K., Révillon, S., Camoin, G., and Poli, E. (2018). The offshore east African rift system: new insights from the Sakalaves seamounts (Davie Ridge, SW Indian Ocean). *Terra Nova*, 30(5), 380–388.

Crisp, J. A. (1984). Rates of magma emplacement and volcanic output. *J. Volcanol. Geotherm. Res.*, 20, 177–211.

Cronin, S. J., Brenna, M., Smith, I. E. M., Barker, S., Tost, M., and Ford, M. (2017). New volcanic island unveils explosive past. *Eos*, 98, 18–23.

Daniel, J., Dupont, J., and Jouannic, C. (1972). Relations Madagascar-archipel des Comores (Nord-Est du canal de Mozambique): sur la nature volcanique du Banc du Leven. *C. R. Acad. Sci. Sér. D: Sciences Naturelles*, 274(12), 1784–1787.

Darnet, M., Wawrzyniak, P., Tarits, P., Hautot, S., and d'Eu, J. F. (2020). Mapping the geometry of volcanic systems with magnetotelluric soundings: results from a land and marine magnetotelluric survey performed during the 2018–2019 Mayotte seismovolcanic crisis. *J. Volcanol. Geotherm. Res.*, 406, article no. 107046.

Davis, A. S. and Clague, D. A. (2006). Volcaniclastic deposits from the North Arch volcanic field, Hawaii: explosive fragmentation of alkalic lava at abyssal depths. *Bull. Volcanol.*, 68(3), 294–307.

Davis, J. K., Lawver, L. A., Norton, I. O., and Gahagan, L. M. (2016). New Somali basin magnetic anomalies and a plate model for the early Indian Ocean. *Gondwana Res.*, 34, 16–28.

Debeuf, D. (2004). *Étude de l'évolution volcano-structurale et magmatique de Mayotte (archipel des Comores, océan Indien)*. PhD thesis, Université de la Réunion, France.

Deplus, C., Feuillet, N., Bachelery, P., Fouquet, Y., Jorry, S., Thinon, I., Pitel-Roudaut, M., et al. (2019). Early development and growth of a deep seafloor volcano: preliminary results from the MAYOBS cruises. In *AGU Fall Meeting Abstracts*, volume 2019, pages V43I–0227. AGU, San Francisco.

Deville, E., Marsset, T., Courgeon, S., Jatiault, R., Ponte, J., Thereau, E., Jouet, G., Jorry, S. J., and Droz, L. (2018). Active fault system across the oceanic lithosphere of the Mozambique channel: implications for the Nubia—Somalia southern plate boundary. *Earth Planet. Sci. Lett.*, 502, 210–220.

Dziak, R. P., Fox, C. G., Bobbitt, A. M., and Goldfinger, C. (2001). Bathymetric map of the Gorda plate: structural and geomorphological processes inferred from multibeam surveys. *Mar. Geophys. Res.*, 22(4), 235–250.

Eagles, G. and König, M. (2008). A model of plate kinematics in Gondwana breakup. *Geophys. J. Int.*, 173(2), 703–717.

Embley, R. W., Chadwick Jr., W. W., Baker, E. T., Butterfield, D. A., Resing, J. A., De Ronde, C. E. J., Tunnicliffe, V., Lupton, J. E., Juniper, S. K., Rubin, K. H., Stern, R. J., Lebon, G. T., Nakamura, K., Merle, S. G., Hein, J. R., Wiens, D. P., and Tamura, Y. (2006). Long-term eruptive activity at a submarine arc volcano. *Nature*, 441, 494–497.

Embley, R. W., de Ronde, C. E. J., Merle, S. G., Davy, B., and Tontini, F. C. (2010). Detailed morphology and structure of an active submarine arc caldera: Brothers volcano, Kermadec arc. *Econ. Geol.*, 107(8), 1557–1570.

Embley, R. W. and Rubin, K. H. (2018). Extensive young silicic volcanism produces large deep submarine lava flows in the NE Lau Basin. *Bull. Volcanol.*, 80, article no. 36.

Emerick, C. M. and Duncan, R. A. (1982). Age progressive volcanism in the Comoros Archipelago, eastern Indian Ocean and implications for Somali plate tectonics. *Earth Planet. Sci. Lett.*, 60(3), 415–428.

Famin, V., Michon, L., and Bourhane, A. (2020). The Comoros archipelago: a right-lateral transform boundary between the Somalia and Lwandle plates. *Tectonophysics*, 789, article no. 228539.

Feuillet, N., Jorry, S. J., Crawford, W., Deplus, C., Thinon, I., Jacques, E., Saurel, J. M., Lemoine, A., Paquet, F., Satriano, C., Aiken, C., Foix, O., Kowalski, P., Laurent, A., Rinnert, E., Cathalot, C., Donval, J. P., Guyader, V., Gaillot, A., Scalabrin, C., Moreira, M., Peltier, A., Beauducel, F., Grandin, R., Ballu, V., Daniel, R., Pelleau, P., Gomez, J., Besançon, S., Geli, L., Bernard, P., Bachèlery, P., Fouquet, Y., Bertil, D., Lemarchand, A., and Van der Woerd, J. (2021). Birth of a large volcanic edifice offshore Mayotte via lithosphere-scale dyke intrusion. *Nat. Geosci.*, 14, 787–795.

Foix, O., Aiken, C., Saurel, J. M., Feuillet, N., Jorry, S. J., Rinnert, E., and Thinon, I. (2021). Offshore Mayotte volcanic plumbing revealed by local passive tomography. *J. Volcanol. Geotherm. Res.*, 420, article no. 107395.

Fouquet, Y., Pelleter, E., Konn, C., Chazot, G., Dupre, S., Alix, A. S., Chéron, S., Donval, J. P., Guyader, V., Etoubleau, J., Charlou, J. L., Labanieh, S., and Scalabrin, C. (2018). Volcanic and hydrothermal processes in submarine calderas: the Kulo Lasi example (SW Pacific). *Ore Geol. Rev.*, 99, 314–343.

Franke, D., Jokat, W., Ladage, S., Stollhofen, H., Klimke, J., Lutz, R., Mahanjane, E. S., Ehrhardt, A., and Schreckenberger, B. (2015). The offshore east African rift system: structural framework at the toe of a juvenile rift. *Tectonics*, 34, 2086–2104.

Gaina, C., Van Hinsbergen, D. J., and Spakman, W. (2015). Tectonic interactions between India and Arabia since the Jurassic reconstructed from marine geophysics, ophiolite geology, and seismic tomography. *Tectonics*, 34(5), 875–906.

Gregg, T. K. and Fink, J. H. (1995). Quantification of submarine lava-flow morphology through analog experiments. *Geology*, 23(1), 73–76.

Head III, J. W. and Wilson, L. (2003). Deep submarine pyroclastic eruptions: theory and predicted landforms and deposits. *J. Volcanol. Geotherm. Res.*, 121(3–4), 155–193.

Iezzi, G., Lanzafame, G., Mancini, L., Behrens, H., Tamburrino, S., Vallefuoco, M., Passaro, S., Signanini, P., and Ventura, G. (2020). Deep sea explosive eruptions may be not so different from subaerial eruptions. *Sci. Rep.*, 10(1), article no. 6709.

Ikegami, F., McPhie, J., Carey, R., Mundana, R., Soule, A., and Jutzeler, M. (2018). The eruption of submarine rhyolite lavas and domes in the deep ocean—Havre 2012, Kermadec arc. *Front. Earth Sci.*, 6, article no. 147.

Jacques, E., Hoste-Colomer, R., Lemoine, A., and Feuillet, N. (2021). Modeling of the stress perturbation revealed by the seismotectonic analysis of the seismic swarm closest to Mayotte Island during the 2018-to-present volcano-tectonic event. In *AGU Fall Meeting Abstracts*, volume 2021, pages V45B–0128. AGU, San Francisco.

Kusky, T. M., Toraman, E., Raharimahefa, T., and

Rasoazanamparany, C. (2010). Active tectonics of the Alaotra–Ankay Graben System, Madagascar: possible extension of Somalian–African diffusive plate boundary? *Gondwana Res.*, 18(2–3), 274–294.

Laurent, A., Satriano, C., Bernard, P., Feuillet, N., and Jorry, S. (2021). Accurate depth determination of VLF events of the ongoing seismovolcanic crisis in Mayotte. In *AGU Fall Meeting Abstracts*, volume 2021, pages V45B–0129. AGU, San Francisco.

Lavayssière, A., Crawford, W. C., Saurel, J. M., Satriano, C., Feuillet, N., Jacques, E., and Komorowski, J. C. (2022). A new 1D velocity model and absolute locations image the Mayotte seismo-volcanic region. *J. Volcanol. Geotherm. Res.*, 421, article no. 107440.

Leinweber, V. T. and Jokat, W. (2012). The Jurassic history of the Africa–Antarctica corridor—new constraints from magnetic data on the conjugate continental margins. *Tectonophysics*, 530, 87–101.

Lemoine, A., Briole, P., Bertil, D., Roullé, A., Foumelis, M., Thinon, I., Raucoules, D., de Michele, M., Valty, P., and Hoste Colomer, R. (2020). The 2018–2019 seismo-volcanic crisis east of Mayotte, Comoros islands: seismicity and ground deformation markers of an exceptional submarine eruption. *Geophys. J. Int.*, 223(1), 22–44.

Mahanjane, E. S. (2012). A geotectonic history of the northern Mozambique basin including the Beira high—a contribution for the understanding of its development. *Mar. Petrol. Geol.*, 36(1), 1–12.

Masquelet, C. et al. (2022). The east-Mayotte new volcano in the Comoros archipelago: structure and timing of magmatic phases inferred from seismic reflection data. *C. R. Géosci.*, 354(S2), 65–79.

Mercury, N. et al. (2022). Onset of a submarine eruption east of Mayotte, Comoros archipelago: the first 10 months seismicity of the seismo-volcanic sequence (2018–2019). *C. R. Géosci.*, 354(S2), 105–136.

Michon, L. (2016). The volcanism of the Comoros archipelago integrated at a regional scale. In *Active Volcanoes of the Southwest Indian Ocean*, pages 333–344. Springer, Cham.

Minami, H. and Ohara, Y. (2018). Detailed volcanic morphology of Daisan-Miyako Knoll in the southern Ryukyu Arc. *Mar. Geol.*, 404, 97–110.

Mueller, C. O. and Jokat, W. (2019). The initial Gondwana break-up: a synthesis based on new potential field data of the Africa–Antarctica corridor. *Tectonophysics*, 750, 301–328.

Nehlig, P., Lacquement, F., Bernard, J., Caroff, M., Deparis, J., Jaouen, T., Pelleter, A. A., Perrin, J., Prognon, C., and Vittecoq, B. (2013). Notice de la carte géologique de Mayotte. BRGM/RP-61803-FR, 135 p., 45 ill., 1 ann, BRGM, Orléans.

Nomikou, P., Carey, S., Papanikolaou, D., Croff, B. K., Sakellariou, D., Alexandri, M., and Bejelou, K. (2012). Submarine volcanoes of the Kolumbo volcanic zone NE of Santorini Caldera, Greece. *Global Planet. Change*, 90–91, 135–151.

Nomikou, P., Papanikolaou, D., Alexandri, M., Sakellariou, D., and Rousakis, G. (2013). Submarine volcanoes along the Aegean volcanic arc. *Tectonophysics*, 597, 123–146.

Nougier, J., Cantagrel, J. M., and Karche, J. P. (1986). The Comores archipelago in the western Indian Ocean: volcanology, geochronology and geodynamic setting. *J. Afr. Earth Sci.*, 5(2), 135–144.

O'Connor, J. M., Jokat, W., Regelous, M., Kuiper, K. F., Miggins, D. P., and Koppers, A. A. (2019). Superplume mantle tracked isotopically the length of Africa from the Indian Ocean to the Red Sea. *Nat. Commun.*, 10(1), article no. 5493.

Pelleter, A. A., Caroff, M., Cordier, C., Bachèlery, P., Nehlig, P., Debeuf, D., and Arnaud, N. (2014). Melilite-bearing lavas in Mayotte (France): an insight into the mantle source below the Comores. *Lithos*, 208, 281–297.

Peltier, A. et al. (2022). Ground deformation monitoring of the eruption offshore Mayotte. *C. R. Géosci.*, 354(S2), 171–193.

Portner, R. A., Dreyer, B. M., and Clague, D. A. (2021). Mid-ocean-ridge rhyolite (MORR) eruptions on the East Pacific Rise lack the fizz to pop. *Geology*, 49(4), 377–381.

Quidelleur, X., Michon, L., Famin, V., Geffray, M. C., Danišík, M., Gardiner, N., Rusquet, A., and Zakaria, M. G. (2022). Holocene volcanic activity in Anjouan Island (Comoros archipelago) revealed by new Cassignol-Gillot groundmass K–Ar and $^{14}C$ ages. *Quat. Geochronol.*, 67, article no. 101236.

REVOSIMA (2019–2022). Bulletin Mensuel du Réseau de surveillance volcanologique et sismologique de Mayotte. http://www.ipgp.fr/fr/revosima/actualites-reseau, https://doi.org/10.18715/MAYOTTE.REVOSIMA, BRGM, Orléans.

Rolandone, F. et al. (2022). Heat flow estimates in the northern Mozambique channel. *C. R. Géosci.*, 354(S2), 35–46.

Saurel, J. M., Jacques, E., Aiken, C., Lemoine, A., Retailleau, L., Lavayssière, A., Feuillet, N., et al. (2022). Mayotte seismic crisis: building knowledge in near real-time by combining land and ocean-bottom seismometers, first results. *Geophys. J. Int.*, 228(2), 1281–1293.

Schnur, S. R., Chadwick Jr., W. W., Embley, R. W., Ferrini, V. L., De Ronde, C. E. J., Cashman, K. V., Deardorff, N., Dziak, R. P., Haxel, J. H., and Matsumoto, H. (2017). A decade of volcanic construction and destruction at the summit of NW Rota-1 seamount: 2004–2014. *J. Geophys. Res.: Solid Earth*, 122, 1558–1584.

Senkans, A., Leroy, S., d'Acremont, E., Castilla, R., and Despinois, F. (2019). Polyphase rifting and breakup of the central Mozambique margin. *Mar. Petrol. Geol.*, 100, 412–433.

Smith, D. K. and Cann, J. R. (1990). Hundreds of small volcanoes on the median valley floor of the mid-Atlantic ridge at 24°–30° N. *Nature*, 348, 152–155.

Smith, D. K., Cann, J. R., Dougherty, M. E., Lin, J., Spencer, S., MacLeod, C., Keeton, J., McAllister, E., Brooks, B., Pascoe, R., and Robertson, W. (1995). Mid-Atlantic ridge volcanism from deep-towed side-scan sonar images, 25–29 N. *J. Volcanol. Geotherm. Res.*, 67(4), 233–262.

Sohn, R. A. et al. (2008). Explosive volcanism on the ultra-slow spreading Gakkel Ridge, Arctic Ocean. *Nature*, 453, 1236–1238.

Stamps, D. S., Saria, E., and Kreemer, C. (2018). A geodetic strain rate model for the East African Rift System. *Sci. Rep.*, 8, article no. 732.

Thinon, I. et al. (2022). Volcanism and tectonics unveiled between the EARS and Madagascar: toward a better understanding of the geodynamics of the Comoros archipelago. *C. R. Géosci.*, 354(S2), 7–34.

Thordarson, T. and Self, S. (1993). The Laki (Skaftár Fires) and Grímsvötn eruptions in 1783–1785. *Bull. Volcanol.*, 55(4), 233–263.

Tzevahirtzian, A., Zaragosi, S., Bachèlery, P., Biscara, L., and Marchès, E. (2021). Submarine morphology of the Comoros volcanic archipelago. *Mar. Geol.*, 432, article no. 106383.

Wessel, P., Sandwell, D., and Kim, S.-S. (2010). The global seamount census. *Oceanography*, 23(1), 24–33.

White, J. D., McPhie, J., and Soule, A. D. (2015a). Ch. 19: submarine lavas and hyaloclastites. In Sigurdsson, H., Houghton, B., McNutt, S. R., Rymer, H., and Stix, J., editors, *The Encyclopedia of Volcanoes*, pages 363–375. Elsevier, Amsterdam.

White, J. D., Schipper, I. C., and Kano, K. (2015b). Ch. 31: submarine explosive eruptions. In Sigurdsson, H., Houghton, B., McNutt, S. R., Rymer, H., and Stix, J., editors, *The Encyclopedia of Volcanoes*, pages 553–569. Elsevier, Amsterdam.

Wiles, E., Watkeys, M., and Jokat, W. (2020). Surface expression of microplate boundary kinematics: an isolated abyssal hill in the Mozambique channel. *J. Afr. Earth Sci.*, 168, article no. 103830.

Yeo, I., Searle, R. C., Achenbach, K. L., Le Bas, T. P., and Murton, B. J. (2012). Eruptive hummocks: building blocks of the upper ocean crust. *Geology*, 40(1), 91–94.

Yeo, I. A. and Searle, R. C. (2013). High-resolution Remotely Operated Vehicle (ROV) mapping of a slow-spreading ridge: mid-Atlantic ridge 45° N. *Geochem. Geophys. Geosyst.*, 14(6), 1693–1702.

Zinke, J., Reijmer, J., Dullo, W. C., and Thomassin, B. A. (2000). Paleoenvironmental changes in the lagoon of Mayotte associated with the Holocene transgression. *Geolines*, 11, 150–153.

Zinke, J., Reijmer, J. J., Taviani, M., Dullo, W. C., and Thomassin, B. (2005). Facies and faunal assemblage changes in response to the Holocene transgression in the Lagoon of Mayotte (Comoro Archipelago, SW Indian Ocean). *Facies*, 50(3), 391–408.

Zinke, J., Reijmer, J. J. G., and Thomassin, B. A. (2003). Systems tracts sedimentology in the lagoon of Mayotte associated with the Holocene transgression. *Sediment. Geol.*, 160(1–3), 57–79.

*Comptes Rendus*
*Géoscience — Sciences de la Planète*
**2022**, Vol. 354, Special Issue S2, p. 105-136
https://doi.org/10.5802/crgeos.191

The Mayotte seismo-volcanic crisis of 2018-2021 in the Comoros archipelago (Mozambique channel) / *La crise sismo-volcanique de 2018-2021 de Mayotte dans l'archipel des Comores (Canal du Mozambique)*

# Onset of a submarine eruption east of Mayotte, Comoros archipelago: the first ten months seismicity of the seismo-volcanic sequence (2018–2019)

**Nicolas Mercury** *, [a], [b], **Anne Lemoine** [b], **Cécile Doubre** [a], **Didier Bertil** [b], **Jérôme Van Der Woerd** [a], **Roser Hoste-Colomer** [b] and **Jean Battaglia** [c]

[a] Institut Terre et Environnement de Strasbourg, CNRS UMR 7063, Université de Strasbourg, 5 rue René Descartes, 67084 Strasbourg Cedex, France

[b] BRGM, Department of Risks and Prevention, 3 av. Claude-Guillemin - BP 36009, 45060 Orléans Cedex 2, France

[c] Laboratoire Magmas et Volcans, UMR 6524 CNRS, UMR 163 IRD, Université Clermont Auvergne, 6 Av. Blaise Pascal, 63170 Aubière, France

*E-mails:* n.mercury@brgm.fr (N. Mercury), a.lemoine@brgm.fr (A. Lemoine), cecile.doubre@unistra.fr (C. Doubre), d.bertil@brgm.fr (D. Bertil), jerome.vanderwoerd@unistra.fr (J. Van Der Woerd), r.hostecolomer@brgm.fr (R. Hoste-Colomer), j.battaglia@opgc.univ-bpclermont.fr (J. Battaglia)

**Abstract.** From 10 May 2018 to 1 November 2022 (time of writing), an unprecedented seismic activity is observed east of Mayotte Island (France), related to the largest submarine eruption ever recorded with offshore geophysical studies. Using signals from regional and local seismic stations, we build a comprehensive catalog of the local seismicity for the first ten months of the sequence. This catalog includes a total of 2874 events of magnitude (Mlv) ranging from 2.4 to 6.0, with 77% of them relocated using a double difference location procedure. The hypocentral locations over this period are highly dependent on the small seismic network available. Therefore we compare the locations of later events using a similar network and those estimated from a local ocean bottom seismometer (OBS) network installed since March 2019. Based on the time space evolution and characteristics of the seismicity, five distinct phases can be identified, corresponding to the successive activation of two deep seismic swarms, related to the lithospheric-scale magma ascent up to the seafloor, along with progressive deepening of the seismicity interpreted as decompression of a 40 km deep reservoir.

**Keywords.** Earthquake catalog, Seismic swarms, Volcano-seismology, Submarine volcanism, Mayotte, Comoros archipelago.

*Published online: 12 January 2023, Issue date: 17 January 2023*

* Corresponding author.

## 1. Introduction

On 10 May 2018, the seismic stations on the western Indian Ocean recorded seismic activity that quickly became an intense sequence, with hundreds of felt earthquakes, including several events of magnitude above 5.0 recorded by the international networks [Cesca et al., 2020, Lemoine et al., 2020a, Bertil et al., 2021]. This unusually deep (40 km) seismicity [Cesca et al., 2020, Lemoine et al., 2020a] occurs in the eastern part of the Comoros archipelago, east of Mayotte, in a region not known previously for being seismically active [Figure 1; Bertil and François, 2016, Bertil et al., 2021]. The magnitude of the seismic events and the duration of the sequence surprised the population, the local authorities, and the scientific community. Past volcanic episodes in the Comoros archipelago, including Mayotte and offshore areas, remain poorly documented [e.g., Zinke et al., 2003a,b, Michon, 2016, Famin et al., 2020], except for the recent volcanic-related seismicity of the Karthala volcano, on Grande Comore [Figures 1 and 2; Bachèlery et al., 2016]. In 2019, one year after the beginning of the sequence, a new 820 m-high volcanic edifice (called "NVE" in Feuillet et al. [2021]) and several subsequent lava flows, corresponding to an estimated volume of 6.55 $km^3$, were discovered on the seafloor 50 km east of Mayotte [Figure 1c; Rinnert et al., 2019, Feuillet et al., 2021, REVOSIMA, 2022]. This seismo-volcanic event is the largest and best-monitored submarine eruption to date [Feuillet et al., 2021].

The largest amount of seismic movement was released within the first two months of the sequence, when the initial seismic monitoring network included only a few stations in Mayotte, Grande Comore, Madagascar and a few further off (Figure 2). Later, through collaborative work of the French scientific community, several additional seismic stations were progressively installed on Mayotte Island at the end of June 2018, at the end of August 2018, and then in March 2019 (Figure 2b,c,d).

In addition, since the end of February 2019, the deployment of a network of 4 to 16 ocean bottom seismometers (OBS) on the seafloor east of Mayotte have been providing better constraints of the seismicity and seismogenic structures [Rinnert et al., 2019, Feuillet et al., 2021, REVOSIMA, 2022, Saurel et al., 2022]. For the first year of the sequence, from May 2018 to February 2019, the geodetic and seismic monitoring has been crucial to understand the processes involved at the onset of this magmatic/volcanic activity, and the building of such an exceptional volcanic edifice [Lemoine et al., 2020a]. Several scenarios are proposed to outline the timeline of magma ascent, based on geophysical and petrological data [Cesca et al., 2020, Lemoine et al., 2020a, Feuillet et al., 2021, Berthod et al., 2021a]. In May 2018, the first cluster of seismicity extended southeast, then a swift upward migration started in early June, going from a depth of 40 km up to the surface within a month. The seismicity highlights the propagation of magma through the lithosphere, from a deep and exceptionally large reservoir up to the seafloor, until the eruption that started between 28 June and 5 July 2018 [Cesca et al., 2020, Lemoine et al., 2020a]. In July 2018, a second cluster progressively appeared, closer to Mayotte, along with intense, very-long-period seismicity (VLP) at more shallow levels [Poli et al., 2019, Satriano et al., 2019, Cesca et al., 2020, Lemoine et al., 2020a, Feuillet et al., 2021, Laurent et al., 2021]. Those two clusters are still active as of October 2022 [REVOSIMA, 2022]. We refer to them as the proximal and distal clusters, relative to Mayotte, following Saurel et al. [2022] (Figures 1c and 3).

The analysis of the seismicity of the first year is challenging due to the poor initial quality of the monitoring network. Therefore, we integrate complementary phases that have been manually picked at a few seismic stations not included in the initial monitoring network, to better specify the locations of the earthquakes over the first ten months of seismicity near Mayotte and to help complete the catalog. We estimate the instrumental bias due to both the network scarcity and geometry, by comparing our locations to those obtained using the subsequent improved monitoring network, including OBS and more inland stations from March 2019. We then relocate 77% of this catalog using a double-difference algorithm to image the seismogenic structures more precisely. Based on this new catalog, we describe the various phases of the rapidly evolving seismicity. Finally, in the light of already published work, we propose a synthetic scenario of the first ten months of the seismo-volcanic sequence of Mayotte.

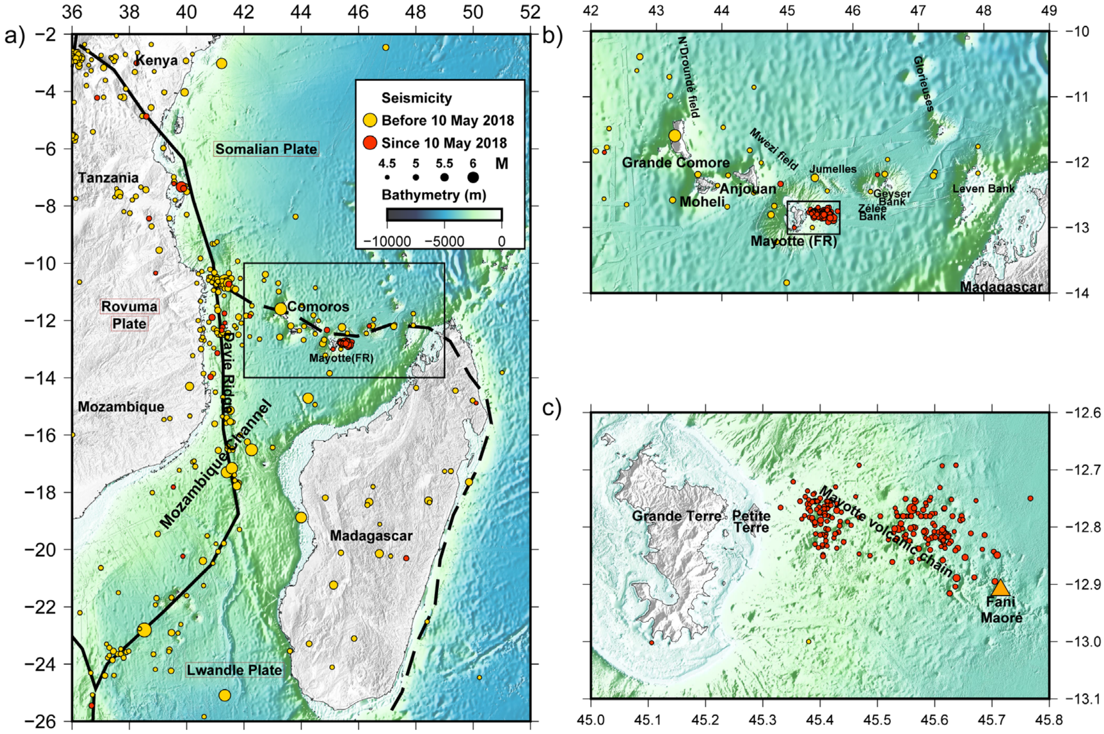


**Figure 1.** Regional historical and instrumental seismicity over the period 1900 to 2020 across the Mozambique channel and the Comoros, and surrounding areas [Bertil et al., 2021]. Black lines are plate boundaries [modified from Stamps et al., 2018]. (a, b) Bathymetry from GEBCO 2014 [Weatherall et al., 2015]. (c) Compilation from Lemoine et al. [2020b] including HOMONIM data [SHOM, 2015] and MAYOBS data [Feuillet et al., 2021]. Red triangle in (c) indicates the position of the Fani Maoré volcano. All figures have been done using GMT 5 [Wessel et al., 2013].

## 2. Geodynamic and seismo-tectonic context of Mayotte

### 2.1. *Tectonic and magmatic activity in the Comoros archipelago*

The four major volcanic islands of the Comoros archipelago are Grande Comore, Moheli, Anjouan, and Mayotte from west to east (Figure 1b). Several marine surveys reveal recent volcanic and tectonic features northward of the archipelago [e.g., N'Droundé and Mwezi fields, Thinon et al., 2022] as well as numerous individual structures [Figure 1b, Audru et al., 2006, Tzevahirtzian et al., 2021, Thinon et al., 2022]. Submarine volcanic ridges connect the four islands [Tzevahirtzian et al., 2021, Thinon et al., 2022]. Major submarine volcano-tectonic structures follow an east–west alignment between Mayotte and the northern part of Madagascar, namely the Jumelles, Geyser, Zélée, and Leven banks. Mayotte is mainly composed of one major island (Grande Terre) and a smaller island to the east (Petite Terre). From Petite Terre, a 50 km long, WNW–ESE volcanic chain is observed on the seafloor, divided into two segments: a western part on the island slope, and an eastern N130°E part mainly composed of what are probably monogenetic cones, up to 500 m high and 2 km wide [Figure 1c; Rinnert et al., 2019, Feuillet et al., 2021, Tzevahirtzian et al., 2021].

Before the ongoing eruption of Mayotte, the active volcanism in the Comoros archipelago was limited to the Karthala volcano, in Grande Comore. The Karthala is one of the world's largest active alkaline basalt shield volcanoes, with almost 20 eruptive sequences within the last century [Bachèlery et al., 2016]. The last eruptive sequence, between 2005 and 2007, resulted in the installation of four broadband

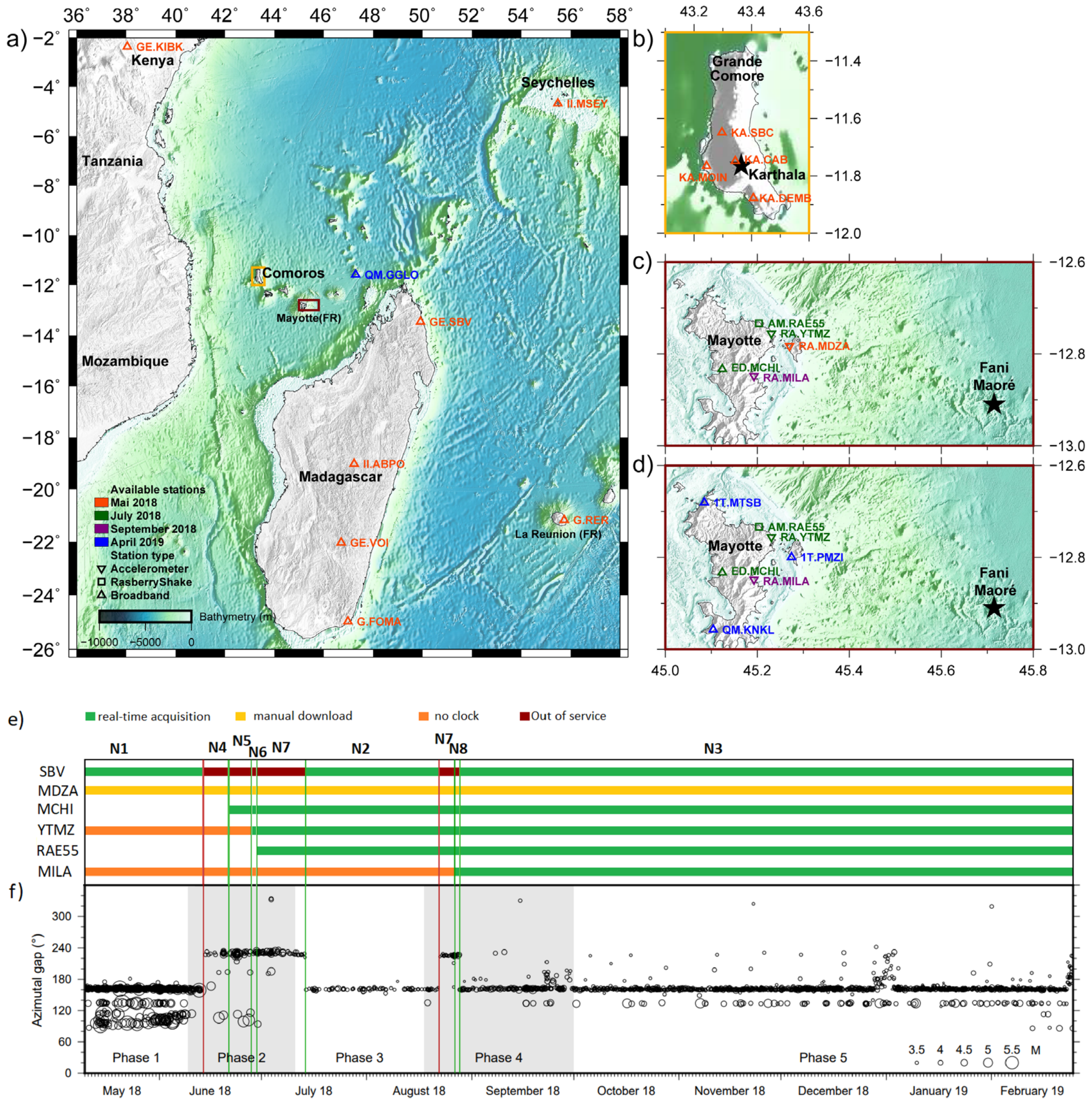


**Figure 2.** (a) Regional seismic stations network. (b) Karthala broadband station network. (c, d) Inland seismic network in Mayotte at two dates, 1 September 2018 and 1 April 2019, respectively. See also Table 1. (e) Period of data acquisition of local and regional stations over the period May 2018 to August 2018. Network geometries N1 to N8 are indicated (see Supplementary document 1). Vertical red and green lines correspond to the loss of the North Madagascar seismic station GE.SBV, and addition or restart of a seismic station, respectively. (f) Azimuthal gap evolution over time. White and grey shading are successive phases (see text for details). Bathymetry: (a) and (b) same as Figure 1a,c and (d) same as Figure 1c.

seismic stations in 2017 to better estimate the volcano hazard. In Mayotte, no active volcanism has been reported prior to the submarine eruption that started in 2018. The southern part of the island is composed of an old volcanic complex, emplaced from 10 Ma to 1.95 Ma. A second phase of volcanism built the northern part of the island, between 8 Ma and 3.8 Ma. Then recent volcanism formed the northeastern part, from 4.4 Ma to 0.15 Ma, with more recent activity that shaped the cones of Petite Terre

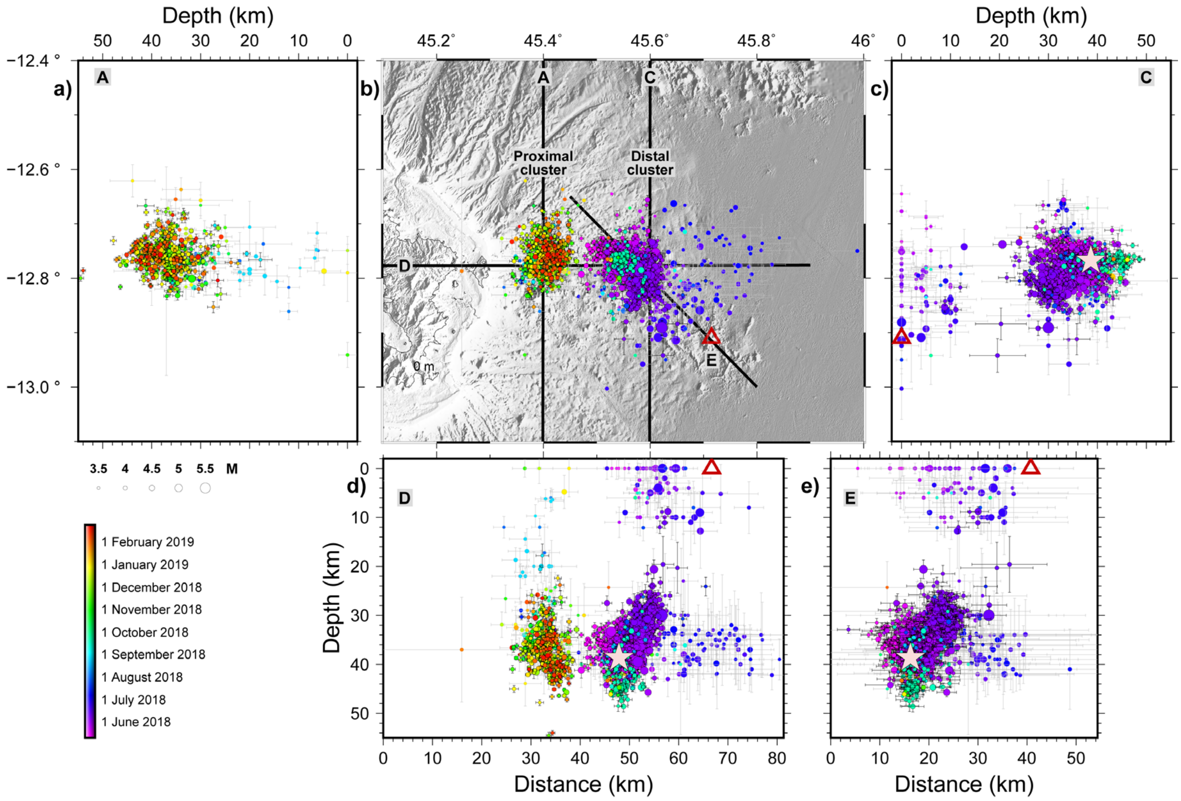


**Figure 3.** Hypocenter distribution of new catalog for the events above Mlv 3.5 of the 10 first months of Mayotte sequence (10 May 2018 to 24 February 2019). (a) N–S section view for the proximal cluster. (b) Map view for both clusters. (c) N–S section view for the distal cluster. (d) E–W section view for both clusters. (e) NW–SE section view for the distal cluster. Relative HypoDD locations and uncertainties are in black, absolute Hypo71 locations and uncertainties are in pale grey. Pale pink star indicates the position of the main shock on 15 May 2018, 15:48 UTC. Red triangle indicates the location of the Fani Maoré volcano. Bathymetry source is the same as Figure 1c.

[Nougier et al., 1983, Zinke et al., 2003a,b, Debeuf, 2009, Nehlig et al., 2013, Michon, 2016].

Although the timing of the formation of the Comoros archipelago is still under debate [e.g., Quidelleur et al., 2022], it is suggested that the volcanism of Mayotte is the oldest [ca 20 Ma in Michon, 2016; ca. 26–27 Ma in Masquelet et al., 2022], whereas volcanism in Anjouan, Moheli, and Grande Comore started later at c.a. 10 Ma [Michon, 2016]. Therefore, there is no simple decrease or increase of the age of volcanism along the Comoros archipelago, as expected in the case of hotspot-related intraplate volcanism. The link between tectonic deformation and volcanic development is under study [Michon, 2016, Famin et al., 2020, Feuillet et al., 2021, Boymond et al., 2022, Thinon et al., 2022], this issue. Geological, geochronological, geomorphological and geophysical datasets tend to confirm the hypothesis of a strong magmatic supply reaching the surface through fractures induced by lithospheric deformation [Michon, 2016, Tzevahirtzian et al., 2021, Famin et al., 2020, Feuillet et al., 2021, Thinon et al., 2022]. The geodynamical context of the east–west trending Comoros archipelago, linking the south-eastern tip of the East African rift to the Madagascar graben system [Figure 1a; e.g., Feuillet et al., 2021], suggests an immature boundary between the tectonic plates of Lwandle and Somalia [Stamps et al., 2018, 2021, Famin et al., 2020, Figure 1a]. Strain from plate tectonics may thus play a role in the origin of the volcanism [Michon, 2016, Famin et al., 2020], in addition to the influence of inherited structures from old oceanic fabric, and of regional mantle dynamics [Thinon et al., 2022].

### 2.2. *Past seismic activity along the Comoros archipelago*

The Comoros archipelago is considered an area of moderate seismicity [Bertil and François, 2016]. The poorly developed monitoring seismic network in the area prevents an exhaustive analysis of the small and moderate magnitude seismicity. According to a recent 120-year compilation of regional seismicity in the North Mozambique channel (1900–2021), most of the earthquakes are concentrated offshore, along the north–south Davie oceanic ridge, and along the east–west trending Comoros archipelago [Figure 1; Bertil et al., 2021]. This regional catalog includes 10 events of magnitude above 5.0, five of them being located around Mayotte [Bertil et al., 2021]. Furthermore, over the previous three centuries, 17th to 19th, only four earthquakes, causing moderate damages on the island, remain in the collective memory of Mayotte [Hachim, 2004, Sira et al., 2018].

### 2.3. *The recent Mayotte seismo-volcanic sequence*

The Mayotte seismic activity started abruptly, unexpectedly, and with intense swarms. Several dozen low to moderate earthquakes occurred daily, and about 280 of them were likely felt during the first two months [according to Peak Ground Acceleration criteria PGA $\geq 0.01$ $m{\cdot}s^{-2}$ on the YTMZ station, Bertil and Hoste-Colomer, 2020]. Quick volunteer response teams organized to estimate the number of events, located the strong magnitude earthquakes, and developed a monitoring network [Sira et al., 2018, Bertil et al., 2019, Lemoine et al., 2020a]. The existing geodetic stations network and InSAR data indicate subsidence and eastward displacement of the island of Mayotte from early July 2018 [Lemoine et al., 2020a].

Given the knowledge of present and past seismicity in the region [Bertil et al., 2021], the pattern of seismicity that occurred east of Mayotte is unprecedented, in light of recorded time sequence data, considering the number and magnitudes of reported seismic events. However, the monogenic volcanoes and more complex submarine systems similar to the NVE covering the seafloor may indicate the previous occurrence of similar episodes [Feuillet et al., 2021, Tzevahirtzian et al., 2021, Thinon et al., 2022].

This seismic activity starts suddenly on 10 May 2018. First seismological catalogs show thousands of events occurring within a year, up to Mw 5.9. The majority of the seismic energy is released during the first six weeks of activity [Cesca et al., 2020, Lemoine et al., 2020a]. This seismicity starts as a swarm 40 km east of Mayotte and around 30–40 km deep, hence below the Moho, estimated to be around 17 km [Jacques et al., 2019, Dofal et al., 2021]. From there, the local and regional networks record a migration of earthquakes southeastwards and upwards, interpreted as magma migration from a deep large reservoir (>10 $km^3$) to the surface [Cesca et al., 2020, Lemoine et al., 2020a, Berthod et al., 2021a]. Seafloor eruption is thought to have started between late June and early July of 2018, hence seven weeks after the onset of the seismic activity, as attested by the beginning of a noticeable deflation signal observed on GNSS stations, along with relative seismic quiescence [Cesca et al., 2020, Lemoine et al., 2020a, Berthod et al., 2021a]. The deep seismicity has remained active since the beginning of the eruption. Oddly intense, monochromatic VLP events were recorded in June 2018 [Laurent et al., 2021], as well as the onset of a second seismic cluster, in July 2018, 10–20 km east of Mayotte [Lemoine et al., 2020a]. Since then, the two deep swarms have remained active; the second has surpassed the first in terms of seismicity rate [Lemoine et al., 2020a, Feuillet et al., 2021, Lavayssière et al., 2022, REVOSIMA, 2022, Saurel et al., 2022]. The seismic sequence is still ongoing in November 2022, with low activity relative to the initial months [REVOSIMA, 2022, Lavayssière et al., 2022, Saurel et al., 2022].

Marine surveys identified the NVE southeastward in the prolongation of the eastward trending Mayotte volcanic chain. This 820 m tall, $5.0 \pm 0.3$ $km^3$ volcanic edifice, now officially called "Fani Maoré", built in one year of eruption [Rinnert et al., 2019, Feuillet et al., 2021], is interpreted as evidence of the damping of a deep and exceptionally large reservoir. This is supported by the large GPS surface displacements, implying a barycenter of deformation located 40 km eastward of Mayotte and 30 km deep [Lemoine et al., 2020a; see also Peltier et al., 2022].

Tomography, petrological studies, and precise relocations of events since March 2019 highlight several volcanic and seismic structures, such as intermediate and deep reservoirs around the seismic swarms (Figure 11), as well as complex magmatic interactions between deep reservoirs and the surface [Berthod et al., 2021a,b, Foix et al., 2021, Lavayssière et al., 2022, Masquelet et al., 2022].

## 3. Data and methods

### 3.1. *Seismic network evolution and data availability*

In order to build the catalog for the first ten months of the Mayotte seismic sequence (Figure 3; Table S1), we first estimated the amount of detected seismic events by performing a STA/LTA method on the vertical component of station YTMZ (Figure 4a and Figure S1). Due to the high level of noise in the signals of this continuous strong-motion station, we applied a Butterworth filter between 1.5 and 15 Hz. Then we selected only events with a STA/LTA ratio above 6.0 and a peak-to-peak amplitude of more than 200 counts. Those parameters reduced the detections of non-seismic sources, such as those of the Mayotte background noise, but likely of small seismic events too. Then, we considered two distinct time periods characterized by different monitoring seismic networks.

For the first four months of the sequence from 10 May to 31 August 2018, we completed the initial catalog of Lemoine et al. [2020a]. In addition to the regional stations (Figure 2a) in Madagascar (GE.SBV, II.ABPO, GE.VOI), Kenya (GE.KIBK), and sparse data from Grande Comore (KA.SBC, KA.CAB, KA.MOIN, Figure 2b), we used additional data from stations located in Seychelles (II.MSEY), La Réunion (G.RER), Madagascar (G.FOMA), and Grande Comore (KA.DEMB). Furthermore, we completed the dataset with GE.SBV signals from May and June 2018, and added missing data from the Grande Comore network (the whole month of May, and short time intervals between June and August 2018). During periods not covered by the GE.SBV station located to the east, we only analyzed events with a well-identified P phase at II.ABPO, to reduce the azimuthal gap. For the local network, since Lemoine et al. [2020a] had integrated MDZA signals only for magnitude $M > 4.0$ events, we enriched the dataset with MDZA signals for smaller events (Figure 2). The local Mayotte network has developed from one to five available stations between May 2018 and February 2019 (see Supplementary Material, Table 1, Figure 2). The picking of the P and S phases was done manually on the continuous signals, using the Seiscomp software [Helmholtz-Centre Potsdam - GFZ German Research Centre for Geosciences and GEMPA GmbH, 2008]. We also checked the previously picked phases from the Lemoine et al. [2020a] catalog and searched for new small events, not previously detected.

From 1 September 2018 to 24 February 2019, events were directly extracted from the database used in Lemoine et al. [2020a] and Bertil et al. [2021], using the stations previously cited. We reviewed and improved the location of more than a hundred earthquakes.

### 3.2. *Absolute locations*

Event absolute locations were processed using the HYPO71 algorithm [Lee and Lahr, 1972, Lee, 1975]. The computer version of HYPO71 [Lee and Valdes, 1985] uses P and S time arrivals to estimate hypocenter locations and magnitude (MLv) for local earthquakes. We used a slightly modified version of the 1D five-layer regional velocity model from Lemoine et al. [2020a], with a regional $V_p/V_s$ value of 1.74 (Table 2). More recent local velocity models were proposed based on the seismic data acquired since the installation of OBS around the Mayotte active zone, using lower and local $V_p/V_s$ values [1.66 in Dofal et al., 2021; around 1.6 in Foix et al., 2021, Saurel et al., 2022, Lavayssière et al., 2022]. However, for earthquake locations, the regional model was more suitable with our network configuration, which included stations beyond 200 km of Mayotte, and no OBS above the active zone. Locations were retained if there were at least eight picked phases on a minimum of four seismic stations, including one in Grande Comore and one in Madagascar.

We compared our MLv estimates with moment magnitudes (Mw) ranging from 4.8 to 5.9 for the 26 Mayotte events located by GCMT (Global Centroid Moment Tensor Project, https://www.globalcmt.org). The magnitude difference (MLv–Mw) varied between −0.1 and +0.7, with a mean difference of 0.1. In order to estimate a seismic moment [M0, Aki and Richards, 2002], even for

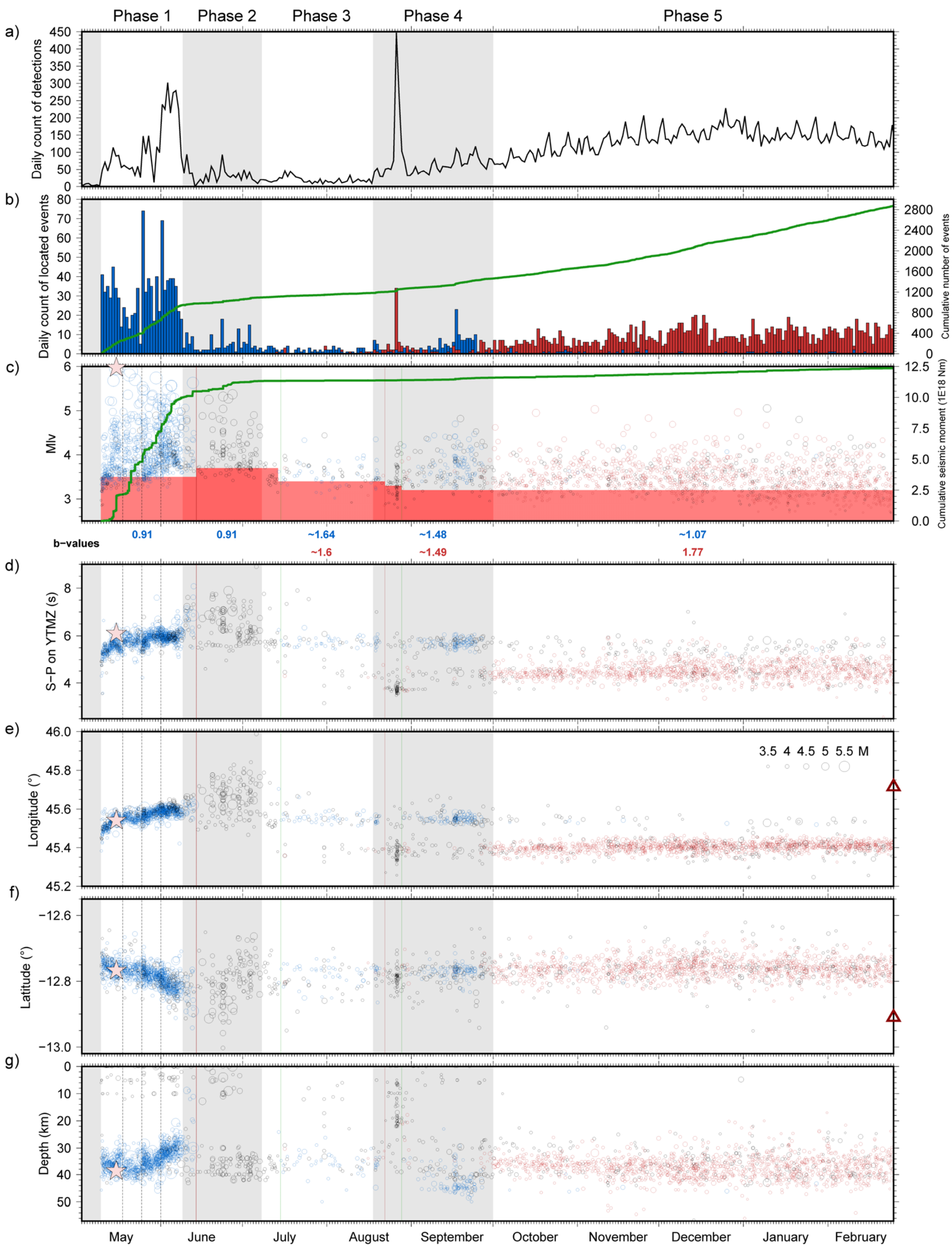


**Figure 4.** Evolution of seismicity from 3 May 2018 to 24 February 2019. Proximal and distal events, located with HypoDD, are identified with red and blue circles, respectively. Earthquakes located with Hypo71 only are identified with black circles. (a) Number of detected events on YTMZ continuous signal, using STA-LTA. (b) Number of events per day for all events within distal (blue) and proximal (red) clusters, and cumulative number of events (green line). (c) Magnitude (Mlv) of events, cumulative seismic moment (green line) and magnitude of completeness (in red). (d) S and P arrival time differences (S–P) at YTMZ station. (e), (f), and (g) are longitude, latitude and depth of events, respectively. The pale pink star indicates the main shock of the sequence, on 15 May 2018, 15:48 UTC. Main phases are indicated by white and grey stripes. Vertical lines correspond to seismic GE.SBV loss (red) and resume (green) of data acquisition. Red triangle in (e) and (f) indicates the position of the Fani Maoré volcano.

**Table 1.** List of local and regional stations

| Station[a] | Longitude | Latitude | Start | End | Type[b] | Min. distance to Mayotte seismic area (km) |
|---|---|---|---|---|---|---|
| RA.MDZA | 45.26°E | 12.78°S | June 2016 | February 2019 | Acc | 3 |
| AM.RCBF0 | 45.27°E | 12.80°S | 15 June 2018 | July 2018 | RaspB | 3 |
| 1T.PMZI | 45.27°E | 12.80°S | March 2019 | — | BB (HH) | 3 |
| RA.YTMZ | 45.23°E | 12.76°S | July 2015 | — | Acc | 8 |
| AM.RAE55 | 45.20°E | 12.73°S | 15 June 2018 | — | RaspB | 12 |
| RA.MILA | 45.19°E | 12.85°S | June 2016 | — | Acc | 14 |
| ED.MCHI | 45.12°E | 12.83°S | 18 June 2018 | — | BB (BH) | 20 |
| 1T.MTSB | 45.08°E | 12.68°S | March 2019 | — | BB (HH) | 28 |
| QM.KNKL | 45.10°E | 12.96°S | March 2019 | — | BB (HH) | 29 |
| KA.MOIN | 43.24°E | 11.77°S | 2017 | — | BB (HH) | 250 |
| KA.SBC | 43.30°E | 11.65°S | 2017 | — | BB (HH) | 250 |
| KA.CAB | 43.34°E | 11.75°S | 2017 | — | BB (HH) | 250 |
| KA.DEMB | 43.41°E | 11.88°S | 2017 | — | BB (HH) | 250 |
| QM.GGLO | 47.29°E | 11.58°S | March 2019 | — | BB (HH) | 250 |
| GE.SBV | 49.92°E | 13.46°S | 2009 | — | BB (HH) | 450 |
| II.ABPO | 47.23°E | 19.02°S | 4 March 2007 | — | BB (HH) | 700 |
| GE.VOI | 46.71°E | 22.03°S | 2009 | — | BB (HH) | 1000 |
| G.FOMA | 46.98°E | 24.98°S | 1 September 2008 | — | BB (HH) | >1000 |
| GE.KIBK | 38.04°E | 2.36°S | 2011 | — | BB (HH) | >1000 |
| II.MSEY | 55.48°E | 4.67°S | 1995 | — | BB (HH) | >1000 |
| G.RER | 55.74°E | 21.17°S | 10 Feb 1986 | — | BB (HH) | >1000 |

[a]Stations come from the following networks: AM: Raspberry Shakes: doi:10.7914/SN/AM; ED: http://www.edusismo.org/; G: Geoscope: doi:10.18715/GEOSCOPE.G; GE: GEOFON: doi:10.14470/TR560404; II: Global Seismic Network IRIS-IDA: doi:10.7914/SN/II; KA: Observatoire Volcanologique du Karthala: http://volcano.ipgp.jussieu.fr/karthala/stationkar.html; RA: RESIF-RAP french accelerometric network: doi:10.15778/RESIF.RA, 1T: Temporal seismological network of Mayotte: doi:10.15778/resif.1t2018, QM: Comoros archipelago seismic and volcanic network: doi:10.18715/MAYOTTE.QM.

[b]Station types: Acc = accelerometer, BB (HH) broadband 0–100 Hz, BB (BH) broadband (0–50 Hz), RaspB: Raspberry Shakes.

smaller magnitudes (Mw < 4.8), we considered at first order that MLv is equivalent to the moment magnitude Mw.

The magnitude of completeness (Mc) evolved with time, as it depended on the quality of the network. Estimated to 3.5 at the onset of the sequence, it slightly increased to 3.7 when the GE.SBV station was down between mid-June and mid-July 2018. Since the improvement of the Mayotte network in September 2018, Mc was estimated to 3.2 (Figure 4c).

We determined $b$-values by calculating a power-law least-square fit to the magnitude-frequency distribution limited to the magnitudes above the estimated Mc [Richter, 1935, Ichimoto and Iida, 1939, Gutenberg and Richter, 1942; Table 3, Figure 4c].

### 3.3. *Uncertainties and estimation of the location reliability*

The HYPO71 algorithm provided uncertainties for the hypocentral locations [Lee and Valdes, 1985]. The

**Table 2.** 1D velocity model used for the location process

| | Depth (km) | $V_p$ (km/s) |
|---|---|---|
| Layer 1 | 0–3 | 3.5 |
| Layer 2 | 3–8 | 5.1 |
| Layer 3 | 8–15 | 6.7 |
| Layer 4 | 15–60 | 8.1 |
| Layer 5 | >60 | 8.15 |

$V_p/V_s$ ratio is fixed at 1.74.

mean uncertainties of the horizontal and vertical locations for the whole catalog were estimated to be 2.3 and 3.2 km, respectively. The mean RMS value was 0.41 s. Because most of the stations of the initial network in Grande Comore and Mayotte were located west of the seismic area, epicentral location accuracies were highly dependent on the signals from the stations GE.SBV to the east, and/or II.ABPO to the southeast (Figure 2a). The average azimuthal gap was 161° with at least one of these stations. The lack of picks in the signals recorded at GE.SBV (Figure 2a) increased the azimuthal gap to 223° (Figure 2f), and uncertainties on earthquake locations along the horizontal and vertical axis up to 4.0 km and 3.8 km, respectively. This was the case mainly for the two periods between 14 June and 14 July 2018 and between 22 and 28 August 2018. Furthermore, the improvement of the Mayotte network with three additional stations at the end of June 2018 (Figure 2d–e) reduced uncertainties by almost 50% on the horizontal axis and by 25% along the vertical axis.

Some calculated uncertainties could be artificially low due to the small number of phases for numerous small earthquakes. Hence, we tested the reliability of our locations and evaluated possible bias within the absolute epicentral positions. To do so, we compared our location procedure performance on a selection of 118 events located using the local OBS and inland stations and a local velocity model [Saurel et al., 2022]. These earthquakes, occurring between May and December 2019, were relocated using different network geometries, corresponding to the network evolution during the period of our catalog (Figure 2 and Figure S2). We used the regional velocity model of this work and the database of P and S pickings [Lemoine et al., 2020a, Bertil et al., 2021]. The results were compared to the well-constrained hypocentral locations of the corresponding events from Saurel et al. [2022] (Figure S2). Despite the challenging geometry of the onshore network, uncertainties are similar for both catalogs, remaining below 5 km along horizontal and vertical axes for most of the events. However, there is a mean horizontal shift of around 4.1 km and 5.5 km westward of our locations for the proximal and distal clusters, respectively, compared to a network including OBS stations above the seismic area, as well as an upward shift of around 4 km of our locations for the proximal cluster [similar results in Aiken et al., 2021].

### 3.4. *Double-difference relocations*

To further improve the locations of the events, we used the HypoDD computer program [Waldhauser, 2001], which is a double difference earthquake location algorithm [Waldhauser and Ellsworth, 2000]: through a least-square procedure, events are relatively relocated by evaluating similarities between pairs of hypocenters. Relocation with HypoDD was applied to the 2395 earthquakes with data at GE.SBV because solutions are unstable without data from this station. HypoDD relocations did not change the absolute positions of the swarms, but improved the locations of the events inside the swarms, significantly decreasing the horizontal (in particular the latitude) and vertical dispersion of the locations. Then, we controlled the HypoDD relocations using the S–P values at YTMZ (Figure 4d). Some events appeared to be located in the distal cluster when they had a low S–P value, or in the proximal cluster when they had a high S–P value. Thus, for those 184 events, we kept the Hypo71 location.

## 4. The 10 first months of the Mayotte seismo-volcanic sequence

The resulting catalog extends from 10 May 2018 to 24 February 2019 (Figure 3; Table S1). It contains 2874 localized earthquakes with a mean of 12 P and S phases per event, counting 43000 manually picked P and S phases: 2211 of these events (77% of the catalog) have a HypoDD relocation.

### 4.1. *Before 10 May 2018*

No significant seismic activity was reported in the area under study before the onset of the Mayotte

**Table 3.** *b*-value as a function of phases and location

| | All data | Proximal cluster | Distal cluster |
|---|---|---|---|
| All phases | 1.06 | 1.60 | 0.96 |
| Phase 1<br>10 May–08 June 2018 | 0.91 | – | 0.91 |
| Phase 2<br>9 June–7 July 2018 | 0.91 | – | 0.91 |
| Phase 3<br>8 July–17 August 2018 | 1.69[a] | >1.6[a] | 1.64[a] |
| Phase 4<br>18 August–30 September 2018 | 1.33 | 1.49[a]<br>APP = 1.34–1.41<br>not APP = 1.69 | 1.48[a] |
| Phase 5<br>1 October 2018–24 February 2019 | 1.67 | 1.77 | 1.07[a] |

[a]Calculated with less than 100 events above the magnitude of completeness.

seismic sequence, despite the installation of the first stations in Mayotte in 2016 [Bertil et al., 2021]. For confirmation we carefully inspected the seismic records of the stations in Mayotte and the whole region (Figure S2), from 1 January to 10 May 2018: no earthquake with S–P values typical of the Mayotte swarms [between 3.5 and 6.5 s] was identified.

### 4.2. *Two clusters of focused seismic activity, east of Mayotte Island*

All the epicenters of our catalog are located between the coasts of Mayotte to 60 km eastward (Figure 3). The epicentral distribution of the seismicity reveals two distinct seismic clusters, spatially separated by an aseismic zone centered around longitude 45.48°E [Cesca et al., 2020, Lemoine et al., 2020a, Feuillet et al., 2021]. The hypocenter depths range between 0 and 50 km, with 90% of them between 25 and 45 km. Overall, the magnitude (Mlv) of the events in our catalog ranges from 2.4 up to 6.0 (Table S1; Figure 4c).

The distal cluster (Figure 3b–e) is located 20 km further east of Petite Terre (Mayotte, Figure 1b), below the eastern N130°E Mayotte volcanic chain [Feuillet et al., 2021, Lavayssière et al., 2022], and nearly extends below Fani Maoré. It is composed of a short 10 km-long E–W segment and a longer 30 km-long NW–SE segment. Most of the earthquakes occur between 25 and 45 km depth, however an upward migration on the eastern segment and a more superficial seismicity (above 15 km depth) is visible during the first two months of the sequence (May–June 2018), as well as a deeper swarm in September 2018 centered around 45 km depth.

The proximal cluster (Figure 3a,b,d) is located between 6 and 20 km east of Petite-Terre (Mayotte). It is more circular in shape, centered on 45.4°E, 12.75°S, below the western and shallower part of the Mayotte volcanic chain [Tzevahirtzian et al., 2021, Feuillet et al., 2021]. Most of the seismicity is located between 25 and 45 km depth, however seismic activity is identified between 4 and 24 km at the end of August 2018 (Figure 4c–g).

In addition to their location, these two clusters differ from each other in seismicity (Figure 4). The distal cluster includes the strongest earthquakes, concentrating 45 of the 47 Mlv ≥ 5.0 events and more than 80% of the earthquakes above magnitude 4.0. The proximal cluster includes far more small earthquakes. Calculated from the magnitude-frequency distribution [Richter, 1935, Ichimoto and Iida, 1939, Gutenberg and Richter, 1942], *b*-values are also different: whereas the *b*-value of the proximal cluster is 1.60, typical of volcanic environments, the estimated *b*-value of the distal cluster is 0.96, corresponding to a more tectonic context [Figure 4c; Table 3; Chiba and Shimizu, 2018].

### 4.3. *Phase descriptions*

Our catalog of the first ten months of the Mayotte seismic sequence with improved locations confirms the previously described clusters and allows a spatio-temporal study of its onset. We identify five distinct phases (Figure 4), based on several criteria, such as the daily number of detected and located earthquakes (Figure 4a,b), the time evolution of the magnitudes (Figure 4c), the S–P value at YTMZ (Figure 4d), the position of the events (longitude, latitude, depth; Figure 4e–g), and the *b*-value (Figure 4c; Table 3).

#### 4.3.1. *Phase 1: 10 May to 8 June 2018*

Phase 1 is characterized by the highest seismicity rate of the whole Mayotte seismic sequence, and the occurrence of numerous large earthquakes (Figures 4 and 5). We detect more than 3500 events and locate 950 events that occurred over 30 days within the distal cluster. This corresponds to an average of 32 earthquakes and 110 detections per day, with a few days peaking at 80 events and 300 detections. 80% of the events with Mlv ≥ 4.5 belong to Phase 1 (Figures 4a–c and 6a–c). In addition, most of the large earthquakes of the catalog occur during this phase, including 38 events (out of 47) with Mlv ≥ 5.0, and 7 events (out of 8) with Mlv ≥ 5.5. The maximum Mlv magnitude reaches 6.0. The *b*-value is 0.91 (Figure 4c; Table 3).

Throughout Phase 1, we observe a mean S–P values increase from 5.0 s to 6.0 s (Figures 4d and 6d), coeval with the variations of longitude, latitude and depth (Figures 4e–g, 5, and 6e–g). The epicenters are concentrated within a 190 km$^2$ seismic zone, migrating to the east the first week, then southeast the third week, and finally south and upward the last week of Phase 1, i.e., away from Mayotte and closer to the Fani Maoré volcano (Figures 5 and 6).

The hypocenters occur at a wide range of depths (Figures 4g, 5c–e, and 6g), with the majority of them located at a depth ranging between 30 km and 40 km. Throughout Phase 1, all the events are deeper than 20 km, except for about 70 events that have no stable relocation with HypoDD. They are most likely deeper since the hypocenters of events equivalent in magnitude and S–P values on YTMZ, and relocated with HypoDD, are between 30 and 40 km. Hence, we believe that this superficial seismicity is an artifact due to the sparse monitoring network.

During Phase 1, the seismicity is characterized by multiple earthquakes that occur in distinct series, each of a few hours duration. We identify 35 pulses as short sequences of eight or more earthquakes, separated by less than an hour from previous and subsequent earthquakes (Figure 6). Most of these pulses (30) are within Phase 1, on average one per day.

The evolution of the seismicity during Phase 1 follows four steps:

- During the first week (10–17 May 2018), the 255 located earthquakes migrate eastward. The Mayotte seismicity starts in a small area, 30 km east of Mayotte, 5 km west of longitude 45.5°E and at depths between 30 and 40 km, between the future positions of the proximal and distal clusters (Figures 4e and 6e). This area has never been active since. These earthquakes consist of Mlv < 4.4 events that rapidly migrate around 5 km eastward on 10 May. Following a Mlv 5.2 event on 13 May, they migrate 5 km further eastward, so that most of the seismicity on 14 May is located on average near longitude 45.55°E (Figures 4e, 5, and 6e). The S–P values increase continuously from 5.0 s to 6.0 s, together with the longitude until 17 May. On 15 May at 15:48 UTC, the Mw5.9 (MLv 6.0) earthquake occurs near the deepest part of the distal cluster, at around 40 km depth, followed by an overall upward migration of 7 ± 1 km until 17 May.
- The second week has a lower activity (18–24 May 2018), with only 140 located events. The seismicity remains focused where it was at the beginning of 15 May, without significant longitudinal or depth changes.
- The third week, an important pulse on 25 May marks the beginning of a 7 ± 1 km migration to the east and south, while the depths range between 30 and 40 km, until 1 June. We locate 260 events within this week.
- The most important pulse, on 1 June, includes 49 earthquakes. Over the next few days (fourth week), until the end of Phase 1, the seismicity goes 10 km south, and upward between depths of 25 and 35 km. With 295 located events and one third of the earthquakes with Mlv ≥ 5.0 of the Mayotte sequence, this week is the most intense of the whole Mayotte sequence (as of November 2022).

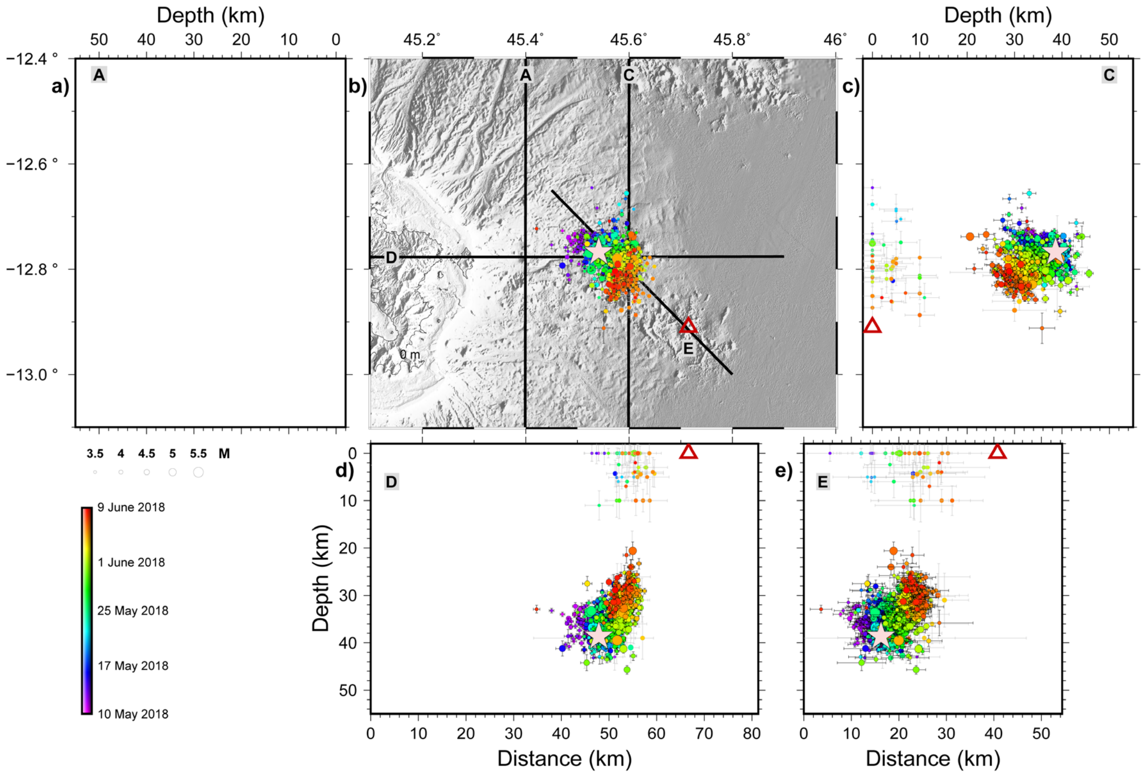


**Figure 5.** Phase 1 (10 May–8 June 2018) hypocentral locations on map and sections (legend details provided in Figure 3).

4.3.2. *Phase 2: 9 June to 7 July 2018*

The beginning of Phase 2 on 9 June is marked by an abrupt drop of the seismicity rate from an average of 32 events per day for Phase 1 to an average of 4 events per day, lasting until 7 July 2018 (Figures 4b and 6b). All the events located during this phase are within the distal cluster (Figure 7). Phase 2 contains two thirds of the Mlv ≥ 4.5 events of the catalog that do not occur during Phase 1 (Figure 4c). Seven Mlv ≥ 5.0 events and one up to Mlv = 5.6 occur, despite an overall decrease in magnitudes (Figures 4c and 6c). The *b*-value of Phase 2 is equal to 0.91, similar to the *b*-value of Phase 1 (Figure 4c; Table 3).

Regarding the largest events (Mlv > 4.7), 83% of them are located in the southeastern part of the distal cluster, i.e., closer to the Fani Maoré volcano, with one half deeper than 30 km and a second half between 0 and 15 km, i.e., shallow depths never found afterwards in the distal cluster. Note that those strong events are more precisely located thanks to the picks on the most distant stations (farther than 800 km, Table 1, Figure 2a). Moreover, even if most of the shallow earthquakes are located with Hypo71 and with more uncertainty due to a less than ideal network configuration, one event is relocated at 8.8 km with HypoDD. Hence, the shallow seismicity is confirmed by HypoDD relocations, as well as by the GCMT international catalog [Dziewonski et al., 1981, Ekström et al., 2012] for the largest events, and full waveform moment tensor inversion and depth phase analysis [Cesca et al., 2020].

Phase 2 is characterized by the largest scattering of seismicity, depicted by the longitude and latitude values, which extends over 45 km and 35 km, respectively. The spatial extent of the activated area is nearly 1600 km$^2$ (Figure 4e,f). We note that most of Phase 2 corresponds to the period without data on station GE.SBV (Figure 4), therefore the resulting locations are less constrained during this phase and must be regarded with caution. We cannot decide

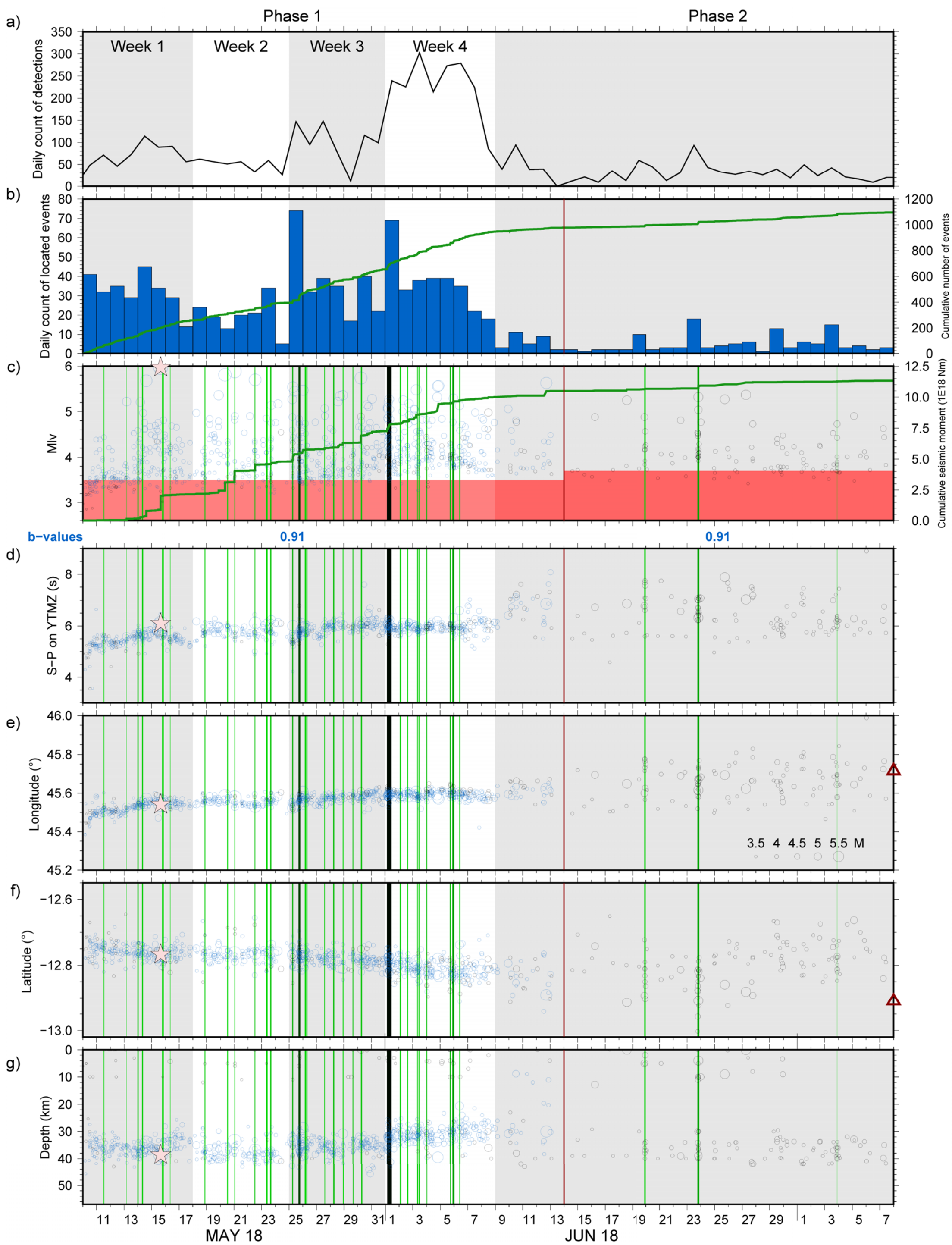


**Figure 6.** Evolution of seismicity of 2 first phases, from 10 May to 7 July 2018 (legend details provided in Figure 4). Green stripes indicate pulses of 8 earthquakes or more (see Section 4.3.1): darkness of green increases with number of earthquakes.

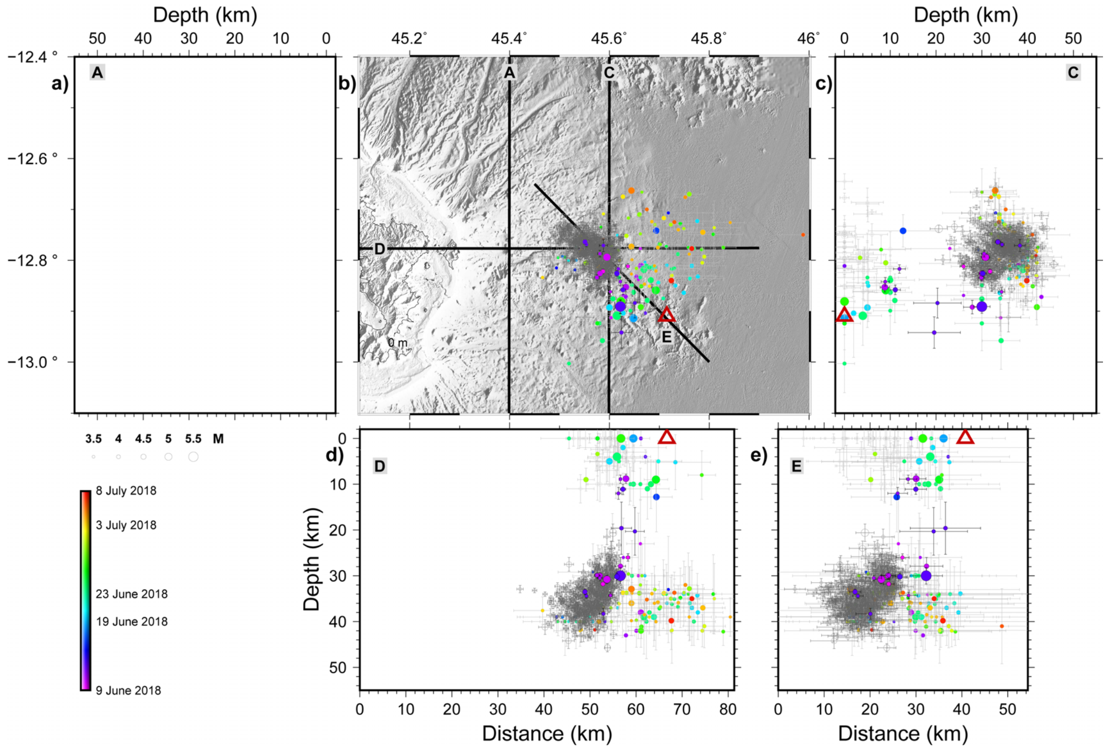


**Figure 7.** Phase 2 (9 June–7 July 2018) hypocentral locations on map and sections (legend details provided in Figure 3).

which of the events located with Hypo71 are well located, considering the sparse locations on the N7 distribution of our reliability test (Figure S2g–h). However, the large range of S–P values (>5.0 s) independent of the location estimates confirms a wider spatial distribution of the hypocentral locations (Figures 4d and 6). More specifically, one feature of Phase 2 is the regular occurrence of seismic events with S–P values on YTMZ station above 6.5 s, and up to 8 s, consistent with locations east of 45.7°E, hence beyond 45 km east of Mayotte (values never found afterwards). Phase 2 includes the easternmost events of the sequence, and a southeastward migration is highlighted by the few earthquakes relocated with HypoDD.

With the previously described criteria, three pulses of activity are identified during Phase 2: 19 June, 23 June and 3 July (Figures 6 and 7). The first two pulses occur on the southeasternmost tip of the distal cluster. The later pulse occurs in the center of the distal cluster. However, the seismicity spreads eastward and upward during this phase, a lower, more focused seismicity remains on the western side of the distal cluster.

At the very beginning of Phase 2, we identify a period without seismicity on 9 June from 04:00 UTC to 22:30 UTC. After this quiet period, the events occur 10 km more east than before this period (Figure 6e). The early seismicity on 10 June is focused on the southeasternmost part of the distal cluster, mainly at depths around 40 km. Phase 2 starts with two consecutive series of successive earthquakes with rapidly increasing S–P values, on 10 and 12 June 2018 (Figure 6).

#### 4.3.3. *Phase 3: 8 July to 17 August 2018*

From 8 July, the seismicity rate drops and remains at the lowest level over the whole period of the catalog, with an average of two events per day, without any pulse of activity (Figure 4b). Within the magnitude range that goes up to 4.4, only two Mlv > 4.0 events are recorded during this phase (Figure 4c).

Most of the localized earthquakes of Phase 3 (84%) are located within the distal cluster (Figure 8). However, the seismicity of the southernmost and easternmost parts of the distal cluster is very low. Most of the epicenters are spread between 45.5°E and 45.6°E in longitude, and 12.75°S and 12.9°S in latitude (Figures 4e,f and 8). This area corresponds to the activated zone at the very early stage of the seismic sequence, around 12–13 May 2018, where some events are located during Phase 2 as well (Figures 5, 6, and 7).

Although the activity within the distal cluster is less intense, Phase 3 corresponds to a major change in the whole Mayotte seismic sequence, since a few small-magnitude events with lower S–P values (below 4.0 s) are located west of the longitude 45.46°E, i.e., at less than 15 km from the east Mayotte coast (Figure 4c,d). Those peculiar events are located where the forthcoming seismicity will be concentrated, i.e., the proximal cluster. From 13 July 2018, the proximal cluster becomes active, with its subsequent events scattered through time until mid-August.

The small number of events during Phase 3, merely 86, prevents an accurate estimate of the *b*-value, but we estimate that it is larger than 1.6, taking into account the seismicity of both clusters. This suggests a drastic change compared to the previous phases.

#### 4.3.4. *Phase 4: 18 August to 30 September 2018*

Phase 4 is characterized by a new increase in the seismicity rate, averaging 75 detections and 6 located events per day, including 35 events with a magnitude between 4.0 and 4.8. The seismic activity resumes with successive pulses of seismicity alternately affecting each cluster (Figure 4d). Similar to Phase 3, the *b*-value of 1.5 of each cluster during Phase 4 confirms that the dynamic differs from the first two phases. Overall, the ratio of "strong to moderate" events (Mlv > 4.5 events relative to Mlv > 3.5 events) is two times lower than during Phases 1 and 2. Most of the events are still located within the distal cluster (60%) with events of higher magnitude on average.

Two periods are of special interest: the end of August and most of the month of September (Figure 4a,b):

- A peculiar seismic activity occurs between 22 August and 6 September 2018, within the proximal cluster, different from its usual and subsequent activity. This 15-day period, the August Proximal Peak (APP), is a series of 62 events identified as distinct from the other proximal and distal events, with S–P values on the YTMZ station of mainly around 3.7 s, and below 4.1 s (Figure 4d). This includes a group of 31 events with S–P values between 3.5 and 4.0 s, forming the pulse of activity on 26 August 2018, the climax of APP. Notably, it corresponds to the maximum of detections on our STA/LTA approach over the whole Mayotte sequence (Figure S1). This is the only example in our catalog of a daily rate above 30 events within the proximal cluster, and the first time where seismicity is mainly located within this cluster in our catalog. The APP events are thus unique, as the depth of many of them range between 0 and 23 km (Figures 4g and 9), while the large majority of the other earthquakes in the proximal cluster are located below 20 km.
- A period of intense seismicity in the distal cluster starts on 11 September. It reaches 100 events between 16 and 30 September, up to 4.7 in magnitude, including 22 Mlv > 4.0 earthquakes, more than one per day on average. The peak of activity is on 17 September, with all events located within the same area as the Phase 3 distal seismicity, but at a lower depth, around 45 km on average (Figures 4g, 8, and 9). This is the last peak of activity in the distal cluster until October 2022. Since the end of September 2018, the daily seismicity rate remains below one located event per day within the distal cluster [Bertil et al., 2019, Lemoine et al., 2020a, REVOSIMA, 2022, Saurel et al., 2022].

#### 4.3.5. *Phase 5: 1 October 2018 to 24 February 2019*

Phase 5 is defined by the fading of the previously predominant activity within the distal cluster, coeval with a significant increase of seismicity in the proximal cluster during the first three months of Phase 5, which then slowly decreases until February 2019 (Figures 4b and 10; see also Figure S1). Over this five month phase, 1070 earthquakes are located, corresponding to a maximum of 200 detections and

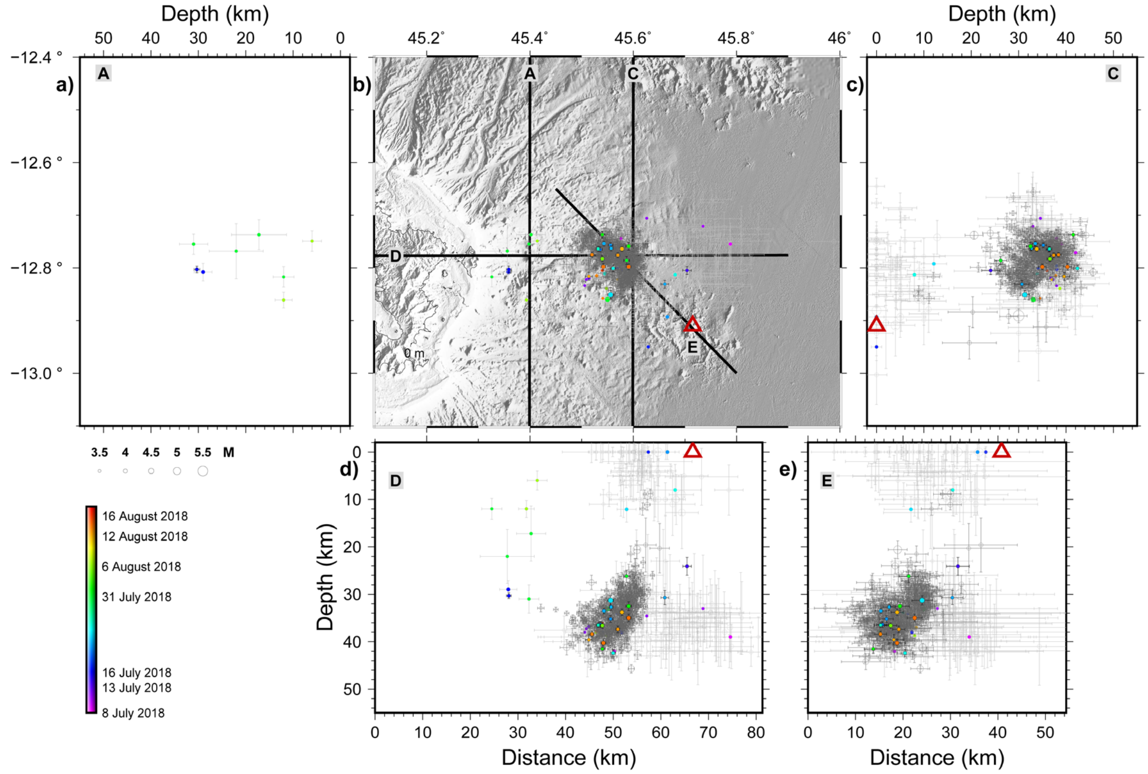


**Figure 8.** Phase 3 (8 July–17 August 2018) hypocentral locations on map and sections (legend details provided in Figure 3).

20 located events per day at the climax of activity (December 2018).

Less than 50 events are located within the distal cluster, with magnitude up to 5.0. We note that the hypocenters are at the same depth (~40 km) than the distal cluster events recorded during Phases 3 and 4. A *b*-value of 1.1 is estimated from those events.

The seismic activity within the proximal cluster corresponds to more than 1000 located events, with 5 to 25 events per day (Figures 4d and 10), and with lower magnitudes in general (93% of them with Mlv $< 4.0$), as part of the proximal cluster (Figures 4c and 10). The epicenters belonging to the proximal cluster during Phase 5 are distributed over a $25 \times 20$ km$^2$ area (Figures 4e,f and 10). The depth of most of them ranges between 20 km and 45 km (Figures 4g and 10). Overall, the events of the proximal cluster are shallower than the distal cluster events. An interesting feature of the proximal cluster is the widening of the depth range over Phase 5, from $36 \pm 2$ km at the beginning of October 2018 to $36 \pm 6$ km at the end of February 2019, together with longitude values focused around 45.4°E in longitude (Figure 4g). A *b*-value of 1.77 is estimated from the events within the proximal cluster during Phase 5.

The observed seismicity distribution (i.e., frequent low magnitude events in the proximal cluster, decreasing proximal activity from April 2019, less frequent but more intense earthquakes in the distal cluster) is observed until the beginning of 2022 [Lemoine et al., 2020a, Lavayssière et al., 2022, Saurel et al., 2022, REVOSIMA, 2022].

## 5. Discussion

### 5.1. *Assessment of data quality*

We build a catalog of seismicity for the first ten months of the sequence, despite the network weaknesses, i.e., the small number of stations and the large azimuthal gap for most of the event locations (Figure 2). The manual identification of new P and

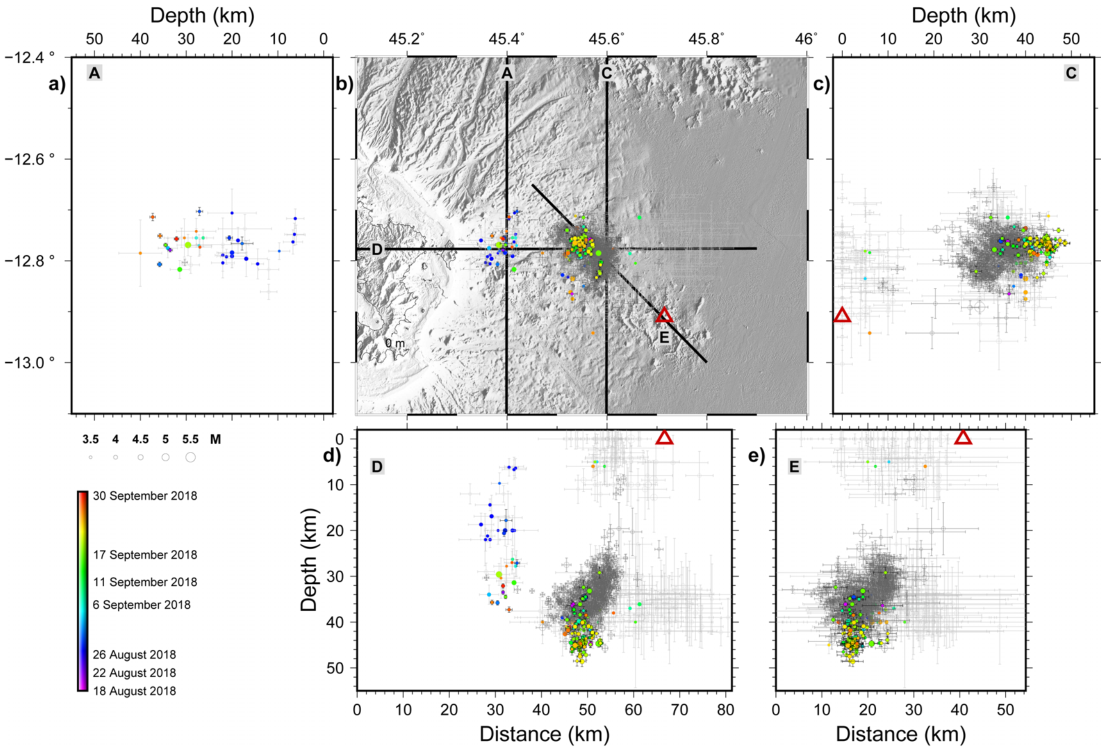


**Figure 9.** Phase 4 (18 August to 30 September 2018) hypocentral locations on map and sections (legend details provided in Figure 3).

S phases from additional local and regional stations lowers the magnitude of completeness to a range from 3.2 to 3.7, depending on the network evolution over the first ten months of the sequence. With 2874 located events, our catalog includes 1.5 times more events than the VT catalog from Cesca et al. [2020] which used only YTMZ local stations (1882 events located at fixed 20 km depth), and 2.9 times more events than the catalog of Lemoine et al. [2020a] which used both local and regional stations (1004 events). The additional P and S wave picks integrated to our location procedure decrease the average hypocentral uncertainties to 2.4 km horizontally and 3.6 km vertically, compared to uncertainties as high as 10 km horizontally and vertically in the previous catalog covering the same period [Lemoine et al., 2020a]. These uncertainties are less than 1 km for the 2211 relative locations (77% of the catalog) (see Section 3.4; Figure 3).

The depth of our locations may be compared to those of Saurel et al. [2022] who use a local OBS network. Regarding the hypocentral depths, our locations within the proximal cluster appear to be 3.7 km shallower than theirs, while the depth differences between the locations belonging to the distal cluster are lower than the 2 km vertical uncertainties of Saurel et al. [2022]. Regarding the epicentral locations, we note that the locations of our catalog for the proximal and distal clusters are on average 4.1 and 5.5 km westward respectively, from those of Saurel et al. [2022], while the location differences in latitude for both clusters are lower than the 2.5 km horizontal uncertainties of Saurel et al. [2022].

The reliability of the hypocenters highly depends on the seismic network distribution, which significantly evolved over the 2018–2019 period (Figure 2), with various network configurations including the GE.SBV data (Figure S2a–c) and one, four or five stations on Mayotte (Figure S2). In all cases, the two clusters remain clearly separated by 5 km. We show that the evolution from one to five stations on Mayotte island does not significantly improve the locations, as suggested by the results of our tests using

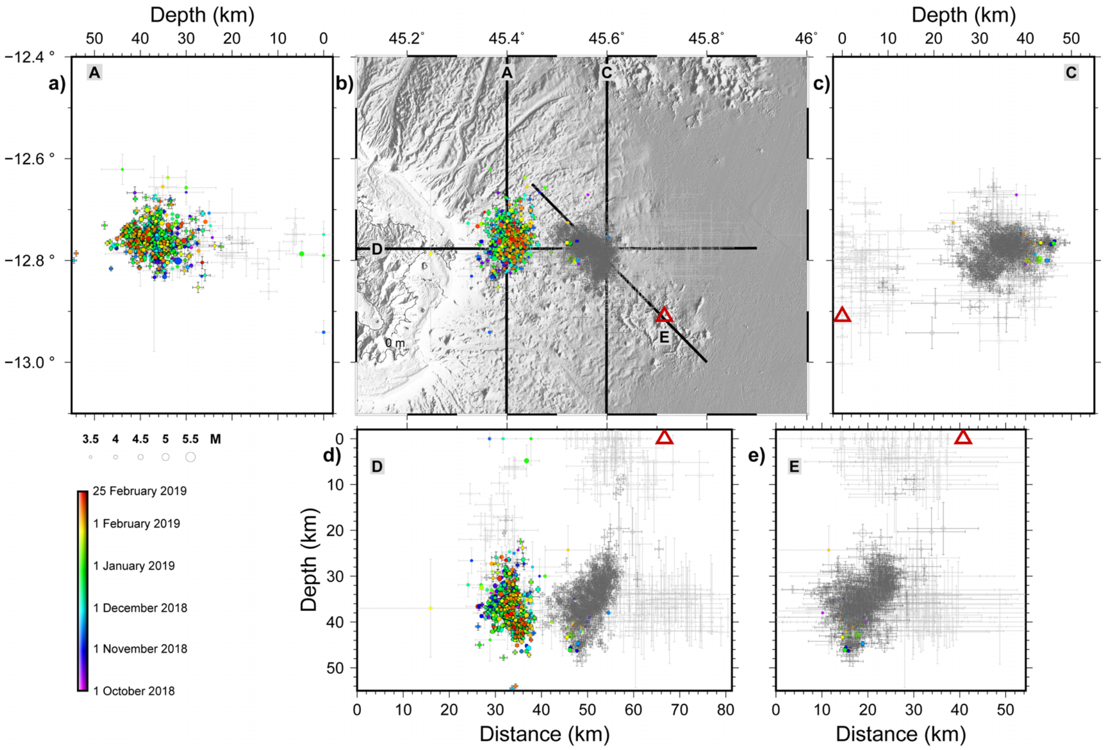


**Figure 10.** Phase 5 (1 october 2018–24 February 2019) hypocentral locations on map and sections (legend details provided in Figure 3).

the N1, N2 and N3 network distributions (Figure S2), whereas data from GE.SBV is crucial for preventing misplaced earthquakes at shallow depth and for clearly distinguishing both clusters laterally (Figure 2f, Figure S2d). Therefore, in light of these results, we consider the locations of our catalog reliable for the periods that include the data from GE.SBV. For periods when data from GE.SBV were not available (Phase 2 and the beginnings of Phase 3 and Phase 4), the results should be analyzed more carefully (Figures 4, 6, 7, 9, and Figure S2), particularly for seismicity upward migration and the lack of events a few km west from Fani Maoré during Phase 2 (Figure 7d). However, the shallower depth (above 25 km) of the events and the southeastward migration of the seismicity (Figures 3, 6, and 7) is confirmed by the evolution of the S–P values at YTMZ station (Figure 6d). Moreover, the shallowness of the seismicity during Phase 2 is documented from various catalogs using distinct methods and data sets [Cesca et al., 2020, Lemoine et al., 2020a, Bertil et al., 2021, Feuillet et al., 2021].

### 5.2. *Chronology of the Mayotte seismo-volcanic sequence*

With the reliability of our catalog, we refine the spatio-temporal variation of seismicity at the beginning of the Mayotte activity (Figures 4 and 11). In the unrest phase of an eruptive context, the seismo-volcanic event migration highlights the magma propagation into the crust and to the surface, as observed in other volcanic areas such as the El Hierro, Canaries [Martí et al., 2013] or the Bárðarbunga, Iceland [Ágústsdóttir et al., 2019].

#### 5.2.1. *The onset of Mayotte seismic sequence (first week of Phase 1: 10–17 May 2018)*

Further analysis of the data in this study confirms a significant lack of seismic activity or surface deformation signal in Mayotte before 10 May 2018, from geodetic and seismic data, respectively (Figure S1). The sequence corresponds to a swarm-like seismicity showing several phases of event migration and

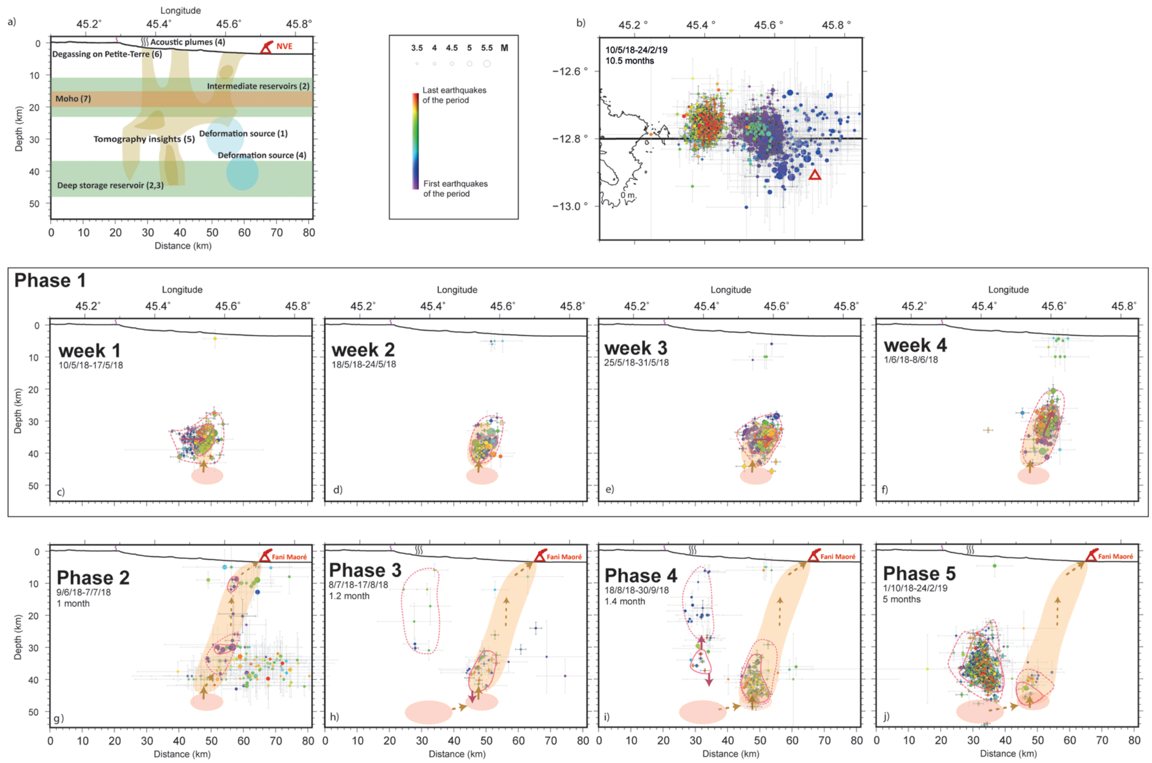

**Figure 11.** Summary eruptive scenario. (a) Synthesis of inferred lithospheric volcanic structures east of Mayotte from previously published studies, with references. (b) Map of the seismicity over the whole period of study. (c–f) Four steps of phase 1. (g–j) Phases 2, 3, 4 and 5. Orange shading highlights inferred extent of magma paths, pink shading are hypothetical reservoirs. Pink lines circle seismically active areas, dashed contour includes most events, continuous contour around denser subset and best-located events. Pink arrows indicate the migration of seismicity, orange arrows indicate inferred direction of magma propagation. Rainbow purple to red color of seismicity is the relative sequence of events for each time window (from blue to red). Black and grey error bars are similar to Figure 3.

pulses of activity encompassing moderate magnitude events (Figures 6, 11b). There is no initial and major shock: the biggest earthquake occurs on 15 May, five days after the beginning of the sequence.

In our catalog, the first detected events (Mlv < 4) occur on 10 May 2018 and are located between the two clusters that are subsequently identified, around 45.45°E and at 30–40 km depth (Figure 5), without any earthquakes being recorded in the following four years of activity. During the two first days, the seismicity rapidly moves to the east (up to 45.5°E) and spreads over a depth range of 30–40 km.

On the one hand, the sudden magmatic activity could be induced by static or dynamic stresses. Several studies such as Feuillet et al. [2006] showed that the destabilization of a deep magma reservoir may be triggered by tectonic transient loading, i.e., by stress induced by the occurrence of one or more earthquakes. The dynamic stresses associated with the seismic waves going through the magma body can also explain the pressure change within the magma reservoir [Walter et al., 2007]. On the other hand, the sudden magmatic activity may be induced by the feeding of the reservoir from a deeper level. Regarding the Mayotte sequence, stresses deduced from focal mechanisms of the 2018-seismic crisis are very consistent with stresses deduced from the regional seismicity before 2018 [Famin et al., 2020], implying that the 2018 earthquakes are in coherency with regional, tectonic stresses. Petrological studies support the tectonic triggering hypothesis [Berthod et al., 2021a]. The seismicity of the first days, confined between the two subsequent clusters, would have initiated the destabilization and damping of the reservoir. The seismic sequence that follows may have resulted from the stress induced by magma injection within the lithosphere and volume change in the reservoir and the conduits.

5.2.2. *The distal cluster: progressive shallowing of the seismicity, in four steps (Phase 1: 10 May–8 June 2018)*

As shown above, the outbreak of Mayotte seismicity is not a continuous sequence of earthquakes. During the one-month long Phase 1, the events cluster during short periods, lasting from half an hour up to eight hours, with a few dispersed events in between (Figure 6). We distinguish four ~week-long steps (Figures 6 and 11b–e). During the first week (10–17 May 2018), the seismicity takes place between the subsequent location of the two clusters. It migrates to the east, while remaining at around the same depths (between 37 and 40 km), and reaches the later location of the distal cluster (currently active). This first week is marked by the occurrence of the largest shock of the sequence. This initial sequence may highlight the overpressure associated with magma injection at depth from the deep reservoir (Figure 11b). During the second week (18–24 May 2018), the earlier earthquakes, including large Mlv > 5.0 shocks, occur at a similar latitude and depth, with small variations along the longitude axis. We propose that during this week the stress may have accumulated locally, with strong earthquakes (Figure 11c). Modeling of the GNSS data with strike-slip faulting only suggests fracturing of the crust and magma intrusion between the middle and end of May 2018 [Lemoine et al., 2020a]. The migration of earthquakes along the E–W direction during the first two weeks of the sequence could highlight the spatial evolution of the propagation front of the magma-filled fractures as observed in more shallow crustal levels along active rifts [Grandin et al., 2011]. Following Cesca et al. [2020] and Feuillet et al. [2021], we suggest that the western part of the active area corresponds to the injection point of magma into the surrounding lithosphere, magma that was previously stored in the deep magma reservoir. This segment of the distal cluster remains active (In October 2022), forming the western, nearly E–W oriented part of the distal cluster [Jacques et al., 2019, Hoste-Colomer et al., 2020, Lavayssière et al., 2022, REVOSIMA, 2022].

Then the intense activity on 25 May, and the seismic climax on 1 June, with dozens of seismic events within three to eight hours, highlight major direction changes in the pathway to the surface. The earthquakes migrate to the southeast from 25 May, and to the south and at a shallower depth (40 to 25 km) from 1 June, which supports the view that seismicity on the eastern segment is associated with the eruptive process of Fani Maoré [Figures 3–7, and 11, Cesca et al., 2020, Lemoine et al., 2020a, Bertil et al., 2021]. Remarkably, there is no seismicity further southeast of the location of Fani Maoré, which suggests that most of the sequence is related to the same magmatic plumbing system. This observation is consistent with the seismo-magmatic crustal episode that occurred along the western Aden ridge, where the dyking-related earthquakes showing a lateral migration affect only one second-order spreading segment of the ridge, with no sign of activity within the adjacent *en-échelon* segments [Ahmed et al., 2016]. We interpret the occurrence of several large seismic events (above magnitude 5.0) in 25 May and 1 June, followed by the direction changes in the migration of the seismicity (Figures 5, 6, and 11d,e), as the ruptures of barriers preventing the magma circulation, as described for example in the 2008 Kasatochi eruption, Alaska [Ruppert et al., 2011].

During Phase 1, the southeastward migration of the seismicity along a lateral distance of 20 km follows the SE-trending regional volcano-tectonic structures: the Jumelles, the Mayotte offshore volcanic chain, and the Mwezi volcanic field [Tzevahirtzian et al., 2021, Thinon et al., 2022]. This suggests that the direction of the magma propagation from the deep magma reservoir at 40 km depth is mostly driven by the regional tectonic stress field with NW–SE and SW–NE-trending maximum and minimum horizontal stresses, respectively [Famin et al., 2020, Lemoine et al., 2020a, Thinon et al., 2022].

5.2.3. *The distal cluster: progress of the seismicity from depth towards the seafloor eruption (Phase 2: 9 June–7 July 2018)*

During Phase 2, the distal cluster is divided into two distinct active areas: a shallow part, interpreted as ruptures that witness the upward magma circulation reaching the surface, and a deep part between 35 km and 40 km.

We interpret this large deep magnitude seismicity between 14 June and 14 July 2018 to be due to the readjustment of stress above the reservoir due to magma withdrawal and its intrusion in the surrounding lithosphere. In other volcanic contexts, usually at shallower depth, events of magnitude above 5.0 are rare and related to large quantities of material from underlying reservoirs being quickly withdrawn, as described in the strongest eruptions of the last decades for instance [Okada, 1983, Mori et al., 1996]. The lateral distribution of the hypocenters and the range of S–P values confirm the large extent of the plumbing system (30 × 30 km).

This seismicity that affects the upper mantle and the crust is interpreted as ruptures associated with the upward magma migration and potentially with the opening of the magma vertical pathways to the surface. Based on the relocations included in our catalog, this seismicity disappears at the end of June 2018. Therefore, the lack of relocated earthquakes above 25 km within the distal cluster suggests that most of the magma ascent from ~25 km up to the surface occurs aseismically from July 2018. In other active volcanic systems, similar observations have been made, where the remaining shallow seismicity remains low once the conduits to the surface are formed and the eruption is set [Roman and Cashman, 2018, and references therein], except during collapse events of the edifice, which has yet to be observed.

Considering that the beginning of the surface deformation signal (related to the magma ascent) is observed since 30 May 2018 [Phase C in Lemoine et al., 2020a], we thus suggest, following Berthod et al. (2020a), that the feeding of the newly formed conduits begins at the very start of the seismic sequence, as early as mid-May 2018. The constant $b$-values (0.91, Figure 4c) over $b$-values of both Phases 1 and 2 (10 May–7 July 2018) suggest that the properties of the surrounding rocks are similar during these first two phases [Schorlemmer et al., 2005]. By contrast, Phase 3 is characterized by a higher $b$-value (1.6), which is usually observed in volcanic contexts [e.g., Wiemer and McNutt, 1997, Chiba and Shimizu, 2018, and references therein], confirming the start of the submarine eruption between Phase 2 and Phase 3. Inland surface deformation measured using GNSS data and associated with the deflation of this deep reservoir begins between 28 June and 3 July 2018 [Cesca et al., 2020, Lemoine et al., 2020a]. This suggests that the magma pathways up to the surface are established at this time, thus the eruption may have started earlier. From our catalog, the start of the submarine eruption appears to be between 17 and 27 June 2018, when the seismicity reaches the surface (Figures 4g, 6g, and 7). This is consistent with the observed diffusion in zoned olivine crystals [Berthod et al., 2021a], which is interpreted as syn-eruptive magma transfer from the deep mantle reservoir, and implies migrations of 25 km east and 10 km south, and upward vertical migration of 40 km in less than seven weeks from the estimated reservoir location. This corresponds to a vertical migration rate of 0.01 to 0.02 $m{\cdot}s^{-1}$ in June, hence a relatively fast magma ascent speed [Cassidy et al., 2015]. This is also among the longest migrations of magma ever monitored and documented during an eruption, with only a few, such as the Pinatubo eruption in 1991, having earthquakes extending laterally for 20 km and from 25 km depth [Mori et al., 1996], or the Bárðarbunga eruption in 2014, occurring at the tip of a 48 km long dyke developed over 13 days, between 0 and 10 km depth [Ágústsdóttir et al., 2016].

#### 5.2.4. *Onset of the proximal cluster (Phase 3: 8 July–17 August 2018)*

Unlike the distal cluster, the seismicity within the proximal cluster starts progressively. The two first events, with an S–P value of ~4.3–4.4 s, are recorded mid-July 2018. Notably this seismicity only starts soon after the beginning of the seafloor eruption, suggesting a relation between the loss of magma volume in the reservoir and the occurrence of the proximal earthquakes. The seismicity of the proximal cluster is interpreted as a subsiding piston-like structure above a depressed magma chamber [Hoste-Colomer et al., 2020, Jacques et al., 2020, Feuillet et al., 2021, Lavayssière et al., 2022]. A complex caldeira-like structure is proposed by seafloor observations above the location of the proximal cluster, with evidence of past eruptive episodes [Berthod et al., 2021a, Feuillet et al., 2021, REVOSIMA, 2022, Puzenat et al., 2022].

The $b$-value estimated from the earthquakes within the proximal cluster (1.6) is higher than in the distal cluster and could indicate a larger amount of fluids within the lithospheric column than for the distal cluster. The identification of potential intermediate reservoirs at 25–30 km depth from petrological and seismic data supports this hypothesis [Figure 11, Berthod et al., 2021a,b, Foix et al., 2021]. Likewise, the VLP events reported during the Mayotte eruption that started mid-June 2018, despite their hardly constrained depth, are located within the proximal cluster area, most likely above the proximal events [Satriano et al., 2019, Laurent et al., 2021]. Those Mayotte VLP events are unique to this area with analogs only found in Polynesia [Talandier et al., 2016, Poli et al., 2019].

#### 5.2.5. *The August Proximal Peak (beginning of Phase 4: 22 August–6 September 2018)*

The APP is located in the area of the proximal cluster, but at a shallower depth (Figures 4 and 9), above what will become the most active area of the proximal cluster [Jacques et al., 2020, Lavayssière et al., 2022]. We may describe it as a third cluster, because its specific characteristics (S–P values on YTMZ, depths, seismicity rate, number of detected events) are different from the past and future proximal cluster dynamics. It occurs shortly after the start of the proximal cluster and after the start of the Fani Maoré eruption. Since May 2019, one year after the onset of the Mayotte seismic sequence, we note that successive MAYOBS cruises have reported hundreds of meters-high, persisting acoustic plumes on top of the caldeira-like edifice on the seafloor above the proximal cluster [Cathalot et al., 2019, Rinnert et al., 2019, Feuillet et al., 2021, Scalabrin et al., 2021, REVOSIMA, 2022, Puzenat et al., 2022]. The beginning of the proximal activity at depth might have destabilized mushes inferred from petrological data around 20 km depth [Berthod et al., 2021a]. We suggest that the APP corresponds to a phase of activation of this area up to the surface, associated with the setting or a renewal of the acoustic plumes above the proximal cluster. As almost continuous gas emissions have been monitored on Petite Terre since 1990 [Sanjuan et al., 2008, Liuzzo et al., 2021, Cadeau et al., 2022], the acoustic plumes might have started before 2018. The APP could mark an enhancement of acoustic plume activity. The depths of the events from 22 to 29 August 2018 range between 0 and 25 km, whereas below Fani Maoré the upward seismic migration on a similar distance takes more than twice this time, associated with larger releases of seismic energy. Because of the low magnitudes, we suggest that the APP occurs in a pre-existing damaged zone, which is still active in October 2022 [REVOSIMA, 2022].

Finally, considering the $5.0 \pm 0.3$ km$^3$ Fani Maoré built up between the end of June 2018 and May 2019, the calculated average eruptive rate of 200 m$^3$/s corresponds to one km$^3$ of erupted material over two months by the end of August. The APP and the following proximal activity could have occurred in response to this already important withdrawal of a large magma volume from a complex plumbing system.

#### 5.2.6. *The distal September 2018 seismicity: opening of a new, deep feeding conduit?*

A renewal of the distal cluster activity occurs from 3 September 2018, right after the APP, with magnitudes up to 4.8. This reactivation is centered around 45 km depth, i.e., below the previous seismically active area (Figures 4, 9). We identify a pulse of activity on 17 September, whose events are within a wider range of depths, between 35 and 50 km, followed by a higher seismicity rate until the end of the month, yet lower than the May and June seismicity rates (Figure 4). There is also an increase of displacement rate within the GNSS data around 8 October 2018. We consequently suppose that a new feeding way may be built in September 2018, allowing a faster withdrawal of magma from a deeper part of the plumbing system. Such downward propagation of swarm-like seismicity, due to decompression of magma reservoirs, has already been observed within the Eyjafjallajökull complex plumbing system, in Iceland [Tarasewicz et al., 2012].

Taking into account the spatial evolution of the hypocenters within the distal cluster, the top of the destabilizing reservoir complex should be located west of 45.5°E and south of 12.75°S, and deeper than 40 km, assuming that the initial seismic activity started above it (Figure 11). This is located below the deflating source in the deformation model proposed by Lemoine et al. [2020a], but is in agreement with the deformation source proposed by Feuillet et al. [2021], the petrological constraints of Berthod et al. [2021a], the tomography studies [Foix et al., 2021], and the previous conceptual models [Feuillet et al., 2021, Lavayssière et al., 2022] (Figure 11a).

## 5.3. *Relations between the seismic clusters and the magmatic plumbing system*

### 5.3.1. *Development of the proximal cluster, link with the Fani Maoré eruption*

The seismicity rate on the proximal cluster remains low until October 2018 (the end of the September distal episode), while the GNSS velocities remain constant [Figure S1; Briole, 2018]. At this point, the proximal cluster progressively becomes predominant. The number of detected events increases until the end of December 2018, as does the effusive rate deducted from GNSS data [Lemoine et al., 2020a]. Then, from the end of 2018, the eruptive rate slowly decreases, as does the seismicity rate within the proximal cluster. We observe that the proximal seismicity rate roughly follows the eruptive rate, suggesting that the seismicity of the proximal cluster is linked to the eruption process, at least in the period covered by this study. The later decreasing eruptive activity, along with the decreasing proximal seismicity rate [Rinnert et al., 2019, REVOSIMA, 2022], tend to show that this proximal seismo-volcanic link continues after March 2019.

The proximal events are focused initially around $36 \pm 4$ km depth. During the following months, the depth range widens (95% of the depth values between 20 km and 50 km, Figure 4g). The majority of the events are 30 km to 45 km deep, meaning that the damaging of a sub-vertical, likely inherited system, propagates slightly downward from the initial active area, consistent with the idea of an underlying collapse [suggested in Hoste-Colomer et al., 2020, Jacques et al., 2020, Lavayssière et al., 2022]. This may favor the circulation of fluids, which would explain the link between the magma drainage and the acoustic plume activity [e.g., Jacques et al., 2020].

The shape of the proximal cluster during Phase 5 tends to show that its seismicity until March 2019 is mainly located on its eastern half [which is the most active part of this swarm during the following years: e.g., Lavayssière et al., 2022, Saurel et al., 2022].

### 5.3.2. *On the link between the two clusters and the dynamic of the feeding system*

Before the proximal cluster becomes intensely active during Phase 5, we observe during Phase 4 that when the activity of one swarm increases, the activity of the other decreases (Figure 4). The distal seismicity lowers during the APP, and then when it increases during the September episode, the proximal activity decreases. Finally, when the proximal cluster becomes predominant within Phase 5, the distal seismicity lessens. We do not identify a direct "seismicity link" between the two clusters, since there is clearly an area without seismicity between them [also observed in the next period with a better monitoring network: e.g., Lavayssière et al., 2022, Saurel et al., 2022]. It is however obvious that both clusters of seismicity are linked to the same eruptive phenomena.

In agreement with already proposed models [Berthod et al., 2021a,b, Feuillet et al., 2021, Lavayssière et al., 2022], we suggest that the distal activity is related to the building and modifications of the feeding system of the Fani Maoré volcano, while the proximal one is linked to the main reservoir drainage and subsequent reequilibration of stresses, and thus the different alternate behaviors.

### 5.3.3. *The ~20 km deep mushes*

Without considering the APP, we observe an area between 13 and 21 km with very few events above magnitude 3.0. Petrological studies highlight an intermediate magma storage at the base of the crust, somewhere in between 11 km and 23 km [Berthod et al., 2021b, Figure 11], as well as tomography work [Foix et al., 2021], where VLP events are located [Satriano et al., 2019, Laurent et al., 2021]. Previous studies have detected a 9 km-thick conductivity anomaly at ~20 km depth [Darnet et al., 2020], interpreted as magmatic underplating [Dofal et al., 2021]. In line with these interpretations, we suggest that this range of depths without seismicity could highlight intermediate magma mushes at the crust-mantle boundary, allowing a non-seismogenic circulation of magma.

## 5.4. *The Mayotte crisis: a unique seismo-volcanic sequence*

Oceanographic campaigns [Audru et al., 2006, Rinnert et al., 2019, Tzevahirtzian et al., 2021, Thinon et al., 2022] uncovered important submarine volcanic chains, with ridges, cones and domes, and complex faulted systems, distributed along the Comoros archipelago. The multiple seafloor marks observed in the archipelago are evidence that important volcanic events such as the Mayotte 2018–2022 eruption might have occurred in the past. Some edifices are of comparable size than Fani Maoré, although this volcano is indeed the highest known submarine volcano within the archipelago.

One particularity of the Mayotte sequence is the amount of earthquakes of magnitude over 5.0. More Mlv > 5.0 events reported within the two first months of the Mayotte sequence than in the previous 50 years within the archipelago, from the Davie ridge to Madagascar [Figure 1; Bertil et al., 2021]. This indicates the high amount of stress applied and the high resistance and/or initial low damage level of the sub-Moho lithosphere (brittle mantle) in this area. No equivalent of this Mayotte seismic sequence can be found within the regional seismicity catalogs: there are neither identified seismic swarms nor focused sequences of earthquakes along the archipelago. Locally within monitored periods, the Mayotte sequence is therefore unique. Collective memory moreover does not recall such an intense crisis, as the oral tradition reports damaging earthquakes only in 1606, 1679, and 1788, without mention of any months-long seismicity [Hachim, 2004].

The Mayotte sequence is a unique laboratory for large-scale eruption study: upper mantle seismicity migrates dozens of kilometers laterally and up to the seafloor, many earthquakes of moderate magnitudes occur for volcano-seismic sequencing, there is the presence of huge emitted volumes of magma and separated clusters with different apparent dynamics. Such magnitudes and sequences of high seismicity rate and duration are highly unusual. In comparison, the off-Ito swarm and eruption, with magnitude up to 5.5 lasted only three months [Okada and Yamamoto, 1991]; see other examples in [McNutt and Roman, 2015].

The size of the destabilized reservoir and the quantity and speed of magma, from depth to surface, is generally related to the associated seismic sequence [Feuillet et al., 2006, Michon et al., 2015]. Furthermore, seismicity is widely used as a precursory eruption warning. Here, the initial Mayotte activity is exceptional, with 45 earthquakes of magnitude between 5.0 and 6.0 and hundreds of felt events within the first two months. Occurrence of seismicity above magnitude 5.0 is rare during volcanic unrest, even though some large events are known, preceding or following large eruptions and/or caldeira collapse. However, none of the eruption-related seismic crises monitored so far, such as the Fernandina 1968 eruption on Galapagos islands [Filson et al., 1973], the Kasatochi 2008 eruption in Alaska [Ruppert et al., 2011], or other examples [e.g., McNutt and Roman, 2015], ever reached the daily rate and durability of Mayotte sequence. The moderate-to-high magnitude sequences of Mayotte could be due to the difficulty to fracture the lithosphere [e.g., Dofal et al., 2021, Masquelet et al., 2022], where no recent eruption had occurred [e.g., Ruppert et al., 2011].

Here, the seismic swarms highlight the exceptional lateral and vertical extension of the magmatic reservoirs and paths. The distal seismicity highlights one of the longest vertical migrations of seismic activity linked to a magma migration ever monitored, from 40 km depth to seafloor bottom at ~3.5 km below sea level, and a 25 km lateral migration to the east then to the south-east. Lateral migrations of dozens of kms, and volcano-seismic sequences that do not happen right below the volcanic edifices, are rare, but have been observed during other dyking events [2011 on El Hierro, Canary islands, Carracedo et al., 2015; 2014 on Bárðarbunga, Iceland, Ágústsdóttir et al., 2016; 2016 on Brava Island, Cabo Verde, Leva et al., 2020].

Similarly, an “aseismic” zone separates our two clusters. We suggest that the two clusters are linked to the eruptive process at the surface, along with the emptying of a deep reservoir. Different clusters can be observed around a same magma body, highlighting its expansion or a spreading eruption [as observed below El Hierro, Cerdeña et al., 2014]. However, in the Mayotte case, the two clusters have different dynamics. The thoroughly researched and monitored example of Bárðarbunga (Iceland) dyke intrusion in 2014 shows a similar pattern: there is evidence of two distincts seismic zones, one linked to a caldeira collapse, the other linked to magma ascent within a 48 km-long dyke reaching the surface [Sigmundsson et al., 2015, Gudmundsson et al., 2016, Ágústsdóttir et al., 2019]. However, in the Bárðarbunga example, the seismicity is above 10 km. The Mayotte eruption is the first observation of a collapsing event in the mantle at depths of 25–50 km.

## 6. Conclusion

We build up an exhaustive catalog of the beginning of the Mayotte seismo-volcanic sequence, from the onset of the seismic sequence on 10 May 2018, to the last day of monitoring without OBS networks on 24 February 2019 [Saurel et al., 2022]. Despite the initial monitoring issues, it is possible to follow up on the crisis and improve the seismic catalog afterwards.

The sequence starts with the propagation of a feeding conduit, built up in segments, from a deep (≥40 km) reservoir. This is highlighted by one month of deep, swarm-like seismicity (10 May–8 June 2018), with a high seismicity rate (30 events per day) and frequent earthquakes above magnitude 5.0 (one a day on average), marking the importance of the stresses applied on barriers, which broke progressively, creating a seismicity in successive pulses. Seismicity migrates from 20 km east of Mayotte and ~40 km depth to almost 50 km east of Mayotte and ~30 km depth, within the so-called distal cluster.

The conduit—dyke—opening up to the surface occurs during the following month (9 June–7 July 2018). Even as the seismicity rate lowers, the magnitudes are as high as in the preceding month. The upward migration is confirmed with GNSS data and international networks [e.g., Cesca et al., 2020, Lemoine et al., 2020a]. The "superficial part" (above 25 km) is less seismic, magma paths perhaps grow through a partially damaged environment and/or pre-existing conduits. Once the conduits are opened on the seafloor, at the end of this phase, there is no more occurrence of seismicity above 25 km within the distal cluster. The seismogenic building of conduits up to the surface, from 10 May to 7 July 2018, cover 25, 10 and 40 km eastward, southward and along the vertical axis, respectively. Superficial earthquakes, i.e., close to the seafloor, occur between 17 and 27 June, marking the end of the conduit building, and likely the beginning of the eruption. The distal cluster activity remains low since October 2018.

The eruption of the Fani Maoré volcano causes a rapid and large deflation of the feeding magmatic system, triggering a deep seismicity extending at depth, highlighted by the proximal cluster located 0 to 20 km east of Mayotte. This seismicity starts in July 2018, at ~30 km depth and develops mainly downward in the following months, to depths ranging between 25 and 40 km in February 2019, with lower seismicity rates and magnitudes. The proximal seismicity rate follows the eruptive rate, but takes place below the complex, westward part of the offshore Mayotte volcanic chain. The following seismicity, since October 2018, is mainly focused on this cluster.

In addition to detailing the two first months migrations, this catalog allow to identify two peculiar episodes of seismicity, one at the end of August 2018 above the proximal cluster, possibly linked to the acoustic plumes, and another in the distal cluster in September 2018, interpreted as the opening of a new feeding pathway allowing for a higher eruptive rate since October 2018.

This seismic sequence questions the state-of-the-art knowledge about the Comoros archipelago lithospheric structure and volcanism. The intense seismicity of the two first months of the Mayotte sequence proves that deep-feeding conduits have not opened for a long period, marking a difficult magma intrusion into the lithosphere. Further investigations of the regional seismicity will help us to understand the link between volcanism, earthquakes, and tectonic activity that much more, and will help us to refine these hypotheses.

## Conflicts of interest

The authors declare no competing interest.

## Acknowledgments

The authors thank Carole Berthod, Pierre Briole, and Chastity Aiken for constructive discussions, which improved this article. They are also grateful to Angèle Laurent and Charles Masquelet, which shared generously unpublished results. This study is part of the ANR COYOTES project (ANR-19-CE31-0018). The authors thank the three anonymous reviewers and the editors for their comments, and Gregory Owcarz for improving the quality of the English.

A large part of the data have been acquired in the framework of the first response team to the Mayotte seismic crisis, including in particular members of the BRGM DRP/RSV unit: A. Colombain, G. Dectot, C. Gracianne, E. Maisonneuve, K. Meza Fajardo, A. Roullé, F. Tronel. This work was possible thanks to the seismic data shared by the Karthala volcanologic observatory (OVK).

This article is part of Nicolas Mercury's thesis at the ITES laboratory (CNRS, University of Strasbourg, ENGEES) funded by BRGM and the French Ministry of Ecological Transition (MTE, DGPR).

## Supplementary data

Supporting information for this article is available on the journal's website under https://doi.org/10.5802/crgeos.191 from the corresponding author.

## References

Ágústsdóttir, T., Winder, T., Woods, J., White, R. S., Greenfield, T., and Brandsdóttir, B. (2019). Intense seismicity during the 2014–2015 Bárðarbunga-Holuhraun rifting event, Iceland, reveals the nature of dike-induced earthquakes and caldera collapse mechanisms. *J. Geophys. Res.: Solid Earth*, 124(8), 8331–8357.

Ágústsdóttir, T., Woods, J., Greenfield, T., Green, R. G., White, R. S., Winder, T., Brandsdottir, B., Steinthorsson, S., and Soosalu, H. (2016). Strike-slip faulting during the 2014 Bárðarbunga-Holuhraun dike intrusion, central Iceland. *Geophys. Res. Lett.*, 43(4), 1495–1503.

Ahmed, A., Doubre, C., Leroy, S., Kassim, M., Keir, D., Abayazid, A., Perrot, J., Audin, L., Vergne, J., Nercessian, A., Jacques, E., Khanbari, K., Sholan, J., Rolandone, F., and Al-Ganad, I. (2016). Seafloor spreading event in western Gulf of Aden during the November 2010–March 2011 period captured by regional seismic networks: Evidence for diking events and interactions with a nascent transform zone. *Geophys. J. Int.*, 205(2), 1244–1266.

Aiken, C., Saurel, J. M., and Foix, O. (2021). Earthquake location and detection modeling for a future seafloor observatory along Mayotte's volcanic ridge. *J. Volcanol. Geotherm. Res.*, 418, article no. 107322.

Aki, K. and Richards, P. G. (2002). *Quantitative Seismology.* University Science Books.

Audru, J. C., Guennoc, P., Thinon, I., and Abellard, O. (2006). Bathymay: la structure sous-marine de Mayotte révélée par l'imagerie multifaisceaux. *C. R. Géosci.*, 338(16), 1240–1249.

Bachèlery, P., Morin, J., Villeneuve, N., Soulé, H., Nassor, H., and Ali, A. R. (2016). Structure and eruptive history of karthala volcano. In Bachèlery, P., Lenat, J., Di Muro, A., and Michon, L., editors, *Active Volcanoes of the Southwest Indian Ocean. Active Volcanoes of the World.* Springer, Berlin, Heidelberg.

Berthod, C., Médard, E., Bachèlery, P., Gurioli, L., Di Muro, A., Peltier, A., Komorowski, J. C., Benbakkar, M., Devidal, J. L., Langlade, J., Besson, P., Boudon, G., Rose-Koga, E., Deplus, C., Le Friant, A., Bickert, M., Nowak, S., Thinon, I., Burckel, P., Hidalgo, S., Kaliwoda, M., Jorry, S., Fouquet, Y., and Feuillet, N. (2021a). The 2018-ongoing Mayotte submarine eruption: magma migration imaged by petrological monitoring. *Earth Planet. Sci. Lett.*, 571, article no. 117085.

Berthod, C., Médard, E., Di Muro, A., Hassen Ali, T., Gurioli, L., Chauvel, C., Komorowski, J. C., Bachèlery, P., Peltier, A., Benbakkar, M., Devidal, J. L., Besson, P., Le Friant, A., Deplus, C., Nowak, S., Thinon, I., Burckel, P., Hidalgo, S., Feuillet, N., Jorry, S., and Fouquet, Y. (2021b). Mantle xenolith-bearing phonolites and basanites feed the active volcanic ridge of Mayotte (Comoros archipelago, SW Indian Ocean). *Contrib. Mineral. Petrol.*, 176(10), 1–24.

Bertil, D. and François, B. (2016). Les stations accélérométriques gérées par le BRGM. In *VIII biennales du RAP*, page 13. https://rap.resif.fr/IMG/pdf/livretrap-reduc.pdf.

Bertil, D. and Hoste-Colomer, R. (2020). Loi Magnitude-Intensité pour Mayotte. Rapport final. Rapport BRGM/RP70297-FR, 52 p., 14 fig., 10 tab., 4 ann.

Bertil, D., Mercury, N., Doubre, C., Lemoine, A., and Van Der Woerd, J. (2021). The unexpected Mayotte 2018–2020 seismic sequence: a reappraisal of the regional seismicity of the Comoros. *C. R. Géosci.*, 353(S1), 211–235.

Bertil, D., Roullé, A., Lemoine, A., Colombain, A., Hoste-Colomer, R., Gracianne, C., Meza-Fajardo, K., Maisonhaute, E., and Dectot, G. (2019). MAYEQSwarm2019: BRGM earthquake catalogue for the Earthquake Swarm located East of Mayotte. 2018 May 10th–2019 May 15th.

Boymond, P., Feuillet, N., Thinon, I., Scholtès, L., Leroy, S., Rusquet, A., Masquelet, C., and Jacques, E. (2022). Volcano-tectonic interactions within two recently discovered submarine volcanic fields: Implication for geodynamics in the Comoros. In *EGU General Assembly 2022, Vienna, Austria 23–27 May 2022, EGU22-10160.*

Briole, P. (2018). Note sur la crise tellurique en cours à Mayotte. http://volcano.iterre.fr/wp-content/uploads/2018/11/mayotte_note_deformation_GPS_20181126.pdf.

Cadeau, P., Jezequel, D., Groleau, A., Di Muro, A., and Ader, M. (2022). Impact of the seismo-volcanic crisis offshore Mayotte on the Dziani Dzaha Lake. *C. R. Géosci.*, 354(S2), 299–316.

Carracedo, J. C., Troll, V. R., Zaczek, K., Rodríguez-González, A., Soler, V., and Deegan, F. M. (2015). The 2011–2012 submarine eruption off El Hierro, Canary Islands: New lessons in oceanic island growth and volcanic crisis management. *Earth-Sci. Rev.*, 150, 168–200.

Cassidy, M., Cole, P. D., Hicks, K. E., Varley, N. R., Peters, N., and Lerner, A. H. (2015). Rapid and slow: Varying magma ascent rates as a mechanism for Vulcanian explosions. *Earth Planet. Sci. Lett.*, 420, 73–84.

Cathalot, C., Rinnert, E., Scalabrin, C., Donval, J. P., Guyader, V., Jorry, S., Gaillot, A., Guérin, C., S., Djedjroh, Y., Fouquet, Y., Leroy, L., Feuillet, N., and Billant, G. (2019). Acoustic and Geochemical Anomalies in the Water Column around the Newly Formed Volcano offshore Mayotte Island. In *AGU Fall Meeting 2019*. (Abstract #V52D-05).

Cerdeña, I. D., Del Fresno, C., and Moreno, A. G. (2014). Seismicity patterns prior to the 2011 El Hierro eruption. *Bull. Seismol. Soc. Am.*, 104(1), 567–575.

Cesca, S., Letort, J., Razafindrakoto, H. N. T., Heimann, S., Rivalta, E., Isken, M. P., Nikkhoo, M., Passarelli, L., Petersen, G. M., Cotton, F., and Dahm, T. (2020). Drainage of a deep magma reservoir near Mayotte inferred from seismicity and deformation. *Nat. Geosci.*, 13(1), 87–93.

Chiba, K. and Shimizu, H. (2018). Spatial and temporal distributions of b-value in and around Shinmoe-dake, Kirishima volcano, Japan. *Earth Planet. Space*, 70(1), 1–9.

Darnet, M., Wawrzyniak, P., Tarits, P., Hautot, S., and d'Eu, J. F. (2020). Mapping the geometry of volcanic systems with magnetotelluric soundings: Results from a land and marine magnetotelluric survey performed during the 2018–2019 Mayotte seismo-volcanic crisis. *J. Volcanol. Geotherm. Res.*, 406, article no. 107046.

Debeuf, D. (2009). *Étude de l'évolution volcano-structurale et magmatique de Mayotte, Archipel des Comores, océan Indien: approches structurale, pétrographique, géochimique et géochronologique*. PhD thesis, Université de la Réunion.

Dofal, A., Fontaine, F. R., Michon, L., Barruol, G., and Tkalčić, H. (2021). Nature of the crust beneath the islands of the Mozambique Channel: Constraints from receiver functions. *J. Afr. Earth Sci.*, 184, article no. 104379.

Dziewonski, A. M., Chou, T.-A., and Woodhouse, J. H. (1981). Determination of earthquake source parameters from waveform data for studies of global and regional seismicity. *J. Geophys. Res.*, 86, 2825–2852.

Ekström, G., Nettles, M., and Dziewonski, A. M. (2012). The global CMT project 2004-2010: Centroid-moment tensors for 13,017 earthquakes. *Phys. Earth Planet. Inter.*, 200–201, 1–9.

Famin, V., Michon, L., and Bourhane, A. (2020). The Comoros archipelago: A right-lateral transform boundary between the Somalia and Lwandle plates. *Tectonophysics*, 789, article no. 228539.

Feuillet, N., Cocco, M., Musumeci, C., and Nostro, C. (2006). Stress interaction between seismic and volcanic activity at Mt Etna. *Geophys. J. Int.*, 164(3), 697–718.

Feuillet, N., Jorry, S., Crawford, W. C., Deplus, C., Thinon, I., Jacques, E., Saurel, J. M., Lemoine, A., Paquet, F., Satriano, C., Aiken, C., Foix, O., Kowalski, P., Laurent, A., Rinnert, E., Cathalot, C., Donval, J. P., Guyader, V., Gaillot, A., Scalabrin, C., Moreira, M., Peltier, A., Beauducel, F., Grandin, R., Ballu, V., Daniel, R., Pelleau, P., Gomez, J., Besançon, S., Geli, L., Bernard, P., Bachèlery, P., Fouquet, Y., Bertil, D., Lemarchand, A., and Van der Woerd, J. (2021). Birth of a large volcanic edifice offshore Mayotte via lithosphere-scale dyke intrusion. *Nat. Geosci.*, 14(10), 787–795.

Filson, J., Simkin, T., and Leu, L. K. (1973). Seismicity of a caldera collapse: Galapagos Islands 1968. *J. Geophys. Res.*, 78(35), 8591–8622.

Foix, O., Aiken, C., Saurel, J. M., Feuillet, N., Jorry, S. J., Rinnert, E., and Thinon, I. (2021). Offshore Mayotte volcanic plumbing revealed by local passive tomography. *J. Volcanol. Geotherm. Res.*, 420, article no. 107395.

Grandin, R., Jacques, E., Nercessian, A., Ayele, A., Doubre, C., Socquet, A., Keir, D., Kassim, M., Lemarchand, A., and King, G. C. P. (2011). Seismicity during lateral dike propagation: Insights from new data in the recent Manda Hararo–Dabbahu rifting episode (Afar, Ethiopia). *Geochem. Geophys. Geosyst.*, 12, article no. Q0AB08.

Gudmundsson, M. T., Jónsdóttir, K., Hooper, A., Holohan, E. P., Halldórsson, S. A., Ófeigsson, B. G., Cesca, S., Vogfjörd, K. S., Sigmundsson, F., Högnadóttir, T., Einarsson, P., Sigmarsson, O., Jarosch, A. H., Jónasson, K., Magnússon, E., Hreinsdóttir, S., Bagnardi, M., Parks, M. M., Hjörleifsdóttir, V., Pálsson, F., Walter, T. R., Schöpfer, M. P. J., Heimann, S., Reynolds, H. I., Dumont, S., Bali, E., Gudfinnsson, G. H., Dahm, T., Roberts, M. J., Hensch, M., Belart, J. M. C., Spaans, K., Jakobsson, S., Gudmundsson, G. B., Fridriksdóttir, H. M., Drouin, V., Dürig, T., Aðalgeirsdóttir, G., Riishuus, M. S., Pedersen, G. B. M., van Boeckel, T., Oddsson, B., Pfeffer, M. A., Barsotti, S., Bergsson, B., Donovan, A., Burton, M. R., and Aiuppa, A. (2016). Gradual caldera collapse at Bárðarbunga volcano, Iceland, regulated by lateral magma outflow. *Science*, 353(6296), article no. aaf8988.

Gutenberg, B. and Richter, C. F. (1942). Earthquake magnitude, intensity, energy, and acceleration. *Bull. Seismol. Soc. Am.*, 32(3), 163–191.

Hachim, S. (2004). Catastrophes: Mayotte perd sa mémoire ! Catastrophes naturelles et mémoire collective à Mayotte. Mémoire de DEA de Géographie, Université Paul Valéry, Montpellier III.

Helmholtz-Centre Potsdam - GFZ German Research Centre for Geosciences and GEMPA GmbH (2008). The SeisComP seismological software package. GFZ Data Services. http://doi.org/10.5880/GFZ.2.4.2020.003.

Hoste-Colomer, R., Jacques, E., Lemoine, A., Lavayssière, A., Crawford, W., Feuillet, N., Fouquet, Y., Jorry, S., Rinnert, E., and Thinon, I. (2020). Seismicity clusters structure of Mayotte volcano-tectonic crisis. In *AGU Fall Meeting 2020*. (Abstract #V040-0001).

Ichimoto, M. and Iida, K. (1939). Observations of earthquakes registered with the microseismograph constructed recently. *Bull. Earthq. Res. Inst.*, 17, 443–478.

Jacques, E., Feuillet, N., Aiken, C., Lemoine, A., Crawford, W. C., Deplus, C., Thinon, I., Saurel, J.-M., Bès de Berc, M., Broucke, C., Colombain, A., Daniel, R., Dectot, G., Dofal, A., Foix, O., Gomez, J., Grunberg, M., Kowalski, P., Laurent, A., Léger, F., Lemarchand, A., and Pelleau, P. (2019). The 2018–2019 mayotte seismic crisis: evidence of an upper mantle rifting event? In *AGU Fall Meeting 2019*. (Abstract #V43I-0221).

Jacques, E., Hoste-Colomer, R., Lavayssière, A., Lemoine, A., Crawford, W. C., Feuillet, N., Fouquet, Y., Jorry, S., Rinnert, E., Thinon, I., and Vanderwoerd, J. (2020). Seismo-tectonic analysis of the ongoing Mayotte crisis suggesting reactivation of a caldera structure below the Moho. In *AGU Fall Meeting 2020*. (Abstract #V040-0006).

Laurent, A., Satriano, C., Bernard, P., Feuillet, N., and Jorry, S. (2021). Accurate Depth Determination of the Very Low Frequency Earthquakes of the Mayotte 2018-2021 Seismo-Volcanic Crisis. In *AGU Fall Meeting 2021, New Orleans, LA and online*.

Lavayssière, A., Crawford, W. C., Saurel, J. M., Satriano, C., Feuillet, N., Jacques, E., and Komorowski, J. C. (2022). A new 1D velocity model and absolute locations image the Mayotte seismo-volcanic region. *J. Volcanol. Geotherm. Res.*, 421, article no. 107440.

Lee, W. H. K. (1975). A computer program for determining hypocenter, magnitude, and first motion pattern of local earthquakes. US Geol. Surv., Open File Report, 75(311), 1–116.

Lee, W. H. K. and Lahr, J. C. (1972). *HYPO71: A computer program for determining hypocenter, magnitude, and first motion pattern of local earthquakes*. US Department of the Interior, Geological Survey, National Center for Earthquake Research.

Lee, W. H. K. and Valdes, C. M. (1985). *HYPO71PC: A personal computer version of the HYPO71 earthquake location program*, volume 85, No. 749. US Geological Survey.

Lemoine, A., Briole, P., Bertil, D., Roullé, A., Foumelis, M., Thinon, I., Raucoules, D., de Michele, M., Valty, P., and Colomer, R. H. (2020a). The 2018–2019 seismo-volcanic crisis east of Mayotte, Comoros islands: seismicity and ground deformation markers of an exceptional submarine eruption. *Geophys. J. Int.*, 223(1), 22–44.

Lemoine, A., Pedreros, R., and Filippini, A. (2020b). Scénarios d'impact des tsunamis pour Mayotte. Final report, http://ficheinfoterre.brgm.fr/document/RP-69869-FR 169 p., 21 ill., 8 Tab., 61 ann.

Leva, C., Rümpker, G., and Wölbern, I. (2020). Remote monitoring of seismic swarms and the August 2016 seismic crisis of Brava, Cabo Verde, using array methods. *Nat. Hazard. Earth Syst. Sci.*, 20(12), 3627–3638.

Liuzzo, M., Di Muro, A., Rizzo, A. L., Caracausi, A., Grassa, F., Fournier, N., Shafik, B., Boudoire, G., Coltorti, M., Moreira, M., and Italiano, F. (2021). Gas geochemistry at grande comore and mayotte volcanic islands (comoros archipelago), Indian Ocean. *Geochem. Geophys. Geosyst.*, 22(8), article no. e2021GC009870.

Martí, J., Pinel, V., López, C., Geyer, A., Abella, R., Tárraga, M., Blanco, M. J., Castro, A., and Rodríguez, C. (2013). Causes and mechanisms of the 2011–2012 El Hierro (Canary Islands) submarine eruption. *J. Geophys. Res.: Solid Earth*, 118(3), 823–839.

Masquelet, C., Leroy, S., Delescluse, M., Chamot-Rooke, N., Thinon, I., Lemoine, A., Franke, D., Watremez, L., Werner, P., and Sauter, D. (2022). The East-Mayotte new volcano in the Comoros archipelago: structure and timing of magmatic phases inferred from seismic reflection data. *C. R. Géosci.*, 354(S2), 65–79.

McNutt, S. R. and Roman, D. C. (2015). Volcanic seismicity. In *The Encyclopedia of Volcanoes*, pages 1011–1034. Academic Press.

Michon, L. (2016). The volcanism of the Comores archipelago integrated at a regional scale. In Bachèlery, P., Lénat, J.-F., Di Muro, A., and Michon, L., editors, *Active Volcanoes of the Southwest Indian Ocean: Piton de La Fournaise and Karthala*, pages 333–344. Springer-Verlag, Berlin and Heidelberg.

Michon, L., Ferrazzini, V., Di Muro, A., Villeneuve, N., and Famin, V. (2015). Rift zones and magma plumbing system of Piton de la Fournaise volcano: How do they differ from Hawaii and Etna? *J. Volcanol. Geotherm. Res.*, 303, 112–129.

Mori, J., White, R. A., Harlow, D. H., Okubo, P., Power, J. A., Hoblitt, R. P., Laguerta, E. P., Lanuza, A., and Bautista, B. C. (1996). Volcanic earthquakes following the 1991 climactic eruption of Mount Pinatubo: Strong seismicity during a waning eruption. In *Fire and Mud: Eruptions and Lahars of Mount Pinatubo, Philippines*, pages 339–350. https://pubs.usgs.gov/pinatubo/.

Nehlig, P., Lacquement, F., Bernard, J., Audru, J., Caroff, M., Deparis, J., Jaouen, T., Pelleter, A. A., Perrin, J., Prognon, C., and Vittecoq, B. (2013). *Notice explicative, carte geol. France (1/30 000), feuille Mayotte (1179)*. BRGM, Orléans. Carte géologique par Lacquement, F., Nehlig, P., Bernard, J. (2013).

Nougier, J., Cantagrel, J. M., and Karche, J. P. (1983). The Comores archipelago in the western Indian Ocean: volcanology, geochronology and geodynamic setting. *J. Afr. Earth Sci.*, 5(2), 135–145.

Okada, H. (1983). Comparative study of earthquake swarms associated with major volcanic activities. In Shimozuru, D. and Yokoyama, I., editors, *Arc volcanism: Physics and Tectonics*, pages 43–61. Terra Scientific Publishing Company, Tokyo.

Okada, Y. and Yamamoto, E. (1991). Dyke intrusion model for the 1989 seismovolcanic activity off Ito, central Japan. *J. Geophys. Res.: Solid Earth*, 96(B6), 10361–10376.

Peltier, A., Saur, S., Ballu, V., Beauducel, F., Briole, P., Chanard, K., Dausse, D., De Chabalier, J. B., Grandin, R., Rouffiac, P., Tranchant, Y. T., Bès de Berc, M., Besançon, S., Boissier, P., Broucke, C., Brunet, C., Canjamalé, K., Carme, E., Catherine, P., Colombain, A., Crawford, W., Daniel, R., Dectot, G., Desfete, N., Doubre, C., Dumouch, T., Griot, C., Grunberg, M., Jund, H., Kowalski, P., Lauret, F., Lebreton, J., Pesqueira, F., Tronel, F., Valty, P., and Van der Woerd, J. (2022). Ground deformation monitoring of the eruption offshore Mayotte. *C. R. Géosci.*, 354(S2), 171–193.

Poli, P., Shapiro, N., and Campillo, M. (2019). Teleseismic detection of very long period signals from Mayotte volcanic crisis. In *AGU Fall Meeting 2019*. (Abstract #V52D-08).

Puzenat, V., Feuillet, N., Komorowski, J. C., Escartin, J., Deplus, C., Bachèlery, P., Berthod, C., Gurioli, L., Scalabrin, C., Cathalot, C., Rinnert, E., Loubrieu, B., Pierre, D., Pitel-Roudaut, M., Tanguy, N., Fouquet, Y., Jorry, S. J., Lebas, E., Paquet, F., and Thinon, I. (2022). Volcano-tectonic structures of Mayotte's upper submarine slope: insights from high-resolution bathymetry and in-situ imagery from a deep towed camera. *C. R. Géosci.*, 354(S2), 81–104.

Quidelleur, X., Michon, L., Famin, V., Geffray, M. C., Danišík, M., Gardiner, N., Rusquet, A., and Zakaria, M. G. (2022). Holocene volcanic activity in Anjouan Island (Comoros archipelago) revealed by new Cassignol-Gillot groundmass K–Ar and 14C ages. *Quat. Geochronol.*, 67, article no. 101236.

REVOSIMA (2022). Bulletin Mensuel du Réseau de surveillance volcanologique et sismologique de Mayotte. http://www.ipgp.fr/sites/default/files/ipgp_revosima_bull_20221107.pdf.

Richter, C. F. (1935). An instrumental earthquake magnitude scale. *Bull. Seismol. Soc. Am.*, 25(1), 1–32.

Rinnert, E., Lebas, E., Jorry, S., Feuillet, N., Thinon, I., and Fouquet, Y. (2019). MAYOBS. https://doi.org/10.18142/291.

Roman, D. C. and Cashman, K. V. (2018). Top–

down precursory volcanic seismicity: implications for 'stealth' magma ascent and long-term eruption forecasting. *Front. Earth Sci.*, 6, article no. 124.

Ruppert, N. A., Prejean, S., and Hansen, R. A. (2011). Seismic swarm associated with the 2008 eruption of Kasatochi Volcano, Alaska: Earthquake locations and source parameters. *J. Geophys. Res.*, 116, article no. B00B07.

Sanjuan, B., Baltassat, J., Bezelgues, S., Brach, M., Girard, J., and Mathieu, F. (2008). Estimation du potentiel géothermique de Mayotte: Phase 2-étape 2. In *Investigations géologiques, géochimiques et géophysiques complémentaires, synthèse des résultats. Synthèse des Résultats (BRGM, 2008).*

Satriano, C., Laurent, A., Bernard, P., Grandin, R., Saurel, J. M., Lemarchand, A., Daniel, R., Jorry, S., Crawford, W. C., and Feuillet, N. (2019). Source process of the very low frequency earthquakes during the Mayotte 2018-2019 seismo-volcanic crisis. In *AGU Fall Meeting 2019.* (Abstract #V43I-0222).

Saurel, J. M., Jacques, E., Aiken, C., Lemoine, A., Retailleau, L., Lavayssière, A., Foix, O., Dofal, A., Laurent, A., Mercury, N., Crawford, W., Lemarchand, A., Daniel, R., Pelleau, P., Bès de Berc, M., Dectot, G., Bertil, D., Roullé, A., Broucke, C., Colombain, A., Jund, H., Besançon, S., Guyavarch, P., Kowalski, P., Roudaut, M., Apprioual, R., Battaglia, J., Bodihar, S., Canjamale, K., Catherine, P., Desfete, N., Doubre, C., Dretzen, R., Dumouche, T., Fernagu, P., Ferrazzini, V., Fontaine, F. R., Gaillot, A., Géli, L., Griot, C., Grunberg, M., Can Guzel, E., Hoste-Colomer, R., Lambotte, S., Lauret, F., Léger, F., Maros, E., Peltier, A., Vergne, J., Satriano, C., Tronel, F., Van der Woerd, J., Fouquet, Y., Jorry, S., Rinnert, E., Thinon, I., and Feuillet, N. (2022). Mayotte seismic crisis: building knowledge in near real-time by combining land and ocean-bottom seismometers, first results. *Geophys. J. Int.*, 228(2), 1281–1293.

Scalabrin, C., Feuillet, N., Fouquet, Y., Thinon, I., Jorry, S., Gaillot, A., Guérin, C., Komorowski, J. C., Rinnert, E., and Cathalot, C. (2021). Acoustic Plumes of the 2019 Mayotte submarine volcanic eruption. In *AGU Fall Meeting 2021.* (Oral session #V53A-05).

Schorlemmer, D., Wiemer, S., and Wyss, M. (2005). Variations in earthquake-size distribution across different stress regimes. *Nature*, 437(7058), 539–542.

SHOM (2015). SHOM. MNT Bathymétrique de façade Atlantique (Projet Homonim). https://doi.org/10.17183/MNT_ATL100m_HOMONIM_WGS84.

Sigmundsson, F., Hooper, A., Hreinsdóttir, S., Vogfjörd, K. S., Ófeigsson, B. G., Heimisson, E. R., Dumont, S., Parks, M., Spaans, K., Gudmundsson, G. B., Drouin, V., Árnadóttir, T., Jónsdóttir, K., Gudmundsson, M. T., Högnadóttir, T., Fridriksdóttir, H. M., Hensch, M., Einarsson, P., Magnússon, E., Samsonov, S., Brandsdóttir, B., White, R. S., Ágústsdóttir, T., Greenfield, T., Green, R. G., Hjartardóttir, A. R., Pedersen, R., Bennett, R. A., Geirsson, H., La Femina, P. C., Björnsson, H., Pálsson, F., Sturkell, E., Bean, C. J., Möllhoff, M., Braiden, A. K., and Eibl, E. P. (2015). Segmented lateral dyke growth in a rifting event at Bárðarbunga volcanic system, Iceland. *Nature*, 517(7533), 191–195.

Sira, C., Schlupp, A., Bontemps, M., Regis, E., and van der Woerd, J. (2018). Essaim sismique à l'est de Mayotte: Analyse pour la période du 10 mai au 15 juin 2018. Note préliminaire du BCSF-RENASS, BCSF-RENASS2018-R4.

Stamps, D. S., Kreemer, C., Fernandes, R., Rajaonarison, T. A., and Rambolamanana, G. (2021). Redefining East African rift system kinematics. *Geology*, 49(2), 150–155.

Stamps, D. S., Saria, E., and Kreemer, C. (2018). Geodetic strain rate model for the East African rift system. *Sci. Rep.*, 8(1), article no. 732.

Talandier, J., Hyvernaud, O., and Maury, R. C. (2016). Unusual seismic activity in 2011 and 2013 at the submarine volcano Rocard, Society hotspot (French Polynesia). *Geophys. Res. Lett.*, 43(9), 4247–4254.

Tarasewicz, J., White, R. S., Woods, A. W., Brandsóttir, B., and Gudmundsson, M. T. (2012). Magma mobilization by downward-propagating decompression of the Eyjafjallajökull volcanic plumbing system. *Geophys. Res. Lett.*, 39, article no. L19309.

Thinon, I., Lemoine, A., Leroy, S., Paquet, F., Berthod, C., Zaragosi, S., Famin, V., Feuillet, N., Boymond, P., Masquelet, C., Mercury, N., Scalabrin, C., Van der Woerd, J., Bernard, J., Bignon, J., Clouard, V., Doubre, C., Jacques, E., Jorry, S. J., Rolandone, F., Chamot-Rooke, N., Delescluse, M., Franke, D., Watremez, L., Bachèlery, P., Michon, L., Sauter, D., Bujan, S., Canva, A., Dassie, E., Roche, V., Ali, S., Sitti Allaouia, A. H., Deplus, C., Rad, S., and Sadeski, L. (2022). Volcanism and tectonics unveiled between the EARS and Madagascar: toward a better understanding of the geodynamics of the Comoros archipelago. *C. R. Géosci.*, 354(S2), 7–34.

Tzevahirtzian, A., Zaragosi, S., Bachèlery, P., Biscara, L., and Marchès, E. (2021). Submarine morphology of the Comoros volcanic archipelago. *Mar. Geol.*, 432, article no. 106383.

Waldhauser, F. (2001). HypoDD: A computer program to compute double-difference earthquake locations. USGS Open File Rep., 01-113.

Waldhauser, F. and Ellsworth, W. L. (2000). A double-difference earthquake location algorithm: Method and application to the northern Hayward fault. *Bull. Seism. Soc. Am.*, 90, 1353–1368.

Walter, T. R., Wang, R., Zimmer, M., Grosser, H., Lühr, B., and Ratdomopurbo, A. (2007). Volcanic activity influenced by tectonic earthquakes: Static and dynamic stress triggering at Mt. Merapi. *Geophys. Res. Lett.*, 34, article no. L05304.

Weatherall, P., Marks, K. M., Jakobsson, M., Schmitt, T., Tani, S., Arndt, J. E., Rovere, M., Chayes, D., Ferrini, V., and Wigley, R. (2015). A new digital bathymetric model of the world's oceans. *Earth Space Sci.*, 2(8), 331–345.

Wessel, P., Smith, W. H. F., Scharroo, R., Luis, J., and Wobbe, F. (2013). Generic Mapping Tools: Improved Version Released, EOS Trans. *Eos Trans. AGU*, 94(45), 409–410.

Wiemer, S. and McNutt, S. R. (1997). Variations in the frequency-magnitude distribution with depth in two volcanic areas: Mount St. Helens, Washington, and Mt. Spurr, Alaska. *Geophys. Res. Lett.*, 24(2), 189–192.

Zinke, J., Reijmer, J. J. G., and Thomassin, B. A. (2003b). Systems tracts sedimentology in the lagoon of Mayotte associated with the Holocene transgression. *Sediment. Geol.*, 160(1–3), 57–79.

Zinke, J., Reijmer, J. J. G., Thomassin, B. A., Dullo, W. C., Grootes, P. M., and Erlenkeuser, H. (2003a). Postglacial flooding history of Mayotte lagoon (Comoro archipelago, southwest Indian Ocean). *Mar. Geol.*, 194(3–4), 181–196.

*Comptes Rendus*
*Géoscience — Sciences de la Planète*
**2022**, Vol. 354, Special Issue S2, p. 137-152
https://doi.org/10.5802/crgeos.150

The Mayotte seismo-volcanic crisis of 2018-2021 in the Comoros archipelago (Mozambique channel) / *La crise sismo-volcanique de 2018-2021 de Mayotte dans l'archipel des Comores (Canal du Mozambique)*

# Exploring the link between large earthquakes and magma transport at the onset of the Mayotte volcano-seismic crisis

**Catalina Morales-Yáñez** [*, a, b], **Zacharie Duputel** [c, d] **and Luis Rivera** [a]

[a] Institut Terre et Environnement de Strasbourg, UMR7063, Université de Strasbourg/EOST, CNRS, Strasbourg, France

[b] Department of Civil Engineering, Universidad Católica de la Santísima Concepción, Concepción, Chile

[c] Observatoire Volcanologique du Piton de la Fournaise, Université de Paris, Institut de Physique du Globe de Paris, CNRS, F-75005, Paris, France

[d] Université de Paris, Institut de physique du globe de Paris, CNRS, F-75005 Paris, France

*E-mails:* catalina.morales@ucsc.cl (C. Morales-Yáñez), duputel@ipgp.fr (Z. Duputel), luis.rivera@unistra.fr (L. Rivera)

**Abstract.** The archipelago of Comoros was generally considered a moderately seismic region. However, since May 2018, unusual seismicity has been observed off the east coast of Mayotte Island. Following this increase of seismic activity, oceanographic campaigns led to the discovery of a new submarine volcano, indicating that the observed seismicity had a volcanic origin. In this study, we estimate Centroid Moment Tensor (CMT) solutions of $M_w \geq 5$ earthquakes of this sequence using 3D Green's functions and analyze their non-double-couple (non-DC) components. Consistently with previous reports, our results indicate that seismicity migrated upward in May–June 2018 with an increasing number of non-DC events. We show that non-DC components observed in our solutions and previously published catalogs cannot correspond to dike opening or closing as the observed rupture durations suggest unrealistically large magma flow rates. Given that waveforms can be relatively well explained with pure-shear sources, we postulate that non-DC components are most likely artifacts due to unmodeled shallow structural heterogeneities. Most $M_w \geq 5$ earthquakes have a strike-slip mechanism consistent with the rupture of pre-existing faults loaded by the regional stress regime and triggered by the increment of stress produced by the upward magma transfer.

**Keywords.** Mayotte, Volcano seismology, Moment tensor inversion, 3D-Green functions, Volcano-tectonic earthquakes.

*Published online: 21 October 2022, Issue date: 17 January 2023*

* Corresponding author.

## 1. Introduction

Mayotte Island is one of the four islands of the Comoros volcanic archipelago. It is located in the Indian Ocean in the Mozambique Channel between Madagascar and Africa. Mayotte Island shows marked volcanic geomorphology. Volcanism in Mayotte started about 10 to 15 My ago [Audru et al., 2010]. This behavior continued during the Quaternary, with the last volcanic eruption occurring 7000 years ago [Zinke et al., 2003]. The source of volcanic activity in Mayotte is still debated. Emerick and Duncan [1982] suggests that the origin of the archipelago is a hotspot, while Nougier et al. [1983] postulates that the volcanism corresponds to the reactivation of old and deep lithospheric fractures. Michon [2016] also rejects the idea of a hotspot and proposes that the Comoros archipelago volcanic activity can be explained by lithospheric deformation related to the southern extension of the East-African rift.

In general, the archipelago of Comoros is considered a moderately seismic region. However, since May 10, 2018, unusual intense seismicity has been observed in the east of Mayotte Island. From May 10, 2018 to July 31, 2019 almost 2000 events with local magnitude $M_L \geq 3.5$, were recorded [REVOSIMA/IPGP, 2019]. The largest earthquake occurred on May 15, 2018, with a magnitude of $M_w = 5.9$. After July 2018, the number of earthquakes decreased, showing less than a hundred earthquakes with magnitude $M_L \geq 3.5$ per month [REVOSIMA/IPGP, 2019, Saurel et al., 2022]. Although the most significant earthquakes occurred at the beginning of the crisis, the region remains active in 2021 with 141 $M_W \geq 1$ Volcano-Tectonic (VT) earthquakes located in December 2021 [REVOSIMA/IPGP, 2021]. Geodetic data recorded in Mayotte show transient displacements of approximately 17–20 cm to the east and subsidence of 8 to 15 cm from the beginning of the crisis until the end of July 2019 [Figures 5 and 6 of the Bulletin number 1; REVOSIMA/IPGP, 2019]. Very long-period events (VLP) with a dominant period of ~15 s have also been reported [Cesca et al., 2020, Lemoine et al., 2020]. An oceanographic campaign in the area led to the discovery of a new submarine volcano in May 2019, located approximately 50 km east of Mayotte, which forms a seamount of approximately 820 m height on the seafloor [Feuillet, 2019]. This campaign and later oceanographic campaigns have revealed several lava flows along with acoustic plumes in the water column. The new volcano is located at the tip of a 50-km-long ridge composed of many recent volcanic edifices, interpreted as an extensional structure within an east–west striking zone between East Africa and Madagascar [Feuillet et al., 2021, Famin et al., 2020]. Assuming that the new volcano edifice began to be built in July 2018, the mean lava flow rate is approximately 180 $m^3 \cdot s^{-1}$ (according to a survey conducted 11 months after onset of eruption [Feuillet et al., 2021]). The extruded volume of lava could be as large as 5 $km^3$ transforming it into the largest active submarine eruption ever documented [Feuillet et al., 2021].

Following the deployment of additional seismological stations both onland and offshore, two separate seismicity clusters are now identified [Saurel et al., 2022]. Most of the large $M_W \geq 5.0$ earthquakes that occurred at the beginning of the crisis were located in a distal cluster connecting deep parts of the plumbing system (at depth of 30–40 km) to the new volcanic edifice on the seafloor [Cesca et al., 2020, Feuillet et al., 2021, Saurel et al., 2022]. This initial seismic sequence was most likely associated with the migration of magma toward the surface. Later, the magnitude of earthquakes decreased progressively and the seismic activity migrated toward Mayotte island. This proximal cluster, located 10 km to the east of Mayotte, has a cylindrical shape that likely corresponds to a ring fault system below an ancient caldera structure [Feuillet et al., 2021].

In this study, we analyze the source of the VT earthquakes to constrain the spatio-temporal properties of magma migration at the onset of Mayotte volcano-seismic activity. The unusual increase of earthquake activity along with the birth of the large volcanic edifice offshore of Mayotte clearly indicate the magmatic origin of the seismic sequence. However, the relationship between the observed large ($M_w \geq 5.0$) earthquakes and the migrating magma pressure source is still elusive. In particular, several VT events in Global CMT [GCMT, Dziewonski et al., 1981, Ekström et al., 2012] and Cesca et al. [2020] catalogs present large non-double-couple (non-DC) components. These non-DC events could potentially correspond to volcanic source processes such as dike opening due to magma migration, resonance of fluid-filled cracks or even complex ruptures on ring-faults [Ekström, 1994, Chouet and Matoza, 2013, Rodríguez-Cardozo et al., 2021]. These non-DC components could also be associated with complex ruptures involving multiple tectonic subfaults or have a spurious origin and be induced by measurement errors (e.g., noise) or modeling uncertainties (e.g., inaccuracy of the Earth model). Here we focus on trying to understand to what extent these earthquakes correspond to opening/closing dykes or whether they correspond to shear faulting caused by stress transfer caused by a migrating magmatic pressure source.

With this purpose, we use long-period waveforms to invert for the source parameters of $M_w \geq 5$ earthquakes that essentially occurred during the first months of the Mayotte seismic crisis (May and June 2018). Unfortunately, few regional stations were available during this period. Hence, the inversion is based on long-period seismological observations, including body and surface waves. To mitigate the impact of lateral heterogeneities that can be particularly large for fundamental mode surface waves, we estimate the Centroid Moment Tensor (CMT) parameters using Green's functions computed for a global 3D Earth model combining S40RTS and CRUST2.0 [Ritsema et al., 2011, Bassin et al., 2000]. We compare our solutions with other studies and discuss the magma transfer at the beginning of the seismo-volcanic crisis.

## 2. Data and methods

We select events from the GCMT catalog located in the vicinity of Mayotte Island in 2018. This selection gives a total of 27 events with $M_w \geq 4.8$, occurring mostly at the beginning of the crisis (i.e. in May–June 2018). We use teleseismic and regional waveforms from stations with an epicentral distance from 0° to 90°. We use a combination of 150 channels from GEOFON [IS, GE, TT; GEOFON Data Centre, 1993], GEOSCOPE [G; Institut de Physique du Globe de Paris (IPGP) and Ecole et Observatoire des Sciences de la Terre de Strasbourg (EOST), 1982], ASL/USGS [AU, IU, IC, GT; Albuquerque Seismological Laboratory (ASL)/USGS, 1988, 1992, 1993], IRIS/IDA [II; Scripps Institution of Oceanography, 1986], MedNet [MN; MedNet Project Partner Institutions, 1990], RESIF [FR, RD; RESIF, 1962, 2018], NARS [NR; Utrecht University (UU Netherlands), 1983], Karthala [KA; Institut de Physique du Globe de Paris (IPGP), 2006] as well as station GULU belonging to a temporary network installed in Uganda to investigate plume-lithosphere interactions [XW; Nyblade, 2017]. Waveform data has been validated at long period by comparing with synthetics from large teleseismic earthquakes. We do not use the YTMZ strong motion station from the French RESIF-RAP network, which was the only station on Mayotte Island at the beginning, due to large errors in the internal clock during the studied time-period.

For each earthquake, we manually reject noisy records and data with dubious metadata. After data screening, moment tensor solutions are obtained using 23 channels in average. The time window used for the waveform inversion starts at the P-wave arrival and includes the first group of surface waves (R1 and L1). For specific stations, we manually change the time window duration to exclude clipped signals in the inversion. A causal bandpass Butterworth filter of order 4 is applied to the data. To mitigate long-period seismic noise, the filter corner periods are adapted as a function of the earthquake magnitude and the epicentral distance of the stations (see Tables 1 and 2). Using the resulting long-period waveforms, we then perform point source inversions to invert for CMT parameters (i.e., moment tensor elements, rupture duration, and centroid location in time and space). We use a modified version of the W-phase inversion method by Duputel and Rivera [2019]. This algorithm relies on a grid-search approach to find the point-source mechanism, time and location that minimizes the root mean square (RMS) waveform misfit. In this study, we assume three different levels of generality for the moment tensor: (1) Full moment tensor (FMT; i.e., six independent elements of the symmetric moment tensor), (2) Deviatoric moment tensor (DMT; i.e., assuming no net volume change during the rupture) and (3) Double-Couple (DC; i.e., assuming a pure shear rupture). While FMT and DMT inversions are linear for a given centroid location, DC solutions are estimated by grid-searching for strike, dip and rake angles corresponding to the minimum RMS misfit. For the sake of consistency, FMT and DC inversions are performed using the same dataset, time shift ($T_s$) and centroid location as those estimated for the DMT solution.

To account for large-scale 3D heterogeneities, we compute Green's functions using SPECFEM3D_GLOBE [Komatitsch et al., 2015] for a global 3D Earth model composed of S40RTS

**Table 1.** Bandpass filter used for records with epicentral distance larger than 4°

| Magnitude | Bandpass |
|---|---|
| $5.3 \leq M_w \leq 5.9$ | 50–150 s |
| $M_w < 5.3$ | 50–100 s |

With the exception of earthquakes 2018-06-04 21:20, $M_w = 5.1$ and 2018-06-01 07:14, $M_w = 4.7$ for which we use 50–150 s and 30–80 s passbands respectively.

**Table 2.** List of events for which an ad-hoc bandpass filter is applied for stations at epicentral distances smaller than 4°

| Event | Magnitude | Bandpass |
|---|---|---|
| 2018-05-15 15:48 | 5.9 | 50–150 s |
| 2018-06-12 17:17 | 5.4 | 50–150 s |
| 2018-06-25 17:41 | 5.3 | 50–150 s |
| 2018-06-27 06:40 | 5.2 | 50–100 s |
| 2018-06-18 13:43 | 5.1 | 50–100 s |
| 2018-06-23 19:45 | 5.0 | 50–100 s |
| 2018-06-05 23:02 | 5.1 | 30–80 s |
| 2018-05-30 05:54 | 5.1 | 30–80 s |
| 2018-05-25 09:32 | 5.0 | 30–80 s |
| 2018-06-07 13:06 | 5.0 | 30–50 s |
| 2018-06-10 13:04 | 4.8 | 30–50 s |

[Ritsema et al., 2011] and CRUST2.0 [Bassin et al., 2000]. Green's functions are calculated for various source locations with depth ranging from 5.0 to 35.0 km (each 2.5 km), latitude ranging from 13.03° S to 12.7° S and longitudes ranging from 45.48° E to 45.83° E (each 0.025°). The definition of this grid was guided by the earthquake centroid locations provided by the GCMT catalog and preliminary tests.

Once we obtain the moment tensor parameters we perform a decomposition of the moment into the double couple (DC), isotropic (ISO), and compensated linear vector dipole (CLVD). For this, we follow the definition of Vavryčuk [2015],

$$M_{\mathrm{ISO}} = \tfrac{1}{3}(M_1 + M_2 + M_3) \tag{1}$$

$$M_{\mathrm{CLVD}} = \tfrac{2}{3}(M_1 + M_3 - 2M_2) \tag{2}$$

$$M_{\mathrm{DC}} = \tfrac{1}{2}(M_1 - M_3 - |M_1 + M_3 - 2M_2|) \quad (M_{\mathrm{DC}} \geq 0) \tag{3}$$

where, $M_1 \geq M_2 \geq M_3$ correspond to the eigenvalues of the moment tensor. Then to measure the relative contribution of each component, we can write,

$$\begin{bmatrix} C_{\mathrm{ISO}} \\ C_{\mathrm{CLVD}} \\ C_{\mathrm{DC}} \end{bmatrix} = \frac{1}{M} \begin{bmatrix} M_{\mathrm{ISO}} \\ M_{\mathrm{CLVD}} \\ M_{\mathrm{DC}} \end{bmatrix} \tag{4}$$

where $M = |M_{\mathrm{ISO}}| + |M_{\mathrm{CLVD}}| + M_{\mathrm{DC}}$ and $|C_{\mathrm{ISO}}| + |C_{\mathrm{CLVD}}| + C_{\mathrm{DC}} = 1$. This relation allows to define the contribution of each component.

## 3. Earthquake migration uncovering a deep magma transfer in May–June 2018

The spatio-temporal distribution of earthquakes after CMT inversion is shown in Figure 1. Events are roughly aligned along a NW–SE structure with deeper earthquakes at the NW and shallower events at the SE (Figure 1a). Although our centroid locations are globally consistent with other catalogs (see comparison with GCMT and Cesca et al. [2020] in Supplementary Figure 1), there are some differences that result from the use of different Earth models, frequency bands and choice of seismological stations. For example, Cesca et al. [2020] use 1D velocity models and includes the local strong-motion station YTMZ (mitigating clock drifting issues by inverting for timeshifts at each station). In contrast, our study is based on a 3D global velocity model and does not include YTMZ. As shown in Figure 1b, the seismic events migrate upward along this NW–SE structure from a depth of ~35 km toward the surface between mid-May and early June 2018. This seismicity migration is a robust feature that is clearly visible in multiple catalogs (GCMT, Cesca et al. [2020] and Lemoine et al. [2020]; cf., Supplementary Figure 1). These migrating earthquakes have been interpreted as the markers of a deep magma transfer at the origin of the new volcano evidenced by Feuillet [2019]. Magma likely originated from one or multiple reservoirs or mushes located at depth ranging from 25 and 60 km depending on the estimates [Lemoine et al., 2020, Cesca et al., 2020, Feuillet et al., 2021]. The absolute centroid depth of earthquakes might depends on the assumed local velocity structure, which is poorly known in the vicinity of Mayotte [Cesca et al., 2020, Dofal et al., 2021].

Earthquake migration associated with magma transfer has been observed in many volcanic areas

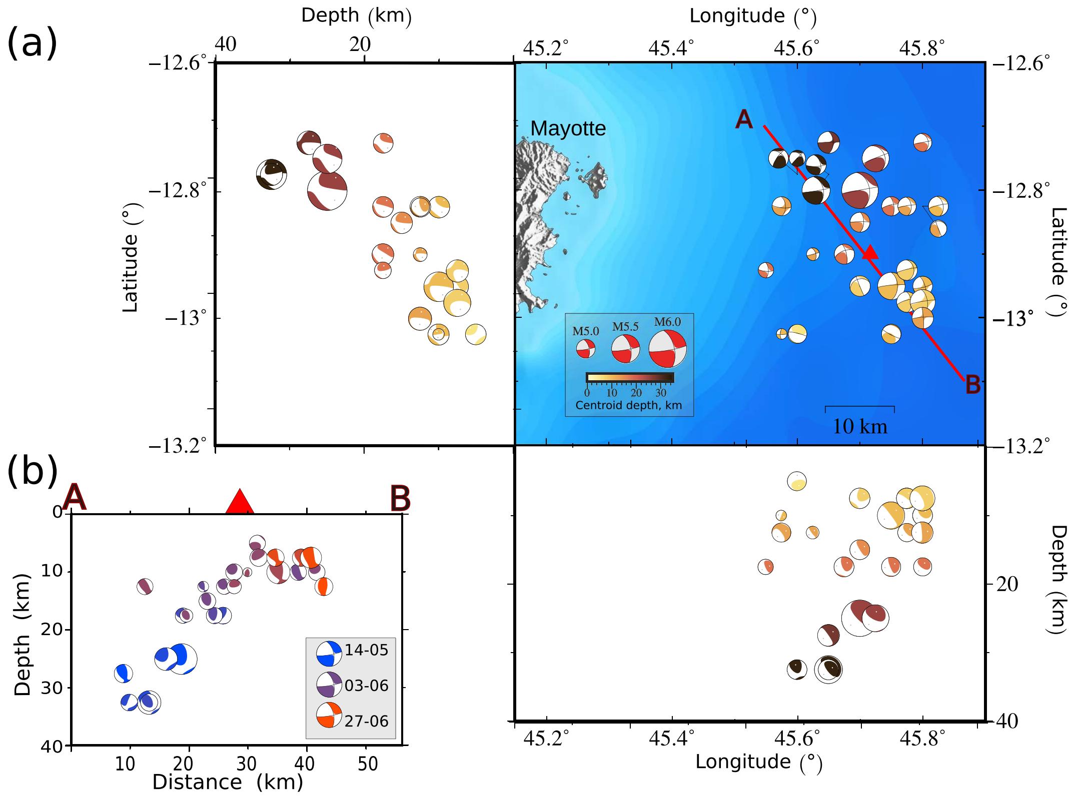


**Figure 1.** Spatial distribution of moment tensor solutions for the deviatoric inversion. (a) The (lower hemisphere) beachballs are positioned on the map at the estimated centroid locations. Colors correspond to the centroid depth. The red triangle indicates the position of the volcano [REVOSIMA/IPGP, 2019]. The two side panels are NS and EW vertical cross sections including beachball visualized from the W and S respectively (back hemisphere beachballs). (b) Vertical A–B cross section. Back hemisphere beachballs (visualized from the SW) are colored according to the event date. Color scale starts on May 14, 2018 (red) and ends on June 27, 2018 (blue). The position of the volcano at the free surface is indicated with a red triangle.

such as the Bároarbunga volcanic system in Iceland [Sigmundsson et al., 2015, Ágústsdóttir et al., 2016], the Kilauea volcanoes in Hawaii [Neal et al., 2019, Lengliné et al., 2021] and the Piton de la Fournaise volcano in La Réunion [Battaglia et al., 2005, Lengliné et al., 2016, Duputel et al., 2019]. However, as noted by Cesca et al. [2020] and Feuillet et al. [2021], deep crustal earthquakes associated with deep magma transfer is less common. Such seismicity at depths larger than 10 km has been previously observed at Lo'ihi and Kilauea volcanoes in Hawaii [Wolfe et al., 2003, Merz et al., 2019]. Deeper seismicity associated with volcano eruption has also been reported in La Palma [Torres-González et al., 2020], with event magnitudes ranging from 0.9 to 2.7 and a depth range of 12 to 33 km, which is comparable to what is observed offshore of Mayotte.

The occurrence of such an intense upward migrating seismicity along with the birth of a new volcano clearly indicate that the earthquakes are caused by a deep magma transfer offshore Mayotte. This sequence is striking for the occurrence of several events of relatively large magnitude ($M_w \geq 5$), which is uncommon in an area formerly considered to be a moderately seismic region. To further analyze the relationship between earthquakes and the migrating magma, our moment tensor estimates are discussed in the next two sections.

## 4. Moment tensor solutions consistent with regional stresses

Moment tensor solutions together with centroid depth, station coverage, and the percentage of CLVD, ISO and DC components are listed in Figures 2 and 3. For each earthquake, deviatoric moment tensor (DMT), full moment tensor (FMT) and double couple (DC) solutions are depicted in red, gray and blue, respectively. DMT and FMT solutions are very similar for most earthquakes, with only minor differences. Some shallow events are associated with large non-DC components, hence with significant differences between DC and moment tensor solutions (i.e., FMT and DMT). This is evidenced in the Hudson diagram [Hudson et al., 1989] presented in Figure 4(a), showing that several earthquakes have a non-negligible CLVD and ISO components. The origin of such large non-DC components is discussed in Section 5.

The dominant strike-slip regime is obvious: almost all earthquakes present a right-lateral strike-slip focal mechanism with a relatively consistent strike angle. This is also visible in Figure 4(b), with P and T axes showing NE–SW extension and NW–SE compression, which is similar to the GCMT catalog and Cesca et al. [2020]. Even earthquakes with a large non-DC component are consistent with this orientation of the principal axes. This observation is in good agreement with regional GNSS observations in the region of the Comoros archipelago [Stamps et al., 2018, Lemoine et al., 2020]. Using a combined stress inversion of focal mechanisms, deformation structures and intrusions, Famin et al. [2020] found that the Comoros archipelago experiences a dextral shear deformation with maximum compressive horizontal stress in the NW–SE direction and NE–SW extension. More locally, earthquakes offshore eastern Mayotte are located beneath a volcanic ridge that exhibits multiple NE–SW extensional features consistent with the direction of our T-axes [Feuillet et al., 2021].

VT earthquakes are generally considered to be brittle ruptures within the volcanic edifice triggered by stress perturbations induced by magma activity. However, different relationships have been observed between VT earthquakes and magma intrusions. In particular, Roman and Cashman [2006] showed that basaltic volcanoes are often associated with migrating earthquakes ahead of the dike tip with focal mechanism P-axes parallel to the regional maximum compressive stress [i.e., dike propagation model; Ukawa and Tsukahara, 1996], while other sequences on strato-volcanoes depict random hypocenter distributions around inflating dikes with focal mechanisms presenting P-axes rotated ~90° from the maximum compressive regional stress [i.e., dike inflation model; Roman, 2005]. These differences are likely related to a number of factors including the existence of pre-existing faults in the vicinity of the dike, the regional stress-field and the properties of the ascending magma.

Observations at the onset of the Mayotte volcano-seismic crisis with migrating seismicity associated with focal mechanisms parallel to regional stresses are more consistent with the dike propagation model proposed by Ukawa and Tsukahara [1996]. The observation of basanitic pillow lava flows following the eruption [reported by Feuillet et al., 2021] thus confirms the idea that VT seismicity at Mayotte reflect stress changes induced by dike propagation. Moreover, given their large magnitudes ($M_w \geq 5.0$), the earthquakes observed at the onset of the sequence probably do not correspond to ruptures of previously intact rocks and rather occur on pre-existing faults that are already loaded by regional stresses. This agrees with stress calculations of Rubin and Gillard [1998], showing that VT events larger than magnitude 1.0 likely occur on pre-existing structures already close to failure. This is also confirmed by observations on volcanoes indicating that earthquakes triggered by dike migration usually occur on pre-existing fault systems [Gargani et al., 2006, Lengliné et al., 2016, Duputel et al., 2019].

## 5. Non-DC component of shallow earthquakes

As pointed out in the previous section, several VT earthquakes are associated with a large non-DC component during the Mayotte sequence (see Figures 2–4). As shown in Figure 5(a), most of earthquakes with large non-DC components (>50%) correspond to events shallower than 15 km. We do not observe any correlation of non-DC components with the event magnitudes. Similar non-DC components have also been reported by Cesca et al. [2020]. To assess the impact of such large non-DC component on waveform fits, we evaluate the ratio of RMS misfits computed for the FMT and DC solutions. Results shown in Figure 5(b) indicate a relatively moderate

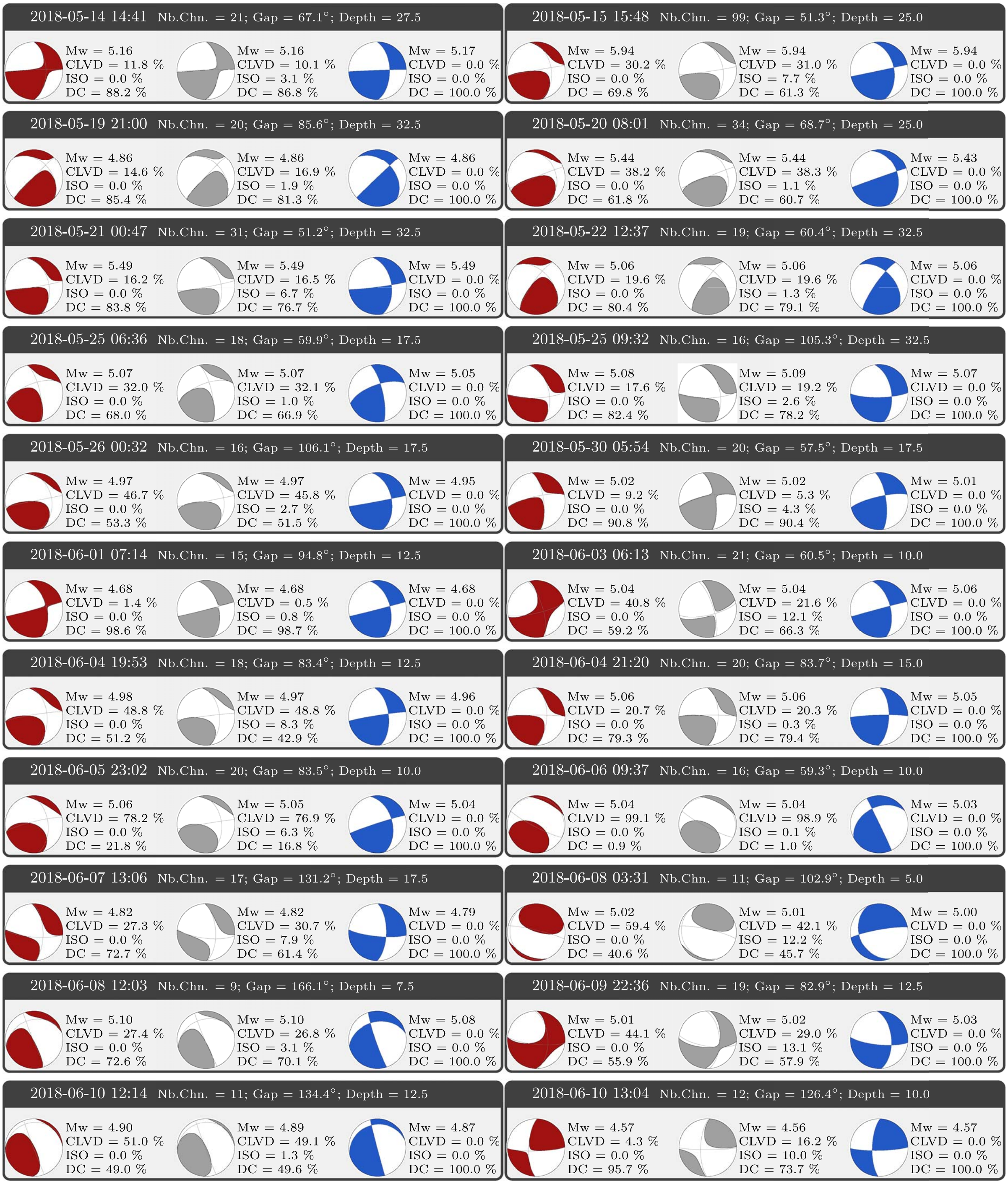


**Figure 2.** Moment tensor solutions for the events analyzed in this study. In red, gray and blue are the beachball obtained from the deviatoric moment tensor (DMT), full moment tensor (FMT), and double couple (DC) inversion, respectively. For each earthquake we present the number of channels, the azimuthal gap of the station coverage, depth and the beachball along with the corresponding CLVD, ISO and DC percentage.

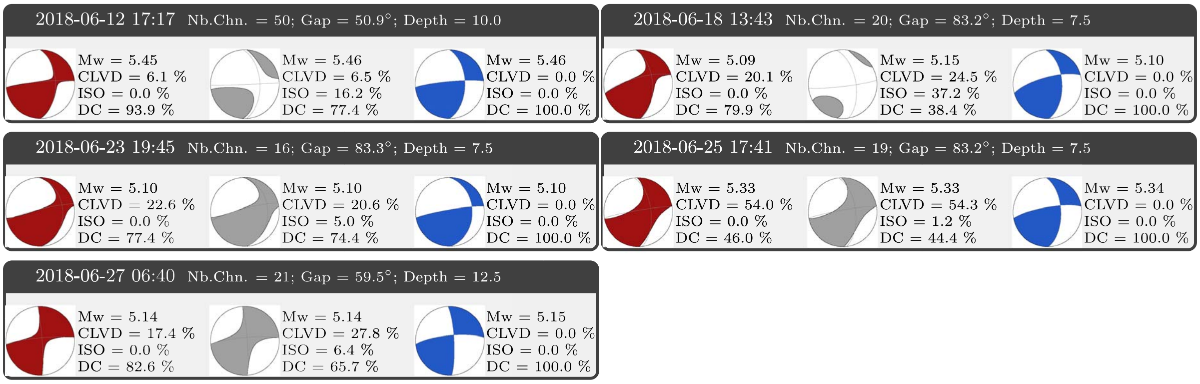


**Figure 3.** Moment tensor solutions for the events analyzed in this study. In red, gray and blue are the beachball obtained from the deviatoric moment tensor (DMT), full moment tensor (FMT), and double couple (DC) inversion, respectively. For each earthquake we present the number of channels, the azimuthal gap of the station coverage, depth and the beachball along with the corresponding CLVD, ISO and DC percentage.

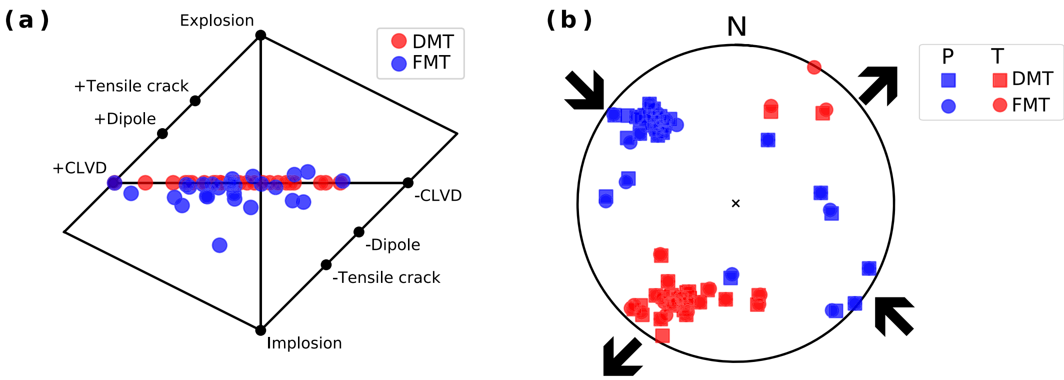


**Figure 4.** Hudson diagram and tension and pressure axis for each earthquake. (a) Hudson diagram Hudson et al. [1989]. Blue and red indicate inversion solutions for FMT and DMT, respectively. (b) Pressure axes (P) are represented in blue. Tension (T) axes are represented in red. Circles and square indicate inversion solutions for FMT and DMT, respectively.

overall reduction of data misfit when inverting for the full moment tensor (i.e., FMT) compared to a DC parametrization. Here, we recall that FMT and DC solutions are inverted independently (i.e., DC parameters are not estimated by decomposing the FMT solution). Unsurprisingly, the reduction of data misfit increases as a function of the non-DC percentage, showing that a DC source cannot fit data as well as a FMT solution for earthquakes with a large non-DC component. This is illustrated in Figure 6 showing the waveform fit of FMT and DC solutions for the earthquake with the largest non-DC component (event ID 2018-06-05 T23:02 in Figure 2). FMT and DMT solutions being very similar for this earthquake, we only show synthetics of the FMT solution. The deterioration of waveform fit for the DC solution is visible at multiple stations (see ABPO, FOMA, LODK and ATD in Figure 6).

Different factors could explain the large non-DC component of earthquakes: one possibility could be crack opening/closure related to volcanic activity (e.g., caldera collapse, dike inflation/deflation, perturbation of magma circulation, etc.). Another possibility could be related to mismodeling of a complex source with a single point source model. Large non-DC components related to dike inflation/deflation

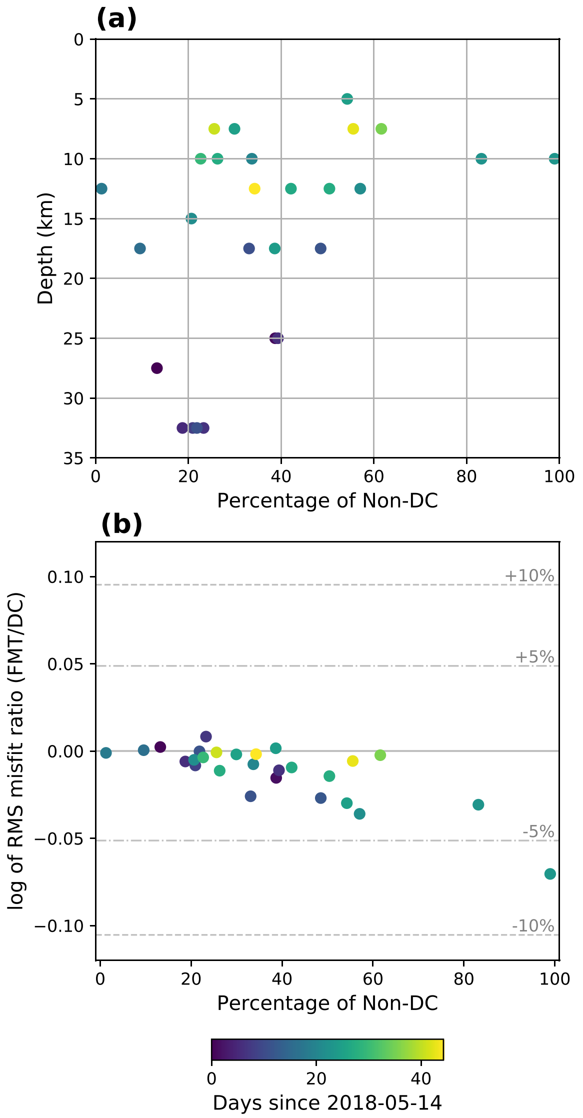


**Figure 5.** Percentage of non-DC components compared to the depth of the events and waveform misfit. (a) Percentage of non-DC as a function of the depth of the events obtained by a full moment tensor inversion. (b) The logarithm of the root means square (RMS) waveform misfit ratio between the solutions obtained with the full moment tensor and the double couple inversion. The colors indicate the days since 2018-05-14.

have been previously reported in Iceland [Hrubcová et al., 2021] for smaller magnitude VT earthquakes ($1 < M \leq 4$). Rodríguez-Cardozo et al. [2021] reported 230 VT earthquakes from $3.7 \leq M_w < 5.5$ and depths between 1–8 km, some of them with considerable non-DC components in the collapse of the Bárðarbunga caldera, Iceland. In particular, they observed that the CLVD component increases with the magnitude, relating it to slip on a curved fault and to the caldera collapse.

However, given the moderate magnitude of earthquakes that we investigate, and the long-period waveforms used in the inversion, the effect of source complexity seems quite unlikely to be the origin of misfit. Finally, there is the possibility of a spurious origin (e.g., contamination by ambient noise or inaccuracies in the Earth model).

In the following, we explore the possibility that the non-DC events observed offshore Mayotte could correspond to the combination of strike-slip motion and dike opening/closing associated with magma propagation. From the equations provided by Dufumier and Rivera [1997, appendix A], we write the surface area of an opening crack as:

$$S = \frac{3M_2^D}{2\mu\Delta u} \tag{5}$$

where $M_2^D$ is the second largest eigenvalue of the deviatoric moment tensor (i.e., $M_2^D = M_2 - (M_1 + M_2 + M_3)/3$, $\mu$ is the shear modulus, and $\Delta u$ is the opening of the dike. If we assume a square dike of characteristic length $L$, we can write

$$L = \sqrt{\frac{3M_2^D}{2\mu\Delta u}}. \tag{6}$$

Assuming that magma is migrating within the opening/closing dike at the timescale of the earthquake source duration, we estimate the average velocity of the migrating magma as:

$$V = \sqrt{\frac{3M_2^D}{2\mu\Delta u T_r^2}} \tag{7}$$

where $T_r$ is the source duration. We can also estimate the magma flow rate $F$ as:

$$F = V L \Delta u \tag{8}$$

$$F = \frac{3M_2^D}{2\mu T_r}. \tag{9}$$

We then estimate the average magma propagation velocity for each event to evaluate if the non-DC component could be related to fluid transport. We consider dike widths ($\Delta u$) ranging from 0.5 m

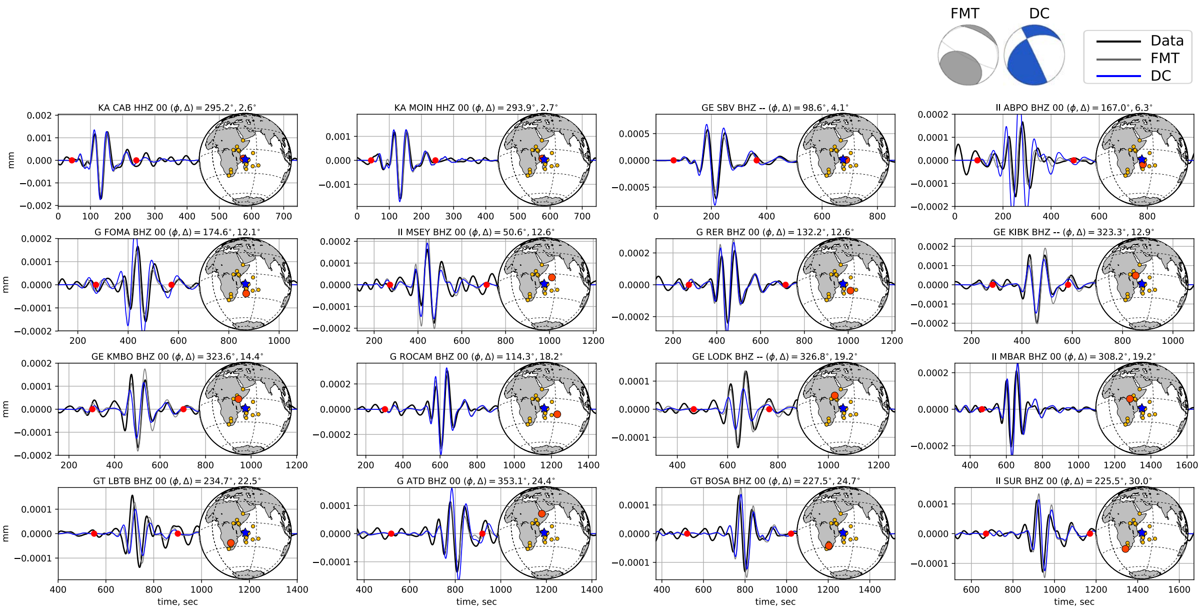


**Figure 6.** Waveform fit for event 2018-06-06 09:37. Observations (black) are compared with predictions created using the same centroid location but different moment tensor solutions. Gray and blue lines correspond to synthetics computed using the full moment tensor (FMT) and double couple (DC) solutions represented at the top of the figure, respectively.

to 10 m. The former value corresponds to a width typically observed on basaltic volcanoes, and the latter is an extremely large value to get a lower bound estimate of the velocity [Rubin, 1995]. For the FMT solutions obtained in this study, we estimate source duration assuming $T_r = 2t_s$, where $t_s$ is the time-shift between the origin time and the centroid time. Centroid time-shift has been proven to provide reliable rupture duration estimates that are less affected by long tails in moment rate functions and by arbitrary modeling choices [Duputel et al., 2013, Meier et al., 2017]. For solutions provided by Cesca et al. [2020], we assume the scaling relation $T_r = 0.6 \times 10^{-8}\ M_0^{1/3}$ [Duputel et al., 2012] since no centroid times are inverted for this catalog. Figure 7 shows the magma migration velocities estimated using (7) with both the Cesca et al. [2020] catalog and our solutions. Estimated velocities range from 44 m/s to 1565 m/s and from 9.9 m/s to 350 m/s for dike openings of 0.5 m and 10 m, respectively. Even considering dike opening of 10 m, most non-DC events are associated with unreasonably large magma migration speeds greater than 100 m/s. For comparison, a rough estimate of the upward migration speed of earthquakes suggest that the dike propagated at an average velocity of 0.05 m/s between 2018/05/19 and 2018/06/08 (see Supplementary Figure 2). To remove any dependency on the dike width, we also estimate the magma flow rate in Figure 8 using (9). The estimated flow rates are globally much larger than the average flow rate of 180 $m^3 \cdot s^{-1}$ estimated by Feuillet et al. [2021].

Shallow moderate magnitude ($M \geq 5$) events with significant non-DC components have been previously observed around active volcanoes. Such earthquakes have been associated with caldera collapses driven by pressure variations in magma reservoirs [e.g., Ekström, 1994, Shuler et al., 2013, Duputel et al., 2019], migration of hydrothermal fluids, perturbation of magma and circulation of gases through shallow conduits [e.g., Chouet and Matoza, 2013], resonance of the fluids [e.g., Maeda and Kumagai, 2017] or complexities in the source [e.g., curved fault slip Rodríguez-Cardozo et al., 2021]. During caldera collapse events, we expect to have many focal mechanisms with vertical T or P axes [Shuler et al., 2013, Duputel and Rivera, 2019]. Even if strike-slip earthquakes occasionally occur on ring fault systems [cf., Rodríguez-Cardozo et al., 2021], there is currently no

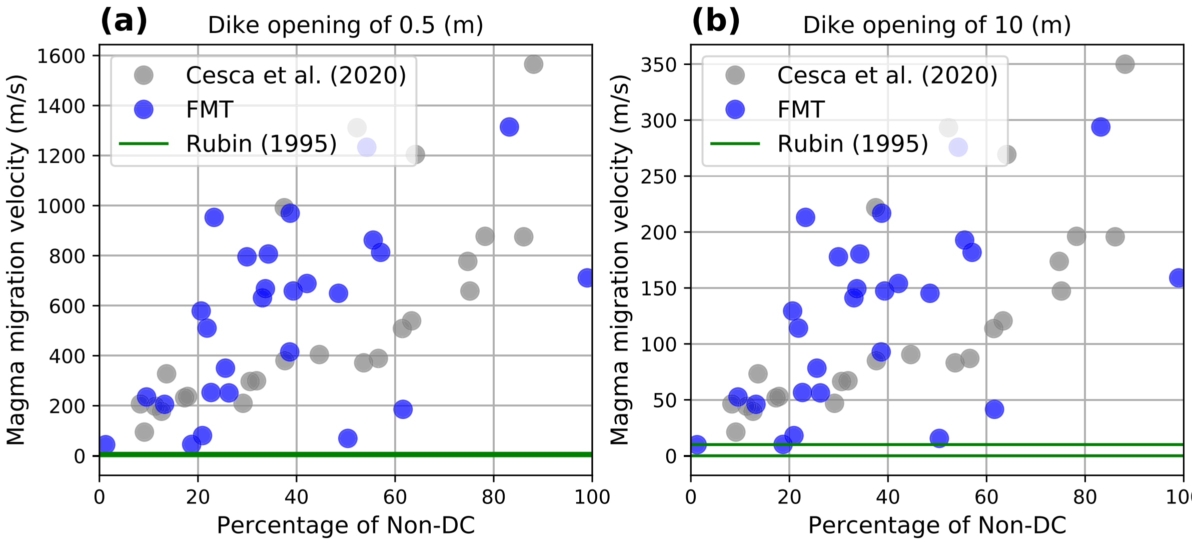


**Figure 7.** Magma migration velocity of the fluid as a function of the non-DC percentage. Gray and blue circles represent the solutions obtained by Cesca et al. [2020] and the present study, respectively. Green lines correspond a propagation velocities for mantle-derived dikes 0.01 and 10 m/s [Rubin, 1995]. We consider dike widths ($\Delta u$) of 0.5 m (a) and 10 m (b).

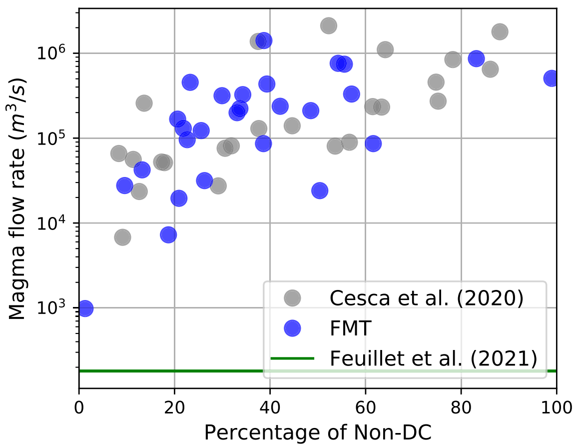


**Figure 8.** Magma flow rate as a function of the non-DC percentage. Gray and blue circles represent the solutions obtained by [Cesca et al., 2020] and the present study, respectively. Green lines correspond to the estimate magma flow rate of Mayotte eruption 180 $m^3/s$ [Feuillet et al., 2021].

indication of any caldera collapse at the location of the distal seismic swarm. There are indications of a resonating magma body (at the origin of VLP signals) with a structure possibly outlining a caldera, but this structure is located closer to Mayotte, in the vicinity of the so-called proximal swarm [Feuillet et al., 2021, Cesca et al., 2020]. Dike resonance also appears unlikely as these phenomena are more typically associated with very long-period signals with marked peak frequencies, while earthquakes studied here have a frequency content similar to regular VT earthquakes.

As mentioned above, large non-DC components can also be associated with spurious origin such as ambient noise or inaccuracies in the Earth model [Šílený, 2009, Kumar et al., 2015]. This seems to be the case in Mayotte as DC solutions fit that data almost as well as FMT solutions (cf., Figures 5 and 6); suggesting that the studied earthquakes correspond to pure-shear ruptures. Moreover, as shown in Supplementary Figure 3, the non-DC part of moment tensors often differs between catalogs. In particular, Cesca et al. [2020] suggests positive isotropic components and negative CLVD for most events while our catalog is dominated by negative isotropic components and positive CLVD. Such variability among catalogs is consistent with bootstrapping results of Cesca et al. [2020], showing that the non-DC components are generally poorly resolved. Uncertainty in the moment tensor solutions increases at shallow depth [Morales-Yáñez et al., 2020, Fukao et al., 2018, Sandanbata et al., 2021]. The enhanced non-DC component of shallow earthquakes could be an artifact due to the mismodeling of the crustal structure in the source region. Depending on the velocity models, the Moho depth in the Mayotte area varies from 5 to 30 km [e.g., Coffin et al., 1986, Laske et al., 2013, Bassin et al., 2000, Pratt et al., 2017, Cesca et al., 2020]. While our 3D Earth model is based on CRUST2.0, which assumes an oceanic crust of thickness 12.5 km, Dofal et al. [2021] proposed recently that the region corresponds to a 17 km-thick continental crust overlying a magmatic underplated layer defining a second interface at a depth of ~27 km.

## 6. Conclusion

Characterizing the source of earthquakes off the east coast of Mayotte is essential to understand the link between magma transport and seismic faulting in the region. Consistently with other catalogs, our CMT solutions indicate an upward migration of seismic events at the onset of the Mayotte seismo-volcanic crisis. Although the region remains seismically active as of January 2022, the largest earthquakes of the sequence with magnitude $M_w \geq 5.0$ occurred during this initial phase in May–June 2018. Most earthquakes have a strike-slip mechanism in agreement with regional stresses in the Comoros archipelago. Our catalog along with solutions by Cesca et al. [2020] and GCMT include some shallow events associated with large non-DC components that could have been interpreted as opening or closing of sub-vertical dikes. However, our analysis indicate that these large non-DC components are probably not physical (i.e., not related to dike opening/closing) and are rather artifacts induced by mismodeling due to inaccuracies in the shallow velocity structure. The migration of earthquakes along with the consistency of focal mechanism with regional stresses suggest that seismic events are triggered by stress perturbations induced by the upward propagation of magma. Given their large magnitudes (i.e., up to $M_w = 5.9$), the triggered seismic events likely occur on pre-existing strike-slip faults already loaded by ambient stresses. This volcano-seismic sequence thus demonstrate how a magma intrusion can induce relatively large earthquakes even in a moderately seismic region.

## Conflicts of interest

The authors declare no competing financial interest.

## Dedication

The manuscript was written through contributions of all authors. All authors have given approval to the final version of the manuscript.

## Acknowledgments

We thank two anonymous reviewers and the editors for their useful comments during the revision process. Dr. Lise Retailleau comments also helped us to improve the manuscript. This work was supported by the Initiative d'Excellence (IDEX) funding framework (Université de Strasbourg). This project has also received funding from the European Research Council (ERC, under the European Union's Horizon 2020 research and innovation program under grant agreement No. 805256) and from Agence Nationale de la Recherche (project ANR-17-ERC3-0010). CMY acknowledges funding from ANID/FONDECYT 3220307 and the "anillo precursor project" ANID PIA Anillo ACT192169. We wish to thank the network and station operators for their commitment to collect high-quality seismic data and the Computational Infrastructure for Geodynamics (http://geodynamics.org) which is funded by the National Science Foundation under awards EAR-0949446 and EAR-1550901.

## Supplementary data

Supporting information for this article is available on the journal's website under https://doi.org/10.5802/crgeos.150 or from the author.

## References

Ágústsdóttir, T., Woods, J., Greenfield, T., Green, R. G., White, R. S., Winder, T., Brandsdóttir, B., Steinthórsson, S., and Soosalu, H. (2016). Strike-slip faulting during the 2014 Bároarbunga-holuhraun dike intrusion, central Iceland. *Geophys. Res. Lett.*, 43(4), 1495–1503.

Albuquerque Seismological Laboratory (ASL)/USGS (1988). Global Seismograph Network (GSN—IRIS/USGS). International Federation of Digital Seismograph Networks.

Albuquerque Seismological Laboratory (ASL)/USGS (1992). New China Digital Seismograph Network. International Federation of Digital Seismograph Networks.

Albuquerque Seismological Laboratory (ASL)/USGS (1993). Global Telemetered Seismograph Network (USAF/USGS). International Federation of Digital Seismograph Networks.

Audru, J.-C., Bitri, A., Desprats, J.-F., Dominique, P., Eucher, G., Hachim, S., Jossot, O., Mathon, C., Nédellec, J.-L., Sabourault, P., Sedan, O., Stollsteiner, P., and Terrier-Sedan, M. (2010). Major natural hazards in a tropical volcanic island: A review for Mayotte Island, Comoros archipelago, Indian Ocean. *Eng. Geol.*, 114(3), 364–381.

Bassin, C., Laske, G., and Masters, G. (2000). The current limits of resolution for surface wave tomography in North America. *EOS Trans. AGU*, 81, article no. F897. https://igppweb.ucsd.edu/~gabi/crust2.html.

Battaglia, J., Ferrazzini, V., Staudacher, T., Aki, K., and Cheminée, J.-L. (2005). Pre-eruptive migration of earthquakes at the Piton de la Fournaise volcano (Réunion Island). *Geophys. J. Int.*, 161(2), 549–558.

Cesca, S., Letort, J., Razafindrakoto, H. N. T., Heimann, S., Rivalta, E., Isken, M. P., Nikkhoo, M., Passarelli, L., Petersen, G. M., Cotton, F., and Dahm, T. (2020). Drainage of a deep magma reservoir near Mayotte inferred from seismicity and deformation. *Nat. Geosci.*, 13, 87–93.

Chouet, B. A. and Matoza, R. S. (2013). A multi-decadal view of seismic methods for detecting precursors of magma movement and eruption. *J. Volcanol. Geotherm. Res.*, 252, 108–175.

Coffin, M. F., Rabinowitz, P. D., and Houtz, R. E. (1986). Crustal structure in the Western Somali Basin. *Geophys. J. Int.*, 86(2), 331–369.

Dofal, A., Fontaine, F., Michon, L., Barruol, G., and Tkalcic, H. (2021). Nature of the crust beneath the islands of the mozambique channel: Constraints from receiver functions. *J. Afr. Earth Sci.*, 184, article no. 104379.

Dufumier, H. and Rivera, L. (1997). On the resolution of the isotropic component in moment tensor inversion. *Geophys. J. Int.*, 131(3), 595–606.

Duputel, Z., Lengliné, O., and Ferrazzini, V. (2019). Constraining spatiotemporal characteristics of magma migration at Piton de la Fournaise volcano from pre-eruptive seismicity. *Geophys. Res. Lett.*, 46(1), 119–127.

Duputel, Z. and Rivera, L. (2019). The 2007 caldera collapse of Piton de la Fournaise volcano: Source process from very-long-period seismic signals. *Earth Planet. Sci. Lett.*, 527, article no. 115786.

Duputel, Z., Rivera, L., Kanamori, H., and Hayes, G. (2012). W phase source inversion for moderate to large earthquakes (1990–2010). *Geophys. J. Int.*, 189(2), 1125–1147.

Duputel, Z., Tsai, V. C., Rivera, L., and Kanamori, H. (2013). Using centroid time-delays to characterize source durations and identify earthquakes with unique characteristics. *Earth Planet. Sci. Lett.*, 374, 92–100. https://www.sciencedirect.com/science/article/pii/S0012821X13002690.

Dziewonski, A. M., Chou, T.-A., and Woodhouse, J. H. (1981). Determination of earthquake source parameters from waveform data for studies of global and regional seismicity. *J. Geophys. Res. Solid Earth*, 86(B4), 2825–2852.

Ekström, G. (1994). Anomalous earthquakes on volcano ring-fault structures. *Earth Planet. Sci. Lett.*, 128(3), 707–712.

Ekström, G., Nettles, M., and Dziewoński, A. (2012). The global cmt project 2004–2010: Centroid-moment tensors for 13,017 earthquakes. *Phys. Earth Planet. Inter.*, 200–201, 1–9.

Emerick, C. and Duncan, R. (1982). Age progressive volcanism in the comores archipelago, western indian ocean and implications for Somali plate tectonics. *Earth Planet. Sci. Lett.*, 60(3), 415–428.

Famin, V., Michon, L., and Bourhane, A. (2020). The comoros archipelago: a right-lateral transform boundary between the Somalia and Lwandle plates. *Tectonophysics*, 789, article no. 228539.

Feuillet, N. (2019). MAYOBS1 French Oceanographic Cruise, RV Marion Dufresne SISMER Database (French Oceanographic Fleet, 2019).

Feuillet, N., Jorry, S., Crawford, W. C., Deplus, C., Thinon, I., Jacques, E., Saurel, J. M., Lemoine, A., Paquet, F., Satriano, C., Aiken, C., Foix, O., Kowalski, P., Laurent, A., Rinnert, E., Cathalot, C., Donval, J.-P., Guyader, V., Gaillot, A., Scalabrin, C., Moreira, M., Peltier, A., Beauducel, F., Grandin, R., Ballu, V., Daniel, R., Pelleau, P., Gomez, J., Besançon, S., Geli, L., Bernard, P., Bachelery, P., Fouquet, Y., Bertil, D., Lemarchand, A., and Van der Woerd, J. (2021). Birth of a large volcanic edifice offshore Mayotte via lithosphere-scale dyke intrusion. *Nat. Geosci.*, 14, 787–795.

Fukao, Y., Sandanbata, O., Sugioka, H., Ito, A., Shiobara, A., Watada, S., and Satake, K. (2018). Mechanism of the 2015 volcanic tsunami earthquake near Torishima, Japan. *Sci. Adv.*, 4(4), article no. eaao0219.

Gargani, J., Geoffroy, L., Gac, S., and Cravoisier, S. (2006). Fault slip and coulomb stress variations around a pressured magma reservoir: consequences on seismicity and magma intrusion. *Terra Nova*, 18(6), 403–411.

GEOFON Data Centre (1993). GEOFON Seismic Network. Deutsches GeoForschungsZentrum GFZ.

Hrubcová, P., Doubravová, J., and Vavryčuk, V. (2021). Non-double-couple earthquakes in 2017 swarm in reykjanes peninsula, sw iceland: Sensitive indicator of volcano-tectonic movements at slow-spreading rift. *Earth Planet. Sci. Lett.*, 563, article no. 116875.

Hudson, J. A., Pearce, R. G., and Rogers, R. M. (1989). Source type plot for inversion of the moment tensor. *J. Geophys. Res. Solid Earth*, 94(B1), 765–774.

Institut de Physique du Globe de Paris (IPGP) (2006). Karthala Volcano Monitoring Network (Karthala).

Institut de Physique du Globe de Paris (IPGP) and Ecole et Observatoire des Sciences de la Terre de Strasbourg (EOST) (1982). GEOSCOPE, French Global Network of broad band seismic stations.

Komatitsch, D., Vilotte, J.-P., Tromp, J., Afanasiev, M., Bozdag, E., Charles, J., Chen, M., Goddeke, D., Hjorleifsdottir, V., Labarta, J., Le Goff, N., Le Loher, P., Liu, Q., Maggi, A., Martin, R., McRitchie, D., Messmer, P., Michea, D., Nissen-Meyer, T., Peter, D., Rietmann, M., de Andrade, S., Savage, B., Schuberth, B., Siemenski, A., Strand, L., Tape, C., Xie, Z., and Zhu, H. (2015). SPECFEM3D GLOBE v7.0.0 [software]. Computational Infrastructure for Geodynamics. https://geodynamics.org/cig/software/specfem3d_globe/.

Kumar, R., Gupta, S., and Kumar, A. (2015). Non-double-couple mechanism of moderate earthquakes occurred in lower siang region of Arunachal Himalaya: Evidence of factors affecting non-DC. *J. Asian Earth Sci.*, 98, 105–115.

Laske, G., Masters, G., Ma, Z., and Pasyanos, M. (2013). Update on crust1. 0—a 1-degree global model of Earth's crust. In *Abstract EGU2013-2658 presented at 2013 Geophysical Research Abstracts*, volume 15, page 2658.

Lemoine, A., Briole, P., Bertil, D., Roullé, A., Foumelis, M., Thinon, I., Raucoules, D., de Michele, M., Valty, P., and Hoste Colomer, R. (2020). The 2018–2019 seismo-volcanic crisis east of Mayotte, Comoros islands: seismicity and ground deformation markers of an exceptional submarine eruption. *Geophys. J. Int.*, 223(1), 22–44.

Lengliné, O., Duputel, Z., and Ferrazzini, V. (2016). Uncovering the hidden signature of a magmatic recharge at Piton de la Fournaise volcano using small earthquakes. *Geophys. Res. Lett.*, 43(9), 4255–4262.

Lengliné, O., Duputel, Z., and Okubo, P. G. (2021). Tracking dike propagation leading to the 2018 Kīlauea eruption. *Earth Planet. Sci. Lett.*, 553, article no. 116653.

Maeda, Y. and Kumagai, H. (2017). A generalized equation for the resonance frequencies of a fluid-filled crack. *Geophys. J. Int.*, 209(1), 192–201.

MedNet Project Partner Institutions (1990). Mediterranean Very Broadband Seismographic Network (MedNet).

Meier, M.-A., Ampuero, J., and Heaton, T. H. (2017). The hidden simplicity of subduction megathrust earthquakes. *Science*, 357(6357), 1277–1281.

Merz, D. K., Caplan-Auerbach, J., and Thurber, C. H. (2019). Seismicity and velocity structure of Lō'ihi submarine volcano and southeastern Hawai'i. *J. Geophys. Res. Solid Earth*, 124(11), 11380–11393.

Michon, L. (2016). The volcanism of the comoros archipelago integrated at a regional scale. In Bachelery, P., Lenat, J.-F., Di Muro, A., and Michon, L., editors, *Active Volcanoes of the Southwest Indian Ocean*, page 481. Springer-Verlag, Berlin, Heidelberg.

Morales-Yáñez, C., Duputel, Z., and Rivera, L. (2020). Impact of 3-D Earth structure on W-phase CMT parameters. *Geophys. J. Int.*, 223(2), 1432–1445.

Neal, C. A., Brantley, S. R., Antolik, L., Babb, J. L., Burgess, M., Calles, K., Cappos, M., Chang, J. C., Conway, S., Desmither, L., Dotray, P., Elias, T., Fukunaga, P., Fuke, S., Johanson, I. A., Kamibayashi, K., Kauahikaua, J., Lee, R. L., Pekalib, S., Miklius, A., Million, W., Moniz, C. J., Nadeau, P. A., Okubo, P., Parcheta, C., Patrick, M. R., Shiro, B., Swanson, D. A., Tollett, W., Trusdell, F., Younger, E. F., Zoeller, M. H., Montgomery-Brown, E. K., Anderson, K. R., Poland, M. P., Ball, J. L., Bard, J., Coombs, M., Dietterich, H. R., Kern, C., Thelen, W. A., Cervelli, P. F., Orr, T., Houghton, B. F., Gansecki, C., Hazlett, R., Lundgren, P., Diefenbach, A. K., Lerner, A. H., Waite, G., Kelly, P., Clor, L., Werner, C., Mulliken, K., Fisher, G., and Damby, D. (2019). The 2018 rift eruption and summit collapse of Kilauea Volcano. *Science*, 363(6425), 367–374.

Nougier, J., Cantagrel, J., and Karche, J. (1983). The Comores archipelago in the western Indian Ocean: volcanology, geochronology and geodynamic setting. *J. Afr. Earth Sci.*, 5(2), 135–145.

Nyblade, A. (2017). Broadband seismic experiment in NE Uganda to investigate plume-lithosphere interactions (NE Uganda) [Data set]. International Federation of Digital Seismograph Networks.

Pratt, M. J., Wysession, M. E., Aleqabi, G., Wiens, D. A., Nyblade, A. A., Shore, P., Rambolamanana, G., Andriampenomanana, F., Rakotondraibe, T., Tucker, R. D., Barruol, G., and Rindraharisaona, E. (2017). Shear velocity structure of the crust and upper mantle of Madagascar derived from surface wave tomography. *Earth Planet. Sci. Lett.*, 458, 405–417.

RESIF (1962). RESIF-RLBP French Broad-band network, RESIF-RAP strong motion network and other seismic stations in metropolitan France.

RESIF (2018). CEA/DASE broad-band permanent network in metropolitan France.

REVOSIMA/IPGP (2019). Bulletin de l'activité sismo-volcanique á Mayotte. Bulletin n°1 du 1 au 31 juillet 2019. http://www.ipgp.fr/sites/default/files/ipgp_1er_bulletin_info_sismo_volcanique_mayotte-cor.pdf.

REVOSIMA/IPGP (2021). Bulletin de l'activité sismo-volcanique á Mayotte. Bulletin n°37 du 1er au 31 décembre 2021. http://www.ipgp.fr/sites/default/files/ipgp_revosima_n37_20220106.pdf.

Ritsema, J., Deuss, A., van Heijst, H. J., and Woodhouse, J. H. (2011). S40rts: a degree-40 shear-velocity model for the mantle from new rayleigh wave dispersion, teleseismic traveltime and normal-mode splitting function measurements. *Geophys. J. Int.*, 184(3), 1223–1236.

Rodríguez-Cardozo, F., Hjörleifsdóttir, V., Jónsdóttir, K., Iglesias, A., Franco, S. I., Geirsson, H., Trujillo-Castrillón, N., and Hensch, M. (2021). The 2014–2015 complex collapse of the bárðarbunga caldera, iceland, revealed by seismic moment tensors. *J. Volcanol. Geotherm. Res.*, 416, article no. 107275. https://www.sciencedirect.com/science/article/pii/S0377027321001049.

Roman, D. C. (2005). Numerical models of volcanotectonic earthquake triggering on non-ideally oriented faults. *Geophys. Res. Lett.*, 32(2), article no. L02304.

Roman, D. C. and Cashman, K. V. (2006). The origin of volcano-tectonic earthquake swarms. *Geology*, 34(6), 457–460.

Rubin, A. M. (1995). Propagation of magma-filled cracks. *Annu. Rev. Earth Planet. Sci.*, 23(1), 287–336.

Rubin, A. M. and Gillard, D. (1998). Dike-induced earthquakes: Theoretical considerations. *J. Geophys. Res. Solid Earth*, 103(B5), 10017–10030.

Sandanbata, O., Kanamori, H., Rivera, L., Zhan, Z., Watada, S., and Satake, K. (2021). Moment Tensors of Ring-Faulting at Active Volcanoes: Insights Into Vertical-CLVD Earthquakes at the Sierra Negra Caldera, Galápagos Islands. *J. Geophys. Res. Solid Earth*, 126(6), article no. e2021JB021693.

Saurel, J.-M., Jacques, E., Aiken, C., Lemoine, A., Retailleau, L., Lavayssière, A., Foix, O., Dofal, A., Laurent, A., Mercury, N., Crawford, W., Lemarchand, A., Daniel, R., Pelleau, P., Bès de Berc, M., Dectot, G., Bertil, D., Roullé, A., Broucke, C., Colombain, A., Jund, H., Besançon, S., Guyavarch, P., Kowalski, P., Roudaut, M., Apprioual, R., Battaglia, J., Bodihar, S., Boissier, P., Bouin, M. P., Brunet, C., Canjamale, K., Catherine, P., Desfete, N., Doubre, C., Dretzen, R., Dumouche, T., Fernagu, P., Ferrazzini, V., Fontaine, F. R., Gaillot, A., Géli, L., Griot, C., Grunberg, M., Guzel, E. C., Hoste-Colomer, R., Lambotte, S., Lauret, F., Léger, F., Maros, E., Peltier, A., Vergne, J., Satriano, C., Tronel, F., Van der Woerd, J., Fouquet, Y., Jorry, S. J., Rinnert, E., Thinon, I., and Feuillet, N. (2022). Mayotte seismic crisis: building knowledge in near real-time by combining land and ocean-bottom seismometers, first results. *Geophys. J. Int.*, 228(2), 1281–1293.

Scripps Institution of Oceanography (1986). Global seismograph network (GSN—IRIS/USGS). International Federation of Digital Seismograph Networks.

Shuler, A., Nettles, M., and Ekström, G. (2013). Global observation of vertical-CLVD earthquakes at active volcanoes. *J. Geophys. Res. Solid Earth*, 118(1), 138–164.

Sigmundsson, F., Hooper, A., Hreinsdóttir, S., Vogfjörd, K. S., Ófeigsson, B. G., Heimisson, E. R., Dumont, S., Parks, M., Spaans, K., Gudmundsson, G. B., Drouin, V., Árnadóttir, T., Jónsdóttir, K., Gudmundsson, M. T., Högnadóttir, T., Fridriksdóttir, H. M., Hensch, M., Einarsson, P., Magnússon, E., Samsonov, S., Brandsdóttir, B., White, R. S., Ágústsdóttir, T., Greenfield, T., Green, R. G., Hjartardóttir, A. R., Pedersen, R., Bennett, R. A., Geirsson, H., La Femina, P. C., Björnsson, H., Pálsson, F., Sturkell, E., Bean, C. J., Möllhoff, M., Braiden, A. K., and Eibl, E. P. S. (2015). Segmented lateral dyke growth in a rifting event at Bároarbunga volcanic system, Iceland. *Nature*, 517, 191–195.

Šílený, J. (2009). Resolution of non-double-couple mechanisms: simulation of hypocenter mislocation and velocity structure mismodeling. *Bull. Seismol. Soc. Am.*, 99(4), 2265–2272.

Stamps, D. S., Saria, E., and Kreemer, C. (2018). A geodetic strain rate model for the East African rift system. *Sci. Rep.*, 8, article no. 732.

Torres-González, P., Luengo-Oroz, N., Lamolda, H., D'Alessandro, W., Albert, H., Iribarren, I., Moure-García, D., and Soler, V. (2020). Unrest signals after 46 years of quiescence at Cumbre Vieja, La Palma, Canary Islands. *J. Volcanol. Geotherm. Res.*, 392, article no. 106757. https://www.sciencedirect.com/science/article/pii/S037702731930366X.

Ukawa, M. and Tsukahara, H. (1996). Earthquake swarms and dike intrusions off the east coast of Izu Peninsula, central Japan. *Tectonophysics*, 253(3), 285–303.

Utrecht University (UU Netherlands) (1983). NARS [Data set]. International Federation of Digital Seismograph Networks.

Vavryčuk, V. (2015). Moment tensor decompositions revisited. *J. Seismol.*, 19, 231–252.

Wolfe, C. J., Okubo, P. G., and Shearer, P. M. (2003). Mantle fault zone beneath Kilauea volcano, Hawaii. *Science*, 300(5618), 478–480.

Zinke, J., Reijmer, J., Thomassin, B., Dullo, W.-C., Grootes, P., and Erlenkeuser, H. (2003). Postglacial flooding history of Mayotte lagoon (Comoro Archipelago, southwest Indian Ocean). *Mar. Geol.*, 194(3), 181–196.

*Comptes Rendus*
*Géoscience — Sciences de la Planète*
**2022**, Vol. 354, Special Issue S2, p. 153-170
https://doi.org/10.5802/crgeos.133

The Mayotte seismo-volcanic crisis of 2018-2021 in the Comoros archipelago (Mozambique channel) / *La crise sismo-volcanique de 2018-2021 de Mayotte dans l'archipel des Comores (Canal du Mozambique)*

# Automatic detection for a comprehensive view of Mayotte seismicity

## *Détection automatique pour une vision globale de la sismicité de Mayotte*

**Lise Retailleau** [*, a, b], **Jean-Marie Saurel** [a], **Marine Laporte** [c], **Aude Lavayssière** [a], **Valérie Ferrazzini** [a, b], **Weiqiang Zhu** [d], **Gregory C. Beroza** [d], **Claudio Satriano** [a], **Jean-Christophe Komorowski** [a] **and OVPF Team** [a, b]

[a] Université Paris Cité, Institut de Physique du Globe de Paris, CNRS, 1 rue Jussieu, F-75005 Paris, France

[b] Observatoire volcanologique du Piton de la Fournaise, Institut de Physique du Globe de Paris, 14 RN3 - Km 27, F-97418 La Plaine des Cafres, La Réunion, France

[c] CEA, DAM, DIF, F-91297 Arpajon, France

[d] Department of Geophysics, Stanford University, 397 Panama Mall, Stanford, CA, USA

*E-mails:* retailleau@ipgp.fr (L. Retailleau), saurel@ipgp.fr (J.-M. Saurel), marinelaporte.ensg@gmail.com (M. Laporte), lavayssiere@ipgp.fr (A. Lavayssière), ferraz@ipgp.fr (V. Ferrazzini), zhuwq@stanford.edu (W. Zhu), beroza@stanford.edu (G. C. Beroza), satriano@ipgp.fr (C. Satriano), jeanchristophe.komorowski@gmail.com (J.-C. Komorowski), peltier@ipgp.fr (OVPF Team)

**Abstract.** The seismic crisis that began in May, 2018 off the coast of Mayotte announced the onset of a volcanic eruption that started two months later 50 km southeast of the island. This seismicity has since been taken as an indicator of the volcanic and tectonic activity in the area. In response to this activity, a network of stations was deployed on Mayotte over the past three years. We used the machine learning-based method PhaseNet to re-analyze the seismicity recorded on land since March 2019. We detect 50,512 events compared to around 6508 manually picked events between March 2019 and March 2021. We locate them with NonLinLoc and a locally developed 1-D velocity model. While eruptions are often monitored through the analysis of Volcano-Tectonic (VT) seismicity (2–40 Hz), we focus on the lower frequency, Long Period (LP) earthquakes (0.5–5 Hz), which are thought to be more directly related to fluid movement at depth. In Mayotte, the VT events are spread between two clusters, whereas the LP events are all located in a single cluster in the bigger proximal

* Corresponding author.

VT cluster, at depths ranging from 25 to 40 km. Moreover, while the VT earthquakes of the proximal cluster occur continuously with no apparent pattern, LP events occur in swarms that last for tens of minutes. We show that during the swarms, LP events generally migrate downward at a speed of 5 m/s. While these events do not appear directly linked to upward fluid migration, their waveform signature could result from propagation through a fluid-rich medium. They occur at a different location than VT earthquakes, also suggesting a different origin which could be linked to the Very Long Period events (VLP) observed above the LP earthquakes in Mayotte.

**Résumé.** La crise sismique qui a commencé à l'Est de l'île de Mayotte en mai 2018 a précédé de deux mois le début d'une éruption volcanique à 50 km au Sud-Est de l'île. Cette sismicité est utilisée depuis comme indicateur de l'activité volcanique et tectonique de la zone. Un réseau de stations a été déployé à Mayotte durant les trois dernières années en réponse à cette activité. Nous avons utilisé la méthode de machine learning PhaseNet afin de ré-analyser la sismicité enregistrée à terre depuis mars 2019. Nous avons identifié 50 512 événements entre mars 2019 et mars 2021, alors que le nombre d'événements identifiés manuellement durant la même période était limité à 6508. Nous avons localisé les événements grâce à l'algorithme NonLinLoc associé à un nouveau modèle de vitesse 1D local. Alors que les éruptions volcaniques sont souvent suivies grâce à l'analyse de la sismicité volcano-tectonique (VT, 2–40 Hz), nous nous sommes concentrés sur les séismes longue période (LP, 0.5–5 Hz), qui sont souvent associés à des mouvements de fluides en profondeur. Les séismes VT sont répartis dans deux zones géographiquement distinctes alors que les LP sont restreints à la zone la plus active et proche de l'île de Mayotte, avec des profondeurs entre 25 et 40 km. De plus, alors que les VT semblent se produire de manière continue sans organisation apparente, les LP se produisent en essaims qui durent quelques dizaines de minutes. A travers cette étude nous avons montré que lors d'un essaim, les séismes LP migrent vers le bas à une vitesse de 5 m/s. Ces événements ne semblent pas directement liés à un mouvement de fluides vers la surface, mais leur forme d'onde pourrait indiquer une propagation à travers un milieu riche en fluides. Ils se produisent en un lieu différent des séismes VT, suggérant aussi une source différente qui pourrait être liée aux événements de très longue période (VLP) qui sont observés à l'aplomb des séismes LP.

**Keywords.** Volcano, Mayotte, Seismicity, Machine learning, Long Period, Volcano-Tectonic, Phase picking.

**Mots-clés.** Volcan, Mayotte, Sismicité, Machine learning, Longue période, Volcano-tectonique, Pointé de phase.

*Published online: 17 June 2022, Issue date: 17 January 2023*

## 1. Introduction

Seismicity usually accompanies volcanic activity. For this reason, it is often used to monitor volcanoes to assess or predict their activity [Chouet and Matoza, 2013] and to anticipate the onset of an eruption [e.g., in Piton de la Fournaise, Peltier et al., 2009]. On remote or inaccessible volcanoes [e.g. Axial seamount Wilcock et al., 2016], seismic signals provide one of the few continuous sources of information directly related to volcano behavior. In Mayotte, the volcanic eruption was first indicated through a strong episode of seismicity [Cesca et al., 2020, Lemoine et al., 2020].

Mayotte is one island of the Comoros archipelago, situated between Africa and Madagascar (Figure 1a). While the origin of the archipelago was associated with a hotspot, recent studies define the area as a shear zone separating the Somalia and Lwandle plates [Famin et al., 2020, Dofal et al., 2021]. Before 2018, the seismicity of the archipelago was moderate [Bertil and Regnoult, 1998, Bertil et al., 2021]. The only volcano known to be active was Karthala, located on Grande Comore, the westernmost island of the archipelago [Bachèlery et al., 2016]. The strong burst of seismicity east of Mayotte that started on May 10th, 2018, with the largest event (magnitude Mw 5.9) on May 15th [Cesca et al., 2020, Lemoine et al., 2020], surprised the inhabitants of the island, the authorities, and the scientific community. A month later, strong deformation signals were observed on a permanent Global Navigation Satellite System (GNSS) station, indicating a likely deformation source to the east of the island [Briole et al., 2018]. Finally, in May, 2019, a new active volcano was discovered 50 km east of Mayotte during a scientific campaign [Mayobs1, Deplus et al., 2019, Feuillet et al., 2021]. The erupted volume and duration [about 6 km$^3$ and over two years, REVOSIMA-IPGP, 2021] of this underwater eruption is unprecedented in the recent history and is second only to the 1783 Laki eruption that lasted eight months and produced 14.7 ± 1.0 km$^3$ of basaltic lava flows [Thordarson and Self, 1993]. The underwater volcanic edifice reached a height of 800 m in one year [REVOSIMA-IPGP, 2021].

The Mayotte submarine eruption was first suspected through the intensity of the seismicity crisis that began on May 10th, 2018. The seismicity is on-going and indicates continuing activity of the system. Studying this seismicity is crucial for understanding this dynamic process and its future evolution. Because no strong seismicity episode or volcanic activity was expected, no seismic monitoring network or monitoring procedures were in place in 2018 and only one permanent seismic station was maintained on the island by the BRGM [RESIF, 1995, Bureau de recherches géologiques et minières]. French scientific institutions organized to monitor the activity with an improved land network and through campaigns at sea, which lead to the creation of the REVOSIMA (Réseau de surveillance volcanologique et sismologique de Mayotte) in 2019. Thanks to this effort, several seismic stations were installed on land and on the ocean bottom to better characterize the seismicity [Saurel et al., 2022]. Before this work and its operational implementation [Retailleau et al., 2022], the seismicity was identified and located mostly manually, which limited catalogs to the strongest activity [usually events greater than M 3; Saurel et al., 2022].

Automatic picking procedures are widely used to analyse large, continuous datasets that can not be easily analysed though hand picking. Automated methods have been extremely useful for real-time detection, when it is not possible for an analyst to continuously pick events, and for reanalysis of long time series. Different automatic detection methods have been used for earthquake detection, ranging from short term/long term amplitude ratios [e.g. STA/LTA, Allen, 1978] to template matching [Shelly et al., 2007, Ross et al., 2019]. While the former is efficient, it may not be effective for detecting small events, especially under noisy conditions. Template matching, on the other hand, can detect very small events (with magnitudes less than 1). However, it is computer-intensive and requires prior information in the form of template waveforms, which limits its ability to detect seismicity changes. We use the machine learning method PhaseNet [Zhu and Beroza, 2019], which allows fast picking of phases while being able to pick small events without prior information. It also identifies both P and S waves, which is crucial for more accurate automatic location.

A wide range of seismic signals are generated by active volcanoes, and they reflect the diversity of source mechanisms [Chouet and Matoza, 2013]. Volcano-Tectonic earthquakes (VT), the most common events, are discrete events with a broad frequency band (2–40 Hz) that are linked to shear failure due to the destabilization of the volcanic edifice. Another common type of seismicity is Long Period earthquakes (LP) which have a narrower and lower frequency band than VT events (0.5–5 Hz). LP earthquakes are usually attributed to resonance in fluid-filled conduit excited by magmatic motion [Chouet, 1996]. Several authors [Shapiro et al., 2017, White and McCausland, 2019] have shown that deep LP events may be precursors of eruptions, making their analysis crucial. In this paper our interest was to detect comprehensively the seismicity and to discriminate between these two main types of events. We analyse their characteristics in the Mayotte system with a focus on LP behavior. We also note the observation of Very Long Period events [VLP or VLF, Cesca et al., 2020, Lemoine et al., 2020, Feuillet et al., 2021, Laurent et al., 2020]. These events have monochromatic signatures and do not have common earthquake characteristics. For this reason, PhaseNet does not detect VLP events, and we do not present their analysis; however, we discuss their observation and their links to other events.

We analyze two years of continuous data recorded by the stations installed on the island of Mayotte using the machine learning-based method PhaseNet [Zhu and Beroza, 2019]. We assess the robustness of P- and S-phase arrival picking by comparing with manual picks from two different catalogs. We associate events when enough phases are detected, and then proceed to locate them. We separate the VT and LP earthquakes through their frequency characteristics and compare their locations and timing.

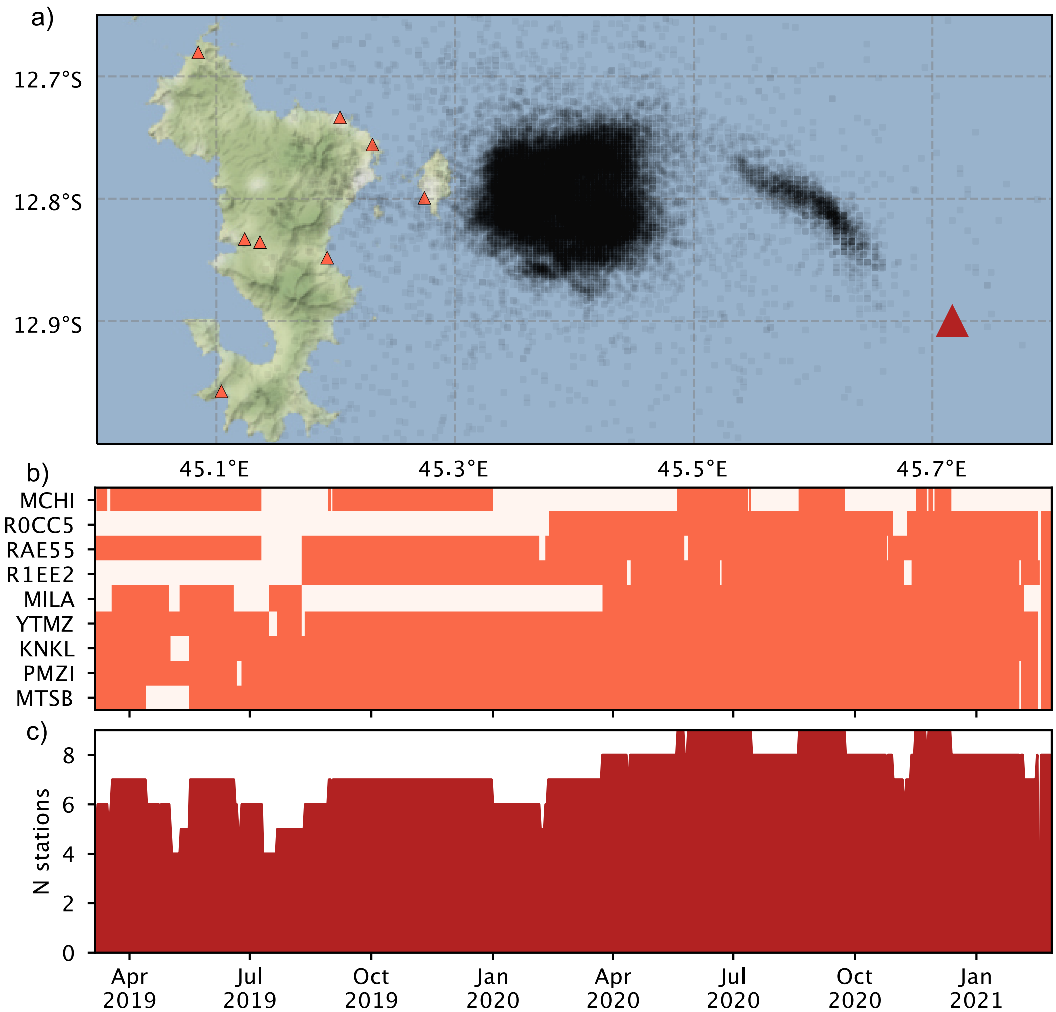


**Figure 1.** (a) Map of Mayotte with the land stations used in this study (orange triangles). The new volcano is represented with the red triangle. The see-through black dots represent the 50,512 earthquakes located in our study. (b) Days processed for the detection for each station (orange). (c) Total number of stations processed over the period.

## 2. Seismicity identification

We detail in this section the event detection process through phase arrival, automatic picking, and event association.

### 2.1. *Automatic detection in continuous time series with PhaseNet*

Only one seismic station was installed on the island of Mayotte before the seismic crisis started [RA.YTMZ RESIF, 1995]; however, the seismic network was progressively extended on the island to record a more extensive dataset, improve the detection level, and increase the location precision of earthquakes [Saurel et al., 2022]. To monitor the early part of the crisis, the regional stations on Grande Comore and Madagascar islands had to be used to locate events, which did not allow precise locations [Lemoine et al., 2020]. Since March 2019, the permanent continuous real-time seismic network has been extended with 2 accelerometers, 4 broadband stations (flat response down to 20 or 120 s), and 2 short-period low-cost stations (flat response down to 1 Hz). Since then, the network aperture has been wide enough to allow stable and robust automatic detection and location of the seismicity with at least 4 stations. Figure 1a shows the stations used on the island of Mayotte for this study and Figure 1b shows data availability for each station throughout the period of interest. The number of stations for which data is available with time is summarized on Figure 1c. Except for a few weeks in June and August 2019, there are always at least 6 stations available. All stations but one feature 3-component sensors with a sample rate higher than 50 Hz.

We use the PhaseNet algorithm to identify P- and S-phase arrivals on the continuous archived data. PhaseNet is a deep-neural-network-based method trained on numerous earthquakes in northern California to pick and identify phases on 3-component seismograms [Zhu and Beroza, 2019]. It generalizes well enough to have been successfully used in diverse tectonic contexts, including: the Ridgecrest earthquake sequence [Liu et al., 2020], induced seismicity in Arkansas [Park et al., 2020], and a year of seismicity in the Appenines [Tan et al., 2021].

We first filter the data with a 0.4–45 Hz frequency band filter, remove the instrument response, then resample at 100 Hz and split into 30 s windows with a 50% overlap. Finally, this data is sent to PhaseNet for pick estimation. For the vertical-only station (AM.RAE55), we add two 0-filled vectors of data as dummy horizontal channels before sending the data to PhaseNet.

We extract all the picks of the different stations. An event is declared when at least 10 P and S picks are within the expected time window for events in the area (2 s time window after the first arrival for the P waves and 8 s time window starting 4.5 s after the first P arrival for the S waves).

### 2.2. *Pick quality estimated from manual catalogs*

PhaseNet was trained on tectonic events. To test how well it generalizes for events that occur in a volcanic environment, we compare its arrival time measurements to reference arrival time measurements performed by skilled analysts. In principle, such a comparison between several observations quantifies uncertainties of arrival-time determination of hand-picked data [Diehl et al., 2012]. It has also been used for performance assessment of various automatic picking procedures [Dai and Macbeth, 1995, Leonard, 2000, Di Stefano et al., 2006].

For their analysis of the Mayotte seismo-volcanic crisis, Cesca et al. [2020] and Lemoine et al. [2020] built seismic catalogues through manual picking using the local station YTMZ. Consequently, we have access to a dataset of events with two independent reference manual estimations of P and S onsets besides PhaseNet picks on YTMZ data. The first catalog of manual picks (from BRGM) contains 1347 P onsets and 1326 S onsets hand-picked by several expert analysts for events of magnitudes above M 3.5 detected between May 10th, 2018 and December 5th, 2019 [Lemoine et al., 2020]. The second catalog (from GFZ institute, GeoForschungsZentrum, Germany) contains 5999 P and 5999 S hand-picked onsets realized by a single expert analyst for events occurring between May 10th, 2018 and February 28th, 2019 [Cesca et al., 2020].

We assess PhaseNet's performance and accuracy by comparing the arrival times automatically picked on YTMZ continuous data by PhaseNet from the beginning of the seismic crisis with the manually picked arrival times for the events of the two manual catalogs. PhaseNet identifies the correct arrival for 99.6% of P onsets and 98.4% of S onsets from the BRGM catalog, forming a comparative dataset of 1342 common P-picks and 1305 common S-picks. Similarly, PhaseNet identifies 97.7% of P onsets and 98.8% of S onsets from the GFZ catalog, forming a comparative dataset of 5858 common P picks and 5924 common S picks. Figure 2 show the time differences between the 3 catalogs and their statistical distributions, for the P-picks and S-picks, excluding outliers. We estimate that two picks are consistent if the difference in arrival-time between them is less than 0.5 s for P phases and less than 0.8 s for S phases. Outliers above the defined threshold mainly result from event or phase mis-identifications. Among the 1342 P and 1305 S arrivals in common with BRGM, 22 (1.6%) and 102 arrivals (7.8%) are outliers, respectively. Among the 5858 P and 5924 S arrivals in common with GFZ, 277 (4.7%) and 506 arrivals (8.5%) are outliers, respectively. The two manual catalogs have 915 common P arrivals, including 21 (2.3%) outliers; and 904 common S arrivals, including 23 outliers (2.5%). Hence, manually hand-picked datasets show less incoherent picks for S arrivals.

In the following analysis, we only consider the arrival time differences that have not been flagged as outliers according to our criteria. Arrival-time differences between independently hand-picked data display a non-Gaussian distribution of pick time differences. To assess the dispersion of pick time differences, we compare the median value and the interquartile range (i.e, containing the closest 25% of the distribution around the median) as it is more suitable for describing non-Gaussian distributions. For the two manual catalogs, the median of manual P pick time differences is 0.01 s and the interquartile range is 0.06 s (Figure 2a, bottom panel). Similarly, the median and the interquartile range for manual S picks time differences is 0.05 s and 0.19 s, respectively (Figure 2b, bottom panel). These values are close to the few values found in the scientific literature for manual picks [Leonard, 2000, Di Stefano et al., 2006]. It supports the common observation that the onset time for P phases are less difficult to measure in a seismic signal than for S phases. In comparison, the median and the interquartile range of the 1320 P pick time differences between the BRGM catalog and PhaseNet is 0.03 s and 0.04 s (Figure 2a, top panel). The median and the interquartile range of 5581 P pick time differences between the GFZ and PhaseNet catalogs is 0.02 s and 0.05 s (Figure 2a, middle panel). These values are close to those obtained between the two manual catalogs even though the statistical population is larger. The precision of PhaseNet thus competes with the precision reached by expert analysts. More precisely, on average, PhaseNet automatic P picks arrive a few milliseconds sooner than the corresponding manual pick, which suggests a greater sensitivity of the neural network to detect an early subtle change in the signal at the true P onset. Regarding S pick time differences, the median and the interquartile range of the 1203 S picks time differences between the BRGM and PhaseNet catalogs is 0.04 s and 0.16 s (Figure 2b, top panel). The median and the interquartile range of 5419 S picks time differences between GFZ and PhaseNet catalogs is 0.01 s and 0.1 s (Figure 2b, middle panel). These values are smaller than the pick time differences observed between the two manual catalogs. PhaseNet S picks are more consistent with the manual picks from GFZ, even though this catalog eventuates smaller magnitudes and presents a larger population. On average, GFZ S picks arrive a few milliseconds sooner than BRGM picks. Similarly, PhaseNet S picks arrive a few milliseconds sooner than BRGM picks but a few milliseconds after GFZ S picks. These results are a representation of the picking precision among the different methods when a phase is correctly identified.

The distribution of arrival differences for S onsets without removing outliers above 0.8 s shows a recurrence of a systematic picking difference at +1.2 s for approximately 44 picks (3%) for the first comparative dataset BRGM-PhaseNet and 188 picks (3%) for the second GFZ-PhaseNet comparative dataset (Supplementary Figure 9). Such a large pick difference suggests a misidentification of the S onset with a precursory seismic arrival. Indeed, the Mayotte seismic sequence occurs within a complex volcanic and underwater environment, which may generate complex seismic waveforms, including P-to-S or a S-to-P phase conversion which are actually expected to arrive approximately one second before the S phase arrival time [Garmany, 1989]. Here, PhaseNet automatic S picks are confused a few times with those precursory arrivals but the confusion has also been seen on some S picks in the catalogs picked manually by expert analysts. It is also possible that the manual training data contained misidentified picks, thus generating these erroneous picks. Further neural training could possibly help correct the confusion between a precursory arrival and an S pick that sometimes happens with PhaseNet.

### 2.3. *Event location*

An advantage of PhaseNet over other auto-picking algorithms is its ability to pick and identify both P and S waves, when picking methods usually only identify the P-wave arrivals. The addition of S waves allows much more precise locations and event depth constraints, which is crucial for accurate hazard assessment. In Mayotte, stations have a limited azimuthal coverage, which makes earthquake location, and particularly depth resolution, particularly challenging.

Each declared event with a set of P and S picks is located with NonLinLoc [Lomax, 2008] using a local 1D velocity model for the east of Mayotte [Lavayssière et al., 2022]. This model was developed with the code VELEST [Kissling et al., 1995] using the 813 most robust earthquake locations (i.e., events with at least 30 phases recorded, azimuthal gap <

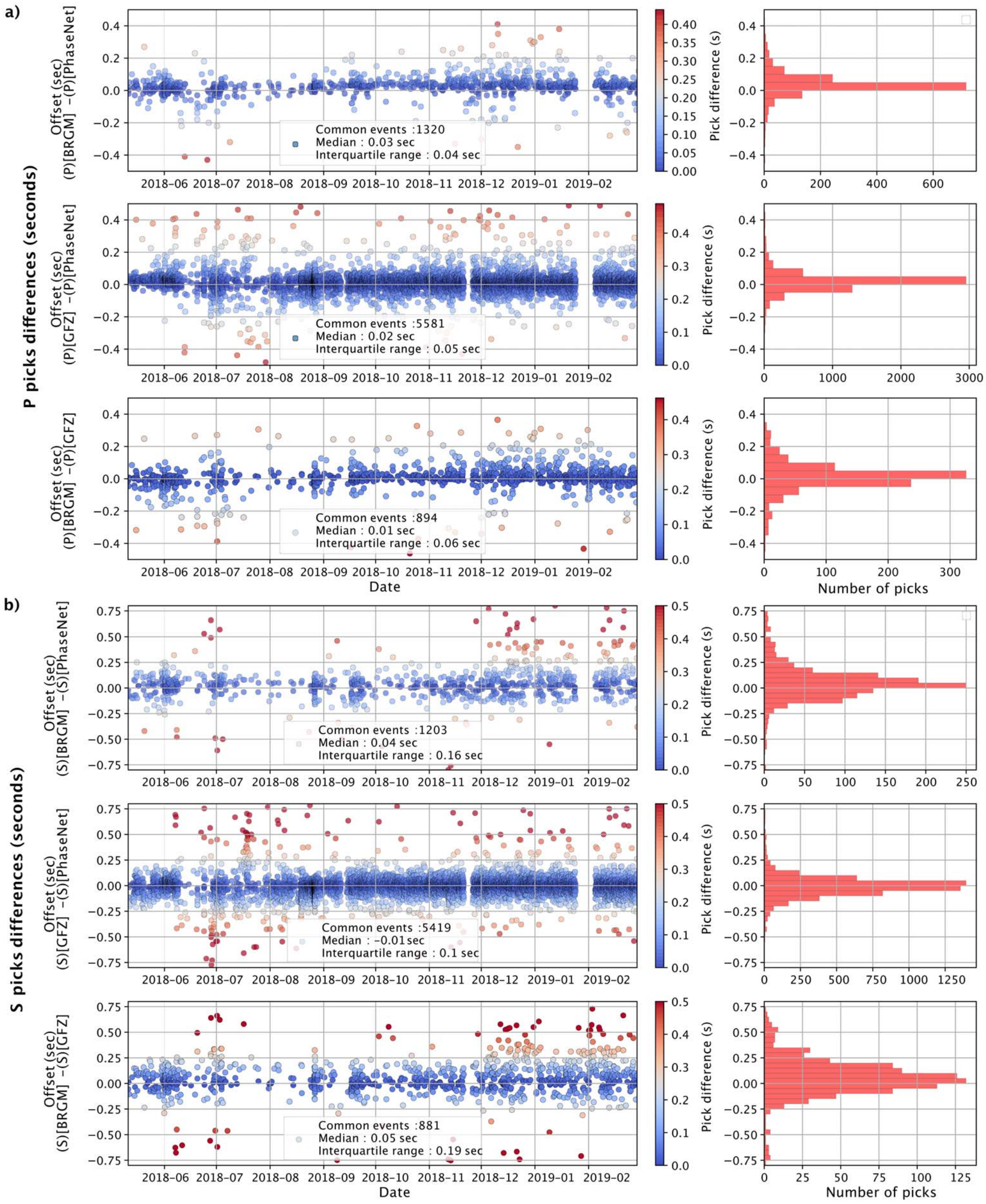


**Figure 2.** (a) P-pick time differences (left, for each event; right, distribution for all events). From top to bottom: comparison between PhaseNet and BRGM catalogs, comparison between PhaseNet and GFZ catalogs, comparison between GFZ and BRGM catalogs. Outliers are not represented. (b) Same as (a) for S-picks.

180°; horizontal error < 2 km and vertical error < 5 km). Lavayssière et al. [2022] selected this subset from events recorded in Mayotte between February 2019 and May 2020 and located manually [Saurel et al., 2022]. The VELEST inversion used picks made both on the land-stations and on Ocean Bottom Seismometers (OBS) to get the most complete set of data and the most well-constrained locations. The goal of this model was to improve the daily monitoring by having more accurate locations of the events using only the land stations, which are all located to the west of the seismicity.

VELEST simultaneously estimates hypocenters and a best-fit velocity model by minimizing the misfit between the arrival times and model predictions using both P- and S-wave arrival time data. In addition to the velocity model, Lavayssière et al. [2022] estimated station corrections to account for lateral heterogeneity and variations in the velocity structure at shallow depth beneath the stations. The velocity model and station corrections obtained hence represent the best 1D approximation of the 3D subsurface structures of the region, which is essential for accurate earthquake location.

Using the P- and S-arrival times identified by PhaseNet with the new velocity model and station corrections, we locate the events using the non-linear probabilistic earthquake-location program NonLinLoc [Lomax, 2008], which calculates a maximum-likelihood hypocenter that represents a global minimum misfit for the spatial location and the origin time of each event.

We represent in Figure 1a the 50,512 events we detected and located accurately. We only keep the events with a final RMS lower than 0.2 s. As shown by Saurel et al. [2022], the seismicity is located in two clusters east of Mayotte: the proximal cluster with a round shape close to the island and the distal cluster with an elongated shape towards the new volcanic edifice.

With this automatic detection and location process, we were able to provide a more complete image of the seismicity, particularly for the distal cluster. Indeed, the catalog of seismicity built through the monitoring work of RENASS (Réseau national de surveillance sismique) and REVOSIMA and made available by RENASS (http://renass.unistra.fr) contains 6508 events for the same period, about 8 times less compared to our new catalog. Furthermore, this method also allowed us to process two different types of seismicity: VT and LP earthquakes.

## 3. Comparative analysis between the VT and LP events

Both VT and LP events are recorded by the seismic stations installed in Mayotte. In this section we detail how we separate them from each other and compare their behavior.

### 3.1. *Event separation*

VT events are commonly observed on volcanoes. These events have a broad frequency range, from 1 Hz to 40 Hz. They are called Volcano-Tectonic earthquakes because their signature is difficult to distinguish from regular tectonic earthquakes as they are associated with shear failure driven by magmatic processes.

Most of the seismicity recorded daily by the stations installed in Mayotte are VT earthquakes. However, LP events are also recorded.

Different definitions have been proposed for LP events [Chouet and Matoza, 2013]. They range from long-period monochromatic signals to signals similar to VT events but with lower frequency content. The events we refer to as LP in Mayotte are similar to VT events, with distinct P- and S-waves, but they have a lower and narrower frequency band. Before our frequency analysis, we filter each signal in a 0.4–45 Hz frequency band, we remove the instrumental response and convert to displacement. Figure 3 shows the resulting signals and spectra of a VT and an LP event recorded by the three component stations on May 21st, 2019, and March 11th, 2019, respectively. The signals (Figure 3a,c) show clearly the difference between the two types of events recorded in Mayotte. The P wave of the VT event has a clear and impulsive onset, while the emergent arrival is very difficult to discern for the LP earthquake. The signal of the S wave can be identified on the horizontal components for both the VT and LP events with a lower dominant frequency for the LP event. Similarly, the spectra shows that the VT event has a broader frequency range than the LP event.

We use this frequency content difference to discriminate between VT and LP events. Our approach is similar to the Frequency Index (FI) proposed by Buurman and West [2010] and Matoza et al. [2014], however, we process the P- and S-waves separately.

For each event, we compute the amplitude ratio of the mean spectrum in two frequency bands (a narrow one at 0.5–6 Hz and a broad one at 0.5–30 Hz) for both the P wave and the S wave on each station. The LP events have a dominant frequency lower than 6 Hz. If the 0.5–6 Hz spectra is strong compared to the broader 0.5–30 Hz spectra, the ratio between the two is large and indicates an LP earthquake. On the

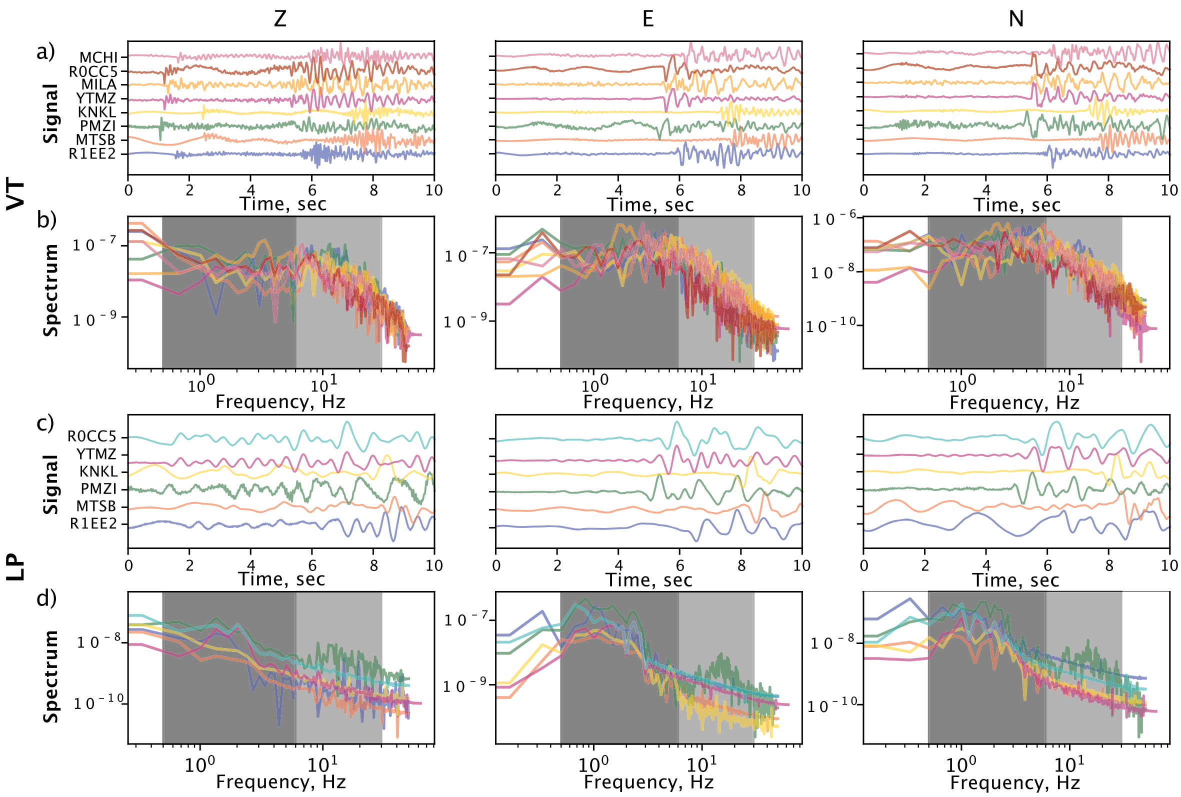


**Figure 3.** Signals (a,c) and spectra (b,d) of a VT earthquake (on May 21, 2019) (a,b) and a LP earthquake (on March 11, 2019) (c,d) recorded by the 3-component stations deployed on Mayotte.

other hand, if the event has a broad frequency band, the 0.5–6 Hz over 0.5–30 Hz spectra ratio is small, indicating a VT earthquake. We compute the ratios for all events, using the vertical component for the P wave and an average of the horizontal components for the S wave. Those ratios are then averaged over all the stations for each event to limit the potential bias of event-to-station path effect [discussed in Matoza et al., 2014].

Figure 4 shows the resulting amplitude ratio distribution for all the events already manually classified. To correctly separate the VT earthquakes from the LP earthquakes, we use the identifications made by the analysts from Observatoire Volcanologique du Piton de la Fournaise (OVPF), one of the Institut de Physique du Globe de Paris (IPGP) French overseas volcano observatories. The earthquakes recorded in Mayotte are identified daily by the analysts of OVPF since February 2020. The color of the dot in Figure 4 shows if the event was manually identified as a VT earthquake (green) or an LP earthquake (yellow). Unsurprisingly, the VT and LP earthquakes separate in two distinct zones. Events of high P and S spectral amplitude ratios are usually LP earthquakes because the high ratios mean that the dominant frequency band is shorter and lower (the 0.5–6 Hz amplitude spectrum is high compared to the broad 0.5–30 Hz amplitude spectrum). From these identifications we separate the spectral ratio diagram in two areas for VT and LP events (green and yellow color respectively in Figure 4). The events are then automatically identified as VT or LP earthquakes depending on where their P and S spectra land on the ratio diagram. Figure 5 represents the vertical component of station KNKL for a few VT and LP earthquakes that have been categorized through our process.

### 3.2. *VT versus LP location and time evolution differences*

After identification of both VT and LP earthquakes we compare their spatial and temporal behavior. For

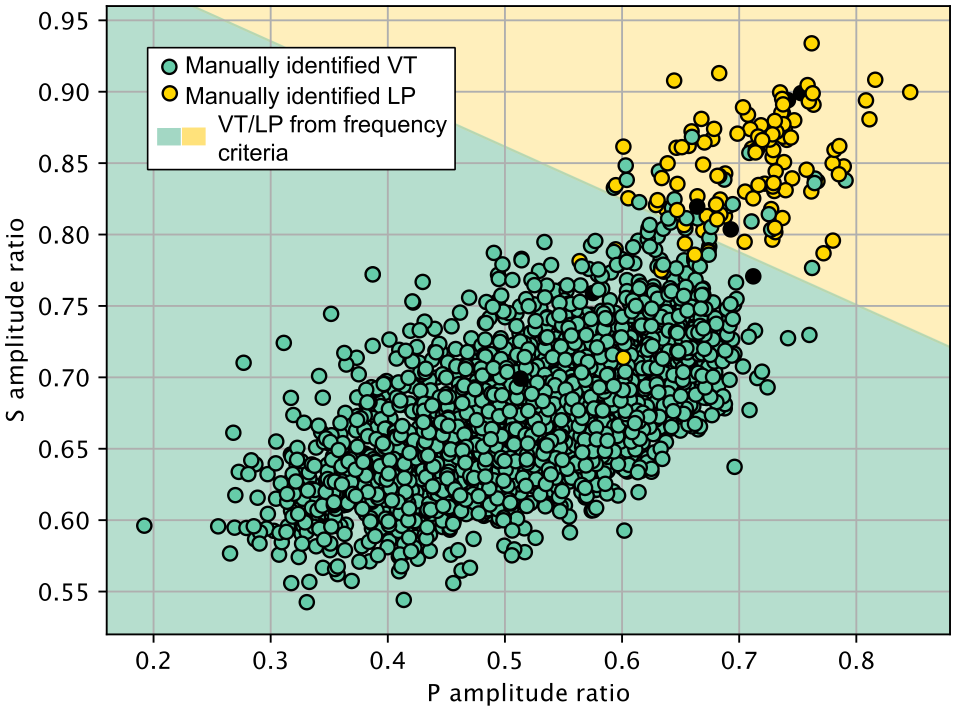


**Figure 4.** Ratios between the 0.5–6 Hz spectrum and the 0.5–30 Hz spectrum averaged over the different 3-component stations for each event. The color of the dot shows how the event was manually classified by the OVPF analysts. The colored domains represent the resulting criteria chosen. The black dots represent regional events.

clarity we represent the events' locations as event count for both VT (in red hues) and LP (with yellow and blue contours) events on Figure 6. As observed in previous publications [e.g. Lemoine et al., 2020, Saurel et al., 2022] and already mentioned in Section 2.3, the seismicity is spread over two clusters. The proximal cluster is closest to the island of Mayotte (about 10 km east) and has a circular shape. Its depth range extends from 20 to 45 km depth. The distal cluster is farther east and is aligned along a $N130°$ axis toward the new volcanic edifice (represented with the red triangle on Figure 6).

The VT earthquakes are spread over the two clusters. We do not explore in this paper the short scale-length spatio-temporal variability of the VT seismicity, which will be analysed in a later study. Remarkably, the LP earthquakes are only observed in the center of the proximal cluster, over a 25–40 km depth range (with most events between 30 and 37 km depths as shown in Figure 6). In this central area, we can see in map view that the density of VT events is lower than in the rest of the proximal cluster, a region which we later refer to as the proximal cluster VT gap. This is not observable in the depth view because all events and thus all the azimuths are shown, the south and north sides masking the central part. We can also note that, in map view, the VT cluster does not appear as a complete ring as shown by previous studies [e.g. Lavayssière et al., 2022]. This is because we plot the event count and most VT events are located in the western part of the proximal cluster. There are thus fewer VT events in its eastern part in comparison. Figure 1a does show clearly the circular shape.

Our catalog is dominated by VT earthquakes with 48,387 events compared to the 2125 LP events, as the histogram in Figure 7a shows. For this reason, before the development of this automatic processing, the LP earthquakes in Mayotte had not been studied and had only been systematically identified as LP through the daily manual screening of continuous data at OVPF, which started in March 2020. Figure 7a shows that the number of VT earthquakes decreased slowly

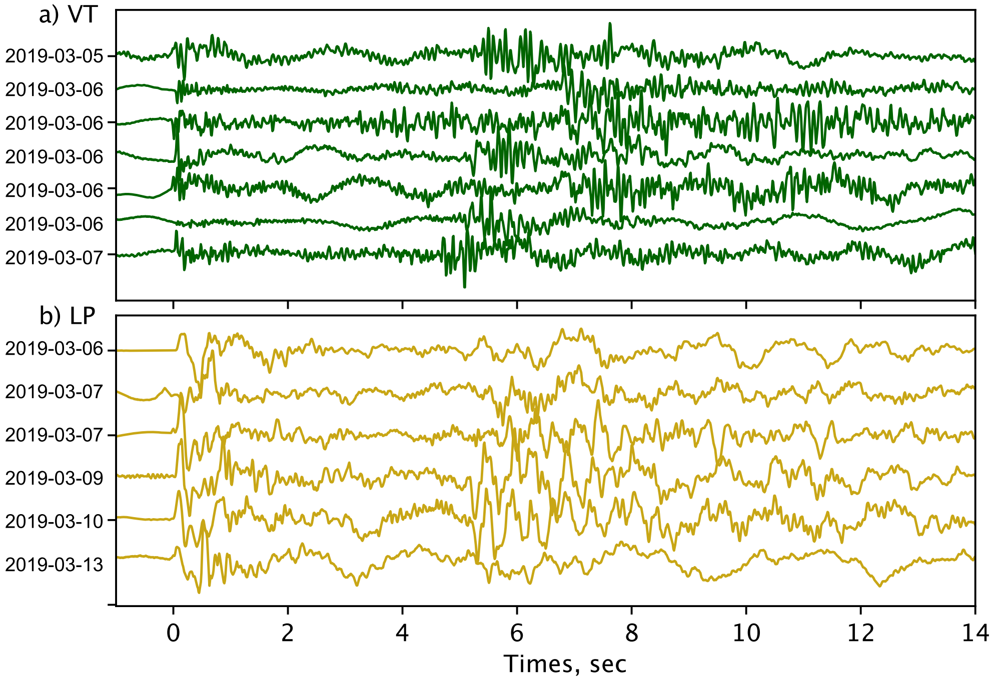


**Figure 5.** Examples of (a) VT and (b) LP earthquakes early March 2019 after event separation.

after a maximum in April, 2019 with some variations. The number of LP events is very small compared to the number of VT events and no clear time evolution is apparent. To observe the temporal evolution of event occurrence, we represent the normalized cumulative rate of both the VT and LP earthquakes (Figure 7b). We estimate the mean seismicity rate over a ten-event sliding window by computing the time difference between the 10th and the 1st event. We then calculate the cumulate of this result. We normalize the results to compare the time evolution of the two types of events. While this representation may be a little unnatural, it clearly shows that the temporal behavior of the VT and LP earthquakes is very different. The VT activity is continuous with a significant slowdown since April 2019, while the LP earthquakes occur episodically in successive swarms. Several LP events occur in a short while (usually less than one hour), followed by a period of sparse activity. Figure 7 also shows that, while the VT activity dominates the LP activity, the latter's activity does not seem to diminish compared to the former.

## 4. Discussion

Using the ability of PhaseNet to pick and identify P- and S-phases we detected over 50,000 earthquakes and separate them into two categories. Indeed, while the seismicity in Mayotte is dominated by VT earthquakes, there is also a substantial population of LP events.

We separated events into these two categories to compare their behavior. The events we define as LP earthquakes look similar to VT earthquakes, but with a lower dominant frequency. In Mayotte, the VT and LP earthquakes also show distinct spatial and temporal features. VT earthquakes are spread over both zones of seismicity (proximal and distal clusters). The VT seismicity of the distal cluster is the first seismicity that was observed in 2018 [Lemoine et al., 2020, Cesca et al., 2020, Feuillet et al., 2021]. It was associated by the authors to magma migration through a dyke feeding the eruption on the seafloor. With its N130 orientation, it is also aligned with a pre-existing ridge with numerous volcanic cones, indicating that faults could have been reactivated by the eruption. This orientation can also be found in other regional geographic features on the seafloor

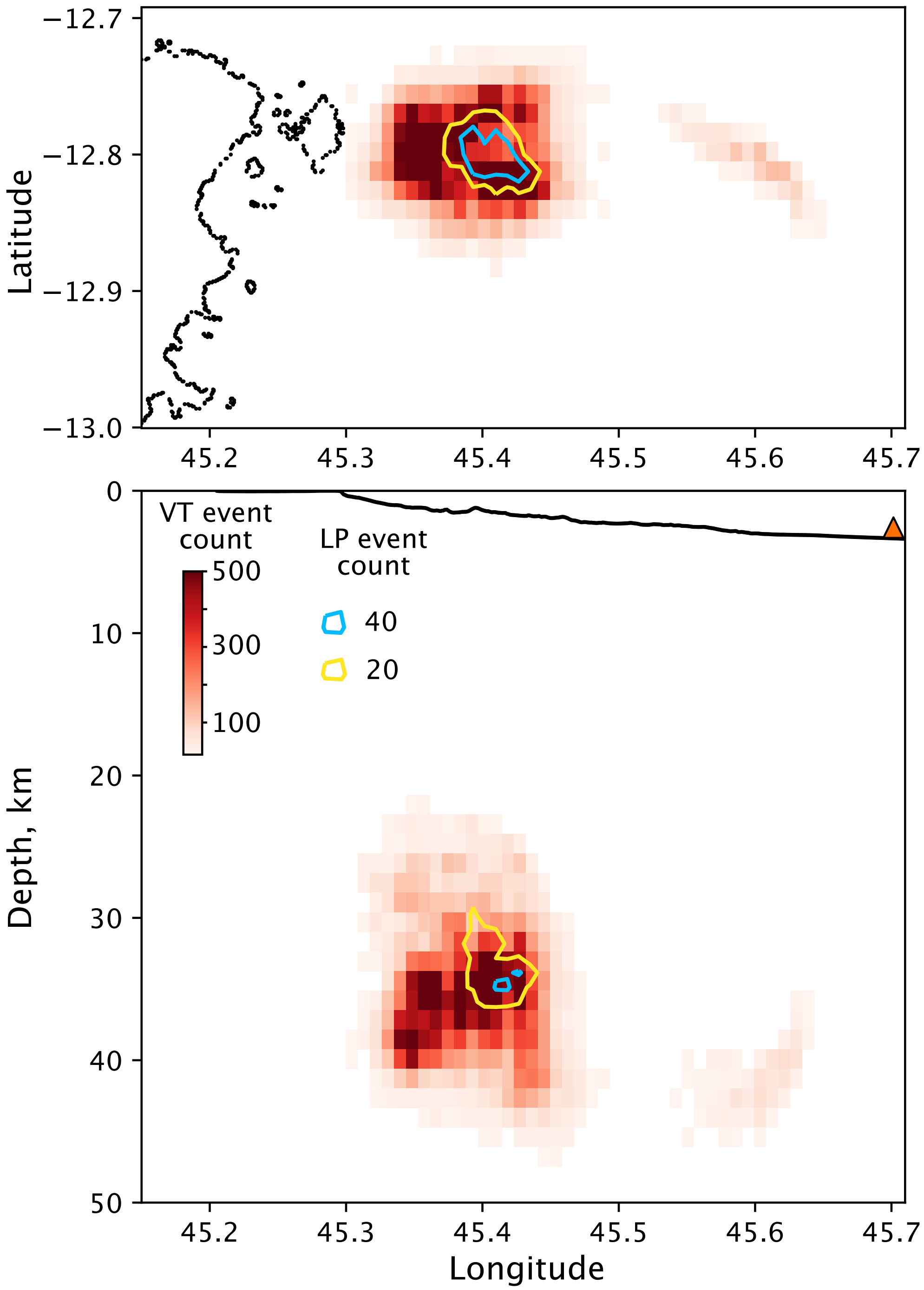


**Figure 6.** Event count of VT (red colors) and LP (yellow and blue contours) earthquakes. The orange triangle represents the location of the new volcano.

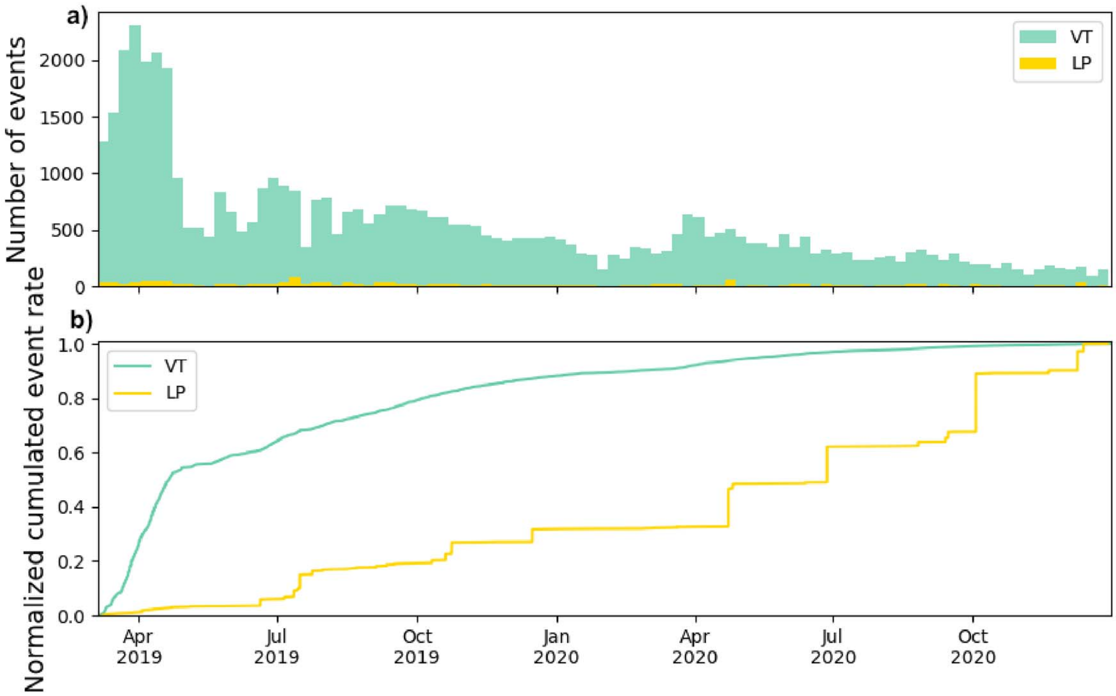


**Figure 7.** (a) 10-days histograms and (b) normalized cumulative rate of the number of VT and LP earthquakes (green and yellow respectively) from March 2019 to March 2021.

[REVOSIMA-IPGP, 2021] and the VT seismicity in the distal cluster can also be linked to the regional tectonic context [Feuillet et al., 2021, Famin et al., 2020].

The proximal cluster is more complex, spread over a broader area, and appears less directly linked to the new volcanic edifice. This seismicity has been linked to the deflation of the main magmatic reservoir [Cesca et al., 2020, Lemoine et al., 2020, Saurel et al., 2022, Lavayssière et al., 2022]. This was deduced because its activity started after the deflation did [modelled from GNSS data, Lemoine et al., 2020]. Moreover, the structure of the seismicity in depth is consistent with ring faults, further supporting the theory of a reservoir below the seismicity. A main reservoir around 40 km depth was suggested by geobarometry analyses of emitted lavas [Berthod et al., 2021] and follows deformation models [Mittal et al., 2022, REVOSIMA-IPGP, 2021]. The drainage of the main reservoir could have generated shear failure or reactivated faults. Indeed, numerous volcanic cones and edifices can be observed on the seafloor above the cluster [REVOSIMA-IPGP, 2021], suggesting a large and complex pre-existing system.

Up to now, seismicity observations of the proximal cluster of Mayotte have been focused on the VT seismicity. The LP seismicity is restricted to the proximal cluster and seems concentrated towards the center east of the cluster, with depths ranging from 25 km to 40 km, and thus directly above the depth suggested by geobarometry and deformation models. This corresponds to a VT seismicity gap in the center of the proximal cluster, also highlighted by previous studies [Saurel et al., 2022, Lavayssière et al., 2022]. A recent tomography analysis by Foix et al. [2021] suggested the presence in this area of a magma chamber between 30 and 50 km depth and a shallower zone of mush and partial melt between 20 and 30 km depth. This is supported by the conceptual model developed by Mittal et al. [2022] which suggests the presence of a porous mush next to the reservoir to explain the deformation estimated through GNSS data. Similarly, Lavayssière et al. [2022] has suggested that the gaps in VT activity could be associated with a magma storage zone.

These observations suggest that the VT seismicity might surround zones of storage [Lavayssière

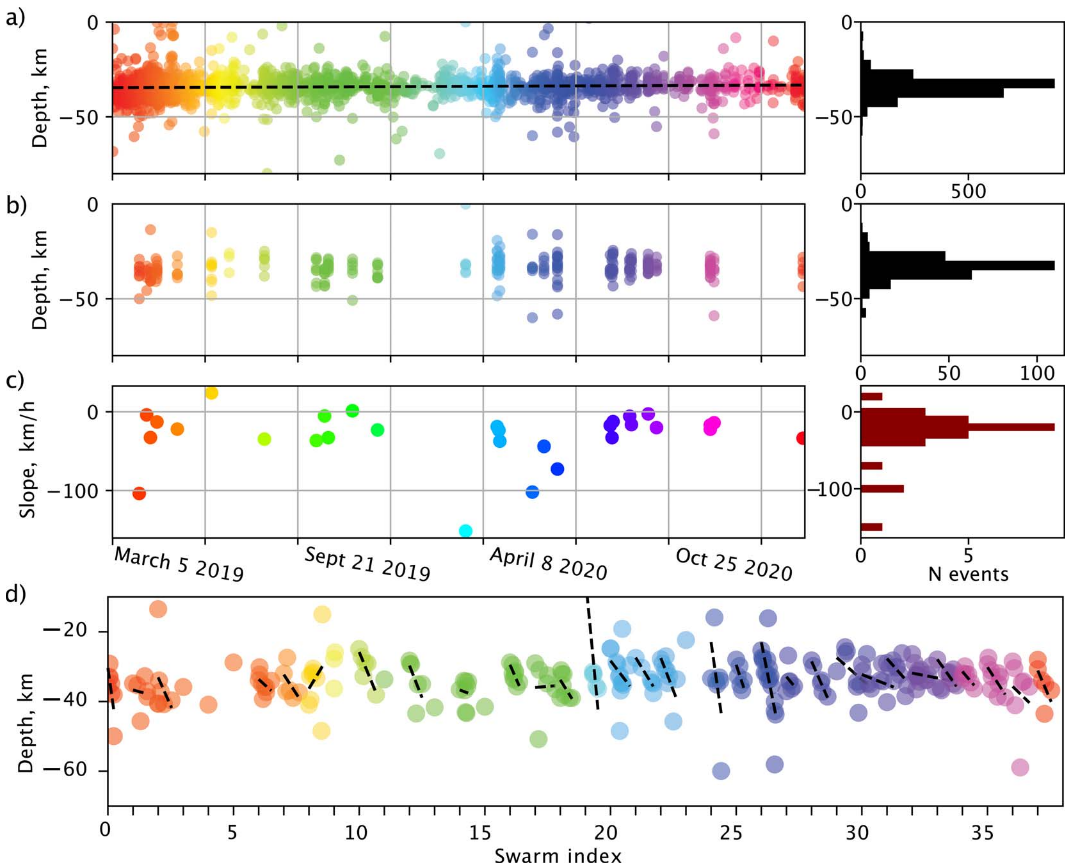


**Figure 8.** (a) All LP earthquakes depths with regards to time, (b) LP earthquakes depths of the main swarms with regards to time, (c) Depth migration velocity estimate during the main LP swarms identified in (b), and (d) Representation in depth of the main LP swarms. Each index also represents one hour. The dashed black lines represent the depth evolution linear regression for each swarm in km·h$^{-1}$.

et al., 2022] while the LP seismicity seems to be located inside these same zones. Clarke et al. [2021] showed that VT sources can appear as LP events when the seismic propagation path passes through highly attenuating areas, such as gas-saturated rocks. They confirmed their laboratory observations using Whakaari volcano shallow-event recordings. While a scaling needs to be done in the Mayotte context, this hypothesis could explain the LP seismicity location in a VT gap as mentioned above. Both LP and VT seismicity could share similar mechanisms, but the LP seismic waves might travel through a few kilometer-wide gas-saturated area that narrow and lower their waveform spectral content. The similarity of frequency content of LP earthquakes inside a swarm, even with their varying depths, also agrees with this idea. These events could be closer to VT earthquakes in mechanism but with a different propagation that lowers their frequency. Studies are ongoing to characterize time evolution and links between VT, LP and VLP types of seismicity.

We represent the depth of the LP earthquakes through time in Figure 8 to focus on their evolution. Figure 8a represents all LP earthquakes and shows that the depths of these events are spread between depths ranging from 25 to 40 km. There is no clear long-term trend of depth change with time. We focus on the main swarms to observe the short-term evolution of the events during a swarm. We flag an LP as part of a swarm when at least 5 LP events occur within one hour around it. The resulting swarms are represented on Figure 8b. For each swarm, we estimate the depth migration speed of the LP earthquakes using a linear regression. We represent in Figure 8c the estimated depth migration speed for each swarm. The histogram shows that this speed is mostly negative, implying that, during a swarm, the LP earthquakes occur at increasing depth with time. During a swarm, the LP earthquakes occur from their shallowest location (around 25 km depth) to their deepest location (around 40 km) at an average speed (removing outliers) of 19.2 km·h$^{-1}$ or 5.3 m·s$^{-1}$. With this average speed, the migration doesn't seem compatible with a migrating fluid (estimated for example at a maximum of 0.3 m·s$^{-1}$ on Piton de la Fournaise volcano by Duputel et al. [2019]). Those two observations suggests that these events are not linked to an ascension of fluids. However, it coincides with the ideas developed in the previous paragraph, and these events could be associated with a propagation through a gas-saturated conduit. Still, their downward propagation remains unexplained.

Since the LP earthquakes occur at a different location than the VT earthquakes, it means that their origin could be different. The LP swarms often coincide temporally with very long period events (VLP) which have been observed along with the rest of the activity and was one of the indicators that the activity had a volcanic origin [Laurent et al., 2020, REVOSIMA-IPGP, 2021]. This implies that their origins could be linked. Although the origin of the LP events could be linked to shear failure generating waves propagating through a gas saturated medium, their trigger seems to have a volcanic origin. A thorough analysis of the links between the different signals will be the subject of another study.

Our interpretation of the LP seismicity is still limited by the lack of focal mechanism solutions that could help distinguish physical processes [Chouet and Matoza, 2013]. The land stations are all distributed to the west of the seismicity, which makes it difficult to obtain reliable focal mechanisms. Broadband OBS surrounding the seismicity in the east would certainly help improve the event location's precision to better understand the process behind this LP seismicity. They could also allow us to perform reliable focal mechanisms to help determine whereas those LP events are volumetric sources or VT sources travelling through a highly attenuating area.

## 5. Conclusions

The use of neural-network-based automatic picking permitted us to precisely re-analyze the seismicity linked to the volcanic system in Mayotte from March 2019 to March 2021. We detected and accurately located 50,512 earthquakes which is close to 8 times more than the 6508 earthquakes in the currently available catalog (RENASS/REVOSIMA). This automatic picking algorithm has been converted into an operational automatic process to monitor the seismic activity in Mayotte since March 2021 [Retailleau et al., 2022]. We separated two types of events from their frequency content as VT and LP earthquakes. These two types of events show a different behavior through time and space. While VT earthquakes are spread over the two clusters observed throughout the crisis, LP earthquakes are restricted to the center of the VT proximal cluster. Moreover, VT earthquakes appear to occur continuously, decaying with time, while LP earthquakes appear to happen episodically in swarms and are on-going. Contrary to VT earthquakes, LP earthquakes may propagate through a fluid area that modified their waveforms and lowered their frequency content. Alternatively, their different location could imply a different source mechanism. In any case, their apparent link to VLP events seems to imply a volcanic trigger, which still needs to be explored.

## Conflicts of interest

The authors declare no competing financial interest.

## Dedication

The manuscript was written through contributions of all authors. All authors have given approval to the final version of the manuscript.

## Acknowledgments

Since June 2019, Mayotte eruption monitoring is funded by le Ministère de l'Enseignement Supérieur, de la Recherche et de l'Innovation (MESRI), le Ministère de la Transition Ecologique (MTE) and le Ministère des Outremers (MOM) with the support of le Ministère de l'Intérieur (MI) and le Ministère des

Armées (MINARM) through the REVOSIMA (Réseau de surveillance volcanologique et sismologique de Mayotte; [Mayotte Volcanological And Seismological Monitoring Network (REVOSIMA) et al., 2021]). AL was partly funded by the European Union's Horizon 2020 research and innovation program under Eurovolc projet (grant agreement No 731070). The authors thank the reviewer Robin Matoza and the editor Jérôme van der Woerd for their reviews which helped improve the manuscript.

OVPF Team: Aline Peltier, Patrice Boissier, Valérie Ferrazzini, Christophe Brunet, Frédéric Lauret, Arnaud Lemarchand, Nicolas Desfete, Kevin Canjamalé, Cyprien Griot, Lise Retailleau, Philippe Catherine, Philippe Kowalski, Andrea di Muro, Fabrice Fontaine, Luciano Garavaglia, Zacharie Duputel, Frédérick Pesqueira.

RA network data available from Résif datacenter [RESIF, 1995]. ED.MCHI station data available at EduSismo. AM network data are available from IRIS and Raspberry Shake SA datacenters [Raspberry Shake, 2016]. 1T and QM data [Mayotte Volcanological And Seismological Monitoring Network (REVOSIMA) et al., 2021] are available upon request.

The catalog of LP earthquakes locations is available on the journal's website.

## Supplementary data

Supporting information for this article is available on the journal's website under https://doi.org/10.5802/crgeos.133 or from the author.

## References

Allen, R. V. (1978). Automatic earthquake recognition and timing from single traces. *Bull. Seismol. Soc. Am.*, 68(5), 1521–1532.

Bachèlery, P., Morin, J., Villeneuve, N., Soulé, H., Nassor, H., and Ali, A. R. (2016). Structure and eruptive history of Karthala Volcano. In *Active Volcanoes of the Southwest Indian Ocean*, pages 345–366. Springer, Cham.

Berthod, C., Médard, E., Bachèlery, P., Gurioli, L., Di Muro, A., Peltier, A., Komorowski, J.-C., Benbakkar, M., Devidal, J.-L., Langlade, J., Besson, P., Boudon, G., E., R.-K., Deplus, C., Le Friant, A., Bickert, M., Nowak, S., Thinon, I., Burckel, P., Hidalgo, S., Kaliwoda, M., Jorry, S. J., Fouquet, Y., and Feuillet, N. (2021). The 2018-ongoing Mayotte submarine eruption: Magma migration imaged by petrological monitoring. *Earth Planet. Sci. Lett.*, 571, article no. 117085.

Bertil, D., Mercury, N., Doubre, C., Lemoine, A., and Van der Woerd, J. (2021). The unexpected Mayotte 2018–2020 seismic sequence: a reappraisal of the regional seismicity of the comoros. *C. R. Géosci.*, 353(S1), 211–235.

Bertil, D. and Regnoult, J. M. (1998). Seismotectonics of madagascar. *Tectonophysics*, 294(1–2), 57–74.

Briole et al. (2018). Note de synthèse. http://volcano.iterre.fr/mayotte-seismo-volcanic-crisis. Accessed 25 May 2021.

Buurman, H. and West, M. (2010). Seismic precursors to volcanic explosions during the 2006 eruption of augustine volcano, chapter 2. In Power, J. A., Coombs, M. L., and Freymueller, J. T., editors, *The 2006 Eruption of Augustine Volcano, Alaska*, volume 1769 of *U.S. Geological Survey Professional Paper*, pages 41–57. SPN, Washington, D.C., https://pubs.usgs.gov/pp/1769/chapters/p1769_chapter02.pdf.

Cesca, S., Letort, J., Razafindrakoto, H. N., Heimann, S., Rivalta, E., Isken, M. P., Nikkhoo, M., Passarelli, L., Petersen, G. M., Cotton, F., and Torsten, D. (2020). Drainage of a deep magma reservoir near Mayotte inferred from seismicity and deformation. *Nat. Geosci.*, 13(1), 87–93.

Chouet, B. A. (1996). Long-period volcano seismicity: its source and use in eruption forecasting. *Nature*, 380(6572), 309–316.

Chouet, B. A. and Matoza, R. S. (2013). A multidecadal view of seismic methods for detecting precursors of magma movement and eruption. *J. Volcanol. Geotherm. Res.*, 252, 108–175.

Clarke, J., Adam, L., and van Wijk, K. (2021). Lp or vt signals? how intrinsic attenuation influences volcano seismic signatures constrained by whakaari volcano parameters. *J. Volcanol. Geotherm. Res.*, 418, article no. 107337.

Dai, H. and Macbeth, C. (1995). Automatic picking of seismic arrivals in local earthquake data using an artificial neural network. *Geophys. J. Int.*, 120(3), 758–774.

Deplus, C., Feuillet, N., Bachelery, P., Fouquet, Y., Jorry, S., Thinon, I., Bermell, S., Besson, F., Gaillot, A., Guérin Sr, C., Le Friant, A., Paquet, F., Pierre, D., and Pitel-Roudaut, M. (2019). Early development and growth of a deep seafloor volcano: Preliminary results from the mayobs cruises. In *AGU Fall Meeting Abstracts*, pages V43I–0227. AGU, Washington, D.C.

Di Stefano, R., Aldersons, F., Kissling, E., Baccheschi, P., Chiarabba, C., and Giardini, D. (2006). Automatic seismic phase picking and consistent observation error assessment: application to the italian seismicity. *Geophys. J. Int.*, 165(1), 121–134.

Diehl, T., Kissling, E., and Bormann, P. (2012). Tutorial for consistent phase picking at local to regional distances. In *New Manual of Seismological Observatory Practice 2 (NMSOP-2)*, pages 1–21. Deutsches GeoForschungsZentrum GFZ.

Dofal, A., Fontaine, F. R., Michon, L., Barruol, G., and Tkalčić, H. (2021). Nature of the crust beneath the islands of the mozambique channel: Constraints from receiver functions. *J. African Earth Sci.*, 184, article no. 104379.

Duputel, Z., Lengliné, O., and Ferrazzini, V. (2019). Constraining spatiotemporal characteristics of magma migration at piton de la fournaise volcano from pre-eruptive seismicity. *Geophys. Res. Lett.*, 46(1), 119–127.

Famin, V., Michon, L., and Bourhane, A. (2020). The comoros archipelago: a right-lateral transform boundary between the somalia and lwandle plates. *Tectonophysics*, 789, article no. 228539.

Feuillet, N., Jorry, S., Crawford, W., Deplus, C., Thinon, I., Jacques, E., Saurel, J.-M., Lemoine, A., Paquet, F., Satriano, C., Aiken, C., Foix, O., Kowalski, P., Laurent, A., Rinnert, E., Cathalot, C., Donval, J.-P., Guyader, V., Gaillot, A., Scalabrin, C., Moreira, M., Peltier, A., Beauducel, F., Grandin, R., Ballu, V., Daniel, R., Pelleau, P., Gomez, J., Besançon, S., Geli, L., Bernard, P., Bachelery, P., Fouquet, Y., Bertil, D., Lemarchand, A., and Van der Woerd, J. (2021). Birth of a large volcanic edifice offshore Mayotte via lithosphere-scale dyke intrusion. *Nat. Geosci.*, 14, 787–795.

Foix, O., Aiken, C., Saurel, J.-M., Feuillet, N., Jorry, S. J., Rinnert, E., and Thinon, I. (2021). Offshore Mayotte volcanic plumbing revealed by local passive tomography. *J. Volcanol. Geotherm. Res.*, 420, article no. 107395.

Garmany, J. (1989). Accumulations of melt at the base of young oceanic crust. *Nature*, 340(6235), 628–632.

Kissling, E., Kradolfer, U., and Maurer, H. (1995). *Program Velest User's Guide—Short Introduction*. Institute of Geophysics, ETH Zurich.

Laurent, A., Satriano, C., Bernard, P., Feuillet, N., and Jorry, S. (2020). Detection, location and characterization of vlf events during the 2018–2020 seismovolcanic crisis in Mayotte. In *AGU Fall Meeting Abstracts*, volume 2020, pages V040–0004. AGU, Washington, D.C.

Lavayssière, A., Crawford, W. C., Saurel, J.-M., Satriano, C., Feuillet, N., Jacques, E., and Komorowski, J.-C. (2022). A new 1d velocity model and absolute locations image the Mayotte seismo-volcanic region. *J. Volcanol. Geotherm. Res.*, 421, article no. 107440.

Lemoine, A., Briole, P., Bertil, D., Roullé, A., Foumelis, M., Thinon, I., Raucoules, D., De Michele, M., Valty, P., and Hoste Colomer, R. (2020). The 2018–2019 seismo-volcanic crisis east of Mayotte, comoros islands: seismicity and ground deformation markers of an exceptional submarine eruption. *Geophys. J. Int.*, 223(1), 22–44.

Leonard, M. (2000). Comparison of manual and automatic onset time picking. *Bull. Seismol. Soc. Am.*, 90(6), 1384–1390.

Liu, M., Zhang, M., Zhu, W., Ellsworth, W. L., and Li, H. (2020). Rapid characterization of the july 2019 ridgecrest, california, earthquake sequence from raw seismic data using machine-learning phase picker. *Geophys. Res. Lett.*, 47(4), article no. e2019GL086189.

Lomax, A. (2008). *The Nonlinloc Software Guide*. ALomax Scientific, Mouans-Sartoux, France, http://alomax.free.fr/nlloc.

Matoza, R. S., Shearer, P. M., and Okubo, P. G. (2014). High-precision relocation of long-period events beneath the summit region of kılauea volcano, hawai'i, from 1986 to 2009. *Geophys. Res. Lett.*, 41(10), 3413–3421.

Mayotte Volcanological And Seismological Monitoring Network (REVOSIMA), Institut de physique du globe de Paris (IPGP), Bureau de recherches géologiques et minières (BRGM), Institut français de recherche pour l'exploitation de la mer (IFREMER), and Centre national de la recherche scientifique (CNRS) (2021). Data collection of the Mayotte volcanological and seismological monitoring network (revosima). http://volobsis.ipgp.fr/revosima/.

Mittal, T., Jordan, J. S., Retailleau, L., Beauducel, F., and Peltier, A. (2022). Mayotte 2018 eruption likely sourced from a magmatic mush. *Earth Planet. Sci. Lett.*, 590, article no. 117566.

Park, Y., Mousavi, S. M., Zhu, W., Ellsworth, W. L., and Beroza, G. C. (2020). Machine-learning-based analysis of the guy-greenbrier, arkansas earthquakes: A tale of two sequences. *Geophys. Res. Lett.*, 47(6), article no. e2020GL087032.

Peltier, A., Bachèlery, P., and Staudacher, T. (2009). Magma transport and storage at piton de la fournaise (la réunion) between 1972 and 2007: A review of geophysical and geochemical data. *J. Volcanol. Geotherm. Res.*, 184(1–2), 93–108.

Raspberry Shake, S. (2016). Raspberry shake. https://www.fdsn.org/networks/detail/AM/.

RESIF (1995). Resif-rap french accelerometric network. https://seismology.resif.fr/networks/#/RA.

Retailleau, L., Saurel, J.-M., Zhu, W., Satriano, C., Beroza, G. C., Issartel, S., Boissier, P., Team, O., and Team, O. (2022). A wrapper to use a machine-learning-based algorithm or earthquake monitoring. *Seismol. Res. Lett.*, 93(3), 1673–1682.

REVOSIMA-IPGP (2021). Bulletin de l'activité sismo-volcanique à Mayotte. www.ipgp.fr/fr/revosima.

Ross, Z. E., Idini, B., Jia, Z., Stephenson, O. L., Zhong, M., Wang, X., Zhan, Z., Simons, M., Fielding, E. J., Yun, S.-H., E., H., Moore, A. W., Liu, Z., and Jung, J. (2019). Hierarchical interlocked orthogonal faulting in the 2019 ridgecrest earthquake sequence. *Science*, 366(6463), 346–351.

Saurel, J.-M., Jacques, E., Aiken, C., Lemoine, A., Retailleau, L., Lavayssière, A., Foix, O., Dofal, A., Laurent, A., Mercury, N., Crawford, W., Lemarchand, A., Daniel, R., Pelleau, P., Bès de Berc, M., Dectot, G., Bertil, D., Roullé, A., Broucke, C., Colombain, A., Jund, H., Besançon, S., Guyavarch, P., Kowalski, P., Roudaut, M., Apprioual, R., Battaglia, J., Bodihar, S., Boissier, P., Bouin, M.-P., Brunet, C., Canjamale, K., Catherine, P., Desfete, N., Doubre, C., Dretzen, R., Dumouche, T., Fernagu, P., Ferrazzini, V., Fontaine, F. R., Gaillot, A., Géli, L., Griot, C., Grunberg, M., Can Guzel, E., Hoste-Colomer, R., Lambotte, S., Lauret, F., Léger, F., Maros, E., Peltier, A., Vergne, J., Satriano, C., Tronel, F., Van der Woerd, J. an Fouquet, Y., Jorry, J. S., Rinnert, E., Thinon, I., and Feuillet, N. (2022). Mayotte seismic crisis: building knowledge in near real-time by combining land and ocean-bottom seismometers, first results. *Geophys. J. Int.*, 228(2), 1281–1293.

Shapiro, N. M., Droznin, D., Droznina, S. Y., Senyukov, S., Gusev, A., and Gordeev, E. (2017). Deep and shallow long-period volcanic seismicity linked by fluid-pressure transfer. *Nat. Geosci.*, 10(6), 442–445.

Shelly, D. R., Beroza, G. C., and Ide, S. (2007). Non-volcanic tremor and low-frequency earthquake swarms. *Nature*, 446(7133), 305–307.

Tan, Y. J., Waldhauser, F., Ellsworth, W. L., Zhang, M., Zhu, W., Michele, M., Chiaraluce, L., Beroza, G. C., and Segou, M. (2021). Machine-learning-based high-resolution earthquake catalog reveals how complex fault structures were activated during the 2016–2017 central italy sequence. *The Seismic Record*, 1(1), 11–19.

Thordarson, T. and Self, S. (1993). The laki (skaftár fires) and grímsvötn eruptions in 1783–1785. *Bull. Volcanol.*, 55(4), 233–263.

White, R. A. and McCausland, W. A. (2019). A process-based model of pre-eruption seismicity patterns and its use for eruption forecasting at dormant stratovolcanoes. *J. Volcanol. Geotherm. Res.*, 382, 267–297. Lessons learned from the recent eruptions of Sinabung and Kelud Volcanoes, Indonesia.

Wilcock, W. S. D., Tolstoy, M., Waldhauser, F., Garcia, C., Tan, Y. J., Bohnenstiehl, D. R., Caplan-Auerbach, J., Dziak, R. P., Arnulf, A. F., and Mann, M. E. (2016). Seismic constraints on caldera dynamics from the 2015 axial seamount eruption. *Science*, 354(6318), 1395–1399.

Zhu, W. and Beroza, G. C. (2019). Phasenet: a deep-neural-network-based seismic arrival-time picking method. *Geophys. J. Int.*, 216(1), 261–273.

*Comptes Rendus*
*Géoscience — Sciences de la Planète*
**2022**, Vol. 354, Special Issue S2, p. 171-193
https://doi.org/10.5802/crgeos.176

The Mayotte seismo-volcanic crisis of 2018-2021 in the Comoros archipelago (Mozambique channel) / *La crise sismo-volcanique de 2018-2021 de Mayotte dans l'archipel des Comores (Canal du Mozambique)*

# Ground deformation monitoring of the eruption offshore Mayotte

## *Suivi des déformations liées à l'éruption au large de Mayotte*

**Aline Peltier** [*, a, b], **Sébastien Saur** [c], **Valérie Ballu** [d], **François Beauducel** [a], **Pierre Briole** [e], **Kristel Chanard** [a], **Denis Dausse** [d], **Jean-Bernard De Chabalier** [a], **Raphael Grandin** [a], **Perrine Rouffiac** [c], **Yann-Treden Tranchant** [d], **Maxime Bès de Berc** [f], **Simon Besançon** [a], **Patrice Boissier** [a, b], **Céleste Broucke** [a, g], **Christophe Brunet** [a, b], **Kevin Canjamalé** [a, b], **Erwan Carme** [h], **Philippe Catherine** [a, b], **Alison Colombain** [i], **Wayne Crawford** [a], **Romuald Daniel** [a], **Grégoire Dectot** [h], **Nicolas Desfete** [a, b], **Cécile Doubre** [f], **Tom Dumouch** [a], **Cyprien Griot** [a, b], **Marc Grunberg** [g], **Hélène Jund** [g], **Philippe Kowalski** [a, b], **Frédéric Lauret** [a, b], **Jacques Lebreton** [a, b], **Frédérick Pesqueira** [a, b], **Frédéric Tronel** [h], **Pierre Valty** [c] and **Jérôme van der Woerd** [f]

[a] Université Paris Cité, Institut de physique du globe de Paris, CNRS, 75005 Paris, France

[b] Observatoire volcanologique du Piton de la Fournaise, Institut de Physique du Globe de Paris, 97418 La Plaine des Cafres, France

[c] Institut national de l'information géographique et forestière, Service de Géodésie et Métrologie, 94165 Saint Mandé, France

[d] LIttoral ENvironnement et Sociétés (LIENSs) UMR7266, La Rochelle Université - CNRS, La Rochelle, France

[e] UMR 8538 CNRS - École normale supérieure - PSL Research University, Laboratoire de Géologie, 24, r. Lhomond, 75231 Paris, France

[f] Institut terre et environnement de Strasbourg, Université de Strasbourg, CNRS, UMR7063 67000 Strasbourg, France

[g] EOST/UAR 830, Université de Strasbourg/CNRS, 5 rue René Descartes, 67084 Strasbourg Cedex, France

[h] Bureau de recherches géologique et minières DAT/OMR/MAY, BP363 97646 Mamoudzou cedex, Mayotte, France

[i] Bureau de recherches géologiques et minières GR/GBS, BP 36009 45060 Orléans Cedex 2, France

* Corresponding author.

*E-mails:* peltier@ipgp.fr (A. Peltier), Sebastien.Saur@ign.fr (S. Saur), valerie.ballu@univ-lr.fr (V. Ballu), beauducel@ipgp.fr (F. Beauducel), briole@ens.fr (P. Briole), chanard@ipgp.fr (K. Chanard), Denis.dausse@univ-lr.fr (D. Dausse), jbdechabalier@ipgp.fr (J.-B. De Chabalier), grandin@ipgp.fr (R. Grandin), Perrine.Rouffiac@ign.fr (P. Rouffiac), yanntreden.tranchant1@univ-lr.fr (Y.-T. Tranchant), mbesdeberc@unistra.fr (M. B. de Berc), sbesancon@ipgp.fr (S. Besançon), boissier@ipgp.fr (P. Boissier), broucke@ipgp.fr (C. Broucke), brunet@ipgp.fr (C. Brunet), canjamale@ipgp.fr (K. Canjamalé), e.carme@brgm.fr (E. Carme), caterine@ipgp.fr (P. Catherine), a.colombain@brgm.fr (A. Colombain), crawford@ipgp.fr (W. Crawford), r.daniel@ipgp.fr (R. Daniel), G.Dectot@brgm.fr (G. Dectot), desfete@ipgp.fr (N. Desfete), cecile.doubre@unistra.fr (C. Doubre), dumouch@ipgp.fr (T. Dumouch), griot@ipgp.fr (C. Griot), marc.grunberg@unistra.fr (M. Grunberg), helene.jund@unistra.fr (H. Jund), kowalski@ipgp.fr (P. Kowalski), lauret@ipgp.fr (F. Lauret), lebreton@ipgp.fr (J. Lebreton), pesqueir@ipgp.fr (F. Pesqueira), F.Tronel@brgm.fr (F. Tronel), Pierre.Valty@ign.fr (P. Valty), jerome.vanderwoerd@unistra.fr (J. van der Woerd)

**Abstract.** In May 2018, the Mayotte island, located in the Indian Ocean, was affected by an unprecedented seismic crisis, followed by anomalous on-land surface displacements in July 2018. Cumulatively from July 1, 2018 to December 31, 2021, the horizontal displacements were approximately 21 to 25 cm eastward, and subsidence was approximately 10 to 19 cm. The study of data recorded by the on-land GNSS network, and their modeling coupled with data from ocean bottom pressure gauges, allowed us to propose a magmatic origin of the seismic crisis with the deflation of a deep source east of Mayotte, that was confirmed in May 2019 by the discovery of a submarine eruption, 50 km offshore of Mayotte [Feuillet et al., 2021]. Despite a non-optimal network geometry and receivers located far from the source, the GNSS data allowed following the deep dynamics of magma transfer, via the volume flow monitoring, throughout the eruption.

**Résumé.** En mai 2018, l'île de Mayotte a été touchée par une crise sismique sans précédent, suivie en juillet 2018 par des déplacements de surface à terre anormaux. En cumulé, du 1$^{er}$ juillet 2018 au 31 décembre 2021, les déplacements horizontaux étaient d'environ 21 à 25 cm vers l'est, et la subsidence d'environ 10 à 19 cm. L'étude des données GNSS à terre, et leur modélisation couplée aux données des capteurs de pression en mer, ont permis de conclure à une origine magmatique de la crise sismique avec la déflation d'une source profonde à l'est de Mayotte, confirmée en mai 2019 par la découverte d'une éruption sous-marine, à 50 km au large de Mayotte [Feuillet et al., 2021]. Malgré une géométrie de réseau non optimale et des récepteurs éloignés de la source, les données GNSS ont permis de suivre la dynamique profonde du transfert magmatique, via la surveillance des flux volumiques.

**Keywords.** GNSS, Pressure gauge, Volcano deformation, Mayotte, GRACE modeling, Joint inversion, Fani Maoré.

**Mots-clés.** GNSS, Capteur de pression, Déformation volcanique, Mayotte, Modélisation GRACE, Inversion jointe, Fani Maoré.

*Published online: 19 December 2022, Issue date: 17 January 2023*

## 1. Introduction

In May 2018, the Mayotte island, located in the Comoros archipelago, in the Indian Ocean, about 300 km north-west of Madagascar, was affected by an unprecedented seismic crisis, with more than 300 earthquakes recorded per day at the beginning of the crisis [Bertil et al., 2021, Cesca et al., 2020, Lavayssière et al., 2022, Lemoine et al., 2020, Feuillet et al., 2021, Retailleau et al., 2022, REVOSIMA, 2019, Saurel et al., 2022, Mercury et al., 2022]. The majority of these earthquakes were of low magnitude (<2.0), but several events of moderate magnitude (3.5 to 5.9) were strongly felt, causing panic among the population [Miki, 2021]. The largest event, of magnitude $M_w = 5.9$, occurred on May 15. The earthquakes were located 5–30 km offshore east of Mayotte with epicenters clustered between 5 and 15 km east of the island and along an alignment of volcanic cones at 25 km east of the island, at depths ranging from 25 and 50 km [Bertil et al., 2021, Lavayssière et al., 2022, Lemoine et al., 2020, Feuillet et al., 2021, Retailleau et al., 2022, REVOSIMA, 2019, Saurel et al., 2022, Mercury et al., 2022]. As of May 2022, the seismicity is still ongoing, although at a much lower intensity and a mean of 10 low-magnitude events per day [REVOSIMA, 2021].

In July 2018, the *Institut national de l'information géographique et forestière* (*IGN*), which is in charge of the French Permanent GNSS (global navigation satellite system) Network (RGP—*réseau GNSS permanent*), started detecting anomalies in the time series of the GNSS stations of Mayotte and issued a warning on the RGP web portal. The anomalous drifts of coordinates were both horizontal and vertical. The latter were intriguing because they could not be fitted with dislocation models assuming crustal earthquakes in the area of the seismic crisis. The first elastic simple models indicated a deflation source located in a range of 30–60 km east of Mayotte, at a depth of 25–50 km, depending on the model and the time periods considered [Lemoine et al., 2020, OVPF, 2019]. The large depth of the deformation source was a strong indicator of a magmatic origin of the phenomenon. Based on the observation of dead benthopelagic fishes by the local population, the scientific community quickly agreed on a submarine volcanic origin of the phenomenon.

Support was given by the French government and scientific institutions to deploy additional instruments both inland (seismometers and GNSS stations) and offshore (Ocean bottom seismometer, pressure gauges) around the active zone from early 2019. In May 2019, the MAYOBS1 cruise discovered a large new volcano edifice, Fani Maoré, at the seafloor around 50 km east of the Mayotte island [Feuillet, 2019, Feuillet et al., 2021]. The eruption is one of the largest effusive eruptions in the world over the last three centuries, with about 5 $km^3$ of lava flow emitted during the first year [Feuillet et al., 2021].

In June 2019, after the discoveries of MAYOBS1, a multi-institutional coordination was created to monitor the phenomenon by means of an array composed of in-land instruments monitored in real time, and periodic campaigns performed inland and offshore to collect data from other instruments as well as geological and geochemical samples. This coordination, called the REVOSIMA (*Réseau de surveillance volcanologique et sismologique de Mayotte*), is operated by IPGP (*Institut de physique du globe de Paris*) through in particular the OVPF-IPGP (*Observatoire volcanologique du Piton de la Fournaise)*, in collaboration with BRGM (*Bureau de recherches géologiques et minières*) through its regional department in Mayotte. REVOSIMA also gathers IFREMER (*Institut français de recherche pour l'exploitation de la mer*), CNRS (*Centre national de la recherche scientifique*), IGN (*Institut national de l'information géographique et forestière*) and several other French entities. For the 24/7 continuous real-time monitoring, the REVOSIMA uses a permanent network installed inland on Mayotte comprising eight seismometers, nine GNSS stations and one gas station (as of January 2022).

GNSS method is now one of the most powerful and widely used methods worldwide, to detect, monitor and model in real-time, the continuous ground deformation associated with volcano unrests and eruptions [e.g. Dzurisin, 2006, Lisowski, 2007, Segall, 2010]. For the seismic crisis affecting Mayotte, GNSS data and their modeling were decisive in understanding its origin. Here, we present first how the GNSS network was expanded in Mayotte through the evolution of the crisis. We then show the time series of GNSS coordinates and their modeling, which provide constraints on the dynamics of magma transfer throughout the lithosphere. Finally, we discuss the contribution of the ocean bottom pressure gauges, installed during the crisis, for modeling.

## 2. GNSS data

### 2.1. *GNSS network in and around Mayotte*

Even though RGP detected the anomalous drifts of coordinates of its 4 GNSS permanent stations as early as July 2018, it quickly became clear that the monitoring of the phenomenon would require a densification of the GNSS network and coordination of all the actions undertaken for that purpose.

Beyond the 4 stations already used (namely MAYG, BDRL, GAMO, KAWE), two other GNSS stations already in operation on the island in 2018 (MTSA and PORO) were used for monitoring, and three others were specifically installed in Mayotte in 2019 (KNKL, PMZI and MTSB; Figure 1a). A GNSS station (GLOR), was also installed on Grande Glorieuse island, about 250 km east north-east of Mayotte (Figure 1b).

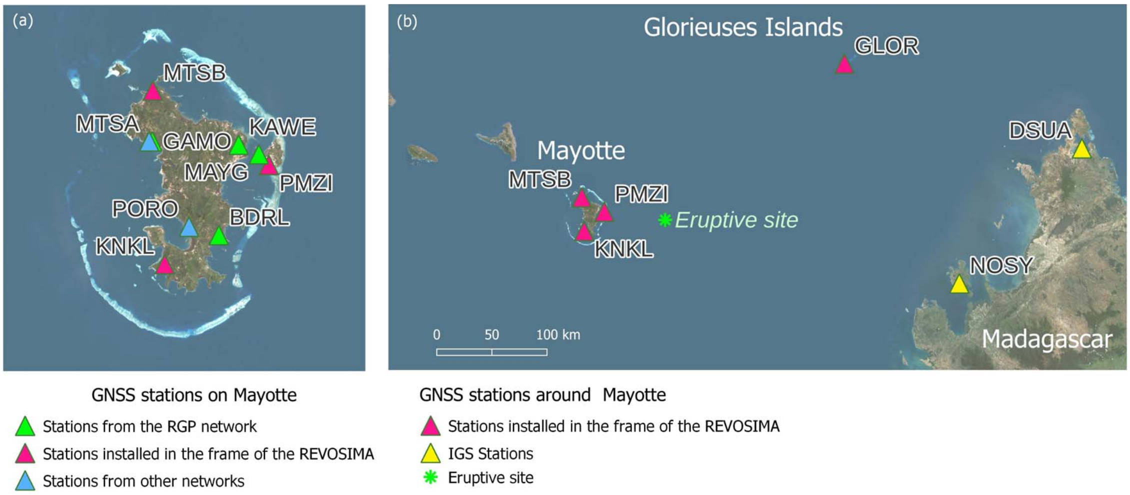


**Figure 1.** (a) Location of the GNSS stations on Mayotte island. (b) Location of the GNSS station located around Mayotte and used by the REVOSIMA. Green star indicates the eruption location.

Two additional stations, DSUA and NOSY, located north of Madagascar (about 400 km east from Mayotte), were also used by the REVOSIMA for processing of the Mayotte data [Figure 1; Bousquet et al., 2020]. However, these stations went quickly out of order, and could not be repaired since then due to the covid-19 pandemic. Also, there is no GNSS data available from the other Comoros islands.

The comprehensive list of the GNSS stations used for the monitoring of the eruption offshore Mayotte is available in Supplementary Material A.

All the GNSS stations are connected to the internet either by 4G networks or by terrestrial link, and queryable in real-time. The four native RGP stations (MAYG, BDRL, GAMO, KAWE) provide multi-GNSS observation hourly files at 1 s sampling rate, whereas the other stations provide hourly or daily files at 30 s sampling rate. All observation files are transformed into daily 30 s files for homogeneous processing.

All the entities involved in the network have come together as a dedicated working group, as early as July 2018, under the coordination of IGN, to achieve a common mode of operation of the stations, and to agree on the centralization and sharing of GNSS data and products, through the operational infrastructure of the RGP, made available by IGN. This working group gathered the following entities in an exemplary public-private partnership: *Institut national de l'information géographique et forestière (IGN), Institut de physique du globe de Paris (IPGP), Observatoire volcanologique du Piton de la Fournaise (OVPF-IPGP), Ecole normale supérieure, Laboratoire de Géologie (ENS), Ecole et observatoire des sciences de la terre de Strasbourg (EOST), Centre national d'études spatiales (CNES), Laboratoire de l'atmosphère et des cyclones, université de La Réunion (LACY), Exagone, Précision Topo.*

## 2.2. *Automatic GNSS data processing*

The GNSS data are routinely and automatically processed by both OVPF-IPGP in charge of the 24/7 continuous and real-time monitoring of Mayotte, and IGN, which is in charge of data distribution (see Data availability statement).

OVPF-IPGP calculates daily solutions with the GipsyX precise point positioning (PPP) software [Bertiger et al., 2020], using the best quality JPL's orbits and the clock products available at the time of calculation (ultra, rapid, then final orbits after a delay of ten days) and provides daily solutions in the ITRF2014 reference frame. The standard deviations of the daily coordinates of MAYG for the years preceding the crisis, detrended from the secular velocity of the station, are 1.9, 1.8, and 5.6 mm for eastern, northern, and vertical components, respectively. The other stations have similar scores. The daily solutions are distributed, processed and displayed on WebObs, a web-based integrated system for data monitoring and networks management routinely used for the crisis management in a dozen volcano observatories worldwide, including the IPGP observatories [Beauducel et al., 2020a]. WebObs is an open source project that includes several specific modules for seismological, geophysical and geochemical data processing in near real-time, one of these modules is dedicated to GNSS solutions.

The resulting outputs from these processes are:

- coordinate files for all the stations used, in the ITRF2014 reference frame;
- time series of the station coordinates with respect to the reference coordinates, for which the horizontal tectonic motion is subtracted using the theoretical velocity given by the tectonic plate model provided by the ITRF;
- time series of the baselines from selected pairs of stations;
- velocities estimated from linear trends for each station at different time windows, represented as vectors on maps;
- source modeling at different time windows (see Section 5.2.2).

IGN calculates the daily solutions with the Bernese GNSS software in double difference mode, including the GNSS stations in and around Mayotte, as described above, and a large number of stations located in Africa, Asia, Madagascar, and on some islands in the Indian Ocean or in the Subantarctic zone. Most of those stations are part of either the RGP or the IGS networks, and their data are available through the RGP and IGS data centers. Depending on their data availability, up to 66 stations are used. The computation is made on a daily basis using the 24 h observation data. The coordinates are produced in the ITRF2014 reference frame. Moreover, a weekly computation is performed, combining the normal equations of the last seven days.

The resulting files from these processes are:

- solution files (normal equations) in the SINEX format;
- coordinate files for all the stations used, in the ITRF2014 reference frame;
- time series of coordinates with respect to the reference coordinates, for which the horizontal tectonic motion is removed using the theoretical velocity given by the tectonic plate model provided by the ITRF.

## 3. Pressure gauge

Ocean bottom pressure (OBP) gauges were deployed by the REVOSIMA in February 2019 along with ocean bottom seismometers (OBS; Figure 2a), with the aim of collecting data as close as possible to the seismic active area and with an azimuthal distribution around the source tailored to best constrain its location and spatial extent. Several SBE 37-SM MicroCat CT Recorder pressure gauges (named SBE 37 hereafter) constructed by Sea-Bird Electronics were therefore installed directly on OBSs frames (Figure 2b), and later redeployed through successive MAYOBS campaigns (Supplementary Materials B and C). Although this type of pressure gauge sensor was not originally designed for geodetic pressure measurements, we deployed them with the first intention of detecting pluri-centimeter co-seismic signals. A previous experiment, made in response to the Santorini volcanic unrest in 2011, showed their potential usefulness in such geodetic studies [Vilaseca et al., 2016]. Figure 2a shows the location of the first pressure gauges deployment, which provided six OBP records from February to May 2019, i.e. nine months after the onset of the crisis. Originally, before the discovery of the offshore eruption, the spatial OBS distribution had been designed wide enough to encompass the entire seismic swarm, therefore its design was not optimal for the deformation monitoring.

For monitoring seafloor deformation through time with OBPs, limitations arise from (1) the instrumental drift and (2) the oceanographic variations. The drift of pressure sensors is usually modeled by combining an exponential term modeling the initial adaptation of the sensor and a long-term linear drift [Wallace et al., 2016, Chierici et al., 2016, Gennerich and Villinger, 2011], which can reach several centimeters per year and be on the same order of magnitude as the vertical signal, one wants to detect.

To address this instrumental issue, and to allow the precise monitoring of slow sea-floor deformation [Wilcock et al., 2021], the SBE 37 pressure gauge network was completed from April 2020 by an A0A pressure gauge (see Supplementary Material B). In the A0A system, the instrumental drift is estimated in-situ by periodic venting from ocean pressures to a reference atmospheric pressure. However, no significant vertical ground displacements are recorded by GNSS stations of Mayotte, Grande Glorieuse and

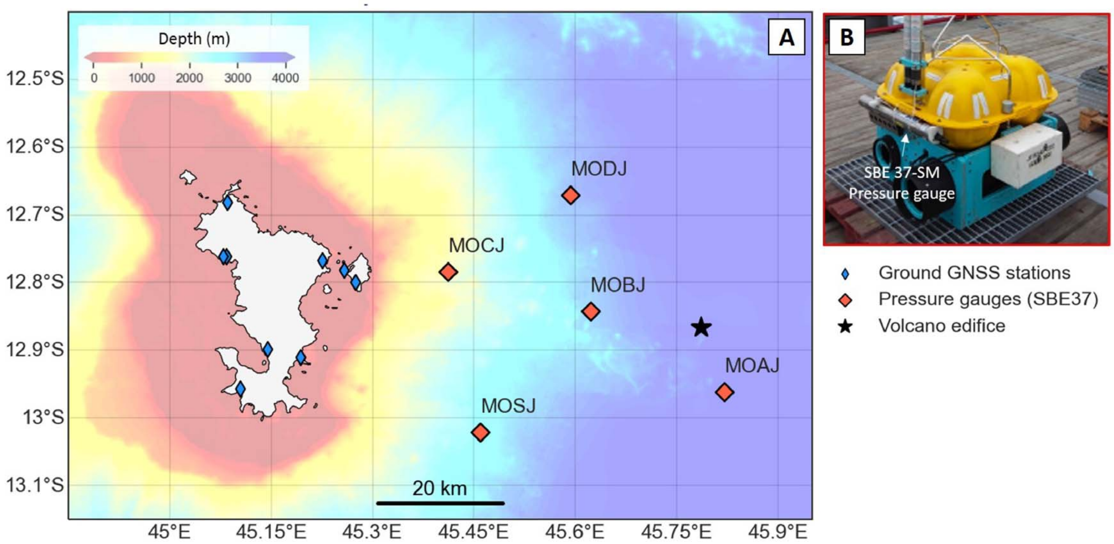


**Figure 2.** (a) First deployment of SBE 37 pressure gauges (red diamonds), deployed in February 2019 and all recovered during the MAYOBS1 campaign in May 2019 [Feuillet, 2019, Rinnert et al., 2019]. The land-based GNSS stations are represented by blue diamonds and the eruption location by the black star. (b) SBE 37-SM pressure sensor equipped on an OBS package.

Madagascar from this period (see Supplementary Material F), and thus we do not expect any seafloor deformation signature in these A0A pressure records. Although these data are not used in this paper in terms of deformation, the drift-controlled records are used hereafter to assess the order of magnitude of SBE 37 pressure gauges instrumental drift by comparing simultaneous and co-located bottom pressure data. The pressure differences between SBE 37 (MOCH and MOCI, see Supplementary Material B) and A0A1 records, deployed from October 2020 to April 2021, are shown in Supplementary Material D. These two comparisons suggest that SBE 37 sensors used in this study have a linear trend below 2 hPa/month (~0.016% per year considering a depth of 1500 m).

The existence of oceanic variations at different timescales is the second major limitation for the detection of seafloor deformation using OBPs. Indeed, while vertical seafloor displacements associated with volcanic activity are expected to be in the order of a few centimeters, oceanic variations can reach tens of centimeters on the same time scales [Dobashi and Inazu, 2021]. The oceanic pressure variations can be partly inferred from ocean circulation models [Dobashi and Inazu, 2021]. For this study, we used bottom pressures from the "cube92" version of the ECCO2 model, which are available at daily resolution on a regular grid (0.25°) from January 1992 to March 2021 [Menemenlis et al., 2008]. Consequently, OBP data recovered after March 2021 were not considered in the present study. Concerning the high-frequency signal, i.e. mostly diurnal and semi-diurnal tides, the OBP records were low-pass filtered at 72 h using a Demerliac tide killer [Demerliac, 1974].

The filtered and corrected pressure anomalies are shown on Figure 3. The 6 OBP records show a pronounced variation over a short initial period of a few days, therefore the first five days of data were removed to reject the main part of the initial instrumental drift (red portions on Figure 3). Adaptation periods, as short as a few days, have been previously observed by Gennerich and Villinger [2011], who speculated that this relative fastness was due to previous immersion of the sensors for long periods at similar depths. All 6 data records exhibit a positive linear trend (dashed lines on Figure 3), ranging from 1.67 hPa per month (MOSO) to 5.34 hPa per month (MOSE), which may correspond both to

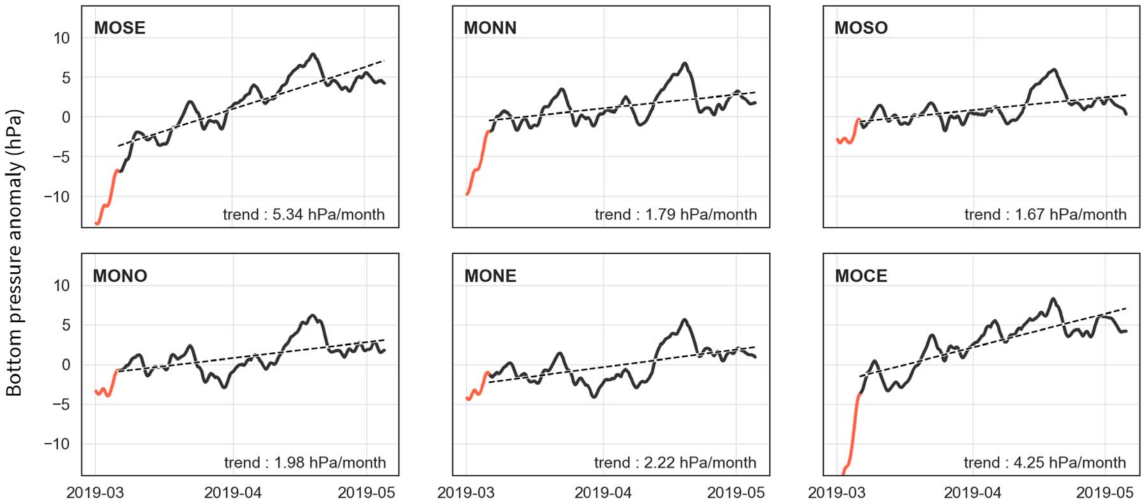


**Figure 3.** Bottom pressure anomalies (BPA) from six OBP records (February to May 2019), after applying the Demerliac filter and correcting the ocean signal contribution from the ECCO2 model. The first five days of data (red portions) are not used in trend estimates. Dashed lines represent the linear trend of each BPA series, for which the value is annotated on the bottom right corner.

a linear instrumental drift and to the signature of the seafloor subsidence in the region during the March–May 2019 period. OBP data from the other campaigns are shown in Supplementary Materials E.

Although associated with large uncertainties (mainly due to uncorrected instrumental drift and the presence of residual oceanic variations), these OBP records are used in this study to demonstrate that it can successfully complement GNSS data in order to improve the determination of the source locations though inversion models (Section 5.2.3).

## 4. Ground displacement trends

### 4.1. *Comparison between Bernese and GipsyX time series*

Before a close inspection and modeling of the GNSS trends, we first compared the time series produced by our GipsyX and Bernese computations. For that, we used MAYG, which is the only station that existed several years before the crisis, as it was installed on December 22, 2013. Figure 4 shows the east, north and vertical time series of the station detrended from a secular velocity.

At first order, the time series are similar in terms of variations and noise (less than 10 mm), except a shift of about 8 mm in July 2015 visible on the east component of Bernese processing (due to the change of calculations in the IGb08 reference system, with the use of the associated antenna calibrations). The annual and semi-annual deformation due to redistribution of hydrological and atmospheric masses on the Earth surface are observed in both processing methods, with a slightly lower amplitude for the Bernese solution. The small differences of a few millimeters between the two solutions do not lead to significant differences in the deformation field given the large amplitude (decimetric) of the displacements recorded during the crisis. Therefore, the two GNSS solutions are equivalent for further modeling and interpretations. In the following, we use the time series of our GipsyX processing, which are used routinely by OVPF-IPGP for the 24/7 continuous and real-time monitoring of Mayotte.

### 4.2. *Evolution of the time series*

Shortly after the onset of the volcanic crisis in May 2018, anomalous displacements were detected from July 2018 by the GNSS network operating on Mayotte. Figure 5 shows the time series of eastward, northward and vertical ground displacements of the GNSS stations computed between January 1, 2017 and December, 31 2021.

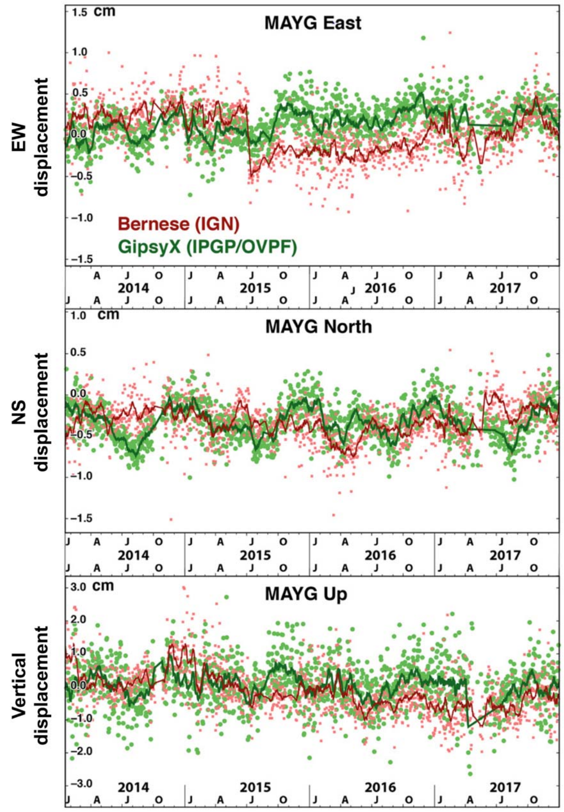


**Figure 4.** Comparison of the MAYG time series processed by the Bernese (in red) and GipsyX (in green) software during the 2014–2017 period preceding the volcano crisis. The points correspond to raw daily solutions, and the lines correspond to 14-day moving average trends.

The GNSS time series show, from July 2018, an overall displacement of the island towards the east and a subsidence [Figures 5 and 6; Lemoine et al., 2020, Feuillet et al., 2021]. Cumulatively from July 1, 2018 to December 31, 2021, these horizontal displacements are approximately 21 to 25 cm eastward, and subsidence of approximately 10 to 19 cm depending on the site (Figure 5, Supplementary Material F). The cumulative horizontal displacements point towards the east, about 20 km offshore the Mayotte coast (Figure 6).

Around April–May 2019, a first slowdown in the trend is observed. Since 2020 movements slow down again and after March 2020 subsidence becomes negligible at several stations, e.g. MTSA, MTSB, PORO (Figure 5, Supplementary Material F). Then, since late 2020 the ground displacements have become so weak that they do not seem to emerge from the noise.

The velocity of MAYG, the only station with a long pre-crisis (4.5 years) time series, has returned, in the three components, to the one observed before 2018.

On the stations located east and south-east of the volcano, further away (more than 250 km), on Grande Glorieuse and Madagascar, no significant deformation has been recorded [Figure 5, Supplementary Material F; Bousquet et al., 2020]. However, in the medium and long term, the data of Grande Glorieuse, in particular, will be important to constrain the geodynamics at the scale of the Comoros archipelago.

## 5. Modeling

### 5.1. *Gravity Recovery and Climate Experiment (GRACE) modeling*

Continuous GNSS-derived land motion measurements in Mayotte are affected, in addition to any seismo-volcanic transient, by (a) steady tectonic plate motion and (b) seasonal variations due to spatio-temporal changes in continental surface water storage, both at local and continental scale. The signature of these processes in the GNSS time-series needs to be characterized to estimate the uncertainty involved in the subsequent inverse modeling of the source.

The area of Mayotte belongs to a diffuse plate boundary between the Somalia, Lwandle and Rovuma tectonic plates, characterized by a transtensional strain regime [Stamps et al., 2018, Famin et al., 2020]. Due to poor constraints on plate kinematic solutions in the area, we use the GNSS time-series at MAYG (available since 2014) to estimate the tectonic trend in Mayotte by fitting a linear regression on the horizontal components. This estimate is used for correcting plate motion at all stations in Mayotte, which implicitly assumes rigid motion and neglects rotation of the island.

After removing the estimated tectonic trend, a quasi-periodic signal is clearly visible in the detrended pre-crisis (2014–2018) time-series at MAYG (Figure 7a). Figures 7b and 7c show that this pre-crisis signal is dominated by a 1-year cyclicity, with a peak-to-peak 30-days sliding average displacement

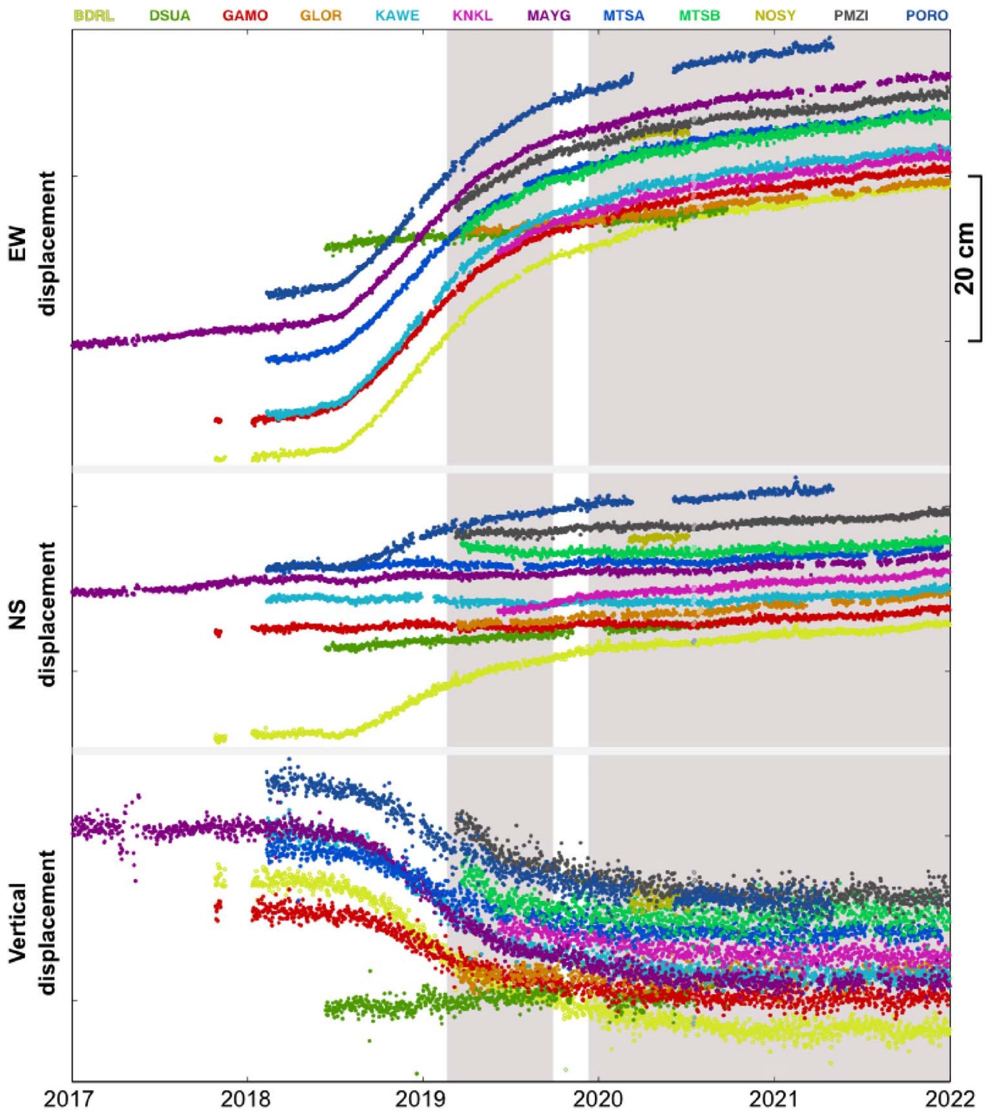


**Figure 5.** Time series of daily solutions of eastward (top), northward (middle), and vertical (bottom) ground displacements as recorded by GNSS stations of Mayotte, Grande Glorieuse (GLOR), and Madagascar (DSUA, NOSY), between January 1, 2017 and December, 31 2021. Time series are not corrected from plate motion; the corrected time series are shown in Supplementary Material F. Shaded grey boxes highlight the periods with OBP measurements.

of 4 mm, 9 mm and 12 mm on the East, North and Up components, respectively. The signal is strongest on the vertical component, with peak downward displacement occurring in August, whereas peak upward displacement occurs in December. The north component shows a clear maximum southward displacement roughly in phase with the vertical, with a peak southward displacement occurring in August–September. Both the vertical and north components show a higher-order periodicity (i.e. fluctuations are not monochromatic), as reflected by a longer transition (8 months) between the upper peak (upwards, northwards, in December) and the lower peak (downwards, southwards, in August), and a shorter

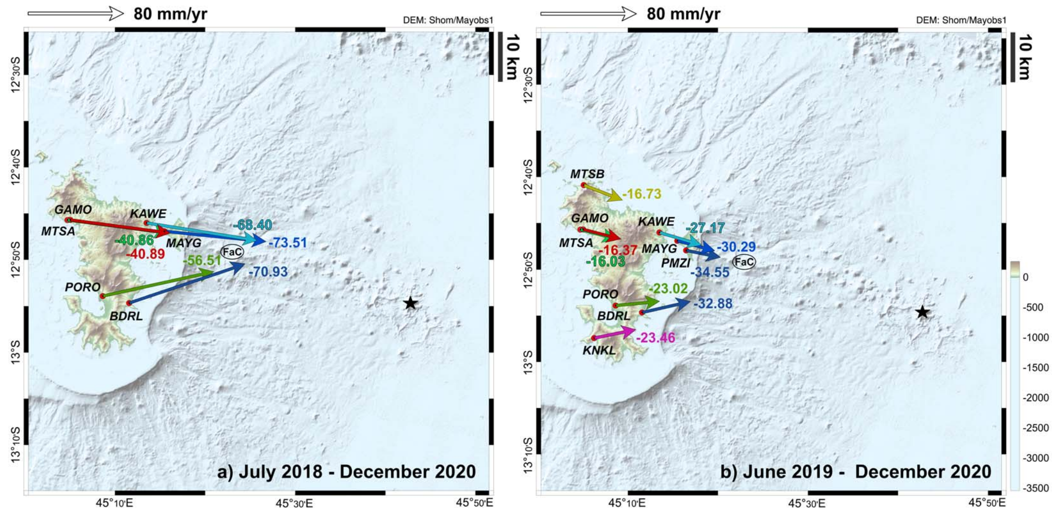


**Figure 6.** Ground displacements recorded on GNSS stations in Mayotte (a) between July 2018 and December 2020 with the stations available from the beginning of the crisis and (b) between June 2019 and December 2020 with all GNSS stations. The horizontal displacements are represented as velocities in vector form and the vertical displacement velocities are indicated by the numerical values in color (in mm/yr). Displacements are corrected from plate velocities. Black star indicates the eruption location. FaC stands for "Fer à Cheval", an old structure where acoustic plumes are observed [REVOSIMA, 2021].

transition (4 months) toward the next upper peak (August to December).

The seasonal fluctuations observed in the pre-crisis MAYG GNSS time-series are interpreted as the result of continental-scale (>1000 km) perturbations of the Earth shape caused by the continental hydrological cycle and external atmospheric forcing [Blewitt et al., 2001]. Surface displacements result from the spatially and temporally variable surface loads occurring at the Earth's surface, convolved with the Earth's deformation response [Tregoning et al., 2009]. Fluctuations typically manifest as periodic signals affecting the GNSS time-series, dominated by a seasonal term (annual), as well as higher-order harmonics.

To confirm the hydrological origin of the quasi-periodic signal visible in Mayotte, we use data from GRACE for the period, April 2002–June 2017 and current GRACE-Follow On (GRACE-FO) from June 2018-present missions. GRACE data provide monthly global measurements of the space and time varying Earth's gravity field, monitoring changes in continental water storage, non-tidal oceanic and atmospheric loading (Figure 7). They can be used to constrain the hydrological source term, which can be subsequently fed into an Earth deformation modeling scheme. Yet, the high level of distinctive unphysical noise in a North–South striping pattern affecting the GRACE data, as well as the temporal gaps (including the long 11 months gap between GRACE and GRACE-FO missions) prevent the interpretation of long-term mass variations. Consequently, we use the Multi-Channel Singular Spectrum Analysis (MSSA) and utilise both spatial and temporal information contained in multiple Level-2 solutions of GRACE and GRACE-FO (CSR, GFZ, JPL, TU-GRAZ) detrended over the 2003–2021 period to fill the observational gaps and develop a data-driven spatio-temporal filter to enhance the data signal-to-noise ratio [Prevost et al., 2019]. Additionally, the non-observable degree-1 spherical harmonics geocenter gravity coefficients are estimated using the degree-1 deformation field inverted from a globally distributed GNSS network corrected for deformation of degree-2 and higher [Chanard et al., 2018]. Moreover C2,0 Earth oblateness and C3,0 gravity coefficients, which are difficult to observe due to the near polar orbit of the GRACE and GRACE-FO missions, are substituted with satellite laser ranging (SLR) observations according to Technical Note 14 [TN-14; Chen et al., 2005, Loomis et al., 2020]. We add

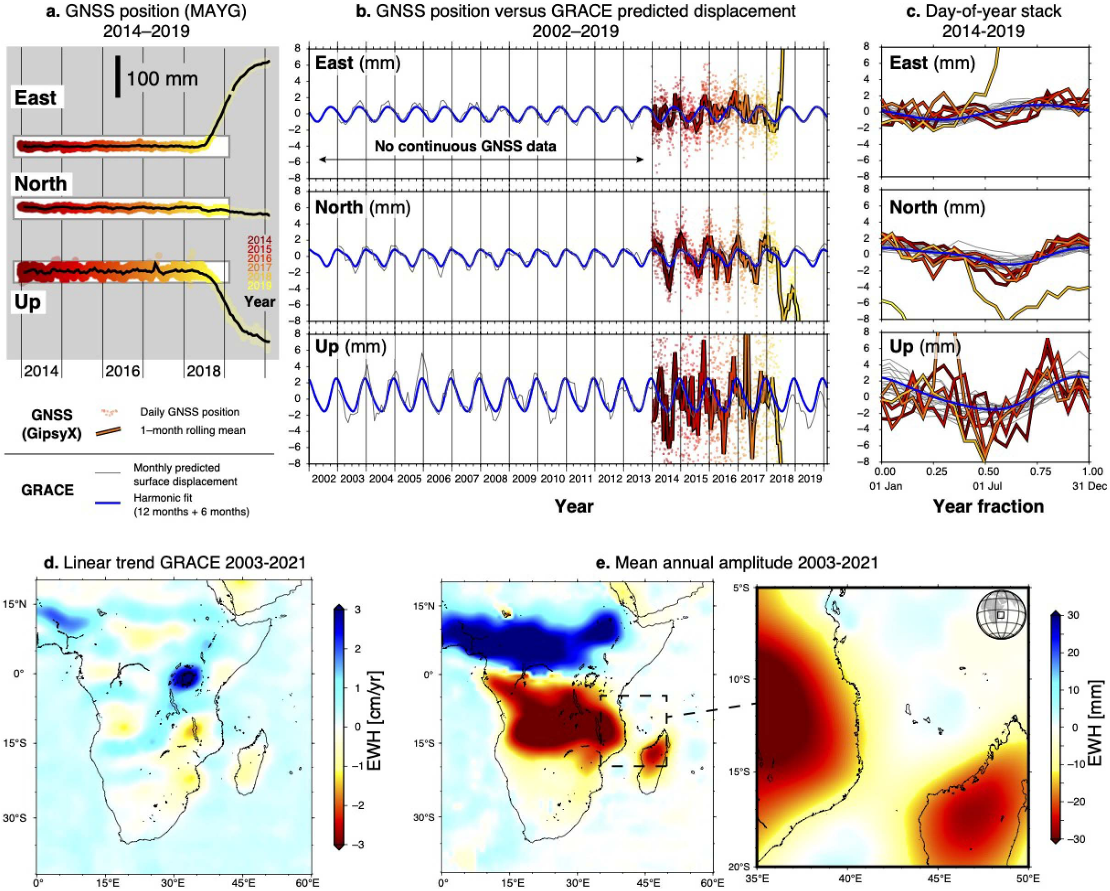


**Figure 7.** (a) Displacements at GNSS station MAYG after removing tectonic trend (GipsyX processing). Each dot corresponds to the position on a 24 h epoch, colored as a function of time. (b) Colored dots: displacement at GNSS station MAYG (same as in (a), with enhanced $Y$-axis scaling); thick colored curve: 30-days running average of surface displacement at GNSS station MAYG; thin black line: monthly-predicted surface displacement deduced from Earth's response to surface loads derived from satellite data of GRACE (2003–June 2017) and GRACE-FO (June 2018–2020) missions; blue curve: best-fitting periodic function adjusted on GRACE-derived predicted surface displacement (black line) using superposition of two harmonic functions with periods of 1 year and 0.5 years, respectively. Each component is adjusted independently. The time interval with available GNSS data prior to the onset of the volcanic crisis is highlighted with a white background. (c) same as (b), with a periodic $X$-axis scaling with duration of 1.0 year, starting from 1 January. GRACE-GRACE-FO M-SSA solution. (d) Mean rate of surface mass density variations from January 2003 to December 2021 expressed in equivalent water height (EWH) per year, given in cm/yr. (e) Mean annual surface mass density variations over the 2003–2021 period.

back the atmospheric and non-tidal oceanic contributions to ensure comparison with the GNSS dataset.

Deformation induced by surface loads, decomposed in the temporal and spatial domains, on a spherical elastic layered Earth model [Dziewonski and Anderson, 1981] is computed based on the Love number formalism [Farrell, 1972, Chanard et al., 2018]. We model the elastic deformation resulting from variations in surface loading measured by the GRACE and GRACE-FO missions at the GNSS MAYG site in Mayotte (Figure 7b,c). Note that considering the large scale resolution of the GRACE and

GRACE-FO measurements (~300 km) compared to the Mayotte GNSS network distribution, the loading model predicts similar deformation at all sites and local effects at sites are not accounted for. The long wavelength annual deformation at all sites is consistent over the 18-year period considered, despite some inter-annual variability.

The agreement between the observed and predicted GNSS displacements at MAYG, mainly on the northward and vertical component, strongly suggests that the GNSS network of Mayotte is affected by quasi-periodic displacement perturbations induced by surface loads generated by surface water storage at regional and/or continental scale. As a result, surface displacements measured during the crisis are contaminated by similar fluctuations. Accordingly, the eastward displacement anomaly of volcanic origin dominates any seasonal fluctuation, and could be safely neglected if the objective was to determine the cumulative displacement affecting the island. The northward component shows a nearly equal partition between the volcanic signal (20 mm cumulated over ~2 years) and the hydrological signal (9 mm peak-to-peak over <6 months). Since the hydrological perturbations are expected to produce a homogeneous effect at the scale of Mayotte, this signal will produce an apparent periodic north–south ~9 mm translation of the whole GNSS network every ~6 months. In other words, the cumulative displacement vectors on Mayotte are expected to be affected by a periodic rotation of 2.5° (peak-to-peak) in the horizontal plane.

In the simplest case where these rotations are uncorrected and incorrectly interpreted as resulting from a true motion of the source of volcanic deformation, the lever arm of ~30 km between the network and the source implies that a 2.5° rotation of displacement vectors on-land will translate into an apparent 1.35 km mislocation of the source of deformation. The effect on the vertical uncertainty of the source location is expected to be slightly larger. Combining horizontal and vertical uncertainties results in an apparent source motion reaching ~3 km, if hydrological load effects are not corrected, which can be considered negligible at first sight.

However, we note that due to higher harmonic components of the hydrological source term with time, these fluctuations can affect the deformation models on time scales as short as 3–4 months (the fastest transition occurs between August and December). We also note that, as the power of the volcanic signal decreases in the extracted vectors (e.g. when investigating the displacement over 6-months temporal windows or shorter, or when approaching the end of the volcanic crisis), the resulting uncertainty on the source location will significantly increase. The 3 km uncertainty reported above should therefore be considered as valid only for models relying on cumulative displacements calculated over time intervals longer than 1 year, and only until early 2020. Since mid-2020, as the volcanic signal has substantially waned, the resulting vector rotation caused by hydrologically-induced fluctuations can easily reach >30°, resulting in an uncertainty of >15 km on the north–south location of the source. This analysis illustrates the difficulty to determine the spatial characteristics of the source of volcanic deformation in Mayotte, as a result of a combination of (a) poor azimuthal coverage of the GNSS network and (b) existence of homogeneous fluctuations of the mean position of the network resulting from large-scale hydrological perturbations. This limitation equally applies if one considers, as here, a single pressure source (Mogi), or a more complex, distributed/multiple source.

## 5.2. *Source modeling*

Displacements subsequently measured from the beginning of the crisis were used to track the transport and storage of magmatic material offshore via numerical modeling.

### 5.2.1. *First modeling*

The first modeling of the deformation was carried out in October 2018, 4 months after the start of the deformation [Lemoine et al., 2020]. The data analyzed were those from the permanent stations available with the RGP at that time: MAYG, BDRL, GAMO and KAWE.

The GNSS time series exhibit a remarkable correlation between the east and the up components. There is also a correlation between east and north components, yet less remarkable for two reasons: (1) because the amplitudes of the north anomalies are small (the deformation source is located to the east of the island) with the uncorrected yearly fluctuations having a magnitude not small with respect

**Table 1.** Scaling coefficient applied to correlate the east and up components and the RMS amplitude of the residual difference for the four stations used in the first modeling

| Station | Scaling factor up | Residual (mm) | Pitch (°) | Scaling factor east | Residual (mm) | Azimuth (°N) |
|---|---|---|---|---|---|---|
| MAYG | 1.146 | 7.2 | 41 | 9.184 | 3 | 96.2 |
| BDRL | 1.321 | 7.2 | 37.1 | 3.065 | 3.5 | 71.9 |
| GAMO | 2.038 | 6.6 | 36.8 | 5.777 | 3.5 | 99.3 |
| KAWE | 1.339 | 6.6 | 26.1 | 6.137 | 3.9 | 97.5 |

to the tectonic signal, (2) because the observations indicate a small seasonal oscillation with time of the north signal.

The Table 1 summarizes the value of the scaling coefficient applied to correlate the east and up components and the root-mean-square (RMS) amplitude of the residual difference for the four stations.

In this first model, the source was a point source located within an elastic medium [Mogi, 1958]. In this model the displacement vector points to the source. This means that we can use the azimuth and pitch angles derived from the above scaling factors to establish the location of the source. This method is expected to be robust and the RMS residuals will teach us about the consistency of the angles indicated by the four GNSS stations.

The best fitting source, recalculated since the first note distributed in October 2018 [Lemoine et al., 2020] by only integrating geometric constraints and not amplitude of the displacement, was found at longitude 45.504° east and latitude 12.81° south. This location of the source is located at 11 km west and 4 km south with respect to the source proposed by Lemoine et al. [2020], and at a depth of 24 km instead of 28 km in this previous study. The source is therefore significantly closer to the island, ~12 km east of the Fer à Cheval [an old structure where acoustic plumes are observed; REVOSIMA, 2021; see location in Figure 6] and 28 km north-west of the new volcano. At this location the seafloor is at 2300 m below sea level. The standard deviation of the pitch angles (1.86°) corresponds to an uncertainty of the determination of the source depth of 1.5 km.

5.2.2. *Automatic processing and modeling*

From mid November 2018, automatic and daily modeling of PPP solutions were set up at IPGP using the WebObs dedicated module "GNSS" [Beauducel et al., 2019, 2020a], in order to characterize the source of deformation and its evolution in real time. The characteristics of a single source (location, depth and volume variation), fitting the observations over a considered period of time, are modeled by a point source of isotropic pressure at depth, in a homogeneous and elastic medium [Mogi, 1958], with topographic effect approximation using the varying-depth formulation [Williams and Wadge, 1998]. These simple models are the most suitable, given the limitations caused by the current geometry of the geodetic measurement network, with stations mostly west of the source [REVOSIMA, 2019]. The inversion method uses a grid-search approach and Bayesian expression of the model probability (calculated from the L1-norm misfit), in order to describe the full model space, i.e., all possible models and not only looking for the "best solution" [Tarantola, 2006].

The system has been configured to process the data independently over several time intervals whose upper limit is always set to current time (real time): 6 months and 1 year sliding windows, and a cumulative window from a reference date before the eruption onset (January 1, 2018). For each time window, velocity trends are estimated at each station, and an inverse problem is computed to look for probable sources. Result is displayed as a probability density function plotted as 3D maps, showing also velocity vectors of observations, vectors computed from the best model, and associated residuals. The Bayesian approach allows us to express in a rational way the *a posteriori* uncertainty on the set of models proposed for each time period. The adequacy of the model with the observations can thus be quantified whatever the signal to noise ratio. This makes the method extremely robust and useful for real-time monitoring [Beauducel et al., 2019, 2020b]. Of course, if the data contain an additional signal related to a poor correction of potential artifacts (tectonic, hydrological or atmospheric for example) or simply to another unidentified phenomenon that produces a compatible deformation signal, even partially, with the model, the result of the inversion will be influenced. As in any modeling, the result will be all the more accurate if all the main sources have been taken into account in the direct problem.

Here, we use all the REVOSIMA stations, including Grande Glorieuse Island, and stations west of Madagascar for which the insignificant deformation signal in the far field also contributes to constrain the source location. We present modeling results obtained after the subtraction of a model accounting for part of non-volcanic seasonal variations (see Section 5.1), using a second-order harmonic fit, 1-year and 6-month sine waves, for which amplitude and phase are estimated from MAYG pre-eruptive time series for each component, equally applied on all the stations. This pre-processing reduces the possible biases previously discussed in Section 5.1, but we must consider that deformation induced by continental hydrology is certainly not purely periodic and may also exist at shorter time scales. As a consequence, some non-volcanic residuals may still affect the source modeling results, in particular when considering time windows shorter than 1 year and/or encompassing a non-integer number of years, and when the volcanic signal amplitude is weak, i.e., before July 2018 and after mid-2020.

In Figure 8, we present a selection of source inversion results from 2018 to 2021, as probability density functions of the source location in space, computed from a 1-year time window velocity trends estimated at each station (see corresponding parameters, and GNSS and calculated velocities for each best source in Table 2 and Supplementary Material G, respectively). First, we clearly see that all models indicate a deflating source located about 50 km east of Mayotte, at a depth around 40 km. But it is clear that determination of both the east–west location and depth of the source, due to the on-land network, is weak. Regarding the time evolution of the source parameters, during the years 2018 and 2019, the deflation corresponds to a volume variation of $-2.6 \pm 0.1$ (km)$^3$ and $-2.5 \pm 0.2$ (km)$^3$, respectively. This value decreases in amplitude to $-0.5 \pm 0.08$ (km)$^3$ in 2020, and becomes insignificant in 2021, while the inversion process still exhibits a slight indication of possible deflation, suggesting that the source is very weak but might be still active.

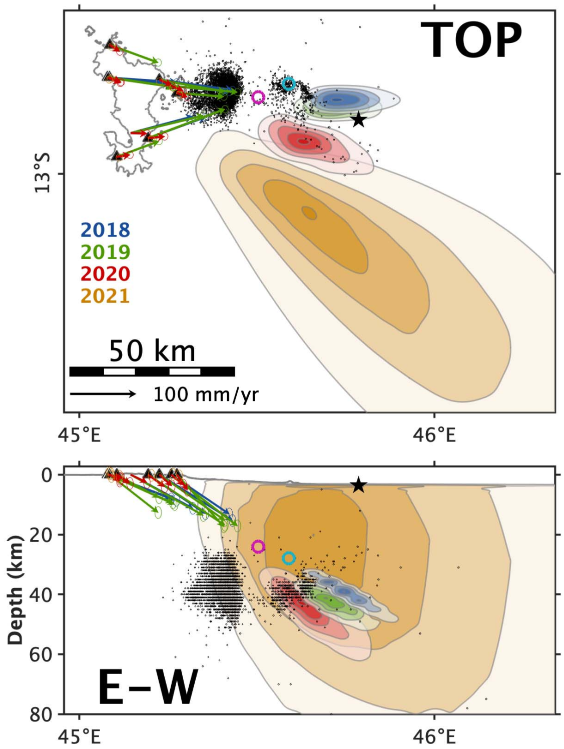


**Figure 8.** Source location estimated from GNSS Bayesian inversions for years 2018 to 2021, as normalized probability density functions in horizontal view and vertical profile, and associated velocity trends vectors with uncertainties. Also indicated the best sources determined from [Lemoine et al., 2020] (Cyan circle) and Section 5.2.1 of this study (Magenta circle). Black star indicates the eruption location. Numerical values are reported in Table 2. 2019-02-25 to 2020-05-10 earthquakes relocated by Saurel et al. [2022] are plotted as black dots (rounded to the nearest km).

In order to follow the possible source characteristics in time, we employ a novel method to compute the time-dependent effusion rate from deformation [Beauducel et al., 2020a, Mittal et al., 2022]. Magma reservoir source location and associated volume variation are computed for a 3-month sliding time window from January 2018 to December 2021, with a 7-day step. For each time window, the linear trend in displacement velocities is estimated from the GNSS data daily solutions previously

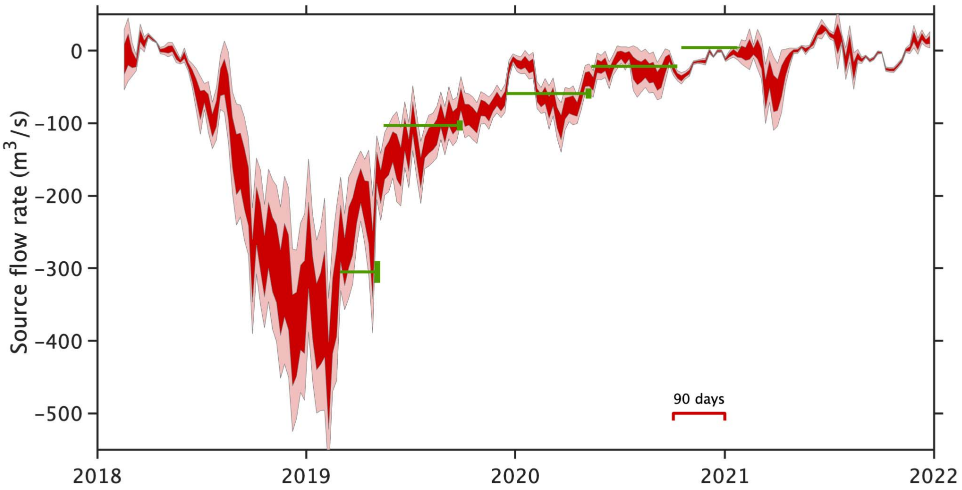


**Figure 9.** Time evolution of the source flow rate computed from inversion of GNSS velocity trends estimated on a 90-day causal sliding window. Uncertainty intervals on the flow rate (dark and light red areas) stands for 1 and 2 sigmas, respectively. Flow rates estimated from joint inversion modeling of GNSS + OBP data for the 5 periods of OBP deployment through successive MAYOBS campaigns (green lines, vertical segment stands for 1 sigma uncertainty).

**Table 2.** Best source parameters obtained from modeling of GNSS data on 1-year time windows (full year from January 1 to December 31) from 2018 to 2021 (see Figure 8). Comparison of source parameters on the OBP first campaign (March 1 to May 5, 2019) using GNSS and GNSS + OBP data (see Figure 10). Uncertainty intervals are given for 1 sigma

| | GNSS 1-year time window | | | | OBP first campaign | |
|---|---|---|---|---|---|---|
| | 2018 | 2019 | 2020 | 2021 | GNSS only | GNSS + OBP |
| Latitude N (°) | $-12.82 \pm 0.04$ | $-12.83 \pm 0.04$ | $-12.92 \pm 0.04$ | $-13.09 \pm 0.3$ | $-12.83 \pm 0.04$ | $-12.82 \pm 0.04$ |
| Longitude E (°) | $45.74 \pm 0.08$ | $45.70 \pm 0.04$ | $45.61 \pm 0.05$ | $45.66 \pm 0.3$ | $45.96 \pm 0.08$ | $46.09 \pm 0.04$ |
| Depth (km) | $39 \pm 2$ | $41 \pm 2$ | $43 \pm 4$ | $20 \pm 15$ | $41 \pm 4$ | $51 \pm 3$ |
| $\Delta V$ ($10^9$ m$^3$) | $-2.6 \pm 0.2$ | $-2.5 \pm 0.3$ | $-0.5 \pm 0.1$ | $-0.06 \pm 0.2$ | $-1.3 \pm 0.2$ | $-1.8 \pm 0.2$ |

corrected from tectonic and hydrological loading. The best solution is computed using a Bayesian inversion in the same conditions as the 1-year modeling performed previously. The method produces a time series of source parameters, more easily comparable to other observables and better suited for monitoring. The result is presented in Figure 9; the source flow rate amplitude varies from low values until July 2018, then increases to a maximum of $-357 \pm 60$ m$^3$/s in average during December 2018 and January 2019, and decreases slowly until 2021, at insignificant values (average of $-5 \pm 7$ m$^3$/s for the 2021 full year).

5.2.3. *Joint modeling of GNSS and OBP observations*

The situation in Mayotte is a textbook case of the difficulty of characterizing a deformation source with an inadequate geodetic network. We believe that Bayesian inversion is probably the best and most robust approach to quantify the *a posteriori* uncertainties associated with such a network inadequacy. One of the main weaknesses of the GNSS network is the lack of near-field observations due to the offshore location of the source, thus pressure gauges should provide an essential complement to improve the inversion results.

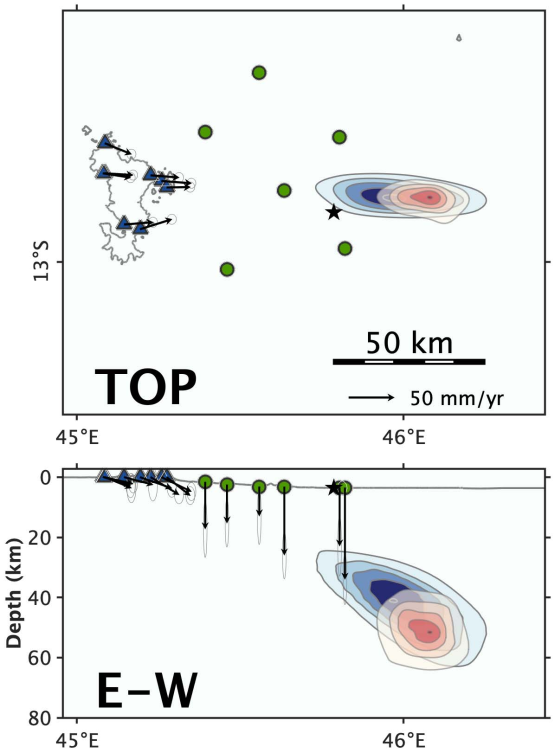


**Figure 10.** Comparison of source modeling location, in map view and along an E–W vertical cross section, as probability density levels using only GNSS data (blue contours) and using both GNSS and OBP data (red contours) recovered during the OBP first campaign (March 1 to May 5, 2019). GNSS stations (blue triangles), OBP stations (green circles), velocity trends and associated uncertainties (black arrows and ellipses), eruption location (black star) are shown. Pressure gauge data have been corrected from tides and oceanic signals and contain only the vertical component of displacement.

In Figure 10, we present the contribution of pressure gauge data to the source modeling, showing the original probability density function when using GNSS data only, and the probability density function when using both GNSS and OBP data recovered during the March 1 to May 5, 2019 period. It is clearly demonstrated that additional observations near the source, even with large *a priori* uncertainties, improve the source location determination with lower *a posteriori* uncertainty, while still remaining within the initial location area of probable models. The source obtained from the joint inversion is a little deeper and associated with a slightly larger deflation volume variation (see Table 2). We show in Supplementary Material H the results for each period of OBP deployment from 2019 to 2021.

In Figure 11 and Supplementary Material H, we present the best model fit in a velocity versus distance from source graph, showing the relatively acceptable adjustment of the OBP data at short distance from the source, while maintaining a very good adjustment of all GNSS data at larger distances. We also computed in Figure 9 flow rates from the best models obtained by the joint inversion of OBP and GNSS for each period of OBP deployment (Figure 10; Supplementary Material H).

## 6. Discussion and conclusions

### 6.1. *Contribution of GNSS in the scientific response to the crisis*

The GNSS method had a major role in the discovery of the magmatic origin of the seismic crisis that started in Mayotte in May 2018, and thus in the discovery of the submarine eruption 50 km offshore Mayotte in May 2019. It is thanks to the detection of anomalies in the ground deformation pattern of the GNSS stations of Mayotte in July 2018 that IGN issued a warning in the RGP web portal, and that the hypothesis of the magmatic origin of the seismic crisis could be confirmed as early as October 2018 when the first modeling of surface displacements recorded on 4 GNSS stations on Mayotte showed a deflation source at $45 \pm 5$ km east of Mayotte center and 28 km depth [Figure 8, Lemoine et al., 2020].

This demonstrates the technical and scientific contribution of: (1) IGN within the French higher education and research consortium, with their deployment and/or supervision of GNSS stations in the geologically active zones of all the national French territory including the overseas territories, and more particularly where no permanent volcano observatories are implemented, as it is the case in Mayotte, and (2) the use of best practice and tools developed into national volcano observatories, which can be easily and quickly implemented into any context.

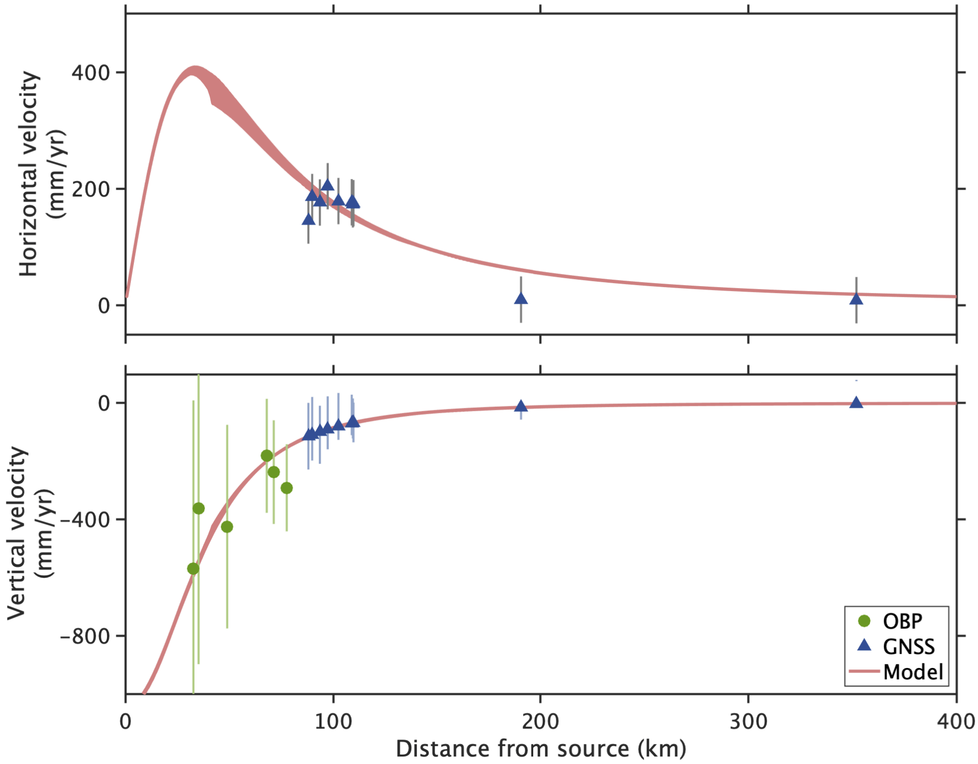


**Figure 11.** Best source modeling from joint inversion of GNSS and OBP data recovered during the OBP first campaign (March 1 to May 5, 2019), displayed as horizontal and vertical velocities versus distance from source. GNSS data and uncertainties (blue triangles), OBP data and uncertainties (green circles), predicted isotropic model with topography (red area) are shown. Pressure gauge data have been corrected from tides and oceanic signals.

GNSS continues to have a crucial role in the follow up, understanding and modeling of the time evolution of the submarine eruptive activity offshore Mayotte and of the magmatic activity in depth. Thanks to the rapid implementation of the WebObs tool [Beauducel et al., 2020a], more complex and automatic models have been quickly implemented, in particular for monitoring the source flow rate in near real-time (Figure 9), which is a crucial parameter for scientific response to the crisis and for which there are no real-time continuous visual constraints in the case of a submarine volcano. This parameter was a proxy of the eruptive activity and allowed an accurate tracking of the activity state of the volcano. GNSS data and modeling are thus of great interest in the scientific crisis management with local authorities and are part of the regular information bulletins (daily and monthly) of REVOSIMA [2019, 2020, 2021].

### 6.2. *Evolution of ground deformation between 2018 and 2021*

A maximum of about 25 cm of cumulative eastern on-land ground displacement and a maximum of about 19 cm of subsidence had been recorded between July 2018 and end of 2020. Since then, no more ground deformation seems to be detectable on Mayotte. This observation and the decrease in the flux deduced from inversion of ground deformation (Figure 9) are in agreement with the flux estimated by bathymetric survey that decrease from 172–181 $m^3/s$ the first year to less than 11 $m^3/s$ at the end of 2020 [Deplus et al., 2019, REVOSIMA, 2021]. Since January 2021, no more new lava flows with thickness more than 10 m have been detected [REVOSIMA, 2021].

The sources modeled with all available data are located to the east and near/below the distal seismic swarm, which extends in the direction of the eruption [Figure 8, Bertil et al., 2021, Cesca et al., 2020, Lavayssière et al., 2022, Lemoine et al., 2020, Feuillet et al., 2021, Retailleau et al., 2022, REVOSIMA, 2019, Saurel et al., 2022, Mercury et al., 2022]. A migration of the deformation source over time to the west and to a greater depth, more or less parallel to the seismic swarm, seems to occur. However, it is compelling to note that the dispersion of the models increased over time, as the signal to noise ratio decreased.

Previous studies mainly based on seismicity, petrology and data from oceanic cruises proposed a complex magma plumbing system feeding the eruption [Cesca et al., 2020, Berthod et al., 2021, Feuillet et al., 2021, Foix et al., 2021, Lavayssière et al., 2022, Mittal et al., 2022], with a main deep magma reservoir (40 to 70 km depth depending of the studies) below the Fer à Cheval, 30 km west of the eruption, and a magma conduit starting from this reservoir to fed the eruptive site. Some studies also proposed intermediates shallower reservoirs [e.g. Berthod et al., 2021, Lavayssière et al., 2022] and porous mush adjacent to the main reservoir [Mittal et al., 2022]. The complexity of the magma plumbing system may partly explain the dispersion of the results of our inversions, as several sources can be active at the same time or, on the contrary, some parts of the complex and extended magma system are not active at the same time. With the configuration of the GNSS network it is difficult to discriminate the effect of several sources. A single source, as modeled in this paper, is certainly an integration of the influence of this whole system that could also be refilled by deeper magma at the same time it was draining to fed the eruption. Over time and with the decline of the eruptive activity, the activation of the shallowest part of the magma feeding system was certainly less visible on the distant ground deformation recorded on-land.

Berthod et al. [2021, 2022] propose several changes in the feeding system during the eruption, with direct feeding from a deep mantle lithospheric reservoir during the first year of the eruption and the involvement of shallower magma batches later. This change revealed by lava petrology would have occurred only close to the eruptive site, as the eruptive activity migrated close to the main volcano edifice, 6 km to the north-west [Deplus et al., 2019, REVOSIMA, 2021], and probably did not influence the ground displacements recorded on-land in Mayotte.

Part of the vector rotation, and the migration of the source to the south observed between 2018 and 2021 could also be explained by a tectonic residue. Supplementary Material I shows the source inversion results from 2018 to 2021, as on Figure 8 but using a tectonic trend correction of +21.20 mm/yr east and +12.5 mm/yr north. This correction minimizes the northern residual for 2021, but does not change the source location from 2018 to 2020. This may be related to the uncertainty of the tectonic correction or to the existence of a new source of deformation in 2021 (magmatic or tectonic signal not clearly identified).

### 6.3. *Limits of the models*

The estimated depth of the modeled sources of deformation ranges from 20 km to 50 km in the oceanic lithospheric upper mantle. At such depth and over years of deformation, the linear elasticity assumption could be invalid, but hopefully with a limited bias at short-time scale.

Nevertheless, we have chosen to keep the use of a simple rheology (elastic and homogeneous medium) because of the limited data quality and the necessity to propose a first-order model of the source. Also, our automatic model processing was already operational, validated on other volcanoes, and quick to set up for the scientific crisis management (see previous section). Even if the estimation of magma volumes and rates, and the exact position of the magma sources could be biasing by the use of an elastic rheology, it allows us to quickly constraint at a first order the source.

In any case, it is rare in volcano contexts to detect geodetic signals of lithospheric source and even more on such length- and time-scales, further detailed studies on these data could be done to better understand, for example, the rheological properties (and layering) of the oceanic crust (intermediate-lower crust) and oceanic upper mantle in this area.

### 6.4. *Limits of the current network and recommendations*

The source of deformation is located far from the island of Mayotte (>40 km of the Mayotte center) under the oceanic crust, so that the network on-land alone is too distant and poorly distributed—mainly west of the source—to efficiently constrain its precise location, its shape and the possible involvement of several sources.

All the GNSS stations added during the crisis improved the redundancy of the network, but did not substantially improve the resolution since they remained located west of the source and installed 8 months after the first signs of ground deformation in Mayotte. The additional observations closer to the source from OBP improves the source location determination (Figure 10). Improving the ability to characterize the source of deformation, in such a context (submarine eruption far from the coast), would require thus complementing available GNSS stations with other types of instruments:

(1) more pressure gauges as close as possible to the supposed source (to capture the maximum amplitude of subsidence above the source) and surrounding the source (to reduce the azimuthal gap), and this from the beginning of the crisis when the deformation was still significant. Even if these data are not real time, they are useful to better constrain the source *a posteriori* (Figure 10, Supplementary Material H). However, exploiting OBP data for seafloor deformation monitoring is still challenging due to several factors including the instrumental drift and the oceanic variations. The emerging generation of angle of attack (AOA) type of sensors offers new opportunities to reduce the impact of instrumental drift and thus increase our ability to monitor slow seafloor motion. In the case of low deformation rates (as it is the case for the latter period in the Mayotte crisis), the usefulness of OBP observations highly relies on our ability to accurately correct the oceanic contribution to the signal. Further studies based on regional modeling approaches and ancillary co-located data (e.g. CTD mooring or glider transects) should be carried out in order to reduce the associated uncertainties and thus improve the detectability of low rate seafloor deformations.
(2) gravimeters on Mayotte to detect mass transfer,
(3) borehole tiltmeters on Mayotte to detect subtle slope variations.

## Data availability statement

IGN supports the REVOSIMA by making the server infrastructure of the RGP available for gathering and distributing GNSS data, metadata and products to the national and international scientific communities, and by coordinating the geodetic field operations in Mayotte. Since May 2018, the operativeness of the RGP has allowed the continuous GNSS monitoring of the crisis.

The technical infrastructure, located in the premises of IGN data center in Saint-Mandé (France), consists mainly of two collection servers that ensure the gathering of the raw observation data by FTP protocol, and one distribution server for data access by users: ftp://rgpdata.ign.fr. Between the reception and the distribution, the following tasks are performed on the observation data:

- files are converted into the RINEX format and renamed according to the standard,
- a quality check is performed to guarantee the usability of the data and to provide quality metadata,
- derivative files are produced if needed, such as sub-sampling from 1 s to 30 s sampling rate and concatenation of hourly file info daily files.

Whatever the type and configuration of the different GNSS receivers, all files are made available in a common and standard format and naming. The folder tree on the distribution server allows users to simply locate the needed files, which enables automation of file search and download. For instance, the generic file path for a 30 s daily RINEX 2 observation file for the station MAYG and for the 152nd day of 2021 will thus be 2021/152/data_30/mayg1520.21d.Z.

The principles used for the data distribution comply with the guidelines of the IGS.

Station metadata are available under the standard sitelog format of the IGS in the "stations" folder on the FTP server. This format records in a human-readable manner, the main characteristics of the station and relevant information about the GNSS equipment installed.

All the data from the RGP stations (MAYG, BDRL, GAMO, KAWE) are distributed under the French open data license ETALAB, compatible with the CC-BY 3.0 license, as well as GNSS products and station metadata. Data from the stations that were installed in the frame of the REVOSIMA (KNKL, PMZI, MTSB and GLOR) are distributed under CC-BY 4.0 license (Supplementary Material A). Data from stations MTSA and PORO is owned by the *Réseau Lél@* and its distribution is restricted to the scientific community.

Data access is made using the FTP protocol in the server ftp://rgpdata.ign.fr. Products and metadata are freely available for any user using an anonymous connection, in the folders "produits" and "stations" respectively. Access to the observation files requires authentication using credentials provided on demand at mayotte.gnss@ign.fr for scientific use.

A dedicated web site (http://mayotte.gnss.fr/) gathers the various information about the GNSS monitoring of the REVOSIMA. Observations and trends are also accessible in the monthly (https://www.ipgp.fr/fr/revosima/actualites-reseau; ISSN 2680-1205) and daily (http://volcano.ipgp.fr/mayotte/Bulletin_quotidien/bulletin.html) bulletins from REVOSIMA.

## Conflicts of interest

Authors have no conflict of interest to declare.

## Acknowledgements

Since June 2019, monitoring of Mayotte eruption is funded by *Ministère de l'Enseignement Supérieur, de la Recherche et de l'Innovation* (MESRI), *Ministère de la Transition Ecologique* (MTE) and *Ministère des Outremers* (MOM) with the support of *Ministère de l'Intérieur* (MI) and *Ministère des Armées* (MINARM) through the REVOSIMA (*Réseau de surveillance volcanologique et sismologique de Mayotte*). Data shown on this paper have been acquired, processed and modeled in the framework of the REVOSIMA, https://doi.org/10.18715/MAYOTTE.REVOSIMA.

The most recent GNSS stations installed on Mayotte and Grande Glorieuse (KNKL, PMZI, MTSB, GLOR) have been funded by the French state via dedicated funding specially released by INSU-CNRS (Institut national des sciences de l'univers—Centre national de la recherche scientifique) after the beginning of the Mayotte seismic crisis. The temporary GNSS stations deployed on the three sites of Mayotte in 2019, before their perpetuation, came from the GPSmob from Résif-Epos. Résif-Epos is a Research Infrastructure (RI) managed by the CNRS-INSU. It is a consortium of eighteen French research organisations and institutions, included in the roadmap of the *Ministère de l'Enseignement Supérieur, de la Recherche et de l'Innovation*. Résif-Epos RI is also supported by the *Ministère de la Transition Ecologique*. The stations NOSY and DSUA were installed by the LACy laboratory (Université de La Réunion) in the framework of the INTERREG-5 Océan Indien 2014–2020 « *ReNovRisk Cyclones et Changement Climatique* » project, funded by the Europe, Région Réunion and the French state [Bousquet et al., 2020].

The station MAYG is part of the REGINA network funded by CNES and co-operated by CNES and IGN (https://regina.cnes.fr/en/general-presentation).
The stations BDRL and GAMO, belonging to the TERIA network, are owned and operated by the Exagone company (https://www.reseau-teria.com/language/en/teria-network/). The stations KAWE, MTSA and PORO, belonging to the *Réseau Lél@* network, are owned and operated by the Precision Topo company (http://www.reseau-lela.com and https://precision-topo.com/). The seafloor data were collected using SBE 37 pressure sensors belonging to the DT-INSU oceanographic facility.

We thank the chief scientists of the MAYOBS1 to MAYOBS21 cruises (DOI: 10.18142/291), Emmanuel Rinnert, Nathalie Feuillet, Yves Fouquet, Stephan Jorry, Isabelle Thinon, Elodie Lebas, Pierre Guyavarch, for the organization of the surveys at sea.

The three anonymous reviewers and the editors are thanked for their constructive and insightful reviews.

## Supplementary data

Supporting information for this article is available on the journal's website under https://doi.org/10.5802/crgeos.176 or from the author.

## References

Beauducel, F., Lafon, D., Béguin, X., Saurel, J.-M., Bosson, A., Mallarino, D., et al. (2020a). WebObs: The volcano observatories missing link between research and real-time monitoring. *Front. Earth Sci.*, 8, article no. 48.

Beauducel, F., Nandaka, M. A., Syahbana, D. K., Suryanto, W., Nurnaning, A., Iguchi, M., et al.

(2019). Real-time magma flux quantization from GNSS as a tool for crisis management. In *VOBP4, Mexico City, November 2019*.

Beauducel, F., Peltier, A., Villié, A., and Suryanto, W. (2020b). Mechanical imaging of a volcano plumbing system from GNSS unsupervised modeling. *Geophys. Res. Lett.*, 47, article no. e2020GL089419.

Berthod, C., Komorowski, J., Gurioli, L., Médard, E., Bachèlery, P., Besson, P., et al. (2022). Temporal magmatic evolution of the Mayotte offshore eruption revealed by in situ submarine sampling and petrological monitoring. *C. R. Géosci.*, 354(S2), 195–223.

Berthod, C., Médard, E., Bachèlery, P., Gurioli, L., Di Muro, A., Peltier, A., et al. (2021). The 2018-ongoing Mayotte submarine eruption: Magma migration imaged by petrological monitoring. *Earth Planet. Sci. Lett.*, 571, article no. 117085.

Bertiger, W., Bar-Sever, Y., Dorsey, A., Haines, B., Harvey, N., Hemberger, D., et al. (2020). GipsyX/RTGx, a new tool set for space geodetic operations and research. *Adv. Space Res.*, 66(3), 469–489.

Bertil, D., Mercury, N., Doubre, C., Lemoine, A., and Van der Woerd, J. (2021). The unexpected Mayotte 2018–2020 seismic sequence: a reappraisal of the regional seismicity of the Comoros. *C. R. Géosci.*, 353(S1), 211–235.

Blewitt, G., Lavallée, D., Clarke, P., and Nurutdinov, K. (2001). A new global mode of Earth deformation: Seasonal cycle detected. *Science*, 294(5550), 2342–2345.

Bousquet, O., Lees, E., Durand, J., Peltier, A., Duret, A., Mekies, D., Boissier, P., Donal, T., Fleischer-Dogley, F., and Zakariasy, L. (2020). Densification of the ground-based GNSS observation network in the Southwest Indian Ocean: current status, perspectives, and examples of applications in meteorology and geodesy. *Front. Earth Sci.*, 8, article no. 566105.

Cesca, S., Letort, J., Razafindrakoto, H. N., Heimann, S., Rivalta, E., Isken, M. P., et al. (2020). Drainage of a deep magma reservoir near Mayotte inferred from seismicity and deformation. *Nat. Geosci.*, 13(1), 87–93.

Chanard, K., Fleitout, L., Calais, E., Rebischung, P., and Avouac, J. P. (2018). Toward a global horizontal and vertical elastic load deformation model derived from GRACE and GNSS station position time series. *J. Geophys. Res. Solid Earth*, 123(4), 3225–3237.

Chen, J. L., Rodell, M., Wilson, C. R., and Famiglietti, J. S. (2005). Low degree spherical harmonic influences on gravity recovery and climate experiment (GRACE) water storage estimates. *Geophys. Res. Lett.*, 32(14), article no. L14405.

Chierici, F., Iannaccone, G., Pignagnoli, L., Guardato, S., Locritani, M., Embriaco, D., Donnarumma, G. P., Rodgers, M., Malservisi, R., and Beranzoli, L. (2016). A new method to assess long-term seabottom vertical displacement in shallow water using a bottom pressure sensor: Application to Campi Flegrei, Southern Italy. *J. Geophys. Res. Solid Earth*, 121, 7775–7789.

Demerliac, M. (1974). Calcul du niveau moyen journalier. *Ann. Hydrogr. du SHOM*, 5, 49–57.

Deplus, C., Feuillet, N., Bachelery, P., Fouquet, Y., Jorry, S., Thinon, I., Bermell, S., Besson, F., Gaillot, A., Guérin, C., Le Friant, A., Paquet, F., Pierre, D., and Pitel-Roudaut, M. (2019). Early development and growth of a deep seafloor volcano: Preliminary results from the MAYOBS cruises. In *Abstract V43I-0227, 2019 Fall Meeting. AGU, San Francisco*.

Dobashi, Y. and Inazu, D. (2021). Improving detectability of seafloor deformation from bottom pressure observations using numerical ocean models. *Front. Earth Sci.*, 8, article no. 598270.

Dziewonski, A. M. and Anderson, D. L. (1981). Preliminary reference Earth model. *Phys. Earth Planet. Inter.*, 25(4), 297–356.

Dzurisin, D. (2006). A comprehensive approach to monitoring volcano deformation as a window on the eruption cycle. *Rev. Geophys.*, 41(1), 1–1–1–29.

Famin, V., Michon, L., and Bourhane, A. (2020). The Comoros archipelago: a right-lateral transform boundary between the Somalia and Lwandle plates. *Tectonophysics*, 789, article no. 228539.

Farrell, W. E. (1972). Deformation of the Earth by surface loads. *Rev. Geophys.*, 10(3), 761–797.

Feuillet, N. (2019). MAYOBS1 cruise. RV Marion Dufresne. https://campagnes.flotteoceanographique.fr/campagnes/18001217/.

Feuillet, N., Jorry, S., Crawford, W. C., Deplus, C., Thinon, I., Jacques, E., et al. (2021). Birth of a large volcanic edifice offshore Mayotte via lithosphere-scale dyke intrusion. *Nat. Geosci.*, 14(10), 787–795.

Foix, O., Aiken, C., Saurel, J. M., Feuillet, N., Jorry, S. J., Rinnert, E., and Thinon, I. (2021). Offshore Mayotte volcanic plumbing revealed by local passive tomography. *J. Volcanol. Geotherm. Res.*, 420, article no. 107395.

Gennerich, H.-H. and Villinger, H. (2011). Deciphering the ocean bottom pressure variation in the Logatchev hydrothermal field at the eastern flank of the Mid-Atlantic Ridge. *Geochem. Geophys. Geosystems*, 12, 1–18.

Lavayssière, A., Crawford, W. C., Saurel, J. M., Satriano, C., Feuillet, N., Jacques, E., and Komorowski, J. C. (2022). A new 1D velocity model and absolute locations image the Mayotte seismo-volcanic region. *J. Volcanol. Geotherm. Res.*, 421, article no. 107440.

Lemoine, A., Briole, P., Bertil, D., Roullé, A., Foumelis, M., Thinon, I., et al. (2020). The 2018–2019 seismo-volcanic crisis east of Mayotte, Comoros islands: seismicity and ground deformation markers of an exceptional submarine eruption. *Geophys. J. Int.*, 223(1), 22–44.

Lisowski, M. (2007). Analytical volcano deformation source models. In *Volcano Deformation*, pages 279–304. Springer, Berlin, Heidelberg.

Loomis, B. D., Rachlin, K. E., Wiese, D. N., Landerer, F. W., and Luthcke, S. B. (2020). Replacing GRACE/GRACE-FO with satellite laser ranging: Impacts on Antarctic Ice Sheet mass change. *Geophys. Res. Lett.*, 47(3), article no. e2019GL085488.

Menemenlis, D., Campin, J.-M., Heimbach, P., Hill, C., Lee, T., Nguyen, A., Schodlok, M., and Zhang, H. (2008). ECCO2: High resolution global ocean and sea ice data synthesis. *Mercator Ocean Q. Newsl.*, 31, 13–21.

Mercury, N., Lemoine, A., Doubre, C., Bertil, D., Van Der Woerd, J., Hoste-Colomer, R., and Battaglia, J. (2022). Onset of a submarine eruption east of Mayotte, Comoros archipelago: the first 10 months seismicity of the seismo-volcanic sequence (2018–2019). *C. R. Géosci.*, 354(S2), 105–152.

Miki, N. (2021). Crisis narratives and (dis)placement: Space, time and earthquakes in Mayotte. *Ampersand*, 8, article no. 100078.

Mittal, T., Jordan, J. S., Retailleau, L., Beauducel, F., and Peltier, A. (2022). Mayotte 2018 eruption likely sourced from a magmatic mush. *Earth Planet. Sci. Lett.*, 590, article no. 117566.

Mogi, K. (1958). Relations between the eruptions of various volcanoes and the deformation of the ground surfaces around them. *Bull. Earthq. Res. Inst., Univ. Tokyo*, 36, 99–134.

OVPF (2019). Monthly bulletin of the Piton de la Fournaise Volcanological Observatory—February 2019. http://www.ipgp.fr/sites/default/files/new_ovpf_20190301_bullmensu_en_2.pdf. ISSN: 2610-5101.

Prevost, P., Chanard, K., Fleitout, L., Calais, E., Walwer, D., van Dam, T., and Ghil, M. (2019). Data-adaptive spatio-temporal filtering of GRACE data. *Geophys. J. Int.*, 219(3), 2034–2055.

Retailleau, L., Saurel, J. M., Laporte, M., Lavayssière, A., Ferrazzini, V., Zhu, W., Beroza, G. C., Satriano, C., and Komorowski, J. C. (2022). Automatic detection for a comprehensive view of Mayotte seismicity. *C. R. Géosci.*, 354(S2), 153–170.

REVOSIMA (2019). Bulletin n° 5 de l'activité sismo-volcanique à Mayotte du 16 au 30 septembre 2019. IPGP, Université de Paris, OVPF, BRGM, Ifremer, CNRS. https://www.ipgp.fr/sites/default/files/ipgp_1er_bulletin_info_sismo_volcanique_mayotte-cor.pdf. ISSN: 2680-1205.

REVOSIMA (2020). Bulletin n° 11 de l'activité sismo-volcanique à Mayotte du 1 au 31 décembre 2019. IPGP, Université de Paris, OVPF, BRGM, Ifremer, CNRS. https://www.ipgp.fr/sites/default/files/ipgp_revosima_n11_07012020.pdf. ISSN: 2680-1205.

REVOSIMA (2021). Bulletin n° 36 de l'activité sismo-volcanique à Mayotte du 1 au 30 novembre 2021. IPGP, Université de Paris, OVPF, BRGM, Ifremer, CNRS. https://www.ipgp.fr/sites/default/files/ipgp_revosima_n36_20211203.pdf. ISSN: 2680-1205.

Rinnert, E., Lebas, E., Jorry, S., Feuillet, N., Thinon, I., and Fouquet, Y. (2019). MAYOBS. https://campagnes.flotteoceanographique.fr/series/291/.

Saurel, J. M., Jacques, E., Aiken, C., Lemoine, A., Retailleau, L., Lavayssière, A., Foix, O., Dofal, A., Laurent, A., et al. (2022). Mayotte seismic crisis: building knowledge in near real-time by combining land and ocean-bottom seismometers, first results. *Geophys. J. Int.*, 228(2), 1281–1293.

Segall, P. (2010). Earthquake and volcano deformation. In *Earthquake and Volcano Deformation*. Princeton University Press, Princeton, NJ.

Stamps, D., Saria, E., and Kreemer, C. (2018). A geodetic strain rate model for the East African rift system. *Sci. Rep.*, 8, article no. 732.

Tarantola, A. (2006). Popper, Bayes and the inverse problem. *Nat. Phys.*, 2(8), 492–494.

Tregoning, P., Watson, C., Ramillien, G., McQueen, H., and Zhang, J. (2009). Detecting hydrologic deformation using GRACE and GPS. *Geophys. Res. Lett.*, 36(15), article no. L15401.

Vilaseca, G., Deplus, C., Escartín, J., Ballu, V., Nomikou, P., Mével, C., and Andreani, M. (2016). Oceanographic signatures and pressure monitoring of seafloor vertical deformation in near-coastal, shallow water areas: a case study from santorini caldera. *Mar. Geod.*, 39, 401–421.

Wallace, L. M., Webb, S. C., Ito, Y., Mochizuki, K., Hino, R., Henrys, S., Schwartz, S. Y., and Sheehan, A. F. (2016). Slow slip near the trench at the Hikurangi subduction zone, New Zealand. *Science*, 352, 701–704.

Wilcock, W. S. D., Manalang, D. A., Fredrickson, E. K., Harrington, M. J., Cram, G., Tilley, J., Burnett, J., Martin, D., Kobayashi, T., and Paros, J. M. (2021). A thirty-month seafloor test of the A-0-A method for calibrating pressure gauges. *Front. Earth Sci.*, 8, article no. 600671.

Williams, C. A. and Wadge, G. (1998). The effects of topography on magma chamber deformation models: application to Mt. Etna and radar interferometry. *Geophys. Res. Lett.*, 25(10), 1549–1552.

*Comptes Rendus*
*Géoscience — Sciences de la Planète*
**2022**, Vol. 354, Special Issue S2, p. 195-223
https://doi.org/10.5802/crgeos.155

The Mayotte seismo-volcanic crisis of 2018-2021 in the Comoros archipelago (Mozambique channel) / *La crise sismo-volcanique de 2018-2021 de Mayotte dans l'archipel des Comores (Canal du Mozambique)*

# Temporal magmatic evolution of the Fani Maoré submarine eruption 50 km east of Mayotte revealed by in situ sampling and petrological monitoring

# *Évolution magmatique temporelle de l'éruption sous-marine de Fani Maoré, située à 50 km à l'est de Mayotte, révélée par un échantillonnage in situ et un suivi pétrologique*

**Carole Berthod[*, a, b], Jean-Christophe Komorowski[c], Lucia Gurioli[b], Etienne Médard[b], Patrick Bachèlery[b], Pascale Besson[c], Pauline Verdurme[b], Oryaëlle Chevrel[b], Andrea Di Muro[c, d], Aline Peltier[c, d], Jean-Luc Devidal[b], Sophie Nowak[c], Isabelle Thinon[e], Pierre Burckel[c], Samia Hidalgo[c], Christine Deplus[c], Benoît Loubrieu[f], Delphine Pierre[f], Sylvain Bermell[f], Mathilde Pitel-Roudaut[f], Yvan Réaud[g], Sacha Fouchard[g], Manon Bickert[h], Anne Le Friant[c], Fabien Paquet[e], Nathalie Feuillet[c], Stephan L. Jorry[f], Yves Fouquet[f], Emmanuel Rinnert[f], Cécile Cathalot[f] and Elodie Lebas[c]**

[a] Université Clermont Auvergne, CNRS, IRD, OPGC, Laboratoire Magmas et Volcans, F-63000 Clermont-Ferrand, France

[b] SEDISOR; Univ. Brest UMR6538, IUEM, Plouzané, France

[c] Université de Paris, Institut de physique du globe de Paris, CNRS, F-75005 Paris, France

[d] Observatoire Volcanologique du Piton de la Fournaise, Institut de physique du globe de Paris, F-97418 La Plaine des Cafres, France

[e] BRGM-French Geological Survey, 3 avenue Claude Guillemin, BP36009, F-45060 Orléans Cédex 2, France

[f] Geo-Ocean, UMR 6538 Ifremer, Université de Bretagne Occidentale, CNRS, F-29280 Plouzané, France

[g] CNRS, Genavir, F-29280 Plouzané, France

* Corresponding author.

[h] Dipartimento di Scienze Chimiche e Geologiche, Università di Modena e Reggio Emilia, Modena, Italy

*E-mails:* berthod@ipgp.fr (C. Berthod), komorow@ipgp.fr (J.-C. Komorowski), lucia.gurioli@uca.fr (L. Gurioli), etienne.medard@uca.fr (E. Médard), Patrick.BACHELERY@uca.fr (P. Bachèlery), besson@ipgp.fr (P. Besson), pauline.verdurme@uca.fr (P. Verdurme), oryaelle.chevrel@uca.fr (M. O. Chevrel), dimuro@ipgp.fr (A. Di Muro), peltier@ipgp.fr (A. Peltier), J.L.Devidal@opgc.univ-bpclermont.fr (J.-L. Devidal), shidalgo@ipgp.fr (S. Nowak), i.thinon@brgm.fr (I. Thinon), burckel@ipgp.fr (P. Burckel), shidalgo@ipgp.fr (S. Hidalgo), deplus@ipgp.fr (C. Deplus), Benoit.Loubrieu@ifremer.fr (B. Loubrieu), Delphine.Pierre@ifremer.fr (D. Pierre), Sylvain.Bermell@ifremer.fr (S. Bermell), mathilde.pitel@ifremer.fr (M. Pitel-Roudaut), Yvan.Reaud@genavir.fr (Y. Réaud), Sacha.Fouchard@genavir.fr (S. Fouchard), mbickert@unimore.it (M. Bickert), lefriant@ipgp.fr (A. Le Friant), F.Paquet@brgm.fr (F. Paquet), feuillet@ipgp.fr (N. Feuillet), Stephan.Jorry@ifremer.fr (S. L. Jorry), Yves.Fouquet@ifremer.fr (Y. Fouquet), Emmanuel.Rinnert@ifremer.fr (E. Rinnert), cecile.cathalot@ifremer.fr (C. Cathalot), elebas@ipgp.fr (E. Lebas)

**Abstract.** The "Fani Maoré" eruption off the coasts of Mayotte has been intensively monitored by applying methods similar to those used for subaerial eruptions. Repeated high-resolution bathymetric surveys and dredging, coupled with petrological analyses of time-constrained samples, allowed tracking the evolution of magma over the whole submarine eruptive sequence. Indeed, after one year of direct ascent (Phase 1), basanitic magma switched to a different pathway that sampled a tephri-phonolitic subcrustal reservoir (Phase 2). Later, the magma pathway shifted again in the crust resulting in a new eruption site located 6 km northwest of the main edifice (Phase 3). The petrological signature of lava flows reveals both an evolution by fractional crystallization and syn-eruptive mixing with a tephri-phonolitic magma.

We demonstrate that high-flux eruption of large volumes of basanitic magma from a deep-seated reservoir can interact with shallower reservoirs and remobilize eruptible magma. This has significant hazards implications with respect to the capacity of such large eruptions to reactivate shallow-seated inactive reservoirs from a transcrustal magmatic system that could be located potentially at a distance from the high-flux eruptive site.

**Résumé.** L'éruption au large de Mayotte a été intensément surveillée en appliquant des méthodes similaires aux éruptions sub-aériennes. Une étude pétrologique et géochimique des échantillons dragués couplée à de nombreux relevés bathymétriques, nous a permis de suivre l'évolution du magma au cours de l'éruption. Le trajet du magma change après un an de remontée directe (Phase 1), un réservoir magmatique sous-crustal et plus différencié est alors échantillonné (Phase 2). Un mois plus tard, le trajet change à nouveau et engendre une migration du site éruptif à 6 km au nord-ouest de l'édifice principal (Phase 3). La signature pétrologique des coulées de lave révèle à la fois une évolution par cristallisation fractionnée et un mélange syn-eruptif avec un magma téphri-phonolitique. Nous démontrons qu'une éruption à haut débit impliquant de grands volumes de magma basanitique et provenant d'un réservoir profond peut interagir avec des réservoirs plus superficiels et remobiliser le magma éruptible. Ceci a des implications significatives en termes de risques quant à la capacité de ces grandes éruptions à réactiver des réservoirs inactifs peu profonds provenant d'un système magmatique transcrustal et potentiellement situé à distance du site éruptif.

**Keywords.** Fractional crystallization, Mixing, Mayotte, Submarine eruption, Dredging, Petrological monitoring, Magmatic system.

**Mots-clés.** Cristallisation fractionnée, Mélange, Mayotte, Éruption sous-marine, Dragage, Suivi pétrologique, Système magmatique.

*Published online: 9 December 2022, Issue date: 17 January 2023*

## 1. Introduction

Volcanic eruptions are monitored using various real-time methods, of which seismology, geodesy, and gas- and water-geochemistry are most commonly used to track magma migration through the Earth's crust. In recent years, with the evolution of sampling methods, and of chemical, petrological and textural analysis techniques applied to solid volcanic products (pyroclasts and lavas), it has become more and more common to carry out near real-time petrological monitoring of eruptions [e.g., Liu et al., 2020, Re et al., 2021, Corsaro and Miraglia, 2022]. The analysis of lava and pyroclasts is carried out after volcanic eruption [Gurioli et al., 2005, Piochi et al., 2005, Di Muro et al., 2014] or occasionally during the eruption [Thivet et al., 2020]. Petrological and geochemical monitoring makes it possible to track the evolution of the magma bodies involved in an eruption, by following the variations in their physical and chemical parameters, such as crystal and gas content, or compositions of solid, liquid and gas phases. These data, when obtained within a short period (a few days to tens of days) after magma emplacement, can be combined with other real-time monitoring data to constrain the magma dynamics during an ongoing eruption. Linking deep magmatic processes to surface geophysical and geochemical records is not only an essential step in interpreting the precursor signals of eruptions but can also be crucial for understanding changes in the eruptive regime during the course of an eruption [Reubi et al., 2019, Gansecki et al., 2019, Bamber et al., 2020, Sundermeyer et al., 2020, Magee et al., 2021].

In contrast with subaerial eruptions, submarine eruptions are much more challenging to monitor. Indeed, their submarine context limits access to direct live observations of the volcanic activity. It is often impossible to know, even approximately, the timing of lava and/or pyroclasts emplacement and, hence, trace their temporal evolution [Resing et al., 2011, Casas et al., 2018, Carey et al., 2018, Clague et al., 2018]. Here, we present new petrological and geochemical evolution of the 2018–2021 submarine eruption that occurred off the eastern coast of Mayotte. This major eruption provided a unique opportunity to carry out frequent and targeted sampling of eruptive products whose emplacement date was constrained with repeated bathymetric surveys. In addition, one active incandescent submarine lava flow was sampled during a dredge (DR18). This sample collection permits constituting one of the most valuable petrological and geochemical databases for any known submarine eruption and particularly given that the eruption occurred at a depth between 2500 and 3500 m below sea level (BSL).

We first report an improved dredging protocol that allowed "surgical strikes" at >2500 m BSL to individually sample each eruptive unit of the newly emplaced volcanic material. Next, we provide a detailed petrological analysis of the most representative formations encountered among the sampled lavas. We use these data to constrain the eruptive history of the Fani Maoré volcanic edifice, taking into account the timing of the lava emplacement, and tracking the magma pathway through the crust.

## 2. Geological setting

Mayotte is the easternmost island of the Comoros Archipelago located in the Mozambique Channel between the eastern coast of Mozambique and the northern tip of Madagascar. This archipelago is composed of four main islands, namely from east to west Mayotte, Anjouan, Moheli, and Grande Comore, which are associated with atolls and partially emerged reef platforms and interconnected by a series of submarine volcanic chains [Tzevahirtzian et al., 2021, Thinon et al., 2022]. The Comoros Archipelago is characterized by active volcanism and tectonics associated with an area of active seismicity that connects the northern extremity of Madagascar in the east to the African coast in the west. This volcanic chain is interpreted as the NW–SE boundary between the Lwandle microplate and the Somalia plate, on the periphery of the East African Rift System [Bertil and Regnoult, 1998, Famin et al., 2020, Feuillet et al., 2021, Thinon et al., 2022] or as a zone of broad deformation extending up to the northern half of Madagascar [Stamps et al., 2021].

Recent volcanic activity has been recorded on Grande Comore [Karthala and La Grille volcanoes, Bachèlery et al., 2016], Anjouan [Quidelleur et al., 2022], and Mayotte [Feuillet et al., 2021]. Karthala Volcano (Grande Comore Island) is one of the largest active volcanoes in the world and the second most active volcano in the Indian Ocean with four eruptions from 2005 to 2007 [Bachèlery et al., 2016, Morin et al., 2016, Thivet et al., 2022]. New K–Ar and $^{14}C$ ages demonstrate that volcanism is still active on Anjouan, with the youngest activity around 9.6 ka [Quidelleur et al., 2022]. Finally, despite Mayotte being the oldest island of the archipelago with

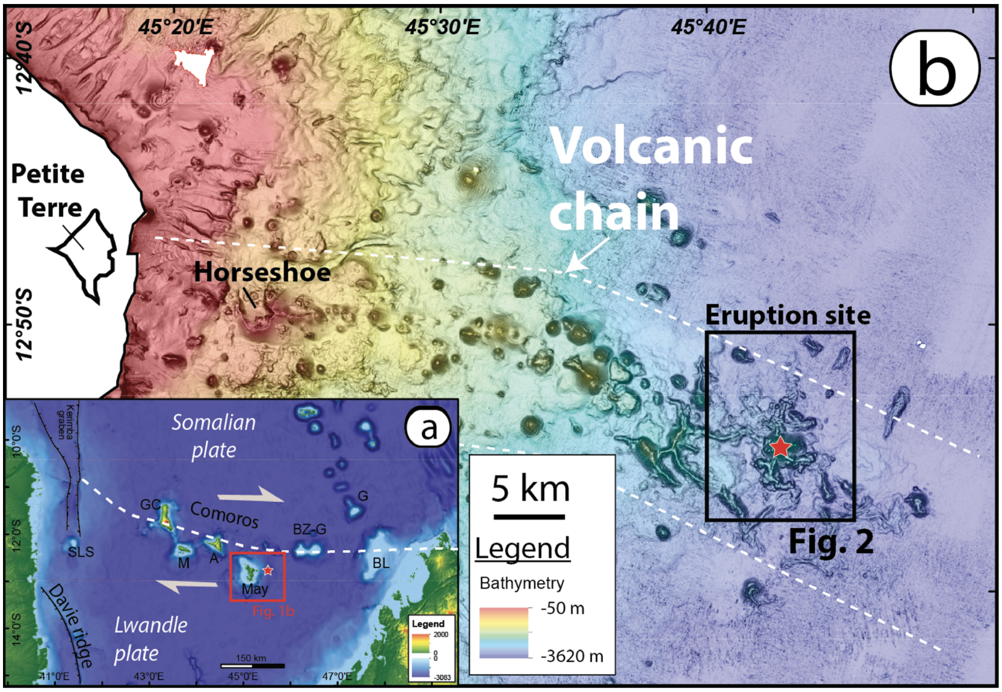


**Figure 1.** Location of the eruptive site off Mayotte's coast. (a) Comoros Archipelago, underlining the NW–SE boundary between the Lwandle microplate and the Somalia plate from Famin et al. [2020] (white dashed line), is composed of two emerged banks (Zelée and Geyser banks) four main volcanic islands, from east to west, Mayotte (May), Anjouan (A), Moheli (M) and Grande Comore (GC). Red star: eruptive site, G: Glorieuses; BL: Leven Bank; SLS: St Lazarus Seamount. (b) Fani Maoré volcanic cone is located 50 km east from offshore Mayotte Island, at the end of the Eastern Volcanic Chain, as delineated by the white dashed lines [Bachèlery et al., 2021, Feuillet et al., 2021].

a maximum age of 28 Ma for the onset of magmatic activity [Masquelet et al., 2022], recent volcanic activity has been documented both on land [possibly as young as 4 ka, Zinke et al., 2003] and on the distal part of a 60 km long WNW–ESE-oriented volcanic chain that extends 50 km off the eastern submarine flank of Mayotte up to the 2018–2021 Fani Maoré new edifice [Figure 1; Berthod et al., 2021b, Feuillet et al., 2021]. Petite Terre, the eastern volcanic island of Mayotte, is characterized by the presence of recent volcanic activity [200 ka, Pelleter et al., 2014] ranging from older mafic Strombolian scoria cones to the younger well-preserved phonolitic tuff rings aligned on N140 trending fractures.

## 3. Eruption phenomenology

The 2018–2021 volcanic activity most likely started in early July 2018 after two months of intense seismic activity at mantle level [Cesca et al., 2020, Lemoine et al., 2020, Bertil et al., 2021], near the eastern end of what is now called the "Eastern Volcanic Chain of Mayotte" [Bachèlery et al., 2021, Feuillet et al., 2021]. When the new volcanic edifice, Fani Maoré was first discovered in May 2019, it had already grown to more than 820 m high above the seafloor, with an estimated lava volume of 5 km$^3$ [Feuillet et al., 2021]. This activity caused a strong mobilization of the French scientific community and the creation of the Mayotte Volcanological and Seismological Monitoring Network [REVOSIMA, 2022] to record seismic and track volcanic activity on Mayotte and thereby provide a better definition of the seismic and volcanic hazards on the island of Mayotte and along the active submarine volcanic chain. In response to this crisis, twenty-six oceanographic campaigns have been carried out since May 2019, six of them deploying rock

**Table 1.** Location of dredges performed during MAYOBS and GEOFLAMME oceanographic campaigns

| Dredges | Oceanographic cruise | DOI https://doi.org/10.18142/291 | Start dredging | | | End dredging | | |
|---|---|---|---|---|---|---|---|---|
| | | | Latitude | Longitude | Depth (m) | Latitude | Longitude | Depth (m) |
| DR01 | MAYOBS 1 | https://doi.org/10.17600/18001217 | 12°54.30′ S | 45°43.13′ E | 3050 | 12°54.51′ S | 45°43.08′ E | 2820 |
| DR08 | MAYOBS 2 | https://doi.org/10.17600/18001222 | 12°56.46′ S | 45°42.88′ E | 3072 | 12°56.05′ S | 45°41.91′ E | 3050 |
| DR10 | MAYOBS 4 | https://doi.org/10.17600/18001238 | 12°54.94′ S | 45°43.31′ E | 3120 | 12°55.05′ S | 45°43.24′ E | 2950 |
| DR11 | MAYOBS 4 | https://doi.org/10.17600/18001238 | 12°54.80′ S | 45°41.57′ E | 3250 | 12°55.20′ S | 45°41.55′ E | 3228 |
| DR12 | MAYOBS 4 | https://doi.org/10.17600/18001238 | 12°52.90′ S | 45°42.94′ E | 3245 | 12°52.97′ S | 45°42.93′ E | 3200 |
| DR14 | MAYOBS 15 | https://doi.org/10.17600/18001745 | 12°51.94′ S | 45°40.65′ E | 3240 | 12°51.94′ S | 45°40.71′ E | 3210 |
| DR15 | MAYOBS 15 | https://doi.org/10.17600/18001745 | 12°52.71′ S | 45°40.34′ E | 3130 | 12°52.80′ S | 45°40.49′ E | 3070 |
| DR18 | MAYOBS 15 | https://doi.org/10.17600/18001745 | 12°52.26′ S | 45°41.17′ E | 3270 | 12°52.27′ S | 45°41.03′ E | 3265 |
| DR19 | GEOFLAMME | https://doi.org/10.17600/18001297 | 12°50.63′ S | 45°40.96′ E | 3363 | 12°50.92′ S | 45°40.81′ E | 3369 |
| DR20 | GEOFLAMME | https://doi.org/10.17600/18001297 | 12°52.09′ S | 45°40.35′ E | 3224 | 12°52.24′ S | 45°40.23′ E | 3135 |

dredges [Feuillet, 2019, Feuillet et al., 2021, Fouquet and Feuillet, 2019, Jorry, 2019, Rinnert et al., 2020, 2021]. These campaigns involve seven multiparameter volcano monitoring cruises [Feuillet, 2019, Fouquet and Feuillet, 2019, Jorry, 2019, Rinnert et al., 2020, 2021], three scientific research campaigns, GEOFLAMME [Rinnert et al., 2021], SISMAORE [Thinon et al., 2021], and SCRATCH [Berthod et al., 2021c], as well as sixteen short campaigns to retrieve and redeploy OBSs (Ocean Bottom Seismometers) every 3–4 months since February 2019.

These campaigns provide an exceptional time-series of bathymetric, textural, petrological, and geochemical data for the 2018–2021 eruptive period (Table 1). Indeed, repeated, high-resolution bathymetric surveys, coupled with dredging of erupted lava at intervals ranging from few hours to few months, allowed us to follow the syn-eruptive evolution of the magma throughout the last two years, until the probable end of the eruption in January 2021 when the last active lava flows were detected.

Using data collected during these oceanographic campaigns, recent studies suggest that the 2018–2021 eruption has been fed by a deep magmatic system rooted in the lithospheric mantle [e.g., Berthod et al., 2021b, Feuillet et al., 2021, Foix et al., 2021, Lavayssiere et al., 2022]. Using dredged volcanic rocks gathered during the first three monitoring campaigns [MAYOBS 1, 2, and 4, Feuillet, 2019, Jorry, 2019, Fouquet and Feuillet, 2019, Rinnert et al., 2019], Berthod et al. [2021b] concluded that primary magma is extracted from the mantle at depths of 80–100 km before being stored in a deep magma reservoir inside the lithospheric mantle. Petrological [Berthod et al., 2021b] and seismic [Feuillet et al., 2021, Foix et al., 2021, Lavayssiere et al., 2022] data indicate that the depth of this reservoir is ≥35 km and probably less than 48 km. After ~50% of crystallization in this deep reservoir, and extremely efficient segregation from its cumulates, an internal or external trigger forced the magma to ascend directly and quickly to the surface where it erupted as aphanitic basanites [Berthod et al., 2021b] from the onset of the eruption (May 2018 to May 2019). After May 2019, the magma output rate slowed down and switched to a different ascent pathway sampling a small shallower evolved magma batch at the base of the crust at a depth of $18 \pm 9$ km [Berthod et al., 2021a].

## 4. Methods

### 4.1. *Dredging protocol*

Despite considerable improvements in navigation and sampling methods in the last decades, including the development of Remotely Operated Vehicles (ROV) and human operated submersibles (e.g., the manned submarine *Nautile*), dredging operations remain fundamental for sampling and characterizing submarine volcanic structures and related products. Its strength relies on its capability to collect a large quantity of material (up to 1000 kg) that can be used for various analyses and can usually be regarded as statistically representative of the studied area. Since dredging requires fewer logistics than submersibles, the related operations are easier to implement, and were, until the late 1960s, the only way to sample the seabed [Kidd et al., 1990]. In recent decades, significant advances have included more accurate navigation systems, improved geophysical survey methods, and monitoring dredge behavior to ensure that dredge sampling is as representative as possible of the geological terrains being investigated. By contrast, the design of the dredge used for geological purposes has remained very simple due to the high risk of equipment breaking during the operation. R/V (Research Vessel) *Marion Dufresne II* and R/V *Pourquoi Pas?* use a cylindrical dredge made of a cylindrical metal base, cut into a 1 m diameter steel pipe with cutting teeth welded at the edge in order to break off samples from outcrops. The dredge is linked to the oceanographic winch cable through swivels, 25 m of cargo ship mooring chain and 150 m of martyr cable. A fuse link is also inserted between the metal bail and the chain connection to ensure the rupture of the martyr cable above a threshold tension of 120–160 kN. Indeed, if the dredge hooks on an outcrop and remains stuck, the increasing tension places the ship's trawl warp at risk of parting. An ultra-short baseline (USBL) acoustic beacon (BUC) is positioned on the trawl cable at about 365 m from the dredge, in order to record the precise 3D location of the dredge during the entire operation.

4.1.1. *Preparation*

An improved preparation procedure was adopted to select the location and the topographic profile to be dredged. Several elements had to be considered beforehand to select the most optimal dredging profile within the studied area:

- For active volcanoes such as Fani Maoré, a bathymetry differential using the ship's multibeam echosounder allowed us to pinpoint potential new eruptive products (such as lava flows). In some cases, bathymetry was acquired by ROV or AUV (Autonomous Underwater Vehicle) with a higher resolution. In addition, if available, the geological map, slope angles and the reflectivity maps were used to better define the sampling area.
- For dredging to be effective, we preferred to operate on a smooth slope (from base to top without major breaks in slope) so that, the dredge would be properly orientated and could easily grab material without emptying on hooking. However, on some occasions, dredges were also successfully performed on nearly flat profiles, where a difference in elevation of only a few meters existed.
- Accounting for meteorological conditions was also critical, and the vessel was aligned as much as possible with the currents and wind directions and preferably facing the wind and the current, so as to simplify the ship's maneuvers during dredging. Note that meteorological conditions could change quickly and on occasions the approach had to be adjusted once the vessel arrived on site. For better efficiency, several topographic profiles with different orientations were prepared in advance using GIS software to quickly adapt the course of the ship if needed.
- The general start and end of the sampling zone of interest was fixed according to the geological and bathymetric information available. The ship's captain could thus plan the location of the entire dredging operation according to the conditions at the time. This requires a precise knowledge of the bathymetry not just in the zone of interest of dredging, but on a longer track that is usually about 7 km.
- The dredge was carefully cleaned to ensure that no rock fragments were retained in the metal mesh. We occasionally attached below the cylindrical dredge a "*baby-dredge*" which consists of a heavy and resistant iron cast tube about 0.5 m long and 20 cm in diameter that hangs with a solid chain below the main dredge in order to sample the finer grained material forming the seabed that easily gets lost filtering through the 3–5 cm sized openings in the metal mesh of the main dredge. This turned out to be extremely useful on submarine pyroclastic cones as it allowed us to sample the pyroclastic matrix of unconsolidated volcanic deposits from submarine explosive activity.

The geographical coordinates of the dredging profile (latitude, longitude, and depth) were then extracted with the help of GIS software (ESRI® ArcGIS or QGIS) to plot the depth profile versus decimal minutes of longitude or latitude at a 1:1 scale. This graph was then used to report the GPS coordinates of the USBL acoustic beacon to track the position of the dredge graphically precisely during the entire process.

#### 4.1.2. *Dredging*

The dredge was launched at the beginning of the profile and deployed by unwinding the cable at a speed of 1 m/s. When the dredge reached the seabed, the vessel started to move towards the end point of the profile at about 0.5 m/s (1 knot) and the cable deployment speed was reduced to about 0.3 m/s. The goal of this step was to tilt the dredge cable line to form an angle of about 40° with the seafloor and to increase the efficiency of dredging. During our campaigns, about 4100 m of cable were deployed for dredging operations at around 3500 m water depth.

Once the optimum tilt was reached, the cable deployment was stopped, the ship slowed down to 0.25 m/s (0.5 knots) and the dredging operation started following the dredge route planned previously. All the information, from the descent to the end of the dredging operation, was recorded. A tensiometer monitored the load on the ship's cable to follow the dredge behavior on the seabed, and to identify potential "hooks" when the dredge was supposedly sampling. For each hook, we recorded on the dredge profile (i) the position of the BUC, (ii) the time, and (iii) the tension of the cable. The known length between the BUC and the dredge (e.g., 365 m during MAYOBS 15 campaign) allowed us to precisely locate the dredge on the seafloor on a 2D plot of the dredge profile. For the latest MAYOBS 21 campaign, dredging was also followed with the software *VGraph3D* in which the topography is shown together with the position of the BUC and the vessel. Careful attention was paid to the time-series of the hooks along the dredging profile to interpret in real-time the behavior of the dredge, whether it was stuck, and whether it had lifted off the seabed, potentially empty. The amplitude of the hooks was carefully monitored so that they do not exceed the 120-kN safety threshold. After half a dozen hooks, the vessel stopped and the hopefully full dredge was brought back on board and its weight recorded. While pulling the dredge, several new hooks were often recorded that might have caused the dredge to get stuck. When this happened, we often managed to free the dredge by driving the vessel backward until it was in vertical alignment with the dredge so that the cable could be rewound a bit thus lifting the dredge off the blockage point.

For sampling sites located at 3500 m BSL, the entire dredging operation usually lasted approximately 6 h: 1.5 h for launching and descent at 1 m/s, 1.5 h for deployment, 1 h for dredging, and 1.5 h for ascent and boarding.

### 4.2. *Chemical analyses*

#### 4.2.1. *X-ray fluorescence analyses (XRF)*

Bulk-rock major element compositions were obtained for forty-seven samples from ten dredges on the eruption site (Table 1). Samples were analyzed with an Epsilon 3 × l X-ray fluorometer (Malvern-Panalytical) at the plateforme "Rayons X"—Université de Paris (Paris, France). The fluorometer is equipped with an Ag X-ray tube operating under He atmosphere, with four conditions during 120 s: 5 kV–60 μA without filter for analysis of Na, Mg, Al and Si, 10 kV–30 μA with a 7 μm titanium filter for the analysis of P, 12 kV–25 μA with a 50 μm aluminum filter for the analysis of Ca, K and Ti, and 20 kV–15 μA with a 200 μm aluminum filter for analysis of Mn and Fe. Samples were mixed with a fluxing agent (0.1136 g of sample, 1.2312 g of fluxing agent, either $LiBO_2$ or $Li_2B_4O_7$) and 0.0187 g of non-wetting agent (LiBr) and melted in a platinum crucible at 1050 °C for 25 min in a fusion instrument (LeNeo fluxer, Claisse). Calibration curves were obtained from identical beads of fifteen geological reference materials (ACE, ANG, BCR-2, BEN, BHVO-2, BIR-1, BXN, DTN, FKN, GSN, MAN, Mica-Fe, Osh BO, UBN and BR24). The curves are perfectly linear over the entire concentration range. Analytical uncertainties ($\pm 1\sigma$) are <5% for $TiO_2$, MnO and $Fe_2O_3$; 5% for MgO, $SiO_2$ and CaO; 10% for $Al_2O_3$, $P_2O_5$ and $K_2O$ and 20% for $Na_2O$.

#### 4.2.2. *ICP-MS analyses*

Trace element concentrations were analyzed by ICP-MS at Institut de Physique du Globe de Paris (IPGP, Paris, France). Around 50 mg of powdered rock samples were digested using a mix of 2 ml concentrated $HNO_3$ and 1 ml concentrated HF, heated in closed Teflon vessels at 110 °C for 24 h. An additional 3 ml of concentrated $HNO_3$ was added to the samples after cooling and the mix was heated for another 24 h at 110 °C. Finally, 45 ml of ultrapure water was added to the samples after cooling and the solutions were sonicated for 4 h. Samples were analyzed 24–48 h later, after an additional 10× dilution with ultrapure water, using an inert introduction system on an Agilent 7900 ICP-MS. Calibration of rock samples was done against a BEN rock standard [Jochum et al., 2016]. Analytical uncertainties are 6% or less for lithophile elements and 15% or less for chalcophile elements.

#### 4.2.3. *Electron probe microanalysis*

The chemical composition of minerals and glasses was analyzed using the CAMECA SXFive Tactis electron microprobe at Laboratoire Magmas et Volcans (LMV, Clermont-Ferrand, France). For minerals, we used a 15 kV accelerating potential and a 15 nA probe current with a focused beam for major and minor elements, with 10 s counting times. We analyzed both mineral rims and cores although no difference was visible except for olivine antecrysts. For glasses, the beam current was reduced to 8 nA, the beam was defocused to a 20 µm diameter, and alkali elements were counted first in order to avoid Na loss caused by beam interaction. Glasses were only analyzed in glassy areas close to pillow rims and away from crystals to avoid any modification due to diffusion during quenching. Natural and synthetic mineral standards, including orthoclase (K, Al), albite (Na), wollastonite (Si, Ca), fayalite (Fe), forsterite (Mg), $TiMnO_3$ (Ti, Mn), NiO (Ni), $Cr_2O_3$ (Cr), and fluorapatite (P) were used for routine calibration.

## 5. Results

### 5.1. *Lava flows chronology*

Repeated bathymetric surveys with the ship's multibeam echosounder have systematically been gathered during the MAYOBS campaigns over the areas of eruptive activity following specific data acquisition protocols, leading to bathymetric grids with a resolution of 7 m to 30 m. Some of the key objectives of these repeated surveys were to be able to track the evolution of the active lava flow field along with the eruptive activity. Due to the depth of the volcano, new volcanic materials can be inferred when depth changes between two surveys exceed 10 m over a sufficiently large area. In some conditions, this depth differential threshold can be as low as 5 m. After each survey, a preliminary analysis of depth differences was achieved, and the results announced by the REVOSIMA. A re-examination of the whole bathymetry dataset is now in progress to quantify more accurately the volumes and flux of erupted material and their evolution over time.

Figure 2 synthesizes the spatio-temporal evolution of the overall contours of the different active lava flows. The compound lava flow field was mapped after each bathymetric survey using a combination of bathymetric data, differential time-lapse bathymetric analysis and ocean bottom reflectivity data. Several phases of lava flow eruption can be identified, ordered chronologically, and matched with the corresponding dredges performed during the different surveys (Figure 2). Phase 1 corresponds to the volcanic field and the new edifice discovered during the first MAYOBS campaign [Feuillet et al., 2021]. The structure, evidenced by comparing their data to those acquired during a 2014 survey by the French Naval Hydrographic and Oceanographic Service (SHOM), is composed of a main central edifice with radial ridges, up to 300 m thick and extending up to 5 km north and south, emplaced between July 2018 and May 2019 [Figure 2a, Feuillet et al., 2021]. Phase 2 marks the emplacement, from new vents, of two widespread lava flow fields in the southern and southwestern distal part of the main edifice. Between August 2019 and January 2021, numerous lava flows were emplaced in a new distinct area, located 6 km northwest from the main central edifice suggesting the occurrence of a third phase (Figure 2a,b). The growth of the main edifice stopped sometime between August 2019 and May 2020. At the time of writing (June 2022), preliminary estimates indicate that the entire eruption produced a bulk volume (not corrected for vesicularity) of about 6.55 $km^3$ of magma [Deplus et al., 2019, REVOSIMA, 2022]. The eruptive flux was very high during Phase 1, on the order of 150 to 200 $m^3/s$ [REVOSIMA, 2019, Deplus et al., 2019] and progressively decreased throughout the eruption (Phase 2) and in particular for lavas emplaced at the northwestern site, during Phase 3 [Berthod et al., 2021b, REVOSIMA, 2020].

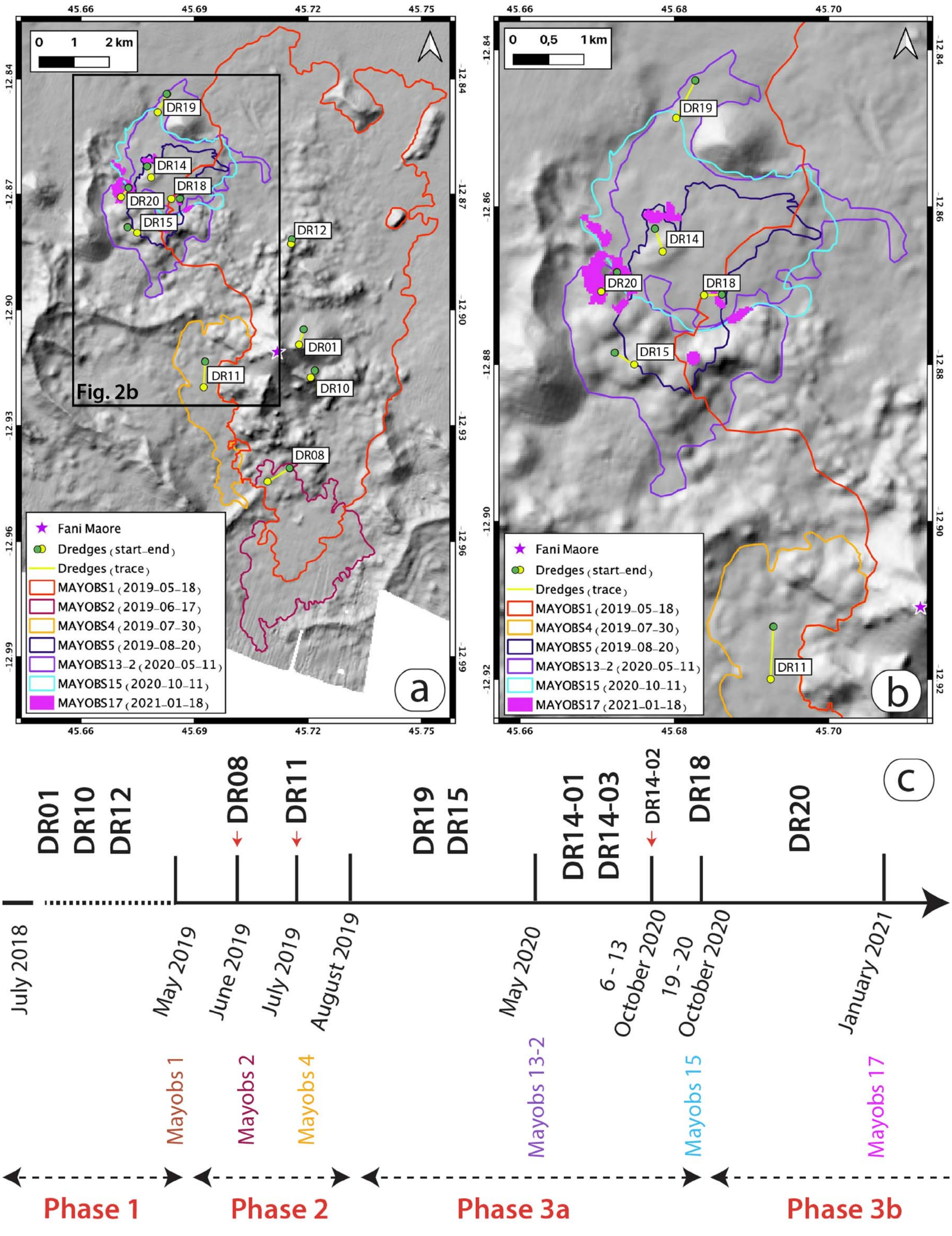


**Figure 2.** Caption continued on next page.

**Figure 2.** (**cont**.) (a) Distinct lava flows identified from bathymetry data collected during the MAYOBS oceanographic campaigns [Feuillet, 2019, Jorry, 2019, Fouquet and Feuillet, 2019, Rinnert et al., 2019] and the GEOFLAMME cruise [Rinnert et al., 2021]. DR labels correspond to the dredges. (b) Close-up view on the last eruptive site, located 6 km northwest of the main volcanic cone and collected during the MAYOBS 15 campaign [Rinnert et al., 2019] and the GEOFLAMME campaign [Rinnert et al., 2021]. (c) Sampling related to eruption timing. DR01, DR10 and DR12 lavas were erupted before May 2019 during the cone-building (Phase 1); DR08 and DR11 are lava flows erupted in June and July 2019 (Phase 2). DR14-01/03 sampled a lava flow erupted between May and October 2020, while DR15 and DR19 sampled different facies of a complex lava flow field erupted between August 2019 and May 2020 (Phase 3a). DR14-02 lava was erupted between the October 6th–13th 2020 and DR18 sampled a lava flow erupted on the night of October 19th–20th 2020 and which has been observed glowing red with the SCAMPI camera during MAYOBS 15 campaign [REVOSIMA, 2020, Rinnert et al., 2020], DR20 erupted between 20 October 2020 and 18 January 2021 (Phase 3b). The subdivision of Phase 3 is proposed from our petrological observations. See Section 5.3 for further explanation.

## 5.2. *Samples*

Most dredged samples are fragments of pillow lavas, centimetric to pluridecimetric in size (Figure 3a), that present five different textural facies that are described as follows from the outside to the inside.

Facies 1 is the quenched, shiny glassy black outer rim with a thickness of about 2–3 cm thick (Figure 3b). This chilled margin, of variable thickness, is cracked and micro-vesiculated. It flakes off easily, sometimes very dynamically as a popping rock, forming numerous glass fragments. The vesicle's concave outer surfaces are often coated with golden metallic deposits giving a very distinctive iridescent sheen to the glassy lava. When preserved, the surface of this facies is wrinkled with millimetric grooves. This surface is often covered with clusters of orange precipitates, which can also fill fractures within the pillow.

Facies 2 is thicker (6–7 cm), less glassy with a less shiny and duller appearance compared to Facies 1. Although it is massive, it is nevertheless characterized by an increase in the size and proportion of vesicles (Figure 3b). The vesicles are mostly sub-spherical with diameters varying between 3.5 mm to 2.0 cm. However, the convoluted shape and irregular outline of the largest vesicles are evidence that coalescence is observable and tends to increase towards the internal part of the pillow lava. All thin sections were made in the outermost chilled margin preserved in the recovered clasts (mostly Facies 1, exceptionally Facies 2) to ensure a rapid quenching in contact with water, and to avoid post-eruptive crystallization processes.

Facies 3 is characterized by the presence of many centimeters long (4–5 cm), tubular but undulating pipes that are oriented perpendicular to the quenched pillow outer surface and that do not penetrate through the lower contact with Facies 2 (Figure 3b).

Facies 4 is characterized by elongated vesicles parallel to the boundary between Facies 3 and Facies 4 (Figure 3b). This part of the pillow is also characterized by prismatic fractures forming a polygonal pattern.

Finally, Facies 5 corresponds to the core of the pillow lava. It often shows a succession of centimetric layers sub-parallel to the outer glassy surface (Facies 1) that are characterized each by a homogeneous vesicularity that differs from the next neighboring layer which can be more vesiculated, in terms of vesicle size and abundance. Vesicles tend to be aligned along a direction sub-parallel to the outer glassy convex surface of the pillow. Vesicles have coalesced to form cavities (2 × 3 cm in size) that have joined together to form radial pipes that are generally perpendicular to the outer pillow's surface (Figure 3b).

## 5.3. *Petrology*

### 5.3.1. *Phase 1: lavas of the main edifice*

Samples from Phase 1 (DR01, DR10, and DR12) are glassy, almost aphyric [<4 vol.% crystals, Berthod et al., 2021b] and highly vesicular (average vesicularity of 35 vol.%). Crystals include 50–700 μm olivine co-crystallizing with smaller 50–100 μm magnetite

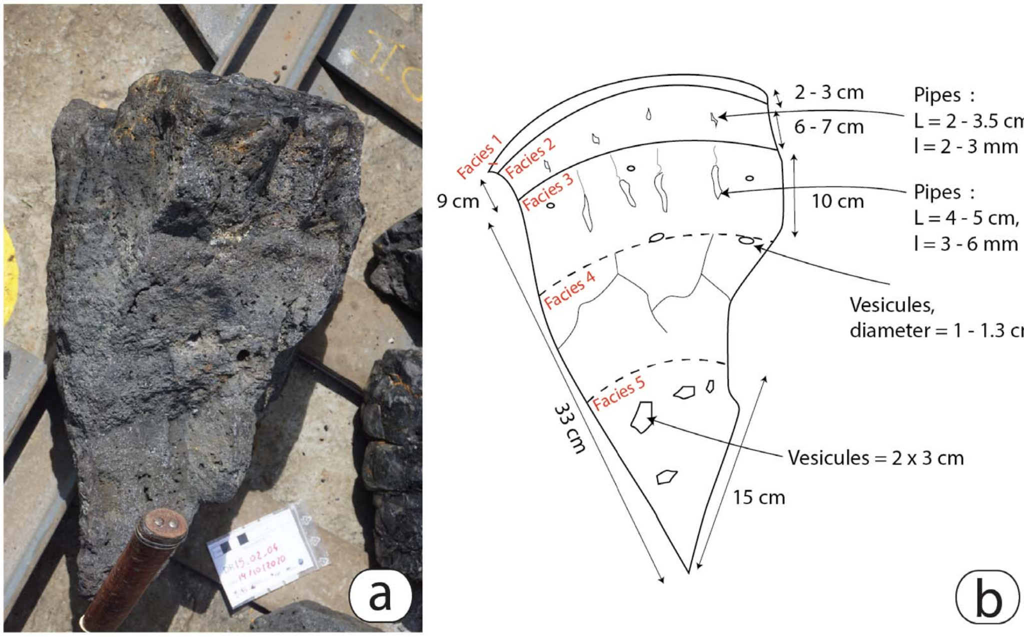


**Figure 3.** (a) Picture and (b) simplified sketch of a poorly fractured pillow-lava dredged during the MAYOBS campaigns (DR15-02), measuring 42 × 39 × 36 cm.

(Figure 4a,b), often grouped as small clusters. Many olivine crystals are skeletal, with numerous inclusions and embayments, although euhedral crystals are also present. Most magnetite crystals display euhedral shapes. Olivine and magnetite crystals are observed in the chilled margins. No apatite or ilmenite have been observed.

### 5.3.2. *Phase 2: distal lavas from the southern and southwestern eruptive vents*

Samples from Phase 2 (DR08 and DR11) display glassy and aphyric textures (Figure 4c,d). Clusters of olivine and magnetite crystals, similar to those observed in Phase 1 samples, are here associated with apatite crystals (up to 20 µm in length). The textural relationships suggest that all three minerals crystallized at the same time. The formation of an early immiscible sulfide melt is evidenced by the presence of small spherical droplets of iron sulfide (<10 µm in diameter).

A small number of large (up to 2.5 mm long) reversely zoned olivine crystals with Fe-rich cores and Mg-rich overgrowths are present in all samples from Phase 2. Since Berthod et al. [2021a] showed that these crystals were sampled by the basanitic magma during its ascent towards the surface, they are interpreted as antecrysts. Some of the cores contain numerous embayments. Contrary to the outer euhedral faces, these embayments do not display overgrowths (Figure 4e). Co-crystallization of magnetite with olivine, as observed within Phase 1 samples, is also found in the Mg-rich overgrowth. Rounded ilmenite grains, surrounded by magnetite overgrowths, are observed in all samples (Figure 4f). Ilmenite inclusions, associated with magnetite and apatite, are observed in some olivine Fe-rich cores. Rare millimetric antecrysts of clinopyroxene and rounded apatite crystals have been described in one sample [Berthod et al., 2021b].

### 5.3.3. *Phase 3a: northwestern eruptive area*

After August 2019, the activity shifted to a new eruptive area 6 km northwest of the main edifice (Figure 2a,b). The petrological description of lava flows from this Phase 3 are presented chronologically (Figures 5 and 6).

The first erupted lava flows at the northwestern site (DR15 and DR19) show a similar mineralogy than Phase 2 samples. They contain clusters of euhedral to skeletal olivine crystals (50 to 500 µm, Figure 5a,b),

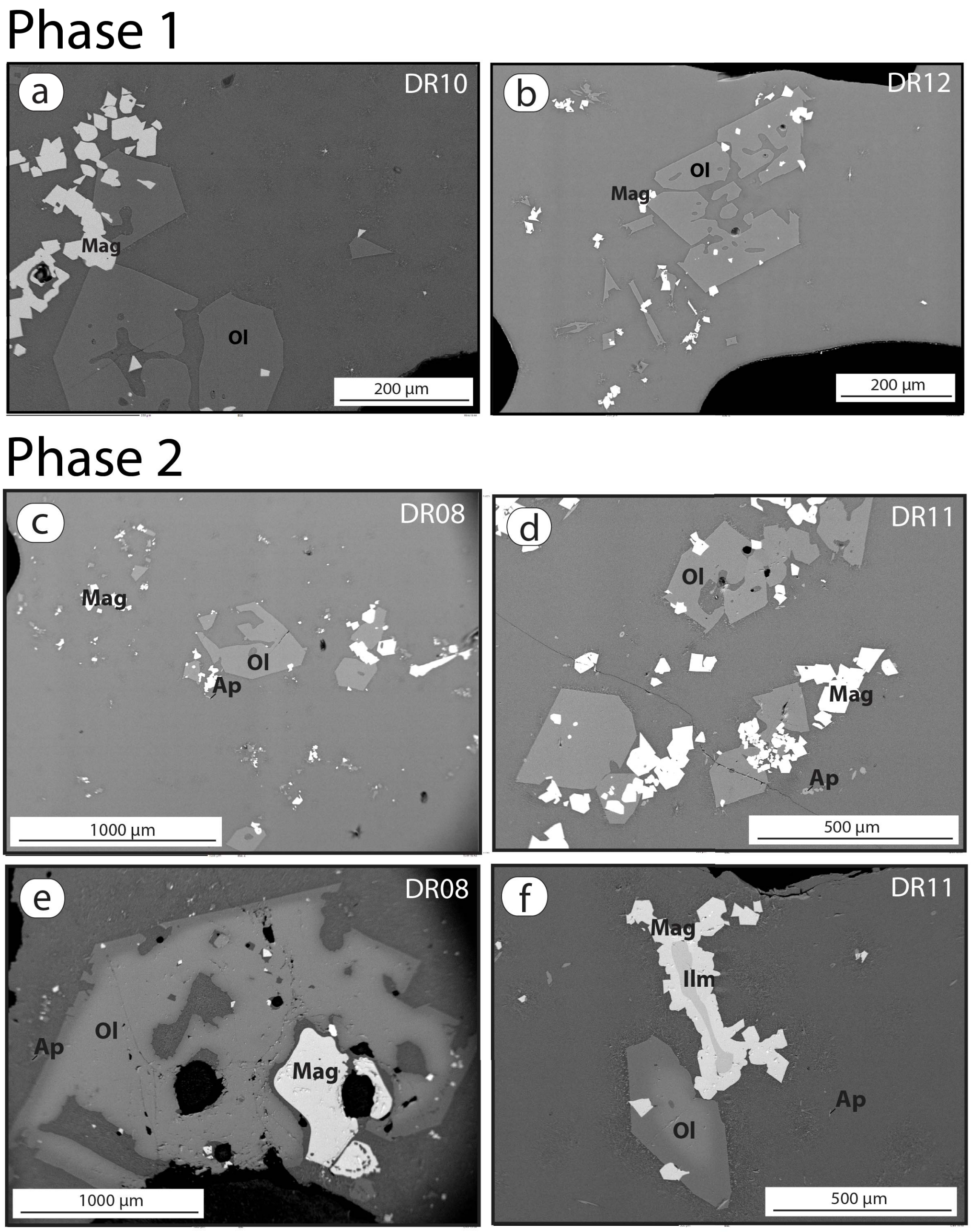


**Figure 4.** Back-scattered electron (BSE) microscope images of samples from Phases 1 and 2, (a) DR10 sample contains clusters made of co-crystallized skeletal olivine and euhedral magnetite crystals. Skeletal olivine in intergrowth with magnetite are also observed in (b) DR12, (c) DR08, and (d) DR11 samples. Apatite crystals also appear in these Phase 2 samples. Reversely zoned olivine with rounded cores and rounded magnetite crystals are present in (e) DR08 and (f) DR11 samples. These Phase 2 lava flows also contain resorbed ilmenite surrounded by magnetite. Ol: Olivine, Mag: Ti-rich Magnetite, Ilm: Ilmenite, Ap: Apatite.

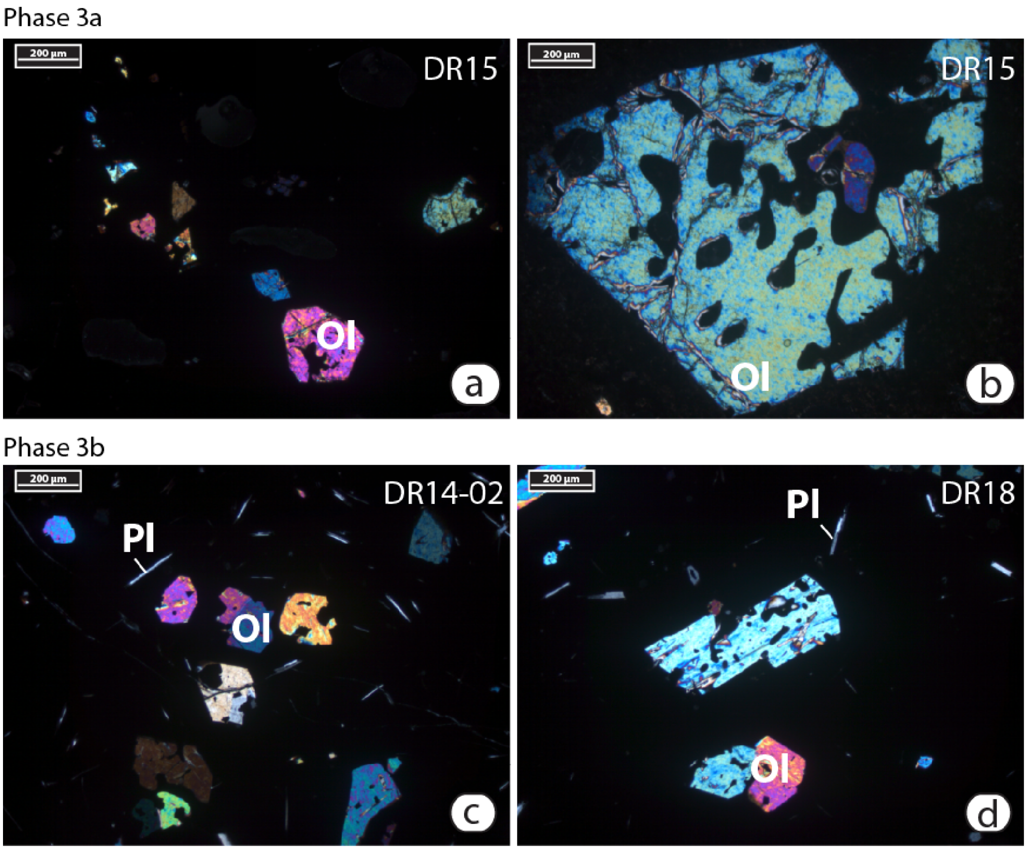


**Figure 5.** Petrographic characteristics of Phase 3 samples from the NW eruptive site viewed under cross-polarized transmitted light (a) typical olivine crystals in sample DR15. (b) Zoned olivine antecryst in sample DR15 with possible dissolution texture. (c) Sample DR14-02 and (d) sample DR18-01 contain plagioclase laths in the matrix. Ol: olivine, Pl: Plagioclase.

in intergrowth with magnetite (up to 200 µm) and apatite crystals. Euhedral to skeletal apatite crystals are more abundant than in Phase 2 samples and can reach 150 µm in length. Droplets of immiscible sulfide melts, up to 20–30 µm in diameter, are associated with or included in magnetite crystals. As with the Phase 2 lavas, those samples also contain an antecryst cargo comprising reversely zoned olivine (0.5–3 mm, Figure 5b) and rounded ilmenite crystals with magnetite rims (up to 800 µm, Figure 6a). No clinopyroxene has been observed.

Three different types of samples were recovered from dredge DR14: (i) samples labeled DR14-03 and DR15 are petrographically identical. (ii) Samples DR14-01 are also similar to DR15 but for the appearance of a few small plagioclase laths (Figure 6b). (iii) The third category of samples, DR14-02 is significantly different from the other DR14 samples and will be described below with the latest eruptive products.

#### 5.3.4. *Phase 3b: most recent eruptive products*

The samples from the most recent lava flows (DR18-01, DR20, and DR14-02) from the NW eruptive area are glassy and contain crystals of olivine (<1000 µm), magnetite (<400 µm), apatite (<200 µm), and plagioclase (<500 µm, average 150 µm, Figures 5c,d and 6c,d). Olivine crystals are often skeletal and contain numerous melt inclusions and embayments. Olivine, apatite, and magnetite crystals show evidence of co-crystallization, whereas plagioclase crystals are isolated. The plagioclase content quickly increases toward the core

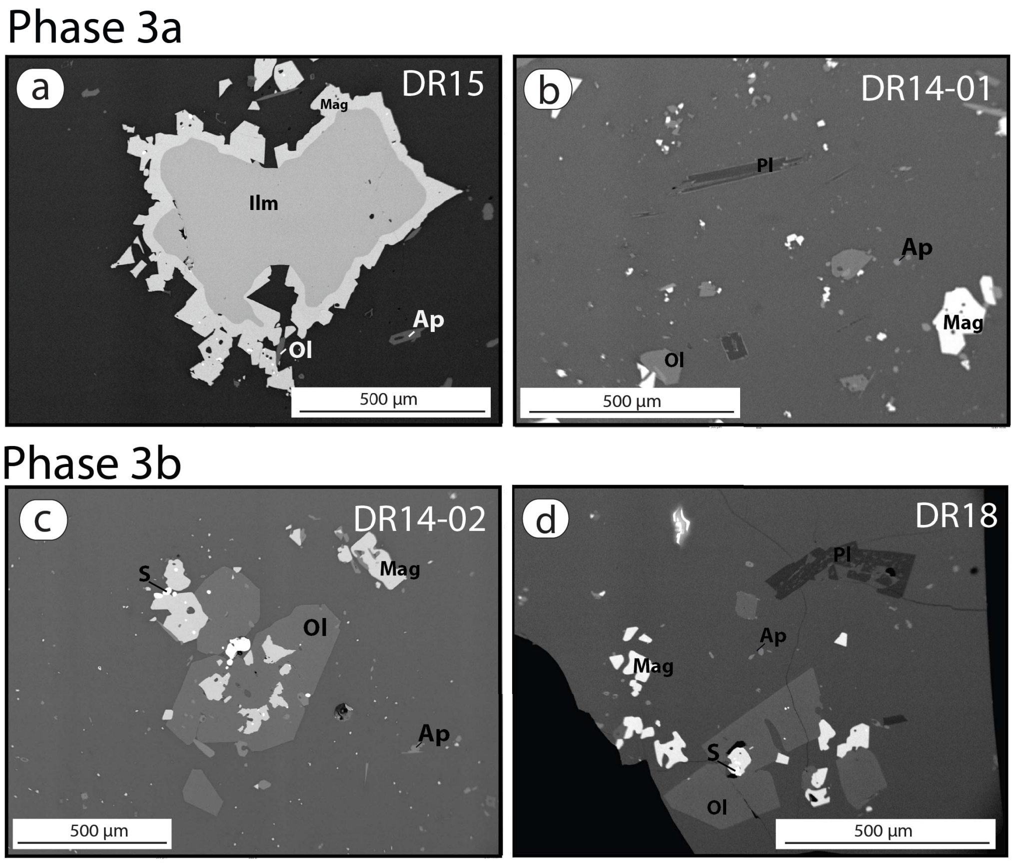


**Figure 6.** Back-scattered electron microscope images of Phase 3 samples from the Phase 3b, on north-western site. (a) Rounded ilmenite antecryst surrounded by magnetite in sample DR15. (b) Crystals of olivine, plagioclase, magnetite, and apatite in sample DR14-01. (c) Olivine-magnetite-sulfide cluster in sample DR14-02 (sulfide are the small light blebs inside the olivine and the larger one in-between the two largest olivine crystals). (d) Olivine, magnetite, plagioclase, and apatite crystals in sample DR18-01. Ol: Olivine, Mag: Ti-rich Magnetite, Ilm: Ilmenite, Ap: Apatite, S: Sulfide blebs.

of the pillow lava fragments, giving them a diktytaxitic texture. Contrary to DR15, DR19, and Phase 2 samples, no reversely zoned olivine or magnetite-rimmed ilmenite have been observed in those samples. Rounded sulfide droplets (up to 100 µm in diameter) are abundant, either as inclusions within oxides and sometimes within olivine, or associated with magnetite-olivine-apatite clusters.

The differences in paragenesis (absence/presence of reversely zoned olivine or magnetite-rimmed ilmenite, and plagioclase) and in droplet contents suggest that Phase 3 can be divided into two sub-phases: Phase 3a (DR14-01, DR14-03, DR15, and DR19) and Phase 3b (DR14-02, DR18-01, and DR20).

### 5.4. *Bulk-rock composition*

All major element data presented here (Figure 7 and Supplementary Table 1) have been normalized to 100%, volatile-free, to facilitate comparisons. Original XRF totals are reported in Supplementary Table 1. Major and trace element compositions are similar to those previously reported for the entire Comoros Archipelago [Späth et al., 1996, Claude-Ivanaj et al., 1998, Class et al., 1998, Deniel, 1998, Bachèlery and Hémond, 2016].

Overall, all erupted samples display a well-defined differentiation trend in all Harker-type element plots (Figure 7). The few outliers are likely due to some

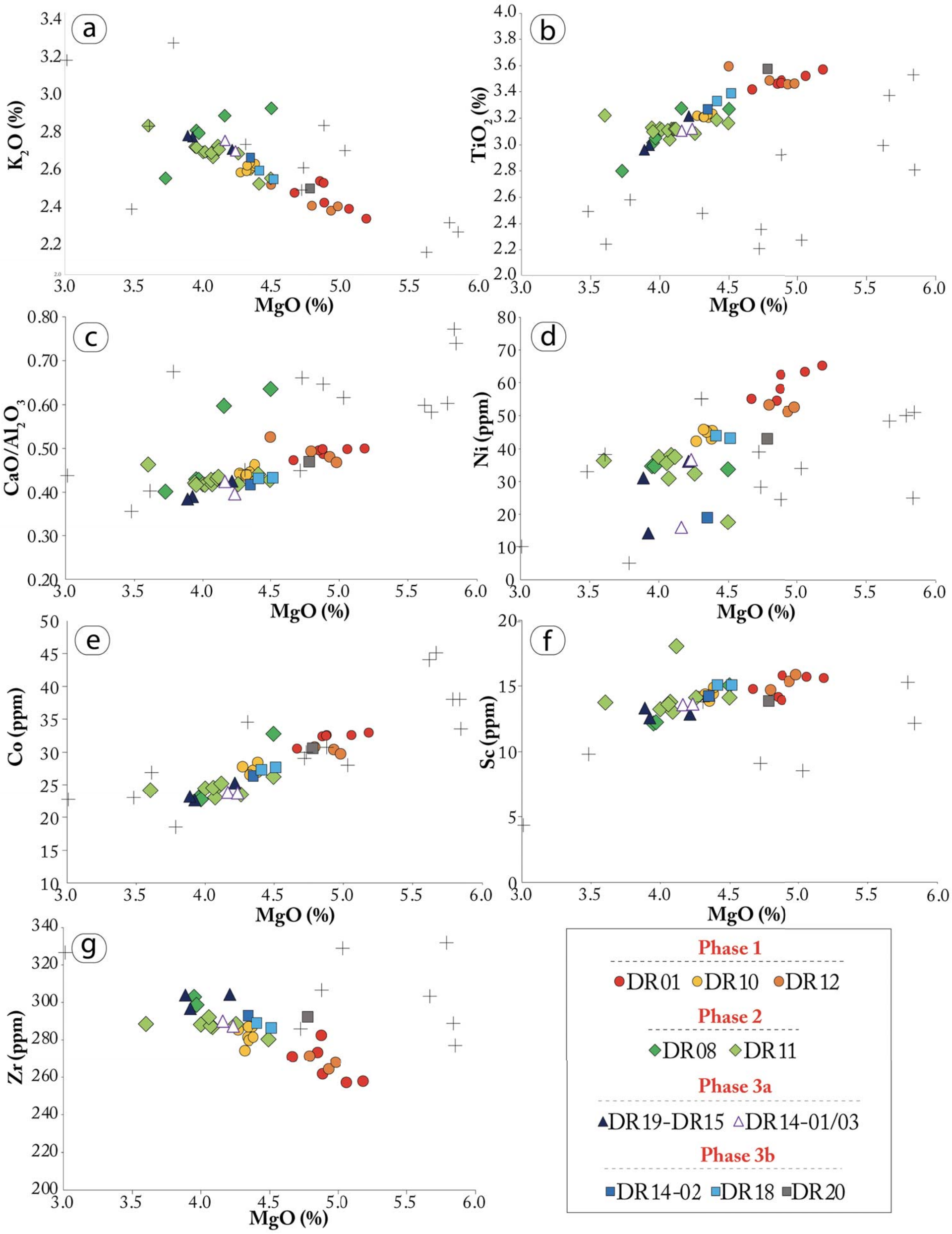


**Figure 7.** Bulk-rock geochemical evolution of dredged lavas from the eruption site. The caption presents dredges in chronological order. Crosses are reference data for Mayotte lavas [Nougier et al., 1986, Späth et al., 1996, Pelleter et al., 2014].

crystal accumulation. The most primitive samples are those erupted during Phase 1 (particularly samples from DR01), the most evolved samples have erupted either during Phase 2 (DR08 and DR11) or at the northwestern eruptive site during Phase 3 (DR15 and DR19).

Early erupted lavas of Phase 1 (DR01, DR10, and DR12) are evolved basanites with a MgO content of 4.0–5.0 wt% and a $K_2O$ content of 2.2–2.5 wt% (Figure 7a,b). In these samples, $TiO_2$, Ni, Co, Sc and Zr contents vary from 3.0–3.4 wt%, 42.3–65.2 ppm, 26.5–32.9 ppm, 0.8–15.9 ppm, and 257–287 ppm respectively (Figure 7c–g). Few variations are observed within the eruptive products of Phase 1, although DR01 is slightly more primitive than DR12 and DR10 with MgO ranging between 4.4–5.0 wt%, 4.3–4.7 wt%, and 4.0–4.2 wt%, respectively. $K_2O$, $TiO_2$, and Ni contents confirm this observation. Phase 2 lavas, sampled by DR08 and DR11 dredges, display more evolved basanitic compositions with 3.4–4.3 wt% MgO and 2.5–3.0 wt% $K_2O$. $TiO_2$ and Ni contents range from 2.4 to 3.1 wt% and 17.7 to 38 wt%, respectively. Co and Sc ranging from 22.8 to 32.8 ppm and from 12.1 to 18.0 ppm, respectively (Figure 7e,f).

The geochemical evolution of the eruptive products tends to continue for Phase 3a lavas on the new northwestern eruptive site (Figure 2a,b), with DR15 and DR19 characterized by the lowest MgO contents (3.6–4.0 wt%). $TiO_2$, Ni, Co, Sc and Zr contents are also slightly lower with values below 3.0 wt%, 36.2 ppm, 25.3 ppm, 13.3 ppm, and 305 ppm, respectively. $K_2O$ content is above 2.5 wt%. Lavas from dredge DR15 are in the phono-tephrite field of a TAS diagram, not the basanite field. In contrast, all other samples still qualify as basanites.

Different types of samples are present within the DR14 dredge (Phase 3). DR14-01 and DR14-03 samples are similar to Phase 2 lavas with 3.8–4.1 wt% MgO, 2.5–2.6 wt% $K_2O$, 2.9–3.0 wt% $TiO_2$, 16.0–36.7 ppm Ni, 23.8 ppm Co, 13.6 ppm Sc, and 286–293 ppm Zr. However, DR14-02, as well as DR18-01, which belong to Phase 3b and are slightly more primitive and similar to Phase 1 (DR10 and DR12). MgO, $K_2O$, $TiO_2$, and Ni contents of DR18-01 and DR14-02 samples range from 4.2–4.4 wt%, 2.4–2.5 wt%, 3.1–3.3 wt%, and 19–43.9 ppm, respectively. Co, Sc, and Zr contents vary between 26.3–27.6 ppm, 14.2–15.1 ppm, and 286–292 ppm, respectively.

Finally, the youngest flow also erupted during Phase 3b, DR20, displays the most primitive composition of the northwestern eruptive site with 4.5 wt% MgO, 2.3 wt% $K_2O$, 3.3 wt% $TiO_2$, 42.9 ppm Ni, 30.5 ppm Co, 13.8 ppm Sc, and 292 ppm Zr.

## 5.5. *Mineral chemistry*

The compositions of olivine crystals in Phase 1 samples (DR01, DR10, and DR12) approximate a Gaussian distribution with a Fo content varying from 70 to 73% (Figure 8 and Supplementary Table 2), suggesting the presence of a single population. Olivine crystals and the borders of reversely zoned olivine antecrysts in Phase 2 samples are slightly more evolved with a Fo content mainly below 71% (68–70% and 69–70% for DR08 and DR11, respectively, Figure 9). As described in previous work [e.g., Berthod et al., 2021b], the core of the zoned olivines have a much more evolved composition than the rims, ranging between $Fo_{56–57}$ and between $Fo_{52–60}$ in DR08 and DR11 samples, respectively. Phase 3a samples erupted at the northwestern site (DR14-01, DR14-03, DR15, and DR19) also contain two distinct populations of olivine: $Fo_{67–70}$ olivine crystals and zoned olivine antecrysts rims, which are more evolved than those from Phase 2, and $Fo_{56–63}$ cores of reversely zoned olivine (Figure 8). No olivine core has been analyzed in DR19 but they are visible in thin sections. The Fo content within the olivine crystals in Phase 3b samples vary from 69 to 72% (DR14-02, DR18-01, and DR20).

In all of our samples, Fe–Ti oxides in intergrowth with olivine crystals are Ti-rich magnetites, with FeO and $TiO_2$ contents ranging from 63.5 to 74.5 wt% and from 12.7 to 22.2 wt%, respectively (Supplementary Table 3). Magnetite-rimmed ilmenite observed in DR08, DR11, DR14, and DR15 samples are characterized by 45.5–50.7 wt% $TiO_2$, and 40.6–45.9 wt% FeO.

DR14-01, DR14-02, DR18-01, and DR20 samples contain plagioclase crystals with compositions at $An_{48–55}Ab_{42–48}Or_3$, $An_{51–58}Ab_{40–46}Or_{2–3}$, $An_{47–63}Ab_{35–49}Or_{2–4}$, and at $An_{53–58}Ab_{40–44}Or_{2–3}$ respectively (Supplementary Table 4).

Rare glassy melt inclusions are found in a variety of crystals (olivine, magnetite) and antecrysts (olivine, ilmenite, and magnetite) but are usually small (<10 μm). In order to identify the parent magma(s) of the antecryst cargo, we carefully looked for melt inclusions in antecrysts. We analyzed one larger inclusion in sample DR14-01, 70 μm in diameter and containing a gas bubble, hosted within the core of a reversely zoned olivine. The inclusion is tephri-phonolitic (56 wt% $SiO_2$ and 10 wt% $Na_2O + K_2O$) when normalized on an anhydrous basis, (Supplementary Table 5), and in equilibrium with its $Fo_{60}$ olivine host [$Kd_{Fe/Mg} = 0.296$ assuming 15% $Fe^{3+}$ in the melt, Roeder and Emslie, 1970].

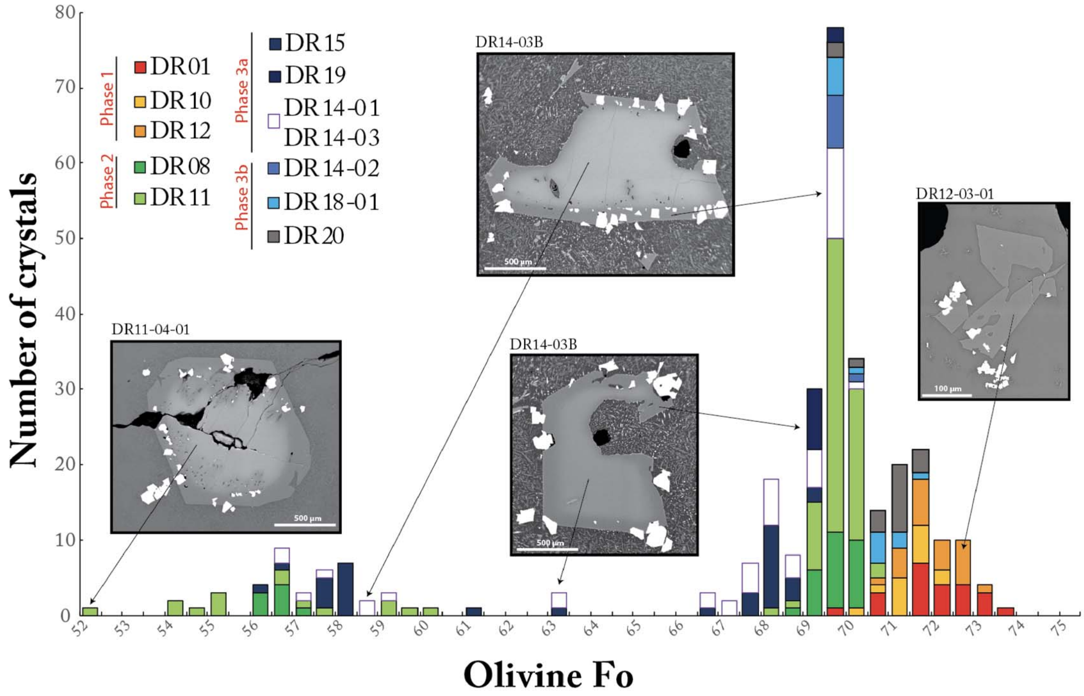


**Figure 8.** Histogram showing bimodal distribution of Fo content of analyzed olivine crystals from the eruption site. Most samples contain one single crystal population with Fo between 67 and 74%, but samples from Phase 2 and the early activity on the northwestern site contain a second population of more evolved olivine cores ($Fo_{52–63}$). Samples in the legend are presented in chronological order, from DR01, DR10, DR12 (Phase 1) to DR20 (Phase 3b, the latest erupted products, Figure 2).

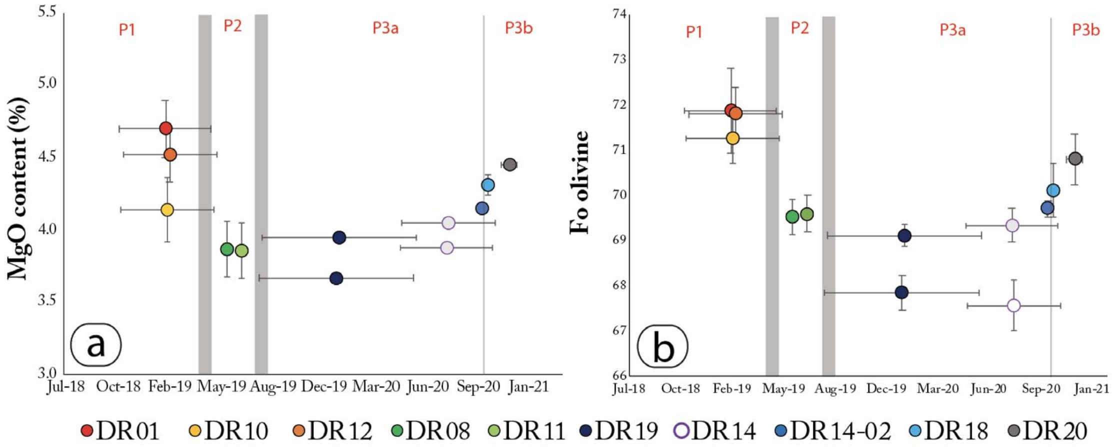


**Figure 9.** Geochemical evolution of the erupted products during the 2018–2021 eruption off the eastern coast of Mayotte. (A) Bulk-rock MgO content, (b) forsterite content in olivine crystals. Vertical error bars are two sigma standard deviations of the dataset for each sample. Uncertainties for the eruption times represent the possible time interval of the eruption, based on differential bathymetry during the various campaigns. P1–P3b: Phase 1 to Phase 3b.

## 6. Discussion

### 6.1. *Syn-eruptive evolution evidenced from high-precision sampling*

Following the methodology developed for subaerial eruptions at monitored volcanoes [Corsaro and Miraglia, 2005, 2022, Di Muro et al., 2014, Edmonds et al., 2013, Gansecki et al., 2019, Gurioli et al., 2018, Re et al., 2021], petrological and geochemical approaches provide an exceptional dataset for a submarine eruption sequence. Here, differential bathymetric datasets and high-precision dredging performed during the MAYOBS campaigns [Rinnert et al., 2019] allowed us to constrain the evolution of magma storage and transfer processes throughout this long-lived voluminous submarine eruption, both in time and space.

Phases 1 and 2 of the eruption were first sampled in May and July 2019, more than ten months after the beginning of the eruption, and when the Fani Maoré volcanic cone was already more than 800 m high. The samples, collected during the first three campaigns [MAYOBS 1, 2, and 4, Feuillet, 2019, Jorry, 2019, Fouquet and Feuillet, 2019, Rinnert et al., 2019], are therefore probably not representative of the very first lavas erupted during this eruption. Phase 1 lavas sampled by the DR01, DR10, and DR12 dredges are crystal-poor basanites (4.0–5.0 wt% MgO, Figure 7) with skeletal crystals (Figure 4a,b) and high pre-eruptive water content [up to 2.3 wt%, Berthod et al., 2021b]. During this first phase that spanned the first year of the eruption (Figure 2), the Fani Maoré eruption was fed by direct ascent of magma from a deep mantle lithospheric reservoir [≥35 km deep, Berthod et al., 2021b] to the surface. The shape and size of crystals (one single population with skeletal habits) indicate that most of the crystallization occurred late, in the shallow part of the ascending dyke. Phase 2 lavas (DR08 and DR11 samples, Figure 2) are more evolved (3.4 to 4.3 wt% MgO, Figure 7) than those from Phase 1. They contain reversely zoned olivine antecrysts ($Fo_{68–70}$ rims surrounding $Fo_{52–60}$ cores, Figures 4c–f and 8). Berthod et al. [2021b] showed that this magmatic evolution is mirrored by a decrease in vesicularity (from an average of 35 vol.% for phase 1 to 18 vol.% for phase 2), vesicle number density and dissolved water content, indicating that Phase 2 lavas were increasingly outgassed. Reverse zoning in olivine antecrysts records the interaction between the hot basanitic magma, ascending from ≥35 km, and more differentiated magma residing at shallower depths. Altogether, Phases 1 and 2 correspond to the eruption of ~5.0 $km^3$ of magma [Deplus et al., 2019, Feuillet et al., 2021].

Using samples collected during the MAYOBS 15 (DR14, DR15, and DR18, Table 1) and GEOFLAMME campaigns (DR19 and DR20, Table 1), we can now provide new petrological evidence on the eruptive sequence. As of August 2019, the eruption switched to a new site located 6 km northwest from the Fani Maoré volcanic edifice, i.e. more than 5 km from the lava flows dredged at the end of Phase 2, in July 2019, west of the main cone (DR11). There is no evidence that these two eruptive sites could have worked simultaneously, but this cannot be completely ruled out either. This change of the eruption site and the construction, at this new eruptive vent, of a large volcanic complex of more than 1.55 $km^3$ between August 2019 and January 2021 [REVOSIMA, 2020, 2022, Deplus et al., 2019], is the result of a significant shift in magma transfer during the eruption. This leads us to define a third phase for the eruptive sequence starting in August 2019. However, it is important to note that the first lava flows emplaced at this NW eruptive vent area (DR15 and DR19, Phase 3a) have similar compositions and mineral assemblages than the 2019 July distal flows (DR08 and DR11), with 3.6–3.7 wt% bulk MgO, $Fo_{67–69}$ olivine crystals, and zoned olivine antecrysts with $Fo_{56–63}$ cores (Figures 5, 7 and 8). Subsequent flows, emplaced between May and October 2020 (DR14-01 and DR14-03 samples, Figures 5, 7, and 8), also share the same characteristics. Phase 3a samples are thus similar to Phase 2 samples but emplaced at a different location.

On the contrary, later eruptive products emplaced at the end of 2020 within the northwestern eruptive area (Phase 3b, after October, Figure 2), are more primitive with whole-rock and mineral compositions and assemblages similar to the early products of Phase 1 (bulk-rock MgO up to 4.5 wt%, $Fo_{70–72}$ olivine, Figures 7 and 8, absence of reversely zoned olivine antecrysts, Figures 5 and 6). So, we consider that the samples from dredges DR18 and DR20 may characterize a new phase of the eruption or an evolution of the Phase 3.

To summarize, we observed a geochemical evolution of the eruptive products towards more evolved composition until October 2020 (Figure 9). Eruptive products then became more primitive, reaching compositions approaching that of the early erupted products. Processes such as (1) fractional crystallization followed by a recharge of a more primitive composition, or (2) mixing with a more differentiated melt until exhaustion of this melt, can account for such geochemical evolution.

### 6.2. *Syn-eruption variations related to fractional crystallization*

Using whole-rock and mineral analyses, we showed a slight geochemical evolution within Phase 1 lavas (Figures 7–9). Bulk MgO content decreases from 4.4–5.0 wt%, 4.3–4.7 wt% to 4.0–4.2 wt% in DR01, DR12, and DR10 samples, respectively (Figures 7 and 9a). Olivine compositions follow the same trend with forsterite content slightly decreasing from 70–73%, 71–73% to 70–72% in DR01, DR12, and DR10 samples, respectively (Figures 8 and 9b).

These small, but significant, compositional variations contrast with the size of the very large 820 m-high Fani Maoré edifice built between July 2018 and May 2019 (Phase 1) during a complex evolution consisting of multiple constructional structures (Figure 2). The dimension of the eruptive area, which extends more than 10 km in latitude and 5 km in longitude, and the morphologies constituting the volcanic edifice (central lava cone, ridges that are probably rift zones, an extensive and well-developed lava tunnel system and distal flows) are consistent with the existence of multiple construction phases. It is important to note that the samples characterizing Phase 1 were collected on the flanks (near the summit and along the ridges) of the Fani Maoré volcanic edifice. They probably are compositions more representative of the end of the construction of this very large and voluminous volcanic cone of several km$^3$, given that the early products were completely buried and/or have not been sampled yet. The overall poorly evolved nature of Phase 1 magmas (44.2–46.3 wt% $SiO_2$ and low 4.0–5.0 wt% MgO, Figure 7), their temperature [1151 ± 20 °C; Berthod et al., 2021b], their aphyric and highly vesicular character, indicate a very low viscosity and confirms that Phase 1 lavas can spread over several kilometers.

The early development and growth of the Phase 1 and Phase 2 edifice may result from (i) multiple vents distributed with a N–S orientation and/or (ii) multiple pulses of magma arriving at the surface with different compositions in distinct sectors. It is likely, as frequently observed during high-eruption rate of voluminous Hawaiian basaltic eruptions [Gansecki et al., 2019], that the eruption started with numerous vents on a linear surface expression of the underlying feeding dyke with high-volume eruption rate and that progressively the activity concentrated to a more localized "cylindrical vent" in order to maintain thermal energy. Our petrological and geochemical data do not allow us to determine which process predominates. Whatever the development and growth of the edifice, our data shows that the slight geochemical evolution found in Phase 1 eruptive products is related to fractional crystallization of the magma in the deep magma reservoir [Berthod et al., 2021b]. Magma evolution of Phases 1 and 2 could be compatible with crystallization of clinopyroxene (decreasing $CaO/Al_2O_3$ and Sc with decreasing MgO, Figure 7c,f) and olivine (decreasing Ni, Co, Cr, and Cu with MgO, Figure 7c,d). A significant decrease in V and FeO may be related to magnetite fractionation although it could at least in part be explained by significant clinopyroxene fractionation. In both Phase 1 and Phase 2 products, there is no evidence of feldspar fractionation: $Na_2O$, $K_2O$, and Ba are strongly incompatible, and Eu concentrations show no anomaly [Berthod et al., 2021b]. In order to quantify this fractional crystallization hypothesis, we used both trace element and Rhyolite-MELTS models [Ghiorso and Sack, 1995, Gualda et al., 2012, Ghiorso and Gualda, 2015].

Using a back-crystallization model similar to the one developed by Späth et al. [1996], Berthod et al. [2021b] concluded that the most primitive basanite erupted by Fani Maoré is derived from primary mantle melts through deep fractionation of a cumulate composed of 80% clinopyroxene and 20% olivine. A similar forward model was computed by adding small increments of equilibrium olivine and clinopyroxene compositions, starting from the most primitive composition DR01-04 (Supplementary Table 1). The proportions of olivine and clinopyroxene were adjusted to fit the general trend of lavas from the eruption site (Figure 10, Supplementary Table 6). The entire trend from the eruption site could be explained by ~7% of crystallization (20% ol + 80% cpx). The fit is usually good, except for

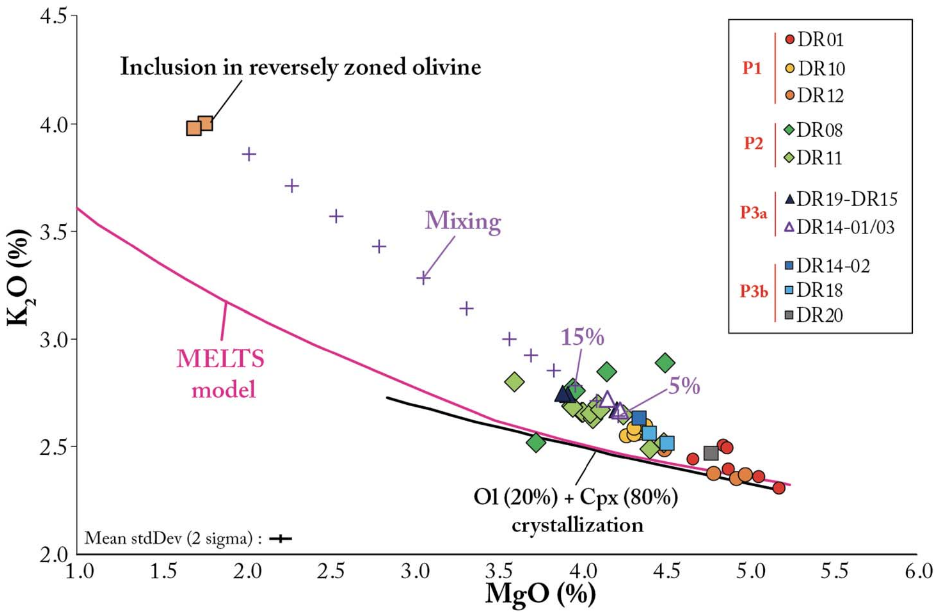


**Figure 10.** Fractional crystallization models (80% cpx and 20% ol crystallization model and Rhyolite-MELTS modeling at 1.0 GPa, FMQ-1, with 2.3 wt% $H_2O$) and mixing model performed to reproduce the syn-eruptive geochemical evolution trend. Our fractional crystallization models fit well with the trend of Phase 1 (DR01, DR10, and DR12). However, none of our fractional crystallization models can explain the rest of the eruptive sequence. We suggest that the geochemical signature of Phase 2 and Phase 3 lava flows is related to different amounts of magma tapping the differentiated subcrustal magma storage zone. Purple crosses represent the mixing line between sample DR10 (composition of the deep basanitic magma at the end of Phase 1) and the melt inclusion in reversely zoned olivine (composition of the tephri-phonolitic magma from the shallower reservoir). P1–P3b: Phase 1 to Phase 3b.

$K_2O$ (and in smaller amounts $Na_2O$) which cannot be fitted by a crystallization model beyond samples from Phase 1. The model also slightly overestimates Ti and Fe, but this could easily be explained by adding small amounts of magnetite crystallization.

A fractional crystallization model was also run using the Rhyolite-MELTS software [Ghiorso and Sack, 1995, Gualda et al., 2012, Ghiorso and Gualda, 2015]. We also use the bulk composition of the most primitive sample, DR01-04, as parental melt. Magma storage conditions were set at 1.0 GPa with 2.3 wt% $H_2O$ and an oxygen fugacity at FMQ-1. Temperature decreased from 1250 to 950 °C, with a 10 °C step. Since no orthopyroxene and garnet crystals were found in Comoros lavas, they were excluded from the crystallizing assemblage.

Except for $P_2O_5$, our modeling results match well for all major elements with the trend defined by the compositions erupted at the beginning of the sequence (Phase 1) and are consistent with an evolution dominated by fractional crystallization producing the slight variability of Phase 1 (Figure 10, Supplementary Table 7). The geochemical differences between DR01 and DR10 samples (Phase 1) can be attributed to 7–9% of fractional crystallization of a crystalline assemblage composed of clinopyroxene, spinel, Fe–Ti oxides, and apatite (Figure 10). This magma evolution by fractional crystallization during part of Phase 1 could reflect progressive cooling of the deep magma reservoir during the first year of the eruption. However, our model cannot account for the evolution of lava composition for the rest of the eruptive sequence (Phases 2 and 3). For example, the evolution of $K_2O$ contents analyzed in lava flows of Phases 2 and 3 shows a clear contrast with the modeled $K_2O$ contents (Figure 10), indicating that another process involving potassium enrichment of the magma must occur.

### 6.3. *Syn-eruptive variations related to mixing*

The presence of reversely zoned olivine and magnetite-rimmed ilmenite in distal lava flows emplaced on the western and southern flanks of the main volcanic cone (Phase 2, DR08 and DR11, Figure 2) and in early lava flows emplaced at the northwestern site (Phase 3, DR15 and DR19, Figure 2) indicates an interaction between the basanitic magma, and a shallower more evolved magma as shown by Berthod et al. [2021b]. Samples from Phase 2 and Phase 3 of the eruption are indeed aligned on a straight line between the later products of Phase 1 (DR10), and a potential composition for the shallower evolved magma, as represented by the composition of the glassy melt inclusions in equilibrium with the $Fo_{59}$ and $Fo_{57}$ cores of reversely zoned olivine (Figure 10).

To quantify the interaction between the two magmas, we use a simple mass balance model between sample DR10 (composition of the deep magma at the end of Phase 1) and the melt inclusions (composition of the evolved magma from the shallower reservoir). The core compositions of reversely zoned olivine antecrysts, although spanning a significant range (Fo contents from 52 to 63%, Figure 8) do not vary systematically during the eruption. The significant range could be explained by the sampling of a mush, and the absence of systematic variation suggests that the composition of the evolved magma varies little during the eruption. Also, reversely zoned olivine or magnetite-rimmed ilmenite represent less than 1% of the crystal cargo and have been only observed as isolated crystals (Figures 4 and 5) indicating that the magma ascending from the depths ≥35 km mainly sampled a melt with few crystals or efficiently dissolved them. We have therefore neglected the crystals in our model. Our results show that the percentage of magma sampled from the evolved shallower magma storage increased up to 14% of the volume released during the second year of the eruption, and then decreased from the beginning of 2020 (Figure 11).

From October 2020, magma composition became more primitive, and only a small percentage of evolved magma can be estimated for DR14-02, DR18-01, and DR20 samples (below standard deviations of the bulk-rock compositions). Evolution towards a more mafic magma during an eruption is usually interpreted as a recharge of the magma system by a more primitive and hotter magma [e.g., Moore et al., 2014]. However, we do not observe any evidence of mixing in crystal textures at the end of the eruption (Figure 6). Instead, we observed the disappearance of reversely zoned olivine or magnetite-rimmed ilmenite in those samples (DR18-01, DR20, and DR14-02, Figure 6) and the increase in the amount of $An_{47–63}Ab_{35–49}Or_{2–4}$ plagioclase in the matrix. This evolution during Phase 3b would rather be explained by a decrease in the amount of evolved magma assimilated by a higher volume of mafic intruded magma or by exhaustion of the mobilizable evolved magma stored in the shallower reservoir, or through a change in the magma ascent path.

Calculations, coupled with our petrological observations, suggest that the tephri-phonolitic shallower magma batch was sampled between May 2019 and mid-2020, and no longer during the last months of the eruption documented here. Using the DR14 samples (Figure 2), we can give a more precise date at which the sampling of this shallower magma batch stopped. Indeed, dredge DR14 sampled two distinct lava flows emplaced between May 2020 and October 2020 (DR14-01 and DR14-03 samples) and between October 6th and October 13th, 2020 (DR14-02 sample). DR14-01 and DR14-03 contain reversely zoned olivine and magnetite-rimmed ilmenite, whereas DR14-02 does not, which thus suggests that the tephri-phonolitic shallower magma storage was no longer sampled as of the beginning of October 2020.

### 6.4. *Magma ascent during the eruption*

We already have evidence of several changes in the dyke pathway during the eruption (Figure 12). Berthod et al. [2021b] suggested that the eruption of a more evolved magma in Phase 2 could have resulted from a change in a dyke pathway around May 2019. As of August, the eruption changed site and continued 6 km NW of the main central edifice leading us to propose the onset of a third phase. We note, however, that the compositions of the lava flows (Phase 3a, DR15 and DR19, Figure 7) are similar to Phase 2 with evolved lavas carrying reversely zoned olivine or magnetite-armored ilmenite (Figures 5 and 6). Therefore, the magma intrusion pathway change, or its northward extension, occurred in the crust above the shallower reservoir. The lack of change in the depth and location of the deep seismic swarm during

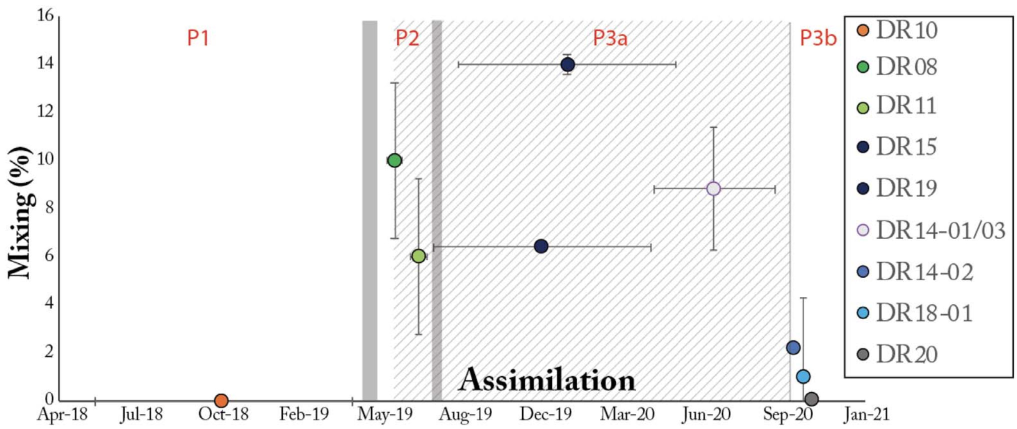


**Figure 11.** Average percentage of magma from the differentiated shallower magma storage in the erupted products calculated for each dredge. These estimates were obtained from a simple mass balance using the DR10 analyses for the deep magma composition. Estimated magma composition from the shallower reservoir was obtained from a glassy magmatic inclusion in the core of a reversely zoned olivine.

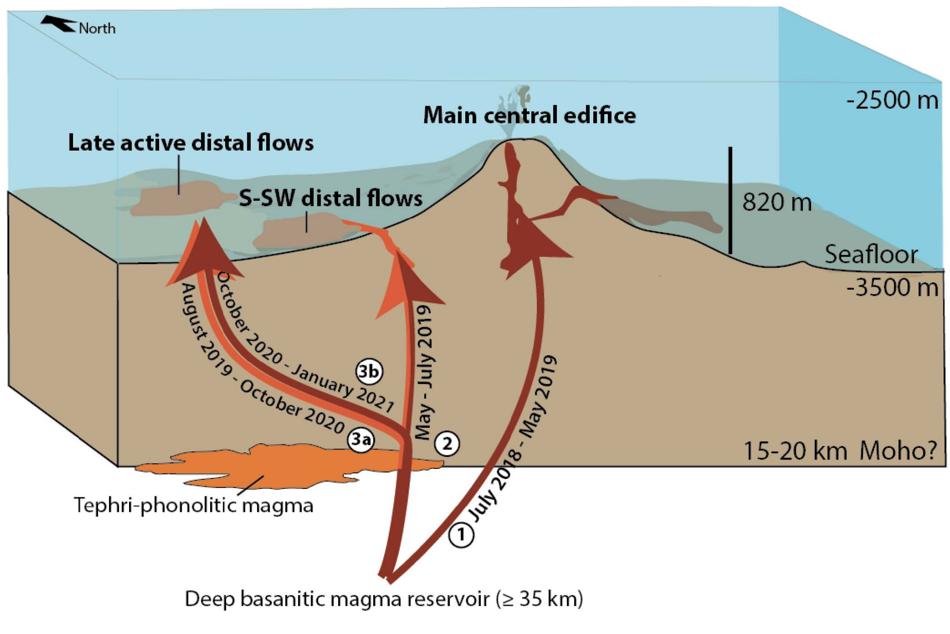


**Figure 12.** Diagram (not to scale) illustrating the dynamics of the magmatic plumbing system feeding the eruption. We propose to divide the eruption sequence into three distinct phases induced by two magma pathway changes. (Phase 1) During the first year of the eruption, the Fani Maoré eruption was fed by direct ascent of a basanitic magma from a deep mantle lithospheric reservoir [≥35 km deep, Berthod et al., 2021b] to the surface. (Phase 2) In May 2019, basanitic magma ascent slowed and switched to a pathway that sampled a shallower and tephri-phonolitic magma batch at the base of the crust [Berthod et al., 2021b]. (Phase 3a) In August 2019, the magma pathway shifted again in the crust resulting in a new eruption site located 6 km northwest of the main edifice. (Phase 3b) Finally, latest petrological and geochemical variations are associated with the exhaustion of the magma stored in the shallower reservoir.

the eruption is consistent with the hypothesis that the petrological variations of lavas, as well as the location of a new eruptive vent 6 km to the northwest of the main edifice, are caused by modifications of the physical properties associated with the more superficial magma reservoir and the crustal zone above it [Lavayssiere et al., 2022]. This change in a dyke pathway could also be related to the significant weight of the 820 m-high Fani Maoré volcanic edifice, which might have made it difficult for magma to rise vertically once the flow rate and overpressure decreased over time. Finally, a Phase 3b can be proposed from October 2020 until January 18, 2021 (the last evidence of new lava eruption at the time of writing in June 2022) with the end of the sampling of the shallower storage. The tephri-phonolitic magma storage has been sampled for almost a year and a half after (Figure 11). Petrological observations, coupled with mass-balance modeling, concluded that this shallow reservoir was no longer sampled as of October 2020. Reversely zoned olivine originating from the shallower reservoir display a Fo content varying from 52 to 63%, which does not change over time (Figure 7), suggesting that this reservoir was homogeneous in composition. A syn-eruptive magma path change is probably not the most likely scenario. In fact, we note that the regular and constant compositional evolution of the latest lavas can be explained by a decrease in the amount of evolved magma assimilated and finally by exhaustion of that evolved magma stored in the shallower reservoir. Therefore, we suggest that this change results from the complete emptying of the magma reservoir.

The petrological signature of the erupted magmas suggests that there are several magma storage zones containing eruptible melt beneath the Eastern Volcanic Chain of Mayotte (Figure 1b), but also that the high-flux eruption of large volumes of magma from a deep-seated reservoir below the Moho can influence and trigger the subsequent tapping of eruptible melt in the crust located at shallower depth just below the Moho [Berthod et al., 2021a]. This has implications with respect to the capacity of such large eruptions to reactivate shallow-seated zones of a large long-lasting magmatic system, which can feed continuing eruptive activity with magmas of different petrological characteristics and different volatile contents [Bachmann and Bergantz, 2004, Wark et al., 2007, Singer et al., 2016]. This conceptual model needs further validation and could be of paramount importance to assess the eruptive potential of the main polybaric magmatic system or mush system below the Horseshoe area of the Mayotte oriental submarine volcanic chain, located within 10 km of Petite Terre and 50 km of the Fani Maoré edifice (Figure 1b), which is probably one of the most active areas of the entire volcanic chain and is currently associated with most of the volcano-tectonic, long-period (LP), and very long-period (VLP) seismicity [Saurel et al., 2022, Retailleau et al., 2020, Lavayssiere et al., 2022] as well as fluid emissions rich in $CO_2$, methane, and $H_2$ [REVOSIMA bulletins; Mastin et al., 2022]. Furthermore, more detailed geomorphological and textural analysis need to be considered to constraint physical properties of the erupted material that controls the ascent dynamics and submarine emplacement.

## 7. Conclusion

With twenty-six oceanographic campaigns, the 2018–2021 Fani Maoré eruption off the coasts of Mayotte is the most intensively monitored submarine eruption. Time-lapsed bathymetric surveys coupled with high-precision submarine dredging allowed us to follow, for the first time, the syn-eruptive evolution of the magma at the submarine eruptive site. Our petrological and geochemical analyses carried out on the dredged lava flows provide an exceptional description of the evolution of the entire submarine eruption sequence that could be tracked and monitored at a regularly spaced interval from May 2019 to January 2021. Our observations enable us to divide the eruption sequence into three main different phases induced by two distinct magma pathway changes: (1) The first year of the eruption (Phase 1) is fed by direct ascent of a basanitic magma (4.0–5.0 wt% MgO) from the deep reservoir to the surface. (2) In May 2019, magma ascent slowed and switched to a pathway that sampled a tephri-phonolitic magma batch at the base of the crust (Phase 2); Lava flows display evidence of assimilation (reversely zoned olivine) and a more evolved composition (3.4–4.3 wt% MgO). (3) Three months later, the activity shifted to a new eruptive area 6 km northwest of the main edifice, Fani Maoré, starting a third phase. Since the Phase 3a lava flows are similar to Phase 2, we suggest that the magma pathway switched again in the crust after the sampling of the tephri-phonolitic magma batch.

Finally, a third evolution is defined in October 2020, associated with the exhaustion of the magma stored in the shallower reservoir (Phase 3b) and a return to compositions similar to Phase 1. From petrological models (crystallization and mass-balance models), we proposed that the initial geochemical evolution (Phase 1) can be explained by 7–9% of fractional crystallization at 1.0 GPa with 2.3 wt% $H_2O$ and an oxygen fugacity at FMQ-1 from the most primitive samples. However, fractional crystallization cannot explain the rest of the eruptive sequence (Phases 2 and 3) and we suggest that the geochemical signature of Phases 2 and 3 is related to mixing with an older differentiated subcrustal magma storage.

These new data help determine the dynamics of the magmatic systems feeding the remarkable Fani Maoré eruption and provide critical constraints on the shallow magma ascent pathway (<20 km) which cannot be imaged geophysically since no seismic signals are recorded at these depths.

## Conflicts of interest

Authors have no conflict of interest to declare.

## Acknowledgements

MAYOBS 1 campaign was funded by the CNRS-INSU TELLUS MAYOTTE program (SISMAYOTTE project). MAYOBS 1, 2, 4, and 15 campaigns were conducted by several French research institutions and laboratories (IPGP/CNRS/BRGM/IFREMER/IPGS). All marine operations are performed as part of the MAYOBS set of campaigns (https://doi.org/10.18142/291) and we thank the captains and crews of the R/V Marion Dufresne (TAAF/IFREMER/LDA), R/V Pourquoi Pas? (GENAVIR/IFREMER, SHOM), R/V Beautemps-Beaupré (SHOM), and R/V Gauss (FUGRO). The GEOFLAMME oceanographic campaign (CNFH; PI C. Cathalot, E. Rinnert, N. Feuillet) also funded marine operations that benefited to this study and provided dredge samples. Analyses were funded by the Service National d'Observation en Volcanologie (SNOV, INSU) and the Réseau de Surveillance Volcanologique et Sismologique de Mayotte (REVOSIMA), a partnership between the Institut de Physique du Globe de Paris (IPGP), the Bureau de Recherches Géologiques et Minières (BRGM), the Observatoire Volcanologique du Piton de la Fournaise (OVPF-IPGP), the Centre National de la Recherche Scientifique (CNRS), and the Institut Français de Recherche pour l'Exploitation de la Mer (IFREMER). Since June 2019, all activities on Mayotte are funded by the Ministère de l'Enseignement Supérieur, de la Recherche et de l'Innovation (MESRI), the Ministère de la Transition Ecologique (MTE), the Ministère des Outremers (MOM), the Ministère de l'Intérieur (MI), and the Ministère des Armées, with the support of the Direction Interministérielle aux Risques Majeurs en Outremer (DIRMOM) and the Mission d'Appui aux Politiques Publiques pour la Prévention des Risques Majeurs en Outremer (MAPPPROM). The authors would like to thank E. Humler for his support and national funding coordination (CNRS, REVOSIMA). Finally, we are also grateful for the helpful reviews provided by the Guest Editors Vincent Famin and Jerome van der Woerd, by Helène Balcone Boissard and an anonymous reviewer. This study contributes to IdEx Université de Paris ANR-18-IDEX-0001. Trace element analyses were supported by IPGP multidisciplinary program PARI and by Paris–IdF region SESAME Grant no. 12015908. This project has received funding from the European Union's Horizon 2020 research and innovation programme under grant agreement no. 731070. This is Labex ClerVolc contribution number 567.

## Supplementary data

Supporting information for this article is available on the journal's website under https://doi.org/10.5802/crgeos.155 or from the author.

## Appendix A. Protocol for sorting and describing samples

Prior to the arrival of the dredge on deck, special care was taken to clean the deck and to ensure that no sample remained from previous dredges to avoid contamination. When the dredge was above deck, it was turned over and emptied. Whenever the dredge contained popping rocks, it was shaken then put "at rest" on deck for a few hours for safety reasons.

An initial description of the contents of the dredge was performed, and pictures of the bulk products were taken, both within the dredge and with the rocks on the deck. These pictures can help to approximately position the first collected samples (at the base of the dredge) and the last ones (at the top).

As soon as we could approach the newly-dredged material, samples were sorted into different lithological and textural categories or types. For instance, for volcanic rocks, categories can be fresh/juvenile, altered and non-juvenile materials. If the juvenile material was effusive, lava fragments were divided according to their typology: whole or fragment (glassy rim, interior) of pillow (see Section 4.2), lava sheet (crust, interior), lava tunnel roof, and column. Descriptions included the vesicle size, density, and morphology (rounded, elongated, pipes), crystal content, crystal nature and size, as well as the presence of enclaves (mingling, xenoliths, cumulates), iron-rich surficial deposits (crust), traces of gas sublimates and/or /hydrothermal mineralization, and datable organic material. Pyroclastic fragments (bombs, lapilli, ashes) were distinguished from their texture (glassy, dense, vesiculated), and their size or coloration. Everything that arguably predates the eruption, that had an altered appearance or had a different color, such as brecciated pyroclastic deposits, hemipelagic sedimentary deposits, organic material, and crystal-rich fragments were considered as non-juvenile to even non volcanic fragments.

After this classification was completed, each sample was then described with a magnifying glass and a binocular microscope, to refine and complete the separation in different lithological types and their description.

The second description step consisted in taking pictures of the selected samples with a scale, a label and a sample number. A consistent numbering scheme has been defined for each campaign off the coasts of Mayotte Mayotte. For instance, for the monitoring survey MAYOBS 15 campaign, the following numbering has been set: MAY15 (campaign number)—DR14 (dredge number) 01 (family number) 01 (subclass number if necessary). To follow standard regulation an International Geo Sample Number (IGSN) had to be given before storage in sample depositaries at Ifremer and IPGP/Chambon.

In general, two boxes (about 30 kg each) were kept as archives in the sample depositaries of IFREMER and IPGP to be available for analytical work and sample requests from the scientific community. An additional 2–3 boxes, based on weight or selected samples for dedicated investigations, were also kept for each participating institution involved in the systematic petrological monitoring. A selection of smaller most important samples including fresh glass were brought back in the airplane by the participating scientists in order to perform rapid geochemical analyses and in some cases geochronological measurements. The bulk of the archived material returns via marine shipping along with the equipment. Unfortunately, not all samples can be brought back, and after careful study on board, samples from the MAYOBS campaigns that are not selected (usually we keep about 200–300 kg of rocks) are stored onboard in a crate that will be emptied at the end of the campaign during transit at the same specific site that is well outside the studied area and well identified in the logbook for future reference (Start: 16°50.40 S, 52°37.67 E; End: 16°51.70 S, 52°38.54 E).

## References


Bachèlery, P., Gurioli, L., Berthod, C., Komorowski, J.-C., Peltier, A., Saurel, J.-M., Lemarchand, A., and REVOSIMA Consortium (2021). European catalogue of volcanoes. UCA-OPGC and IPGP. Retrieved from https://volcanos.eurovolc.eu/?volcano=MAY#.

Bachèlery, P. and Hémond, C. (2016). Geochemical and petrological aspects of Karthala volcano. In Bachèlery, P., Lénat, J.-F., Di Muro, A., and Michon, L., editors, *Active Volcanoes of the Southwest Indian Ocean: Piton de la Fournaise and Karthala. Active Volcanoes of the World*, pages 367–384. Springer-Verlag, Berlin and Heidelberg. Chap. 23.

Bachèlery, P., Morin, J., Villeneuve, N., Soulé, H., Nassor, H., and Ali, A. R. (2016). Structure and eruptive history of Karthala volcano. In Bachèlery, P., Lénat, J.-F., Di Muro, A., and Michon, L., editors, *Active Volcanoes of the Southwest Indian Ocean: Piton de la Fournaise and Karthala. Active Volcanoes of the World*, pages 345–366. Springer-Verlag, Berlin and Heidelberg. Chap. 22.

Bachmann, O. and Bergantz, G. W. (2004). On the origin of crystal-poor rhyolites: Extracted from batholithic crystal mushes. *J. Petrol.*, 45(8), 1565–1582.

Bamber, E. C., Arzilli, F., Polacci, M., Hartley, M. E., Fellowes, J., Di Genova, D., Chavarria, D., Armando Ceballos, J., and Burton, M. R. (2020).

Pre-and syn-eruptive conditions of a basaltic Plinian eruption at Masaya Volcano, Nicaragua: the Masaya Triple Layer (2.1 ka). *J. Volcanol. Geotherm. Res.*, 392, article no. 106761.

Berthod, C., Médard, E., Bachèlery, P., Gurioli, L., Di Muro, A., Peltier, A., Komorowski, J.-C., Benbakkar, M., Devidal, J.-L., Langlade, J., Besson, P., Boudon, G., Rose-Koga, E., Deplus, C., Le Friant, A., Bickert, M., Nowak, S., Thinon, I., Burckel, P., Hidalgo, S., Kaliwoda, M., Jorry, S., Fouquet, Y., and Feuillet, N. (2021a). The 2018-ongoing Mayotte submarine eruption: Magma migration imaged by petrological monitoring. *Earth Planet. Sci. Lett.*, 571, article no. 117085.

Berthod, C., Médard, E., Di Muro, A., Hassen Ali, T., Gurioli, L., Chauvel, C., Komorowski, J.-C., Benbakkar, M., Devidal, J.-L., Besson, P., Le Friant, A., Deplus, C., Nowak, S., Thinon, I., Burckel, P., Hidalgo, S., Feuillet, N., Jorry, S., and Fouquet, Y. (2021b). Mantle xenolith-bearing phonolites and basanites feed the active volcanic ridge of Mayotte (Comoros archipelago, SW Indian Ocean). *Contrib. Mineral. Petrol.*, 176(10), 1–24.

Berthod, C., Zaragosi, S., and Famin, V. (2021c). SCRATCH cruise. RV Marion Dufresne.

Bertil, D., Mercury, N., Doubre, C., Lemoine, A., and Van der Woerd, J. (2021). The unexpected Mayotte 2018–2020 seismic sequence: a reappraisal of the regional seismicity of the Comoros. *C. R. Géosci.*, 353(S1), 211–235.

Bertil, D. and Regnoult, J. M. (1998). Seismotectonics of Madagascar. *Tectonophysics*, 294, 57–74.

Carey, R., Soule, S. A., Manga, M., White, J. D. L., McPhie, J., Wysoczanski, R., Jutzeler, M., Tani, K., Yoerger, D., Fornari, D., Caratori-Tontini, F., Houghton, B., Mitchell, S., Ikegami, F., Conway, C., Murch, A., Fauria, K., Jones, M., Cahalan, R., and McKenzie, W. (2018). The largest deep-oceansilicic volcanic eruption of the past century. *Sci. Adv.*, 4, article no. e1701121.

Casas, D., Pimentel, A., Pacheco, J., Martorelli, E., Sposato, A., Ercilla, G., et al. (2018). Serreta 1998–2001 submarine volcanic eruption, offshore terceira (azores): Characterization of the vent and inferences about the eruptive dynamics. *J. Volcanol. Geotherm. Res.*, 356, 127–140.

Cesca, S., Letort, J., Razafindrakoto, H. N. T., Heimann, S., Rivalta, E., Isken, M. P., Nikkhoo, M., Passarelli, L., Petersen, G. M., Cotton, F., and Dahm, T. (2020). Drainage of a deep magma reservoir near Mayotte inferred from seismicity and deformation. *Nat. Geosci.*, 13, 87–93.

Clague, D. A., Paduan, J. B., Dreyer, B. M., Chadwick Jr, W. W., Rubin, K. R., Perfit, M. R., and Fundis, A. T. (2018). Chemical variations in the 1998, 2011, and 2015 lava flows from Axial Seamount, Juan de Fuca Ridge: Cooling during ascent, lateral transport, and flow. *Geochem. Geophys. Geosyst.*, 19, 2915–2933.

Class, C., Goldstein, S. L., Altherr, R., and Bachèlery, P. (1998). The process of plume–lithosphere interactions in the ocean basins—the case of Grande Comore. *J. Petrol.*, 39, 881–903.

Claude-Ivanaj, C., Bourdon, B., and Allègre, C. J. (1998). Ra–Th–Sr isotope systematics in Grande Comore Island: a case study of plume–lithosphere interaction. *Earth Planet. Sci. Lett.*, 164, 99–117.

Corsaro, R. A. and Miraglia, L. (2005). Dynamics of 2004–2005 Mt. Etna effusive eruption as inferred from petrologic monitoring. *Geophys. Res. Lett.*, 32, article no. L13302.

Corsaro, R. A. and Miraglia, L. (2022). Near real-time petrologic monitoring on volcanic glass to infer magmatic processes during the February–April 2021 Paroxysms of the South-East Crater, Etna. *Front. Earth Sci.*, 10, article no. 828026.

Deniel, C. (1998). Geochemical and isotopic (Sr, Nd, Pb) evidence for plume–lithosphere interactions in the genesis of Grande Comore magmas (Indian Ocean). *Chem. Geol.*, 144, 281–303.

Deplus, C., Feuillet, N., Bachelery, P., Fouquet, Y., Jorry, S., Thinon, I., Bermell, S., Besson, F., Gaillot, A., Guérin, C., Le Friant, A., Paquet, F., Pierre, D., and Pitel-Roudaut, M. (2019). Early development tand growth of a deep seafloor volcano: Preliminary results from the MAYOBS cruises. In *Abstract V43I-0227, 2019 Fall Meeting*. AGU, San Francisco.

Di Muro, A., Métrich, N., Vergani, D., Rosi, M., Armienti, P., Fougeroux, T., Deloule, E., Arienzo, I., and Civetta, L. (2014). The shallow plumbing system of Piton de la Fournaise Volcano (La Réunion Island, Indian Ocean) revealed by the major 2007 caldera forming eruption. *J. Petrol.*, 55, 1287–1315.

Edmonds, M., Sides, I. R., Swanson, D. A., Werner, C., Martin, R. S., Mather, T. A., Herd, R. A., Jones, R. L., Mead, M. I., and Sawyer, G. (2013). Magma storage, transport and degassing during the 2008–10 summit eruption at Kilauea Volcano, Hawai'i. *Geochim. Cosmochim. Acta*, 123, 284–301.

Famin, V., Michon, L., and Bourhane, A. (2020). The Comoros archipelago: a right-lateral transform boundary between the Somalia and Lwandle plates. *Tectonophysics*, 789, article no. 228539.

Feuillet, N. (2019). MAYOBS1 cruise. RV Marion Dufresne.

Feuillet, N., Jorry, S., Crawford, W., Deplus, C., Thinon, I., Jacques, E., Saurel, J.-M., Lemoine, A., Paquet, F., Satriano, C., Aiken, C., Foix, O., Kowalski, P., Laurent, A., Rinnert, E., Cathalot, C., Donval, J. P., Guyader, V., Gaillot, A., Scalabrin, C., Moreira, M., Peltier, A., Beauducel, F., Grandin, R., Ballu, V., Daniel, R., Pelleau, P., Gomez, J., Besançon, S., Géli, L., Bernard, P., Bachèlery, P., Fouquet, Y., Bertil, D., Lemarchand, A., and Van Der Woerd, J. (2021). Birth of a large volcanic edifice offshore Mayotte via lithosphere-scale dyke intrusion. *Nat. Geosci.*, 14(10), 787–795.

Foix, O., Aiken, C., Saurel, J. M., Feuillet, N., Jorry, S. J., Rinnert, E., and Thinon, I. (2021). Offshore Mayotte volcanic plumbing revealed by local passive tomography. *J. Volcanol. Geotherm. Res.*, 420, article no. 107395.

Fouquet, Y. and Feuillet, N. (2019). MAYOBS4 cruise. RV Marion Dufresne.

Gansecki, C., Lee, R. L., Shea, T., Lundblad, S. P., Hon, K., and Parcheta, C. (2019). The tangled tale of Kīlauea's 2018 eruption as told by geochemical monitoring. *Science*, 366, article no. eaaz0147.

Ghiorso, M. S. and Gualda, G. A. (2015). An H2O-CO2 mixed fluid saturation model compatible with rhyolite-MELTS. *Contrib. Mineral. Petrol.*, 169, 1–30.

Ghiorso, M. S. and Sack, R. O. (1995). Chemical mass transfer in magmatic processes IV. A revised and internally consistent thermodynamic model for the interpolation and extrapolation of liquid–solid equilibria in magmatic systems at elevated temperatures and pressures. *Contrib. Mineral. Petrol.*, 119, 197–212.

Gualda, G. A., Ghiorso, M. S., Lemons, R. V., and Carley, T. L. (2012). Rhyolite-MELTS: a modified calibration of MELTS optimized for silica-rich, fluid-bearing magmatic systems. *J. Petrol.*, 53, 875–890.

Gurioli, L., Di Muro, A., Vlastélic, I., Moune, S., Thivet, S., Valer, M., Villeneuve, N., Boudoire, G., Peltier, A., and Bachèlery, P. (2018). Integrating field, textural, and geo-chemical monitoring to track eruption triggers and dynamics: a case study from Piton de la Fournaise. *Solid Earth*, 9, 431–455.

Gurioli, L., Houghton, B. F., Cashman, K. V., and Cioni, R. (2005). Complex changes in eruption dynamics and the transition between Plinian and phreatomagmatic activity during the 79 AD eruption of Vesuvius. *Bull. Volcanol.*, 67, 144–159.

Jochum, K. P., Weis, U., Schwager, B., Stoll, B., Wilson, S. A., Haug, G. H., Andreae, M. O., and Enzweiler, J. (2016). Reference values following ISO guidelines for frequently requested rock reference materials. *Geostand. Geoanal. Res.*, 40, 333–350.

Jorry, S. J. (2019). MAYOBS2 cruise. RV Marion Dufresne.

Kidd, R. B., Huggett, Q. J., and Ramsay, A. T. S. (1990). The status of geological dredging techniques. *Mar. Geol. Surv. Sampl.*, 12, 131–143.

Lavayssiere, A., Crawford, W. C., Saurel, J.-M., Satriano, C., Feuillet, N., Jacques, E., and Komorowski, J.-C. (2022). A new 1d velocity model and absolute locations image the Mayotte seismo-volcanic region. *J. Volcanol. Geotherm. Res.*, 421, article no. 107440.

Lemoine, A., Briole, P., Bertil, D., Roullé, A., Foumel, M., Thinon, I., Raucoules, D., de Michele, M., and Valty, P. (2020). The 2018–2019 seismo-volcanic crisis east of Mayotte, Comoros islands: seismicity and ground deformation markers of an exceptional submarine eruption. *Geophys. J. Int.*, 223(1), 22–44.

Liu, E. J., Cashman, K. V., Miller, E., Moore, H., Edmonds, M., Kunz, B. E., Jenner, F., and Chigna, G. (2020). Petrologic monitoring at Volcán de Fuego, Guatemala. *J. Volcanol. Geotherm. Res.*, 405, article no. 107044.

Magee, R., Ubide, T., and Caulfield, J. (2021). Days to weeks of syn-eruptive magma interaction: High-resolution geochemistry of the 2002–03 branched eruption at Mount Etna. *Earth Planet. Sci. Lett.*, 565, article no. 116904.

Masquelet, C., Leroy, S., Delescluse, M., Chamot-Rooke, N., Thinon, I., Lemoine, A., Franke, D., Watremez, L., Werner, P., Paquet, F., Berthod, C., Cabiativa, V., and Sauter, D. (2022). The East-Mayotte new volcano in the Comoros archipelago: structure and timing of magmatic phases inferred from seismic reflection data. *C. R. Géosci.*, 354(S2), 65–79.

Mastin, M., Cathalot, C., Rouxel, O., Gaucher, E. C., Donval, J. P., Guyader, V., Germain, Y., Scalabrin, C., Jouenne, S., Dehez, S., and Rinnert, E. (2022). Strong geochemical anomalies following active submarine eruption offshore Mayotte. In *Ocean Sciences Meeting 2022, DS08 The Impact of Submarine Hydrothermal and Volcanic Activity on Ocean Chemistry and Biology 03. 24 February–4 March 2022*. ASLO, Waco, TX.

Moore, A., Coogan, L. A., Costa, F., and Perfit, M. R. (2014). Primitive melt replenishment and crystal-mush disaggregation in the weeks preceding the 2005–2006 eruption 9 50′ N, EPR. *Earth Planet. Sci. Lett.*, 403, 15–26.

Morin, J., Bachèlery, P., Soule, H., and Nassor, H. (2016). Volcanic risk and crisis management on Grande Comore island. In Bachèlery, P., Lénat, J.-F., Di Muro, A., and Michon, L., editors, *Active Volcanoes of the Southwest Indian Ocean: Piton de la Fournaise and Karthala. Active Volcanoes of the World*, pages 403–422. Springer-Verlag, Berlin and Heidelberg. Chap. 25.

Nougier, J., Cantagrel, J. M., and Karche, J. P. (1986). The Comores archipelago in the Western Indian Ocean: Volcanology, geochronology and geodynamic setting. *J. Afr. Earth Sci. (1983)*, 5(2), 135–144.

Pelleter, A. A., Caroff, M., Cordier, C., Bachèlery, P., Nehlig, P., Debeuf, D., and Arnaud, N. (2014). Melilite-bearing lavas in Mayotte (France): An insight into the mantle source below the Comores. *Lithos*, 208, 281–297.

Piochi, M., Mastrolorenzo, G., and Pappalardo, L. (2005). Magma ascent and eruptive processes from textural and compositional features of Monte Nuovo pyroclastic products, Campi Flegrei, Italy. *Bull. Volcanol.*, 67, 663–678.

Quidelleur, X., Michon, L., Famin, V., Geffray, M. C., Danišík, M., Gardiner, N., Rusquet, A., and Zakaria, M. G. (2022). Holocene volcanic activity in Anjouan Island (Comoros archipelago) revealed by new Cassignol-Gillot groundmass K–Ar and $^{14}$C ages. *Quat. Geochronol.*, 67, article no. 101236.

Re, G., Corsaro, R. A., D'Oriano, C., and Pompilio, M. (2021). Petrological monitoring of active volcanoes: A review of existing procedures to achieve best practices and operative protocols during eruptions. *J. Volcanol. Geotherm. Res.*, 419, article no. 107365.

Resing, J. A., Rubin, K. H., Embley, R. W., Lupton, J. E., Baker, E. T., Dziak, R. P., et al. (2011). Active submarine eruption of boninite in the northeastern Lau Basin. *Nat. Geosci.*, 4, 799–806.

Retailleau, L., Saurel, J.-M., Issartel, S., Zhu, W., Beroza, G. C., Satriano, C., Ferrazzini, V., and Komorowski, J.-C. (2020). Automatic detection of the seismicity associated to the Maytte volcanic crisis. In *Fall Meeting 2020*. American Geophysical Union, Washington, DC. Abstract #V040-0002.

Reubi, O., Blundy, J., and Pickles, J. (2019). Petrological monitoring of Volcán de Colima magmatic system: the 1998 to 2011 activity. In *Volcán de Colima*, pages 219–240. Springer, Berlin, Heidelberg.

REVOSIMA (2019). Bulletin n°2 du 1 au 15 août 2019, Bulletin bi-mensuel de l'activité sismo-volcanique à Mayotte. IPGP, Université de Paris, OVPF, BRGM, Ifremer, CNRS, January, 6th, 2021, http://www.ipgp.fr/revosima, http://www.ipgp.fr/sites/default/files/ipgp_1er_bulletin_info_sismo_volcanique_mayotte-cor.pdf.

REVOSIMA (2020). Bulletin n°24 de l'activité sismo-volcanique à Mayotte. IPGP, Université de Paris, OVPF, BRGM, Ifremer, CNRS, January, 6th, 2021, http://www.ipgp.fr/revosima, http://www.ipgp.fr/sites/default/files/ipgp_revosima_n24_08122020.pdf.

REVOSIMA (2022). Bulletin n°38 de l'activité sismo-volcanique à Mayotte. 1 au 31 janvier 2022, IPGP, Université de Paris, OVPF, BRGM, Ifremer, CNRS, 4 février 2022, http://www.ipgp.fr/revosima, http://www.ipgp.fr/sites/default/files/ipgp_revosima_n38_20220204.pdf.

Rinnert, E., Cathalot, C., and Feuillet, N. (2021). GEOFLAMME cruise. RV Pourquoi Pas?

Rinnert, E., Feuillet, N., Fouquet, Y., Jorry, S., Thinon, I., and Lebas, E. (2019). MD 228/MAYOBS.

Rinnert, E., Thinon, I., and Feuillet, N. (2020). MD 228/MAYOBS15 cruise. RV Marion Dufresne, https://doi.org/10.17600/18001745.

Roeder, P. L. and Emslie, R. F. (1970). Olivine-liquid equilibrium. *Contrib. Mineral. Petrol.*, 29, 275–289.

Saurel, J. M., Jacques, E., Aiken, C., Lemoine, A., Retailleau, L., Lavayssiere, A., Foix, A., Dofal, A., Laurent, A., Mercury, N., Crawford, W., Lemarchand, A., Daniel, R., Pelleau, P., Bes de Berc, M., Dectot, G., Bertil, D., Roullé, A., Broucker, C., Colombain, A., Besancon, S., Guyavarch, P., Kowalski, P., Roudaut, M., Battaglia, J., Bodihar, S., Bouin, M. P., Canjamale, K., Desfete, N., Doubre, C., Dretzen, R., Ferrazzini, V., Fontaine, F., Geli, L., Griot, C., Grunberg, M., Can Guzel, E., Hoste-Colomer, R., Lambotte, S., Leger, F., Vergnes, J., Satriano, C., Tronel, F., Van der Woerd, J., Feuillet, N., Fouquet, Y., Jorry, S. J., Rinnert, E., and Thinon, I. (2022). Mayotte seismic crisis: building knowledge in near real-time by combining land and ocean-bottom seismometers, first results. *Geophys. J. Int.*, 228(2), 1281–1293. Publisher's official version: https://doi.org/10.1093/gji/ggab392. Open Access version: https://archimer.ifremer.fr/doc/00724/83604/.

Singer, B. S., Costa, F., Herrin, J. S., Hildreth, W., and Fierstein, J. (2016). The timing of compositionally-zoned magma reservoirs and mafic "priming" weeks before the 1912 Novarupta-Katmai rhyolite eruption. *Earth Planet. Sci. Lett.*, 451, 125–137.

Späth, A., Roex, A. P. L., and Duncan, R. A. (1996). The geochemistry of lavas from the Comores Archipelago, Western Indian Ocean: petrogenesis and mantle source region characteristics. *J. Petrol.*, 37, 961–991.

Stamps, D. S., Kreemer, C., Fernandes, R., Rajaonarison, T. A., and Rambolamanana, G. (2021). Redefining East African rift system kinematics. *Geology*, 49(2), 150–155.

Sundermeyer, C., Di Muro, A., Gordeychick, B., and Wörner, G. (2020). Timescales of magmatic processes during the eruptive cycle 2014–2015 at Piton de la Fournaise, La Réunion, obtained from Mg-Fe diffusion modelling in olivine. *Contrib. Mineral. Petrol.*, 175, 1–16.

Thinon, I., Lemoine, A., Leroy, S., Paquet, F., Famin, V., Feuillet, N., Berthod, C., Doubre, C., Jacques, E., Zaragosi, S., Clouard, V., Bernard, J., Delescluse, M., Franke, D., Jorry, S. J., Van der Woerd, J., Watremez, L., Boymond, P., Masquelet, C., Rusquet, A., Mercury, N., Roche, V., Bachèlery, P., Sauter, D., Michon, L., Chamot-Rooke, N., Rolandone, F., Scalabrin, C., Deplus, C., Rad, S., Bujan, S., Dassie, E., Bignon, J., Canva, A., Sitti allaouia, S., Ali, S., Morvan, L., Hardouin, E., and Sadeski, L. (2022). Volcanism and tectonics unveiled between the EARS and Madagascar: toward a better understanding of the geodynamics of the Comoros archipelago. *C. R. Géosci.*, 354(S2), 7–34.

Thinon, I., Leroy, S., and Lemoine, A. (2021). SISMAORE cruise. RV Pourquoi Pas?

Thivet, S., Carlier, J., Gurioli, L., Di Muro, A., Besson, P., Smietana, M., Boudon, G., Bachelery, P., Eychenne, J., and Nedelec, J.-M. (2022). Magmatic and phreatomagmatic contributions on the ash-dominated basaltic eruptions: insights from the April and November–December 2005 eruptions at Karthala volcano, Comoros. *J. Volcanol. Geotherm. Res.*, 424, article no. 107500.

Thivet, S., Gurioli, L., and Di Muro, A. (2020). Basaltic dyke eruptions at Piton de La Fournaise: characterization of the eruptive products with implications for reservoir conditions, conduit processes and eruptive dynamics. *Contrib. Mineral. Petrol.*, 175, article no. 26.

Tzevahirtzian, A., Zaragosi, S., Bachèlery, P., Biscara, L., and Marchès, E. (2021). Submarine morphology of the Comoros volcanic archipelago. *Mar. Geol.*, 432, article no. 106383.

Wark, D. A., Hildreth, W., Spear, F. S., Cherniak, D. J., and Watson, E. B. (2007). Pre-eruption recharge of the Bishop magma system. *Geology*, 35(3), 235–238.

Zinke, J., Reijmer, J. J. G., Thomassin, B. A., Dullo, W. C., Grootes, P. M., and Erlenkeuser, H. (2003). Postglacial flooding history of Mayotte lagoon (Comoro archipelago, southwest Indian Ocean). *Mar. Geol.*, 194(3–4), 181–196.

*Comptes Rendus*
*Géoscience — Sciences de la Planète*
**2022**, Vol. 354, Special Issue S2, p. 225-256
https://doi.org/10.5802/crgeos.182

The Mayotte seismo-volcanic crisis of 2018-2021 in the Comoros archipelago (Mozambique channel) / *La crise sismo-volcanique de 2018-2021 de Mayotte dans l'archipel des Comores (Canal du Mozambique)*

# Experimental evidence for the shallow production of phonolitic magmas at Mayotte

## *Evidence expérimentale de la production de magmas phonolitiques à faible profondeur à Mayotte*

**Joan Andújar** [*, a], **Bruno Scaillet** [a], **Manuel Moreira** [a], **Ida Di Carlo** [a], **Anne Le Friant** [b], **Manon Bickert** [c], **Fabien Paquet** [d], **Stephan Jorry** [e] **and Nathalie Feuillet** [b]

[a] Institut des Sciences de la Terre d'Orléans (ISTO), UMR 7327, Université d'Orléans, CNRS, BRGM, 1A rue de la Férollerie, F-45071 Orléans, France

[b] Université de Paris, Institut de physique du globe de Paris, CNRS, F-75005 Paris, France

[c] Dipartimento di Scienze Chimiche e Geologiche, Università di Modena e Reggio Emilia, Modena, Italy

[d] BRGM-French geological survey, DGR/GBS, 3 avenue Claude Guillemin, BP36009, F-45060 Orleans Cedex 2, France

[e] Geo-Ocean, Univ Brest, Ifremer, CNRS, Technopole La Pointe du Diable, 29280 Plouzané, France

*E-mails:* juan.andujar@cnrs-orleans.fr (J. Andújar), bscaille@cnrs-orleans.fr (B. Scaillet), manuel.moreira@cnrs-orleans.fr (M. Moreira), ida.di-carlo@cnrs-orleans.fr (I. Di Carlo), Lefriant@ipgp.fr (A. Le Friant), manon.bickert@gmail.com (M. Bickert), F.Paquet@brgm.fr (F. Paquet), Stephan.Jorry@ifremer.fr (S. Jorry), feuillet@ipgp.fr (N. Feuillet)

**Abstract.** Since May 2018 till the end of 2021, Mayotte island has been the locus of a major submarine volcanic eruption characterized by the offshore emission of more than 6.5 $km^3$ of basanitic magma. The eruption occurred along a WNW–ESE trending submarine ridge on the east flank of the island where, in addition, several seemingly recent phonolitic bodies were also identified close to the island. To define realistic scenarios of magma ascent and potentially predict the style of an upcoming event, it is crucial to have a precise understanding on the plumbing system operating below volcanoes. The putative relationships between basanites emitted by the new volcano and these recent phonolites have been experimentally explored by performing crystallization experiments on a representative basanite over a large range of pressures (up to

* Corresponding author.

400 MPa). The results show that the crystallization of basanite at crustal levels (≤12–15 km) yields a phonolitic residual liquid containing up to 3–4 wt% $H_2O$ after ≥65 wt% of an assemblage of olivine+plagioclase+amphibole+clinopyroxene+biotite+magnetite+ilmenite+apatite. The final iron content of the residual phonolitic liquids is strongly controlled by the depth/pressure of fractionation. Fe-rich phonolites from the submarine ridge are produced at 6–8 km depth, while a shallower differentiation (≤4–5 km) results in the production of liquids with trachyte–benmoreite affinities. If the fractionation process occurs at depths higher than 8 km, the resulting phonolitic melts are progressively enriched in $SiO_2$–$Al_2O_3$ but depleted in FeO*, ie unlike those erupted. We therefore conclude that phonolitic magma production and storage at Mayotte is a rather shallow process.

**Résumé.** Depuis mai 2018 et jusqu'à la fin de l'année 2021, l'île de Mayotte a été le scenario d'une éruption volcanique sous-marine majeure caractérisée par l'émission en mer de plus de 6,5 km$^3$ de magma basanitique. L'éruption s'est produite le long d'une ride sous-marine orientée ONO–ESE sur le flanc est de l'île où, entre autre, plusieurs corps phonolitiques d' aspect récent ont également été identifiés à proximité de l'île. Pour définir des scénarios réalistes d'ascension du magma et potentiellement prévoir le style d'un événement à venir, il est crucial d'avoir une compréhension précise du système de plomberie magmatique opérant sous les volcans. Les relations génétiques potentielles entre les basanites émises par le nouveau volcan et ces phonolites récentes ont été explorées expérimentalement en effectuant des expériences de cristallisation sur une basanite représentative, et ce sur une large gamme de pressions (jusqu'à 400 MPa). Les résultats montrent que la cristallisation de la basanite à des profondeurs crustales (≤12–15 km) produit un liquide résiduel phonolitique contenant jusqu'à 3–4 % en poids (pd.%) de $H_2O$, après la précipitation d'au moins 65 pd.% d'un assemblage d'olivine+plagioclase+amphibole+clinopyroxène+biotite+magnétite+ilménite+apatite. La teneur finale en fer des liquides phonolitiques résiduels est fortement contrôlée par la profondeur/pression de cristallisation. Les phonolites riches en fer de la dorsale sous-marine sont produites à 6–8 km de profondeur, tandis qu'une différenciation moins profonde (≤4–5 km) entraîne la production de liquides à affinités trachyte–benmoreite. Si le processus de fractionnement se produit à des profondeurs supérieures à 8 km, les liquides phonolitiques résultants sont progressivement enrichis en $SiO_2$–$Al_2O_3$ mais appauvris en FeO*, c'est-à-dire différents des phonolites naturelles. Nous concluons donc que la production et le stockage de magma phonolitique à Mayotte est un processus plutôt superficiel.

**Keywords.** Mayotte, Phase equilibria, Phonolite, Iron-enrichment, Basanite.

**Mots-clés.** Mayotte, Equilibres de phases, Phonolite, Enrichement en fer, Basanite.

*Published online: 12 January 2023, Issue date: 17 January 2023*

## 1. Introduction

Understanding the plumbing systems feeding volcanic eruptions is critical for providing an accurate interpretation of the different signals (seismicity, surface deformation, gas emissions) generated during periods of volcanic reactivation or eruption. Having accurate constraints on magma temperature, storage depths and on the amount of volatiles ($H_2O$, $CO_2$, S, F, Cl… etc.) dissolved in the magma allow to define more realistic scenarios for simulating the ascent and potentially predict the style of the upcoming event. In systems where different types of magmas (i.e., mafic to felsic) are emitted, an important question is to understand under which conditions basaltic melts evolve towards felsic compositions, and in particular whether this process occurs in a single or in multiple reservoirs located at different depths. This is crucial for understanding the final storage level of more evolved compositions and the structure of the plumbing system beneath a volcano, as the generation level of the felsic melts may not correspond to that of their pre-eruptive storage. In this contribution, we address this issue by unravelling the parental relationships between recent erupted basanites and phonolites at Mayotte (North Mozambique channel) using an experimental approach.

Between May 2018 and the end of 2021, Mayotte island has experienced a major submarine volcanic eruption characterized by the emission of more than 6.55 km$^3$ of magma [Feuillet, 2019, ReVoSiMa, 2022]. Prior to this event, the island has not experienced historical episodes of reactivation, and the latest known volcanic event occurred some 7000 yrs ago on Petite Terre [Zinke et al., 2003]. The 2018–2021 eruption occurred along a WNW–ESE trending submarine ridge on the east flank of the island (Figure 1).

Two main seismic swarms are still active below the ridge: a proximal and a distal cluster [Bertil et al., 2021, Cesca et al., 2020, Feuillet et al., 2021,

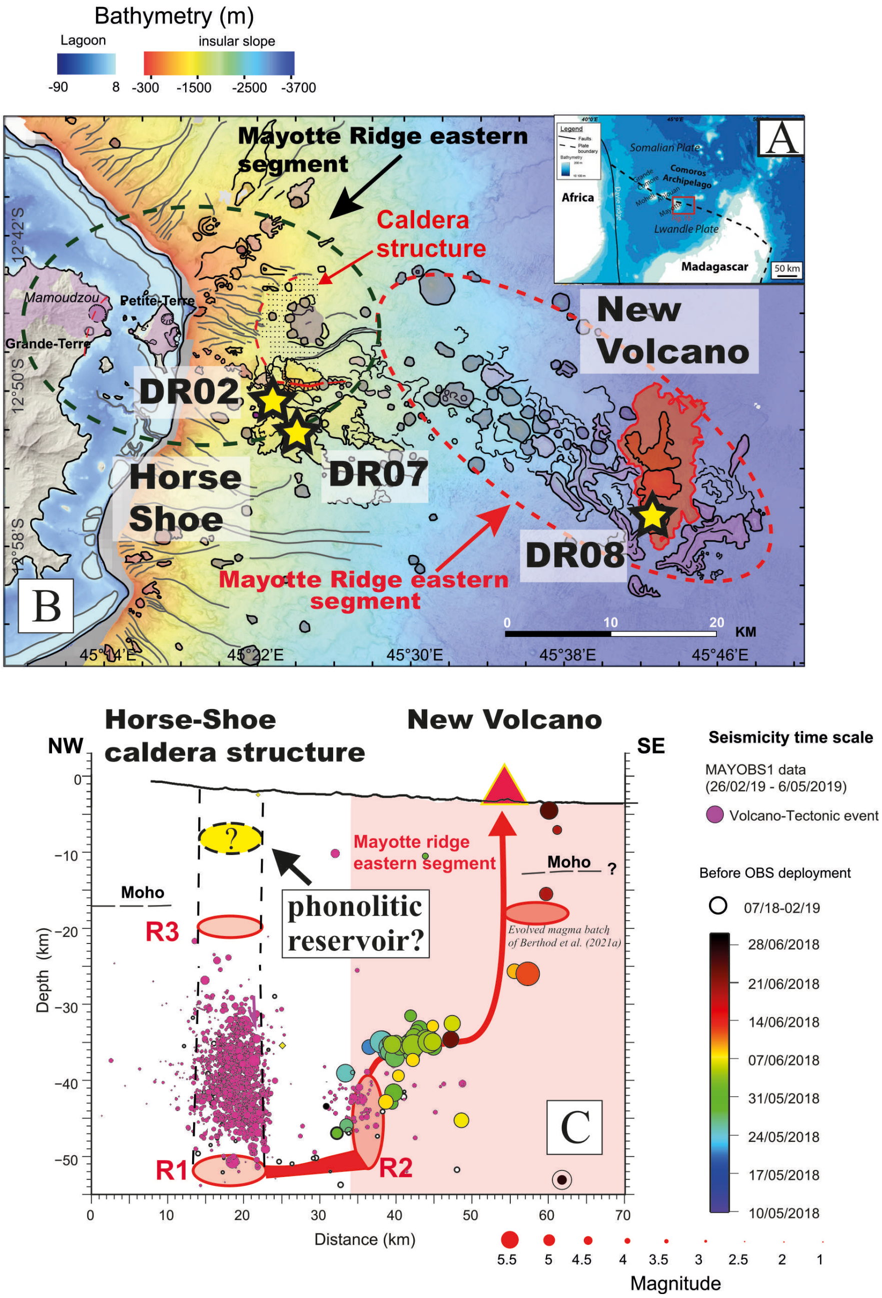


**Figure 1.** (A) Location of Comoros archipelago in the Mozambique channel. (B) Geological map of the active submarine volcanic ridge at Mayotte (modified from Feuillet et al. [2021]) showing the locations of the new volcano, and the Horse-shoe zone having active submarine degassing. The location of the dredged samples considered in this study is marked by yellow stars (modified from Berthod et al. [2021b]). (C) Depth distribution of the two well identified seismic swarms over the submarine ridge of Mayotte (modified from Feuillet et al. [2021]). The three seismically active zones R1, R2, R3 identified during this eruption, and the petrologically inferred reservoir located below the volcano and intercepted by the rising magma, are also shown [Feuillet et al., 2021, Foix et al., 2021 and Berthod et al., 2021b]. The emptying of a potential shallow phonolitic reservoir, as inferred in this work, could have produced the Horseshoe structure (see text for details).

Lavayssière et al., 2022, Lemoine et al., 2020, Saurel et al., 2021]. The distal cluster is located 30 km far from the eastern coast of Petite Terre whereas the proximal one is much closer (5–10 km from Petite Terre). Feuillet et al. [2021] inferred that the distal swarm was promoted by the drainage and consecutive stress changes around a ~40 km deep magmatic reservoir (R2). Relocations of seismic events recorded by seismic stations onshore within the first weeks of the crisis show that a dike propagated from this reservoir R2 to transport the magma toward the seafloor at the eruption site [Feuillet et al., 2021]. Following the eruption, the proximal cluster was activated likely following the drainage of deeper (55 km) reservoir R1 and the consecutive collapse of a deep caldera structure above [Feuillet et al., 2021]. The proximal cluster is located below an old caldera structure where sits the Horseshoe zone [Figures 1B–C, Feuillet et al., 2021]. Active degassing is observed in this zone, giving rise to submarine plumes but without emission of fresh lava [Feuillet et al., 2021]. Ground deformation modeling revealed the drainage of about 5 km$^3$ of a deep -seated reservoir [Lemoine et al., 2020], inferred to be R2 [Feuillet et al., 2021].

Recent passive tomography data [Foix et al., 2021], along with the detection of an important number of very low frequency events at ~20 km [VLF; Laurent et al., 2021], suggest the presence of a third reservoir (R3; Figure 1C) above the deep caldera structure. The reactivation of this reservoir could be at the origin of the gas-emissions observed on the horseshoe region [Foix et al., 2021].

Geothermobarometry calculations broadly support the above seismic depths for the deep reservoirs (volume ≥ 10 km$^3$; depths ≥ 37 km), in which the hydrous (2.3 wt% $H_2O$ dissolved in melt, $H_2O_{melt}$) evolved basanite (generated by ~50% of crystallization of a more primitive magma; Berthod et al. [2021a]) was sourced. Berthod et al. [2021a] further proposed that during its uprise, the basanite intercepted a shallower pre-existing reservoir at 17 ± 6.5 km below the new volcano (Figure 1C), in which a more evolved magma originated during recent magmatic episodes was residing.

The appearance of the dense seismic swarm beneath the Horseshoe region (Figure 1C) and the discovery of intensive submarine gas plumes, prompted the community for sampling this zone located 15 km away from Petite Terre. The study of samples dredged in this area revealed the presence of a bimodal compositional distribution of the emitted magmas in contrast to the new volcano, where basanite flows predominate. Within the Horseshoe region, several phonolitic bodies occur in abundance in addition to basanites, outcropping on the caldera borders and flowing downwards (Figure 1B; Berthod et al. [2021a,b]). The possible genetic link between the submarine basanites and phonolites was explored in Berthod et al. [2021b] through fractional crystallization modelling of major and trace elements along with Rhyolite-MELTs simulations [Ghiorso and Gualda, 2015]. These modelling results show that the production of phonolite liquids from a hydrous (2.3 wt% $H_2O_{melt}$) basanite requires 80% of fractional crystallization of a mineral assemblage consisting of clinopyroxene (Cpx), olivine (Ol), magnetite (Mt), apatite (Ap), ilmenite (Ilm) and anorthoclase alkali feldspar (Afs) at ≤1000 °C, $P \geq 600$ MPa and $fO_2 \sim$ FMQ-1. Cpx–Opx barometry performed on mantle xenoliths carried by both phonolitic and basanitic samples from the Horseshoe region, yields similar storage conditions (15–20 km; Figure 1C). Based on these lines of evidence, these authors conclude that crystallisation of evolved basanitic melts at low oxygen fugacity produced the erupted Fe-rich phonolitic melts at Moho levels [Dofal et al., 2021].

It is worth noting that most of the phonolitic magmas known worldwide evolve at relatively shallow conditions [$P \leq 200$ MPa or ≤6–8 km; Andújar et al., 2008, 2010, 2013, Berndt et al., 2001, Harms et al., 2004, Moussallam et al., 2013, Scaillet et al., 2008]. However, rare are the cases concerning mantle-xenolith bearing phonolites [e.g. Berthod et al., 2021b, Dautria et al., 1983]. At first sight, the presence of mantle fragments within phonolitic magmas, along with thermobarometric calculations, hint at a rapid ascent of these magmas from deep mantle levels. Yet, examples of mafic to intermediate magmas containing significant amounts of different types of mantle xenoliths are manifold in alkaline series [e.g., La Palma, Klügel et al., 1999, 2022, Lanzarote, Neumann et al., 1995, La Garrotxa, Spain, Pedrazzi et al., 2022]. Since the products and mineralogy of evolved phonolites often show evidence of mixing-mingling with more mafic melts [i.e. mixed pumices, presence of inverse zonations in feldspars, olivine; Andújar et al., 2013, Andújar and Scaillet, 2012, Berthod et al., 2021b, Wolff, 1985; among others], the injection of mantle-bearing mafic magmas into phonolitic reservoirs could also account for the occurrence of these mantle fragments into the phonolites.

Another point worth of note is the use of thermobarometric equations [e.g., Putirka, 2008] along with thermodynamic algorithms like MELTS or Rhyolite-MELTS [Gualda et al., 2012] for retrieving the ponding conditions and/or modelling the crystallization behavior of felsic alkaline magmas. These thermobarometric calibrations have important associated uncertainties on intensive parameters, in particular *P* [e.g. ±50 °C for *T* and ±150–400 MPa for *P* or 5–12 km in depth; Berthod et al., 2021a,b, Putirka, 2008, 2016, Ubide et al., 2019] which limit their practical use in volcanological contexts, notably for inferring precisely storage conditions or comparing them to geophysical data. In particular, recent works have shown that amphibole- and Cpx- based geobarometers either do not capture real pressure [Erdmann et al., 2014] or overestimate considerably it [Hammer et al., 2016], in particular when applied to alkaline magmas [Hammer et al., 2016].

Similarly, while MELTs algorithm can faithfully simulate the evolution of anhydrous mafic melts at low pressures, the application of this model to the study of hydrous mafic melts is still limited, in large part because it cannot predict the crystallization of important hydrous phases such as amphibole or biotite. Significant differences in the crystallization temperatures and stability fields of phases like Cpx or Plagioclase in hydrous systems have also been reported [Freise et al., 2009, MacDonald et al., 2021].

Whereas the above approaches remain valuable for a first order evaluation of the ponding and evolution conditions of crystal-bearing magmas, the uncertainties and lack of calibration issues outlined above indicate that these methods are not standalone tools, and still need to be confronted to experimental results whenever possible. Accordingly, here we report experimental data gained on mafic magmas from Mayotte in order to put constraints on the generation conditions of phonolitic melts in this area.

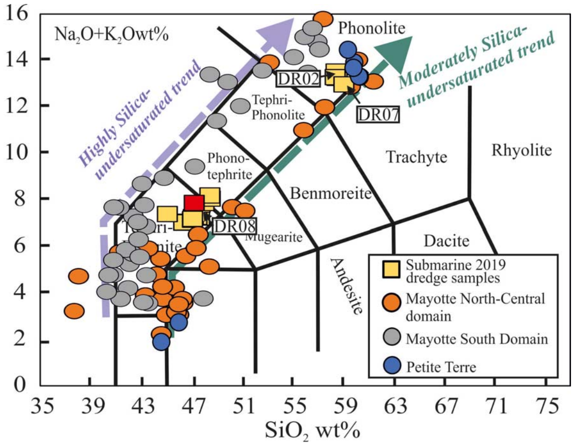


**Figure 2.** Total alkali ($Na_2O + K_2O$) versus $SiO_2$ diagram [TAS after Le Bas and Streckeisen, 1991] showing the two different liquid lines of descent of Mayotte magmas: highly silica-undersaturated and moderately silica-undersaturated trends. The products dredged on the active submarine ridge and those from Petite Terre are also shown. Compositional data are from Pelleter et al. [2014] and Berthod et al. [2021a,b].

## 2. Geological setting

Mayotte is the easternmost and oldest island of the Comoros archipelago, composed of a main volcanic island (Grande Terre) and a volcanic islet (Petite Terre) located 4 km away to the east (Figure 1B). Mayotte was constructed in three main different phases of volcanism: the first stage corresponds to the shield-building phase, between 20 and 3.8 Ma, followed by a fissure-erupted post erosional phase (3.8–2.5 Ma) and a final episode [2.4–1.5 Ma; Späth et al., 1996]. In detail, the volcanic activity of Grande Terre migrated from the southern part of the island during early stages (10.6–1.9 Ma) towards the north (5–0.75 Ma) and north-east (0.75–Present), with periods of quiescence in between [Debeuf, 2004, Nehlig et al., 2013]. This period of activity may also concern offshore WNW–ESE volcanic chains extending from Petite-Terre down to the newly discovered Fani Maore offshore volcano, Feuillet et al. [2021].

The compositions of magmas erupted on Mayotte islands and along the 60 km of submarine ridge clearly define two distinct magmatic lineages. Whereas magmas from the southern Mayotte region are alkali-rich and highly silica undersaturated, those from north central-east sectors and the most recent Holocene products (including the 2018–2021 submarine eruption) are also silica-undersaturated but show a moderate alkali enrichment (Figure 2). Compositional differences between these two series are readily explained by the mineralogical heterogeneity of their source regions [Späth et al., 1996]. In both cases, crystal-fractionation has been proposed to be the main mechanism controlling magma evolution [Berthod et al., 2021a,b, Pelleter et al., 2014, Späth et al., 1996]. Despite their different sources, the magmas from these two series are dominated by the same mineralogy sensu latto. Ol+Cpx operate at the very initial stages of the fractionation process, being joined, and progressively replaced by, Fe–Ti oxides, feldspar and amphibole, as well as accessory amounts of apatite and titanite with increasing degrees of differentiation [Debeuf, 2004, Pelleter et al., 2014, Späth et al., 1996].

## 3. Experimental work

### 3.1. *Preparation of the starting material*

The starting material used for our experiments is the sample DR08 that was dredged during the early phases of the 2018–2021 eruption by the MAYOBS-2 oceanographic campaign [Figure 1B; Table 1; Jorry, 2019]. This sample has been petrologically characterized by Berthod et al. [2021a]; according to these authors (see their Tables 2–4), it is an evolved glassy popping-rock basanite (Mg ~ 4.5 wt%; Table 1) with normative olivine content being ≥10%, moderately vesicular (~31%) with 5–9% (calculated on a bubble-free basis) of olivine (~Fo72 ± 2 mol%), and trace amounts of Ti-magnetite and apatite.

Several pieces of this glassy rock were first finely ground in an agate mortar, put in a Pt crucible at 1400 °C and melted twice, with grinding in between, during 5 h in open atmosphere. Electron microprobe analyses (EMPA) of the starting glass show a homogeneous composition with no significant Na or Fe loss compared to data from Berthod et al. [2021a, Table 1]. The resulting dry glass was then ground to obtain the powder that was used as starting material for the phase equilibrium experiments and stored in an oven at 120 °C.

### 3.2. *Experimental equipment and strategy*

In total, six experiments were performed (Table 2) at the ISTO experimental laboratory, using the same experimental apparatus and procedure of Andújar et al. [2013], Moussallam et al. [2013], Scaillet et al. [1992], which are briefly summarized below. Experiments were carried out in an Internally Heated Pressure Vessel (IHPV) operating vertically, loaded with Ar–$H_2$ mixtures at room temperature to achieve the desired $fO_2$ conditions (see below). Total pressure was recorded by a transducer calibrated against a Heise Bourdon gauge with an uncertainty of ±20 bars. A double-winding kanthal furnace was used as this allows to achieve near-isothermal conditions (gradient <2–3 °C/cm) along a 3 cm long hot spot. Temperature was measured using K-type thermocouples with an accuracy of ±5 °C. A rapid-quench technique was systematically used, imparting isobaric cooling rates of >100 °C/s [e.g., Andújar et al., 2013, 2015, Scaillet et al., 2008]. In all runs reported here, the drop quench was successful as indicated by the rise in total pressure upon the falling of the sample holder into the cold (bottom) part of the vessel.

Experiments were mainly conducted at *T*–*P* conditions covering those determined for similar phonolites worldwide [e.g., Andújar et al., 2008, 2010, 2013, Andújar and Scaillet, 2012, Giehl et al., 2013, Moussallam et al., 2013, Scaillet et al., 2008]. Temperature was set at 925 and 950 °C whereas explored pressures were 100, 150, 200 and 400 MPa. Based on the iron-rich character of the Mayotte phonolites [Berthod et al., 2021b], the initial $fO_2$ was set at ≤ NNO buffer (where NNO refers to the Ni–NiO buffer) as Fe enrichment in magmas is favoured by low $fO_2$ [e.g., Giehl et al., 2013, Moussallam et al., 2013, Toplis and Carroll, 1995].

### 3.3. *Capsule preparation*

We used Au gold capsules (1.5 cm long, 2.5 mm inner diameter, 0.2 mm wall thickness) since this metal minimizes the Fe-loss towards the capsule walls under reducing conditions. Distilled $H_2O$ was first loaded, then silver oxalate as the source of $CO_2$ for $H_2O$-undersaturated runs, and then the glass powder. Capsules were weighed and then welded using an arc-electric welder. After welding, capsules were re-weighed and if no significant weight loss occurred (considered to occur for a difference >0.0004 g (or ≤0.1% of the final weight of the capsule)), they were left in an oven for a few hours at 100 °C, to ensure homogeneous volatiles distribution. Both the amount of $H_2O + CO_2$ and fluid/silicate ratio were maintained constant (3 ± 0.5 mg of $H_2O + CO_2$, and 30 mg silicate). At a given *T*–*P* conditions, various starting

$H_2O$–$CO_2$ mixtures were explored: $XH_2O_{in}$, defined as $H_2O/(H_2O + CO_2)$ (in moles), varied in the range 1–0.08 (Table 2).

A typical experiment contained five or six capsules, each loaded with a different $H_2O/CO_2$ ratio. Run duration varied between 64 and 74 h, depending on temperature. Experiments were terminated by using the drop quench device and then switching off the power supply. After the experiments, capsules were checked for leaks, opened, and half of the run product was embedded in a probe mount with an epoxy resin and polished for optical observation, and carbon coated for subsequent EMPA and scanning electron microscopy (SEM) characterisation.

### 3.4. *Water content, $fH_2$, $fO_2$ in the capsules*

The variation of the $XH_2O_{in}$ in the capsules allowed us to explore different water fugacities, and thus different $H_2O_{melt}$ (Table 2). The amount of dissolved water ($XH_2O_{in}$) in the glass of the different $H_2O$-saturated charges was calculated using the $H_2O$-solubility model of Jiménez-Mejías et al. [2021] which is suited for basanitic–phonotephritic compositions. The water contents of charges with $XH_2O_{in} < 1$ ran at the same temperature and pressure than the $H_2O$-saturated charge, were calculated by mass balance using the constraint of equilibrium fugacities of $H_2O$ and $CO_2$ species between melt and fluid, along with the $H_2O$–$CO_2$ solubility model of Jiménez-Mejías et al. [2021].

The $fH_2$ of the experiments was determined using an empirical calibration curve established in previous experimental works, relating the $H_2$ pressure loaded initially to the autoclave at room temperature to the final $fH_2$ as determined using NiPd sensors run at similar $P$–$T$–$fO_2$ [Andújar and Scaillet, 2012, Andújar et al., 2015, Romano et al., 2018]. Once the prevailing $fH_2$ is known, the $fO_2$ can be determined by using the dissociation constant of water [Robie et al., 1979], knowing the $fH_2O$ at the experimental temperature and pressure. $fH_2O$ was calculated as $fH_2O = XH_2O_{in} * fH_2O^o$ where $fH_2O^o$ is the fugacity of pure water [Burnham et al., 1969]. Afterwards, the $fO_2$ for each capsule was calculated (Table 2) (see Andújar and Scaillet [2012] for further details). The experiments were conducted at oxygen fugacities around NNO $\pm$ 0.3 at $H_2O$-saturation. As $fO_2$ decreases with $XH_2O_{in}$ [e.g., Andújar and Scaillet, 2012, Freise et al., 2009, Scaillet et al., 1995, Webster et al., 1987], at fixed $T$, $P$, $fH_2$, for water-undersaturated charges the prevailing oxygen fugacity is necessarily <NNO $\pm$ 0.3. As a result, in a single experimental series, the decrease in $XH_2O_{in}$ from 1 to 0.08 decreased the $fO_2$ up to about 2.5 log units below the NNO buffer (or ~1.8 log units below the Fayalite-Magnetite-Quarz buffer, FMQ; Table 2).

### 3.5. *Analytical techniques*

Experimental runs were first characterized using a Zeiss Merlin Compact electron microscope equipped with an EDS micro-analysis system (Bruker-Quantax-XFlash6) at ISTO. EDS spectra allowed a first order identification of the minerals present in each charge. Experimental phases were analyzed using a Cameca SX-Five EPMA with an acceleration voltage of 15 kV, a sample current of 6 nA, and a counting time of 10 s. For glasses, a defocused beam of 20 μm was used whereas for minerals a focused beam was employed instead. Sodium and potassium were analyzed first and a Phi-Rho-Z correction procedure was applied. Major elements calibration was done using the following standards: albite (Na, Si), orthoclase (K), andradite (Ca), apatite (P), chromite (Cr), corundum (Al), magnesium oxide (Mg), hematite (Fe) and pyrophanite (Mn, Ti). The relative analytical errors are 1% ($SiO_2$, $Al_2O_3$, CaO), 3% (FeO, MgO, $TiO_2$) and 5% (MnO, $Na_2O$, $K_2O$, $P_2O_5$).

In the case of experimental plagioclase (Pl), the small size of this phase in the charges (usually ≤3 μm) along with the presence of small (≤0.5 μm) Fe–Ti oxides-apatite inclusions inside the crystals, made difficult the proper analysis of this phase with EPMA. To circumvent this problem, Pl composition was obtained via using a SEM-EDS calibrated analysis: albite, orthose and andradite EMPA standards were analyzed first with a focused beam (1 μm), a voltage of 15 kV and counting times of 15 s for the different elements (Na, K, Si, Al, Ca, Na, K). SEM-EDS compositions of the standards were found to be within ≤5% to those obtained by EMPA (see Supplementary Table). Consequently, experimental plagioclases were determined by SEM-EDS in each charge, using the same conditions and the average SEM-EDS calibrated compositions fulfilling the stoichiometric requirements for this phase (see Supplementary Table).

**Table 1.** 100 wt% anhydrous composition of the starting glass DR08, dredge bulk-rock compositions for submarine basanite DR08 and phonolites [Berthod et al., 2021a,b]; North-central onland phonolites

| DR08 | DR08 Starting Glass | sd | Bulk-rock submarine basanite Berthod et al. [2021a,b] | | Bulk-rock submarine phonolites | | | | | North central onland-phonolites [Pelleter et al., 2014, Späth et al., 1996] | | | | |
|---|---|---|---|---|---|---|---|---|---|---|---|---|---|---|
| | | | DR0801-ALF | DR080102 | DR020202 | DR020401 | DR060204 | DR070201 | DR0701 | M29 (aphyric) | M31 | M76 | Ma-5 | Ma65 |
| *n* | 15 | | | | | | | | | | | | | |
| $SiO_2$ | 47.45 | 0.33 | 47.65 | 47.44 | 58.54 | 58.50 | 58.59 | 58.43 | 59.12 | 61.47 | 57.60 | 59.65 | 60.10 | 58.65 |
| $TiO_2$ | 2.87 | 0.13 | 2.90 | 2.92 | 0.37 | 0.36 | 0.36 | 0.35 | 0.36 | 0.35 | 0.87 | 0.56 | 0.58 | 0.81 |
| $Al_2O_3$ | 15.35 | 0.16 | 15.69 | 15.53 | 18.51 | 18.47 | 18.65 | 18.67 | 18.37 | 19.79 | 20.24 | 19.95 | 19.91 | 19.14 |
| FeO* | 13.61 | 0.35 | 13.74 | 14.00 | 6.47 | 6.44 | 6.50 | 6.68 | 6.48 | 3.15 | 4.75 | 4.01 | 3.77 | 5.12 |
| MnO | 0.19 | 0.04 | 0.24 | 0.25 | 0.26 | 0.26 | 0.27 | 0.27 | 0.27 | 0.12 | 0.14 | 0.13 | 0.14 | 0.17 |
| MgO | 4.57 | 0.10 | 4.43 | 4.46 | 0.62 | 0.63 | 0.46 | 0.40 | 0.47 | 0.49 | 1.02 | 0.46 | 0.45 | 0.79 |
| CaO | 6.61 | 0.06 | 6.53 | 6.53 | 1.57 | 1.55 | 1.63 | 1.62 | 1.65 | 1.45 | 3.16 | 2.26 | 1.97 | 3.03 |
| $Na_2O$ | 4.79 | 0.06 | 4.48 | 4.62 | 7.97 | 8.05 | 7.64 | 7.67 | 7.48 | 7.38 | 7.36 | 7.66 | 8.07 | 7.67 |
| $K_2O$ | 2.74 | 0.11 | 2.75 | 2.63 | 5.39 | 5.47 | 5.61 | 5.60 | 5.48 | 5.70 | 4.62 | 5.20 | 4.91 | 4.40 |
| $P_2O_5$ | 1.81 | 0.05 | 1.58 | 1.60 | 0.31 | 0.28 | 0.31 | 0.31 | 0.32 | 0.09 | 0.25 | 0.11 | 0.08 | 0.22 |
| Sum | 100.00 | | 100 | 100 | 100 | 100 | 100 | 100 | 100 | 100 | 100 | 100 | 100 | 100 |
| P.I. | 0.71 | | 0.66 | 0.68 | 1.03 | 1.04 | 1.01 | 1.01 | 1.00 | 0.93 | 0.85 | 0.92 | 0.94 | 0.91 |
| Normative Nepheline (wt%) | | | | | 12.6 | 13.2 | 11.5 | 11.8 | 9.4 | 7.4 | 10.8 | 10.4 | 10.7 | 9.4 |

*n*: Number of analysis.

sd: Standard deviation.

P.I: Peralkaline index calculated as the (Na+K)/Al in moles.

**Table 2.** Experimental run conditions and phase proportions (wt%)

| Charge | $T$ (°C) | $P$ | $XH_2O_{in}$ | $XH_2O_{fin}$ | $H_2O$ (wt%) | $CO_2$ (ppm) | $fH_2O$ | $\log fO_2$ | $\Delta$NNO | $\Delta$QFM | Ol | Mt | Ilm | Ap | Cpx | Pl | Kr | Bt | Observations | % crystals | R2 |
|---|---|---|---|---|---|---|---|---|---|---|---|---|---|---|---|---|---|---|---|---|---|
| **950 °C/400 MPa; $t$ = 73 h** | | | | | | | | | | | | | | | | | | | | | |
| DR08-140 | 950 | 400 | 1.00 | 1.00 | 6.78 | 0 | 3880 | −10.7 | 0.3 | 0.87 | | 7.7 | | 3.8 | | | 12.4 | 5.2 | | 29.1 | 0.61 |
| DR08-141 | 950 | 400 | 0.72 | 0.52 | 4.78 | 4593 | 2015 | −11.3 | −0.3 | 0.30 | | 6.15 | 0.1 | 3.3 | | | 25.8 | 2.5 | | 37.85 | 0.42 |
| DR08-142 | 950 | 400 | 0.49 | 0.27 | 3.40 | 5483 | 1062 | −11.9 | −0.8 | −0.25 | 2.9 | 5.6 | 0.37 | 4.7 | | | 20.6 | 2.1 | | 36.27 | 0.23 |
| DR08-143 | 950 | 400 | 0.26 | 0.10 | 1.97 | 5974 | 381 | −12.8 | −1.7 | −1.15 | 14.05 | 0.94 | 3.4 | 3.86 | | 34.07 | 9 | 0.7 | | 66.02 | 0.73 |
| DR08-144 | 950 | 400 | 0.14 | 0.04 | 1.29 | 6108 | 172 | −13.5 | −2.4 | −1.83 | X | X | X | X | | X | X | X | | | |
| DR08-145 | 950 | 400 | 0.09 | 0.03 | 0.96 | 6154 | 100 | −13.9 | −2.9 | −2.31 | X | X | X | X | X | X | X | X | | | |
| **925 °C/400 MPa; $t$ = 71.5 h** | | | | | | | | | | | | | | | | | | | | | |
| DR08-152 | 925 | 400 | 1.00 | 1.00 | 6.69 | 0 | 3779 | −11.2 | 0.2 | 0.81 | | 7.6 | 0.2 | 4.01 | | | 15.6 | 7.8 | | 35.21 | 0.38 |
| DR08-154 | 925 | 400 | 0.50 | 0.31 | 3.59 | 5402 | 1173 | −12.2 | −0.8 | −0.21 | | 5.6 | 0.51 | 3.5 | | 14.4 | 25.7 | 7.8 | | 57.51 | 0.75 |
| DR08-155 | 925 | 400 | 0.29 | 0.16 | 2.51 | 5850 | 599 | −12.8 | −1.4 | −0.79 | X | X | X | X | | X | X | X | | | |
| DR08-156 | 925 | 400 | 0.18 | 0.09 | 1.86 | 6030 | 340 | −13.3 | −1.9 | −1.29 | X | X | X | X | | X | X | X | | | |
| DR08-157 | 925 | 400 | 0.08 | 0.03 | 1.09 | 6170 | 127 | −14.2 | −2.7 | −2.14 | X | X | X | X | X | X | X | X | | | |
| **DR08-950 °C, 200 MPa, $t$ = 68 h** | | | | | | | | | | | | | | | | | | | | | |
| DR08-56 | 950 | 200 | 0.90 | 0.85 | 4.65 | 249 | 1527 | −11.6 | −0.5 | 0.81 | 2.3 | 8.8 | | 3.2 | | | 20 | 2.6 | | 36.9 | 1.2 |
| DR08-58 | 950 | 200 | 0.51 | 0.34 | 2.73 | 908 | 613 | −12.3 | −1.3 | 1.03 | 3.01 | 7.1 | | 3.6 | | | 25 | 2.1 | | 40.81 | 0.93 |
| **DR08-925 °C/200 MPa, 69.5 h** | | | | | | | | | | | | | | | | | | | | | |
| DR08-129 | 925 | 200 | 1.00 | 1.00 | 5.06 | – | 1764 | −11.9 | −0.4 | 0.14 | | 7.1 | | 3.97 | | | 26.5 | 2.3 | Quench | 39.87 | 0.96 |
| DR08-130 | 925 | 200 | 0.88 | 0.82 | 4.52 | 287 | 1452 | −12.1 | −0.6 | −0.02 | | 5.7 | | 2.4 | | | 30.5 | 3.8 | | 42.4 | 0.99 |
| DR08-131 | 925 | 200 | 0.69 | 0.60 | 3.76 | 596 | 1060 | −12.3 | −0.8 | −0.30 | 15.9 | 1 | 3.8 | 4.3 | | 31.29 | 8.2 | 0.4 | | 64.89 | 0.67 |
| DR08-132 | 925 | 200 | 0.45 | 0.35 | 2.73 | 900 | 614 | −12.8 | −1.3 | −0.77 | x | x | x | x | x | x | x | x | | | |
| DR08-133 | 925 | 200 | 0.34 | 0.25 | 2.27 | 1004 | 449 | −13.1 | −1.6 | −1.04 | x | x | x | x | x | x | | x | | | |
| DR08-134 | 925 | 200 | 0.19 | 0.13 | 1.49 | 1138 | 226 | −13.7 | −2.2 | −1.66 | x | x | x | x | x | x | | ? | | | |
| DR08-135 | 925 | 200 | 0.09 | 0.05 | 0.84 | 1215 | 93 | −14.4 | −2.9 | −2.45 | x | x | x | x | x | x | | ? | | | |

(continued on next page)

**Table 2.** (continued)

| Charge | $T$ (°C) | $P$ | $XH_2O_{in}$ | $XH_2O_{fin}$ | $H_2O$ (wt%) | $CO_2$ (ppm) | $fH_2O$ | $\log fO_2$ | ΔNNO | ΔQFM | Ol | Mt | Ilm | Ap | Cpx | Pl | Kr | Bt | Observations | % crystals | R2 |
|---|---|---|---|---|---|---|---|---|---|---|---|---|---|---|---|---|---|---|---|---|---|
| **DR08-925 °C/150 MPa; $t$ = 71, 5h** | | | | | | | | | | | | | | | | | | | | | |
| DR08-158 | 925 | 150 | 1.00 | 1.00 | 3.85 | 0 | 1339 | −11.8 | −0.3 | 0.26 | | 7.72 | | 4.01 | | | 20.6 | 4.8 | | 37.13 | 0.32 |
| DR08-159 | 925 | 150 | 0.90 | 0.86 | 3.56 | 259 | 1154 | −11.9 | −0.4 | 0.13 | | 7.74 | | 3.72 | | 3.74 | 22.7 | 3.1 | | 41 | 0.5 |
| DR08-160 | 925 | 150 | 0.65 | 0.52 | 2.72 | 998 | 698 | −12.3 | −0.8 | −0.31 | 7.44 | 7.76 | 1.73 | 3.59 | 2.3 | 12.8 | 18.4 | 0.9 | | 54.92 | 0.33 |
| DR08-161 | 925 | 150 | 0.54 | 0.45 | 2.52 | 1164 | 603 | −12.5 | −1.0 | −0.44 | X | X | X | X | X | X | X | X | | | |
| DR08-162 | 925 | 150 | 0.30 | 0.21 | 1.66 | 1719 | 277 | −13.1 | −1.6 | −1.11 | X | X | X | X | X | X | | X | | | |
| DR08-163 | 925 | 150 | 0.18 | 0.12 | 1.26 | 1897 | 165 | −13.6 | −2.1 | −1.58 | X | X | X | X | X | X | | X | | | |
| **DR08-925 °C/100 MPa; $t$ = 64 h** | | | | | | | | | | | | | | | | | | | | | |
| DR08-164 | 925 | 100 | 1.00 | 1.00 | 3.14 | 0 | 915 | −11.8 | −0.3 | 0.18 | 2.45 | 8.18 | | 3.7 | | 14.5 | 18.9 | 3.1 | | 50.83 | 0.56 |
| DR08-165 | 925 | 100 | 0.88 | 0.84 | 2.87 | 168 | 772 | −12.0 | −0.5 | 0.03 | 5.33 | 7.6 | 1.09 | 4.03 | 6.39 | 21.3 | 2.9 | 5.5 | | 54.14 | 0.4 |
| DR08-166 | 925 | 100 | 0.71 | 0.62 | 2.44 | 424 | 571 | −12.3 | −0.7 | −0.23 | X | X | X | X | X | X | | X | | | |
| DR08-167 | 925 | 100 | 0.47 | 0.37 | 1.86 | 741 | 341 | −12.7 | −1.2 | −0.68 | X | X | X | X | X | X | | X | | | |
| DR08-168 | 925 | 100 | 0.33 | 0.24 | 1.46 | 921 | 217 | −13.1 | −1.6 | −1.07 | X | X | X | X | X | X | | X | | | |

Ol: olvine, Mt: magnetite, ilm: ilmenite, Ap: apatite, Cpx: Clinopyroxene, Pl: plagioclase, Kr: Kaersutite/Amphibole, Bt: biotite.

$XH_2O_{in}$ =, initial $H_2O/(H_2O+CO_2)$ in the charge.

$XH_2O_{fin}$ = final $H_2O/(H_2O+CO_2)$ in the charge.

$H_2O$ wt%, water content in the melt in wt%.

$CO_2$ content in the melt ppm.

$\log fO_2$(bar), logarithm of the oxygen fugacity calculated from the experimental $fH_2$.

ΔNNO = $\log fO_2$ experiment-$\log fO_2$ of the NNO buffer calculated at experimental $T$–$P$ after Pownceby and O'Neill [1994].

ΔQFM = $\log fO_2$ experiment-$\log fO_2$ of the QFM buffer calculated at experimental $T$ after Chou [1978].

X, mineral phase identified by SEM but, its abundance could not be calculated.

$fH_2$(bar), hydrogen fugacity of the experiment. See text for details.

**Table 3.** Experimental olivine compositions (wt%)

| Charge | $T$ (°C) | $P$ (MPa) | $n$ | $SiO_2$ | $TiO_2$ | $Al_2O_3$ | FeO* | MnO | MgO | CaO | $Na_2O$ | $K_2O$ | Sum | Fo% |
|---|---|---|---|---|---|---|---|---|---|---|---|---|---|---|
| DR08-142 | 950 | 400 | 3 | 33.5 | 0.2 | 0.2 | 43.8 | 1.1 | 19.9 | 0.7 | 0.1 | 0.0 | 99.5 | 44.8 |
| sd | | | | 0.4 | 0.1 | 0.2 | 1.0 | 0.1 | 0.3 | 0.4 | 0.1 | 0.0 | 0.7 | 0.2 |
| DR08-143 | 950 | 400 | 2 | 32.9 | 0.3 | 0.1 | 47.3 | 1.2 | 17.6 | 0.9 | 0.1 | 0.0 | 100.5 | 39.9 |
| sd | | | | 0.0 | 0.0 | 0.0 | 0.2 | 0.1 | 0.2 | 0.1 | 0.0 | 0.0 | 0.0 | 0.3 |
| DR08-144 | 950 | 400 | 1 | 32.8 | 0.5 | 0.7 | 48.9 | 1.3 | 16.4 | 0.8 | 0.1 | 0.1 | 101.7 | 37.5 |
| DR08-145 | 950 | 400 | 1 | 34.2 | 0.3 | 1.5 | 45.0 | 1.6 | 15.0 | 1.1 | 0.3 | 0.2 | 99.2 | 37.3 |
| DR08-155 | 925 | 400 | 2 | 32.7 | 0.2 | 0.1 | 50.3 | 1.8 | 13.9 | 1.3 | 0.1 | 0.1 | 100.5 | 33.0 |
| sd | | | | 0.5 | 0.1 | 0.1 | 1.0 | 0.1 | 0.5 | 0.2 | 0.0 | 0.1 | 0.7 | 0.4 |
| DR08-157 | 925 | 400 | 1 | 32.7 | 0.5 | 0.5 | 49.3 | 1.4 | 13.5 | 1.6 | 0.1 | 0.1 | 99.6 | 32.8 |
| DR08-58 | 950 | 200 | 2 | 33.3 | 0.3 | 0.1 | 40.2 | 1.2 | 21.6 | 1.2 | 0.0 | 0.0 | 97.9 | 49.0 |
| sd | | | | 0.4 | 0.3 | 0.1 | 0.3 | 0.1 | 0.6 | 0.5 | 0.0 | 0.0 | 0.2 | 0.9 |
| DR08-131 | 925 | 200 | 1 | 33.5 | 0.2 | 0.5 | 42.6 | 1.7 | 19.2 | 1.0 | 0.2 | 0.1 | 98.9 | 44.5 |
| DR08-132 | 925 | 200 | 2 | 32.1 | 0.8 | 0.6 | 42.4 | 1.5 | 18.6 | 1.3 | 0.2 | 0.1 | 97.5 | 43.9 |
| sd | | | | 1.0 | 0.5 | 0.3 | 1.1 | 0.1 | 0.5 | 0.2 | 0.0 | 0.0 | 1.2 | 0.5 |
| DR08-160 | 925 | 150 | 1 | 34.8 | 0.1 | 0.0 | 40.6 | 1.4 | 22.4 | 0.5 | 0.0 | 0.0 | 99.8 | 49.6 |
| DR08-161 | 925 | 150 | 2 | 34.8 | 0.1 | 0.6 | 40.6 | 1.7 | 22.2 | 0.4 | 0.3 | 0.1 | 100.8 | 49.4 |
| sd | | | | 0.1 | 0.1 | 0.1 | 0.5 | 0.3 | 0.3 | 0.1 | 0.0 | 0.0 | 0.8 | 0.6 |
| DR08-162 | 925 | 150 | 1 | 31.6 | 1.3 | 0.5 | 44.0 | 1.3 | 18.6 | 1.7 | 0.1 | 0.1 | 99.3 | 42.9 |
| DR08-164 | 925 | 100 | 2 | 34.3 | 0.1 | 0.4 | 38.8 | 1.4 | 22.8 | 1.8 | 0.1 | 0.0 | 99.8 | 51.1 |
| sd | | | | 0.7 | 0.1 | 0.1 | 0.2 | 0.0 | 0.0 | 0.4 | 0.1 | 0.0 | 0.3 | 0.1 |
| DR08-165 | 925 | 100 | 1 | 32.1 | 1.0 | 0.2 | 40.4 | 1.3 | 22.0 | 1.6 | 0.0 | 0.1 | 98.7 | 49.2 |
| DR08-166 | 925 | 100 | 2 | 32.7 | 1.0 | 0.8 | 40.1 | 1.3 | 20.9 | 2.0 | 0.2 | 0.1 | 99.2 | 48.2 |
| sd | | | | 0.6 | 0.4 | 0.2 | 0.3 | 0.1 | 0.3 | 0.2 | 0.1 | 0.0 | 0.5 | 0.1 |

$n$: number of analysis.

sd: standard deviation.

FeO*: Total iron reported as $Fe^{2+}$.

Fo mole(%) = 100 Mg/(Mg + Fe*) in olivine.

It should be noted that, compared to EMPA analyses, which are characterized by lower standard deviations (see Tables 3–8), SEM-EDS compositions are slightly more variable (see Supplementary Table), with a variation of ~2–3 mol% on end-member molecules. However, despite this, we can still use these compositions for comparison purposes.

### 3.6. *Attainment of equilibrium*

The crystallization experiments performed in this work share similar phase stabilities, textural and compositional characteristics to those found in equivalent studies performed on alkali-rich basalts [e.g., Andújar et al., 2015, Freise et al., 2009, Iacovino et al., 2016] using a similar procedure. As in these works, the following observations show that near-equilibrium conditions were attained in our experiments: the euhedral shape of crystals, the homogeneous distribution of phases within the charges, the smooth variation of phase proportions and compositions with changes in experimental conditions, and the small sum of residuals of mass-balance (generally ≤1; Table 2). Since each experimental charge is a

**Table 4.** Experimental amphibole compositions (wt%). Classification after Ridolfi [2021]

| Charge | $T$ (°C) | $P$ (MPa) | $n$ | $SiO_2$ | $TiO_2$ | $Al_2O_3$ | FeO* | MnO | MgO | CaO | $Na_2O$ | $K_2O$ | Sum | Species | Si | AlIV | Ti | T sum | AlVI | Ti | Cr | $Fe^{3+}$ | Mg | $Fe^{2+}$ | Mn | C sum | Ca | Na | B sum | Na | K | A sum | OH | F | Cl | W sum | Charge | Mg/(Mg + $Fe^{2+}$) | Mg# | Al# | AlT |
|---|---|---|---|---|---|---|---|---|---|---|---|---|---|---|---|---|---|---|---|---|---|---|---|---|---|---|---|---|---|---|---|---|---|---|---|---|---|---|---|---|---|
| DR08-140 | 950 | 400 | 5 | 39.85 | 2.91 | 11.07 | 13.14 | 0.25 | 11.23 | 9.97 | 2.71 | 0.87 | 92.41 | Mg-hastingsite | 6.24 | 1.76 | 0.00 | 8.00 | 0.28 | 0.34 | 0.00 | 0.45 | 2.62 | 1.27 | 0.03 | 5.00 | 1.67 | 0.33 | 2.00 | 0.49 | 0.17 | 0.67 | 2.00 | 0.00 | 0.00 | 2.00 | 45.55 | 0.67 | 0.60 | 0.14 | 2.04 |
| sd | | | | 0.53 | 0.23 | 0.35 | 1.00 | 0.07 | 0.76 | 0.08 | 0.05 | 0.10 | 0.89 | | | | | | | | | | | | | | | | | | | | | | | | | | | | |
| DR08-141 | 950 | 400 | 2 | 39.16 | 3.72 | 12.10 | 16.20 | 0.28 | 9.97 | 11.72 | 2.75 | 0.91 | 96.83 | Pargasite | 6.00 | 2.00 | 0.00 | 8.00 | 0.18 | 0.43 | 0.00 | 0.12 | 2.28 | 1.95 | 0.04 | 5.00 | 1.92 | 0.08 | 2.00 | 0.74 | 0.18 | 0.92 | 2.00 | 0.00 | 0.00 | 2.00 | 45.88 | 0.54 | 0.52 | 0.08 | 2.18 |
| sd | | | | 0.73 | 0.60 | 1.09 | 1.07 | 0.14 | 0.68 | 1.81 | 0.00 | 0.09 | 1.25 | | | | | | | | | | | | | | | | | | | | | | | | | | | | |
| DR08-142 | 950 | 400 | 3 | 39.41 | 5.14 | 12.22 | 14.83 | 0.19 | 11.01 | 10.51 | 2.68 | 0.95 | 96.94 | kaersutite | 5.91 | 2.09 | 0.00 | 8.00 | 0.07 | 0.58 | 0.00 | 0.52 | 2.46 | 1.34 | 0.02 | 5.00 | 1.69 | 0.31 | 2.00 | 0.47 | 0.18 | 0.65 | 2.00 | 0.00 | 0.00 | 2.00 | 45.48 | 0.65 | 0.57 | 0.03 | 2.16 |
| sd | | | | 0.97 | 0.35 | 0.57 | 0.58 | 0.06 | 0.39 | 0.36 | 0.20 | 0.12 | 0.68 | | | | | | | | | | | | | | | | | | | | | | | | | | | | |
| DR08-143 | 950 | 400 | 3 | 38.60 | 5.55 | 11.77 | 16.27 | 0.36 | 9.23 | 11.83 | 2.71 | 1.12 | 97.44 | kaersutite | 5.95 | 2.05 | 0.00 | 8.00 | 0.09 | 0.64 | 0.00 | 0.00 | 2.12 | 2.10 | 0.05 | 5.00 | 1.95 | 0.05 | 2.00 | 0.76 | 0.22 | 0.98 | 2.00 | 0.00 | 0.00 | 2.00 | 46.27 | 0.50 | 0.50 | 0.04 | 2.14 |
| sd | | | | 0.79 | 0.55 | 0.57 | 1.03 | 0.10 | 0.18 | 0.78 | 0.10 | 0.06 | 0.66 | | | | | | | | | | | | | | | | | | | | | | | | | | | | |
| DR08-144 | 950 | 400 | 2 | 41.10 | 5.05 | 10.50 | 18.19 | 0.25 | 9.07 | 10.80 | 2.96 | 1.14 | 99.04 | low-Mg | 6.20 | 1.80 | 0.00 | 8.00 | 0.06 | 0.57 | 0.00 | 0.02 | 2.04 | 2.27 | 0.03 | 5.00 | 1.74 | 0.26 | 2.00 | 0.61 | 0.22 | 0.83 | 2.00 | 0.00 | 0.00 | 2.00 | 45.98 | 0.47 | 0.47 | 0.03 | 1.87 |
| sd | | | | 0.11 | 0.03 | 0.28 | 0.89 | 0.05 | 0.26 | 0.48 | 0.03 | 0.09 | 1.54 | | | | | | | | | | | | | | | | | | | | | | | | | | | | |
| DR08-145 | 950 | 400 | | | | | | | | | | | | | | | | | | | | | | | | | | | | | | | | | | | | | | | |
| DR08-152 | 925 | 400 | 3 | 40.44 | 3.07 | 11.78 | 13.30 | 0.31 | 12.71 | 11.49 | 2.66 | 0.86 | 96.63 | Mg-hastingsite | 6.04 | 1.96 | 0.00 | 8.00 | 0.12 | 0.35 | 0.00 | 0.53 | 2.83 | 1.14 | 0.04 | 5.00 | 1.84 | 0.16 | 2.00 | 0.61 | 0.16 | 0.78 | 2.00 | 0.00 | 0.00 | 2.00 | 45.47 | 0.71 | 0.63 | 0.06 | 2.08 |
| sd | | | | 0.57 | 0.19 | 0.70 | 0.40 | 0.06 | 0.50 | 0.21 | 0.10 | 0.08 | 0.92 | | | | | | | | | | | | | | | | | | | | | | | | | | | | |
| DR08-154 | 925 | 400 | 4 | 40.25 | 3.79 | 11.11 | 18.85 | 0.42 | 9.00 | 10.41 | 2.98 | 0.68 | 97.48 | Mg-hastingsite | 6.10 | 1.90 | 0.00 | 8.00 | 0.09 | 0.43 | 0.00 | 0.56 | 2.04 | 1.83 | 0.05 | 5.00 | 1.69 | 0.31 | 2.00 | 0.57 | 0.13 | 0.70 | 2.00 | 0.00 | 0.00 | 2.00 | 45.44 | 0.53 | 0.46 | 0.04 | 1.99 |
| sd | | | | 0.94 | 0.15 | 0.19 | 0.51 | 0.12 | 0.30 | 0.23 | 0.10 | 0.04 | 0.89 | | | | | | | | | | | | | | | | | | | | | | | | | | | | |
| DR08-155 | 925 | 400 | 6 | 39.33 | 4.04 | 10.40 | 19.05 | 0.45 | 8.12 | 10.80 | 3.01 | 0.85 | 96.06 | low-Mg | 6.16 | 1.84 | 0.00 | 8.00 | 0.08 | 0.48 | 0.00 | 0.11 | 1.90 | 2.38 | 0.06 | 5.00 | 1.81 | 0.19 | 2.00 | 0.73 | 0.17 | 0.89 | 2.00 | 0.00 | 0.00 | 2.00 | 45.89 | 0.44 | 0.43 | 0.04 | 1.92 |
| sd | | | | 0.61 | 0.20 | 0.23 | 0.40 | 0.05 | 0.20 | 0.26 | 0.07 | 0.03 | 0.47 | | | | | | | | | | | | | | | | | | | | | | | | | | | | |
| DR08-156 | 925 | 400 | 1 | 39.48 | 4.32 | 10.75 | 18.24 | 0.45 | 7.66 | 11.42 | 2.98 | 0.92 | 96.23 | low-Mg | 6.22 | 1.78 | 0.00 | 8.00 | 0.22 | 0.51 | 0.00 | 0.00 | 1.80 | 2.41 | 0.06 | 5.00 | 1.93 | 0.07 | 2.00 | 0.84 | 0.18 | 1.02 | 2.00 | 0.00 | 0.00 | 2.00 | 46.42 | 0.43 | 0.43 | 0.11 | 2.00 |
| DR08-157 | 925 | 400 | 1 | 40.53 | 3.89 | 12.15 | 17.63 | 0.32 | 7.00 | 10.99 | 3.23 | 0.96 | 96.70 | low-Mg | 6.33 | 1.67 | 0.00 | 8.00 | 0.57 | 0.46 | 0.00 | 0.00 | 1.63 | 2.30 | 0.04 | 5.00 | 1.84 | 0.16 | 2.00 | 0.82 | 0.19 | 1.01 | 2.00 | 0.00 | 0.00 | 2.00 | 46.66 | 0.41 | 0.41 | 0.25 | 2.24 |
| sd | | | | | | | | | | | | | | | | | | | | | | | | | | | | | | | | | | | | | | | | | |
| DR08-56 | 950 | 200 | 5 | 39.495 | 4.4431 | 11.74 | 12.44 | 0.27 | 12.61 | 11.03 | 2.62 | 0.85 | 95.50 | kaersutite | 5.96 | 2.04 | 0.00 | 8.00 | 0.05 | 0.50 | 0.00 | 0.48 | 2.84 | 1.09 | 0.03 | 5.00 | 1.78 | 0.22 | 2.00 | 0.55 | 0.16 | 0.71 | 2.00 | 0.00 | 0.00 | 2.00 | 45.52 | 0.72 | 0.64 | 0.03 | 2.09 |
| sd | | | | 0.2655 | 0.2434 | 0.22 | 0.11 | 0.05 | 0.15 | 0.23 | 0.13 | 0.08 | 0.44 | | | | | | | | | | | | | | | | | | | | | | | | | | | | |
| DR08-58 | 950 | 200 | 5 | 39.336 | 5.0109 | 11.10 | 14.51 | 0.28 | 10.84 | 11.56 | 2.68 | 0.98 | 96.30 | kaersutite | 6.04 | 1.96 | 0.00 | 8.00 | 0.04 | 0.58 | 0.00 | 0.00 | 2.48 | 1.86 | 0.04 | 5.00 | 1.90 | 0.10 | 2.00 | 0.70 | 0.19 | 0.89 | 2.00 | 0.00 | 0.00 | 2.00 | 46.03 | 0.57 | 0.57 | 0.02 | 2.01 |
| sd | | | | 0.1415 | 0.3008 | 0.36 | 0.69 | 0.07 | 0.08 | 0.53 | 0.12 | 0.10 | 0.88 | | | | | | | | | | | | | | | | | | | | | | | | | | | | |

(continued on next page)

**Table 4.** (continued)

| Charge | $T$ (°C) | $P$ (MPa) | $n$ | $SiO_2$ | $TiO_2$ | $Al_2O_3$ | FeO* | MnO | MgO | CaO | $Na_2O$ | $K_2O$ | Sum | Species | Si | AlIV | Ti | T sum | AlVI | Ti | Cr | $Fe^{3+}$ | Mg | $Fe^{2+}$ | Mn | C sum | Ca | Na | B sum | Na | K | A sum | OH | F | Cl | W sum | Charge | Mg/(Mg + $Fe^{2+}$) | Mg# | Al# | AlT |
|---|---|---|---|---|---|---|---|---|---|---|---|---|---|---|---|---|---|---|---|---|---|---|---|---|---|---|---|---|---|---|---|---|---|---|---|---|---|---|---|---|---|
| DR08-129 | 925 | 200 | 3 | 38.76 | 3.58 | 12.34 | 13.13 | 0.32 | 11.82 | 11.33 | 2.65 | 0.86 | 94.78 | Mg-hastingsite | 5.94 | 2.06 | 0.00 | 8.00 | 0.17 | 0.41 | 0.00 | 0.40 | 2.70 | 1.29 | 0.04 | 5.00 | 1.86 | 0.14 | 2.00 | 0.65 | 0.17 | 0.82 | 2.00 | 0.00 | 0.00 | 2.00 | 45.60 | 0.68 | 0.62 | 0.07 | 2.23 |
| sd | | | | 0.12 | 0.16 | 0.08 | 0.08 | 0.07 | 0.28 | 0.26 | 0.07 | 0.16 | 0.17 | | | | | | | | | | | | | | | | | | | | | | | | | | | | |
| DR08-131 | 925 | 200 | 3 | 39.08 | 3.78 | 11.19 | 16.27 | 0.33 | 10.49 | 10.75 | 2.83 | 0.84 | 95.57 | Mg-hastingsite | 6.00 | 2.00 | 0.00 | 8.00 | 0.03 | 0.44 | 0.00 | 0.55 | 2.40 | 1.54 | 0.04 | 5.00 | 1.77 | 0.23 | 2.00 | 0.61 | 0.16 | 0.78 | 2.00 | 0.00 | 0.00 | 2.00 | 45.45 | 0.61 | 0.53 | 0.01 | 2.03 |
| sd | | | | 0.05 | 0.08 | 0.00 | 0.31 | 0.03 | 0.21 | 0.10 | 0.13 | 0.02 | 0.14 | | | | | | | | | | | | | | | | | | | | | | | | | | | | |
| DR08-158 | 925 | 150 | 3 | 40.12 | 3.67 | 11.78 | 15.39 | 0.26 | 11.38 | 11.22 | 2.82 | 0.68 | 97.34 | Mg-hastingsite | 6.01 | 1.99 | 0.00 | 8.00 | 0.09 | 0.41 | 0.00 | 0.53 | 2.54 | 1.40 | 0.03 | 5.00 | 1.80 | 0.20 | 2.00 | 0.62 | 0.13 | 0.75 | 2.00 | 0.00 | 0.00 | 2.00 | 45.47 | 0.65 | 0.57 | 0.04 | 2.08 |
| sd | | | | 0.83 | 0.23 | 0.25 | 0.30 | 0.10 | 0.28 | 0.23 | 0.02 | 0.15 | 0.84 | | | | | | | | | | | | | | | | | | | | | | | | | | | | |
| DR08-159 | 925 | 150 | 3 | 40.63 | 3.68 | 11.43 | 15.42 | 0.36 | 11.21 | 11.07 | 2.89 | 0.69 | 97.38 | Mg-hastingsite | 6.09 | 1.91 | 0.00 | 8.00 | 0.10 | 0.41 | 0.00 | 0.45 | 2.50 | 1.48 | 0.05 | 5.00 | 1.78 | 0.22 | 2.00 | 0.62 | 0.13 | 0.75 | 2.00 | 0.00 | 0.00 | 2.00 | 45.55 | 0.63 | 0.56 | 0.05 | 2.02 |
| sd | | | | 0.16 | 0.14 | 0.06 | 0.55 | 0.13 | 0.11 | 0.30 | 0.10 | 0.09 | 0.29 | | | | | | | | | | | | | | | | | | | | | | | | | | | | |
| DR08-160 | 925 | 150 | 3 | 39.45 | 3.93 | 10.65 | 15.66 | 0.37 | 10.56 | 11.71 | 3.01 | 0.86 | 96.19 | Pargasite | 6.10 | 1.90 | 0.00 | 8.00 | 0.04 | 0.46 | 0.00 | 0.00 | 2.43 | 2.02 | 0.05 | 5.00 | 1.94 | 0.06 | 2.00 | 0.84 | 0.17 | 1.01 | 2.00 | 0.00 | 0.00 | 2.00 | 46.00 | 0.55 | 0.55 | 0.02 | 1.94 |
| sd | | | | 0.38 | 0.11 | 0.38 | 0.43 | 0.09 | 0.43 | 0.62 | 0.04 | 0.10 | 0.76 | | | | | | | | | | | | | | | | | | | | | | | | | | | | |
| DR08-161 | 925 | 150 | 1 | 40.30 | 4.19 | 10.89 | 16.32 | 0.44 | 10.64 | 11.03 | 2.89 | 0.85 | 97.56 | Mg-hastingsite | 6.08 | 1.92 | 0.00 | 8.00 | 0.02 | 0.48 | 0.00 | 0.38 | 2.39 | 1.68 | 0.06 | 5.00 | 1.78 | 0.22 | 2.00 | 0.63 | 0.16 | 0.79 | 2.00 | 0.00 | 0.00 | 2.00 | 45.62 | 0.59 | 0.54 | 0.01 | 1.94 |
| DR08-164 | 925 | 100 | 4 | 39.99 | 4.23 | 11.07 | 14.57 | 0.28 | 11.14 | 11.70 | 2.81 | 0.71 | 96.51 | Pargasite | 6.10 | 1.90 | 0.00 | 8.00 | 0.09 | 0.49 | 0.00 | 0.05 | 2.53 | 1.81 | 0.04 | 5.00 | 1.91 | 0.09 | 2.00 | 0.74 | 0.14 | 0.88 | 2.00 | 0.00 | 0.00 | 2.00 | 45.95 | 0.58 | 0.58 | 0.04 | 1.99 |
| sd | | | | 0.18 | 0.25 | 0.16 | 0.24 | 0.10 | 0.14 | 0.25 | 0.10 | 0.05 | 0.29 | | | | | | | | | | | | | | | | | | | | | | | | | | | | |
| DR08-165 | 925 | 100 | 2 | 39.74 | 4.36 | 10.53 | 14.83 | 0.34 | 10.85 | 12.21 | 2.91 | 0.83 | 96.60 | kaersutite | 6.13 | 1.87 | 0.00 | 8.00 | 0.04 | 0.51 | 0.00 | 0.00 | 2.49 | 1.91 | 0.04 | 5.00 | 2.02 | -0.02 | 2.00 | 0.89 | 0.16 | 1.05 | 2.00 | 0.00 | 0.00 | 2.00 | 46.25 | 0.57 | 0.57 | 0.02 | 1.91 |
| sd | | | | 0.54 | 0.16 | 0.34 | 0.12 | 0.05 | 0.09 | 0.59 | 0.07 | 0.00 | 0.68 | | | | | | | | | | | | | | | | | | | | | | | | | | | | |
| DR08-166 | 925 | 100 | 2 | 39.54 | 4.46 | 10.17 | 14.92 | 0.25 | 10.59 | 12.29 | 2.88 | 0.93 | 96.04 | kaersutite | 6.17 | 1.83 | 0.00 | 8.00 | 0.04 | 0.52 | 0.00 | 0.00 | 2.46 | 1.95 | 0.03 | 5.00 | 2.05 | -0.05 | 2.00 | 0.93 | 0.19 | 1.11 | 2.00 | 0.00 | 0.00 | 2.00 | 46.41 | 0.56 | 0.56 | 0.02 | 1.87 |
| sd | | | | 0.27 | 0.12 | 0.68 | 0.05 | 0.12 | 0.21 | 0.72 | 0.01 | 0.04 | 0.79 | | | | | | | | | | | | | | | | | | | | | | | | | | | | |

$n$: number of analysis.

sd: standard deviation.

FeO*: Total iron reported as $Fe^{2+}$.

**Table 5.** Experimental biotite composition

| Charge | $T$ (°C) | $P$ (MPa) | $n$ | $SiO_2$ | $TiO_2$ | $Al_2O_3$ | FeO* | MnO | MgO | CaO | $Na_2O$ | $K_2O$ | Sum | Mg# |
|---|---|---|---|---|---|---|---|---|---|---|---|---|---|---|
| DR08-140 | 950 | 400 | 2 | 35.02 | 3.67 | 14.25 | 11.51 | 0.10 | 15.30 | 0.10 | 1.40 | 7.19 | 88.55 | 70.33 |
| sd | | | | 0.83 | 0.02 | 0.38 | 0.06 | 0.04 | 0.68 | 0.08 | 0.13 | 0.08 | 0.24 | |
| DR08-141 | 950 | 400 | 1 | 34.77 | 5.54 | 15.35 | 16.50 | 0.09 | 12.35 | 0.11 | 1.27 | 7.17 | 93.15 | 57.16 |
| DR08-145 | 950 | 400 | 1 | 38.21 | 7.24 | 14.21 | 17.26 | 0.13 | 8.51 | 3.04 | 1.63 | 6.46 | 96.70 | 46.78 |
| DR08-152 | 925 | 400 | 1 | 37.27 | 3.96 | 15.79 | 16.29 | 0.18 | 12.79 | 0.37 | 1.50 | 7.14 | 95.28 | 58.32 |
| DR08-130 | 925 | 200 | 1 | 34.77 | 5.81 | 15.40 | 18.24 | 0.11 | 12.23 | 0.55 | 1.24 | 7.18 | 95.53 | 54.44 |
| DR08-158 | 925 | 150 | 1 | 37.86 | 4.87 | 16.12 | 15.23 | 0.15 | 11.85 | 0.51 | 1.43 | 6.50 | 94.51 | 58.11 |
| DR08-159 | 925 | 150 | 1 | 34.11 | 5.56 | 14.27 | 16.37 | 0.26 | 13.18 | 0.27 | 1.34 | 6.73 | 92.08 | 58.93 |

$n$: number of analysis.

sd: standard deviation.

FeO*: Total iron reported as $Fe^{2+}$.

Mg# = 100*(MgO/MgO + FeO*).

closed-system, the low-residuals indicate that there was no mass loss or gain during the experiments, and that no major mineral phase has been omitted in our calculations.

## 4. Results

Phase proportions were obtained by mass-balance calculations of the charges using the bulk rock composition and the composition of the different mineral and glass phases. Results are provided in Table 2.

### 4.1. *Phase relationships*

The main mineral phases crystallizing in our runs are Bt (biotite), Amp (Kaersutite-type), Ol, Mt, Ilm, Ap, Pl and Cpx, with different glass proportions. Variations in temperature, pressure and $H_2O_{melt}$ directly affect the stability and relationships of the different minerals. These changes are displayed in two isothermal-polybaric sections described below (Figure 3).

At 925 °C, the water-rich part of the diagram ($H_2O_{melt}$ > 4 wt%) is dominated by the assemblage Bt+Amp+Mt+Ap+melt, followed by Ilm, Pl and Cpx with decreasing $H_2O_{melt}$ (Figure 3A). Cpx coexists in a relatively narrow $H_2O_{melt}$ region with Amp, both being involved along with Pl and melt, in a reaction-relationship that results in the disappearance of Amp at lower $H_2O_{melt}$ (Figure 3A). Bt is stable everywhere in the $P$–$H_2O_{melt}$ space explored. However, the decrease of its modal proportion with $H_2O_{melt}$ (Table 2) and the consequent enrichment of the residual liquid in $K_2O$ point towards its instability in the driest part of the system (Figure 3A). Hence, at 925 °C and for $H_2O_{melt}$ < 1 wt%, the mineral assemblage that dominates the explored $P$-$H_2O_{melt}$ region is Ol+Cpx+Pl+Ap+Mt+Ilm.

At this temperature and for pressures between 100 and 200 MPa, the Amp-out and Cpx, Ol, Ilm and Pl-in curves display steep or even vertical slopes, all occurring in a narrow $H_2O_{melt}$ interval between 2.5–3 wt% (Figure 3A). Above 200 MPa, Cpx-in and Amp-out curves shrink towards lower $H_2O_{melt}$ (≤2 wt%) whereas Ilm stability shifts towards higher $H_2O_{melt}$. Pressure does not have any major effect on Ol and Pl saturation curves.

At 950 °C, the general topology is broadly similar to that at 925 °C (Figure 3B), with Pl and Cpx appearing at $H_2O_{melt}$ < 2–3 wt%, as anticipated, and Ol crystallizing first relative to Pl.

### 4.2. *Phase proportions*

Since experiments were performed at relatively low temperatures, liquidus conditions were not reached during the experiments. Charges always contained different amounts of crystals, which vary between 29 and 66 wt% (Figure 4A). In general, at fixed $P$–$T$ conditions, the crystal proportions increase as $H_2O_{melt}$ decreases (Figure 4A). Amp is the dominant phase

**Table 6.** Experimental Magnetite and ilmenite compositions (wt%)

| Charge | $T$ (°C) | $P$ (MPa) | $n$ | $SiO_2$ | $TiO_2$ | $Al_2O_3$ | FeO* | MnO | MgO | CaO | $Na_2O$ | $K_2O$ | $Cr_2O_3$ | Sum | X-Usp | X-Ilm |
|---|---|---|---|---|---|---|---|---|---|---|---|---|---|---|---|---|
| DR08-140 | 950 | 400 | 1 | 0.17 | 20.16 | 3.45 | 72.00 | 0.70 | 2.70 | 0.19 | 0.06 | 0.10 | 0.46 | 100 | 0.60 | |
| DR08-141 | 950 | 400 | 1 | 1.80 | 49.68 | 1.82 | 41.63 | 0.78 | 2.26 | 1.41 | 0.33 | 0.21 | 0.09 | 100 | | 0.99 |
| DR08-141 | 950 | 400 | 1 | 0.11 | 21.47 | 4.31 | 71.25 | 0.64 | 2.00 | 0.08 | 0.05 | 0.07 | 0.03 | 100 | 0.67 | |
| DR08-142 | 950 | 400 | 1 | 0.10 | 50.89 | 0.38 | 44.61 | 1.07 | 2.50 | 0.29 | 0.04 | 0.09 | 0.03 | 100 | | 0.95 |
| DR08-142 | 950 | 400 | 1 | 0.12 | 21.43 | 4.59 | 71.06 | 0.66 | 1.92 | 0.15 | 0.03 | 0.01 | 0.04 | 100 | 0.67 | |
| DR08-143 | 950 | 400 | 1 | 0.10 | 21.79 | 4.22 | 71.05 | 0.66 | 1.93 | 0.10 | 0.04 | 0.05 | 0.05 | 100 | 0.68 | |
| DR08-152 | 925 | 400 | 1 | 0.11 | 49.52 | 0.20 | 46.08 | 0.96 | 2.82 | 0.20 | 0.04 | 0.05 | 0.02 | 100 | | 0.92 |
| DR08-152 | 925 | 400 | 1 | 0.03 | 19.91 | 3.07 | 73.05 | 0.95 | 1.94 | 0.11 | 0.06 | 0.07 | 0.81 | 100 | 0.59 | |
| DR08-154 | 925 | 400 | 1 | 0.72 | 21.63 | 3.02 | 70.50 | 1.11 | 1.53 | 0.29 | 0.03 | 0.12 | 1.04 | 100 | 0.67 | |
| DR08-56 | 950 | 200 | 3 | 0.37 | 21.93 | 3.66 | 69.75 | 0.78 | 2.94 | 0.28 | 0.03 | 0.06 | 0.14 | 100 | 0.66 | |
| sd | | | | 0.18 | 0.33 | 0.05 | 0.98 | 0.05 | 0.03 | 0.05 | 0.02 | 0.04 | 0.03 | | | |
| DR08-58 | 950 | 200 | 1 | 0.33 | 24.63 | 3.20 | 67.79 | 0.78 | 2.74 | 0.33 | 0.00 | 0.15 | 0.00 | 100 | 0.74 | |
| DR08-129 | 925 | 200 | 1 | 0.46 | 20.15 | 3.45 | 71.65 | 0.92 | 2.41 | 0.31 | 0.04 | 0.07 | 0.53 | 100 | 0.61 | |
| DR08-131 | 925 | 200 | 1 | 0.32 | 20.06 | 3.88 | 70.74 | 0.96 | 2.14 | 0.26 | 0.00 | 0.07 | 1.58 | 100 | 0.62 | |
| DR08-158 | 925 | 150 | 1 | 0.71 | 18.75 | 3.57 | 72.26 | 0.79 | 2.37 | 0.92 | 0.07 | 0.03 | 0.53 | 100 | 0.57 | |
| DR08-159 | 925 | 150 | 1 | 0.44 | 18.16 | 3.61 | 73.69 | 0.87 | 2.34 | 0.76 | 0.00 | 0.08 | 0.04 | 100 | 0.54 | |
| DR08-160 | 925 | 150 | 1 | 0.28 | 20.01 | 2.82 | 72.36 | 0.94 | 2.27 | 0.23 | 0.00 | 0.02 | 1.06 | 100 | 0.59 | |
| DR08-161 | 925 | 150 | 1 | 0.11 | 21.76 | 2.27 | 70.29 | 1.13 | 2.21 | 0.20 | 0.04 | 0.07 | 1.91 | 100 | 0.63 | |
| DR08-165 | 925 | 100 | 1 | 1.89 | 18.78 | 3.22 | 69.89 | 0.98 | 2.41 | 0.34 | 0.20 | 0.15 | 2.14 | 100 | 0.61 | |
| DR08-165 | 925 | 100 | 1 | 0.06 | 51.45 | 0.18 | 41.95 | 1.57 | 4.58 | 0.18 | 0.00 | 0.02 | 0.02 | 100 | | 0.94 |
| DR08-166 | 925 | 100 | 1 | 1.67 | 19.18 | 2.92 | 70.17 | 0.94 | 2.14 | 0.38 | 0.17 | 0.14 | 2.29 | 100 | 0.61 | |
| DR08-166 | 925 | 100 | 1 | 0.17 | 50.35 | 0.18 | 43.95 | 1.47 | 3.50 | 0.26 | 0.05 | 0.07 | 0.00 | 100 | | 0.93 |

$n$: number of analysis.

sd: standard deviation.

FeO*: Total iron reported as $Fe^{2+}$.

X-Ilm: Ilmenite fraction in in ilmenite calculated as in Andersen and Lindsley [1998].

X-Usp: Ulvöspinel fraction in Magnetite calculated as in Andersen and Lindsley [1998].

**Table 7.** Experimental clinopyroxenes composition (wt%)

| Charge | *T* (°C) | *P* (MPa) | *n* | $SiO_2$ | $TiO_2$ | $Al_2O_3$ | FeO* | MnO | MgO | CaO | $Na_2O$ | $K_2O$ | Total | En | Fs | Wo | Mg# |
|---|---|---|---|---|---|---|---|---|---|---|---|---|---|---|---|---|---|
| DR08-145 | 950 | 400 | 1 | 47.78 | 1.45 | 4.03 | 10.89 | 0.29 | 10.73 | 20.54 | 0.95 | 0.37 | 97.03 | 33.77 | 19.23 | 46.47 | 63.72 |
| DR08-160 | 925 | 150 | 3 | 49.09 | 0.95 | 2.96 | 11.78 | 0.62 | 11.71 | 20.76 | 0.72 | 0.08 | 98.65 | 34.86 | 19.67 | 44.43 | 63.94 |
| | | | | 0.60 | 0.19 | 0.16 | 0.57 | 0.09 | 0.13 | 0.19 | 0.09 | 0.04 | 0.66 | 0.15 | 0.70 | 0.82 | 0.85 |

*n*: number of analysis.

sd: standard deviation.

FeO*: Total iron reported as $Fe^{2+}$.

**Table 8.** Composition of experimental glasses normalized to 100% anhydrous (wt%)

| Charge | $T$ (°C) | $P$ (MPa) | $n$ | $SiO_2$ | $TiO_2$ | $Al_2O_3$ | FeO* | MnO | MgO | CaO | $Na_2O$ | $K_2O$ | $P_2O_5$ | Total | Original sum | P.I. = (Na + K/Al) | Normative Nepheline (wt%) |
|---|---|---|---|---|---|---|---|---|---|---|---|---|---|---|---|---|---|
| DR08-140 | 950 | 400 | 5 | 58.57 | 0.99 | 18.37 | 6.83 | 0.17 | 1.61 | 4.33 | 5.98 | 2.75 | 0.39 | 100 | 85.72 | 0.70 | |
| sd | | | | 0.42 | 0.08 | 0.25 | 0.22 | 0.07 | 0.08 | 0.07 | 0.56 | 0.15 | 0.07 | | 0.53 | | |
| DR08-141 | 950 | 400 | 7 | 59.95 | 0.68 | 19.60 | 5.71 | 0.15 | 1.00 | 2.90 | 6.35 | 3.24 | 0.43 | 100 | 93.86 | 0.72 | |
| sd | | | | 0.58 | 0.08 | 0.10 | 0.25 | 0.08 | 0.03 | 0.03 | 0.34 | 0.10 | 0.08 | | 0.78 | | |
| DR08-142 | 950 | 400 | 3 | 60.50 | 0.68 | 19.97 | 6.13 | 0.15 | 1.00 | 2.90 | 6.53 | 3.24 | 0.19 | 100 | 95.13 | 0.72 | |
| sd | | | | 0.61 | 0.18 | 0.18 | 0.21 | 0.06 | 0.20 | 0.04 | 0.29 | 0.07 | 0.01 | | 0.83 | | |
| DR08-143 | 950 | 400 | 1 | 60.68 | 0.51 | 18.36 | 4.79 | 0.15 | 0.58 | 1.77 | 7.60 | 5.24 | 0.32 | 100 | 88.50 | 1.00 | 7.2 |
| sd | | | | | | | | | | | | | | | | | |
| DR08-152 | 925 | 400 | 3 | 60.41 | 0.78 | 18.98 | 5.66 | 0.15 | 0.97 | 3.71 | 6.34 | 2.59 | 0.42 | 100 | 88.08 | 0.70 | |
| sd | | | | 0.34 | 0.13 | 0.23 | 0.46 | 0.11 | 0.16 | 0.06 | 0.18 | 0.05 | 0.20 | | 0.36 | | |
| DR08-154 | 925 | 400 | 1 | 62.53 | 0.42 | 18.20 | 5.15 | 0.03 | 0.51 | 1.83 | 7.40 | 3.54 | 0.39 | 100 | 95.23 | 0.88 | |
| DR08-56 | 950 | 200 | 2 | 58.01 | 0.95 | 18.59 | 7.08 | 0.29 | 1.50 | 3.87 | 6.25 | 3.19 | 0.30 | 100 | 92.90 | 0.74 | |
| sd | | | | 0.44 | 0.09 | 0.09 | 0.21 | 0.01 | 0.07 | 0.01 | 0.16 | 0.03 | 0.02 | | 0.93 | | |
| DR08-58 | 950 | 200 | 2 | 58.58 | 0.77 | 18.50 | 7.41 | 0.22 | 0.86 | 2.57 | 6.45 | 4.22 | 0.41 | 100 | 94.58 | 0.83 | 0.1 |
| sd | | | | 0.53 | 0.05 | 0.07 | 0.37 | 0.11 | 0.00 | 0.07 | 0.08 | 0.09 | 0.15 | | 0.28 | | |
| DR08-129 | 925 | 200 | 2 | 58.84 | 0.62 | 18.71 | 6.96 | 0.18 | 0.73 | 3.47 | 6.40 | 3.16 | 0.91 | 100 | 94.39 | 0.75 | |
| sd | | | | 0.09 | 0.04 | 0.01 | 0.59 | 0.01 | 0.07 | 0.15 | 0.06 | 0.23 | 0.09 | | 0.34 | | |
| DR08-130 | 925 | 200 | 2 | 59.00 | 1.09 | 18.96 | 6.55 | 0.17 | 0.67 | 3.16 | 6.32 | 3.24 | 0.83 | 100 | 93.87 | 0.74 | |
| sd | | | | 0.38 | 0.71 | 0.50 | 0.02 | 0.11 | 0.01 | 0.01 | 0.16 | 0.03 | 0.22 | | 1.34 | | |
| DR08-131 | 925 | 200 | 1 | 59.23 | 0.49 | 18.39 | 7.16 | 0.05 | 0.49 | 1.76 | 7.30 | 4.96 | 0.16 | 100 | 97.57 | 0.95 | 6.4 |

(continued on next page)

**Table 8.** (continued)

| Charge | $T$ (°C) | $P$ (MPa) | $n$ | $SiO_2$ | $TiO_2$ | $Al_2O_3$ | FeO* | MnO | MgO | CaO | $Na_2O$ | $K_2O$ | $P_2O_5$ | Total | Original sum | P.I. = (Na + K/Al) | Normative Nepheline (wt%) |
|---|---|---|---|---|---|---|---|---|---|---|---|---|---|---|---|---|---|
| DR08-158 | 925 | 150 | 9 | 60.78 | 0.68 | 19.29 | 5.02 | 0.16 | 1.01 | 3.04 | 6.51 | 3.21 | 0.31 | 100 | 92.67 | 0.74 | |
| sd | | | | 0.34 | 0.09 | 0.34 | 0.21 | 0.08 | 0.03 | 0.07 | 0.28 | 0.14 | 0.05 | | 0.68 | | |
| DR08-159 | 925 | 150 | 9 | 60.81 | 0.74 | 19.18 | 4.82 | 0.18 | 0.92 | 2.78 | 6.77 | 3.47 | 0.33 | 100 | 93.44 | 0.78 | |
| sd | | | | 0.56 | 0.07 | 0.25 | 0.56 | 0.05 | 0.10 | 0.14 | 0.20 | 0.10 | 0.08 | | 0.47 | | |
| DR08-160 | 925 | 150 | 2 | 60.52 | 0.63 | 19.25 | 4.92 | 0.16 | 0.80 | 2.73 | 6.75 | 3.80 | 0.44 | 100 | 95.98 | 0.79 | |
| sd | | | | 0.82 | 0.04 | 0.13 | 0.10 | 0.15 | 0.06 | 0.68 | 0.02 | 0.28 | 0.45 | | 1.23 | | |
| DR08-164 | 925 | 100 | 3 | 61.71 | 0.53 | 18.63 | 5.00 | 0.11 | 0.73 | 2.28 | 6.71 | 3.99 | 0.31 | 100 | 95.89 | 0.83 | |
| sd | | | | 0.03 | 0.03 | 0.23 | 0.15 | 0.04 | 0.05 | 0.11 | 0.17 | 0.18 | 0.07 | | 0.94 | | |
| DR08-165 | 925 | 100 | 2 | 61.81 | 0.59 | 19.39 | 5.02 | 0.00 | 0.74 | 2.10 | 6.44 | 3.78 | 0.14 | 100 | 94.98 | 0.76 | |
| sd | | | | 0.07 | 0.04 | 0.45 | 0.18 | 0.00 | 0.02 | 0.02 | 0.13 | 0.25 | 0.15 | | 0.35 | | |

$n$: number of analysis.

sd: standard deviation.

FeO*: Total iron reported as $Fe^{2+}$.

P.I: peralkaline index calculated as the (Na + K)/Al in moles.

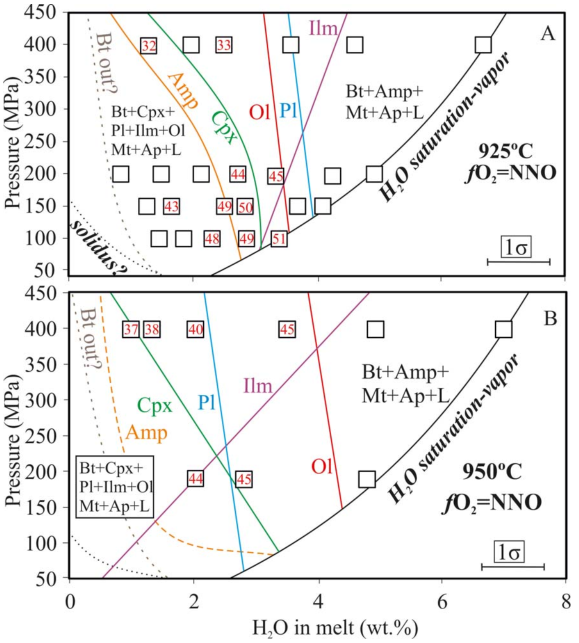


**Figure 3.** Isothermal phase relationships of the DR08 sample at (A) 925 °C and (B) 950 °C for different pressures and water contents in the melt. $fO_2$ ~ NNO: oxygen fugacity at water-saturation conditions. The decrease in $XH_2O$ (hence $H_2O_{melt}$) results in a decrease in $fO_2$ in the capsules (see text for details). Mt: magnetite, Bt: biotite, Cpx: clinopyroxene, Ilm: ilmenite, Amp: amphibole, Pl: plagioclase, Ap: apatite; Ol: olivine, L: liquid. Dashed lines are estimated phase boundaries. Numbers inside squares indicate the forsterite content (Fo) in moles of the crystallizing olivines (see text for details).

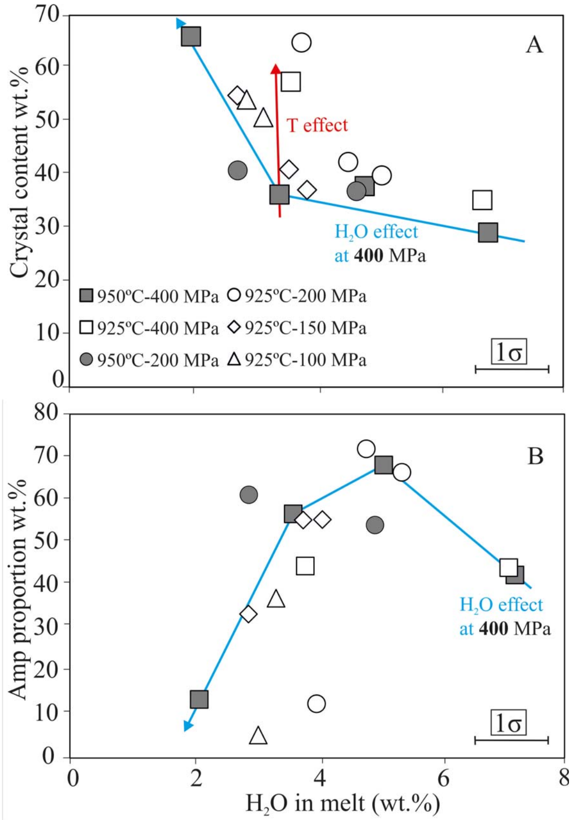


**Figure 4.** (A) Total crystal content of charges versus $H_2O_{melt}$. (B) Amph proportion in the fractionating crystal assemblage versus $H_2O_{melt}$. Vertical errors equal to symbol size.

whenever present, with proportions of up to 50–70 wt% of the crystallizing assemblage (Figure 4B); as $H_2O_{melt}$ decreases, the Amp content decreases below 15 wt%. With decreasing $H_2O_{melt}$, Mt, Bt and Ap proportions steadily decrease while Ol, Ilm, Cpx and Pl increase. However, compared to Amp, any of these phases never exceed 15–25 wt% (Table 2).

### 4.3. *Phase compositions*

Experimental phase compositions (minerals and glass) are displayed in Tables 3–9, in supplementary and their variation with experimental variables ($P$–$T$ and $H_2O_{melt}$) is discussed in the following sections.

#### 4.3.1. *Olivine*

Ol crystallizing in our charges varies between $Fo_{51-33}$, with relatively constant contents of MnO (1.4 ± 0.2 wt%), depending on $H_2O_{melt}$, temperature and pressure conditions (Table 3). At a given $P$ and $T$, a decrease in $H_2O_{melt}$ decreases the Fo and increases the CaO content of Ol, similarly to the trends observed in other basaltic compositions [Andújar et al., 2015, 2017, Berndt et al., 2005, Di Carlo et al., 2006]. This is well exemplified at 400 MPa and 950 °C where a decrease in $H_2O_{melt}$ of 2.5 wt% produces a diminution of 8 mol% of Fo (Figure 5A) and an increase of ~0.5 wt% in the CaO content of Ol (Figure 5B). A drop of 25 °C results in a relatively modest variation of Fo content, generally <5 mol% (Figure 5A). Series conducted at 925 °C allow to assess the effect of pressure on Ol composition. Considering a

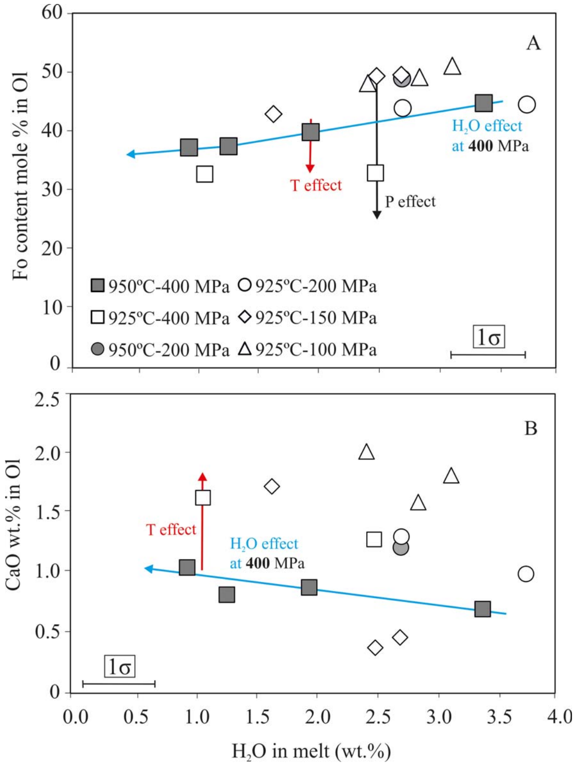


**Figure 5.** Composition of experimental olivine. (A) Fo content, (B) CaO (wt%) in Ol versus $H_2O_{melt}$. Vertical errors are equal to size symbols.

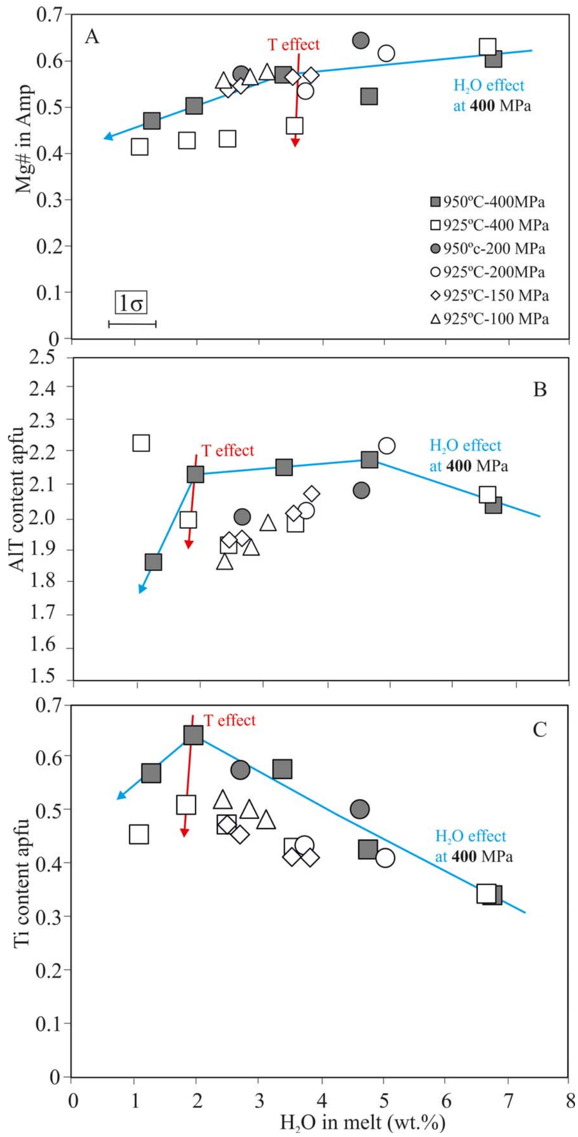


**Figure 6.** Composition of experimental amphibole. (A) Al total cations in atoms per formula unit (apfu), (B) Ti content and (C) Mg# = (Mg/Mg+$Fe_{total}$) versus $H_2O_{melt}$. Vertical errors equal to symbol size.

fixed $H_2O_{melt}$ (e.g. 2.5–3 wt%), runs conducted between 100–150 MPa crystallized Ol with a similar composition (e.g. ~$Fo_{50}$). Increasing $P$ by 50 MPa (so up to 200 MPa) produces changes in Ol composition that are equivalent to those observed with a $T$ diminution (i.e., decrease of 8 mol% in Fo; Figure 5A). At higher pressures, the effect of this parameter in olivine composition is more pronounced, since at 400 MPa, crystallizing Ol are highly more fayalitic ($Fo_{33}$) compared to their shallower counterparts (e.g., $Fo_{45-50}P \leq 200$ MPa). The average Ol–liquid exchange (KdFe*–Mg; using FeO* as total iron) is $0.29 \pm 0.1$ (varying between 0.25 and 0.44).

### 4.3.2. *Amphibole*

Based on Ridolfi [2021], Amp that were synthetized in our runs vary between pargasite, Mg-hastingsite and kaersutite (Table 4). At a fixed $P$, amphibole Mg# (calculated with Fe* in atoms per formula unit, apfu), $Al_{tot}$ and $Al_{IV}$ decrease by ~20% relative (Figure 6A,B), while Ti increases, as $H_2O_{melt}$ decreases (Figure 6C; Table 4). In series run at $P \leq 200$ MPa, a decrease of 25 °C does not significantly affect the composition of Amp. The variations of $Al_{tot}$, $Al_{IV}$ and $Al_{VI}$ with temperature and pressure have been widely used as a basis of empirical thermometers and barometers to infer crystallization conditions of Amp-bearing magmas. In this work, however, neither $Al_{IV}$ nor $Al_{VI}$ show obvious correlations with pressure/temperature changes. Only Amp crystallized at 950 °C, 2–5 wt% $H_2O_{melt}$ and 400 MPa have higher $Al_{tot}$ contents (0.1–0.2 apfu) than their 200 MPa counterparts (Figure 6B).

### 4.3.3. *Biotite*

Representative analyses are presented in Table 5. The Mg# (calculated with FeO*) varies between 70 and 47 when $H_2O_{melt}$ decreases from 7 to 1 wt%. $TiO_2$ content is inversely correlated with water content, the maximum (7 wt%) being achieved at ~1 wt% $H_2O_{melt}$ and conditions of 950 °C–400 MPa. Water-saturated charges (DR08-140 and DR08-152) at 400 MPa show a difference of 10% in Mg# when $T$ is decreased by 25 °C. Otherwise, under water-rich conditions and at constant $T$ (e.g. 925 °C), the decompression of the system from 400 to 200 MPa produces Ti-rich biotites. The limited set of data does not allow us to provide further constraints on the effect of pressure or temperature on Bt composition.

### 4.3.4. *Fe–Ti oxides*

Mt has a relatively constant $TiO_2$ content at ~22 ± 2.5 wt%, with more variable FeO* (68–74 wt%). When present, Ilm was often too small to obtain reliable compositions by EPMA. Nevertheless, analyzed Ilm in 5 charges have almost constant $TiO_2$, at 50 wt%, and FeO* contents in the range 42–46 wt% (Tables 6–7). As for other phases, changes in experimental parameters affect Mt and Ilm compositions. The effect of $H_2O_{melt}$ is significant: for example, in charges annealed at 950 °C–400 MPa, a decrease of 4 wt% $H_2O_{melt}$ decreases Mg# by ~4% (Figure 7A), FeO* by 1.5 wt% and increases %Ulvöspinel from 60 to 70% (Figure 7B). The other experimental series display quite similar trends (Figure 7). A decrease in temperature of 25 °C produces similar changes. As for olivine, the effect of pressure on Mt composition is enhanced within the interval 200–400 MPa, low pressure Mt being enriched in Mg# and depleted in FeO* and %Ulvöspinel (compare series run at 950 °C–400 and 200 MPa in Figure 7).

### 4.3.5. *Plagioclase*

Pl are mostly andesines with compositions between $An_{27}$–$An_{42}$ [Deer et al., 1972]. The most evolved Pl (oligoclase) crystallized instead in charges DR08-132, 155 and 161. As already observed in previous experimental studies performed on hydrous basaltic or basaltic andesite melts, Pl composition is highly sensitive to changes in $H_2O_{melt}$ [e.g. Andújar et al., 2015, 2017]. The most important compositional variations are observed in charges run at 925 °C and $P \leq 150$ MPa, where the decrease in 2 wt% $H_2O_{melt}$ results in a reduction of 10% in the mole fraction of An (see Supplementary Table). Similar variations in the CaO content of the experimental plagioclases can be produced when pressure decreases from 200 to 150 or 100 MPa at a given $H_2O_{melt}$, an effect that is again in agreement with the results of previous works [e.g. Andújar et al., 2015, 2017].

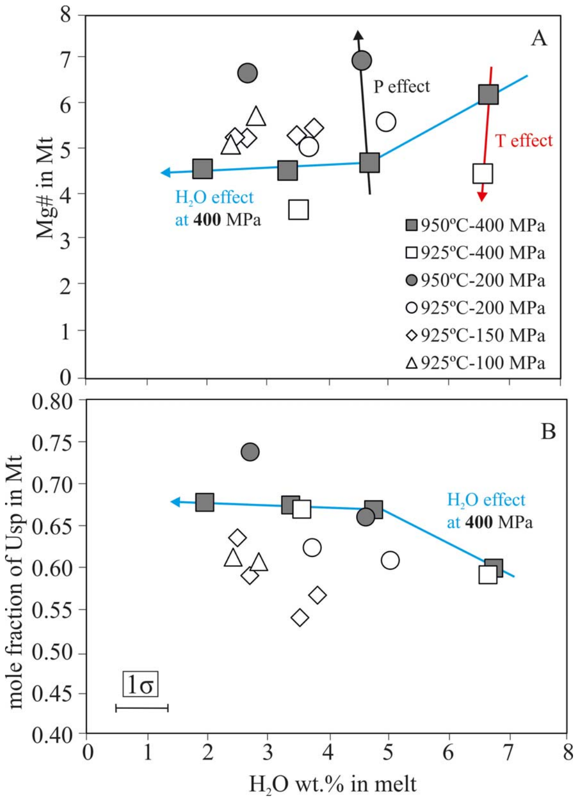


**Figure 7.** Composition of experimental magnetite. (A) Mg# = (MgO/MgO + FeO*), (B) Ulvöspinel content [calculated as in Andersen and Lindsley, 1998] versus $H_2O_{melt}$. Vertical errors equal to symbol size.

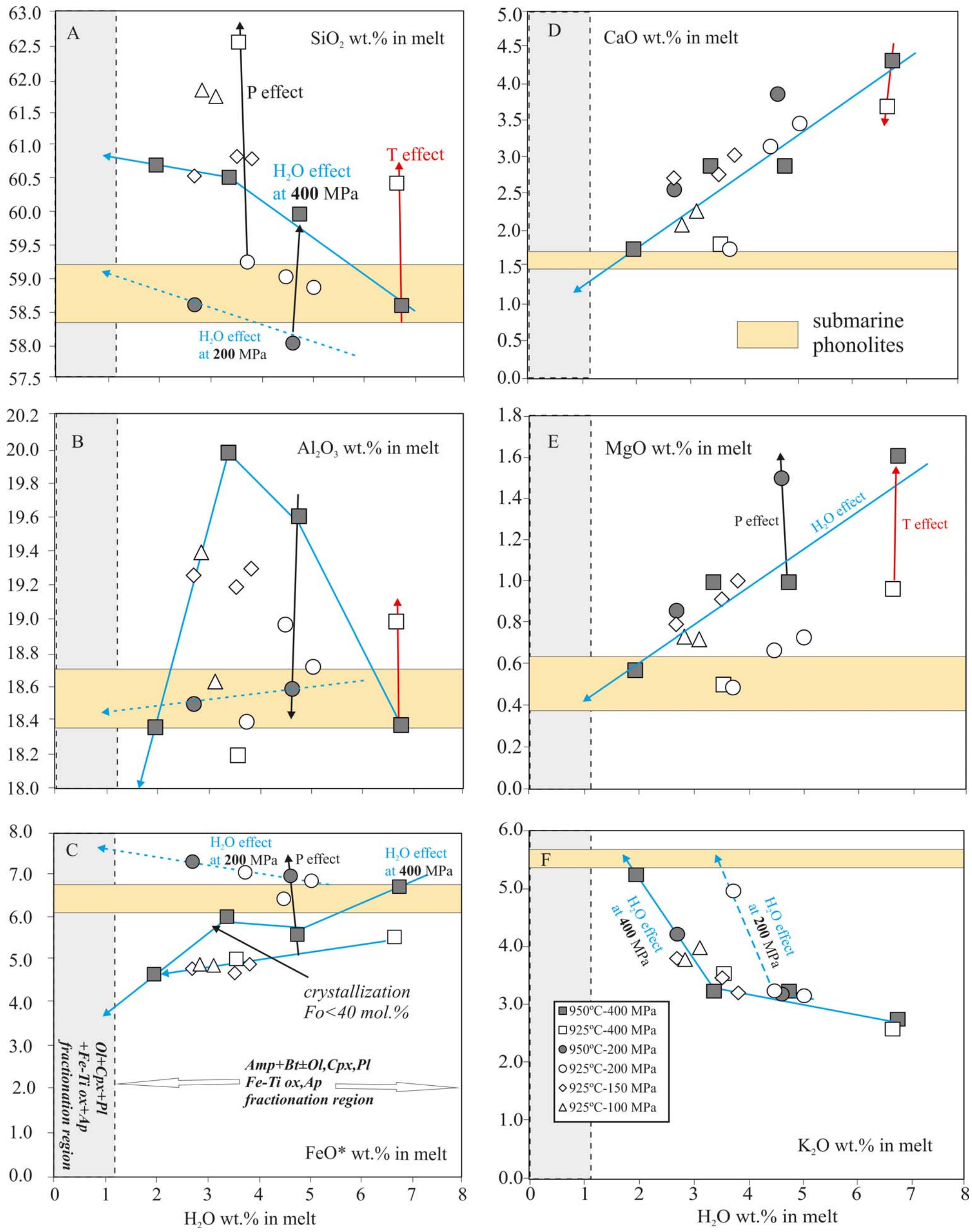


**Figure 8.** Experimental glass compositional variations of major and minor oxides versus $H_2O_{melt}$. For each graph, the yellow horizontal bar shows the natural compositions of phonolites dredged on the Horseshoe site (Table 1). Grey vertical bar shows the fractionation region for Ol+Cpx+Mt+Ilm+Ap (see text for details). Vertical errors equal the symbol sizes.

### 4.3.6. *Experimental glasses*

Residual glass compositions (calculated on a 100% anhydrous basis) have benmoreitic–trachytic affinities (according to the classification of Le Bas and Streckeisen [1991] with P.I. (peralkaline indice, =Na+K/Al in moles) at 0.7–1 (Figures 8–9, Table 9). Only charges DR08-143 and DR08-131 produced liquids that straddle the phonolite–trachyte boundary line (Figure 9), having a P.I. = 0.95–1, normative nepheline (6.5–7%) and containing 2–4 wt% $H_2O_{melt}$ (Table 8). The production of benmoreitic–trachytic–phonolitic liquids reflects the significant degree of crystallization of the charges. In the range of temperatures explored in this work, crystallization is dominated by Amp+Bt along with different proportions of Fe–Ti oxides+Ap for $H_2O_{melt}$ in the range 2–7 wt% (Figures 3–4, Table 2). The onset of Pl+Ol+Cpx crystallization results in a drastic decrease of Mt, Amp and Bt proportions until the breakdown of the two last phases which occurs at ≤2 wt% $H_2O_{melt}$ (Figure 3). The combination of the above factors increases both the $SiO_2$ and the alkalinity of the residual melt, which reaches the phonolitic field (Figure 9A). In parallel, $TiO_2$ (not shown), CaO and MgO decrease (Figure 8B,D). In contrast, FeO* may even slightly increase when $H_2O_{melt}$ decreases (Figure 8C), though by a modest amount (usually <0.5 wt%). This Fe-enrichment is due to the changing proportions of hydrous Fe–Mg phases and Mt (Table 2). In comparison, a decrease of 200 MPa lowers FeO* by ∼1.5–2 wt% for a given $H_2O_{melt}$ (Figure 8C). Below 3 wt% $H_2O_{melt}$, the liquid produced at 400 MPa are even more depleted in FeO* (Figure 8C). This is due to the fact that, at 200 MPa, the precipitation of a relatively Fe-poor Ol ($Fo_{45-40}$) enhances the iron-enrichment process. In contrast, at 400 MPa, the crystallization of significant amounts of relatively fayalitic-rich Ol (e.g., Fo ≤ 38) counteracts the depleting role of Mt at higher $H_2O_{melt}$ (Figures 3, 8C). Such a difference explains why charges at 200 MPa yield melts with the highest analyzed FeO* contents (7.4 wt%) compared to their high-pressure counterparts, which achieved only a maximum of 6.7 wt% FeO*, and under very high $H_2O_{melt}$.

Another striking point concerns the charges annealed at 100–150 MPa since these yield residual melt compositions overlaping those produced at higher $P$ (≥200 MPa), not only in terms of iron but also in the other major elements (Figure 8). In fact, despite the presence of moderate proportions of olivine with compositions $Fo_{51-43}$ (Figure 5A, Table 3), which according to 200 MPa data promotes the Fe-enrichment of the melt, the co-crystallization of ∼8 wt% of Fe-rich magnetite and different amounts of Cpx+Pl±Bt±Amp inhibit the Fe-enrichment process and drive the residual melt towards more Si- and Al-rich and low P.I. compositions [Figures 8–9; Table 8; Botcharnikov et al., 2008, Giehl et al., 2013, Scaillet and MacDonald, 2006, Toplis and Carroll, 1995]. The effect of $P$ variation is not restricted to FeO*; as pressure increases, the $SiO_2$, CaO increase with decreasing $Al_2O_3$ content, MgO and alkalis being somewhat less affected (Figure 8).

It should be also noted that between 7 and 3 wt% $H_2O_{melt}$, the precipitation of Amp along with Bt in amounts, representing 60–80% of the total crystal cargo, increases the $SiO_2$ and $Al_2O_3$ content but buffers $K_2O$ at ∼3 wt% (Figure 8F). Below this $H_2O_{melt}$, the crystallization of Ol+Cpx+Pl, along with a drastic drop of Amp+Bt+Mt proportions, increases the potassium content of the melt by ∼50% relative (Figure 8F). $Na_2O$ follows a similar trend but the observed enrichment is less significant compared to $K_2O$. The evolution of $Al_2O_3$ is well illustrated in series run at 200–400 MPa where $Al_2O_3$ increases when $H_2O_{melt}$ decreases until the onset of Pl crystallization (Figure 8B). Pl crystallization in relative high proportions (up to ∼30 wt%; Table 2) decreases the $Al_2O_3$ and accelerates the evolution of the residual melts towards alkali-rich compositions.

Aside from water and pressure, temperature is also an important parameter controlling melt composition. At lower temperatures (i.e. 925 °C) and for a fixed $H_2O_{melt}$, residual liquids tend to be enriched in $SiO_2$ and $Na_2O$ but depleted in $TiO_2$, MgO and CaO when compared to melts produced at 950 °C. FeO*, $K_2O$ and $Al_2O_3$ do not show any clear relationship with $T$ in charges run at $P$ ≤ 200 MPa. Only those at 400 MPa and 950 °C have higher $Al_2O_3$ and FeO compared to their colder counterparts (Figure 8).

In summary, the fractionation of a relatively hydrous basanite under low oxygen fugacity conditions ($fO_2$ ≤ FMQ; Table 2), at temperatures between 925–950 °C and 200–400 MPa (corresponding to depths of 6–12 km) produces Fe-rich phonolitic liquids containing 2–4 wt% dissolved $H_2O$. In the next section, we use the composition of the natural phonolites dredged along the Mayotte submarine ridge or collected on-land to shed light on the conditions needed to generate this type of evolved melts at Mayotte.

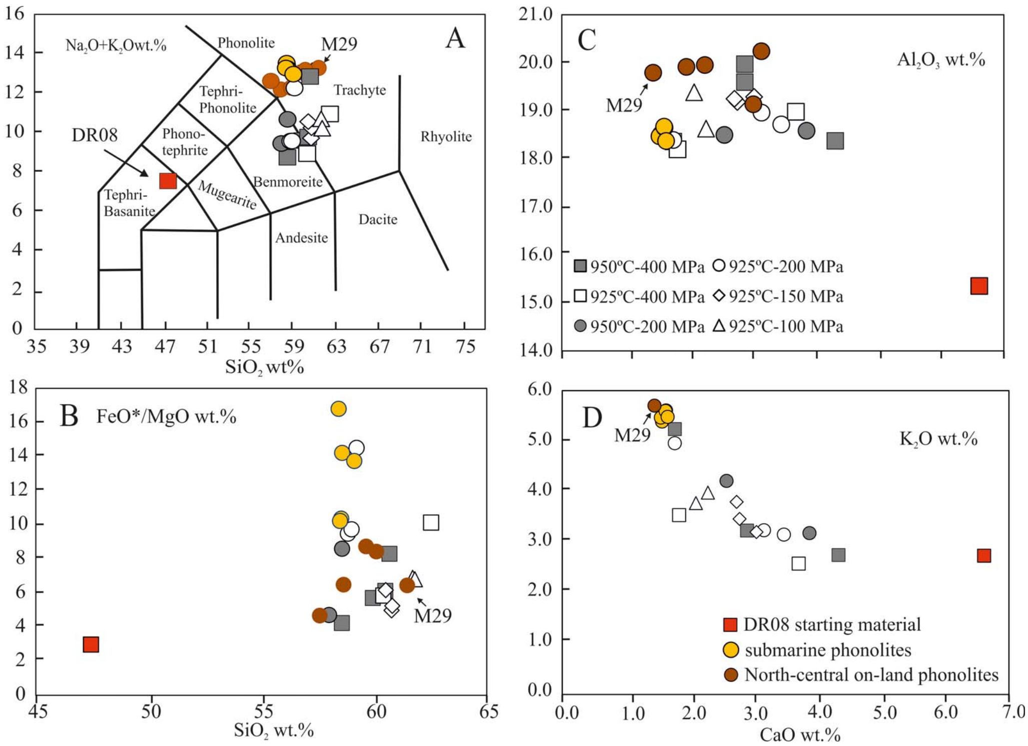


**Figure 9.** (A) Total alkalis ($Na_2O + K_2O$) versus $SiO_2$ diagram [after Le Bas and Streckeisen, 1991] showing the composition of the experimental glasses, the DR08 starting material, and onland/offshore phonolites at Mayotte (Table 1). (B) FeO*/MgO versus. $SiO_2$ wt%, (C) $Al_2O_3$ versus CaO wt%, (D) $K_2O$ versus CaO wt%. Legend as in previous figures. Vertical errors are equal to symbol size.

## 5. Discussion

As stated in the previous sections, most of the seismo-volcanic activity recorded during the 2018–2021 eruptive episode (and up to date) occurred along the 60 km long submarine volcanic ridge located eastward of Mayotte (Figure 1B). Dredged samples along this ridge define a bimodal distribution of basanites and phonolites [Berthod et al., 2021a,b], phonolites mostly outcropping in the Horseshoe region (Figure 1). Submarine mafic magmas are chemically and petrologically similar to the on-land counterparts from the moderately silica-undersaturated Comoros chemical trend [Bachèlery et al., 2016, Berthod et al., 2021b, Pelleter et al., 2014]. Dredged phonolites have major and trace elements that are also compatible with this magmatic lineage. However, when compared to their on-shore equivalents, they are slightly enriched in Fe–Mg–Ca and have lower Al-total alkalis content, both akin to the somewhat less evolved character of these magmas [Pelleter et al., 2014]. This is also reflected by differences between submarine and on-shore phonolites in their mineralogy. Whereas offshore phonolites are moderate porphyritic magmas with small crystals (≤200 µm) of fayalitic Ol (Fo ≤ 32 mol%), Pl (An ≤ 24 mol%), Ap and Fe–Ti oxides microcrystals [Ox; Berthod et al., 2021b], those on land are characterized by the presence of an amphibole-bearing assemblage consisting of Cpx+Amp+Afs+Ap+Ox±nepheline (Nph) [Debeuf, 2004, Pelleter et al., 2014]. It is worth noting that Ol-bearing phonolites are not restricted to the submarine domain since they were also identified onshore at Mayotte [Berthod et al., 2021b, Debeuf, 2004]. Based on our experimental results, the differences in phase assemblage and composition observed between these two groups can potentially be related to changes in the evolution conditions of the parental basanitic magma ($P$–$T$–$H_2O$), as we discuss below.

### 5.1. *Production of phonolitic liquids at the WNW–ESE submarine volcanic ridge of Mayotte*

The low porphyritic character of the submarine phonolites dredged in the vicinity of the active Horseshoe structure of Mayotte [Berthod et al., 2021a,b] allows us to consider the bulk-rock composition as representative of liquids. Accordingly, the experimental results detailed above are useful for understanding the conditions for the production of phonolitic melts at this site (Figures 8–9, Tables 1 and 8). Although glasses produced at conditions of 925 °C–200 MPa and 950 °C–400 MPa with 2–7 wt% $H_2O_{melt}$ broadly reproduce the $SiO_2$, $Al_2O_3$, MgO and CaO contents of natural phonolites (Figure 8), only the residual glasses of charges DR08-143 (950 °C–400 MPa; ~2 wt% $H_2O_{melt}$) and DR08-131 (925 °C–200 MPa; ~4 wt% $H_2O_{melt}$) closely match the phonolitic affinities (P.I. ~ 0.9–1) of the natural products (Figure 9A; Table 1). Both charges have the same mineral assemblage and phase proportions (~65 wt% of Ol+Pl+Amp+Mt+Ilm+Ap±Bt; Table 2), but differ in the composition of the phases (see above). In detail, only the 200 MPa experiment closely reproduces the FeO* and $SiO_2$ contents (and other oxides) as well as the FeO*/MgO ratios (Figure 9B). The glass produced at 400 MPa has a FeO* content ~2 wt% lower and a higher $SiO_2$ with respect to the dredged phonolites (Figure 9B). Our data therefore show that the crystallization of DR08 basanite at 925 °C–200 MPa (corresponding to depths of 6–8 km) and under relatively reduced conditions ($fO_2$ ~ FMQ; Table 2) generates phonolitic melts (with up to 3.8 wt% $H_2O_{melt}$) with FeO* contents and FeO*/MgO ratios similar to phonolites sampled offshore. Whereas such T–P–$H_2O_{melt}$ estimates are in agreement with the conditions set for most of the phonolites and evolved peralkaline magmas worldwide [Andújar et al., 2008, 2010, 2013, Andújar and Scaillet, 2012, Di Carlo et al., 2010, Giehl et al., 2013, Moussallam et al., 2013, Romano et al., 2018, Scaillet and MacDonald, 2006, Scaillet et al., 2008], they strongly differ from those inferred by Berthod et al. [2021b], in particular with respect to pressure conditions: as stated previously, these authors conclude that the fractionation of a 80 wt% dry mineral assemblage from a hydrous basanite (2.3 wt% $H_2O_{melt}$) at mantle depths (18–20 km, 600 MPa) produces the Fe-rich phonolites of the ridge. However, in this model, no role is given to the hydrous phases like amphibole or biotite in the evolutionary process. Assuming that $H_2O_{melt}$ (2.3 wt%) determined in olivine melt inclusions in DR08 sample by Berthod et al. [2021b] is representative, a fractionating assemblage lacking Amp with such an $H_2O_{melt}$ requires a maximum pressure of ~200 MPa (Figure 3). Our results show, however, that basanite crystallization under such wet conditions (i.e., ending with residual liquids with $H_2O_{melt}$ > 6 wt%, as required by the largely incompatible behaviour of $H_2O$, for 80 wt% crystallization of a basanite with 2.3 wt% $H_2O_{melt}$) produces mostly trachytic melts (Figure 9A), true phonolites requiring drier conditions (<3–4 wt%). This mismatch is seemingly due to the fact that MELTs does not incorporate amphibole, which is an important fractionating phase in hydrous basanite as our experiments demonstrate.

It should be also stressed here that the differences between MELTs calculations and our results not only concern the role of hydrous phases in the fractionating process, but also the composition of feldspar that is in equilibrium with these Fe-rich phonolitic melts. Whereas the calculations of Berthod et al. [2021b] predict the precipitation of at least 30% of alkali feldspar (anorthoclase) to produce the phonolitic melts, the experimental charges yielding to such type of liquids are instead characterized by the presence of relatively primitive Plagioclase (oligoclase) with composition ~27 mol% in the fractionating mineral assemblage. The submarine phonolites have a dominant alkali feldspar population at ≤$An_{15}$ mol%, but also contain a few more calcic cores ($An_{24}$ mol%) [Berthod et al., 2021b]. The latter is close to that of experimental Pl ($An_{27\pm3}$ mol%) produced in charge DR08-131 (925 °C–200 MPa), which is as shown above, in equilibrium with a Mayotte-type phonolitic liquid. Hence, the more calcic Pl cores in the natural phonolite can be considered as crystals inherited from the fractionation process involving the crystallization of the mineral assemblage Ol+Pl+Amp+Mt+Ilm+Ap±Bt down to the phonolitic production stage. The less calcic and dominant variety of feldspar microphenocrysts in the phonolite is likely the result of a small increment of crystallization that occurred after the phonolitic liquid was extracted from its parental basanitic magma, perhaps due to an adiabatic cooling effect upon decompression that took place when the phonolitic melt had left the basanitic reservoir.

Hence, we conclude that conditions of 950/925 °C–200 MPa with $H_2O_{melt}$ ≤ 3–4 wt% are best suited for the production of Fe-rich phonolites at Mayotte. Deeper conditions produce significantly different compositions, as stated previously (Figure 8).

## 5.2. *The production of the north-central Mayotte Karthala type phonolites*

As stated in previous sections, the compositions of the magmas at Mayotte clearly define two distinct magmatic series. Since our starting basanitic composition belongs to the moderate-silica undersaturated series (i.e. Karthala type), our results primarily apply to this specific compositional lineage (Figure 2).

Detailed mineralogical information concerning the phonolitic products of Mayotte is scarce, however: only the works of Pelleter et al. [2014] and Späth et al. [1996] provide bulk-rock information and few mineral data from these evolved compositions (Table 1). For comparison purposes, we have only considered the bulk-rock compositions having MgO contents up to 0.4 wt%, since these are the maximum amounts of our experimental melts (Table 8). The phonolites-trachytes with MgO contents lower than ~0.25 wt% represent the most evolved products of the Karthala LLD [Pelleter et al., 2014, Späth et al., 1996]. In this case, the liquids produced in our experiments possibly represent the parental compositions from which the Mayotte on-land phonolites derive.

Compared to phonolites from the submarine ridge, those from Mayotte island are characterized by a contrasted mineralogy [Amp+Cpx+Mt+Ilm+Afs+Ap±Nph) and have slightly lower Fe-contents (between 3.7 to 5.1 wt%; Pelleter et al., 2014]. Rare Ol+Afs bearing phonolites [i.e., equivalent to the dredged products; Berthod et al., 2021b], and aphyric glassy samples [sample M29 in Pelleter et al., 2014; Table 1] can be also found in the northern-central parts of Mayotte.

Apart from sample M29, the Mayotte phonolites are reproduced by the 200–400 MPa series products on TAS, FeO*/MgO, CaO, $Al_2O_3$ versus $SiO_2$ Harker diagrams (Figure 9), suggesting that these melts could have been potentially generated at ~300 MPa (9 km depth). This pressure is about 100 MPa (3 km) higher (deeper) than that determined for the conditions of production of their 2018–2021 submarine equivalents. However, both the lower iron content of the Mayotte island phonolites compared to the submarine ridge products and the presence of Amp in these compositions (Amp stability is enhanced with pressure; Figure 3), support deeper conditions for generation of the on-land phonolites.

The M29 aphyric sample has the highest $SiO_2$ (61.5 wt%) and the lowest FeO* (3.2 wt%) contents of all phonolites considered in this work (Table 1). According to our results, the production of this phonolitic composition will require ponding conditions of a DR08 type basanite at pressures ≥400 MPa. In fact, the melt from the charge DR08-143 run at 400 MPa closely matches the total alkalis and $SiO_2$ contents of this phonolite (Figure 9A). However, when it comes to FeO*/MgO ratio and $TiO_2$ and CaO contents, the best fits are obtained by charges produced at 925 °C–100 MPa (Figure 9, Table 8). The absence of phenocrysts in the natural sample does not allow us to use the mineralogical information to discriminate between these conditions. However, we cannot exclude that this aphyric phonolite was produced by the fractionation of a basanitic magma at low-pressure (≤100 MPa) and under relatively dry (≤3 wt%) and hot (?) conditions.

As stated above, the existence of phonolites, with MgO contents <0.4 wt% containing a mineral assemblage Amp+Cpx+Pl+Fe–Ti oxides [Debeuf, 2004, Pelleter et al., 2014], suggests that, even if these magmas evolved from liquids similar to those produced in this work, their composition and mineralogy [low-Mg number of amphiboles, Debeuf, 2004] do not necessary reflect the production level: they could reflect shallower final ponding conditions. This observation highlights the need for detailed petrographic data on Mayotte phonolites, especially those on-land, if we are to define more precisely the pre-eruptive conditions of Khartala-type phonolites.

## 5.3. *Various levels of phonolite production/storage at Mayotte*

The crystallization experiments, performed on a representative evolved basanitic sample from the 2018–2021 eruption, allowed us to define the best conditions ($T$–$P$–$f O_2$–$f H_2O$) for producing the characteristical compositional variability of phonolites from the north-central parts of the Grand Terre island, Petite Terre and NE active submarine ridge of Mayotte. In particular, these experiments show the ease of producing phonolitic melts in the shallow crust, as observed in many other settings. Phonolitic melts containing up to ~3–4 wt% of $H_2O_{melt}$ are produced by the extensive crystallization of at least 65 wt% of a mineral assemblage consisting of Ol+Pl+Amp+Cpx+Bt+Mt+Ilm+Ap, at crustal levels ≤12–15 km. Pressure (hence depth) appears to be an important factor controlling the final FeO* content of residual phonolitic liquids. This oxide could be potentially used as a geobarometer (for this type of magma series) to infer the generation/storage depths of corresponding magmas.

A conceptual model summarizing our view on Mayotte phonolites is shown in Figure 10. Considering the above water-contents, the differentiation of basanitic magmas at depths ≤4–5 km produces residual liquids with trachyte–benmoreite affinities. The Fe-enriched phonolite compositions found in the Mayotte system are instead produced at around 6–8 km, whereas at greater depths, the fractionation process results in the generation of phonolitic melts which are progressively enriched in $SiO_2$–$Al_2O_3$ and depleted in FeO*.

Hence, the production of phonolitic melts with the Karthala affinities of Mayotte island occurs at multiple depths above the local Moho [16–17 km, Dofal et al., 2021]. However, the presence of highly evolved phonolitic magmas (i.e. MgO poor) suggests that these magmas experienced a later episode of crystallization and fractionation at shallower levels, prior to their eruption. The occurrence of relatively shallow phonolitic reservoirs below the Horseshoe region (Figure 1C) would have permitted their subsequent rapid emptying and collapse during past eruptions, which would readily explain the presence of a caldera-looking depression at this point, since relatively shallow depths of magma reservoirs favors the formation of caldera structures [e.g. Martí et al., 2008].

Our results contrast with the conditions inferred from mineral geobarometers and MELTS simulations, which for producing the Fe-rich phonolites from Mayotte, predict the crystallization of a dry mineral assemblage at significantly higher pressures than those determined in this work (600 versus 200 MPa). This difference highlights the still poor resolution that these two methods have for predicting the depths of magma evolution in alkaline systems, and calls for additional calibration of these tools.

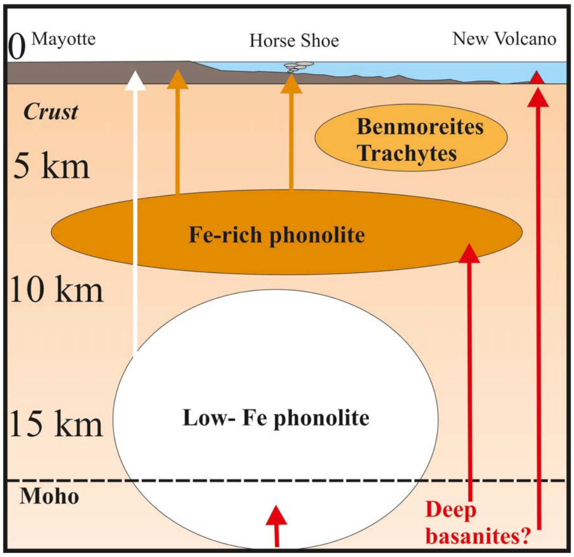


**Figure 10.** Conceptual model of the plumbing system operating at Mayotte for producing Fe-rich, Low-Fe phonolites and benmoreite–trachyte compositions (see text for details). Moho location from Dofal et al. [2021].

## Conflicts of interest

Authors have no conflict of interest to declare.

## Acknowledgments

The authors thank Patricia Benoist for the technical support with SEM and EMPA. We thank the scientific party of the MAYOBS 2 (DR08 sampling) campaign that was conducted by several French research institutions and laboratories (IPGP/CNRS/BRGM/IFREMER/IPGS). All marine operations are performed as part of the MAYOBS set of campaigns (https://doi.org/10.18142/291), under the supervision of REVOSIMA (Réseau de Surveillance Volcanologique et Sismologique de Mayotte; REVOSIMA), a partnership between the Institut de Physique du Globe de Paris (IPGP), the Institut Français de Recherche pour l'Exploitation de la Mer (IFREMER), the Bureau de Recherches Géologiques et Minières (BRGM), the Centre National de la Recherche Scientifique (CNRS) and the REVOSIMA consortium. We thank the captain and crew of the R/V Marion Dufresne (TAAF/IFREMER/LDA). R. Cioni and an anonymous reviewer are thanked for the detailed reviews of this work. We want also to thank the editorial handling of editor Jérôme Van der Woer.

## Funding

This work was supported by the Institut des Sciences de la Terre d'Orléans (ISTO-CNRS), the LABEX VOLTAIRE (ANR-10-LABX-100-01) and the EQUIPEX PLANEX (11-EQPX-0036). Since June 2019, all activities on Mayotte, including MAYOBS campaigns, are funded by le Ministère de l'Enseignement Supérieur, de la Recherche et de l'Innovation (MESRI), le Ministère de la Transition Ecologique (MTE), le Ministère des Outremers (MOM), le Ministère de l'Intérieur (MI), and le Ministère des Armées with the support of the DIRMOM (Direction Interministérielle aux Risques Majeurs en Outremer) and the MAPPPROM (Mission d'appui aux politiques publiques pour la prévention des risques majeurs en Outremer).

## Supplementary data

Supporting information for this article is available on the journal's website under https://doi.org/10.5802/crgeos.182 or from the author.

## References

Andersen, D. J. and Lindsley, D. H. (1998). Internally consistent solution models for Fe–Mg–Mn–Ti oxides: Fe–Ti oxides. *Am. Mineral.*, 73, 714–726.

Andújar, J., Costa, F., and Martí, J. (2010). Magma storage conditions of the last eruption of Teide volcano (Canary Islands, Spain). *Bull. Volcanol.*, 72, 381–395.

Andújar, J., Costa, F., Martí, J., Wolff, J. A., and Carroll, M. R. (2008). Experimental constraints on pre-eruptive conditions of phonolitic magma from the caldera-forming El Abrigo eruption, Tenerife (Canary Islands). *Chem. Geol.*, 257, 173–191.

Andújar, J., Costa, F., and Scaillet, B. (2013). Storage conditions and eruptive dynamics of central versus flank eruptions in volcanic islands: the case of Tenerife (Canary Islands, Spain). *J. Volcanol. Geotherm. Res.*, 260, 62–79.

Andújar, J., Martel, C., Pichavant, M., Samaniego, P., Scaillet, B., and Molina, I. (2017). Structure of the plumbing system at Tungurahua volcano, Ecuador: Insights from phase equilibrium experiments on July–August 2006 eruption products. *J. Petrol.*, 58, 1249–1278.

Andújar, J. and Scaillet, B. (2012). Experimental constraints on parameters controlling the difference in the eruptive dynamic of phonolitic magmas: the case from Tenerife (Canary Islands). *J. Petrol.*, 53, 1777–1806.

Andújar, J., Scaillet, B., Pichavant, M., and Druitt, T. H. (2015). Differentiation conditions of a basaltic magma from Santorini, and its bearing on the production of andesite in arc settings. *J. Petrol.*, 56, 765–794.

Bachèlery, P., Morin, J., Villeneuve, N., Soulé, H., Nassor, H., and Ali, A. R. (2016). Structure and eruptive history of Karthala volcano. In *Active Volcanoes of the Southwest Indian Ocean*, pages 345–366. Springer-Verlag, Berlin and Heidelberg.

Berndt, J., Holtz, F., and Koepke, J. (2001). Experimental constraints on storage conditions in the chemically zoned phonolitic magma chamber of the Laacher See Volcano. *Contrib. Mineral. Petrol.*, 140, 469–486.

Berndt, J., Koepke, J., and Holtz, F. (2005). An experimental investigation of the influence of water and oxygen fugacity on differentiation of MORB at 200 MPa. *J. Petrol.*, 46, 135–167.

Berthod, C., Médard, E., Bachèlery, P., Gurioli, L., Di Muro, A., Peltier, A., Komorowski, J., Benbakkar, M., Devidal, J., Langlade, J., Besson, P., Boudon, G., Rose-Koga, E., Deplus, C., Le Friant, A., Bickert, M., Nowak, S., Thinon, I., Burckel, P., Hidalgo, S., Jorry, S., Fouquet, Y., and Feuillet, N. (2021a). The 2018-ongoing Mayotte submarine eruption: magma migration imaged by petrological monitoring. *Earth Planet. Sci. Lett.*, 571, article no. 117085.

Berthod, C., Médard, E., Di Muro, A., Hassen Ali, T., Gurioli, L., Chauvel, C., Komorowski, J.-C., Benbakkar, M., Devidal, J.-L., Besson, P., Le Friant, A., Deplus, C., Nowak, S., Thinon, I., Burckel, P., Hidalgo, S., Feuillet, N., Jorry, S., and Fouquet, Y. (2021b). Mantle xenolith-bearing phonolites and basanites feed the active volcanic ridge of Mayotte

(Comoros archipelago, SW Indian Ocean). *Contrib. Mineral. Petrol.*, 176(10), 1–24.

Bertil, D., Mercury, N., Doubre, C., Lemoine, A., and Van Der Woerd, J. (2021). The unexpected Mayotte 2018–2020 seismic sequence: a reappraisal of the regional seismicity of the Comoros. *C. R. Géosci.*, 353, 211–235.

Botcharnikov, R. E., Almeev, R. R., Koepke, J., and Holtz, F. (2008). Phase relations and liquid lines of descent in hydrous ferrobasalt-implications for the Skaergaard intrusion and Columbia river flood basalts. *J. Petrol.*, 49, 1687–1727.

Burnham, C. W., Holloway, J. R., and Davis, N. F. (1969). *Thermodynamic Properties of Water to 10000 °C and 10,000 Bars*, volume 132. Geological Society of America Publ., Special Paper No. 132.

Cesca, S., Letort, J., Razafindrakoto, H. N. T., Heimann, S., Rivalta, E., Isken, M. P., Nikkhoo, M., Passarelli, L., Petersen, G. M., Cotton, F., and Dahm, T. (2020). Drainage of a deep magma reservoir near Mayotte inferred from seismicity and deformation. *Nat. Geosci.*, 13, 87–93.

Chou, I.-M. (1978). Calibration of oxygen buffers at elevated P and T using the hydrogen fugacity sensor. *Am. Mineral.*, 63, 690–703.

Dautria, J. M., Girod, M., and Rahaman, O. (1983). The upper mantle beneath eastern Nigeria: inferences from ultramafic xenoliths in Jos and Biu volcanics. *J. African Earth Sci.*, 1, 331–338.

Debeuf, D. (2004). *Étude de l'évolution volcano-structurale et magmatique de Mayotte (archipel des Comores, océan Indien)*. PhD thesis, Université de la Reunion.

Deer, W. A., Howie, R. A., and Zussman, J. (1972). *Rock-Forming Minerals, Volume 4: Framework Silicates*. Longmans, Green and Co. Ltd., London.

Di Carlo, I., Pichavant, M., Rotolo, S. G., and Scaillet, B. (2006). Experimental crystallization of a High-K arc basalt: the golden pumice, Stromboli volcano (Italy). *J. Petrol.*, 47, 1317–1343.

Di Carlo, I., Rotolo, S. G., Scaillet, B., Buccheri, V., and Pichavant, M. (2010). Phase equilibrium constraints on pre-eruptive conditions of recent felsic explosive volcanism at Pantelleria Island, Italy. *J. Petrol.*, 51, 2245–2276.

Dofal, A., Fontaine, F. R., Michon, L., Barruol, G., and Tkalcic, H. (2021). Nature of the crust beneath the islands of the Mozambique channel: Constraints from receiver functions. *J. African Earth Sci.*, 184, article no. 104379.

Erdmann, S., Martel, C., Pichavant, M., and Kushnir, A. (2014). Amphibole as an archivist of magmatic crystallization conditions: problems, potential, and implications for inferring magma storage prior to the paroxysmal 2010 eruption of Mount Merapi, Indonesia. *Contrib. Mineral. Petrol.*, 167, article no. 1016.

Feuillet, N. (2019). MAYOBS1 cruise, RV Marion Dufresne. https://doi.org/10.17600/18001217.

Feuillet, N., Jorry, S., Crawford, W., Deplus, C., Thinon, I., Jacques, E., Saurel, J.-M., Lemoine, A., Paquet, F., Satriano, C., Aiken, C., Foix, O., Kowalski, P., Laurent, A., Rinnert, E., Cathalot, C., Donval, J. P., Guyader, V., Gaillot, A., Scalabrin, C., Moreira, M., Peltier, A., Beauducel, F., Grandin, R., Ballu, V., Daniel, R., Pelleau, P., Gomez, J., Besançon, S., Géli, L., Bernard, P., Bachèlery, P., Fouquet, Y., Bertil, D., Lemarchand, A., and Van der Woerd, J. (2021). Birth of a large volcanic edifice offshore Mayotte via lithosphere-scale dyke intrusion. *Nat. Geosci.*, 14(10), 787–795.

Foix, O., Aiken, C., Saurel, J. M., Feuillet, N., Jorry, S. J., Rinnert, E., and Thinon, I. (2021). Offshore Mayotte volcanic plumbing revealed by local passive tomography. *J. Volcanol. Geotherm. Res.*, 420, article no. 107395.

Freise, M., Holtz, F., Nowak, M., Scoates, J. S., and Strauss, H. (2009). Differentiation and crystallization conditions of basalts from the Kerguelen large igneous province: an experimental study. *Contrib. Mineral. Petrol.*, 158, 505–527.

Ghiorso, M. S. and Gualda, G. A. R. (2015). An $H_2O$-$CO_2$ mixed fluid saturation model compatible with rhyolite-MELTS. *Contrib. Mineral. Petrol.*, 169, 1–30.

Giehl, C., Marks, M., and Nowak, M. (2013). Phase relations and liquid lines of descent of an iron-rich peralkaline phonolitic melt: an experimental study. *Contrib. Mineral. Petrol.*, 165, 283–304.

Gualda, G. A. R., Ghiorso, M. S., Lemons, R. V., and Carley, T. L. (2012). Rhyolite-MELTS: a modified calibration of MELTS optimized for silica-rich, fluid-bearing magmatic systems. *J. Petrol.*, 53, 875–890.

Hammer, J., Jacob, S., Welsch, B., Hellebrand, E., and Sinton, J. (2016). Clinopyroxene in postshield Haleakala ankaramite: 1. Efficacy of thermobarometry. *Contrib. Mineral. Petrol.*, 171, article no. 7.

Harms, E., Gardner, J. E., and Schmincke, H. U. (2004). Phase equilibria of the lower Laacher See Tephra (East Eifel, Germany): constraints on pre-eruptive storage conditions of a phonolitic magma reservoir. *J. Volcanol. Geotherm. Res.*, 134, 135–148.

Iacovino, K., Oppenheimer, C., Scaillet, B., and Kyle, P. (2016). Storage and evolution of mafic and intermediate alkaline magmas beneath Ross Island, Antarctica. *J. Petrol.*, 57, 93–118.

Jiménez-Mejías, M., Andújar, J., Scaillet, B., and Casillas, R. (2021). Experimental determination of $H_2O$ and $CO_2$ solubilities of mafic alkaline magmas from Canary Islands. *C. R. Géosci.*, 353, 289–314.

Jorry, S. J. (2019). MAYOBS2 cruise, RV Marion Dufresne. https://doi.org/10.17600/18001222.

Klügel, A., Albers, E., and Hansteen, T. H. (2022). Mantle and crustal xenoliths in a tephriphonolite from La Palma (Canary Islands): implications for phonolite formation at oceanic island Volcanoes. *Front. Earth Sci.*, 10, article no. 761902.

Klügel, A., Schmincke, H. U., White, J. D. L., and Hoernle, K. A. (1999). Chronology and volcanology of the 1949 multi-vent rift-zone eruption on La Palma (Canary Islands). *J. Volcanol. Geotherm. Res.*, 94, 267–282.

Laurent, A., Satriano, C., and Bernard, P. (2021). Accurate depth determination of VLF events of the ongoing seismo-volcanic crisis in Mayotte. In *5èmes Rencontres Scientifiques et Techniques Résif, Nov 2021 Obernai (67210), France*. https://hal.archives-ouvertes.fr/hal-03481002. HAL Id: hal-03481002.

Lavayssière, A., Crawford, W. C., Saurel, J.-M., Satriano, C., Feuillet, N., Jacques, E., and Komorowski, J.-C. (2022). A new 1D velocity model and absolute locations image the Mayotte seismo-volcanic región. *J. Volcanol. Geotherm. Res.*, 421, article no. 107440.

Le Bas, M. J. and Streckeisen, A. L. (1991). The IUGS systematics of igneousrocks. *J. Geol. Soc. Lond.*, 148, 825–833.

Lemoine, A., Briole, P., Bertil, D., Roullé, A., Foumel, M., Thinon, I., Raucoules, D., de Michele, M., and Valty, P. (2020). The 2018–2019 seismo-volcanic crisis east of Mayotte, Comoros islands: seismicity and ground deformation markers of an exceptional submarine eruption. *Geophys. J. Int.*, 223(1), 22–44.

MacDonald, R., White, J. C., and Belkin, H. E. (2021). Peralkaline silicic extrusive rocks: magma genesis, evolution, plumbing systems and eruption. *C. R. Géosci.*, 353, 7–59.

Martí, J., Geyer, A., Folch, A., and Gottsmann, J. (2008). Chapter 6. A Review on collapse caldera modelling. In Gotssmann, J. and Martí, J., editors, *Caldera Volcanism, Analysis, Modelling and Respons*, Developments in Volcanology, page 492. Elsevier, Amsterdam, the Netherlands.

Moussallam, Y., Oppenheimer, C., Scaillet, B., and Kyle, P. R. (2013). Experimental phase-equilibrium constraints on the phonolite magmatic system of Erebus Volcano, Antarctica. *J. Petrol.*, 54, 1285–1307.

Nehlig, P., Lacquement, F., Bernard, J., Caroff, M., Deparis, J., Jaouen, T., Pelleter, A. A., Perrin, J., Prognon, C., and Vittecoq, B. (2013). Notice de la carte géologique de Mayotte. BRGM/RP-61803-FR, 135 p., 45 ill., 1 ann.

Neumann, E.-R., Wulff-Pedersen, E., Johnsen, K., Andersen, T., and Krogh, E. (1995). Petrogenesis of spinel harzburgite and dunite suite xenoliths from Lanzarote, eastern Canary Islands: implication for the upper mantle. *Lithos*, 35, 83–107.

Pedrazzi, D., Cerda, D., Geyer, A., Martí, J., Aulinas, M., and Planagumà, L. (2022). Stratigraphy and eruptive history of the complex Puig de La Banya del Boc monogenetic volcano, Garrotxa volcanic field. *J. Volcanol. Geotherm. Res.*, 423, article no. 107460.

Pelleter, A. A., Caroff, M., Cordier, C., Bachelery, P., Nehlig, P., Debeuf, D., and Arnaud, N. (2014). Melilite-bearing lavas in Mayotte (France): An insight into the mantle source below the Comores. *Lithos*, 208–209, 281–297.

Pownceby, M. I. and O'Neill, H. St. C. (1994). Thermodynamic data redox reactions at high temperatures. III. Activity-composition relations in Ni-Pd alloys from EMF measurements at 850–1250 K and calibration of the NiO + Ni–Pd assemblage a redox sensor. *Contrib. Mineral. Petrol.*, 116, 327–339.

Putirka, K. D. (2008). Thermometers and barometers for volcanic systems. *Rev. Mineral. Geochem.*, 69, 61–120.

Putirka, K. D. (2016). Amphibole thermometers and barometers for igneous systems and some implications for eruption mechanisms of felsic magmas at arc Volcanoes. *Am. Mineral.*, 101, 841–858.

ReVoSiMa (2022). Bulletin no 39 de l'activité sismo-volcanique à Mayotte, du 1er au 28 fevrier 2022. http://www.ipgp.fr/sites/default/files/ipgp_revosima_n39_20220304.pdf. ISSN: 2680-1205.

Ridolfi, F. (2021). Amp-TB2: an updated model for calcic amphibole thermobarometry. *Minerals*, 11(3), article no. 324.

Robie, R. A., Hemingway, B. S., and Fisher, J. R. (1979). Thermodynamic properties of minerals and related substances at 298.15 K and 1 bar (105 pascals) pressure and at higher temperatures. *US Geol. Surv. Bull.*, 1452.

Romano, P., Andújar, J., Scaillet, B., Romengo, N., Di Carlo, I., and Rotolo, S. G. (2018). Phase equilibria of Pantelleria Trachytes (Italy): constraints on pre-eruptive conditions and on the Metaluminous to Peralkaline transition in silicic magmas. *J. Petrol.*, 59, 559–588.

Saurel, J. M., Retailleau, L., Weiqiang, Z., Issartel, S., Satriano, C., and Beroza, G. C. (2021). Implementation of a new real time seismicity detector for the Mayotte crisis. EGU21-10646. https://doi.org/10.5194/egusphere-egu21-1-10646.

Scaillet, B. and MacDonald, R. (2006). Experimental constraints on pre-eruption conditions of pantelleritic magmas: evidence from the Eburru complex, Kenya Rift. *Lithos*, 91, 95–108.

Scaillet, B., Pichavant, M., and Cioni, R. (2008). Upward migration of Vesuvius magma chamber over the past 20,000 years. *Nature*, 455, 216–219.

Scaillet, B., Pichavant, M., and Roux, J. (1995). Experimental crystallization of leucogranite magmas. *J. Petrol.*, 36, 663–705.

Scaillet, B., Pichavant, M., Roux, J., Humbert, G., and Lefévre, A. (1992). Improvements of the Shaw membrane technique for measurement and control of fH2 at high temperatures and pressures. *Am. Mineral.*, 77, 647–655.

Späth, A., Roex, A. P. L., and Duncan, R. A. (1996). The geochemistry of lavas from the Comores Archipelago, Western Indian Ocean: petrogenesis and mantle source region characteristics. *J. Petrol.*, 37, 961–991.

Toplis, M. J. and Carroll, M. R. (1995). An experimental study of the influence of oxygen fugacity on fe-ti oxide stability, phase relations, and mineral-melt equilibria in ferro-basaltic systems. *J. Petrol.*, 36, 1137–1170.

Ubide, T., Mollo, S., Zhao, J., Nazzari, M., and Scarlato, P. (2019). Sector-zoned clinopyroxene as a recorder of magma history, eruption triggers, and ascent rates. *Geochim. Cosmochim. Acta*, 251, 265–283.

Webster, J. D., Holloway, J. R., and Hervig, R. L. (1987). Phase equilibria of a Be, U and F-enriched vitrophyre from Spor Mountain, Utah. *Geochim. Cosmochim. Acta*, 51, 389–402.

Wolff, J. A. (1985). Zonation, mixing and eruption of silica-under-saturated alkaline magma: a case study from Tenerife, Canary1986 Mount St. Helens eruptions. *J. Geophys. Res.*, 98, 19667–19685. Islands. Geol. Mag., 122, 623–640.

Zinke, J., Reijmer, J. J. G., Thomassin, B. A., Dullo, W.-C., Grootes, P. M., and Erlenkeuser, H. (2003). Postglacial flooding history of Mayotte lagoon (Comoro archipelago, southwest Indian Ocean). *Mar. Geol.*, 194, 181–196.

*Comptes Rendus*
*Géoscience — Sciences de la Planète*
**2022**, Vol. 354, Special Issue S2, p. 257-273
https://doi.org/10.5802/crgeos.119

The Mayotte seismo-volcanic crisis of 2018-2021 in the Comoros archipelago (Mozambique channel) / *La crise sismo-volcanique de 2018-2021 de Mayotte dans l'archipel des Comores (Canal du Mozambique)*

# Initial results from a hydroacoustic network to monitor submarine lava flows near Mayotte Island

## *Premiers résultats d'un réseau hydroacoustique pour surveiller les coulées de lave sous-marines près de l'île de Mayotte*

**Sara Bazin *, [a], Jean-Yves Royer [a], Flavie Dubost [b], Fabien Paquet [c], Benoît Loubrieu [a], Aude Lavayssière [d], Christine Deplus [d], Nathalie Feuillet [d], Éric Jacques [d], Emmanuel Rinnert [a], Isabelle Thinon [c], Élodie Lebas [d], Delphine Pierre [a], Lise Retailleau [e], Jean-Marie Saurel [d], Alexey Sukhovich [a], Robin Bonnet [a] and the REVOSIMA group**

[a] Université Brest, CNRS, Ifremer, UMR6538 Geo-Ocean, 29280 PLOUZANÉ, France

[b] ENSTA Bretagne, 2 rue François Verny, 29806 BREST Cedex 09, France

[c] BRGM, 3 avenue Claude-Guillemin, BP 36009, 45060 ORLÉANS Cedex 2, France

[d] Université de Paris, Institut de Physique du Globe de Paris, CNRS, 1 rue Jussieu, 75005 PARIS, France

[e] Observatoire Volcanologique du Piton de la Fournaise, Institut de Physique du Globe de Paris, 14 RN3 - Km 27, 97418 LA PLAINE DES CAFRES, Réunion, France

*E-mails:* sara.bazin@univ-brest.fr (S. Bazin), jyroyer@univ-brest.fr (J.-Y. Royer), flavie.dubost@ensta-bretagne.org (F. Dubost), f.paquet@brgm.fr (F. Paquet), benoit.loubrieu@ifremer.fr (B. Loubrieu), lavayssiere@ipgp.fr (A. Lavayssière), deplus@ipgp.fr (C. Deplus), feuillet@ipgp.fr (N. Feuillet), jacques@ipgp.fr (É. Jacques), emmanuel.rinnert@ifremer.fr (E. Rinnert), i.thinon@brgm.fr (I. Thinon), elebas@ipgp.fr (É. Lebas), delphine.pierre@ifremer.fr (D. Pierre), retailleau@ipgp.fr (L. Retailleau), saurel@ipgp.fr (J.-M. Saurel), alexey.sukhovich@univ-brest.fr (A. Sukhovich), robin.bonnet15@gmail.com (R. Bonnet)

**Abstract.** In 2019, a new underwater volcano was discovered at 3500 m below sea level (b.s.l.), 50 km east of Mayotte Island in the northern part of the Mozambique Channel. In January 2021, the submarine eruption was still going on and the volcanic activity, along with the intense seismicity that accompanies this crisis, was monitored by the recently created REVOSIMA (MAyotte VOlcano and Seismic Monitoring) network. In this framework, four hydrophones were moored in the SOFAR channel in October 2020. Surrounding the volcano, they monitor sounds generated by the volcanic activity and the

* Corresponding author.

lava flows. The first year of hydroacoustic data evidenced many earthquakes, underwater landslides, large marine mammal calls, along with anthropogenic noise. Of particular interest are impulsive signals that we relate to steam bursts during lava flow emplacement. A preliminary analysis of these impulsive signals (ten days in a year, and only one day in full detail) reveals that lava emplacement was active when our monitoring started, but faded out during the first year of the experiment. A systematic and robust detection of these specific signals would hence contribute to monitor active submarine eruptions in the absence of seafloor deep-tow imaging or swath-bathymetry surveys of the active area.

**Résumé.** En 2019, un nouveau volcan sous-marin a été découvert par 3500 m de profondeur, à 50 km à l'est de l'île de Mayotte dans la partie Nord du Canal du Mozambique. Le RÉseau de surveillance VOlcanologique et SIsmologique de MAyotte (REVOSIMA) a été mis en place pour surveiller l'activité sous-marine de ce nouveau volcan ainsi que l'intense crise sismique qui a débuté en Mai 2018 et qui est toujours en cours. Dans ce cadre, quatre mouillages équipés d'hydrophones ont été déployés en octobre 2020 autour du volcan, à la profondeur du canal SOFAR. L'objectif est, entre autres, d'enregistrer les sons générés par l'activité volcanique sous-marine, notamment par l'éruption de coulées de lave. Plusieurs sources d'ondes hydroacoustiques ont été identifiées pendant la première année d'écoute : séismes, glissements de terrain sous-marins, cris de mammifères marins de différentes espèces et bruit anthropogénique. Parmi ces sons, des signaux impulsionnels ont retenu notre attention. Nous les associons à des formations de vapeur liées à l'épanchement de coulées volcaniques. L'analyse préliminaire de ces signaux (10 jours répartis sur la première année, dont 24 h dépouillées finement) révèle que la forte activité éruptive observée à 10 km au NW du nouveau volcan au début de la surveillance hydroacoustique a fortement diminué pendant la première année d'enregistrement. Une détection systématique robuste de ces signaux offrirait la possibilité de dater et localiser l'activité éruptive, en l'absence de levés bathymétriques et d'imagerie répétée de la zone active.

**Keywords.** Underwater volcano, Hydroacoustic, Submarine lava flow, Seismo-volcanic monitoring, Geophysics.

**Mots-clés.** Volcan sous-marin, Hydroacoustique, Coulée de lave, Surveillance sismo-volcanique, Géophysique.

*Published online: 9 December 2022, Issue date: 17 January 2023*

## 1. Introduction

The soundscape of the oceans has changed greatly since the industrial revolution and has become a growing field of research [Duarte et al., 2021]. Sound propagates well underwater and transmits information efficiently over great distances. Mooring acoustic recorders in the Sound Fixing and Ranging (SOFAR) channel greatly expands their detection range, since the SOFAR acts as an acoustic waveguide carrying sounds over thousands of kilometers [Fox et al., 2001]. Networks of moored autonomous hydrophones (AuHs) can thus be an efficient way to monitor oceanic sound sources such as earthquakes and submarine volcanic eruptions, marine mammals, iceberg cracking, sea-state, as well as ship noise [e.g. Royer et al., 2015]. A moored AuH array unveiled the first detailed spatial and temporal distribution of seismicity along the central Mid-Atlantic Ridge [Smith et al., 2003]. The Sound Surveillance System (SOSUS), a US Navy hydrophone array deployed for anti-submarine warfare during the Cold War, has been used for three decades now to detect seismic and volcanic activity in the Northeast Pacific Ocean [Dziak et al., 2011]. For nearly 20 years, the laboratory Geo-Ocean has been maintaining hydroacoustic networks in the open ocean. Among them, the OHASISBIO network in the southern Indian Ocean, with 7 to 9 distant AuHs, has been monitoring the seismic and volcanic activity of the three Indian spreading ridges, as well as the presence and migration patterns of large whales, and oceanic ambient noise in general, since 2010 [e.g. Royer et al., 2015]. Analyses of hydroacoustic event clusters can also reveal the relative contribution of tectonic and volcanic activities associated with seafloor spreading along the Southwest Indian Ridge [Ingale et al., 2021].

One of the biggest challenges in monitoring underwater volcanoes is the fact that the eruptive activity is not as visible as on land. Furthermore, accessing real-time data, easy and common on land, is much more complex in a marine environment. Several early studies have evidenced submarine volcanic activity from hydroacoustic $T$-waves recorded by island or coastal seismic stations, corresponding to the conversion of hydroacoustic waves to seismic waves on island slopes [e.g. Talandier and Okal, 1998, Reymond et al., 2003]. The SOSUS array detected two major eruptive episodes along the northern Gorda Ridge in 1996 [Fox and Dziak, 1998] and Axial Volcano in 1998 [Dziak and Fox, 1999]. Chadwick et al. [2008] reported the first simultaneous hydroacoustic and video recordings of an active submarine volcanic eruption in the Mariana Arc (Rota-1 Volcano). Sounds from that shallow eruption, in the form of continuous gas-driven lava fragmentation, were captured in 2006 by a portable AuH at a distance of 40 m from the vent, at 530 m b.s.l. Few years later, Resing et al. [2011] documented explosive magmatic degassing at the Hades and Prometheus vents on West Mata Volcano at 1200 m b.s.l., within the NE Lau Basin, again with simultaneous AuH and video recordings. Since these first observations, the use of hydroacoustic arrays to monitor underwater volcanoes has developed and expanded [e.g. Dziak et al., 2015]. For instance, Axial Seamount, the most active submarine volcano in the NE Pacific [e.g. Chadwick et al., 2016], now hosts the world's first underwater volcano observatory, at a node of the OOI (Ocean Observatories Initiative, www.oceanobservatories.org) regional cabled array (RCA).

Ocean Bottom Seismometers (OBS) and hydrophones have also sometimes detected waterborne acoustic phases associated with submarine eruptions, but either related to explosions or implosions during lava flow emplacement on the seafloor. For instance, during the 2015 eruption at Axial Seamount, OOI seismometers detected tens of thousands of impulsive signals near the lava flows while they were being emplaced [Wilcock et al., 2016, Caplan-Auerbach et al., 2017, Le Saout et al., 2020]. Moreover, Chadwick et al. [2016] observed numerous explosion pits on the 2015 lava flow field and, hence, regarded the impulsive signals as resulting from steam bursts as lava drained out of individual lava lobes beneath a solidified crust. Similar signals were also recorded along the East Pacific Rise at 9° 50′ N [Tan et al., 2016] and on the Gakkel ridge [Schlindwein et al., 2005, Schlindwein and Riedel, 2010] suggesting that these types of impulsive sounds may be common during submarine eruptions. Hence, one of the main goals of this study is to determine whether similar hydroacoustic processes have occurred during the Mayotte eruption.

## 2. Geological setting

Mayotte is a volcanic island of the Comoros Archipelago, located in the northern part of the Mozambique Channel, between Africa and Madagascar [Michon, 2016]. Although there is still debate about its origin and its geodynamic setting, observations indicate that the archipelago was formed by intraplate volcanism either on a ~150 Ma old oceanic crust [e.g. Talwani, 1962, Davis et al., 2016, Phethean et al., 2016, Leroux et al., 2020, Vormann et al., 2020], or on a thin continental crust [e.g. Flower, 1972, Roach et al., 2017, Dofal et al., 2021], overlain by a thick sedimentary cover. Near Mayotte, the sedimentary cover reaches a thickness estimated at 1 to 2 km [Coffin et al., 1986], and more recently, at up to 3 km under the new eruption site [Masquelet et al., 2022]. From multichannel seismic reflection profiles, Malod et al. [1991] identified N130° E trending structures within the Comoros Basin that are parallel to the movement of Madagascar with respect to the African Plate. These structures are compatible with linear features highlighted in recently re-processed gravity data and orthogonal to the regional magnetic anomalies [Phethean et al., 2016]. From newly acquired marine geophysical datasets, Thinon et al. [2022] show that the recent volcanic and tectonic deformation fits with the fossil oceanic crustal fabric in the western part of the Comoros Archipelago. It is also consistent either with a current regional transpression along an immature and dextral Somalia–Lwandle plate boundary [Famin et al., 2020] or a transtension in between the East African rifts and Malagasy graben [Feuillet et al., 2021].

## 3. Volcanological and seismological monitoring of a new submarine volcano

Since 10/05/2018, Mayotte Island has experienced intense seismicity [Cesca et al., 2020, Lemoine et al., 2020, Saurel et al., 2021]. The first monitoring cruise was carried out a year later in May 2019, after the onset of the seismic activity, MAYOBS1 [Feuillet, 2019]. It revealed that these seismic events were linked to the birth of a 820 m tall and 5 km wide new volcanic edifice (NVE), whose summit reached 2800 m b.s.l. [Feuillet et al., 2021]. Several radial ridges, up to 5 km in length, grew around the summit, giving the edifice a starfish shape. Feuillet et al. [2021] estimated the volume of material that erupted to be at least 5 $km^3$. It is the largest historical submarine eruption ever observed. As of September 2021, twenty other monitoring cruises have followed MAYOBS1 to investigate the volcanic and seismic activity offshore Mayotte [REVOSIMA, 2021b, Rinnert et al., 2019]. A combination of on-land seismic stations and OBS have recorded the seismicity since March 2019 [Saurel et al., 2021]. The seismicity forms two clusters: (i) a proximal one located 10 km east of Mayotte and (ii) a distal one situated between the proximal one and the NVE [Cesca et al., 2020, Lemoine et al., 2020, Feuillet et al., 2021, Lavayssière et al., 2021, Saurel et al., 2021, Retailleau et al., 2022]. The seismic events within these two clusters occur between 25 and 50 km depth, with only very few shallow earthquakes detected.

The submarine volcanic activity has been monitored by repeated ship-borne multibeam bathymetric surveys. Bathymetric differences between successive surveys (from MAYOBS1 to MAYOBS21) allow the documentation of the spatial evolution of the volcanic activity along with pinpointing the superposition of new lava flows. For instance, from May 2019 [MAYOBS1, Feuillet, 2019] to July 2019 [MAYOBS4, Fouquet and Feuillet, 2019], the main summit of the volcanic edifice stopped growing and only lateral expansions of the lava flow field occurred [Deplus et al., 2019]. From August 2019 [MAYOBS5, SHOM, 2019] and January 2021 [MAYOBS17, Thinon et al., 2021], the active lava flows were located 10 km NW of the main NVE summit. They gradually filled a circular area, ~5 km diameter, hereafter called Tiktak area. A deep-tow camera survey observed incandescent lava flows in October 2020 near the center of the Tiktak area [MAYOBS15, Rinnert et al., 2020b]. Fresh samples of these lava flows were also dredged, leading to "popping rocks" on board the ship [Berthod et al., 2021, Feuillet et al., 2021].

## 4. MAHY hydroacoustic monitoring network

### 4.1. *Instrument description*

The AuHs deployed offshore Mayotte Island were designed after those of NOAA's Pacific Marine Environmental Laboratory [PMEL, Fox et al., 2001]. They continuously record low-frequency sounds (0–120 Hz). The sensor (a HTI90 hydrophone) consists of a piezoelectric ceramic cylinder with a flat frequency response between 2 Hz and 20 kHz. The data logger is based on a low-power microprocessor CF2 Persistor, sampling at 240 Hz and storing data on a SD (Secure Digital) card. A high-precision TCXO (Temperature Compensated Crystal Oscillator) clock is synchronized with the GPS clock prior to deployment and after recovery. The instrument's clock drift is usually on the order of 1–2 s over a 1-year deployment; the correction is applied before any data processing. Lithium batteries provide an autonomy of over 2 years, but since their transportation has become more and more restricted, we are currently testing alkaline batteries to simplify network maintenance in the future. The mooring line is anchored with a disposable weight of 400 kg at the sea bottom. An immersed buoy maintains the hydrophone at the SOFAR depth (~1300 m b.s.l.). An acoustic release triggered from the surface can free the mooring line for its subsequent recovery. The position of the acoustic release is either obtained by acoustic triangulation, or from a LBL (Long BaseLine acoustic positioning) beacon. Mooring deployment or recovery takes about 2 h.

### 4.2. *MAHY deployments*

During the MAYOBS15 cruise [Rinnert et al., 2020b] in October 2020, we deployed four AuHs around the NW–SE-oriented volcanic ridge that bridges Mayotte Island and the NVE (Figure 1). The array has a radius of ~50 km around the NVE. The instruments were then turned around in April 2021 [MAYOBS18, Rinnert et al., 2021a] and in October 2021 [MAYOBS21, Rinnert et al., 2021b]. The first deployments (MAYOBS15) were named MAHY01 to MAHY04, and the second deployments (MAYOBS18) were named MAHY11 to MAHY14.

During the first 6-month deployment, from mid-October 2020 to mid-April 2021, the four AuHs recorded data 100% of the time (Figure 2). In the following 5.5-month deployment, from mid-April 2021 to the end of September 2021, they recorded 86% (MAHY11), 77% (MAHY12), 100% (MAHY13, Figure 3), and 96% (MAHY14) of the time. MAHY11, MAHY12, and MAHY14 stopped recording, 22, 36, and 6 days before their recovery, respectively (see Supplementary Materials S1 and S2 for all spectrograms). MAHY11 failure was due to battery problems while that of MAHY12 is not yet understood. As for

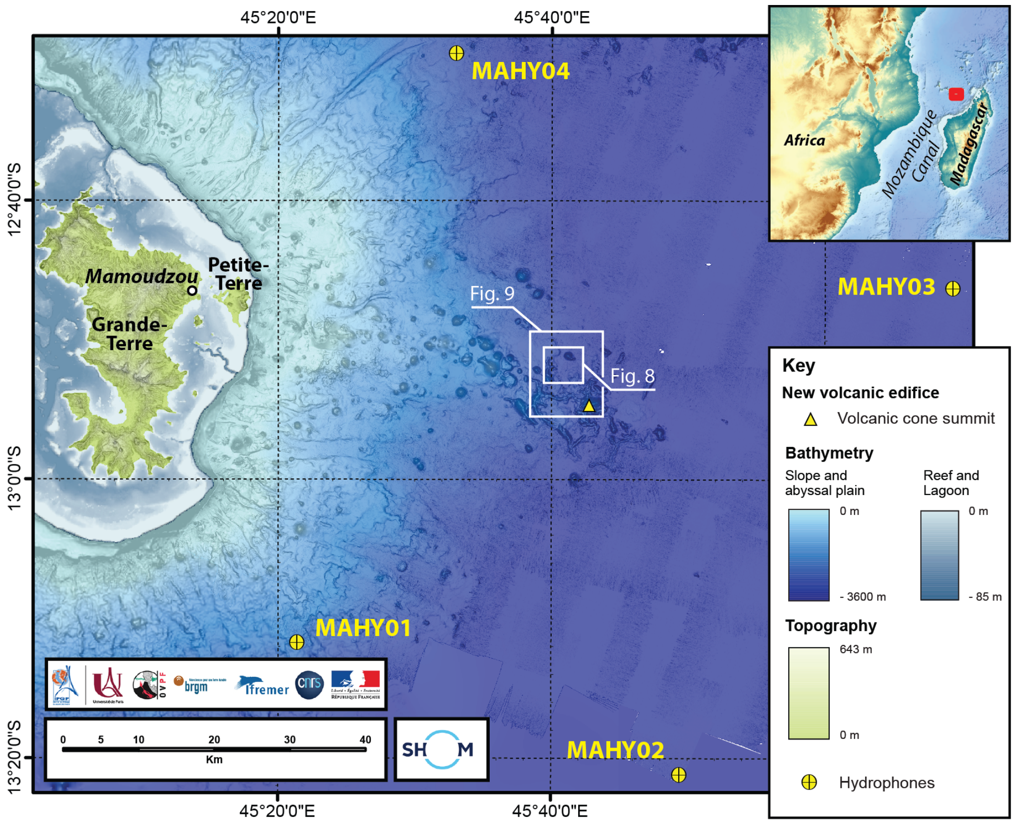


**Figure 1.** MAHY hydroacoustic array (yellow circles) located ~50 km around the new underwater volcano (yellow triangle) SE of Mayotte Island. The bathymetry is from MAYOBS1 survey [Feuillet, 2019, Feuillet et al., 2021] and SHOM [2016].

MAHY14, the failure is related to a SD card problem and recovery of the data might still be possible. The next maintenance of the AuHs is scheduled for Summer 2022.

Various types of sounds were highlighted in the data, including marine mammal calls, anthropogenic noise [Figures 2 and 3; Bazin et al., 2021], but only those related to the ongoing submarine volcanic activity are reported here. The data are obscured by seismic shots from three exploration surveys that took place in the Mozambique Channel: from 27/12/2020 to 04/02/2021 (SISMAORE [Thinon et al., 2020] and MAYOBS17 [Thinon et al., 2021] campaigns), and from 20/02/2021 to 07/03/2021 [CARAPASS (Division Plans de DMI—SHOM) campaign]. As a consequence, only a subset of the hydroacoustic dataset has been analyzed so far.

### 4.3. *Data processing*

PMEL developed an AuH data processing and visualization software called Seas [Fox et al., 2001]. This software, written in the IDL language, includes a range of tools for spectral analysis, filtering, audio conversion, and localization. All these functions are used through an interactive menu (Figure 4). The operator can visually identify events in the spectrograms from their spectral signature. Using at least three arrival times, the software can determine an initial location and then resynchronize the signals in time, so that all signals related to the same event are horizontally aligned in the display window. The display can be zoomed in for a more precise picking of the arrival times, so that the event location can be iteratively improved. The source location and origin time are estimated by a non-linear least-square

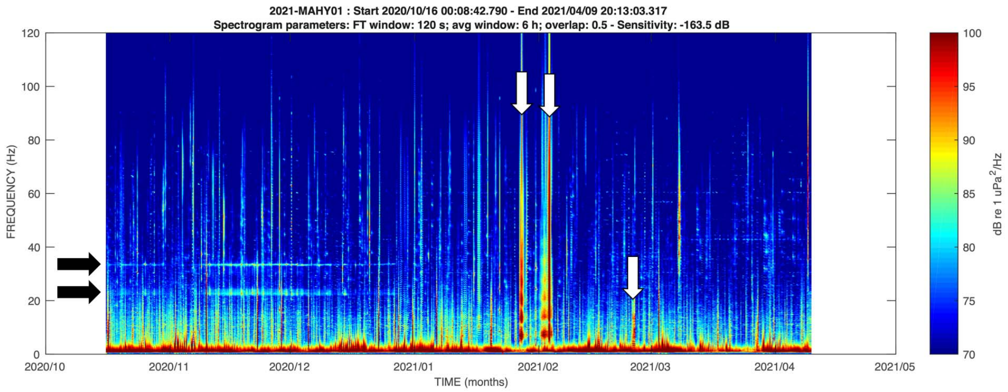


**Figure 2.** Spectrogram of the first 6 months of MAHY01 data from mid-October 2020 to mid-April 2021. The horizontal bands in Fall correspond to marine mammal calls (marked with black arrows), while the vertical stripes correspond to temporary nonvolcanic sound sources such as seismic surveys (marked with white arrows). Transiting ships are discernible as vertical (dotted) lines in the spectrograms.

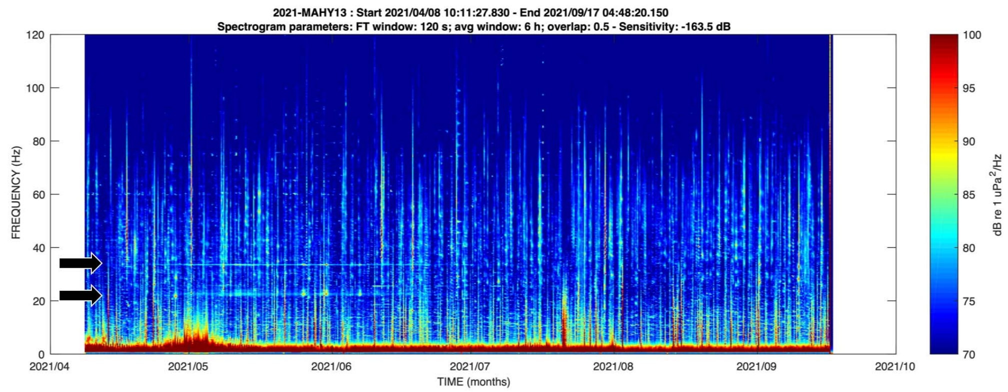


**Figure 3.** Spectrogram of the following 5.5 months of MAHY13 data from mid-April 2021 to mid-September 2021. The horizontal bands in Spring correspond to marine mammal calls (marked with black arrows).

minimization of the arrival times. The location can then be saved in a file containing the latitude and longitude, the origin time, the names of AuHs that recorded the event, the residuals, the uncertainties in the location and time of origin, the source acoustic level (SL) and the error on this level, along with sound velocities used during the inversion. The uncertainties in latitude, longitude and origin time are estimated from the covariance matrix of this least-square minimization. The distances and travel times to each AuH are calculated using the seasonal sound velocity from the Global Digital Environment Model (GDEM) and averaged along great circle paths joining the source to each of the AuHs [Teague et al., 1990].

### 4.4. *Impulsive hydroacoustic events*

Local and regional seismicity is recorded by the AuHs as $T$-waves (marked in green in Figure 5), which results from the conversion of the seismic waves at the crust/ocean interface (i.e. the seafloor) into hydroacoustic phases. So, the localization of $T$-wave sources actually corresponds to the conversion area (i.e. acoustic radiator on the seafloor) which may not always coincide with the earthquake epicenters, particularly when their sources are 25 to 50 km deep, as is the case in Mayotte. The AuHs seismic catalog is therefore not so useful for locating deep earthquakes. Nevertheless, each AuH also detected many

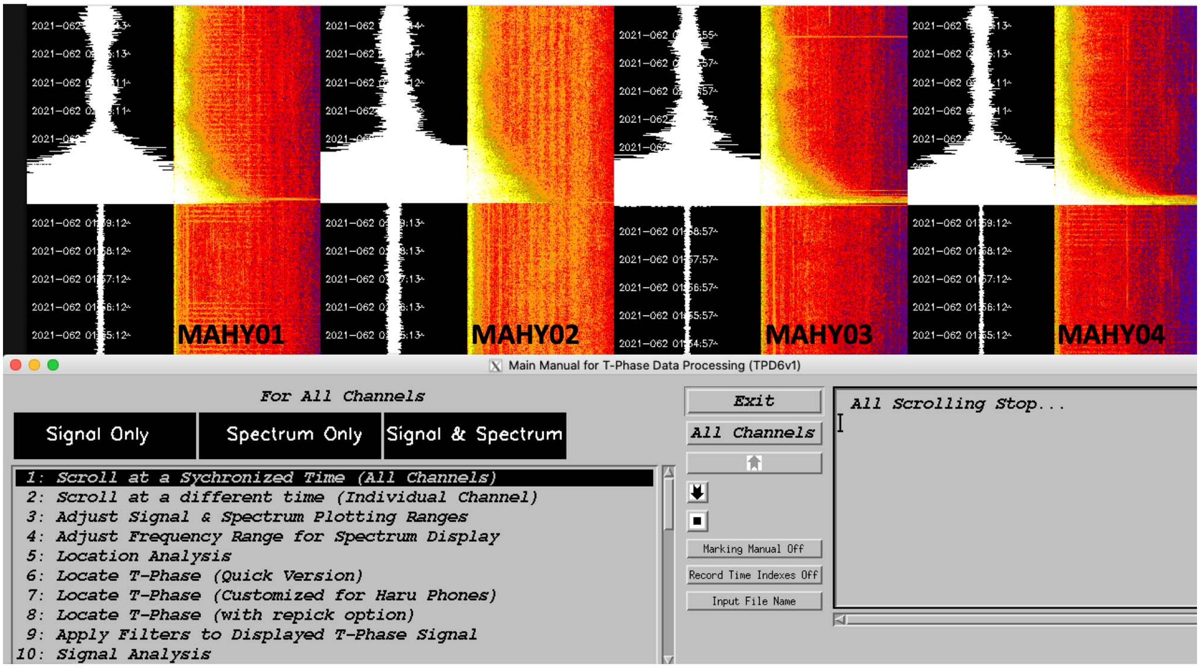


**Figure 4.** Seas visualization and processing software of hydroacoustic data developed by PMEL [Fox et al., 2001]. The raw signal is shown in white and the spectrum in colors between 0 and 120 Hz, for the four AuHs. Each time-mark corresponds to 1 min. Notice the energetic $T$-wave generated by the 3/3/2021 M4.5 local earthquake, as well as the background noise before and after the earthquake corresponding to regular seismic shots (CARAPASS seismic survey more than 600 km away, in the southern part of the Mozambique Channel, only visible in the spectrum).

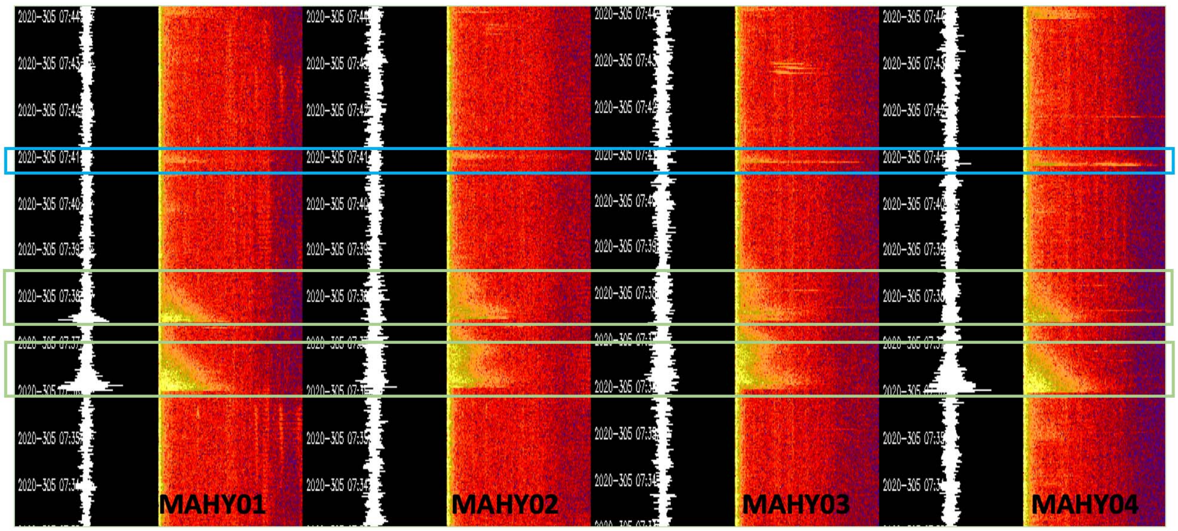


**Figure 5.** Seas visualization (same as in Figure 4) of regular $T$-waves from local earthquakes (2 events, outlined in green) and of an impulsive event (outlined in blue), both in the time and spectral domains.

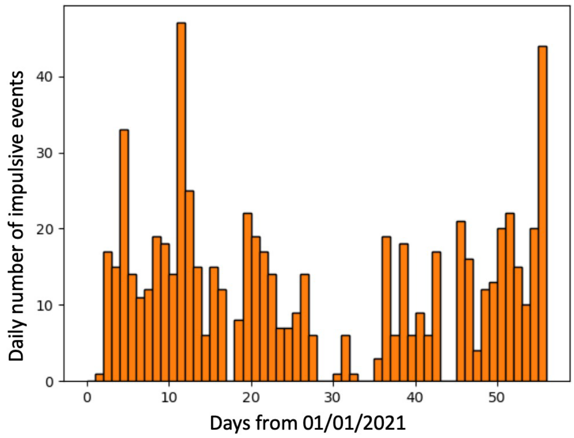


**Figure 6.** Histograms of the impulsive events detected by visual inspection during the months of January 2021 and February 2021.

unusual impulsive events that are very energetic and very short (<10 s duration, marked in blue in Figure 5) compared to the $T$-waves [Ingale et al., 2021]. Their short durations and their high-frequency content (up to 50–100 Hz) indicate that they are $H$-waves (only water borne), meaning that the energy is released directly into the water and does not travel into the solid crust as for regular $T$-waves.

Because of the large amount of data that has been recorded over the 11.5 months of the experiment, we have, so far, only examined in detail and handpicked a subset of data (Table 1 and Figure 6). Our strategy was to pick all impulsive signals identified within a period of 4 h, and then extrapolate their number to obtain an average rate over 24 h. We did this for eight different days between October 2020 and December 2020, which were selected based on their high signal-to-noise ratio (SNR). The rate of impulsive events was very high at the beginning of the recording period (October–November 2020), with a maximum of 600 events per day on November 14th, 2020, and then significantly decayed in December 2020 (Table 1). In January 2021 and February 2021, the occurrence of impulsive events decreased even further, so that it became possible to hand-pick them one by one 24/7 (Table 1). A daily average of 13 and 11 impulsive events was observed in January 2021 and February 2021, respectively, with a daily occurrence varying between 0 and 47 events (Table 1, Figure 6).

We also tested a simple automatic detector tuned for these impulsive events based on the amplitude variations in the spectrograms of the four AuHs. The threshold levels (minimum amplitude level in the spectrum, minimum amplitude drop, maximum event duration, etc) were adjusted by fitting the previously handpicked detections during mid-November 2020 on the MAHY04 dataset. Daily automatic detections for the four AuHs is presented in Figure 7. The automatic detections led to the identification of more impulsive events than the events picked manually due to false detections related to the high noise level in the data (i.e., seismic shots or whale pulses). In addition, the high rate of automatic detections in April 2021 is likely an artifact due to the start of MAYOBS18 (ship noise) on site. Moreover, two AuHs (MAHY02 and MAHY03) are more sensitive to ship traffic (see Supplementary Material S1) and present higher automatic detection rates than the two other near-shore instruments (MAHY01 and MAHY04). Due to the high automatic detection rate during the SISMAORE, MAYOBS17 and CARAPASS seismic surveys, we concluded that this method of automatic detection was not effective in a poor SNR context for assessing the occurrence of impulsive events. In such a context, automatic recognition methods based on machine learning may be more successful and will be explored.

### 4.5. *Localization of hydroacoustic activity*

From a visual inspection of the days with a high SNR on the four AuH datasets (those with good detections of impulsive events), 15/11/2020 appears as one of the most active days. Hence, we focussed our analysis on this specific date. Hand picking the impulsive events on this day resulted in a catalog of 81 events containing information on their latitude, longitude, SL and uncertainties. In fact, there were more impulsive events detected by the AuHs during that day, especially by MAHY04, but only 81 of them were clearly recorded simultaneously by the four AuHs. The picking uncertainty is on the order of 6 s. The mean error on the positions is 1654 m while the mean error in origin time of the source is 0.87 s. All the events identified on 15/11/2020 are located in the Tiktak area of the new lava flow field that was emplaced between May 2020 and January 2021. Re-picking these 81 events in a zoomed time window (the procedure

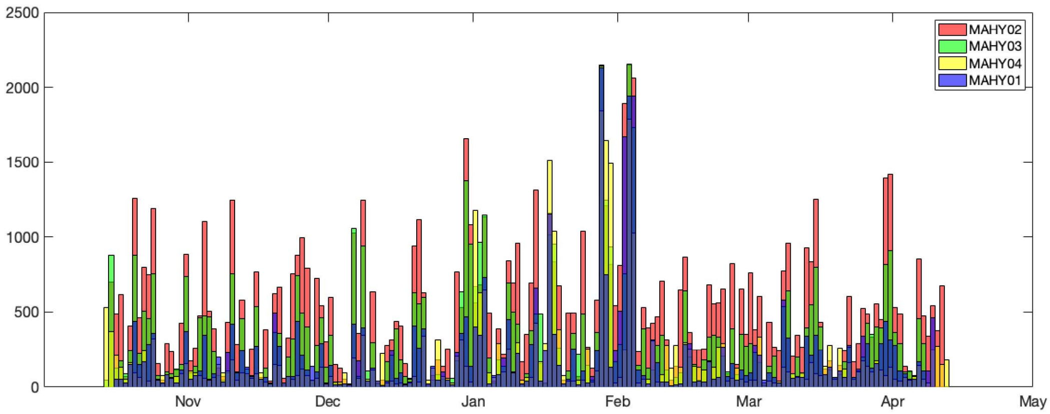


**Figure 7.** Histograms of the daily number of impulsive events detected by a simple automatic detection on the four AuH records during the first 6 months of the experiment (mid-October 2020 to mid-April 2021). The high level of automatic detections in January 2021 and February 2021 is an artifact due to poor SNR during seismic surveys. Indeed, the picks observed during the two time windows on 29–30/01/2021 and 2–4/02/2021 correspond to zero detection by visual inspection in Figure 6.

**Table 1.** Summary of the number of impulsive events detected by visual inspection of the first five months of data

| Months | Analysis window | Count over 4 h | Minimum over 24 h | Maximum over 24 h | Average over 24 h | Context |
|---|---|---|---|---|---|---|
| Oct 2020 | Count in 00:00TU–04:00TU, day 31 | 50 | | | 300 | Noisy during MAYOBS15 |
| Nov 2020 | Count in 00:00TU–04:00TU, day 07 | 40 | | | 240 | |
| | Count in 00:00TU–04:00TU, day 14 | 100 | | | 600 | |
| | Count in 00:00TU–04:00TU, day 21 | 50 | | | 300 | |
| | Count in 00:00TU–04:00TU, day 28 | 30 | | | 180 | |
| Dec 2020 | Count in 00:00TU–04:00TU, day 5 | 50 | | | 300 | |
| | Count in 00:00TU–04:00TU, day 12 | 50 | | | 300 | |
| | Count in 00:00TU–04:00TU, day 25 | 10 | | | 60 | |
| Jan 2021 | Count in 00:00TU–04:00TU, everyday | | 0 | 47 | 13 | Noisy during seismic survey |
| Feb 2021 | Count in 00:00TU–04:00TU, everyday | | 0 | 22 | 11 | Noisy during seismic survey |

Our strategy was to estimate as fast as possible the level of activity (illustrated with orange–red colors) throughout the experiment. A subset of eight days was handpicked during the time of high activity from October 2020 to December 2020, and 59 days were handpicked during the time of low activity in January 2021 and February 2021 (Figure 6).

is explained in the Data Processing paragraph, see also see Supplementary Material S3) reduced the position errors to 258 m on average, and to 0.13 s in origin time. All the 15/11/2020 re-picked events are clustered near the small Tiktak mount, which is ~60 m high and located near the center of the new lava flow field (Figure 8). The estimation of location errors (258 m) is based only on the Seas inversion. Uncertainties due to bathymetric effects, 3D variation in sound speed, or buoy displacements are not taken into account, but are likely to be limited and similar for all events.

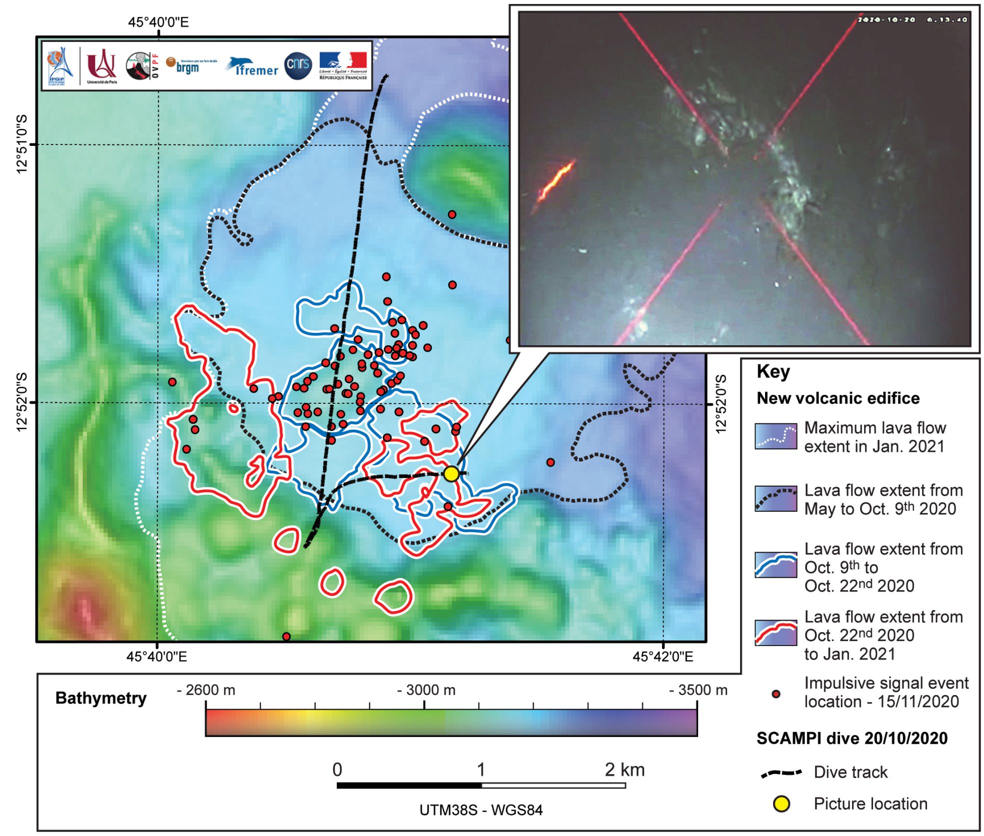


**Figure 8.** Impulsive events (red circles) detected on 15/11/2020 and located in the Tiktak area. The dashed black line tracks the SCAMPI deep-towed camera transect BS15-135. The black dotted line, blue solid line, and red solid lines outline the most recent lava flows detected by multibeam bathymetry between May 2020 and January 2021 (see key for detail). The deep-towed camera recorded a glimpse of incandescent lava at the position marked by a yellow circle as shown in the top left inset photograph. Red diagonal lines are lasers used for scale.

During MAYOBS15, a 5632 m-long dive with a towed camera (SCAMPI) across the Tiktak region (Transect BS15-135; Figure 8) recorded, for the first time, a glimpse of incandescent lava at the end of the transect on 20/10/2020 at 06:13:40TU, at position 12° 52.27′ S and 45° 41.15′ E [REVOSIMA, 2021a, see inset in Figure 8]. The impulsive events are clustered in the Tiktak area which is the active lava flow field at that time. Hence, we regard these events as implosions when hot lava interacts with seawater. They correspond to the sound generated by the gas bubbles that implode under the effect of pressure. Both Wilcock et al. [2016] and Tan et al. [2016] documented similar signals in association with steam bursts, on the East Pacific Rise. These impulsive events appear to be associated with the emplacement of new lava flows, and therefore represent a potential new method for monitoring submarine volcanic activity.

## 5. History and morphological evolution of the Tiktak flow field

To examine the relationships between the temporal and spatial distribution of the impulsive events and the lava flow field in the Tiktak region, we examined the available bathymetric data. Ship-borne multibeam echosounder data was acquired during three successive cruises (MAYOBS13-2, MAYOBS15 and MAYOBS17). The datasets were re-processed

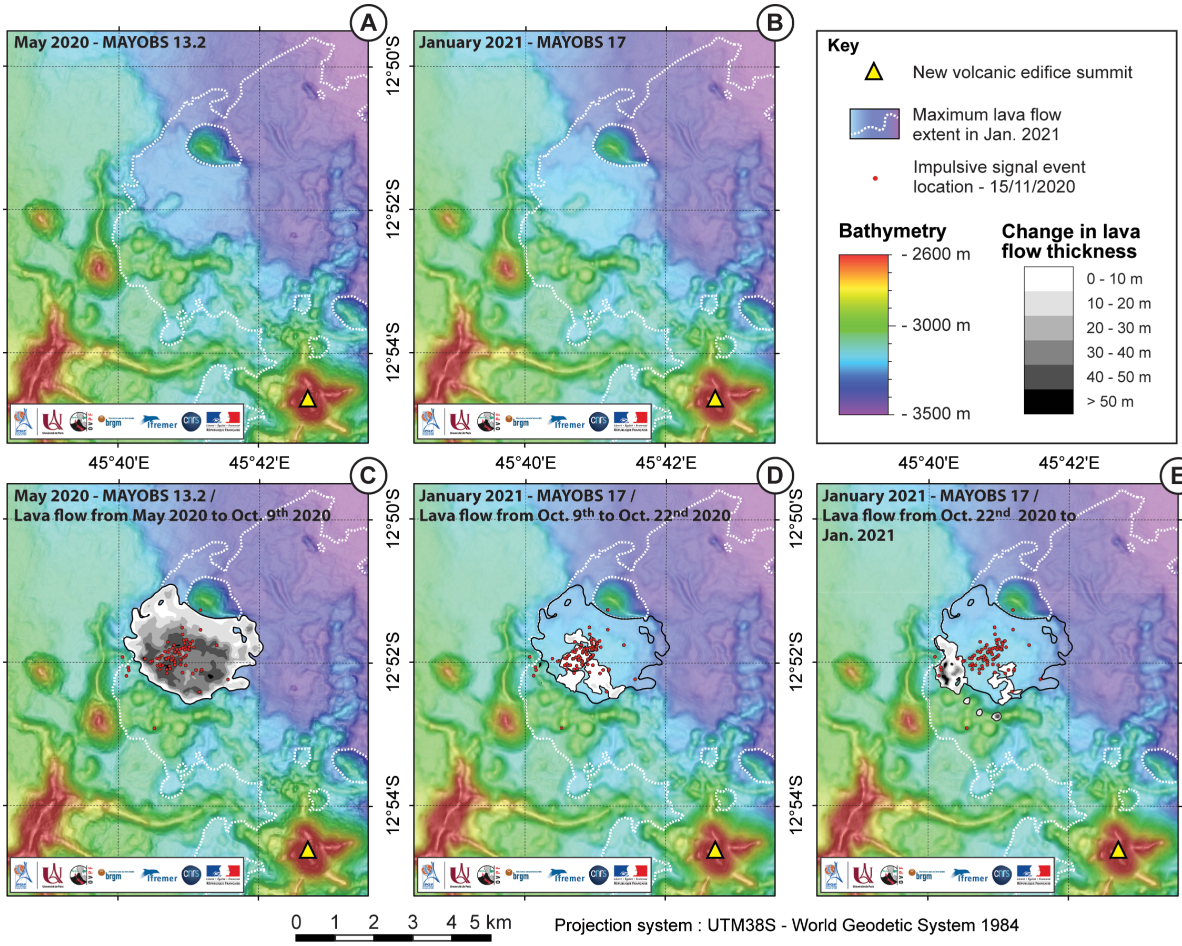


**Figure 9.** Chronological evolution of the Titkak lava flow field based on bathymetric data from successive multibeam surveys. Panels A and B show the bathymetric maps acquired in May 2020 [MAYOBS13-2, Rinnert et al., 2020a] and in January 2021 [MAYOBS17, Thinon et al., 2021]. Panels C, D, and E highlight depth changes (i.e. change in thicknesses of the new lava flows) between May 2020 and 09/10/2020 (C), [MAYOBS15, Rinnert et al., 2020b], between 09/10/2020 and 22/10/2020 (D), and between 22/10/2020 and January 2021 (E). All the impulsive events detected on 15/11/2020 (red circles) are located in the area covered with lava that erupted between May 2020 and January 2021. The lava flows which were emplaced during the period that brackets the hydroacoustic observations are less voluminous and therefore closer to the multibeam echosounder detection threshold (E).

with the GLOBE software [GLobal Oceanographic Bathymetry Explorer, Poncelet et al., 2022] to produce digital terrain models (30-m grid-cell spacing) and seafloor backscatter imagery. Successive surveys were compared to detect depth changes due to new lava deposits and to estimate their area and thickness (Figure 9). Assuming a vertical resolution of 5 m, new volcanic material can be inferred when depth changes exceed 10 m over a sufficiently large area. The data show up to 60 m-thick new lava flow between May 2020 and October 2020 in the Tiktak area. It continued growing after October 2020, but had stopped growing by January 2021. The AuH array was deployed during the last months of activity of the Tiktak lava flows. The impulsive events detected on 15/11/2020 can be seen as a snapshot of the eruptive activity and we suggest that they highlight areas of active flow emplacement.

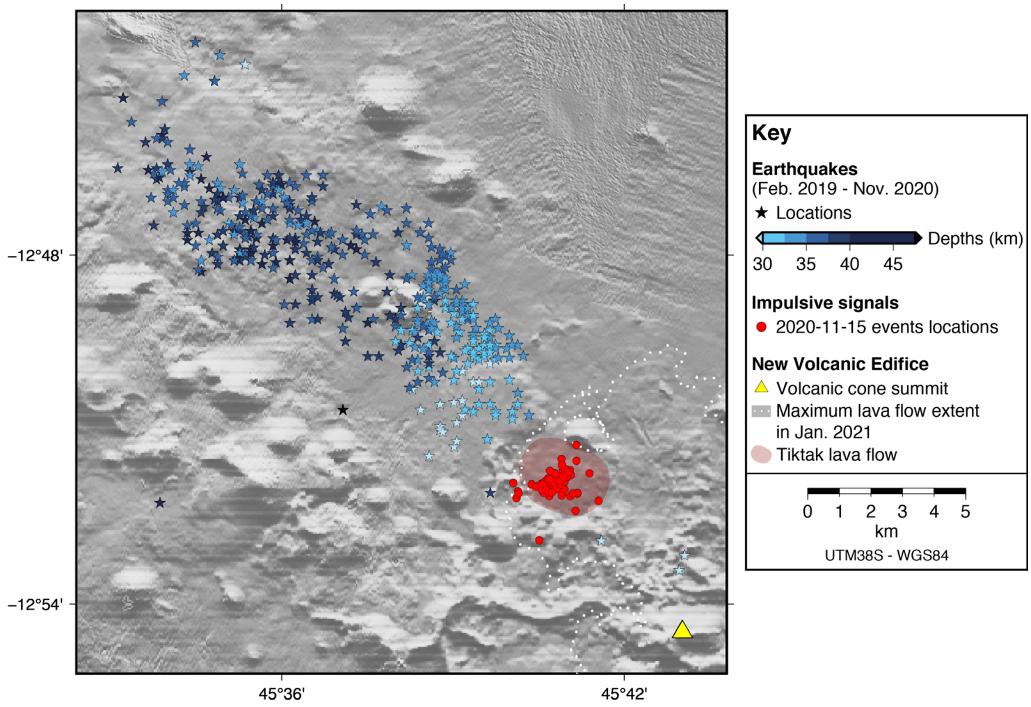


**Figure 10.** The hydroacoustic impulsive signals (red dots) interpreted as lava emplacement lie at the southern tip of the seismic swarm (colored stars). The events of the seismic swarm are the best-constrained locations from 25/02/2019 to 11/11/2020, using OBS and land seismic stations. The colors used for the earthquakes illustrate the depth of the epicenters: they show the upward and southeastward injection of magma through the feeding dyke [modified from Lavayssière et al., 2021].

## 6. Perspectives

We investigate the hydroacoustic data to track the sounds generated as hot lava interacted with cold seawater. Such signals could either be produced near the outlet or at the flow fronts [Le Saout et al., 2020]. Further examination will be necessary to investigate their detailed relation with flow emplacement. Anyhow, these impulsive sounds can indicate the start and end of submarine eruptions. As observed by the rate of impulsive events, the eruption activity in the Tiktak area was highest in October–November 2020, significantly decayed in December 2020 until it stopped. Fortunately, the AuHs were deployed before the end of the eruption and are now in place to detect potential restart. Hydroacoustic monitoring can indeed be used as a proxy for the duration of the eruptive activity [e.g. Chadwick et al., 2016]. When combined with detailed seafloor mapping, it can reveal lava emplacement in time and space. Extrusion rates can then be estimated to study the dynamics of the eruption [Le Saout et al., 2020]. Here, this preliminary analysis reveals only a snapshot of the Tiktak eruption. A more detailed analysis should elucidate the time–space pattern of the impulsive sounds. Estimation of extrusion rates will be possible when seafloor morphology analysis and ROV bathymetry data become available.

The time pattern of the impulsive events may also help to detect missed events in the OBS data. Interestingly, they lie at the southern tip of the distal seismic swarm which is interpreted as a feeder dyke [Figure 10, Feuillet et al., 2021, Lavayssière et al., 2021, Retailleau et al., 2022]. However there is so far no sign of seismic activity in the upper crust above 25 km depth, nor in the overlying first kilometers of the sedimentary cover [Coffin et al., 1986, Masquelet et al., 2022]. The occurrence of this seismic cluster only between 25 and 50 km depth is still unexplained. We suppose that a more detailed analysis possibly using template matching might reveal nonvolcano-tectonic events in the so-called aseismic zone [e.g. Duputel et al., 2019]. The available hydroacoustic data do not provide the reason for why the upward and southward migration of magma in the crust seem silent, nevertheless it can pinpoint the time windows where available OBS data could be further analyzed.

Streaming real-time data to shore is not yet available and one can mitigate this problem by making frequent access to the hydroacoustic network, at short range from Mayotte. However, deploying and recovering the current AuH moorings requires vessels with an A-frame or a small crane, and a winch, which are not available in Mayotte. The recent development of a long-term hydrophone prototype [HYDROBS for HYDROacoustic OBServatory, Royer et al., 2019] may facilitate more efficient data recovery. It is equipped with three shuttles (13″ glass spheres) that can be released on demand to collect the data. Data is duplicated once per day from the data logger to the shuttles wirelessly (1 Mb/s digital inductive through water). The shuttles can be recovered with any small vessel and are designed to be handled by nonspecialists. For instance, prior to its release, the shuttle synchronizes with the logger clock and when it surfaces, it automatically synchronizes with GPS time and stores the clock drift. Shuttles can be located on the sea surface with an AIS-like (Automatic Identification System) system. We plan to deploy an array of such moorings on the Mayotte volcano area in the near future.

## 7. Conclusions

Although the hydrophones were deployed more than two years after the onset of the eruption, they were able to record numerous impulsive events in the vicinity of the NVE. The coincidence of the location of the impulsive events with the area of active lava flow emplacement supports the interpretation that they are directly related to lava–water interactions, and as such, monitoring these acoustic events provides a way to remotely detect and locate ongoing submarine eruptions. However, the automatic detection and location of such impulsive events needs to be improved before the scientific value of the full dataset can be revealed and these new methods can be used for risk assessment and monitoring.

A new research and monitoring endeavor focussed on Mayotte has just started in France, with the MARMOR (Marine Advanced geophysical Research equipment and Mayotte multidisciplinary Observatory for Research and response) project funded by the 2021 PIA3-EQUIPEX plan. Similar to the Ocean Observatories Initiative [OOI, Kelley et al., 2014] that has streamed data live to shore since 2014 at Axial Seamount, MARMOR will finance a permanent cabled observatory to monitor the new Mayotte volcanic area with a network of multidisciplinary instruments deployed on the seafloor and in the water column, including hydrophones (HYDROBS type). These preliminary results show the potential value of hydroacoustic monitoring to better understand volcanic processes occurring on the seafloor during submarine eruptions.

## Conflicts of interest

Authors have no conflict of interest to declare.

## Acknowledgments

Since June 2019, all activities performed on Mayotte by the REVOSIMA (https://doi.org/10.18715/mayotte.revosima) monitoring network are funded by MESRI (Higher Education, Research and Innovation Ministry), MTE (Environment Ministry) and MOM (Overseas Territory Ministry) with the support from MI (Interior Ministry), MINARM (Armed Forces Ministry), DIRMOM (joint-government department for Major Hazards in the Overseas). All marine operations are performed as part of the MAYOBS set of cruises (https://doi.org/10.18142/291) and we thank the captains and crews of the R/V Marion Dufresne, R/V Pourquoi Pas? and BSAOM Champlain. We thank W. Chadwick and an anonymous reviewer for their very constructive comments on this publication. We express our gratitude to M. Beauverger for providing technical support, A. Lemarchand for logistical support, and C. Quinio for administrative support. FD was financially supported by IUEM (UAR3113 and UMR6538). The data contributes to the Service National d'Observation en Volcanologie (SNOV).

## Supplementary data

Supporting information for this article is available on the journal's website under https://doi.org/10.5802/crgeos.119 or from the author.

## References


Bazin, S., Dubost, F., Torterotot, M., Royer, J.-Y., Samaran, F., and Retailleau, L. (2021). Hydroacoustic observatory of Mayotte volcano: preliminary results. In *E-Poster at the EMSO Time Series Conference Observing Ocean Sounds, 20–22 October 2021, Telde, Gran Canaria, Spain.* (poster P10 available at https://tsc2021.emso.eu/poster).

Berthod, C., Médard, E., Bachèlery, P., Gurioli, L., Di Muro, A., Peltier, A., Komorowski, J.-K., Benbakkar, L., Devidal, J., Langlade, J., Besson, P., Boudon, G., Rose-Koga, E., Deplus, C., Le Friant, A., Bickert, M., Nowak, S., Thinon, I., Burckel, P., Hidalgo, S., Jorry, S., Fouquet, Y., and Feuillet, N. (2021). The 2018-ongoing Mayotte submarine eruption: Magma migration imaged by petrological monitoring. *Earth Planet. Sci. Lett.*, 571, article no. 117085.

Caplan-Auerbach, J., Dziak, R. P., Haxel, J., Bohnenstiehl, D. R., and Garcia, C. (2017). Explosive processes during the 2015 eruption of Axial Seamount, as recorded by seafloor hydrophone. *Geochem. Geophys. Geosyst.*, 18, 1761–1774.

Cesca, S., Letort, J., Razafindrakoto, H. N. T., Heimann, S., Rivalta, E., Isken, M. P., Nikkhoo, M., Passarelli, L., Petersen, G. M., and Cotton, F. (2020). Drainage of a deep magma reservoir near Mayotte inferred from seismicity and deformation. *Nat. Geosci.*, 13, 87–93.

Chadwick, W. W., Cashman Jr., K. V., Embley, R. W., Matsumoto, H., Dziak, R. P., de Ronde, C. E. J., Lau, T. K., Deardorff, N. D., and Merle, S. G. (2008). Direct video and hydrophone observations of submarine explosive eruptions at NW Rota-1 volcano, Mariana arc. *J. Geophys. Res.*, 113, article no. B08S10.

Chadwick, W. W., Paduan Jr, J. B., Clague, D. A., Dreyer, B. M., Merle, S. G., Bobbitt, A. M., Caress, D. W., Philip, B. T., Kelley, D. S., and Nooner, S. L. (2016). Voluminous eruption from a zoned magma body after an increase in supply rate at Axial Seamount. *Geophys. Res. Lett.*, 43, 12063–12070.

Coffin, M. F., Rabinowitz, P. D., and Houtz, R. E. (1986). Crustal structure in the western Somali Basin. *Geophys. J. Int.*, 86(2), 331–369.

Davis, J. K., Lawver, L. A., Norton, I. O., and Gahagan, L. M. (2016). New Somali Basin magnetic anomalies and a plate model for the early Indian Ocean. *Gondwana Res.*, 34, 16–28.

Deplus, C., Feuillet, N., Bachelery, P., Fouquet, Y., Jorry, S., Thinon, I., Bermel, I. S., Besson, F., Gaillot, A., Guérin, C., Le Friant, A., Paquet, F., Pierre, D., and Pitel-Roudaut, M. (2019). Early development and growth of a deep seafloor volcano: preliminary results from the MAYOBS cruises. In *AGU Fall Meeting, 9–13 December 2019, San Francisco, USA, Abstract V43I-022.*

Dofal, A., Fontaine, F. R., Michon, L., Barruol, G., and Tkalcic, H. (2021). Nature of the crust beneath the islands of the Mozambique Channel: Constraints from receiver functions. *J. Afr. Earth Sci.*, 184, article no. 104379.

Duarte, C. M., Chapuis, L., Collin, S. P., Costa, D. P., Devassy, R. P., Eguiluz, V. M., et al. (2021). The soundscape of the Anthropocene ocean. *Science*, 371(6529), article no. eaba4658.

Duputel, Z., Lengliné, O., and Ferrazzini, V. (2019). Constraining spatiotemporal characteristics of magma migration at Piton de la Fournaise volcano from pre-eruptive seismicity. *Geophys. Res. Lett.*, 46, 119–127.

Dziak, R. P., Bohnenstiehl, D. R., Baker, E. T., Matsumoto, H., Caplan-Auerbach, J., Embley, R. W., Merle, S. G., Walker, S. L., Lau, T.-K., and W.W.Jr, C. (2015). Long-term explosive degassing and debris flow activity at West Mata submarine volcano. *Geophys. Res. Lett.*, 42, 1480–1487.

Dziak, R. P. and Fox, C. G. (1999). The January 1998 earthquake swarm at Axial Volcano, Juan de Fuca Ridge: Hydroacoustic evidence of seafloor volcanic activity. *Geophys. Res. Lett.*, 26(23), 3429–3432.

Dziak, R. P., Hammond, S. R., and Fox, C. G. (2011). A 20-year hydroacoustic time series of seismic and volcanic events in the Northeast Pacific Ocean. *Oceanography*, 24, 280–293.

Famin, V., Michon, L., and Bourhane, A. (2020). The Comoros archipelago, a right-lateral transform boundary between the Somalia and Lwandle plates. *Tectonophysics*, 789, article no. 228539.

Feuillet, N. (2019). MAYOBS1 cruise, RV Marion

Dufresne, https://doi.org/10.17600/18001217.

Feuillet, N., Jorry, S., Crawford, W. C., et al. (2021). Birth of a large volcanic edifice offshore Mayotte via lithosphere-scale dyke intrusion. *Nat. Geosci.*, 14, 787–795.

Flower, M. F. J. (1972). Petrology of volcanic rocks from Anjouan, Comores archipelago. *Bull. Volcanol.*, 36(1), 238–250.

Fouquet, Y. and Feuillet, N. (2019). MAYOBS4 cruise, RV Marion Dufresne, https://doi.org/10.17600/18001238.

Fox, C. G. and Dziak, R. P. (1998). Hydroacoustic detection of volcanic activity on the Gorda Ridge, February-March 1996. *Deep-Sea Res. II*, 45, 2513–2530.

Fox, C. G., Matsumoto, H., and Lau, T.-K. A. (2001). Monitoring Pacific Ocean seismicity from an autonomous hydrophone array. *J. Geophys. Res.*, 106, 4183–4206.

Ingale, V. V., Bazin, S., and Royer, J.-Y. (2021). Hydroacoustic observations of two contrasted seismic swarms along the southwest Indian ridge in 2018. *Geosciences*, 11, article no. 225.

Kelley, D. S., Delaney, J. R., and Juniper, S. K. (2014). Establishing a new era of submarine volcanic observatories: Cabling Axial Seamount and the Endeavour Segment of the Juan de Fuca Ridge. *Mar. Geol.*, 352, 426–450.

Lavayssière, A., Crawford, W., Saurel, J.-M., Satriano, C., Feuillet, N., Jacques, E., and Komorowski, J.-C. (2021). A new 1D velocity model and absolute locations image the Mayotte seismo-volcanic region. *J. Volcanol. Geophys. Res.*, 421, article no. 107440.

Le Saout, M., Bohnenstiehl, D. R., Paduan, J. B., and Clague, D. A. (2020). Quantification of eruption dynamics on the north rift at Axial Seamount. Juan de Fuca Ridge. *Geochem. Geophys. Geosyst.*, 21, article no. e2020GC009136.

Lemoine, A., Briole, P., Bertil, D., Roullé, A., Foumelis, M., Thinon, I., et al. (2020). The 2018–2019 seismo-volcanic crisis east of Mayotte, Comoros islands: seismicity and ground deformation markers of an exceptional submarine eruption. *Geophys. J. Int.*, 223(1), 22–44.

Leroux, E., Counts, J. W., Jorry, S. J., Jouet, G., Révillon, S., BouDagher-Fadel, M. K., Courgeon, S., Berthod, C., Ruffet, G., Bachélery, P., and Grenard-Grand, E. (2020). Evolution of the glorieuses seamount in the SW Indian ocean and surrounding deep Somali basin since the cretaceous. *Mar. Geol.*, 427, article no. 106202.

Malod, J. A., Mougenot, D., Raillard, S., and Maillard, A. (1991). Nouvelles contraintes sur la cinématique de Madagascar : les structures de la chaîne de Davie. *C. R. Acad. Sci. Paris*, 312(Série II), 1639–1646.

Masquelet, C., Leroy, S., Delescluse, M., Chamot-Rooke, N., Thinon, I., Lemoine, A., Franke, D., Watremez, L., Werner, P., and Sauter, D. (2022). The East-Mayotte new volcano in the Comoros archipelago: structure and timing of magmatic phases inferred from seismic reflection data. *C. R. Géosci.*, 354(S2), 65–79.

Michon, L. (2016). The volcanism of the Comores archipelago integrated at a regional scale. In Bachèlery, P., Lénat, J.-F., Di Muro, A., and Michon, L., editors, *Active Volcanoes of the Southwest Indian Ocean*, pages 333–344. Springer-Verlag, Berlin and Heidelberg.

Phethean, J. J. J., Kalnins, L. M., van Hunen, J., Biffi, P. G., Davies, R. J., and Mccaffrey, K. J. W. (2016). Madagascar's escape from Africa: A high-resolution plate reconstruction for the Western Somali Basin and implications for supercontinent dispersal. *Geochem. Geophys. Geosyst.*, 17, 5036–5055.

Poncelet, C., Billant, G., and Corre, M.-P. (2022). Globe (global oceanographic bathymetry explorer) software. seanoe.

Resing, J., Rubin, K., Embley, R., et al. (2011). Active submarine eruption of boninite in the northeastern Lau Basin. *Nat. Geosci.*, 4, 799–806.

Retailleau, L., Saurel, J.-M., Zhu, W., Satriano, C., Beroza, G. C., Issartel, S., and Boissier, P. (2022). A Wrapper to Use a Machine-Learning-Based Algorithm or Earthquake Monitoring. *Seismological Res. Lett.*, 93(2A).

REVOSIMA (2021a). Bulletin de l'activité sismo-volcanique à mayotte, 27. http://www.ipgp.fr/revosima. ISSN 2680-1205.

REVOSIMA (2021b). Data collection of the Mayotte volcanological and seismological monitoring network (REVOSIMA) (Version 1.0). Institut De Physique Du Globe De Paris (IPGP), Bureau De Recherches Géologiques Et Minières (BRGM), Institut Français De Recherche Pour L'exploitation De La Mer (IFREMER), Centre National De La

Recherche Scientifique (CNRS).

Reymond, D., Hyvernaud, O., Talandier, J., and Okal, E. A. (2003). T-wave detection of two underwater explosions off Hawaii on 13 April 2000. *Bull. Seismol. Soc. Am.*, 93(2), 804–816.

Rinnert, E., Feuillet, N., Fouquet, Y., Jorry, S., Thinon, I., and Lebas, E. (2019). MAYOBS cruises.

Rinnert, E., Feuillet, N., and Thinon, I. (2020a). MAYOBS13-2 cruise, RV Gauss (FUGRO).

Rinnert, E., Thinon, I., and Feuillet, N. (2020b). MD 228/MAYOBS15 cruise, RV Marion Dufresne.

Rinnert, E., Thinon, I., and Lebas, E. (2021a). MAYOBS18 cruise, RV Pourquoi Pas?

Rinnert, E., Thinon, I., and Lebas, E. (2021b). MAYOBS21 cruise, RV Marion Dufresne.

Roach, P., Milsom, J., Toland, C., Matchette-Downes, C., Budden, C., Riaroh, D., and Houmadi, N. (2017). New evidence supports presence of continental crust beneath the Comoros. In *PESGB/HGS Africa Conference, August 2017, London, England.* Abstract.

Royer, J.-Y., Chateau, R., Dziak, R. P., and Bohnenstiehl, D. R. (2015). Seafloor seismicity, Antarctic ice-sounds, cetacean vocalizations and long-term ambient sound in the Indian Ocean basin. *Geophys. J. Int.*, 2, 748–762.

Royer, J.-Y., Hello, Y., Rozen, J., and Yegikian, M. (2019). HYDROBS: a versatile long-term datalogger with messengers for monitoring the water column. In *21st EGU General Assembly, EGU2019, Proceedings from the Conference, 7–12 April 2019, Vienna, Austria.* id. 16793.

Saurel, J.-M., Jacques, E., Aiken, C., Lemoine, A., Retailleau, L., Lavayssière, A., Foix, O., Dofal, A., Laurent, A., Mercury, N., Crawford, W., Lemarchand, A., Daniel, R., Pelleau, P., Bès de Berc, M., Dectot, G., Bertill, D., Roullé, A., Broucke, C., Coombain, A., Jund, H., Besançon, S., Guyavarch, P., Kowaski, P., Roudaut, M., Aprioual, R., Battaglia, J., Bodihar, S., Boissier, P., Bouin, M.-P., Brunet, C., Canjamale, K., Catherine, P., Desfete, N., Doubre, C., Dretzen, R., Dumouche, T., Fernagu, P., Ferrazzini, V., Fontaine, F., Gaillot, A., Géli, L., Griot, C., Grunberg, M., Can Guzel, E., Hoste-Colomer, R., Lambotte, S., Lauret, F., Léger, F., Maros, E., Peltier, A., Vergne, J., Satriano, C., Tronel, F., Van der Woerd, J., Fouquet, Y., Jorry, S., Rinnert, E., Thinon, I., and Feuillet, N. (2021). Mayotte seismic crisis: building knowledge in near real-time by combining land and ocean-bottom seismometers, first results. *Geophys. J. Int.*, 228(2), 1281–1293.

Schlindwein, V., Muller, C., and Jokat, W. (2005). Seismoacoustic evidence for volcanic activity on the ultraslow-spreading Gakkel Ridge, Arctic Ocean. *Geophys. Res. Lett.*, 32, article no. L18306.

Schlindwein, V. and Riedel, C. (2010). Location and source mechanism of sound signals at Gakkel ridge, Arctic Ocean: Submarine Strombolian activity in the 1999–2001 volcanic episode. *Geochem. Geophys. Geosyst.*, 11.

SHOM (2016). MNT bathyétrique de la façade de Mayotte (Projet Homonim).

SHOM (2019). Division plans de dmi. Levés Mayotte BBP Août 2019 cruise, BHO Beautemps-Beaupré.

Smith, D. K., Escartin, J., Cannat, M., Tolstoy, M., Fox, C. G., Bohnenstiehl, D. R., and Bazin, S. (2003). Spatial and temporal distribution of seismicity along the northern Mid-Atlantic Ridge (15°–35° N). *J. Geophys. Res.*, 108(B3), article no. 2167.

Talandier, J. and Okal, E. A. (1998). On the mechanism of conversion of seismic waves to and from T waves in the vicinity of island shores. *Bull. Seismol. Soc. Am.*, 88(2), 621–632.

Talwani, M. (1962). Gravity measurements on HMS Acheron in south atlantic and indian oceans. *Geol. Soc. Am. Bull.*, 73(9), 1171–1182.

Tan, Y. J., Tolstoy, M., Waldhauser, F., and Wilcock, W. (2016). Dynamics of a seafloor-spreading episode at the east pacific rise. *Nature*, 540, 261–265.

Teague, W. J., Carron, M. J., and Hogan, P. J. (1990). A comparison between the Generalized Digital Environmental Model and Levitus climatologies. *J. Geophys. Res.*, 95(C5), 7167–7183.

Thinon, I., Lemoine, A., Leroy, S., et al. (2022). Volcanism and tectonics unveiled between the EARS and Madagascar: toward a better understanding of the geodynamics of the Comoros archipelago. *C. R. Géosci.*, 354(S2), 7–34.

Thinon, I., Leroy, S., and Lemoine, A. (2020). SISMAORE cruise, RV Pourquoi Pas?

Thinon, I., Rinnert, E., and Feuillet, N. (2021). MAYOBS17 cruise, RV Pourquoi Pas?

Vormann, M., Franke, D., and Jokat, W. (2020). The crustal structure of the southern Davie Ridge offshore northern Mozambique – a wide-angle seismic and potential field study. *Tectonophysics*, 778, article no. 228370.

Wilcock, W. S. D., Tolstoy, M., Waldhauser, F., Garcia, C., Tan, Y. J., Bohnenstiehl, D. R., Caplan-Auerbach, J., Dziak, R. P., Arnulf, A. F., and Mann, M. (2016). Seismic constraints on caldera dynamics from the 2015 Axial Seamount eruption. *Science*, 354(6318), 1395–1399.

*Comptes Rendus*
*Géoscience — Sciences de la Planète*
**2022**, Vol. 354, Special Issue S2, p. 275-298
https://doi.org/10.5802/crgeos.148

The Mayotte seismo-volcanic crisis of 2018-2021 in the Comoros archipelago (Mozambique channel) / *La crise sismo-volcanique de 2018-2021 de Mayotte dans l'archipel des Comores (Canal du Mozambique)*

# The composition of gas emissions at Petite Terre (Mayotte, Comoros): inference on magmatic fingerprints

**Marco Liuzzo** [*, a, b], **Andrea Di Muro** [c, d], **Andrea Luca Rizzo** [a, e], **Fausto Grassa** [a], **Massimo Coltorti** [b] and **Magali Ader** [c]

[a] Istituto Nazionale di Geofisica e Vulcanologia, Sezione di Palermo, Italy

[b] Università di Ferrara, Dipartimento di Fisica e Scienze della Terra, Italy

[c] Université de Paris, Institut de physique du globe de Paris, CNRS, F-75005 Paris, France

[d] Observatoire volcanologique du Piton de la Fournaise, Institut de physique du globe de Paris, F-97418 La Plaine des Cafres, France

[e] Istituto Nazionale di Geofisica e Vulcanologia, Sezione di Milano, Italy

*E-mails:* marco.liuzzo@ingv.it (M. Liuzzo), dimuro@ipgp.fr (A. Di Muro), andrea.rizzo@ingv.it (A. L. Rizzo), fausto.grassa@ingv.it (F. Grassa), clt@unife.it (M. Coltorti), ader@ipgp.fr (M. Ader)

**Abstract.** The Comoros archipelago is an active geodynamic region located in the Mozambique Channel between East continental Africa and Madagascar. The archipelago results from intra-plate volcanism, the most recent eruptions having occurred on the youngest island of Grande Comore and on the oldest one of Mayotte. Since 2018, the eastern submarine flank of Mayotte has been the site of one of the largest recent eruptive events on Earth in terms of erupted lava volume. On land, the most recent volcanic activity occurred in Holocene on the eastern side of Mayotte, corresponding to the small Petite Terre Island, where two main and persistent gas seep areas are present (Airport Beach, namely BAS, and Dziani Dzaha intracrateric lake). The large submarine eruption at the feet of Mayotte (50 km offshore; 3.5 km b.s.l.) is associated with deep (mantle level) seismic activity closer to the coast (5–15 km offshore) possibly corresponding to a single and large magmatic plumbing system. Our study aims at characterizing the chemical and isotopic composition of gas seeps on land and assesses their potential link with the magmatic plumbing system feeding the Mayotte volcanic ridge and the recent submarine activity. Data from bubbling gases collected between 2018 and 2021 are discussed and compared with older datasets acquired between 2005 and 2016 from different research teams. The relation between $^3He/^4He$ and $\delta^{13}C\text{-}CO_2$ shows a clear magmatic origin for Mayotte bubbling gases, while the variable proportions and isotopic signature of $CH_4$ is related to the occurrence of both biogenic and abiogenic sources of methane. Our new dataset points to a time-decreasing influence of the recent

* Corresponding author.

seismo-volcanic activity at Mayotte on the composition of hydrothermal fluids on land, whose equilibrium temperature steadily decreases since 2018. The increased knowledge on the gas-geochemistry at Mayotte makes the results of this work of potential support for volcanic and environmental monitoring programs.

**Keywords.** Gas-geochemistry, Hydrothermal system, Biogenic vs abiogenic $CO_2$ & $CH_4$, Stable and noble gas isotopes, Mayotte, Comoros.

*Published online: 15 September 2022, Issue date: 17 January 2023*

## 1. Introduction

The Comoro Islands form an archipelago located in the Mozambique Channel between the east coast of Africa and the north-western coast of Madagascar. The formation of a huge submarine volcanic edifice since 2018, about 50 km offshore east of Mayotte, has focused the attention of the volcanological community with an increasing number of geophysical, petrological and geochemical studies [Bachèlery et al., 2019, Berthod et al., 2021a,b, Cesca et al., 2020, Feuillet et al., 2019, Lemoine et al., 2020, Liuzzo et al., 2021, Foix et al., 2021, Aiken et al., 2021].

The archipelago consists of four major volcanic islands from NW to SE: Grande Comore, Moheli, Anjouan, and Mayotte (Figure 1). Among them, Grande Comore hosts the frequently active basaltic shield Karthala volcano, whose last eruption occurred in 2007 [Thivet et al., 2022]. Subaerial Holocene volcanic activity related to alkaline magmas whose composition ranges from basanite to phonolite has been documented on the other islands [Bachèlery and Hémond, 2016, Michon, 2016, Tzevahirtzian et al., 2021, Quidelleur et al., 2022]. Based on a review of the existing morphological, geological and chronological data of The Comoro Islands, Tzevahirtzian et al. [2021] suggest that Mayotte and Moheli are the oldest islands, while Anjouan and Grande Comore are the most recent ones. The Comoro Islands are considered as part of the potentially diffuse Lwandle–Somali sub-plate boundary and possibly related to the SE extension of the East African Rift System [Michon, 2016, Famin et al., 2020, Stamps et al., 2021].

The islands of the Comoros archipelago are located within a particularly complex geodynamic region, whose volcanic and tectonic features are yet to be definitively constrained [Coffin et al., 1986, Gaina et al., 2013, Lemoine et al., 2020, Phethean, 2016]. In this complex frame, only limited information exists on the signatures and sources of fluids and their potential link with the recent volcano-tectonic activity [Liuzzo et al., 2021].

At Mayotte, volcanic products becomes increasingly older moving from the eastern side (Petite Terre island), to the western main island (Grande Terre) [Nehlig et al., 2013]. The large-volume and long-lasting submarine eruption of Mayotte, the largest submarine event ever detected by monitoring networks [Berthod et al., 2021a,b, Cesca et al., 2020, Famin et al., 2020, Lemoine et al., 2020, Feuillet et al., 2021] is likely to have had a large scale impact on fluid emissions and compositions. Since 2018, about 6.5 $km^3$ of evolved basanite lava have been emitted on the 3.5 km deep seafloor, 50 km east south-east from Mayotte from a deep source located in the upper lithospheric mantle [Bachèlery et al., 2019, Berthod et al., 2021a,b, Lemoine et al., 2020, Feuillet et al., 2021]. The new volcano grows on a N120° oriented volcanic ridge, which runs along the eastern submarine flank of Mayotte and its western subaerial tip is the small island of Petite Terre [Tzevahirtzian et al., 2021]. Since the beginning of the crisis, the region has experienced thousands of earthquakes with $M > 3.5$, related to deep (25–55 km depth) sources and distributed in two main swarms: a distal one (25 km away from Petite Terre) and a proximal one (5–15 km from Petite Terre) [Foix et al., 2021]. The important subsidence recorded by GNSS and Insar at Mayotte has been related to the drainage of a large magma reservoir located at mantle level [Lemoine et al., 2020], possibly located at a relatively small distance (13–22 km) from Petite Terre [Foix et al., 2021]. Mayotte Island is thus an ideal playground to study the possible influence of large mafic eruptions on the fluid emissions at regional scale.

On Petite Terre, recent volcanic activity has resulted in a set of Holocene basaltic scoria cones and phonolitic maars formed upon the existing coral reef [Zinke et al., 2001, Nehlig et al., 2013], as well as two main areas of low-temperature $CO_2$-rich gas seeps (Figure 1). A first bubbling area occurs in the NE part of Petite Terre (Figure 1c) inside the crater lake hosted by the Dziani Dzaha phonolitic maar. Dziani Dzaha

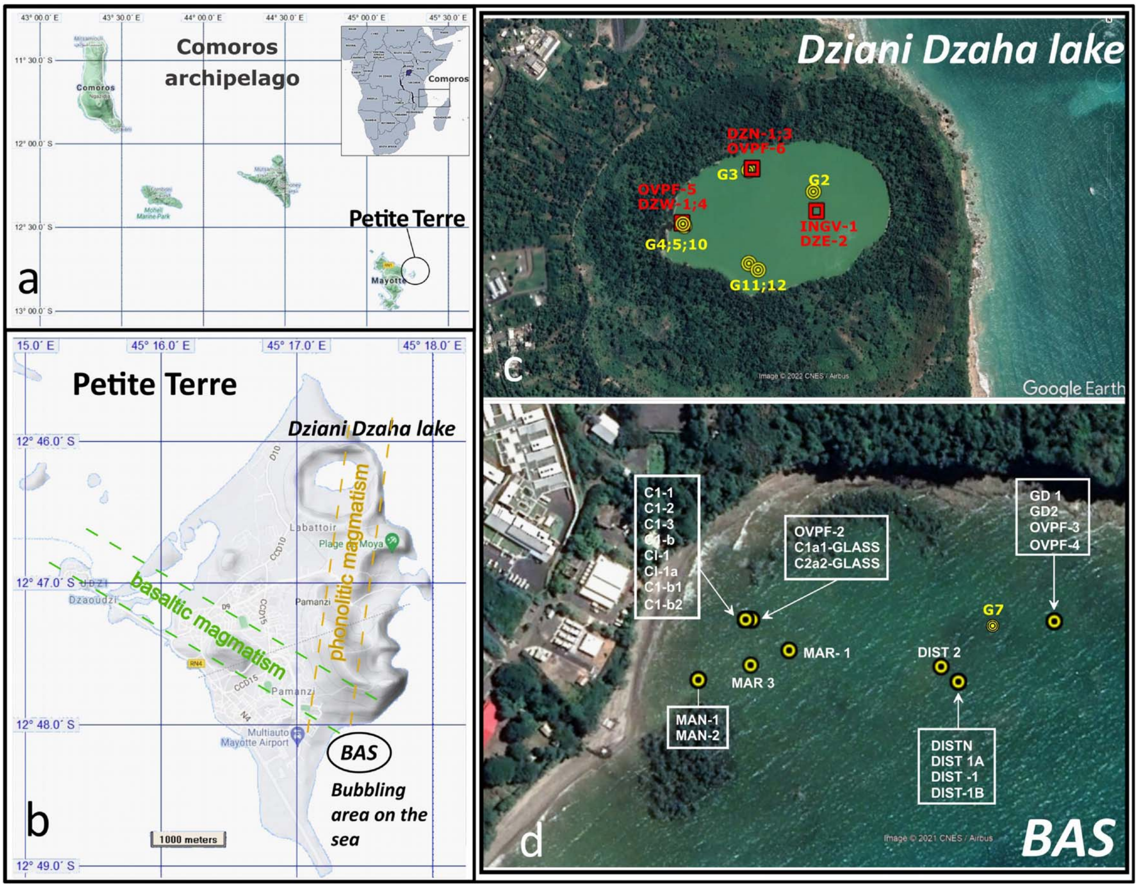


**Figure 1.** Map of the Comoros archipelago located in the northern part of the Mozambique Channel between Africa and Madagascar. In (b) the map of the Petite Terre Island on the east coast of Mayotte hosting the two main areas of gas seeps on land and where all samples discussed in this paper have been collected. In (c) and (d) the Dziani Dzaha Lake and bubbling area Airport tidal flat (BAS area) respectively. Labeled spots correspond to the location of sampled bubbling pools.

Lake is a meromictic lake with a maximum depth ranging between 4.5 m to around 18 m in a sub-central narrow depression and the bubbling emissions are heterogeneously distributed along the lake margins and in the central area, therefore upwelling through a variable water column in term of depth. Several $CO_2$-rich and high-flux bubbling areas occur along the lake margins and a main $CH_4$-rich spot made of myriads of small bubbles occurs close to the deepest part of the lake [Milesi et al., 2020]. A second bubbling area—first described in 1998 on the eastern tidal flat of Petite Terre—is located close to the locality named "Airport beach" [Figure 1d, BAS site; Traineau et al., 2006, Sanjuan et al., 2008]. There, tens of bubbling spots with variable flux occur at the southern base of the large "Vigie" phonolitic maar, on a muddy flat area exposed to significant tide and extended for about 250 × 300 m from the beach.

In this work, we focus on these two bubbling emission zones on Petite Terre Island, with the aim of characterizing their geochemical and isotopic signatures, by constraining their sources and assessing the potential influence of the still ongoing submarine volcano-tectonic activity.

## 2. Materials and methods

Since the beginning of the seismo-volcanic crisis in May 2018 at Mayotte [Feuillet et al., 2021], five campaigns including geochemical surveys were carried out, i.e. in December 2018, April 2019, September 2019, November 2020 and September 2021 (Tables 1a–1e).

Bubbling gases were sampled using a steel funnel (on the tidal flat) or a floating plastic funnel (on the Dziani Dzaha Lake) connected to a three-way valve equipped with a syringe and a tube connected to two-stopcock glass bottles of 250 mL (for general chemistry and C–H isotopic analysis), two-stopcock steel bottles of 100 mL (noble gases elemental and isotopic analysis), and pre-weighed evacuated bottles containing 4N NaOH absorbing alkaline solution (for noble gases elemental and isotopic analysis) following the method of Giggenbach and Goguel [1989].

All gas samples were analyzed at the laboratories of the INGV (Istituto Nazionale di Geofisica e Vulcanologia; Section of Palermo), for their chemistry and for the isotopic compositions of noble gases (He, Ne, and Ar), C of $CO_2$, and C and H of $CH_4$, except for the last campaign of September 2021 for which only the chemistry of the gases was analyzed and discussed in this work. Results are reported in Tables 1a–1e.

The gas chemistry was determined using a gas chromatograph (GC, Agilent 7890 equipped with PPU and MS5A columns) associated with a MicroGC module (equipped with a PPU column) and a double detector (TCD and FID) using argon as carrier gas. The analytical errors were <3%.

The C-isotope composition of $CO_2$ (expressed as $\delta^{13}$C‰ versus V-PDB) was determined using a continuous-flow isotope-ratio mass spectrometer (Thermo Delta Plus XP, Finnigan), connected to a gas chromatograph (Trace GC) and an interface (Thermo GC/C III, Finnigan). The gas chromatograph and its column (length = 30 m and i.d. = 0.32 mm; Poraplot-Q) were operated at a constant temperature of 50 °C using He as carrier gas. The analytical errors were <0.1‰. The same instrument was used for measuring the $\delta^{13}$C and $\delta^2$H of $CH_4$, where a combustion interface (Thermo GC III, Finnigan) was used to produce $CO_2$ from $CH_4$ and a gas-chromatograph/thermal-conversion interface provided online high-temperature conversion of $CH_4$ into $H_2$. The SDs for the $\delta^{13}$C and $\delta^2$H measurements of $CH_4$ were <0.2 and <2.5‰, respectively.

The He, Ne and Ar isotopic compositions were measured at the noble-gas laboratory of the INGV-Palermo. The $^3$He and $^4$He were measured into a split flight tube mass spectrometer (GVI-Helix SFT), after purification of the sample from the major gaseous species using four GP-50 Zr–Al getters and separation from the other noble gases with a trap filled with active charcoal and submerged in liquid nitrogen (for adsorbing argon), and a cryogenic trap equipped with a cold head (Janis Research) cooled down at a temperature of 10 K by a helium compressor and temperature controller that allows regulating the T in order to adsorb and release helium and neon. The $^{20}$Ne was measured by admitting Ne into a multicollector mass spectrometer (Thermo-Helix MC plus), after purification procedure into a stainless steel ultra-high vacuum line distinct from that used for He and Ar. The $^3$He/$^4$He ratio is expressed as R and normalized to $R_a$, the atmospheric helium isotope ratio equal to $1.39 \times 10^{-6}$. Analytical uncertainty ($1\sigma$) varied between 0.5 and 1.1%. Further details on the purification and analytical procedures can be found in Rizzo et al. [2019].

In the following section, we discuss the $^3$He/$^4$He ratio corrected for atmospheric contamination (expressed as $R_c/R_a$) using the measured $^4$He/$^{20}$Ne ratio (see Appendix A, Equation (A1) for the mathematical treatment). The Ar elemental and isotopic compositions ($^{36}$Ar, $^{38}$Ar, and $^{40}$Ar) were quantified in a multicollector mass spectrometer (Helix MC-GVI). The analytical uncertainty ($1\sigma$) for single $^{40}$Ar/$^{36}$Ar measurements was <0.1%. The $^{40}$Ar was corrected for air contamination ($^{40}$Ar$^*$) in samples showing $^{40}$Ar/$^{36}$Ar > 315 to exclude the most air contaminated samples, whose $^{40}$Ar correction could lead to over corrections (i.e., underestimation of $^{40}$Ar$^*$), assuming that the detected $^{36}$Ar was derived from atmosphere (Appendix A, Equation (A2)). The analytical uncertainty ($1\sigma$) of $^4$He/$^{40}$Ar$^*$ and $^4$He/$^{20}$Ne ratios is below 0.8 and 0.7%, respectively. Typical blanks for He, Ne, and Ar were $<10^{-11}$, $<10^{-12}$, and $<10^{-10}$ cc STP, respectively, and are at least two orders of magnitude lower than the signals obtained during sample measurements. Further details on sample purification and analyses are described by Rizzo et al. [2019] and Boudoire et al. [2020].

## 3. Results

Tables 1a–1e show the analyses of all samplings, also including the analyses of some data that, by their nature, were affected by air contamination during

**Table 1a.** Chemical composition of major and minor gaseous components and isotopic values of $CO_2$ and $CH_4$ from bubbling area at Petite Terre (surveys 2018–2020)

| Sampling date | Sample | Lat | Long | Site | Major (Raw) | | | | | | | $\delta^{13}C$ (‰) | | $\delta D$ (‰) |
|---|---|---|---|---|---|---|---|---|---|---|---|---|---|---|
| | | | | | $CO_2$ (vol%) | CO (ppmv) | $CH_4$ (ppmv) | $N_2$ (vol%) | $O_2$ (vol%) | $H_2$ (ppmv) | He (ppmv) | $CO_2$ | $CH_4$ | $CH_4$ |
| 08/11/2020 | OVPF-1 | −12.8002 | 45.2874 | BAS | 97.5 | 0.8 | 3859.0 | 0.7 | 0.1 | 18.0 | 26.0 | −4.4 | −18.9 | |
| 08/11/2020 | C1a1-glass | −12.8002 | 45.2874 | BAS | 51.8 | 1.3 | 2046.0 | 36.9 | 10.0 | 3.8 | 13.0 | | | |
| 08/11/2020 | OVPF-2 | −12.8002 | 45.2874 | BAS | 97.2 | 0.6 | 3787.0 | 0.6 | 0.2 | 17.0 | 23.0 | −4.3 | −19.1 | |
| 08/11/2020 | C2a2-glass | −12.8002 | 45.2874 | BAS | 0.9 | 1.4 | 16.0 | 76.4 | 20.4 | 4.0 | 4.7 | | | |
| 08/11/2020 | OVPF-3 | −12.8002 | 45.2895 | BAS | 97.7 | 36.0 | 5291.0 | 0.5 | 0.0 | 82.0 | 20.0 | −4.2 | −19.2 | −135.0 |
| 08/11/2020 | GD-1 | −12.8002 | 45.2895 | BAS | 49.5 | 1.5 | 2495.0 | 38.7 | 10.4 | 3.7 | 9.0 | | | |
| 08/11/2020 | OVPF-4 | −12.8002 | 45.2895 | BAS | 97.7 | bdl | 5145.0 | 0.6 | 0.1 | 218.0 | 19.0 | −4.2 | −19.9 | −138.0 |
| 08/11/2020 | GD-2 | −12.8002 | 45.2895 | BAS | 73.6 | bdl | 3600.0 | 20.7 | 5.4 | 2.4 | 13.0 | | | |
| 10/11/2020 | C1-b1 | −12.8002 | 45.28736 | BAS | 97.1 | bdl | 3958.0 | 0.7 | 0.1 | 28.0 | 28.0 | −4.6 | −19.1 | −125.0 |
| 10/11/2020 | C1-b2 | −12.8002 | 45.28736 | BAS | 98.8 | bdl | 3907.0 | 0.4 | 0.1 | bdl | 26.0 | | | |
| 08/09/2019 | Dist N | −12.8006 | 45.28883 | BAS | 97.1 | | 2854.0 | 0.3 | 0.0 | | 25.0 | −4.1 | −21.6 | |
| 08/09/2019 | Dist N | −12.8006 | 45.28883 | BAS | 98.5 | | 2982.0 | 0.4 | 0.0 | 112.0 | 26.0 | −4.0 | −21.8 | |
| 08/09/2019 | C1-2 | −12.8002 | 45.28736 | BAS | 98.7 | | 2444.0 | 0.3 | 0.1 | | 29.0 | −4.7 | −21.0 | |
| 08/09/2019 | C1-2 | −12.8002 | 45.28736 | BAS | 97.3 | | 2384.0 | 0.5 | 0.1 | 16.0 | 28.0 | −4.7 | −19.2 | |
| 13/09/2019 | Dist 2 | −12.8005 | 45.28871 | BAS | 98.3 | 1.2 | 2914.0 | 0.3 | 0.1 | | 27.0 | −3.8 | −22.0 | |
| 08/09/2019 | DIST-1 | −12.8006 | 45.28883 | BAS | | 18.0 | 390000.0 | 43.1 | 15.8 | 8.0 | 3558.0 | | −22.1 | −137.8 |
| 08/09/2019 | C1-2 | −12.8002 | 45.28736 | BAS | | 4.1 | 455400.0 | 48.0 | 3.0 | 11.0 | 5528.0 | | −19.6 | −118.1 |
| 06/04/2019 | Dist 1-A | −12.8006 | 45.28883 | BAS | 97.1 | 1.2 | 2442.0 | 0.5 | 0.2 | <1 | 21.0 | −3.7 | −24.4 | |
| 06/04/2019 | Dist 1-B | −12.8006 | 45.28883 | BAS | 95.8 | 2.4 | 2426.0 | 1.7 | 0.5 | <1 | 20.0 | −3.6 | | |
| 06/04/2019 | Dist 2 | −12.8005 | 45.28871 | BAS | 97.3 | 2.1 | 2406.0 | 0.3 | 0.1 | <1 | 19.0 | −3.5 | −21.4 | |
| 06/04/2019 | C1-1 | −12.8002 | 45.28736 | BAS | 97.0 | 2.1 | 2088.0 | 0.8 | 0.2 | <1 | 23.0 | −4.2 | −19.0 | |
| 06/04/2019 | C1-3 | −12.8002 | 45.28736 | BAS | 97.0 | 5.0 | 2036.0 | 0.9 | 0.2 | <1 | 23.0 | −4.3 | −19.0 | |
| 06/04/2019 | MAR 3 | −12.8005 | 45.28740 | BAS | 96.5 | 10.0 | 2725.0 | 1.6 | 0.4 | <1 | 27.0 | −4.2 | −21.0 | |
| 16/12/2018 | MAR-1 | −12.8004 | 45.28766 | BAS | 63.3 | 1.6 | 1209.0 | 27.8 | 7.5 | 2.2 | 7.0 | | | |
| 16/12/2018 | MAR-1 | −12.8004 | 45.28766 | BAS | | | | | | | | −4.8 | | |
| 16/12/2018 | CI-1a | −12.8002 | 45.28736 | BAS | 28.7 | 2.1 | 416.0 | 55.0 | 15.0 | <1 | bdl | −4.5 | −18.7 | |
| 16/12/2018 | C1-b | −12.8002 | 45.28736 | BAS | 97.9 | 1.7 | 2130.0 | 0.7 | 0.1 | 318.0 | 23.0 | −4.5 | | |
| 16/12/2018 | CI-1 | −12.8002 | 45.28736 | BAS | | | | | | | | −4.9 | | |
| 16/12/2018 | MAN-1 | −12.8006 | 45.28705 | BAS | 95.5 | 0.7 | 4587.0 | 2.5 | 0.2 | <1 | 107.0 | −5.1 | −12.4 | |
| 16/12/2018 | MAN-1 | −12.8006 | 45.28705 | BAS | | | | | | | | −5.6 | | |
| 16/12/2018 | MAN-2 | −12.8006 | 45.28705 | BAS | 83.5 | 8.0 | 4621.0 | 12.0 | 2.7 | <1 | 110.0 | −5.0 | −11.7 | |
| 16/12/2018 | MAN-2 | −12.8006 | 45.28705 | BAS | | | | | | | | −5.7 | | |
| 09/11/2020 | OVPF-5 | −12.7708 | 45.2858 | DZIANI | 93.2 | bdl | 4707.0 | 3.3 | 1.2 | 11.0 | 41.0 | −3.1 | −27.1 | −145 |
| 09/11/2020 | DZW-1 | −12.7708 | 45.2858 | DZIANI | 97.3 | 0.3 | 4825.0 | 1.1 | 0.9 | 8.0 | 38.0 | −2.6 | −26.9 | −161 |
| 09/11/2020 | DZW-4 | −12.7708 | 45.2858 | DZIANI | bdl | 8.0 | 258400.0 | 40.8 | 31.0 | 392.0 | 2322.0 | | −26.9 | −148 |
| 09/11/2020 | DZW4-dupl | −12.7708 | 45.2858 | DZIANI | | | | | | | | | | |
| 09/11/2020 | OVPF-6 | −12.7694 | 45.2877 | DZIANI | 85.8 | bdl | 37800.0 | 8.5 | 0.3 | 12.0 | 1013.0 | −0.9 | −24.6 | −124 |
| 09/11/2020 | DZN-1 | −12.7694 | 45.2877 | DZIANI | 85.8 | bdl | 39700.0 | 9.1 | 0.5 | bdl | 958.0 | | | |
| 09/11/2020 | DZN-3 | −12.7694 | 45.2877 | DZIANI | bdl | bdl | 283500.0 | 64.5 | 2.6 | 24.0 | 7823.0 | | −24.8 | −141 |
| 09/11/2020 | DZN-3-dupl | −12.7694 | 45.2877 | DZIANI | | | | | | | | | | |
| 09/11/2020 | INGV-01 | −12.7710 | 45.2903 | DZIANI | 0.2 | 6.0 | 81900.0 | 73.6 | 16.5 | 39.0 | 478.0 | −6.3 | −38.4 | −184 |
| 09/11/2020 | DZE-2 | −12.7710 | 45.2903 | DZIANI | 0.3 | 1.2 | 3897.0 | 77.6 | 20.6 | 3.8 | 9.0 | | | |

**Table 1b.** Isotopic values of the noble gases from bubbling area at Petite Terre (surveys 2018–2020)

| Sampling date | Sample | Lat | Long | Site | Noble gases isotopes | | | | | | | | | | | |
|---|---|---|---|---|---|---|---|---|---|---|---|---|---|---|---|---|
| | | | | | $R/R_a$ | $^4He/^{20}Ne$ | $[^4He]$ (ppm) | $[^{20}Ne]$ (ppm) | $R_c/R_a$ | $^{40}Ar$ (ppm) | $^{38}Ar$ (ppm) | $^{36}Ar$ (ppm) | $^{40}Ar^*$ (ppm) | $^{40}Ar$ (atm) | $^{40}Ar/^{36}Ar$ (corr) | $^{38}Ar/^{36}Ar$ (corr) |
| 08/11/2020 | OVPF-1 | −12.8002 | 45.2874 | BAS | 5.86 | 199.45 | 28.25 | 0.14 | 5.87 | 110.71 | 0.06 | 0.31 | 18.86 | 91.85 | 355.50 | 0.19 |
| 08/11/2020 | C1a1-glass | −12.8002 | 45.2874 | BAS | | | | | | | | | | | | |
| 08/11/2020 | OVPF-2 | −12.8002 | 45.2874 | BAS | 5.92 | 136.09 | 24.49 | 0.18 | 5.94 | 91.41 | 0.05 | 0.25 | 18.86 | 72.55 | 371.61 | 0.19 |
| 08/11/2020 | C2a2-glass | −12.8002 | 45.2874 | BAS | | | | | | | | | | | | |
| 08/11/2020 | OVPF-3 | −12.8002 | 45.2895 | BAS | 5.54 | 108.44 | 19.72 | 0.18 | 5.55 | 90.47 | 0.05 | 0.26 | 13.30 | 77.17 | 345.67 | 0.19 |
| 08/11/2020 | GD-1 | −12.8002 | 45.2895 | BAS | | | | | | | | | | | | |
| 08/11/2020 | OVPF-4 | −12.8002 | 45.2895 | BAS | 5.46 | 78.22 | 19.89 | 0.25 | 5.48 | 98.17 | 0.05 | 0.29 | 13.31 | 84.86 | 341.19 | 0.19 |
| 08/11/2020 | GD-2 | −12.8002 | 45.2895 | BAS | | | | | | | | | | | | |
| 10/11/2020 | C1-b1 | −12.8002 | 45.28736 | BAS | 5.53 | 99.83 | 26.99 | 0.27 | 5.55 | 72.16 | 0.03 | 0.18 | 19.54 | 52.62 | 404.40 | 0.19 |
| 10/11/2020 | C1-b2 | −12.8002 | 45.28736 | BAS | 5.55 | 237.19 | 31.63 | 0.13 | 5.56 | 87.63 | 0.04 | 0.23 | 18.54 | 69.08 | 373.95 | 0.19 |
| 08/09/2019 | Dist N | −12.8006 | 45.28883 | BAS | 6.86 | 329.38 | 24.41 | 0.07 | 6.87 | 59.28 | 0.03 | 0.15 | 14.92 | 44.36 | 392.00 | 0.19 |
| 08/09/2019 | Dist N | −12.8006 | 45.28883 | BAS | 6.94 | 261.61 | 25.05 | 0.10 | 6.95 | 55.17 | 0.02 | 0.13 | 16.35 | 38.82 | 418.02 | 0.19 |
| 08/09/2019 | C1-2 | −12.8002 | 45.28736 | BAS | 7.23 | 529.11 | 27.50 | 0.05 | 7.24 | 62.81 | 0.03 | 0.14 | 20.24 | 42.56 | 434.13 | 0.19 |
| 08/09/2019 | C1-2 | −12.8002 | 45.28736 | BAS | 7.12 | 152.41 | 26.03 | 0.17 | 7.14 | 125.30 | 0.07 | 0.36 | 19.62 | 105.68 | 348.11 | 0.19 |
| 13/09/2019 | Dist 2 | -12.8005 | 45.28871 | BAS | 7.19 | 310.71 | 25.67 | 0.08 | 7.20 | 72.00 | 0.04 | 0.19 | 15.38 | 56.63 | 374.36 | 0.19 |
| 08/09/2019 | DIST-1 | −12.8006 | 45.28883 | BAS | 6.90 | | | | | | | | | | | |
| 08/09/2019 | C1-2 | −12.8002 | 45.28736 | BAS | 7.17 | | | | | | | | | | | |
| 06/04/2019 | Dist 1-A | −12.8006 | 45.28883 | BAS | 7.07 | 167.74 | 21.20 | 0.13 | 7.08 | 87.28 | 0.05 | 0.24 | 15.06 | 72.22 | 354.85 | 0.19 |
| 06/04/2019 | Dist 1-B | −12.8006 | 45.28883 | BAS | | 1663.88 | | | | | | | | | | |
| 06/04/2019 | Dist 2 | −12.8005 | 45.28871 | BAS | | | | | | | | | | | | |
| 06/04/2019 | C1-1 | −12.8002 | 45.28736 | BAS | 7.52 | 219.30 | 22.48 | 0.10 | 7.53 | 105.50 | 0.06 | 0.30 | 16.16 | 89.34 | 347.41 | 0.18 |
| 06/04/2019 | C1-3 | −12.8002 | 45.28736 | BAS | 7.26 | 138.87 | 22.47 | 0.16 | 7.27 | 141.91 | 0.08 | 0.43 | 15.90 | 126.01 | 331.79 | 0.19 |
| 06/04/2019 | MAR 3 | −12.8005 | 45.28740 | BAS | 7.24 | 107.84 | 27.16 | 0.25 | 7.26 | 238.96 | 0.14 | 0.75 | 17.44 | 221.52 | 318.11 | 0.19 |
| 16/12/2018 | MAR-1 | −12.8004 | 45.28766 | BAS | 3.24 | 1.07 | 8.20 | 7.65 | 4.18 | 3346.63 | 2.15 | 11.53 | - | - | 290.73 | 0.19 |
| 16/12/2018 | MAR-1 | −12.8004 | 45.28766 | BAS | | | | | | | | | | | | |
| 16/12/2018 | CI-1a | −12.8002 | 45.28736 | BAS | | | | | | | | | | | | |
| 16/12/2018 | C1-b | −12.8002 | 45.28736 | BAS | 7.13 | 200.34 | 23.19 | 0.12 | 7.14 | 75.08 | 0.04 | 0.19 | 18.51 | 56.57 | 390.28 | 0.19 |
| 16/12/2018 | CI-1 | −12.8002 | 45.28736 | BAS | | | | | | | | | | | | |
| 16/12/2018 | MAN-1 | −12.8006 | 45.28705 | BAS | 6.40 | 222.22 | 102.00 | 0.46 | 6.41 | 497.76 | 0.26 | 1.41 | 81.33 | 416.43 | 352.77 | 0.19 |
| 16/12/2018 | MAN-1 | −12.8006 | 45.28705 | BAS | | | | | | | | | | | | |
| 16/12/2018 | MAN-2 | −12.8006 | 45.28705 | BAS | 6.93 | 43.59 | 113.25 | 2.60 | 6.97 | 1762.78 | 1.07 | 5.71 | 74.57 | 1688.20 | 308.79 | 0.19 |
| 16/12/2018 | MAN-2 | −12.8006 | 45.28705 | BAS | | | | | | | | | | | | |
| 09/11/2020 | OVPF-5 | −12.7708 | 45.2858 | DZIANI | 5.82 | 54.00 | 42.51 | 0.79 | 5.85 | 405.89 | 0.24 | 1.24 | 39.52 | 366.37 | 326.89 | 0.19 |
| 09/11/2020 | DZW-1 | −12.7708 | 45.2858 | DZIANI | 5.28 | 48.62 | 42.45 | 0.87 | 5.31 | 281.37 | 0.16 | 0.85 | 31.40 | 249.97 | 331.99 | 0.19 |
| 09/11/2020 | DZW-4 | −12.7708 | 45.2858 | DZIANI | 6.82 | 577.25 | 2322.33 | 4.02 | 6.83 | 9088.27 | 4.72 | 25.11 | 1669.59 | 7418.68 | 362.06 | 0.19 |
| 09/11/2020 | DZW4-dupl | −12.7708 | 45.2858 | DZIANI | 6.74 | 575.22 | 2438.49 | 4.24 | 6.74 | 9634.94 | 5.01 | 26.56 | 1786.22 | 7848.72 | 362.81 | 0.19 |
| 09/11/2020 | OVPF-6 | −12.7694 | 45.2877 | DZIANI | 6.67 | 628.12 | 1139.54 | 1.81 | 6.67 | 2055.13 | 0.82 | 4.42 | 749.02 | 1306.11 | 463.77 | 0.19 |
| 09/11/2020 | DZN-1 | −12.7694 | 45.2877 | DZIANI | | | | | | | | | | | | |
| 09/11/2020 | DZN-3 | −12.7694 | 45.2877 | DZIANI | 6.42 | 1994.54 | 8223.72 | 4.12 | 6.42 | 15342.65 | 6.07 | 32.85 | 5636.66 | 9705.99 | 467.01 | 0.18 |
| 09/11/2020 | DZN-3-dupl | −12.7694 | 45.2877 | DZIANI | 6.42 | 2122.31 | 8439.59 | 3.98 | 6.42 | 15764.01 | 6.22 | 33.62 | 5828.82 | 9935.20 | 468.76 | 0.19 |
| 09/11/2020 | INGV-01 | −12.7710 | 45.2903 | DZIANI | 6.39 | 33.31 | 620.22 | 18.62 | 6.44 | 12340.99 | 7.63 | 40.26 | 444.49 | 11896.50 | 306.44 | 0.19 |

acquisition operations, or are referable to emission sources that underwent secondary processes that altered their initial elemental and/or isotopic composition. In what follows, we will attempt to provide a description of these samples as well, however they will no longer be taken into account in the interpretative considerations (and related graphs).

## 3.1. *Gas composition*

With the exception of one $CH_4$-rich bubbling spot in the Dziani Dzaha Lake (DZE), all studied samples of

**Table 1c.** Corrected data for air contamination from the samples listed in Table 1a (surveys 2018–2020)

| Sampling date | Sample | Lat | Long | Site | Corrected for air contamination | | | | | | |
|---|---|---|---|---|---|---|---|---|---|---|---|
| | | | | | He (ppm) | $H_2$ (ppm) | $O_2$% | $N_2$% | $CH_4$ (ppm) | CO (ppm) | $CO_2$% |
| 08/11/2020 | OVPF-1 | −12.8002 | 45.2874 | BAS | 26.47 | 18.34 | 0.00 | 0.24 | 3932.82 | 0.81 | 99.37 |
| 08/11/2020 | C1a1-glass | −12.8002 | 45.2874 | BAS | 20.30 | 6.85 | 0.00 | −0.46 | 3949.21 | 2.28 | 100.07 |
| 08/11/2020 | OVPF-2 | −12.8002 | 45.2874 | BAS | 23.53 | 17.42 | 0.00 | 0.04 | 3881.17 | 0.61 | 99.57 |
| 08/11/2020 | C2a2-glass | −12.8002 | 45.2874 | BAS | −31.26 | 270.09 | 0.00 | 29.85 | 1112.06 | 89.66 | 70.00 |
| 08/11/2020 | OVPF-3 | −12.8002 | 45.2895 | BAS | 20.27 | 83.16 | 0.00 | 0.33 | 5365.96 | 36.51 | 99.11 |
| 08/11/2020 | GD-1 | −12.8002 | 45.2895 | BAS | 12.90 | 6.93 | 0.00 | −0.38 | 5033.43 | 2.78 | 99.88 |
| 08/11/2020 | OVPF-4 | −12.8002 | 45.2895 | BAS | 19.26 | 221.11 | 0.00 | 0.38 | 5218.42 | 0.00 | 99.07 |
| 08/11/2020 | GD-2 | −12.8002 | 45.2895 | BAS | 15.62 | 3.03 | 0.00 | 0.81 | 4825.20 | −0.09 | 98.70 |
| 10/11/2020 | C1-b1 | −12.8002 | 45.28736 | BAS | 28.60 | 28.63 | 0.00 | 0.27 | 4047.28 | 0.00 | 99.32 |
| 10/11/2020 | C1-b2 | −12.8002 | 45.28736 | BAS | 26.17 | 0.00 | 0.00 | 0.04 | 3936.47 | 0.00 | 99.57 |
| 08/09/2019 | Dist N | −12.8006 | 45.28883 | BAS | 25.62 | 0.00 | 0.00 | 0.15 | 2925.35 | 0.00 | 99.56 |
| 08/09/2019 | Dist N | −12.8006 | 45.28883 | BAS | 26.22 | 112.99 | 0.00 | 0.29 | 3008.39 | 0.00 | 99.39 |
| 08/09/2019 | C1-2 | −12.8002 | 45.28736 | BAS | 29.26 | 0.00 | 0.00 | 0.12 | 2467.35 | 0.00 | 99.63 |
| 08/09/2019 | C1-2 | −12.8002 | 45.28736 | BAS | 28.62 | 16.36 | 0.00 | 0.22 | 2438.25 | 0.00 | 99.53 |
| 13/09/2019 | Dist 2 | −12.8005 | 45.28871 | BAS | 27.39 | 0.00 | 0.00 | −0.06 | 2958.37 | 1.22 | 99.76 |
| 08/09/2019 | DIST-1 | −12.8006 | 45.28883 | BAS | | | | | | | |
| 08/09/2019 | C1-2 | −12.8002 | 45.28736 | BAS | | | | | | | |
| 06/04/2019 | Dist 1-A | −12.8006 | 45.28883 | BAS | 21.57 | | 0.00 | −0.12 | 2512.60 | 1.23 | 99.87 |
| 06/04/2019 | Dist 1-B | −12.8006 | 45.28883 | BAS | 20.74 | | 0.00 | −0.26 | 2531.98 | 2.50 | 100.01 |
| 06/04/2019 | Dist 2 | −12.8005 | 45.28871 | BAS | 19.47 | | 0.00 | −0.07 | 2469.39 | 2.15 | 99.82 |
| 06/04/2019 | C1-1 | −12.8002 | 45.28736 | BAS | 23.61 | | 0.00 | 0.01 | 2148.01 | 2.16 | 99.77 |
| 06/04/2019 | C1-3 | −12.8002 | 45.28736 | BAS | 23.56 | | 0.00 | 0.14 | 2090.69 | 5.13 | 99.65 |
| 06/04/2019 | MAR 3 | −12.8005 | 45.28740 | BAS | 27.74 | | 0.00 | 0.22 | 2809.43 | 10.31 | 99.49 |
| 16/12/2018 | MAR-1 | −12.8004 | 45.28766 | BAS | 8.10 | 3.18 | 0.00 | | 1910.79 | 2.39 | 100.01 |
| 16/12/2018 | MAR-1 | −12.8004 | 45.28766 | BAS | | | | | | | |
| 16/12/2018 | CI-1a | −12.8002 | 45.28736 | BAS | | | 0.00 | | 1483.76 | 6.87 | 102.53 |
| 16/12/2018 | C1-b | −12.8002 | 45.28736 | BAS | 23.32 | 322.78 | 0.00 | 0.38 | 2162.05 | 1.72 | 99.37 |
| 16/12/2018 | CI-1 | −12.8002 | 45.28736 | BAS | | | | | | | |
| 16/12/2018 | MAN-1 | −12.8006 | 45.28705 | BAS | 109.57 | | 0.00 | 1.72 | 4699.48 | 0.71 | 97.80 |
| 16/12/2018 | MAN-1 | −12.8006 | 45.28705 | BAS | | | | | | | |
| 16/12/2018 | MAN-2 | −12.8006 | 45.28705 | BAS | 127.26 | | 0.00 | 2.27 | 5378.54 | 9.27 | 97.18 |
| 16/12/2018 | MAN-2 | −12.8006 | 45.28705 | BAS | | | | | | | |
| 09/11/2020 | OVPF-5 | −12.7708 | 45.2858 | DZIANI | 44.00 | 11.86 | 0.00 | −1.28 | 5089.07 | −0.02 | 100.76 |
| 09/11/2020 | DZW-1 | −12.7708 | 45.2858 | DZIANI | 39.50 | 8.34 | 0.00 | −2.26 | 5044.09 | 0.30 | 101.75 |
| 09/11/2020 | DZW-4 | −12.7708 | 45.2858 | DZIANI | | | | | | | |
| 09/11/2020 | DZW4-dupl | −12.7708 | 45.2858 | DZIANI | | | | | | | |

(continued on next page)

**Table 1c.** (continued)

| Sampling date | Sample | Lat | Long | Site | Corrected for air contamination | | | | | | |
|---|---|---|---|---|---|---|---|---|---|---|---|
| | | | | | He (ppm) | $H_2$ (ppm) | $O_2$% | $N_2$% | $CH_4$ (ppm) | CO (ppm) | $CO_2$% |
| 09/11/2020 | OVPF-6 | −12.7694 | 45.2877 | DZIANI | 1043.35 | 12.35 | 0.00 | 7.64 | 38935.48 | 0.00 | 88.36 |
| 09/11/2020 | DZN-1 | −12.7694 | 45.2877 | DZIANI | 984.77 | −0.01 | 0.00 | 7.63 | 40814.10 | −0.01 | 88.19 |
| 09/11/2020 | DZN-3 | −12.7694 | 45.2877 | DZIANI | | | | | | | |
| 09/11/2020 | DZN-3-dupl | −12.7694 | 45.2877 | DZIANI | | | | | | | |
| 09/11/2020 | INGV-01 | −12.7710 | 45.2903 | DZIANI | 2301.87 | 187.42 | 0.00 | 59.24 | 397823.18 | 28.19 | 0.73 |
| 09/11/2020 | DZE-2 | −12.7710 | 45.2903 | DZIANI | 257.75 | 219.69 | 0.00 | 54.91 | 260997.01 | 63.93 | 18.94 |

**Table 1d.** Chemical composition of major and minor gaseous components from bubbling area at Petite Terre (survey 2021)

| Sampling date | Sample | Lat | Long | Site | Major (Raw) | | | | | | |
|---|---|---|---|---|---|---|---|---|---|---|---|
| | | | | | $CO_2$ (vol%) | CO (ppmv) | $CH_4$ (ppmv) | $N_2$ (vol%) | $O_2$ (vol%) | $H_2$ (ppmv) | He (ppmv) |
| 5/9/2021 | C1-2 | −12.800117 | 45.2873 | BAS | 97.7 | 0.8 | 5099 | 0.25 | 0.0705 | bdl | 22 |
| 5/9/2021 | C1-1 | −12.80015 | 45.28736 | BAS | 97.45 | 0.9 | 5158 | 0.68 | 0.27 | bdl | 2021 |
| 5/9/2021 | MAN | −12.80064 | 45.28705 | BAS | 96.94 | 1.5 | 6654 | 1.59 | 0.45 | bdl | 38 |
| 5/9/2021 | MAR | −12.80045 | 45.28873 | BAS | 97.73 | 0.9 | 5838 | 0.43 | 0.23 | bdl | 15 |
| 5/9/2021 | DIST | −12.799917 | 45.28612 | BAS | 97.62 | 1.4 | 6637 | 0.5 | 0.24 | bdl | 2021 |
| 7/9/2021 | DZW | −12.770833 | 45.28582 | DZIANI | 97.28 | 1.1 | 6126 | 1.2021 | 0.73 | bdl | 54 |
| 7/9/2021 | DZN | −12.769403 | 45.28771 | DZIANI | 89.71 | 1 | 24,400 | 6.5 | 1.98 | bdl | 330 |

**Table 1e.** Corrected data for air contamination from the samples listed in Table 1d (survey 2021)

| Sampling date | Sample | Lat | Long | Site | Corrected for air contamination | | | | | | |
|---|---|---|---|---|---|---|---|---|---|---|---|
| | | | | | He (ppm) | $H_2$ (ppm) | $O_2$% | $N_2$% | $CH_4$ (ppm) | CO (ppm) | $CO_2$% |
| 5/9/2021 | C1-2 | −12.800117 | 45.2873 | BAS | 22.384 | | 0.07 | 0.254368318 | 5188.096214 | 0.814 | 99.2 |
| 5/9/2021 | C1-1 | −12.80015 | 45.28736 | BAS | 21.34 | | 0.27 | 0.691000802 | 5241.444318 | 0.9146 | 98.5 |
| 5/9/2021 | MAN | −12.80064 | 45.28705 | BAS | 37.834 | | 0.45 | 1.583044892 | 6624.89353 | 1.4934 | 97.3 |
| 5/9/2021 | MAR | −12.80045 | 45.28873 | BAS | 15.172 | | 0.23 | 0.434934814 | 5904.998706 | 0.9103 | 98.7 |
| 5/9/2021 | DIST | −12.799917 | 45.28612 | BAS | 21.28 | | 0.24 | 0.506657787 | 6725.375469 | 1.4186 | 98.6 |
| 7/9/2021 | DZW | −12.770833 | 45.28582 | DZIANI | 58.525 | | 0.79 | 1.311395671 | 6639.347007 | 1.1922 | 97.2 |
| 7/9/2021 | DZN | −12.769403 | 45.28771 | DZIANI | 1026 | | 6.16 | 20.20949473 | 75863.33407 | 3.1092 | 65.9 |

the Mayotte gas seeps are $CO_2$-dominated. The Mayotte noble gas show a more variable composition for the Dziani Dzaha Lake than for the Airport tidal flat (BAS; Tables 1a–1e), with $^4$He ranging between 8.2 and 113 ppm at BAS and between 42.5 and 1139.5 for the Dziani Dzaha Lake. The $^{20}$Ne values for the BAS zone range from 0.1 to 7.7 ppm and between 0.8 and 18.6 for the Dziani Dzaha Lake. Finally, the $^{40}$Ar is in the range 55.2–3346.6 ppm in BAS and 281.4–2055.1 for the Dziani Dzaha Lake. Some of the samples in both Dziani and BAS areas have a significant air contamination showing concentrations of $N_2$ and $O_2$ up to 76.4% and 20.4% respectively (Tables 1a–1e, Figure 2a).

The BAS bubbling gases from the tidal flat show a $CO_2$ dominated composition with concentrations up to 98.8% and a variable concentration in $CH_4$ ranging between 16 and 5291 ppm with the lowest value

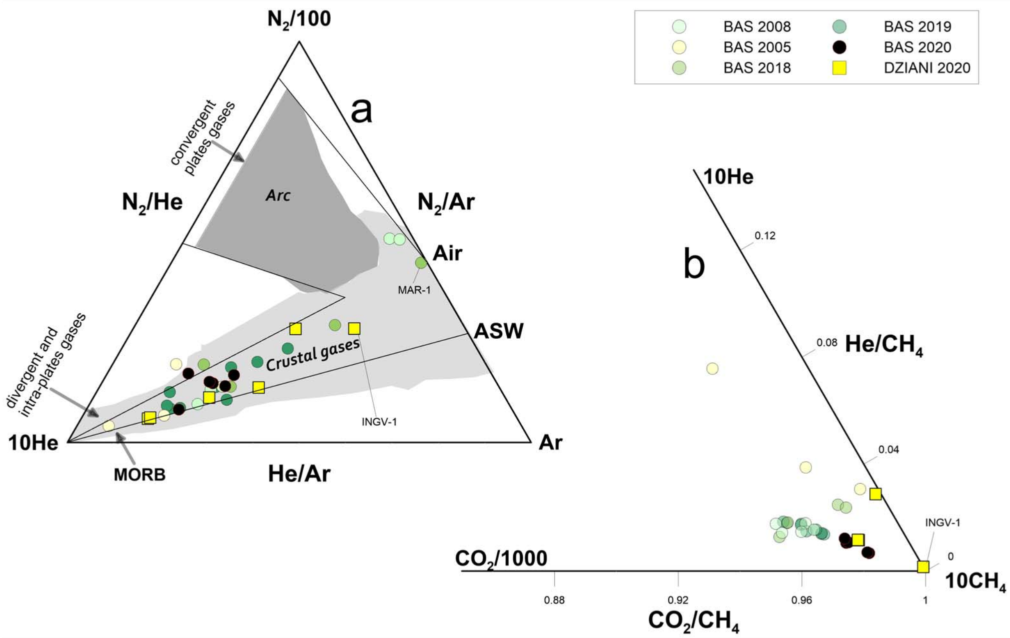


**Figure 2.** Relative proportion of He–Ar–$N_2$ in Mayotte bubbling gases (a); the fields of composition of gases emitted in crustal and arc settings are also shown. Data collected at Petite Terre show variable degrees of air and ASW contamination. In (b) $CO_2$–$CH_4$–He ternary diagram shows that the $CO_2$-rich Mayotte gases contain a significant amount of $CH_4$ with the highest proportion of methane recorded in the Dziani Dzaha Lake. Areas in different shades of grey distinguish gases from arc- and crustal geodynamic environments—from literature data.

related to an air-contaminated sample ($C_2a_2$-glass). The BAS gases show low concentrations in $H_2$ and CO, ranging from below detection limit to 11 ppm for $H_2$ and to 18 ppm for CO (higher values for $H_2$ and CO in Tables 1a–1e refer to samples collected in steel samplers, which we do not consider reliable, as discussed in Section 4.3). At the Dziani Dzaha Lake, $CO_2$ is also the dominant gas species in two of the three analyzed spots (DZW, DZN), with values up to 97.3%, while $CH_4$ is variable between 3897 and 81,900 ppm, except in the third spot (DZE) where $CH_4$ is the dominant gas. The $H_2$ and CO are generally present in low concentrations.

The chemical composition of the Mayotte gases plotted in a $N_2$, He and Ar ternary diagram (Figure 2a) follows a mixing trend between a He-rich component and an atmospheric component (air or air-saturated water—ASW). The bubbling gases from both areas at Mayotte show a variable degree of contamination by an atmospheric end-member, and its contribution is probably slightly higher for air than for ASW at least in BAS. On the whole, the He–Ar–$N_2$ variability falls within a typical compositional range of gases emitted in intraplate or extensive tectonic settings. The two dominant mixing sources appear to be atmospheric and MORB-type mantle, and they are distinct from typical subduction-related gases, which have higher $N_2$/Ar ratios due to the $N_2$ excess released to the wedge by subducting sediments [e.g., Barry and Hilton, 2016]. With regard to the helium variability, the similarity between Dziani Dzaha Lake and BAS is interesting, as there seems to be no appreciable difference in the air-MORB mixing trends. This suggests that shallow processes do not significantly affect helium abundances at Petite Terre.

The chemical composition in relation to the plot of $CO_2$–$CH_4$–He (Figure 2b) highlights that low temperature gas seeps of Petite Terre have a general high $CH_4$ concentration. A relatively higher abundance of $CH_4$ in Dziani than in BAS tidal flat is likewise evident. Since the beginning of the seismo-volcanic crisis, the $CO_2$-rich bubbling spots of the two sites show comparable abundances of $CH_4$, and Dziani still hosts the only $CH_4$-dominated bubbling area. The INGV-1 sample in Dziani is the most enriched in methane (Figure 1c); however, it should also be noted that this specific sample is also affected by air contamination.

## 3.2. *Systematics of noble gas isotope ratios,* $CO_2$ *and* $CH_4$ *isotopes*

Tables 1a–1e report the isotopic compositions of noble gases, $CO_2$ and $CH_4$ in the sampled gases from the two bubbling areas of Petite Terre. Regarding the measured $^3He/^4He$ ratios, these vary between 5.45 and 7.5 $R_a$ in BAS, and between 5.3 and 6.8 $R_a$ in Dziani Dzaha Lake (Figure 3). It is worth noting that the range of $R/R_a$ values is very similar between BAS and Dziani, although it should be noted that less data is available for Dziani and that they are only related to the 2020 campaign. In both BAS and Dziani, a few samples show a clear air contamination as recorded by relatively high content of $N_2$ and $O_2$. It is possible that these samples underwent some issues during the sampling operations or during the storage and transport to the laboratory that fractionated the $^3He/^4He$, (for example MAR-1 Figure 3) leading us to exclude them for further discussion. The majority of samples do not show significant air contamination as indicated by both the chemistry of gases and the noble gas systematics (Tables 1a–1e). For instance, the $^4He/^{20}Ne$ ratios is at least 2 orders of magnitude higher than the ratio in air (0.318) reaching 1663 in the BAS (this study) and up to 2750 in the survey carried out by BRGM in 2008 [Sanjuan et al., 2008], while is reaches up to 2122 in the Dziani Dzaha Lake.

The $^{40}Ar/^{36}Ar$ values range from the atmospheric ratios up to 434 in BAS, and up to 468 in the Dziani Dzaha Lake. The few air contaminated samples have lower ratios, like MAR-1 and MAN-2 in BAS site ($^{40}Ar/^{36}Ar$ = 290 and 308; and $^4He/^{20}Ne$ = 1.07 and 43.59, respectively), and INGV-01 in the Dziani Dzaha Lake ($^{40}Ar/^{36}Ar$ = 306 and $^4He/^{20}Ne$ = 33.3).

With the exception of a few air-contaminated samples, the difference between $R/R_a$ and $R_c/R_a$ is almost negligible.

The $^4He/^{40}Ar^*$ ratio of BAS gases ranges between 1.3 and 1.7, with a general overlap of values between different sampled pools and sampling periods, and they are within 1.1 and 1.5 in Dziani Dzaha Lake, irrespective of the variable $CH_4/CO_2$ ratios. These values fall within the typical range of mantle production ratio [$^4He/^{40}Ar^*$ = 1–5; Marty, 2012] and magmatic values from other geodynamic settings [e.g., Reunion hot spot, Boudoire et al., 2018; Eger Rifţ intra-plate in Europe, Bräuer et al., 2011; Etna intra-plate, Paonita et al., 2012; Kolumbo arc volcano in Greece, Rizzo et al., 2019].

The $^4He/^{40}Ar^*$ variability is commonly used to track magmatic degassing processes due to the ~7–10 times lower solubility in silicate melts of Ar

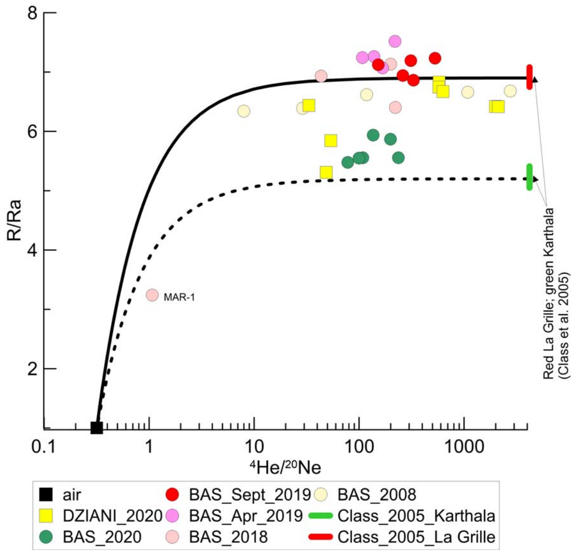


**Figure 3.** $^4He/^{20}Ne$ versus $^3He/^4He$ ($R/R_a$) ratios in Mayotte bubbling gas. Continuous and dashed black lines correspond to mixing trend between air and magmatic gases. Magmatic signature is constrained using the analyses of mineral crushing of Class et al. [2005] from La Grille and Karthala volcanoes [see also Liuzzo et al., 2021]. The two solid red and green bars correspond to the range of the $R/R_a$ variability in La Grille and Karthala datasets [Class et al., 2005]. La Grille is the older and rarely active volcano in the north of Grande Comore (last dated eruption: 1029–1424 CE) [Bachèlery and Hémond, 2016, and references therein], while Karthala is the most active volcano of Grande Comore (last eruption: 2007).

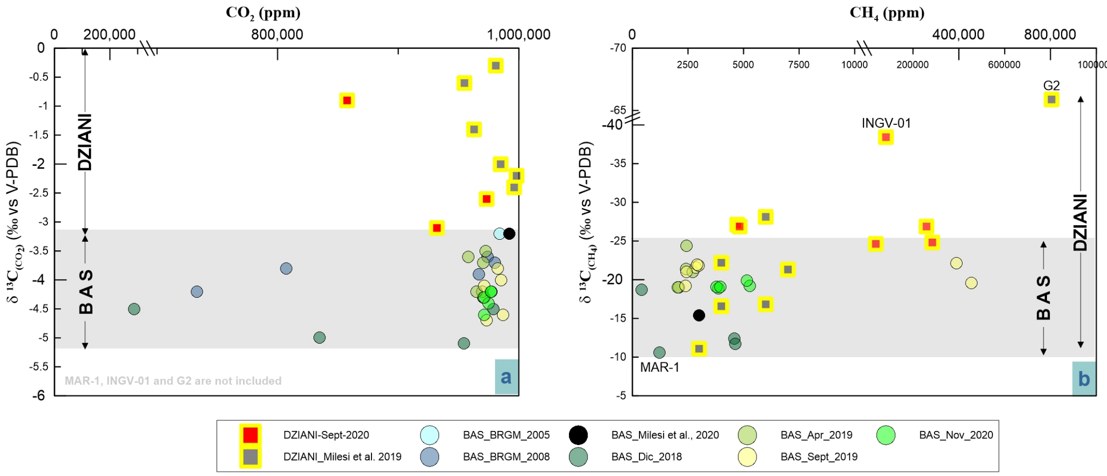


**Figure 4.** Comparison of carbon isotopic variability in $CO_2$ (left) and $CH_4$ (right) and elemental composition of the two main bubbling areas of Mayotte–Petite Terre (BAS tidal flat and Dziani Dzaha intracrateric lake).

than He [e.g. Burnard, 2001, Paonita et al., 2012, Barry et al., 2014, Boudoire et al., 2018]. $^4He/^{40}Ar^*$ ratios at Petite Terre do not show systematic variations as a function of location or time. Liuzzo et al. [2021] suggest that this homogeneous signature reflects that all bubbling spots are related to a single degassing source and pressure, likely related to magmas stored close to the mantle-crust underplating depth (15–20 km depth), as observed in other magmatic systems [e.g., Reunion, Boudoire et al., 2018]. This depth range corresponds to the shallower part of the magmatic plumbing system below Mayotte, where evolved basanitic magma differentiate to form phonolitic melts [Berthod et al., 2021a,b, Foix et al., 2021].

The C-isotope compositions of $CO_2$ ($\delta^{13}C_{CO_2}$) at BAS gases vary from −5.7‰ and −3.5‰, where the most negative ratios are those measured in samples from MAN-1 and MAN-2 a sampling pool with relatively low gas flux and located close to a dense area of Mangrove trees on the airport flat. At Dziani Dzaha Lake the variability is much wider with $\delta^{13}C_{CO_2}$ spanning between −0.9 and −6.3‰ (data from this work), where the most negative value is that of the sample INGV-01 from the $CH_4$-rich plume (DZE). Interestingly, previous data collected in 2016 from Milesi et al. [2019] show an even higher variability with $^{13}C_{CO_2}$ between −0.3 and −20.1, where the most negative correspond to G2 sample in Milesi et al. (2019) collected in the same area of DZE. Figure 4a shows the $\delta^{13}C_{CO_2}$ distribution and highlights a significant separation of the C isotope signature between the two bubbling areas, where Dziani is systematically more positive than BAS (with the exception of G2 not represented in the plot) and where the $\delta^{13}C_{CO_2}$ in BAS are confined to a narrow range of about 2 delta units.

On the contrary, the distribution of the C-isotope composition of $CH_4$ ($\delta^{13}C_{CH_4}$) (Figure 4b) partly overlaps in BAS and Dziani areas, with the BAS site showing again a fairly narrow range of variability, (from −25‰ to −10‰). At BAS, the least negative values are found in the MAN low-flux pool located close to the mangrove area (MAN-1 and MAN-2 samples) that is considered affected by gas–water dissolution by Liuzzo et al. [2021]. The site of Dziani Dzaha Lake shows a wider variation in $\delta^{13}C_{CH_4}$ fluctuating from minimum values of more than −65‰ (DZE area) to maximum values of −11‰ (DZW area). The different isotopic variability of carbon in a $\delta^{13}C_{CO_2}$ and $\delta^{13}C_{CH_4}$ space is evident in Figure 5, where the two markers are linearly and negatively correlated ($R^2$ = 0.7) in the BAS site and positively correlated in the Dziani Dzaha Lake. Interestingly our new dataset on the Dziani Dzaha Lake clearly shows more negative $\delta^{13}C_{CH_4}$ values with respect to that

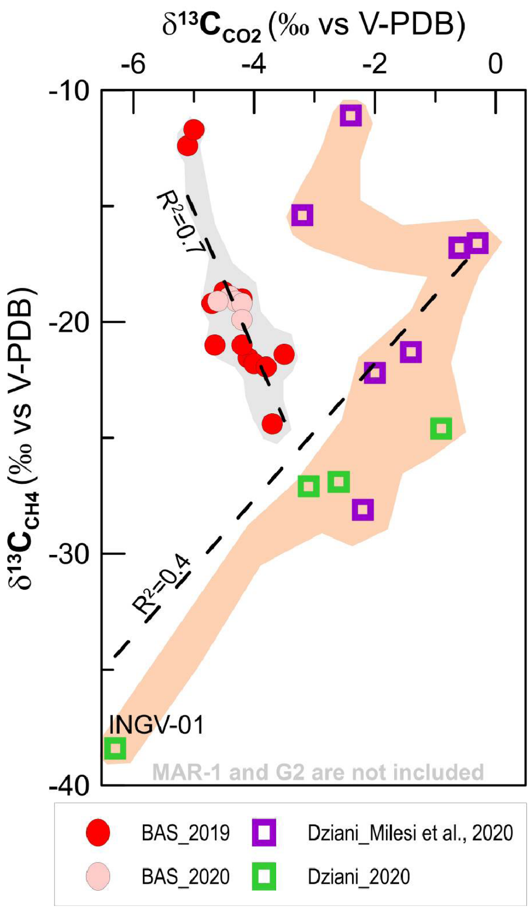


**Figure 5.** Carbon isotopic composition in $CO_2$ and $CH_4$ in the two gas seeps areas of Mayotte (BAS tidal flat and Dziani Dzaha Lake). Milesi et al. [2020] data were collected in 2016, before the beginning of the seismo-volcanic crisis in 2018.

of Milesi et al. [2020]. Regarding hydrogen isotopic values in $CH_4$ ($\delta D_{CH_4}$), our samples yielded a δD of −118.1‰ and −137.8‰ V-SMOW, respectively in BAS and −124‰ and −184‰ V-SMOW in Dziani.

## 4. Discussion

### 4.1. $CO_2$ *origin and gas–water interaction*

In order to assess the origin of $CO_2$ rich gas emissions in Mayotte, we followed the approach used in Sano and Marty [1995] and we extended the dataset from the BAS area discussed in Liuzzo et al. [2021] with new gas sampling made in 2020 in BAS and in the Dziani Dzaha Lake. In order to discriminate the possible contributions from various sources (magmatic, organic and marine sediments), we considered the isotopic variability of carbon in $CO_2$ versus $CO_2/^3He$ ratio (Figure 6). The two mixing curves were modeled between the local mantle endmember resulting from the average values of our data (in which we only considered data that were not modified by secondary processes), data from literature [$CO_2/^3He = 5.0 \times 10^9$ and $\delta^{13}C = -4.3$‰, Liuzzo et al., 2021] and an organic ($\delta^{13}C = -25$‰) and limestone endmember ($\delta^{13}C = 0$‰) from Hoefs [2015]. For both organic and limestone carbon endmembers, a value of $CO_2/^3He = 1.0 \times 10^{13}$ is assumed. Finally, in order to evaluate the secondary processes of gas–water interaction, we have considered data corrected for air only for samples having $N_2 < 22\%$, following the approach of Liuzzo et al. [2021].

The distribution of the data for the two degassing areas at Petite Terre shows clear differences. With the exception of the MAN-1 and MAN-2 samples, the BAS area shows little variability in bulk chemistry and C isotopy and are reasonably interpretable as being related to an outgassing process from a deep magmatic source. Conversely, the gas samples from the Dziani Dzaha Lake area have a larger scattering.

Gas–water interaction effects previously highlighted for some samples from the BAS area by Liuzzo et al. [2021] likely play an even more important role in the Dziani Dzaha Lake. We modeled four possible Rayleigh fractionation curves by assuming gas dissolution in water under equilibrium conditions (Appendix A, Equation (A3)). However, whereas in the case of the BAS zone a simple dissolution process can be assumed (MAN 1-2 curve Rf-1) [Liuzzo et al., 2021], in the case of Dziani, a single dissolution step cannot reproduce the measured large scattering. Moreover, when considering the typical parameters of the Dziani Dzaha Lake (pH = 9 and temperature of 36 °C from Milesi et al. [2020]) the corresponding curve Rf-2 clearly does not fit with any Dziani Dzaha Lake data. The pH value of up to 9 in Diazni Dzaha Lake can potentially facilitate calcite precipitation. However, the precipitation of calcite, by subtracting the heavier isotope, would produce a more negative $\delta^{13}C$ component in the gas phase (resulting in a curve that would overlap with Rf-2), but in our case the trend of the values measured in the lake is the

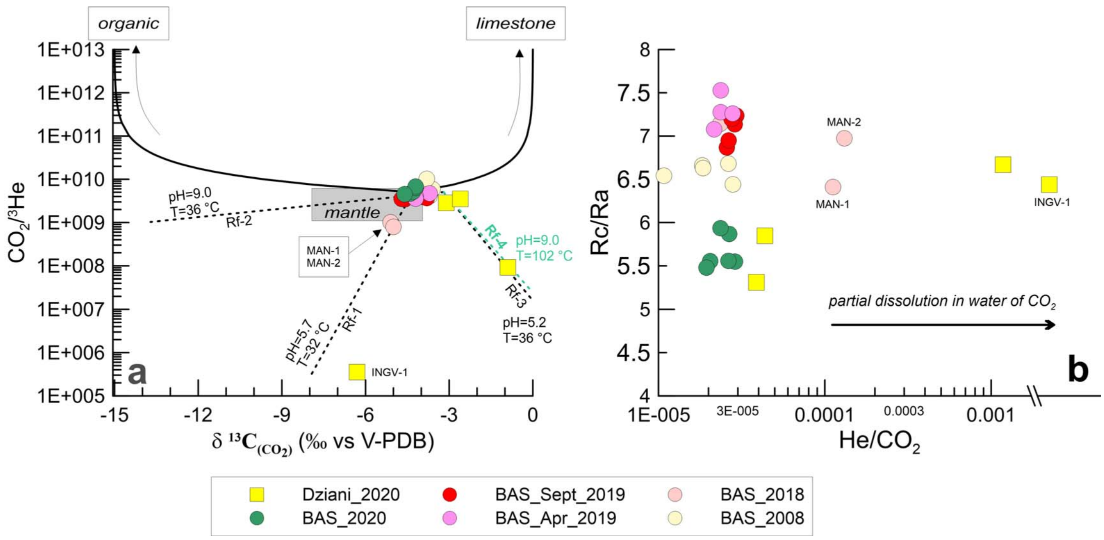


**Figure 6.** In (a) $\delta^{13}$C of $CO_2$ versus $CO_2/^3He$ diagram of bubbling gases at Petite Terre (Mayotte). In (b) $He/CO_2$ versus $R_c/R_a$. Diagram 6a shows that gases at Petite Terre are in the field of mantle-like sources with no evident organic or limestone contributions. Solid lines are mixing curves between organic, mantle and limestone endmembers. The dashed lines indicates Rayleigh fractionation (Rf) trends related to gas dissolution in water under four different pH–T conditions (see text for discussion and interpretation). Diagram 6b displays the effect of variable degree of water-gas interaction controlling $CO_2/He$ variability.

opposite. In order to fit the Dziani Dzaha Lake gases in the range of temperatures of 32–36 °C, much more acid pH of about 5.2–5.7 are needed (Rf-3 path). If, on the other hand, fractionation in equilibrium with the lake's pH of about 9 is considered, the temperature required to obtain a good fit on the data (Rf-4 path) should be about 102 °C. However, these high temperatures are not realistic, nor have such temperature anomalies ever been found in any of the surveys performed in the lake before or after the beginning of the seismic crisis. Modeling seems to suggest that simple fractionation does not occur in the water column of the Dziani Dzaha Lake, on the other hand if the fractionation process occurs in the aquifer and does not undergo major changes in the lake, the Rf-3 model is likely the most plausible.

Nevertheless, the variability of $He/CO_2$ versus $R_c/R_a$ shown in Figure 6b, evidences that a partial dissolution in water did play a role in modifying the composition of gas bubbling streaming through the Dziani Dzaha Lake, and appears to be notably extreme in the $CH_4$-rich INGV-1 sample. In particular, this sample is collected in correspondence of the deepest portion of the lake (Figure 1c), and as already noted for sample G2 in Milesi et al. [2020], may have been significantly affected by the gas transfer and residence in the higher water column.

The current dataset does not permit to exclude that gaseous emissions from Dziani Dzaha Lake undergo gas–water interaction processes under non-equilibrium conditions and/or the occurrence of other fractionation processes than those here modeled. Among these, isotope exchange in Dziani between $\delta^{13}C_{CO_2}$ and $\delta^{13}C_{TDIC}$ could lead to the less negative isotopic values measured at the Dziani Dzaha Lake with respect to BAS, if we consider that water lake reaches DIC concentrations up to 0.2 mol/L and $\delta^{13}C_{TDIC}$ up to +13‰ [Cadeau et al., 2020]. The acquisition of more data on both exsolved and dissolved gases in the future is thus needed in order to better constrain the processes controlling the variability of the carbon isotopic signature in the Dziani Dzaha Lake. All of these effects need to be evaluated and eventually filtered out in order to calculate the thermobarometric conditions of the hydrothermal system feeding the gas seeps (see next section), as it has been recognized in other studies of hydrothermal gases [Capasso et al., 2005, Gilfillan et al., 2009, Rizzo et al., 2019]. In fact, besides $\delta^{13}C$ isotopic signature, the $CO_2/^3He$, $He/CO_2$, $CH_4/CO_2$ ratios can also be potentially modified by oxydation/reduction reactions and/or by gas–water interaction in which $CO_2$ dissolves preferentially with respect to the other species.

### 4.2. $CH_4$ *origin and* $\delta^{13}C$ *versus* $\delta^2H$ *variability*

For the samples collected in the 2019–2020 campaigns, it was possible to define the isotopic signature of carbon and hydrogen in methane in both BAS and the Dziani Dzaha Lake sites and compare them with previous data of Dziani Dzaha Lake from Milesi et al. [2020]. The results are plotted in the classification diagram proposed by Schoell [1980] (Figure 7). It must be stressed that distinguishing between methanogenesis processes of biological origin and thermogenic processes at the origin of $CH_4$ [Mazzini et al., 2011, Schoell, 1980, Welhan, 1988] is complicated by the possible mixing between endmembers with different isotopic signatures [Taran et al., 2010a,b], or by the occurrence of oxidation processes [e.g., Batista Cruz et al., 2019].

Although with some relative variability, the isotopic signature of methane in BAS falls in the field of abiogenic origin, together with sample G7, acquired in 2016 in this area by Milesi et al. [2020]. This confirms that outgassing in the BAS tidal area originates from a homogeneous and unique source, particularly if we also take into account the stable and low variability of $R_c/R_a$ and $\delta^{13}C$-$CO_2$ values (Figures 3–5). The situation in the Dziani Dzaha Lake is more complex. The $CH_4$-rich $G_2$ sample collected near the deepest part of the lake corresponds to a gas that has clearly undergone a reduction process by microbial methanogenesis, as already highlighted in Milesi et al. [2020]. Our INGV-01 sample from this area (Tables 1a–1e), records a possible strong interaction in water or in the sediments (Figure 6b). The isotopic characteristics of methane for this sample can be consistent with a thermogenic origin or with mixing between abiogenic and biogenic endmembers. In the Dziani Dzaha Lake, the isotopic signature of the $CH_4$-rich bubbling is thus distinct from that of the $CO_2$-rich bubbling (ex. G3), which have abiogenic signature similar to the samples in BAS, but with a less negative proportion of $\delta^2H$. The remaining samples from the 2020 campaign in Dziani have a signature intermediate between abiogenic and thermogenic fields (DZN 1-2; OVPF-5; DZW 1-4). The variability of methane isotopic characteristics in distinct outgassing areas in Dziani thus appears to be much more complex than measured in BAS, which is confirmed also by the wider variability in $\delta^{13}C$ signature in $CO_2$ (Figures 4, 5). This again suggests that several processes may operate in the lake, including abiotic degassing of gases, microbial production and oxidation of methane, and partial dissolution of $CO_2$ in water, all of which contribute to varying degrees to the greater chemical and isotopic variability compared to the more homogeneous BAS area.

It is therefore clear that further data are needed to better constrain the origin of methane in the Dziani Dzaha Lake, and we are aware that the debate on methane origin is open within the scientific community, in particular in order to justify its possible abiotic origin assuming a “magmatic” or “late magmatic” origin [Etiope and Sherwood Lollar, 2013]. However, answering this question is not trivial, considering that the recent submarine eruption only 50 km off-shore from Petite Terre represents by far the largest known submarine eruption until now and that intense seismicity occurs at variable distance from the island [Feuillet et al., 2021, Berthod et al., 2021a,b, Foix et al., 2021]. In this context, a further clue is given by the isotopic signature of helium involved in the outgassing process at Petite Terre, which can be useful in discerning and assessing the deep origin of the gas. Therefore, we considered the isotopic variability of methane by comparing it with the percentage of mantle-related helium, following the approach indicated in Etiope and Sherwood Lollar [2013] (Figure 8). In our case, the Petite Terre gases fall within the area where magmatic $CH_4$ inputs are clearly recognized (EPR—East Pacific Rise, Socorro, Lost City [Proskurowski et al., 2008, Taran et al., 2010a, Welhan and Craig, 1983]). This leads us to conclude that input of gas of magmatic origin contributes to the general outgassing at Petite Terre, and specifically even regarding a not negligible contribution of methane, which in turn, particularly in the Dziani Dzaha Lake area, has undergone further transformation processes by microbial activity.

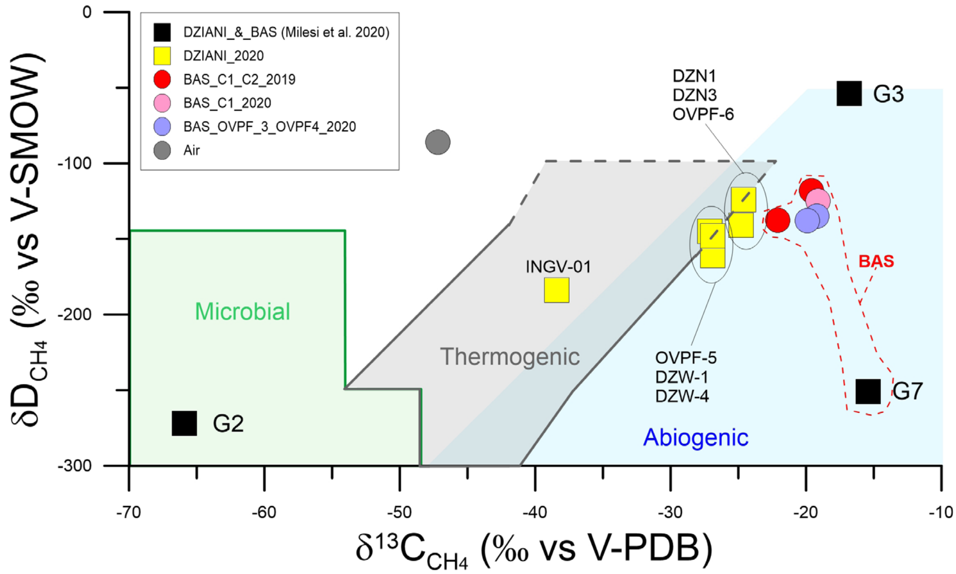


**Figure 7.** $\delta^{13}C_{CH_4}$ versus $\delta D_{CH_4}$ classification diagram (modified from Schoell [1980]). G2, G3 and G7 data acquired in 2016 from Milesi et al. [2020]. Most samples collected in the Mayotte gas seeps fall in the typical abiogenic fields, while a clear microbial signature is found in the sample collected by Milesi in 2016. The sample INGV-01 collected in the same area of G2 have an intermediate composition between biotic and abiotic end-members.

### 4.3. *Equilibrium temperature of hydrothermal gases*

The elemental composition of the gases of Petite Terre shows a general low concentration of $H_2$ and CO in both BAS and Dziani Dzaha Lake areas. Therefore, although $H_2$ and CO are considered useful geo-indicators for equilibrium temperature and pressure in the hydrothermal system, we did not consider these species to be suitable for thermobarometric purposes in the study of Mayotte fluids. On the contrary, the amounts of $CO_2$ and methane (Tables 1a–1e) are high enough to have good analytical precision in both concentration and isotopic data. Therefore, we used the approach adopted by Liuzzo et al. [2021], assuming that in the hydrothermal system an equilibrium is attained between the dominant species $H_2O$–$H_2$–$CO_2$–CO–$CH_4$, in which the formation of methane is favoured by the decreasing temperature from the reaction (A4) indicated in Appendix A.4. For this system, the temperature has been calculated assuming a condition of thermal equilibrium between $CH_4$ and $CO_2$ by (A5) in Appendix A.4 as proposed by Giggenbach [1992]. Moreover, in order to further constrain the possible evidence of recent input of deep fluids in the Mayotte hydrothermal system, we evaluated the thermal equilibrium in combination with their isotopic signatures based on their $\delta^{13}C$ isotopic fractionation factor between $CO_2$ and $CH_4$. To this aim, we combined the temperatures obtained from (A5) with the temperatures calculated using (A6) proposed by Bottinga [1969], valid for temperatures ranging between 0–700 °C (Appendix A.4), following the approach proposed in Ono et al. [1993], and recently applied in the Comoros area by Liuzzo et al. [2021], finally obtaining (A7). On this basis, the curves of thermal equilibrium were modeled assuming that both chemical and isotopic equilibrium is maintained with a fixed $\delta^{13}C_{C02}$ representative of the possible range of magmatic signature; here we considered a range of $\delta^{13}C_{C02}$ magmatic signatures from −4‰ to −8‰ when coupling (A5) and (A6).

The results are shown in Figure 9, which allows to extend the preliminary study made by Liuzzo et al. [2021], taking into account recent gas sampling in 2020 at both BAS and Dziani Dzaha Lake areas of Petite Terre. The data considered are those in which there are no obvious secondary variations and/or

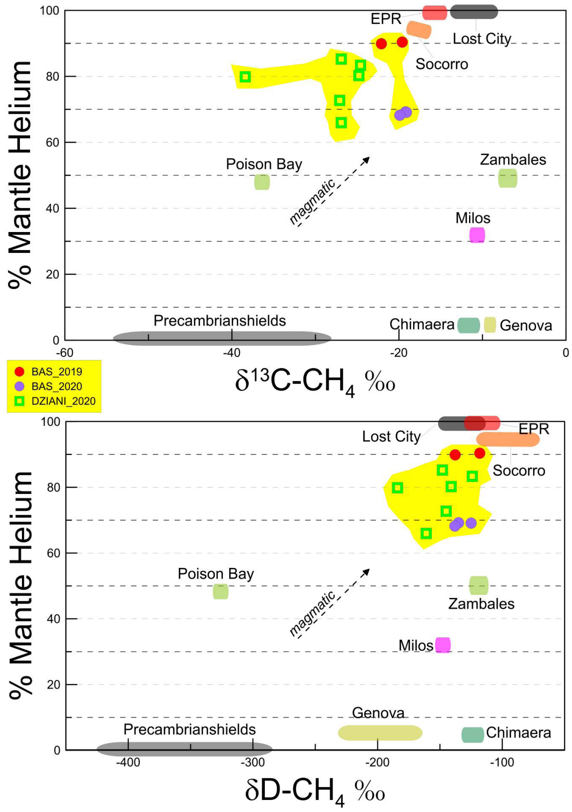


**Figure 8.** $\delta^{13}C$ and $\delta D$ in $CH_4$ versus the proportion of He sourced from the mantle (%He). The Petite Terre data are compared with a larger dataset from various geodynamic origins from Etiope and Sherwood Lollar [2013], and appear consistent with environments where methane of magmatic origin is clearly recognized.

gas–water interactions.

The methane-rich gases at the Dziani Dzaha Lake are certainly conditioned by the microbial activity in lacustrine waters and sediments; the range of variability of $\delta^{13}C_{(CH_4)}$ and $\delta D$ is high, and the values are generally scattered. The variability of $\delta^{13}C_{(CO_2)}$ is less than for $\delta^{13}C_{(CH_4)}$; however, $\delta^{13}C_{(CO_2)}$ of gases bubbling through the Dziani Dzaha Lake show a wider range of variability than BAS. As noted in the previous sections, this leads us to conclude that outgassing in Dziani Dzaha Lake is probably affected by several physicochemical processes and are related to several sources. Their isotopic variability is related to variable degrees of mixing between organic and abiotic components [Milesi et al., 2020]. Figure 9 also shows that isotopic equilibrium is not reached between $CO_2$ and $CH_4$, as all sampled gases at Dziani Dzaha Lake have variable $\delta^{13}C_{(CH_4)}$ values above the calculated equilibrium curves. Bacterial oxidation of $CH_4$ likely controls isotopic fractionation, determining an increase in the isotopic ratio in the residual methane [Baker and Fritz, 1981, Coleman et al., 1981, Horita, 2001], and this process is expected to be significant in the Dziani Dzaha Lake, where an extensive microbial activity has been well documented.

Regarding the BAS area, the range of variability of $\delta^{13}C_{(CH_4)}$ is consistent with an abiogenic source [Schoell, 1980], and the data also show moderate variability in their isotopic signature. Therefore, a single degassing source produces the bubbling observed at BAS. In the 2020 samples, however, a significant shift of the methane toward heavier isotopic concentrations, as observed in Liuzzo et al. [2021] is still evident. Although a carbon isotopic fractionation of methane cannot be excluded in BAS area as in Dziani, Liuzzo et al. [2021] have shown that isotopic signature of the hydrothermal gases in the BAS area likely records a quenching effect. In this interpretation, $CO_2$ and $CH_4$ are considered initially in isotopic equilibrium during outgassing of the deep (mantle level) magmatic source. In this interpretation, isotopic disequilibrium is a consequence of fast ascent of the gases to shallow crustal layers, with little time for isotopic re-equilibration. Such a quenching effect is expected because of the much faster rate of re-equilibration (about 100 times) of the elemental reaction with respect to the isotopic one [Giggenbach, 1982]. Our new dataset confirms that isotopic disequilibrium between $CO_2$ and $CH_4$ previously shown in 2018–2019 samples, is still well recorded by the 2020 samples. An important consequence of the disequilibrium is that the actual temperatures could be higher than those calculated from the equilibrium obtained from (A5), as discussed by Liuzzo et al. [2021]. This is because, having numerically simulated a thermal isotopic-chemical equilibrium between $CO_2$, $CH_4$ and their d $\delta^{13}C$, the corresponding $\delta^{13}C$ values of methane would be in equilibrium if they intersected the corresponding curve. However, the $\delta^{13}C(CH_4)$ values would have to shift to the left to meet the equilibrium curve and thus would have even higher temperatures.

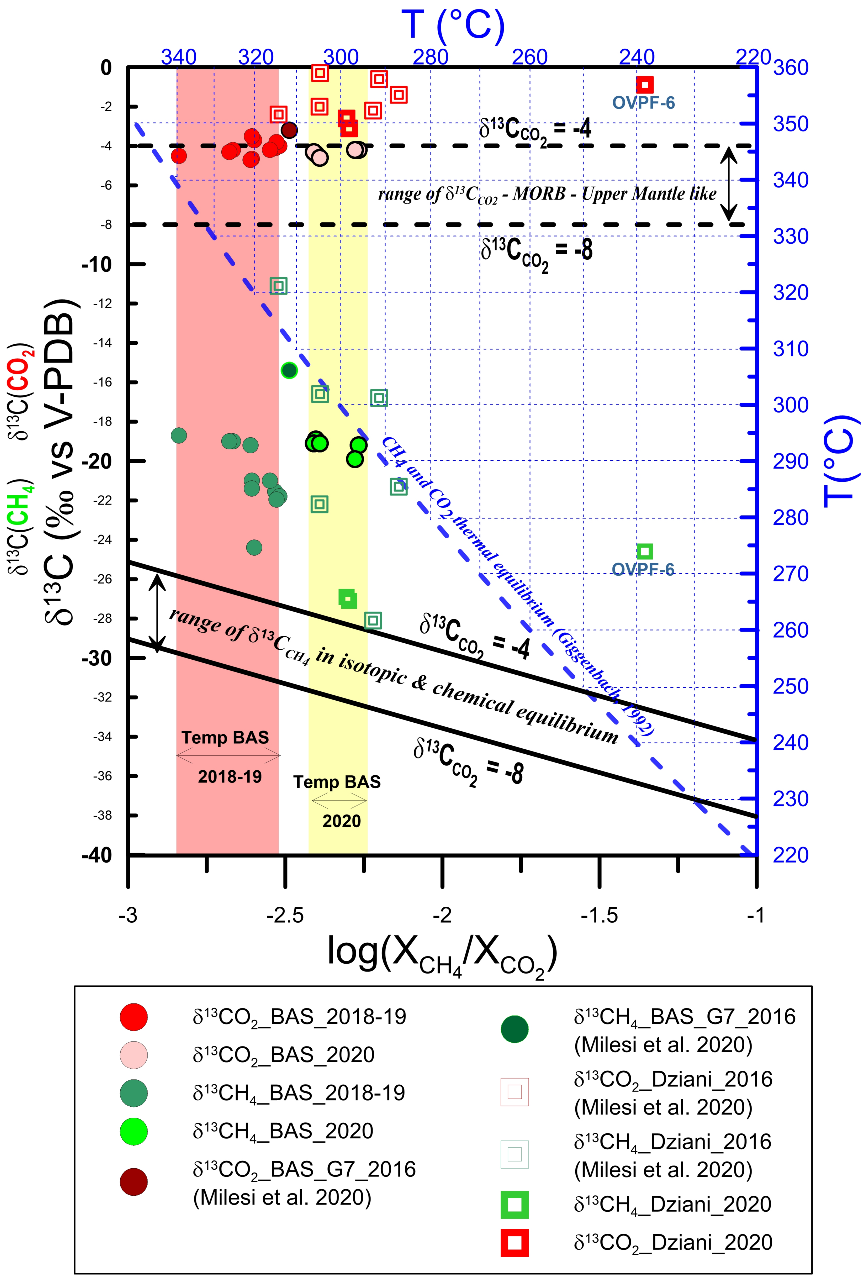


**Figure 9.** $\delta^{13}C$ in $CO_2$ (red) and $CH_4$ (green) versus $\log(X_{CH_4}/X_{CO_2})$ for Petite Terre bubbling gases. Red and yellow areas correspond to the range of equilibrium temperature of the hydrothermal gas samples collected in the BAS area between 2018 and 2020, respectively. The blue dashed line corresponds to the $CH_4$ and $CO_2$ thermal equilibrium expressed in (A5) in Appendix A.4 [Giggenbach, 1992]; the continuous black lines are calculated following (A7) in Appendix A.4 by assuming isotopic and chemical equilibrium between $CH_4$ and $CO_2$ for two possible end-members of $\delta^{13}C$ ($CO_2$) at −4‰ and −8‰, which in turn are indicated as horizontal black dashed lines.

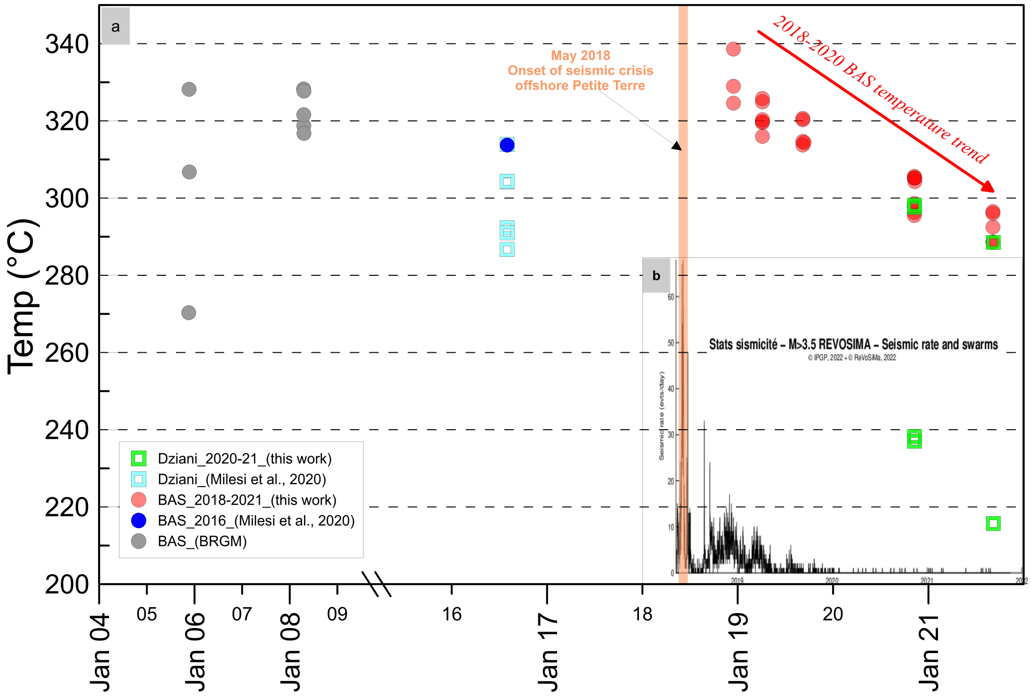


**Figure 10.** (a) Time evolution of equilibrium temperature in hydrothermal fluids of Mayotte (Petite Terre) calculated by using (A4) from Giggenbach, 1992 (Appendix A.4). In box (b), overlaid in time, the declining rate of seismicity (event/day for M > 3.5 earthquakes; from REVOSIMA Monthly Bulletin—December 2021) since the beginning of the volcano-tectonic crisis in 2018.

The occurrence of isotopic disequilibrium implies that the hydrothermal system at BAS may have recently received new input of deep-hot $CO_2$ and $CH_4$-rich gases possibly before or at the beginning of the volcanic activity in 2018.

This hypothesis is further supported by the time evolution of the equilibrium temperatures (calculated with (A5)) over years in both the BAS and Dziani areas (Figure 10). In the BAS area, a well-defined trend of cooling can be observed between 2018 and 2021. The equilibrium temperature of gases collected in the Dziani Dzaha Lake follows the same trend even if the dataset is smaller and the gases have been variably affected by secondary processes. The cooling trend recorded by equilibrium temperatures mimics that of progressive decrease of the seismic activity and magma extrusion rate over the same time period [Bachèlery et al., 2019, Berthod et al., 2021a,b, Cesca et al., 2020, Feuillet et al., 2021, Lemoine et al., 2020, REVOSIMA, 2019; REVOSIMA Monthly Bulletin, December 2021]. It is therefore reasonable to assume that a deep fluid input, which was somehow related to the most intense phase of submarine eruptive activity, may have reached the outgassing areas of Petite Terre, resulting in the initial increase in equilibrium temperature and isotopic disequilibrium in the hydrothermal system, which then over time fell steadily, as the seismo-volcanic crisis declined. The existence of this link is expected as most of the seismicity and the deep sources of magma feeding the distal submarine eruption are located close to Petite Terre (5–15 km) [Foix et al., 2021] and the involved volumes of magma are huge and $CO_2$-rich [Feuillet et al., 2021, Berthod et al., 2021a,b].

## 5. Conclusion

This study has investigated the geochemistry of the two main areas of low-T gas seeps occurring at Mayotte (Petite Terre): the Airport tidal flat (BAS) and the

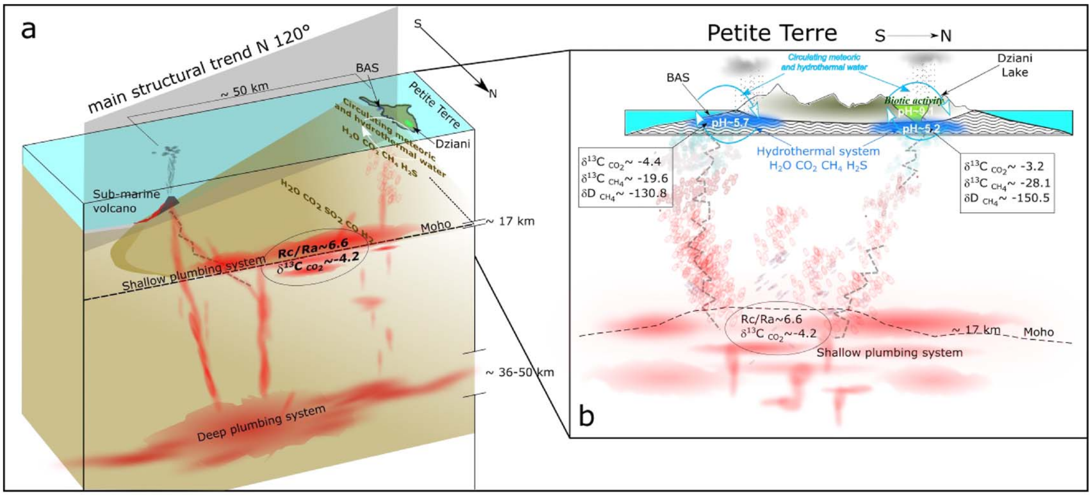


**Figure 11.** (a) Conceptual diagram of the deep and shallow magma and fluid plumbing system [modified from Berthod et al., 2021a,b] beneath the eastern flank of Mayotte Island. (b) Detail of the signatures and transfer of magmatic fluids reaching the two gas seep areas of Petite Terre (BAS and Dziani Dzaha Lake).

intracrateric Dziani Dzaha Lake. The chemical and isotopic study has permitted to constrain both the sources and the secondary processes controlling the signature of the bubbling hydrothermal fluids.

The $CO_2$-rich bubbling gases streaming through Petite Terre Island are sourced by the shallower part of the deep magmatic plumbing located near the Moho at about 17 km b.s.l. [Foix et al., 2021, Berthod et al., 2021a,b] (Figure 11a). This inference stems from the homogeneous and low He/Ar* ratios of Mayotte gases and the absence of crustal signature in their chemical and isotopic signatures. The seismically very active magmatic system is located close to the island (5–15 km) and has likely provided the $CO_2$–He rich fluids percolating through the whole deep magma plumbing system, whose deeper part is located in the mantle (around 36–50 km depth), has a basanitic composition and is expected to be very $CO_2$ rich [Berthod et al., 2021a,b]. Petrological and geophysical data show that both the deep (mantle) and the shallow (crustal underplating) parts of the plumbing systems were drained to feed the recent submarine eruptive activity responsible for the construction of the huge volcanic edifice about 50 km offshore Petite Terre [Berthod et al., 2021a, Cesca et al., 2020, Feuillet et al., 2019, Lemoine et al., 2020]. Seismic and eruptive activity have steadily declined since the beginning of the crisis in 2018. This evolution is likely recorded by the decrease over time of equilibrium temperatures in Petite Terre hydrothermal fluids.

Hydrothermal gases bubbling in both the BAS and Dziani Dzaha Lake reflect primarily the signature of deep gases in terms of geochemical tracers such as $R/R_a$ $\delta^{13}$C in carbon and methane (Figure 11b), however their chemical and isotopic composition is partly affected by secondary processes that produce some variability between the two areas. The Dziani Dzaha Lake hosts the only $CH_4$-dominated bubbling area and gases streaming through the lake are variable and in some cases significantly affected by microbial activity in a meromictic lake environment. In the BAS tidal area, the influence of the microbial activity and of the gas–water interaction is certainly less significant. Secondary processes in the Dziani Dzaha Lake explain the significant difference in the methane isotopic signature. Conversely, the He content and isotopic signature is much less affected by late-stage processes and preserved the signature of the pristine deep source.

The recognition in the BAS area of deep gases related to the several stages of outgassing from the magmatic plumbing system and not affected by secondary processes, make this area the most suitable area for volcano monitoring purposes.

## Conflicts of interest

Authors have no conflict of interest to declare.


## Acknowledgements

This work is part of the PhD (XXXIV cycle) of Marco Liuzzo at the University of Ferrara. The work has been partially funded by INGV (GECO project Fondi Ricerca libera 2019 INGV) and by REVOSIMA Consortium (IPGP, CNRS, BRGM, IFREMER) for fieldwork and and by the Interreg "Hatari" (IPGP/OVPF) for analytical activities. The authors are very thankful to INGV, Sezione di Palermo, for allowing the access to the analytical facilities and to the BRGM Mayotte for their support during fieldwork.


## Appendix A.

### A.1. $R_c/R_a$ *calculation*

The $^3He/^4He$ ratio is expressed as $R/R_a$ (being $R_a$ the He isotope ratio of air and equal to $1.39 \times 10^{-6}$) with an analytical uncertainty ($1\sigma$) below 0.3%. The $^3He/^4He$ ratio corrected for atmospheric contamination has been calculated using the measured $^4He/^{20}Ne$ ratio following Sano and Wakita [1985] and is reported in units of $R_c/R_a$, as follows:

$$\frac{R_c}{R_a} = \frac{\left(\frac{R_m}{R_a}\right) \cdot \left(\frac{4\mathrm{He}}{20\mathrm{Ne}}\right)_m - \left(\frac{4\mathrm{He}}{20\mathrm{Ne}}\right)_a}{\left(\frac{4\mathrm{He}}{20\mathrm{Ne}}\right)_m - \left(\frac{4\mathrm{He}}{20\mathrm{Ne}}\right)_a} \tag{A1}$$

where subscripts $m$ and $a$ refer to measured and atmosphere theoretical values respectively [$(\mathrm{He/Ne})_a = 0.318$ [Ozima and Podosek, 1983]]. As a consequence of a very low air contamination the correction on the $^3He/^4He$ ratio is small or negligible for most of the gas samples $(^4\mathrm{He}/^{20}\mathrm{Ne})_m \gg (^4\mathrm{He}/^{20}\mathrm{Ne})_a$.

### A.2. *Argon correction*

$^{40}Ar$ was corrected for air contamination ($^{40}Ar^*$) in samples showing $^{40}Ar/^{36}Ar > 315$ assuming that the $^{36}Ar$ present derived from atmosphere, as follows:

$$^{40}\mathrm{Ar}^* = {}^{40}\mathrm{Ar}_{\mathrm{sample}} - {}^{36}\mathrm{Ar}_{\mathrm{sample}} \cdot \left(\frac{^{40}\mathrm{Ar}}{^{36}\mathrm{Ar}}\right)_{\mathrm{air}}. \tag{A2}$$

### A.3. $\delta^{13}C_{CO_2}$ *calculation in a Rayleigh fractionation under dissolution equilibrium*

In order to constrain the pristine C isotopic signature of $CO_2$ in Mayotte, we modeled a Rayleigh fractionation assuming dissolution under equilibrium conditions based on the approach used in Rizzo et al. [2019] and Liuzzo et al. [2021] for the application in the previous study for Comoros archipelago. The Clark and Fritz [1997] equation is as follows:

$$\delta^{13}C_{CO_2} = (\delta^{13}C_{CO_2})_0 + \varepsilon \ln(f) \tag{A3}$$

where the subscript 0 indicates the initial $CO_2$ isotope composition and $f$ is the fraction of the residual gas phase, while $\varepsilon$ is the fractionation factor between DIC (dissolved inorganic carbon) and gaseous $CO_2$ ($CO_{2\cdot(g)}$). In turn, $\varepsilon$ depends on water temperature and pH, which are unknown. In the discussion, the values of temperature and pH 5.7 and $T = 32$ °C (curve Rf-1; Figure 5a) correspond to those measured in the marine water of the Mayotte tidal flat by BRGM surveys [Sanjuan et al., 2008, Traineau et al., 2006]. The curve Rf-2 has been calculated using a pH = 9 and $T = 36$ °C, that correspond to the parameters measured in Dziani by Milesi et al. [2020]. Further fractionation lines were calculated either for lower pH (Rf-3 trend; pH = 5.2 and $T = 36$ °C) or higher temperature (Rf-4 trend; pH = 9 and $T = 102$ °C).

### A.4. *Equilibrium temperature*

Assuming that in the hydrothermal system an equilibrium is attained between the dominant species $H_2O$–$H_2$–$CO_2$–$CO$–$CH_4$, methane can form inorganically from the Sabatier reaction [Hulston and McCabe, 1962]:

$$CO_2 + 4H_2 = CH_4 + 2H_2O \tag{A4}$$

where the formation of methane is favoured by the decreasing temperature. For this system, we calculated the condition of thermal equilibrium between $CH_4$ and $CO_2$ following the equation proposed by Giggenbach [1992]:

$$\log(X_{CH_4}/X_{CO_2}) = 4625/(t_e + 273) - 10.4. \tag{A5}$$

The equilibrium temperature for the isotopic fractionation of $\delta^{13}C$ between $CO_2$ and $CH_4$ was calculated using the equation proposed by Bottinga [1969] valid for temperatures ranging between 0–700 °C:

$$\Delta = 22166/(t_e + 273) - 13.8 \tag{A6}$$

where $\Delta$ is the difference between $\delta^{13}C_{CO_2}$ and $\delta^{13}C_{CH_4}$ values.

In Figure 7 the thick black lines were modeled assuming that both chemical and isotopic equilibrium is maintained with a fixed $\delta^{13}C_{C02}$ corresponding to the range of magmatic signature (−4‰ and −8‰; dashed black lines) by coupling the Equations (A5) and (A6):

$$\log\left(\frac{X_{CH_4}}{X_{CO_2}}\right) = \frac{4625(\Delta + 13.8)}{22166} - 10.4. \quad \text{(A7)}$$

## References

Aiken, C., Saurel, J. M., and Foix, O. (2021). Earthquake location and detection modeling for a future seafloor observatory along Mayotte's volcanic ridge. *J. Volcanol. Geotherm. Res.*, 418, article no. 107322.

Bachèlery, P., Berthod, C., Di Muro, A., Gurioli, L., Besson, P., Caron, B., Jorry, S., Fouquet, Y., Nowak, S., Burckel, P., Devidal, J. L., Deplus, C., Thinon, I., Bickert, M., Boudon, G., Moreira, M. A., Chauvel, C., Le Friant, A., and Feuillet, N. (2019). Petrological and geochemical characterization of the lava from the 2018–2019 mayotte eruption: first results. In *AGU Fall Meeting Abstracts*, pages V52D–06. AGU, Washington, DC.

Bachèlery, P. and Hémond, C. (2016). Geochemical and petrological aspects of karthala volcano. In Bachèlery, P., Lénat, J.-F., Di Muro, A., and Michon, L., editors, *Active Volcanoes of the Southwest Indian Ocean: Piton de La Fournaise and Karthala*, pages 367–384. Springer-Verlag, Berlin, Heidelberg.

Baker, J. F. and Fritz, P. (1981). Carbon isotope fractionation during microbial methane oxidation. *Nature*, 293, 289–291.

Barry, P. H. and Hilton, D. R. (2016). Release of subducted sedimentary nitrogen throughout Earth's mantle. *Geochem. Perspect. Lett.*, 2, 148–159.

Barry, P. H., Hilton, D. R., Füri, E., Halldórsson, S. A., and Grönvold, K. (2014). Carbon isotope and abundance systematics of Icelandic geothermal gases, fluids and subglacial basalts with implications for mantle plume-related $CO_2$ fluxes. *Geochim. Cosmochim. Acta*, 134, 74–99.

Batista Cruz, R. Y., Rizzo, A. L., Grassa, F., Bernard Romero, R., González Fernández, A., Kretzschmar, T. G., and Gómez-Arias, E. (2019). Mantle degassing through continental crust triggered by active faults: The case of the Baja California Peninsula, Mexico. *Geochem. Geophys. Geosyst.*, 20(4), 1912–1936.

Berthod, C., Médard, E., Bachèlery, P., Gurioli, L., Di Muro, A., Peltier, A., Komorowski, J., Benbakkar, M., Devidal, J., Langlade, J., Besson, P., Boudon, G., Rose-Koga, E., Deplus, C., Le Friant, A., Bickert, M., Nowak, S., Thinon, I., Burckel, P., Hidalgo, S., Jorry, S., Fouquet, Y., and Feuillet, N. (2021a). The 2018-ongoing Mayotte submarine eruption: magma migration imaged by petrological monitoring. *Earth Planet Sci. Lett.*, 571, article no. 117085.

Berthod, C., Médard, E., Di Muro, A., Hassen Ali, T., Gurioli, L., Chauvel, C., Komorowski, J.-C., Bachèlery, P., Peltier, A., Benbakkar, M., Devidal, J.-L., Besson, P., Le Friant, A., Deplus, C., Nowak, S., Thinon, I., Burckel, P., Hidalgo, S., Feuillet, N., Jorry, S., and Fouquet, Y. (2021b). Mantle xenolith-bearing phonolites and basanites feed the active volcanic ridge of Mayotte (Comoros archipelago, SW Indian Ocean). *Contrib. Mineral. Petrol.*, 176, article no. 75.

Bottinga, Y. (1969). Calculated fractionation factors for carbon and hydrogen isotope exchange in the system calcite-carbon dioxide-graphite-methane hydrogen-water vapor. *Geochim. Cosmochim. Acta*, 33, 49–64.

Boudoire, G., Rizzo, A. L., Arienzo, I., and Di Muro, A. (2020). Paroxysmal eruptions tracked by variations of helium isotopes: inferences from Piton de la Fournaise (La Réunion island). *Sci. Rep.*, 10, article no. 9809.

Boudoire, G., Rizzo, A. L., Di Muro, A., Grassa, F., and Liuzzo, M. (2018). Extensive $CO_2$ degassing in the upper mantle beneath oceanic basaltic volcanoes: First insights from Piton de la Fournaise volcano (La Réunion Island). *Geochim. Cosmochim. Acta*, 235, 376–401.

Bräuer, K., Kämpf, H., Koch, U., and Strauch, G. (2011). Monthly monitoring of gas and isotope compositions in the free gas phase at degassing locations close to the Nový Kostel focal zone in the western Eger Rifţ Czech Republic. *Chem. Geol.*, 290, 163–176.

Burnard, P. (2001). Correction for volatile fractionation in ascending magmas: noble gas abundances in primary mantle melts. *Geochim. Cosmochim. Acta*, 65(15), 2605–2614.

Cadeau, P., Jézéquel, D., Leboulanger, C., Fouilland, E., Le Floc'h, E., Chaduteau, C., Milesi, V., Guélard, J., Sarazin, G., Katz, A., d'Amore, S., Bernard, C., and Ader, M. (2020). Carbon isotope evidence for large methane emissions to the Proterozoic atmosphere. *Sci. Rep.*, 10, article no. 18186.

Capasso, G., Carapezza, M. L., Federico, C., Inguaggiato, S., and Rizzo, A. (2005). Geochemical variations in fluids from Stromboli volcano (Italy): early evidences of magma ascent during 2002-2003 eruption. *Bull. Volcanol.*, 68, 118–134.

Cesca, S., Letort, J., Razafindrakoto, H. N., Heimann, S., Rivalta, E., Isken, M. P., Nikkhoo, M., Passarelli, L., Petersen, G. M., Cotton, F., and Dahm, T. (2020). Drainage of a deep magma reservoir near Mayotte inferred from seismicity and deformation. *Nat. Geosci.*, 13(1), 87–93.

Clark, I. D. and Fritz, P. (1997). *Environmental Isotopes in Hydrogeology*. CRC Press, Boca Raton, FL.

Class, C., Goldstein, S. L., Stute, M., Kurz, M. D., and Schlosser, P. (2005). Grand Comore Island: a well-constrained "low $^{3}$He/$^{4}$He". *Earth Planet. Sci. Lett.*, 233, 391–409.

Coffin, M. F., Rabinowitz, P. D., and Houtz, R. E. (1986). Crustal structure in the western Somali Basin. *Geophys. J. Int.*, 86(2), 331–369.

Coleman, D. D., Risatti, J. B., and Schoell, M. (1981). Fractionation of carbon and hydrocarbon isotopes by methane-oxidizing bacteria. *Geochim. Cosmochim. Acta*, 45, 1033–1037.

Etiope, G. and Sherwood Lollar, B. (2013). Abiotic methane on Earth. *Rev. Geophys.*, 51, 276–299.

Famin, V., Michon, L., and Bourhane, A. (2020). The Comoros archipelago: a right-lateral transform boundary between the Somalia and Lwandle plates. *Tectonophysics*, 789, article no. 228539.

Feuillet, N., Jorry, S., Crawford, W. C., Deplus, C., Thinon, I., Jacques, E., Saurel, J. M., Lemoine, A., Paquet, F., Daniel, R., Gaillot, A., Satriano, C., Peltier, A., Aiker, C., Foix, O., Kowalski, P., Laurent, A., Beauducel, F., Grandin, R., Ballu, V., Bernard, P., Donval, J. P., Géli, L., Gomez, J., Pelleau, P., Guyader, V., Rinnert, E., Besancon, S., Bertil, D., Lemarchand, A., and Vanderwoerd, J. (2019). Birth of a large volcano offshore Mayotte through lithosphere-scale rifting. In *Proceedings of the AGU Fall Meeting 2019*. AGU, Washington, DC.

Feuillet, N., Jorry, S., Crawford, W. C., Deplus, C., Thinon, I., Jacques, E., Saurel, J. M., Lemoine, A., Paquet, F., Satriano, C., Aiken, C., Foix, O., Kowalski, P., Laurent, A., Rinnert, E., Cathalot, C., Donval, J.-P., Guyader, V., Gaillot, A., Scalabrin, C., Moreira, M., Peltier, A., Beauducel, F., Grandin, R., Ballu, V., Daniel, R., Pelleau, P., Gomez, J., Besançon, S., Geli, L., Bernard, P., Bachelery, P., Fouquet, Y., Bertil, D., Lemarchand, A., and Van der Woerd, J. (2021). Birth of a large volcanic edifice offshore Mayotte via lithosphere-scale dyke intrusion. *Nat. Geosci.*, 14, 787–795.

Foix, O., Aiken, C., Saurel, J. M., Feuillet, N., Jorry, S. J., Rinnert, E., and Thinon, I. (2021). Offshore Mayotte volcanic plumbing revealed by local passive tomography. *J. Volcanol. Geotherm. Res.*, 420, article no. 107395.

Gaina, C., Torsvik, T. H., van Hinsbergen, D. J. J., Medvedev, S., Werner, S. C., and Labails, C. (2013). The African Plate: a history of oceanic crust accretion and subduction since the Jurassic. *Tectonophysics*, 604, 4–25.

Giggenbach, W. F. (1982). Carbon-13 exchange between $CO_2$ and $CH_4$ under geothermal conditions. *Geochim. Cosmochim. Acta*, 46, 159–165.

Giggenbach, W. F. (1992). Chemical techniques in geothermal exploration. Applications of geochemistry in geothermal reservoir development. In D'Amore, F., editor, *Activities at the UNITAR/UNDP Centre on Small Energy Resources for 1988*, pages 119–143. UNITAR/UNDP Centre on Small Energy Resources, Rome.

Giggenbach, W. F. and Goguel, R. L. (1989). Methods for the collection and analysis of geothermal and volcanic water and gas samples. New Zealand Department of Scientific and Industrial Research, Chemistry Division Report 2387, 53 p.

Gilfillan, S., Lollar, B., Holland, G., Blagburn, D., Stevens, S., Schoell, M., Cassidy, M., Ding, Z., Zhou, Z., Lacrampe-Couloume, G., and Ballentine, C. J. (2009). Solubility trapping in formation water as dominant $CO_2$ sink in natural gas fields. *Nature*, 458, 614–618.

Hoefs, J. (2015). *Stable Isotope Geochemistry*. Springer International Publishing, Switzerland, 7th edition. ISBN 978-3-319-19715-9.

Horita, J. (2001). Carbon isotope exchange in the system $CO_2$–$CH_4$ at elevated temperatures. *Geochim. Cosmochim. Acta*, 65(12), 1907–1919.

Hulston, J. R. and McCabe, W. J. (1962). Mass spectrometer measurements in the thermal areas of

New Zealand: Part 1. Carbon dioxide and residual gas analyses. *Geochim. Cosmochim. Acta*, 26(3), 383–397.

Lemoine, A., Briole, P., Bertil, D., Roullé, A., Foumelis, M., Thinon, I., Raucoules, D., de Michele, M., Valty, P., and Hoste Colomer, R. (2020). The 2018–2019 seismo-volcanic crisis east of Mayotte, Comoros islands: seismicity and ground deformation markers of an exceptional submarine eruption. *Geophys. J. Int.*, 23(1), 22–44.

Liuzzo, M., Di Muro, A., Rizzo, A. L., Caracausi, A., Grassa, F., Fournier, N., Shafik, B., Boudoire, G., Coltorti, M., Moreira, M., and Italiano, F. (2021). Gas geochemistry at Grande Comore and Mayotte volcanic islands (Comoros archipelago). *Indian Ocean Geochem. Geophys. Geosyst.*, 22, article no. e2021GC009870.

Marty, B. (2012). The origins and concentrations of water, carbon, nitrogen and noble gases on earth. *Earth Planet. Sci. Lett.*, 313–314, 56–66.

Mazzini, A., Svensen, H., Etiope, E., Onderdonk, N., and Banks, D. (2011). Fluid origin, gas fluxes and plumbing system in the sediment-hosted Salton Sea Geothermal System (California, USA). *J. Volcanol. Geotherm. Res.*, 205, 67–83.

Michon, L. (2016). The volcanism of the Comoros archipelago integrated at a regional scale. In Bachèlery, P., Lénat, J.-F., Di Muro, A., and Michon, L., editors, *Active Volcanoes of the Southwest Indian Ocean:Piton de La Fournaise and Karthala*, pages 333–344. Springer-Verlag, Berlin and Heidelberg.

Milesi, V. P., Debure, M., Marty, N. C. M., Capano, M., Jézéquel, D., Steefel, C., Rouchon, V., Albéric, P., Bard, E., Sarazin, G., Guyot, F., Virgone, A., Gaucher, E. C., and Ader, M. (2020). Early diagenesis of lacustrine carbonates in volcanic settings: the role of magmatic $CO_2$ (Lake Dziani Dzaha, Mayotte, Indian Ocean). *ACS Earth Space Chem.*, 4(3), 363–378.

Milesi, V. P., Jézéquel, D., Debure, M., Cadeau, P., Guyot, F., Sarazin, G., Claret, F., Vennin, E., Chaduteau, C., Virgone, A., Gaucher, E. C., and Ader, M. (2019). Formation of magnesium-smectite during lacustrine carbonates early diagenesis: Study case of the volcanic crater lake Dziani Dzaha (Mayotte Indian Ocean). *Sedimentology*, 66, 983–1001.

Nehlig, P., Lacquement, F., Bernard, J., Audru, J., Caroff, M., Deparis, J., Jaouen, T., Aziliz Pelleter, A., Perrin, J., Prognon, C., and Vittecoq, B. (2013). *Notice explicative de la carte géologique Mayotte à 1/30.000 feuille Mayotte*, volume 1179. BRGM, Orléans. Carte géologique par Lacquement F., Nehlig P., Bernard J. (2013).

Ono, A., Sano, Y., Wakita, H., and Giggenbach, W. F. (1993). Carbon isotopes of methane and carbon dioxide in hydrothermal gases of Japan. *Geochem. J.*, 27(4–5), 287–295.

Ozima, M. and Podosek, F. A. (1983). *Noble Gas Geochemistry*. Cambridge University Press, New York, NY.

Paonita, A., Caracausi, A., Iacono-Marziano, G., Martelli, M., and Rizzo, A. (2012). Geochemical evidence for mixing between fluids exsolved at different depths in the magmatic system of Mt Etna (Italy). *Geochim. Cosmochim. Acta*, 84, 380–394.

Phethean, J. J. J. (2016). Madagascar's escape from Africa: a high-resolution plate reconstruction for the Western Somali Basin and implications for supercontinent dispersal. *Geochem. Geophys. Geosyst.*, 17, 5036–5055.

Proskurowski, G., Lilley, M. D., Seewald, J. S., Früh-Green, G. L., Olson, E. J., Lupton, J. E., Sylva, S. P., and Kelley, D. S. (2008). Abiogenic hydrocarbon production at Lost City hydrothermal field. *Science*, 319, 604–607.

Quidelleur, X., Michon, L., Famin, V., Geffray, M. C., Danišík, M., Gardiner, N., Rusquet, A., and Zakaria, M. G. (2022). Holocene volcanic activity in Anjouan Island (Comoros archipelago) revealed by new Cassignol–Gillot groundmass K–Ar and 14C ages. *Quat. Geochronol.*, 67, article no. 101236.

REVOSIMA (2019). Bulletin n°1 de l'activité sismo-volcanique à Mayotte, IPGP. Université de Paris, OVPF, BRGM, Ifremer, CNRS, 23 August 2019, http://www.ipgp.fr/sites/default/files/ipgp_1er_bulletin_info_sismo_volcanique_mayotte-cor.pdf and http://www.ipgp.fr/revosima.

REVOSIMA (2021). Bulletin n°1 de l'activité sismo-volcanique à Mayotte. IPGP, Université de Paris, OVPF, BRGM, Ifremer, CNRS, 31 December 2021, http://www.ipgp.fr/sites/default/files/ipgp_revosima_n37_20220106.pdf and http://www.ipgp.fr/revosima.

Rizzo, A. L., Caracausi, A., Chavagnac, V., Nomikou, P., Polymenakou, P. N., Mandalakis, M., Kotoulas, G., Magoulas, A., Castillo, A., Lampridou, D., Marusczak, N., and Sonke, J. E. (2019). Geochemistry of $CO_2$-Rich Gases Venting From Submarine Volcanism: The Case of Kolumbo (Hellenic Volcanic Arc, Greece). *Front. Earth Sci.*, 7, article no. 60.

Sanjuan, B., Baltassat, J.-M., Bezelgues, S., Brach, M., Girard, J.-F., and Mathieu, F. (2008). Estimation du potentiel géothermique de Mayotte: Phase 2 - Etape 2. Investigations géologiques, géochimiques et géophysiques complémentaires, synthèse des résultats. BRGM/RP-568082 Final reports, 82 p., 18 Figure, 3 Tables, 6 ann. BRGM, Orléans.

Sano, Y. and Marty, B. (1995). Origin of carbon in fumarolic gases from island arcs. *Chem. Geol.*, 119, 265–274.

Sano, Y. and Wakita, H. (1985). Geographical distribution of $^3He/^4He$ ratios in Japan: implications for arc tectonics and incipient magmatism. *J. Geophys. Res.*, 90, 8729–8741.

Schoell, M. (1980). The hydrogen and carbon isotopic composition of methane from natural gases of various origins. *Geochim. Cosmochim. Acta*, 44, 649–661.

Stamps, D. S., Kreemer, C., Fernandes, R., Rajaonarison, T. A., and Rambolamanana, G. (2021). Redefining east African rift system kinematics. *Geology*, 49(2), 150–155.

Taran, J. A., Varley, N. R., Inguaggiato, S., and Cienfuegos, E. (2010b). Geochemistry of $H_{2-}$ and $CH_4$-enriched hydrothermal fluids of Socorro Island, Revillagigedo Archipelago, Mexico. Evidence for serpentinization and abiogenic methane. *Geofluids*, 10, 542–555.

Taran, Y. A., Kliger, G. A., Cienfuegos, E., and Shuykin, A. N. (2010a). Carbon and hydrogen isotopic compositions of products of open-system catalytic hydrogenation of $CO_2$: implications for abiogenic hydrocarbons in Earth's crust. *Geochim. Cosmochim. Acta*, 74, 6112–6125.

Thivet, S., Carlier, J., Gurioli, L., Di Muro, A., Besson, P., Smietana, M., Boudon, G., Bachèlery, P., Eychenne, J., and Nedelec, J.-M. (2022). Magmatic and phreatomagmatic contributions on the ash-dominated basaltic eruptions: insights from the April and November–December 2005 paroxysmal events at Karthala volcano, Comoros. *J. Volcanol. Geotherm. Res.*, 424, article no. 107500.

Traineau, H., Sanjuan, B., Brach, M., and Audru, J.-C. (2006). Etat des connaissances du potentiel géothermique de Mayotte. Rapport final. BRGM/RP-54700-FR.

Tzevahirtzian, A., Zaragosi, S., Bachèlery, P., Biscara, L., and Marchès, E. (2021). Submarine morphology of the Comoros volcanic archipelago. *Mar. Geol.*, 432, article no. 106383.

Welhan, J. A. (1988). Origins of methane in hydrothermal systems. *Chem. Geol.*, 71, 183–198.

Welhan, J. A. and Craig, H. (1983). Methane, hydrogen and helium in hydrothermal fluids of 21″ N on the East Pacific Rise. In Rona, P. A., Bostriim, K., Laubier, L., and Smith Jr., K. L., editors, *Hydrothermal Processes at Seafloor Spreading Centers*, pages 391–409. Plenum, New York, NY.

Zinke, J., Reijmer, J. J. G., and Thomassin, B. A. (2001). Seismic architecture and sediment distribution within the Holocene barrier reef–lagoon complex of Mayotte (Comoro archipelago, SW Indian Ocean). *Palaeogeogr. Palaeoclimatol. Palaeoecol.*, 175(1–4), 343–368.

*Comptes Rendus*
*Géoscience — Sciences de la Planète*
**2022**, Vol. 354, Special Issue S2, p. 299-316
https://doi.org/10.5802/crgeos.172

The Mayotte seismo-volcanic crisis of 2018-2021 in the Comoros archipelago (Mozambique channel) / *La crise sismo-volcanique de 2018-2021 de Mayotte dans l'archipel des Comores (Canal du Mozambique)*

# Impact of the seismo-volcanic crisis offshore Mayotte on the Dziani Dzaha Lake

**Pierre Cadeau** *, [a], [b], **Didier Jézéquel** [b], [c], **Alexis Groleau** [b], **Andrea Di Muro** [b], [d] **and Magali Ader** [b]

[a] Sorbonne Université, CNRS, EPHE, PSL, UMR METIS, F-75005 Paris, France

[b] Université Paris Cité, Institut de physique du globe de Paris, CNRS, F-75005 Paris, France

[c] UMR CARRTEL, INRAE & Université Savoie Mont Blanc, 74200 Thonon-les-Bains, France

[d] Observatoire Volcanologique du Piton de la Fournaise, Institut de physique du globe de Paris, 97418, La Plaine des Cafres, France

*E-mails:* pierre.cadeau@gmail.com (P. Cadeau), jezequel@ipgp.fr (D. Jézéquel), groleau@ipgp.fr (A. Groleau), dimuro@ipgp.fr (A. Di Muro), ader@ipgp.fr (M. Ader)

**Abstract.** Since May 2018, an unexpected long and intense seismic crisis started offshore Mayotte (Indian Ocean, France). This ongoing seismic sequence is associated with the birth of a newly discovered submarine volcano 50 km east of Petite Terre. Here, we investigate the indirect impact of this crisis on the stability of an atypical ecosystem located in Mayotte, the Dziani Dzaha Lake. This lacustrine system presented physical, chemical and biogeochemical characteristics that were distinct from those classically observed in modern lakes or seawater, e.g. high salinity (up to 70 psu), lack of nitrate, sulfate content below 3 mM, and permanent water column anoxia below ca. 1.5 m depth (2012–2017 period). Based on three surveys conducted in 2020 and 2021, we documented an episode of water column oxygenation, a significant pH decrease and an impressive change in the carbon isotope signatures. These preliminary data suggest that the functioning of biogeochemical cycles in the Dziani Dzaha Lake is impacted by increased $CO_2$ inputs and the changes in the lake mixing dynamics, which is an indirect consequence of the ongoing seismo-volcanic crisis.

**Keywords.** Dziani Dzaha Lake, Mayotte, Seismo-volcanic crisis, Carbon isotopes, Nitrogen isotopes, Volcanic $CO_2$ degassing.

*Published online: 9 December 2022, Issue date: 17 January 2023*

## 1. Introduction

Mayotte Island is one of the four main volcanic islands of the Comoros Archipelago located in the Indian Ocean. The earliest step of magmatic activity is around 11 Ma [Debeuf, 2004, Pelleter et al., 2014], and the last eruptive events are estimated to have occurred between 7 and 4 ka [Zinke et al., 2003]. Until the present seismo-volcanic crisis offshore Mayotte that started in May 2018, the volcanic islands of

* Corresponding author.

the Comoros Archipelago were known for their diffuse and moderate seismicity with few historically felt events. The ongoing seismic sequence is thus unexpected and remarkable with regard to its duration and intensity (i.e. earthquakes of magnitude 5.9 on 15 May 2018). After the first two months of intense seismicity at the beginning of the crisis, seismicity still persisted a long time with numerous small earthquakes [Bertil et al., 2019], and ground deformation was observed [Lemoine et al., 2020]. A new submarine volcano was discovered at 50 km east of Petite Terre [Feuillet et al., 2019, 2021], and significant subsidence of Mayotte Island (up to 20 cm) was attributed to the drainage of a deep magma chamber near the coast [Foix et al., 2021]. This long-term seismic sequence and the associated new active volcano offshore Mayotte led the scientific community to investigate further the seismo-volcanic hazard in this area [Feuillet et al., 2019, Cesca et al., 2020, Darnet et al., 2020, Lemoine et al., 2020, Berthod et al., 2021, Foix et al., 2021, Saurel et al., 2022]. This seismo-volcanic crisis has been monitored since the beginning of May 2018; numerous studies were performed and many others are in progress to gain further information about the deep volcanic system, to better constrain the seismo-volcanic hazard for Mayotte and its population (e.g. seismicity, slope instability, tsunami, island subsidence or even new volcanic activity onshore).

On the Petite Terre Island in Mayotte, one of the latest eruptive events proposed at around 7 and 4 ky is probably at the origin of the Dziani Dzaha Lake formation [Zinke et al., 2003]. For the last decade, this atypical lacustrine system has been extensively studied [Leboulanger et al., 2017, Cellamare et al., 2018, Gérard et al., 2018, Milesi et al., 2019, Aucher et al., 2020, Jovovic et al., 2020, Sala et al., 2022]. Based on its water chemistry, the lake was most likely initially filled with seawater [Sarazin et al., 2021], and has since evolved as a closed system. Before the seismo-volcanic crisis, the physical, chemical and biological features of this ecosystem were far from those observed in a modern oceanic or lacustrine environment (details in Study site section). The ongoing seismo-volcanic crisis offshore Mayotte could have a significant impact on the stability and the functioning of this ecosystem through the reactivation of fractures in the crater/basement, the infiltration of fresh/sea water and/or the increase in magmatic bubbling and degassing through its waters [Liuzzo et al., 2021].

In order to investigate the impact of the perturbations related to the growth of the submarine volcano offshore Mayotte on this lacustrine system, we conducted three field trips in 2020 and 2021 on the Dziani Dzaha Lake. We documented the evolution of the physical and chemical properties in the water column (e.g. [$O_2$], pH, salinity, T), as well as the carbon and nitrogen isotopic signatures of dissolved inorganic carbon (DIC) and suspended particulate matter (SPM)) within it (i.e. $\delta^{15}N_{SPM}$, $\delta^{13}C_{DIC}$, $\delta^{13}C_{SPM}$). The comparison of these results with those obtained before the seismo-volcanic crisis illustrates the response of this lacustrine system to this kind of geological perturbations.

## 2. Study site

The Dziani Dzaha Lake is a shallow maar lake located on the Petite Terre Island of Mayotte (Figure 1). This lake is small (i.e. $2.36 \times 10^5$ m$^2$), close to sea level and separated from the nearby seashore by a 220-m-thick crater wall [Rouwet et al., 2021]. The lake watershed is restricted to the volcanic crater (i.e. ~1 km in diameter and 50–100 m height). The average depth of the Dziani Dzaha Lake is about 3 m with a narrow depression reaching 18 m depth (Figure 1), likely related to the chimney of the phreatomagmatic eruption at the origin of this lake. Magmatic gases bubble through the water column in several locations [Milesi et al., 2020, Liuzzo et al., 2021] mostly in shallow areas of the lake, with one bubbling site in the central part for which a strong increase in the bubbling activity has been observed since 2020 compared to our last observations from 2012 to 2017 (Figure 1).

From 2010 to 2017, i.e. before the beginning of the seismo-volcanic crisis in May 2018, the lake water column showed an atypical combination of physical and chemical features for a modern lacustrine system [e.g. Sarazin et al., 2021]. Salinity measured was between 35 and 70 psu (practical salinity unit), nearly twice the usual salinity of seawater. The alkalinity was also very high, with values ranging from ca. 0.1 to 0.2 M (nearly 100 times the alkalinity of seawater), and pH ranged between 9 and 9.5. The water column was periodically stratified with a sharp halocline at ca. 2 m depth about half of the year, driven by the salinity decrease in surface waters as a result

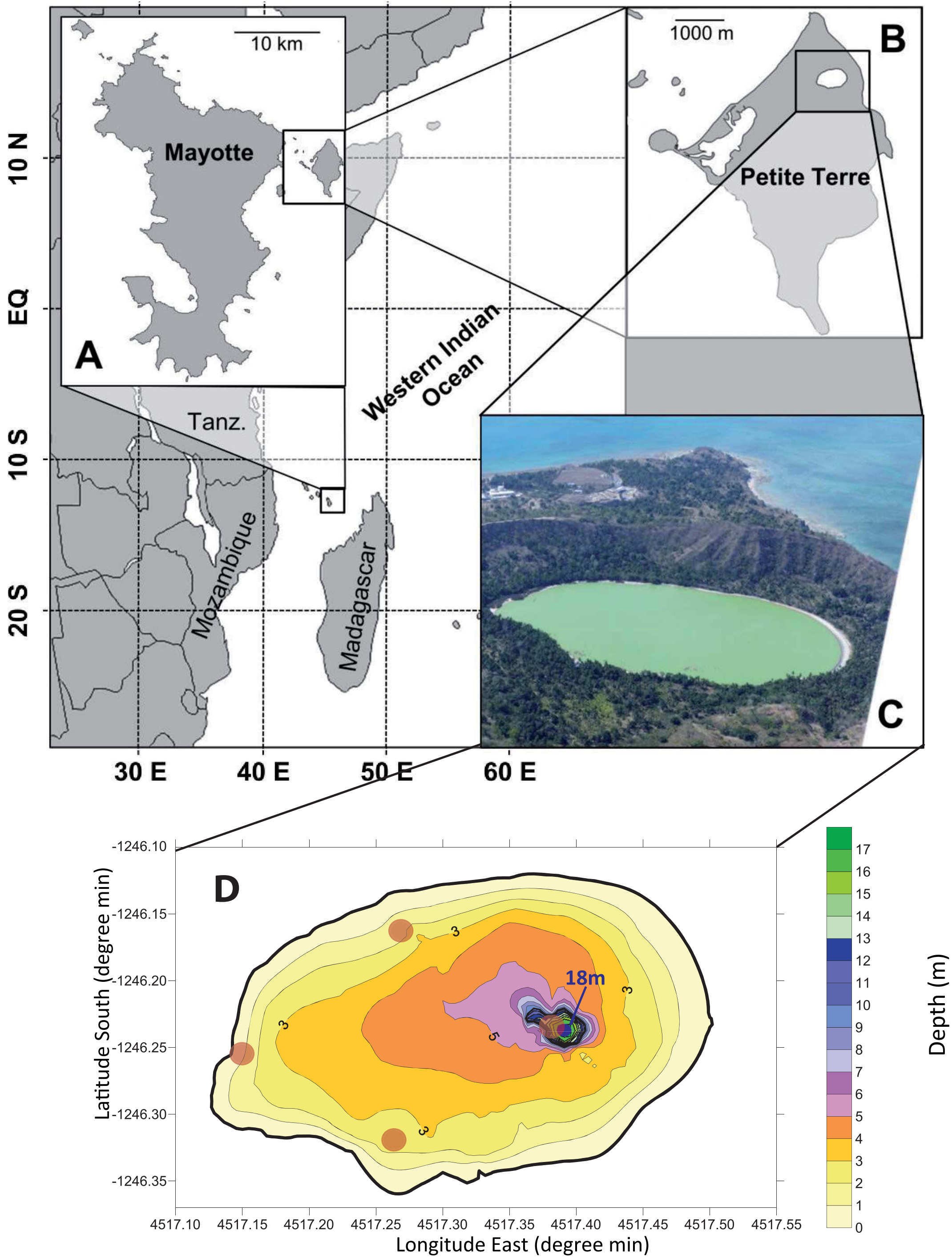


**Figure 1.** Location and bathymetric maps of the Dziani Dzaha Lake on Mayotte Islands (Indian Ocean). (A) Mayotte Islands in Western Indian Ocean, (B) Dziani Dzaha Lake in Petite Terre Island on Mayotte, (C) Picture of the lake taken in October 2014, and (D) Bathymetric map of the lake, with blue circle representing the water column sampling location and the red circles representing the identified bubbling areas at the water–air interface (modified from Leboulanger et al. [2017] and Cadeau et al. [2022]).

of increasing precipitation during the rainy season. A permanent chemocline was also present at ca. 14 m depth in the narrow depression [Sarazin et al., 2021]. Importantly, the lake was permanently anoxic below ca. 1.5 m depth despite seasonal variations in its water column structure, and was strongly euxinic (sulfides $H_2S/HS^-$ concentration ranging from 2 to 6 mM) below 2 m depth when the halocline is present (during the stratified period), or only below a 14 m depth when it is not [during the non-stratified period, Sarazin et al., 2021]. Details on the evolution of the physical and chemical parameters according to stratification are available in previous works [e.g. Leboulanger et al., 2017, Cadeau et al., 2020, Sarazin et al., 2021]. All our field trips done since the beginning of the crisis were conducted during non-stratified periods (i.e. from August to December). Before the crisis, these non-stratified periods were characterized by the absence of halocline (except at ca. 14 m depth). As a result, most physical, chemical and biological parameters were constant with depth down to the deep chemocline at 14 m depth, except for the dissolved oxygen that was only present down to a maximum of 1.5 m depth depending on the photosynthetic activity. The fact that $O_2$ saturation values fluctuate widely (from 0 to 350%) is related to large nycthemeral fluctuations in the balance between the activities of photosynthesis (which produces $O_2$) and respiration (which consumes it) in this biologically very active lacustrine system [e.g. Leboulanger et al., 2017, Cadeau et al., 2020]. The salinity was close to 60 psu, the alkalinity close to 0.14 M, the pH close to 9.2, the $[SO_4^{2-}]$ content close to 3 mM, $[H_2S]$ content close to 0.1 mM, and a relatively homogeneous diversity of cyanobacteria, bacteria, and archaea was observed along the water column [Hugoni et al., 2018]. Below the 14 m deep chemocline, the salinity and alkalinity increased to 70 psu and 0.2 M, respectively, the pH decreased to a value close to 9, no $SO_4^{2-}$ was observed while $H_2S$ accumulated up to 6 mM. Our previous work has demonstrated that the characteristics of non-stratified seasons have remained stable since 2010 [e.g. Leboulanger et al., 2017, Hugoni et al., 2018, Bernard et al., 2019, Sarazin et al., 2021].

## 3. Materials and methods

The isotope signatures in this study were acquired on samples from surveys conducted in November 2020, September 2021 and December 2021. A nomenclature consistent with previous publications was used to identify each sample taken during the different surveys. For example, for the sample "DZ21-9 2m," "DZ" indicates the Dziani Dzaha Lake, "21-9" indicates the year (2021) and month (September) of the survey, "2m" refers to sampling depth of the water column station called "18m" as shown on Figure 1.

Water samples were collected using a horizontal 1.2 L Niskin bottle along a vertical profile at the 18 m depth station for each survey. For each sampling depth, samples were taken in 500 mL plastic bottles. Each sample was then filtered onto precombusted Whatman GF/F glass fiber filters (0.7 µm) and quartz Millipore AQFA (size cut-off ca. 3 µm) for $\delta^{13}C_{POC}$ and $\delta^{15}N_{PON}$ analysis, and a 12 mL Labco Exetainer glass tube was filled with the filtrate and fixed with 0.2 mL of saturated $HgCl_2$ solution for DIC and $\delta^{13}C_{DIC}$ analyses. The GF/F filters with SPM were decarbonated by exposure to concentrated HCl fumes in a desiccator for 12 h to avoid loss of material.

### 3.1. *Physical and chemical in situ measurements*

*In situ* profiling were performed with a CTD multiparameter EXO2 probe (temperature, conductivity/salinity, pH, ORP, $O_2$, turbidity, chlorophyll, phycocyanine (PC) and fDOM) and a turbidity AQUAlogger 210 TYPT Aquatec probe. The pH electrode was calibrated using pH 4.00, 7.01 and 10.00 NBS-NIST buffers; $O_2$ optode was calibrated at 100% saturation in wet air; salinity sensor was calibrated with a 34.271 psu seawater. Other sensors have not been calibrated and the corresponding parameters are used as relative values; nevertheless, most of these sensors offer quite stable response (especially T, turb., chl., PC, fDOM), at the exception of oxidation-reduction potential (ORP) electrode which can only be used as relative values. In addition, two $O_2$ NKE SDOT optodes were deployed at 0.25 m depth from 10/09 to 13/12 2021 near the central gas bubbling zone (at ca. 1–3 m from the outlet, respectively), and a water level probe (OTT Orpheus Mini) was installed in September 2021 in the NO part of the lake.

### 3.2. *Carbon and nitrogen isotope measurements*

DIC and $\delta^{13}C_{DIC}$ were measured using an AP2003 mass spectrometer. Phosphoric acid (100% $H_3PO_4$)

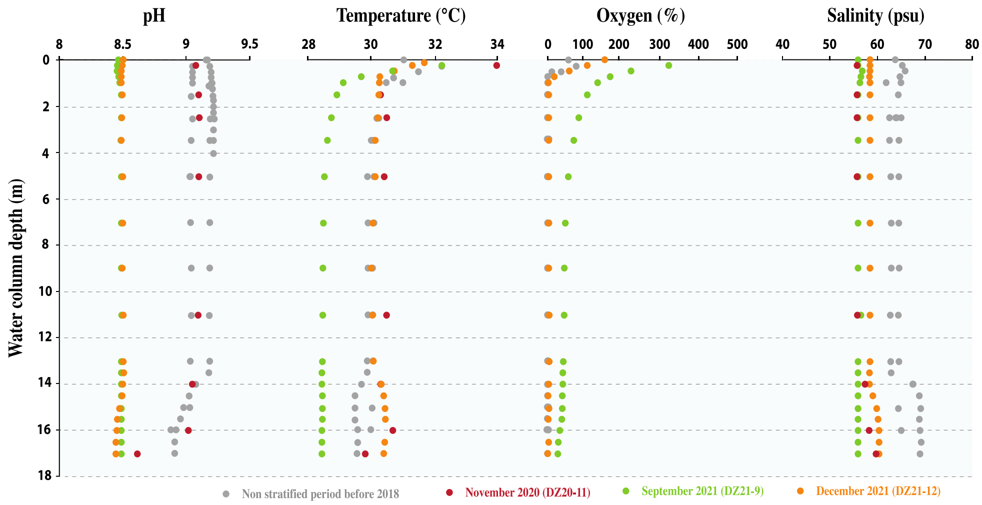


**Figure 2.** Vertical profiles of physical and chemical parameters recorded during each survey including salinity (psu), temperature (°C), pH and dissolved oxygen (%). The grey profiles correspond to previous data obtained before 2018 from Cadeau et al. [2022].

was injected into 12 mL Labco Exetainer tubes that were then flushed with helium. For each sample, 0.1 mL water was sub-sampled and transferred into the acidified Labco Exetainer tubes. The samples were agitated for 15–24 h so that $CO_2$ in the water was in equilibrium with the $CO_2$ in the headspace. The $CO_2$ in the headspace gas was then separated by gas chromatography with helium as a carrier gas and analyzed using the AP2003 mass spectrometer. Solutions presenting a range of DIC were prepared using sodium hydrogen carbonate for DIC calibration. Three internal carbonate standards with known isotopic compositions (Across, Merck and Rennes II) were used for isotopic composition calibration. The standard carbonate powder was loaded into 12 mL Labco Exetainer tubes with 0.1 mL distilled water before being flushed with helium and then analyzed in the same way as DIC. DIC values are expressed in $mol \cdot L^{-1}$ with a reproducibility of $\pm 0.01$ $mol \cdot L^{-1}$, and $\delta^{13}C_{DIC}$ values are expressed in ‰ relative to Vienna Pee Dee Belemnite (VPDB) with a reproducibility of $\pm 0.1$‰ ($1\sigma$).

The $\delta^{13}C_{POC}$ and $\delta^{15}N_{PON}$ of the decarbonated filters were measured using a Flash EA1112 elemental analyzer coupled to a Thermo Finnigan Deltaplus XP mass spectrometer via a Conflo IV interface (Thermo Fisher Scientific, Waltham, MA, USA). The decarbonated samples were loaded into tin capsules and heated to 1200 °C in a combustion tube with a mixture of chromium oxide and silver cobalt oxides. The combustion gases were carried by helium through a reduction column and a gas chromatography column to separate $CO_2$ from $N_2$ and from the other gases. $CO_2$ and $N_2$ were successively injected into the mass spectrometer for isotopic analysis. For the isotope calibration, four internal standards of organic-rich soil or sediment were analyzed in the same way. $\delta^{13}C_{POC}$ values are expressed as ‰ relative to VPDB with a reproducibility of $\pm 0.2$‰ ($1\sigma$) and $\delta^{15}N^{PON}$ are expressed as ‰ relative to air with a reproducibility of $\pm 0.3$‰ ($1\sigma$).

## 4. Results

### 4.1. *Physical and chemical features of the water column*

In September 2020, salinity was constant down to 14 m depth with an average value close to 55.6 psu and increased below this depth up to 59.7 psu (Figure 2, Table 1). pH was constant down to 14 m depth with an average value of 9.1 and decreased below this depth down to 8.6. Temperature decreased in surface waters from 34 °C to 30.3 °C at 1.5 m depth, and remained constant with depth down to the lake bottom. In September 2021, salinity, pH and temperature significantly decreased in the water column.

**Table 1.** Salinity (psu), temperature (°C), pH and dissolved oxygen (%) measured in November 2020, September 2021 and December 2021 in the Dziani Dzaha Lake

| Sample (name) | Depth (cm) | Temperature (°C) | pH | $[O_2]$ (%) | Salinity (psu) |
|---|---|---|---|---|---|
| DZ20-11 | 0.25 | 34 | 9.07 | | 55.6 |
| DZ20-11 | 1.5 | 30.3 | 9.09 | | 55.6 |
| DZ20-11 | 2.5 | 30.5 | 9.095 | | 55.6 |
| DZ20-11 | 5 | 30.4 | 9.093 | | 55.6 |
| DZ20-11 | 11 | 30.5 | 9.083 | | 55.8 |
| DZ20-11 | 14 | 30.3 | 9.038 | | 57.3 |
| DZ20-11 | 16 | 30.7 | 9.009 | 0.2 | 58.1 |
| DZ20-11 | 17 | 29.8 | 8.610 | | 59.7 |
| DZ21-9 | 0.25 | 32.2 | 8.6 | 327 | 55.1 |
| DZ21-9 | 0.50 | 30.4 | 8.6 | 212 | 55.8 |
| DZ21-9 | 0.75 | 29.5 | 8.6 | 149 | 55.6 |
| DZ21-9 | 1.01 | 29.1 | 8.6 | 128 | 55.3 |
| DZ21-9 | 1.25 | 29.0 | 8.6 | 116 | 55.2 |
| DZ21-9 | 1.50 | 28.9 | 8.6 | 100 | 55.2 |
| DZ21-9 | 1.75 | 28.8 | 8.6 | 93 | 55.1 |
| DZ21-9 | 2.01 | 28.8 | 8.6 | 91 | 55.1 |
| DZ21-9 | 2.26 | 28.7 | 8.6 | 84 | 55.1 |
| DZ21-9 | 2.51 | 28.7 | 8.6 | 80 | 55.1 |
| DZ21-9 | 2.76 | 28.7 | 8.6 | 73 | 55.1 |
| DZ21-9 | 3.01 | 28.6 | 8.6 | 70 | 55.1 |
| DZ21-9 | 3.26 | 28.6 | 8.6 | 67 | 55.1 |
| DZ21-9 | 3.51 | 28.6 | 8.6 | 65 | 55.1 |
| DZ21-9 | 3.76 | 28.6 | 8.6 | 64 | 55.1 |
| DZ21-9 | 4.00 | 28.6 | 8.5 | 61 | 55.1 |
| DZ21-9 | 4.50 | 28.5 | 8.5 | 53 | 55.1 |
| DZ21-9 | 5.00 | 28.5 | 8.5 | 51 | 55.1 |
| DZ21-9 | 5.51 | 28.5 | 8.5 | 48 | 55.2 |
| DZ21-9 | 6.61 | 28.5 | 8.5 | 47 | 55.2 |
| DZ21-9 | 7.01 | 28.5 | 8.5 | 45 | 55.2 |
| DZ21-9 | 7.47 | 28.5 | 8.5 | 43 | 55.2 |
| DZ21-9 | 8.18 | 28.5 | 8.5 | 43 | 55.2 |
| DZ21-9 | 8.50 | 28.5 | 8.5 | 43 | 55.2 |
| DZ21-9 | 8.86 | 28.5 | 8.5 | 42 | 55.2 |
| DZ21-9 | 9.58 | 28.5 | 8.5 | 42 | 55.2 |
| DZ21-9 | 10.00 | 28.5 | 8.5 | 42 | 55.2 |
| DZ21-9 | 11.04 | 28.5 | 8.5 | 41 | 55.2 |
| DZ21-9 | 11.51 | 28.5 | 8.5 | 40 | 55.2 |
| DZ21-9 | 12.01 | 28.5 | 8.5 | 39 | 55.2 |

(continued on next page)

**Table 1.** (continued)

| Sample (name) | Depth (cm) | Temperature (°C) | pH | $[O_2]$ (%) | Salinity (psu) |
|---|---|---|---|---|---|
| DZ21-9 | 13.01 | 28.4 | 8.5 | 39 | 55.2 |
| DZ21-9 | 13.51 | 28.4 | 8.5 | 37 | 55.2 |
| DZ21-9 | 14.51 | 28.4 | 8.5 | 36 | 55.2 |
| DZ21-9 | 15.00 | 28.4 | 8.5 | 35 | 55.2 |
| DZ21-9 | 16.00 | 28.4 | 8.5 | 29 | 55.2 |
| DZ21-9 | 17.01 | 28.4 | 8.5 | 23 | 55.2 |
| DZ21-12 | 0.25 | 31.4 | 8.6 | 152 | 57.9 |
| DZ21-12 | 0.50 | 30.4 | 8.6 | 58 | 58.2 |
| DZ21-12 | 0.75 | 30.3 | 8.6 | 22 | 58.1 |
| DZ21-12 | 1.00 | 30.3 | 8.5 | 7 | 58.1 |
| DZ21-12 | 1.25 | 30.2 | 8.5 | 5 | 58.1 |
| DZ21-12 | 1.50 | 30.2 | 8.5 | 4 | 58.1 |
| DZ21-12 | 1.75 | 30.2 | 8.5 | 2 | 58.1 |
| DZ21-12 | 2.00 | 30.2 | 8.5 | 2 | 58.1 |
| DZ21-12 | 2.25 | 30.2 | 8.5 | 2 | 58.1 |
| DZ21-12 | 2.50 | 30.2 | 8.5 | 2 | 58.1 |
| DZ21-12 | 2.75 | 30.2 | 8.5 | 2 | 58.1 |
| DZ21-12 | 3.00 | 30.2 | 8.5 | 1 | 58.1 |
| DZ21-12 | 3.25 | 30.1 | 8.5 | 1 | 58.1 |
| DZ21-12 | 3.50 | 30.1 | 8.5 | 1 | 58.1 |
| DZ21-12 | 3.75 | 30.1 | 8.5 | 1 | 58.1 |
| DZ21-12 | 4.01 | 30.1 | 8.5 | 1 | 58.1 |
| DZ21-12 | 4.50 | 30.1 | 8.5 | 1 | 58.1 |
| DZ21-12 | 4.99 | 30.1 | 8.5 | 1 | 58.1 |
| DZ21-12 | 5.51 | 30.1 | 8.5 | 1 | 58.1 |
| DZ21-12 | 6.00 | 30.1 | 8.5 | 1 | 58.1 |
| DZ21-12 | 6.50 | 30.1 | 8.5 | 1 | 58.1 |
| DZ21-12 | 7.01 | 30.1 | 8.5 | 1 | 58.1 |
| DZ21-12 | 7.50 | 30.0 | 8.5 | 1 | 58.1 |
| DZ21-12 | 8.01 | 30.0 | 8.5 | 1 | 58.1 |
| DZ21-12 | 8.51 | 30.0 | 8.5 | 1 | 58.1 |
| DZ21-12 | 9.00 | 30.0 | 8.5 | 1 | 58.0 |
| DZ21-12 | 9.50 | 30.0 | 8.5 | 1 | 58.1 |
| DZ21-12 | 10.00 | 30.0 | 8.5 | 1 | 58.1 |
| DZ21-12 | 10.49 | 30.0 | 8.5 | 1 | 58.1 |
| DZ21-12 | 11.01 | 30.0 | 8.5 | 1 | 58.1 |
| DZ21-12 | 11.50 | 30.1 | 8.5 | 1 | 58.1 |
| DZ21-12 | 12.01 | 30.1 | 8.5 | 0 | 58.1 |

(continued on next page)

**Table 1.** (continued)

| Sample (name) | Depth (cm) | Temperature (°C) | pH | $[O_2]$ (%) | Salinity (psu) |
|---|---|---|---|---|---|
| DZ21-12 | 12.49 | 30.1 | 8.5 | 0 | 58.1 |
| DZ21-12 | 13.01 | 30.1 | 8.5 | 0 | 58.1 |
| DZ21-12 | 13.50 | 30.1 | 8.5 | 0 | 58.1 |
| DZ21-12 | 14.01 | 30.3 | 8.5 | 0 | 58.2 |
| DZ21-12 | 14.50 | 30.4 | 8.5 | 0 | 58.7 |
| DZ21-12 | 15.02 | 30.4 | 8.4 | 0 | 59.5 |
| DZ21-12 | 15.50 | 30.4 | 8.4 | 0 | 59.8 |
| DZ21-12 | 16.00 | 30.5 | 8.4 | 0 | 60.0 |
| DZ21-12 | 16.50 | 30.5 | 8.4 | 0 | 60.2 |
| DZ21-12 | 17.00 | 30.4 | 8.4 | 0 | 60.2 |

Salinity and pH values were still constant with depth throughout the whole water column but with average values close to 55 psu and 8.5, respectively. Temperature decreased from 32 °C in surface water to 28.2 °C at about 2 m depth, and then remained constant with depth down to the lake bottom. Dissolved oxygen was present throughout the whole water column. Surface waters showed very high $O_2$ saturation values (i.e. up to 327%, Figure 2) that are related to the high photosynthetic activity similar to before the volcanic crisis. Surprisingly however, the deeper part of the lake, which was anoxic all year long before the crisis was oxygenated at 20% of $O_2$ saturation. In December 2021, the temperature decreased from about 32 °C in surface waters to 30 °C at about 2 m depth. Temperature then remained constant down to 14 m and increased to values close to 30.5 °C below 14 m depth. Salinity was constant down to 14 m depth with an average value close to 58 psu and increased below this depth up to 60.2 psu. pH was constant with depth throughout the water column with an average value close to 8.5. Dissolved oxygen was only present in surface water down to 0.8 m; below this depth the water column remained completely anoxic.

Physical and chemical features of the water column in September 2020 were similar to those observed during the surveys conducted before the seismo-volcanic crisis offshore Mayotte (Figure 2), except for the salinity which was already lower than those observed previously. In contrast, salinity and pH values were significantly lower in September 2021 compared to the pre-seismo-volcanic crisis values observed, whereas dissolved oxygen was distributed in the water column, which had never been observed before. In December 2021 the pH still remained as low as in September 2021, the salinity increased by 2.8 psu compared to September 2021 (up to about 5 psu in the deeper part of the lake), and the water column was anoxic again below 1.5 m depth. In addition, based on $O_2$ optode placed in the central part of the lake, monitoring of dissolved oxygen content indicates that oxygenation of the entire water column lasted for several months between September and December 2021 (Figure 3).

### 4.2. *Carbon and nitrogen isotopic signature in the water column*

In the Dziani Dzaha Lake water column, the DIC concentrations ranged from 0.15 to 0.21 M with an average value of 0.19 ± 0.02 M in November 2020, from 0.16 to 0.22 M with an average value of 0.20 ± 0.02 M in September 2021, and from 0.17 to 0.23 M with an average value of 0.21 ± 0.02 M in December 2021 (Figure 4, Table 2). An increasing trend with depth was observed below the deep chemocline at 14 m depths in November 2020 from 0.15 to 0.21 M. In September and December 2021, the DIC concentrations decreased between 6 and 12 m depths. Overall, these concentration data show some variability but remain around an average value close to 0.2 M throughout the water column, which is similar to the DIC concentrations observed before the seismo-volcanic crisis (Figure 4).

The DIC isotopic compositions ($\delta^{13}C_{DIC}$) ranged between 12.2 and 13.0‰ with an average value of

**Table 2.** [DIC], $\delta^{13}C_{DIC}$, $\delta^{13}C_{POC}$ and $\delta^{15}N_{PON}$ measured in November 2020, September 2021 and December 2021 in the Dziani Dzaha Lake

| Sample (name) | Depth (cm) | [DIC] (M) | $\delta^{13}C_{DIC}$ (±0.2‰) | $\delta^{13}C_{POC}$ (±0.2‰) | $\delta^{15}N_{PON}$ (±0.2‰) |
|---|---|---|---|---|---|
| DZ20-11 | 0.25 | 0.17 | 12.36 | −14.01 | 7.86 |
| DZ20-11 | 0.25 | 0.18 | 13.01 | −14.13 | 8.10 |
| DZ20-11 | 1.5 | 0.20 | 12.41 | −14.01 | 8.14 |
| DZ20-11 | 2.5 | 0.19 | 12.66 | −13.78 | 8.14 |
| DZ20-11 | 3.5 | 0.21 | 12.59 | −13.95 | 8.17 |
| DZ20-11 | 5 | 0.18 | 12.73 | −13.82 | 7.83 |
| DZ20-11 | 11 | 0.19 | 12.55 | −13.55 | 7.92 |
| DZ20-11 | 14 | 0.15 | 12.19 | −13.04 | 8.68 |
| DZ20-11 | 16 | 0.18 | 12.51 | −12.24 | 9.03 |
| DZ20-11 | 17 | 0.21 | 12.94 | −9.99 | 10.70 |
| DZ20-11 | 17 | — | — | −10.33 | 10.46 |
| DZ21-9 | 0.25 | 0.21 | 9.93 | −18.74 | 7.71 |
| DZ21-9 | 0.75 | 0.21 | 9.73 | −18.68 | 7.78 |
| DZ21-9 | 1.5 | 0.19 | 9.94 | −18.77 | 7.73 |
| DZ21-9 | 1.5 | 0.22 | 9.63 | — | — |
| DZ21-9 | 2 | 0.20 | 9.88 | −18.57 | 7.63 |
| DZ21-9 | 2.5 | 0.21 | 9.77 | −18.68 | 7.72 |
| DZ21-9 | 5 | 0.20 | 9.78 | −18.63 | 7.80 |
| DZ21-9 | 7 | 0.16 | 9.93 | −18.38 | 7.54 |
| DZ21-9 | 11 | 0.21 | 9.89 | −18.40 | 7.65 |
| DZ21-9 | 14 | 0.21 | 9.85 | −18.37 | 7.83 |
| DZ21-9 | 16 | 0.21 | 9.92 | −18.55 | 7.36 |
| DZ21-9 | 17 | 0.21 | 9.78 | −18.01 | 7.43 |
| DZ21-12 | 0.25 | 0.18 | 9.78 | −18.07 | 7.55 |
| DZ21-12 | 0.75 | 0.21 | 9.51 | −17.89 | 8.01 |
| DZ21-12 | 1.5 | — | — | −17.96 | 8.02 |
| DZ21-12 | 2.5 | 0.23 | 9.43 | −17.91 | 7.83 |
| DZ21-12 | 5 | 0.21 | 9.56 | −17.91 | 7.94 |
| DZ21-12 | 7 | 0.19 | 9.66 | −17.92 | 7.99 |
| DZ21-12 | 11 | 0.17 | 9.73 | −17.85 | 7.97 |
| DZ21-12 | 13 | 0.23 | 9.51 | −17.79 | 8.06 |
| DZ21-12 | 14 | 0.22 | 9.44 | −17.90 | 8.01 |
| DZ21-12 | 15 | 0.22 | 9.57 | −17.79 | 8.35 |
| DZ21-12 | 16 | 0.22 | 9.50 | −17.86 | 7.90 |
| DZ21-12 | 17 | 0.21 | 9.32 | −17.50 | 8.24 |
| DZ21-12 | 17 | 0.21 | 9.46 | −16.93 | 8.42 |

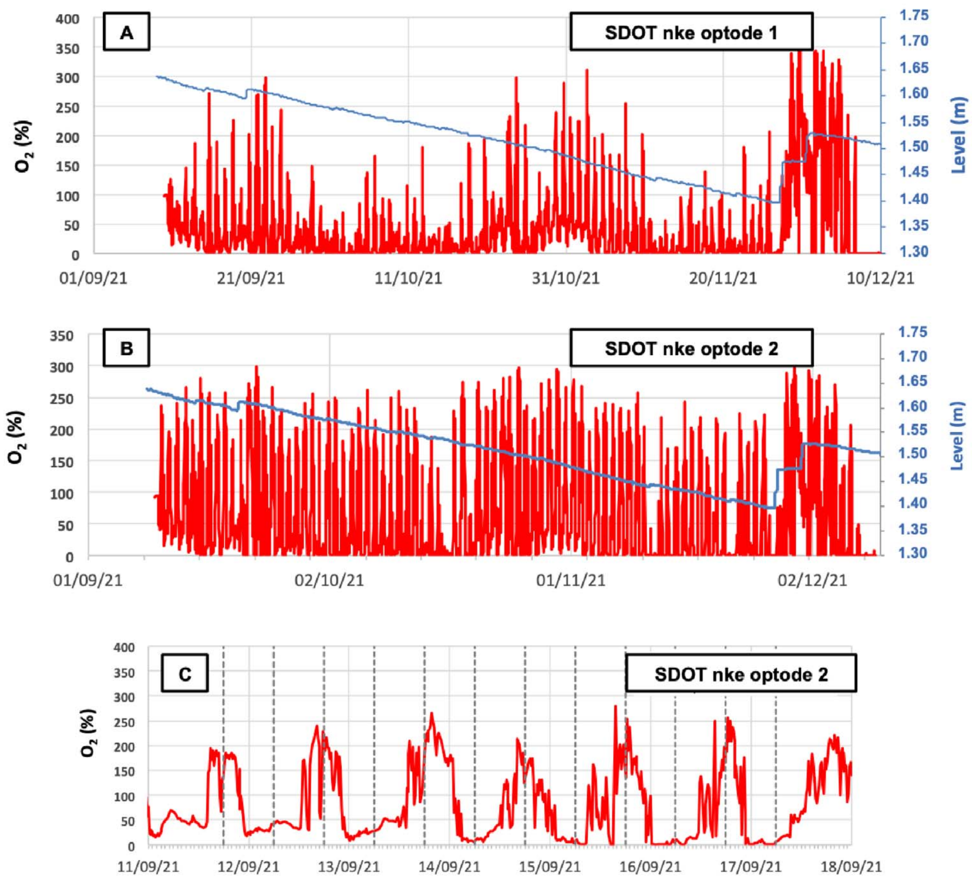


**Figure 3.** Evolution of dissolved oxygen content at 25 cm depth at station 18 m (in red) and relative water column level (in blue) from September to December 2021 ((A, B) two NKE SDOT optodes, (C) zoom on several nycthemeral cycles from the NKE SDOT optode 2).

12.6±0.2‰ in November 2020, between 9.6 and 9.9‰ with an average value of 9.8 ± 0.1‰ in September 2021, and between 9.3 and 9.8‰ with an average value of 9.5 ± 0.1‰ in December 2021 (Figure 4). The $\delta^{13}C_{DIC}$ was constant with depth during these three surveys. The $\delta^{13}C_{DIC}$ observed in November 2020 was similar to the $\delta^{13}C_{DIC}$ measured before 2018 (i.e. average value of 12.1‰, Figure 4), while the isotopic signatures observed in September and December 2021 were depleted in $^{13}C$ by almost 3‰ compared to the $\delta^{13}C_{DIC}$ measured before 2018.

The particulate organic carbon (POC) isotopic signatures ($\delta^{13}C_{POC}$) ranged from −14.1 to −10‰ with an average value of −13 ± 1.5‰ in November 2020, from −18.8 to −18‰ with an average value of −18.5 ± 0.2‰ in September 2021, and from −18 to −16.9‰ with an average value of −17.8 ± 0.3‰ in December 2021 (Figure 4). In November 2020, the $\delta^{13}C_{POC}$ was constant with depth from the surface water to the deep chemocline at 14 m depth with an isotopic signature close to −14‰, and significantly increased below it to −10‰. These isotopic signatures and this isotopic pattern with depth are similar to the $\delta^{13}C_{POC}$ observed before 2018 (i.e. average value of −14‰, Figure 4). In contrast, the $\delta^{13}C_{POC}$ in September and December 2021 were constant with depth throughout the whole water column and strongly depleted in $^{13}C$ compared to the $\delta^{13}C_{POC}$ observed before 2018.

The particulate organic nitrogen (PON) isotopic signatures ($\delta^{15}N_{PON}$) ranged from 7.8 to 10.7‰ with an average value of 8.6 ± 1‰ in November 2020, from 7.4 to 7.8‰ with an average value of 7.7 ± 0.1‰ in

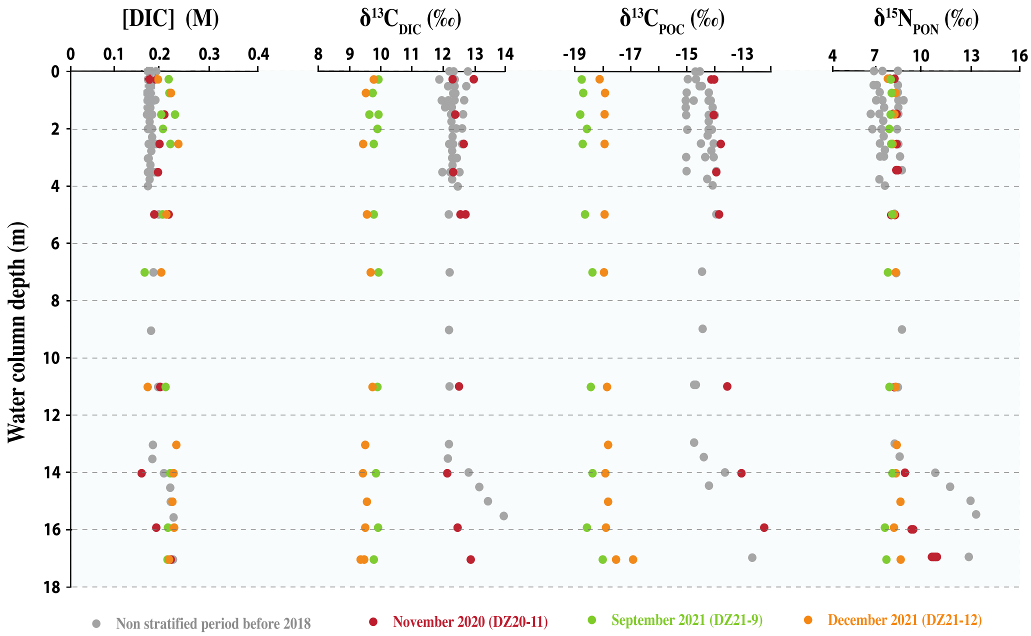


**Figure 4.** Vertical profiles of [DIC], $\delta^{13}C_{DIC}$, $\delta^{13}C_{POC}$ and $\delta^{15}N_{PON}$ in the Dziani Dzaha Lake water column. The grey profiles correspond to previous data obtained before 2018 from Cadeau [2017] and Cadeau et al. [2020, 2021, 2022].

September 2021, and from 7.5 to 8.4‰ with an average value of 8 ± 0.2‰ in December 2021 (Figure 4). Overall, during these three surveys the $\delta^{15}N_{PON}$ values were close to 8‰ and constant with depth throughout the water column, except in November 2020 when a significant isotopic enrichment was observed below 14 m depth, up to a value of 10.7‰. This isotopic enrichment is similar to the isotopic enrichments observed before 2018 ($\delta^{15}N_{PON}$ values up to 13‰), and contrasts with the constant isotopic values observed in September and December 2021 (Figure 4).

## 5. Discussion

### 5.1. *Physical and chemical features in the water column*

The evolution of the physical and chemical parameters observed in the Dziani Dzaha Lake water column during the surveys conducted after the beginning of the seismo-volcanic crisis illustrates significant modifications of the water column characteristics. Indeed, before 2018, one of the main features of this lacustrine system was its great stability (since it was first studied in 2010), with a permanent anoxia of the water column below ca. 1.5 m depth [sometimes shallower depending on photosynthetic activity in surface water, e.g. Sarazin et al., 2021]. The oxygenation of the whole water column, as well as a significant decrease in salinity and pH values, had never been observed. These represent major perturbations of this lacustrine system. Two distinct processes related to the seismo-volcanic crisis may be invoked to explain these observations: (i) an impact of seawater or freshwater infiltration into the lake in response to the subsidence, and (ii) an intensification of volcanic degassing into the lake (with physical, chemical and biological impacts).

Water chemistry of the Dziani Dzaha Lake and the ocean are very different. A contribution of an oxygenated, more neutral and less salty water from the ocean (or from groundwater) into the lake could have a consistent impact with what is observed in the Dziani Dzaha Lake water column in September 2021. However, firstly, after infiltration into bedrock, ocean or groundwater is unlikely to remain well-oxygenated. Moreover, given the very high organic matter content in the water column [Leboulanger et al., 2017, Cadeau et al., 2020], an oxygen supply from episodic water inputs into the lake would probably be quickly consumed through oxygenic organic matter degradation. Secondly, to significantly change the chemistry of the whole water column in the Dziani Dzaha Lake, water inputs would have to be significant, which seems unrealistic. Considering seawater and freshwater inputs with a salinity of 35 psu and 0 psu ($\text{Salinity}_{\text{input}}$ in (1)), respectively, and a lake salinity before the seismo-volcanic crisis near 63.5 psu ($\text{Salinity}_{\text{pre-2020}}$ in (1)), the impact of water input on salinity can be tested using mass balance equations as follows:

$$V_{\text{post-2020}} \times \text{Salinity}_{\text{post-2020}} = V_{\text{input}} \times \text{Salinity}_{\text{input}} + V_{\text{pre-2020}} \times \text{Salinity}_{\text{pre-2020}}. \tag{1}$$

For instance, based on water volume calculations [e.g. Cadeau et al., 2022], an increase of the water level of about 20 cm (corresponding to the subsidence of Mayotte Island) would represent a water input of about 7.2% of the total water volume ($V_{\text{input}}$ in (1)). From this, the calculated salinities considering seawater or freshwater inputs are close to 61.4 psu or 58.9 psu, respectively. In September 2021, salinity was close to 55 psu. According to the mass balance equation, to obtain a calculated salinity of 55 psu it would be necessary to consider a freshwater input representing 12.7% of the total water volume. In addition, the origin of potential freshwater inputs is difficult to constrain, because it could also be related to an increase of precipitation water inputs as observed in surface waters during the period when the lake is stratified [e.g. Sarazin et al., 2021]. Although oceanic or freshwater inputs cannot be dismissed, it seems unrealistic to assume that this process alone could be responsible for all the modifications observed in the physical and chemical features in 2020 and 2021, but could at least in part explain the salinity decrease.

Before the beginning of the seismo-volcanic crisis offshore Mayotte, several bubbling areas were identified at the water–air interface of the Dziani Dzaha Lake. The volcanic origin of these degassing into the atmosphere was confirmed by the $CO_2$ carbon isotopic composition, which was typically of magmatic origin [around −3‰, Milesi et al., 2020, Liuzzo et al., 2021]. Yet, since a large part of these degassing was ebullitive, the contribution of this carbon source to the lake water column was difficult to estimate [Cadeau et al., 2020]. In addition, degassing areas were mainly located in the shallow parts of the lake (<2 m depth, Figure 1), with only one weakly bubbling area in the central part of the lake. An intensification of volcanic degassing through the Dziani Dzaha Lake water column related to the seismicity associated with the submarine volcano growth offshore Mayotte could impact both the oxygenation state and the pH of the water column. Indeed, an intense and permanent degassing in the central part of this lacustrine system, as observed during the surveys conducted in 2020 and 2021, could generate a convective plume that would significantly increase the mixing of the water column, favoring oxygenation events throughout the water column. Based on $[O_2]$ data from two $O_2$ NKE SDOT optodes deployed at 0.25 m depth between September 10th and December 10th 2021 near the central plume, long-term water column oxygenation is highlighted (Figure 3). From 10th September to 7th December, day–night cycles of oxygenation are observed, which reflect the relative variations of photosynthesis and respiration activity in this highly productive lacustrine system [e.g. Leboulanger et al., 2017]. As the optodes are under the central plume influence, water comes from the bottom part of the lake (ca. 5 m depth at this point), which suggests the presence of dissolved oxygen at depth at least part of the day ($O_2$ decreases according to the respiration activity at night). Since magmatic gases do not contain $O_2$, the only explanation for the presence of $O_2$ in the deeper part of the lake (at least at 5 m depth) would be a more active water column mixing (i.e. which was never observed before 2018) introducing $O_2$ from the surface waters to the deep waters. This increase of the mixing dynamics probably results from the water uplift induced by the more active central degassing in the absence of strong salinity gradient. After December 7th, these day–night cycles of oxygenation stopped, indicating a reduction of the water column mixing dynamics. We assume here that the water uplift due to the central degassing zone was not strong enough to fight the onset of the water column stratification. This is consistent with an increase in precipitation water inputs in late November and early December leading to a rise of the lake level (Figure 3), and the beginning of haline stratification. In addition to the water column mixing, this intense and long-term central plume could also increase the dissolution of volcanic $CO_2$ in the lake waters, decreasing the pH. Although this process might explain both the dissolved oxygen content increase (i.e. physical mixing of the water column) and the pH decrease (i.e. dissolution of $CO_2$), the volcanic $CO_2$ contribution to the dissolved inorganic pool in the lake is difficult to constrain and it seems unrealistic to propose that the significant pH decrease is entirely related to it. In addition, pH value represents the balance of many processes, such as photosynthesis/respiration or sulfate reduction, which may also have changed.

Based on the three surveys conducted in 2020 and 2021, physical and chemical properties in the Dziani Dzaha Lake water column have already been impacted by the seismo-volcanic crisis offshore Mayotte. It is probably related to a combination of a dilution by precipitation water (explaining the salinity decrease), an infiltration of low salinity groundwater and an intensification of volcanic degassing (explaining both the oxygenation of the whole water column, through a mixing process, and at least a part of the pH decrease). These results provide a first assessment of the extent to which the Dziani Dzaha Lake functioning is impacted by the consequence of the birth of this submarine volcano.

## 5.2. *The Carbon biogeochemical cycle*

Since the beginning of the seismo-volcanic crisis offshore Mayotte, the three surveys conducted in the Dziani Dzaha Lake indicate: (i) similar but more variable DIC concentrations, and (ii) a significant depletion in $^{13}C$ since 2021 of about 3‰ (Figure 4). These results could be explained by (i) an input of a carbon source isotopically lighter than the DIC pool, or (ii) a modification in the respective influence of the processes that regulate the carbon cycle in the Dziani Dzaha Lake.

Two main parameters related to the seismo-volcanic crisis offshore Mayotte need to be considered to discuss the potential impact of an isotopically lighter carbon source in the lake: the subsidence of Mayotte and the seismicity affecting these islands for 4 years now. This combination of parameters might favor both water input through the bedrock and an increase of volcanic $CO_2$ input in the lake. Based on the chemical and physical parameters (e.g. salinity, pH, $[O_2]$), no seawater input has been identified since the study of the Dziani Dzaha Lake in 2010 and until 2018. In contrast, volcanic $CO_2$ inputs have already been highlighted by previous studies [Cadeau et al., 2020, Milesi et al., 2020], mostly thanks to the observation of several bubbling areas at the water/air interface. The contribution of volcanic $CO_2$ to the Dziani Dzaha Lake carbon cycle was difficult to constrain, and $CO_2$ dissolution in the water could be limited by a mainly ebullitive degassing through the water column. In addition, since 2018 the activity of the degassing area located in the central part of the lake has strongly increased, which must have increased water column mixing and $CO_2$ dissolution. These carbon sources present a significantly lighter $\delta^{13}C$ value compared to the $\delta^{13}C_{DIC}$ values in the Dziani Dzaha Lake, i.e. close to 0‰ and −3‰ for seawater DIC and volcanic $CO_2$, respectively [Cadeau et al., 2020]. Considering the strong modifications of the physico-chemical parameters observed in the lake since 2018 (e.g. $[O_2]$, pH, Figure 2), both water inputs and increased $CO_2$ inputs through old fractures in the volcanic basement are strongly suspected. However, considering the very high DIC concentrations in the lake (i.e. about 100 times seawater concentrations), it is unlikely that these two sources alone are responsible for the $^{13}C$ depletion observed in September and December 2021. The impact of these sources can be tested using isotopic and mass balance equation as follows:

$$X_{\text{post-2020}} \times \delta^{13}C_{\text{DIC-post-2020}} = X_{\text{input}} \times \delta^{13}C_{\text{DIC-input}} + X_{\text{pre-2020}} \times \delta^{13}C_{\text{DIC-pre-2020}}. \tag{2}$$

With $X$ representing the amount of DIC considering the concentrations and water volumes, and $\delta^{13}C$ the calculated or measured carbon isotopic compositions of DIC. Based on the (2), considering the concentrations and isotopic signatures of the lake and ocean DIC (i.e. 200 mM and 12‰ for the lake, and 2 mM and 0‰ for the ocean), an input of seawater equivalent to 7.2% of the lake volume as mentioned previously would modify the lake $\delta^{13}C_{DIC}$ by less than 0.1‰. The effect of an increase of volcanic $CO_2$ dissolution with a $\delta^{13}C$ of −3‰ would have a similar impact.

As mentioned previously, water input or most likely an intensification of $CO_2$ volcanic input through the central plume have the ability to strongly and quickly impact the oxygenation state of the water column, which is a key parameter in the regulation of the carbon cycle by exercising a strong control on the organic matter degradation pathways.

Previous studies have shown that the strongly positive $\delta^{13}C_{DIC}$ in the Dziani Dzaha Lake was the consequence of organic matter degradation by methanogenesis associated with methane degassing into the atmosphere, which results from the complete sulfate consumption in an anoxic water column [Cadeau et al., 2020, 2022]. In contrast to other lacustrine systems in which methanogenesis has been suggested to explain $^{13}C$ enrichment observed in the sediment record or in the water column [Talbot and Kelts, 1986, Valero-Garcés et al., 1999, Gu et al., 2004, Anoop et al., 2013, Zhu et al., 2013, Birgel et al., 2015], the Dziani Dzaha Lake exhibits similar carbon isotope signatures in the lake waters and in the sediment, as well as a long-term steady state [Cadeau et al., 2020]. Oxygenation of the water column necessarily modified the carbon cycle functioning by limiting the methanogenesis activity in favor of an aerobic degradation of the organic matter, and by fostering methane oxidation in the water column, hence limiting methane degassing into the atmosphere. Using the isotopic and mass balance equation described below, the impact of methane oxidation in the water column can be tested with the following equation:

$$\delta^{13}C_{\text{DIC-post-2020}} = X_{CH_4\text{-pre-2020}} \times \delta^{13}C_{CH_4\text{-pre-2020}} + X_{\text{DIC-pre-2020}} \times \delta^{13}C_{\text{DIC-pre-2020}}. \quad (3)$$

With $X$ representing the amount of DIC or $CH_4$ considering the concentrations and water volumes, and $\delta^{13}C$ the calculated or measured carbon isotopic compositions of DIC or $CH_4$. Based on the (3) and considering a methane concentration close to 2 mM (i.e. hundred times lower than DIC which is of 200 mM) and its isotopic signature close to −65‰, as observed in the water column before 2018 [e.g. Cadeau et al., 2020, Sarazin et al., 2021], methane oxidation would decrease the $\delta^{13}C_{DIC}$ by only 0.8‰. This illustrates that punctual and complete methane oxidation in the water column (i.e. simulating an extreme oxygenation episode) would have a limited impact on $\delta^{13}C_{DIC}$.

Although such punctual perturbation has a limited impact on the $\delta^{13}C_{DIC}$, a modification of the Dziani Dzaha Lake steady state related to seismo-volcanic crisis perturbations could easily explain the $\delta^{13}C_{DIC}$ decrease. Based on the steady state box model proposed in Cadeau et al. [2020], a decrease in methane degassing into the atmosphere of about 10% of methane generated, a decrease of about 10% of the amount of organic matter degradation through methanogenesis, or a combination of both, would be sufficient to explain 3‰ decrease in $\delta^{13}C_{DIC}$ as observed in September and December 2021. The $\delta^{13}C_{DIC}$ significantly depleted in $^{13}C$ is thus most probably the consequence of the limitation in both organic matter degradation by methanogenesis and methane degassing to the atmosphere related to the oxygenation of the water column.

Based on the three surveys conducted in 2020 and 2021, the carbon cycle in the Dziani Dzaha Lake seems to be significantly impacted by the seismo-volcanic crisis offshore Mayotte most likely because of the intensification of volcanic $CO_2$ degassing into the lake, resulting in water column oxygenation and modifications of the organic matter degradation pathways within it. Future work is needed to determine the spatial extent and the persistence of these processes, as well as determine whether the carbon cycle is temporarily or permanently modified.

### 5.3. *The nitrogen biogeochemical cycle*

The particulate organic nitrogen isotope signatures ($\delta^{15}N_{PON}$) observed since 2018 are very similar to those observed before the beginning of the seismo-volcanic crisis offshore Mayotte, i.e. close to 8‰ and constant with depth (Figure 4). The only difference is the absence of significant isotopic increase below 14 m depth for the samples collected in September and December 2021.

In a previous study, we have suggested that the isotopic enrichment observed in the $\delta^{15}N_{PON}$ evolution in the deeper part of the water column or in the surface sediments results from a $^{15}N$-enriched ammonium ($NH_4^+$) assimilation, which itself results from $NH_4^+$ dissociation to ammonia ($NH_3$) associated with a strong isotopic fractionation under basic and anoxic conditions [Cadeau et al., 2021]. As also shown for other modern basic lacustrine environments [Menzel et al., 2013] and sedimentary records of past lacustrine environments [Stüeken et al., 2020, 2019, 2015], pH and oxygenation state are thus major parameters in the regulation of the nitrogen cycle in the Dziani Dzaha Lake.

The oxygenation state of the water column controls the speciation of dissolved nitrogen into ammonium *versus* nitrate. Water column oxygenation, as observed in September 2021, should prevent any $NH_4^+$ accumulation by inducing its oxidation. In addition, even when the water column remains anoxic as observed in December 2021, the significant decrease in pH can be predicted to limit the dissociation of $NH_4^+$ into $NH_3$. Based on the average pH value of 8.5 and on the isotopic fractionation associated with the $NH_4^+/NH_3$ dissociation reaction [Li et al., 2012], only about 15% of the $NH_4^+$ dissociates into $NH_3$, resulting in an isotopic enrichment of the residual $NH_4^+$ of only about 7‰. These predicted amounts of dissociated $NH_4^+$ and isotopic enrichment of residual $NH_4^+$ are significantly lower than those estimated before the seismo-volcanic crisis event [i.e. about 45–72% of $NH_4^+$ dissociated with an isotopic enrichment of residual $NH_4^+$ comprised between 20 and 32‰, Cadeau et al., 2021]. The perturbations related to the seismo-volcanic crisis 2018 should therefore have had a significant impact on the $\delta^{15}N_{PON}$ in the Dziani Dzaha Lake.

Surprisingly however, nitrogen isotope signatures are quite similar to those observed before the beginning of the ongoing crisis. The only difference is that in September and December 2021, $\delta^{15}N_{PON}$ values are constant over the whole water column, including the deeper part of the water column, while up until 2020 a marked isotopic increase was observed in the deep part of the water column. These constant nitrogen isotopic signatures observed in September and December 2021 are probably related to the assimilation of $NH_4^+$ only slightly enriched in $^{15}N$ as a consequence of a less basic condition in the deeper and $NH_4^+$-rich part of the water column. We predict that this minor change in the $\delta^{15}N_{PON}$ pattern represents the premise of bigger changes, should the lower pH and the periods of oxygenation persist or aggravate in the future.

## 6. Conclusion

Since the beginning of the lake study in 2010 and until the beginning of the seismo-volcanic crisis in 2018, the Dziani Dzaha Lake presented an atypical combination of physical, chemical and biological features, as well as a high stability. Among them, the permanent anoxia of the water column and the pH exerted a strong control on the carbon and nitrogen cycles through: (i) an organic matter degradation by methanogenesis coupled to methane degassing into the atmosphere following the quantitative sulfate consumption in the water column, and (ii) a $^{15}N$-enriched $NH_4^+$ assimilation in the deeper part of the lake related to the dissociation of $NH_4^+$ to $NH_3$ under basic conditions. Three years after the onset of the seismo-volcanic crisis, the submarine volcano growth and its associated perturbations are already having an impact on the biogeochemical functioning of the lake. Through water infiltration into the lake or/and an increase of volcanic $CO_2$ degassing into the lake, the water column oxygenation and the strong decrease of the pH value have: (i) modified the organic matter degradation pathways by limiting both the methanogenesis activity and methane degassing into the atmosphere, which is illustrated by a significant decrease in the $\delta^{13}C_{DIC}$, and (ii) limited the $NH_4^+$ dissociation into $NH_3$ and the isotopic enrichment of the residual $NH_4^+$, which is illustrated by the absence of $\delta^{15}N$ increase with depth. These results constitute a first assessment of the present-day impact of the seismo-volcanic crisis on the lake. Although the perturbations affecting the Dziani Dzaha Lake are difficult to constrain now, studying this lacustrine system is an exciting opportunity to explore the resilience of these ecosystems to such geological disturbances.

## Data availability

All the data generated and analyzed in this study are available in the paper.

## Conflicts of interest

The authors declare no competing financial interests.

## Author contributions

MA designed the study. MA, DJ and AD collected the samples. DJ and AG measured the physical and chemical parameters on the Dziani Dzaha Lake. PC performed the isotopic analyses and took the lead in the interpretation and writing the original draft. All authors provided critical feedback in shaping both the research results and the manuscript.

## Acknowledgements

Research was supported by the Réseau de Surveillance Volcanologique et Sismologique de Mayotte (REVOSIMA), a partnership between the Institut de Physique du Globe de Paris (IPGP), the Bureau de Recherches Géologiques et Minières (BRGM), and the Observatoire Volcanologique du Piton de la Fournaise (OVPF-IPGP), the Centre National de la Recherche Scientifique (CNRS), and the Institut Français de Recherche pour l'Exploitation de la Mer (IFREMER). The funders had no role in study design, data collection and analysis, decision to publish, or preparation of the manuscript. The authors also wish to thank the Conservatoire du littoral for their support.


## References


Anoop, A., Prasad, S., Plessen, B., Basavaiah, N., Gaye, B., Naumann, R., Menzel, P., Weise, S., and Brauer, A. (2013). Palaeoenvironmental implications of evaporative gaylussite crystals from Lonar Lake, central India. *J. Quat. Sci.*, 28, 349–359.

Aucher, W., Delafont, V., Ponlaitiac, E., Alafaci, A., Agogué, H., Leboulanger, C., Bouvy, M., and Héchard, Y. (2020). Morphology and ecology of two new amoebae, isolated from a Thalassohaline Lake, Dziani Dzaha. *Protist*, 171, article no. 125770.

Bernard, C., Escalas, A., Villeriot, N., Agogué, H., Hugoni, M., Duval, C., Carré, C., Got, P., Sarazin, G., Jézéquel, D., Leboulanger, C., Grossi, V., Ader, M., and Troussellier, M. (2019). Very low phytoplankton diversity in a tropical saline-alkaline lake, with co-dominance of Arthrospira fusiformis (Cyanobacteria) and Picocystis salinarum (Chlorophyta). *Microb. Ecol.*, 78, 603–617.

Berthod, C., Médard, E., Bachèlery, P., Gurioli, L., Di Muro, A., Peltier, A., Komorowski, J.-C., Benbakkar, M., Devidal, J.-L., Langlade, J., Besson, P., Boudon, G., Rose-Koga, E., Deplus, C., Le Friant, A., Bickert, M., Nowak, S., Thinon, I., Burckel, P., Hidalgo, S., Kaliwoda, M., Jorry, S., Fouquet, Y., and Feuillet, N. (2021). The 2018-ongoing Mayotte submarine eruption: Magma migration imaged by petrological monitoring. *Earth Planet. Sci. Lett.*, 571, article no. 117085.

Bertil, D., Roullé, A., Lemoine, A., Colombain, A., Hoste-Colomer, R., Gracianne, C., Meza-Fajardo, K., Maisonhaute, E., and Dectot, G. (2019). MAYEQSwarm2019: BRGM earthquake catalogue for the Earthquake Swarm located East of Mayotte. May 2018–May 2019. http://ressource.brgm.fr/data/data/937d4fef5c0b-4580-b1ad-2723393b68b6.

Birgel, D., Meister, P., Lundberg, R., Horath, T. D., Bontognali, T. R. R., Bahniuk, A. M., de Rezende, C. E., Vasconcelos, C., and Mckenzie, J. A. (2015). Methanogenesis produces strong $^{13}C$ enrichment in stromatolites of Lagoa Salgada, Brazil: a modern analogue for Palaeo-/Neoproterozoic stromatolites? *Geobiology*, 13, 245–266.

Cadeau, P. (2017). *Cycles biogéochimiques du carbone, de l'azote et du soufre dans un analogue des océans précambriens : le lac Dziani (Mayotte)*. PhD thesis, Université Sorbonne-Paris Cité.

Cadeau, P., Ader, M., Jézéquel, D., Chaduteau, C., Sarazin, G., Bernard, C., and Leboulanger, C. (2021). Nitrogen isotope discrepancy between primary producers and sediments in an anoxic and alkaline lake. *Front. Earth Sci.*, 9, article no. 787386.

Cadeau, P., Cartigny, P., Thomazo, C., Jézéquel, D., Leboulanger, C., Sarazin, G., and Ader, M. (2022). The Dziani Dzaha Lake: a long-awaited modern analogue for superheavy pyrites. *Geobiology*, 20, 444–461.

Cadeau, P., Jézéquel, D., Leboulanger, C., Fouilland, E., Le Floc'h, E., Chaduteau, C., Milesi, V., Guélard, J., Sarazin, G., Katz, A., d'Amore, S., Bernard, C., and Ader, M. (2020). Carbon isotope evidence for large methane emissions to the Proterozoic atmosphere. *Sci. Rep.*, 10, article no. 18186.

Cellamare, M., Duval, C., Drelin, Y., Djediat, C., Touibi, N., Agogué, H., Leboulanger, C., Ader, M., and Bernard, C. (2018). Characterization of phototrophic microorganisms and description of new cyanobacteria isolated from the saline-alkaline crater-lake Dziani Dzaha (Mayotte, Indian Ocean). *FEMS Microbiol. Ecol.*, 94, article no. fiy108.

Cesca, S., Letort, J., Razafindrakoto, H. N. T., Heimann, S., Rivalta, E., Isken, M. P., Nikkhoo, M., Passarelli, L., Petersen, G. M., Cotton, F., and Dahm, T. (2020). Drainage of a deep magma reservoir near Mayotte inferred from seismicity and deformation. *Nat. Geosci.*, 13, 87–93.

Darnet, M., Wawrzyniak, P., Tarits, P., Hautot, S., and D'Eu, J. F. (2020). Mapping the geometry of volcanic systems with magnetotelluric soundings: Results from a land and marine magnetotelluric survey performed during the 2018–2019 Mayotte seismovolcanic crisis. *J. Volcanol. Geotherm. Res.*, 406, article no. 107046.

Debeuf, D. (2004). *Étude de l'évolution volcano-structurale et magmatique de Mayotte (archipel des Comores, océan Indien)*. Université de la Réunion, Réunion.

Feuillet, N., Jorry, S., Crawford, W. C., Deplus, C., Thinon, I., Jacques, E., Saurel, J. M., Lemoine, A., Paquet, F., Satriano, C., Aiken, C., Foix, O., Kowalski, P., Laurent, A., Rinnert, E., Cathalot, C., Donval, J.-P., Guyader, V., Gaillot, A., Scalabrin, C., Moreira, M., Peltier, A., Beauducel, F., Grandin, R., Ballu, V., Daniel, R., Pelleau, P., Gomez, J., Besançon, S., Geli, L., Bernard, P., Bachelery, P., Fouquet, Y., Bertil, D., Lemarchand, A., and Van der Woerd, J. (2021). Birth of a large volcanic edifice offshore Mayotte via lithosphere-scale dyke intrusion. *Nat. Geosci.*, 14, 787–795.

Feuillet, N., Jorry, S., Rinnert, E., Thinon, I., and Fouquet, Y. (2019). MAYOBS. In *French Oceanographic Cruises*. Sismer, Paris.

Foix, O., Aiken, C., Saurel, J.-M., Feuillet, N., Jorry, S. J., Rinnert, E., and Thinon, I. (2021). Offshore Mayotte volcanic plumbing revealed by local passive tomography. *J. Volcanol. Geotherm. Res.*, 420, article no. 107395.

Gérard, E., De Goeyse, S., Hugoni, M., Agogué, H., Richard, L., Milesi, V., Guyot, F., Lecourt, L., Borensztajn, S., Joseph, M.-B., Leclerc, T., Sarazin, G., Jézéquel, D., Leboulanger, C., and Ader, M. (2018). Key role of alphaproteobacteria and cyanobacteria in the formation of stromatolites of Lake Dziani Dzaha (Mayotte, Western Indian Ocean). *Front. Microbiol.*, 9, article no. 796.

Gu, B., Schelske, C. L., and Hodell, D. A. (2004). Extreme $^{13}$C enrichments in a shallow hypereutrophic lake: implications for carbon cycling. *Limnol. Oceanogr.*, 49, 1152–1159.

Hugoni, M., Escalas, A., Bernard, C., Nicolas, S., Jézéquel, D., Vazzoler, F., Sarazin, G., Leboulanger, C., Bouvy, M., Got, P., Ader, M., Troussellier, M., and Agogué, H. (2018). Spatiotemporal variations in microbial diversity across the three domains of life in a tropical thalassohaline lake (Dziani Dzaha, Mayotte Island). *Mol. Ecol.*, 27, 4775–4786.

Jovovic, I., Grossi, V., Adam, P., Simon, L., Antheaume, I., Gelin, F., Ader, M., and Cartigny, P. (2020). Quantitative and specific recovery of natural organic and mineral sulfur for (multi-)isotope analysis. *Org. Geochem.*, 146, article no. 104055.

Leboulanger, C., Agogué, H., Bernard, C., Bouvy, M., Carré, C., Cellamare, M., Duval, C., Fouilland, E., Got, P., Intertaglia, L., Lavergne, C., Le Floc'h, E., Roques, C., and Sarazin, G. (2017). Microbial diversity and cyanobacterial production in Dziani Dzaha Crater Lake, a unique tropical thalassohaline environment. *PLoS ONE*, 12, article no. e0168879.

Lemoine, A., Briole, P., Bertil, D., Roullé, A., Foumelis, M., Thinon, I., Raucoules, D., de Michele, M., Valty, P., and Hoste Colomer, R. (2020). The 2018–2019 seismo-volcanic crisis east of Mayotte, Comoros islands: seismicity and ground deformation markers of an exceptional submarine eruption. *Geophys. J. Int.*, 223, 22–44.

Li, L., Lollar, B. S., Li, H., Wortmann, U. G., and Lacrampe-Couloume, G. (2012). Ammonium stability and nitrogen isotope fractionations for – NH3(aq)–NH3(gas) systems at 20–70 °C and pH of 2–13: applications to habitability and nitrogen cycling in low-temperature hydrothermal systems. *Geochim. Cosmochim. Acta*, 84, 280–296.

Liuzzo, M., Di Muro, A., Rizzo, A. L., Caracausi, A., Grassa, F., Fournier, N., and Italiano, F. (2021). Gas geochemistry at Grande Comore and Mayotte volcanic islands (Comoros archipelago), Indian Ocean. *Geochem. Geophys. Geosyst.*, 22(8), article no. e2021GC009870.

Menzel, P., Gaye, B., Wiesner, M. G., Prasad, S., Stebich, M., Das, B. K., Anoop, A., Riedel, N., and Basavaiah, N. (2013). Influence of bottom water anoxia on nitrogen isotopic ratios and amino acid contributions of recent sediments from small eutrophic Lonar Lake, central India. *Limnol. Oceanogr.*, 58, 1061–1074.

Milesi, V. P., Debure, M., Marty, N. C. M., Capano, M., Jézéquel, D., Steefel, C., Rouchon, V., Albéric, P., Bard, E., Sarazin, G., Guyot, F., Virgone, A., Gaucher, É. C., and Ader, M. (2020). Early diagenesis of lacustrine carbonates in volcanic settings: the role of Magmatic $CO_2$ (Lake Dziani Dzaha, Mayotte, Indian Ocean). *ACS Earth Space Chem.*, 4, 363–378.

Milesi, V. P., Jézéquel, D., Debure, M., Cadeau, P., Guyot, F., Sarazin, G., Claret, F., Vennin, E., Chaduteau, C., Virgone, A., Gaucher, E. C., and Ader, M. (2019). Formation of magnesium-smectite during lacustrine carbonates early diagenesis: study case of the volcanic crater lake Dziani Dzaha (Mayotte—Indian Ocean). *Sedimentology*, 66, 983–1001.

Pelleter, A.-A., Caroff, M., Cordier, C., Bachelery, P., Nehlig, P., Debeuf, D., and Arnaud, N. (2014). Melilite-bearing lavas in Mayotte (France): an insight into the mantle source below the Comores. *Lithos*, 208–209, 281–297.

Rouwet, D., Nemeth, K., Tamburello, G., and Calabrese, S. (2021). Volcanic lakes in Africa: the VOLADA_Africa 2.0 Database, and implications for volcanic hazard. *Front. Earth Sci.*, 9, article no. 717798.

Sala, D., Grossi, V., Agogué, H., Leboulanger, C., Jézéquel, D., Sarazin, G., Antheaume, I., Bernard, C., Ader, M., and Hugoni, M. (2022). Influence of aphotic haloclines and euxinia on organic biomarkers and microbial communities in a thalassohaline and alkaline volcanic crater lake. *Geobiology*, 20, 292–309.

Sarazin, G., Jézéquel, D., Leboulanger, C., Fouilland, E., Le Floc'h, E., Bouvy, M., Gérard, E., Agogué, H., Bernard, C., Hugoni, M., Grossi, V., Troussellier, M., and Ader, M. (2021). Geochemistry of an endorheic thalassohaline ecosystem: the Dziani Dzaha crater lake (Mayotte Archipelago, Indian Ocean). *C. R. Géosci.*, 352, 559–577.

Saurel, J.-M., Jacques, E., Aiken, C., Lemoine, A., Retailleau, L., Lavayssière, A., Foix, O., Dofal, A., Laurent, A., Mercury, N., Crawford, W., Lemarchand, A., Daniel, R., Pelleau, P., Bès de Berc, M., Dectot, G., Bertil, D., Roullé, A., Broucke, C., Colombain, A., Jund, H., Besançon, S., Guyavarch, P., Kowalski, P., Roudaut, M., Apprioual, R., Battaglia, J., Bodihar, S., Boissier, P., Bouin, M. P., Brunet, C., Canjamale, K., Catherine, P., Desfete, N., Doubre, C., Dretzen, R., Dumouche, T., Fernagu, P., Ferrazzini, V., Fontaine, F. R., Gaillot, A., Géli, L., Griot, C., Grunberg, M., Guzel, E. C., Hoste-Colomer, R., Lambotte, S., Lauret, F., Léger, F., Maros, E., Peltier, A., Vergne, J., Satriano, C., Tronel, F., Van der Woerd, J., Fouquet, Y., Jorry, S. J., Rinnert, E., Thinon, I., and Feuillet, N. (2022). Mayotte seismic crisis: building knowledge in near real-time by combining land and ocean-bottom seismometers, first results. *Geophys. J. Int.*, 228, 1281–1293.

Stüeken, E. E., Buick, R., and Schauer, A. J. (2015). Nitrogen isotope evidence for alkaline lakes on late Archean continents. *Earth Planet. Sci. Lett.*, 411, 1–10.

Stüeken, E. E., Martinez, A., Love, G., Olsen, P. E., Bates, S., and Lyons, T. W. (2019). Effects of pH on redox proxies in a Jurassic rift lake: implications for interpreting environmental records in deep time. *Geochim. Cosmochim. Acta*, 252, 240–267.

Stüeken, E. E., Tino, C., Arp, G., Jung, D., and Lyons, T. W. (2020). Nitrogen isotope ratios trace high-pH conditions in a terrestrial Mars analog site. *Sci. Adv.*, 6, article no. eaay3440.

Talbot, M. R. and Kelts, K. (1986). Primary and diagenetic carbonates in the anoxic sediments of Lake Bosumtwi, Ghana. *Geology*, 14, 912–916.

Valero-Garcés, B. L., Delgado-Huertas, A., Ratto, N., and Navas, A. (1999). Large $^{13}C$ enrichment in primary carbonates from Andean Altiplano lakes, northwest Argentina. *Earth Planet. Sci. Lett.*, 171, 253–266.

Zhu, Z., Chen, J., and Zeng, Y. (2013). Abnormal positive $\delta^{13}C$ values of carbonate in Lake Caohai, southwest China, and their possible relation to lower temperature. *Quat. Int.*, 286, 85–93.

Zinke, J., Reijmer, J. J. G., Thomassin, B. A., Dullo, W.-C., Grootes, P. M., and Erlenkeuser, H. (2003). Postglacial flooding history of Mayotte Lagoon (Comoro Archipelago, southwest Indian Ocean). *Mar. Geol.*, 194, 181–196.

*Comptes Rendus*
*Géoscience — Sciences de la Planète*
**2022**, Vol. 354, Special Issue S2, p. 317-341
https://doi.org/10.5802/crgeos.151

The Mayotte seismo-volcanic crisis of 2018-2021 in the Comoros archipelago (Mozambique channel) / *La crise sismo-volcanique de 2018-2021 de Mayotte dans l'archipel des Comores (Canal du Mozambique)*

# Site effects observations and mapping on the weathered volcanic formations of Mayotte Island

## *Observations et cartographie des effets de site sur les formations volcaniques altérées de l'île de Mayotte*

**Agathe Roullé** [*, a], **Marie Baillet** [b], **Didier Bertil** [a] **and Cécile Cornou** [c]

[a] BRGM, Department of Risks and Prevention, 3 av. Claude-Guillemin - BP 36009, 45060 5 Orléans Cedex 2, France

[b] CNRS, UMR Géoazur, Cellule Education, Campus Azur du CNRS, 250 rue Albert Einstein - CS 10269 - F 06905 SOPHIA ANTIPOLIS Cedex, France

[c] ISTerre (Institut des Sciences de la Terre), Université Grenoble Alpes, CS 40700, 38058 GRENOBLE Cedex 9, France

*E-mails:* a.roulle@brgm.fr (A. Roullé), marie.baillet@geoazur.unice.fr (M. Baillet), d.bertil@brgm.fr (D. Bertil), cecile.cornou@univ-grenoble-alpes.fr (C. Cornou)

**Abstract.** Since the 2000s, local seismic hazard studies have shown that Mayotte Island presented superficial geological formations prone to lithological site effects. The seismic sequence initiated in May 2018 confirmed the importance of such effects, both in terms of intensity and spatial extension. The analysis of the recorded strong motions showed that weathered volcanic formations are prone to significant site effects with mean amplification factors for peak ground acceleration (PGA) between 1.4 and 4.9 and that a complex combination of lithological and topographic site effects is in action. We thus implement a regional scale map of site effects for the fast calculation of strong motion and damage maps for crisis management purposes. We also provide a first estimate of key site parameters for eight stations: surface geology, resonance frequency, an amplification factor proxy for PGA, a $V_{S,30}$ value, if available, and an estimated EC8 soil class.

**Résumé.** Depuis les années 2000, les études d'aléa sismique local réalisées à Mayotte ont montré que les formations géologiques superficielles présentes sur l'île étaient susceptibles de présenter des effets de site lithologiques. La séquence sismique initiée en mai 2018 a confirmé l'importance de ces effets, aussi bien en termes d'intensité que d'étendue spatiale. L'analyse des enregistrements des mouvements forts a montré notamment que les formations volcaniques altérées pouvaient être soumises à des effets de site significatifs avec des facteurs d'amplification moyens du PGA compris entre 1,4 et 4,9, et que ces effets résultaient probablement d'une combinaison complexe d'effets lithologiques et topographiques. Nous avons ensuite produit une carte d'effets de site à l'échelle

* Corresponding author.

régionale pour permettre le calcul en temps réel de cartes de mouvements forts et de dommages à des fins de gestion de crise. Enfin, pour les 8 sites de stations sismologiques étudiés dans cet article, nous proposons une première estimation des paramètres de sites clefs, à savoir : la géologie superficielle, la fréquence de résonance, un facteur d'amplification du PGA, une valeur du paramètre $V_{S,30}$, si disponible, et une estimation de la classe de sol EC8 au site.

**Keywords.** Site effects, Weathering, Mayotte, Seismic hazard, Seismic risk, Volcanic formations.

**Mots-clés.** Effets de site, Altération, Mayotte, Risque sismique, Aléa sismique, Formations volcaniques.

*Published online: 9 December 2022, Issue date: 17 January 2023*

## 1. Introduction

After the seismic sequence, initiated in May 2018, and characterized by hundreds of felt earthquakes and consecutive building damages [Sira et al., 2018], the evaluation of the seismic hazard in the whole of Mayotte territory became an imperative need for both crisis management and risk mitigation.

Mayotte is a cluster of volcanic islands on the southern part of the Somalia basin between Africa and Madagascar. It is part of the Comoros archipelago and comprises two main islands: Grande Terre on the west and Petite Terre on the east. Since 2011, the Mayotte territory must comply with the French Building Code regulations, which classifies it as a moderate seismicity level area (decrees 2010-1254 and 2010-1255). In May 2018, an exceptional telluric activity started ~50 km east of Mayotte, and remains active after more than two years, with 29 events of magnitude greater than 5, the highest magnitude reaching Mw 5.9 [Cesca et al., 2020, Lemoine et al., 2020, Bertil et al., 2021, Feuillet et al., 2021]. Until June 2018, only three accelerometric stations were operating on the island and could record the earthquakes: the two RESIF-RAP stations YTMZ and MDZA [RESIF, 1995] and the BRGM station MILA. During the main shock of May 15, 2018, the peak ground acceleration (PGA) reached 180 mg at the MILA station, located at Iloni on the eastern coast of Mayotte, near the top of a hill with outcropping clayey weathered formations, whereas the PGA recorded at the YTMZ station, situated on a rock site, at the same epicentral distance, was about 50 mg. These observations remind us that local geology plays an important role in modifying the characteristics of strong ground motion, both in terms of amplification and duration of seismic waves. The particularity of the superficial geological formations of Mayotte lies in their ancient volcanic origin [Nehlig et al., 2013] and the tropical conditions, which induces strong weathering of outcropping formations. The presence of those particular formations is a complex subject, which is still difficult to take into account, especially in a tropical volcanic context. While many papers show examples of weathering profile imaging [for example Anbazhagan and Sitharam, 2009 in India; Wang et al., 2019, Keifer et al., 2019 in Wyoming, United States] with some of them being applied in geological contexts similar to Mayotte [Von Voigtlander et al., 2018, Nelson and McBride, 2019, in Hawaï], a few of them intended to address site effects. Nevertheless, there are some precedents such as Davis [1995] who modelled the effect of the presence of a weathered layer on the seismic response of a site or Spudich et al. [1996] and Graizer [2009] who studied the directional amplification effects related to topography and the amplification effects related to the soft surface layer (weathered shale) at the Tarzana site in California. Narayan and Kumar [2015] and Kumar et al. [2017] also worked on the effects of weathering on seismic motion on a hillside via 2D modelling. In a similar manner, Wang et al. [2018] performed 3D modelling of lithological and topographic effects under weathering conditions in Hong Kong. Some authors also treated site effects in weathered areas for the estimation of induced ground motion, as is the case of Havenith et al. [2002] on the Ananevo site in Kyrgyzstan on weathered granite or of Ma et al. [2019] in Tokushima, Japan. In both cases, the authors used H/V ratios to analyze the directivity of the seismic response according to geomorphological criteria. Di Naccio et al. [2017] analyzed the amplification effects related to the shape of the topography and the presence of fractures on the surface via, in particular, the polarization analysis of H/V signals. This work on the San Gregorio site in Italy, located on fractured rock and which suffered significant damage during the L'Aquila earthquake, shows the importance of weathering in the directionality of seismic motion. All these works show the importance of weathering in seismic strong motions, both in terms of amplification, modification of the spectral content and directivity of the seismic energy. Since the 2000s, site effects have been studied on the island of Mayotte through specific site studies prior to the construction of public buildings [mainly scholarly buildings, e.g., Rey et al., 2012, Roullé et al., 2019]. Informative maps, including lithological and topographical site effect maps, were also produced in 2004 for the atlas of natural hazards on behalf of the local authorities [Audru et al., 2010]. Those maps were based on a "solid geology" low-resolution version of the geological map [Stieltjes, 1988] and are now regarded as obsolete in terms of description and mapping of superficial formations. Despite this limitation, they have shown high susceptibility to site effects of the volcanic formations of Mayotte. The seismic sequence initiated in 2018 led us (i) to update the site effects mapping to account for the amplification of strong motion related to the surficial geology in crisis management tools such as shake maps and damage scenarios and (ii) to characterize site effects at the seismological station sites in order to improve the metadata of the stations used for seismic monitoring of the territory.

## 2. Geological context

Mayotte Island is made up of a succession of volcanic deposits: the oldest goes back to 10 My in the south and the north-west, the most recent, found in Petite Terre, has been proposed to be of Holocene age [Zinke et al., 2013], but these deposits have not been dated. The succession of eruptive phases and quiescence, which allowed weathering and erosion, have shaped the present geology of Mayotte [for detailed information on the geological history of Mayotte, see Stieltjes, 1988, Debeuf, 2004, Audru et al., 2006, 2010, Nehlig et al., 2013]. The tropical climate of Mayotte is characterized by high rainfall levels, with an average annual rainfall exceeding 1500 mm over the whole island (http://www.meteofrance.yt/climat/description-du-climat, last access 14/12/2021). Coupled with the age of the rocks, this is largely responsible for the strong weathering of Mayotte's superficial formations.

In 2013, a 1:30,000 geological map of Mayotte [Lacquement et al., 2013, Nehlig et al., 2013], with focus on superficial geology and natural hazards, was produced with an attempt to better characterize weathering levels. A simplified version of this map is given in Figure 1. The main geological units that outcrop on land are basaltic, phonolitic or trachytic lavas (later referred to as lava formations), volcaniclastic deposits and large thicknesses of weathered rocks (later referred to as superficial formations). It distinguishes, among the superficial formations, the anthropic deposits, the autochthonous formations resulting from supergene weathering processes (e.g., alloterites and isalterites) and the allochthonous formations which bring together all the sedimentary deposits from erosion and transport process (e.g., alluvium, beach sands and slope formations as collu-vium or screes). A conceptual diagram to explain the typical pattern of the weathering profiles of Mayotte and the relation between the geological formations of Figure 1 is given in Figure 2.

## 3. Data description

### 3.1. *Earthquake records*

The earthquake data used in this paper come from the records of the YTMZ, MCHI, MILA, MTSB, KNKL, PMZI and R1EE2 stations described in Bertil et al. [2021] and Saurel et al. [2022] which provide continuous data in the framework of the Mayotte seismo-volcanic monitoring network (Réseau de surveillance volcanologique et sismologique de Mayotte—REVOSIMA). The geographic location of these stations is shown in Figure 3 and these are described in terms of name, network and type in Table 1. A particular case is the TBAD station, which corresponds to a test site for the future installation of a permanent seismological station on Petite Terre to replace the PMZI temporary station. The analyzed seismic events occurred from 08/03/2018 to 09/02/2020 and include the strongest events of the seismo-volcanic crisis initiated in May 2018 (Figure 4). Their locations are extracted from the work of Lemoine et al. [2020] until May 2019 and Bertil et al. [2021] from June 2019 up to February 2020. All their magnitudes come from Bertil et al. [2021] and correspond to local $M_{lv}$ magnitudes estimated from the regional localizations, generally stronger than the magnitudes calculated from the global networks. In the catalogue of Bertil et al. [2021], the comparison between the $M_w$ value given by G-CMT [Dziewonski et al., 1981, Ekström et al., 2012] and $M_{lv}$ (for $M_w$ between 4.9 and 5.9) and between the $m_b$ value given by the International Seismological Centre [2016] and $M_{lv}$ (between $m_b$ = 4.0 and 5.9) shows that $M_{lv}$ overestimates

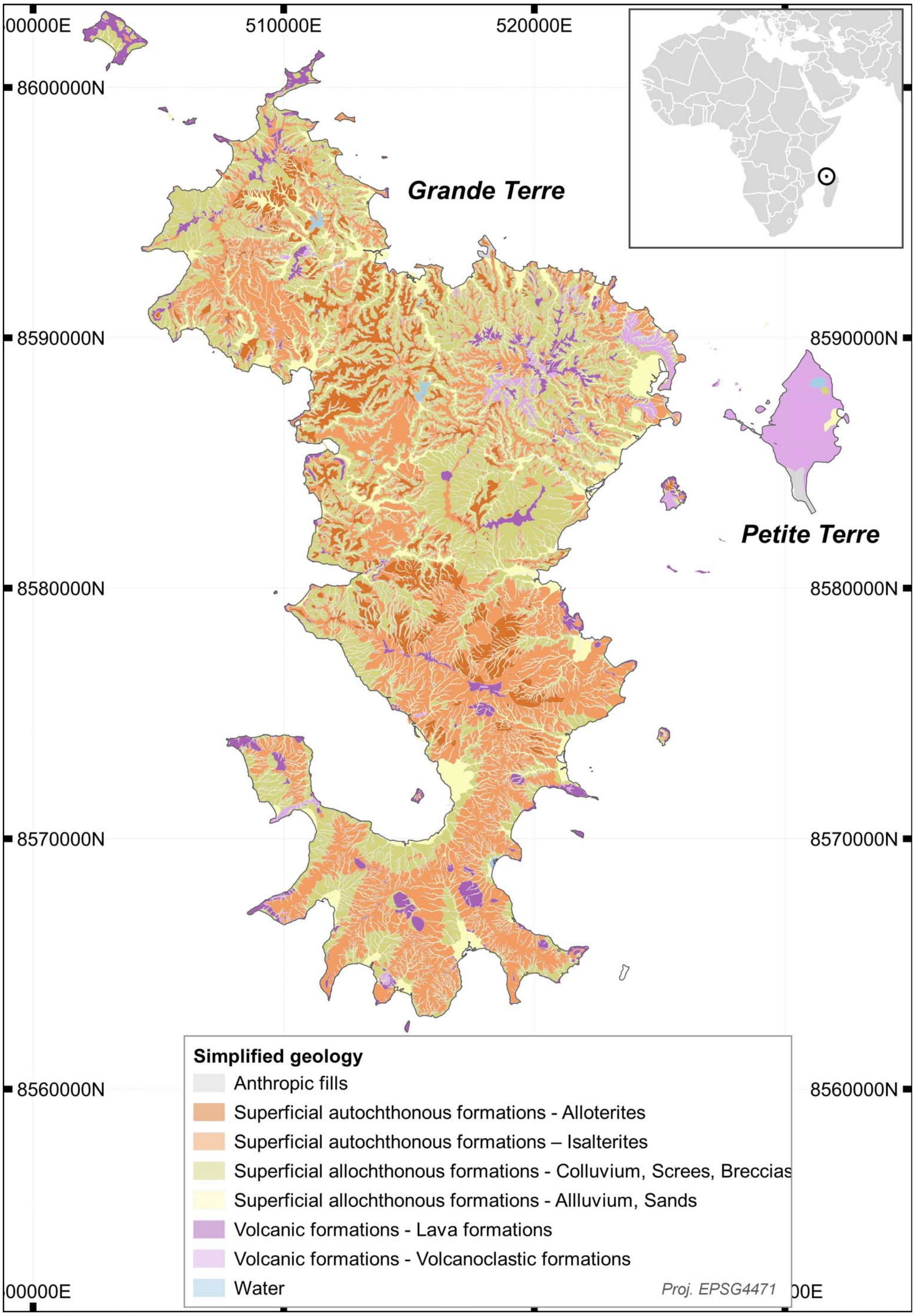


**Figure 1.** Simplified geology of Mayotte derived from Lacquement et al. [2013].

$M_w$ by 0.3 on average and $m_b$ by 0.4 on average. From this main dataset, regrouping more than 4900 events, we extracted a subset of 84 events in order to calculate H/V earthquake spectral ratios (i.e., the

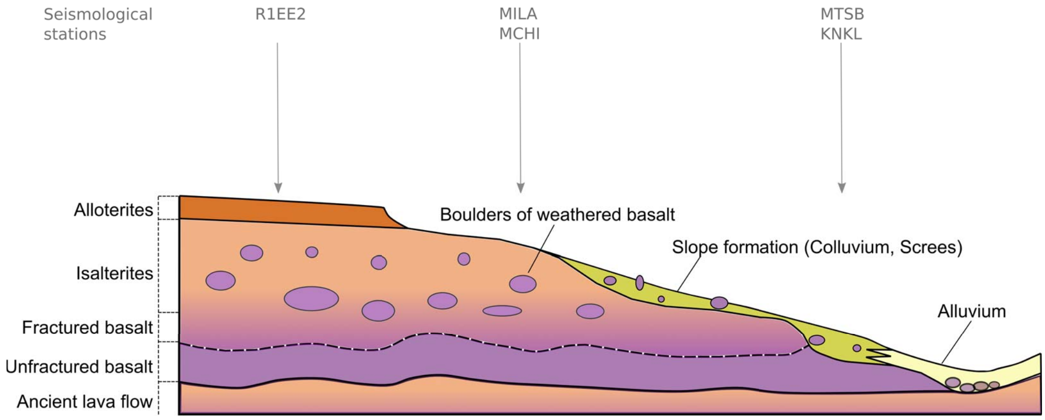


**Figure 2.** Conceptual diagram representing the typical weathering profile in Mayotte [modified from Nehlig et al., 2013]. Alloterites thicknesses are generally about few meters, whereas isalterites thicknesses can reach 20–70 m depending on the area.

ratio between the Fourier amplitude spectra of the horizontal and the vertical components of seismic motion, Lermo and Chávez-García [1993]; see Supplementary Table S1). This subset of data includes (i) the 53 highest magnitude earthquakes ($M_{lv} > 5$) recorded between 08/03/2018 and 27/06/2018 for stations YTMZ and MILA (the only stations operating during this period) and (ii) 31 additional earthquakes with magnitudes between 2.8 and 5.0 recorded between 25/05/2019 and 08/02/2020 for stations YTMZ, MCHI, MILA, MTSB, KNKL, PMZI and R1EE2.

### 3.2. *H/V noise spectral ratios and MASW profiles*

For 20 years, BRGM has been carrying out seismic hazard studies on sites in Mayotte Island. These studies generally include a lithological site effects analysis and have led us to acquire numerous geophysical measurements to characterize (i) the resonance frequency of the sites via the calculation of the H/V noise spectral ratio [i.e., the ratio between the Fourier spectra of the horizontal and the vertical components of the seismic noise recorded at the surface, Nakamura, 1989] and (ii) the S-wave velocity profile with depth inferred from the MASW active surface wave method (Multichannel Analysis of Surface Wave). The compilation of all these data allowed us to obtain 557 H/V measurements and 117 MASW profiles distributed over the whole island (Figure 3). An exhaustive list of the public reports from which the H/V and MASW data were collected is given in Supplementary Table S2.

## 4. Method of analysis

### 4.1. *Peak ground accelerations*

The PGA, defined as the highest amplitude of the absolute value of a signal in acceleration between the two horizontal components of the ground motion, is a common parameter to describe strong ground motion for seismic damage evaluation and mitigation purposes. PGAs were extracted directly from the raw signals through the scwfparam module of the Seiscomp monitoring tool [Cauzzi et al., 2013]. This module uses distance and magnitude criteria to select the signals to be processed and the size of the time window. The PGA is calculated on a filtered signal cut at 40 Hz for signals with a signal-to-noise ratio superior to a fixed threshold.

### 4.2. *H/V noise spectral ratios*

We calculated the H/V noise spectral ratio following the method proposed by Nakamura [1989] to characterize the site resonance frequency. The method assumes that the spectral ratio between the horizontal and vertical component of seismic noise is a good indicator for site effect evaluation in 1D subsurface conditions. In case of high impedance contrast between soft filling and stiff basement and under the 1D assumption, the H/V peak frequency can be associated to the fundamental resonance frequency of

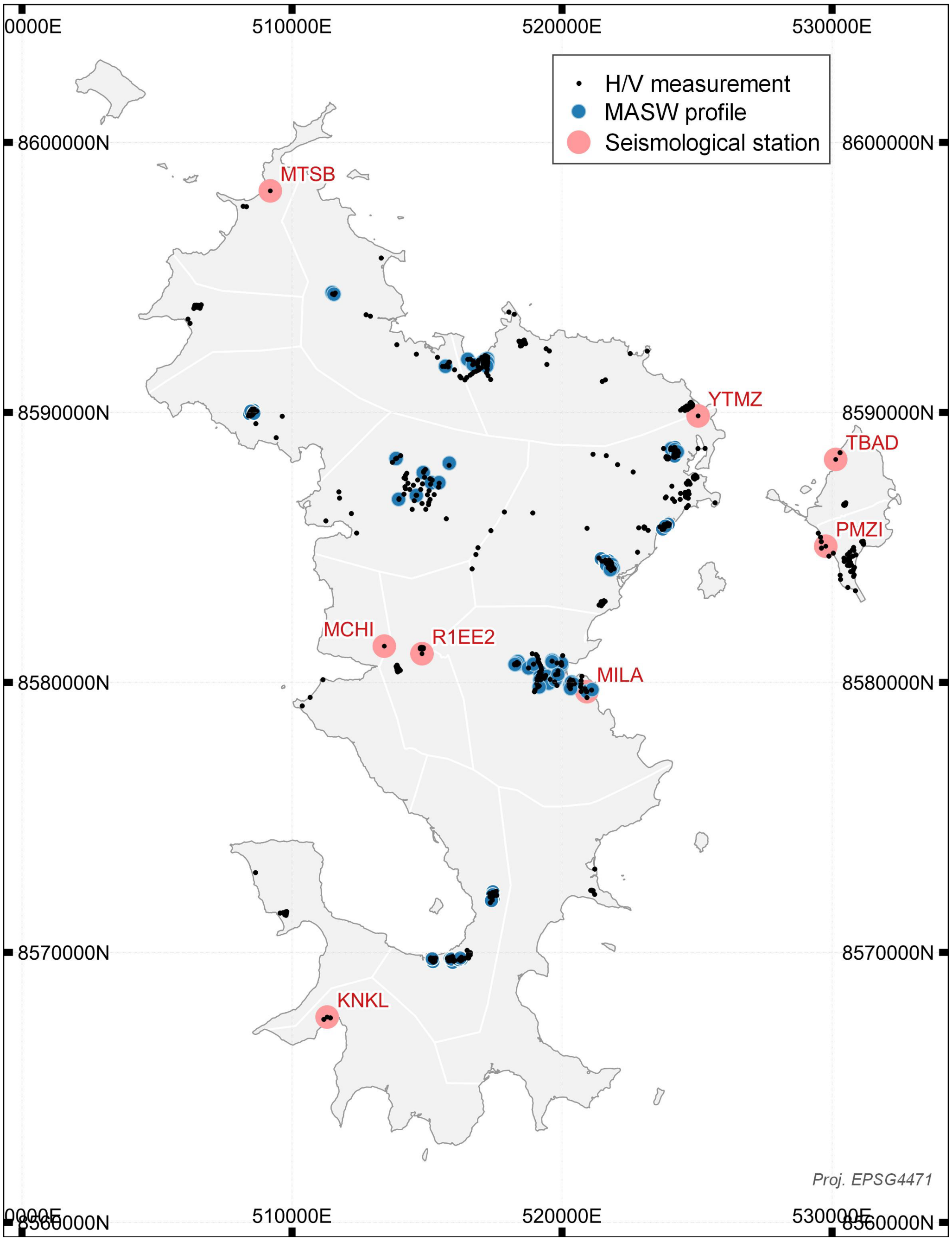


**Figure 3.** Location of the H/V noise spectral ratios data (black dot), the MASW profiles (blue dot), and the seismological stations (red dot) used in this paper.

the soft soil [e.g., Field and Jacob, 1995, Bonnefoy-Claudet et al., 2006] following the equation:

$$f_0 = V_S/4H, \qquad (1)$$

where $H$ corresponds to the thickness of the soft layer and $V_S$ is the average shear-wave velocity in the soft layer.

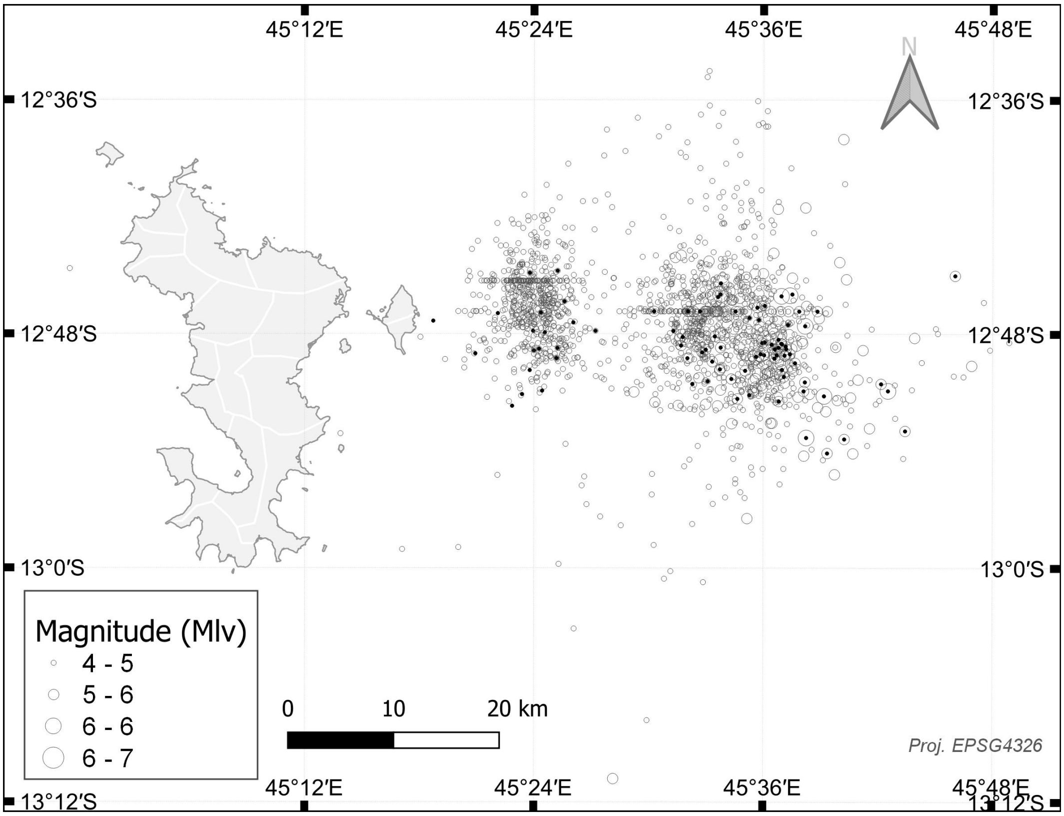


**Figure 4.** Location of the seismic events used in this paper, from Lemoine et al. [2020] and Bertil et al. [2021]. The full set of earthquakes considered are represented in grey while the black dots indicate the subset of the data of 84 earthquakes used to calculate the H/V earthquake spectral ratios.

**Table 1.** Description of seismic stations

| Stations | YTMZ | MILA | MTSB | MCHI | KNKL | TBAD | PMZI | R1EE2 |
|---|---|---|---|---|---|---|---|---|
| Network | RA | RA | 1T | ED | QM | None | 1T | AM |
| Site name | Mamoudzou | Iloni | M'Tsamboro | Chiconi | Kani-Keli | Badamiers | Pamandzi | Coconi |
| Latitude | −12.7577 | −12.8481 | −12.6804 | −12.8329 | −12.9571 | −12.770231 | −12.7993 | −12.8354 |
| Longitude | 45.2307 | 45.1928 | 45.0847 | 45.1237 | 45.1042 | 45.277658 | 45.2743 | 45.1365 |
| Sensor type | Acc | Acc | BB (HH) | BB (BH) | BB (HH) | BB (HH) | BB (HH) | RaspB |

Station types are: Acc = accelerometer; BB (HH) = broadband 0–100 Hz; BB (BH) = broadband 0–50 Hz; RaspB = Raspberry shakes. Networks references are: AM [Raspberry Shake Community, 2016]; ED = http://www.edusismo.org/; RA [RESIF, 1995]; 1T [Feuillet et al., 2022] and QM: CNRS-INSU Tellus SISMAYOTTE project.

For characterization of seismological stations, we calculated the H/V noise spectral ratios by extracting 1 h of signal from the continuous data stream of the station during the night (quiet period). The calculations were made following the guidelines from the SESAME project [SESAME, 2004] using the Geopsy software [Wathelet et al., 2020]. We used the following parameters for calculations of the H/V spectral ratios: data were filtered with a bandpass filter between 0.1 and 20 Hz, the selected windows are 50 s long, and

**Table 2.** Minimum, maximum and average S-wave window lengths in seconds used for the H/V earthquake spectral ratio calculations

| | MCHI | MILA | MTSB | KNKL | YTMZ |
|---|---|---|---|---|---|
| Minimum | 62.3209 | 44.3768 | 25.6447 | 13.5924 | 26.6476 |
| Maximum | 147.9226 | 136.0315 | 114.9714 | 57.8797 | 87.2135 |
| Average | 101.0179 | 92.7994 | 50.2577 | 35.2106 | 56.2333 |

we applied a 40% Kono–Homachi smoothing on the Fourier spectra.

### 4.3. *H/V earthquake spectral ratios*

For seismological stations YTMZ, MCHI, MILA, MTSB and KNKL (see Figure 3 for stations location), the H/V noise spectral ratios were compared with the H/V earthquake spectral ratios from the subset of data comprising the 84 earthquakes listed in Supplementary Table S1. To calculate them, we followed the procedure described by Lermo and Chávez-García [1993], keeping only the S-wave part of our records. This work has been done manually. Selected window lengths vary between 13 s and 136 s, with an average length greater than 50 s for four of the five studied stations (Table 2). Discrepancies between window lengths are due to the available signal for each event at each station. The shortest windows occur when events happened in bursts. The filtering and smoothing parameters are the same as those used for the H/V noise spectral ratio calculation to obtain comparable spectral ratios.

For stations PMZI and R1EE2, we only calculated the H/V noise spectral ratio, mainly because of data availability problems due to the late installation of these stations. However, we chose to include our results to provide preliminary indications of site effects at these stations.

### 4.4. *Azimuthal variation of H/V noise spectral ratios*

We computed the azimuthal variation of H/V curves. The direction of the maximum H/V ratio in the horizontal plane is used as an estimate of the predominant polarization [Di Giulio et al., 2015]. This tool allows to study the directivity of the seismic response as a function of the morphology and geological structure of a site [Theodoulidis et al., 2018], for example as a function of slope [Del Gaudio et al., 2008], rock fracturing [Di Naccio et al., 2017], or more broadly as a function of weathering and the presence of a soft layer on the surface [Havenith et al., 2002, Ma et al., 2019]. In this paper, we only show those analyses indicating a strong directivity effect, i.e., for which the amplitude of the H/V peaks varies with azimuth.

### 4.5. *Damping*

We finally used the damping tool available in Geopsy package [Wathelet et al., 2020] to check the natural origin of the resonance frequency [Dunand et al., 2002]. Following Dunand et al. [2002] and the SESAME guidelines [2004], we consider that the damping of a natural origin peak will present very low values (<1%). The damping test has been done in a systematic way but only the particular case of the temporary station TBAB has been presented in this article.

## 5. Site effects analysis at seismological station sites

### 5.1. *Peak ground acceleration comparisons*

In this paragraph, we compared the PGAs extracted from the earthquake signals listed in the Lemoine et al. [2020] catalog for the MILA, KNKL, MCHI, MTSB, MPZI and R1EE2 stations with those of the YTMZ station, which is considered as the reference station in Mayotte and which recorded the whole seismo-volcanic crisis initiated in 2018 (Figure 5). For each station and each PGA value, a PGA correction was applied to account for the difference in hypocentral distance between the considered station and the YTMZ station. For this, we applied the empirical relationship between PGA, local magnitude and hypocentral distance proposed by Bertil and Hoste-Colomer [2020] for Mayotte:

$$\log(\mathrm{PGA}) = 0.757 \times \mathrm{M_{lv}} - 5.79 \times 10^{-5} \times R_{\mathrm{hypo}} - \log R_{\mathrm{hypo}} - 4.433 \pm 0.29, \qquad (2)$$

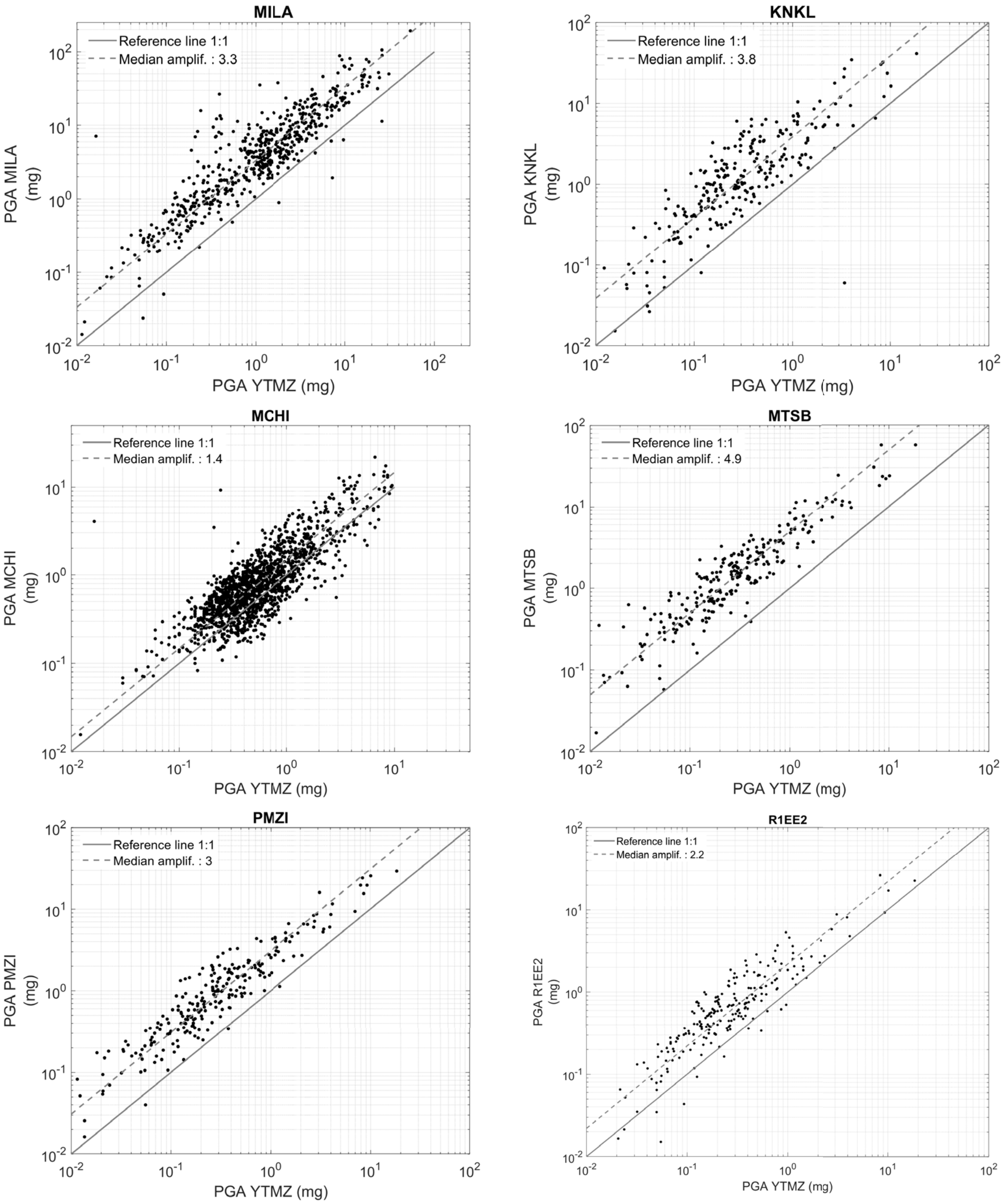


**Figure 5.** Comparison of PGAs between the reference station YTMZ and the considered station. Black dots give the value of PGA for each recorded event, the grey line represents the reference line for which $PGA_{YTMZ} = PGA_{station}$, the dotted grey line represents the median amplification coefficient line. The median amplification coefficient corresponds to the ratio between $PGA_{station}$ and $PGA_{YTMZ}$ and is indicated in the legend.

where $R_{\text{hypo}}$ represents the hypocentral distance in km, $M_{\text{lv}}$ is the local magnitude on the vertical component, PGA unit is g.

We have a good sampling of PGA values between 0.1 and 10 mg with little data above 10 mg except for the MILA station, which has recorded the strongest ground motions of the crisis. In general, we observe that the PGA values at the stations studied are mostly higher than those observed at the YTMZ station, with median amplification values ranging from 1.4 for MCHI to 4.9 for MTSB. Except for station MCHI, these coefficients are superior to the soil coefficients given by the French building code (between 1.35 for soil class B and 1.8 for soil class E). We also observe a strong variability of PGA ratios between the considered station and YTMZ, with amplifications that can go from a factor of 1 to factors greater than 8 on some earthquakes (e.g., on MILA).

### 5.2. *Earthquake and noise spectral ratios*

We then calculated the H/V noise spectral ratios for each station of the study and compared them to the H/V earthquake spectral ratio if available (Figures 6 and 7). For all the stations, H/V noise spectral ratios and H/V earthquake spectral ratios show similar shapes, particularly in terms of resonance frequency. The amplitude of the H/V earthquake spectra ratio is higher than that of the noise one as observed before [see for example Haghshenas et al., 2008, for a detailed comparisons between noise and earthquake H/V spectral ratios], especially at frequencies lower than the resonance frequency.

The YTMZ station, located on recent volcaniclastic formations with little alteration, is considered since the beginning of the seismo-volcanic crisis as the reference station. It is a key station for monitoring the crisis since it is the only one that recorded the entire crisis. The H/V noise spectral ratio shows a value close to 1 for most of the frequency range and a slight amplification around 2.5 Hz. This amplification is not visible on the H/V earthquake spectral ratio, which shows a slight amplification at low frequencies. Although these spectral ratios are not perfectly flat and equal to 1 over the entire frequency range considered (the ideal case of a rocky site with no site effect), the observed amplifications have much lower amplitudes than those observed at the other sites. We can therefore consider that this station does not present a significant site effect and is a good reference station for Mayotte.

The MILA station, located on a hill of about 50 m height made of isalterites, presents two close peaks at 1.6 and 2.2 Hz on the H/V ratios, both for the noise and earthquake spectral ratios. MASW measurements made at the site yield an S-wave velocity of approximately 290 m/s between 0 and 15 m depth as shown in Figure 8. The $V_{S,30}$ value could be estimated by extrapolating the $V_S(z)$ profile using Boore's [2004] formula and is about 350 m/s, which would correspond to a minimum thickness of soft formation at the surface of 40 m if (1) is considered, consistent with the geological knowledge of the site. For this station, the azimuthal analysis of the H/V noise spectral ratio (Figure 9) shows a variation in the amplitude of the H/V peaks but without the disappearance of any peak, with a maximum amplitude between N060 and N170, indicating a potential geometric effect. These observations suggest a complex combination of effects related to the nature of the involved rocks and the topography as observed by Spudich et al. [1996] on the Tarzana hill during the 1994 Northridge earthquake, or on the Rognes hill which suffered severe damages during the 1909 Provence earthquake [Glinsky et al., 2019], or in a fractured rock site subjected to significant damages during the L'Aquila earthquake in Italy [Di Naccio et al., 2017], or even in landslide areas as studied for example by Del Gaudio et al. [2014] in the Terano landslide site, Italy. In all those cases, both the geomechanical characteristics of the geological layers (fracturing, presence of a fault, presence of a low velocity layer in surface), combined with a geometric effect linked to the surrounding topography, produced important amplifications of ground motion associated with strong directivity patterns. The MTSB and KNKL stations, both located at the bottom of the slope on colluvium, show a single resonance centered around 5 Hz (Figure 6), corresponding to soft material of lesser thickness than on MILA, in coherence with the alteration model proposed in Figure 2 and the known geology. For these two stations, the study of the directivity of the H/V noise spectral ratio shows a strong variability of the peaks according to the azimuth (Figure 9). This is of particular interest for the MTSB station for which we observe a H/V resonance peak of lower amplitude than the other stations and spread between 4.5 and 6.5 Hz, and for which the directivity analysis of

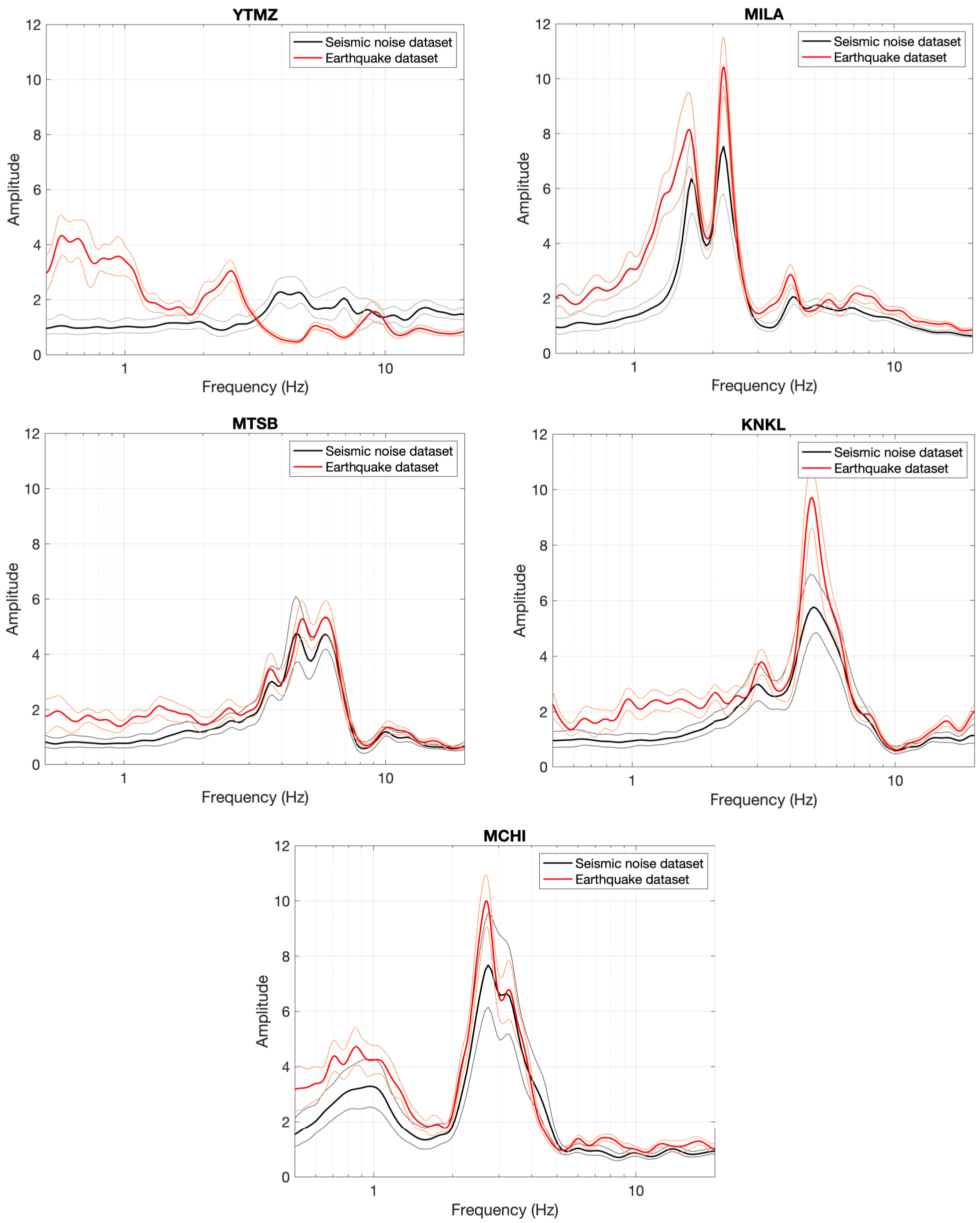


**Figure 6.** Comparison of H/V spectral ratios performed on earthquake and on seismic noise for stations YTMZ, MILA, MTSB, KNKL and MCHI.

the H/V ratio indicates a predominance of the lowest resonance frequency (around 4.5 Hz) at N080 and a predominance of the highest resonance frequency (around 6.5 Hz) at N180. This could correspond to a topography-related surface wave separation [Roten et al., 2006] with the predominance of Love waves at low frequency and N080 and Rayleigh waves at higher frequency and N180. For the KNKL station, the observed resonance seems simpler with a very strong peak at 5 Hz and the appearance of a secondary peak around 3 Hz for azimuths N040 to N080. Here again, geometric effects are possible.

The MCHI station shows a lower frequency peak around 2.9 Hz, with a very good correspondence

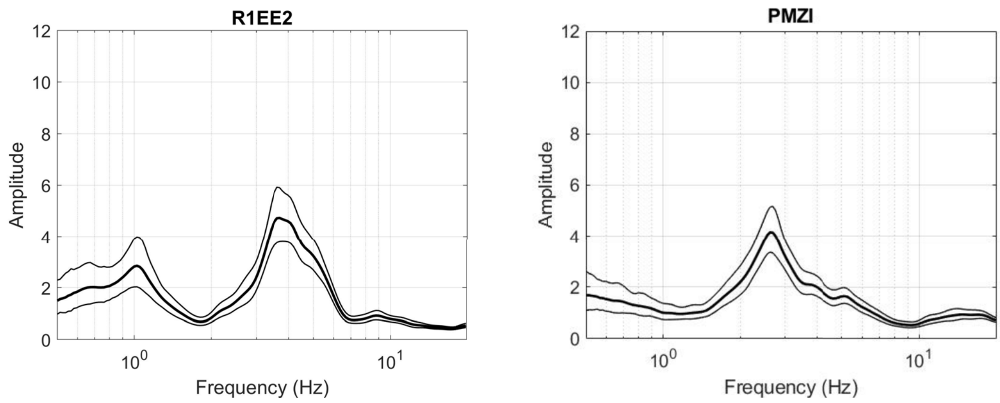


**Figure 7.** H/V noise spectral ratio for stations R1EE2 and PMZI.

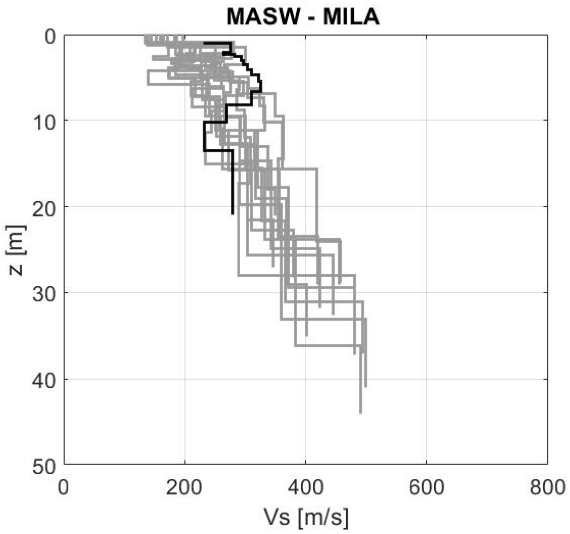


**Figure 8.** MASW profiles for the seismological station MILA. The black profile was acquired on the station site whereas the grey profiles were acquired at 200 m of the station site. Each grey $V_S(z)$ profile corresponds to a different shot of the same MASW profile.

between the H/V noise and earthquake spectral ratios both in terms of frequency and amplitude (Figure 6). This station is located on a high plateau area filled by a large thickness of isalterites (Combani paleosurface), consistent with the observed resonance frequency, which corresponds to a filling of several tens of meters thickness (of the order of 25 m thickness according to (1) if we consider a $V_S$ value of the order of 305 m/s as indicated in Table 4, in the next section). For this station, the H/V directivity analysis (not shown here) indicates a stable peak in amplitude, independent of the azimuth considered, in coherence with the flat topography of the site.

The Station R1EE2, located on alloterites at the top of the alteration profile, has two distinct resonance frequencies (Figure 7): one, not very pronounced, around 1 Hz and the second, of higher amplitude, at 3.7 Hz. This weak low frequency amplification is also found on the MCHI station located about 1.5 km east of R1EE2 and on the H/V noise spectral ratios acquired north of the area, in Combani, in a similar geological context. The response of this station would therefore correspond to the presence of two distinct interfaces: one quite deep, around 75 m deep, and the other, more superficial, around 20 m deep, assuming a tabular environment with a surface layer of $V_S = 300$ m/s. These hypotheses will need to be validated by a more detailed study of the 3D structure underlying the station. The PMZI station, located on the volcaniclastic formations of Petite Terre, presents a unique amplification at 2.6 Hz, probably corresponding to a rather thick soft layer (several tens of meters). The absence of MASW data in the vicinity of the area and the high spatial variability of the volcaniclastic formations do not allow us to go further in the interpretation of the data. The last station analyzed here is the Badamiers site, TBAD. It is in fact a site located to the north of Petite Terre, on the volcaniclastic formations, and potentially intended to host a permanent seismological station as part of the seismological monitoring of the Mayotte territory to

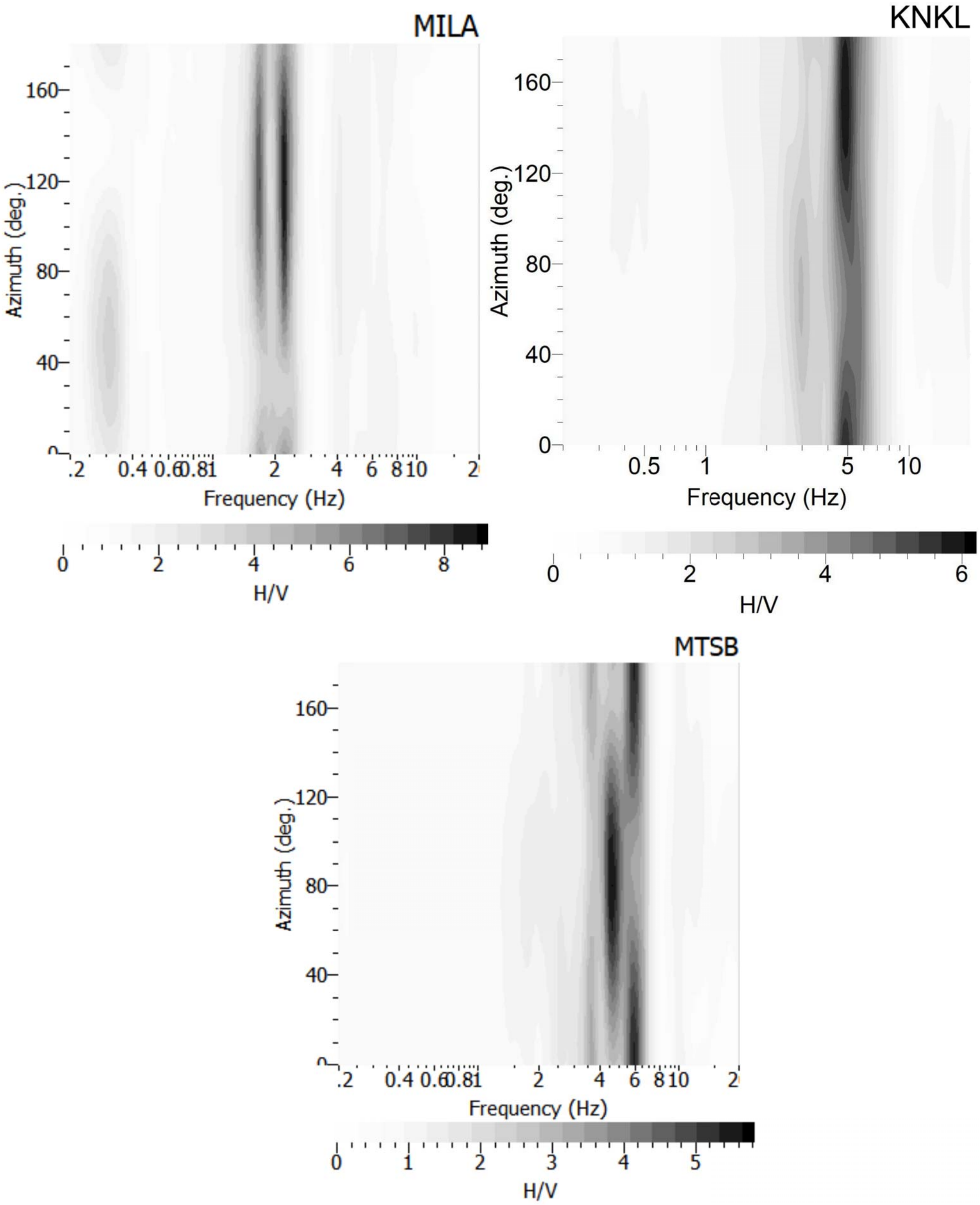


**Figure 9.** Azimuthal variation of H/V spectral ratio for stations MILA, MTSB and KNKL.

replace the PMZI temporary station currently used. Although this station was installed for a short time in 2020 and therefore does not have a sufficient earthquake record dataset for a complete analysis of site effects on its site, we have chosen to show the preliminary results obtained on this site to demonstrate the importance of analyzing site effects before any permanent installation. The H/V ratio of the TBAD station (Figure 10) shows a rather peculiar pattern with peaks at 1.5 Hz, 8.3 Hz, and 12.4 Hz. The analysis of the damping on each of these frequencies confirms the natural origin of the peak at 1.5 Hz with an attenuation value of 4% and shows us that the peak at 8 Hz is of anthropic origin with a damping lower than 1% [Dunand et al., 2002, Guillier et al., 2007]. We observe the same result at 12 Hz. Looking at the H/V

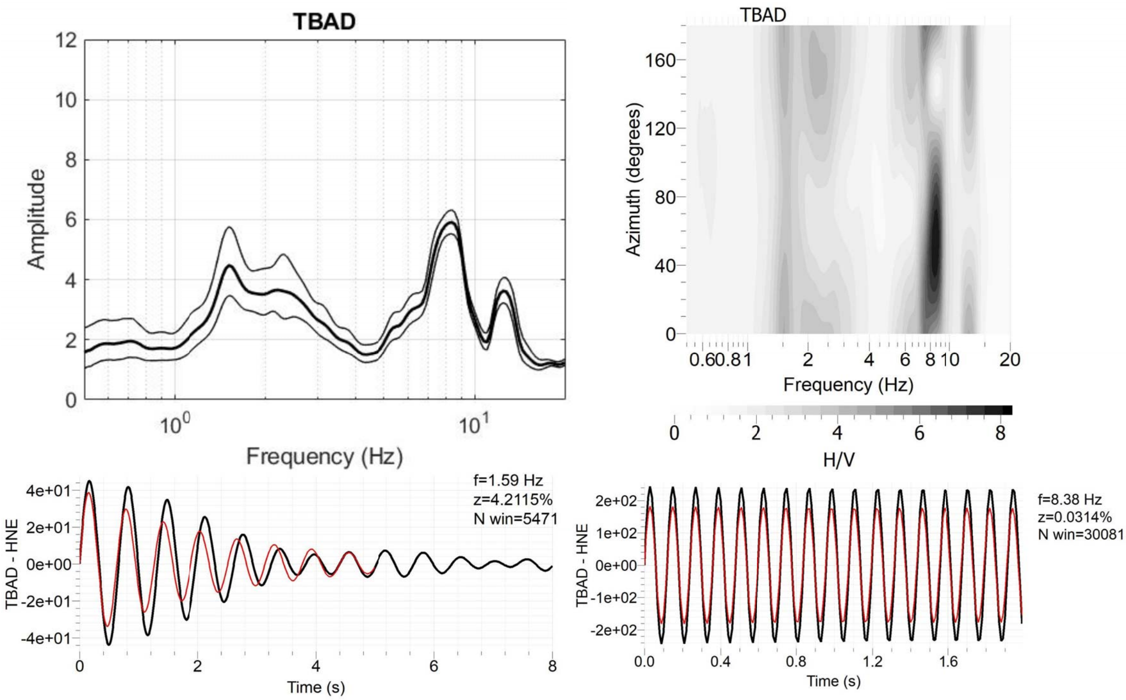


**Figure 10.** H/V noise spectral ratio (top left), azimuthal variation of H/V spectral ratio (top right) and damping at 1.5 Hz (bottom left) and 8.3 Hz (bottom right) at the station site TBAD.

ratio directivity, we can see a strong H/V peak directivity at 8 Hz, with a maximum amplitude between N020 and N080. This could correspond to the signature of the thermal power plant located about 500 m north of this site, in the N040 direction.

## 6. Preliminary geology-based site effects mapping at regional scale

The strong ground motion observations made during the seismo-volcanic crisis confirmed that the superficial geology of the island could lead to significant site effects, including on weathered volcanic formations [Bertil et al., 2019, 2021, Roullé et al., 2022]. Since the beginning of the 2000s, numerous local seismic hazard studies have shown that the Mayotte territory presents superficial geological formations likely to undergo lithological site effects [e.g., Audru et al., 2002, 2010]. This led us to produce, in the first months of the crisis, a new lithological site effects map at regional scale dedicated to the calculation of strong motion maps and damage scenarios for crisis management purposes [Taillefer et al., 2019, 2022]. This map has been upgraded since then including the analysis done in the framework of the revision of the local seismic hazard mapping of Mayotte, a study in progress on behalf of the local authorities. This paper describes the upgraded version of the preliminary map described in Taillefer et al. [2019, 2022].

For practical reasons of constrained time delays and costs, we decided to use only the available data (i.e., without carrying out additional measurement) and to base our site effects classification on the soil classes A–E derived from the European building code EuroCode 8 (EC8) [NF EN 1998-5, 2005] and described in Table 3. Our site effects map is based on the 1:30,000 geological map of Mayotte Island [Nehlig et al., 2013, Lacquement et al., 2013, see Figure 1]. To complete the geological data, we compiled the geophysical data of the local seismic hazard studies realized by BRGM since 2000 (Figure 3). The H/V measurements and MASW profiles have been analyzed respectively in terms of resonance frequency $f_0$, corresponding to the frequency of the maximum peak of the H/V spectral ratio, and $V_{S,30}$ value, a site effect proxy from EC8 soil classification. This is calculated

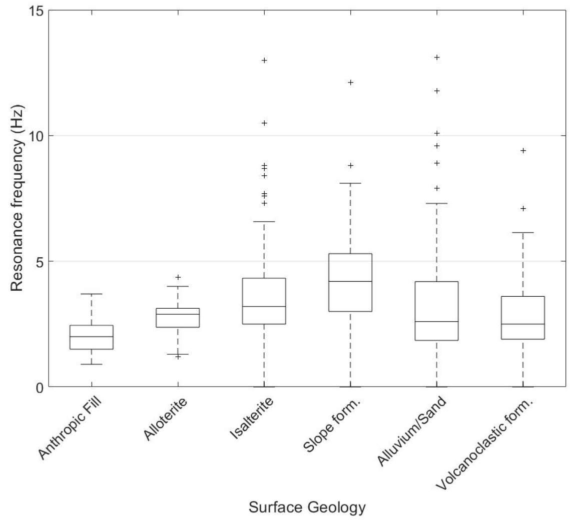


**Figure 11.** Distribution of the H/V peak values (dominant resonance frequency) regarding simplified surface geology given in Figure 1. For each box, the central line represents the median, the edges of the box represent the 25th and 75th percentiles, the whiskers (dotted lines) extend to 1.5 times the interquartile ranges, and the outliers (data with values beyond the ends of the whiskers) are plotted individually (crosses). Corresponding values are indicated in Table 4.

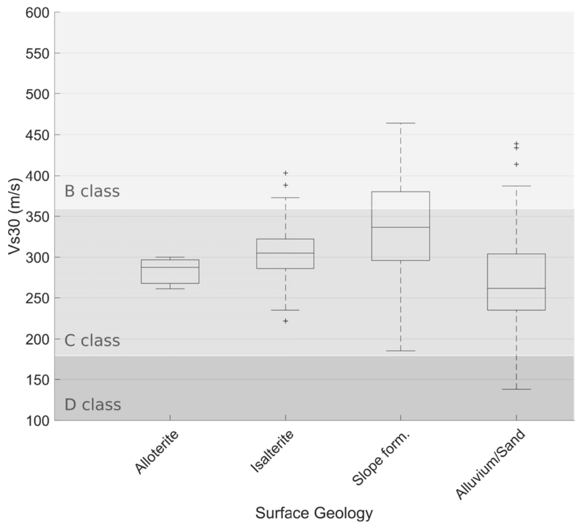


**Figure 12.** Distribution of $V_{S,30}$ values regarding simplified surface geology. The box description is the same as for Figure 11. Corresponding Q25, Q50 and Q75 values are indicated in Table 4.

following the equation [Borcherdt, 1994]:

$$V_{S,30} = \frac{30}{\sum\limits_{i=1,N} \frac{h_i}{V_i}}, \tag{3}$$

where $h_i$ and $V_i$ represent respectively the thickness and shear wave velocity of the $i$th layer and $N$ corresponds to the number of layers identified in the upper 30 m of the ground. The $f_0$ and $V_{S,30}$ values were directly extracted from existing reports with no extra calculation. For the geological formations for which geophysical data were available, we calculated the distribution of the $f_0$ and $V_{S,30}$ parameters (Figures 11 and 12).

The first observation that can be made is that all the considered geological formations present a significant site effect with resonance frequencies globally between 1 and 5 Hz (Figure 11 and Table 4). If we consider a single layer medium characterized by shear-wave velocities between 200 and 300 m/s according to the available MASW profiles [see for example Rey et al., 2012, Roullé et al., 2019], this would correspond to thicknesses of superficial formations up to several tens of meters. These values are consistent with the geological outcrop data acquired for the achievement of the 2013 geological map where weathering profile thicknesses from 20 m to 70 m were observed [see Nehlig et al., 2013]. These observations corroborate the importance of site effects on Mayotte observed in Figure 5 both in terms of amplification and spatial extent. The spatial variability of the observed resonance frequencies can occur over distances of the order of a few hundred meters as shown by the example of the Dembeni site (Figure 13). On this example, we observe a strong variability of $f_0$ values on the isalterite formations located on the south-western zone of the map with values ranging from 3.7 to 13 Hz in less than 200 m of distance. On the contrary, the $f_0$ values observed on the south-eastern hill with outcropping isalterites (values ranging from 2.2 to 3.5 over a distance of 200 m) are rather stable. A detailed knowledge of the geometry and geomechanical characteristics of those weathered formations would be necessary to better understand such variability patterns. The analysis of

**Table 3.** Description of the EC8 soil classes used in this paper

| Soil class | Description of soil profile | $V_{S,30}$ parameter (m/s) |
|---|---|---|
| A | Rock or other rock-like geological formation, including at most 5 m of weaker material at surface | >800 |
| B | Deposits of very dense gravel, or very stiff clay, at least several tens of m in thickness, characterized by a gradual increase of mechanical properties with depth | 360–800 |
| C | Deep deposits of dense or medium-dense sand, gravel or stiff clay with thickness from several tens to many hundreds of m | 180–360 |
| D | Deposits of loose-to-medium cohesionless soil (with or without some soft cohesive layers), or of predominantly soft-to-firm cohesive soil | <180 |
| E | A soil profile consisting of a surface alluvium layer with $V_{S,30}$ values of type C or D and thickness varying between about 5 m to 20 m, underlain by stiffer material with $V_{S,30}$ > 800 m/s | |

**Table 4.** Statistical values for $f_0$ and $V_{S,30}$ parameters distribution (data count, Q25, Q50 and Q75) and EC8 soil class according to the simplified geology

| Simplified geology | $f_0$ (count) | $f_0$ (Q25) | $f_0$ (Q50) | $f_0$ (Q75) | $V_{S,30}$ (count) | $V_{S,30}$ (Q25) | $V_{S,30}$ (Q50) | $V_{S,30}$ (Q75) | EC8 class |
|---|---|---|---|---|---|---|---|---|---|
| Anthropic fills | 23 | 1.5 | 2.0 | 2.4 | 1 | — | — | — | As surrounding formation |
| Alloterites | 25 | 2.4 | 2.9 | 3.1 | 3 | 267 | 287 | 297 | C |
| Isalterites | 111 | 2.5 | 3.2 | 4.3 | 23 | 285 | 305 | 322 | C |
| Slope formations (colluvium, screes, breccias) | 153 | 3 | 4.2 | 5.3 | 42 | 296 | 336 | 380 | B or C or E |
| Alluvium, beach sands | 176 | 1.8 | 2.6 | 4.2 | 46 | 235 | 261 | 304 | C |
| Volcaniclastic formations | 66 | 1.9 | 2.5 | 3.6 | 0 | — | — | — | A on Grande-Terre island, B or C on Petite Terre island |
| Lava formations | 3 | — | — | — | 1 | — | — | — | A |

the $V_{S,30}$ parameter distribution (Figure 12) shows a quite similar trend for the four analyzed geological formations with most of the $V_{S,30}$ distribution (i.e., the interval between Q25 and Q75) ranging from 230 to 380 m/s. The autochthonous altered volcanic formations (alloterites and isalterites), which form the upper weathering profile on top of the fractured lava formations (see Figure 2 for a conceptual presentation of a characteristic weathering profile in Mayotte Island), present values around 270–320 m/s. Both their lithological characteristics, geometry, and $V_{S,30}$ values lead us to consider them as a C soil class. The allochthonous formations classified as slope formations (mainly colluvium) present higher $V_{S,30}$ values between 300 and 380 m/s. These formations drape the sides of the reliefs: their thickness is prone to increase downstream and can reach 10 m at particular areas of accumulation. They present different facies from fine colluvium to boulder colluvium with strong lateral variations of facies and thickness. At the bottom of the reliefs, these formations tend to rest directly on bedrock with a clear contact between the two formations. Those formations are thus difficult to classify following EC8 criteria since they can

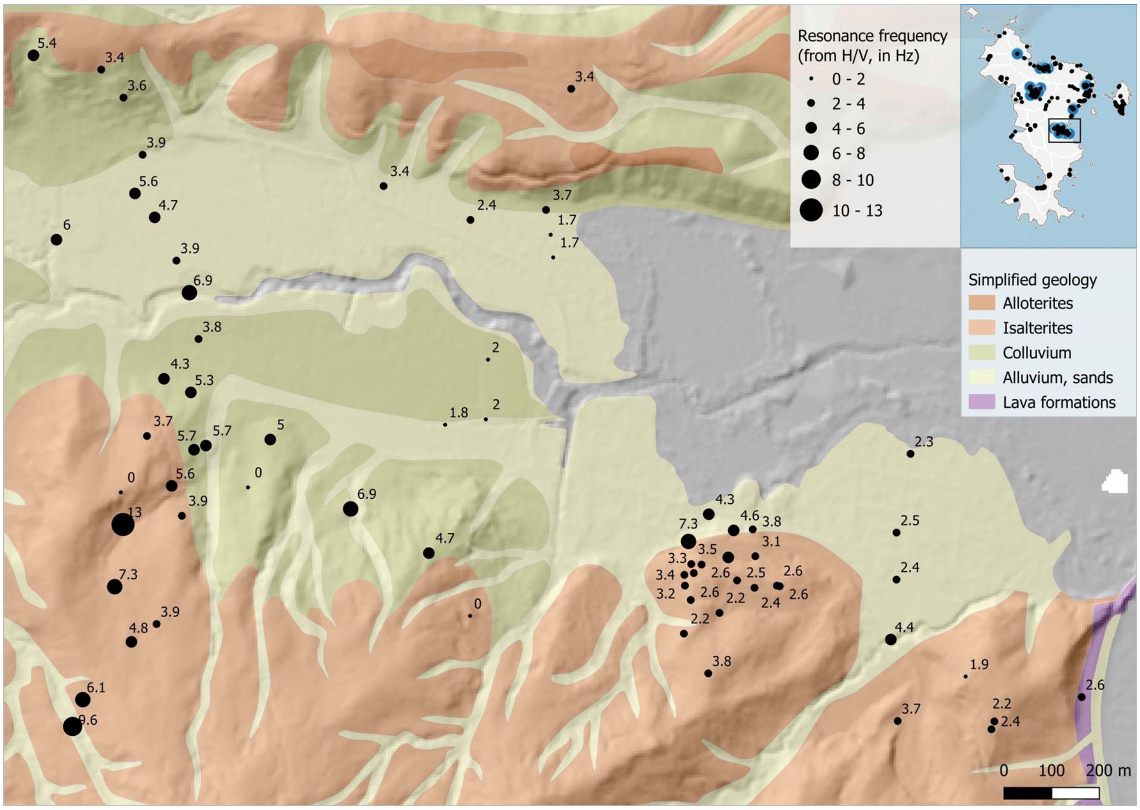


**Figure 13.** Dominant resonance frequencies $f_0$ observed at the Dembeni site on a simplified geological map and topographic background. The location of the site is indicated by a rectangle in the map at the top right. The colours correspond to the geological formations shown in Figure 1. The shading used as a base map corresponds to the IGN DEM at a 5 m resolution.

be considered either as B, C or even E soil class in certain configurations. At present, neither geological nor geomorphological information permits us to distinguish the different possible configurations: so we decided to keep a B, or C or E classification in our preliminary map but this point should be clarified in future works. The alluvium and beach sands, on the other hand, present $V_{S,30}$ values mainly between 235 and 304 m/s (Q25–Q75 interval) with a median value of 261 m/s, which corresponds clearly to a C soil class. The visible spread towards higher values of $V_{S,30}$ (above 300 m/s) corresponds to areas at the edge of the basins where the alluvial deposit is thinner. For geological formations without sufficient $V_{S,30}$ measurements to lead to a simple EC8 classification (anthropic fills and lava or volcaniclastic formations), we proceeded by expert analysis. Thus, as the anthropic fills present variable mechanical characteristics and relatively small thicknesses and a very small area (less than 1% of the entire area of the island), we preferred to assign them an EC8 soil class similar to the surrounding geological formation. As for the lava formations, corresponding to the least altered volcanic deposits of the island and essentially present on the coasts, the tops of crests and the bottoms of gullies, we considered them as bedrock, that is to say, as an A soil class.

Finally, the case of volcaniclastic formations is more complex. They consist mainly in the phreatomagmatic projections of Petite Terre and Mamoudzou, which are characterized by ash deposits that are often poorly consolidated but very heterogeneous both in terms of granulometry and lithology. The $f_0$ resonance frequency values issued from the H/V measurements available to date indicate the presence of lithological site effects on these formations (Figure 11 and Table 4), but the spatial distribution of the H/V measurements, mostly around the airport area on Petite Terre, does not allow us to confirm that observation on a more expanded area. In addition, the reference station YTMZ used to monitor the seismo-volcanic crisis and situated in Grande Terre, is also located on these formations and does not present a significant site effect (Figure 6). This station being preponderant in the calculation of the strong motion maps, we decided to assign the A soil class to all the volcaniclastic formations located on Grande Terre Island and a B or C soil class for the specific deposits of phreatomagmatic projections of Petite Terre. This decision ensures that strong motions are not overestimated during the real-time shake map calculation process, based on the acceleration values observed at terrestrial seismological stations and which takes into account station site conditions. Work in progress for the local authorities of Mayotte, with a forthcoming H/V and MASW survey on Petite Terre, should make it possible to modulate this classification in the future. The EC8 soil classes assigned to each surficial geological formation defined in Figure 1 allowed us to build a preliminary lithological site effects map (Figure 14) based on a simplified geology of the island and usable for real-time calculation of strong motion maps (shakemaps) and damage maps (SEISAID releases) in case of significant seismic event [Auclair et al., 2015, Guérin-Marthe et al., 2021]. The results show that only 6% of the Mayotte territory can be considered as EC8 site class A (rock site). Consequently, the urban areas are mainly located on soils prone to site effects, which could imply severe consequences in terms of seismic risk. This map was built from existing and partial data, especially in terms of spatial distribution. It therefore needs to be improved to better take into account the geometric complexity and spatial variability of the geological formations, for example for volcaniclastic formations. Work is currently underway as part of a project to revise the local seismic hazard on behalf of the local authorities. The idea is to integrate information on the weathering thickness and geometry of surface formations via additional in-situ geophysical measurements and analysis of airborne EM data. This study could lead us shortly to revise the preliminary lithological site effects map presented in this paper.

## 7. Discussion and conclusion

The seismo-volcanic crisis initiated in May 2018 in Mayotte led us to assess the strong motions on the territory for crisis management and seismic monitoring purposes via the calculation of strong motion and damage maps (for risk scenarios, shake maps, seismological bulletins, etc ...). In this context, an estimation of the site effects, potentially responsible for a local amplification of the seismic motion, is essential.

We first reanalyzed all the H/V and MASW data acquired in the last 20 years by comparing them to the recent geological map of the surface formations of Mayotte, which takes into account the levels of weathering of the various outcropping geological formations [Lacquement et al., 2013, Nehlig et al., 2013]. The results show that the alteration of volcanic rocks in Mayotte induces generalized site effects since all the geological formations for which we have data show a clear resonance (Figure 4, Table 4) and low values of $V_{S,30}$ (Figure 5, Table 4).

These results are based on weak ground motion (seismic noise) and need to be validated by comparison with strong ground motion observations. The seismo-volcanic crisis initiated in 2018 has allowed the constitution of an unparalleled set of strong ground motion data for the study of the response of highly weathered volcanic formations under seismic load. The first analyses show the importance of the amplifications observed on the analyzed seismological stations, with median amplification factors of 1.4 to 4.9 for the PGA compared to the reference station YTMZ (Table 5). In addition, the analysis of the H/V spectral ratios showed the possible combination of lithological effects linked to the presence of soft layers on the surface and topographical effects linked to the geometry of the site (relief in particular), as is the case, for example, at the MILA station, which recorded the strongest motions (180 mg) during the main earthquake of 15/05/2018 (Mw = 5.9). However, the work done here presents several limitations since it only covers PGA values between 0.1 and 10 mg with little data above 10 mg (except for the MILA station) and present a strong bias in azimuthal covering since most of the analyzed event epicenters are located full east. It would be interesting to pursue the data collection and analysis to complete those preliminary results. Further works on this ex-

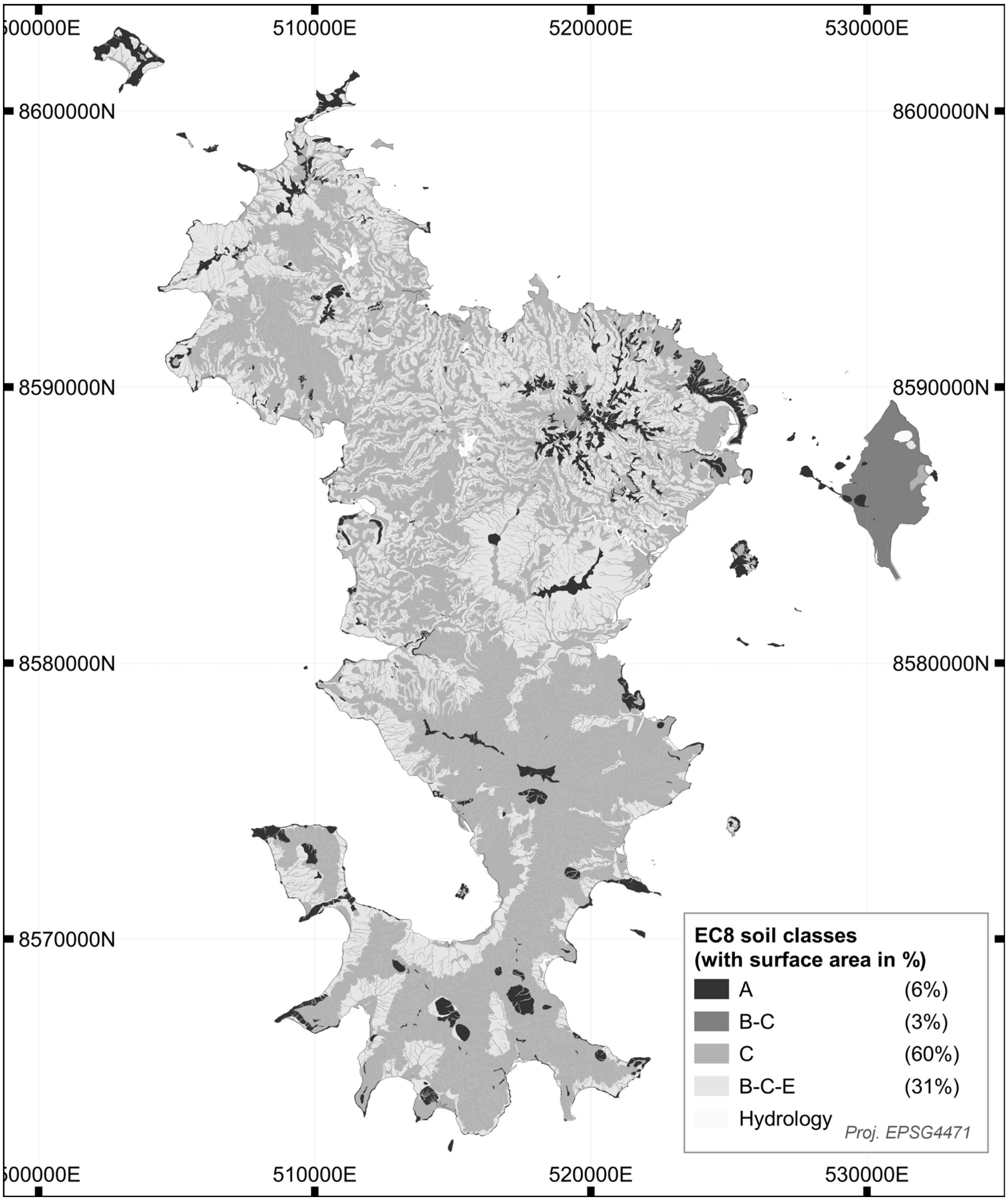


**Figure 14.** Geology-based lithological site effects map in terms of EC8 soil classes. The corresponding surface areas for each soil class are indicated in the legend.

ceptional dataset should advance our understanding of site effects in a highly weathered volcanic environment with direct operational application in Mayotte but also in the West Indies, the highest seismic hazard zone in France.

Beyond the analysis of this exceptional strong ground motion dataset, we also proposed a preliminary lithologic site effects map based on the 1:30,000 geological map produced in 2013 and EC8-derived soil classes estimated from the existing geophysical database (Figure 7). It shows that 94% of the Mayotte territory is likely to present a site effect linked to its superficial geology. This map is intended to be used in the framework of crisis management and seismic

**Table 5.** Summary of the information characterising the sites of the seismological stations studied in this paper

| Stations | YTMZ | MILA | MTSB | MCHI | KNKL | TBAD | PMZI | R1EE2 |
|---|---|---|---|---|---|---|---|---|
| Network | RA | RA | 1T | ED | QM | None | 1T | AM |
| Site name | Mamoudzou | Iloni | M'Tsamboro | Chiconi | Kani-Keli | Badamiers | Pamandzi | Coconi |
| Superficial geology | Volcaniclastic formation | Isalterites | Colluvium | Isalterites | Colluvium | Volcaniclastic formation | Volcaniclastic formation | Alloterites |
| Lithological effect | No | Yes | Yes | Yes | Yes | Yes | Yes | Yes |
| Suspected topographical site effect | | Yes | Yes | | Yes | | | |
| Resonance frequencies (Hz) | | 1.6 and *2.2* | 5 | 1 and *2.8* | 4.8 | 1.5 | 2.6 | 1 and *3.7* |
| Median PGA ratio between the station and YTMZ | 1 | 3.3 | 4.9 | 1.4 | 3.8 | Not calculated | 3.0 | 2.2 |
| $V_{S,30}$ (m/s) | | 350 | | | | | | |
| Estimated EC8 class | A | C | B–C–E | C | B–C–E | B–C | B–C | C |

For each station, we indicate: the station code, its corresponding network, the name of the site, the simplified surface geology (Figure 1) from the 1:30,000 geological map of Mayotte [Lacquement et al., 2013], the presence or absence of a lithological and topographical site effect on the station, the associated resonance frequency, the median PGA ratio between the site and the reference station YTMZ on the analyzed earthquakes, and the measured $V_{S,30}$ value, if available. In case of double H/V peaks, both frequencies are indicated and the dominant one (with the maximum amplitude) is underlined.

monitoring. Nevertheless, it presents several limitations:

- a poor spatial distribution of collected geophysical data, including a lack of data inland and in the south of the island, outside the main urban areas (Figure 2);
- a lack of knowledge of the 3D geometry of the interfaces of interest, which does not allow us, for example, to distinguish between soil classes B, C and E at the colluvium level (Figures 6 and 7);
- a lack of knowledge of the spatial variability of the geological formations concerned, which does not allow us, for example, to objectively characterize the volcaniclastic formations present especially on Petite Terre (Figure 7).

The mapping carried out will therefore evolve as knowledge of the Mayotte subsoil improves, particularly in terms of the thickness of surface layers and their geomechanical characteristics. Finally, the importance of the site effects observed on the strong recordings analyzed in this paper leads us to recommend a systematic characterisation of the site parameters of the seismological stations in place within the REVOSIMA framework, following the recommendations of the European SERA project [Cultrera et al., 2021, Di Giulio et al., 2021] on the key parameters to be estimated as a priority and the protocols to be used to obtain good quality information. The most relevant indicators identified by Cultrera et al. [2021] are: the fundamental resonance frequency, the shear-wave velocity profile, the time-averaged shear-wave velocity over the first 30 m, the depth of both seismological and engineering bedrock, surface geology and soil class. A systematic calculation of the Frequency-Scaled Curvature proxy developed by Maufroy et al. [2015] should also provide information on whether a site is prone to such effect or not. In our case, the synthesis of the site characteristics from our work (Table 5) shows that a dedicated geophysical measurement campaign would provide the main missing proxy, namely the velocity profile $V_S(z)$ and the resulting parameter $V_{S,30}$, and thus complete the site metadata of each station to obtain a standardised characterisation according to European quality criteria.

## Conflicts of interest

Authors have no conflict of interest to declare.

## Acknowledgments

We thank all the technicians, engineers and researchers who participated in the installation and operation of the Mayotte seismological stations. RESIF data centre provides data of RA and 1T networks stations (YTMZ, MILA, MTSB and PMZI). We thank IPGP for having shared the data of QM network station KNKL, EDUSISMO (www.edusismo.org) for having installed and maintained the station MCHI, and IRIS data centre and Raspberry Shake SA data centre for having provided R1EE2 data.

We also thank J.-M. Saurel for providing the TBAD data.

This work was funded by the Ministry of Environment (Ministère de la Transition Ecologique—MTE), the Department of the Environment, Planning and Housing (DEAL) of Mayotte, and the Ministry of Research (Ministère de l'Enseignement Supérieur et de la Recherche et de l'Innovation) through the BRGM own funds.

Detailed comments provided by Julie Régnier, Vincent Famin and one anonymous reviewer greatly improved the manuscript.

## Supplementary data

Supporting information for this article is available on the journal's website under https://doi.org/10.5802/crgeos.151 or from the author.

## References

Anbazhagan, P. and Sitharam, T. G. (2009). Spatial variability of the depth of weathered and engineering bedrock using multichannel analysis of surface wave method. *Pure Appl. Geophys.*, 166, 409–428.

Auclair, S., Monfort, D., Colas, B., Langer, T., and Perrier, P. (2015). Evaluation rapide des bilans matériels et humains: une aide essentielle à la gestion opérationnelle des crises sismiques. In *9ème Colloque National AFPS*.

Auclair, S., Vanoudheusden, E., Rey, J., Roullé, A., Audru, J.-C., and Eucher, G. (2006). Projet de piste longue de l'aéroport de Pamandzi (Mayotte) - Étude de l'aléa sismique et détermination des mouvements sismiques. Rapport BRGM/RP-55151-FR, 55 p.

Audru, J.-C., Bitri, A., Desprats, J.-F., Dominique, P., Eucher, G., Hachim, S., Jossot, O., Mathon, C., Nédellec, J.-L., Sabourault, P., Sedan, O., Stollsteiner, P., and Terrier-Sedan, M. (2010). Major natural hazards in a tropical volcanic island: a review for Mayotte Island, Comoros archipelago, Indian Ocean. *Eng. Geol.*, 114, 264–381.

Audru, J.-C., Bitri, A., Desprats, J.-F., Mathon, C., Maurillon, N., Sabourault, P., Terrier-Sedan, M., and Sedan, O. (2002). Projets risques naturels et érosion à Mayotte : résultats d'année 1. Rapport BRGM/RP-51738-FR, 49 p.

Audru, J. C., Guennoc, P., Thinon, I., and Abellard, O. (2006). BATHYMAY: underwater structure of Mayotte Island revealed by multibeam bathymetry. *C. R. Géosci.*, 338, 1240–1249.

Bertil, D. and Hoste-Colomer, R. (2020). Loi Magnitude-Intensité pour Mayotte. Rapport final. Rapport BRGM/RP-70297-FR, 54 p.

Bertil, D., Lemoine, A., and Roullé, A. (2019). Evaluation d'un niveau d'aléa sismique probabiliste à Mayotte et à la Réunion. Rapport final. Rapport BRGM/RP69481-FR, 93 p.

Bertil, D., Mercury, N., Doubre, C., Lemoine, A., and Van der Woerd, J. (2021). The unexpected Mayotte 2018-2020 seismic sequence: a reappraisal of the regional seismicity of the Comoros. *C. R. Géosci.*, 353, 211–235.

Bonnefoy-Claudet, S., Cotton, F., and Bard, P. Y. (2006). The nature of noise wavefield and its applications for site effects studies: a literature review. *Earth-Sci. Rev.*, 79(3–4), 205–227.

Boore, D. M. (2004). Estimating Vs30 (or NEHRP site classes) from shallow velocity models (depths <30 m). *Bull. Seismol. Soc. Am.*, 94(2), 591–597.

Borcherdt, R. D. (1994). Estimates of site-dependent response spectra for design (methodology and justification). *Earthq. Spectra*, 10(4), 617–653.

Cauzzi, C., Clinton, J., Becker, J., and Kästli, P. (2013). Scwfparam: a tool for rapid parameterisation of ground motions and input to ShakeMap in SeisComP3. In *SSA2013 Annual Meeting, 17–19 April, Salt Lake City—Abstract no. 13-347*.

Cesca, S., Letort, J., Razafindrakoto, H. N. T., Heimann, S., Rivalta, E., Isken, M. P., Passarelli, L., Petersen, G. M., Cotton, F., and Dahm, T. (2020). Drainage of a deep magma reservoir near Mayotte inferred from seismicity and deformation. *Nat. Geosci.*, 13, 87–93.

Cochery, R., Lauret, G., Rey, J., and Forestier, L. (2014). Caractérisation des aléas mouvements de terrain, inondation et sismiques sur le futur site d'implantation du futur lycée de la Kwalé. Rapport BRGM/RP-63836-FR, 78 p.

Cultrera, G., Cornou, C., Di Giulio, G., and Bard, P.-Y. (2021). Indicators for site characterization at seismic station: recommendation from a dedicated survey. *Bull. Earthq. Eng.*, 19, 4171–4195.

Davis, R. (1995). Effects of weathering on site response. *Earthq. Eng. Struct. Dyn.*, 24, 301–309.

Debeuf, D. (2004). *Étude de l'évolution volcano-structurale et magmatique de Mayotte, Archipel des Comores, Océan Indien: approches structurale, pétrographique, géochimique et géochronologique.* Doctoral dissertation, Université de la Réunion, https://tel.archives-ouvertes.fr/tel-00646477.

Del Gaudio, V., Coccia, S., Wasowski, J., Gallipoli, M. R., and Mucciarelli, M. (2008). Detection of directivity in seismic site response from microtremor spectral analysis. *Nat. Hazards Earth Syst. Sci.*, 8, 751–762.

Del Gaudio, V., Muscillo, S., and Wasowski, J. (2014). What we can learn about slope response to earthquakes from ambient noise analysis: an overview. *Eng. Geol.*, 182, 182–200.

Di Giulio, G., Amoroso, S., Di Naccio, D., Falcucci, E., Gori, S., Hailemikael, S., Vasallo, M., Ciampaglia, A., De Luca, G., Del Grosso, A., Di Marcantonio, P., D'Onofrio, K., Porreca, M., Trotta, D., Villani, F., and Milana, G. (2015). The seismic microzonation of San Gregorio through a multidisciplinary approach. Seismic amplification in a stiff site. *Eng. Geol. Soc. Territ.*, 5, 1137–1141.

Di Giulio, G., Cultrera, G., Cornou, C., Bard, P.-Y., and Al-TFaily, B. (2021). Quality assessment for site characterization at seismic stations. *Bull. Earthq. Eng.*, 19, 4643–4691.

Di Naccio, D., Vassallo, M., Di Giulio, G., Amoroso, S., Cantore, L., Hailemikael, S., Falcucci, E., Gori, S., and Milana, G. (2017). Seismic amplification in a fractured rock site. The case study of San Gregorio (L'Aquila, Italy). *Phys. Chem. Earth, Parts A/B/C*, 98, 90–106.

Dunand, F., Bard, P. Y., Chatelain, J. L., Guéguen, P., Vassail, T., and Farsi, M. N. (2002). Damping and frequency from Randomdec method applied to in situ measurements of ambient vibrations. Evidence for effective soil structure interaction. In *12th European Conference on Earthquake Engineering, London.* Paper (Vol. 869).

Dziewonski, A. M., Chou, T. A., and Woodhouse, J. H. (1981). Determination of earthquake source parameters from waveform data for studies of global and regional seismicity. *J. Geophys. Res.*, 86, 2825–2852.

Ekström, G., Nettles, M., and Dziewonski, A. M. (2012). The global CMT project 2004–2010: centroid-moment tensors for 13,017 earthquakes. *Phys. Earth Planet. Inter.*, 200–201, 1–9.

Feuillet, N., Jorry, S., Crawford, W., Deplus, C., Thinon, I., Jacques, E., Saurel, J. M., Lemoine, A., Paquet, F., Satriano, C., Aiken, C., Foix, O., Kowalski, P., Laurent, A., Rinnert, E., Cathalot, C., Donval, J. P., Guyader, V., Gaillot, A., Scalabrin, C., Moreira, M., Peltier, A., Beauducel, F., Grandin, R., Ballu, V., Daniel, R., Pelleau, P., Besancon, S., Geli, L., Bernard, P., Bachelery, P., Fouquet, Y., Bertil, D., Lemarchand, A., and Van der Woerd, J. (2021). Birth of a large volcano offshore Mayotte through lithosphere-scale rifting. *Nat. Geosci.*, 14, 787–795.

Feuillet, N., Van der Woerd, J., and RESIF (2022). Seismic sequence monitoring on land and at sea in Mayotte: SISMAYOTTE (RESIF-SISMOB) [Data set]. RESIF - Réseau Sismologique et géodésique Français.

Field, E. H. and Jacob, K. H. (1995). A comparison and test of various site-response estimation techniques, including that are not reference-site dependent. *Bull. Seismol. Soc. Am.*, 85, 1127–1143.

Glinsky, N., Bertrand, E., and Régnier, J. (2019). Numerical simulation of topographical and geological site effects. Applications to canonical topographies and Rognes hill, South East France. *Soil Dyn. Earthq. Eng.*, 116, 620–636.

Graizer, V. (2009). Low-velocity zone and topography as a source of site amplification effect on Tarzana hill, California. *Soil Dyn. Earthq. Eng.*, 29(2), 324–332.

Guérin-Marthe, S., Gehl, P., Fayjaloun, R., Caterina, N., and Auclair, S. (2021). Rapid earthquake response: the state-of-the art and recommendations with a focus on European systems. *Int. J. Disaster*

*Risk Reduct.*, 52, article no. 101958.

Guillier, B., Chatelain, J.-L., Bonnefoy-Claudet, S., and Haghshenas, E. (2007). Use of ambient noise: from spectral amplitude variability to H/V stability. *J. Earthq. Eng.*, 11(6), 925–942.

Haghshenas, E., Bard, P. Y., and Theodulidis, N. (2008). Empirical evaluation of microtremor H/V spectral ratio. *Bull. Earthq. Eng.*, 6(1), 75–108.

Havenith, H.-B., Jongmans, D., Faccioli, E., Abdrakhmatov, K., and Bard, P.-Y. (2002). Site effect analysis around the seismically induced Ananevo Rockslide. *Kyrgyzstan Bull. Seismol. Soc. Am.*, 92, 3190–3209.

International Seismological Centre (2016). On-line Bulletin, http://www.isc.ac.uk, Internatl. Seismol. Cent., Thatcham, United Kingdom.

Keifer, I., Dueker, K., and Chen, P. (2019). Ambient Rayleigh wave field imaging of the critical zone in a weathered granite terrane. *Earth Planet. Sci. Lett.*, 510, 198–208.

Kumar, V., Narayan, J. P., and Kumar, M. (2017). Numerical study of effect of ridge-weathering thickness effect on the ground motion amplification. *Earth Sci. India*, 10, 167–178.

Lacquement, F., Nehlig, P., and Bernard, J. (2013). *Carte géol. France (1/30,000), feuille Mayotte (1179)*. BRGM, Orléans.

Lemoine, A., Briole, P., Bertil, D., Roullé, A., Foumelis, M., Thinon, I., Raucoules, D., de Michele, M., Valty, P., and Hoste Colomer, R. (2020). The 2018–2019 seismo-volcanic crisis east of Mayotte, Comoros islands: seismicity and ground deformation markers of an exceptional submarine eruption. *Geophys. J. Int.*, 223, 22–44.

Lermo, J. and Chávez-García, F. J. (1993). Site effect evaluation using spectral ratios with only one station. *Bull. Seismol. Soc. Am.*, 83(5), 1574–1594.

Ma, N., Wang, G., Kamai, T., Doi, I., and Chigira, M. (2019). Amplification of seismic response of a large deep-seated landslide in Tokushima, Japan. *Eng. Geol.*, 249, 218–234.

Maufroy, E., Cruz-Atienza, V. M., Cotton, F., and Gaffet, S. (2015). Frequency-scaled curvature as a proxy for topographic site-effect amplification and ground-motion variability. *Bull. Seismol. Soc. Am.*, 105(1), 354–367.

Nakamura, Y. (1989). A method for dynamic characteristics estimation of subsurface using microtremor on the ground surface. *Railw. Tech. Res. Inst. Q. Rep.*, 30(1), 25–33.

Narayan, J. P. and Kumar, V. (2015). A numerical study of effects of ridge-weathering and ridge-shape-ratio on the ground motion characteristics. *J. Seismol.*, 19(1), 83–104.

Nehlig, P., Lacquement, F., Bernard, J., Caroff, M., Deparis, J., Jaouen, T., Pelleter, A.-A., Perrin, J., Prognon, C., and Vittecoq, B. (2013). *Notice explicative, Carte géol. France (1/30,000), feuille Mayotte (1179)*. BRGM, Orléans.

Nelson, S. and McBride, J. (2019). Application of HVSR to estimating thickness of laterite weathering profiles in basalt. *Earth Surf. Process. Landf.*, 44(7), 1365–1376.

NF EN 1998-5 (2005). *Eurocode 8 - Calcul des structures pour leur résistance aux séismes - Partie 5 : Fondations, ouvrages de soutènement et aspects géotechniques (P 06-035-1).* AFNOR.

Oppermann, A., Auclair, S., Bitri, A., Nédellec, J. L., Rey, J., Roullé, A., and Vanoudheusden, E. (2009). Evaluation de l'aléa sismique sur les sites de l'extension du collège de Labattoir, de la construction du collège de Bouéni, et du lycée de Chirongui (Mayotte). Rapport BRGM/RP-57715-FR, 126 p.

Raspberry Shake Community (2016). OSOP, S.A.; Gempa GmbH.

RESIF (1995). RESIF-RAP French Accelerometric Network. RESIF – Réseau Sismologique et géodésique Français.

Rey, J., Auclair, S., Vanoudheusden, E., Oppermann, A., François, B., and Bitri, A. (2010). Evaluation de l'aléa sismique sur le site de l'extension de la maison d'arrêt de Majicavo-Lamir (Mayotte). Rapport BRGM/RP-58025-FR, 73 p.

Rey, J., Bastone, V., Bitri, A., Cochery, R., François, B., Roullé, A., and Tardy, D. (2012). Evaluation de l'aléa sismique pour 8 sites prévus pour la construction d'établissements scolaires à Mayotte. Rapport BRGM/RP-61170-FR, 176 p.

Rey, J., Bastone, V., Bitri, A., François, B., Lauret, G., and Tardy, D. (2013a). Evaluation de l'aléa sismique pour 3 sites d'extensions d'établissements scolaires à Mayotte. Rapport BRGM/RP-62972-FR, 67 p.

Rey, J., Bastone, V., Bitri, A., François, B., Lauret, G., and Tardy, D. (2013b). Evaluation de l'aléa sismique pour le site du projet d'extension de la Préfecture de Mayotte. Rapport BRGM/RP-62965-FR, 38 p.

Rey, J. and Cochery, R. (2012). Evaluation de l'aléa sismique selon la nouvelle réglementation pour la construction d'un collège à Bambo Ouest à Mayotte. Rapport BRGM/RP-61593-FR, 32 p.

Rey, J., Roullé, A., De Martin, F., Audru, J.-C., and Eucher, G. (2006a). Étude de l'aléa sismique et détermination des mouvements sismiques. Lycée de Pamandzi (Mayotte). Rapport BRGM/RP-54471-FR, 31 p., 7 Illust., 6 tabl., 1 annexe.

Rey, J., Roullé, A., De Martin, F., Audru, J.-C., Miehe, J.-M., Bitri, A., and Nédellec, J.-L. (2006b). Étude de l'aléa sismique et détermination des mouvements sismiques. LEP de Kaouéni (Mayotte). Rapport BRGM/RP-54470-FR, 49 p.

Rey, J., Roullé, A., De Martin, F., Audru, J.-C., Miehe, J.-M., Nédellec, J.-L., Eucher, G., and Bitri, A. (2006c). Étude de l'aléa sismique et détermination des mouvements sismiques. Futur lycée de Dembéni (Mayotte). Rapport BRGM/RP-54467-FR, 45 p.

Rey, J., Roullé, A., Vanoudheusden, E., and Audru, J. C. (2006d). Étude de l'aléa sismique et détermination des mouvements sismiques sur le site de l'IFM de Dembéni (Mayotte). Rapport BRGM/RP-54960-FR, 31 p.

Rey, J., Vanoudheusden, E., and Lauret, G. (2013c). Evaluation de l'aléa sismique pour le site du projet d'extension du Centre Hospitalier de Mamoudzou (CHM). Rapport BRGM/RP-63175-FR, 34 p.

Roten, D., Fäh, D., Cornou, C., and Giardini, D. (2006). Two-dimensional resonances in Alpine valleys identified from ambient vibration wavefields. *Geophys. J. Int.*, 165, 889–905.

Roullé, A., Audru, J.-C., Bernardie, S., and Nédellec, J.-L. (2005a). Étude de l'aléa sismique et détermination des mouvements sismiques sur le site du lycée de Chirongui (Mayotte). Rapport BRGM/RP-53832-FR, 61 p.

Roullé, A., Belvaux, M., Abad, J., François, B., Colombain, A., and Noury, G. (2019). Evaluation de l'aléa sismique pour 10 sites de construction/extension d'établissements scolaires à Mayotte. Rapport BRGM/RP-68294-FR, 236 p.

Roullé, A., Bernardie, S., Bitri, A., Miehe, J. M., Audru, J. C., and Eucher, G. (2005b). Étude de l'aléa sismique et détermination des mouvements sismiques sur le site de l'hôpital de Mamoudzou (Mayotte). Rapport BRGM/RC-53975-FR, 45 p., 11 fig., 11 tabl., 2 annexes.

Roullé, A., Raingeard, A., Cochery, R., Baptiste, J., Vanoudheusden, E., Reninger, P. A., Bitri, A., Sadeski, L., Beaubois, F., and Dectot, G. (2022). Méthodologie de révision de l'aléa sismique local et de la liquéfaction : application aux zones pilotes de Dembeni, Longoni et Combani. Rapport final. BRGM/RP-71365-FR.

Sabourault, P., Sedan, O., Audru, J. C., Mathon, C., Nédellec, J. L., Bitri, A., Bour, M., and Lebrun, B. (2002). Microzonage sismique de Mamoudzou centre, Mayotte. Rapport BRGM/RP-51839-FF, 107 p.

Saurel, J.-M., Jacques, E., Aiken, C., Lemoine, A., Retailleau, L., Lavayssière, A., Foix, O., Dofal, A., Laurent, A., Mercury, N., Crawford, W., Lemarchand, A., Daniel, R., Pelleau, P., Bès de Berc, M., Dectot, G., Bertil, D., Roullé, A., Broucke, C., Colombain, A., Jund, H., Besançon, S., Guyavarch, P., Kowalski, P., Roudaut, M., Apprioual, R., Battaglia, J., Bodihar, S., Boissier, P., Bouin, M. P., Brunet, C., Canjamale, K., Catherine, P., Desfete, N., Doubre, C., Dretzen, R., Dumouche, T., Fernagu, P., Ferrazzini, V., Fontaine, F. R., Gaillot, A., Géli, L., Griot, C., Grunberg, M., Can Guzel, E., Hoste-Colomer, R., Lambotte, S., Lauret, F., Léger, F., Maros, E., Peltier, A., Vergne, J., Satriano, C., Tronel, F., Van der Woerd, J., Fouquet, Y., Jorry, S. J., Rinnert, E., Thinon, I., and Feuillet, N. (2022). Mayotte seismic crisis: building knowledge in near real-time by combining land and ocean-bottom seismometers, first results. *Geophys. J. Int.*, 228(2), 1281–1293.

SESAME (2004). Guidelines for the implementation of the H/V spectral ratio technique on ambient vibrations measurements, processing and interpretation. Available at http://sesame-fp5.obs.ujf-grenoble.fr/Papers/HV_User_Guidelines.pdf.

Sira, C., Schlupp, A., Bontemps, M., Regis, E., and Van der Woerd, J. (2018). Essaim sismique à l'est de Mayotte. Analyse pour la période du 10 mai au 15 juin 2018. Note préliminaire du BCSF-RENASS, BCSF-RENASS2018-R4, 62 p.

Spudich, P., Hellweg, M., and Lee, W. H. K. (1996). Directional topographic site response at Tarzana observed in aftershocks of the 1994 Northridge, California, earthquake: implications for mainshock motions. *Bull. Seismol. Soc. Am.*, 86(1B), S193–S208.

Stieltjes, L. (1988). *Geological map of Mayotte at 1/50,000.* BRGM, Orléans.

Taillefer, N., Bertil, D., Negulescu, C., Roullé, A., Iasio, C., Auclair, S., and Quique, R. (2022). Seismic damage scenarios for Mayotte: a tool for disaster management. *C. R. Géosci.*, 354(S2), 343–359.

Taillefer, N., Negulescu, C., Iasio, C., Bertil, D., and Roullé, A. (2019). Scénarios de dommages sismiques pour Mayotte. Rapport final. BRGM/RP-69518 –FR, 63 p.

Theodoulidis, N., Cultrera, G., Cornou, C., Bard, P. Y., Boxberger, T., DiGiulio, G., Imtiaz, A., Kementzetzidou, D., Makra, K., and the Argostoli NERA Team (2018). Basin effects on ground motion: the case of a high-resolution experiment in Cephalonia (Greece). *Bull. Earthq. Eng.*, 16(2), 529–560.

Vermeersch, F., Auclair, S., Vanoudheusden, E., Rey, J., Roullé, A., Bitri, A., and Cluzet, C. (2008). Étude de l'aléa sismique et détermination des mouvements sismiques. Futur lycée de Dembéni, site de Tsararano (Mayotte). Rapport BRGM/RP-56431-FR, 52 p.

Von Voigtlander, J., Clark, M. K., Zekkos, D., Greenwood, W. W., Anderson, S. P., Anderson, R. S., and Godt, J. W. (2018). Strong variation in weathering of layered rock maintains hillslope-scale strength under high precipitation. *Earth Surf. Process. Landforms*, 43(6), 1183–1194.

Wang, G., Du, C., Huang, D., Jin, F., Koo, R. C., and Kwan, J. S. (2018). Parametric models for ground motion amplification considering 3D topography and subsurface soils. *Soil Dyn. Earthq. Eng.*, 115, 41–54.

Wang, W., Chen, P., Keifer, I., Dueker, K., Lee, E. J., Mu, D., Jiao, J., Zhang, Y., and Carr, B. (2019). Weathering front under a granite ridge revealed through full-3D seismic ambient-noise tomography. *Earth Planet. Sci. Lett.*, 509, 66–77.

Wathelet, M., Chatelain, J. L., Cornou, C., Giulio, G. D., Guillier, B., Ohrnberger, M., and Savvaidis, A. (2020). Geopsy: a user-friendly open-source tool set for ambient vibration processing. *Seismol. Res. Lett.*, 91(3), 1878–1889.

Zinke, J., Reijmer, J. J. G., Thomassin, B. A., Dullo, W.-C., Grootes, P. M., and Erlenkeuser, H. (2013). Postglacial flooding history of Mayotte Lagoon (Comoro Archipelago, southwest Indian Ocean). *Mar. Geol.*, 194, 181–196.

*Comptes Rendus*
*Géoscience — Sciences de la Planète*
**2022**, Vol. 354, Special Issue S2, p. 343-359
https://doi.org/10.5802/crgeos.120

The Mayotte seismo-volcanic crisis of 2018-2021 in the Comoros archipelago (Mozambique channel) / *La crise sismo-volcanique de 2018-2021 de Mayotte dans l'archipel des Comores (Canal du Mozambique)*

# Seismic damage scenarios for Mayotte: a tool for disaster management

**Nicolas Taillefer**[*, a], **Didier Bertil** [a], **Caterina Negulescu** [a], **Agathe Roullé** [a], **Christian Iasio** [a], **Samuel Auclair** [a] and **Robin Quique** [a]

[a] BRGM, 3 avenue C Guillemin, 45060 Orléans Cedex 2, France
*E-mails:* n.taillefer@brgm.fr (N. Taillefer), d.bertil@brgm.fr (D. Bertil), C.Negulescu@brgm.fr (C. Negulescu), a.roulle@brgm.fr (A. Roullé), c.iasio@brgm.fr (C. Iasio), s.auclair@brgm.fr (S. Auclair), r.quique@brgm.fr (R. Quique)

**Abstract.** A new marine volcano is erupting offshore Mayotte since May 2018, generating numerous earthquakes. The population felt many of them and the stronger shaking of the ongoing sequence caused slight damage to buildings. Historical records also confirm that damaging earthquakes had occurred in the past in this region. Seismic damage scenarios are a key tool for supporting the decision-making process, the preparedness, and for designing appropriate emergency responses. This paper provides the outcomes of a work consisting in improving the seismic risk assessment as a part of disaster risk governance and exposes the scientific background of this workflow. It illustrates its use with two earthquakes. Related post-seismic surveys provide observations that are useful to check the validity of the reference dataset. The paper also discusses the main characteristics of the rapid loss assessment tool that has been developed to provide operational information for crisis management.

**Keywords.** Mayotte, Damage scenarios, Vulnerability, Site amplification, Earthquakes, Rapid loss assessment.

*Published online: 13 December 2022, Issue date: 17 January 2023*

## 1. Introduction

Mayotte is an island located in the Indian Ocean, East of Africa, in the Mozambique Channel. Since 2011, it got the administrative status of France's departments. The French seismic regulatory zonation (2010) classifies Mayotte's territory as a zone of moderate seismicity (Zone 3 out of 5). Nevertheless, most of the buildings date from before the enforcement of seismic regulation. The recent demographic evolution is rapid and it is strongly affecting the dynamics of construction in the island. It is leading to the spread of informal housing and low-quality buildings. For these reasons, the level of seismic performance of the global building stock diverts significantly from the regulation's standards.

The ongoing seismic sequence results from a submarine eruption [Cesca et al., 2020, Feuillet et al., 2021, Lemoine et al., 2020]. The population felt hundreds of earthquakes, mainly during the first month of the crisis. The largest earthquake reached magnitude $M_w = 5.9$ and is reported to have damaged some

* Corresponding author.

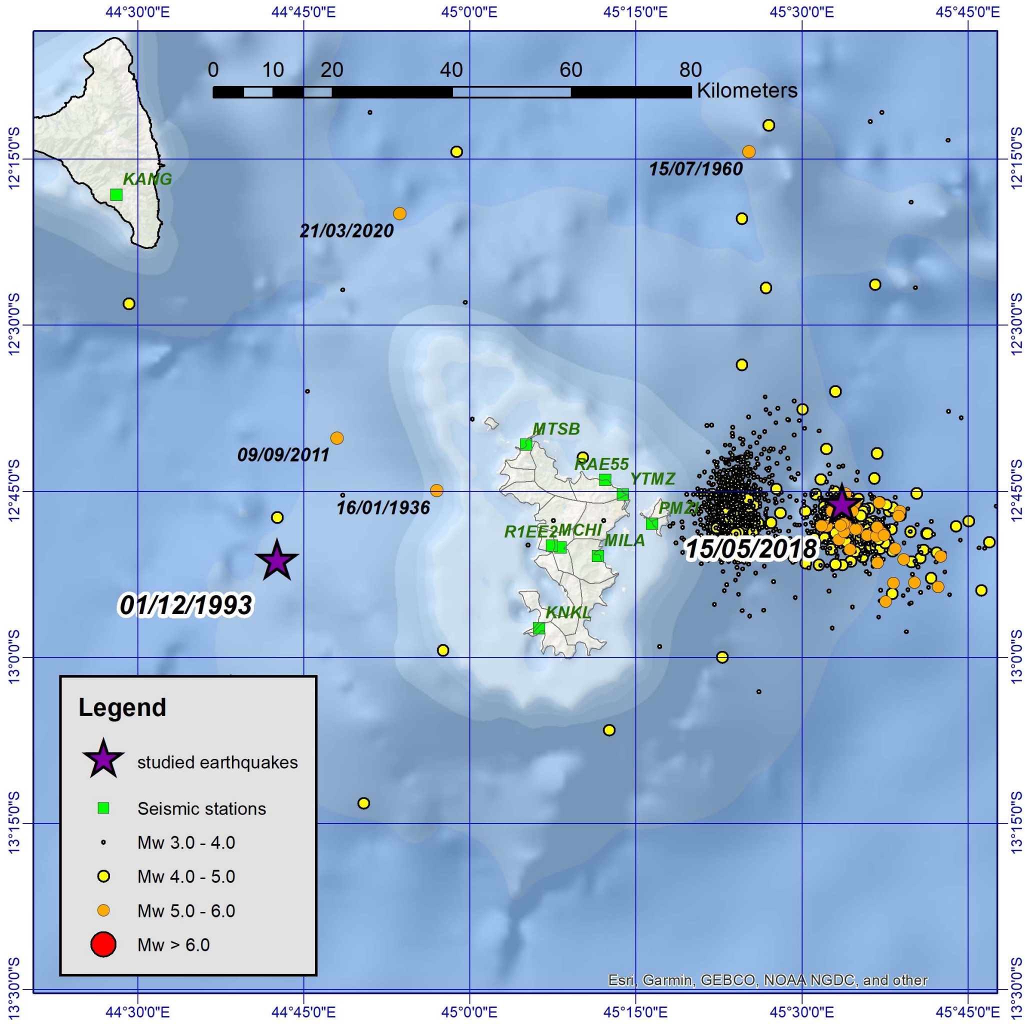


**Figure 1.** Localization of earthquakes of the ongoing sequence and historical events.

buildings. Historical records also report that some destructive events have hit the island in the 20th century, for example in 1993 ($M_b = 5.3$, according to ISC, $M_w = 5.5$ [Bertil et al., 2021]) and in 1936 (see the historical database SisFrance Indian Ocean for example) (Figure 1). Consequently, prevention policies have to consider preparation for a destructive earthquake on the island as an important component of action plans.

The article focuses on the seismic risk in Mayotte, whether it results from the ongoing volcanic event or from the regional tectonics. It documents and releases a reliable dataset and an operational workflow for rapid loss assessment, considering the latest developments about the geodynamical context. The dataset is ready to assess consequences of future events, as well as to build realistic seismic loss scenarios that can illustrate the potential impacts of earthquakes. Two past earthquakes are simulated, for which there is documentation about their impacts on buildings: 1993 December 1 earthquake and 2018 May 15 main shock. Simulation results describe the operational outcomes of the workflow and set a basis for comparison between simulation and field observations, that contributes to justify the reliability of the key parameters provided as a reference dataset

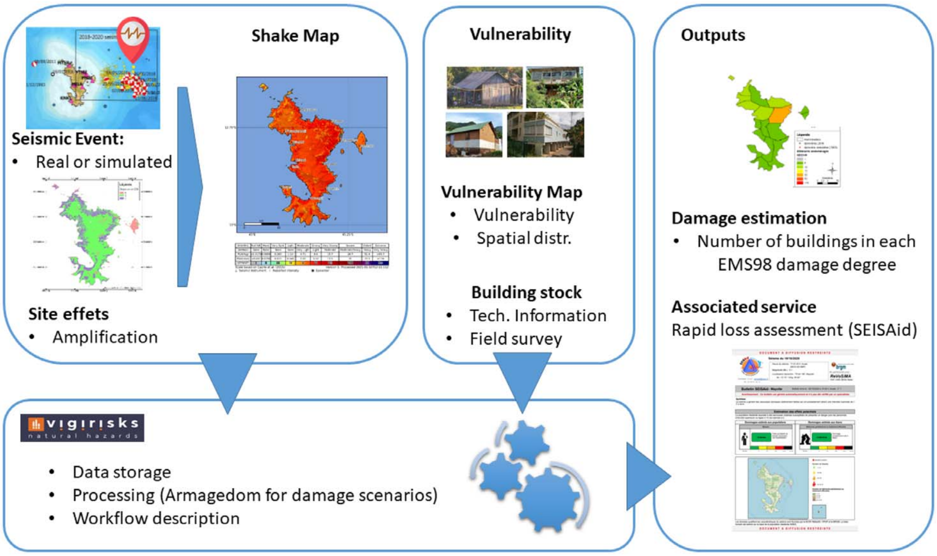


**Figure 2.** General procedure and workflow for the damage scenarios.

for seismic risk assessments.

## 2. Approach

Damage scenarios consist in simulating the damage on buildings resulting from a selected seismic configuration (also called event description or seismic scenario) and represent it in a way that can support decision-making process. Building realistic scenarios implies namely:

(i) to consider historical and recent seismicity,
(ii) to take into account most recent data regarding geology and site effects,
(iii) to derive vulnerability indexes taking into account the characteristics of local building stock,
(iv) to elaborate a new geospatial dataset describing the distribution of the building stock by different typologies,
(v) to release results in a format that directly matches the needs of the decision makers.

The procedure for damage assessment follows the framework developed in the European project RISK-UE [Lagomarsino et al., 2002, RISK-UE, 2003] for the European countries, which was also successfully applied on French overseas territories and other countries [Monfort et al., 2019, Negulescu et al., 2020, 2019, Sedan et al., 2013]. Slight adaptations of the vulnerability indexes that statistically describe the response of structures to shakings are required to fit the local building's characteristics. It is important to mention that the approach is based on vulnerability indexes and is relevant statistically, but should not be applied to assess the potential damage to a specific building. Consequently, the results should be displayed only at a scale that is compatible with the precision of the entry data, in particular those describing site effects and building characteristics.

The VIGIRISKS platform, developed at BRGM, the French Geological Survey [Tellez-Arenas et al., 2019, Negulescu et al., 2019], is a tool that comprises risk computation modules, a data management system, and a convenient user interface. The computing module of the platform runs the algorithm of the Armagedom software [Sedan et al., 2013], which crosses geospatial information (acceleration, site amplification, and building types) to assess and to map damage indexes (Figure 2).

The classification of damage in five grades introduced in the European EMS-98 macro seismic scale [Grunthal, 1998] is the reference for ranking the level of damage for common buildings (housing) in our simulations. This facilitates comparison of the results of the simulations with field data collected by GIM (Macro seismic field survey group) in 2018 and published in their field survey report [Sira et al., 2018].

Data and simulations are stored through the platform VIGIRISKS for future use. Thanks to web services, the calculation codes hosted by VIGIRISKS can also be used independently from the platform. For instance, the SEISAid tool developed by BRGM [see Section 4 and Guérin-Marthe et al., 2020] uses the code Armagedom, one component of the platform VIGIRISKS. It assesses automatically the probable losses associated to shake-maps [Gehl et al., 2017, Worden et al., 2018] for earthquakes that have just occurred on the French territory, and quickly produces reports for the local authorities. On the other hand, this damage assessment code makes it possible to pre-calculate credible scenarios for crisis management purposes and land use planning. They are also good communication supports to enhance risk-awareness: the French Ministry in charge of disaster prevention required such scenarios for the territory of Mayotte to BRGM.

Therefore, the workflow can handle either characteristics of pre-defined event or real events. In this article, the following configurations are considered (Table 1), as totemic events regarding seismic risk in Mayotte:

- The earthquake of 15 May 2018 (Magnitude $M_w$ = 5.9), which is the main shock of the ongoing swarm.
- The earthquake of 1 December 1993 (Magnitude $M_b$ = 5.3, $M_w$ = 5.5), which occurred in the west of the island, and which was until 2018 one of the main regional earthquake to be considered for Seismic Hazard Assessment in Mayotte.

Both earthquakes produced slight structural damage to buildings, as detailed in post-event field survey reports [Europact, 1995, Potin, 1993, Sira et al., 2018].

## 3. Data collection

The reference dataset takes into account the results of the latest studies concerning geology and ground classification in Mayotte as well as the outcome of a dedicated field survey for building classification and distribution. Field investigations have completed existing data about the structural characteristics of the local building stock.

The key data for establishing the scenarios are:

- The shake-map corresponding to the scenario earthquake, which gives the spatial distribution of intensity measurements (IM) expressed in terms of peak ground acceleration (PGA) or macro seismic intensity (MI). The calculation of this shake-map requires in particular the characteristics of the earthquake scenario (magnitude, location, and depth), regional models of attenuation (Ground Motion Prediction Equations—GMPEs) and conversion between PGA and MI (Ground Motion to Intensity Conversion Equations—GMICEs), and a local model to take into account site effects, taking the form of an amplification factors map.
- Spatial distribution of buildings considering their level of vulnerability.

### 3.1. *Site effects*

Locally, site conditions influence the amplitude of the ground motion and result in very significant amplifications, causing additional damage to buildings if compared to those on rocky sites. Lithology, geometry of the outcropping geological formations or topography are main factors. This study only considers lithology. Since 2000, BRGM has done more than 30 seismic hazard assessments all over the island, for projects of educational estates for example. Consequently, it acquired both geotechnical and geophysical (H/V noise spectral ratio and MASW active surface wave method) data. Those data, combined with the latest release of the geological map at a scale of 1:30,000 [Nehlig et al., 2013, BRGM, 2013] are the basis of the work, and is detailed in Roullé et al. [2022]. The map predicting lithological site effects according to the Eurocode 8 standard soil classes (class A to E) [NF EN 1998-1, 2005] and their spatial extension uses the superficial weathering formations. Class A (rock) represents about 10% of the surface of the island and the remaining 90% lay on soil with amplification. Considering geological data and geophysical measures available in past studies, it appeared that class C reasonably represents the behaviour of these soils. Then, the corresponding site effects can be computed using soil related parameters in the GMPE used in the software ShakeMap 4.0 [Worden et al., 2020]. In the selected GMPE, the soil velocity (parameter Vs30 is the proxy for the type of

**Table 1.** Seismological characteristics of 1993 and 2018 earthquakes

| | Earthquake of 1 December 1993 | Earthquake of 15 May 2018 |
|---|---|---|
| Magnitude | $M_w$ = 5.5 [Bertil et al., 2021]<br>$M_b$ = 5.3 (ISC) | $M_w$ = 5.9 (GCMT)<br>$M_b$ = 5.6 (ISC) |
| Coordinate of epicentre (Lat/Lon °) | −12.85; 44.71 | −12.80; 45.54 |
| Depth | 13 km | 40 km |
| Source hypocenter | ISC | Regional location from Bertil et al. [2021] |
| Distance to the coast | 40 km | 27 km |
| Distance to Mamoudzou | 59 km | 35 km |

soil: Vs30 = 800 m/s for soil A, Vs30 = 270 m/s for soil C). The map in Figure 3 shows Vs30 values with a step of 100 m.

### 3.2. *Ground motion*

GMPEs are components of the analysis since they support the calculation of ground motion at every point of the model. Many GMPEs exist in the literature, and new ones are released regularly [Douglas and Edwards, 2016]. Nevertheless, these equations are generally valid for a limited regional domain, a limited magnitude range, or are relevant only at large scale. Bertil et al. [2019] made a review of existing laws and proposed seven GMPEs that are compatible with seismological data about the regional seismicity of Mayotte (both historical and instrumental) in a perspective of Probabilistic Seismic Hazard Assessments, or for the establishment of shake-maps [Bertil and Hoste-Colomer, 2020]. On the other hand, three accelerometric stations were operating when the main shock occurred in Mayotte in 2018 (YTMZ, MILA, PMZY on the map Figure 1). Consequently, measured accelerations are available for this earthquake. The PGA obtained from stations helped to select best fitting models. Considering all the records available, including events that occurred before the ongoing sequence, Bertil and Hoste-Colomer [2020] concludes that the equation proposed by Atkinson and Boore [2006] fits best with data, on the range of magnitude $M_w$ = 3.0 to $M_w$ = 5.0. It slightly underestimates PGA for earthquakes of magnitude 6 or stronger, but still gives better prediction than the other equations. USGS' ShakeMap 4.0 tool [Worden et al., 2020] is used to establish the shake-maps in acceleration for the two events (Figures 4a and 5a), selecting the GMPE from Atkinson and Boore [2006], and introducing the Vs30 values of Figure 3 for local amplifications. The PGA values for the 2018 earthquake coming from measures at the two local seismological stations that are on a rocky-type soil, YTMZ and PMZY, provide control points to correct the shake map (Figure 5b). The software calculates a general correction factor for results coming from the model (GMPE). A slight underestimation of PGA by the model can be noticed, consistent with Bertil's conclusion stating that the selected GMPE underestimates accelerations for earthquakes of magnitudes around 6. The PGA calculated by the model differs only slightly from measured values (less than 5%, a PGA of 5.3% g is measured on the YTMZ station, located on a rock-like soil, whereas the estimated intensity is V).

A complementary set of shake-maps expressed in MI is produced using the GMICE from Caprio et al. [2015]. The historical database SISFRANCE (www.SisFrance.net), hosted in BRGM and extended to French overseas territories, contains information about the 1993 earthquake. It provides IM for each municipality, determined from post-seismic field survey reports and other documentation. The shake-maps in intensity (Figure 4b) were updated by these observations. To do it, the software calculates back the PGA corresponding to the observed IM values from the model (GMICE, GMPE and amplification factors for site effects), and then calculates a correction factor. There is a difference of about 1 point between intensities calculated by the model and IM; the correction on PGA values reaches 30%.

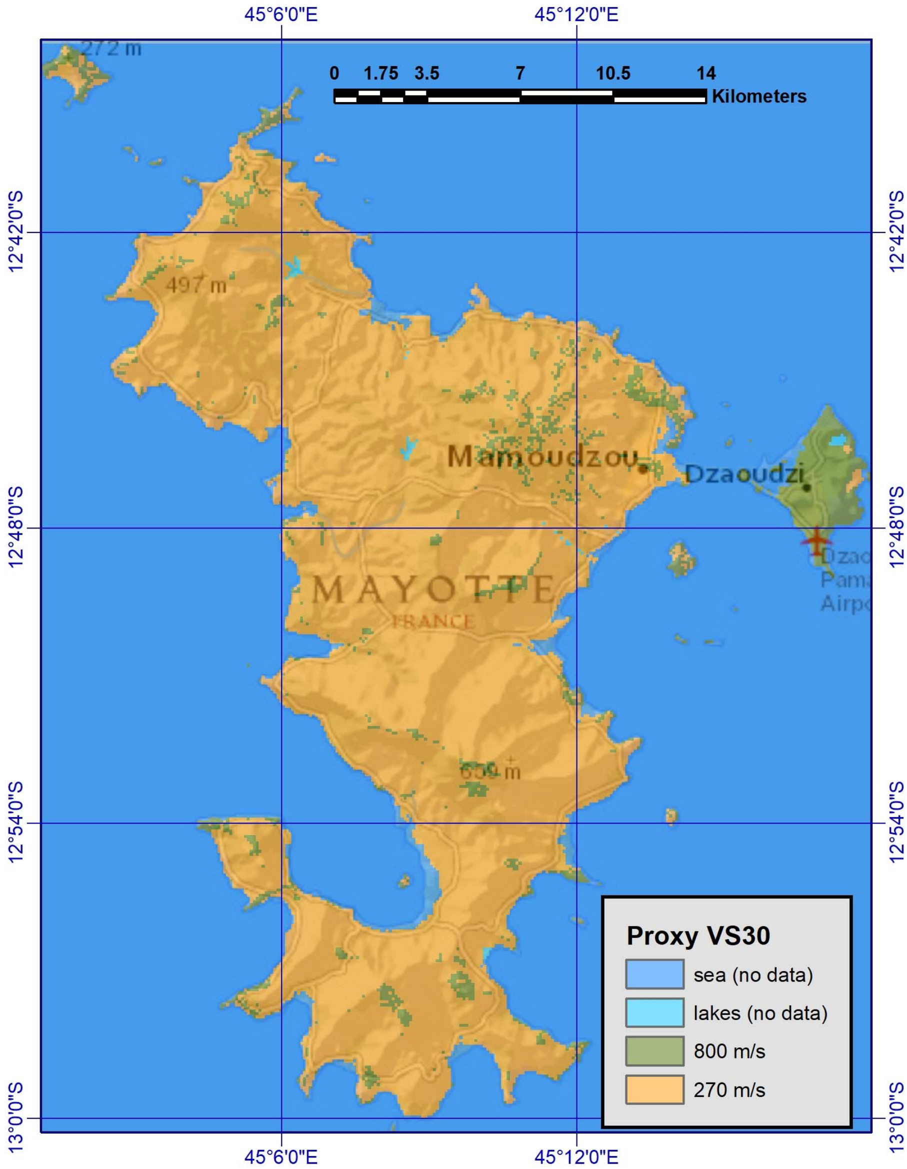


**Figure 3.** Map of the proxy for the site effects, based on the geological map of Mayotte from Nehlig et al. [2013]. Two soil categories, defined by their mean values of the soil velocity are considered in the calculations.

Comparison between shake-maps shows that:

- The geological site effect zoning used in this study results in strong local amplifications of MI (and in particular of IM), especially for soil of type C, that is rather common in urbanized areas,
- PGA values predicted by the GMPE from Atkinson and Boore [2006] fit well the acceleration recorded during the earthquake of May 15, 2018 (i.e. good agreement between Figures 5a and b),
- Concerning the earthquake of December 1, 1993, whereas the shake-map calculated directly from the GMPE (i.e. without any cal-

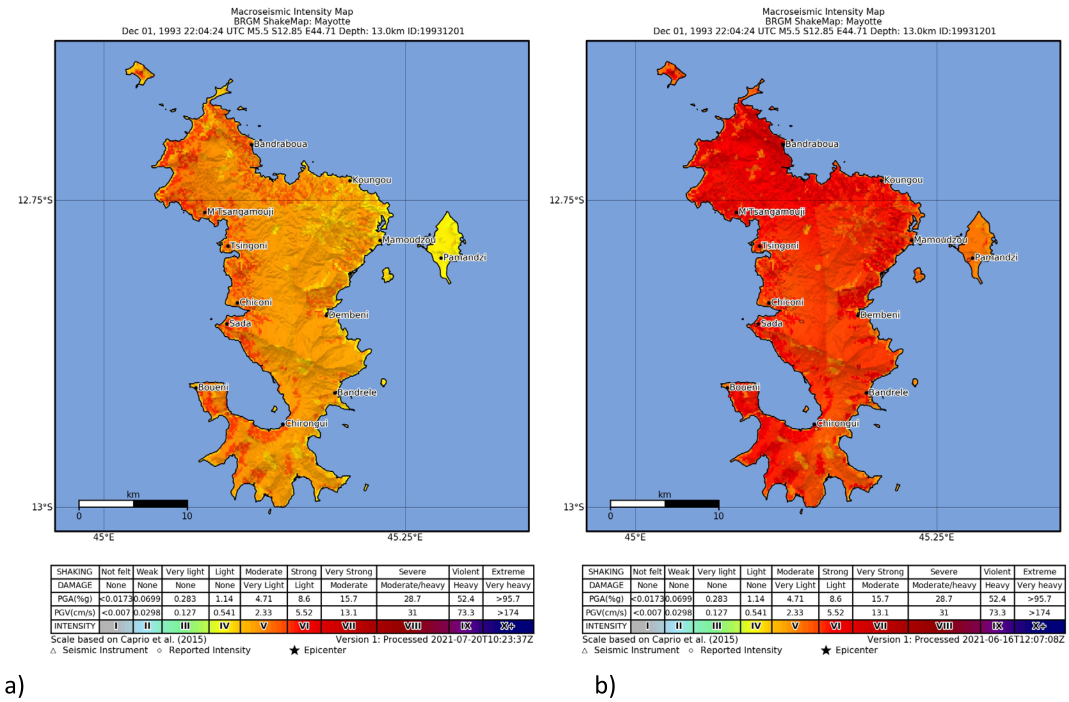


**Figure 4.** Shake-maps in MI of the 1993 EQ (a) calculated from GMPE and GMICE, (b) corrected with field intensity values (SISFRANCE).

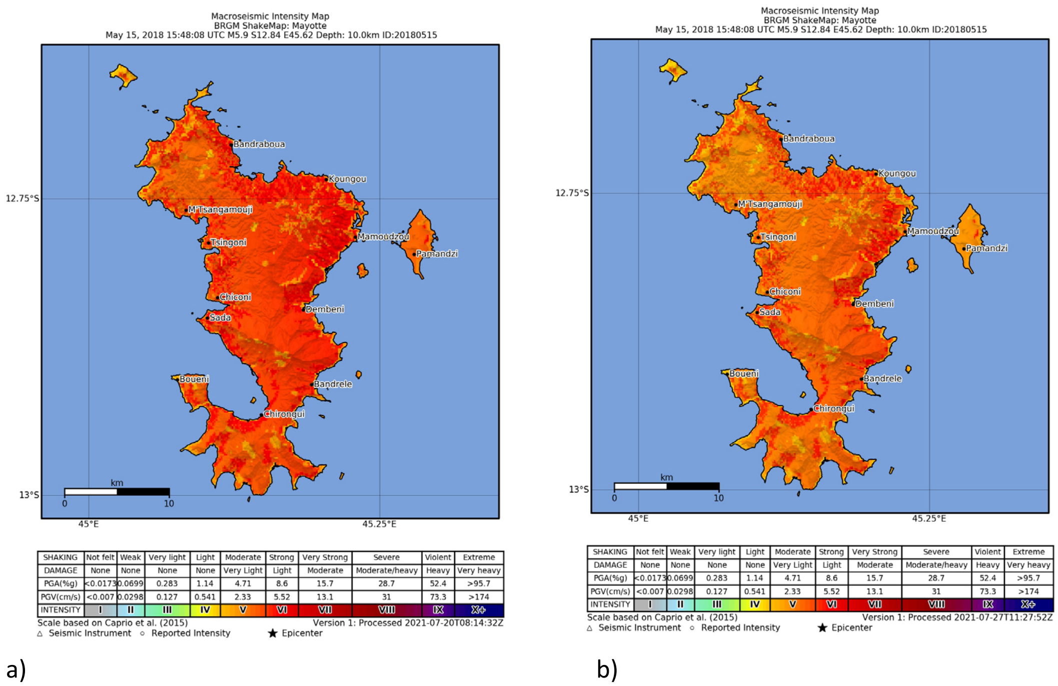


**Figure 5.** Shake-maps in MI of the 2018 EQ (a) calculated from GMPE and GMICE, (b) corrected with instrumental PGA values.

ibration with instrumental or macro seismic observations) seems consistent with the distance to the epicentre (i.e. overall attenuation of intensity of the ground motion with the distance, from west to east), it significantly underestimates MI values compared to the ones established following post-seismic observations. This results in a large discrepancy between Figures 4a and b, with stronger yet smoother values in Figure 4b.

### 3.3. *Buildings' response and vulnerability*

The study considers only the residential building stock. According to official statistics, it counts about 64,500 units for an official population of 257,000 inhabitants in 2017. The political, demographic and economic changes that the island faced in the last decades led to a drastic evolution of the construction landscape, especially for the residential stock. Individual houses made of masonry, poor construction types made of steel sheets and light structures rapidly replaced traditional construction. Collective residential buildings are still quite rare.

The description of the characteristics of a building type, together with its spatial distribution, is necessary to produce damage maps. Then, the Risk-UE method associates a vulnerability index to each building type, depending on its structural features and additional vulnerability factors. Several technical reports provide detailed information about construction techniques and physical characteristics of local material. Site investigations helped also to examine more precisely construction features and building type repartition. Finally, four types of building cover the vulnerability information for the analysis. For each type of building, the application of the Risk-UE methods gives a range of the vulnerability index, taking into account the average characteristics of the real buildings (Table 2). Factors like the number of floors, irregularities, and effect of aggregate buildings can amplify the vulnerability. In this study, the vulnerability index is calculated considering the mean value of the Risk-UE method and additional vulnerability factors that are representative of the buildings observed during the field survey. Then the field work helped in assessing the distribution of building types in each district. Despite it being convenient to represent large stocks of buildings, this method has some limitations: local variations of the vulnerability due to additional site factors (slope for example), and induced effects of earthquake (liquefaction, landslides) are not taken into account.

According to most recent data, poor housing represents one third of the residential stock, masonry individual houses quite exclusively complete the stock in 2018, but were quite rare in 1993 (Figure 6). This type of building is not properly addressed in the Risk-UE methodology. It was decided to affect a high value of the vulnerability index to it, considering the fact that their quality and resistance is very poor. Moreover, for moderated earthquakes, it is possible that the effects of inertia are lower than the action of wind, which such constructions regularly face. This means that they could withstand moderate earthquake shaking but they are probably very vulnerable to larger shakings or induced effect like slope destabilization. Given the number of such housing in the building stock in 2018, results in terms of damaged building should be considered with caution.

The next step consists in mapping the distribution of each building type in the different urbanized areas of the Island. Two levels of description of the building stock are used. The first level is the municipality (Mayotte has 17 municipalities), using the statistics released by the French National Institutes for Statistics [INSEE, 2018], which are available from the 1980s, and comparing them to the data issued in the 2018 field survey [Sira et al., 2018]. A more detailed level considers districts that result from the subdivision of the administrative perimeter of the municipalities and present a homogeneous repartition of the different types of buildings. Crossing this geographically small district and detailed soil map provides better assessment of the damages.

For the analysis at the district level, ESRI World Atlas images (small and medium scale TerraColor imagery mainly provided by Digital Globe and GeoEye) at 1:10.000 scale were interpreted, with sporadic and random verification by more recent high resolution imagery (mainly provided by Airbus through Google Maps) at working scale of 1:5.000. An aggregation of building types at the municipality scale, were each municipality territory forms a polygon with a specific distribution of building types provides results that can be compared with the previous approach. It shows significant discrepancies in the distribution of building types for some municipalities, even if at the

**Table 2.** Building types, distribution and associated vulnerability indexes

| Photo | Type and description | Vulnerability index Vi | % of total number of buildings (number) | |
|---|---|---|---|---|
| | | | In 1993 | In 2018 |
|  | Type 1: Poor living units made of steel sheets, wood or mud bricks [no corresponding type, to be compared to the method most vulnerable type M1.1 Fieldstone] | 0.85 [0.87] | 2% (400) | 27% (17,000) |
|  | Type 2: Traditional one-story houses, brick masonry houses without steel reinforcement [M3.1 Masonry] | 0.74 [0.74] | 73% (14,000) | 2% (1000) |
|   | Type 3: Masonry houses with steel reinforcement [M3.4 Masonry with reinforced concrete slab] | 0.65 [0.62] | 25% (4800) | 71% (46,000) |
|  | Type 4: Collective residential buildings, reinforced concrete structure or concrete block masonry with steel reinforcement [M4 or RC2] | 0.58 [0.39 to 0.45] | 0% (~10) | 0.2% (150) |

Corresponding Risk-UE Model building classes, and their mean vulnerability index are indicated with brackets.

scale of the entire island the distribution rate is the same. This is because aerial images do not capture all the characteristics needed to determine the vulnerability of buildings.

Using population census data from INSEE [2018] for past years, and the evolution of buildings' characteristics, the buildings' distribution has been assessed, at the municipality scale for the year 1993. Available data are not detailed enough to do this assessment at the scale of districts. Comparison of damage results using both scales of building distribution for the 2018 scenario confirmed that the aggregation of building's distribution at the municipality level, even if less precise locally, keep providing satisfying results for total number of damaged buildings in the island.

## 4. Damage scenarios for past events

Table 3 shows the simulation results, figuring the number of damaged buildings in the two main scenarios: The 15 May 2018 earthquake and the 1 December 1993 earthquake, considering today's population and urbanization, and assessing the urban-

**Table 3.** Results of the simulations for different seismic scenarios

| Scenario | SM | EQ | Level of precision | $M_w$ | Population | Total no. of buildings | ND2+ | ND3+ | %D2+ | %D3+ |
|---|---|---|---|---|---|---|---|---|---|---|
| 93-93-m | Figure 4a | 1993 | Municip. | 5.5 | 94,000 | 19,237 | 149 | 14 | 0% | 0% |
| **93-93-m*** | **Figure 4b** | | | | **94,000** | **19,237** | **327** | **34** | **2%** | **0%** |
| 18-18-m | Figure 5a | 2018 | | 5.9 | 257,000 | 64,633 | 1345 | 163 | 2% | 0% |
| **18-18-d*** | **Figure 5b** | | District | | **257,000** | **64,633** | **1808** | **248** | **3%** | **0%** |
| Optimized | Figure 5b | | | | 257,000 | 64,633 | 204 | 17 | 0% | 0% |

Scenarios with an asterisk (∗) means that they used shake-maps calibrated on observations. Column SM refers to the shake-map used for ground motion (reference of the figures in this article). Columns with “D2+”/“D3+” correspond to the number (“N”) and percentage (“%”) of buildings reaching or exceeding the damage grades 2 (light structural damage in masonry buildings, cracks in many walls or partitions) and 3 (moderate structural damage in masonry buildings, large cracks and some collapsed walls) respectively, according to the EMS-98 scale.

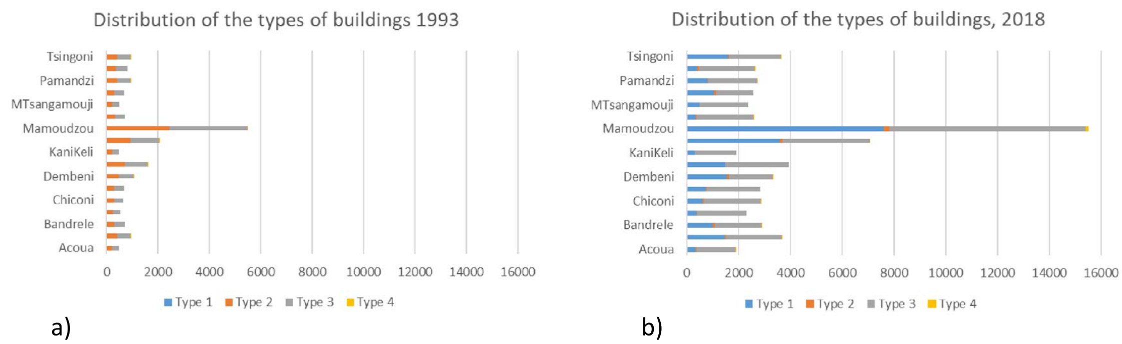


**Figure 6.** Distribution of the types of buildings for nine cities in Mayotte, (a) in 1993, estimated from INSEE census data, and (b) in 2018, from data from Sira et al. [2018] and the local office for environment and construction. A map of Mayotte is given on Figure 7.

ization in 1993. It is expressed as the number of buildings and the percentage of the total buildings stock of constructions, damaged at different grade, according to EMS-98 scale [Grunthal, 1998]. A complementary scenario, called “optimized” scenario calculates back the vulnerability index for type 3 houses that best fits the post-earthquake data for the 2018 earthquake.

For all the simulated cases, the number of severely damage buildings (level D4 or D5) is close to zero, and does not reach the level of statistical significance.

The “optimized” scenario neutralizes the vulnerability of type 1 houses and effects a vulnerability index of Vi* = 0.52 to type 3 houses. It uses the calibrated shake-map, considering it provides the most precise information about the ground motion.

The dataset was prepared for future simulations and stored in the VIGIRISKS platform. It is available for running new simulations aimed to provide seismic damage assessment for any specific uses (preparation of emergency strategy, illustration of prevention recommendations, risk awareness), or rapid loss estimation following a major event.

### 4.1. *From off-line damage scenario to real-time rapid loss assessment*

In case of a major earthquake, the authorities need to draw up as quickly as possible a “rough picture” of the situation, in order to adequately assess the operational response (organization of assistance to the victims, delimiting sectors of search and rescue operations, etc.) and anticipate requests for reinforcement as well as longer-term actions.

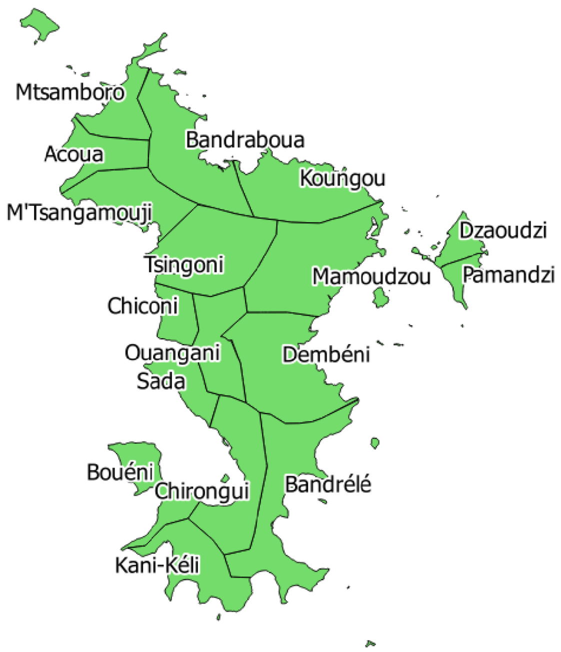


**Figure 7.** Map of Mayotte.

In the first phases of disaster relief and crisis management, to get reliable trends quickly about the extent of the crisis is more important than precise estimates, which would require time-consuming feedback from the field. Experience demonstrates that after a destructive earthquake, it often takes many hours, even days, to obtain a realistic picture of the overall number of the human and material losses. Based on numerous feedbacks from earthquakes that occurred in Japan, Tang et al. [2019] have established empirical models describing the average temporal progression of the rate of knowledge concerning the number of deceased victims, according to the size of the earthquake. According to these models, it takes 24 h to confirm information on death toll for an earthquake causing less than 100 casualties, and up to five days for earthquakes with between 100 to 1000 deceased victims.

In this context, the local authorities and the French civil protection asked the BRGM to set up a tool for rapid and automatic assessment of the extent of losses caused by earthquakes in the territory of Mayotte (SEISAID-Mayotte system). Inspired by PAGER automatic reports produced by the US Geological Survey [Earle et al., 2009], this system is designed to quickly estimate human and material losses, and to deliver reports tailored for actors involved in crisis management, 30 min after a detected event. Reports deal with two parameters relevant to crisis management: the number of partially or totally collapsed buildings (damage levels D4 and D5) and the number of injured people. These indicators support decision-making for setting priorities for search activities and allocation of rescue resources. The SEISAID tool uses the VIGIRISKS platform's damage assessment modules to automatically produce reports in case of earthquakes of magnitude 4 or greater. Figure 8 shows two example bulletins, corresponding to 1993 and 2018 earthquake scenarios that were detailed in the preceding sections.

## 5. Discussion

The opportunity to compare simulation results with field data from post-seismic surveys is a chance (Table 4). Following the 1993 and 2018 earthquakes, field surveys produced key information for a benchmark of simulation tools. Reports about the 1993 earthquake compile field data and inhabitants' damage declarations in technical documents in order to justify the allocation of repair funds. They contain valuable details about the observed damage and the vulnerability of constructions. The reliability of figures about damaged buildings is nevertheless questionable, since there was no systematic checking of the information at that time and the mechanism of damage declaration for insurance purpose frequently produces some biases. Authors themselves point to this limit.

Regarding simulation results of the 1993 earthquake, the representativeness of input data is difficult to crosscheck. Recent changes in Mayotte drastically affected the disposition of population and urbanization, making it difficult to represent precisely the real exposition to seismic risk in the past. Strong hypotheses and estimations were necessary concerning the number, type and vulnerability of buildings as well as the localization and real extension of urbanized area. The order of magnitude seems nevertheless consistent with observations. Post-event field surveys conducted estimate a total of 113 houses having been rebuilt and 1210 houses needing repair [Europact, 1995]. Deeper analysis of the report shows that repair claims concerned also houses with rather

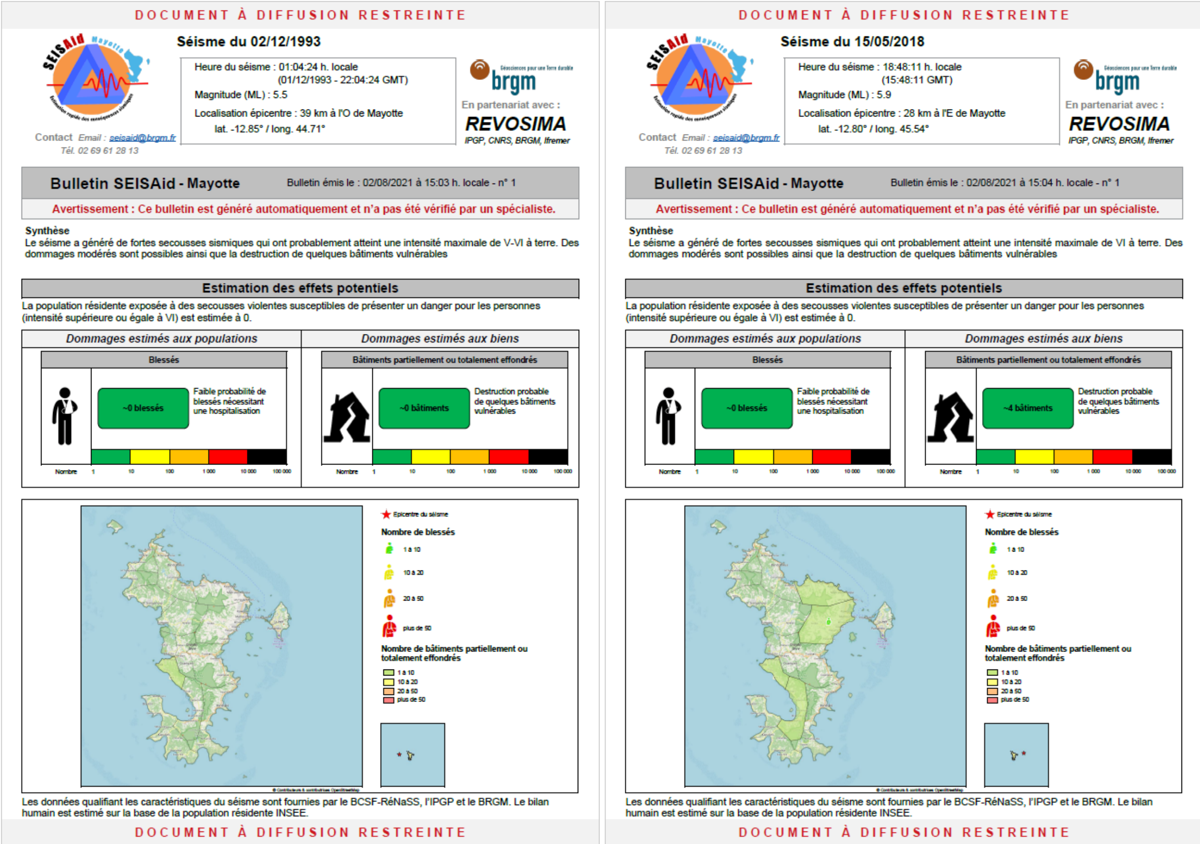


**Figure 8.** SEISAID reports corresponding to 1993 and 2018 EQ (scenario mode).

**Table 4.** Comparison of simulation and field data

| Earthquake | Simulation | | Observation | | |
|---|---|---|---|---|---|
| | D2+ | D3+ | Claims | D2+ | D3+ |
| 2018 | 1345–1808 | 163–248 | 1000 | 200 | <10 |
| 1993 | 149–327 | 14–34 | 1210 (113 rebuilt) | | |

Columns with "D2+"/"D3+" correspond to the number of buildings reaching or exceeding the damage grades 2 (light structural damage in masonry buildings, cracks in many walls or partitions) and 3 (moderate structural damage in masonry buildings, large cracks and some collapsed walls) respectively, according to the EMS-98 scale. Claims refer to claims for repair.

small damages (some maybe only corresponding to level D1). So, the total amount of claim cannot directly be compared to the number of buildings reaching D1 or D2 level in the simulation, but probably something in between. Scenario 93-93-m, based on the non-calibrated shake-map (Figure 4a), and scenario 93-93-m*, taking into account the observations-calibrated shake-map, predict 14 to 34 building with significant damage, which is rather consistent with the number of housing rebuilt. A more precise look at the number of damaged buildings per municipality did not show good agreement, tending to support the thinking that at least locally, damages could be overestimated in repair claims.

Other factors can also contribute to the discrepancies, linked to the macroseismicity values themselves. At that time, intensities were scaled according to the MSK scale, that differs slightly from the EMS98 one used for simulations. When considering the basis for intensity assessment, SisFrance does not refer to the above quoted detailed reports but on news reports, that seems to be much less detailed, and were not checked with direct field observations. Cumulated uncertainties in simulations as well as limits of data used for shakemaps should lead to high caution on interpreting the results of comparisons between these approaches.

The comparison of the scenarios obtained for the 2018 earthquake (18-18-d, 18-18-d* and "optimized") with field observations coming from Sira et al. [2018] also shows some discrepancies. Since the type of buildings are not identical, it is not easy to compare intensity results, but the number of damaged buildings are of relevance. Field observations report 1000 claims for repairs, for damage corresponding mainly to levels D1 to D2. However, it appears that many of damaged building suffer pre-existing damage. The total number of buildings damaged to level D2 is roughly estimated to be around 200, and less than ten to level D3. These values are much lower than those estimated by the simulations, which estimate between 1300 and 1800 buildings to be impacted at damage level D2 and more. One factor accounting for these differences is the behaviour of type 1 buildings. The report shows no evidence of poor housing being extensively damaged, whereas this type of building represents the majority of damaged buildings in simulation, due to the value of the vulnerability index that has been selected. On the contrary, when type 1 buildings are neutralized (artificially setting a very low vulnerability index to them), the total number of damaged buildings is much closer to the observations. In addition, when slightly modifying the vulnerability index of type 3 buildings from 0.58 to 0.52, results show very good agreement with observations (see "optimized scenario", Table 3). This value is still compatible with the Risk-UE methodology, and the range of variation acceptable for the vulnerability index. It seems that the vulnerability of type 3 buildings is a bit lower than when taking into account all the factors of vulnerability cumulatively.

The May 15, 2018 earthquake is part of a long sequence of shakings. The state of damage observed probably results from the cumulative effects of repeated ground motion. Consequently, one could expect that the damage state observed is greater than the damage state due to a single earthquake, as simulated. Nevertheless, there is no direct evidence that smaller earthquakes that occurred before the May 15 one did affect the vulnerability of the buildings. No significant damage has been reported in the first stage of the swarm, even if a dozen of earthquakes have been felt. It is worth mentioning that the magnitude scale is logarithmic and that the level of acceleration produced by most earthquakes during the sequence did not reach a level that produced structural impact. The impact of repeated low-level ground shaking deserve more investigations, but from the data available, it seems that the cumulative effect can be neglected when comparing the results of simulations with field observations.

Even if the observations of damages produced by a relatively moderate earthquake tends to support a rather good behaviour of the building stock, nonlinearity could affect the results for stronger events, especially if the shaking triggers landslides or other induced phenomena. Consequently, the reference dataset keeps recommended values of the vulnerability index, since it use by tools dedicated to crisis management accommodates better overestimation than underestimation of damages. Recommended values benefit from larger support from field observations on a broader range of magnitude considered in the Risk-UE project, even if they are less specific to the territory. There is still a need to find an appropriate way to handle the behaviour of poor housing (type 1 buildings), which represent locally a significant part of the building stock.

It is then important to note that the method used for rapid damage modeling intrinsically bears high reliability limits. Unlike damage scenario calculations, for which the user sets the seismic parameters with precision, rapid loss assessment tools are supposed to use the data available immediately after an earthquake, which is often tainted with high uncertainty. This is especially the case for rather moderate earthquakes in regions covered by a loose monitoring network, like in the Comoros region. The parameters of the earthquake (location, depth of the epicenter, and magnitude) can evolve with time, when more data become progressively available for computation. In addition to the uncertainty inherent in the methodology itself, there are several important sources of uncertainty related to the data used, including:

- Uncertainty factors related to the rapid intensity assessment:
  - Epicenter parameters (location, magnitude, depth);
  - Empirical models for taking into account lithological site effects and topographical site effects (not done here);
  - Empirical equations used for accounting for attenuation (GMPEs) and conversion between PGA and MI (GMICEs);
  - Source and directivity effects of seismic wave propagation not taken into account.
- Uncertainty factors related to the characterization of the assets at risk and their vulnerability:
  - Application of building vulnerability indices deduced at the scale of urban areas and not of individual buildings, based on an interpretation from statistical data;
  - Modeling of human losses on the basis of statistical damage/victimology correlations;
  - Exposed population considered as static, by ventilation in buildings of the resident population as described in the population census data.

Despite these limits, the comparison of simulations and real events proved its statistical robustness. It is therefore well suited for identifying trends a few minutes after the event, in the initial phase of the rescue, since very few reliable observations are available. However, it does not intent to provide indicators with high resolution (spatially or numerically). Calibration of shake-maps with measured values for ground acceleration is also a promising way to reduce uncertainty affecting the earthquake parameters.

## 6. Conclusions and perspectives

The study produced a reliable set of data for damage assessment and loss simulations that fits closely Mayotte's geographical and physical characteristics. Its implementation into the VIGIRISKS platform and its exploitation by the rapid loss estimation tool SEISAID opens perspectives for operational support to decision making regarding prevention, preparedness and crisis management.

The approach of the study, deeply rooted in the Risk-UE methodology, is robust and consistent with other damage assessment made in mainland France and overseas territories. By construction, its use is strictly limited to statistical analysis on rather large-scale territories. Results at the scale of the entire island or at the municipality level are the most relevant. Nevertheless, uncertainties about the extension of urbanized area and the assessment of site-effects, the definition of vulnerability typology and associated indexes, as well as parameters used to calculate the ground motion affects the results in terms of damage. It is recommended to run different simulations to capture variations and obtain a range of probable results, and prefer order of magnitudes of numerical values to support the decision.

The reference case, calibrated on the ongoing swarm's main shock (15 May 2018), confirms that damaging earthquakes can occur, and that a total number of several hundreds of damaged buildings should be anticipated even for a rather moderate earthquake ($M < 6$). Simulation of the 1993 event and field surveys provide additional evidences of the general vulnerability of Mayotte residential stock. This means that reducing seismic risks implies working hard on building better and reducing vulnerability.

More generally, taking into account the seismic risk of this region, the wider dissemination and adoption of good construction practices, along with the improvement in the quality of masonry building appear to be encouraging trends for leveraging a more disaster-safe and resilient territory.

## Conflicts of interest

Authors have no conflict of interest to declare.

## Acknowledgments

This work was supported by the Ministry for the Ecological Transition's General Directorate for Risk Prevention.

Seismic data from Mayotte's stations are shared within REVOSIMA, Mayottes' seismic and volcanic monitoring network.

## Glossary

BCSF-RENASS (Bureau central de sismologie français – Réseau National de surveillance sismique) : entity in charge of the seismic monitoring network part of the national seismic monitoring facility.

BRGM (Bureau de recherche géologiques et minières) : French geological survey

DEAL (Direction de l'environement et de l'aménagement) : local entity représentions the Ministry of Environment for the enforcement of the prevention policies.

DGPR (Direction générale de la prévention des risques) : Department of the French Ministry of environement in charge of the natural risks prevention policy.

DGSCGC (Direction générale de la sécurité ciile et de la gestion de crise) : Department of the French Ministy of Interiors in charge of the civil protection and crisis management.

GIM (Groupe d'intervention macrosismique) : scientific initiative that gathers researchers from different institutions in order to assess the macroseismic intensity of earthquakes occurring in France.

INSEE (Institut National des statistiques et des études économiques) : French national institute for Statistics and Economic studies, in charge of the census.

REVOSIMA (Réseau de surveillance volcanique et sismologique de Mayotte) : Scientific consortium operating the monitoring network and the marine campaigns in Mayotte. IPGP and BRGM operate REVOSIMA with Observatoire volcanologique du Piton de la Fournaise, IFREMER and CNRS. REVOSIMA is supported by a scientific consortium including IPGS, RENASS-BCSF, IRD, IGN, ENS, Université de Paris, Université de la Réunion, Université Clermont Auvergne, LMV et OPGC, Université de Strasbourg, Université Grenoble Alpes, ISTerre, Université de La Rochelle, Université Paul Sabatier, Toulouse, GET-OMP, GéoAzur, CNES, Météo France, SHOM, and TAAF. Observation data are produced by the consortium and financed by the French government.

## References


Atkinson, G. M. and Boore, D. M. (2006). Earthquake ground-motion prediction equations for eastern North America. *Bull. Seismol. Soc. Am.*, 96(6), 2181–2205.

Bertil, D. and Hoste-Colomer, R. (2020). Loi Magnitude-Intensité pour Mayotte. Rapport final. Rapport BRGM/RP70297-FR, accessible on https://infoterre.brgm.fr/rapports/RP-70297-FR.pdf.

Bertil, D., Lemoine, A., and et Roullé, A. (2019). Evaluation d'un niveau d'aléa sismique probabiliste à Mayotte et à la Réunion. Rapport final. Rapport BRGM/RP69481-FR, accessible on https://infoterre.brgm.fr/rapports/RP-69481-FR.pdf.

Bertil, D., Mercury, N., Doubre, C., Lemoine, A., and Van der Woerd, J. (2021). The unexpected Mayotte 2018–2020 seismic sequence: A reappraisal of the regional 1 seismicity of the Comoros. *C. R. Géosci.*, 353(S1), 211–235.

BRGM (2013). Carte géologique de Mayotte, Notice explicative par Nehlig et al.

Caprio, M., Tarigan, B., Worden, C. B., Wiemer, S., and Wald, D. J. (2015). Ground motion to intensity conversion equations (GMICEs): A global relationship and evaluation of regional dependency. *Bull. Seismol. Soc. Am.*, 105(3), 1476–1490.

Cesca, S., Letort, J., Razafindrakoto, H. N. T., et al. (2020). Drainage of a deep magma reservoir near Mayotte inferred from seismicity and deformation. *Nat. Geosci.*, 13, 87–93.

DEAL Mayotte (2018). Note à la DGPR " Estimation des " typologies constructives" du bâti à Mayotte" du 5 juin 2018.

Douglas, J. and Edwards, B. (2016). Recent and future developments in earthquake ground motion estimation. *Earth-Sci. Rev.*, 160, 203–219.

Earle, P. S., Wald, D. J., Jaiswal, K. S., Allen, T. I., Marano, K. D., Hotovec, A. J., et al. (2009). In *Prompt Assessment of Global Earthquakes for Response (PAGER): A System for Rapidly Determining the Impact of Global Earthquakes Worldwide (Open-File Report 2009-1131)*, page 15. US Geological Survey, Reston, VA.

Europact (1995). Aide aux populations victimes du séisme à Mayotte. Rapport d'opération suite à la visite du 14 au 21 janvier 1995- Programme Europact, 9 février 1995.

Feuillet, N., Jorry, S., Crawford, W., Deplus, C., Thinon, I., Jacques, E., Saurel, J. M., Lemoine, A., Paquet, F., Satriano, C., Aiken, C., Foix, O., Kowalski, P., Laurent, A., Rinnert, E., Cathalot, C., Donval, J. P., Guyader, V., Gaillot, A., Scalabrin, C., Moreira, M., Peltier, A., Beauducel, F., Grandin, R., Ballu, V., Daniel, R., Pelleau, P., Besancon, S., Geli, L., Bernard, P., Bachelery, P., Fouquet, Y., Bertil, D., Lemarchand, A., and Van der Woerd, J. (2021). Birth of a large volcanic edifice offshore Mayotte via lithosphere-scale dyke intrusion. *Nat. Geosci.*, 14, 787–795.

Gehl, P., Douglas, J., and d'Ayala, D. (2017). Inferring earthquake ground-motion fields with bayesian networks. *Bull. Seismol. Soc. Am.*, 107(6), 2792–2808.

Grunthal, G. (1998). *European Macroseismic Scale*, volume 15. Centre Européen de Géodynamique et de Séismologie, Luxembourg.

Guérin-Marthe, S., Gehl, P., Fayjaloun, R., Negulescu, C., and Auclair, S. (2020). Rapid earthquake response: The state-of-the art and recommendations with a focus on European systems. *Int. J. Disaster Risk Reduct.*, 52, article no. 101958.

INSEE (2018). Census data available on the website, http://www.insee.fr.

Lagomarsino, S., Giovinazzi, S., Podestà, S., and Resemini, S. (2002). *WP4 - Vulnerability Assessment of Current Buildings: I Level Methodology for the Vulnerability Assessment of Current Buildings and Guidelines for the Implementation, RISK-UE Project: An Advanced Approach to Earthquake Risk Scenarios with Applications to Different European Towns.* Contract No. EVK4-CT- 2000-00014.

Lemoine, A., Briole, P., Bertil, D., Roullé, A., Foumelis, M., Thinon, I., Raucoules, D., de Michele, M., Valty, P., and Colomer, R. H. (2020). The 2018–2019 seismo-volcanic crisis east of Mayotte, Comoros Islands: Seismicity and ground deformation markers of an exceptional submarine eruption. *Geophys. J. Int.*, 223, 22–44.

Monfort, D., Negulescu, C., and Belvaux, M. (2019). Remote sensing vs. field survey data in a post-earthquake context: Potentialities and limits of damaged building assessment datasets. *Remote Sens. Appl.: Soc. Environ.*, 14, 46–59.

Negulescu, C., Benaïchouche, A., Lemoine, A., Le Roy, S., and Pedreros, R. (2020). Adjustability of exposed elements by updating their capacity for resistance after a damaging event: application to an earthquake–tsunami cascade scenario. *Nat. Hazards*, 104, 753–793.

Negulescu, C., Hohmann, A., Tellez-Arenas, A., and Smaï, F. (2019). VIGIRISKS A Web Platform for Storing, Sharing and Executing Scientific Workflows for Natural Risk Assessment: Part 1–Eata, Approaches and Case Studies. In *Geophysical Research Abstracts*, volume 21. European Geosciences Union.

Nehlig, P., Lacquement, F., Bernard, J., Caroff, M., Deparis, J., Jaouen, T., Pelleter, A.-A., Perrin, J., Prognon, C., and Vittecoq, B. (2013). Notice de la carte géologique de Mayotte. BRGM/RP-61803-FR, 135 p., 45 ill., 1 ann.

NF EN 1998-1 (2005). *Eurocode 8 — Design of Structures for Earthquake Resistance. Part 1: General Rules, Seismic Actions and Rules for Buildings.*

Potin, J. (1993). *Etat des observations des désordres sismiques du 2 décembre 1993 à l'île de Mayotte.* Socotec Réunion.

RISK-UE (2003). In Milutinovic, Z. V. and Trendafiloski, G. S., editors, *RISK-UE WP4 Handbook. Vulnerability of Current Buildings - An Advanced Approach to Earthquake Risk Scenarios with Applications to Different European Towns.*

Roullé, A., Baillet, M., Bertil, D., and Cornou, C. (2022). Site effects observation and mapping on the weathered volcanic formations of Mayotte Island. *C. R. Géosci.*, 354(S2), 317–341.

Sedan, O., Negulescu, C., Terrier, M., Roullé, A., Winter, T., and Bertil, D. (2013). Armagedom—a tool for seismic risk assessment illustrated with applications. *J. Earthq. Eng.*, 17(2013), 253–281.

Sira, C., Schlupp, A., Bontemps, M., Regis, E., and Van der Woerd, J. (2018). Essaim sismique à l'est de Mayotte. Analyse pour la période du 10 mai au 15 juin 2018, Note préliminaire du BCSF-RENASS, BCSF-RENASS2018-R4, 62 pages, 4 tableaux, 47 Fig., 5 annexes.

Tang, B., Chen, Q., Liu, X., Liu, Z., Liu, Y., Dong, J., and Zhang, L. (2019). Rapid estimation of earthquake fatalities in China using an empirical regression method. *Int. J. Disaster Risk Reduct.*, 41, article no. 101306.

Tellez-Arenas, A., Hohmann, A., Quentin, A., Negulescu, C., and Smaï, F. (2019). VIGIRISKS A Web Platform for Storing, Sharing and Executing Scientific Workflows for Natural Risk Assessment: Part 2-Description of an Interoperable Architecture Based on Open-Source. In *Geophysical Research Abstracts*, volume 21. European Geosciences Union.

Worden, C. B., Thompson, E. M., Baker, J. W., Bradley, B. A., Luco, N., and Wald, D. J. (2018). Spatial and spectral interpolation of ground-motion intensity measure observations. *Bull. Seismol. Soc. Am.*, 108(2), 866–875.

Worden, C. B., Thompson, E. M., Hearne, M., and Wald, D. J. (2020). *ShakeMap Manual Online: Technical Manual, User's Guide, and Software Guide*. U. S. Geological Survey, http://usgs.github.io/shakemap/.

*Comptes Rendus*
*Géoscience — Sciences de la Planète*
**2022**, Vol. 354, Special Issue S2, p. 361-390
https://doi.org/10.5802/crgeos.138

The Mayotte seismo-volcanic crisis of 2018-2021 in the Comoros archipelago (Mozambique channel) / *La crise sismo-volcanique de 2018-2021 de Mayotte dans l'archipel des Comores (Canal du Mozambique)*

# Numerical simulation of submarine landslides and generated tsunamis: application to the on-going Mayotte seismo-volcanic crisis

## *Simulation numérique de glissements sous-marins et des tsunamis associés : application à la crise sismo-volcanique en cours à Mayotte*

**Pablo Poulain** [*, a, b], **Anne Le Friant** [a], **Rodrigo Pedreros** [b], **Anne Mangeney** [a], **Andrea G. Filippini** [b], **Gilles Grandjean** [b], **Anne Lemoine** [b], **Enrique D. Fernández-Nieto** [c], **Manuel J. Castro Díaz** [d] and **Marc Peruzzetto** [b]

[a] Institut de Physique du Globe de Paris, Université Paris Cité, France

[b] BRGM, France

[c] Departamento de Matematica Aplicada, Universidad de Sevilla, Spain

[d] Departamento de Analisis Matematico, Universidad de Malaga, Spain

*E-mails:* poulain@ipgp.fr (P. Poulain), lefriant@ipgp.fr (A. Le Friant), r.pedreros@brgm.fr (R. Pedreros), mangeney@ipgp.fr (A. Mangeney), a.filippini@brgm.fr (A. G. Filippini), g.grandjean@brgm.fr (G. Grandjean), A.Lemoine@brgm.fr (A. Lemoine), edofer@us.es (E. D. Fernández-Nieto), castro@anamat.cie.uma.es (M. J. Castro Díaz), m.peruzzetto@externe.brgm.fr (M. Peruzzetto)

**Abstract.** Since May 2018, Mayotte Island has been experiencing seismo-volcanic activities that could trigger submarine landslides and, in turn, tsunamis. To address these hazards, we use the HySEA numerical model to simulate granular flow dynamics and the Boussinesq FUNWAVE-TVD numerical model to simulate wave propagation and subsequent inundations. We investigate 8 landslide scenarios (volumes from $11.25 \times 10^6$ m$^3$ to $800 \times 10^6$ m$^3$). The scenario posing the greatest threat involves destabilization on the eastern side of Mayotte's lagoon at a shallow depth and can generate sea-surface deformations of up to 2 m. We show that the barrier reef surrounding Mayotte plays a prominent role in controlling water-wave propagation and in protecting the island. The tsunami travel time to the coast is very short (a few minutes) and the tsunami is not necessarily preceded by a sea withdrawal. Our simulation results provide a key to establishing hazard maps and evacuation plans and improving early-warning systems.

* Corresponding author.

**Résumé.** Depuis mai 2018, l'île de Mayotte connaît une activité sismo-volcanique importante susceptible de déclencher des glissements de terrain sous-marins générant des tsunamis. Pour faire face à ces aléas, nous utilisons deux modèles numériques complémentaires : le modèle HySEA (simulant la dynamique des écoulements granulaires) et le modèle Boussinesq FUNWAVE-TVD (simulant la propagation des vagues et les inondations) pour étudier 8 scénarios de glissements sous-marins potentiels (volumes de $11{,}25 \times 10^6$ $m^3$ à $800 \times 10^6$ $m^3$). Les scénarios ayant le plus d'impact se situent à proximité de Petite Terre et à faible profondeur. Ils peuvent générer une élévation de la surface de la mer jusqu'à 2 m en zone habitée à Petite Terre. Nous montrons que la barrière de corail entourant Mayotte joue un rôle prépondérant dans le contrôle de la propagation des vagues et dans la protection de l'île. Le temps de trajet du tsunami jusqu'à la côte est très court (quelques minutes) et le tsunami n'est pas nécessairement précédé d'un retrait maritime. De telles observations sont essentielles pour construire des cartes d'aléas précises et des plans d'évacuation afin d'aider la population.

**Keywords.** Mayotte, Seismo-volcanic crisis, Submarine landslide, Debris-avalanches, Tsunamis, Numerical modeling, Coastal flooding hazard.

**Mots-clés.** Mayotte, Crise sismo-volcanique, Glissement sous-marin, Avalanches de débris, Tsunamis, Modélisation numérique, Risque d'inondation.

*Published online: 29 July 2022, Issue date: 17 January 2023*

## 1. Introduction

The Comoros archipelago is composed of four volcanic islands (Grande Comore, Mohéli, Ajouan and Mayotte) with volcanic activities recorded from the Miocene to the Holocene [Debeuf, 2004]. Since May 2018, the island of Mayotte has registered intense seismic activities related to the birth of a large new submarine volcano 50 km offshore Petite Terre, with a volume estimated to be around 5 $km^3$ [Feuillet et al., 2021]. The epicenters of the seismic swarms are located between 5 and 15 km east of Petite Terre for the proximal swarm (Figure 1) and from 25 km to 50 km east of Petite Terre for the distal swarm [Lemoine et al., 2020a, Saurel et al., 2022]. Perturbations in the water column associated with plumes likely linked to magmatic activity were reported in the new volcano area and in the vicinity of the seismic swarm closest to Petite Terre [Feuillet et al., 2021, Scalabrin et al., 2021]. Although variations in the frequency of earthquakes and their distribution have been observed since the start of the eruption in early July 2018 [Cesca et al., 2020, Lemoine et al., 2020a, Mercury et al., 2020, Saurel et al., 2022], persistence of continuous seismicity could generate earthquakes of magnitudes close to Mw4, or even higher, that would be widely felt by the population. Since May 10, 2018, 2054 earthquakes with magnitudes greater than 3.5 have been recorded, including 36 with recorded magnitudes greater than 5 (REVOSIMA bulletin no. 33, August 2021). These strong seismic activities are located near the island of Mayotte and mainly east of Petite Terre where steep submarine slopes are observed (Figure 1). The intense seismo-volcanic crisis that has affected Mayotte since 2018, the location of earthquakes near the steep slopes surrounding the island and the construction of a new volcanic structure [Feuillet et al., 2021] may trigger submarine instabilities offshore Mayotte (and in particular to the east). The triggering of tsunamigenic submarine landslides by intense seismic activity has already been documented, for instance in 2018 in Palu Bay (Sulawesi, Indonesia) after a Mw 7.8 earthquake [Liu et al., 2020]. However, recent studies show that low amplitude ($M < 3$) but cumulative seismicity may also trigger landslides [Bontemps et al., 2020]. Gravitational instabilities could occur on steep submarine slopes offshore Mayotte but also on the new submarine volcano 50 km offshore Petite Terre: such instabilities are not new on volcano edifices [e.g. Lebas et al., 2018, Le Friant et al., 2015, 2019, Lipman et al., 1988, Moore et al., 1989, Paris et al., 2020, Sassa et al., 2016, Watt et al., 2014]. For instance, the collapse of the Anak Krakatau volcano in Indonesia in 2018 [93 $Mm^3$, Gouhier and Paris, 2019] triggered a tsunami that hit the coast of the Sunda Strait with waves of up to 80 m [Grilli et al., 2019, Paris et al., 2020]. Stromboli is also a tsunamigenic volcano that triggered five tsunamis from 1916 to 1954 [Maramai et al., 2005] and one in 2002 [Tinti et al., 2006]. Another occurrence is the Soufrière volcano on Montserrat Island (Lesser Antilles), where a 200 $Mm^3$ dome collapse generated a tsunami in 2003, with waves of up to 2 m [Pelinovsky et al., 2004]. Potential instabilities and resulting tsunamis of the submarine volcano Kick-'em-Jenny (Grenada, Lesser

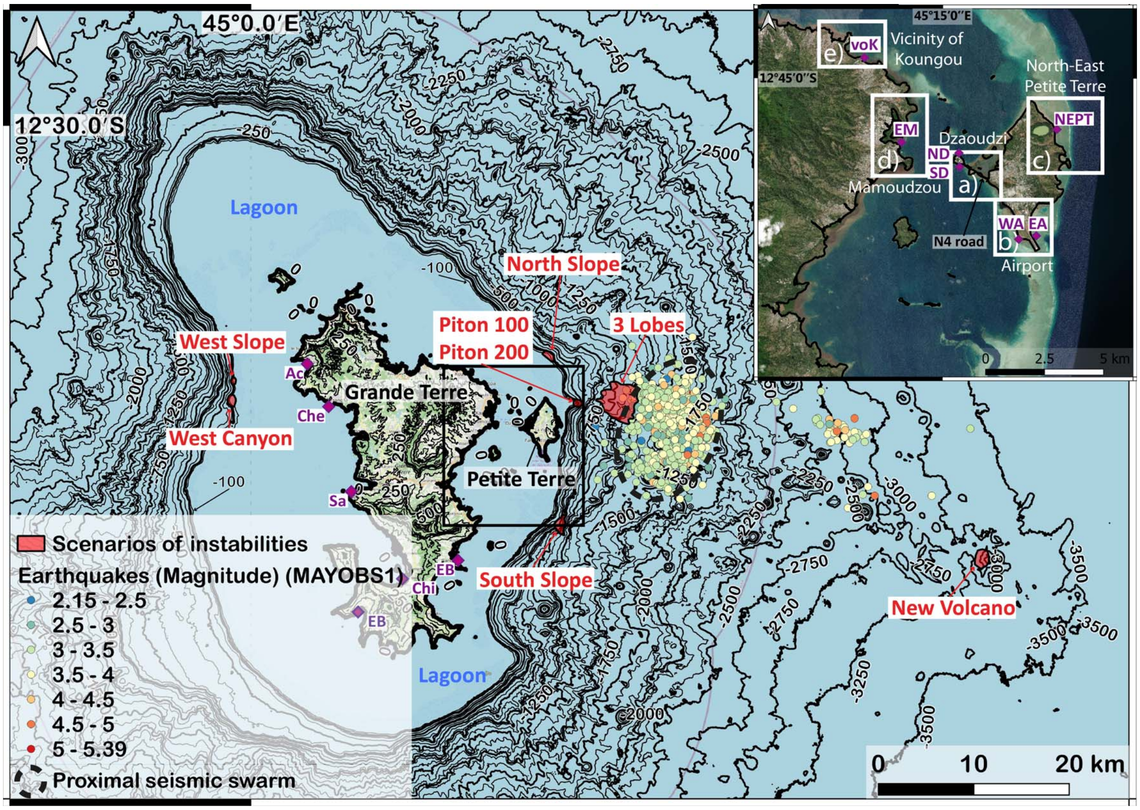


**Figure 1.** Bathymetry from Lemoine et al. [2020b] based on: Gebco 2014 (https://www.gebco.net), HOMONIM SHOM DTM (100 m resolution, https://data.shom.fr), MAYOBS 1 [Feuillet et al., 2021, 30 m resolution], bathymetric surveys of SHOM (25 m resolution, https://data.shom.fr), litto3D (lidar data at 1 m resolution, https://data.shom.fr). The main seismic swarm related to the on-going volcano seismic crisis is indicated as well as the new volcano. The scenarios of potential submarine instabilities are indicated in red. The location of the gauge EB is indicated. The insert (corresponding to the black rectangle in the main map) defines five strategic areas that will be discussed and shows the locations of the gauges voK, EM, ND, SD, WA, EA, NEPT.

Antilles) have been studied by Dondin et al. [2016].

As discussed by Roger [2019], landslide-generated tsunamis could have a significant impact on Mayotte's population and infrastructure. This impact can be quantified through hazard assessment. One of the main difficulties for hazard assessment is to identify the most probable landslide scenarios. Lemoine et al. [2020b] estimated the impact of 32 potential scenarios of submarine landslides on the slopes of Mayotte or on the new volcano. They then identified the scenarios that would be the most impactful for Mayotte. As a first attempt to assess tsunami hazards in Mayotte for national and local authorities in charge of risk mitigation, the deformation of the sea surface generated by each of the potential submarine landslides was calculated with the TOPICS software [Tsunami Open and Progressive Initial Condition System; Watts et al., 2003], based on simple empirical relations for the landslide description [Le Roy et al., 2015, Poisson and Pedreros, 2010 and Di Risio et al., 2011 for a review of such empirical relations]. These relations represented the landslide motion as a rigid block moving along a constant slope. The displacement of the free surface of the water is modeled through empirical relationships that relate the geometric and physical characteristics of the landslide to the initial amplitude and wavelength of the generated tsunamis. However, beyond simple empirical relations or block models [Gylfadóttir et al., 2017], more realistic models describing the landslide exist (see for example the large number of models already used to simulate the 2018 Anak Krakatau landslide-generated tsunami listed in Grilli et al. [2021]). They may be used for hazard assessment as done for example by Giachetti et al. [2012] and Heinrich et al. [1998] who simulated tsunami waves generated by potential landslides on Anak Krakatau and Montserrat, respectively. A few years after these studies, landslides on these two volcanoes actually occurred. The generated tsunamis had characteristics (e.g. height and impacted areas) with orders of magnitude that were similar to the characteristics of the previously simulated tsunamis. As a result, despite the high uncertainty in such simulations [Løvholt et al., 2020] related to the potential scenario (location, volume, shape), the rheological laws describing these complex natural materials, and the model approximations, such numerical codes provide a unique tool to build hazard maps that are as physics based as possible. Full 3D models [e.g. Abadie et al., 2012, Rauter et al., 2022 and references in Romano, 2020 and Grilli et al., 2021] or a combination of 3D and 2D models [Grilli et al., 2019, Løvholt et al., 2008] have been developed. As such models have huge computational costs, a significant number of shallow depth-averaged numerical models of tsunamis generated by landslides have also been developed over the past decades and applied to natural events [e.g. Abadie et al., 2010, Giachetti et al., 2012, Gittings, 1992, Heinrich et al., 2001b,a, Kelfoun et al., 2010, Mangeney et al., 2000, Paris et al., 2019, 2020]. For tsunami wave simulation, most of the models applied at the field scale solve shallow (i.e. hydrostatic pressure) depth-averaged equations for a two-layer flow made of a layer of granular material moving beneath a water layer [Fine et al., 2003, 2005, Fernández-Nieto et al., 2008, Giachetti et al., 2011, Jiang and LeBlond, 1992, Majd and Sanders, 2014, Yavari-Ramshe and Ataie-Ashtiani, 2015, and references within]. For the water wave propagation part, more advanced depth-averaged models, based on Boussinesq-type equations (non-hydrostatic pressure) that are weakly dispersive [e.g. Kirby et al., 2013, Popinet, 2015, Zhou et al., 2011] are available. In particular, these non-hydrostatic models are necessary at least to accurately simulate tsunami wavelengths of about the same order of magnitude as the water depth [Gylfadóttir et al., 2017, Kirby et al., 2022 for a benchmark; Yavari-Ramshe and Ataie-Ashtiani, 2016].

Submarine landslides are known to generate waves with wavelengths of a few kilometers [Papadopoulos and Kortekaas, 2003]. In the seismo-volcanic context of Mayotte, the potential areas of instabilities are close to the island (as shown by the presence of confirmed past submarine instabilities on the slope and foot of the island [Thinon et al., 2021]). In these conditions, the water wave wavelengths could be about the same order of magnitude as the water depth (wavelengths from 1000 m to 5000 m [Lemoine et al., 2020b]). Consequently, to investigate the impact of tsunamis generated by submarine landslides, we need to use models that take into account the landslide dynamics but that also solve Boussinesq-type equations for the tsunami propagation. These models do not yet include an accurate description of the source (for instance accounting for correct topography effects [Delgado-Sánchez et al., 2020, Ma et al., 2015]) together with a precise simulation of the wave propagation. For instance, in his analysis of landslide-generated tsunamis in Mayotte with the GEOWAVE software, Roger [2019] first simulated the submarine landslide and then used the corresponding deformation as a source term for the tsunami simulation with the FUNWAVE model [Shi et al., 2012]. This strategy presents two drawbacks: (i) the landslide and the wave generation are not simulated in a single simulation and (ii) the shallow-water assumption inherent to FUNWAVE is not valid at the beginning of the simulation. To overcome this issue, we propose a framework for coupling two near-field and far-field numerical models as done for example by Grilli et al. [2019], each model being efficient to describe a specific part of the physical processes involved. We thus combine the HySEA model [Macías et al., 2017], used to describe the submarine avalanche and initiate the waves, with the widely used Boussinesq FUNWAVE-TVD model [Abadie et al., 2020, Grilli et al., 2019, Le Roy and Legendre, 2017, Rohmer et al., 2017, Shi et al., 2012], used to propagate the wave and compute the flooding on the Mayotte coast. To implement this approach, we: (i) analyze morphological data offshore Mayotte to define scenarios of potential submarine landslides by reconstructing precise topography, (ii) process numerical simulation of the submarine landslide including a detailed description of the sources and of the granular flow, (iii) simulate the waves generated by the landslide, its propagation, and the coast inundation and discuss the pertinence of the combination of models.

## 2. Submarine landslide scenarios

The two islands of Mayotte (Petite Terre and Grande Terre) are surrounded by a well-developed shallow submarine shelf (defining the lagoon) extending offshore from 0.5 km east of Petite Terre to 17 km at certain locations around Grande Terre (Figure 1). The shelf-to-slope transition occurs at depths of 30 to 100 m. It corresponds to a significant topography slope break, from shallow slopes on the shelf (<9°) to flanks with maximum slopes of 25° to 60° locally. The slopes then decline away from the shelf-break, towards the more subdued topography of the surrounding area. In deeper water, many gullies and canyons (up to 150 m depth) form tributaries of large valleys. These canyons and discontinuities are present all around the island and may control the circulation of sediments.

In their exploratory study, Lemoine et al. [2020b] considered 62 scenarios around Mayotte that could generate tsunamis (32 instability scenarios located in Figure S1, 19 earthquake scenarios and 11 caldera collapse scenarios) and a sensitivity study was carried out on the density of collapsed material and tides. They concluded that the most impactful scenarios were associated with gravitational instabilities located on the slopes close to the reef and at the foot of the slope to the east of Petite Terre (see Figure S1). Repeated earthquakes located between 5 and 15 km from the coast east of Petite Terre could weaken the sedimentary pile and trigger tsunamigenic gravitational instabilities. The results of Lemoine et al. [2020b], combined with the location of the seismo-volcanic crisis, led us to focus our attention on the eastern coast of Mayotte. We performed a morphological analysis of the submarine slopes east of Mayotte using new bathymetric data collected in 2019 [MAYOBS 1 cruise in 2019, Feuillet et al., 2021] but we also considered scenarios on the western part of Mayotte that were considered by Lemoine et al. [2020b]. The extent, the depth, and the geometry of collapse structures were constrained by a geomorphological analysis of bathymetric surveys. The collapse structure was then constructed by digging into the present submarine slope within the defined extent. Sensitivity tests on the volumes and associated geometries of the collapsing mass are presented in Section 6.1, showing that they strongly influence wave generation. Thus, we consider 8 scenarios with different volumes and depths for numerical simulations to get an idea of the magnitude of the potential generated tsunami. The list of scenarios is not exhaustive and other scenarios could be considered in the future. We summarize the characteristics of the collapse scenarios in Table 1 [with reference to the scenarios used in Lemoine et al., 2020b] and in Figures 1 and 2.

The volumes of the landslide scenarios vary from $11.25 \times 10^6$ m$^3$ to $800 \times 10^6$ m$^3$. Six scenarios involve shallow depths: Piton 100, Piton 200, North Slope and South Slope to the east of Petite Terre and West Slope and West Canyon to the west of Grande Terre. Two scenarios are also considered at greater depths: the 3 Lobes scenario involves the morphological lobes close to the seismic swarm at middle depth and the New Volcano scenario involves the new submarine volcano at 3300 m depth. The Piton 200 scenario is located at the shelf to slope transition close to Petite Terre (2.5 km) at depths between 50 and 600 m below sea level. It probably involves a volcanic morphology (one volcano or a complex of volcanic cones) and a volume of $200 \times 10^6$ m$^3$ (Figure 2a). The Piton 100 scenario is similar to that of Piton 200 but with a shallower profile and a volume of $100 \times 10^6$ m$^3$. The 3 Lobes scenario is constrained by morphological discontinuities and gullies east of Petite Terre at depths between 850 and 1350 m below sea level and involves a volume of $800 \times 10^6$ m$^3$ (Figure 2b). The South Slope (Figure 2c) and North Slope (Figure 2d) scenarios are located on the steep slopes at the shelf break at depths between 400 and 1000 m and 50 and 250 m respectively and involve volumes of $290 \times 10^6$ m$^3$ and $11.25 \times 10^6$ m$^3$. The West Slope (Figure 2e) and West Canyon (Figure 2f) are both located to the west of Grande Terre at depths between 30 m and 300 m and involve volumes of $19 \times 0^6$ m$^3$ and $69 \times 10^6$ m$^3$. The New Volcano scenario involves the western part of the volcano (that will flow towards the west). It is located at depths between 2600 and 3150 m and involves a volume of $260 \times 10^6$ m$^3$ (Figure 2g).

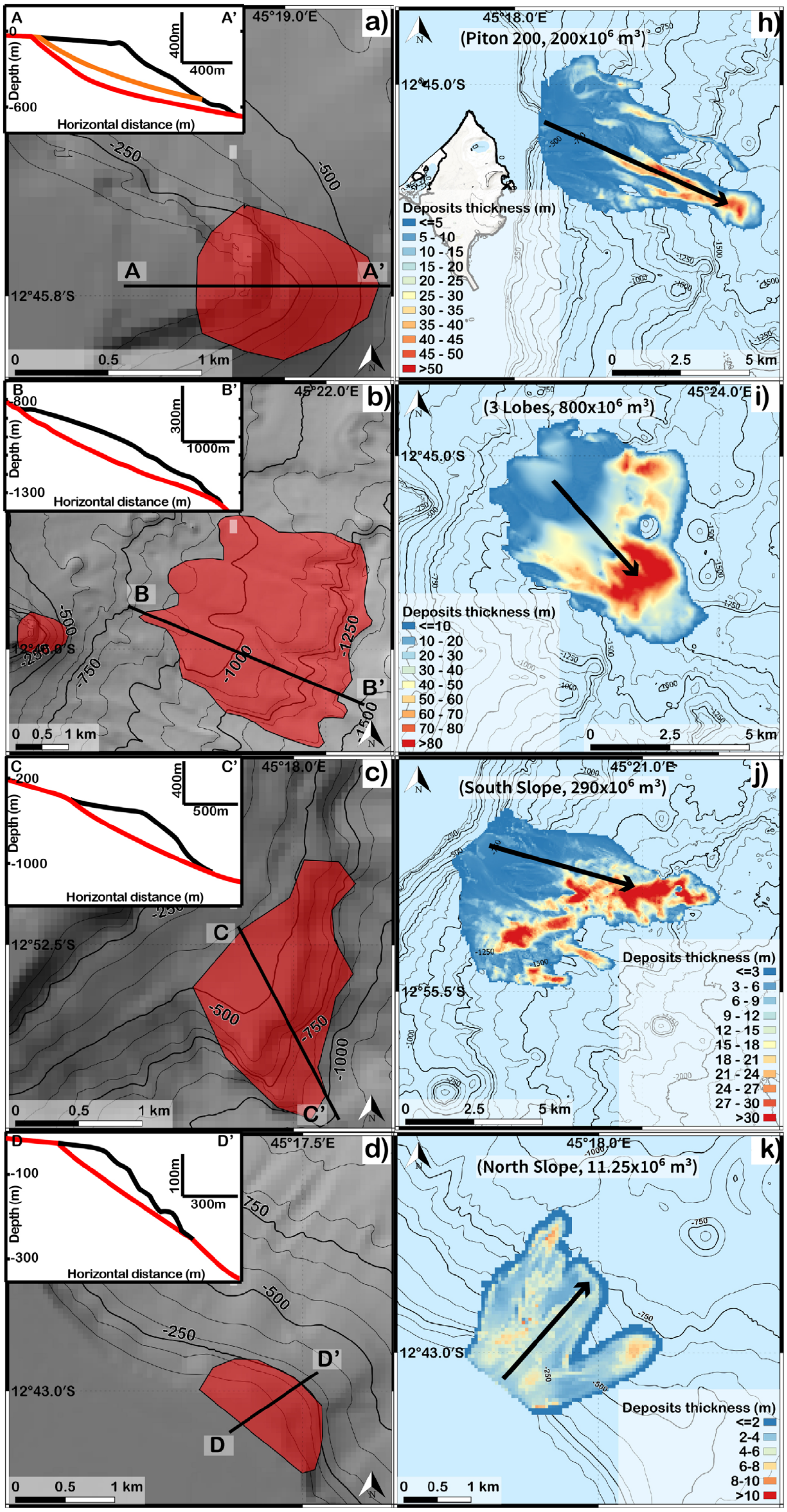


**Figure 2.** Continued on next page.

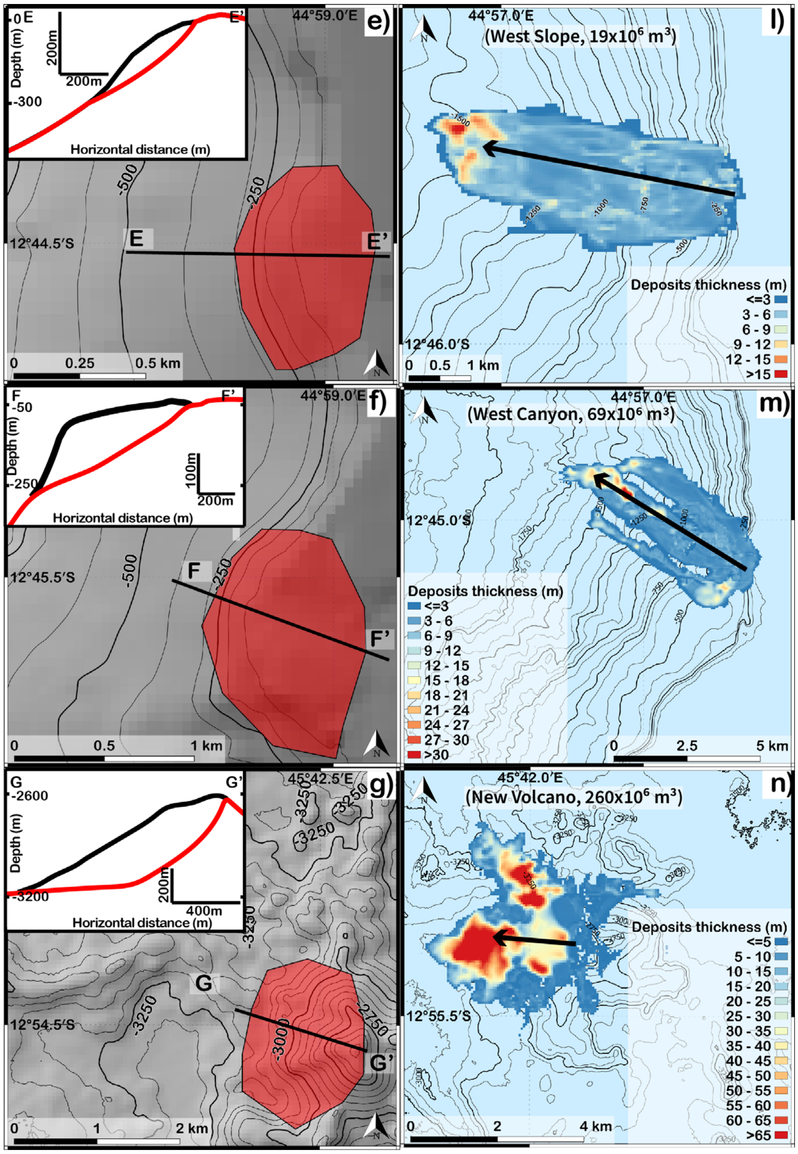


**Figure 2 (cont.).** Left column (a–g): location of scenarios of instabilities on bathymetry and associated cross-sections (the black curve represents the bathymetry before sliding and the red and orange curves represent the bathymetry after sliding) (a) Piton 200 (red) and Piton 100 (orange), (b) 3 Lobes, (c) south slope, (d) north slope, (e) west slope, (f) west Canyon, (g) new volcano; right column (h–n): thickness of the deposits calculated using HySEA for seven scenarios: (h) Piton 200, (i) 3 Lobes, (j) south slope, (k) north slope, (l) west slope, (m) west Canyon, (n) new volcano.

## 3. Numerical models and coupling

Let us briefly describe the two numerical models, HySEA and FUNWAVE-TVD, that will be used to simulate landslide dynamics and wave generation, and wave propagation, respectively, as well as the strategy adopted to couple these models.

### 3.1. *HySEA*

The two-layer hydrostatic HySEA code is a 2D extension of the model proposed by Fernández-Nieto et al. [2008], but using Cartesian coordinates. It describes submarine avalanches and the water motion on top of them. As in most landslide-generated tsunami

**Table 1.** Characteristics of the eight scenarios (volume, bathymetry) and parameters (friction angles and coupling time) used for the numerical simulations

| Type of source | Name of the scenario | Volume ($10^6$ m$^3$) | Bathymetry shallower/ deeper (m) | Pouliquen friction angle (deg.) | | | Coupling time (s) | Scenario with comparable volume and placement [Lemoine et al., 2020b] |
|---|---|---|---|---|---|---|---|---|
| | | | | $\delta_1$ | $\delta_2$ | $\delta_3$ | | |
| Active volcano | New volcano | 260 | −2600/−3150 | 6 | 16 | 8 | 26 | Sce_47 |
| Bottom of the slope | 3 Lobes | 800 | −850/−1350 | 6 | 16 | 8 | 28 | Sce_35 |
| East reef | Piton 200 | 200 | −50/−600 | 7 | 17 | 9 | 35 | Sce_48 |
| | Piton 100 | 100 | −50/−500 | 7 | 17 | 9 | 30 | Sce_36 |
| | North slope | 11.25 | −50/−250 | 10 | 20 | 12 | 28 | Sce_53 |
| Bottom of east reef | South slope | 290 | −400/−1000 | 6 | 16 | 8 | 30 | Sce_42 |
| West reef | West Canyon | 69 | −30/−300 | 8 | 18 | 10 | 20 | Sce_40 |
| | West slope | 19 | −30/−300 | 9 | 19 | 11 | 23 | Sce_39 |

models, the fluid and the granular mass are assumed to be incompressible and homogeneous. This means that the landslide is considered as an effective media described by an empirical rheological law, as discussed below. Therefore, the natural complexity of the phenomena is not fully taken into account. For instance, we do not take into account material heterogeneity, segregation and fragmentation processes, bed erosion and incorporation of air and/or water, or density variations that can be caused by the expansion or contraction of the material and their impact on pore fluid pressure [see Delannay et al., 2017 for a review of processes]. HySEA was developed by the EDANYA group [Asunción-Hernández et al., 2012, Asunción et al., 2013, Castro Díaz et al., 2005, 2006, 2008a,b, Macías et al., 2015] and has been successfully used to simulate tsunamis generated by landslides [Kirby et al., 2022 (for a benchmarking exercise); Macías et al., 2021, Esposti Ongaro et al., 2021]. From the depth-averaged equations, six unknowns are solved by the model, $(h_1, u_{1x}, u_{1y})$ and $(h_2, u_{2x}, u_{2y})$, representing the vertical height and horizontal velocity of the fluid (index 1) and granular layer (index 2), respectively, averaged in the vertical direction. The HySEA code is based on an efficient hybrid finite-volume-finite-difference numerical scheme on GPU architectures [Macías et al., 2020]. The equations are solved numerically using a relaxation method, as described in Escalante et al. [2019].

The appropriate rheology for subaerial and submarine landslides is still an open issue. Indeed, the high mobility of these gravitational flows [Lucas et al., 2014] and their complex deposit shape [Kelfoun et al., 2008] have only been reproduced by empirical laws with no clear physical origin. The empirical laws used in submarine landslide simulations include the simple Coulomb friction law [Brunet et al., 2017], the Voellmy rheology [Salmanidou et al., 2018], a retarding stress [Giachetti et al., 2012], the viscous law [Grilli et al., 2021], the friction-weakening law [Lucas et al., 2014], and the $\mu(I)$ rheology [Brunet et al., 2017], the latter being derived from lab-scale experiments on granular flows. The $\mu(I)$ rheology, resulting in the Pouliquen and Forterre [2002] flow law in depth-averaged models, includes the dependence of the friction coefficient on the velocity and thickness of the flow. Note that the thickness dependency behavior is qualitatively similar to that of the retarding stress. Following Brunet et al. [2017], we use this law here with empirical parameters. Indeed, as in most landslide simulations, the parameters of the laws have no physical meaning but result from empirical fits obtained to reproduce past events. The frictional rheology and in particular $\mu(I)$ made it possible to reproduce the main characteristics of landslide dynamics and deposits [Brunet et al., 2017, Le Friant et al., 2003, Lucas et al., 2014, Moretti et al., 2015].

In depth-averaged models with frictional rheologies, the empirical friction coefficient $\mu = \tan(\delta)$, with $\delta$ the constant or flow-dependent friction angle, can be seen as a representation of the mean dissipation during the flow [Mangeney et al., 2007a, Pouliquen, 1999, Pouliquen and Forterre, 2002]. Pouliquen and Forterre [2002] developed a friction law for the whole range of possible thicknesses and Froude numbers

($Fr$) even though the experimental data only concerned steady and uniform flows. Depending on the value of the Froude number, the flow is assumed to be in a dynamic, intermediate or static regime and the friction coefficient can be written in each regime as a function of four parameters: $L$, which is a characteristic length of the grain diameter, and $\mu_1 = \tan(\delta_1)$, $\mu_2 = \tan(\delta_2)$ and $\mu_3 = \tan(\delta_3)$, which are the tangents of the critical angles, $\delta_1$, $\delta_2$ and $\delta_3$. The angle $\delta_3$ corresponds to the asymptote of the curve $\theta_{\text{start}}(h)$, representing the slope angle at which a layer of thickness $h$ is mobilized. Two other empirical parameters $\beta$ and $\gamma$ appear in the rheological law describing (i) the critical Froude number above which the flow is assumed to be in the dynamic regime ($Fr > \beta$) and (ii) the transition between the static and dynamic regime ($\gamma$), respectively. Several studies have shown that this law well reproduces laboratory experiments on granular flows such as erosion/deposition waves [Edwards and Gray, 2014, Edwards et al., 2017, 2019, Mangeney et al., 2007b, Russell et al., 2019] or self-channeling flows and levee formation [Mangeney et al., 2007a, Rocha et al., 2019]. It has also made possible the production of conclusive results for submarine landslides in the Antilles [Brunet et al., 2017, Le Friant et al., 2003]. More precisely, a detailed comparison of the simulated and observed deposit of a submarine avalanche showed that the simulation with the $\mu(I)$ rheology better reproduces observations than the simple Coulomb friction law [Brunet et al., 2017]. Following these studies and in order to only have one free empirical parameter ($\mu_1$), we assume that $\delta_2 - \delta_1 = 10°$ and $\delta_3 - \delta_1 = 2°$ are constants, their values corresponding to those measured at the lab-scale, and we fix $L = 1$ m. We also fix the parameters $\beta = 0.136$ and $\gamma = 10^{-3}$ as in Pouliquen and Forterre [2002] and Mangeney et al. [2007a]. Note that the value of $\gamma$ has been shown to poorly affect the results in these studies. Finally, the value of $\mu_1$ is first based on the volume-dependent friction law of Lucas et al. [2014], $\mu_1 = \tan(\delta_1) = V^{-0.0774}$, empirically defined to fit the deposit of a series of almost dry landslides of different volumes $V$. We then subtract approximately 6° from $\delta_1$ as was done empirically in Peruzzetto et al. [2019] and Moretti et al. [2015] to roughly account for water effect. Table 1 summarizes the angles used for each scenario. The effect of the friction between the landslide layer and the water layer $m_f$ is small in our case as discussed in Section 6.1 [Macías et al., 2021].

In our simulations, as in most landslide simulations in the literature [Yavari-Ramshe and Ataie-Ashtiani, 2016], the initial mass is instantaneously released from rest at the initial instant, without considering the transition phase from a coherent mass to a granular flow.

### 3.2. *FUNWAVE-TVD*

The FUNWAVE-TVD code, widely used in the literature [e.g. Grilli et al., 2019], employs an enhanced version of the fully non-linear Boussinesq equations derived by Wei et al. [1995]. Chen [2006] improved the original equations of Wei et al. [1995] in order to include the vertical vorticity, which is well suited to describe wave-induced currents [Chen et al., 2003]. They also incorporated the adaptive vertical reference level of Kennedy et al. [2001] to improve the non-linear representation of the model. The FUNWAVE-TVD code solves either fully non-linear equations in a Cartesian framework [Shi et al., 2012] or a weakly non-linear spherical coordinate formulation with Coriolis effects [Kirby et al., 2013] to take into account Earth curvature. It uses a TVD shock-capturing algorithm with a hybrid finite-volume and finite-difference scheme. Following the approach of Tonelli and Petti [2009], wave breaking is detected when the ratio between wave height and water depth exceeds 0.8. The subsequent coastal inundation is simulated by cancelling off dispersive terms, hence solving the non-linear shallow-water equations. The third order strong stability preserving (SSP) Runge–Kutta scheme is adopted for time stepping.

The code is fully parallelized using the Message Passing Interface (MPI) protocol and efficient algorithms, ensuring a substantial acceleration of the computations with the number of cores. For operational uses, FUNWAVE-TVD has received many convenient features, such as the use of nested grids to refine the simulations in the interest areas or the use of heterogeneous Manning coefficients to characterize bottom friction.

### 3.3. *Coupling between HySEA and Funwave-TVD*

Coupling two numerical codes is a complex task because they are generally developed using different numerical schemes, computing libraries and language versioning. This is the case with HySEA and

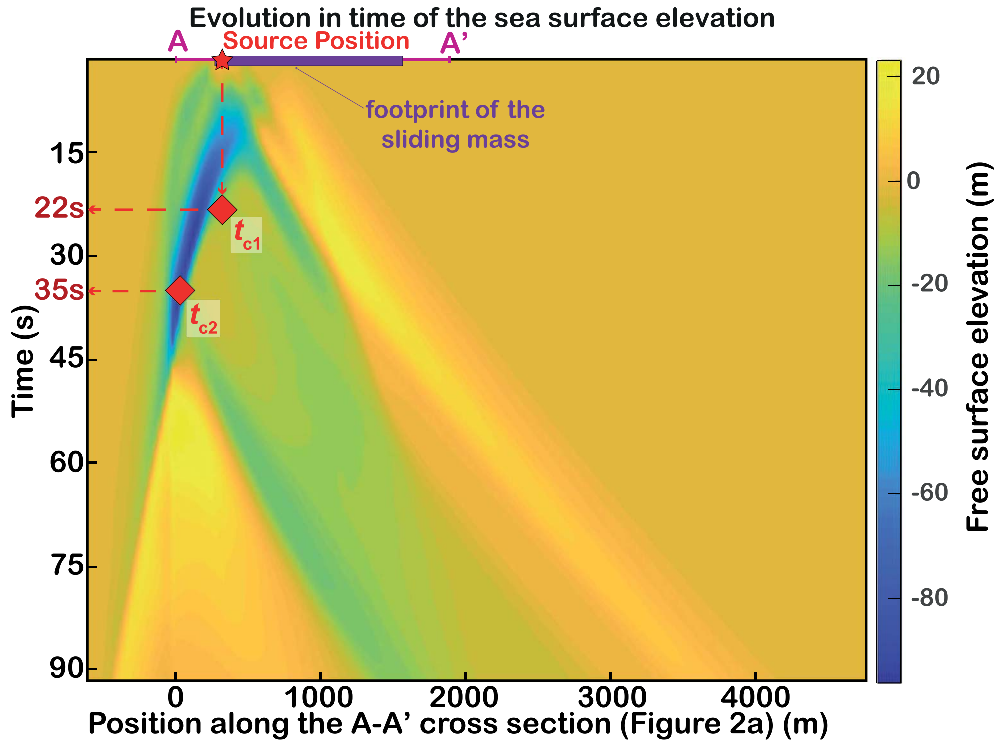


**Figure 3.** Evolution in time of the sea-surface elevation along a longitudinal plane collinear to the sliding direction. Source Position: location of the initial movement; $t_{c1}$: time at which the wave is entirely formed at the free surface; $t_{c2}$: time at which the maximum of energy is transmitted to the free surface.

Funwave-TVD. To prevent any intrusive coupling option that could produce errors and numerical instabilities, we choose to run each of them sequentially, so that after simulating the initiation of the landslide and the associated waves with HySEA, and at a time $t_c$ (coupling time), HySEA results are passed on as initial conditions for FUNWAVE-TVD. This choice ensures that all parameters (wave velocities and free-surface elevation) are correctly transmitted from one numerical environment to the other. In order to explain our choice of $t_c$, we represent, for the Piton 200 scenario, the free-surface elevation computed by HySEA along the main propagation line, from 0 to 90 s, roughly the time when the waves have vanished (Figure 3). We can identify in Figure 3 various times:

- early times when the first wave is emerging and is not yet formed;
- the time $t_{c1}$ when the landslide has moved enough to generate a completely shaped wave at the sea surface located directly above. At this time, around 22 s, the wave amplitude has completely returned to zero (orange color) after negative (blue color) then positive (yellow colors) values;
- the time $t_{c2}$, around 35 s, when the wave has reached a maximum of amplitude (dark blue color) at the free surface surrounding the source area. At $t_{c2}$, the initial first wave has grown and it can be considered to be completely formed because of the level of energy transmitted by the granular flow;
- later times where secondary waves are propagating.

To define $t_c$ for each scenario, we consider (i) situations where the sliding mass has transmitted a sufficient level of energy to the free surface to generate a complete wave and (ii) minimal errors introduced by the HySEA hydrostatic approximation when simulating wave propagation. In order to be sure to form a maximal amplitude wave (and so being conservative enough in terms of final impacts) while minimizing non-hydrostatic effects during propagation, we decided to fix $t_c$ at the value of $t_{c2}$. Table 1 summarizes the coupling times chosen for each scenario.

## 4. Model setup

The numerical simulations of landslide and sea-surface deformation were carried out under the following conditions:

- wave propagation was simulated in mean high water springs (+1.92 m at Dzaoudzi to the Mayotte vertical datum IGN1950 following the RAM 2017), which, in most cases, reduces the protective effect of the reef [Thran et al., 2021], compared to the other reference tide levels (e.g. mean high water neaps or mean tide level with values of 1.02 and 0.35 m/IGN1950 respectively),
- a global island subsidence of 0.15 m linked to the deflation phenomenon that has been observed since summer 2018 [Cesca et al., 2020, Lemoine et al., 2020a, Feuillet et al., 2021], without taking into account the west-east differential visible in GNS measurements,
- two DTM (Digital Terrain Model) with spatial resolutions of 50 m and 10 m were used. They are the same as those in Lemoine et al. [2020b]. They are based on: Gebco 2014 (https://www.gebco.net), HOMONIM SHOM DTM (100 m resolution, https://data.shom.fr), MAYOBS 1 [Feuillet et al., 2021, 30 m resolution], bathymetric surveys of SHOM (25 m resolution, https://data.shom.fr), and litto3D (lidar data at 1 m resolution, https://data.shom.fr). The 50 m DTM is used for the landslide and wave propagation simulation, and the 10 m DTM for the inundation. The mesh resolution remains constant throughout the domain. It is either 50 m when performing the large-scale simulation for the propagation of the waves and 10 m when performing the inundation simulation. The extent of the 10 m mesh grid is however smaller than that of the 50 m mesh grid to limit simulation time and focus on specific areas,
- in FUNWAVE-TVD, one-way nested grids are used to simulate inundation together with wave propagation. The 10 m DTM receives as boundary conditions the free-surface elevation and flow velocities from the simulation on the 50 m DTM. Absorbing layers are used as boundary conditions for the wave propagation simulation on the 50 m DTM,
- in FUNWAVE-TVD, the spatial changes in the bottom friction (related to land use) are taken into account by the model using Manning's roughness coefficients, $n$ [see details in Lemoine et al., 2020b]. Typical values of $n$ are determined from the literature [see e.g. Bunya et al., 2010] and vary for example between 0.02 $s/m^{1/3}$ for the deep ocean and 0.14 $s/m^{1/3}$ for the mangrove forest. Note that $n$ is constant in HySEA (see sensitivity test in figure of Section 6.1),
- in FUNWAVE-TVD: the wave breaking approach of Tonelli and Petti [2009] is activated and the simulations at 10 m resolution are conducted with a one-way nested grids (DTM at 10 m receives as boundary conditions the free-surface elevation and flow velocities from the simulation at 50 m resolution). For the boundary conditions of the model at 50 m resolution, we consider absorbing layers.

For the eight scenarios, the landslides and the tsunamis (generation, propagation and inundation phases) were first simulated with a 50 m mesh grid surrounding the whole island of dimensions 151.2 km by 110.4 km (part of it is represented in Figure 4). The results are presented with maps of the extension of landslide deposits (Figure 2h–n) and maps of maximum sea-surface elevation due to the tsunami including Grande Terre and Petite Terre (Figure 4a–h). In this paper, the term sea-surface elevation refers to the deformation in sea level caused by the generated tsunami and not an absolute elevation value. For the most impactful tsunamis, the one-way nested grid approach was used for a realistic simulation of the flooding (10 m resolution) in terms of extension, water depth (sea-surface elevation—bottom elevation) and currents. For these simulations, we focus on strategic areas provided by the local authorities: (a) Dzaouzi, (b) Airport, (c) Northeast Petite Terre, (d) Mamoudzou, (e) Vicinity of Koungou (Figure 1).

The simulations performed with FUNWAVE-TVD were run on a cluster composed of 4 to 8 nodes, each with 24 CPU processing cores. Simulations on the

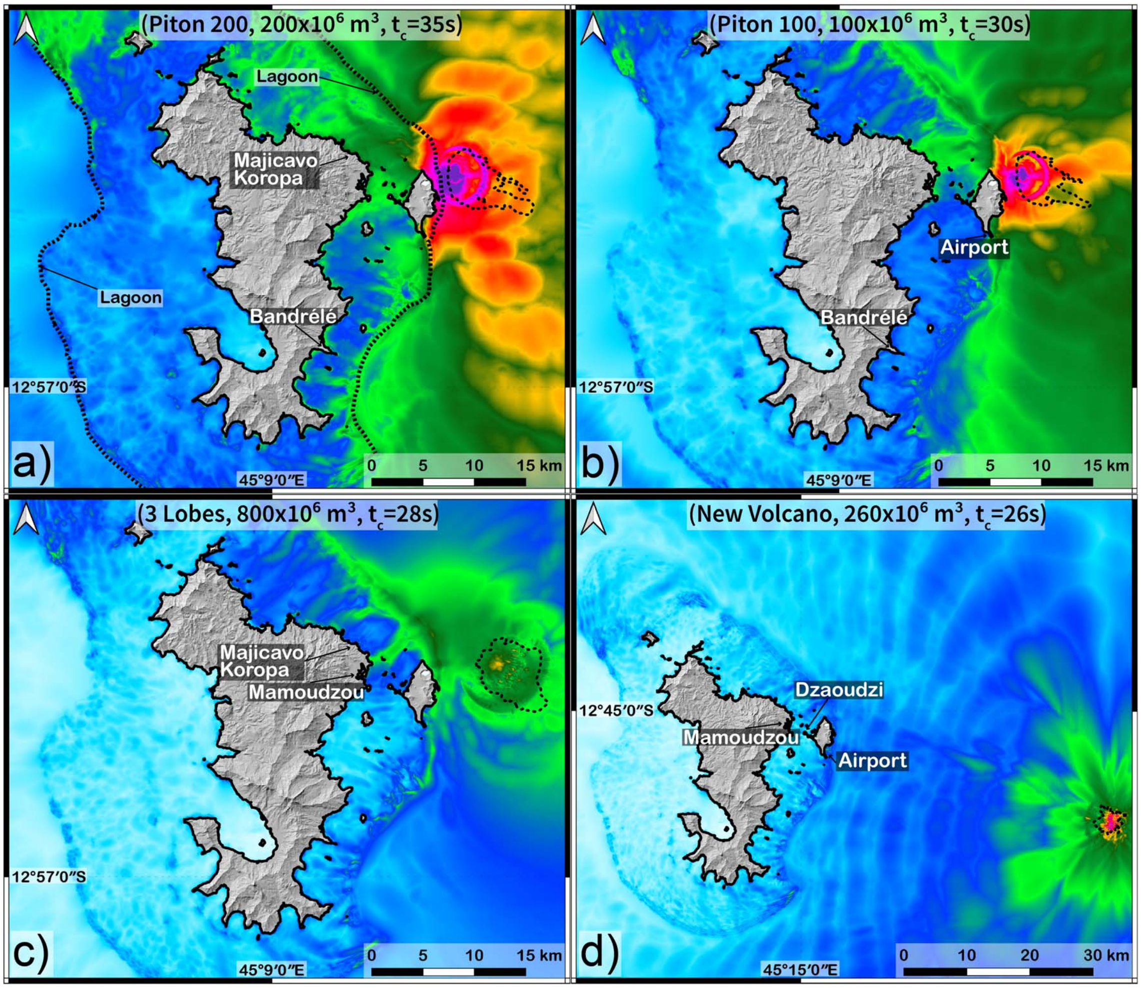


**Figure 4.** Continued on next page.

50 m DEM take between 15 and 36 h. Simulations on the 10 m DEM last between 28 and 50 h.

## 5. Results

### 5.1. *Landslide simulation at low resolution (50 m)*

We first simulate the submarine landslides and tsunamis with HySEA. For the Piton 200 scenario, the velocity of the front of the avalanche varies from 53 m/s at 40 s to 25 m/s at 150 s. Considering the steep slope and the volume of the slide, these velocities values seem to be around what can be found in the literature, even if 53 m/s is at the upper limit for submarine slides. Indeed, the velocity for the landslide of the 1741 Oshima–Oshima tsunami was estimated to be around 100 m/s [Satake, 2001], which is similar to the velocities of the subaerial flank collapse of Mount St Helens [70 m/s Voight et al., 1983]. Other studies show lower slide velocity values such as Ward and Day [2003] who estimated an average velocity of 40 m/s for Ritter Island (supposedly, the front is faster). In our simulation, the landslide stops at 260 s, extending over an area of 28 km$^2$ with a maximum thickness of 52 m (Figure 2h). We simulated the landslide deposits for all 8 scenarios (Figure 2h–n). The deposit extension varies from 12 km$^2$ to 36 km$^2$ and the maximum deposit thicknesses vary from 30 m to 90 m. The runout distance (distance between scar highest point and deposit front) varies from 2.3 km to 9.2 km. As expected, higher friction angles induce smaller runouts and deposit areas

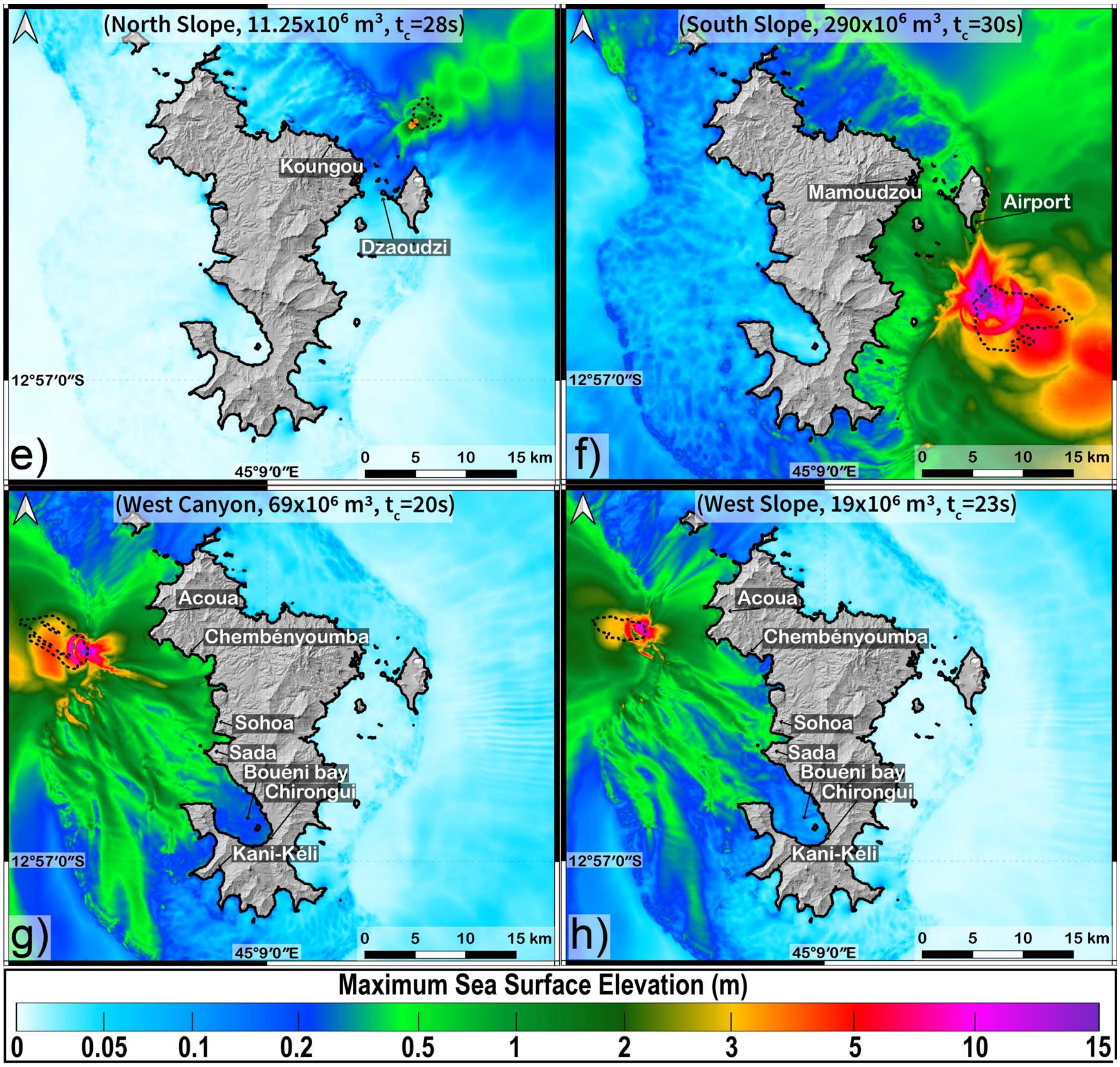


**Figure 4 (cont.).** Maximum sea-surface elevation (MSSE) in meters calculated for the eight scenarios (resolution: 50 m): (a) Piton 200, (b) Piton 100, (c) 3 Lobes, (d) new volcano, (e) north slope, (f) south slope, (g) west Canyon and (h) west slope. The volumes of the landslides and the coupling times used are indicated for each scenario. The bold black line is the Histolitt coastline from SHOM.

(see Section 6.1). The topography strongly controls the dynamics and emplacement of the landslide (Figure 2h–n) as found for instance by Peruzzetto et al. [2019, 2021] and Fischer et al. [2012].

## 5.2. *Tsunami propagation simulations at low resolution (50 m)*

The sea-surface elevation at low resolution (50 m) for the 8 landslide scenarios (Figure 4) is simulated with FUNWAVE-TVD:

- *Piton 200* ($V = 200 \times 10^6$ $m^3$): This scenario is located in shallow water. Results of the numerical simulations show an impact offshore the east coast of Petite Terre and mainly on the northeast coast of Grande Terre (Figure 4a). The shallow depth of the landslide (between 50 and 600 m) and its location close to Petite Terre lead to sea-surface elevations at the coasts of more than 10 m northeast of Petite Terre in uninhabited areas (with a maximum at 15 m, 19 m very locally) and 2.3 m to the northeast of Grande Terre near Majicavo Koropa, an inhabited area (Figure 4a).

- *Piton 100* ($V = 100 \times 10^6\ m^3$): The Piton 100 scenario is located at the same place as the Piton 200 scenario but only half of the volume is involved. Figure 4b shows sea-surface elevations at the coasts of maximum 10 m northeast of Petite Terre (uninhabited area) and 1.2 m northeast of Grande Terre (inhabited area). Off the airport, the maximum sea surface recorded is 2.3 m while it is 1.2 m northeast of Grande Terre and 0.4 m at the N4 road. Note that reducing the volume of the landslide by two does not decrease the sea-surface elevation by the same factor (Figure 4b). Off the coast of Grande Terre, where the sea-surface elevation was between 1 m and 3 m in the Piton 200 scenario, the maximum difference between the 100 and 200 scenarios is about 0.5 m. In the area close to the source of the landslide (northeast of Petite Terre) these differences are greater than 1 m or even 3 m locally where sea-surface elevations calculated for Piton 200 were between 5 m and 10 m.
- *3 Lobes* ($V = 800 \times 10^6\ m^3$): This scenario mobilizes the largest volume and is located at a greater depth. This scenario therefore has less impact than other scenarios on the Mayotte coasts (Figure 4c). Only the eastern coast of Petite Terre appears to be impacted with water elevations up to almost 2 m reached in the uninhabited areas northeast of Petite Terre. For Grande Terre, the elevations at the coasts are about 1 m (near Majicavo Koropa) and 1.3 m locally near Mamoudzou (Figure 4c).
- *New Volcano* ($V = 260 \times 10^6\ m^3$): This scenario investigates a landslide on the flank of the new volcano located 50 km east of Mayotte at more than 3000 m below sea level (Figure 4d). Although the volume is high ($260 \times 10^6$ m$^3$), the sea-surface elevation off the coasts of Mayotte is low. We observe that the maximum sea-surface elevation reaches 0.7 m very locally on the east coast of Petite Terre. Offshore Mamoudzou, the maximum elevation of the sea surface is 1 m locally but most of the values are less than 0.2 m (around 0.15 m). The maximum sea-surface elevations calculated offshore Dzaoudzi and the airport are 0.8 m and 0.5 m respectively (Figure 4d).
- *North Slope* ($V = 11.25 \times 10^6\ m^3$): This landslide scenario is located at a shallow depth and close to the reef, however it has little impact on the coasts of Mayotte with sea-surface elevations about 0.2 m offshore Koungou and Dzaoudzi, with local maximums at 0.7 m and 0.9 m respectively (Figure 4e).
- *South Slope* ($V = 290 \times 10^6\ m^3$): This scenario investigates a landslide located south of Petite Terre. It has a strong impact on the east southeast coasts of Grande Terre and mainly on the east coast of Petite Terre. The location of the landslide near the entrance of the lagoon leads to a sea-surface elevation of more than 7 m southeast of Petite Terre in uninhabited areas and about 1.8 m off the coasts near Mamoudzou (inhabited area) (Figure 4f). The airport area is also fairly exposed with a maximum sea-surface elevation of 3.4 m.
- *West Canyon* ($V = 69 \times 10^6\ m^3$): This scenario is located offshore the western coast of Grande Terre. It has a fairly limited impact off the west coast of Mayotte and has little or no impact off the east coast. The maximum sea-surface elevation reaches up to 4 m locally (Figure 4g). In the Sada and Sohoa region, the maximum sea-surface elevation reaches 2.4 and 2.8 m respectively. Offshore the Chembényoumba and the Acoua area, the maximum sea-surface elevations are 2.2 m and 2.1 m respectively.
- *West Slope* ($V = 19 \times 10^6\ m^3$): This scenario located offshore the west coast of Grande Terre has a limited impact off the west coast of Grande Terre and no impact off the east coast. The maximum sea-surface elevations reach up to 3 m locally (Figure 4h). Offshore the Sada and Sohoa region, the maximum sea-surface elevation reaches 1.2 and 2 m

**Table 2.** Times of arrival of the first tsunami wave at the gauges placed around Mayotte for each simulated scenario (locations of the gauges in Figure 1)

| Scenario | Airport | Dzaoudzi | Koungou | Mamoudzou | Bandrélé |
|---|---|---|---|---|---|
| Piton 200 | 3′55″ | 8′35″ | 11′35″ | 8′25″ | 8′35″ |
| Piton 100 | 2′50″ | 9′30″ | 12′30″ | 11′30″ | 10′30″ |
| 3 Lobes | 3′48″ | 12′28″ | 13′48″ | 14′08″ | 6′08″ |
| New volcano | 6′46″ | 14′56″ | 17′46″ | 18′16″ | 11′26″ |
| North slope | 4′28″ | 10′28″ | 9′28″ | 12′28″ | 15′28″ |
| South slope | 5′30″ | 11′20″ | 15′30″ | 13′50″ | 7′10″ |
| Scenario | Acoua | Chembényoumba | Sada | Chirongui | Kani-Kéli |
| West Canyon | 7′10″ | 9′ | 10′50″ | 20′10″ | 20′40″ |
| West slope | 6′13″ | 9′03″ | 10′43″ | 19′03″ | 20′53″ |

respectively. Offshore Chembényoumba and Acoua, the maximum sea-surface elevations are 1.3 m and 2 m respectively.

Table 2 summarizes the tsunami travel time at different strategic zones defined in Figure 1 for all the scenarios. We describe here the time series of the sea-surface elevation for three of the most impactful cases identified on the low-resolution simulations (50 m), Piton 200 (Figure 5), South Slope and West Canyon (Figures S2, S3). Digital gauges have been chosen close to specific strategic sites in order to capture the evolution of the free-surface (see locations on insert in Figure 1).

- *Piton 200* ($V = 200 \times 10^6$ $m^3$): 1 min after the start of the simulation, the first waves reach the east coast of Petite Terre (Figure 5a–d). The airport area is reached by waves in 3′55″. At 6′, the first waves propagate in the lagoon towards the northeast of Grande Terre and Dzaoudzi. The waves reach the coasts of Grande Terre at 8′25″ for the south of the east coast and 10′35″ for the northeast coast. Mamoudzou is only hit by the waves at 11′15″. At 20′, the waves have not yet reached the west coast of Grande Terre; they are just starting to propagate in this part of the lagoon. Note that the tsunami is not necessarily preceded by a withdrawal of the sea and that the first wave does not always have the highest elevation as seen on the pink plot (Figure 5d).
- *South Slope* ($V = 290 \times 10^6$ $m^3$): 2′ after the start of the wave propagation, the first waves reach the east coast of Petite Terre (Figure S2a–d). The airport area is reached by waves in 5′30″, but the interior of the lagoon remains protected. Still at 5′30″, the first waves propagate in the lagoon towards the southeast of Grande Terre and Dzaoudzi. The waves reach Dzaoudzi at 11′20″, then continue to propagate in the lagoon and reach Mamoudzou in 13′50″. 15′ after the beginning of the propagation of the waves, the northeast coast of Grande Terre is reached by the waves.
- *West Canyon* ($V = 69 \times 10^6$ $m^3$): 7′10″ after the start of the landslide, the first waves reach the west coast of Grande Terre starting with the Acoua region, then the Chembeyoumba area at 9′ (Figures S3a–d). The waves then propagate in the Lagoon towards the southwest of Grande Terre. The Sada region is reached by the waves at 10′50″ before the waves propagate in Bouéni bay and reach Chirongui at 20′10″. Finally, the southwest coast of Mayotte is reached at 20′40″ with the Kani-Kéli region.

### 5.3. *Coastal flooding simulations and hazard mapping at high resolution (10 m)*

To get precise results near the coast of Mayotte, high resolution simulations (10 m) were performed

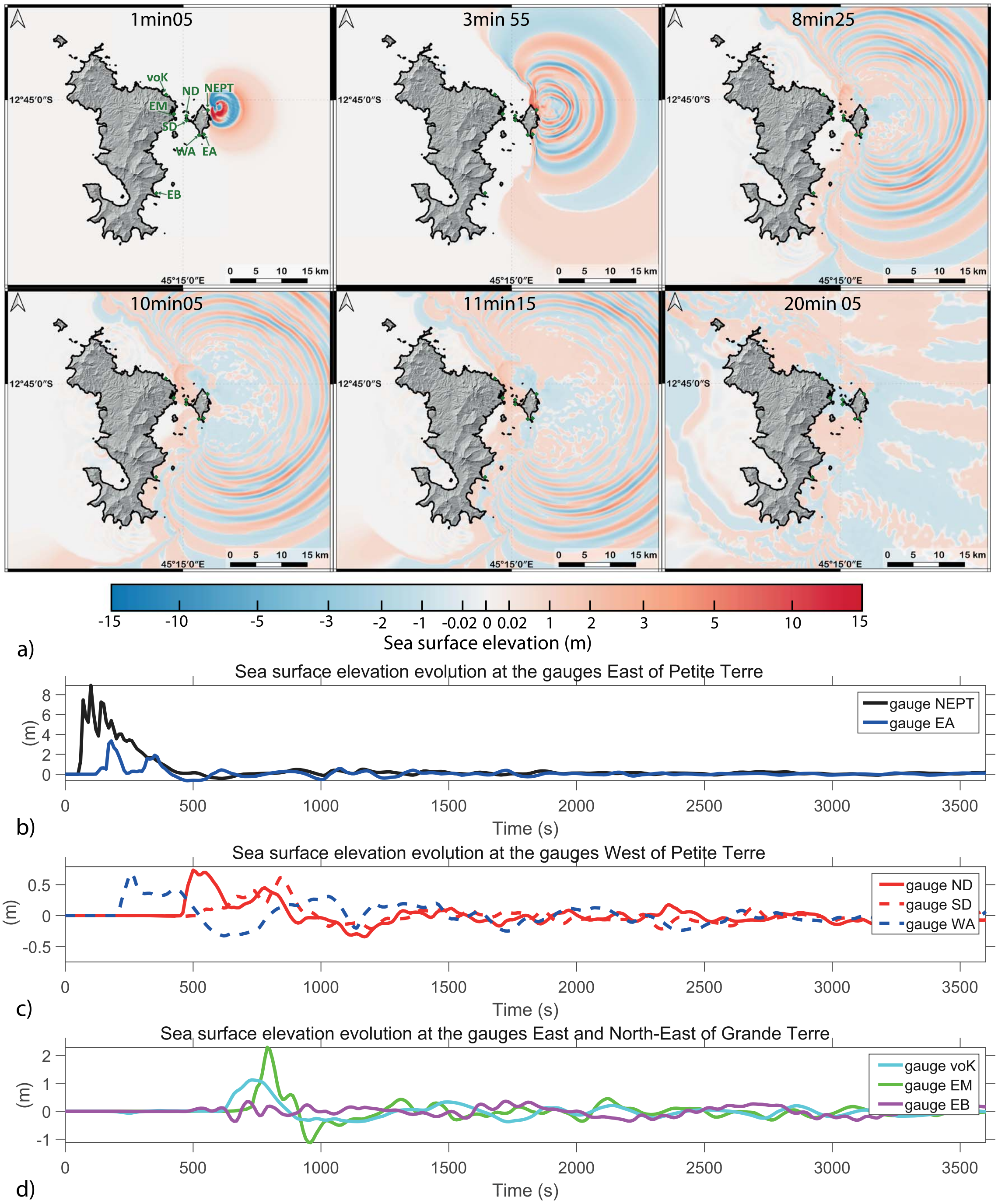


**Figure 5.** (a) Piton 200 scenario (resolution: 50 m): wave propagation from 1 min to 20 min after the landslide. The color scale represents the elevation of the calculated sea surface at a given time. The green dots on the maps indicate the locations of the gauges. (b–d) Evolution of the elevation of the sea surface at different gauges (NEPT, EA, ND, SD, WA, voK, EM, EB). The locations of the gauges are indicated in Figures 1 and 5(a).

at the local scale for the Piton 200 and South Slope scenarios as they are the most impactful (Figure 4) in the area of the current seismo-volcanic activity. We described here the results for Piton 200 ($V = 200 \times 10^6$ m$^3$) which is the most impactful scenario. The results were post-processed to obtain the maximum water depth (Figure 4 (cont.)) and maximum flow velocities (Figure 4 (cont.)). Results for the South Slope scenario are shown in Figures S4 and S5.

Figure 4 (cont.)a shows that the N4 road leading from Labatoir to Dzaoudzi is partially submerged with water depth varying from 10 cm to 1.5 m. The airport area is also subject to partial flooding with water depths of up to 35 cm on the runway and 1.50 m near the runway (Figure 4 (cont.)b). At Mamoudzou, maximum water depths of 1.50 m are reached (Figure 4 (cont.)c) north of the large Mamoudzou market. In the Koungou region, maximum water depths of 2.60 m are reached on the first buildings (such as in Majicavo Koropa, Figure 4 (cont.)d) and up to 1.90 m at a distance of 50 m from the shore. In the northern part of Petite Terre (Figure 4 (cont.)e), water depths of 6 m are reached in an uninhabited area and 8 m near Moya beach.

Figure 4 (cont.) shows that the maximum velocities are reached on the eastern side of Petite Terre and can exceed 3 m/s close to the airport (Figure 4 (cont.)b) and Moya beach (Figure 4 (cont.)d). These values are lower in the lagoon, where the depth is greater, and do not exceed 0.75 m/s (e.g. Figure 4 (cont.)a). Finally, significant velocities of 1 to 3 m/s can be observed again near the coastline and on land in some bays such as Mamoudzou (Figure 4 (cont.)c) and Koungou (Figure 4 (cont.)d) as well as on the west coast of Petite Terre (Figures 4 (cont.)a and 4 (cont.)b).

## 6. Summary and discussion

### 6.1. *Sensitivity analysis*

As discussed above, significant uncertainties are associated with these landslide and tsunami simulations [Løvholt et al., 2020]. We have tested the effect of the main assumptions and parameters involved in the models: the landslide volume, the friction law and parameters involved, the Manning coefficient, and the hydrostatic approximation. When the friction coefficient $\mu_1$ of the friction law increases to reach typical values used for dry avalanches of similar volumes ($\delta_1 = 13°$, $\delta_2 = 23°$ and $\delta_3 = 15°$) compared to our so-called reference case (*Pouliquen friction law*, $\delta_1 = 7°$, $\delta_2 = 17°$ and $\delta_3 = 9°$, $L =$ 1 m, $n = 0.025$ m$^{-1/3}$, $m_f = 0$, *Hydrostatic version of HySEA*), the landslide runout is much smaller (Figure 4 (cont.)a) and the maximum generated waves are about two meters smaller at gauge 2 (Figure 4 (cont.)c). Decreasing the typical diameter of the granular material involved ($L = 0.1$ m instead $L = 1$ m) in the $\mu(I)$ rheology does not change the maximum amplitude but slightly changes the wave shape after the first wave arrival. When $L = 0.1$ m, the simulated water wave becomes closer to the simulation using the Coulomb friction law with $\delta = 7°$. Indeed, in the $\mu(I)$ rheology, when $L$ gets smaller, $\mu$ tends to $\mu_1$. The difference between the landslide deposits simulated with the $\mu(I)$ rheology and the Coulomb friction laws is however significant (Figure 4 (cont.)a). The friction between the landslide layer and the water layer $m_f$ and the Manning coefficient $n$ poorly affect the generated wave for typical values of $m_f$ between 0 and $10^{-4}$ m$^{-1}$ and Manning $n$ between 0 and 0.05 [e.g. Macías et al., 2021, González-Vida et al., 2019] (Figure 4 (cont.)b,c), at least during the first tens of seconds before the coupling time $t_c$. The strongest effect is related to the hydrostatic assumption. Indeed, in the particular case of Mayotte, the non-hydrostatic simulations give very different results with a more rounded and longer-period wave with a maximum amplitude of the same order of magnitude (a few meters), but more than two times smaller than the hydrostatic simulation at gauge 2. The picked waves obtained with the hydrostatic assumption are typical of such approximation (see e.g. Figure 3b of Giachetti et al. [2012] or Figures 9 and 10 of Gylfadóttir et al. [2017]). Finally, the maximum wave amplitude increases as the landslide volume increases (Figure S6) and the waveform changes.

### 6.2. *Numerical models and coupling approach*

We used here the depth-averaged hydrostatic version of HySEA (i.e. with one layer for the avalanche and another layer for the water column, as opposed to the multilayer HySEA model where the water column is divided into several layers). The depth-averaged hydrostatic version of HySEA has been already applied to real landslides and tsunamis [Macías et al.,

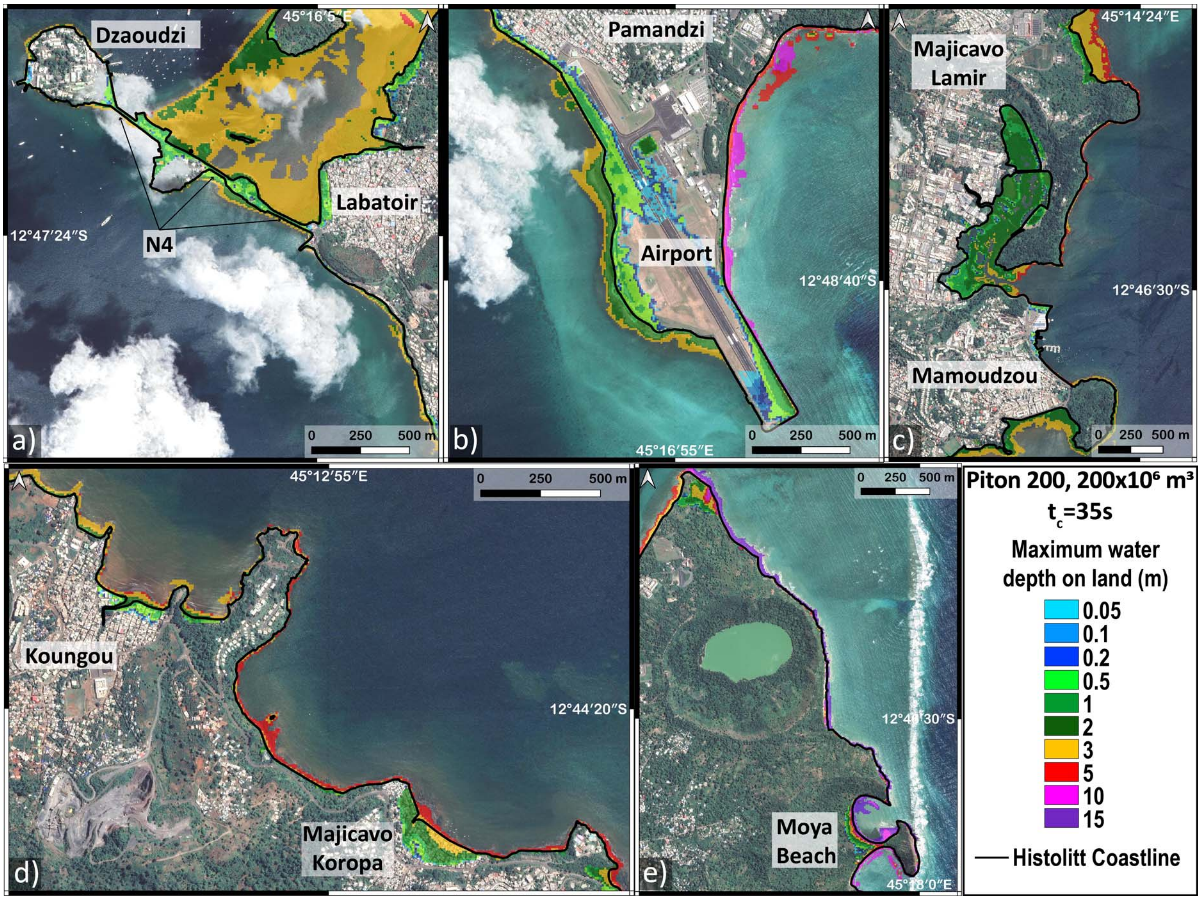


**Figure 4 (cont.).** Maximum water depths (MWD) with 10 m resolution for the Piton 200 scenario. The color scale represents the value of MWD calculated for each point: (a) Dzaoudzi and route N4, (b) airport and Pamandzi, (c) Mamoudzou, (d) northeast coast of Petite Terre, and (e) Koungou. The bold black line is the Histolitt coastline from SHOM.

2017, 2020]. The accuracy of hazard maps related to landslide-generated tsunamis would be significantly improved by more advanced models accounting for non-hydrostatic effects in the landslide [Garres-Díaz et al., 2021] and water wave propagation, different coordinate systems for the landslide and avalanche [Delgado-Sánchez et al., 2020], in-depth variations [Garres-Díaz et al., 2021], and grain–fluid interactions [Bouchut et al., 2016]. However, some of these models are not yet applicable for field-scale simulations or require more parameters that are not easy to calibrate, which could lead to significant uncertainties.

In order to preserve the numerical stability of each code (HySEA and FUNWAVE-TVD) when coupling them and to be the least intrusive possible, the coupling consisted in considering the wave parameters (velocities and free-surface elevation) computed by HySEA at a certain time as initial conditions of FUNWAVE. This protocol needs to evaluate the coupling time ($t_c$) so that it reflects the best continuity between the two codes. Thus, the choice of $t_c$ is important because it affects the simulated impact of the scenarios. Taken too early, the landslide will not yet have fully formed the water wave and the impact will be reduced. Taken too late, the wave will have started to spread with hydrostatic conditions and the impact may be overestimated. This time also depends on the characteristics of the landslide (depth, thickness, volume, slope, etc.) and its interaction with the topography. Starting the FUNWAVE-TVD simulation later increases the impacted area and the elevations of wa-

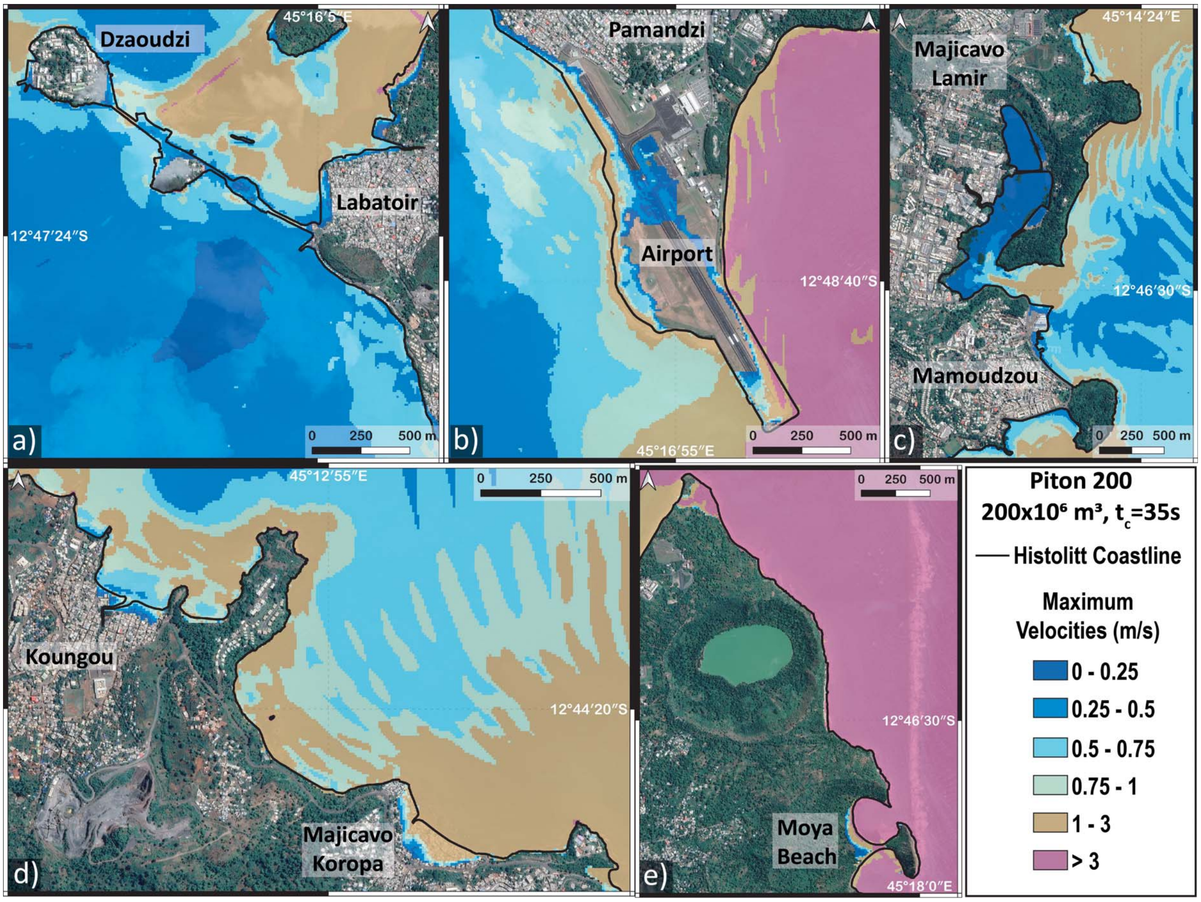


**Figure 4 (cont.).** Maximum water velocities in m/s with 10 m resolution for the Piton 200 scenario. The color scale represents the value of the maximum water velocity calculated for each point: (a) Dzaoudzi and route N4, (b) airport and Pamandzi, (c) Mamoudzou, (d) northeast coast of Petite Terre, and (e) Koungou. The bold black line is the Histolitt coastline from SHOM.

ter at the coasts. For example, in the Piton 200 scenario, if we start the FUNWAVE-TVD 13 s before $t_{c2}$, the maximum water elevation is reduced by 3.1 m at the airport and by 0.8 m in Dzaoudzi. Thus, using a slightly longer coupling time is a way to obtain envelope scenarios satisfying precautionary principles in terms of hazard assessment, as done in this work.

### 6.3. *Tsunami generation, wave propagation and inundation by combining the scenarios*

Figure 4 (cont.) displays the maximum sea-surface elevation obtained by combining the results of numerical simulations from all the eight scenarios simulated for a 50 m mesh grid. The most penalizing scenarios can locally generate elevations of the water level greater than 1 m, in particular along the eastern coast of Petite Terre where they can reach several meters locally for the most impactful scenarios. The scenarios considered here are associated with rather maximizing assumptions. The most impactful sources are linked to sliding masses of large volume and occurring at shallow depths, i.e. close to the reef and along the slope east of Petite Terre. A good example is the Piton 200 scenario (Figure 4a) that mainly participates in defining the map of the maximum elevations of the water body (Figure 4 (cont.)) for the east part of Petite Terre. Other considered scenarios have a limited impact, with elevations of the water level less than 30 cm at the coast of the lagoon and the reef. This point is particularly illustrated by the impact of the 3 lobe scenarios (huge volume at middle depth) and the South-Slope and North-Slope scenarios (small volume at shallow depth) (Figure 4). This also concerns the collapses of the new volcanic edifice, corresponding to one of the most significant cases in terms of destabilized volume. However, the movements transmitted to the water are so deep that the impact at the free surface is strongly attenuated and the impact along the coasts is low.

The impact on the coast of simulated potential tsunamis is heterogeneous and depends not only on the considered scenarios but also on the coastal areas as is generally the case. Globally, modeled impacts of tsunamis along the coast of Mayotte can be considered as moderate, except for some maximizing scenarios along the eastern side of the island. This side of the island is the most exposed since we considered potential landslides in this area, associated with the ongoing seismo-volcanic activity. However, the reef plays an essential protective role since it can dissipate much of the energy of tsunamis coming westward, as it does for cyclonic waves [Kunkel et al., 2006, De la Torre et al., 2008]. The east coast of Petite Terre is much more exposed because of the lack of a reef. Elsewhere, coastal morphologies characterized by steep slopes associated with the presence of mangroves also mitigate the impact of submersion due to dissipation processes. Given the orders of magnitude of the modeled events, it is essential to take into account the tides and the subsidence linked to regional deflation (phenomenon of emptying of the magmatic chamber [Cesca et al., 2020, Lemoine et al., 2020a, Feuillet et al., 2021]). In our study, unfavorable assumptions (full spring tide and homogeneous subsidence of 15 cm) have been considered during the modeling of tsunamis in order to conserve the logic of the "worst credible risky case".

More locally, in addition to the exposure to the phenomenon, the level of risk depends on the presence of buildings, roads or particular infrastructures such as the airport or administrative centers and their vulnerability. The most exposed areas (in terms of wave height) are not associated with a high level of risk as they are located along the eastern coast of Petite Terre that is almost uninhabited (beaches surrounded by relief and cliffs). Higher resolution simulations (10 m resolution) were carried out for some of the most impactful scenarios such as Piton 200 and South Slope in order to model the potential flooding. To engage operational communication with local authorities, we were encouraged to map a simplified parameter representing the intensity of flooding along the coasts. Because it has been computed by integrating all the most impactful scenarios, it reflects the intensity, from low to very high, on a specific area, as defined by the French coastal risk prevention plan guide [MEDDE, 2014] (Table 3). The resulting mapping is thus obtained by combining the water depths and flow velocities simulated for the most impactful scenarios, and for simplification, it has been associated with the notion of hazard (or pseudo-hazard), even if it is not feasible or realistic to associate a probability with the considered simulated scenarios. However, the performed simulations show that inundations located on Petite Terre, and in particular at the airport and Dzaoudzi, lead to a high pseudo-hazard level. On Grande Terre, specific local conditions (mangrove, steep slopes) mitigate the impact of inundation. Figure 4 (cont.) exhibits such high to very high pseudo-hazard levels along the entire coastline studied, impacting in particular some coastal urbanized sectors (e.g. Figure 4 (cont.)d) and coastal infrastructures (Figure 4 (cont.)a,b). In addition, tsunami arrival times for these scenarios are around a few minutes (Figure 4 (cont.)), which is relatively short to set up an early warning system.

## 7. Conclusion

Since May 2018, Mayotte Island has experienced intense seismic activities linked to the on-going seismo-volcanic crisis. This could weaken the submarine slopes of Mayotte and trigger submarine landslides associated with tsunamis. To address the hazards associated with such events, we have combined two complementary numerical models (the HySEA and the Boussinesq FUNWAVE-TVD models) to numerically simulate eight potential submarine landslides and the associated generation and propagation of waves. Our results show that, for the most penalizing scenarios, the generated elevations of the water level are generally around 1 m, except in Petite Terre where they can reach very locally

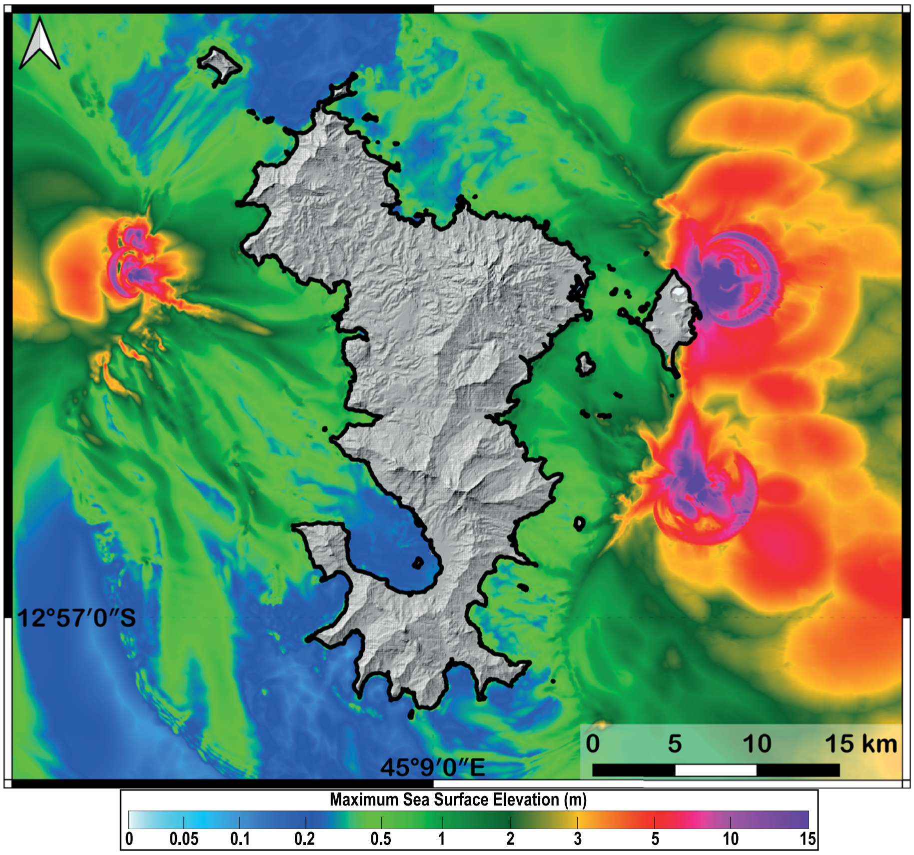


**Figure 4 (cont.).** Map of the maximum sea-surface elevation (values in m) combining the results of the eight simulated scenarios (resolution: 50 m). The bold black line is the Histolitt coastline from SHOM.

**Table 3.** Parameters used to represent the intensity of the flooding, as defined in the French coastal risk prevention plan guide [MEDDE, 2014]

| Water height (m) | Submersion dynamics: velocities | | |
|---|---|---|---|
| | $0\ \mathrm{m/s} < V < 0.2\ \mathrm{m/s}$ | $0.2\ \mathrm{m/s} \leq V < 0.5\ \mathrm{m/s}$ | Fast: $V \geq 0.5\ \mathrm{m/s}$ |
| $H < 0.5$ m | Low | Medium | High |
| $0.5\ \mathrm{m} \leq H \leq 1$ | Medium | Medium | High |
| $H \geq 1$ m | High | High | Very high |

more than 15 m in an uninhabited area. Indeed, the most impactful sources are linked to sliding masses of large volumes and occurring at shallow depths, i.e. close to the reef and along the slope east of Petite Terre, as represented by the Piton 200 scenario. Other considered scenarios have a limited impact, with less than 30 cm elevations of the sea level at the coast of the lagoon and the reef. The impact on the coast is therefore non-uniform and depends on the side of the island. Globally, the eastern side of the island is the most exposed since it faces the location of landslides potentially generated by the seismo-volcanic activity. Fortunately, at this location, the reef plays a key protective role by dissipating much of the energy of tsunamis coming westward. Preserving the reef is therefore crucial to maintain this natural protection.

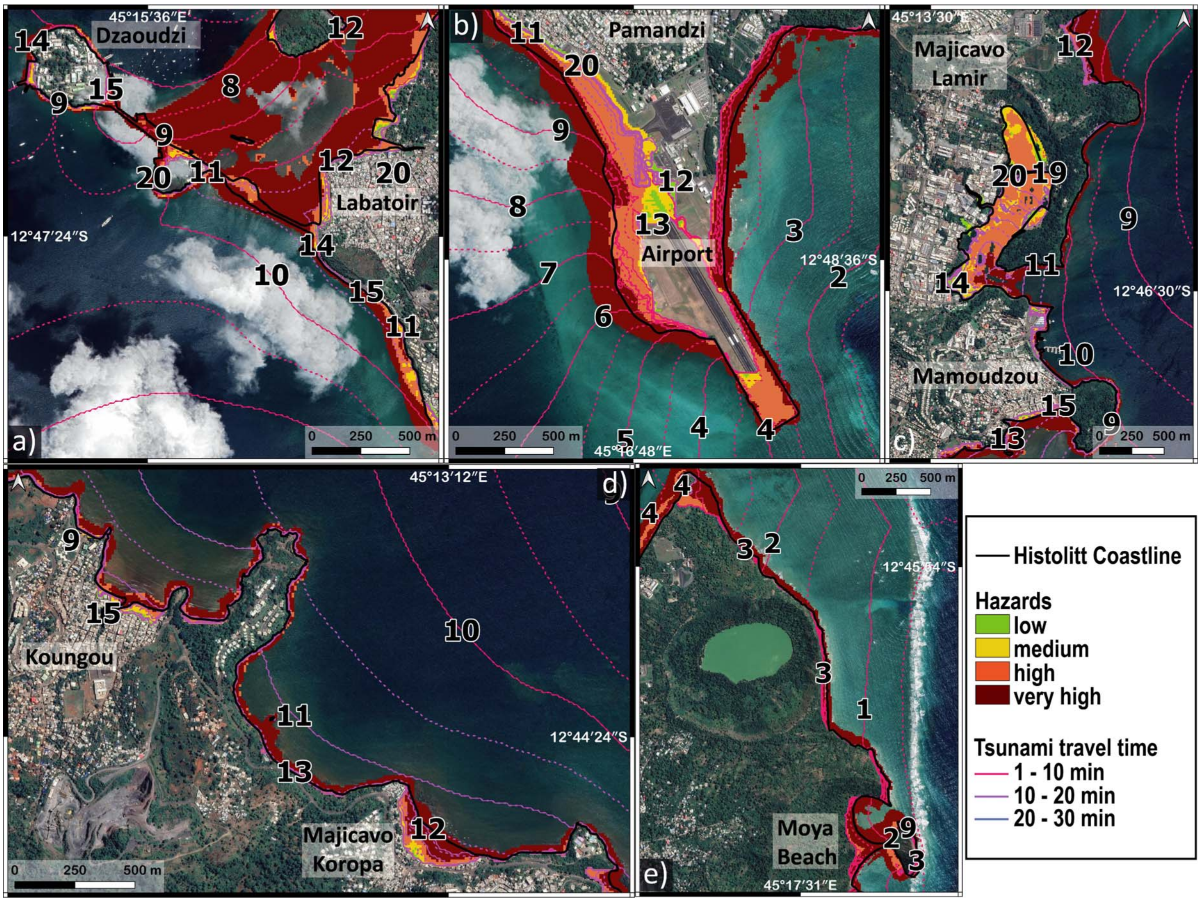


**Figure 4 (cont.).** Hazard value and time of travel of the tsunami from the combined results of the most impactful scenarios (Piton 200 and South Slope) with a 10 m resolution. The color scale represents the value of the hazard calculated for each point: (a) Dzaoudzi and route N4, (b) airport and Pamandzi, (c) Mamoudzou, (d) northeast coast of Petite Terre, and (e) Koungou. The bold black line is the Histolitt coastline from SHOM. The colored lines and dashed lines represent the travel times of the tsunami in minutes.

Our simulations show that, for some of the most impactful scenarios, such as Piton 200 and South Slope, inundations located on Petite Terre, and in particular at the airport and Dzaoudzi (up to 1.5 m), can lead locally to a very high hazard level. On Grande Terre, specific local conditions (mangrove, steep slopes) mitigate the impact of any inundation. Note that preserving the mangroves is also crucial to reduce flooding.

Our study paves way to the development and use of complex numerical models to simulate both landslides and wave propagation processes [e.g. Rauter et al., 2022, Yavari-Ramshe and Ataie-Ashtiani, 2016, for a review], instead of simple empirical laws for the landslides [Lemoine et al., 2020b]. This should improve hazard and risk assessment strategies in contexts similar to Mayotte, i.e. in active seismo-volcanic contexts near the coast. To understand the results presented in this study, it is essential to be aware of the uncertainties linked to the scenario definition, model approximations, empirical rheological laws, and the simplification of natural complexity (see Section 6.1 and Figure S6). Each of these parameters affect the tsunami wave, but the non-hydrostatic effects dominate in such a context and should thus be accounted for in the future. Furthermore, we have

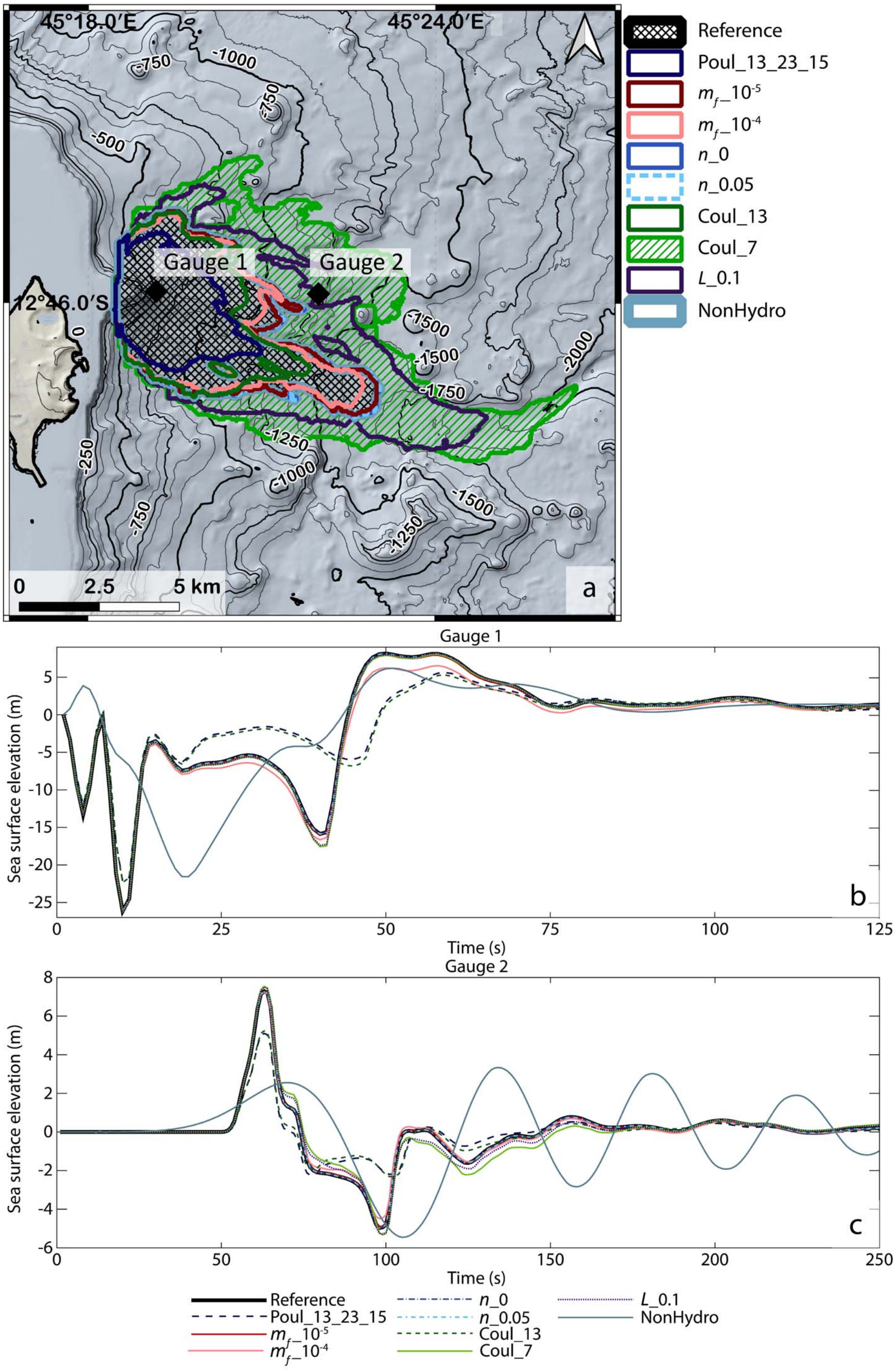


**Figure 4 (cont.).** Sensitivity tests performed on the Piton 200 scenario with varying Manning coefficient $n$, friction angles $\delta_i$, water landslide friction $m_f$, value of the typical grain diameter $L$, and version of HySEA (parameters can be found in Table 4). (a) Deposit extension for each sensitivity test and locations of the gauges, (b) sea-surface elevation at gauge 1, (c) sea-surface elevation at gauge 2. The reference simulation is the thick black curve.

**Table 4.** Parameters involved in the sensitivity tests performed by varying the landslide volume $V$, the friction law and associated friction angles $\delta_i$, the Manning coefficient $n$, the typical grain diameter $L$ in the Pouliquen ($\mu(I)$) flow law, friction between the avalanche and water layer $m_f$, and version of the model (hydro and non-hydro)

| No of the simulation | Name | Volume ($10^6$ m$^3$) | Friction law | Friction angle (deg.) | | | $L$ in m Pouliquen law | Manning $n$ (m$^{-1/3}$·s) | Water-landslide friction $m_f$ (m$^{-1}$) | Version of HySEA |
|---|---|---|---|---|---|---|---|---|---|---|
| | | | | $\delta_1$ | $\delta_2$ | $\delta_3$ | | | | |
| 1 | Reference | 200 | Pouliquen | 7 | 17 | 9 | 1 | 0.025 | 0 | Hydro |
| 2 | Poul_13_23_15 | 200 | Pouliquen | 13 | 23 | 15 | 1 | 0.025 | 0 | Hydro |
| 3 | $m_f$_$10^{-5}$ | 200 | Pouliquen | 7 | 17 | 9 | 1 | 0.025 | 0.00001 | Hydro |
| 4 | $m_f$_$10^{-4}$ | 200 | Pouliquen | 7 | 17 | 9 | 1 | 0.025 | 0.0001 | Hydro |
| 5 | $n$_0 | 200 | Pouliquen | 7 | 17 | 9 | 1 | 0 | 0 | Hydro |
| 6 | $n$_0.05 | 200 | Pouliquen | 7 | 17 | 9 | 1 | 0.05 | 0 | Hydro |
| 7 | Coul_13 | 200 | Coulomb | 13 | | | | 0.025 | 0 | Hydro |
| 8 | Coul_7 | 200 | Coulomb | 7 | | | | 0.025 | 0 | Hydro |
| 9 | L_0.1 | 200 | Pouliquen | 7 | 17 | 9 | 0.1 | 0.025 | 0 | Hydro |
| 10 | NonHydro | 200 | Pouliquen | 7 | 17 | 9 | 1 | 0.025 | 0 | Non hydro |
| 11 | $V$_$100 \times 10^6$ | 100 | Pouliquen | 7 | 17 | 9 | 1 | 0.025 | 0 | Hydro |
| 12 | $V$_$50 \times 10^6$ | 50 | Pouliquen | 8 | 18 | 10 | 1 | 0.025 | 0 | Hydro |

not taken into account the heterogeneity of the material involved, grain/fluid interactions, and the transition phase from an initially coherent mass to a granular flow. However, the purpose of these simulations is to give the order of magnitude of waves, for a set of realistic submarine landslide scenarios, using state-of-the-art models. Thus, our results confirm the potential of advanced numerical models to build precise hazard maps suitable for use in land-use planning or the design of evacuation plans [Leone et al., 2021].

This approach can be advanced in different aspects. More precise scenarios could be determined using new geological data from future marine surveys and drilling in the targeted areas. From the modeling point of view, the simulation accuracy could be significantly improved by developing more advanced numerical models for landslide and tsunami waves accounting for non-hydrostatic effects, different coordinate systems for the landslide and the tsunami, grain–fluid interactions in the granular mass, and multilayer approaches for the landslide and tsunami wave. Another key improvement would be to account for uncertainties and develop probabilistic approaches in the simulated hazard maps [Løvholt et al., 2020], based notably on series of simulations using for example statistical emulation [e.g. Salmanidou et al., 2019].

## Conflicts of interest

Authors have no conflict of interest to declare.

## Acknowledgements

We thank staff scientists and crew for the data provided by MAYOBS 1 cruise that was funded by the CNRS-INSU TELLUS MAYOTTE program (SISMAYOTTE project). This study was supported by the Réseau de Surveillance Volcanologique et Sismologique de Mayotte (REVOSIMA). Since June 2019, all activities on Mayotte are funded by le Ministère de l'Enseignement Supérieur, de la Recherche et de l'Innovation (MESRI), le Ministère de la Transition Ecologique (MTE), le Ministère des Outremers (MOM), le Ministère de l'Intérieur (MI), and le Ministère des Armées with the support of the DIRMOM (Direction Interministérielle aux Risques Majeurs en Outremer) and the MAPPPROM (Mission d'appui aux politiques publiques pour la prévention des risques majeurs en Outremer) throughout the REVOSIMA. The work was also funded by the contract ERC-CG-2013-PE10-617472 SLIDEQUAKES along with the Spanish Government and FEDER through the Research Project MTM2015-70490-C2-2-R. This study contributes to the IdEx Université de Paris ANR contract ANR-18-IDEX-0001.

## Supplementary data

Supporting information for this article is available on the journal's website under https://doi.org/10.5802/crgeos.138 or from the author.

## References


Abadie, S., Morichon, D., Grilli, S. T., and Glockner, S. (2010). Numerical simulation of waves generated by landslides using a multiple-fluid Navier–Stokes model. *Coast. Eng.*, 57, 779–794.

Abadie, S., Paris, A., Ata, R., Le Roy, S., Arnaud, G., Poupardin, A., Clous, L., Heinrich, P., Harris, J. C., Pedreros, R., and Krien, Y. (2020). La Palma landslide tsunami: computation of the tsunami source with a calibrated multi-fluid Navier–Stokes model and wave impact assessment with propagation models of different types. *Nat. Hazards Earth Syst. Sci.*, 20, 3019–3038.

Abadie, S. M., Harris, J. C., Grilli, S. T., and Fabre, R. (2012). Numerical modeling of tsunami waves generated by the flank collapse of the Cumbre Vieja Volcano (La Palma, Canary Islands): Tsunami source and near field effects. *J. Geophys. Res.*, 117, article no. C05030.

Asunción, M. D., Castro, M. J., Fernández-Nieto, E. D., Mantas, J. M., Ortega Acosta, S., and González-Vida, J. M. (2013). Efficient GPU implementation of a two waves TVD-WAF method for the two-dimensional one layer shallow water system on structured meshes. *Comput. Fluids*, 80, 441–452.

Asunción-Hernández, M. D., Parés-Madroñal, C. M., Díaz-del Río-Español, V., Castro-Díaz, M. J., Macías-Sánchez, J., Vázquez, J. T., Fernández-Salas, L. M., Bárcenas-Gascón, P., González-Vida, J. M., and Morales-de Luna, T. (2012). *Deslizamientos submarinos y tsunamis en el Mar de Alborán. Un ejemplo de modelización numérica.* Instituto Espanol de Oceanographia.

Bontemps, N., Lacroix, P., Larose, E., Jara, J., and Taipe, E. (2020). Rain and small earthquakes maintain a slow-moving landslide in a persistent critical state. *Nat. Commun.*, 11(780), 1–10.

Bouchut, F., Fernández-Nieto, E. D., Mangeney, A., and Narbona-Reina, G. (2016). A two-phase two-layer model for fluidized granular flows with dilatancy effects. *J. Fluid Mech.*, 801, 166–221.

Brunet, M., Moretti, L., Le Friant, A., Mangeney, A., Fernández Nieto, E. D., and Bouchut, F. (2017). Numerical simulation of the 30–45 ka debris avalanche flow of Montagne Pelée volcano, Martinique: from volcano flank collapse to submarine emplacement. *Nat. Hazards*, 87, 1189–1222.

Bunya, S., Dietrich, J. C., Westerink, J. J., Ebersole, B. A., Smith, J. M., Atkinson, J. H., Jensen, R. E., Resio, D. T., Luettich, R. A., Dawson, C. N., Cardone, V. J., Cox, A. T., Powell, M. D., Westerink, H. J., and Roberts, H. J. (2010). A high-resolution coupled riverine flow, tide, wind, wind wave, and storm surge model for Southern Louisiana and Mississippi. Part I: Model development and validation. *Mon. Weather. Rev.*, 138(2), 345–377.

Castro Díaz, M. J., Ferreiro, A. M., García-Rodríguez, J. A., González-Vida, J. M., Macias, J., Parés, C., and Vázquez-Cendón, M. E. (2005). The numerical treatment of wet/dry fronts in shallow flows: application to one-layer and two-layer systems. *Math. Comput. Model.*, 42(3–4), 419–439.

Castro Díaz, M. J., Gallardo, J. M., and Parés, C. (2006). High order finite volume schemes based on reconstruction of states for solving hyperbolic systems with nonconservative products. Applications to shallow-water systems. *Math. Comput.*, 75, 1103–1134.

Castro Díaz, M. J., López, J. A., and Madroñal, C. P. (2008a). Finite volume simulation of the geostrophic adjustment in a rotating shallow-water system. *SIAM J. Sci. Comput.*, 31, 444–477.

Castro Díaz, M. J., Rebollo, T. C., Fernández-Nieto, E. D., Vida, J. M., and Parés, C. (2008b). Well-balanced finite volume schemes for 2D non-homogeneous hyperbolic systems. Application to the dam-break of Aznalcóllar. *Comput. Methods Appl. Mech. Eng.*, 197, 3932–3950.

Cesca, S., Letort, J., Razafindrakoto, H. N., Heimann, S., Rivalta, E., Isken, M. P., Nikkhoo, M., Passarelli, L., Petersen, G. M., Cotton, F., and Dahm, T. (2020). Drainage of a deep magma reservoir near Mayotte inferred from seismicity and deformation. *Nat. Geosci.*, 13, 87–93.

Chen, Q. (2006). Fully nonlinear Boussinesq-type equations for waves and currents over porous beds. *J. Eng. Mech.*, 132(2), 220–230.

Chen, Q., Kirby, J. T., Dalrymple, R. A., Shi, F., and Thornton, E. B. (2003). Boussinesq modeling of longshore currents. *J. Geophys. Res.*, 108(C11), article no. 3362.

De la Torre, Y., Lecacheux, S., Pedreros, R., and

Balouin, Y. (2008). Modélisation de la houle cyclonique dans le lagon de Mayotte. In *Xèmes Journées Nationales Génie Côtier*. Génie Civil, Sophia Antipolis.

Debeuf, D. (2004). *Etude de l'évolution volcano-structurale et magmatique de Mayotte, Archipel des Comores, océan Indien: approches structurales, pétrographique, géochimique et géochronologique*. PhD thesis, La Réunion University. 277 p.

Delannay, R., Valance, A., Mangeney, A., Roche, O., and Richard, P. (2017). Granular and particle-laden flows: from laboratory experiments to field observations. *J. Phys. D*, 50, article no. 053001.

Delgado-Sánchez, J. M., Bouchut, F., Fernández-Nieto, E. D., Mangeney, A., and Narbona-Reina, G. (2020). A two-layer shallow flow model with two axes of integration, well-balanced discretization and application to submarine avalanches. *J. Comput. Phys.*, 406, article no. 109186.

Di Risio, M., De Girolamo, P., and Beltrami, G. (2011). Forecasting landslide generated tsunamis: a review. In Marner, N.-A., editor, *The Tsunami Threat—Research and Technology*. IntechOpen, London.

Dondin, F. J.-Y., Heap, M. J., Robertson, R. E. A., Dorville, J.-F. M., and Carey, S. (2016). Flank instability assessment at Kick-'em-Jenny submarine volcano (Grenada, Lesser Antilles): A multidisciplinary approach using experiments and modeling. *Bull. Volcanol.*, 79(1), article no. 5.

Edwards, A. N. and Gray, J. M. (2014). Erosion–deposition waves in shallow granular free-surface flows. *J. Fluid Mech.*, 762, 35–67.

Edwards, A. N., Russell, A. S., Johnson, C. G., and Gray, J. M. (2019). Frictional hysteresis and particle deposition in granular free-surface flows. *J. Fluid Mech.*, 875, 1058–1095.

Edwards, A. N., Viroulet, S., Kokelaar, B. P., and Gray, J. M. (2017). Formation of levees, troughs and elevated channels by avalanches on erodible slopes. *J. Fluid Mech.*, 823, 278–315.

Escalante, C., Dumbser, M., and Castro, M. J. (2019). An efficient hyperbolic relaxation system for dispersive non-hydrostatic water waves and its solution with high order discontinuous Galerkin schemes. *J. Comput. Phys.*, 394, 385–416.

Esposti Ongaro, T., de'Michieli Vitturi, M., Cerminara, M., Fornaciai, A., Nannipieri, L., Favalli, M., Calusi, B., Macías, J., Castro, M. J., Ortega, S., González-Vida, J. M., and Escalante, C. (2021). Modeling tsunamis generated by submarine landslides at Stromboli volcano (Aeolian Islands, Italy): a numerical benchmark study. *Front. Earth Sci.*, 9, article no. 628652.

Fernández-Nieto, E. D., Bouchut, F., Bresch, D., Díaz, M. J., and Mangeney, A. (2008). A new Savage-Hutter type model for submarine avalanches and generated tsunami. *J. Comput. Phys.*, 227, 7720–7754.

Feuillet, N., Jorry, S. J., Crawford, W. C., Deplus, C., Thinon, I., Jacques, E., Saurel, J., Lemoine, A., Paquet, F., Satriano, C., Aiken, C., Foix, O., Kowalski, P., Laurent, A., Rinnert, E., Cathalot, C., Donval, J. P., Guyader, V., Gaillot, A., Scalabrin, C., Moreira, M., Peltier, A., Beauducel, F., Grandin, R., Ballu, V., Daniel, R., Pelleau, P., Gomez, J., Besançon, S., Géli, L., Bernard, P., Bachélery, P., Fouquet, Y., Bertil, D., Lemarchand, A., and Van der Woerd, J. (2021). Birth of a large volcanic edifice offshore Mayotte via lithosphere-scale dyke intrusion. *Nat. Geosci.*, 14, 787–795.

Fine, I. V., Rabinovich, A. B., Thomson, R. E., and Kulikov, E. A. (2003). *Numerical Modeling of Tsunami Generation by Submarine and Subaerial Landslides*. Springer, Cham.

Fine, I. V., Rabinovichb, A. B., Bornholdt, B. D., Thomson, R. E., and Kulikovb, E. A. (2005). The Grand Banks landslide-generated tsunami of November 18, 1929: preliminary analysis and numerical modeling. *Mar. Geol.*, 215, 45–57.

Fischer, J.-T., Kowalski, J., and Pudasaini, S. P. (2012). Topographic curvature effects in applied avalanche modeling. *Cold Reg. Sci. Technol.*, 74–75, 21–30.

Garres-Díaz, J., Fernández-Nieto, E. D., Mangeney, A., and Luna, T. M. (2021). A weakly non-hydrostatic shallow model for dry granular flows. *J. Sci. Comput.*, 86(2), article no. 25.

Giachetti, T., Paris, R., Kelfoun, K., and Ontowirjo, B. (2012). Tsunami hazard related to a flank collapse of Anak Krakatau Volcano, Sunda Strait, Indonesia. *Geol. Soc. Lond. Spec. Publ.*, 361, 79–90.

Giachetti, T., Paris, R., Kelfoun, K., and Pérez-Torrado, F. J. (2011). Numerical modelling of the tsunami triggered by the Güimar debris avalanche, Tenerife (Canary Islands): comparison with field-based data. *Mar. Geol.*, 284, 189–202.

Gittings, M. L. (1992). SAIC's adaptive grid Eulerian hydrocode. In *Defense Nuclear Agency Numeri-*

*cal Methods Symposium*, pages 28–30. Defense Nuclear Agency, Alexandria, VA.

González-Vida, J. M., Macías, J., Castro, M. J., Sánchez-Linares, C., de la Asunción, M., Ortega-Acosta, S., and Arcas, D. (2019). The Lituya Bay landslide-generated mega-tsunami—numerical simulation and sensitivity analysis. *Nat. Hazards Earth Syst. Sci.*, 19, 369–388.

Gouhier, M. and Paris, R. (2019). SO2 and tephra emissions during the December 22, 2018 Anak Krakatau eruption. *Volcanica*, 2(2), 91–103.

Grilli, S., Tappin, D., Carey, S., Watt, S., Ward, S., Grilli, A., Engwell, S., Zhang, C., Kirby, J., Schambach, L., and Muin, M. (2019). Modelling of the tsunami from the December 22, 2018 lateral collapse of Anak Krakatau volcano in the Sunda Straits, Indonesia. *Sci. Rep.*, 9, article no. 11946.

Grilli, S. T., Zhang, C., Kirby, J. T., Grilli, A. R., Tappin, D. R., Watt, S. F. L., Hunt, J. E., Novellino, A., Engwell, S., Nurshal, M. E. M., Abdurrachman, M., Cassidy, M., Madden-Nadeau, A. L., and Day, S. (2021). Modeling of the Dec. 22nd 2018 Anak Krakatau volcano lateral collapse and tsunami based on recent field surveys: Comparison with observed tsunami impact. *Mar. Geol.*, 440, article no. 106566.

Gylfadóttir, S., Kim, J., Helgason, J. K., Brynjólfsson, S., Hoskuldsson, A., Jóhannesson, T., Harbitz, C., and Løvholt, F. (2017). The 2014 Lake Askja rockslide-induced tsunami: Optimization of numerical tsunami model using observed data. *J. Geophys. Res. Oceans*, 122, 4110–4122.

Heinrich, P., Boudon, G., Komorowski, J., Sparks, R. S., Herd, R. A., and Voight, B. (2001a). Numerical simulation of the December 1997 Debris Avalanche in Montserrat, Lesser Antilles. *Geophys. Res. Lett.*, 28, 2529–2532.

Heinrich, P., Piatanesi, A., and Hébert, H. (2001b). Numerical modelling of tsunami generation and propagation from submarine slumps: the 1998 Papua New Guinea event. *Geophys. J. Int.*, 145, 97–111.

Heinrich, Ph., Mangeney, A., Guilbourg, S., Roche, R., Boudon, G., and Cheminée, J. L. (1998). Numerical simulation of a potential landslide-generated tsunami in Monserrat. *Geophys. Res. Lett.*, 25(19), 3697–3700.

Jiang, L. and LeBlond, P. H. (1992). The coupling of a submarine slide and the surface waves which it generates. *J. Geophys. Res.*, 97, 12731–12744.

Kelfoun, K., Druitt, T., van Wyk de Vries, B., and Guilbaud, M.-N. (2008). Topographic reflection of the Socompa debris avalanche, Chile. *Bull. Volcanol.*, 70, 1169–1187.

Kelfoun, K., Giachetti, T., and Labazuy, P. (2010). Landslide–generated tsunamis at Réunion Island. *J. Geophys. Res. Earth Surf.*, 115, article no. F04012.

Kennedy, A. B., Kirby, J. T., Chen, Q., and Dalrymple, R. A. (2001). Boussinesq-type equations with improved nonlinear performance. *Wave Motion*, 33, 225–243.

Kirby, J., Grilli, S., Horrillo, J., Liu, P., Nicolsky, D., Abadie, S., Ataie-Ashtiani, B., Castro, M., Clous, L., Escalante Sánchez, C., Fine, I., González-Vida, J., Løvholt, F., Lynett, P., Ma, G., Macías, J., Ortega, S., Shi, F., Yavari, S., and Zhang, C. (2022). Validation and inter-comparison of models for landslide tsunami generation. *Ocean Model.*, 170, article no. 101943.

Kirby, J. T., Shi, F., Tehranirad, B., Harris, J. C., and Grilli, S. T. (2013). Dispersive tsunami waves in the ocean: Model equations and sensitivity to dispersion and Coriolis effects. *Ocean Model.*, 62, 39–55.

Kunkel, C. M., Hallberg, R., and Oppenheimer, M. (2006). Coral reefs reduce tsunami impact in model simulations. *Geophys. Res. Lett.*, 33, article no. L23612.

Le Friant, A., Ishizuka, O., Boudon, G., Palmer, M. R., Talling, P., Villemant, B., Adachi, T., Aljahdali, M., Breitkreuz, C., Brunet, M., Caron, B., Coussens, M., Deplus, C., Endo, D., Feuillet, N., Fraas, A. J., Fujinawa, A., Hart, M. B., Hatfield, R. G., Hornbach, M., Jutzeler, M., Kataoka, K. S., Komorowski, J.-C., Lebas, E., Lafuerza, S., Maeno, F., Manga, M., Martínez-Colón, M., McCanta, M., Morgan, S., Saito, T., Slagle, A., Sparks, S., Stinton, A., Stroncik, N., Subramanyam, K. S. V., Tamura, Y., Trofimovs, J., Voight, B., Wall-Palmer, D., Wang, F., and Watt, S. F. L. (2015). Submarine record of volcanic island construction and collapse in the Lesser Antilles arc: First scientific drilling of submarine volcanic island landslides by IODP Expedition 340. *Geochem. Geophys. Geosyst.*, 16(2), 420–442.

Le Friant, A., Lebas, E., Brunet, M., Lafuerza, S., Hornbach, M., Coussens, M., Watt, S. F. L., Cassidy, M., and Talling, P. J. (2019). Submarine landslides around volcanic islands: A review of what can be learned from the Lesser Antilles Arc. In Ogata, K., Festa, A., and Pini, G. A., editors, *Submarine Land-*

*slides: Subaqueous Mass Transport Deposits from Outcrops to Seismic Profiles*. AGU.

Le Friant, A. L., Heinrich, P., Deplus, C., and Boudon, G. (2003). Numerical simulation of the last flank-collapse event of Montagne Pelée, Martinique, Lesser Antilles. *Geophys. Res. Lett.*, 30(2), article no. 1034.

Le Roy, S., Pedreros, R., Monfort, D., and Terrier, M. (2015). Simulations numériques de tsunamis sur la côte méditerrannéenne Française: le cas d'Antibes. *La Houille Blanche*, 101(6), 12–20.

Le Roy, S. A. and Legendre, Y. (2017). Détermination de la submersion marine liée aux tsunamis en Martinique. Rapport final BRGM/RP-66547-FR p 177p.

Lebas, E., Lebas, E., Friant, A. L., Deplus, C., and Voogd, B. D. (2018). Understanding the evolution of an oceanic intraplate volcano from seismic reflection data: A new model for La Réunion, Indian Ocean. *J. Geophys. Res.*, 123, 1035–1059.

Lemoine, A., Briole, P., Bertil, D., Roullé, A., Foumelis, M., Thinon, I., Raucoules, D., de Michele, M., Valty, P., and Hoste Colomer, R. (2020a). The 2018–2019 seismo-volcanic crisis east of Mayotte, Comoros islands: seismicity and ground deformation markers of an exceptional submarine eruption. *Geophys. J. Int.*, 223, 22–44.

Lemoine, A., Pedreros, R., and Filippini, A. (2020b). Scénarios d'impact de tsunamis pour Mayotte. BRGM/RP-69869-FR.

Leone, F., Gherardi, M., Péroche, M., Idaroussi, F., and Lagahé, E. (2021). Planifier les évacuations préventives face au risque de tsunami à Mayotte. https://arcg.is/1be4iC0. Rapport intermédiaire du projet EVACTSU Mayotte pour le compte de la DIRMOM.

Lipman, P. W., Normark, W. R., Moore, J. G., Wilson, J. B., and Gutmacher, C. E. (1988). The giant submarine Alika Debris slide, Mauna Loa, Hawaii. *J. Geophys. Res.*, 93, 4279–4299.

Liu, P. L.-F., Higuera, P., Husrin, S., Prasetya, G. S., Prihantono, J., Diastomo, H., Pryambodo, D. G., and Susmoro, H. (2020). Coastal landslides in Palu Bay during 2018 Sulawesi earthquake and tsunami. *Landslides*, 17, 2085–2098.

Løvholt, F., Glimsdal, S., and Harbitz, C. (2020). On the landslide tsunami uncertainty and hazard. *Landslides*, 17, 2301–2315.

Løvholt, F., Pedersen, G., and Gisler, G. (2008). Oceanic propagation of a potential tsunami off La Palma Island. *J. Geophys. Res.*, 113(C9), article no. C09026.

Lucas, A., Mangeney, A., and Ampuero, J. P. (2014). Frictional velocity-weakening in landslides on Earth and on other planetary bodies. *Nat. Commun.*, 5, article no. 3417.

Ma, G., Kirby, J. T., Hsu, T., and Shi, F. (2015). A two-layer granular landslide model for tsunami wave generation: Theory and computation. *Ocean Model.*, 93, 40–55.

Macías, J., Castro, M. J., Ortega, S., and González-Vida, J. M. (2020). Performance assessment of Tsunami-HySEA model for NTHMP tsunami currents benchmarking. Field cases. *Ocean Model.*, 152, article no. 101645.

Macías, J., Escalante, C., and Castro, M. J. (2021). Multilayer-HySEA model validation for landslide-generated tsunamis—Part 2: Granular slides. *Nat. Hazards Earth Syst. Sci.*, 21, 791–805.

Macías, J., Escalante Sánchez, C., Castro, M., González Vida, J., and Ortega, S. (2017). HySEA model. NTHMP Landslide Benchmarking Results.

Macías, J., Vazquez, J. T., Fernández-Salas, L. M., González-Vida, J. M., Bárcenas, P., Castro, M. J., Díaz-del Río, V., and Alonso, B. (2015). The Al-Borani submarine landslide and associated tsunami. A modelling approach. *Mar. Geol.*, 361, 79–95.

Majd, M. and Sanders, B. F. (2014). The LHLLC scheme for Two-Layer and Two-Phase transcritical flows over a mobile bed with avalanching, wetting and drying. *Adv. Water Resour.*, 67, 16–31.

Mangeney, A., Bouchut, F., Thomas, N., Vilotte, J., and Bristeau, M. (2007a). Numerical modeling of self-channeling granular flows and of their levee-channel deposits. *J. Geophys. Res. Earth Surf.*, 112, article no. F02017.

Mangeney, A., Heinrich, P., Roche, R., Boudon, G., and Cheminée, J. L. (2000). Modeling of debris avalanche and generated water waves: Application to real and potential events in Montserrat. *Phys. Chem. Earth Part A-Solid Earth Geodesy*, 25, 741–745.

Mangeney, A., Tsimring, L. S., Volfson, D., Aranson, I. S., and Bouchut, F. (2007b). Avalanche mobility induced by the presence of an erodible bed and associated entrainment. *Geophys. Res. Lett.*, 34, article no. L22401.

Maramai, A., Graziani, L., and Tinti, S. (2005).

Tsunamis in the Aeolian Islands (southern Italy): A review. *Mar. Geol.*, 215, 11–21.

MEDDE (2014). Guide Méthodologique. Plan de Prévention des Risques Littoraux, 05-2014, 169 p.

Mercury, N., Lemoine, A., Bertil, D., Vanderwoerd, J., Doubre, C., and Hoste-Colomer, R. (2020). The 2018–2020 seismo-volcanic crisis, east of Mayotte, Comoros islands: in-depth study of poorly instrumented first months of crisis. In *AGU Fall Meeting Abstracts*, volume 2020, pages V040–0007. AGU.

Moore, J. G., Clague, D. A., Holcomb, R. T., Lipman, P. W., Normark, W. R., and Torresan, M. E. (1989). Prodigious submarine landslides on the Hawaiian Ridge. *J. Geophys. Res.*, 94, 17465–17484.

Moretti, L., Allstadt, K. E., Mangeney, A., Capdeville, Y., Stutzmann, É., and Bouchut, F. (2015). Numerical modeling of the Mount Meager landslide constrained by its force history derived from seismic data. *J. Geophys. Res.*, 120, 2579–2599.

Papadopoulos, G. and Kortekaas, S. (2003). Characteristics of landslide generated tsunamis from observational data. In *Submarine Mass Movements and Their Consequences*, volume 19, pages 367–374. Springer, Dordrecht.

Paris, A., Heinrich, P., Paris, R., and Abadie, S. (2020). The December 22, 2018 Anak Krakatau, Indonesia, landslide and tsunami: Preliminary modeling results. *Pure Appl. Geophys.*, 177, 571–571.

Paris, A., Okal, E. A., Guerin, C., Heinrich, P., Schindelé, F., and Hébert, H. (2019). Numerical modeling of the June 17, 2017 landslide and tsunami events in Karrat Fjord, West Greenland. *Pure Appl. Geophys.*, 176, 3035–3057.

Pelinovsky, E. N., Zahibo, N., Dunkley, P., Edmonds, M., Herd, P., Talipove, T., Kozelkov, A., and Nikolkina, I. (2004). Tsunami generated by the volcano eruption on July 12–13, 2003 at Montserrat, Lesser Antilles. *Sci. Tsunami Hazards*, 22, 44–57.

Peruzzetto, M., Komorowski, J., Le Friant, A., Rosas-Carbajal, M., Mangeney, A., and Legendre, Y. (2019). Modeling of partial dome collapse of La Soufrière of Guadeloupe volcano: implications for hazard assessment and monitoring. *Sci. Rep.*, 9, article no. 13105.

Peruzzetto, M., Mangeney, A., Bouchut, F., Grandjean, G., Levy, C., Thiery, Y., and Lucas, A. (2021). Topography curvature effects in thin-layer models for gravity-driven flows without bed erosion. *J. Geophys. Res. Earth Surf.*, 126, article no. e2020JF005657.

Poisson, B. and Pedreros, R. (2010). Numerical modelling of historical landslide-generated tsunamis in the French Lesser Antilles. *Nat. Hazards Earth Syst. Sci.*, 10, 1281–1292.

Popinet, S. (2015). A quadtree-adaptive multigrid solver for the Serre-Green-Naghdi equations. *J. Comput. Phys.*, 302, 336–358.

Pouliquen, O. (1999). Scaling laws in granular flows down rough inclined planes. *Phys. Fluids*, 11, 542–548.

Pouliquen, O. and Forterre, Y. (2002). Friction law for dense granular flows: application to the motion of a mass down a rough inclined plane. *J. Fluid Mech.*, 453, 133–151.

Rauter, M., Viroulet, S., Gylfadottir, S., Fellin, W., and Løvholt, F. (2022). Granular porous landslide tsunami modelling—the 2014 Lake Askja flank collapse. *Nat. Commun.*, 13, article no. 678.

Rocha, F. M., Johnson, C. G., and Gray, J. M. (2019). Self-channelisation and levee formation in monodisperse granular flows. *J. Fluid Mech.*, 876, 591–641.

Roger, J. (2019). Potential tsunami hazard related to the seismic activity East of Mayotte Island, Comoros Archipelago. *Sci. Tsunami Hazards: J. Tsunami Soc. Int.*, 38(3), 118–131.

Rohmer, J., Rousseau, M., Lemoine, A., Pedreros, R., Lambert, J., and Benki, A. (2017). Source characterisation by mixing long-running tsunami wave numerical simulations and historical observations within a metamodel-aided ABC setting. *Stoch. Environ. Res. Risk Assess.*, 32, 967–984.

Romano, A. (2020). Physical and numerical modeling of landslide-generated tsunamis: A review. In Essa, K. S. et al., editors, *Geophysics and Ocean Waves Studies*. IntechOpen, London.

Russell, A. S., Johnson, C. G., Edwards, A. N., Viroulet, S., Rocha, F. M., and Gray, J. M. (2019). Retrogressive failure of a static granular layer on an inclined plane. *J. Fluid Mech.*, 869, 313–340.

Salmanidou, D., Heidarzadeh, M., and Guillas, S. (2019). Probabilistic landslide-generated tsunamis in the Indus Canyon, NW Indian Ocean, using statistical emulation. *Pure Appl. Geophys.*, 176, 1–16.

Salmanidou, D. M., Georgiopoulou, A., Guillas, S., and Dias, F. (2018). Rheological considerations for the modelling of submarine sliding at Rockall Bank, NE Atlantic Ocean. *Phys. Fluids*, 30, article no. 030705.

Sassa, K., Dang, K., Yanagisawa, H., and He, B. (2016). A new landslide-induced tsunami simulation model and its application to the 1792 Unzen-Mayuyama landslide-and-tsunami disaster. *Landslides*, 13, 1405–1419.

Satake, K. (2001). Tsunami modeling from submarine landslides. *ITS Proc.*, 6(6–4), 665–674.

Saurel, J.-M., Jacques, E., Aiken, C., Lemoine, A., Retailleau, L., Lavayssière, A., Foix, O., Dofal, A., Laurent, A., Mercury, N., Crawford, W., Lemarchand, A., Daniel, R., Pelleau, P., Bès de Berc, M., Roullé, A., Broucke, C., Colombain, A., Besançon, S., Guyavarch, P., Kowalski, P., Roudaut, M., Battaglia, J., Bodihar, S., Bouin, M.-P., Canjamale, K., Desfete, N., Doubre, C., Dretzen, R., Ferrazzini, V., Fontaine, F., Géli, L., Griot, C., Grunberg, M., Guzel, E. C., Hoste Colomer, R., Lambotte, S., Léger, F., Vergne, J., Satriano, C., Tronel, F., Van der Woerd, J., Feuillet, N., Fouquet, Y., Stéphan, J., Rinnert, E., and Thinon, I. (2022). Mayotte seismic crisis: building knowledge in near real-time by combining land and ocean-bottom seismometers, first results. *Geophys. J. Int.*, 228(2), 1281–1293.

Scalabrin, C., Feuillet, N., Fouquet, Y., Thinon, I., Jorry, S., Gaillot, A., Guérin, C., Komorowski, J.-C., Rinnert, E., and Cathalot, C. (2021). Acoustic plumes of the 2019 Mayotte submarine volcanic eruption. In *AGU Fall Meeting 2021*. AGU, Washington, DC.

Shi, F., Kirby, J. T., Harris, J. C., Geiman, J. D., and Grilli, S. T. (2012). A high-order adaptive time-stepping TVD solver for Boussinesq modeling of breaking waves and coastal inundation. *Ocean Model.*, 43, 36–51.

Thinon, I., Lemoine, A., Leroy, S., Berthod, C., Bernard, J., Bignon, J., Boymond, P., Bujan, S., Canva, A., Chamot-Rooke, N., Clouard, V., Dassie, E., Delescluse, M., Doubre, C., Famin, V., Roche, V., Rolandone, F., Rusquet, A., Sadeski, L., Scalabrin, C., Abdoulhamid, S. A., van Der Woerd, J., Watremez, L., Zaragosi, S., Michon, L., Bachelery, P., Deplus, C., and Sauter, D. (2021). Discovery of recent volcanic and tectonic provinces along the Comoros archipelago (North Mozambique Channel). Preliminary results of the SISMAORE oceanographic cruise (ANR-COYOTES project). RST—27e édition de la Réunion des Sciences de la Terre, Lyon, France. hal-03375817v2.

Thran, M. C., Brune, S., Webster, J. M., Dominey-Howes, D., and Harris, D. (2021). Examining the impact of the Great Barrier Reef on tsunami propagation using numerical simulations. *Nat. Hazards*, 108, 347–388.

Tinti, S., Pagnoni, G., and Zaniboni, F. (2006). The landslides and tsunamis of the 30th of December 2002 in Stromboli analysed through numerical simulations. *Bull. Volcanol.*, 68, 462–479.

Tonelli, M. and Petti, M. (2009). Hybrid finite volume—finite difference scheme for 2DH improved Boussinesq equations. *Coast. Eng.*, 56, 609–620.

Voight, B., Janda, R. J., Glicken, H., and Douglass, P. M. (1983). Nature and mechanics of the Mount St Helens rockslide-avalanche of 18 May 1980. *Géotechnique*, 33, 243–273.

Ward, S. N. and Day, S. (2003). Ritter island volcano—lateral collapse and the tsunami of 1888. *Geophys. J. Int.*, 154, 891–902.

Watt, S. F., Talling, P. J., and Hunt, J. E. (2014). New insights into the emplacement dynamics of volcanic island landslides. *Oceanography*, 27(2), 46–57.

Watts, P., Grilli, S. T., Kirby, J. T., Fryer, G. J., and Tappin, D. R. (2003). Landslide tsunami case studies using a Boussinesq model and a fully nonlinear tsunami generation model. *Nat. Hazards Earth Syst. Sci.*, 3, 391–402.

Wei, G., Kirby, J. T., Grilli, S. T., and Subramanya, R. (1995). A fully nonlinear Boussinesq model for surface waves. Part 1. Highly nonlinear unsteady waves. *J. Fluid Mech.*, 294, 71–92.

Yavari-Ramshe, S. and Ataie-Ashtiani, B. (2015). A rigorous finite volume model to simulate subaerial and submarine landslide-generated waves. *Landslides*, 14, 203–221.

Yavari-Ramshe, S. and Ataie-Ashtiani, B. (2016). Numerical modeling of subaerial and submarine landslide-generated tsunami waves—recent advances and future challenges. *Landslides*, 13, 1325–1368.

Zhou, H., Moore, C. W., Wei, Y., and Titov, V. V. (2011). A nested-grid Boussinesq-type approach to modelling dispersive propagation and runup of landslide-generated tsunamis. *Nat. Hazards Earth Syst. Sci.*, 11, 2677–2697.

*Comptes Rendus*
*Géoscience — Sciences de la Planète*
**2022**, Vol. 354, Special Issue S2, p. 391-415
https://doi.org/10.5802/crgeos.149

The Mayotte seismo-volcanic crisis of 2018-2021 in the Comoros archipelago (Mozambique channel) / *La crise sismo-volcanique de 2018-2021 de Mayotte dans l'archipel des Comores (Canal du Mozambique)*

# Mayotte's seismo-volcanic "crisis" in news accounts (2018–2021)

## *La crise sismo-volcanique de Mayotte dans la presse (2018–2021)*

**Maud H. Devès** [*, a, b], **Sophie Moirand** [c], **Louise Le Vagueresse** [a] **and Geoffrey Robert** [a]

[a] Université Paris Cité, Institut de physique du globe de Paris, CNRS, F-75005 Paris, France

[b] Université Paris Cité, Centre de Recherche Psychanalyse Médecine et Société, CNRS, F-75006 Paris, France

[c] Université Sorbonne nouvelle, EA CLESTHIA, Axe Sens et Discours, Maison de la Recherche, 4 rue des Irlandais, 75005 Paris, France

*E-mails:* deves@ipgp.fr (M. H. Devès), sophie.moirand@sorbonne-nouvelle.fr (S. Moirand), levagueresse@ipgp.fr (L. Le Vagueresse), robert@ipgp.fr (G. Robert)

**Abstract.** Mayotte's seismo-volcanic crisis gave rise to extensive media coverage in the local, regional and national daily press. Analyzing the *news narratives* allows us to bring to light the representations that readers are confronted with when they try to inform themselves about the situation. This article brings together the sciences of risk, language and communication in order to analyse these *pluri-vocal* narratives, in which the scientific community is given pride of place. It shows how the voices of the main actors (the inhabitants, the administrative and scientific authorities) are put on the stage, conveying differing representations, differing forms of explanation and contributing to an effect of "enunciatory muddling". It aims to provide food for thought for people called upon to intervene in the media, in Mayotte or elsewhere.

**Résumé.** La crise sismo-volcanique de Mayotte a donné lieu à une large couverture médiatique dans la presse quotidienne locale, régionale et nationale. L'analyse de ces *récits médiatiques* permet de mettre en lumière les représentations auxquelles les lecteurs sont confrontés lorsqu'ils tentent de s'informer sur la situation. Cet article associe les sciences du risque, du langage et de la communication afin d'analyser ces récits *à plusieurs voix*, dans lesquels la place accordée à la communauté scientifique apparaît centrale. Il montre comment les paroles des principaux acteurs (la population, les autorités administratives et les scientifiques) sont mises en scène, véhiculant des représentations qui empruntent à différentes formes et fonctions de l'explication et contribuant à un effet de « brouillage énonciatif ». Il vise ainsi à nourrir la réflexion des personnes conduites à intervenir dans les médias, à Mayotte ou ailleurs.

* Corresponding author.

**Keywords.** Seismo-volcanic crisis, Mayotte, Press narratives, Risk communication, Public information, Explanation, Uncertainty.

**Mots-clés.** Crise sismo-volcanique, Mayotte, Récit médiatique, Communication des risques, Information des populations, Explication, Incertitude.

*Published online: 21 October 2022, Issue date: 17 January 2023*

## 1. Introduction

The news accounts that the media builds around events such as health crises, earthquakes, volcanic eruptions, tsunamis, and so on, contribute to how the main actors—including the populations exposed to the event—perceive, interpret and react in the face of risk [Coleman, 1993, Quarantelli, 2002, Wachinger et al., 2013]. The local and national media constitute a privileged source of information, in particular in crisis situations when people are searching for information to help them decide upon a course of action to protect themselves and their close ones [Burkhart, 1990, Allan et al., 2000, Scanlon, 2007]. Furthermore, the media are closely followed by crisis management teams, impacting upon their communication strategies [Fisher III, 1994, Rodriguez et al., 2007]. Further still, many studies have shown that the adequate informing of populations nowadays constitutes one of the principal levers by which to progress towards more efficient risk management [Courant et al., 2021]. Thus, news reports, and notably *real time* news reports in the daily media, constitute an important, but still understudied, object of research for risk specialists.

What scientists have called the Mayotte seismo-volcanic "crisis" gave rise to wide media coverage not only in the local daily press, but also in the regional, national and, less extensively, international press. The present article is the result of interdisciplinary work bringing together earth sciences, risk sciences and language and communication sciences. It relates the observation, description and analysis of published news reports concerned with Mayotte's seismo-volcanic "crisis". The analysis of the news reports on this event brings to light the *representations* that readers of the press are confronted with when they try to inform themselves about the situation. This study tackles the question of how populations at risk are kept abreast of events. It complements the recent works carried out by Fallou et al. [2020] on how Mayotte's inhabitants seized upon social media in order to overcome the sense of a lack of information at the start of the crisis, and by Devès et al. [2022] on the discrepancy that exists between the information published by those in charge of the monitoring and management of risk and the general expectations of populations at risk.

Section 2 relates some elements of the political and societal context of the "crisis". Section 3 presents the theoretical and methodological background to the analysis: the choice of "discursive moments" and the analysis of "small corpora" to analyze items in current news affairs as well as elements of reflection on the news accounts. Section 4 aims to acquaint the reader with the corpus and to shed light on some of its key properties, and in particular the explicative aim of these accounts. Section 5 gives an overview of the various forms and functions of explanation that have been mobilized, to the extent that "to tell is to explain," "the act of narrating (being) an ordering of the real, designed to understand it" [Arquembourg and Lambert, 2005, p. 7]. Section 6 concludes with lessons that can be learnt from analysis of the news accounts, in the hope of feeding reflection on the part of those led to intervene in the media or in response to the media, in Mayotte or in the framework of other similar events.

## 2. Political and social context of the seismo-volcanic "crisis"

We shall first relate some elements of the political and social context that contributed to the transformation of a seismo-volcanic phenomenon with, so far—and as discussed below—relatively minor consequence, into a crisis for Maore society. Geoscientists are accustomed to speaking of seismic-volcanic "crises", although the use of the term "crisis" is not always relevant to disaster risk management definitions. However, in the case of Mayotte, the observed activity did indeed give rise, at least initially, to a crisis situation that required the intervention of the authorities in charge of civil protection and crisis management.

The activity started on the night of 10 to 11 May 2018 with an earthquake of magnitude ML 4.3 felt by the population. Seismicity intensified on 15 May 2018 with several earthquakes of magnitude >4, all largely felt, and an event of magnitude ML 5.8 (MW 5.9) [Lemoine et al., 2020]. Although diminishing over time, seismic activity has continued since and is still active at the time of writing. Prior to May 2018, regional instrumental seismicity was known to be moderate [Roulle et al., 2019] but the ability to identify and precisely locate the earthquakes was hindered by a lack of proper instrumentation. The geodynamic context of the zone had been little studied and there were large uncertainties about the nature of the seismicity, its cause and its possible evolution.

The earthquakes affected a vulnerable territory. Mayotte, which became a French Department in 2011, is marked by great poverty and high social inequality [Roinsard, 2014]. In a population of 256,000, 77% live under the poverty line and over 30% are unemployed, 48% are foreign (and often undocumented), 30% have no access to clean drinking water, and four in ten live in informal housing [INSEE, 2021 with data of 2017]. Mayotte's multiculturalism is a wealth that can prove difficult to manage for the authorities whose duty is to inform the widest possible public: 45% of the population is from the Comoros [INSEE, 2021], and while French remains the official language, about 37% of the population do not speak it [INSEE, 2021]. Oral culture is the dominant one and the commonly spoken languages are Shimaore and Shibushi. Ninety-five percent of the population is Muslim [Ministère des Outre-Mer, 2016] and there is no real integration between the traditional culture of the villages and the more westernized culture of large cities [Lambek, 2018]. The relationship with state authorities is also complicated by the island's colonial past and by a sense of disappointment among the population, who expected more rapid changes to bring the island up to French standards after departmentalization in 2011 [Roinsard, 2019]. Since then, Mayotte has been regularly shaken by social crises. Widespread strikes and roadblocks had been marring everyday life on the island for several months when the seismic crisis began [Roinsard, 2019, Mori, 2021]. Lastly, the absence in living memory of seismic and volcanic events in Mayotte meant that part of the inhabitants were relatively naïve about such risks [although people coming from the neighboring Comoros islands might have experienced previous seismic and volcanic crises as four eruptions occurred in 2005, 2006 and 2007, see Morin et al., 2016].

Although the earthquakes were of moderate intensity, they affected vulnerable buildings, and their repetition caused the appearance of cracks, leading some municipalities to close schools [Sira et al., 2018]. Local observers reported strong anxiety among inhabitants, many people leaving their houses to sleep outside [Mori, 2021, Fallou and Bossu, 2019, Fallou et al., 2020]. They also testified to a general feeling of confusion linked to the unfamiliar nature of the hazard and to a lack of public information. The mobilization of scientists, whom the state tasked with finding an "explanation" for the tremors felt by the inhabitants, was made more complicated by the distance from mainland France (where most of the expert earth-science institutions are located) and by the red tapism around the raising of funds necessary for scientific instrumentation in the zone [Devès et al., 2022]. It would take a whole year before the official declaration of the discovery of the largest underwater eruption ever recorded, at around 30 miles off the Mayotte coast. During this lapse of time, rumors circulated [Fallou et al., 2020] and both the people and their representatives became impatient, criticizing a "chaotic" and sometimes contradictory communication [cf. the questions addressed to the government by the Mayotte deputy in Ali, 2018, as well as the open letter addressed to the authorities and the scientists by a citizens' collective in February 2019, Picard, 2019]. The official announcement of the creation of a Scientific Network for Volcanological and Seismological Monitoring in Mayotte (REVOSIMA: Réseau scientifique de surveillance volcanologique et sismologique de Mayotte), which was tasked with improving the state of knowledge, and monitoring and identifying risks linked to this unusual seismo-volcanic activity, finally took place one year and four months after the start of the seismic "crisis" in August 2019, during a visit from the Minister of the Overseas (article in the *Journal de Mayotte*, 27-08-2019). At the time of writing, REVOSIMA is still active, and in spite of significant effort and constant progress regarding instrumentation and knowledge (reported in the other articles in this same issue), uncertainties remain strong, in particular concerning the possible evolution of the activity [Feuillet et al., 2021].

The initial communication crisis seems to have eased in part nowadays. This is probably, as Devès et al. [2022] suggest, due to the combination of several factors: better organization of communication—likewise made more consistent by scientific advances, the perceived decline in seismic activity, and the gradual disinterest of the inhabitants in a hazard whose manifestations are rare and indirect. But the scientists and the civil services are still regularly taken to task, especially on social media [see the recent commentaries by members of the Facebook STTM group reported on by Devès et al., 2022].

## 3. An interdisciplinary approach to media accounts

The approach adopted here is based on a theoretical and conceptual background borrowed from the sciences of language and communication (Section 3.1). This underpins the choice of categories of analysis: the notions of narrative (Ricoeur) and discursive formation (Foucault), borrowed from philosophy, those of polyphony, dialogism and spheres of language activity, reworked on the basis of the work of Bakhtin and Voloshinov [Todorov, 1981], as well as that of social actor, borrowed from *Critical Discourse Analysis* [Fairclough, 2003, Van Leeuwen, 2009]. This also determines the methodological approach adopted for the collection (Section 3.2) and analysis of data (Section 3.3). Interdisciplinarity relies on the fact that risk sciences are necessary to understand the context of production of the media discourses. The work on a media corpus has to be completed by a work on a "reference corpus". The latter aims at documenting and understanding contextual elements (which can be scientific, historical, political, sociological). Such an understanding is essential to a sound analysis of media discourses. Working in interdisciplinarity also led us to reexamine concepts and notions that were used differently in our core disciplines. Hence, we explored the role and function of explanation, risk and uncertainty, both in the discourse of the daily press but also in the speech of social actors (as it is reported by the press).

### 3.1. *Theoretical positioning*

Unlike historical accounts and novelistic narratives, news reports are not produced in line with an end that is already known [Arquembourg and Lambert, 2005, Moirand, 2021]. They are in a state of constant reconfiguration, following the evolution of the media event they are recounting—and this is especially true in the case of Mayotte, where the origin of the earthquakes felt by the inhabitants was demonstrated by scientists over a year after the first events. Indeed, media reports "exist only in the state of a puzzle, scattered fragments posted from day-to-day on various platforms and then loosely assembled in reference to headlines or the use of a few enunciatory indexes" [Arquembourg, 2011, p. 37]. Rather than a coherent system that can be grasped as a whole, news reports correspond more to a succession of "discursive moments," that is to say, "the sudden appearance in the media of an intense and diverse discursive production regarding a single event [⋯]," which allows for the "constitution of a corpus upon other bases besides sociological characteristics" [Moirand in Charaudeau and Maingueneau, 2002, p. 389; Moirand, 2007, p. 4].

For discourse analysts who specialize in sciences of language—beyond the reflections initiated by, among others, Foucault [1969, pp. 44–54] on "discursive formations," which are still at the center of theoretical debates in the domain—the media constitutes places where different spheres of language activity come together [Moirand et al., 2016]. In a single article, the reader is effectively confronted with comments from local inhabitants, from scientists, from administrative and/or political authorities and from journalists. Now, each of these communities constitutes a distinct community of experience, which is also a community of interpretation and, ultimately, a distinct discursive community [cf. Devès, 2018, on the different discourses referring to the notion of disaster/catastrophe]. The scientific event constituted by the discovery of Mayotte's underwater volcano has thus given rise to *a polyphonic text*, in which there has been a mixing and even an interpenetration of the voices of actors who belong to different discursive communities. Discourse analysis allows, then, for an exploration, not only of the meaning that the words take on in their co-texts and contexts, but also of the social and even political meaning that they take on for the actors whose comments are reported. To put it another way, analysis of the news reports allows for clarification of the "verbal" behavior of the social actors such as it is "shown" in the media.

Following the work of Fairclough [2003] and Van Leeuwen [2009] in *Critical Discourse Analysis*, we prefer to speak here of "represented discourses" or "representations of discourses" rather than "reported discourses" [Petitclerc and Schepens, 2009]. The discourses of social actors are more "represented" here: it is often a question of short fragments of speech juxtaposed in the press, whereas they have been uttered in diverse locations and in situations that sometimes predate the publication date of the newspaper. These words, signposted by quotation marks, give a particular structure to the press text. To speak of "represented discourses" is to admit that those who have drafted the articles are those who have chosen to "stage" them by extracting them from the context and co-texts in which they were uttered (the situation, the moment, and sometimes the place), and by placing them anew on the space of the page with titles, subtitles and inter-titles, together with the infographics, photos, maps, and so on, that sometimes accompany them.

The co-texts of reported words (and which are therefore "shown" as exterior to the author of the article) constitute a means of access to representations of the discursive communities who are present. They function as indexes for contextualization, which allow the situation in which they have been spoken to be inferred. Over the long duration of the event, they thus constitute *an inter-discursive memory* of the interpretation of the events on the basis of references and quotations borrowed from earlier discourses, and notably from discourses on events of the same type [Moirand, 2007, pp. 114–150].

### 3.2. *Data collection*

Since May 2018, and despite the concurrence of the health crisis linked to Covid-19, the local, regional and national media have continued to offer regular coverage of the events linked to the scientific, political and administrative management of the seismo-volcanic crisis in Mayotte. The research team of the MAY'VOLCANO project[1] (which the authors are part of) was thus able to assemble a large database of non-specialist press articles written in French, from which we have extracted the corpus used here.

At the time of writing, the MAY'VOLCANO corpus comprises 365 articles published between May 10, 2018 and May 1, 2021. It thus covers the first three years of seismo-volcanic activity and contains the entirety of articles published by six French-language daily papers that address different readerships:

- *Le Figaro* and *Le Monde* are national daily papers addressed primarily to a public in mainland France; *Le Figaro* is the national paper that has devoted the highest number of articles to the seismo-volcanic crisis in Mayotte. *Le Monde*, though less verbose, is the most read payment-access newspaper in France and the most widely available abroad.
- Narrowing down to the Indian Ocean, *Le Journal de l'île de la Réunion* and *L'Express de Madagascar,* address the inhabitants of the French island of Réunion and Madagascar respectively. *Le Journal de l'île de la Réunion*, whose readership has been mindful of seismo-volcanic risk due to the very active volcano of Piton de la Fournaise, has dedicated extensive coverage to the seismo-volcanic crisis in Mayotte; furthermore, Réunion island also hosts the prefecture of the Indian Ocean Zone which in turn includes the prefecture of the Mayotte *département*,[2] and it constitutes a logistical way-station for civil protection between mainland France and Mayotte. *L'Express de Madagascar* with text in both French and Malagasy, has also covered the events widely and is one of the most read newspapers in the region.
- Narrowing further to Mayotte itself, the corpus is constituted of the publications of the *Journal de Mayotte* and *Mayotte la 1ère*. *Le Journal de Mayotte* is among the most read French-language publications on the island. It is also the one that has published most on the subject of the "crisis" that we are working on. *Mayotte la 1ère* is a radio station, an online newspaper and a television channel that broadcasts content in French and in Shimaore. A branch of the public service, it offers news with no subscription fee and has

[1] The research project entitled MAY'VOLCANO is funded by the Centre des Politiques de la Terre with the support of Université Paris Cité, Sciences Po and ANR. It is an interdisciplinary project dedicated to the study of the circulation of knowledge between scientists, risk and crisis management actors, the media, and the population of Mayotte during the ongoing seismo-volcanic crisis.

[2] In France, prefectures are administrations that belong to the Ministry of Interior and act as local government.

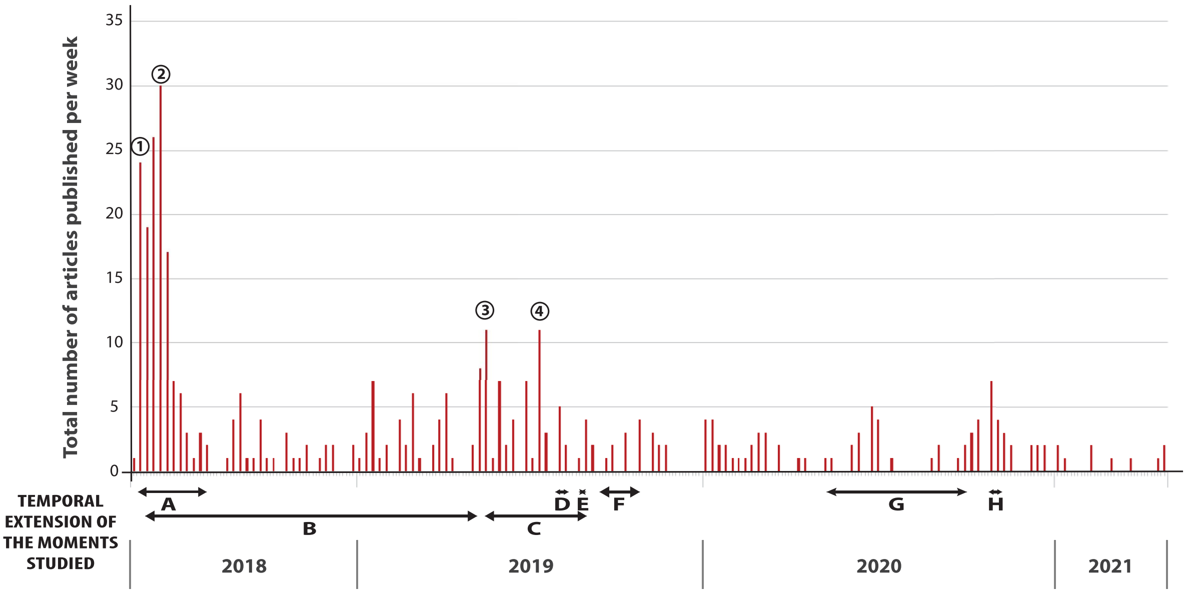


**Figure 1.** Histogram representing the number of articles published per week between May 10, 2018 and May 1, 2021 in newspapers from the MAY'VOLCANO corpus. Black arrows beneath the histogram indicate the temporal extension of the moments studied (Table 1). The numbers under each event show: (1) The week marked by the occurrence of the strongest earthquake during the crisis (magnitude 5.8), which gave rise to intensified seismicity monitoring and the issuing of security instructions; (2) The arrival in Mayotte of the inter-ministerial mission of experts to take stock of the seismic activity and its associated risks; (3) The "discovery" of the "new volcano"; (4) The announcement of the MAYOBS 3 Oceanographic campaign among articles that still concerned the discovery of the volcano (with, in particular, the publication of a series of four articles in *Le Monde* that same week).

a wide audience in Mayotte, notably through other local newspapers.

### 3.3. *Analysis through "discursive moments"*

Rather than carry out exhaustive statistical analysis of the MAY'VOLCANO corpus, we have chosen here to focus on the media coverage of key moments during the seismo-volcanic "crisis". Indeed, what was particular to this event was how it set in for a long duration. It comprises a series of distinct "discursive moments" which are most pertinently analyzed independently of one another (Figure 1). Analysis through "moments" also allows the media accounts to be studied in their evolution over time.

The discursive moments under study are eight in number. They have been defined on the basis of the work carried out by Devès et al. [2022], which led to the identification of the social actors implicated in the experience and the management of the crisis and the events that marked the first three years of seismo-volcanic activity. The whole corresponds to a corpus of 244 articles (out of the 356 articles of the MAY'VOLCANO corpus) (Table 1).

Press interest in the subject of the seismo-volcanic crisis in Mayotte shows variation over time in keeping with the local, regional and national integration of the newspapers under consideration (Figure 2). During the first three years of the crisis, the local press published approximately six times more articles than the regional press, and almost ten times more than the national press.

The number of articles published is especially high at the start of the seismic crisis, when the number of felt earthquakes was at its highest, that it to say, between May and June 2018 (moment A). This is the only period that can truly be qualified as a "crisis" to the extent that the social actors do effectively at-

**Table 1.** Presentation of the eight moments studied

| | | |
|---|---|---|
| (A) | First months of seismic crisis | 133 articles from May 10, 2018 to July 26, 2018: *le Journal de Mayotte* (76 articles), *Mayotte la 1ère* (26), *l'Express de Madagascar* (12), *le Journal de l'Île de la Réunion* (9), *Le Figaro* (8), *Le Monde* (2) |
| (B) | Volcanic hypothesis and subsidence data predating the discovery of the volcano | 29 articles from May 24, 2018 to May 10, 2019: *le Journal de Mayotte* (15 articles), *Mayotte la 1ère* (3), *le Journal de l'Île de la Réunion* (4), *L'Express de Madagascar* (3), *Le Figaro* (3), *Le Monde* (1) |
| (C) | Discovery of the volcano | 51 articles from May 16, to August 30, 2019: *le Journal de Mayotte* (22 articles), *Mayotte la 1ère* (16), *l'Express de Madagascar* (3), *le Journal de l'Île de la Réunion* (1), *Le Monde* (6), *Le Figaro* (3) |
| (D) | Press conference to the local representatives | 7 articles from July 31 to August 9, 2019: *le Journal de Mayotte* (3 articles), *Mayotte la 1ère* (3), *Le Figaro* (1) |
| (E) | Visit from the minister of the overseas | 5 articles from August 27 to 30, 2019: *le Journal de Mayotte* (2 articles), *Mayotte la 1ère* (1), *l'Express de Madagascar* (1), *le Journal de l'Île de la Réunion* (1) |
| (F) | Scientific press conference at the Institut de Physique du Globe de Paris | 5 articles from September 4, to October 26, 2019: *le Journal de Mayotte* (2 articles), *Le Figaro* (2), *Le Monde* (1) |
| (G) | MAYOBS 13-1 and MAYOBS 13-2 oceanographic campaigns | 6 articles from May 4 to September 28, 2020: *le Journal de Mayotte* (3 articles), *Mayotte la 1ère* (1), *le Journal de l'Île de la Réunion* (1) |
| (H) | "Volcano week" and installation of the first alert siren in Dembeni | 8 articles from October 28 to November 3, 2020: *le Journal de Mayotte* (4 articles), *Mayotte la 1ère* (4) |

test to a crisis experience, which led the Mayotte administration to activate a "crisis cell". Reading the articles (prior to systematic thematic analysis) reveals that, throughout this period, the media accounts focus on: the unprecedented character of the seismic crisis, which was of unexpected intensity and duration for this region; the disquiet of the inhabitants; the measures taken by the authorities—in particular the Mayotte prefecture; and the difficulties experts had when it came to "explaining" the phenomenon. The local newspapers follow the communiqués from the prefecture attentively [daily news "updates" over the first months, Devès et al., 2022], and regularly publish lists of the earthquakes' characteristics (magnitude, location), as well as security instructions.

In the long term, the seismic activity (and notably the number of felt earthquakes) diminishes from June 2018 onwards. Even though it was to increase again at different moments, for the next three years it was never to reach the same level as at the start of the seismic crisis [cf. Figure 3 in Devès et al., 2022]. From June 2018 onwards, the number of articles per week also trails off and a progressive shift in the themes treated can be observed: the specific issues involved in managing the seismic crisis give way to the question of the origin of this unusual activity (moment B). Only the local press continues to regularly follow the situation updates from the experts in charge of monitoring the seismicity, which are relayed by the prefecture on a regular basis. The articles published between September 2018 and the announcement of the "discovery of the underwater volcano" in May 2019 relay the hypotheses given by the scientists and examine new observations enabled by GPS and seismic data [Briole, 2018, Cesca et al., 2020], as well as the organization of the first "Tellus-

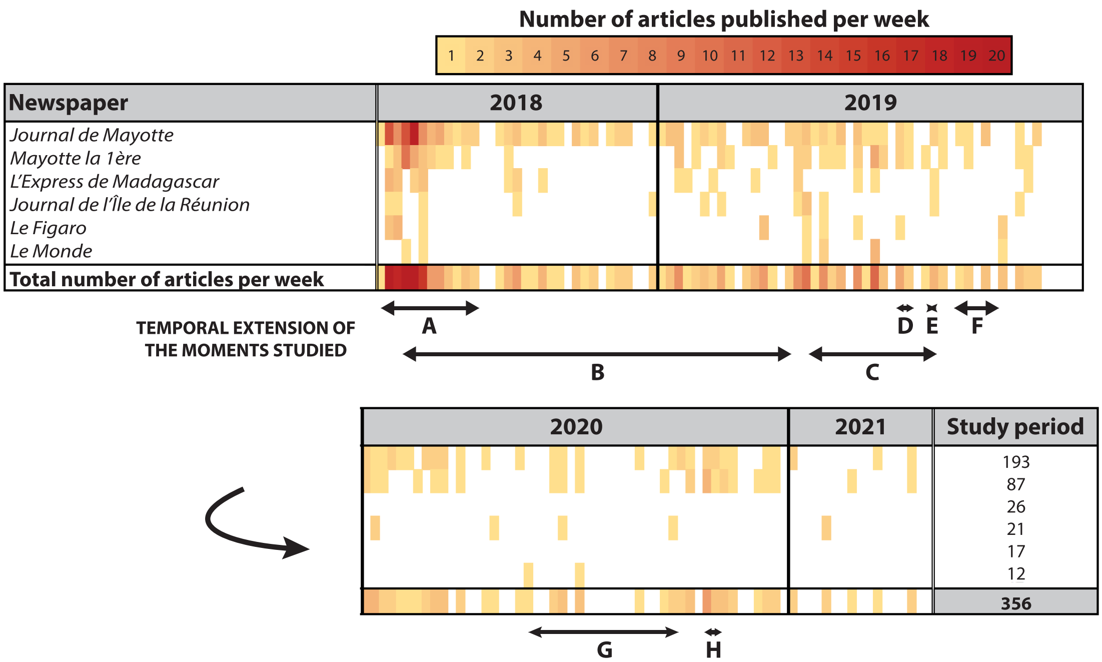


**Figure 2.** Number of articles published per week and per newspaper between May 10, 2018 and May 1, 2021. The figures in the right-hand column indicate the full number of articles published per newspaper over the entirety of the study period. In total 356 articles were published.

Mayotte" scientific campaigns, but also the discovery of dead fish coming from the deep-sea by Mayotte fishermen.

The announcement of the discovery of the volcano in May 2019 (moment C) is the event that received the second most coverage in the media. It closes the narrative arc, opened a year earlier, which examined the cause of the seismicity and underlined the unprecedented and mysterious character of the phenomenon. It is the occasion, for the national newspapers in particular, to cast a retrospective eye over the year that has passed. The evidence for the volcanic origin of the activity opens at last new horizons of questioning, relative to the knowledge, the uncertainties and the means to be implemented so that a phenomenon qualified as "exceptional" may be studied, but also relative to the risks and opportunities associated with the presence of a volcanic zone in such close proximity to the island. Since the time of the "discovery" of the volcano, Mayotte has been spoken of more frequently in the national and international press, which sends back a "positive image" of the French *département*. In the local press, the journalists' accounts started to oscillate between an account of the disquiet produced by the discovery of a volcano so close to the island and the hope that this might offer a different image of Mayotte to the one thus far conveyed by the media (notably by the media in mainland France). The article published in the *Journal de Mayotte* on May 20, 2018, for example, carries the following headline: "*Le volcan, nouvelle vitrine de Mayotte*" ("Volcano, the new Mayotte showcase"). The extraordinary mobilization that this natural phenomenon provoked was to generate genuine enthusiasm, as much within the scientific community as among the services of the state and in the press—which, we may recall, would still be covering the subject three years after the start of the crisis, even though the seismic activity was no longer hampering the everyday life of the inhabitants, and this in spite of the spate of large-scale health and social crises.

The ensuing media coverage appears to follow the rhythm of the communications as orchestrated by the authorities: press conferences organized by the prefecture intended for local agents (an example of moment D), a bimonthly and then monthly publication of REVOSIMA bulletins from August 2019 onwards, declarations from the government regarding actions undertaken and the various means mobilized (example of moment E), a scientific conference aiming to take stock of the state of knowledge (example of the conference organized by REVOSIMA in October 2019, moment F), and lastly, the publication of official communiqués concerning the successive scientific campaigns organized by the prefecture and/or organizations in partnership with REVOSIMA (example of moment G). An awareness week called "the volcano week" organized in October 2019 was followed in some depth by the local press (moment H).

The health crisis linked to Covid-19 has probably affected media coverage. A visible effect of the Spring 2020 lockdown can be observed. Since the start of 2021, media coverage has been chiefly local, and articulated around communiqués to do with scientific campaigns. The national newspapers have nevertheless been publishing overviews, in particular on their "science" pages.

More widely, it has been observed that the national press has shown a fairly minor interest in the subject of the seismo-volcanic "crisis" in Mayotte, which seems to be driven essentially by the unprecedented character of the phenomenon and of the scientific means mobilized in order to study it. The national daily papers react more to events on a national scale (inter-ministerial communiqués announcing the discovery of the volcano, a scientific conference organized at the Institut de Physique du Globe de Paris) than to events of a more local scale (there was no publication on the occasion of the visit by the Minister of the Overseas announcing the creation of REVOSIMA, nor was there any publication concerning the awareness events organized during the "volcano week"). A large portion of the articles published by these daily newspapers feature in the "Science" pages (which are not a daily column), which tends to accentuate a more scientific treatment of the subject to the detriment of information about the monitoring and management of risk, which are crucial for the Mayotte inhabitants. The regional press dedicates more words to the seismo-volcanic "crisis" than does the national press, but still far fewer than the local press. Nevertheless, it does show itself to be more sensitive to the ultramarine issues, relaying for example information concerning governmental visits and announcements or concerning organizational issues to do with monitoring. As for the local press, it has been following the evolution of the situation very closely, with the *Journal de Mayotte* and *Mayotte la 1ère* publishing several articles per day during the more intense moments of the three years studied.

## 4. Observing the corpus for a better understanding

In order to study the *representations* conveyed by the daily press regarding the seismo-volcanic "crisis" in Mayotte, we begin by identifying the different actors who are present, how they are designated, the syntaxico-semantic place they occupy in the narrative, as well as the words that are attributed to them (Section 4.1). This identification shows the polyphonic character of the news accounts, which we discuss in Section 4.2. In the remainder of the article, we illustrate the results of the analysis using extracts from the corpus, in which we underline those elements that refer back to the *three discursive communities* identified, and we indicate in bold the *connectors* and *lexical words* that allow for a semantic interpretation of the "micro-narratives" identified throughout the article.

### 4.1. *The three main discursive communities "represented"*

Extracts from the corpus illustrate "the place" that the media accounts attribute to the actors and what they say:

(1) "Since Thursday, several seismic tremors have been felt in a number of localities of the Mayotte *département*," the prefecture **explains** in a communiqué, but "at this stage, no damage has been observed in the wake of these low-intensity tremors."[3]

Today, fresh earthquakes have been felt, one of which registered a magnitude of 4.6 and another a magnitude of 5.1. On social

[3]We underline those elements that refer back to the *three discursive communities* identified, and we indicate in bold the *connectors* and *lexical words* that allow for a semantic interpretation of the "micro-narratives" identified throughout the article.

media, many Mahorais have **gone into a panic** about these tremors.[4]

[*Le Figaro*, 14-05-2018, moment A]

(2) **There is no risk** of a tsunami **but** emergency teams are ready to be dispatched from Paris and from Reunion Island where tents and medication are stocked. [...]

**But** the watchword is to reassure the population. "On the global scale, these are micro-phenomena, underlines Etienne Guillet [cabinet director of the prefecture]. The cluster of earthquakes is "**apparently** linked to the East-African rift" and to "a sliding of tectonic plates." **There is no risk of subduction, therefore there is no risk of a tsunami** [...] **Potentially**, a plate may have splintered," he adds, while some inhabitants see this as a divine punishment and a number of people on the internet say they have been unable to sleep.

"A fear in the stomach has set in" observes Muriel Lignon, a teacher [...]

[*Le Figaro*, 21-05-2018, moment A][5]

(3) "Following the conclusions of the governmental mission that went to Mayotte at the behest of the prefecture, France's Central Bureau for Seismology (BCSF) and the National Network for Seismic Monitoring (RENASS) have engaged a mission from the Group for Macroseismic Intervention (GIM) on the Mayotte island from June 11 to 15" **explains** the prefecture in a communiqué.

[*L'Express de Madagascar*, 13-06-2018, moment A][6]

Three main discursive communities are represented here: Mayotte's inhabitants, the political and administrative authorities (foremost among them the prefecture plays a pivotal role), and the scientists. These three communities are called upon to communicate with one another throughout the event, but each of them occupies a different discursive "place". Mayotte's inhabitants "gets in a panic" on Twitter and in the remarks reported by the journalists, while the scientists "try to understand" and the prefecture "tries to reassure" the population. The "subject" position in the sentence, in French, does not imply that one is the "agent of an action": the administrative authorities and the scientists "act", while the inhabitants are asked to "give feedback" to the authorities and "follow" instructions relayed by local journalists, thus casting them in the position of "counter-agent" (drawing on the theory of the US semantician Fillmore [1968, 1972], that is to say, on the orders of an agent representing authority.

Furthermore, not all social actors play the same role in the circulation of discourses. The Mayotte prefecture constitutes a locus of intermediate discourse between the central power (Paris) and the local administrators (nominated or elected), between the ground-level observations, the results of the scientific missions, the rumors that circulate on social media, and the words of the islanders and media. The local journalists also occupy a specific position, both interested parties in the crisis and authors of the narratives that speak of it. This position allows them to position themselves as "mediators" of the crisis. This is the case of the journalists of the *Journal de Mayotte* (designated by "us") who, at the height of the seismic

[4]« De nombreuses secousses sismiques ont été ressenties depuis jeudi dans plusieurs localités du département de Mayotte », explique la préfecture dans un communiqué, mais « à ce stade aucun dégât n'a été constaté suite à ces secousses de faible intensité ». Aujourd'hui de nouveaux séismes ont ainsi été ressentis, dont un de magnitude 4.6 et un autre de magnitude 5.1. Sur les réseaux sociaux, de nombreux Mahorais s'affolent de ces secousses. [*Le Figaro*, 14-05-2018, moment A].

[5]Il n'y a pas de risques de tsunami mais des équipes de secours sont prêtes à être dépêchées depuis Paris et la Réunion où des tentes et des médicaments sont stockés. [...] Mais le mot d'ordre est de rassurer la population. « On est dans des micro-phénomènes à l'échelle géologique, souligne Etienne Guillet [directeur de cabinet du préfet]. L'essaim de séismes est « lié à priori au rift est-africain » et à « un glissement de plaques ». Il n'y a pas de risques de subduction donc pas de risque de tsunami [...] C'est potentiellement une plaque qui se serait scindé », détaille-t-il, alors que certains habitants y voient une punition divine et que de nombreux internautes signalent avoir perdu le sommeil. « On a la peur dans le ventre qui s'est installé » livre Muriel Lignon, professeur [...] [*Le Figaro,* 21-05-2018, moment A].

[6]« Suite aux conclusions de la mission gouvernementale qui s'est rendu à Mayotte à la demande du préfet, le Bureau Central Sismologique Français (BCSF) et le Réseau National de Surveillance Sismique (RENASS) engagent une mission du Groupe d'Intervention Macrosismique (GIM) sur l'île de Mayotte du 11 au 15 juin » explique la préfecture dans un communiqué. [*L'Express de Madagascar*, 13-06-2018, moment A].

crisis, attempt to forge a link between their readers (designated by "you") and the "state services":

(4) "First-hand accounts of earthquakes in Mayotte are multiplying. The strongest was stressed on Thursday night—Friday morning at about 2.20 am, but many of **you** informed **us** of other tremors last night.

The prefecture has confirmed to **us** that no less than 13 tremors have been registered in Mayotte these last two days. The strongest was magnitude 4.5 and the epicenter was located 35 miles East of Mamoudzou. This event was too weak to generate the slightest fear of a tsunami, **the state services** have reassured…"

[*Le Journal de Mayotte*, 12-05-2018, moment A][7]

The national, regional or local integration of the newspapers influences the diversity of actors who are "on the scene" and the way in which they are represented. It may thus be noted that the national daily papers report more frequently what is said by actors in mainland France, or actors operating on the national level of crisis or risk management. This is even more visible after "the discovery of the volcano" when the articles focus on the scientific dimension. The local press seems to report comments by a wider diversity of actors, and notably those local actors who are sometimes forgotten by the national press (local representatives, associations or personalities). The regional and national newspapers are confined to a commentator role and base their accounts on testimonies taken from the local press, on the content of AFP dispatches, and on interviews with authorities and scientists present in mainland France.

### 4.2. *A polyphonic discourse*

Readers of these news accounts often find themselves confronted with many voices: those of the different discursive communities whose words are being reported. This is visible in extracts 1, 2 and 4. The following extract, the account of the visit to Mayotte by the Minister of the Overseas, also illustrates this:

(5) Yesterday in Mayotte, the Minister of the Overseas, Annick Girardin, indicated as a preamble to the announcement of measures for the development of the territory that the series of tremors felt there over the last few days **"does not seem to present any risk of damage on land, nor of a tsunami in the sea."**

A hundred or so micro-tremors, "about fifteen of which were stronger than magnitude 3.0," have been recorded in Mayotte since Thursday, indicated the prefecture of the ultramarine *département* on Monday.

The minister, who has herself felt some tremors since her arrival on Sunday, recognized that the event could "be a source of worry for citizens."

"**I want to share with you the most recent information we** have from the **Bureau for Geological and Mining Research (BRGM)**. This cluster of tremors is being felt in spite of its low intensity because it is located 35 miles from the coast and its point of origin is not very deep," she **explained**.

"It doesn't **seem to present any risk of damage on land, nor of a tsunami in the sea**, and **should not at present be stronger** than level 5 on the BRGM scale," she added.

The minister asked the prefecture to "provide daily information on the evolution of the phenomenon and **to anticipate any foreseeable** risk to the population," she further added.

[*L'Express de Madagascar* 16/05/2018, moment A][8]

---

[7]« Les témoignages liés à des tremblements de terre se multiplient à Mayotte. Le plus fort a été souligné dans la nuit de jeudi à vendredi vers 2h20 du matin, mais vous avez été nombreux à nous faire part d'autres secousses la nuit dernière. La préfecture nous confirme que pas moins de 13 secousses ont été enregistrées à Mayotte ces deux derniers jours. La plus forte était d'une magnitude de 4,5 et l'épicentre a été localisé à 55 km à l'est de Mamoudzou. Un événement trop faible pour générer la moindre crainte de tsunami, rassurent les services de l'Etat… ». [*Le Journal de Mayotte*, 12-05-2018, moment A].

[8]La ministre des Outre-mer Annick Girardin a indiqué, mardi à Mayotte, en préambule à l'annonce de mesures pour le développement du territoire, que la série de séismes ressentis ces derniers jours sur place « ne présente a priori pas de risques de dégât sur terre, ni de tsunami en mer ». Une centaine

The very functioning of the press text, which is determined by constraints of place and by the necessity of giving an account of the plurality of viewpoints, leads to the juxtaposition of different discursive genres that in turn include first-hand testimony, research discourse, the discourse for the relaying of scientific findings, and the discourse of the administrative and political authorities. In extract 5, for example, we can see the minister taking up "the explanation" by BRGM in order to "share it" with her audience and reassure them. But the linking-up of discourses borrowed from different spheres of language activity demands an attentive reading, which is not always practiced. Even though this juxtaposition intends to give an account of the reality of the situation—that of the existence of a diversity of actors and viewpoints—it tends to thrust the comments from the different actors onto a single plane and thus contributes to the "muddling" of communication,[9] particularly at times of crisis when uncertainties run high and when opinions diverge and even contradict one another.

de micro-séismes, dont « une quinzaine avec des magnitudes supérieures à 3.0 », ont été enregistrés depuis jeudi à Mayotte, a indiqué lundi la préfecture du département ultramarin. La ministre, qui a eu elle-même l'occasion de ressentir les secousses depuis son arrivée dimanche, a reconnu que l'événement pouvait « être une source d'inquiétude pour les citoyens ». « Je veux partager avec vous les dernières informations que nous avons du Bureau de recherches géologiques et minières (BRGM). Cet essaim de séismes est ressenti malgré sa faible intensité car il est situé à 50 kilomètres des côtes et que son origine est assez peu profonde », a-t-elle expliqué. « Il ne présente a priori pas de risques de dégât sur terre, ni de tsunami en mer et ne dépasserait pas jusqu'à présent le niveau 5 sur l'échelle du BRGM », a-t-elle ajouté. La ministre a demandé à la préfecture de « produire une information journalière sur l'évolution du phénomène et d'anticiper tout risque prévisible pour la population », a-t-elle précisé. [*L'Express de Madagascar* 16/05/2018, moment A].

[9]We are borrowing this image from Varga [2020], who used it in the context of the Covid-19 health crisis, and, in a somewhat different sense, regarding controversies between scientists participating in television broadcasts (see also Moirand [2021]). In the case of Mayotte, we have come across few controversies between scientists, at least as mentioned in the media. In the texts from the corpus, we read rather a kind of "enunciatory muddling" [see Lejeune [2005], and Léglise and Garric (editors) [2012], "L'intensification du brouillage énonciatif dans *le Monde*," pp. 68–70], and which here results in the juxtaposition of comments from different social actors who are not to be "seen," in contradistinction to the television broadcasts and certain social media.

## 5. Accounts with an explicative aim

The preceding accounts show a prefect, a deputy prefect and then a minister who "explain" the state of the situation or the "latest information" produced by the scientists, as well as journalists who try to provide "explanations" to the questions from their readers and even to anticipate these queries. These few examples illustrate an observation that can be generalized for the full corpus studied, and which accords with the observation by Arquembourg and Lambert [2005] quoted in the introduction: in recounting what was happening in Mayotte, the journalists set about "explaining," that is to say, they strive to give meaning to the events and to the comments made by the different actors. Furthermore, the situation is qualified in turn by the actors themselves as "unknown," "unprecedented," "exceptional," "never before observed," these being a host of modalities that, referring neither to the facts nor to specialist knowledge, invite people to seek out explanations. It will also be remarked that, with their explicative aim (Section 5.1), the news reports on the seismo-volcanic "crisis" in Mayotte draw on different forms of explanation (Section 5.2), without managing to account for the uncertainties specific to the crisis situation and to the very notion of "risk" mobilized by the actors.

### 5.1. *Different forms of explanation*

Explanation has many semantic facets which correspond to different activities dependent on the actors who are implicated in the press narratives. A social actor can reply to one explicit request for information (e.g. in the summary of a press conference or an information meeting). One might also participate in a dialogue between one who does not know and one who is in a position of "knowing" (implicit expectation of explanation). A scientist might also seek to anticipate the requests of his audience or readership.

We can observe here that the media accounts very frequently refer the reader to what has been said by the scientific community. The scientific community even appears to be particularly central. This is linked in part to the fact that comments from other communities who are present, on this occasion those of the authorities, who try to "explain" the situation and to "justify" the decisions they take, themselves borrow from the field of scientific discourse. This is all the more so given how, in Mayotte, the seismo-volcanic activity is perceived only in an indirect manner. Certainly the islanders feel the strongest earthquakes and can observe other manifestations like gas release and dead fish, but it is principally by means of scientific instruments and interpretations that the situation comes to be "told." In fact, the authorities themselves necessarily draw on arguments and lines of argumentation produced by the scientists.

The studies carried out in the field of the relaying of scientific findings have led to an updating of the prototypical forms and functionings of "explanation" [Claudel et al., 2008, Moirand, 2003, 2008b,a, von Münchow and Rakotonoelina, 2010]. Press texts give rise to different verbal constructions in relation to "explanation":

X explains Y (one fact "explains" another fact)

Y is due to X (one fact is due to another fact)

Z (the journalist) tells the public that S (the scientists) explain that X would be due to Y,

Etc.

Forms such as these can be identified in the studied articles, in particular the moment C relative to the discovery of the volcano, which comes to close a year of questioning as to the "causes" of the seismicity:

(6) A scientific mission has drawn attention to the formation of an underwater volcano some 35 miles east of Mayotte and two miles deep. **This allows for an explanation** for the earthquakes that have been observed on this French island in the Indian Ocean for a year now, with more than 1800 tremors of magnitude 3.5 or higher, the strongest being 5.8. The size of the volcano "has been assessed at 2600 feet in height with a base of 2 $\frac{1}{2}$ to 3 miles in diameter. The 6500-feet plume of volcanic fluids does not reach the surface of the water," explain the scientists, who speak of an "exceptional geological phenomenon."

[*Le Figaro*, 27-05-2019, corpus C][10]

(7) The scientists have been mobilized in order to **treat, analyze and interpret** the multitude of data gathered during these last months. This operation will necessitate in-depth work in order to evaluate **the risks** occasioned for Mayotte in matters of seismic risk, volcanic risk and tsunami risk.

[*Le journal de Mayotte*, 16-05-2019, corpus C][11]

But, for the media audience, to "explain" refers most often to a didactic situation in which "someone explains something to someone else" (which corresponds to a dissymmetry in knowledge), or else someone asks for "an explanation" (often with regard to a specialist word or a new object"), or explanation for behavior ("why should one stay at home when there are earthquakes?"), or else advice on what to do if such and such should happen. In the information narrative, the request is not necessarily worded in this way, but the journalist often anticipates questions from the readership (which falls under a dialogism that is said to be "interactional"), as indeed do the specialists in charge of disseminating scientific findings in their speeches: "What is a seismograph? A seismograph is...," "What should we do if there is an earthquake or if there is a tsunami? Well, one should not run outside... one should..."

To explain "to the other" (a word, steps to be taken, a scientific discovery, etc.) implies a dissymmetry in knowledge between the one who is asking for explanations and the one who is providing the explanations,[12] the forms of explanation hinging then on

[10] Une mission scientifique a mis en évidence la naissance d'un volcan sous-marin à 50 km à l'est de Mayotte et à 3500 mètres de profondeur. Ceci permet d'expliquer les séismes constatés sur cette île française de l'océan Indien depuis un an, avec plus de 1800 secousses de magnitude supérieure ou égale à 3,5, dont la plus forte a été de 5,8. La taille du nouveau volcan « est évaluée à 800 mètres de hauteur avec une base de 4 à 5 km de diamètre. Le panache des fluides volcaniques de 2 km de hauteur n'atteint pas la surface de l'eau », expliquent les scientifiques qui parlent d'un « phénomène géologique exceptionnel ». [*Le Figaro*, 27-05-2019, corpus C].

[11] Les scientifiques sont mobilisés pour traiter, analyser et interpréter la multitude de données acquises durant ces derniers mois. Cette exploitation nécessitera des travaux approfondis pour évaluer les risques induits pour Mayotte en matière de risque sismique, risque volcanique et de tsunami. [*Le journal de Mayotte*, 16-05-2019, corpus C].

[12] This dissymmetry harks back to the one that exists between layperson and expert, see thus e.g., the definition that Roqueplo [1997] gives for the expert: "someone who must take a decision wishes to do so in full knowledge of the facts. He appeals therefore to a person or to an institution that he deems competent in the domain of this decision, so that it will provide him with these facts in full or in part." See also Léglise and Garric [2012] on the

comparisons, analogies, metaphors, and so on. In the following extract, the scientist quoted begins by giving a scientific explanation, but ends with another "image" that is closer to the non-expert audience:

(8) "Often, when the magma has found its path, which is the case for our new volcano, there is no seismicity under the volcano. The magma continues to flow freely. It follows its course and it does not fracture the rock, she [the scientist] explained.

Furthermore, she confirmed that Mayotte was still sinking and moving. "There is a draining of the reservoir and, at the same time, of the magma, which is rising to the surface. **It's like** squeezing a toothpaste tube deep down, and the lava comes out.

[*Le Figaro*, 31-07-2019, corpus C][13]

This form of comparison is typical of the forms used by scientific journalists, but nor do scientists hesitate to use them in press conferences, or in Frequently Asked Questions (like those offered by the prefecture of Mayotte in May 2019).[14]

But the juxtaposition of these two forms of explanation (the relation between two facts that have been observed, measured or modeled vs. explanation with a didactic aim) in the press texts also contributes to the "enunciatory muddling" mentioned above:

(9) • Where has Mayotte's subsidence got to?

At the current time, the island of Mayotte "has sunk five inches since July," indicates Nathalie Feuillet, the delegation head onboard the Marion Dufresne and a physicist from the observatories at the Paris Globe Institute for Physics. This shift is rapid and on a geological scale. "These movements **could be explained** by the draining of a deep reservoir, some 25 miles down," the geologist continues. [...]

• What have the seismometers installed out at sea revealed?

[...] As soon as it [the Marion Dufresne vessel] arrived in the zone, the seismologists picked up the eight devices set out on the ocean floor to analyze their data. [...] It transpires that the epicenters are not located between 20 and 40 miles from Mayotte as they have believed over this last year, but only six miles from our island! [...] "The new 2500-feet-high volcano indicated by an arrow forms **a limited cluster about half a dozen miles from Petit Terre**" indicates Nathalie Feuillet. Still, there is no cause for panic, because while they are closer in "epicentral" distance, **that is to say**, horizontally, they are further away than previously thought in "hypercentral" distance, **that is to say**, in depth. [...]

These new data reinforce the fascinating character of this unusual natural phenomenon. To such an extent that it would not be surprising to see researchers from the world over showing up soon, attracted by this major scientific case. A rather unexpected form of tourism for Mayotte, but which won't do any harm.

[*Le Journal de Mayotte*, 17-05-2019, corpus C][15]

discourse of experts and expertise.

[13] « Souvent, quand le magma a trouvé son chemin, ce qui est le cas pour notre nouveau volcan, il n'y a pas du coup de sismicité sous le volcan. Le magma continue de s'écouler tranquillement, il suit son chemin et ça ne fracture pas la roche, a-t-elle expliqué. Elle a par ailleurs confirmé que Mayotte continuait à s'enfoncer et à se déplacer. « On a le vidage du réservoir et en même temps du magma qui sort à la surface. C'est comme si on appuyait sur un tube de dentifrice en profondeur, la lave sort. [Le Figaro, 31-07-2019, corpus C].

[14] https://www.mayotte.gouv.fr/content/download/14333/108957/file/FAQ_mai2019-2.pdf.

[15] Où en est l'enfoncement de Mayotte ? A l'heure actuelle, l'île de Mayotte « s'est enfoncée de 13 centimètres depuis juillet », indique Nathalie Feuillet, cheffe de mission à bord du Marion Dufresne et physicienne des observatoires à l'Institut de physique du Globe de Paris. Ce déplacement est rapide à l'échelle géologique. « Ces mouvements pourraient être expliqués par la vidange d'un réservoir profond, à environ 40 km de profondeur » poursuit la géologue. [...]—Qu'ont révélé les sismomètres installés au large ? [...] Dès son arrivée sur zone [le bateau Marion Dufresne], les sismologues ont relevé les huit appareils disposés au fond de la mer pour en analyser les données. [...] Il en ressort que les épicentres ne sont pas situés entre 30 et 60 km de Mayotte comme on l'a cru depuis un an, mais à seulement 10 km de notre île ! [...] « Le nouveau volcan de 800 m de haut indiqué par une flèche forme un essaim restreint à une dizaine de km de Petite Terre » indique Nathalie Feuillet. Toutefois pas de panique car s'ils sont plus proches en distance « épicentrale », c'est-à-dire à l'horizontale, ils sont plus loin que prévu en distance « hyper-

This extract brings on to the same place the scientific explanation (*epicentral* or *hypercentral distance*) and didactic explanation (*that is to say…*), the consequences in terms of risk and fascination for the volcano, which might attract tourists, without letting uninitiated readers perceive the difference in status of these explanations in terms of scientific robustness and in terms of consequences for life on Mayotte.

Other forms of explanation also arise from the media narratives we have studied. This is the case below, in the article that gives an account of a *Journal de Mayotte* interview with the Civil Protection mission dispatched to Mayotte in June 2018. The questions here correspond to other representations of explanation, because they ask those in charge of the delegation dispatched from mainland France at the behest of the prefecture, not to explain what might occur, but to "explain themselves" on what they have come to do in Mayotte:

(10) To begin with, what is civil protection? […] What exactly have you come to do in Mayotte? […] Do you plan to look again at the cartography of the marine submersion made in 1984? Does your calendar have to adapt to the one for the scientific discoveries around the volcano? Have you carried out observations on the cracks in buildings? Is there any risk of a tsunami, in the wake of a collapse or subsiding on the east of the island? What is the current state of the "PREPARETOI*" plan? […] What is the main risk to be taken in account right now in Mayotte?

[*Le Journal de Mayotte*, 03-06-2019, corpus C]

*Acronym for *Prévention et Recherche Pour l'Atténuation du Risque Tsunami dans l'Océan Indien.*

If, with regard to the "meaning" of *explanation*, we begin by consulting, as linguists most generally do, what a commonly used dictionary says, for example *Le Petit Robert de la langue française* (2012, p. 983), we find, as a first acceptation of "*expliquer*," "*faire connaître ou comprendre*" ["to make known or understood"], as a second acceptation, "*rendre clair, faire comprendre*" ["to make clear, understood"], and only as a third acceptation, "*faire connaître la raison, la cause de (qqch). Expliquer un phénomène. Expliquer pourquoi*" ["to make known the reason, the cause of (something). To explain a phenomenon. To explain why"]. But we find no example borrowed from the discourse of science. We cannot therefore trust in the high frequency of this verb identified in the media by lexicometric software to interpret the meaning of its use. Only analysis of "close" and "remote" co-texts allows us to give "a meaning" to the requirements of explanation for extract 10, in which there is no trace of the signifier "*expliquer*/explain," but which ends with a request for explanation as to the nature of the risk.

## 5.2. *Speaking of risk and uncertainty*

Over the course of the explanations relayed in the corpus we can see relations emerging between verbs that account for the activity of the researchers (treating, analyzing, interpreting, assessing, ...) and the notion of risk. This notion appears essentially in the remarks made by the authorities (the Prime Minister, the Minister of the Overseas, the prefect and the elected representatives of the island (deputy, senator and mayors of the *département*). From the viewpoint of the state services, "quantifying risk", "risk assessment" or even "appropriating the culture of risk" is an indispensible precondition for any efficient action in matters of "reduction of risk of catastrophe" (the terminology used accounts very well for the prevalence of the notion). But it extends also to the activities of the scientists, to the extent that it is thanks to science that one can hope to be able to understand and assess risk. It will be noted, however, that the notion of risk remains absent from the remarks made by lay people. What is verbalized by the inhabitants of Mayotte, at least through the channel of the press, is not so much the apprehension of risk as the disquiet felt in the face of a new threat.

Studying the corpus shows that, having perceived the disquiet among the population, the response

centrale », c'est-à-dire en profondeur. […] Ces nouvelles données renforcent le caractère fascinant de ce phénomène naturel hors norme. A tel point qu'il ne serait pas étonnant de voir débarquer prochainement des chercheurs du monde entier, attirés par ce cas scientifique majeur. Un tourisme assez inattendu pour Mayotte, mais qui ne ferait pas de mal. [*Le Journal de Mayotte*, 17-05-2019, corpus C].

adopted by the public authorities, but also by journalists, consists of "explaining" in order to reassure. Thus, for example, we can read:

(11) "First-hand accounts of earthquakes in Mayotte are multiplying. The strongest was stressed on Thursday night–Friday morning at about 2.20 am, but many of you informed us of other tremors last night. [...] This event was too weak to generate the slightest fear of a tsunami, **the state services have reassured**.

This series of tremors, the number of which might seem overwhelming, has not caused any damage, and at present there is no need to fear a stronger earthquake. [...] In this precise case, **the prefecture assures** that the magnitude is too weak to generate "violent" aftershocks, or else this would be due to another event.

[*Le Journal de Mayotte*, 12-05-2018, moment A][16]

These few lines show the embarrassment generated by the uncertainty as to the origin of the tremors: "the prefecture 'assures that' ..." is contradicted by the use of the conditional and the introduction of an eventuality that refers to a threat of the unknown: "or else this would be due to another event."

In each case, the scientific explanation is supposed to function as a defense against unrest, as the following extract shows:

(12) **Many irrational reactions, faced with which the BRGM explains** that while the seismicity in this region is still at the present time **fairly poorly understood**, the distancing of Madagascar from the East-African shore (from which it has detached) is continuing, causing a widening of the East-African rift which is continuing out at sea, "by utilizing the fracture system of the Davie ridge."

A phenomenon that "seems to be progressing toward the south-east, that is to say, towards the Comoros and Madagascar. It is probable that this phenomenon is reactivating the ancient faults in these two sectors, and in particular the **submeridian faults parallel to the East African Rift and the Davie Ridge"**

[*Le Journal de Mayotte*, 23-05-2018, moment A][17]

What raises a question here is the contrast that is being made between the comments from the scientific expert (the BRGM) who "explains," and "the irrational reactions" of the population at risk. The disquiet of the inhabitants and the comprehension of the geodynamic context of the zone are thus placed on a single plane, as though the emotion kindled by feeling earthquakes could be absorbed, or offset, by turning to a higher rationality, that of scientific explanation. Furthermore, this is a rationality whose foundations are not provided, because the knowledge is here delivered without anyone knowing what allowed it to be established and validated, nor what the uncertainties correlative to its constitution might be.

It will be remarked more generally that in the explanations given in the news accounts studied there is an absence of any nuance specific to scientific discourse. Indeed, scientific deontology prefers that the presentation of what is known should be made with regard to what is not known. Turning to the notion of uncertainty allows for a more precise delimitation of the limits of a given knowledge and for an account of the existence of irreducible gray zones in knowledge. We distinguish *a minima* between two types of

[16] Les témoignages liés à des tremblements de terre se multiplient à Mayotte. Le plus fort a été souligné dans la nuit de jeudi à vendredi vers 2h20 du matin, mais vous avez été nombreux à nous faire part d'autres secousses la nuit dernière. [...] Un événement trop faible pour générer la moindre crainte de tsunami, rassurent les services de l'État. Cette série de secousses qui peut impressionner par leur nombre n'a pas causé de dégâts, et il n'y a pas à craindre de tremblement de terre plus fort l'heure actuelle. [...] Dans ce cas précis, la préfecture assure que la magnitude est trop faible pour générer des répliques « violentes » ou alors ce serait dû à un autre événement. [*Le Journal de Mayotte*, 12-05-2018, moment A].

[17] Beaucoup de réactions irrationnelles, en face desquelles le BRGM explique que si la sismicité dans cette région demeure à ce jour assez mal connues, l'éloignement de Madagascar de la côte est-africaine africaine (d'où elle s'était détachée) se poursuit provoquant l'ouverture du rift Est-Africain qui se poursuit en mer, « en utilisant le système de failles de la ride de Davie ». Un phénomène qui « semble progresser vers le sud-est, c'est-à-dire vers les Comores et Madagascar. Il est probable que ce phénomène remette en activité les anciennes failles de ces deux secteurs, et en particulier les failles subméridiennes parallèles au rif Est-Africain et à la ride de Davie » [*Le Journal de Mayotte*, 23-05-2018, moment A].

uncertainty: instrumental incertitude, linked to the imprecision inherent in any instrument or method of measure, which is in part quantifiable, and epistemic incertitude, linked to the limits intrinsic to any knowledge, and which could never be quantified because it touches on the domain of what is not yet known. From the scientific point of view, the beginning of the seismic crisis in Mayotte is marked by great uncertainties that are both instrumental and epistemic. It will be noted, however, that these two types of uncertainty are explicitly distinguished neither by the journalists nor by the actors from whom certain comments are borrowed. This contributes to a "muddling" of the explanation:

(13) The epicenter of the current earthquakes is located in the sea, some 30 to 40 miles off the Mayotte coast, estimates the BRGM. A tremor of higher magnitude than those already observed **cannot be ruled out**", **even if** the probability of an earthquake of much higher force **is unlikely**. "At [magnitude] 6, we would indeed have greater damage," Étienne Guillet, cabinet director of the prefecture recognized on Monday morning during a meandering discussion with worried inhabitants [...]

But the watchword is to reassure the population. "On the global scale, these are microphenomena, underlines Etienne Guillet. The cluster of earthquakes is "apparently linked to the East-African rift" and to "a sliding of tectonic plates." **There is no risk of subduction therefore there is no risk of a tsunami** [...] **Potentially**, a plate may have splintered," he adds, while some inhabitants see this as a divine punishment and a number of people on the internet say they have been unable to sleep.

[*Le Figaro*, 22-05-2018, moment A][18]

The statement that "a tremor of higher magnitude cannot be ruled out" sends a message of alert that is hardly softened by the more technical—and less emotionally marking—statement that "its probability" remains "unlikely." Especially as the next part of the explanation ventures a paradoxical image that binds the idea of "micro-phenomena" to the idea of a potential rupture of the tectonic plate on which the island of Mayotte sits, a plate which we may suppose to be of dimensions that have nothing microscopic about them.

Instrumental incertitude, being very technical by its nature, rarely becomes an object of discussion in the general media. We can, however, find some examples. The *Journal de Mayotte* comes back to the polemic around the detection of the earthquakes:

(14) **Divergences in the Localization of Earthquakes between Different Operators: the BRGM Explains Itself** [headline]

Enthusiasts of the app receive data, almost in real time, on the daily tremors in Mayotte. Magnitude, epicenter, depth ... almost nothing escapes the web users. But sometimes there is divergence in the data.

This was the case on Tuesday May 22, when a new tremor was felt at 15:37. The prefecture reports that, "the Bureau of Geological Research (BRGM) recorded a new tremor at 15:37 felt by the population at a magnitude of 5.0 with an epicenter located 30 miles to the east of Mamoudzou.

On the smartphones, the "quake" application showed for that same time a comparable magnitude, of 5.1, but for an epicenter 20 miles from Mayotte, thus much closer to our island. Data issued by the USGS, United States Geological Survey.

The divergences show up in red and blue on a seismicity map published by the BRGM on its site [...]. It can be seen that the blue points symbolizing the epicenters are much

[18] « L'épicentre des séismes actuels est situé en mer, vers 50 à 60 km au large de Mayotte, estime le BRGM. Une secousse de magnitude supérieure à celles déjà observées ne peut être exclue », même si la probabilité d'un séisme nettement plus puissant est peu probable. « À 6 [de magnitude, NDLR], on aurait effectivement plus de dégâts », reconnaît lundi matin Étienne Guillet, directeur de cabinet du préfet lors d'une discussion à bâtons rompus avec des habitants inquiets [...] Mais le mot d'ordre est de rassurer la population. « On est dans des micro-phénomènes à l'échelle géologique », souligne Étienne Guillet. L'essaim de séismes est « lié a priori au rift est-africain » et à « un glissement de plaques. Il n'y a pas de subduction donc pas de risque de tsunami [...] C'est potentiellement une plaque qui se scinderait », détaille-t-il alors que certains habitants y voient une punition divine et que de nombreux internautes signalent avoir perdu le sommeil. [*Le Figaro*, 22-05-2018, moment A].

more dispersed than those of the BRGM, which explains this as follows: "The USGS uses remote seismic stations, the closest of which is 400 miles from Mayotte and up to 3000 miles away. The seismic phases are difficult to visualize on these remote stations for magnitudes lower than 4.5. This results in greater incertitude than is to be seen with the dispersion of epicenters on the map."

On its side, the BRGM carries out localizations with four stations: those of Kaweni and Iloni, 30 miles from the epicenter, and those of Madagascar and Kenya. The low distance of the Mayotte stations heightens the precision of the localizations (points in grey and red on the map), "but we are limited by the visualization of signals on the remote stations (KIBK in Kenya, 750 miles away). We only localize in this way those tremors of a magnitude higher than 4.2–4.3. The smaller tremors are caught by the Mayotte stations but do not allow for reliable localization.

[*Le Journal de Mayotte*, 23-05-2018, moment A]

This long explanation, which is almost cut and paste, undoubtedly conveys a real difficulty in translating the experts' remarks for a wider audience. Indeed, many questions arise which are not explicitly explained: what is a seismic phase? Why are many stations used? Why is the distance between them so important?

The diminishing seismic activity (which was accompanied by an exit from the emergency experience and from crisis communication), progress in scientific knowledge (with, notably, the discovery of the volcanic source of the activity), and the organization of the actors in an organized network for monitoring with a coordinated communication strategy (via the REVOSIMA), have allowed for the progressive emergence of more structured and coherent media narratives in matters of explanation, notably on the scientific side. But in spite of the first scientific campaigns, and notably those of May 2019 that led to the announcement of the "discovery of the new volcano," the "lack of information" is still "giving rise to some disquiet" among inhabitants:

(15) Fresh lava flow and earthquakes closer than thought […]

**"Nothing is being hidden"** assure the Mayotte prefecture in concert with its cabinet director. **While this detail is important, the lack of information, above all on social media, is giving rise to some disquiet and even to conspiracism of all kinds**. The Marion Dufresne thus hosted local representatives on Tuesday morning, and press delegations in the afternoon, for a "transparency" operation. But transparency is not always synonymous with omniscience and many questions remain unanswered, generating frustration, starting with the scientists themselves […]

**And the prefecture has as many of these unanswered questions as the journalists.**

**"Even more still"** notes the new prefect […]

**We respond to a risk when we are aware of it"** says Jean-François Collombet.

[*Le journal de Mayotte*, 01-08-2019, sous-corpus D][19]

It is the case, then, that the rigorous application of the scientific approach brings as many "unanswered questions" as responses, and "discovering" the volcano is insufficient when it comes to characterizing the threats that its presence causes to weigh down on the island. In this sense, the advance in knowledge shows itself to be frustrating for the inhabitants, for the authorities, and for journalists alike. The prefect's words sum up very well the situation of the powerlessness of the public authorities, who can hardly move forward in the definition of a strategy for protecting the population because "we respond to a risk when we are aware of it."

[19]Une nouvelle coulée de lave et des séismes plus proches qu'on ne le pensait […] « On ne cache rien » assurent de concert le préfet de Mayotte et son directeur de cabinet. Si la précision est utile, c'est que le manque d'informations, surtout sur les réseaux sociaux, suscite quelques inquiétudes voir complotisme de tout poil. Le Marion Dufresne a donc accueilli mercredi matin les élus du département, et l'après-midi la presse, pour une opération de « transparence ». Mais transparence ne rime pas toujours avec omniscience et de nombreuses questions restent en suspens, générant de la frustration, à commencer par les scientifiques eux-mêmes. […] Et des questions en suspens, la préfecture en a autant que les journalistes. h« Voire plus encore » note le nouveau préfet […] On répond à un risque quand on le connaît » dit Jean-François Collombet. [*Le journal de Mayotte*, 01-08-2019, sous-corpus D].

The expression of incertitude in the news accounts thus shifts from the questions of the "cause of the seismicity" toward that of possible scenarios and risks. One will note that, in both cases, the scientific community remains central in the news accounts, because only the scientists harbor the means to reduce these uncertainties.

## 6. Discussion

The study undertaken here on six non-specialist French-language newspapers would gain additional depth by including further local, regional and national daily papers in the corpus, perhaps even others written in other languages, and further media such as television, radio, or social networks. To the extent that a large number of Mayotte's inhabitants neither read nor understand French, analysis of the corpus informs us only as to representations circulating in the newspapers studied, and not those circulating among the Mayotte population. The non-specialist daily press nevertheless remains a firm candidate for studying representations conveyed by the media as a whole, especially given the tendency for almost instantaneous relaying of news broadcast from one media to another, whether this be the press, television, radio or internet [Cagé et al., 2017]. This is why the corpus retained here seems to us to be sufficiently representative of the French-language media narratives that circulated on the seismo-volcanic "crisis" in Mayotte during the period of time studied, that is to say, between spring 2018 and spring 2021.

With regard to the representation of social actors in the media accounts, three discursive communities are foregrounded here and the place ascribed to each of them is different: people "endure and get into a panic," while the authorities "take measures" and "strive to reassure," but often under the cover of what the scientists are "striving to understand." This observation is coherent with the previously conducted research, which shows the media putting on stage "officials [who] must be careful about issuing warnings because of the danger of panic" and "victims [who] will be dazed and confused, perhaps in shock, and must be cared for by others" [Scanlon, 2007, p. 416]. Even if, in the case of Mayotte, no disaster crisis in the strict sense came about, one can nevertheless notice strong similarities in the way the actors are represented. Indeed, these representations are deemed "inaccurate, biased and often exaggerated" by specialists in research on catastrophes [Rodriguez et al., 2007, p. 482]. Such representations merely corroborate certain myths already circulating in society, largely deconstructed by the social sciences, but which persist in spite of everything [Mileti, 1999]. Quarantelli [2008] thus reminds us that panic is such a rare phenomenon in emergency situations that it becomes hard for researchers to study it, adding that the populations affected, rather than becoming confused, passive and irrational, are on the contrary extremely pragmatic and proactive in the face of danger. He also underlines that the representations that western societies have of catastrophe are largely inspired by those circulating in the media, because catastrophes are, *in fine*, fairly rare in these societies. Thus, media narratives contribute to the reinforcement of such myths. In the case of Mayotte, the words of the different actors, selected and rearranged by the journalists, are inserted into a narrative that undeniably echoes this.

We have also shown that the scientific community occupied a particular place among the actors put on the stage in these media narratives: it appears to be far more central. The CNRS ethics committee (COMETS) made a similar observation concerning scientific communication during the health crisis linked to Covid-19 [Lettelier et al., 2021]. But has the scientific community taken full measure of its "centrality," especially when what is at stake is an event said to be "natural"? In our western democracies, the scientific system for validating evidence is one of the levers upon which officials ground the legitimacy of the decisions they take [Jasanoff, 2005]. Opinions held by officials thus tend to refer the listener or reader systematically to what has been said by the scientific community, which places the latter implicitly in a situation of a third-party guarantee, if not for the truth, then at least for the fairness of the opinions held. This effect is even stronger in the case of Mayotte given that the seismo-volcanic activity only manifested itself indirectly, and the "new volcano" has been visible only through instrumentation and scientific interpretation. But scientific discourse in itself does not say very much about decision-making. The basis of a decision is, further to elements of scientific evidence, those elements of context and situation that are not the province of science. All the more so when uncertainty runs high, which is the case here. The narratives that tend, then, to maintain confusion between “what is scientific” and what is not do a disservice to the decision-making process as a whole [see the discussion on this topic engaged by Devès et al., 2022, which concerns communication from state officials in the framework of the Mayotte crisis].

The analysis comprehensively highlights the temporal difference that exists between the practices of the different actors, not only among themselves, but also with the media. The discursive moments studied fall under the “hot news” timeframe [Pilmis and Rouquette, 2016], a journalistic temporality that does not correspond to the temporalities of scientific research, of monitoring, or even risk and crisis management. Media demand, which is very strong when the seismic crisis was at its height, forces the actors to express themselves in the here and now, even when they have nothing (by their own standards) new to say. As Fallou et al. [2020] have underlined for the case of Mayotte, but other authors too with regard to other crises, it nevertheless remains crucial that actors, and the authorities in particular, should express themselves promptly so as not to allow space for rumor to gather [Lagadec, 1993, Scanlon, 2007]. We have been able to glimpse this here: what is at stake is to express oneself while trying to avoid contradictions, which cannot fail to emerge as awareness about the situation becomes more precise. Through their construction, based as we have seen on the juxtaposition of remarks made by different actors, the news accounts tend to highlight these possible contradictions. Platt [1999] goes so far as to assert that media enthusiasm for extreme situations contributes, by putting local protagonists in the spotlight, to a politicization of the situation in a way that is not helpful while preventing the actors from reacting correctly.

Reviewing the corpus has revealed that most of the accounts studied had an explicative aim. This is not so surprising when one considers that, faced with the threat of catastrophe, which is often perceived (as we have said) as threatening the social fabric, journalists, and in particular local journalists who are in the front line, contribute through their accounts to maintaining the bond between individuals and the group. Many contributions have shown the importance of the media in the face of a risk of catastrophe (the media play the role of sounding the alarm but also of transmitting information about zones affected, the localization and distancing of danger, and for each of these reasons give life to the bond between the individual and the group, etc.) [Scanlon, 2007]. In the case of Mayotte, a similar tendency can be observed at the height of the seismic crisis at the level of the local press. We have also seen how journalists mean to contribute to “reassurance” in order to avoid panic, which translates into a wish to “rationally” express what is happening by turning to scientific arguments. The influence of the major myths mentioned above is here met again.

Besides the incompatibility between this stance and the reality described by the analysis of real catastrophes [Quarantelli, 2008], analysis reveals a number of factors inherent to press writing that are liable to contribute to a “muddling effect” on explanation; an effect that is all the more present in that often one skims over the zone of the page or screen, rather than reading in depth:

- A first factor is the one introduced by recourse to scare quotes to represent the speech of different actors. It translates into a polyphony that is sometimes hard for the reader to decipher insofar as these are often fairly short segments borrowed from different discursive formations which are almost juxtaposed. This way of structuring the news account contributes to the placing of the opinions of different actors on a single plane, be they first-hand testimony of something felt, the announcement of a measure for civil protection, or the sharing of scientific results. Indeed, the opinions held by the different actors when speaking to journalists refer implicitly to their own value systems, references and practices. But the journalists do not always translate these implicit meanings, and sometimes do not even perceive them. The fragmentation of the meaning of the original words into a plurality of decontextualized extracts makes them lose their own specific value, which might for one person strive to articulate a subjective truth, and which might for another describe a factual truth or a piece of scientific evidence.
- A second “muddling” factor is the use of

specialist terms without necessarily defining them or placing them in their context. Thus, we have been able to highlight on several occasions how hard it has been to translate certain terms of scientific concepts. The concept of "risk," of "seismic constellation," of "intensity" or even the explanation of uncertainties linked to the spatial arrangement of seismic networks, are typical examples from the corpus studied.

- A third "muddling" factor is the superimposition of different forms of explanation. Didactic explanation superposes onto scientific explanation or explicative argumentation, and comparisons that are supposed to facilitate comprehension are not always pertinent for readers who are often far removed from the images of mainland France, and which are chosen by editors and scientists who in some cases are far removed from everyday life in Mayotte.
- A fourth "muddling" factor is the treatment of uncertainties themselves. The sharing of uncertainty is complicated by the very structure of the media account. The fragmentation of scientific speech hampers the development of a well-supported line of scientific argumentation. Another limit is the difficulty of transcribing the difference between what is known and what is not, between what is due to an epistemic incertitude and what is due to an instrumental incertitude. And the multiplicity of expressions of uncertainty, a polysemic term if ever there was, does not help to clarify the sentiment.

But one might equally see in "this muddling" (the term is not a pejorative one) an inevitable tendency of media communication, and even of political communication, which borrows from social media as much as from science, to the point of giving rise to an inevitable "permeability of borders between the ordinary and the specialized in both genres and discourse" [Rakotonoelina, 2014]. What is being sought here is to show how an account of the "instant" is being constructed (rather than a retrospective account that could be given in a few years' time) of the birth of a submarine volcano near Mayotte and what this has provoked in terms of changes in Mayotte's history. While the narrative is developed on the basis of the words of different social actors, its finality is to inform about what is being said and done by representatives of the different discursive formations implicated in the narrative at the $x$ moment when the newspaper comes out.

What analysis has confirmed, regardless of the references in use [from the perspective of the work on the enunciation of analysis of French discourse, Chauvin-Vileno and Rabatel 2006; and/or that of *Critical Discourse Analysis*—Petitclerc and Schepens, 2009], is that these narratives of information, which could be extended to news programs on local and regional television stations, "are not organized by the descriptions of an end that is known by the narrator, but under the control of the situation of utterance, which is in the course of occuring at the moment when the narrator is speaking, filming or writing. This anchorage in the situation of enunciation explains in part the disintegration of accounts of events that seem to have no end, if not that the media stops speaking about them" [Arquembourg, 2011, pp. 40–41]. And yet these narratives may be merely provisional, to the extent that work on the event [Londei et al., 2013] "is ongoing, which leads the narrative to reemerge and to become extended later on" adds Arquembourg [2011, pp. 40–41], who suggests distinguishing between two types of media narrative in accordance with their different temporalities [Arquembourg, 2011, p. 41]: "finished accounts that bring about a retrospective return to the facts and deeds, and which are oriented toward a past that is more or less close" and "emerging narratives, which offer an account of what is taking place and which are oriented both toward the future and toward the horizon of an account yet to come." This remains a project for the future, notably in reference to newspapers and monthly magazines, the science pages of daily newspapers, and some television programs and webinars on the submarine volcanism near Mayotte.

We have also brought to light how, in something of a contrast with the health crisis due to Covid-19, no polemic was "shown" here between scientists, nor among or with other actors, which changes considerably the structure of these narratives, hence the apparent juxtaposition of words from the three discursive formations; formations which do not seem to be in a debate either mutually or internally. And yet the past seismo-volcanic crises, foremost among them the eruption of the Soufrière in Guadeloupe in 1976 [Devès et al., 2016], have shown that the domain of earth sciences has not been free of controversy. Was Mayotte spared this by what was ultimately a very moderate scale of impact on the everyday life of the inhabitants? And what might happen were some of the danger scenarios envisaged come to pass?

## 7. Conclusion

Analysis of news accounts from the daily press on the seismo-volcanic "crisis" in Mayotte has enabled us to explore the forms of the media narratives emerging in a context marked by great uncertainties that were both scientific and political.

We have shown the important place taken by three main discursive communities: the scientists, the authorities, and the population at risk, as well as the role played by myths circulating in our western societies regarding the role played by the different parties in a situation, if not of catastrophe, then at least of crisis. We have highlighted the importance of the scientific community in these accounts, even though this sometimes occurred very much against its will. We have underscored some of the difficulties presented by the differences in temporality between the timeframe of the media (especially the daily outlets) and the timeframe of scientific research, of the monitoring or the management of risk and crisis. We have shown that, although all news accounts tend to adopt an explicative aim, the various discursive communities rely on differing forms of explanation, which can contribute to an effect of 'enunciatory muddling'.

But we have not exhausted the data from the different discursive moments that we collected and further work is in course to complete the analysis. Apart from the work on uncertainty that we have sketched out here and which would benefit from additional study, it has emerged that re-contextualizing the different moments of time and place of the daily papers retained for analysis would be helpful, in keeping with what has been proposed by, for example, Idelson [2007] on the treatment of the Chikungunya crisis in Reunion, Mauritius and the Seychelles. On the one hand, it will be a matter of differentiating between the newspapers retained in accordance with their distance from Mayotte, questioning journalists on the priorities they set for themselves at the start of the event and throughout its evolution, and questioning Mayotte's inhabitants in person (interviews had been planned, but the Covid-19 crisis has led to their postponement for the time being), because, beyond the discursive communities and the discourses they speak, one might equally examine the way in which these same communities function as "interpretative communities" [Idelson, 2011]. This could be useful for scientific missions sent to the Indian Ocean, or elsewhere in the world. Indeed, as discussed earlier, all actors do not share a similar interpretative framework. Efficient risk communication relies on the ability of the ones who "communicate" i.e., the scientists and the authorities to understand these differing frameworks.

## Conflicts of interest

Authors have no conflict of interest to declare.

## Authors' contributions

MHD and SM were responsible for the conceptualization of the study, the administration of the project, the methodology and the writing of the document. MHD and GR were responsible for the design of the MAY'VOLCANO corpus, GR and LV for collecting the press articles and LV and MHD for validation. MHD selected the corpus studied here. MHD and SM undertook the formal analysis together. MHD and LV worked on the figures.

## Acknowledgements

This research has been supported by the IdEx Université de Paris (Université Paris Cité), Centre des Politiques de la Terre, ANR-18-IDEX-0001. The authors would like to thank Robin Lacassin, Sandrine Reboul-Touré, Pascal Brunner, Emilie Née, all members of the MAY'VOLCANO team, for their thoughtful comments on the original version of the paper, and Adrian Price for translating in English the French version of the paper.

## References

Ali, R. (2018). Question écrite à M. le ministre d'État, ministre de l'intérieur sur la crise sismique à Mayotte, Pub. L. No. 8992, 23AN. *J. Officiel Assemblée Nationale 4665.* Retrieved from https://www2.assemblee-nationale.fr/questions/detail/15/QE/8992.

Allan, S., Adam, B., and Carter, C. (2000). Introduction: The media politics of environmental risk. In *Environmental Risks and the Media*, pages 17–42. Routledge, UK.

Arquembourg, J. (2011). Les enjeux politiques des récits d'information : d'un objet introuvable à l'institution d'un monde commun. *Quad. Commun. Technol. Pouvoir*, 74, 37–45.

Arquembourg, J. and Lambert, F. (2005). Présentation. *Réseaux*, 132(4), 9–23. Les Récits médiatiques.

Briole, P. (2018). Mayotte seismo-volcanic crisis. http://www.geosciences.ens.fr/volcanologie/actualites/mayotte/. (last access: 8 January 2021).

Burkhart, F. N. (1990). *Media, emergency warnings and citizen response.* PhD thesis, Arizona state university.

Cagé, J., Hervé, N., and Viard, M.-L. (2017). *L'information à tout prix.* Ina éditions, Paris, https://hal-sciencespo.archives-ouvertes.fr/hal-01521888.

Cesca, S., Letort, J., Razafindrakoto, H. N. T., Heimann, S., Rivalta, E., Isken, M. P., et al. (2020). Drainage of a deep magma reservoir near Mayotte inferred from seismicity and deformation. *Nat. Geosci.*, 13(1), 87–93.

Charaudeau, P. and Maingueneau, D. (2002). *Dictionnaire d'analyse du discours.* Seuil, Paris.

Chauvin-Vileno, A. and Rabatel, A. (2006). Énonciation et responsabilité dans les médias. *Semen*, 22, 5–24. Revue de sémio-linguistique des textes et des discours, Collection Annales Littéraires, Presses universitaires de france comté.

Claudel, C., Doury, M., and Moirand, S. (2008). Quelques discours 'ordinaires' sur la question des risques alimentaires. In Hudelot, C., Salazar Orvig, A., and Venezia, E., editors, *L'explication : enjeux cognitifs et communicationnels*, pages 99–111. Peeters, Louvain.

Coleman, C. L. (1993). The influence of mass media and interpersonal communication on societal and personal risk judgments. *Commun. Res.*, 20(4), 611–628.

Courant, F., Biscay, J.-F., Boutillet, D., Rizza, C., Vinet, F., and Weiss, K. (2021). *Rapport de la mission sur la transparence, l'information et la participation de tous à la gestion des risques majeurs, technologiques ou naturels. June 2021.* Ministère de la transition écologique, France.

Devès, M., Lacassin, R., Pécout, H., and Robert, G. (2022). Risk communication during seismo-volcanic crises: the example of Mayotte, France. *Nat. Hazards Earth Syst. Sci.*, 22, 2001–2029.

Devès, M. H. (2018). The ecological war: A reflection on the conflictive dimension of humankind's relations with its environment. *Int. J. Psychoanal.*, 99(6), 1391–1408.

Devès, M. H., Ribémont, T., Kaminski, E., and Komorowski, J.-C. (2016). « La spécialisation des experts scientifiques comme facteur de vulnérabilité : étude comparée de deux crises volcaniques ». In dans Clinchamps, N., Cournil, C., Fabregoule, C., and Ganapathy-Doré, G., editors, *Sécurité et Environnement*, pages 219–236. Academia-Bruylant, Louvain.

Fairclough, N. (2003). *Analysing Discourse: Textual Analysis for Social Research.* Routledge, London.

Fallou, L. and Bossu, R. (2019). Taking into account the cultural context to improve scientific communication – Lessons learned from earthquakes in Mayotte. https://blogs.egu.eu/divisions/sm/2019/03/08/taking-intoaccount-the-cultural-context-to-improve-scientific. (last access: 15 October 2020).

Fallou, L., Bossu, R., Landès, M., Roch, J., Roussel, F., Steed, R., and Julien-Laferrière, S. (2020). Citizen seismology without seismologists? Lessons learned from Mayotte leading to improved collaboration. *Front. Commun.*, 5, article no. 49.

Feuillet, N., Jorry, S., Crawford, W. C., Deplus, C., Thinon, I., Jacques, E., et al. (2021). Birth of a large volcanic edifice offshore Mayotte via lithosphere-scale dyke intrusion. *Nat. Geosci.*, 14(10), 787–795.

Fillmore, C. J. (1968). The case for case. In Bach, E. and Harms, R. T., editors, *Universals in Linguistic Theory*, pages 1–88. Holt, Rineart and Winston, New York.

Fillmore, C. J. (1972). Subjects, speakers and roles. In Davidson, D. and Harman, G., editors, *Semantics of Natural Language*, pages 1–24. Reidel, Dordrecht.

Fisher III, H. W. (1994). *Response to Disaster: Fact Versus Fiction and its Perpetuation: The Sociology of Disaster.* University Presses of America, New York.

Foucault, M. (1969). *L'archéologie du Savoir.* Gallimard, Paris.

Idelson, B. (2007). L'épidémie de Chikungunya à la Réunion, medias, opinion publique et pouvoirs publiques dans la crise. In *Abstracts, Chikungunya et autres arboviroses émergentes en milieu tropical*, page 339. CRVOI and INVS, 3–4 December 2007, Saint-Pierre, La Réunion.

Idelson, B. (2011). Figures de journalismes indo-océaniques. Analyse comparée du traitement médiatique de la crise du chikungunya à la Réunion, à Maurice et aux Seychelles (2005–2006). In Idelson, B. and Ledengen, G., editors, *Chikungunya: la médiatisation d'une crise*, pages 43–62. Éditions EME, Belgique.

INSEE (2017). Mayotte: les langues en 2007—Insee. Retrieved March 22, 2021, from https://www.insee.fr/fr/statistiques/2569783.

INSEE (2021). L'essentiel sur… Mayotte—Insee. Retrieved March 22, 2021, from https://www.insee.fr/fr/statistiques/4632225.

Jasanoff, S. (2005). *Designs on Nature: Science and Democracy in Europe and the United States.* Princeton University Press, Princeton.

Lagadec, P. (1993). *Preventing Chaos in a Crisis.* McGraw-Hill, Maidenhead.

Lambek, M. (2018). *Island in the Stream: An Ethnographic History of Mayotte.* University of Toronto Press, Toronto.

Léglise, I. and Garric, N. (2012). *Discours d'experts et d'expertise.* Peter Lang, Berne.

Lejeune, P. (2005). Le brouillage énonciatif dans le compte-rendu de documents techniques: le cas du Monde et des Notes de conjoncture de de l'Insee. In *Dans la Jungle des Discours. Genres de Discours et Discours Rapporté*, pages 237–248. Universidad de Cádiz, Servicio de Publicaciones, Cádiz, http://digital.casalini.it/3135477.

Lejeune, P. (2012). Le discours d'expert de l'analyse conjoncturelle du Monde et à l'INSEE. In Léglise, I. and Garric, N., editors, *Discours d'experts et d'expertise*, pages 47–76. Peter Lang, Berne.

Lemoine, A., Briole, P., Bertil, D., Roullé, A., Foumelis, M., Thinon, I., Raucoules, D., de Michele, M., Valt, P., and Colomer, R. H. (2020). The 2018–2019 seismo-volcanic crisis east of Mayotte, Comoros islands: seismicity and ground deformation markers of an exceptional submarine eruption. *Geophys. J. Int.*, 223, 22–44.

Lettelier, L. et al. (2021). Avis du COMETS - CNRS : « Communication scientifique en situation de crise sanitaire : profusion, richesse et dérives » (no. 2021-42). approuvé le 25 juin 2021.

Londei, D., Moirand, S., Reboul-Touré, S., and Reggiani, L. (2013). Les sens de l'événement, Présentation. In *Dire l'événement. Langage, mémoire, société*, pages 11–20. Presses Sorbonne Nouvelle, Paris.

Mileti, D. (1999). *Disasters by Design: A Reassessment of Natural Hazards in the United States.* National Academies Press, Washington DC. ISBN: 0-309-51849-0.

Ministère des Outre-Mer (2016). *Mayotte–Culture.* Retrieved March 22, 2021, from https://outre-mer.gouv.fr/mayotte-culture.

Moirand, S. (2003). Communicative and cognitive dimensions on science in the French mass medias. *Discourse Stud.*, 5(2), 175–206. Online.

Moirand, S. (2007). *Les discours de la presse quotidienne. Observer, analyser, comprendre.* PUF, Paris. traduction en arabe : 2009, en espagnol et en italien : 2018, 2020, avec une postface et une bibliographie réactualisée.

Moirand, S. (2008a). Le modèle du Cercle de Bakhtine à l'épreuve des genres de la presse. *Linx*, 56, 91–108.

Moirand, S. (2008b). Un modèle dialogique de l'explication. In Hudelot, C., Salazar Orvig, A., and Veneziano, E., editors, *L'explication : enjeux cognitifs et communicationnels*, pages 77–88. Peeters, Louvain.

Moirand, S. (2021). Instants discursifs d'une pandémie sous l'angle des chiffres, des récits médiatiques et de la confiance. *Repères DoRif*, 24. Constellations discursives en temps de pandémie, DoRif Universita, Roma.

Moirand, S., Reboul-Touré, S., and Ribeiro, M. P. (2016). La vulgarisation scientifique au croisement de nouvelles sphères d'activité langagière. *Bakhtiniana, Rev. Estud. Discurso*, 11, 137–161.

Mori, M. (2021). Crisis narratives and (dis)placement: Space, time and earthquakes in Mayotte. *Ampersand*, 8, article no. 100078.

Morin, J., Bachèlery, P., Soulé, H., and Nassor, H. (2016). Volcanic risk and crisis management on Grande Comore Island. In *Active Volcanoes of the Southwest Indian Ocean*, pages 403–422. Springer, Berlin, Heidelberg.

Petitclerc, A. and Schepens, P. (2009). Critical Analysis. Les notions de contexte et d'acteurs sociaux. *Semen*, 2011(93), 137–143.

Picard, Y. (2019). Plus d'informations et de communication sur les séismes à Mayotte. Retrieved January 7, 2021, from https://www.change.org/p/m-le-préfet-de-mayotte-plus-d-informations-et-de-communication-sur-les-séismes-à-mayotte.

Pilmis, O. and Rouquette, N. (2016). Introduction. *Temporalités*, 23. [En ligne]. mis en ligne le 12 octobre 2016, consulté le 02 septembre 2022. URL: http://journals.openedition.org/temporalites/3350.

Platt, R. H. (1999). *Disasters and Democracy: The Politics of Extreme Natural Events*. Island Press, Washington DC.

Quarantelli, E. (2008). Conventional beliefs and counterintuitive realities. *Soc. Res. Int. Quart.*, 75(3), 873–904. Retrieved from https://muse.jhu.edu/article/527617.

Quarantelli, E. L. (2002). The role of the mass communication system in natural and technological disasters and possible extrapolation to terrorism situations. *Risk Manag.*, 4(4), 7–21.

Rakotonoelina, F. (2014). Perméabilité des frontières entre l'ordinaire et le spécialisé dans les genres et les discours. In *Les Carnets du Cediscor*, volume 12. Presses Sorbonne nouvelle, Paris.

Rodriguez, H., Diaz, W., Santos, J. M., and Aguirre, B. E. (2007). Communicating risk and uncertainty: science, technology, and disasters at the crossroads. In *Handbook of Disaster Research*, pages 476–488. Springer, New York.

Roinsard, N. (2014). Conditions de vie, pauvreté et protection sociale à Mayotte: une approche pluridimensionnelle des inégalités. *Rev. Fr. Aff. Soc.*, 4, 28–49.

Roinsard, N. (2019). Une jeunesse en insécurité. *Plein droit*, 1, 32–35.

Roqueplo, P. (1997). *Entre savoir et décision, l'expertise scientifique*. Éditions Quae, INRA, Paris.

Roulle, A., Bertil, D., Colombain, A., and François, B. (2019). Effets de site sur les stations sismologiques de Mayotte. In *Rencontres scientifiques et techniques*. RESIF 2019. Novembre 2019. <hal−02416124>.

Scanlon, J. (2007). Unwelcome irritant or useful ally? The mass media in emergencies. In *Handbook of Disaster Research*, pages 413–429. Springer, New York.

Sira, C., Schlupp, A., Regis, E., and Van der Woerd, J. (2018). *BCSF—Essaim sismique à l'est de Mayotte. Analyse pour la période du 10 mai au 15 juin 2018*. (Note préliminaire du BCSF-RENASS No. BCSF-RENASS2018-R4) (p. 62). BCSF-RENASS. Retrieved from http://www.franceseisme.fr/donnees/intensites/2018/180515_1548/Note_macro-BCSF-RENASS-Mayotte-13-07-2018-BD.pdf.

Todorov, T. (1981). *Mikhaïl Bakhtine. Le principe dialogique suivi de Écrits du Cercle de Bakhtine*. Éditions du Seuil, Paris.

Van Leeuwen, T. (2009). Représenter les acteurs sociaux, traduction de A. Petitclerc et P. Shepens. *Semen*, 27, 34–67.

Varga, R. (2020). 'La polémique Raoult' : brouillage de la communication. In *Revue de Recherches Francophones en Sciences de l'Information et de la Communication*. Communication de crise, médias et gestion des risques du COVID-19. http://www.refsicom.org/783.

von Münchow, P. and Rakotonoelina, F. (2010). Questions and explanations in French and Anglo-American usenet newsgroups. *Discourse Stud.*, 12, 311–329.

Wachinger, G., Renn, O., Begg, C., and Kuhlicke, C. (2013). The risk perception paradox—implications for governance and communication of natural hazards. *Risk Anal.*, 33(6), 1049–1065.

*Comptes Rendus*
*Géoscience — Sciences de la Planète*
**2022**, Vol. 354, Special Issue S2, p. 417-437
https://doi.org/10.5802/crgeos.131

The Mayotte seismo-volcanic crisis of 2018-2021 in the Comoros archipelago (Mozambique channel) / *La crise sismo-volcanique de 2018-2021 de Mayotte dans l'archipel des Comores (Canal du Mozambique)*

# Storytelling, language, and the earthquake swarm of May 2018: Insights into Shimaore and Kibushi from narrative analysis

## *Les récits, le langage et l'essaim de séismes de mai 2018 : les perceptions du shimaore et du kibushi à partir d'une analyse narrative*

**Miki Mori** [a]

[a] Centre universitaire de formation et de recherche de Mayotte; CNRS UMR 5267 Praxiling, 8 rue de l'Université, Iloni, BP 53 97660 Dembeni, France

*E-mails:* miki.mori@univ-mayotte.fr, mikimorimayotte@gmail.com

**Abstract.** The earthquake swarm that struck Mayotte in 2018 incited panic and various reactions among the local population. Because earthquakes are rare on the island, people were beside themselves, with many leaving their homes to wait out the night under the open air. This article analyzes 36 short narratives that recount events surrounding the crisis. Told in Shimaore and Kibushi, these stories describe what happened at night, particularly when people sought refuge in open spaces, fearing another earthquake might strike. The article focuses on the language used in the stories to discuss earthquakes and the earthquake swarm. Analyses reveal that the stories have a similar structure and language related to space, movement, affect and evaluation are parallel in the two languages. Some differences between the two languages are observed regarding terminology, such as the noun form for "earthquake." Narratives reveal evaluative language that negatively portrays the events, and the language that stresses the collective experience on the island.

**Résumé.** L'essaim de séismes qui a frappé Mayotte en 2018 a suscité la panique, la détresse et diverses réactions parmi la population locale. Les tremblements de terre étant une rareté sur l'île, les gens étaient inquiets, beaucoup quittaient leurs maisons pour attendre la nuit à l'air libre. Cet article analyse 36 courts récits qui relatent les événements entourant la crise. Racontées en shimaore et en kibushi, ces histoires décrivent ce qui s'est passé la nuit, en particulier lorsque les gens ont quitté leurs maisons pour se réfugier dans des espaces ouverts, craignant qu'un autre tremblement de terre ne se produise. Dans l'ensemble, les histoires ont une structure similaire, et le langage lié à l'espace, le mouvement, l'affect et l'évaluation sont parallèles dans les deux langues. Certaines différences sont observées concernant la terminologie, comme la forme nominale pour « tremblement de terre » dans les deux langues.

**Keywords.** Narrative, Language, Chronotope, Evaluation, Shimaore, Kibushi, Earthquake.
**Mots-clés.** Récit, Langue, Chronotope, Evaluation, Shimaore, Kibushi, Séisme.

*Published online: 20 July 2022, Issue date: 17 January 2023*

## 1. Introduction

Earthquakes and earthquake swarms are commonplace in many parts of the world, including on various islands. Mayotte island was an exception to this before May 2018, when inhabitants experienced hundreds of earthquakes within a period of two months, including the largest recorded earthquake on May 15, 2018, which was a 5.9 on the Richter scale. These earthquakes, whose epicenters are located about 50 km east of Mayotte [Bertil et al., 2021], were felt throughout the island. While structural damage to buildings did occur [see Sira et al., 2018], fortunately no major catastrophic destruction happened. Nevertheless, the earthquake swarm incited panic and distress among the local population, to the point that governmental entities set-up hotlines for psychological support. Considering this unprecedented swarm, people were beside themselves, with many leaving their homes to wait out the night under the open air. From afar, these reactions could appear exaggerated, but it is important to understand what happened from the point of view of those living through the earthquakes. Mayotte is not safe from natural disasters, such that studying how people experienced this unpredictable and disturbing event may help future awareness-raising efforts. Storytelling can provide various types of insight into such occasions, such as revealing awareness, reaction, and language regarding earthquakes, the latter of which is particularly pertinent in contexts with complex, multilingual landscapes. The goal of this study is to provide a modest linguistic analysis of 36 short narratives as told by Maore (inhabitants of Mayotte) who faced the earthquake swarm. It is written for non-specialists to provide a small lexicography and corpus of the language used to describe the events surrounding the earthquakes, and this in the two dominant local languages of the island—Shimaore and Kibushi. It seeks to answer the question of how language is used in short narratives.

## 2. Literature review

### 2.1. *Considering language, storytelling, and earthquakes in disaster communication*

Researchers in many disciplines across the globe have looked at the intersection of natural disasters, narratives[1] and language. Language can be studied from various approaches, be it issues of translation, evaluation or creative expression for healing. First, considering narratives, people around the globe encounter natural disasters, including earthquakes and people, no matter their background, tell stories as a way to share their experiences. After harrowing events such as earthquakes, people sometimes tell stories to help understand the disasters [Iida, 2016, Parr, 2015], to work on identity construction [Delante, 2019, McKinnon et al., 2016] and to share their experiences with others [Childs et al., 2017, Wu, 2014]. Linguistic expression has proven to be an important research avenue, and some have explored the use of poetry to express survival and trauma, for example with the Great East Japan Earthquake of 2011 [Iida, 2016, 2020] or with the typhoon Yolanda in the Philippines [Parr, 2015]. Short texts such as tweets can be analyzed to understand how emotion is expressed, such as signaling fear and anxiety during the Great East Japan Earthquake [Vo and Collier, 2013]. Large-scale projects exist that solicit narratives for various purposes, such as the UC QuakeBox Project, which collected oral histories surrounding the 2011 Christchurch earthquake [Clark et al., 2016]. Storytelling in seen as a way to heal after destructive earthquakes such as the 2008 Wenchuan earthquake [Wu, 2014, Xu, 2013]. Indeed, stories can help individuals make sense of disasters and they provide insight into the role of belief systems and religion [Abbott and White, 2019].

Besides aspects of identity and affect, earthquake stories are studied in order to understand their structure such as linguistic markers and coherence in narratives [Luebs, 1992], the use of reported speech in earthquake narratives [Gawne and Hildebrandt, 2020], or other broad language documentation questions [Hildebrandt et al., 2019]. This is particularly interesting considering the fact that narrative structures vary according to language, even among bilingual speakers [Pavlenko, 2008, 2014]. That is, language use and form are important factors for

[1] It is beyond the scope of the study to define the term narrative and narrative research in an exhaustive manner. In this article, I define "narrative" as a "recount (of) events in a sequential order" [De Fina, 2003, p. 1].

understanding how individuals react to and process natural disasters.

Narratives exist en masse as well in the media and government discourses surrounding disasters, and they are known to (re)construct disasters and the collective memory via language. Some studies look at larger socio-political constructions of a shared narrative, such as how political leaders discuss natural disasters to help their political agenda [Windsor et al., 2015]. Media coverage of natural disasters provide a rich area for understanding how journalists (re)create history, engage in narrative, and play with affect during coverage. For example, narratives from inhabitants have been used in the Indonesian media to discuss earthquakes in ways that demonstrate biases in event coverage [Irawanto, 2018]. In addition, reflecting on distant earthquakes via narratives is a way for media to shape collective memory and reconstruct the past, as could be seen with the 1999 "921" earthquake in Taiwan [Su, 2012].

Beyond narratives, communication during and after disasters—particularly with government bodies—can be limited and inefficient, even when a common language is shared [Hong et al., 2018]. As seen in many disasters, multilingualism in a population can complicate information dissemination. Language minority speakers and immigrants who do not have their language represented in the media or in governmental communication face particular barriers during earthquakes, whether in receiving information or communicating in the aftermath. Such is the case for Mayotte, where there is no written media coverage in Shimaore or Kibushi. For television and radio, there is news coverage in Shimaore but not Kibushi, and most happens in French. This even though a sizeable percentage of the population does not understand nor speak the language [Insee Mayotte Infos, 2014, Insee, 2007].

Studies have highlighted the need to better understand local language difficulties in order to address risk management in societies. For example, earthquake relief efforts were met with problems regarding language with local Tibetan varieties in China during a 2010 earthquake, since media coverage and governmental aide was mainly in Chinese [Chunying and Shujun, 2015]. Similar observations have been observed with immigrants and minority language speakers affected by the 2011 Great East Japan Earthquake [Kawasaki et al., 2018, Shinya, 2019] and the 2011 Christchurch earthquake [Shinya, 2019]. People in these regions faced real-time issues with understanding risk, such as evacuation procedures and recovery-related services. Lack of multilingual resources concerning natural disasters remain a concern. Recent studies push for the need for bilingual resources concerning risk with earthquakes, such as with Spanish and English in the U.S. [Bravo et al., 2019]. Be it in the moment or in the aftermath, communication issues related to multilingualism needs to be addressed.

There are many ways and reasons to look at how natural disasters are discussed by people in the aftermath of an event such as an earthquake. Discourse, particularly narratives, provide insight into how experiences are lived, perceived, and assessed in retrospect. Storytelling can be found across cultures and is an easy way to solicit lived experiences and crises. This study focuses on how Maore recount the earthquake swarm, including the language they use and how they evaluate reactions in the stories. The purpose of this study is to understand how speakers used Shimaore and Kibushi when talking about the events. Specifically, it looks at language use in the context of the narratives themselves, considering the overall structure, including the main events, and any evaluative or emotional aspects found within. There is little to no research on how Maore express themselves in Shimaore and Kibushi regarding earthquakes. This is a problem considering recent efforts to bring awareness to risk concerning natural disasters on the island, including those related to earthquakes. This article offers a modest contribution to understanding how Maore talk about earthquakes, to gleam insight into lexical and grammatical considerations, including questions of shared language, formulaic language [Wray, 2002], and lexical bundles [Biber et al., 2004].

### 2.2. *Mayotte in context of the earthquake swarm*

It is beyond the scope of this article to give an exhaustive look into Mayotte, its rich history, and its diverse population. For robust insight into the island culture and languages, see Blanchy [1988], Lambek [2018], Martin [2010], Rombi [1984] and Walker [2019]. In order to contextualize the earthquake stories, I provide as much insight as needed regarding Mayotte during the earthquake swarms in 2018 and the narrative recordings in 2019, including background information on the geological, linguistic and cultural characteristics of the island. First, inhabitants in Mayotte rarely experience earthquakes nor do they have an earthquake-related culture, unlike in other regions of the world such as countries located on the Pacific Ring of Fire (Japan, Chile, U.S. to name a few). Before 2018, the largest recorded earthquake occurred in 1993 and was a magnitude 5.2 on the Richter scale, located about 30–40 km west of the island [Bertil et al., 2021, "Essaim de séismes" 2019]. Small tremors may be felt occasionally, but there is no precedent in the collective memory of Mayotte that could compare to the earthquake swarm that started in May 2018. To summarize, Maore are not accustomed to earthquakes.

Because of this, one can imagine the reaction when over several months, islanders felt hundreds of earthquakes, with the largest ever recorded embedded within that time period. People were panicked, and news coverage of that period show worried villagers gathering outside at night to seek safety. Governmental entities and the scientific community were also taken aback by the events and were unprepared to respond with clear explanations for the phenomenon. In fact, it took about a year to discover that volcanic activity off the coast of Mayotte was the source of the swarm. While fortunately no major damage or direct deaths occurred, the population was under stress and indirect injury most likely did occur. Besides distress, this unprecedented event evoked confusion, as again people did not understand the origins of the swarm of earthquakes. One reaction observed in media coverage involved soliciting a higher power for protection and mercy. Some inhabitants believed the earthquakes were God's punishment for indecent behavior [Fallou et al., 2020]. Indeed, the vast majority of inhabitants in Mayotte practice a Sunni Shafi'i Islam [Blanchy, 1988, Lambek, 2018, Philip-Gay, 2018, Rombi, 1984]. Calls to prayer are heard five times a day from multiple mosques in villages, with even the smallest village of only a few hundred habitants having a mosque (such as Mbouini). Due to its proximity to the equator, the time of the call to prayers is relatively stable, with the first, Fajr, occurring between 4:00 and 5:00 am. Islam as a belief and practice can be seen in various aspects of island life, such as the fact that children often attend religious schools (*shioni* or *madras*) in addition to secular French public schools. Finally, it should be noted that Ramadan started on May 17, 2018, which is a month of daytime fasting and religious reflection. Just before the earthquake, Mayotte had undergone months of social and economic distress with roadblocks and the closing of various services, including the university center, due to insecurity and immobility.

There are two main local languages spoken in Mayotte. The first is a Sabaki Bantu language, Shimaore, (Guthrie classification G44d) [Nurse and Hinnebusch, 1993, Patin et al., 2019] spoken by roughly 80% of inhabitants. There are various varieties of the Bantu language spoken here, but there are two which are the most predominant and which are mutually intelligible: Shimaore (from Mayotte) and Shindzuani (from Anjouan), the presence of the latter due to a high influx of immigration from the neighboring island of Anjouan, located only 65 miles northwest of Mayotte, as seen in Figure 1. Considering birth and immigration statistics [Insee, 2021], an increasing number of Bantu speaking inhabitants speak a Shindzuani variety. Estimates suggest 41% of the habitants speak Shimaore and 31% speak a variety of the three Comorian dialects Shingazidja, Shimwali and Shindzuani [Insee Mayotte Infos, 2014], with the latter dialect representing a large proportion. Given the demographic situation (such as mixed families, contact in neighborhoods and schools), these two varieties are in contact and are probably undergoing various changes because of it.

Nevertheless, in everyday discourse, people use the term Shimaore to indicate the Bantu language variety spoken on the island in comparison with Kibushi, the Austronesian language spoken by about 15% of islanders [Jamet, 2016]. Kibushi itself has two varieties, Kisalakava, the most common and Kiantalautsi, a variety spoken only by a few thousand inhabitants in two villages: Poroani and Ouangani. The Bantu and Austronesian languages spoken in Mayotte are not mutually intelligible, even if there are shared words such as for "thank you" (*marahaba*), "each" (*kula*), or "really" (*swafi*), which are terms arguably borrowed from Shimaore. Figure 2 shows a rough estimate of language varieties spoken in Mayotte. As seen, Kibushi is present in parts of the West and South of the island, whereas Shimaore and Shindzuani are spoken in villages all over the island. Some villages have a mix of Kibushi and


Wikimedia commons https://commons.wikimedia.org/wiki/File:Comoros_rel91.jpg

**Figure 1.** Map of the Comorian Archipelago in the Mozambique Channel.

Shimaore such as M'tsangamouji or Ouangani. Dense urban areas on the northeast part of the island such as Mamoudzou, prove to be complex in terms of variation and language contact, such that identifying them just as influenced from Shindzuani can be limiting.

## 3. Methods

### 3.1. *Setting*

The short stories were collected at the Centre universitaire de formation et de recherche (CUFR) of Mayotte during a larger sociolinguistic study


Image by author with Wikimedia commons map
https://commons.wikimedia.org/wiki/File:Mayotte_administrative_map-fr.svg

**Figure 2.** Approximate distribution of the local languages and their varieties in Mayotte.

concerning the local languages carried out between March and November 2019. Participants were recorded in a soundproof booth to avoid recording noise issues often encountered on the field.

## 3.2. *Participants*

As for participants, 36 individuals, of which nine men, partook in the study, who were for the most part local university students and personnel. Participant age ranged from 22 to 49 years of age, with most being women in their early 20s. Except for one participant, I know all the individuals personally, having worked with them or taught them for months or years. Among participants, 28 were bilingual French–Shimaore speakers and eight were French–Kibushi speakers. Recordings were done in Shimaore and Kibushi, and discussion with participants in French. Besides language, other demographic information varied such as income, village of residency, as well as family history with Mayotte. Participants lived in villages throughout Mayotte, such that one region or village was not representative. Some participants came from families having lived for generations in Mayotte, while others were first generation immigrants from Anjouan, often with modest living conditions. Because of this, the "Shimaore" speakers in the study spoke either a Shimaore with little influence from Shindzuani or a variety heavily based on Shindzuani. Due to the voluntary nature of the study, gender, language, and age are not representative.

### 3.3. *Procedure*

As discussed in Section 3.1, these stories come from a larger study, which used sociolinguistic interview methods to elicit various types of data [Schilling, 2013]. First, the participant and I discussed in French the earthquake swarm experienced the year before, and we talked about the fact that on at least a couple nights, many villagers left their homes to be in an open space. All participants recalled these events and were eager to discuss with me. Next, I expressed my desire to hear them describe their experiences in Shimaore or Kibushi and asked them to imagine that they were discussing these events with a friend or family member who was not in Mayotte when the earthquake swarm occurred. One reason I did this was to record participants paying little attention to their speech, as they are concentrating on telling a story charged with emotion, what Labov calls the "danger of death" story type [Labov, 1972]. The other reason was to better understand how some Maore lived through the earthquake crisis, since I knew it was a harrowing experience for some. After the storytelling, we discussed again the events and I have remained in contact with some of them. Recordings varied from 30 s to 7 min, with an average duration of 2.5 min.

### 3.4. *Analyses*

Recordings were transcribed and translated by bilingual French–Shimaore and French–Kibushi speakers. Transcriptions and translations were then analyzed to look at morphology and to facilitate refined translations and glossing using FieldWorks 9.0 ["Fieldworks", 2020]. For Section 4.1, stories were thematically analyzed using RQDA [Huang, 2012] for chronotopic features, including deixis of time, space, and person. Orthography of the languages aligned with suggestions made by the Association Shime [2016] and the Conseil Départemental de Mayotte [2020] in that the orthography is as transparent as possible, privileging IPA (International Phonetic Alphabet) symbols for phonemes. Various lexical resources were used including the dictionaries from Blanchy [1996], Gueunier [2016], and Jamet [2016], the latter two being for Kibushi. The dissertations of Blanchy [1988], Johansen Alnet [2009] and Rombi [1984] on Shimaore were also consulted, as well as Ahmed-Chamanga's [2017] text on the grammar of Shindzuani. Standard Leipzig glossing rules are used in examples 1–50 ["The Leipzig Glossing Rules," 2015]. Glossing is included for eventual insight into the structure of the language for non-linguists. The intention is to have a small contribution to understanding theses languages, particularly because no written grammar exists for either one.

## 4. Results

### 4.1. *Overall story structure via chronotope*

Before describing various linguistic aspects of the narratives, a brief description of the overall patterns for the narratives and the organization of the stories along the time and space axis is provided. This is because the language analyzed in the studies is closely linked to the overall narrative structure and thus it is important to describe it. For an in-depth narrative analyses, see Mori [2021]. Most stories begin with individuals inside their houses. They start with an orientating action [Labov and Waletzky, 1967] in a certain time and space envelope, also known as chronotope [Silverstein, 2005]. In this study, the time and

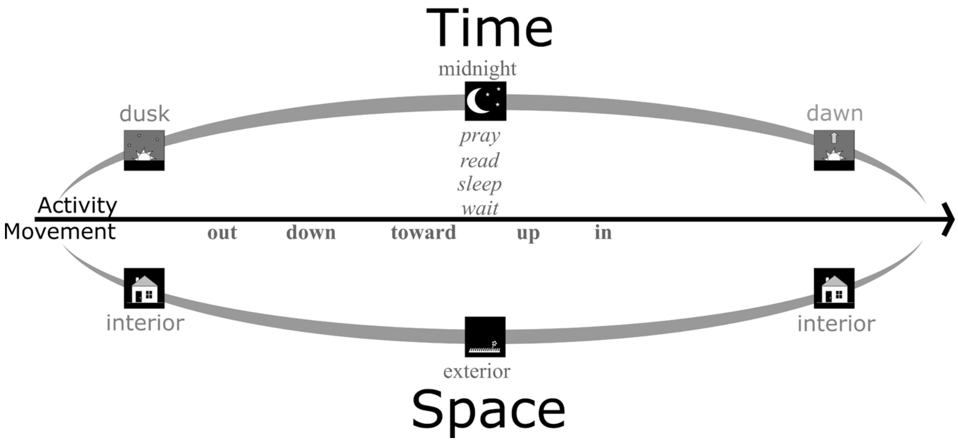


**Figure 3.** Diagram of the time and space envelope (chronotope) for the earthquake stories.

space envelope is night in Maore villages during the earthquake swarm and is represented in Figure 3 [from Mori, 2021]. This figure shows the chronotope in which the stories develop. Read from left to right, a "there-and-back again" pattern can be observed, in which people start inside their homes in the earlier part of the night before leaving to an open area, only to return indoors near dawn. Various activities can be observed during the time spent outside.

The complicating action occurs with storytellers either waking up to an earthquake or receiving an urgent notice that they must immediately leave the house to find shelter in an open area or to pray for mercy. These notifications come in various forms such as from a relative in the house (10 occurrences), a neighbor (3), a phone call (13) or a text message (6). Most storytellers describe deciding to go outside as requested, and they move toward parking lots, courtyards, soccer fields or in front of mosques. As for why they leave their homes, storytellers talk about the fact that a large earthquake (15) or a wave (3) was going to arrive. Others are motivated by the fear of falling debris (14) or because they need to invoke God's mercy through prayer (10), this latter being potentially linked to why people gathered around mosques, as they are seen as a point of refuge.

Once outside, storytellers describe how people, in mass, engage in various activities but principally read holy texts (21 occurrences) and prayed (21). Some read the news or social networks on their phones (6), and some talk (5) while others wait (6) or sleep (6). In addition, some stories describe seeing individuals heading up to higher grounds to take refuge from an earthquake or rising waters. Many stories are resolved with individuals returning to their houses at dawn (14) or when overcome by fatigue (8). The resolution is the return home, to the inside of a building, and some include a coda in which they summarize the story events. Only two stories include the storyteller staying inside their house and refusing to join the others outside.

### 4.2. *Language used to describe earthquakes*

As seen in Section 4.1, the stories often start with discussion about an incoming earthquake or an earthquake being felt. Storytellers use one of two ways to describe the earth shaking. For one, they employ a noun meaning "earthquake" or simply "quake", such as *mdjidjimiyo* (Shimaore, from now on Sh). The other way to discuss this phenomenon is through describing the earth's movement in a phrase, such as *mana tani mihetsiki* (Kibushi, from now on Ki), "because the earth moves." In these phrases, a noun describes the earth or the ground and a verb describing some sort of movement meaning to shake or tremble. To facilitate discussion, the two languages are from now on considered separately. First, for Shimaore, the most common way to describe the event was to use a phrase with the word *ntsi* or *tsi* (earth or ground) as the subject followed by a conjugated form of *udjidjima* (to shake), as seen in Figure 4. Examples 1 and 2 (Sh) show these verbs in use. See the

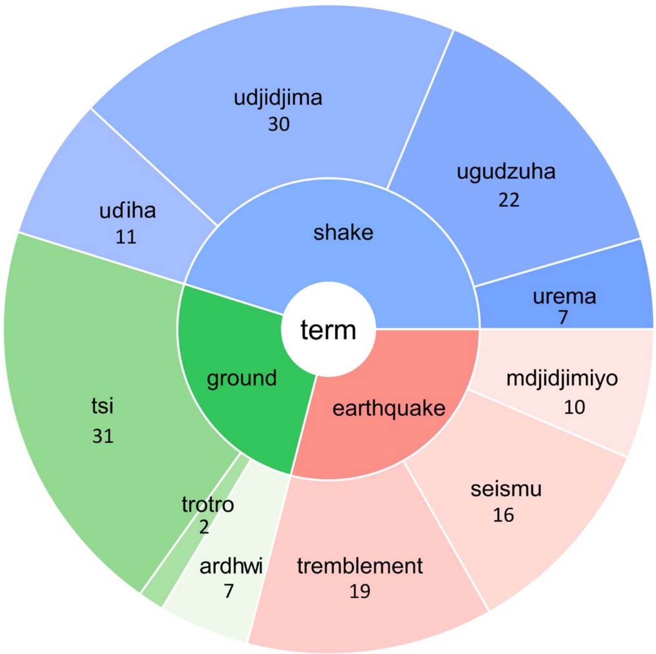


**Figure 4.** Earthquake-related terms in Shimaore and their frequency.

Appendix for the interlinear abbreviations from the Leipzig Glossing Rules, such as CL9 = the nominal class 9 and FUT = the future tense marker, as seen in Example 1. *i-* marks the nominal class 9 and *-tso-* indicates the future tense.

(1) Tsi[2] itsodjidjima.
tsi i-tso-djidjima
earth CL9-FUT-shake
"The earth will shake."

(2) Shivandre ya ntsi isigudzuha.
shivandre y-a ntsi i-si-gudzuha
surface CL9-GEN earth CL9–PRS.PROG-shake
surface of earth is shaking
"The earth's surface is shaking."

The noun phrase *shivandre ya tsi* (the surface of the earth/land/ground) was common in the stories told in Shimaore. Other words to discuss the earth or the ground are *trotro* and *ardhwi*, the latter derived from Arabic, as seen in Figure 4. Verbs besides *udjidjima* are used in the stories to describe the movement of the earth shaking; this includes *ugudzua* and *uɗiha*. These verbs, while synonyms, have slightly different meanings. *Udjidjima* means to tremble or shiver, whereas *ugudzua* is closer to the verbs shake, shift, or stir [Blanchy, 1996]. *Uɗiha* is an intransitive verb and similar to shift or move but can also mean to reanimate [Blanchy, 1996]. Sometimes people used the word *urema* (to hit or strike) when talking about a *seismu* (earthquake) occurring, thus expressing the notion that an earthquake can strike. These verbs were conjugated into various tenses and aspects, including simple future, present progressive, present simple and past imperfect, as seen in 3 through 7.

(3) Yakodjidjima.
ya-ko-djidjima
CL9-PST.IPFV-shake
"(It) was shaking."

(4) Isidjidjima.
i-si-djidjima
CL9-PRS.PROG- shake
"(It) is shaking."

(5) Iɗiha.
i-∅-ɗiha
CL9-PST-shake
"(It) shook."

[2]Note that there is variation among certain vocabulary, such as the word for "earth/ground." This can be *tsi* and *ntsi*.

(6) Ika igudzuha.

i-ka i-∅-gudzuha
CL9.IPFV CL9-PST-tremble

"It had shaken."

(7) Itsogudzuha.

i-tso-gudzuha
CL9-FUT-tremble

"(It) will shake."

Regarding noun forms for discussing the earthquakes, speakers used nouns borrowed from French: *tremblement* (tremor) and *seismu* (earthquake) (see Figure 4). There were occurrences of one nominalized form, *mdjidjimiyo*, derived from the verb *udjidjima* (to tremble). This nominalized word means tremor or quake. The prefix *m-* is the nominal prefix and in combination with the suffix *-iyo* (or *-io*), creates an abstract noun form [Ahmed-Chamanga, 2017]. This latter suffix is similar to the suffixes *-tion* and *-sion* in English. Examples 8–10 show how the noun forms are used. As we see, it is used to describe an entity that existed (8) and that can be modified, such as being described as "big" (9) (*mɓole*) and "of the earth" (10) (*ya iardhwi*). This use is not unlike ways of describing the phenomenon in English (an earthquake) or French (*un tremblement de terre*).

(8) Mana mdjidjimiyo uka swafi ta vuhidjiri adjali Kaweni.

mana mdjidjimiyo uka swafi ta
because quake CL1-PST-be really until
vu-∅-hidjiri adjali Kaweni
CL16.PST-provoke accident Kaweni

"Because the earthquake that night was so intense to the point that it caused an accident in Kaweni."

(9) Tsika hatru suku vwakoja mdjidjimiyo mɓole.

tsi-∅-ka h-atru suku vw-a-ko-ja
1CL1-PST-be CL1-GEN day CL16-be-PST.IPFV-come
mdjidjimiyo m-ɓole
quake CL9-big

"I was at home the day that there was going to be a big earthquake."

(10) Mwaha jana vuka vureme mdjidjimiyo ya iardhwi hunu Maore.

mwaha jana vu-∅-ka vu-∅-reme mdjidjimiyo
year last CL16.PST-be CL16-struck quake
y-a irardhwi hunu Maore
CL9-GEN CL9-earth here Mayotte

"Last year, a ground tremor struck here in Mayotte."

As for Kibushi, there was much less variation in the way the phenomenon was expressed, as seen in Figure 5. This may be due to sample size, or this may reflect stable terminology in this language. Nevertheless, in the stories told in Kibushi, speakers used the noun phrase *horuhoru tani* (earthquake), *horuhoru* meaning a tremor and *tani* meaning the earth, as seen in examples 11 and 12. Like the stories in Shimaore, there are instances of the French words *tremblement* and *seisme* (example 13). Furthermore, as seen in examples 14 and 15, some storytellers also used verb phrases, using the verb *mihetsiki* (shake) and once, *bouger*, borrowed from the French verb "to move" or "to shift". As seen, the term used for the earth or ground is unequivocally *tani*.

(11) Zuva ni horuhoru tani yi zi tani *mois de mai*.

zuva ni horuhoru tani yi zi tan' *mois de mai*
day of tremor earth here it in month of May

"The day of the earthquake was in the month of May."

(12) Mwaka djana nisi zuva reki zeŋi halinyi misi horuhoru tani.

mwaka djana n-isi zuva reki zeŋi halinyi
year last PST-have day one this night
m-isi horuhoru tani
PRS-have tremor earth

"Last year there was one day where at night there was an earthquake."

(13) Mana lera ni tremblement vou itamponu koni.

mana lera ni tremblement vou n-itampono
because time of tremor recent PST-start
koni
really

"Because at that time the tremor had just really started."

(14) Nisi tani mihetsiki ata fa nanpatahutru Maore etu.

n-isi tani m-ihetsiki ata fa nanpatahutru
PST-have earth PRS-shake until but scare
Maore etu
Maore here

"There was an earthquake that but scared the Maore people here".

(15) Zeyi nandri *et* ze naharenyi mahala dja ni*bouger*.

zeyi n-andri *et* ze n-aharenyi mahala dja
we PST-sleep and we PST-hear place all
ni-*bouger*
PST-move

"We were sleeping and we heard movement all around."

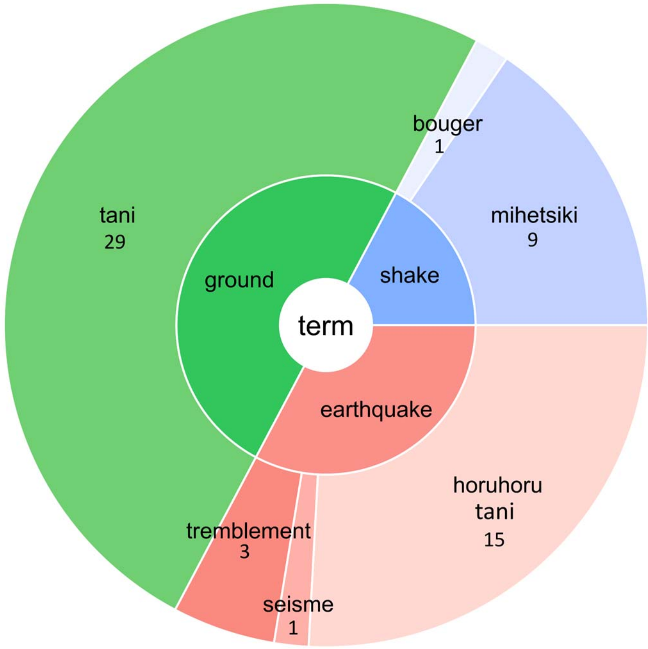


**Figure 5.** Earthquake-related terms in Kibushi and their frequency.

When comparing how the shaking of the earth is described in the two languages, we notice a difference in terms of nominalization. Kibushi has an established, transparent term (noun) for “earthquake” with *horuhoru tani* (quake earth), which is similar to the compound noun in English (earthquake) and the noun phrase in French (*tremblement de terre*). However, seeing that French loanwords nouns are used more often than *mdjidjimiyo*, Shimaore does not have an established, widely used nominalized form, though this may change over time with the increasing occurrences of earthquakes and heightened media and governmental attention. In addition, though not used by any participant in this data, there is an expression for describing earthquakes *nyombe ya uzima*, which means “zebu” (*nyombe*) “down below” (*uzimu*). This expression is known by many, with some stressing that it is an old, playful way of describing earthquakes, where it is said that the ground shaking comes from an underground “zebu” (an African humped cattle) moving its tail or ear. It is unclear why this expression was not used by any participant in this study, but it may be due to the young age of respondents. The only noun form used in Shimaore was *mdjidjimiyo*.

### 4.3. *Language for describing movement and space*

As discussed in Section 4.1, movement and position in space and time are an important element of these stories. The “there and back again” structure provides insight into how movement and position can be described in Shimaore and Kibushi. Table 1 shows frequent words (verbs, prepositions, and adverbs) used for discussing movement, activity, and position. A principal observation is that movement, activity, and position are similar regardless of the language. Spatial language is frequently employed, as storytellers orient themselves in the village once outside. Examples 16–24 show how these terms for space and location are used in the stories.

#### 4.3.1. *Shimaore*

(16) Be watru kawakojua amba mbani ɗe aka arongoa amba ritsolawa vwendze.

| ɓe | wa-tru | ka-wa-ko-jua | amba | mbani |
|---|---|---|---|---|
| but | 3CL2-person | NEG-3CL2-IPFV-know | that | who |

| ɗe | a-ka | arongoa | amba | ri-tso-lawa |
|---|---|---|---|---|
| that is | 3CL1.PST-be | say | that | 1CL2-FUT-leave |

vwendze
outside

**Table 1.** Terms for movement, position, and activity while outdoors in Shimaore and Kibushi

| Space | English | Shimaore | Frequency | Kibushi | Frequency |
|---|---|---|---|---|---|
| Movement | Leave | ulawa | 142 | miboka | 26 |
| Movement | Return | uregea (urudi) | 9 (4) | mipudi | 2 |
| Movement | Ascend | uhea | 14 | manunga | 3 |
| Movement | Descend | ushuka | 21 | midzutsu | 4 |
| Position | Above | uju | 11 | | |
| Position | Below | (h)utsini | 11 | anbani | 2 |
| Position | Outside | vwendze (mwendze) | 78 (31) | antani | 11 |
| Position | Inside | | | aŋati* | 8 |
| Activity | Sit | uksetsi | 82 | mipetraka | 23 |
| Activity | Sleep | ulala | 63 | mandri | 9 |
| Activity | Wait | uɓaki | 21 | miambinyi | 1 |
| Activity | Pray | ufanya/utoa ɗua | 16 | mikuswali | 2 |
| Activity | Read | usoma | 50 | midzoru | 6 |
| Activity | Discuss | uhadisi | 12 | | |

*For phonetic transparency, [ŋ] is used. Jamet [2016] uses the grapheme "ñ" for this sound.

"But people didn't know who had said for them to go outside."

(17) Tsiwono piya watru waka walawa vwendze.

tsi-∅-wono piya wa-tru wa-ka wa-lawa
1CL1-PST-see all 3CL2-person 3CL2-be 3CL2–leave
vwendze
outside

"I saw everyone go outside."

(18) Vanu risilawa vwendze.

vanu ri-si-lawa vwendze
ici 1CL2-PRS.PROG-leave outside

"We are leaving outside here."

(19) Piya watru wakoria du ku piya watru walawa mwendze.

piya wa-tru wa-ko-ria du ku piya
all 3CL2-person 3CL2-IPFV-afraid *du coup* all
wa-tru wa-∅-lawa mwendze
3CL2-person 3CL2-PST-leave outside

"Everyone was afraid, so everyone left outside."

(20) Riregea malagoni rilala ta asuɓuhi.

ri-∅-regea ma-lago-ni ri-∅-lala
1CL2-PST-return CL6-house-LOC 1CL2-PST-sleep
ata asuɓuhi
until morning

"We returned to our homes and we slept until morning."

### 4.3.2. *Kibushi*

(21) Kula ze maharenyi drrdrrr ze milumeyi ze miboka antani.

kula ze m-aharenyi drrdrr ze m-ilumeyi ze
each we PRS-hear boomboom we PRS-run we
m-iboka antani
PRS-leave outside

"Each of us hear the boomboom, we run, and we go outside."

(22) Anba holu dja... niboka antani.

anba holu dja n-iboka antani
that person all PST-leave outside

"That everyone... left outside."

(23) Za nilumeyi za niboka antani ou, holu djabi aŋati traŋu to niboka antani.

za n-ilumeyi za n-iboka antani ou holu djabi
I PST-run I PST-leave outside there person all
aŋati traŋu to n-iboka antani
inside house before PST-leave outside

"I ran, I went outside there, everyone that was inside their house before left outside."

(24) Kula holu nipudi antanana nandeha nandri.

kula holu n-ipudi an-tanana n-andeha
each person PST-return LOC-home PST-leave
n-andri
PST-sleep

"Everyone returned home, they left and slept."

We see a nearly formulaic phrase for the act of leaving the house, which is a key moment in the stories. The subject is often either the first-person plural (we) or third person plural (they) and the verbs are often conjugated in the past tense. The adverb to describe outside, *vhendze* (Sh), *mwendze* (Sh) or *antani* (Ki) follows the verb. Other verbs to express movement in space are used, as participants move up or down in the village as a group and eventually return to their houses near dawn or when overcome with fatigue, as seen in examples 25–33. As seen, movement and location in space and time are important in these stories, as certain places become indexed with danger, such as home interiors.

#### 4.3.3. *Shimaore*

(25) Wasi rikia amba vwa watru wawo waka wahea mulimaju.

wasi ri-∅-kia amba vw-a wa-tru
us 1CL2-PST-hear that CL16-be 3CL2-person
wa-wo wa-ka wa-hea mulima-ju
CL2-DEM 3CL2-PST.be 3CL2-ascend mountain-LOC

"Us, we heard that there were people who went up on the mountain."

(26) Piya watru waka ɗagoni Sada utsini wahea terin ya futru terin ya basketi.

piya wa-tru w-a-ka ɗago-ni Sada
all 3CL2-person 3CL2-PST.be home-LOC Sada
utsini wa-∅-hea terin ya futra terin ya
below 3CL2-ascend field GEN *future* field GEN
basketi
basketball

"Everyone at home below in Sada went up to the court-the future basketball court."

(27) Tsirongoa wami nisishuka nalale.

tsi-∅-rongoa wami ni-si-shuka
1CL1-PST-say me 1CL1-PRS.PROG-descend
ni-a-lal-e
1CL1-REL-sleep-SBJV

"I said, me I'm going down to sleep."

(28) Mana wawo uketsi uju hoho.

mana wa-wo uketsi u-ju hoho
because 3CL2-GEN sit above there

"Because them, they sat up above there."

(29) Karitsokodza fetre neka ringia utsini na zilatabu.

ka-ri-tso-kodza fetre neka ringia utsini na
NEG-1CL2-FUT-hurt well if put under with
zi-latabu
CL8-table

"We will not get hurt if we go under the tables."

#### 4.3.4. *Kibushi*

(30) Ze kaza mipetraka aŋati traŋu ou mahala misi raha meti latsaka aŋabuneyi.

ze kaza m-ipetraka aŋati traŋu ou mahala
we NEG PRS-sit inside house there place
m-isi raha meti latsaka aŋabu-neyi
PRS-have something can fall on-us

"That we shouldn't sit inside the house where something could fall on us."

(31) za nidzeri neka horuhoru tani maresaka, ranu meti manunga. Ou ro raha nampatahutru za swafi.

za n-idzeri neka horuhoru tani maresaka ranu
I PST-think if tremor earth strong water
meti m-anunga.
going PRS-rise.

ou ro raha n-ampa-tahutru za swafi
There it's this something PST-CAUS-fear me really

"I thought that if the earthquake is strong, the water is going to rise. It's this sort of thing that really scared me."

(32) Ze swafi niboka zeyi nidzutsu tan mkiri.

ze swafi n-iboka zeyi n-idzutsu tan' mkiri
we really PST-leave we PST-descend at mosque

"We left and went all the way down to the mosque."

(33) Tani tsika ti havi idzutsu anbanibani, hukurora.

tani-tsika ti havi idzutsu an-bani-bani
earth-ours here going descend LOC-below-below
hu-kurora
FUT-sink

"Our earth here is going to go down below-below, it'll sink (it'll be the end)."

Finally, as discussed in Section 4.1, once outside, several activities are described, the most prominent being waiting, reading, and sleeping. These activities were discussed as happening in mass, with the subject pronouns in first or third person. In this context, reading refers to reading of holy texts (the Quran, certain chapters like the Yassine) and prayers. Most stories describe people staying up and waiting, but some also talk about sleeping outside on the ground or on mattresses brought outside. To give context to the words in Table 1 regarding action verbs that occurred while outside, examples 34–40 are provided below. Once again activities are described as happening collectively, with subjects being in plural form "we" or "they." The examples also reveal motivations for some activities such as in 37 and 38 or they made connections between two actions, such as in 34 and 40.

### 4.3.5. *Shimaore*

(34) Riɓaki riɓaki ata karisikia trongo.

ri-∅-ɓaki  ri-∅-ɓaki  ata
1CL2-PST-wait  1CL2-PST-wait  until
ka-ri-si-kia  trongo
NEG-1CL2-PRS.PROG-hear  thing

"We waited, we waited until we didn't hear a thing."

(35) Watru waendre waketsi mkirini, wakotowa ɗua.

wa-tru  wa-∅-endra  wa-ketsi  mkiri-ni
3CL2-person  3CL2-PST-go  3CL2-sit  mosque-LOC
wa-ko-towa  ɗua
3CL2-IPFV-emit  prayer

"People went to sit at the mosque and they sent up prayers."

(36) Watru waketsi piya vhavho, watru wasome.

wa-tru  wa-∅-ketsi  piya  vhavho  wa-tru
3CL2-person  3CL2-PST-sit  all  there  3CL2-person
wa-som-e
3CL2-read-SBJV

"Everyone sat there, people read."

(37) Waketsi mwendze tan wakosoma kuruani mana wakoria ata huku ushe.

wa-∅-ketsi  mwendze  tan  wa-ko-soma  kuruani
3CL2-PST-sit  outside  until  3CL2-IPFV-read  Quran
mana  wa-ko-ria  ata  huku  ushe
because  3CL2-IPFV-afraid  until  night  fell

"They sat outside and just read the Quran because they were afraid until night ended."

### 4.3.6. *Kibushi*

(38) Be holu tsi mpetraka aŋati traŋu, mana holu ka aŋati traŋu mbu hazu toiambu.

be  holu  tsi  m-petraka  aŋati  traŋu  mana
but  person  NEG  PRS-wait  inside  house  because
holu  ka  aŋati  traŋu  mbu  hazu  toiambu
person  if  inside  house  will  get  problem

"But people don't wait inside their houses, because if they wait inside, there will be problems."

(39) Safke holu djabi antanana mandri.

safke  holu  djabi  an-tanana  m-andri
so  person  all  LOC-home  PRS-sleep

"So everyone were in their homes sleeping."

(40) Holu djabi niboka antani be tsinisi ata raha.

holu  djabi  n-iboka  an-tani  be  tsi-n-isi
person  all  PST-leave  LOC-earth  but  NEG-PST-have
ata  raha
until  something

"Everyone left outside but there wasn't anything."

## 4.4. *Evaluative language in the stories*

Perhaps unsurprisingly, these short stories are filled with evaluative language [Martin and White, 2005] given the highly disruptive nature of the earthquakes on people's lives, particularly during the night. Indeed, the stories are filled with language that shows emotion and judgement, such as how people assess events. Starting with language expressing affect, "fear", "surprise", and "shock" were the principal emotions described in the stories via verb forms indicating "to be afraid" or "to be shocked", as seen in Table 2. The verb for "shock" is similar in the two languages, -*shanga*, and this word can also describe a sense of worry depending on the context. Shimaore stories had another prominent verb, *uria*, which means to be afraid or to fear. In Kibushi, this is *mavuzu*. Terms for fear were often used to describe the overall reaction to the earthquakes in the night and the reason for going outside. Others feared that the house would collapse if they stayed inside.

The expression for shock or worry, -*shanga*, was employed in a similar way, as people were likely to be in shock after an earthquake. This feeling motivates many to go outside together, and is the reason why they could not sleep. When describing being woken up to the noise or movement of the earth shaking, storytellers use the verb *umaruha* (Sh) and the adjective *tehitri* (Ki), both of which describe being suddenly awakened or the state of being startled. We also see people describing their concern that the houses will be destroyed or damaged because of the tremors (*komoha*, Sh; *midzutsu*, Ki). While outside, storytellers describe hearing people crying and children screaming. Thus, we see various reactions to different aspects of the earthquakes: the act itself during the night, its potential occurrence, and the physical damage it could cause on the houses. Examples 41 through 48 show these words in context.

### 4.4.1. *Shimaore*

(41) Lera rilawa vwendze rihono piya watru, kula mutru ashanga, ana hamu.

lera  ri-∅-lawa  vwendze  ri-∅-ono  piya
when  1CL2-PST-leave  outside  1CL2-PST-see  all
wa-tru  kula  mu-tru  a-∅-shanga
3CL2-person  each  3CL1-person  3CL1-PST-shock
a-na  hamu
3CL1.PRS.-have  sadness

"When we left outside, we saw everyone, every single person was in shock and is sad."

**Table 2.** Terms for evaluation in Shimaore and Kibushi

| Space | English | Shimaore | Frequency | Kibushi | Frequency |
|---|---|---|---|---|---|
| Affect | Cry | *keme* | 11 | | |
| Affect | Afraid | *ria* | 37 | *mavuzu* | 3 |
| Affect | Shock | *shanga* | 15 | *kushanga* | 3 |
| Affect | Sad | *hamu* | 3 | *mafurenyi* | 0 |
| Affect | Problem | *taãɓu* | 5 | *toiambu* | 1 |
| Affect | Startle(d) | *umaruha* | 6 | *tehitri* | 6 |
| Affect | Difficult | *dziro* | 7 | *mavestra* | 1 |
| Affect | Destroy | *komoha* | 6 | *midzutsu* | 4 |
| Affect | Heart/soul | *roho* | 10 | *ratsi* | 1 |
| Affect | Tranquil | *trulia* | 8 | *kutrulia* | 1 |
| Affect | Mean | | | *ratsi* | 1 |
| Quantity | Everyone | *piya* | 42 | *djabi* | 15 |
| Quantity | We | *wasi* | 7 | *atsika (zeheyi)* | 7(1) |
| Quantity | Them | *wawo* | 5 | *reu/ro* | 24 |
| Quantity | Alone | *weke* | 42 | *areki* | 1 |
| Quantity | I | *wami* | 9 | *zahu* | 44 |
| Quantity | Each person | *kula mutru* | 15 | *kula holu* | 5 |
| Faith | God | *(mwezi)mungu (allah)* | 15(4) | *draŋahari (mugu)* | 2(1) |

(42) Wakoria ɗagoni amba vutsokomoha.

| | | | |
|---|---|---|---|
| wa-ko-ria | ɗago-ni | amba | vu-tso-komoha |
| 3CL2-IPFV-fear | house-LOC | that | CL16-FUT-collapse |

"They were afraid that their house would collapse."

(43) Lera wakia mwadini kawakia tsena trongo ile roho zijatrulia

| | | | | |
|---|---|---|---|---|
| lera | wa-∅-kia | mwadini | ka-wa-kia | tsena |
| when | 3CL2-PST-hear | muezzin | NEG-3CL2-hear | again |
| trongo | ile | roho | zi-ja-trulia | |
| thing | so that | heart | CL10-come-calm | |

"When they heard the muezzin, they didn't hear anything else so that their heart/spirit was calmed."

### 4.4.2. *Kibushi*

(44) Holu djabi mpetraka ari midzoru, mangataka, mavuzu, mpetraka tu arinyi.

| | | | | | |
|---|---|---|---|---|---|
| holu | djabi | m-petraka | ari | m-idzoru | m-angataka |
| person | all | PRS-sit | that | PRS-read | PRS-ask |
| m-avuzu | m-petraka | tu | arinyi | | |
| PRS-fear | PRS-wait | just | there | | |

"Everyone is sitting and reading, wondering, being scared, just waiting there."

(45) Ze tunga yo mpetraka kula holu masu maventi kushanga.

| | | | | | | |
|---|---|---|---|---|---|---|
| ze | tunga | yo | m-petraka | kula | holu | masu |
| we | arrived | there | PRS-sit | each | person | eyes |
| maventi | kushanga | | | | | |
| big | shock. | | | | | |

"Once there, we wait and everyone's eyes are wide open in shock."

(46) Holu dja tehitri zuvan yo. holu djabi natahutru.

| | | | | | | |
|---|---|---|---|---|---|---|
| holu | dja | tehitri | zuva-n | yo | holu | djabi |
| person | all | surprise | day-LOC | there | person | all |
| n-atahutru | | | | | | |
| PST-afraid | | | | | | |

"Everybody was surprised that day, everyone was afraid."

(47) Atsika angataka duwa fo tani drewu havi ihetsiki

| | | | | | | |
|---|---|---|---|---|---|---|
| atsika | angataka | duwa | fo | tani | drewu | havi |
| we | implore | dua | but | earth | going | come |
| m–ihetsiki | | | | | | |
| PRS-shake | | | | | | |

"Let's evoke prayers, the earth is going to shake yet."

(48) Tani inyi nihetsiki ata za naharenye djirani dja nireska

| | | | | | | |
|---|---|---|---|---|---|---|
| tani | inyi | n-ihetsiki | ata | za | n-aharenye | djirani |
| earth | thise | PST-shook | until | I | PST-hear | neighbor |
| dja | n-ireska | | | | | |
| all | PST-scream | | | | | |

"The earth shook to the point that I heard the neighbors screaming."

As seen, much of the evaluative language in the stories is negative, evoking undesirable sentiments and feelings. One expression used in the stories in Shimaore concerns the heart and/or soul, *roho*. Several participants use *roho*, with some talking about their hearts and/or souls being calmed when they heard the first call to prayer and knew that the night was over. Some storytellers spoke of God and desiring his mercy and forgiveness. Besides appealing to God for mercy prayers were made and the Quran was read to appease fears and anxieties. Terms used to refer to holy texts in the stories include *yasini*, *msaafu* and *koran*.

Another important linguistic aspect of the stories is the stress on the collective, which is a judgement made by the storyteller. Throughout the stories, activities and reactions are described in the plural form, either by using the expressions for describing "everyone" or conjugating verbs in plural form, both first person and third person. One Shimaore storyteller used the word *piya* (all/everyone) nine times in his short narrative and as seen in many examples, including 49 (Sh) and 50 (Ki). Participants repeated the adjectives to express that the actions in the stories—leaving, waiting, being shocked—were done not just by a handful of individuals, but by all of Mayotte. Repetition of these adjectives shows the stress put on the magnitude of the earthquakes in terms of their effects on the islanders. These were not some small tremors with little repercussion. Rather, storytellers position themselves via language as just one of many individuals who reacted in the same way during the night.

(49) Igudzuha swafi ta vhani piya watru rilawa piya vwendze... piyasi rilawe vwendze.

| | | | | | |
|---|---|---|---|---|---|
| i-∅-gudzuha | swafi | ta | vhani | piya | wa-tru |
| CL9.PST-tremble | really | until | here | all | 3CL2-person |

| | | | | |
|---|---|---|---|---|
| ri-∅-lawa | piya | vwendze | piya-si | ri-∅-lawa |
| 1CL2-PST-leave | all | outside | all-CL2 | 1CL2-PST-leave |

vwendze
outside

"(The earth) shook so much until everyone here, we all left outside... everyone left outside."

(50) Tani maore dja nifoha matuŋalinyi iu, djabi tani maore nifoha tehitri.

| | | | | | | |
|---|---|---|---|---|---|---|
| tani | maore | dja | n-ifoha | matuŋalinyi | iu | djabi |
| earth | Mayotte | all | PST-wake | midnight | this | all |

| | | | |
|---|---|---|---|
| tani | maore | n-ifoha | tehitri |
| earth | Mayotte | PST-wake | shock |

"Everyone in Mayotte awoke at midnight, all of Mayotte awoke in shock."

## 5. Discussion and conclusion

The goal of this article was to look at how language is used via narrative to recount the earthquake swarms of 2018 in Mayotte, including expressions regarding space, movement, and evaluation. It specifically looked at how Maore recounted, in Shimaore and Kibushi, their experiences during the earthquake swarm when they were compelled to leave their houses to seek refuge outside at night. Regarding the terminology for earthquakes, there appears to be a preference for the nominalized term in Kibushi, an established noun for "earthquake", which is *horuhoru tani*. While some storytellers used a nominalized form in Shimaore, *mdjidjimiyo*, it was more common to use a verbal phrase equivalent to "the earth shook" or to borrow the French noun-forms. It is unclear why this difference exists for these two languages. Concerning the verbs used in the phrases describing the earth shaking in Shimaore, three stand out: *udjidjima*, *ugudzua* and *udiha*. While synonyms, these verbs appear to have slightly different semantic meanings: "tremble", "shake" and "shift", respectively. The word for "shake", *ugudzua*, was used the most to describe the ground's movement. Finally, in Shimaore, participants sometimes mentioned the earth or ground (*tsi*) itself moving but also sometimes talked about the surface of the earth moving (*shivandre ya tsi*).

Regarding other linguistic observations, the stories revealed a range of expressions for describing displacement either through verbs, such as those for "leaving", "going up" or "going down", or with prepositions and other markers of location and placement and various formulaic language was observed. Various activities were expressed in both languages. One principal observation is that the language used in the stories was very similar for Shimaore and Kibushi. Regardless of language (and by corollary, village), storytellers described their nighttime outdoor activities during the earthquake as including reading, waiting, sitting, and praying. This suggests that while there are villages that differ by language, there are strong cultural similarities. Finally, these similarities are also seen when storytellers evaluate events. The Shimaore and Kibushi terms for "shock" and "startle" are frequently used, suggesting that villagers all over the island experienced the earthquake swarm in a similar manner. We see via repeated, common language that storytellers express the extent to which many Maore acted similarly during the earthquake swarms, particularly at night. Emphasis on language that expresses an inclusive "all" and plurality such as activities being done by "us" and "them" shows how these activities are portrayed as occurring on a large scale, not just by a select, scared few. Various formulaic language was identified in the analyses, which could be exploited during awareness-raising campaigns. Little divergence between the two languages was observed considering the stories themselves or the language used in them, besides the nominalization of the word for "earthquake."

The unprecedented earthquake swarm that struck Mayotte in 2018 incited unprecedented reactions from inhabitants. These reactions were better understood by asking people to recount their experiences during the months of relentless earthquakes, which is an established methodology (see Section 2.1). Narrative analysis revealed underlying similarities across villages in that people gathered in mass outside in order to wait out the night. In both local languages, storytellers describe villagers being afraid, in shock and startled. Movement in time and space plays an important part in the stories, which have a "there-and-back again" structure, in which the building interiors get indexed with danger and the exterior places index safety and unity. This indexing changes over time, because as the night wears on, the interiors become indexed with refuge, particularly once dawn arrives. Understanding reaction to this shared experience is important for risk management planning programs. For example, the fact that people gathered around mosques or that they read holy texts and prayed shows the importance of the Islamic faith on the island in moments of crisis and should not be ignored when considering how to approach risk prevention in Mayotte. Seeing that villagers all over the island left their homes and gathered in open areas indicates that certain spaces are privileged by default during certain crises. These aspects of the stories can be used when considering the local context for disaster planning.

Once again considering the local context, looking at how these events are recounted in Kibushi and Shimaore provide a small lexicography concerning earthquakes as well as spatial and evaluative language. There is still much to be learned about these two languages, particularly how they are used in specific contexts. While the study was modest in size and scope, it provides information on language in use on the island, such as established terms for "earthquake" or how the action associated with it is expressed. Linguistic analyses also offer insight into language use in a specific time and space envelope and how terms related to movement, emotion and evaluation are used. The various provided examples add to the existing literature on the languages, and can be exploited to help organizations charged with risk prevention and communication efforts in Mayotte's local languages. There is still much to be learned and more research is needed looking at discourses of risk in Mayotte as realized by the population, including studies that include a larger and more diverse population sample. In addition, the media and governmental discourses around the earthquake swarms are yet to be fully understood, whether communicating in French, Shimaore or Kibushi. For the local languages, little media coverage exists, but the little that does, such as the televised evening news segment in Shimaore, has yet to be analyzed for its earthquake and other disaster narratives.

## Conflicts of interest

The author has no competing interests to declare.

## Acknowledgements

I would like to thank the participants for sharing their stories with me, the students who transcribed and translated texts, and Ahamada Kassime for his feedback on some grammatical aspects of Kibushi. I would also like to thank Narivelo Rajaonarimanana, Noel Gueunier, Mohamed Ahmed Chamanga, and the anonymous reviewers for their thoughtful and thorough feedback. Any errors are my own. The Conseil scientifique of the CUFR helped fund transcription and translation services.

## Appendix. Leipzig glossing rules abbreviations included in the article

| | |
|---|---|
| 1 | First person |
| 2 | Second person |
| 3 | Third person |
| CAUS | Causative |
| CL | Nominal class, numbered 1–11, 14–18 |
| DEM | Demonstrative |
| FUT | Future |
| GEN | Genitive |
| IPFV | Imperfective |
| LOC | Locative |

| | |
|---|---|
| NEG | Negation, negative |
| PRS | Present |
| PROG | Progressive |
| PST | Past |
| REL | Relative |
| SBJV | Subjunctive |

## References


Abbott, R. P. and White, R. S. (2019). *Narratives of Faith from the Haiti Earthquake*. Routledge, Oxfordshire.

Ahmed-Chamanga, M. (2017). *Introduction à la grammaire structural du comorien, Volume II: le shiNdzuani*. KomEDIT, Moroni.

Association SHIME (2016). *Aprenons le shimaore. Narifundrihe Shimaore*. Armen Factory, Mayotte.

Bertil, D., Mercury, N., Doubre, C., Lemoine, A., and Van der Woerd, J. (2021). The unexpected Mayotte 2018–2020 seismic sequence: a reappraisal of the regional seismicity of the Comoros. *C. R. Géosci.*, 353(1), 211–235.

Biber, D., Conrad, S., and Cortes, V. (2004). If you look at …: lexical bundles in university teaching and textbooks. *Appl. Linguist.*, 25(3), 371–405.

Blanchy, S. (1988). La vie quotidienne à Mayotte (Comores) : essai d'anthropologie compréhensive. Anthropologie sociale et ethnologie. Doctoral dissertation, Université de la Réunion.

Blanchy, S. (1996). *Dictionnaire mahorais-français, français-mahorais*. L'Harmattan, Paris.

Bravo, T. K., Welti, R., Hubenthan, M., Johnson, J. A., and Dordevic, M. (2019). *Spanish Language Earthquake Resources Yield U.S. and International Impacts*. American Geophysical Union, Washington, D.C. Fall Meeting 2019.

Childs, G., Craig, S., Dhakal, D. N., Donohue, M., and Hildebrandt, K. (2017). Narrative disaster through participatory research: Perspectives from post-earthquake Nepal. *Collab. Antrhopol.*, 10(1–2), 207–236.

Chunying, S. and Shujun, Y. (2015). In Yuming, L. and Wei, L., editors, *Language Barrier and Assistance During the Earthquake Relief Operations in Yushu, Qinghai Province*, volume 3, 2009–2010, pages 123–136. De Gruyter Mouton, Berlin.

Clark, L., MacGougan, H., Hay, J., and Walsh, L. (2016). "Kia ora. This is my earthquake story". Multiple applications of a sociolinguistic corpus. *Ampersand*, 3, 13–20.

Conseil Departemental de Mayotte (2020). Alphabets "des langues mahoraises". Retrieved October 1, 2021 from https://www.cg976.fr/services-en-ligne/vie-pratique/documentation/telechargements.

De Fina, A. (2003). *Identity in Narrative*. John Benjamins, Amsterdam.

Delante, N. (2019). Natural disasters reconstruct the self: A thematic analysis of youth survivors' narratives about typhoon haiyan. *J. Narrat. Lang. Stud.*, 7(13), 113–129.

Essaim de séismes à Mayotte: FAQ scientifique (2019). Bureau de recherches géologiques et minières. Retrieved from https://www.brgm.fr/content/essaim-seismes-mayotte-faq-scientifique.

Fallou, L., Bossu, R., Landès, M., Roch, J., Roussel, F., Steed, R., and Julien-Laferrière, S. (2020). Citizen seismology without seismologists? Lessons learned from Mayotte leading to improved collaboration. *Front. Commun.*, 5(49), 1–17.

FieldWorks 9.0 (2020). Software retrieved from https://github.com/sillsdev/FieldWorks.

Gawne, L. and Hildebrandt, K. A. (2020). Reported speech in earthquake narratives from six Tibeto–Burman languages. *Stud. Language*, 44(2), 461–499.

Gueunier, N. J. (2016). *Dictionnaire du dialecte malgache de Mayotte (Comores)*. KomEDIT, Moroni.

Hildebrandt, K. A., Burge-Beckley, T., and Sebok, J. (2019). Language documentation in the aftermath of the 2015 Nepal earthquakes: A guide to two archives and a web exhibit. *Lang. Doc. Conserv.*, 13, 618–651.

Hong, L., Fu, C., Wu, J., and Frias-Martinez, V. (2018). Information needs and communication gaps between citizens and local governments online during natural disasters. *Inf. Syst. Front.*, 20, 1027–1039.

Huang, R. (2012). RQDA: R-based Qualitative Data Analysis. R package version 0.2-3. URL: http://rqda.r-forge.r-project.org/.

Iida, A. (2016). Exploring earthquake experiences: A study of second language learners' ability to express and communicate deeply traumatic events in poetic form. *System*, 57, 120–133.

Iida, A. (2020). I feel like I can't avoid dying": A poetic representation of a survivor's traumatic experience in the Great East Japan earthquake. *Qual. Inq.*, 27(1), 45–58.

Insee (2007). *Mayotte: les langues en 2007*. Retrieved October 1, 2021 from https://www.insee.fr/fr/statistiques/2569783#consulter.

Insee (2021). *L'essentiel sur... Mayotte*. Retrieved October 1, 2021 from https://www.insee.fr/fr/statistiques/4632225#consulter.

Insee Mayotte Infos (2014). Les difficultés face à l'écrit en langue française. Quatre jeunes sur dix en grande difficulté à l'écrit à Mayotte. *Population*, 70, 1–6.

Irawanto, B. (2018). Narratives of natural disaster survivors in Indonesian media: The case of Tempo magazine. *Pac. J. Rev.*, 24(1), 37–51.

Jamet, R. (2016). *Dictionnaire kibushi-français*. Association SHIME, Dzoumogné.

Johansen Alnet, A. (2009). The clause structure of the Shimaore dialect of Comorian (Bantu). Doctoral dissertation, University of Illinois at Urbana-Champaign.

Kawasaki, A., Henry, M., and Meguro, K. (2018). Media preference, information needs, and the language proficiency of foreigners in Japan after the 2011 Great East Japan earthquake. *Int. J. Disaster Risk Sci.*, 9, 1–15.

Labov, W. (1972). *Sociolinguistic Patterns*. Blackwell, Oxford.

Labov, W. and Waletzky, J. (1967). Narrative analysis: Oral versions of personal experience. In Helm, J., editor, *Essays on the Verbal and Visual Arts*, pages 12–44. University of Washington Press, Seattle.

Lambek, M. (2018). *Island in the Stream: An Ethnographic History of Mayotte*. University of Toronto Press, Toronto.

Luebs, M. (1992). Earthquake narratives. In *Proceedings of the Eighteenth Annual Meeting of the Berkeley Linguistics Society: General Session and Parasession on the Place of Morphology in a Grammar*, pages 157–165. BLS, Berkeley, CA.

Martin, J. (2010). *Histoire de Mayotte, département français*. Indes Savantes, Paris.

Martin, J. R. and White, P. R. R. (2005). *The Language of Evaluation: Appraisal in English*. Palgrave Macmillan, New York.

McKinnon, S., Gorman-Murray, A., and Dominey-Howes, D. (2016). "The greatest loss was a loss of our history": natural disasters, marginalised identities and sites of memory. *Soc. Cult. Geogr.*, 17(8), 1120–1139.

Mori, M. (2021). Crisis narratives and (dis)placement: Space, time and earthquakes in Mayotte. *Ampersand*, 8, article no. 100078.

Nurse, D. and Hinnebusch, T. J. (1993). *Swahili and Sabaki: A Linguistic History*. University of California Publ. in Linguistics 121. University of California Press, Berkeley.

Parr, R. A. (2015). The use of expressive arts in making sense of traumatic experiences. *Philipp. J. Psychol.*, 48(2), 133–159.

Patin, C., Mohamed-Soyir, K., and Kisseberth, C. (2019). Ngazidja G44A. In Van de Velde, M., Bostoen, K., Nurse, D., and Philippson, G., editors, *The Bantu Languages*, pages 591–614. Routledge, London.

Pavlenko, A. (2008). Narrative analysis. In Wei, L. and Moyer, M. G., editors, *The Blackwell Guide to Research Methods in Bilingualism and Multilingualism*, pages 311–325. Wiley-Blackwell, Hoboken, NJ.

Pavlenko, A. (2014). *The Bilingual Mind: And What it Tells Us about Language and Thought*. Cambridge University Press, Cambridge.

Philip-Gay, M. (2018). Valeurs de la République et islam à Mayotte. *Revue du droit des religions*, 6, 59–76.

Rombi, M. F. (1984). *Le shimaore: Première approche d'un parler de la langue comorienne, île de Mayotte, Comores*. Peeters Publishers, Leuven.

Schilling, N. (2013). *Sociolinguistic Fieldwork*. Cambridge University Press, Cambridge.

Shinya, U. (2019). Disaster linguicism: Linguistic minorities in disasters. *Lang. Soc.*, 48(3), 353–375.

Silverstein, M. (2005). Axes of evals: Token versus type interdiscursivity. *J. Linguist. Anthropol.*, 15(1), 6–22.

Sira, C., Schlupp, A., Bontemps, M., Regis, E., and Van der Woerd, J. (2018). Essaim sismique à l'est de Mayotte: Analyse pour la période du 10 mai au 15 juin 2018. Technical report, Bureau central sismologique français (BCSF)-Réseau national de surveillance sismique. (Rénass).

Su, C. (2012). One earthquake, two tales: Narrative analysis of the tenth anniversary coverage of the 921 earthquake in Taiwan. *Media Cult. Soc.*, 34(3), 280–295.

"The Leipzig Glossing Rules" (2015). Conventions for interlinear morpheme-by-morpheme glosses.

Retrieved October 1, 2021 from https://www.eva.mpg.de/lingua/pdf/Glossing-Rules.pdf.

Vo, B. H. and Collier, N. (2013). Twitter emotion analysis in earthquake situations. *Int. J. Comput. Linguist. Appl.*, 4(1), 159–173.

Walker, I. (2019). The production of identities on the island of Mayotte: A historical perspective. In Shnepel, B. and Sen, T., editors, *Travelling Pasts: The Politics of Cultural Heritage in the Indian Ocean World*, pages 246–270. Brill, Leiden.

Windsor, L. C., Dowell, N., and Graesser, A. (2015). The language of autocrats: Leaders' language in natural disaster crises. *Risk Hazards Crisis Public Policy*, 5(4), 446–467.

Wray, A. (2002). *Formulaic Language and the Lexicon.* Cambridge University Press, Cambridge.

Wu, H. (2014). Post-Wenchuan earthquake rural reconstruction and recovery in Sichuan China: Memory, civic participation and government intervention. Doctoral dissertation, University of British Columbia, Vancouver.

Xu, K. (2013). In the wake of the Wenchuan earthquake: the function of story-sharing in rebuilding communities in the quake disaster zone. *Asian J. Commun.*, 23(2), 152–174.

*Comptes Rendus*

*Géoscience*

**Objet de la revue**

Les *Comptes Rendus Géoscience* sont une revue électronique évaluée par les pairs de niveau international, qui couvre l'ensemble des domaines des sciences de la Terre et du développement durable. Ils publient des articles originaux de recherche, des articles de revue, des mises en perspective historiques, des textes à visée pédagogique ou encore des actes de colloque, sans limite de longueur, en anglais ou en français. Les *Comptes Rendus Géoscience* sont diffusés selon une politique vertueuse de libre accès diamant, gratuit pour les auteurs (pas de frais de publication) comme pour les lecteurs (libre accès immédiat et pérenne).



**À propos de la revue**

Toutes les informations concernant la revue, y compris le texte des articles publiés qui est en accès libre intégral, figurent sur le site https://comptes-rendus.academie-sciences.fr/geoscience/.

**Informations à l'attention des auteurs**

Pour toute question relative à la soumission des articles, les auteurs peuvent consulter le site https://comptes-rendus.academie-sciences.fr/geoscience/.

**Contact**

Académie des sciences
23, quai de Conti, 75006 Paris, France
Tél. : (+33) (0)1 44 41 43 72
CR-Geoscience@academie-sciences.fr

# Comptes Rendus de l'Académie des sciences

## Géoscience

### Sciences de la Planète

Volume 354, nº S2, 2022


**Special issue / *Numéro thématique***

The Mayotte seismo-volcanic crisis of 2018-2021 in the Comoros archipelago (Mozambique channel) / *La crise sismo-volcanique de 2018-2021 de Mayotte dans l'archipel des Comores (Canal du Mozambique)*

**Guest editors / *Rédacteurs en chef invités***

Jérôme Van der Woerd (Institut Terre Environnement de Strabourg, UMR 7063 CNRS / Université de Strasbourg, 67084 Strasbourg, France), Vincent Famin (Laboratoire Géosciences Réunion, Université de La Réunion - IPGP, 97744 Saint-Denis, France)
Eric Humler (Professeur Université de Nantes, Laboratoire de Planétologie et Géosciences, UMR 6112, Faculté des Sciences et Techniques, Nantes Université, 44322 Nante, France)

**Cover illustration / *Illustration de couverture***

Discovery of the 800 m-tall submarine volcanic edifice of Fani Maoré, the 4th active French volcano, 40 km east of Mayotte with the 12 kHz multi-beam echosounder aboard R/V Marion Dufresne in May 2019 during Mayobs-1 oceanic cruise. Clearly visible in the water column above the volcano, the acoustic-eruptive plume extends from the volcano summit 2600 m below sea level up to 800 m from the surface (Feuillet 2019, MAYOBS1 cruise, RV Marion Dufresne, https://doi.org/10.17600/18001217). Figure réalisée par Cyrille Poncelet et Carla Scalabrin à partir des données de Mayobs-1 avec le logiciel Globe (Poncelet Cyrille, Billant Gael, Corre Marie-Paule, GLobal Oceanographic Bathymetry Explorer Software, SEANOE, 2022, https://doi.org/10.17882/70460). CC-BY 4.0

1778-7025 (electronic)

Comptes Rendus
de l'Académie des sciences

*Géoscience*

Volume 354, nº S2, 2022